Eocene Exhumation and Lake Basin Development in the North American Cordilleran Hinterland, Northeastern Nevada, U.S.A.

A Dissertation

Presented in Partial Fulfillment of the Requirements for the

Degree of Doctor of Philosophy

with a

Major in Geology

in the

College of Graduate Studies

University of Idaho

by

Andrew Scott Canada

Major Professor: Elizabeth Cassel, Ph.D.

Committee Members: Michael E. Smith, Ph.D.; Sean Long, Ph.D.; Peter Isaacson, Ph.D.

Department Administrator: Leslie Baker, Ph.D.

May 2019

Authorization to Submit Dissertation

This dissertation of Andrew S. Canada, submitted for the degree of Doctor of Philosophy with a Major in Geology and titled "Eocene Exhumation and Lake Basin Development in the North American Cordilleran Hinterland, Northeastern Nevada, U.S.A.," has been reviewed in final form. Permission, as indicated by the signatures and dates below, is now granted to submit final copies to the College of Graduate Studies for approval.

Major Professor: _____ Date: _____
Elizabeth Cassel, Ph.D.

Committee Members: _____ Date: _____
Michael E. Smith, Ph.D.

_____ Date: _____
Sean Long, Ph.D.

_____ Date: _____
Peter Isaacson, Ph.D.

Department Administrator: _____ Date: _____
Leslie Baker, Ph.D.

ABSTRACT

The crustal and mantle dynamics of subduction-driven orogenesis and subsequent lithospheric thinning are preserved in Phanerozoic sedimentary deposits of the North American Cordillera. The hinterland of the North American Cordillera, the area between the magmatic arc and the frontal Sevier fold-thrust belt, records a protracted history of crustal thickening and surface uplift as well as subsequent orogenic collapse to form the modern Basin and Range Province. By the Paleogene, continued orogenesis led to the formation of a high-elevation plateau in what is now eastern Nevada and western Utah. The topography and hydrology of this plateau and its relation to tectonic processes is enigmatic, largely because this history is obscured by later Basin and Range extension. Terrestrial basins that were once situated across a large expanse of this plateau preserve a detailed record of this landscape and enable reconstruction of the paleogeographic and tectonic development of the hinterland.

Eocene fluvial and lacustrine deposits are spread across much of eastern Nevada and reflect the evolution of several long-lived terrestrial basins. These deposits provide a critical record of drainage patterns, paleolake evolution, and the nature of upper-crustal exhumation prior to orogenic collapse. Lacustrine strata of the Elko Formation and related fluvial and volcanic units were deposited across a large area of northeastern Nevada during the early–middle Eocene. The mechanisms that facilitated the accumulation of these Eocene sediments and the past controls on their observed heterogeneity remain uncertain (e.g., Satarugsa and Johnson, 2000; Haynes, 2003; Henry, 2008; Smith et al., 2017). To resolve this uncertainty, detailed study and correlation of time-equivalent hinterland strata is essential. The research presented in this dissertation includes a study of the sedimentology, stratigraphy, geochemistry, geochronology, and thermochronology of Elko Formation and equivalent strata in northeastern Nevada. This interdisciplinary approach permits the first detailed assessment of Eocene paleogeographic evolution in the central North American Cordilleran hinterland at high spatial and temporal resolution. The primary goal of this research is to gain a better understanding of the Paleogene-Neogene landscape evolution of the hinterland, and to determine tectonic and climatic drivers for changes to the surface record.

Chapter I presents a detrital geochronologic and thermochronologic evaluation of early–middle Eocene sedimentary rocks to determine sediment provenance and hinterland

exhumation rates across an ~8 m.y. time span. By applying (U-Th)/(He-Pb) double dating of detrital zircon and (U-Th)/He thermochronology of detrital apatite from precisely dated Paleogene terrestrial strata (cf. Smith et al., 2017), we determine the timing and approximate magnitude of upper-crustal exhumation across this interval. This facilitates interpretation of possible links between tectonic unroofing, magmatism, and basin development. Nearly all Eocene fluvial strata sampled contain detrital zircon with long lag times (i.e., the time between cooling and deposition) of >100 m.y., indicating sediment recycling and prolonged retention at upper-crustal depths. However, 43–41 Ma strata contain nonvolcanic detrital zircon with <10 m.y. lag times, indicating rapid cooling of proximal source terranes. These data reflect accelerated exhumation (with rates of >1 km/m.y.) synchronous with the onset of magmatism in northeastern Nevada. This chapter is in press for publication in the *Geological Society of America Bulletin* in 2019.

Chapter II provides a reconstruction of the Paleogene exhumation history of the Copper Mountains and the development of the extensional Copper Basin during the middle Eocene through Oligocene. This area preserves one of the most complete records of Paleogene Cordilleran hinterland extension to date, which is preserved in both synextensional hanging wall strata and footwall rocks. We evaluate the precise timing and style of extensional deformation via $^{40}Ar/^{39}Ar$ and (U-Th)/He thermochronology of hanging wall and footwall rocks. This thermochronology demonstrates the Late Cretaceous Coffeepot Stock was uplifted in the footwall and cooled through the zircon (U-Th)/He closure temperature between ~90 and 70 Ma and the apatite (U-Th)/He closure temperature between 43 and 40 Ma. Plutonic grains of the Coffeepot Stock are identified in Copper Basin strata using (U-Th)/(He-Pb) double dating and REE chemistry. When combined with precise depositional ages for Copper Basin strata, detrital cooling ages reveal rapid exhumation of this source during 8–12 km of middle Eocene–early Oligocene slip along the Copper Creek normal fault. This history of rapid extension in the Copper Mountains is correlative to the pattern noted in the regional synthesis of exhumation rates in Chapter I. Taken together, these data indicate a substantial transition in the style of near-surface hinterland deformation and terrestrial ponding during the middle and late Eocene that was likely driven by dynamic and thermal effects of Farallon slab and/or lower lithosphere removal. Chapter II is accepted pending revision for publication in *Geosphere*.

Chapter III summarizes a geochemical study of Elko Formation strata that investigates Eocene lake water chemistry to constrain paleolake extent and connectivity, sediment provenance, and controls on lake evolution. Evaluation of the stable isotope geochemistry of lacustrine carbonates using multiple geochemical tracers ($^{87}Sr/^{86}Sr$, $\delta^{13}C$, and $\delta^{18}O$) permits assessment of intrinsic and external drivers for observed stratigraphic changes. Low $^{87}Sr/^{86}Sr$ ratios for most samples collected across the stratigraphic range of the Elko Formation (mean = 0.70857; $\sigma = 0.0007$) indicates that bedrock underlying the Elko Basin catchment consisted predominantly of late Paleozoic sedimentary strata and/or recent volcaniclastic sediments for the duration of lacustrine deposition. Covariance in $^{87}Sr/^{86}Sr$, $\delta^{13}C$, and $\delta^{18}O$ values across multiple field areas implies prolonged lacustrine connectivity across a >1000 km^2 area between ca. 43 and 41 Ma. Heightened $\delta^{13}C$ and $\delta^{18}O$ values and a progressive 38–52% in δD_{glass} values for tuff intercalated with Elko Formation lacustrine sediments deposited after ca. 42.1 Ma signifies enhanced evaporation prior to basin closure by ca. 40 Ma. Chemostratigraphic variations recorded in multiple proxies indicate substantial variation in the source, intensity, and chemistry of hydrologic inflow to and outflow from Elko Basin lakes. These data indicate lake expansion occurred coeval to the middle Eocene acceleration of source exhumation rates highlighted in Chapter I and that subsequent basin closure was closely related to the arrival of encroaching volcanism, likely triggered by Farallon slab removal. This chapter will be submitted to *Geochimica et Cosmochimica Acta*.

Chapter IV presents results of detailed sedimentology and stratigraphy of the Elko Formation, informed by the data presented in Chapters I–III and the age model of Smith et al. (2017). Several previous workers have described various aspects of the stratigraphy of the Elko Formation (e.g., Van Houten, 1956; Smith and Ketner, 1976; Solomon et al., 1979; Moore et al., 1983; Haynes, 2003; Horner, 2015; Johnson and Birdwell, 2016), but no study has integrated outcrop, core, and well data with detailed stratigraphic correlations. As a result, numerous hypotheses exist for how and why paleolake systems developed in the hinterland. Stratigraphic characterization indicates the Elko Basin was filled by >1.2 km of fluvial, lacustrine, and volcaniclastic sediment during two distinct phases of tectonic subsidence in the early and middle Eocene. Two lake-type transitions from fluvial-lacustrine to fluctuating profundal conditions (cf. Carroll and Bohacs, 1999) at 49.0 Ma and 42.4 Ma signify changes in lake water chemistry and depositional character driven by external controls. Lake

expansion-contraction cycles can be correlated regionally in both fluctuating profundal and fluvial-lacustrine strata, potentially implying regional paleolake connectivity. Lake transgression occurred during intense regional magmatism and extension within the basin catchment, both of which are reflected in the lithology and structure of sedimentary facies. Reconstruction of the subsidence history of the Elko Basin and comparison with other hinterland basins reveals a similar tectonic subsidence history that is generally distinct from other basin types. This chapter will be submitted to *Basin Research*.

ACKNOWLEDGEMENTS

I would like to thank the members of my committee, Drs. Elizabeth Cassel, Michael E. Smith, Sean Long, and Peter Isaacson for their guidance and assistance throughout the course of my graduate studies. Drs. Cassel and Smith developed the original framework for this project and secured NSF support that enabled the interdisciplinary and collaborative aspects of this work. I also thank Drs. Cassel and Smith for joining me in the field and for providing research suggestions that greatly benefitted my field campaigns. I am grateful for Dr. Cassel's continued support to pursue the extensive field and laboratory work that has made this dissertation possible. I am very appreciative of Dr. Smith for first introducing me to geology, for providing inspiration and mentorship while I was an undergraduate at Sonoma State University, and for sharing the original NSF research proposal that started the research enclosed in this dissertation. Dr. Smith's expertise in lacustrine stratigraphy and geochronology was instrumental to the development of this research. Dr. Long's vast knowledge of Nevada geology and his constant willingness to provide suggestions and feedback was also highly valuable, particularly for development of the research presented in Chapters I–II. I also greatly appreciate Dr. Isaacson's continued support and insight on the Paleozoic history of the North American Cordillera.

I would also like to thank the large number of coauthors, collaborators, and field assistants who have contributed to this research over the last few years. These individuals generously provided their time, insight, and assistance, which improved the scope and quality of this dissertation. Dr. Smith worked in the WiscAr lab at the University of Wisconsin-Madison with Drs. Brad Singer and Brian Jicha to complete single crystal sanidine $^{40}Ar/^{39}Ar$ geochronology. Dr. Danny Stockli generously provided laboratory support and facilities over the course of several visits to the UT Chron facilities at the University of Texas-Austin for both U-Pb and (U-Th)/He dating. Dr. Stockli also provided his time and expertise toward the analysis and interpretation of geochronology and thermochronology data. Laboratory work at the University of Texas-Austin was also made possible by guidance, instruction, and assistance from Doug Barber, Kelly Thompson, Cody Colleps, Patrick Body, Renas Koshnaw, Emily Cooperdock, Lisa Stockli, and Dr. Federico Galster. I am particularly grateful to Doug Barber and Dr. Galster for helping with apatite U-Pb geochronology and

laser ablation-split stream analysis. Drs. Daniel Breecker and Toti Larson provided guidance on carbonate $\delta^{13}C$ and $\delta^{18}O$ analysis and volcanic glass δD analysis in the Light Isotope Lab at the University of Texas-Austin. Peter Carlson helped provide instruction on $\delta^{13}C$ and $\delta^{18}O$ data reduction. Dr. Peter Larson and Charles Knaack supported additional carbonate $\delta^{13}C$ and $\delta^{18}O$ analyses in the Washington State University GeoAnalytical Lab. Dr. Jeff Vervoort helped develop a Sr separation protocol and provided his clean laboratory facilities for Sr sample separation and preparation. Chao Zhang generously provided additional laboratory support and geochemical methods instruction. I am also thankful for the instruction and laboratory support of Drs. Brian Kennedy and Jens Hegg at the University of Idaho TIMS Lab during Sr analyses. Dr. Tom Williams and Cody Steven provided instruction on carbonate X-ray diffraction analysis in the Electron Microscopy Center at the University of Idaho. Core and cuttings observations/sampling and access to well records at the Great Basin Science Sample and Records Library was graciously supported by Charlotte Stock, David Davis, Jerry Walker, and Dr. James Faulds. I am very appreciative of the enthusiastic collaborations of Dr. Allen McGrew, of the University of Dayton, who provided critical support and interpretations for the research presented in Chapter II. Discussions with Drs. Chris Henry and Mike Ressel of the Nevada Bureau of Mines and Geology regarding eastern Nevada paleogeography, magmatism, and basin development greatly improved several aspects of this dissertation. Thoughtful manuscript reviews by Drs. Chris Henry, Jeffrey Rahl, and Chris Painter greatly improved Chapters I and II. Field assistance from Emily White, Cameron Carlson, Zach Foster-Baril, Eduardo Gonzalez-Lugo, Kimberly Mendez, Eric Stauffer, Mikahala Waters, Ron Canada, and Diane Canada facilitated several productive yet highly enjoyable field seasons in eastern Nevada. I am particular grateful for the assistance and companionship of Emily White and Cameron Carlson, who both devoted many weeks of their time to helping me with sample and data collection in eastern Nevada.

Thanks also to the many people who have supported me and made my time at the University of Idaho memorable. I am indebted to Debbie Jensen, Terry Evans, and Mickey Gunter for endless administrative and logistical support. Many UI and WSU grad students have helped me and shared great memories over the years, particularly Tom, Cody, Marian, Kristina, Thomas, Courtney, Zach, Russ, Jeff, Gabi, Meg, Anthony, Brigid, Emma, Aaron, Daisuke, Ryan, Bev, Bridget, and Luke. Thanks to Mom, Pop, David, and Holly for their

constant love and encouragement to follow my passion. And to Emily. You brighten every day and I have been fortunate to have your endless love and support from the very start of this journey. Every step of this research has benefitted from your inspiration.

Finally, I am very thankful for the number of organizations that have provided generous financial support to numerous aspects of this study. National Science Foundation grant EAR-1322073 supported my graduate student tuition/stipend as well as initial field and laboratory work. Student grants from the University of Idaho College of Science (2015) and Graduate and Professional Student Association (2015, 2016, 2017, 2018), the Association American Association of Petroleum Geologists Grants-in-Aid (2015 Paul Danheim Nelson Memorial Grant, 2016 Kenneth H. Crandall Memorial Grant), the Rocky Mountain Association of Geologists (2016 Norman H. Foster Memorial Scholarship), the Society for Sedimentary Geology (2015, 2016), the Geological Society of America (2015, 2016), the Tobacco Root Geological Society (2016, 2017), the Nevada Petroleum and Geothermal Society (2017), the Society of Economic Geologists (Hugh McKinstry Fund, 2017), and the Geological Society of Nevada-Elko Chapter (2016, 2017, 2018).

TABLE OF CONTENTS

LIST OF FIGURES

LIST OF TABLES

STATEMENT OF CONTRIBUTION

Chapter I is part of a collaborative work with Drs. Elizabeth Cassel (University of Idaho), Daniel Stockli (University of Texas-Austin), Michael E. Smith (Northern Arizona University), and Brian Jicha and Brad Singer (University of Wisconsin-Madison). Canada completed fieldwork, sample preparation and detrital double dating at UT-Austin under the supervision of Stockli, time-temperature modeling, original manuscript writing, and figure preparation. Cassel completed additional sample collection and detrital U-Pb geochronology. Smith, Stockli, Jicha, and Singer all contributed to data analysis and integration. All authors contributed to multiple aspects of the revision of the text contained within this chapter.

Chapter II is part of a collaborative work with Drs. Elizabeth Cassel (University of Idaho), Allen McGrew (University of Dayton), Michael E. Smith (Northern Arizona University), Daniel Stockli (University of Texas-Austin), Kenneth Foland (Ohio State University), and Brian Jicha and Brad Singer (University of Wisconsin-Madison). Canada completed fieldwork, detrital geo- and thermochronology under the supervision of Stockli, time-temperature modeling, and manuscript/figure preparation. Cassel completed additional fieldwork and detrital zircon U-Pb geochronology. McGrew completed independent fieldwork, and geo- and thermochronology in collaboration with Foland. Smith completed geochronology data recalibration and reduction in cooperation with Jicha and Singer. All authors contributed to multiple aspects of the writing and revision of this chapter.

CHAPTER I

Accelerating Exhumation in the Eocene North American Cordilleran Hinterland: Implications from Detrital Zircon (U-Th)/(He-Pb) Double Dating

In Press as:

Canada, A.S., Cassel, E.J., Stockli, D.F., Smith, M.E., Jicha, B.R., and Singer B.S., 2019, Accelerating exhumation in the Eocene North American Cordilleran hinterland: Implications from detrital zircon (U-Th)/(He-Pb) double dating: Geological Society of America Bulletin, doi:10.1130/B35160.1.

ABSTRACT

Basins in orogenic hinterlands are directly coupled to crustal thickening and extension through landscape processes and preserve records of deformation that are unavailable in footwall rocks. Following prolonged late Mesozoic–early Cenozoic crustal thickening and plateau construction, the hinterland of the Sevier orogen of western North America underwent late Cenozoic extension and formation of metamorphic core complexes. While the North American Cordillera is one of Earth's best-studied orogens, estimates for the spatial and temporal patterns of initial extensional faulting differ greatly and thus limit understanding of potential drivers for deformation. We employed (U-Th)/(He-Pb) double dating of detrital zircon and (U-Th)/He thermochronology of detrital apatite from precisely dated Paleogene terrestrial strata to quantify the timing and magnitude of exhumation and explore the linkages between tectonic unroofing and basin evolution in northeastern Nevada. We determined sediment provenance and lag time evolution (i.e., the time between cooling and deposition, which is a measure of upper-crustal exhumation) during an 8 m.y. time span of deposition within the Eocene Elko Basin. Fluvial strata deposited between 49 and 45 Ma yielded Precambrian (U-Th)/He zircon cooling 40 ages (ZHe) with 105–740 m.y. lag times dominated by unreset detrital ages, suggesting limited exhumation and Proterozoic through

early Eocene sediment burial (<4–6 km) across the region. Minimum nonvolcanic detrital ZHe lag times decreased to <100 m.y. in 45–43 Ma strata and to <10 m.y. in 43–41 Ma strata, illustrating progressive and rapid hinterland unroofing in Eocene time. Detrital apatite (U-Th)/He ages present in ca. 44 and 39 Ma strata record Eocene cooling ages with 1–20 m.y. lag times. These data reflect acceleration of basement exhumation rates by >1 km/m.y., indicative of rapid, large-magnitude extensional faulting and metamorphic core complex formation. Contemporaneous with this acceleration of hinterland exhumation, syntectonic freshwater lakes developed in the hanging wall of the Ruby Mountains–East Humboldt Range metamorphic core complex at ca. 43 Ma. Volcanism driven by Farallon slab removal migrated southward across northeastern Nevada, resulting in voluminous rhyolitic eruptions at 41.5 and 40.1 Ma, and marking the abrupt end of fluvial and lacustrine deposition across much of the Elko Basin. Thermal and rheologic weakening of the lithosphere and/or partial slab removal likely initiated extensional deformation, rapidly unroofing deeper crustal levels. We attribute the observed acceleration in exhumation, expansion of sedimentary basins, and migrating volcanism across the middle Eocene to record the thermal and isostatic effects of Farallon slab rollback and subsequent removal of the lowermost mantle lithosphere.

INTRODUCTION

In large orogenic belts, major shortening-related crustal thickening can result in kilometer-scale surface uplift in the hinterland and form an orogenic plateau in the region between the active magmatic arc and frontal fold-and-thrust belt (e.g., DeCelles, 2004; Snell et al., 2014). These high-elevation hinterland plateaus are commonly characterized by voluminous siliceous magmatism, lithospheric mantle removal, and thick crust, despite comparatively low internal shortening magnitudes and internally drained basins, as well as syn- or postorogenic extensional deformation (e.g., Humphreys, 1995; Platt, 2007; Long, 2012; Horton, 2018). These plateaus control continent-scale drainage systems, global climate and atmospheric circulation, and gravitational potential energy, yet fundamental uncertainties exist in the processes that govern their formation, uplift, and eventual collapse and demise (e.g., DeCelles and Graham, 2015). For example, contractional deformation and surface

uplift are frequently accompanied by or followed by crustal extension in the hinterland regions (e.g., England and Houseman, 1989; Wells et al., 1990, 2012; Wells, 1997; Bonev and Beccaletto, 2007; Molnar et al., 2010; Long et al., 2015; Horton, 2018; Rabillard et al., 2018), but the early phases of extension are often enigmatic because synorogenic stratigraphic records within these systems are limited or poorly preserved (Dickinson, 2006; Henry et al., 2011; Ramos et al., 2014). Extensionally unroofed lower-plate rocks are also commonly strongly overprinted by magmatism or yield contradictory and complex thermobarometric histories (Hodges et al., 1992; Camilleri and Chamberlain, 1997; McGrew et al., 2000; Colgan et al., 2010; Hallett and Spear, 2014). The North American Cordilleran hinterland plateau (Fig. 1.1A), from eastern Nevada to western Utah, is an ancient analog for Earth's largest plateaus, such as the central Andean Plateau of Bolivia and northern Argentina (e.g., Allmendinger et al., 1997; DeCelles, 2004; Dickinson, 2006; Long, 2012; Cassel et al., 2014, 2018), the Pamir-Tibetan Plateau (e.g., Beghoul et al., 1993; Dilek and Moores, 1999; Molnar, 2015; Hyndman, 2017), and the Iranian and Anatolian Plateau (e.g., Dilek and Moores, 1999; Schemmel et al., 2013). These modern plateaus are all characterized by varying degrees of synconvergent crustal extension that initiated in the Miocene or earlier and continues to the present (Bussell and Pitcher, 1985; Allmendinger et al., 1997; Dilek and Moores, 1999; Bonev and Beccaletto, 2007; Horton, 2018). Kinematic alternations between shortening and extension are documented within a wide variety of orogens (Burchfiel and Royden, 1985; Wells et al., 1990; Lister et al., 2001; Horton, 2018). Syncontractional extensional deformation is related to delamination of the lower crust and/or mantle lithosphere (Platt, 2007; Wells and Hoisch, 2008; Wells et al., 2012; Best et al., 2016) and/or gravitational collapse of thick crust (Coney and Harms, 1984; Wells et al., 1990; Druschke et al., 2009b), which may be associated with the degree of mechanical coupling between the subducting and overriding plates (Ramos et al., 2014; Horton, 2018). Postcontractional extensional deformation requires fundamentally different tectonic mechanisms related to slab removal (Lister et al., 2001; Beltrando et al., 2007; Cassel et al., 2018) or kinematic boundary condition changes (Dickinson, 2006; Colgan and Henry, 2009). In order to understand the mechanisms that govern the growth and maintenance of high topography and

the drivers for lithospheric thinning and orogenic collapse, it is critical to constrain the timing and duration of hinterland extension and its relationship to surface elevation.

The role of crustal extension in accommodating exhumation in the North American Cordillera is widely debated (Fig. 1.2; McGrew and Snee, 1994; Camilleri, 1996; Camilleri and Chamberlain, 1997; Henry et al., 2001, 2011; Rahl et al., 2002; Cline et al., 2005; Druschke et al. 2009a; Colgan et al., 2010; Long et al., 2015). The footwalls (or lower plates) of metamorphic core complexes are regions of localized high-magnitude extension that exhume medium- to high-grade metamorphic rocks (DeCelles, 2004; Rey et al., 2009a; Long and Soignard, 2016). Metamorphic core complexes run north to south along the metamorphic axis of the Cordilleran hinterland and represent the location of a Paleogene welt of 50–60-km-thick crust (Fig. 1.2C; Coney and Harms, 1984; Dilek and Moores, 1999). While the timing of crustal extension and metamorphic core complex formation was likely spatially and temporally variable and included multiple stages, it continues to be widely debated (Table 1). Within the greater Ruby Mountains–East Humboldt Range–Wood Hills–Pequop Mountains metamorphic core complex, initial core complex exhumation has been variably assigned to the Late Cretaceous (Hodges et al., 1992; Camilleri and Chamberlain, 1997; McGrew et al., 2000), Eocene (Wright and Snoke, 1993; McGrew and Snee, 1994; MacCready et al., 1997; Litherland and Klemperer, 2017), or Oligocene–Miocene (Fig. 1.2B; Dokka et al., 1986; Hurlow et al., 1991; Colgan et al., 2010; Haines and van der Pluijm, 2010). In this metamorphic core complex, basement thermobarometry and U-Pb crystallization ages have been interpreted to record exhumation from Cretaceous midcrustal depths (20–30 km; e.g., Dallmeyer et al., 1986; Mueller and Snoke, 1993; Camilleri and Chamberlain, 1997; McGrew et al., 2000; Druschke et al., 2009a; Hallett and Spear, 2014), mica $^{40}Ar/^{39}Ar$ thermochronology suggests rocks in the southern Ruby Mountains passed through the ~400 °C isotherm between 33 and 21 Ma (Dallmeyer et al., 1986; McGrew and Snee, 1994), and apatite (U-Th)/He thermochronometry recorded cooling to <70 °C between 17 and 10 Ma (Colgan et al., 2010). However, all of these thermochronometric data do not constrain the crustal thermal evolution prior to cooling through the ~400 °C isotherm and are hence insensitive to the pre–33 Ma exhumation history, despite general agreement on evidence for some degree of Late Cretaceous through Oligocene exhumation (e.g., Snoke and Miller,

1988; McGrew et al., 2000; Satarugsa and Johnson, 2000; Hallett and Spear, 2015; Litherland and Klemperer, 2017). Widespread deposition of Paleogene clastic sedimentary rocks, preserved across the hinterland, spanned this time interval and so Paleogene basins would have received both volcanic influx and possible synextensional lower plate detritus at the time. Detrital zircon U-Pb and (U-Th)/He double dating permits identification of volcanic detritus so that it can be excluded from lag-time analysis (Saylor et al., 2012) and exhumation patterns can be assessed. Resulting lag times of Eocene strata provide critical new insights into the kinematic and exhumation history of the hinterland.

Eocene fluvial and lacustrine strata in northeastern Nevada range in age from ca. 50 to 38 Ma (Rahl et al., 2002; Smith et al., 2017). Terrestrial strata of the Elko Basin include fluvial sandstones and pebble to cobble conglomerates and a variety of lacustrine facies (Fig. 1.2; Moore et al., 1983; Haynes, 2003; Cassel et al., 2014). The lowermost lacustrine interval contains micritic carbonate with freshwater mollusks, carbonaceous shale, and abundant plant matter indicative of fluvial-lacustrine deposition in Lake Elko by ca. 43.5 Ma (Cassel et al., 2014; Smith et al., 2017). After ca. 42.8 Ma, lake transgression was followed by increased salinity and alkalization of lacustrine waters, recorded by fluctuating profundal facies, including organic-rich laminated mudstone and microbialitic carbonate, which continued until ca. 40 Ma (Smith and Ketner, 1976; Solomon et al., 1979; Smith et al., 2017). Lacustrine strata of the Elko Formation reflect increasing drainage isolation across this interval, but they lack evidence of growth strata or coarse-grained footwall-generated alluvium (Smith et al., 2017). Hydrogen isotope ratios (δD) of volcanic glass deposited in adjacent nonlacustrine strata show that deposition occurred at elevations of ~2.8–3.0 km (Fig. 1.2; Cassel et al., 2014, 2018). While this early Cenozoic sedimentary record was disrupted by widespread high-angle Neogene extensional faulting and unconformity (Haynes, 2003; Lund Snee et al., 2016; Camilleri et al., 2017), surviving strata are well dated via single-crystal sanidine $^{40}Ar/^{39}Ar$ geochronology (Smith et al., 2017), providing a basis for correlation and reconstruction of basin formation and evolution (Fig. 1.1A).

Detrital zircon (U-Th)/(He-Pb) double dating, where a U-Pb crystallization age and a (U-Th)/He cooling age (ZHe) are obtained from the same detrital zircon grain, permits cross correlation of provenance and assessment of regional exhumation trends (e.g., Reiners et al.,

2005; Thomson et al., 2017). In contrast to traditional low-temperature thermochronometry, which is commonly applied through analysis of basement samples collected along a bedrock or structural transect (e.g., Stockli et al., 2000), double dating of detrital zircon extracted from sedimentary strata can elucidate the timing and paleogeographic evolution of multiple orogenic events across a large area (e.g., Painter et al., 2014; Thomson et al., 2017). This technique has great utility in the Cordilleran hinterland, where Eocene sedimentary deposits are widely dispersed (Fig. 1.2), and they contain zircon grains with complex thermal histories that span the Phanerozoic. When combined with depositional age control from $^{40}Ar/^{39}Ar$ geochronology and volcanic zircons constraining maximum depositional ages, detrital zircon double dating provides time-temperature paths of many individual zircon crystals with varying geologic histories and permits documentation of exhumation rates across a large area. This also allows for estimation of lag times, which can be used to reconstruct the early Cenozoic exhumation history of the Cordilleran hinterland in northeastern Nevada. The zircon (U-Th)/(He-Pb) double dating approach is critical for this type of study because first-cycle volcanic zircons (U-Pb age = ZHe age) must be excluded for robust and reliable lag-time analysis (Saylor et al., 2012). The studied basin record in northeastern Nevada, integrated with the existing thermochronologic record from footwall rocks, provides a new framework for understanding the kinematics and drivers of core complex formation and hinterland orogenic evolution.

GEOLOGIC SETTING

The orogenic thickening of the North American Cordillera reflects the combination of multiple contractional tectonic events from the late Paleozoic to the Paleogene (e.g., Dickinson, 2006), as well as protracted rifted- and passive-margin sediment accumulation that resulted in an ~11-km-thick succession of Proterozoic–Paleozoic strata in eastern Nevada (Miller et al., 1992; Camilleri and Chamberlain, 1997; Crafford, 2008; Pape et al., 2016). During the Late Devonian to early Mississippian Antler orogeny, Cambrian through Devonian deep-marine rocks of the Roberts Mountains allochthon were emplaced above the Roberts Mountains thrust over coeval shelf facies of the Cordilleran passive-margin sequence

(Fig. 1.1; Trexler et al., 2004; Gehrels and Pecha, 2014; Linde et al., 2016). The last stages of Antler orogenesis shed up to 2.5 km of clastic detritus (Mississippian Diamond Peak Formation) into the Antler foreland basin of eastern Nevada (Fig. 1.1B; Poole, 1974; Silitonga, 1974; Poole and Sandberg, 1977). Modest burial of Antler and subsequent overlap strata is indicated by low (≤2.5) conodont color alteration indices (CAI) for Pennsylvanian–Triassic rocks (Harris and Crafford, 2007). In contrast, Roberts Mountains allochthon strata, particularly Ordovician strata of the Vinini Formation and Devonian strata of the Slaven Chert, commonly exhibit CAI >3 (Fig. 1.1A; Harris and Crafford, 2007), implying temperatures of at least 200 °C (Long and Soignard, 2016) and likely complete postdepositional thermal resetting of ZHe ages.

During late Mesozoic times, Farallon plate subduction led to voluminous arc and backarc magmatism (Miller and Hoisch, 1995; Dickinson, 2006) and contractional deformation within the Sierran magmatic arc (Mookerjee et al., 2016), across hinterland fold-and-thrust belts (Long, 2012), and within the Sevier fold-and-thrust belt (DeCelles, 2004). In eastern Nevada, Mesozoic deformation was characterized by low-angle faults, long-hinged folds, development of ~2 km of structural relief, and ~10 km of shortening within the Central Nevada fold-and-thrust belt (DeCelles, 2004; Long, 2012, 2015). In the Late Cretaceous, contraction shifted to a SW-NE orientation and arc magmatism ceased as the angle of the subducting plate shallowed (Humphreys, 2009; Heller et al., 2013). This appears to have been associated with minor post-Sevier upper-crustal extension in eastern Nevada (e.g., Druschke et al., 2011). By this time, the Cordilleran hinterland region had attained elevations of ≥2 km (Snell et al., 2014) and reached up to 3.5 km by the late Oligocene (Cassel et al., 2014). Farallon slab rollback induced southwest propagating volcanism, basin formation, <1 km of surface uplift, and drainage migration in the Eocene and Oligocene (Janecke and Snee, 1993; Smith et al., 2014, 2017; Cassel et al., 2014, 2018). The potential drivers of hinterland exhumation during this time are uncertain and include thermal weakening induced by slab rollback volcanism (e.g., Gans et al., 1989; Axen et al., 1993; Humphreys, 1995; Dinter, 1998; Rahl et al., 2002; Bendick and Baldwin, 2009; Brun et al., 2016), gravitational collapse of isostatically compensated crust (e.g., Burchfiel and Royden, 1985; Dewey, 1988; Platt,

2007), and lithospheric removal (e.g., Houseman et al., 1981; Göğüş and Pysklywec, 2008; Wells and Hoisch, 2008; Platt, 2007; DeCelles et al., 2015; Smith et al., 2017).

METHODS AND MATERIALS

Detrital Zircon (U-Th)/(He-Pb) Double Dating and Detrital Apatite (U-Th)/He Thermochronometry

Detrital zircon from Eocene sandstone samples was double dated using (U-Th)/(He-Pb), and detrital apatite was analyzed using (U-Th)/He thermochronometry (Fig. 1.3). In order to more fully understand the detrital signatures of the proximal source regions, zircon from a sample of the Mississippian Diamond Peak Formation was also double dated. Medium- to coarse-grained (250–750 μm) sandstones were collected to minimize the effects of hydrodynamic sorting and fractionation (e.g., Malusà et al., 2016). Zircon and apatite were separated using standard mineral separation techniques, including crushing, water table, magnetic, and heavy liquid procedures and mounted on double-sided tape on a 1 in. (2.5 cm) acrylic disc. U-Pb detrital zircon geochronology by depth-profile laser ablation-inductively coupled plasma-mass spectrometry (LA-ICP-MS) was conducted following procedures outlined in Hart et al. (2016), and zircon and apatite (U-Th)/He dating was conducted following procedures detailed in Wolfe and Stockli (2010; see also Supplementary Materials herein). All analytical work was carried out at the UTChron facility at the University of Texas at Austin. Following U-Pb analysis, a subset of zircon grains from each significant U-Pb age component was selected for (U-Th)/He analysis. Significant (U-Th)/He age components are defined as including three or more grains for which ages overlapped given the analytical uncertainties (Saylor et al., 2012; Thomson et al., 2017). Saylor et al. (2012) demonstrated that the selection of zircons for (U-Th)/He analysis based on prior knowledge of their U-Pb ages does not bias the resulting (U-Th)/He age distribution.

(U-Th)/(He-Pb) detrital double dating refers to obtaining a U-Pb crystallization age and a (U-Th)/He cooling age (He age) on the exact same zircon grain (Reiners et al., 2005). While detrital zircon U-Pb ages are commonly used to assess provenance, the ZHe age data are needed to discriminate between sources with similar U-Pb age populations and to

elucidate the thermo-tectonic evolution of the source terrane (Thomson et al., 2017). In particular, multicycle sediment often contains material with a complex array of thermal histories that can only be elucidated using combined thermochronologic techniques (Campbell et al., 2005; Painter et al., 2014; Fosdick et al., 2015). Importantly, the zircon (U-Th)/(He-Pb) double dating approach also allows for the identification of first-cycle volcanic zircons (U-Pb age = ZHe age) and their exclusion from lag-time calculations (Saylor et al., 2012).

Given the thermal sensitivity window of zircon (U-Th)/He ages (140–180 °C; Wolfe and Stockli, 2010), we supplemented the detrital zircon double dating with detrital apatite (U-Th)/He thermochronometry. The apatite (U-Th)/He system is particularly applicable for study of upper crustal extension due to its substantially lower closure temperature (~70 °C; Farley, 2000) and thus sensitivity to lower-magnitude extensional unroofing. Apatite grains were carefully examined petrographically, and large (60–110 μm width), euhedral, inclusion-free, detrital apatite grains were analyzed to minimize potential inaccuracies introduced by excessive alpha ejection (Farley et al., 1996; Farley, 2000; Farley and Stockli, 2002).

Radiation damage has been shown to modulate He diffusion through trapping in apatite (Shuster et al., 2006; Flowers et al., 2009) or causing damage to interconnective (percolation) networks in zircon (Guenthner et al., 2013; Ketcham et al., 2013), which can lead to anomalous zircon and apatite He ages. While these effects become more amplified in samples with pre-Cenozoic cooling histories, we chose to minimize these effects: No metamict grains were selected; all selected double-dated zircon grains had eU concentrations of <800 ppm; and >97% of analyzed grains had eU concentrations of <400 ppm, based on the LA-ICP-MS U-Pb analyses of the same grains (Fig. 1.4). Hence, all zircon analyzed was characterized by low eU and low radiation damage (Fosdick et al., 2015; Thomson et al., 2017). Nearly all detrital zircon and apatite grains that met the selection criteria discussed above and were not volcanic in origin (U-Pb age older than Eocene) were selected from each U-Pb dated sample for thermochronology.

Lag-Time Analysis

Lag time (L) is the difference between the cooling age and the depositional age for an

individual detrital grain, and it provides a measure of hinterland exhumation rate, ignoring the fluvial transport duration (Brandon and Vance, 1992; Garver et al., 1999; Carrapa et al., 2003; Ruiz et al., 2004; Carrapa and DeCelles, 2008; Painter et al., 2014; Thomson et al., 2017). In order to do so, however, volcanic first-cycle zircon has to be excluded because it, by definition, will have L = 0 m.y., which would severely compromise this approach. As previously noted, (U-Th)/(He-Pb) double dating obviates this complication and allows selection of nonvolcanic zircons for (U-Th)/He analysis. By performing thermochronometric lag-time analysis from a range of stratigraphic levels, lag-time trends can be identified that might be interpreted as changes in source area or source exhumation rates (e.g., Ruiz et al., 2004; Saylor et al., 2012). While most detrital thermochronometric studies use the youngest cooling age in each sample to assess lag time (Garver et al., 1999; Ruiz et al., 2004; Carrapa et al., 2003, Carrapa and DeCelles, 2008; Painter et al., 2014), we applied the more conservative method of Saylor et al. (2012), using the two youngest overlapping He ages to determine the regional lag-time trend. Following this approach, decreasing lag times represent increasing exhumation rates, constant lag times represent steady-state exhumation, and increasing lag times represent decreasing exhumation rates, or introduction of a new source terrane (Fig. 1.3; Garver et al., 1999; Ruiz et al., 2004). In addition to the exclusion of first-cycle volcanic grains, for the lag time method to be valid, the (U-Th)/He ages must not be partially or fully reset after deposition (e.g., Fosdick et al., 2015; Thomson et al., 2017). However, this can be evaluated, because (U-Th)/He ages, including first-cycle volcanic grains, must be older than the depositional age (Thomson et al., 2017). The accuracy of lag-time analysis is therefore fundamentally dependent on the precision and accuracy of sample stratigraphic (i.e., depositional) ages. We used recently published high precision single-crystal sanidine $^{40}Ar/^{39}Ar$ radiogenic ages of interbedded volcanic ash beds (Smith et al., 2017) and detrital zircon U-Pb maximum depositional ages to determine sample stratigraphic age (Table 2).

RESULTS

Detrital (U-Th)/(He-Pb) Double Dating

We generated 949 detrital zircon U-Pb ages and 137 detrital zircon (U-Th)/He ages from Eocene Elko Formation samples (Table 2). No zircon He ages were younger than the depositional age within 2σ uncertainties. Of samples deposited between 50 and 38 Ma, 9% of all double-dated detrital grains yielded Eocene cooling ages, whereas 31% yielded identical cooling and crystallization ages between 52 and 38 Ma. Of the remaining 69% of detrital zircon grains, 22% yielded crystallization and cooling ages consistent with local Jurassic and Cretaceous backarc plutons, and 46% resembled detrital zircon populations observed in proximal Paleozoic marine strata (Fig. 1.5). Kernel density estimates (KDEs) and histograms of detrital zircon U-Pb ages, as well as weighted mean plots of sample maximum depositional ages, are shown in Supplementary Figures A1–A7 (see footnote 1). Mississippian–Pennsylvanian and Eocene conglomerates are compositionally similar, but the Diamond Peak Formation sample analyzed here lacked a Cenozoic zircon U-Pb grain age population that is present in proximal Elko Formation samples (Hollingsworth et al., 2018).

Most analyzed grains exhibited a moderate to high fractional loss of helium (f = 30%–95%, where $f = \left[\frac{\text{He age}}{\text{U–Pb age}}\right] \times 100$) and low effective uranium (eU) content (<300 ppm; Fig. 1.4). Of the four zircon grains that had relatively high eU (>600 ppm; Fig. 1.4), two grains gave Jurassic–Cretaceous U-Pb ages and Eocene He ages. Two Elko Formation samples and the Diamond Peak Formation sample showed a negative ZHe age–eU correlation (NV12–040CM, NV15–168RM, and NV15–013PR; Fig. 1.4). For all other samples, there was no discernible relationship between zircon He age and eU content or grain size (Fig. 1.4). The low-eU material analyzed and the absence of a clear relationship between these parameters for nearly all samples indicate that radiation damage alone cannot account for the observed cooling patterns, although it likely accounts for some of the ZHe age scatter (Fig. 1.5), particularly for grains with higher eU.

Zircon grains extracted from multiple stratigraphic levels yielded a wide spectrum of He ages (>1000 m.y.; Fig. 1.5). Thermochronometric lag times also ranged from <1 m.y. to >1000 m.y. (Fig. 1.3). This indicates that zircon He ages were not reset as a result of either

burial or thermal effects of proximal magmatism. From 50 to 40 Ma, detrital zircon grains show an up section shift from predominantly long (>100 m.y.) to short (<10 m.y.) lag times across the Eocene. The 50–45 Ma samples yielded >70% of grains with >100 m.y. zircon lag times and no grains with <25 m.y. lag times (Table 2). In contrast, middle to late middle Eocene samples showed a substantial component of very long (>500 m.y.) zircon grain lag times, but they also had zircon and apatite grains with <10 m.y. lag-time values. Inverse thermal modeling of grains with <10 m.y. lag times (see Supplementary Fig. A8) shows rapid cooling by 42 ± 2 Ma and continuing until at least 39.3 ± 2.1 Ma (Table 2). This abrupt middle Eocene transition from low to high zircon grain cooling rates was both spatially and temporally synchronous with lake basin expansion and the arrival of volcanism at ca. 44 Ma (Fig. 1.2).

Detrital Apatite (U-Th)/He Results

Detrital apatite extracted from three Eocene samples (n = 20) yielded predominantly late Cenozoic (U-Th)/He ages and lesser amounts of Eocene and Cretaceous cooling ages (Fig. 1.6). Prior determination of CAI values for Paleozoic–Mesozoic strata in northeastern Nevada showed that Mississippian–Triassic strata proximal to the Elko Basin generally have low values (CAI ≤2.5) that imply a lack of postdepositional heating beyond ~140 °C (Harris and Crafford, 2007). Additionally, the Mississippian Diamond Peak Formation sample (Fig. 1.1A; 013PR) contained 50% Cretaceous, 33% Eocene, and 17% Oligocene apatite He grain ages, suggestive of incomplete postdepositional resetting. Low CAI values for proximal Paleozoic sedimentary rocks indicate that preservation of only partially reset pre-Neogene apatite He ages in Mississippian–Triassic strata is plausible. The Roberts Mountains allochthon, however, lies to the west of the Elko Basin and commonly exhibits CAI >3 (Harris and Crafford, 2007), indicating substantial postdepositional heating (>200 °C; Fig. 1.1A). Elko Formation strata deposited near the Ruby Mountains–East Humboldt Range (e.g., 102EH) contain apatite that was thermally reset during postdepositional burial and later exhumed during Miocene Basin and Range extension, with 89% of grains possessing 20–9 Ma He ages. The Eocene apatite He ages that were not reset suggest cooling of proximal source terranes at ca. 44 Ma and continued cooling until at least 39 Ma (Fig. 1.3).

DISCUSSION

Hinterland Sediment Dispersion

Eocene detrital zircon grains have crystallization and cooling ages that reflect a variety of Precambrian to Eocene tectonic pathways. Precambrian U-Pb detrital zircon ages are interpreted to be derived from the Appalachians (Dickinson and Gehrels, 2009), and of those grains, 25% yielded Late Devonian–Late Triassic ZHe ages recording either the widespread thermo-tectonic effects of Antler and Sonoma orogenesis or thermo-tectonic events in the original Appalachian sources (Fig. 1.5A). Post-Mississippian pooled ZHe ages from the Elko Formation clustered in at least five groups that loosely correlate with apparent cooling events during the Early Permian, Early–Middle Triassic, Late Jurassic, Early Cretaceous, and middle Eocene (Fig. 1.6). We interpret the Early Permian ages to result from Antler orogenic deformation (e.g., Trexler et al., 2004).

Precambrian zircon U-Pb crystallization age populations (1.8, 2.1, and 2.7 Ga) in several Eocene samples resemble the detrital zircon populations from the proximal Mississippian Diamond Peak Formation (Fig. 1.5A). Grains interpreted to be derived from the Diamond Peak Formation are characterized by 64% Precambrian ZHe ages and 28% Paleozoic ZHe ages, and only 2 out of 24 grains have post-Mississippian ZHe ages (Fig. 1.5A). Eocene samples that preserve pre-Mississippian cooling ages therefore possibly reflect derivation from the Diamond Peak Formation and likely other strata of the Late Devonian–middle Pennsylvanian Antler foreland basin. Similarly, Cretaceous sediments of the Newark Canyon Formation are also inferred to have been derived from erosion of proximal Antler foreland basin strata (Druschke et al., 2011), based on detrital zircon results, and they may also have sourced zircon grains with Precambrian crystallization ages.

We used the above information to highlight four schematic cooling trajectories for Elko Formation detrital zircon grains (Fig. 1.6), including (A) erosion of Roberts Mountains allochthon strata followed by Cretaceous and Eocene recycling at shallow crustal depths, (B) recycling of Roberts Mountains allochthon strata into the Antler foreland basin (Diamond Peak Formation) and retention in the shallow crust, (C) burial of Roberts Mountains allochthon strata during the Antler orogeny followed by late Paleozoic cooling above the

zircon closure temperature, and (D) burial of Roberts Mountains allochthon strata during the Antler orogeny, retention below the zircon closure temperature, and rapid Eocene exhumation. Of these trajectories, only time temperature path D can account for zircon grains with pre-Jurassic U-Pb ages and Eocene He ages.

A comparison of He and depositional ages for detrital zircon grains with Jurassic and Cretaceous U-Pb ages (200–110 Ma) showed that a subset of these grains was rapidly exhumed from ~6 to 9 km depth between ca. 45 and 40 Ma (Fig. 1.3). These grains were likely sourced from local tectonically exhumed backarc plutons with crystallization ages between ca. 160 and ca. 150 Ma (Miller and Hoisch, 1995; du Bray, 2007). Thermobarometry of Late Jurassic backarc plutons in eastern Nevada and western Utah delineates a zone of relatively shallow (<7 km) plutonic emplacement roughly to the north and west of the Ruby Mountains–East Humboldt Range–Wood Hills–Pequop Mountains metamorphic core complex and a zone of deeper (>7 km) plutonic emplacement to the east and south of the metamorphic core complex (Miller and Hoisch, 1995). Samples collected closest to the Ruby Mountains (168RM, 241RM, and 102EH) have the lowest Δt values: ~25 m.y. for Jurassic and Cretaceous detrital zircon grains, where Δt is the time between crystallization and cooling (Fig. 1.5B). These relatively low Δt values imply either derivation from dikes or plutons emplaced at hypabyssal depths (<~5 km) or rapid exhumation following pluton emplacement. Late Jurassic–Early Cretaceous volcanic zircon grains (169–142 Ma) were likely derived from air-fall tuffs associated with a Sierra Nevada high-flux event (Fig. 1.5B; DeCelles and Graham, 2015) or the Jurassic Frenchie Creek Volcanics in the proximal Cortez Mountains (Muffler, 1964; Hollingsworth et al., 2018). Several samples deposited between 50 and 39 Ma contained detrital zircon grains with Δt values that equal zero within 2σ analytical uncertainty, suggesting these are first-cycle volcanic grains. These first cycle volcanic grains have ages consistent with both extraregional (52–45 Ma; 27%) and regional (44–38 Ma; 73%) volcanism (Fig. 1.5B). All double-dated zircon grains with Eocene U-Pb ages were found to be first-cycle volcanic in nature ($L = 0$), implying that Eocene plutons were likely not yet unroofed at this time. If Eocene plutons were synkinematically emplaced during rapid exhumation, however, they may approximate $L = 0$.

Regional Exhumation across the Paleogene

Lag-time trends and detrital He age distributions in the early and middle Eocene were evaluated for three intervals: 50–45 Ma (n = 43), 45–43 Ma (n = 12), and 43–41 Ma (n = 53) to determine sediment recycling and exhumation trends and ultimately to reconstruct the tectonic setting during deposition and basin development.

50–45 Ma

At the onset of Elko Formation deposition, detrital zircon grains with Proterozoic U-Pb ages, Paleozoic–Mesozoic ZHe ages, and predominantly long (>100 m.y.) lag times accumulated in braided streams east of the Cordilleran paleodivide (Fig. 1.3; Smith et al., 2017; Cassel et al., 2018). At this time, initial lacustrine sedimentation occurred within an isolated subbasin near Coal Mine Canyon (Fig. 1.7; Smith et al., 2017). A sample from near the base of the Coal Mine Canyon section contains ubiquitous (56%) 54–45 Ma detrital zircon U-Pb grain ages with identical He ages, indicative of volcanic derivation, possibly from the age-equivalent Challis volcanic field (Sanford, 2005; Fig. 1.1). All early to early–middle Eocene samples also contained zircon with U-Pb ages consistent with derivation from the proximal Roberts Mountains allochthon and Antler foreland basin strata. Long-term storage of this sediment in the shallow crust is reflected by overlapping U-Pb age distributions of Paleozoic passive-margin strata (Fig. 1.1B) and the similarity of clast assemblages in Eocene, Cretaceous, and Mississippian–Permian clastic strata (Silitonga, 1974; Haynes, 2003; Druschke et al., 2011). White et al. (2016) presented heavy mineral analysis of a subset of Elko Formation samples (n = 7 samples) and demonstrated that zircon makes up >94% of grains with a density >2.8 g/cm3, which also supports persistent sediment recycling. In addition, the negative zircon He age–eU correlation observed for several samples (Fig. 1.5) suggests an effect of accumulated radiation damage due to prolonged (>100 m.y.) residence at upper-crustal temperatures (Guenthner et al., 2013). Together, these data indicate slow exhumation rates across this region and likely an absence of extensional faulting coeval with initial Elko Formation deposition.

45–43 Ma

Detrital zircon U-Pb ages indicate that the Elko Basin collected increasingly more volcaniclastic material as slab removal volcanism progressed into northern Nevada by 44 Ma (Henry, 2008; Henry and John, 2013). A sample collected from the Tuscarora Mountains contains 51% middle Eocene detrital zircon U-Pb grain ages, implying substantial sediment contributions from proximal volcanic rocks by 44 ± 0.4 Ma. Numerous volcanic and volcaniclastic horizons, commonly <10 cm thick, are intercalated with Elko Formation strata and represent ash-fall deposits from encroaching volcanism (Smith et al., 2017). Limited ignimbrites from this early volcanism in Nevada accumulated in preexisting paleovalleys. At ca. 43 Ma, volcanic detrital zircon grains with 56–45 Ma U-Pb ages appear to have been abruptly cut off from the basin, possibly reflecting drainage reorganization and/or increased erosion or unroofing of new proximal sources coeval with lake expansion (Fig. 1.7). Despite increased accommodation within the Elko Basin, detrital zircon grains deposited at this time are characterized by >50 m.y. lag times, signifying continued slow tectonic exhumation across this area. Two detrital apatite grains deposited at 43.9 ± 0.5 Ma near Robinson Mountain, however, have Eocene He ages (55.5± 3.3 Ma and 53.2 ± 3.2 Ma) that may reflect incipient upper-crust unroofing not yet recorded by the ZHe ages. We interpret these detrital apatite grains to be sourced from Jurassic plutonic rocks exposed ~20 km to the west in the Cortez Mountains (Hollingsworth et al., 2018). Detrital zircon grains from this sample include 39% Jurassic U-Pb ages, which match these sources as well. Since apatite grains were not double dated, it is also possible that apatite grains with Eocene AHe ages are volcanic in origin. For this reason, all apatite grains were excluded from lag-time analysis. We support the interpretation that these detrital apatite grains are likely nonvolcanic, however; all Elko Formation samples with predominant populations of volcanic grains possess only minor detrital apatite and no apatite grains of a suitable size for thermochronology. In contrast, large and euhedral apatite grains are found in backarc plutons throughout northeastern Nevada (e.g., Muffler, 1964; Seymour, 1980; Rahl et al., 2002; Colgan et al., 2010). Deposition of these relatively low-lag-time apatite grains (<15 m.y.) may therefore mark a ca. 44 Ma transition to more accelerated exhumation of plutonic sources proximal to the Elko Basin.

43–41 Ma

A subgroup of He ages of detrital zircon grains deposited across the Elko Basin shows a sharp increase in apparent source exhumation rates and the onset of rapid tectonic unroofing by ca. 42 Ma. Elko Formation deposition occurred over the largest area during this time interval as Lake Elko transitioned from freshwater to increasingly saline and alkaline conditions after ca. 42.8 Ma (Smith et al., 2017). Rapid exhumation coeval with lacustrine sedimentation is recorded regionally in short-lag-time zircon sampled from Emigrant Pass, Robinson Mountain, and Eureka (Figs. 2 and 3). We interpret this sudden shift to rapid regional exhumation rates to signify extensional deformation within the catchment of the Elko Basin. Detrital apatite and zircon cooling ages between ca. 44 and 40 Ma are consistent with cooling rates along extensional faults and metamorphic core complex detachments (Stockli, 2005; Colgan et al., 2010; Wildman et al., 2016; Brown et al., 2017; Cochran et al., 2017). Sustained rapid cooling rates indicated by ZHe ages during ca. 42–40 Ma necessitate cooling from depths of ~6–9 km. Alternative potential drivers of this abrupt acceleration in source exhumation, such as changes to the erosion rate or geothermal gradient (e.g., Fosdick et al., 2015), are unlikely to account for the observed dramatic reduction in lag times. Large climate-induced changes to the erosion rate are also unlikely during the studied time interval as (1) the Cordilleran hinterland is broadly characterized by low magnitude erosional exhumation (Long, 2012), (2) Elko Formation deposition did not coincide with the middle Eocene climatic optimum (MECO; Smith et al., 2017), and (3) there is no notable increase in Elko Basin sediment accumulation rates. An elevated geothermal gradient during the middle Eocene, however, is possibly supported by $^{40}Ar/^{39}Ar$ and U-Pb dating of proximal Carlin trend mineralization to between 42 and 36 Ma (Arehart et al., 2003; Cline et al., 2005). However, even assuming an extremely high geothermal gradient of ~130 °C/km during middle Eocene regional magmatism (Giordano et al., 2016), rapid cooling rates and exhumation of >1 km/m.y. would still be required within the Elko Basin catchment.

Exhumation in the Hinterland

We interpret these results to record spatially isolated extensional faulting within northeastern Nevada beginning at ca. 44 Ma and accommodating increased exhumation by

42 Ma. Rapid exhumation is recorded by only a small subset of zircon grains, suggesting tectonic unroofing was spatially confined to isolated source regions within the local catchments. This rapid tectonic unroofing, recorded by ZHe cooling ages, contemporaneous regional northwest striking dike swarms and shallow pluton emplacement (Henry and Boden, 1997, 1998; Henry et al., 1999; Ressel and Henry, 2006), evidence for extensional reactivation of pre-Mesozoic faults (Cline et al., 2005; Ressel and Henry, 2006), and associated Au mineralization along the western margin of the Elko Basin (Arehart et al., 2003; Cline et al., 2005) all support extensional deformation within the Elko Basin catchment at this time. Several studies have also used mapped angular unconformities within volcanic rocks overlying Elko Formation strata to document surface-breaching extensional deformation during this time (e.g., Brooks et al., 1995; Mueller et al., 1999; Henry et al., 2001; Haynes, 2003; Lund Snee et al., 2016; Pape et al., 2016). The noted absence of distinctive synextensional Elko Formation strata may reflect extensive Miocene sediment burial and cover of Eocene strata (Moore et al., 1983; Camilleri et al., 2017) or only limited fault control on basin accommodation (Fig. 1.7; Smith et al., 2017). This study is the first to provide quantitative constraints on the magnitude and precise timing of Paleogene exhumation using the sedimentary record, which permits evaluation of the drivers of hinterland extension and the resulting implications for the evolution of the Cordilleran hinterland plateau.

Metamorphic Core Complexes and Magmatism

Zircon grains with <10 m.y. lag times show rapid exhumation in northeastern Nevada from 42 to 40 Ma. Across this time interval (ca. 55–40 Ma), the Ruby Mountains–East Humboldt Range–Wood Hills–Pequop Mountains metamorphic core complex is believed to record ~400 MPa of near-isothermal decompression at temperatures of ~600 °C (Fig. 1.8; Rey et al., 2009b; Hallett and Spear, 2015), indicative of a major phase of core complex development. Within the East Humboldt Range and northern Ruby Mountains, crustal flow and extensional exhumation along the mylonitic shear zone are thought to have initiated in the Eocene (Mueller and Snoke, 1993; MacCready et al., 1997), but the thermochronologic record of rocks currently exposed at the surface are dominated by late Oligocene–Miocene

cooling ages (Fig. 1.8). To ascertain the nature of Eocene core complex development, additional thermochronology of rocks from a wider range of structural levels is needed, including directly beneath the Ruby detachment fault. It is also possible, however, that this early exhumation record is eroded and only now preserved within the Elko Basin (Fig. 1.8). While mylonitic clasts of the core complex do not appear in adjacent basins until the Miocene (Colgan et al., 2010; McGrew and Snoke, 2015; Lund Snee et al., 2016), unroofing of >6 km of Precambrian–Pennsylvanian sedimentary strata (Colgan et al., 2010) prior to exposure of the mylonitic crystalline core may have initiated during the Eocene (McGrew and Snee, 1994; MacCready et al., 1997; McGrew et al., 2000; Litherland and Klemperer, 2017). Several metamorphic core complexes in the northern Rocky Mountains record cooling ages that possibly correlate with this initial phase of rapid extension at ca. 50 Ma (cf. Bendick and Baldwin, 2009), which is within an analogous ~2–3 m.y. window of initial slab removal volcanism within these areas (Konstantinou et al., 2013; Smith et al., 2014). The high middle Eocene cooling rates from samples collected near the incipient Ruby Mountains–East Humboldt Range–Wood Hills–Pequop Mountains metamorphic core complex may reflect cooling of partially molten crust along a high geothermal gradient (Whitney et al., 2013). If these short-lag-time grains were sourced from the Ruby Mountains–East Humboldt Range–Wood Hills–Pequop Mountains metamorphic core complex, it would imply that the core complex was characterized by episodes of fast cooling initiating in the middle Eocene, rather than monotonous and protracted cooling (i.e., Rey et al., 2009b).

Volcanism in northern Nevada began as early as 45–44 Ma (Fig. 1.2; Henry, 2008; Henry et al., 2012; Henry and John, 2013; Smith et al., 2017). Basin-proximal magmatism began in the Tuscarora volcanic field at 40.2 Ma (Henry, 2008), and Eocene dikes and plutons intruded this area from 41 to 39 Ma (Henry and Boden, 1997, 1998; Henry et al., 1999; Ressel and Henry, 2006). The thermal effects of slab removal may induce localized extension, including initial core complex extension, directly prior to voluminous phases of volcanism associated with the rollback-driven influx of asthenosphere (Lister and Davis, 1989; Smith et al., 2014). Middle Eocene Y-rich growth zones on metamorphic zircons in the East Humboldt Range, as well as volcanic and intrusive rocks across northeastern Nevada

(e.g., Henry and Boden, 1997; du Bray, 2007), record this peak phase of heating during slab-removal magmatism from ca. 40 to 32 Ma (Hallett and Spear, 2015). However, elevated lithospheric temperatures across this area beginning at ca. 42 Ma, synchronous with rapid extension, are supported by both the coeval initiation of Carlin-type Au mineralization (Arehart et al., 2003) and intrusion of plutons in the Ruby Mountains (Dallmeyer et al., 1986; Wright and Snoke, 1993; MacCready et al., 1997; Litherland and Klemperer, 2017). This phase of magmatism is theorized to have induced midcrustal flow that spurred upper-crustal extension in northeastern Nevada (Fig. 1.7; Gans et al., 1989; Axen et al., 1993; MacCready et al., 1997; Litherland and Klemperer, 2017). The synchronicity of magmatism and rapid cooling rates documented at multiple localities indicates that this extension was fundamentally reliant on lithospheric heating and weakening from slab rollback.

Extension and Slab Removal

Identification of rapid middle Eocene cooling rates during a previously unconstrained phase of deformation in the Cordilleran hinterland reveals a pivotal transition from slow to rapid exhumation, accommodated by an initial pulse of extensional deformation. Recent paleoaltimetry shows that this region remained at high elevations of 2.7–3.1 km from 41 to 28 Ma (Cassel et al., 2014, 2018) and indicates that this extension did not result in widespread surface lowering. The ensuing 35–17 Ma southward migration of volcanism and sedimentation (Henry et al., 2011, 2012; Lund Snee et al., 2016) accompanied postremoval surface uplift of 400–600 $^{+390}/_{-270}$ m, resulting from the combined effects of slab removal, heating, and lithospheric delamination (Cassel et al., 2018). During the late Eocene and early Oligocene, an unconformity across most of northeastern Nevada indicates that slab removal was followed by ~20 m.y. of diminished surface deformation, prior to Miocene orogenic collapse (Colgan and Henry, 2009).

A compilation of magmatic and syn- to postcontractional records of extension within the North American Cordillera reveals several similarities to the tectonic evolution of other regions that have a history of synextensional magmatism and/or slab rollback (e.g., Stockli, 2005; Bonev and Beccaletto, 2007; Druschke et al., 2009b; Molnar et al., 2010; Wells et al., 2012; Horton, 2018; Rabillard et al., 2018). For example, the Aegean/Cycladic region of the

eastern Mediterranean is characterized by ≤20 km of tectonic burial with peak temperatures (>700 °C) and pressures attained between ca. 73 and 42 Ma (Whitney and Dilek, 1997; Liati and Gebauer, 1999). At ca. 40 Ma, initial exhumation of metamorphic core complexes was accompanied by Paleogene basin formation and synextensional magmatism (Jolivet et al., 2003; Bonev and Beccaletto, 2007). The Basin and Range and Aegean/Cycladic provinces therefore share a history of postcontractional basin formation and initial core complex exhumation during volcanism, all prior to widespread extension >20 m.y. later (Jolivet et al., 2003; Dickinson, 2006; Bendick and Baldwin, 2009; Brun et al., 2016). This supports the theory that while complete orogenic collapse is predicated on kinematic boundary condition changes, magmatism and thermal weakening of the lithosphere result in clear kinematic changes in regions of thickened crust. Slab removal drives magmatism and lithospheric weakening, slab suction and mantle flow, and isostatic changes that include mantle lithospheric delamination, indicating that slab-removal processes are an important trigger of exhumation and extension in orogenic hinterland plateaus (e.g., Rahl et al., 2002; Heuret and Lallemand, 2005; Hall, 2013; Nakakuki and Mura, 2013; Sternai et al., 2014).

CONCLUSIONS

(1) (U-Th)/(He-Pb) double dating shows that zircon grains in Eocene fluvial strata were predominantly derived from local Paleozoic strata, Jurassic–Cretaceous backarc plutons, and Eocene felsic volcanic rocks. Eocene sandstones contain multicycle zircon grains with Precambrian crystallization ages and Precambrian through Eocene cooling ages, as well as an increasing proportion of younger (150–40 Ma) ZHe ages up section, suggesting formation or capture of newly exhumed source terranes.

(2) Early to middle Eocene samples contain abundant 56–45 Ma volcanic detritus that likely originated from the Challis volcanic province. We interpret an up-section decrease in sediment source diversity based on the sudden middle Eocene disappearance of Challis-age grains and coincident increase in 43–39 Ma volcaniclastic material, reflecting increased exhumation and erosion of proximal sources.

(3) Many detrital zircon grains extracted from Eocene sedimentary rocks preserve

Precambrian (32%) and Paleozoic (13%) cooling ages, and several samples show a negative correlation between He age and eU concentration, indicative of muted exhumation and prolonged sediment recycling in the upper crust across the contractile phase of the North American Cordillera.

(4) A progressive decrease in lag times of detrital grains up section indicates acceleration of source exhumation from rates of <0.01 km/m.y. to >1 km/m.y. between 45 and 41 Ma. We attribute the subsequent low lag times between 42 and 39 Ma to extensional deformation coincident with and following the removal of the Farallon slab and/or mantle lithospheric delamination. This extension was localized in spatial extent, with consistent recycling of Paleozoic bedrock detritus, and it likely signifies the initiation of rapid core complex exhumation. An ~15 m.y. hiatus in terrestrial sediment accumulation across northeastern Nevada followed this rate change, which we interpret as the result of regional uplift and erosion.

(5) The coincidence of increased exhumation rates and core complex formation with volcanism and drainage disruption due to slab removal indicates a fundamental link between metamorphic core complexes and slab and mantle lithosphere removal. Rapid exhumation and core complex formation do not, however, necessitate orogenic collapse of hinterland plateaus. This deformation preceded the transition to surface lowering and distributed Basin and Range extension by ~20 m.y.

ACKNOWLEDGEMENTS

National Science Foundation grant EAR-1322073 and student grants from the Geological Society of America, American Association of Petroleum Geologists, Rocky Mountain Association of Geologists, Geological Society of Nevada, Nevada Petroleum and Geothermal Society, Society for Sedimentary Geology (SEPM), and Tobacco Root Geological Survey supported this research. This work greatly benefited from discussions with S. Long and C. Henry, as well as field assistance from E. White, A. Wilson, C. Carlson, E. Stauffer, N. Seymour, and Z. Foster-Baril. We also would like to acknowledge laboratory

assistance by L. Stockli, D. Patterson, and K. Thomson. We also thank C. Painter and an anonymous reviewer for thoughtful reviews that greatly improved the manuscript.

REFERENCES

Allmendinger, R.W., Jordan, T.E., Kay, S.M., and Isacks, B.L., 1997, The evolution of the Altiplano-Puna Plateau of the Central Andes: Annual Review of Earth and Planetary Sciences, v. 25, p. 139–174, https://doi.org/10.1146/annurev.earth.25.1.139.

Arehart, G.B., Chakurian, A.M., Tretbar, D.R., Christensen, J.N., McInnes, B.A., and Donelick, R.A., 2003, Evaluation of radioisotope dating of Carlin-type deposits in the Great Basin, western North America, and implications for deposit genesis: Economic Geology and the Bulletin of the Society of Economic Geologists, v. 98, p. 235–248, https://doi.org/10.2113/gsecongeo.98.2.235.

Axen, G.J., Taylor, W.J., and Bartley, J.M., 1993, Space-time patterns and tectonic controls of Tertiary extension and magmatism in the Great Basin of the western United States: Geological Society of America Bulletin, v. 105, p. 56–76, https://doi.org/10.1130/0016-7606(1993)105<0056:STPATC>2.3.CO;2.

Beghoul, N., Barazangi, M., and Isacks, B.L., 1993, Lithospheric structure of Tibet and western North America: Mechanisms of uplift and a comparative study: Journal of Geophysical Research, v. 98, no. B2, p. 1997–2016, https://doi.org/10.1029/92JB02274.

Beltrando, M., Hermann, J., Lister, G., and Compagnoni, R., 2007, On the evolution of orogens: Pressure cycles and deformation mode switches: Earth and Planetary Science Letters, v. 256, no. 3–4, p. 372–388, https://doi.org/10.1016/j.epsl.2007.01.022.

Bendick, R., and Baldwin, J., 2009, Dynamic models for metamorphic core complex formation and scaling: The role of unchannelized collapse of thickened continental crust: Tectonophysics, v. 477, no. 1–2, p. 93–101, https://doi.org/10.1016/j.tecto.2009.03.017.

Best, M.G., Christiansen, E.H., de Silva, S., and Lipman, P.W., 2016, Slab-rollback ignimbrite flareups in the southern Great Basin and other Cenozoic American arcs: A distinct style of arc volcanism: Geosphere, v. 12, no. 4, p. 1097–1135, https://doi.org/10.1130/GES01285.1.

Bonev, N., and Beccaletto, L., 2007, From syn- to post-orogenic Tertiary extension in the north Aegean region: Constraints on the kinematics in the eastern Rhodope-Thrace, Bulgaria- Greece, and the Biga Peninsula, NW Turkey, *in* Taymaz, T., Yilmaz, Y., and Dilek, Y., eds., The Geodynamics of the Aegean and Anatolia: Geological Society [London] Special Publication 291, p. 113–142, https://doi.org/10.1144/SP291.6.

Brandon, M.T., and Vance, J.A., 1992, Tectonic evolution of the Cenozoic Olympic subduction complex, Washington State, as deduced from fission track ages for detrital zircons: American Journal of Science, v. 292, p. 565–636, https://doi.org/10.2475/ajs.292.8.565.

Brooks, W.E., Thorman, C.H., and Snee, L.W., 1995, The 40Ar/39Ar ages and tectonic setting of the middle Eocene northeast Nevada volcanic field: Journal of Geophysical Research, v. 100, no. B7, p. 10,403–10,416, https://doi.org/10.1029/94JB03389.

Brown, S.J., Thigpen, J.R., Spotila, J.A., Krugh, W.C., Tranel, L.M., and Orme, D.A., 2017, Onset timing and slip history of the Teton fault, Wyoming: A multidisciplinary reevaluation: Tectonics, v. 36, no. 11, p. 2669–2692, https://doi.org/10.1002/2016TC004462.

Brun, J.P., Faccenna, C., Gueydan, F., Sokoutis, D., Philippon, M., Konstantinos, K., and Gorini, C., 2016, The two-stage Aegean extension, from localized to distributed, a result of slab rollback acceleration: Canadian Journal of Earth Sciences, v. 53, p. 1142–1157, https://doi.org/10.1139/cjes-2015-0203.

Burchfiel, B.C., and Royden, L.H., 1985, North-south extension within the convergent Himalayan region: Geology, v. 13, no. 10, p. 679–682, https://doi.org/10.1130/0091-7613(1985)13<679:NEWTCH>2.0.CO;2.

Bussell, M.A., and Pitcher, W.S., 1985, The structural controls of batholith emplacement, *in* Pitcher, W.S., et al., eds., Magmatism at a Plate Edge: The Peruvian Andes: New York, John Wiley and Sons, p. 167–176, https://doi.org/10.1007/978-1-4899-5820-4_15.

Camilleri, P.A., 1996, Evidence for Late Cretaceous–Early Tertiary(?) extension in the Pequop Mountains, Nevada: Implications for the nature of the Early Tertiary unconformity, *in*

Taylor, W.J., and Holly, L., eds., Cenozoic Structure and Stratigraphy of Central Nevada, 1996 Field Conference Volume: Reno, Nevada, Nevada Petroleum Society Inc., p. 23–31.

Camilleri, P.A., and Chamberlain, K.R., 1997, Mesozoic tectonics and metamorphism in the Pequop Mountains and Wood Hills region, northeast Nevada: Implications for the architecture and evolution of the Sevier orogeny: Geological Society of America Bulletin, v. 109, p. 74–94, https://doi.org/10.1130/0016-7606(1997)109<0074:MTAMIT>2.3.CO;2.

Camilleri, P., Deibert, J., and Perkins, M., 2017, Middle Miocene to Holocene tectonics, basin evolution, and paleogeography along the southern margin of the Snake River Plain in the Knoll Mountain–Ruby–East Humboldt Range region, northeastern Nevada and south-central Idaho: Geosphere, v. 13, no. 6, p. 1901–1948, https://doi.org/10.1130/GES01318.1.

Campbell, I.H., Reiners, P.W., Allen, C.M., Nicolescu, S., and Upadhyay, R., 2005, He-Pb double dating of detrital zircons from the Ganges and Indus Rivers: Implication for quantifying sediment recycling and provenance studies: Earth and Planetary Science Letters, v. 237, no. 3–4, p. 402–432, https://doi.org/10.1016/j.epsl.2005.06.043.

Carrapa, B., and DeCelles, P.G., 2008, Eocene exhumation and basin development in the Puna of northwestern Argentina: Tectonics, v. 27, TC1015, https://doi.org/10.1029/2007TC002127.

Carrapa, B., Wijbrans, J., and Bertotti, G., 2003, Episodic exhumation in the western Alps: Geology, v. 31, no. 7, p. 601–604, https://doi.org/10.1130/0091-7613(2003)031<0601:EEITWA>2.0.CO;2.

Carrapa, B., Strecker, M.R., and Sobel, E.R., 2006, Cenozoic orogenic growth in the Central Andes: Evidence from sedimentary rock provenance and apatite fission track thermochronology in the Fiambala Basin, southernmost Puna Plateau margin (NW

Argentina): Earth and Planetary Science Letters, v. 247, no. 1–2, p. 82–100, https://doi.org/10.1016/j.epsl.2006.04.010.

Cassel, E.J., Breecker, D.O., Henry, C.D., Larson, T.E., and Stockli, D.F., 2014, Profile of a paleo-orogen: High topography across the present-day Basin and Range from 40 to 23 Ma: Geology, v. 42, no. 11, p. 1007–1010, https://doi.org/10.1130/G35924.1.

Cassel, E.J., Smith, M.E., and Jicha, B.R., 2018, The impact of slab rollback on Earth's surface: Uplift and extension in the hinterland of the North American Cordillera: Geophysical Research Letters, v. 45, no. 20, p. 10,996–11,004, https://doi.org/10.1029/2018GL079887.

Cline, J.S., Hofstra, A.H., Muntean, J.L., Tosdal, R.M., and Hickey, K.A., 2005, Carlin-type gold deposits in Nevada: Critical geologic characteristics and viable models: Economic Geology and the Bulletin of the Society of Economic Geologists, v. 100, p. 451–484.

Cochran, W.J., Spotila, J.A., Prince, P.S., and McAleer, R.J., 2017, Rapid exhumation of Cretaceous arc-rocks along the Blue Mountains restraining bend of the Enriquillo-Plantain Garden fault, Jamaica, using thermochronometry from multiple closure systems: Tectonophysics, v. 721, p. 292–309, https://doi.org/10.1016/j.tecto.2017.09.021.

Colgan, J.P., and Henry, C.D., 2009, Rapid middle Miocene collapse of the Sevier orogenic plateau in north-central Nevada: International Geology Review, v. 51, no. 9–11, p. 920–961, https://doi.org/10.1080/00206810903056731.

Colgan, J.P., Howard, K.A., Fleck, R.J., and Wooden, J.L., 2010, Rapid middle Miocene extension and unroofing of the southern Ruby Mountains, Nevada: Tectonics, v. 29, TC6022, https://doi.org/10.1029/2009TC002655.

Coney, P.J., and Harms, T.A., 1984, Cordilleran metamorphic core complexes: Cenozoic extensional relics of Mesozoic compression: Geology, v. 12, no. 9, p. 550–554, https://doi.org/10.1130/0091-7613(1984)12<550:CMCCCE>2.0.CO;2.

Crafford, E.J., 2008, Paleozoic tectonic domains of Nevada: An interpretive discussion to accompany the geologic map of Nevada: Geosphere, v. 4, no. 1, p. 260–291, https://doi.org/10.1130/GES00108.1.

Dallmeyer, R.D., Snoke, A., and McKee, E.H., 1986, The Mesozoic–Cenozoic tectonothermal evolution of the Ruby Mountains, East Humboldt Range, Nevada: A Cordilleran metamorphic core complex: Tectonics, v. 5, no. 6, p. 931–954, https://doi.org/10.1029/TC005i006p00931.

DeCelles, P.G., 2004, Late Jurassic to Eocene evolution of the Cordilleran thrust belt and foreland basin system, western U.S.A.: American Journal of Science, v. 304, no. 2, p. 105–168, https://doi.org/10.2475/ajs.304.2.105.

DeCelles, P.G., and Graham, S.A., 2015, Cyclical processes in the North American Cordilleran orogenic system: Geology, v. 43, no. 6, p. 499–502, https://doi.org/10.1130/G36482.1.

DeCelles, P.G., Carrapa, B., Horton, B.K., McNabb, J., Gehrels, G.E., and Boyd, J., 2015, The Miocene Arizaro Basin, central Andean hinterland: Response to partial lithosphere removal?, *in* DeCelles, P.G., et al., eds., Geodynamics of a Cordilleran Orogenic System: The Central Andes of Argentina and Northern Chile: Geological Society of America Memoir 212, p. 359–386, https://doi.org/10.1130/2015.1212(18).

Dewey, J.F., 1988, Extensional collapse of orogens: Tectonics, v. 7, no. 6, p. 1123–1139, https://doi.org/10.1029/TC007i006p01123.

Dickinson, W.R., 2006, Geotectonic evolution of the Great Basin: Geosphere, v. 2, no. 7, p. 353–368, https://doi.org/10.1130/GES00054.1.

Dickinson, W.R., and Gehrels, G.E., 2009, Use of U-Pb ages of detrital zircons to infer maximum depositional ages of strata: A test against a Colorado Plateau Mesozoic database: Earth and Planetary Science Letters, v. 288, no. 1–2, p. 115–125, https://doi.org/10.1016/j.epsl.2009.09.013.

Dilek, Y., and Moores, E.M., 1999, A Tibetan model for the Early Tertiary western United States: Journal of the Geological Society [London], v. 156, no. 5, p. 929–941, https://doi.org/10.1144/gsjgs.156.5.0929.

Dinter, D.A., 1998, Late Cenozoic extension of the Alpine collisional orogen, northeastern Greece: Origin of the north Aegean basin: Geological Society of America Bulletin, v. 110, no. 9, p. 1208–1230, https://doi.org/10.1130/0016-7606(1998)110<1208:LCEOTA>2.3.CO;2.

Dokka, R.K., Mahaffie, M.J., and Snoke, A.W., 1986, Thermochronologic evidence of major tectonic denudation associated with detachment faulting, northern Ruby Mountains–East Humboldt Range, Nevada: Tectonics, v. 5, no. 7, p. 995–1006, https://doi.org/10.1029/TC005i007p00995.

Druschke, P., Hanson, A.D., and Wells, M.L., 2009a, Structural, stratigraphic, and geochronologic evidence for extension predating Palaeogene volcanism in the Sevier hinterland, east-central Nevada: International Geology Review, v. 51, no. 7–8, p. 743–775, https://doi.org/10.1080/00206810902917941.

Druschke, P., Hanson, A.D., Wells, M.L., Rasbury, T., Stockli, D.F., and Gehrels, G., 2009b, Synconvergent surface-breaking normal faults of Late Cretaceous age within the Sevier hinterland, east-central Nevada: Geology, v. 37, no. 5, p. 447–450, https://doi.org/10.1130/G25546A.1.

Druschke, P., Hanson, A.D., Wells, M.L., Gehrels, G.E., and Stockli, D., 2011, Paleogeographic isolation of the Cretaceous to Eocene Sevier hinterland, east-central Nevada: Insights from U-Pb and (U-Th)/He detrital zircon ages of hinterland strata: Geological Society of America Bulletin, v. 123, no. 5, p. 1141–1160, https://doi.org/10.1130/B30029.1.

Dubiel, R.F., Potter, C.J., Good, S.C., and Snee, L.W., 1996, Reconstructing an Eocene extensional basin: The White Sage Formation, eastern Great Basin, *in* Beratan, K.K., ed., Reconstructing the History of Basin and Range Extension Using Sedimentology and Stratigraphy: Geological Society of America Special Paper 303, p. 1–14, https://doi.org/10.1130/0-8137-2303-5.1.

du Bray, E.A., 2007, Time, space, and composition relations among northern Nevada intrusive rocks and their metallogenic implications: Geosphere, v. 3, no. 5, p. 381–405, https://doi.org/10.1130/GES00109.1.

Effimoff, I., and Pinezich, A.R., 1981, Tertiary structural development of selected valleys based on seismic data: Basin and Range Province, northeastern Nevada: Philosophical Transactions of the Royal Society of London, v. 300, no. 1454, p. 435–442, https://doi.org/10.1098/rsta.1981.0074.

England, P.C., and Houseman, G.A., 1989, Extension during continental convergence, with application to the Tibetan Plateau: Journal of Geophysical Research, v. 94, p. 17,561–579, https://doi.org/10.1029/JB094iB12p17561.

Farley, K.A., 2000, Helium diffusion from apatite: General behavior as illustrated by Durango fluorapatite: Journal of Geophysical Research, v. 105, no. B2, p. 2903–2914, https://doi.org/10.1029/1999JB900348.

Farley, K.A., and Stockli, D.F., 2002, (U-Th)/He dating of phosphates: Apatite, monazite, and xenotime: Reviews in Mineralogy and Geochemistry, v. 48, no. 1, p. 559–577, https://doi.org/10.2138/rmg.2002.48.15.

Farley, K.A., Wolf, R.A., and Silver, L.T., 1996, The effects of long alpha-stopping distances on (U-Th)/He ages: Geochimica et Cosmochimica Acta, v. 60, no. 21, p. 4223–4229, https://doi.org/10.1016/S0016-7037(96)00193-7.

Flowers, R.M., Ketcham, R.A., Shuster, D.L., and Farley, K.A., 2009, Apatite (U-Th)/He thermochronometry using a radiation damage accumulation and annealing model: Geochimica et Cosmochimica Acta, v. 73, no. 8, p. 2347–2365, https://doi.org/10.1016/j.gca.2009.01.015.

Fosdick, J.C., Grove, M., Graham, S.A., Hourigan, J.K., Lovera, O., and Romans, B.W., 2015, Detrital thermochronologic record of burial heating and sediment recycling in the Magallanes foreland basin, Patagonian Andes: Basin Research, v. 27, p. 546–572, https://doi.org/10.1111/bre.12088.

Gans, P.B., Mahood, G.A., and Schermer, E., 1989, Synextensional Magmatism in the Basin and Range Province: A Case Study from the Eastern Great Basin: Geological Society of America Special Paper 233, 53 p., https://doi.org/10.1130/SPE233-p1.

Garver, J.I., Brandon, M.T., Roden-Tice, M.K., and Kamp, P.J.J., 1999, Exhumation history of orogenic highlands determined by detrital fission track thermochronology, *in* Ring, U., et al., eds., Exhumation Processes: Normal Faulting, Ductile Flow, and Erosion: Geological Society [London] Special Publication 154, p. 283–304.

Gehrels, G., and Pecha, M., 2014, Detrital zircon U-Pb geochronology and Hf isotope geochemistry of Paleozoic and Triassic passive margin strata of western North America: Geosphere, v. 10, no. 1, p. 49–65, https://doi.org/10.1130/GES00889.1.

Gilbert, H., 2012, Crustal structure and signatures of recent tectonism as influenced by ancient terranes in the western United States: Geosphere, v. 8, no. 1, p. 141–157, https://doi.org/10.1130/GES00720.1.

Giordano, G., Ahumada, F., Aldega, L., Baez, W., Becchio, R., Bigi, S., Caricchi, C., Chiodi, A., Corrado, S., De Benedetti, A.A., Favetto, A., Filipovich, R., Fusari, A., Groppelli, G., Invernizzi, C., Maffucci, R., Norini, G., Pinton, A., Pomposiello, C., Tassi, F., Taviani, S., and Viramonte, J., 2016, Preliminary data on the structure and potential of the Tocomar Geothermal Field (Puna Plateau, Argentina): Energy Procedia, v. 97, p. 202–209, https://doi.org/10.1016/j.egypro.2016.10.055.

Göğüş, O.H., and Pysklywec, R.N., 2008, Mantle lithosphere delamination driving plateau uplift and synconvergent extension in eastern Anatolia: Geology, v. 36, no. 9, p. 723–726, https://doi.org/10.1130/G24982A.1.

Guenthner, W.R., Reiners, P.W., Ketcham, R.A., Nasdala, L., and Giester, G., 2013, Helium diffusion in natural zircon: Radiation damage, anisotropy, and the interpretation of zircon (U-Th)/He thermochronology: American Journal of Science, v. 313, no. 3, p. 145–198, https://doi.org/10.2475/03.2013.01.

Haines, S.H., and van der Pluijm, B.A., 2010, Dating the detachment fault system of the Ruby Mountains, Nevada: Significance for the kinematics of low-angle normal faults: Tectonics, v. 29, TC4028, https://doi.org/10.1029/2009TC002552.

Hall, R., 2013, Contraction and extension in northern Borneo driven by subduction rollback: Journal of Asian Earth Sciences, v. 76, p. 399–411, https://doi.org/10.1016/j.jseaes.2013.04.010.

Hallett, B.W., and Spear, F.S., 2014, The *P-T* history of anatectic pelites of the northern East Humboldt Range, Nevada: Evidence for tectonic loading, decompression, and anatexis: Journal of Petrology, v. 55, no. 1, p. 3–36, https://doi.org/10.1093/petrology/egt057.

Hallett, B.W., and Spear, F.S., 2015, Monazite, zircon, and garnet growth in migmatitic pelites as a record of metamorphism and partial melting in the East Humboldt Range, Nevada: The American Mineralogist, v. 100, no. 4, p. 951–972, https://doi.org/10.2138/am-2015-4839.

Harris, A.G., and Crafford, A.E.J., 2007, A Digital Conodont Database of Nevada: U.S. Geological Survey Data Series 249, 46 p.

Hart, N.R., Stockli, D.F., and Hayman, N.W., 2016, Provenance evolution during progressive rifting and hyperextension using bedrock and detrital zircon U-Pb geochronology, Mauléon Basin, western Pyrenees: Geosphere, v. 12, no. 4, p. 1166–1186, https://doi.org/10.1130/GES01273.1.

Haynes, S.R., 2003, Development of the Eocene Elko Basin, Northeastern Nevada: Implications for Paleogeography and Regional Tectonism [M.S. thesis]: Vancouver, British Columbia, Canada, University of British Columbia, 159 p.

Heller, P.L., Mathers, G., Dueker, K., and Foreman, B., 2013, Far-traveled latest Cretaceous–Paleocene conglomerates of the Southern Rocky Mountains, USA: Record of transient Laramide tectonism: Geological Society of America Bulletin, v. 125, no. 3/4, p. 490–498, https://doi.org/10.1130/B30699.1.

Henry, C.D., 2008, Ash-flow tuffs and paleovalleys in northeastern Nevada: Implications for Eocene paleogeography and extension in the Sevier hinterland, northern Great Basin: Geosphere, v. 4, no. 1, p. 1–35, https://doi.org/10.1130/GES00122.1.

Henry, C.D., and Boden, D.R., 1997, Eocene magmatism of the Tuscarora volcanic field, Elko County, Nevada, and implications for Carlin-type mineralization, *in* Vikre, P., et al., eds., Guidebook for the Society of Economic Geologists Field Conference: Littleton, Colorado, Society of Economic Geologists, v. 28, p. 193–202, https://doi.org/10.1130/0091-7613(1998)026<1067:EMTHSF>2.3.CO;2.

Henry, C.D., and Boden, D.R., 1998, Geologic Map of the Southern Part of the Mount Blitzen Quadrangle, Nevada: Nevada Bureau of Mines and Geology Map 110, 20 p.

Henry, C.D., and Faulds, J.E., 1999, Preliminary Geologic Map of the Emigrant Pass Quadrangle, Nevada: Nevada Bureau of Mines and Geology Open-File Report 99–9, scale 1:24,000, 20 p.

Henry, C.D., and John, D.A., 2013, Magmatism, ash-flow tuffs, and calderas of the ignimbrite flareup in the western Nevada volcanic field, Great Basin, USA: Geosphere, v. 9, p. 951–1008, https://doi.org/10.1130/GES00867.1.

Henry, C.D., Boden, D.R., and Castor, S.B., 1999, Geologic map of the Tuscarora Quadrangle, northeastern Nevada: Nevada Bureau of Mines and Geology Map 116, scale 1:24,000, 20 p.

Henry, C.D., Faulds, J.E., Boden, D.R., and Ressel, M.W., 2001, Timing and styles of Cenozoic extension near the Carlin Trend, northeastern Nevada: Implications for the formation of Carlin-type gold deposits, *in* Shaddrick, D.R., Zbinden, E., Mathewson, D.C., and Prenn, C., eds., Regional Tectonics & Structural Control of Ore: The Major Gold Trends of Northern Nevada: Geological Society of Nevada Special Publication 33, p. 115–128.

Henry, C.D., McGrew, A.J., Colgan, J.P., Snoke, A.W., and Brueseke, M.E., 2011, Timing, distribution, amount, and style of Cenozoic extension in the northern Great Basin, *in* Lee, J., and Evans, J.P., eds., Geologic Field Trips to the Basin and Range, Rocky Mountains, Snake River Plain, and Terranes of the U.S. Cordillera: Geological Society of America Field Guide 21, p. 27–66, https://doi.org/10.1130/2011.0021(02).

Henry, C.D., Hinz, N.H., Faulds, J.E., Colgan, J.P., John, D.A., Brooks, E.R., Cassel, E.J., Garside, L.J., Davis, D.A., and Castor, S.B., 2012, Eocene–early Miocene paleotopography of the Sierra Nevada–Great Basin–Nevadaplano based on widespread ash-flow tuffs and paleovalleys: Geosphere, v. 8, no. 1, p. 1–27, https://doi.org/10.1130/GES00727.1.

Heuret, A., and Lallemand, S., 2005, Plate motions, slab dynamics, and back-arc deformation: Physics of the Earth and Planetary Interiors, v. 149, no. 1–2, p. 31–51, https://doi.org/10.1016/j.pepi.2004.08.022.

Hodges, K.V., Snoke, A.W., and Hurlow, H.A., 1992, Thermal evolution of a portion of the Sevier hinterland: The northern Ruby Mountains–East Humboldt Range and Wood Hills, northeastern Nevada: Tectonics, v. 11, no. 1, p. 154–164, https://doi.org/10.1029/91TC01879.

Hollingsworth, E., Ressel, M.W., and Henry, C., 2018, Early coarse clastic deposition in the western Elko Basin, Piñon Range, northeastern Nevada: Implications for basin evolution and petroleum potential: American Association of Petroleum Geologists Search and Discovery Article 90323.

Horton, B.K., 2018, Sedimentary record of Andean mountain building: Earth-Science Reviews, v. 178, p. 279–309, https://doi.org/10.1016/j.earscirev.2017.11.025.

Houseman, G.A., McKenzie, D.P., and Molnar, P., 1981, Convective instability of a thickened boundary layer and its relevance for the thermal evolution of continental convergent belts: Journal of Geophysical Research, v. 86, no. B7, p. 6115–6132, https://doi.org/10.1029/JB086iB07p06115.

Humphreys, E., 1995, Post-Laramide removal of the Farallon slab, western United States: Geology, v. 23, no. 11, p. 987–990, https://doi.org/10.1130/0091-7613(1995)023<0987:PLROTF>2.3.CO;2.

Humphreys, E., 2009, Relation of flat subduction to magmatism and deformation in the western United States, *in* Kay, S.M., et al., eds., Backbone of the Americas: Shallow Subduction, Plateau Uplift, and Ridge and Terrane Collision: Geological Society of America Memoir 204, p. 85–98, https://doi.org/10.1130/2009.1204(04).

Hurlow, H.A., Snoke, A.W., and Hodges, K.V., 1991, Temperature and pressure of mylonitization in a Tertiary extensional shear zone, Ruby Mountains–East Humboldt Range, Nevada: Tectonic implications: Geology, v. 19, no. 1, p. 82–86, https://doi.org/10.1130/0091-7613(1991)019<0082:TAPOMI>2.3.CO;2.

Hyndman, R.D., 2017, Lower-crustal flow and detachment in the North American Cordillera: A consequence of Cordillera-wide high temperatures: Geophysical Journal International, v. 209, no. 3, p. 1779–1799, https://doi.org/10.1093/gji/ggx138.

Janecke, S.U., and Snee, L.W., 1993, Timing and episodicity of middle Eocene volcanism and onset of conglomerate deposition, Idaho: The Journal of Geology, v. 101, no. 5, p. 603–621, https://doi.org/10.1086/648252.

Jolivet, L., Faccenna, C., Goffé, B., Burov, E., and Agard, P., 2003, Subduction tectonics and exhumation of high-pressure metamorphic rocks in the Mediterranean orogens: American Journal of Science, v. 303, no. 5, p. 353–409, https://doi.org/10.2475/ajs.303.5.353.

Ketcham, R.A., Guenthner, W.R., and Reiners, P.W., 2013, Geometric analysis of radiation damage connectivity in zircon and its implications for helium diffusion: The

American Mineralogist, v. 98, no. 2–3, p. 350–360, https://doi.org/10.2138/am.2013.4249.

Konstantinou, A., Strickland, A., Miller, E., Vervoort, J., Fisher, C.M., Wooden, J., and Valley, J., 2013, Synextensional magmatism leading to crustal flow in the Albion–Raft River–Grouse Creek metamorphic core complex, northeastern Basin and Range: Tectonics, v. 32, no. 5, p. 1384–1403, https://doi.org/10.1002/tect.20085.

Liati, A., and Gebauer, D., 1999, Constraining the prograde and retrograde *P-T-t* path of Eocene HP rocks by SHRIMP dating of different zircon domains: Inferred rates of heating, burial, cooling and exhumation for central Rhodope, northern Greece: Contributions to Mineralogy and Petrology, v. 135, no. 4, p. 340–354, https://doi.org/10.1007/s004100050516.

Liberty, L.M., Heller, P.L., and Smithson, S.B., 1994, Seismic reflection evidence for two-phase development of Tertiary basins from east-central Nevada: Geological Society of America Bulletin, v. 106, no. 12, p. 1621–1633, https://doi.org/10.1130/0016-7606(1994)106<1621:SREFTP>2.3.CO;2.

Linde, G.M., Trexler, J.H., Cashman, P.H., Gehrels, G., and Dickinson, W.R., 2016, Detrital zircon U-Pb geochronology and Hf isotope geochemistry of the Roberts Mountains allochthon: New insights into the early Paleozoic tectonics of western North America: Geosphere, v. 12, no. 3, p. 1016–1031, https://doi.org/10.1130/GES01252.1.

Lister, G.S., and Davis, G.A., 1989, The origin of metamorphic core complexes and detachment faults formed during Tertiary continental extension in the northern Colorado River region, USA: Journal of Structural Geology, v. 11, no. 1–2, p. 65–94, https://doi.org/10.1016/0191- 8141(89)90036-9.

Lister, G.S., Forster, M.A., and Rawling, T.J., 2001, Episodicity during orogenesis, *in* Miller, J.A., et al., eds., Continental Reactivation and Reworking: Geological Society [London] Special Publication 184, p. 89–113, https://doi.org/10.1144/GSL.SP.2001.184.01.06.

Litherland, M.M., and Klemperer, S.L., 2017, Crustal structure of the Ruby Mountains metamorphic core complex, Nevada, from passive seismic imaging: Geosphere, v. 13, no. 5, p. 1506–1523, https://doi.org/10.1130/GES01472.1.

Long, S.P., 2012, Magnitudes and spatial patterns of erosional exhumation in the Sevier hinterland, eastern Nevada and western Utah, USA: Insights from a Paleogene paleogeographic map: Geosphere, v. 8, no. 4, p. 881–901, https://doi.org/10.1130/GES00783.1.

Long, S.P., 2015, An upper-crustal fold province in the hinterland of the Sevier orogenic belt, eastern Nevada, U.S.A.: A Cordilleran Valley and Ridge in the Basin and Range: Geosphere, v. 11, no. 2, p. 404–424, https://doi.org/10.1130/GES01102.1.

Long, S.P., and Soignard, E., 2016, Shallow-crustal metamorphism during Late Cretaceous anatexis in the Sevier hinterland plateau: Peak temperature conditions from the Grant Range, eastern Nevada, U.S.A.: Lithosphere, v. 8, no. 2, p. 150–164, https://doi.org/10.1130/L501.1.

Long, S.P., Thomson, S.N., Reiners, P.W., and Di Fiori, R.V., 2015, Synorogenic extension localized by upper-crustal thickening: An example from the Late Cretaceous Nevadaplano: Geology, v. 43, no. 4, p. 351–354, https://doi.org/10.1130/G36431.1.

Lund Snee, J.E., Miller, E.L., Grove, M., Hourigan, J.K., and Konstantinou, A., 2016, Cenozoic paleogeographic evolution of the Elko Basin and surrounding region, northeast Nevada: Geosphere, v. 12, no. 2, p. 464–500, https://doi.org/10.1130/GES01198.1.

MacCready, T., Snoke, A.W., Wright, J.E., and Howard, K.A., 1997, Mid-crustal flow during Tertiary extension in the Ruby Mountains core complex, Nevada: Geological Society of America Bulletin, v. 109, no. 12, p. 1576–1594, https://doi.org/10.1130/0016-7606(1997)109<1576:MCFDTE>2.3.CO;2.

Malusà, M.G., Resentini, A., and Garzanti, E., 2016, Hydraulic sorting and mineral fertility bias in detrital geochronology: Gondwana Research, v. 31, p. 1–19, https://doi.org/10.1016/j.gr.2015.09.002.

McGrew, A.J., and Snee, L.W., 1994, 40Ar/39Ar thermochronologic constraints on the tectonothermal evolution of the northern East Humboldt Range metamorphic core complex, Nevada: Tectonophysics, v. 238, no. 1–4, p. 425–450, https://doi.org/10.1016/0040-1951(94)90067-1.

McGrew, A.J., and Snoke, A.W., 2015, Geologic Map of the Welcome Quadrangle and an Adjacent Part of the Wells Quadrangle, Elko County, Nevada: Nevada Bureau of Mines and Geology Map 184, scale 1:24,000, 40 p.

McGrew, A.J., Peters, M.T., and Wright, J.E., 2000, Thermobarometric constraints on the tectonothermal evolution of the East Humboldt Range metamorphic core complex, Nevada: Geological Society of America Bulletin, v. 112, no. 1, p. 45–60, https://doi.org/10.1130/0016-7606(2000)112<45:TCOTTE>2.0.CO;2.

Miller, D.M., and Hoisch, T.D., 1995, Jurassic tectonics of northeastern Nevada and northwestern Utah from the perspective of barometric studies, *in* Miller, D.M., and Busby, C., eds., Jurassic Magmatism and Tectonics of the North American Cordillera: Geological Society of America Special Paper 299, p. 267–294, https://doi.org/10.1130/SPE299-p267.

Miller, D.M., Hillhouse, W.C., Zartman, R.E., and Lanphere, M.A., 1987, Geochronology of intrusive and metamorphic rocks in the Pilot Range, Utah and Nevada, and comparison with regional patterns: Geological Society of America Bulletin, v. 99, no. 6, p. 866–879, https://doi.org/10.1130/0016-7606(1987)99<866:GOIAMR>2.0.CO;2.

Miller, E.L., Miller, M.M., Stevens, C.H., Wright, J.E., and Madrid, R., 1992, Late Paleozoic paleogeographic and tectonic evolution of the western U.S. Cordillera, *in* Burchfiel, B.C., et al., eds., The Cordilleran Orogen: Conterminous U.S.: Boulder, Colorado, Geological Society of America, The Geology of North America, v. G-3, p. 57–106.

Molnar, P., 2015, Gravitational instability of mantle lithosphere and core complexes: Tectonics, v. 34, no. 3, p. 478–487, https://doi.org/10.1002/2014TC003808.

Molnar, P., Boos, W.R., and Battisti, D.S., 2010, Orographic controls on climate and paleoclimate of Asia: Thermal and mechanical roles for the Tibetan Plateau: Annual Review of Earth and Planetary Sciences, v. 38, p. 77–102, https://doi.org/10.1146/annurev-earth-040809-152456.

Mookerjee, M., Canada, A., and Fortescue, F.Q., 2016, Quantifying thinning and extrusion associated with an oblique subduction zone: An example from the Rosy Finch shear zone: Tectonophysics, v. 693, p. 290–303, https://doi.org/10.1016/j.tecto.2016.06.012.

Moore, S.W., Madrid, H.B., and Server, G.T., 1983, Results of oil-shale investigations in northeastern Nevada: U.S. Geological Survey Open-File Report 83–586, 18 p.

Mueller, K.J., and Snoke, A.W., 1993, Progressive overprinting of normal fault systems and their role in Tertiary exhumation of the East Humboldt–Wood Hills metamorphic complex northeastern Nevada: Tectonics, v. 12, no. 2, p. 361–371, https://doi.org/10.1029/92TC01967.

Mueller, K.J., Cerveny, P.K., Perkins, M.E., and Snee, L.W., 1999, Chronology of polyphase extension in the Windermere Hills, northeast Nevada: Geological Society of America Bulletin, v. 111, no. 1, p. 11–27, https://doi.org/10.1130/0016-7606(1999)111<0011:COPEIT>2.3.CO;2.

Muffler, L.J.P., 1964, Geology of the Frenchie Creek Quadrangle, North-Central Nevada: U.S. Geological Survey Bulletin 1179, 99 p.

Muntean, J.L., and Henry, C.D., 2007, Preliminary Geologic Map of the Jerritt Canyon Mining District, Elko County, Nevada: Nevada Bureau of Mines and Geology Open-File Report 07– 3, scale 1:24,000.

Nakakuki, T., and Mura, E., 2013, Dynamics of slab rollback and induced back-arc basin formation: Earth and Planetary Science Letters, v. 361, p. 287–297, https://doi.org/10.1016/j.epsl.2012.10.031.

Painter, C.S., Carrapa, B., DeCelles, P.G., Gehrels, G.E., and Thomson, S.N., 2014, Exhumation of the North American Cordillera revealed by multi-dating of Upper Jurassic–Upper Cretaceous foreland basin deposits: Geological Society of America Bulletin, v. 126, no. 11–12, p. 1439–1464, https://doi.org/10.1130/B30999.1.

Palmer, H.C., MacDonald, W.D., and Hayatsu, A., 1991, Magnetic, structural and geochronologic evidence bearing on volcanic sources and Oligocene deformation of ash flow tuffs, northeast Nevada: Journal of Geophysical Research, v. 96, no. B2, p. 2185–2202, https://doi.org/10.1029/90JB02224.

Pape, J.R., Seedorff, E., Baril, T.C., and Thompson, T.B., 2016, Structural reconstruction and age of an extensionally faulted porphyry molybdenum system at Spruce Mountain, Elko County, Nevada: Geosphere, v. 12, no. 1, p. 237–263, https://doi.org/10.1130/GES01249.1.

Platt, J.P., 2007, From orogenic hinterlands to Mediterranean-style back-arc basins: A comparative analysis: Journal of the Geological Society [London], v. 164, p. 297–311, https://doi.org/10.1144/0016-76492006-093.

Poole, F.G., 1974, Flysch deposits of Antler foreland basin, western United States, *in* Dickinson, W.R., ed., Tectonics and Sedimentation: Society of Economic Paleontologists and Mineralogists (SEPM) Special Publication 22, p. 58–82, https://doi.org/10.2110/pec.74.22.0058.

Poole, F.G., and Sandberg, C.A., 1977, Mississippian paleogeography and tectonics in the Western United States, *in* Stewart, J.H., et al., eds., Paleozoic Paleogeography of the Western United States: Bakersfield, California, Society of Economic Paleontologists and Mineralogists (SEPM), Pacific Coast Paleogeography Symposium 1, p. 67–85.

Potter, C.J., Dubiel, R.F., Snee, L.W., and Good, S.C., 1995, Eocene extension of early Eocene lacustrine strata in a complexly deformed Cordilleran hinterland, northwest Utah and northeast Nevada: Geology, v. 23, no. 2, p. 181–184, https://doi.org/10.1130/0091-7613(1995)023<0181:EEOEEL>2.3.CO;2.

Rabillard, A., Jolivet, L., Arbaret, L., Bessière, E., Laurent, V., Menant, A., Augier, R., and Beaudoin, A., 2018, Synextensional granitoids and detachment systems within Cycladic metamorphic core complexes (Aegean Sea, Greece): Toward a regional tectono-magmatic model: Tectonics, v. 37, no. 8, p. 2328–2362, https://doi.org/10.1029/2017TC004697.

Rahl, J.M., McGrew, A.J., and Foland, K.A., 2002, Transition from contraction to extension in the northeastern Basin and Range: New evidence from the Copper Mountains, Nevada: The Journal of Geology, v. 110, no. 2, p. 179–194, https://doi.org/10.1086/338413.

Ramos, V.A., Litvak, V.D., Folguera, A., and Spagnuolo, M., 2014, An Andean tectonic cycle: From crustal thickening to extension in a thin crust (34°–37°SL): Geoscience Frontiers, v. 5, no. 3, p. 351–367, https://doi.org/10.1016/j.gsf.2013.12.009.

Reiners, P.W., Campbell, I.H., Nicolescu, S., Allen, C.M., Hourigan, J.K., Garver, J.I., Mattinson, J.M., and Cowan, D.S., 2005, (U-Th)/(He-Pb) double dating of detrital

zircons: American Journal of Science, v. 305, no. 4, p. 259–311, https://doi.org/10.2475/ajs.305.4.259.

Ressel, M.W., and Henry, C.D., 2006, Igneous geology of the Carlin Trend, Nevada: Development of the Eocene plutonic complex and significance for Carlin-type gold deposits: Economic Geology and the Bulletin of the Society of Economic Geologists, v. 101, p. 347–383, https://doi.org/10.2113/gsecongeo.101.2.347.

Rey, P.F., Teyssier, C., and Whitney, D.L., 2009a, Extension rates, crustal melting, and core complex dynamics: Geology, v. 37, no. 5, p. 391–394, https://doi.org/10.1130/G25460A.1.

Rey, P.F., Teyssier, C., and Whitney, D.L., 2009b, The role of partial melting and extensional strain rates in the development of metamorphic core complexes: Tectonophysics, v. 477, no. 3–4, p. 135–144, https://doi.org/10.1016/j.tecto.2009.03.010.

Ruiz, G.M.H., Seward, D., and Winkler, W., 2004, Detrital thermochronology—A new perspective on hinterland tectonics, an example from the Andean Amazon Basin, Ecuador: Basin Research, v. 16, no. 3, p. 413–430, https://doi.org/10.1111/j.1365-2117.2004.00239.x.

Sanford, R.F., 2005, Geology and Stratigraphy of the Challis Volcanic Group and Related Rocks, Little Wood River Area, South-Central Idaho, with a Section on Geochronology by Lawrence W. Snee: U.S. Geological Survey Bulletin 2064-II, 22 p.

Satarugsa, P., and Johnson, R.A., 2000, Cenozoic tectonic evolution of the Ruby Mountains metamorphic core complex and adjacent valleys, northeastern Nevada: Rocky Mountain Geology, v. 35, no. 2, p. 205–230, https://doi.org/10.2113/35.2.205.

Saylor, J.E., Stockli, D.F., Horton, B.K., Nie, J., and Mora, A., 2012, Discriminating rapid exhumation from syndepositional volcanism using detrital zircon double dating: Implications for the tectonic history of the Eastern Cordillera, Colombia: Geological Society of America Bulletin, v. 124, no. 5/6, p. 762–779, https://doi.org/10.1130/B30534.1.

Schemmel, F., Mikes, T., Rojay, B., and Mulch, A., 2013, The impact of topography on isotopes in precipitation across the Central Anatolian Plateau (Turkey): American Journal of Science, v. 313, no. 2, p. 61–80, https://doi.org/10.2475/02.2013.01.

Schmauder, G.C., Arehart, G.B., and Donelick, R.A., 2005, Thermal and chemical profiling of the Bald Mountain district, White Pine County, Nevada, *in* Rhoden, H.N., et al., eds., Window to the World: Geological Society of Nevada Symposium 2005: Reno, Nevada, Geological Society of Nevada, p. 531–542.

Seymour, R.S., 1980, Petrology and Geochemistry of the Coffeepot Stock, N.E. Nevada: A record of crystallization history and hydrothermal fluid migrations [M.S. thesis]: Eugene, Oregon, University of Oregon, 273 p.

Shuster, D.L., Flowers, R.M., and Farley, K.A., 2006, The influence of natural radiation damage on helium diffusion kinetics in apatite: Earth and Planetary Science Letters, v. 249, no. 3–4, p. 148–161, https://doi.org/10.1016/j.epsl.2006.07.028.

Silitonga, P.H., 1974, Geology of part of the Kittridge Springs Quadrangle, Elko County, Nevada [M.S. thesis]: Golden, Colorado, Colorado School of Mines, 88 p.

Smith, J.F., and Ketner, K.B., 1976, Stratigraphy of post-Paleozoic rocks and summary of resources in the Carlin-Piñon Range area, Nevada: U.S. Geological Survey Professional Paper 867-B, p. B1–B48.

Smith, J.F., Ketner, K., Hernandez, G.X., Harris, A.G., Stamm, R.G., and Smith, M.C., 1990, Geologic Map of the Summer Camp Quadrangle and Part of the Black Butte Quadrangle, Elko County, Nevada: U.S. Geological Survey Miscellaneous Investigations Series Map I-2097, scale 1:24,000.

Smith, M.E., Carroll, A.R., Jicha, B.R., Cassel, E.J., and Scott, J.J., 2014, Paleogeographic record of Eocene Farallon slab rollback beneath western North America: Geology, v. 42, no. 12, p. 1039–1042, https://doi.org/10.1130/G36025.1.

Smith, M.E., Cassel, E.J., Jicha, B.R., Singer, B.S., and Canada, A.S., 2017, Hinterland drainage closure and lake formation in response to middle Eocene Farallon slab removal, Nevada, U.S.A.: Earth and Planetary Science Letters, v. 479, p. 156–167, https://doi.org/10.1016/j.epsl.2017.09.023.

Snell, K.E., Koch, P.L., Druschke, P., Foreman, B.Z., and Eiler, J.M., 2014, High elevation of the 'Nevadaplano' during the Late Cretaceous: Earth and Planetary Science Letters, v. 386, p. 52–63, https://doi.org/10.1016/j.epsl.2013.10.046.

Snoke, A.W., and Miller, D.M., 1988, Metamorphic and tectonic history of the northeastern Great Basin, *in* Ernst, W.G., ed., Metamorphism and Crustal Evolution of the Western United States: Englewood Cliffs, New Jersey, Prentice Hall, p. 606–648.

Solomon, B.J., McKee, E.H., and Andersen, D.W., 1979, Stratigraphy and depositional environments of Paleogene rocks near Elko, Nevada, *in* Armentrout, J.M., et al., eds., Cenozoic Paleogeography of the Western United States: Bakersfield, California, Pacific Section, Society of Economic Paleontologist and Mineralogists (SEPM), Pacific Coast Paleogeography Symposium 3, p. 75–88.

Sternai, P., Jolivet, L., Menant, A., and Gerya, T., 2014, Driving the upper plate surface deformation by slab rollback and mantle flow: Earth and Planetary Science Letters, v. 405, p. 110–118, https://doi.org/10.1016/j.epsl.2014.08.023.

Stewart, J.H., and Carlson, J.E., 1981, Geologic Map of Nevada G81386: U.S. Geological Survey and Nevada Bureau of Mines and Geology, scale 1:500,000, https://doi.org/10.3133/70046281.

Stockli, D.F., 2005, Application of low-temperature thermochronometry to extensional tectonic settings: Reviews in Mineralogy and Geochemistry, v. 58, no. 1, p. 411–448, https://doi.org/10.2138/rmg.2005.58.16.

Stockli, D.F., Farley, K.A., and Dumitru, T.A., 2000, Calibration of the apatite (U-Th)/He thermochronometer on an exhumed fault block, White Mountains, California: Geology, v. 28, no. 11, p. 983–986, https://doi.org/10.1130/0091-7613(2000)28<983:COTAHT>2.0.CO;2.

Thomson, K.D., Stockli, D.F., Clark, J.D., Puigdefàbregas, C., and Fildani, A., 2017, Detrital zircon (U-Th)/(He-Pb) double-dating constraints on provenance and foreland basin evolution of the Ainsa Basin, south-central Pyrenees, Spain: Tectonics, v. 36, no. 7, p. 1352–1375, https://doi.org/10.1002/2017TC004504.

Thorman, C.H., and Snee, L.W., 1988, Thermochronology of metamorphic rocks in the Wood Hills and Pequop Mountains, northeastern Nevada: Geological Society of America Abstracts with Programs, v. 20, p. A18.

Trexler, J.H., Cashman, P.H., Snyder, W.S., and Davydov, V.I., 2004, Late Paleozoic tectonism in Nevada: Timing, kinematics, and tectonic significance: Geological Society of America Bulletin, v. 116, no. 5–6, p. 525–538, https://doi.org/10.1130/B25295.1.

Vandenberghe, N., Hilgen, F.J., and Speijer, R.P., 2012, The Paleogene period, *in* Gradstein, F.M., et al., eds., The Geologic Time Scale 2012: Amsterdam, Netherlands, Elsevier, p. 855–921, https://doi.org/10.1016/B978-0-444-59425-9.00028-7.

Wells, M.L., 1997, Alternating contraction and extension in the hinterlands of orogenic belts: An example from the Raft River Mountains, Utah: Geological Society of America Bulletin, v. 109, no. 1, p. 107–126, https://doi.org/10.1130/0016-7606(1997)109<0107:ACAEIT>2.3.CO;2.

Wells, M.L., and Hoisch, T.D., 2008, The role of mantle delamination in widespread Late Cretaceous extension and magmatism in the Cordilleran orogen, western United States: Geological Society of America Bulletin, v. 120, no. 5–6, p. 515–530, https://doi.org/10.1130/B26006.1.

Wells, M.L., Dallmeyer, R.D., and Allmendinger, R.W., 1990, Late Cretaceous extension in the hinterland of the Sevier thrust belt, northwestern Utah and southern Idaho: Geology, v. 18, no. 10, p. 929–933, https://doi.org/10.1130/0091-7613(1990)018<0929:LCEITH>2.3.CO;2.

Wells, M.L., Hoisch, T.D., Cruz-Uribe, A.M., and Vervoort, J.D., 2012, Geodynamics of synconvergent extension and tectonic mode switching: Constraints from the Sevier-Laramide orogen: Tectonics, v. 31, no. 1, TC1002, https://doi.org/10.1029/2011TC002913.

White, E.J., Cassel, E.J., Anfinson, O.A., and Henry, C.D., 2016, Heavy mineral analysis of Eocene sediments deposited on the high-elevation North American Cordilleran Plateau: Geological Society of America Abstracts with Programs, v. 48, no. 6, paper 24-4, https://doi.org/10.1130/abs/2016RM-276242.

Whitney, D., and Dilek, Y., 1997, Core complex development in central Anatolia, Turkey: Geology, v. 25, no. 11, p. 1023–1026, https://doi.org/10.1130/0091-7613(1997)025<1023:CCDICA>2.3.CO;2.

Whitney, D.L., Teyssier, C., Rey, P., and Buck, W.R., 2013, Continental and oceanic core complexes: Geological Society of America Bulletin, v. 125, no. 3–4, p. 273–298, https://doi.org/10.1130/B30754.1.

Wildman, M., Brown, R., Beucher, R., Persano, C., Stuart, F., Gallagher, K., Schwanethal, J., and Carter, A., 2016, The chronology and tectonic style of landscape evolution along the elevated Atlantic continental margin of South Africa resolved by joint apatite fission track and (U-Th-Sm)/He thermochronology: Tectonics, v. 35, no. 3, p. 511–545, https://doi.org/10.1002/2015TC004042.

Wolfe, M.R., and Stockli, D.F., 2010, Zircon (U-Th)/He thermochronometry in the KTB drill hole, Germany, and its implications for bulk He diffusion kinetics in zircon: Earth and Planetary Science Letters, v. 295, no. 1–2, p. 69–82, https://doi.org/10.1016/j.epsl.2010.03.025.

Wright, J.E., and Snoke, A.W., 1993, Tertiary magmatism and mylonitization in the Ruby–East Humboldt metamorphic core complex, northeastern Nevada: U-Pb geochronology and Sr, Nd, and Pb isotope geochemistry: Geological Society of America Bulletin, v. 105, no. 7, p. 935–952, https://doi.org/10.1130/0016-7606(1993)105<0935:TMAMIT>2.3.CO;2.

Yonkee, W.A., Dehler, C.D., Link, P.K., Balgord, E.A., Keeley, J.A., Hayes, D.S., Wells, M.L., Fanning, C.M., and Johnston, S.M., 2014, Tectono-stratigraphic framework of Neoproterozoic to Cambrian strata, west-central U.S.: Protracted rifting, glaciation, and evolution of the North American Cordilleran margin: Earth-Science Reviews, v. 136, p. 59–95, https://doi.org/10.1016/j.earscirev.2014.05.004.

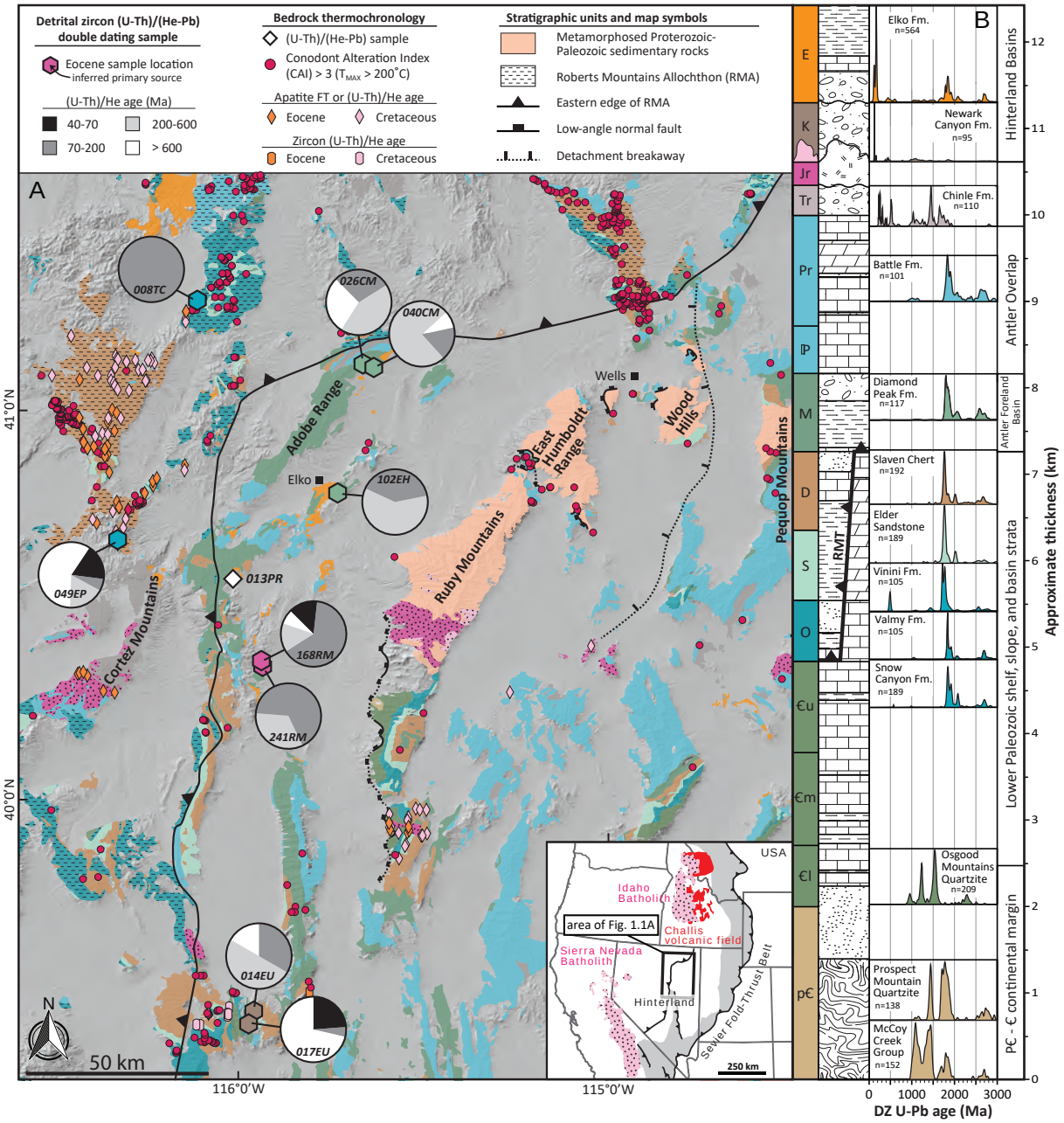
Detrital zircon (U-Th)/(He-Pb) double dating sample
Eocene sample location
inferred primary source
(U-Th)/He age (Ma)
40-70
200-600
70-200
> 600
Bedrock thermochronology
(U-Th)/(He-Pb) sample
Conodont Alteration Index (CAI) > 3 (T_MAX > 200°C)
Apatite FT or (U-Th)/He age
Eocene
Cretaceous
Zircon (U-Th)/He age
Eocene
Cretaceous
Stratigraphic units and map symbols
Metamorphosed Proterozoic-Paleozoic sedimentary rocks
Roberts Mountains Allochthon (RMA)
Eastern edge of RMA
Low-angle normal fault
Detachment breakaway
A
008TC
026CM
040CM
102EH
049EP
013PR
168RM
241RM
014EU
017EU
Adobe Range
Elko
Wells
East Humboldt Range
Wood Hills
Pequop Mountains
Ruby Mountains
Cortez Mountains
RMT
41°0'N
40°0'N
116°0'W
115°0'W
N
50 km
USA
Idaho Batholith
area of Fig. 1.1A
Challis volcanic field
Sierra Nevada Batholith
Hinterland
Sevier Fold-Thrust Belt
250 km
B
E
K
Jr
Tr
Pr
P
M
D
S
O
€u
€m
€l
p€
Elko Fm. n=564
Newark Canyon Fm. n=95
Chinle Fm. n=110
Battle Fm. n=101
Diamond Peak Fm. n=117
Slaven Chert n=192
Elder Sandstone n=189
Vinini Fm. n=105
Valmy Fm. n=105
Snow Canyon Fm. n=189
Osgood Mountains Quartzite n=209
Prospect Mountain Quartzite n=138
McCoy Creek Group n=152
Hinterland Basins
Antler Overlap
Antler Foreland Basin
Lower Paleozoic shelf, slope, and basin strata
P€ - € continental margin
Approximate thickness (km)
0
1000
2000
3000
DZ U-Pb age (Ma)

Figure 1.1. (A) Simplified geologic map of northeastern Nevada with (U-Th)/(He-Pb) sample locations and He age populations. Binned He ages exclude volcanic grains. Distribution of map units is from Stewart and Carlson (1981), Smith et al. (1990), Camilleri and Chamberlain (1997), Muntean and Henry (2007), Colgan et al. (2010), and Lund Snee et al. (2016); conodont color alteration indices are from Harris and Crafford (2007); bedrock zircon and apatite fission track (FT) and (U-Th)/He thermochronology is from Cline et al. (2005), Schmauder et al. (2005), Colgan et al. (2010), and Long et al. (2015); location of Roberts Mountains thrust (RMT) is from Long (2012); location of normal faults and detachment breakaway are from Camilleri and Chamberlain (1997), Colgan et al. (2010), and Camilleri et al. (2017). Colors of map units and hexagons of double dating sample localities correspond to stratigraphy in B. Inset map: overview of batholiths, Challis volcanic field, and thrust belts from Long (2012), Konstantinou et al. (2013), and DeCelles and Graham (2015). (B) Generalized stratigraphy of Precambrian–Eocene strata in eastern Nevada modified from Camilleri and Chamberlain (1997). Detrital zircon (DZ) geochronology for Precambrian–Paleozoic strata is from Gehrels and Pecha (2014), Yonkee et al., (2014), and Linde et al. (2016) and geochronology for the Newark Canyon Formation is from Druschke et al. (2011). Time scale abbreviations: p€—Precambrian, €l—lower Cambrian, €m—middle Cambrian, €u—upper Cambrian, O—Ordovician, S—Silurian, D—Devonian, M—Mississippian, P—Pennsylvanian, Pr—Permian, Tr—Triassic, Jr—Jurassic, K—Cretaceous, E—Eocene.

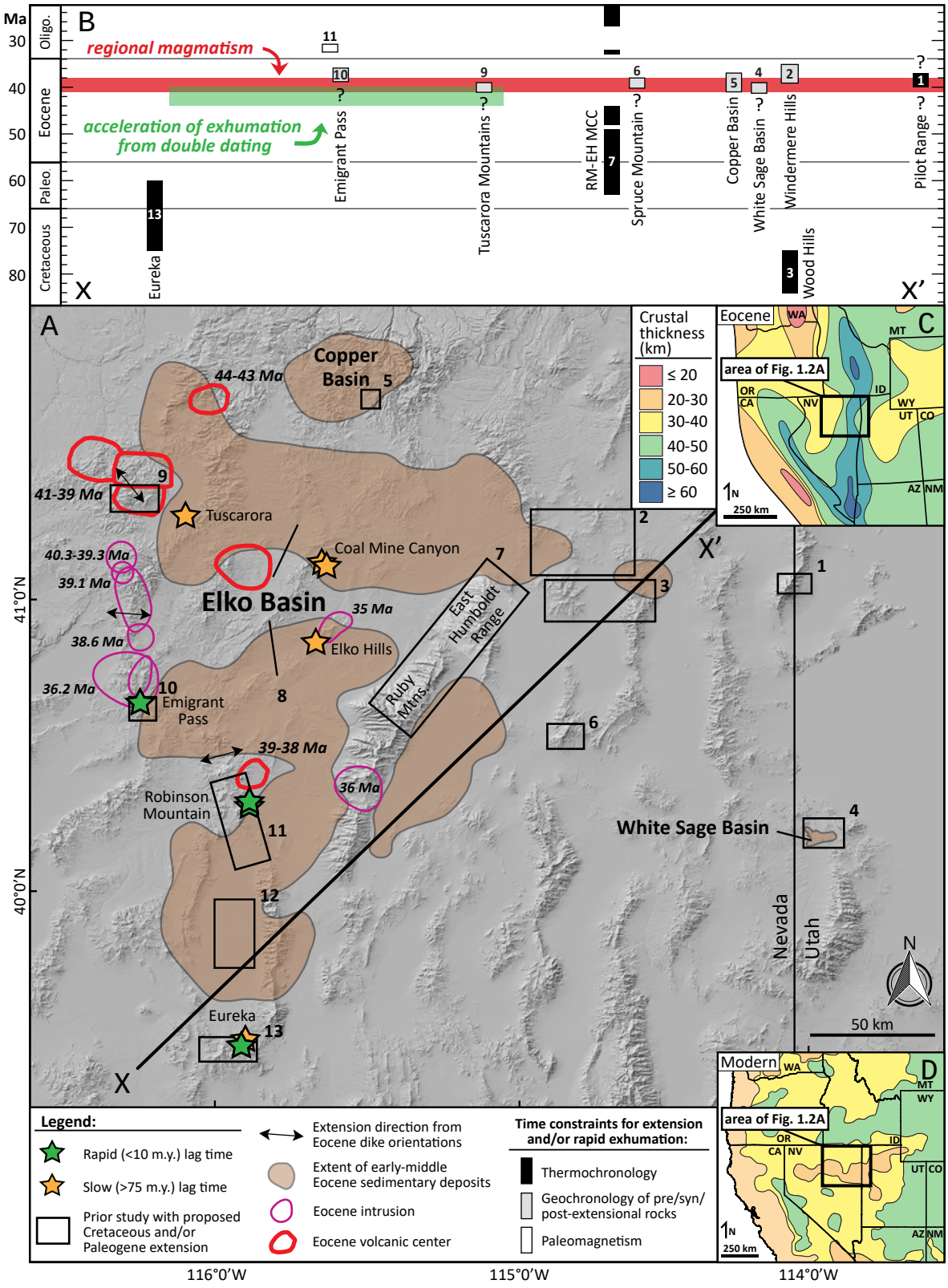
B
Ma
30
40
50
60
70
80
Oligo.
Eocene
Paleo.
Cretaceous
regional magmatism
acceleration of exhumation from double dating
X
X'
Eureka
Emigrant Pass
Tuscarora Mountains
RM-EH MCC
Spruce Mountain
Copper Basin
White Sage Basin
Windermere Hills
Wood Hills
Pilot Range
A
Copper Basin
44-43 Ma
41-39 Ma
Tuscarora
Coal Mine Canyon
40.3-39.3 Ma
39.1 Ma
Elko Basin
35 Ma
Elko Hills
38.6 Ma
36.2 Ma
Emigrant Pass
East Humboldt Range
Ruby Mtns.
39-38 Ma
36 Ma
Robinson Mountain
White Sage Basin
Eureka
Nevada
Utah
41°0'N
40°0'N
116°0'W
115°0'W
114°0'W
50 km
N
Crustal thickness (km)
≤ 20
20-30
30-40
40-50
50-60
≥ 60
Eocene
Modern
C
D
area of Fig. 1.2A
WA
MT
OR
CA
NV
ID
WY
UT
CO
AZ
NM
250 km
Legend:
Rapid (<10 m.y.) lag time
Slow (>75 m.y.) lag time
Prior study with proposed Cretaceous and/or Paleogene extension
Extension direction from Eocene dike orientations
Extent of early-middle Eocene sedimentary deposits
Eocene intrusion
Eocene volcanic center
Time constraints for extension and/or rapid exhumation:
Thermochronology
Geochronology of pre/syn/post-extensional rocks
Paleomagnetism

Figure 1.2. (A) Overview map of select tectonic features in northeastern Nevada. Areal extent of hinterland basins in northeastern Nevada is from Smith et al. (2017); Eocene volcanic centers are from Henry et al. (2011); Eocene intrusions and dike orientations are from Henry et al. (2001); Ressel and Henry (2006); and du Bray (2007). (B) Time constraints for previously proposed Cretaceous–Paleogene rapid exhumation and extension in northeastern Nevada (numbers correspond to field localities in Table 1). RM-EH MCC—Ruby Mountains-East Humboldt Range metamorphic core complex. (C) Palinspastic and paleoisopach reconstruction of Eocene crustal thickness from Coney and Harms (1984). (D) Simplified map of modern crustal thickness from Gilbert (2012). State abbreviations: WA—Washington, OR—Oregon, CA—California, NV—Nevada, ID—Idaho, MT—Montana, WY—Wyoming, UT—Utah, CO—Colorado, AZ—Arizona, NM—New Mexico.

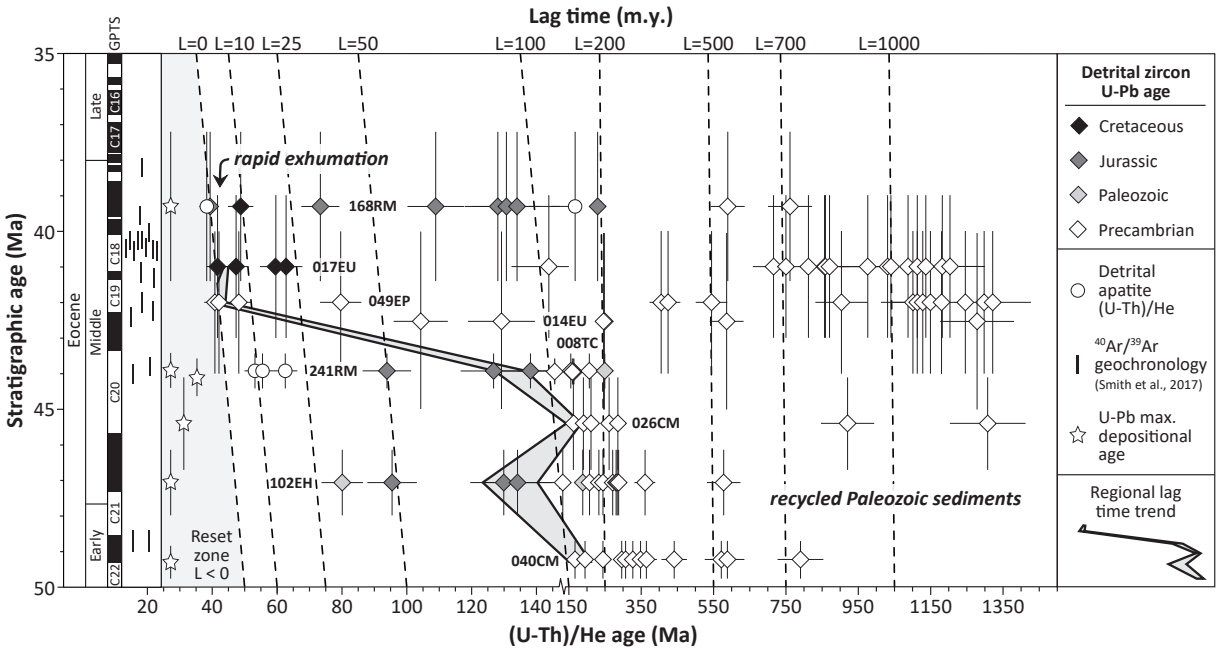

Figure 1.3. Lag time (*L*) of double-dated detrital zircon and detrital apatite plotted with respect to stratigraphic ages from single crystal sanidine $^{40}Ar/^{39}Ar$ weighted mean ages of tuffs (Smith et al., 2017) and U-Pb maximum depositional ages. The youngest two He ages in each sample that overlap within analytical uncertainty are connected for lag-time analysis (Saylor et al., 2012). Volcanic grains were excluded from lag-time analysis. Note change in (U-Th)/He scale at 150 Ma. Geomagnetic polarity timescale (GPTS 2012) is from Vandenberghe et al. (2012).

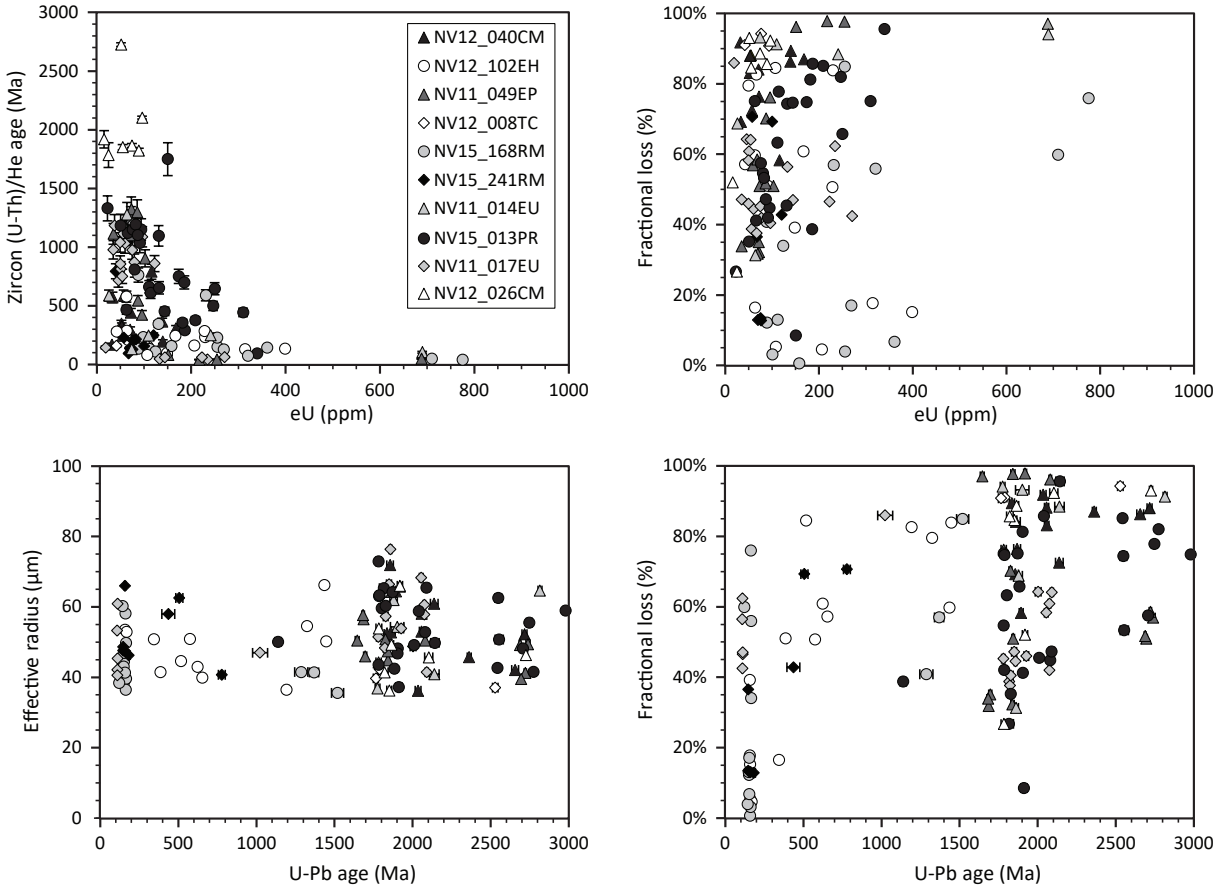

Figure 1.4. Detrital zircon U-Pb and (U-Th)/He results for the Elko Basin and Mississippian Diamond Peak Formation (NV15-013PR) showing the relationships among cooling age (Ma), effective uranium content (eU), fractional helium loss (%), effective radius (μm), and crystallization age (Ma).

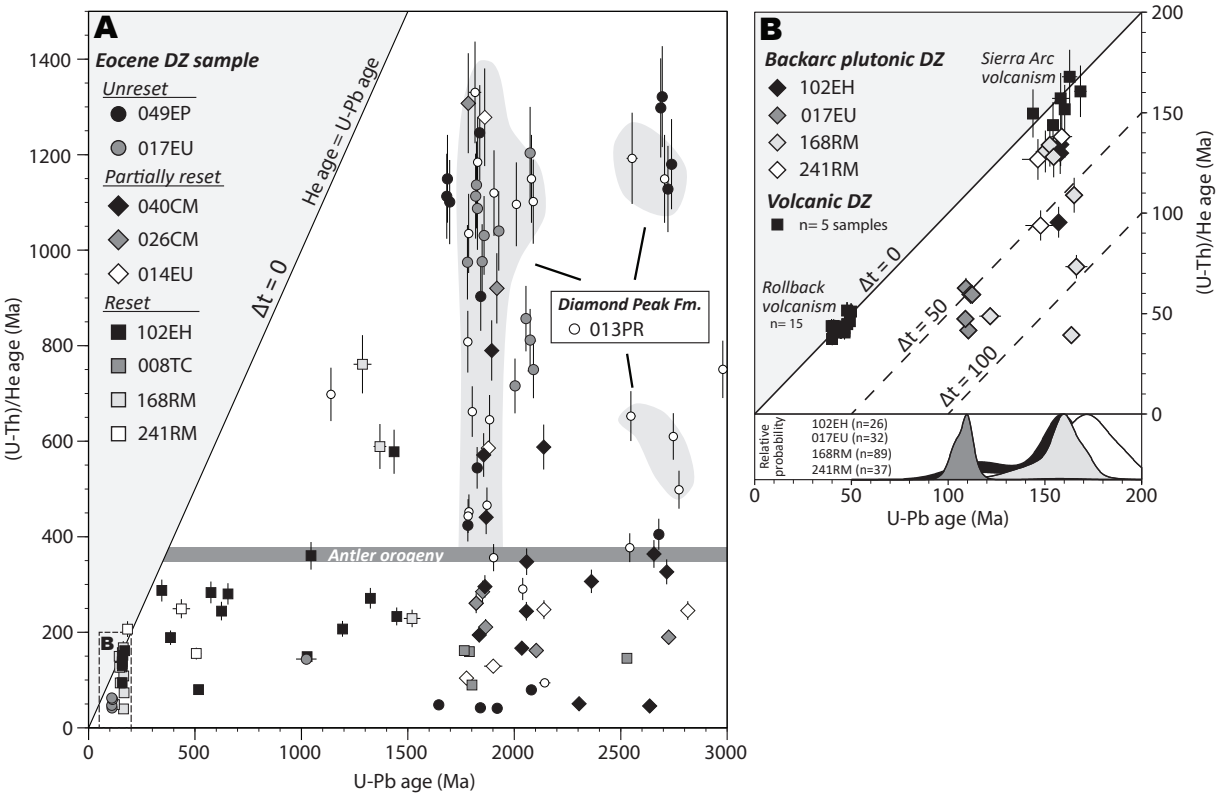

Figure 1.5. (A) (U-Th)/(He-Pb) double-dated detrital zircon (DZ) grains extracted from Eocene sedimentary rocks. The Δt value is the difference between crystallization and cooling age for the same zircon grain. Samples are grouped based on the following: most zircon grains in each sample are inferred to be reset after the Antler orogeny (or are plutonic in origin; squares), most were not reset during the Antler orogeny (circles), or approximately half of all zircon grains were reset during the Antler orogeny (diamonds). Thermal signature of the Mississippian Diamond Peak Formation is drawn from (U-Th)/(He-Pb) double-dated grains (white circles) extracted from a sample collected in the Pinon Range (Fig. 1A). (B) Double-dated detrital zircon grains that are interpreted to be sourced from proximal plutonic rocks or volcanic rocks.

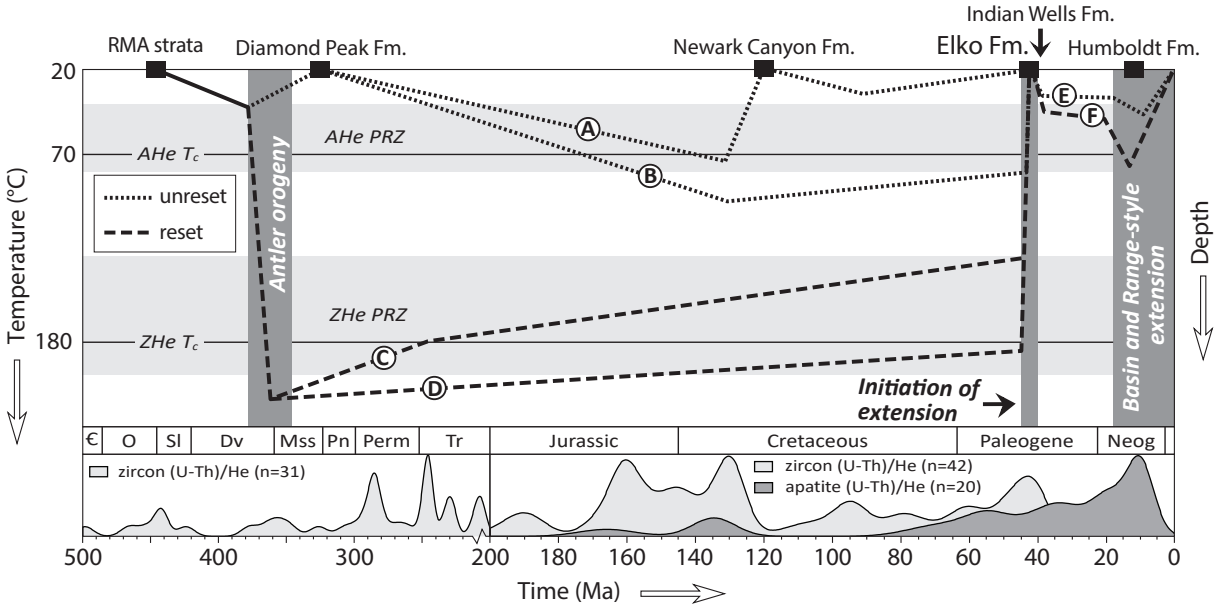

Figure 1.6. Schematic cartoon depicting four potential cooling trajectories that can explain the provenance and predepositional cooling histories of Elko Formation zircon grains (A–D) as well as two hypothetical post-Eocene cooling histories (E and F). Detrital zircon and apatite (U-Th)/He age (ZHe, AHe) kernel density estimates are for grains extracted from the Elko Formation. Timing of the Antler orogeny and Basin and Range-style extension from Dickinson (2006). RMA—Roberts Mountains Allochthon; PRZ—partial retention zone; T_c—closure temperature. Time scale abbreviations: €—Cambrian, O—Ordovician, Sl—Silurian, Dv—Devonian, Mss—Mississippian, Pn—Pennsylvanian, Perm—Permian, Tr—Triassic, Jr—Jurassic, Neog—Neogene.

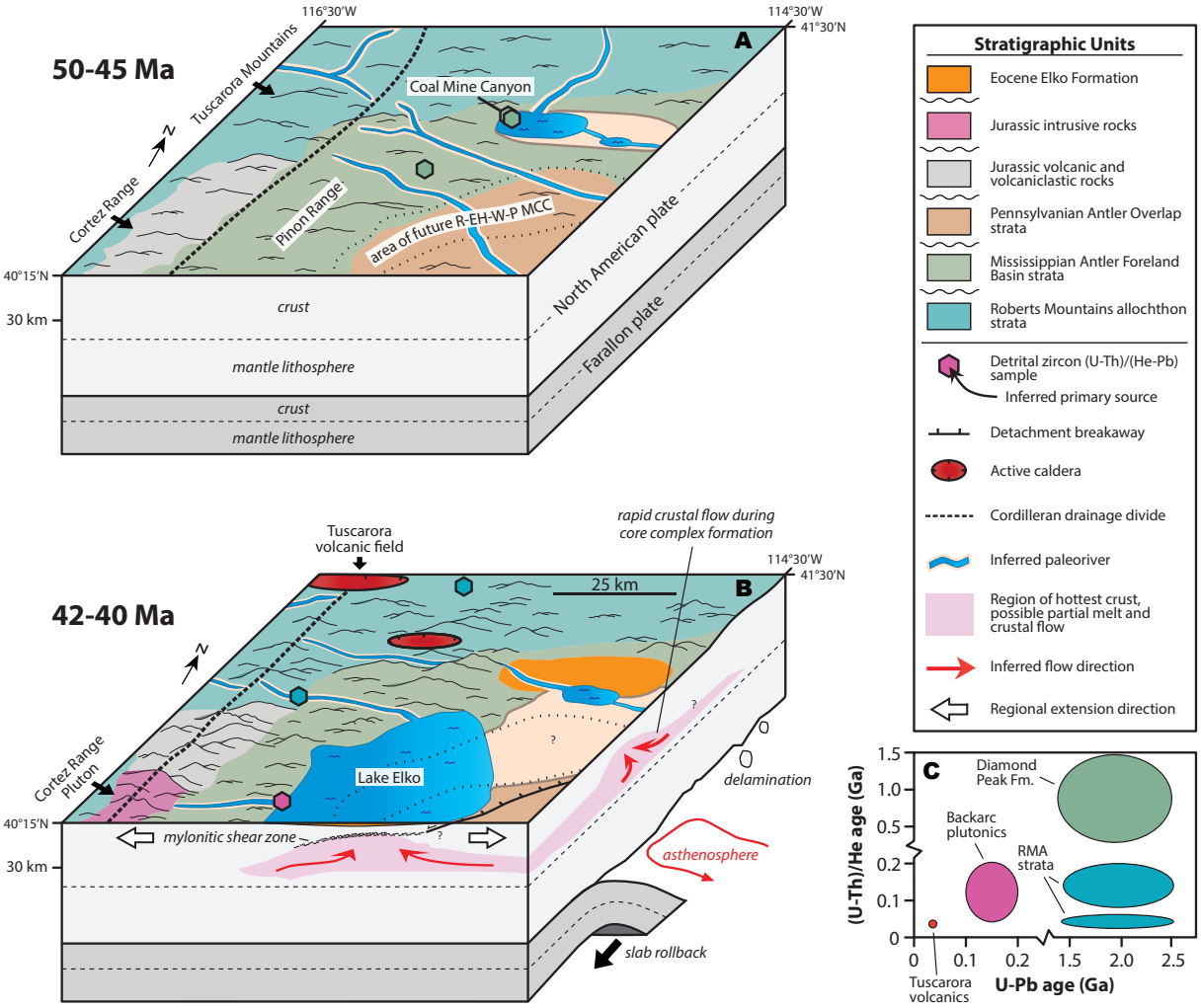

Figure 1.7. Schematic block diagrams of tectonic and paleogeographic evolution of the Elko Basin during (A) early–middle Eocene, and (B) late–middle Eocene deposition of the Elko Formation. Paleohydrology is simplified from Smith et al. (2017). Topography is not drawn to scale. Crustal-flow region and direction and paleo-Moho depth modified from Litherland and Klemperer (2017). R-EH-W-P—Ruby Mountains–East Humboldt Range–Wood Hills–Pequop Mountains metamorphic core complex. (C) Anticipated (U-Th)/(He-Pb) double-dating pattern for grains derived from five predominant sediment sources contributing to the Elko Basin. RMA—Roberts Mountains Allochthon.

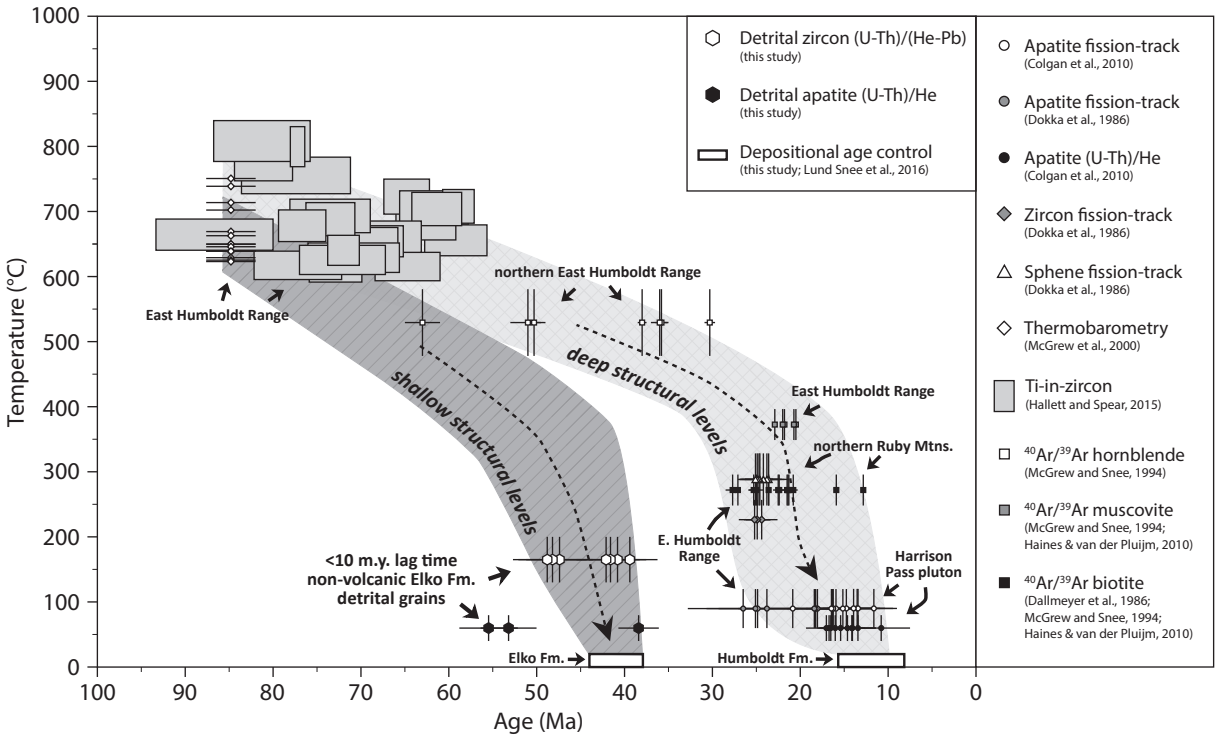

Figure 1.8. Summary of thermochronologic and thermobarometric constraints for the northern East Humboldt Range and Ruby Mountains as well as low-lag-time detrital grains extracted from the Elko Formation. Large arrows and schematic cooling envelopes show interpreted paths for shallow and deep structural levels within the Ruby Mountains–East Humboldt Range metamorphic core complex.

TABLE 1.1. SUMMARY OF PRIOR EVIDENCE FOR SYNOROGENIC EXTENSION IN NORTHEASTERN NEVADA

Location†	Age (Ma)	Displacement	Method(s)	Reference(s)
Pilot Range				
1	≥40 to ≤37	E-W extension, detachment faulting	Biotite K-Ar and zircon U-Pb, geologic mapping	Miller et al., 1987
Windermere Hills				
2	39–35	13–25 km displacement along an E-rooted low-angle normal fault system	Biotite and sanidine $^{40}Ar/^{39}Ar$, geologic mapping	Mueller and Snoke, 1993; Mueller et al. 1999
Pequop Mountains and Wood Hills				
3	84–75	≤10 km exhumation by top-to-the-W to NW extension along the Pequop normal fault	Sphene U-Pb† and muscovite, biotite, and amphibole $^{40}Ar/^{39}Ar$*, structural analysis	Thorman and Snee, 1988; Camilleri, 1996; †Camilleri and Chamberlain, 1997
White Sage Basin				
4	≤63 to ≥39	~1 km of displacement along high-angle N-S-striking faults	Molluscan paleontology†, biotite and hornblende $^{40}Ar/^{39}Ar$† of volcanic rocks, geologic mapping	Potter et al., 1995; †Dubiel et al., 1996
Copper Basin				
5	41–37	8–12 km displacement along NE-striking low-angle fault	Biotite and sanidine $^{40}Ar/^{39}Ar$, structural analysis	Rahl et al., 2002
Spruce Mountain				
6	?–38	~5.4 km of E-W extension	Zircon U-Pb dating of volcanic rocks, structural analysis	Pape et al., 2016
Ruby Mountains-East Humboldt Range				
7	63–49† 48–44‡ 33–32* 27–21†*	≥30 km of exhumation§ partially accommodated by detachment faulting	Hornblende‡†, muscovite†, biotite*†, and k-feldspar† $^{40}Ar/^{39}Ar$; sphene, zircon, and apatite fission track^	‡*Dallmeyer et al., 1986; ^Dokka et al., 1986; †McGrew and Snee, 1994; §Henry et al., 2011
Elko Basin				
8	42–39† 46.1–39‡ 40–38.5†	E-W to NW-SE extension	Stratigraphy†, geologic mapping†‡, sanidine $^{40}Ar/^{39}Ar$†‡, apatite fission track*	†Haynes, 2003; *Cline et al., 2005; ‡Henry, 2008
Tuscarora Mountains				
9	≥40 to 38	Regional NW-SE extension	Sanidine $^{40}Ar/^{39}Ar$ of generally NE-striking dikes	Henry and Boden, 1997; Henry et al., 1999, 2001
Emigrant Pass				
10	≥38 to 36	Regional extension oriented NW-SE	Sanidine and hornblende $^{40}Ar/^{39}Ar$† of generally N-S striking dikes, geologic mapping.	†Henry and Faulds, 1999; Henry et al., 2001
Robinson Mountain				
11	32.5–30.8	Down-to-the-SW extension	Paleomagnetism, AMS, and $^{40}K/^{39}Ar$ of tuffs	Palmer et al., 1991

Diamond Valley and Railroad Valley				
12	66–?	2.4–4.5 km displacement along W-dipping low-angle faults*	Seismic interpretation	Effimoff and Pinezich, 1981*; Liberty et al., 1994
Eureka				
13	75–60	2–4 km of throw along down-to-the-W normal faults	Zircon and apatite (U-Th)/He and fission track, structural analysis	Long et al., 2015

Note: Symbols in reference column refer to corresponding symbols within each row.
†number corresponds to field locality shown in Fig. 2

TABLE 1.2. LAG TIME ANALYSIS

Sample	Depositional Age (Ma)	*N* (zircon)	*N* (apatite)	Lag time (*L*) <10 (m.y.)	10-100 (m.y.)	100-200 (m.y.)	>250 (m.y.)
NV15-168RM	41.4-37.2[§]	10	2	25%	42%	17%	17%
NV11-017EU	43.0-39.0*[†]	18	-	11%	17%	6%	67%
NV11-049EP	44.0-40.0*[†]	17	-	18%	6%	0%	76%
NV11-014EU	45.0-40.0*[†]	6	-	0%	22%	22%	22%
NV15-241RM	44.4-43.4[§]	6	3	11%	56%	33%	0%
NV12-008TC	44.3-43.6*[§]	3	-	0%	0%	100%	0%
NV11-026CM	46.7-44.1[§]	7	-	0%	0%	43%	57%
NV12-102EH	48.0-46.1[§]	15	9	0%	27%	29%	40%
NV12-040CM	49.8-48.7*[§]	12	-	0%	0%	25%	75%

*Based on Smith et al. (2017) $^{40}Ar/^{39}Ar$ geochronology
[†]Based on stratigraphic correlation (Table S1)
[§]Based on detrital zircon maximum depositional age

CHAPTER II

Eocene Exhumation and Extensional Basin Formation in the Copper Mountains, Nevada, U.S.A.

Accepted Pending Review as:
Canada, A.S., Cassel, E.J., McGrew, A.J., Smith, M.E., Stockli, D.F., Foland, K.A., Jicha, B.R., and Singer B.S., 2019, Eocene exhumation and extensional basin formation in the Copper Mountains, Nevada, U.S.A.: Geosphere, submitted December 5, 2018.

ABSTRACT

Within extended orogens, records that reflect the driving processes and dynamics of early extension are often overprinted by subsequent orogenic collapse. The Copper Mountains of northeastern Nevada preserve an exceptional record of hinterland extensional deformation and high-elevation basin formation, but current geo- and thermochronology is insufficient to relate this to broader structural trends in the region. This extension occurred concurrent with volcanism commonly attributed to Farallon slab removal. We combine thermochronology of both synextensional hanging wall strata and footwall rocks to comprehensively evaluate the precise timing and style of this deformation. Specifically, we apply (U-Th)/(He-Pb) double dating of minerals extracted from Eocene–Oligocene Copper Basin strata with multi-mineral (U-Th)/He and $^{40}Ar/^{39}Ar$ thermochronology of rocks sampled across a ~20 km transect of the Copper Mountains. We integrate basement and detrital thermochronology records to comprehensively evaluate the timing and rates of hinterland extension and basin sedimentation. Cooling and U-Pb crystallization ages show that the Coffeepot Stock, which spans the width of the Copper Mountains, was emplaced at ~109–108 Ma, and then cooled through the $^{40}Ar/^{39}Ar$ muscovite and biotite closure temperatures by ~90 Ma, the zircon (U-Th)/He closure temperature between ~90 and 70 Ma, and the apatite (U-Th)/He closure temperature between 43 and 40 Ma. Detrital apatite and zircon (U-Th)/(He-Pb) double dating of late Eocene fluvial and lacustrine strata of the Dead Horse

Formation and early Oligocene fluvial strata of the Meadow Fork Formation, both deposited in Copper Basin, shows that Early Cretaceous age detrital grains have a cooling history that is analogous to proximal intrusive rocks of the Coffeepot Stock. Cooling and depositional ages for Copper Basin strata reveal rapid exhumation of proximal source terranes (cooling rate of ~37 °C/m.y.) at ca. 38 Ma, in which 8–12 km of slip along the low-angle Copper Creek normal fault exhumed the Coffeepot Stock in the footwall. Late Eocene–early Oligocene slip along this fault and an upper fault splay, the Meadow Fork Fault, created a half graben that accommodated ~1.4 km of volcaniclastic strata, including ~20 m of lacustrine strata that preserve the renowned Copper Basin flora. Single crystal sanidine $^{40}Ar/^{39}Ar$ geochronology of interbedded tuffs in Copper Basin constrains the onset of rapid exhumation to 38.0 ± 0.9 Ma, indicating that surface-breaching extensional deformation was coincident with intense proximal volcanism. Coarse-grained syndeformational sediments of the Oligocene Meadow Fork Formation were deposited just prior to formation of an extensive regional Oligocene–Miocene unconformity and represent one of the most complete hinterland stratigraphic records of this time. We interpret this history of rapid late Eocene exhumation across the Copper Mountains, coeval volcanism, and subsequent unconformity formation, to reflect dynamic and thermal effects associated with Farallon slab removal. The final phase of extension is recorded by late, high-angle normal faults that cut and rotate the early middle Miocene Jarbidge Rhyolite sequence, deposited unconformably in the hanging wall. These results provide an independent record of episodic Paleogene to Miocene exhumation documented in Cordilleran metamorphic core complexes and establish that substantial extension occurred locally in the hinterland prior to province-wide Miocene extensional break-up.

INTRODUCTION

In the hinterland of the Sevier orogenic belt, from eastern Nevada to western Utah, the potential links between Eocene magmatism, extension, and sedimentation are widely debated (Fig. 2.1; Armstrong, 1982; Axen et al., 1993; McGrew and Snee, 1994; Brooks et al., 1995; Rahl et al., 2002; Henry, 2008; Druschke et al., 2009a). Hinterland deformation in

this area associated with Miocene Basin and Range extension is well documented (e.g., Colgan et al., 2010; Brueseke et al., 2014; Lund Snee et al., 2016; Camilleri et al., 2017), but the importance of an earlier, Eocene or Oligocene, phase of extension is supported by relatively few studies (e.g., Axen et al., 1993; Potter et al., 1995; Rahl et al., 2002; Cline et al., 2005; Long et al., 2018). This uncertainty reflects the absence of quantitative constraints on both the timing and magnitude of Eocene and Oligocene extensional deformation in the Cordilleran hinterland (Henry et al., 2011). During the Paleozoic and Mesozoic, the Sevier hinterland region underwent protracted contractional deformation (Trexler and Nitchman, 1990; Miller and Hoisch, 1995; DeCelles, 2004; Trexler et al., 2004; Long et al., 2014) to form a belt of 50–60-km-thick crust (Coney and Harms, 1984; McGrew et al., 2000) that supported a Paleogene orogenic plateau with elevations of ≥2 km by the Late Cretaceous (Snell et al., 2014) and up to 3.5 km by the late Oligocene (Thorman et al., 1991; Axelrod, 1997; Camilleri and Chamberlain, 1997; Best et al., 2009; Cassel et al., 2014, 2018). From the Paleogene to the early Miocene, a chain of metamorphic core complexes formed across the hinterland, from British Columbia to Arizona, some of which brought middle and lower crustal rocks from depths of ~35–40 km to the surface (Armstrong, 1982; Dokka et al., 1986; Hodges et al., 1992; McGrew and Snee, 1994; Henry et al., 2011; Hallett and Spear, 2014). Well-documented thermochronologic trajectories of multiple Cordilleran metamorphic core complexes suggest that initial metamorphic core complex exhumation occurred during the Late Cretaceous and/or Paleogene (Snoke and Miller, 1988; Wright and Snoke, 1993; Wells, 1997; McGrew et al., 2000), and was potentially aided by the onset of magmatism (MacCready et al., 1997; Bendick and Baldwin, 2009; Smith et al., 2014; 2017; Hallett and Spear, 2015). However, this metamorphic core complex record of partial melting, crustal flow, and exhumation is not clearly reflected in the stratigraphic record (Colgan et al., 2010; Lund Snee et al., 2016; Smith et al., 2017; Canada et al., 2019). Outside or peripheral to the metamorphic core complexes, existing structural histories of Paleogene hinterland extension also commonly lack a well-preserved complementary stratigraphic record or constraints on the magnitude and/or timing of deformation (e.g., Camilleri and Chamberlain, 1997; Long et al., 2015; Pape et al., 2016). These uncertainties present a considerable obstacle for

deciphering the spatial partitioning of strain at this time and its implications for the tectonic evolution of the North American Cordilleran hinterland.

Copper Basin, located in the Copper Mountains of northeastern Nevada, is characterized as a half graben that contains ~1.4 km of middle Eocene to early Oligocene volcaniclastic and alluvial-fluvial strata that accumulated during 8–12 km of displacement along the northeast-trending Copper Creek normal fault (Fig. 2.2; Coats, 1964; Axelrod, 1966a; Rahl et al., 2002). Here we present precise measurements of the timing of extension in the Copper Mountains and the implications of this deformation for Eocene tectonics in the Cordilleran hinterland. This is accomplished by integrating (1) multi-mineral $^{40}Ar/^{39}Ar$ (hornblende, biotite, muscovite, and K-feldspar) and (U-Th)/He thermochronology (zircon, titanite, and apatite) of igneous and metamorphic rocks sampled across a structural transect of the Copper Mountains (Fig. 2.1) with (2) (U-Th)/(He-Pb) double dating of detrital apatite and zircon grains from late Eocene–early Oligocene Copper Basin strata (Fig. 2.2), which provides both a U-Pb crystallization age and (U-Th)/He cooling age for each individual grain. These methods show agreement between source exhumation and basin sedimentation trends and permit evaluation of the potential association of hinterland deformation with magmatism. $^{40}Ar/^{39}Ar$ geochronology of abundant tuffs exposed within Copper Basin (Fig. 2.2; e.g., Rahl et al., 2002; Henry et al., 2011; Smith et al., 2017) facilitates basin-wide correlation of strata and depositional age assessment for sediment lag time calculations. Lag time is defined as the difference between the cooling and depositional ages of detrital minerals and can therefore be used to provide quantitative constraints on exhumation trends (e.g., Brandon and Vance, 1992; Garver et al., 1999; Ruiz et al., 2004; Saylor et al., 2012; Thomson et al., 2017; Canada et al., 2019). By combining cooling histories of detrital minerals with depositional ages and bedrock thermochronology of rocks exposed across the Copper Mountains, we constrain the timing and magnitude of Eocene extension in the central Cordilleran hinterland and evaluate the response of this high-elevation landscape to magmatism induced by removal of the Farallon slab and/or progressive delamination of the mantle lithosphere.

GEOLOGIC SETTING

North American Cordilleran Hinterland

The Late Cretaceous to Eocene Cordilleran hinterland is often described as a low exhumation, eroding bedrock highland with low (~2 km) structural relief (Armstrong, 1968; Coney and Harms, 1984; Vandervoort and Schmitt, 1990; Thorman et al., 1991; Long, 2012; Best et al., 2016; Camilleri et al., 2017), where high-magnitude (>1 km throw) surface-breaching normal faults may have been rare until the Miocene (Long, 2019). By combining lower bounds for paleoelevation estimates of 2.0 ± 0.2 km from leaf physiognomic methods in Copper Basin (Wolfe et al., 1998) with upper bound elevation estimates of ~4.2 km (Mix et al., 2011; Chamberlain et al., 2012), Chamberlain et al. (2012) suggested that middle Eocene topographic relief of up to 2.2 km existed in northeastern Nevada. Based on the depth of inferred paleovalleys, Henry (2008) reached an estimate of up to 1.6 km of Eocene relief across this same area, concluding that this reflects deep incision into Paleozoic basement, which was potentially augmented by limited Eocene extension. A pre-Miocene phase of extension is supported by isolated Cretaceous–Eocene hinterland basins and angular unconformities documented within Paleogene strata (Brooks et al., 1995; Dubiel et al., 1996; Mueller et al., 1999; Satarugsa and Johnson, 2000; Henry et al., 2001; Haynes, 2003; Cline et al., 2005; Henry, 2008; Druschke et al., 2009b). Widespread hinterland sedimentation occurred during the Eocene, primarily within several lacustrine-dominated basins that have been largely interpreted to signify extensional basin formation at relatively high elevations (Axelrod, 1966a, 1966b; Rahl et al., 2002; Haynes, 2003; Druschke et al., 2009a). In east-central Nevada, Cretaceous to middle Eocene alluvial and lacustrine rocks of the Sheep Pass Formation are scattered across a 15,000 km^2 area adjacent to the Snake Range metamorphic core complex (Druschke et al., 2009b). Deposition of these sediments is interpreted to reflect accommodation formed during 4 km of throw along the Ninemile fault system, but this deformation is broadly attributed to episodic Late Cretaceous–Oligocene extension (Druschke et al., 2009b). To the north, fluvial and lacustrine rocks of the Elko Formation cover a 23,000 km^2 area adjacent to the Ruby Mountains-East Humboldt Range metamorphic core complex (Coats, 1987; Haynes, 2003), but are not unequivocally diagnostic of

deposition within an extensional basin (Henry, 2008; Smith et al., 2017). Elko Formation strata are interpreted to be locally tilted 10–15° to the southeast prior to eruption of ca. 40–38 Ma ignimbrites, which is inferred to indicate extension contemporaneous with late Eocene magmatism (Brooks et al., 1995; Henry and Faulds, 1999; Haynes, 2003; Hickey et al., 2005). The degree of discordance between Elko Formation strata and overlying volcanic rocks is interpreted to vary across northeastern Nevada (Brooks et al., 1995). This may partly relate to inclined fabrics created through tractional aggradation in pyroclastic debris flows, which may be misinterpreted as bedding (Branney and Kokelaar, 2002). Similar angular unconformities (10–15° westward tilting) in proximal volcanic rocks of the Robinson Mountain volcanic field are interpreted by Lund Snee et al. (2016) to represent a maximum of 1 km of extension. This limited and often enigmatic record of Paleogene crustal deformation across the hinterland hinders development of a clear understanding of the relationship between Eocene accommodation and crustal extension.

Volcanism migrated to the southwest across a >200 km transect of northeastern Nevada from ca. 44 Ma to ca. 38 Ma (Henry and John, 2013) and across a >110 km transect of central Nevada during the ca. 36–18 Ma Great Basin ignimbrite flareup (Best et al., 2009; Henry and John, 2013). The comparatively slow migration of volcanism across central Nevada (~11 km/m.y. compared to ~31 km/m.y. for northeastern Nevada; Henry et al., 2012), in addition to the widespread volcanism in this area, may reflect a major change in subduction geometry (Best et al., 2016) and/or a transition from predominantly slab rollback volcanism to mantle lithosphere delamination (Best et al., 2009, 2016; DeCelles et al., 2009). Calderas associated with this volcanism erupted up to 3000 km^3 of silicic volcanic rocks, some of which can be geochemically correlated over areas exceeding 55,000 km^2 (Best et al., 2009; Cassel et al., 2009; Henry et al., 2012; Henry and John, 2013). In northeastern Nevada, the uneven spatial distribution of these volcanic rocks indicates many of them were deposited in preexisting valleys (Henry, 2008).

Copper Mountains Geology

The Copper Mountains preserve Neoproterozoic to early Paleozoic metasedimentary rocks that record prolonged passive margin sedimentation, tectonic burial, and Cenozoic

extension (Rahl et al., 2002; Crafford, 2008; Linde et al., 2016). This includes phyllite and quartzite of the Neoproterozoic McCoy Creek Group and Neoproterozoic–Cambrian Prospect Mountain Quartzite (Misch and Hazzard, 1962; Woodward, 1967), which form the main bedrock lithologies exposed adjacent to Copper Basin (Fig. 2.1). Rocks of this age are sparsely exposed across northeastern Nevada, but equivalent strata are inferred to be 3 km thick beneath >5 km of Paleozoic strata in the southern Ruby Mountains (Colgan et al., 2010; Pape et al., 2016) and ~3 km thick in the Schell Creek Range of east-central Nevada (Young, 1960; Dechert, 1967; Norman, 2013). In the Copper Mountains, these metasedimentary rocks are overlain by ~1.6 km of shale and limestone of the Ordovician Tennessee Mountain Formation (Bushnell, 1967). Crafford (2008) assigned these strata to the Nolan Belt Domain because they exhibit a complex polyphase deformation history that is distinct from proximal rocks of the same age. Ordovician strata are unconformably overlain by ~1.3 km of conglomerate and limestone of the Pennsylvanian to Permian Sunflower Formation (Bushnell, 1967), deposited within the Antler overlap assemblage, and Mississippian–Permian strata that were emplaced along the Golconda thrust around Early Triassic time (Silberling, 1975; Crafford, 2008). In the Copper Mountains, this sequence of Proterozoic–late Paleozoic passive margin strata is intruded by rocks associated with the Cretaceous Coffeepot intrusive suite, which locally cut Paleozoic thrust faults to the north of Copper Mountain (Fig. 2.1; McGrew et al., 2000; Rahl et al., 2002).

The Coffeepot Stock is one of the largest backarc plutons exposed in northeastern Nevada and part of a series of east-west trending 110–75 Ma Cretaceous granitoids that are exposed near the Nevada-Idaho border (Supplemental Fig. B5; Seymour, 1980; Stewart and Carlson, 1981; Miller et al., 1990; du Bray, 2007). Over 90% of the total volume of the stock is comprised of coarse-grained biotite quartz monzonite, monzogranite, and granodiorite that is locally cut by late-stage alaskitic, aplitic and pegmatitic dikes and veins (Seymour, 1980; Rahl et al., 2002; Supplemental Table B1, Fig. B1). Despite the homogeneity of the stock and lack of assimilated material, geochemical data indicate an inward progression of fractional crystallization that implies crystallization was time-transgressive (Seymour, 1980). At the contact with the Tennessee Mountain Formation, amphibolite facies metamorphism from localized metasomatism formed a broad contact aureole: the Tennessee Mountain skarn

(Lapointe et al., 1991; Rahl et al., 2002). The mineralogy of this skarn is attributed by Coats and McKee (1972) to the relatively high content of hyperfusible material and the high intrusion temperature of Coffeepot Stock magma. Rahl et al. (2002) used high-grade mineral assemblages in this skarn to estimate peak metamorphic pressures of <375 MPa as well as muscovite-bearing granitoids with fibrolitic sillimanite in the structurally-deepest eastern portion of the pluton to record emplacement pressures of ≥220 MPa, indicating emplacement depths of 8–14 km.

The Copper Mountains are separated from Copper Basin by the east-dipping, low-angle Copper Creek and Meadow Fork normal faults (Figs. 2.2–2.3; Rahl et al., 2002). The Copper Creek Fault (CCF) places Cambrian to Ordovician Tennessee Mountain Formation strata in contact with Neoproterozoic–Lower Cambrian rocks of the McCoy Creek Group and Prospect Mountain Quartzite (Rahl et al., 2002). The CCF fault zone is characterized by mylonitized rocks that are locally brecciated and contain slickenlines that imply dip slip towards the southeast (Rahl et al., 2002). The Meadow Fork Fault (MFF) splays off the CCF and separates Meadow Fork Formation strata from the Tennessee Mountain Formation. In the northern part of Copper Basin, Tennessee Mountain Formation strata contain a skarn associated with a granitoid intrusion, both of which were likely transported along the CCF from the Tennessee Mountain area (Fig. 2.1; Rahl et al., 2002).

Stratigraphy of Copper Basin

Copper Basin consists of ~1.4 km of middle Eocene to early Oligocene strata that accumulated in the hanging wall of the Meadow Fork Fault between ca. 43 and 29 Ma (Fig. 2.4; Coats, 1964; Henry, 2008). The age model for these strata integrates new single crystal sanidine $^{40}Ar/^{39}Ar$ geochronology (Henry, 2008; Smith et al., 2017) and legacy biotite $^{40}Ar/^{39}Ar$ ages (Rahl et al., 2002) recalculated to the 28.201 Ma age for Fish Canyon Tuff sanidine (Fig. 2.2; cf. Smith et al., 2017). The middle to late Eocene Dead Horse Formation is comprised of ~1 km of volcaniclastic strata that is dominated by ignimbrites and ash-fall tuffs deposited unconformably on Paleozoic limestone (Fig. 2.4; Rahl et al., 2002). The upper portion of the Dead Horse Formation contains laterally discontinuous beds of tuffaceous sandstone and pebble–cobble conglomerate with planar-tabular and trough cross-bedding and

thin pebble lags (Fig. 2.5). These beds are often scoured at the base, but also contain rippled tops preserved in thin interbeds of siltstone and shale (Fig. 2.5). These characteristics are indicative of channel and overbank deposits of braided streams (e.g., Cassel et al., 2012), which are broadly correlative to basal Elko Formation facies, deposited as paleovalley fill (Henry, 2008; Smith et al., 2017). Conglomerate clast lithology counts show that coarse-grained detritus was primarily derived from volcanic and proximal Precambrian–early Paleozoic metasedimentary rocks (Fig. 2.4). Paleocurrent measurements taken near the Meadow Fork Formation contact suggest that paleoflow was predominantly oriented towards the south during the late Eocene (mean trend 187°; Fig. 2.5). A thin (<25-m-thick) section of tuffaceous siltstone and claystone near the top of the Dead Horse Formation preserves abundant Eocene paleoflora assemblages (e.g., Axelrod, 1966a; 1997), including conifer and alder species (Fig. 2.5) that are interpreted to signify paleoelevations ranging from 1.1 to 2.8 km based on a range of paleoclimate techniques (Axelrod, 1966b; Chase et al., 1998; Wolfe et al., 1998). Mix et al. (2011) used $\delta^{18}O$ values of smectites extracted from Dead Horse Formation strata to estimate hinterland elevations of up to ~3.4 km by the late Eocene. In comparison, by using δD values of volcanic glasses from across eastern Nevada and western Utah, Cassel et al. (2014, 2018) estimate Eocene and early Oligocene hinterland plateau elevations of 2.7–3.1 km. Two tuff samples collected from the Dead Horse Formation contain glass with δD values of -90.6‰ ± 4.0‰ and -100.7‰ ± 2.5‰, indicating evaporative enrichment of meteoric waters in a fluctuating profundal lacustrine environment (cf. Smith et al., 2017; Cassel and Breecker, 2018).

The late Eocene to early Oligocene Meadow Fork Formation consists of ~400 m of coarse-grained fluvial and alluvial strata and interbedded tuffs that rest conformably above Dead Horse Formation strata (Fig. 2.4; Coats, 1964; Henry, 2008). The Meadow Fork Formation is distinguished by poorly sorted, non-traction-structured pebble–cobble conglomerate beds that contain angular to sub-rounded clasts of marble, quartzite, phyllite, and granite up to 1 m in diameter (Fig. 2.6). All of the strata within Copper Basin thicken to the northwest, towards the Meadow Fork Fault, but this is most pronounced within the coarse-grained clastic strata of the Meadow Fork Formation. These stratal geometries and

facies characteristics are interpreted to signify deposition in debris-flow-dominated alluvial fans that transported local detritus from the relatively steep northwestern margin of the basin.

MATERIALS AND METHODS

Detrital Zircon and Apatite (U-Th)/(He-Pb) Double Dating

Detrital (U-Th)/(He-Pb) double dating refers to the process of obtaining a U-Pb crystallization age and a (U-Th)/He cooling age for the same detrital grain (Reiners et al., 2005). This combined history of crystallization and cooling permits discrimination between potential sources with similar U-Pb age populations as well as quantification of source exhumation rates (Saylor et al., 2012; Painter et al., 2014; Thomson et al., 2017). Here we apply (U-Th)/(He-Pb) double dating of both detrital zircon and detrital apatite to determine the provenance of detrital minerals and assess the timing of high-magnitude extensional deformation (full analytical data and procedures listed in Supplemental Materials). Apatite dating is not typically used for detrital studies, because apatite has low U concentrations, high concentrations of common Pb, and low resistance to physical and chemical abrasion in comparison to zircon (Thomson et al., 2012). Copper Basin strata, however, contain large, euhedral, and inclusion-free detrital apatite grains suitable for double dating. The apatite (U-Th)/He system has a substantially lower closure temperature (~70 °C; Farley, 2000) than the zircon (U-Th)/He system (~180 °C; Wolfe and Stockli, 2010), which makes it an excellent complementary technique for deciphering near-surface processes.

Detrital apatite grains were analyzed by laser ablation split stream–inductively coupled plasma mass spectrometry (LASS–ICPMS) at the UTChron facility at the University of Texas at Austin, which simultaneously generates precise U-Pb isotopic ratios and trace element concentrations (Kylander-Clark et al., 2013; Supplemental Section 1, 4). These were used to determine sediment provenance in an area with geochemically and geochronologically distinct source areas (Supplemental Fig. B5). Apatite U-Pb ages are inferred to be equivalent to the lower intercept of a chord fit to all apatite grain ages on a Tera-Wasserburg projection (Tera and Wasserburg, 1972; Kirkland et al., 2018). Since the amount of ^{204}Pb is generally significant in apatite, this graphical approach allows estimation

of an age of initial crystallization using only $^{207}Pb/^{206}Pb$ and $^{238}U/^{206}Pb$ ratios, assuming original isotopic homogeneity and no subsequent disturbance of the system (Tera and Wasserburg, 1972; Ludwig, 1998). Apatite U-Pb ages were also determined using the ^{204}Pb correction of Stacey and Kramers (1975), where $^{207}Pb/^{206}Pb$ ages are used as an initial estimate for model ^{204}Pb composition (Supplemental Fig. B4). Correction of ^{206}Pb, ^{207}Pb, and ^{208}Pb peaks was completed by measurement of ^{202}Hg to correct for ^{204}Hg isobaric interference and application of Stacey and Kramers (1975) common lead model. We then used the iterative process of Thomson et al. (2012) to calculate new $^{206}Pb/^{238}U$ ratios and ages. ^{204}Pb corrected ages yield a weighted mean age that is within 2σ uncertainty of the lower intercept age of the Tera-Wasserburg projection. During detrital apatite ablation, simultaneous analysis of the same ablation volume, using a secondary ICPMS, measured ^{43}Ca, ^{44}Ca, ^{87}Sr, ^{89}Y, ^{137}Ba, ^{139}La, ^{140}Ce, ^{141}Pr, ^{146}Nd, ^{147}Sm, ^{153}Eu, ^{157}Gd, ^{159}Tb, ^{163}Dy, ^{165}Ho, ^{166}Er, ^{169}Tm, ^{172}Yb, ^{175}Lu, ^{232}Th, and ^{238}U to evaluate potential correspondence between grain age, grain trace element geochemistry, and source geochemistry (see Supplementary Materials).

Following U-Pb geochronology, zircon and apatite grains from each major grain age population, defined as including three or more grains whose ages overlap given the analytical uncertainties (Saylor et al., 2012; Thomson et al., 2017), were picked from mounts and analyzed using (U-Th)/He thermochronology following the procedures of Wolfe and Stockli (2010) at the University of Texas at Austin (see also Supplemental Section 1). Apatite, zircon, and titanite extracted from granitoid samples in the Copper Mountains (Table 1) were analyzed for (U-Th)/He thermochronology following the procedures of Wolfe and Stockli (2010) at the University of Kansas (Supplemental Section 5).

$^{40}Ar/^{39}Ar$ Thermochronology and U-Pb Geochronology

Igneous and metamorphic rocks were sampled for $^{40}Ar/^{39}Ar$ thermochronology along a transect across the Copper Mountains to constrain the timing of plutonic emplacement, the cooling history of footwall rocks, and depositional ages within Copper Basin (Figs. 2.3–2.4). Incremental-heating and single crystal laser-fusion experiments were conducted at Ohio State University on a range of minerals extracted from these rocks (i.e., hornblende, muscovite,

biotite, and K-feldspar). Full results of these analyses are reported in Table 2 and methods are discussed in detail in Supplemental Section 1 (see also Supplemental Section 6). For incremental-heating experiments, all reported plateau ages are >70% concordant and contain >50% cumulative ^{40}Ar released within the plateau fraction. For single crystal laser-fusion experiments, weighted mean ages were calculated using all analyses that attained >90% ^{40}Ar released. Ages were calculated using the 28.201 Ma age for Fish Canyon Tuff sanidine (FCs) and the equations of Kuiper et al. (2008) and Renne et al. (1998).

Crystallization ages were determined using zircon U-Pb geochronology (Fig. 2.7) for samples within the western fault block (980730-5), the eastern fault block (000714-1), and the displaced cupola within the northern part of Copper Basin (970721-4C) (Figs. 2.1–2.2). Zircon geochronology was completed using high resolution laser ablation–inductively coupled plasma–mass spectrometry (LA–HR–ICP–MS) at the UTChron facility at the University of Texas at Austin (analytical data and procedures listed with Supplemental Material).

RESULTS

Zircon U-Pb Geochronology

Figure 2.7 shows concordia diagrams of zircon U-Pb ages. Most zircon grains have concordant ages that imply mean crystallization ages for the Coffeepot Stock between 108.4 ± 0.5 Ma and 111.0 ± 0.5 Ma (Fig. 2.7), which is in excellent agreement with prior estimates inferred from hornblende and biotite ^{40}Ar/^{39}Ar geochronology (109–108 Ma; Rahl et al., 2002). One sample taken at the southeastern extent of the pluton (000714-1) contains a bimodal distribution of Cretaceous and Jurassic (176–157 Ma) ages that we infer to reflect inheritance (Fig. 2.7). This interpretation is supported by the uneven profile of ^{238}U/^{206}Pb ratios during laser ablation, which show Cretaceous rim and Jurassic core ages for many of the Jurassic age zircon grains.

Detrital Zircon and Apatite U-Pb Geochronology and Trace Element Chemistry

Detrital zircon U-Pb geochronology of four sandstone samples from the Dead Horse Formation and one sandstone sample from the Meadow Fork Formation show an up-section transition from Eocene volcaniclastic to Cretaceous plutonic grain age populations (Fig. 2.8; Supplemental Table S2). Samples from the upper part of the Dead Horse Formation (NV12-181CB, NV12-169CB, and NV12-159CB) with maximum depositional ages ranging from 39.4 ± 0.2 Ma to 37.1 ± 0.1 Ma are comprised of >99% Eocene volcanic grains (Supplemental Fig. B2–B3). A sample taken from near the top of the Dead Horse Formation (NV12-176CB) has a bimodal distribution of 45–35 Ma volcanic grains (79%) and 111–101 Ma plutonic grains (17%). A sample taken from the base of the Meadow Fork Formation (NV12-162CB) includes 43–34 Ma (4%), 115–100 Ma (61%), and 130–116 Ma (32%) detrital zircon grain ages (Fig. 2.8). The largest of these detrital zircon U-Pb age groups (115–100 Ma) is consistent with crystallization ages obtained for the Coffeepot Stock, but the source of the older (130–116 Ma) zircon grain ages is uncertain; it may reflect an early phase of crystallization within the Coffeepot intrusive suite. This sudden introduction of plutonic detritus at the contact of the Dead Horse Formation and Meadow Fork Formation is also reflected in conglomerate clast lithology counts throughout Copper Basin, which show the Meadow Fork Formation consists of ~50% granitic clasts and <10% volcanic clasts (Figs. 2.4 and 2.6).

Lower intercepts on Tera-Wasserburg plots, calculated by regressing 129 apatite grains from these same samples, yield mean U-Pb ages of 106 ± 9 Ma and 108 ± 10 Ma with an MSWD of <2 (Fig. 2.9), which are within 2σ uncertainty of the ca. 109 Ma crystallization age of the Coffeepot Stock (Fig. 2.7). We therefore interpret these ages to represent the time of apatite crystallization within the Coffeepot Stock, suggesting the stock was emplaced at relatively shallow depths. REE concentrations and patterns are similar for all apatite grains from both detrital samples (Fig. 2.9) but observed variations in trace-element composition likely reflect evolution in the parental melt composition or late crystallization from residual melts (Belousova et al., 2002). The low slope of the REE pattern, low Ce/Yb ratios, and HREE enrichment are all indicative of a granitic source (Belousova et al., 2001; 2002). The weak negative Eu anomaly indicates less fractionation and that the ratio of plagioclase to

potassium feldspar in the host rocks was relatively high (Belousova et al., 2002; Kirkland et al., 2018), which is consistent with chemical analyses of the Coffeepot Stock (i.e., Seymour, 1980; Supplemental Section 2). As discussed above, detrital zircon U-Pb geochronology reveals Copper Basin samples yield two significant age populations that represent volcanic (45–35 Ma) and plutonic (130–100 Ma) detritus. Since volcanic grains have statistically equivalent crystallization and cooling ages (Ruiz et al., 2004; Saylor et al., 2012), the plutonic age population was targeted for (U-Th)/He analysis to assess source exhumation trends.

(U-Th)/He and $^{40}Ar/^{39}Ar$ Thermochronology

Several samples of the Coffeepot Stock were analyzed for zircon, titanite, and apatite (U-Th)/He thermochronology following the procedures of Wolfe and Stockli (2010) at the University of Kansas. In the western fault block, these samples have zircon (U-Th)/He (ZHe) ages that range from ~89.2–69.6 Ma and apatite (U-Th)/He (AHe) ranging from ~52.2–27.0 Ma (Fig. 2.3; Table 1). Both ZHe and AHe ages generally decrease towards the west, where a steep (~75° dip) normal fault bounds the western margin of the pluton. These ages suggest that this fault was active during Cretaceous–Oligocene exhumation of the western part of the Coffeepot Stock. In the eastern fault block, between the Bruneau Valley Fault and Copper Creek Fault, ZHe ages decrease from 53.7 ± 3.2 Ma in the west to 37.2 ± 1.9 Ma in the east (Figs. 2.2–2.3). This progression of ages records footwall exhumation along the Copper Creek Fault and tilting along the Bruneau Valley Fault. In the northern part of Copper Basin, a sample of the allochthonous plutonic body has a ZHe age of 81.3 ± 3.8 Ma and an AHe age of 32.6 ± 2.0 Ma, which is consistent with Coffeepot Stock cooling ages near Tennessee Mountain, where this body is inferred to have originated (Figs. 2.1–2.3; cf. Rahl et al., 2002).

$^{40}Ar/^{39}Ar$ thermochronology of a range of minerals separated from the same samples as Rahl et al. (2002), as well as several new samples, yields new constraints on the thermal history of footwall rocks exposed in the Copper Mountains. Single crystal K-feldspar $^{40}Ar/^{39}Ar$ analyses yield weighted mean ages of 70.73 ± 1.41 Ma and 71.87 ± 1.65 Ma for samples collected in the eastern fault block (Table 2), indicating cooling through the ~200 °C K-feldspar closure temperature during the latest Cretaceous (Fig. 2.3; Reiners and Brandon,

2006). A sample collected near the western margin of the eastern fault block, however, has multi-crystal muscovite and biotite $^{40}Ar/^{39}Ar$ ages of 91.37 ± 0.64 Ma and 55.39 ± 2.39 Ma, respectively, suggesting slower cooling through the ~310 °C biotite closure temperature (Fig. 2.3; Reiners and Brandon, 2006). In Copper Basin, a tuff located near the base of the Meadow Fork Formation yields a biotite plateau age of 32.92 ± 0.29 Ma and is separated by ~150 m of coarse-grained alluvial strata from a tuff with a biotite $^{40}Ar/^{39}Ar$ age of 29.77 ± 0.53 Ma (Figs. 2.2 and 2.4). These ages yield maximum age constraints for the final period of deposition within Copper Basin.

Detrital Zircon and Apatite (U-Th)/(He-Pb) Double Dating

Of the two dominant U-Pb age populations in Copper Basin samples, volcanic grains (45–35 Ma) have statistically equivalent crystallization and cooling ages (Ruiz et al., 2004; Saylor et al., 2012), so grains with U-Pb ages of 130–100 Ma were targeted to assess source terrane exhumation trends. Detrital (U-Th)/(He-Pb) double dating is critical in this circumstance to eliminate first-cycle volcanic zircon and apatite grains and select non-volcanic detrital grains for (U-Th)/He analysis (cf. Saylor et al., 2012). Double dated detrital grains with Cretaceous U-Pb ages extracted from the uppermost Dead Horse Formation have 89.6–64.8 Ma zircon He ages and 106.5–39.8 Ma apatite He ages (Fig. 2.9). 71% of detrital apatite grains from this sample have Eocene He ages. Detrital grains with Cretaceous U-Pb ages extracted from the base of the Meadow Fork Formation have 139.6–64.7 Ma zircon He ages and 21.7–15.3 Ma apatite He ages. These ages imply post-depositional heating and thermal resetting resulting from elevated near-surface temperatures, between the apatite He and zircon He closure temperatures, during the early Miocene.

DISCUSSION

Emplacement and Cooling History of the Coffeepot Stock

We divide the Copper Mountains into three structural blocks that record discrete exhumation histories, separated by the Bruneau Valley Fault and the Copper Creek Fault (Figs. 2.1–2.3). In addition, we infer that the entire western margin of the Coffeepot Stock is

bound by a high-angle down-to-the-west normal fault here named the Tennessee Mountain Fault. Dipping ~75^{o} W, the Tennessee Mountain Fault juxtaposes the stock against a hanging wall carrying ~900 m of ca. 15 Ma Jarbidge Rhyolite (Bushnell, 1967; Brueseke et al., 2014). The western block also preserves a 10–15^{o} east-tilted unconformity on its eastern flank, overlain by at least 200 m of Jarbidge Rhyolite (Figs. 2.1–2.3). Westward projection of the nonconformity surface suggests a minimum of 2 km of throw on the Tennessee Mountain Fault. Consequently, the western part of the pluton appears to be tilted gently eastward, exposing progressively deeper structural levels of the pluton west toward the Tennessee Mountain Fault. Thermochronological results support this inference, showing progressively younger ages toward the west. Samples collected across the western block of the Coffeepot Stock yield hornblende $^{40}Ar/^{39}Ar$ ages of ~106.5–105.1 Ma, biotite $^{40}Ar/^{39}Ar$ ages of ~104.6 to 100.5 Ma, and K-feldspar $^{40}Ar/^{39}Ar$ ages of ~93.7 to 91.8 Ma (Table 2). These Coffeepot Stock $^{40}Ar/^{39}Ar$ ages are interpreted to record cooling directly following pluton emplacement in the late Early Cretaceous. We interpret the hornblende $^{40}Ar/^{39}Ar$ ages to correspond to crystallization at relatively shallow depths. Using biotite and K-feldspar closure temperatures of 310 °C and 200 °C, respectively (Reiners and Brandon, 2006), these ages correlate to an estimated cooling rate of ~10 °C/m.y. between the biotite and K-feldspar partial retention zones. The nearly equivalent hornblende and biotite $^{40}Ar/^{39}Ar$ ages for the Coffeepot Stock show quick cooling to below ~310 °C following crystallization, as would be expected for a relatively shallowly emplaced pluton.

To derive time-temperature (*t*-*T*) paths for the Coffeepot Stock and to test whether geologically reasonable thermal histories can satisfy AHe, ZHe, and THe data, we used the HeFTy software (Ketcham, 2005) to complete inverse models. We focused *t*-*T* modeling on the western fault block, where ZHe ages for the Coffeepot Stock decrease from 89.2 ± 4.1 Ma in the east to 69.6 ± 3.2 Ma in the west and AHe ages decrease from 42.1 ± 2.7 in the east to 27.0 ± 1.3 Ma near the Tennessee Mountain Fault (Table 1). Figure 2.10 shows *t*-*T* paths for the western block using time constraints for cooling of the western Coffeepot Stock through the biotite $^{40}Ar/^{39}Ar$ closure and mean (U-Th)/He data for several samples collected across the block. Taken together, these samples define a protracted cooling history from the Late Cretaceous to the Oligocene, with the most prominent phase of cooling being in the Late

Cretaceous following emplacement of the Coffeepot Stock. Rapid Late Cretaceous cooling through the ZHe closure temperature within 15–35 m.y. of crystallization signifies pronounced exhumation, which may be related to other episodes of synorogenic extension documented in eastern Nevada (e.g., Camilleri and Chamberlain, 1997; Druschke et al., 2009a; Long et al., 2015). This initial exhumation in the Copper Mountains, however, is not clearly associated with surface-breaching extensional deformation. We relate a late Eocene cooling phase, evident from middle–late Eocene AHe ages of samples collected across multiple structural levels, to exhumation along the Copper Creek Fault system. A later Oligocene to Miocene cooling phase is recognizable only in the AHe data from immediately beneath the Tennessee Mountain Fault (980730-1). The younger, 27-Ma AHe age from directly beneath the Tennessee Mountain Fault could be a partial retention age or it could record cooling associated with Oligocene extension contemporaneous with deposition of the Meadow Fork Formation farther east.

In the northern part of Copper Basin, a 109.2 ± 0.3 Ma body of granodiorite has Late Cretaceous hornblende, biotite, and K-feldspar $^{40}Ar/^{39}Ar$ ages, a ZHe age of 81.3 ± 3.8 Ma, and an AHe age of 32.6 ± 2.0 Ma, all of which are consistent with cooling ages of the Coffeepot Stock in the Tennessee Mountain area and significantly different from cooling ages in the proximal eastern block (Figs. 2.1–2.2). Thermal modeling indicates samples collected from this granodiorite body and from near the Tennessee Mountain skarn both had pronounced Late Cretaceous cooling (Fig. 2.10). This supports the interpretation of Rahl et al. (2002) that this granodiorite body represents an allochthonous slice of the Coffeepot Stock with adjacent Tennessee Mountain Formation skarn that was transported ~10 km eastward during 8 to 12 km of slip along the Copper Creek normal fault. Figure 2.11A shows thermochronologic ages of samples collected in the footwall of the Copper Creek fault plotted against horizontal distance from the fault (e.g., Stockli, 2005). Linear regression of ZHe ages indicate a nominal slip rate of ~0.44 mm/yr, but a large component of this slip (≥ 2 km) likely occurred between ca. 45 and ca. 38 Ma. The AHe age of 32.6 ± 2.0 Ma from this sample closely corresponds with the onset of coarse clastic deposition recorded by the Meadow Fork Formation in the hanging wall of the Meadow Fork normal fault. This, too, is consistent with the inference of Rahl et al. (2002) that the detached fault slice initially was

transported with the hanging wall of the Copper Creek Fault but was subsequently transferred to the footwall during the initiation of the Meadow Fork Fault. This makes the Meadow Fork Fault, together with its rotated syntectonic strata (the Meadow Fork Formation), the only clearly documented evidence of Oligocene extension in northeastern Nevada. Miocene volcanic rocks (ca. 17–15 Ma; Table 2) are deposited unconformably above both hanging wall and footwall strata near Copper Basin (Figs. 2.1 and 2.3), providing a youngest age constraint on the timing of deformation along the Copper Creek and Meadow Fork Faults.

In the eastern fault block, a sample from the eastern margin of the Coffeepot Stock (970709-3C) has a biotite $^{40}Ar/^{39}Ar$ age of 94.21 ± 0.66 Ma and a K-feldspar $^{40}Ar/^{39}Ar$ age of 71.87 ± 1.65 Ma. Rahl et al. (2002) interpreted these younger cooling ages to imply that the eastern part of the pluton intruded deeper structural levels and cooled more slowly than the western part of the pluton, which is consistent with the greenschist facies metamorphism and solid-state foliation that is only present in the eastern part of the pluton (Supplemental Fig. B6). Samples of muscovite-biotite schist within the eastern fault block yield biotite $^{40}Ar/^{39}Ar$ ages of 88.94 ± 0.90 Ma in the east (970726-5) and 55.39 ± 2.39 Ma near the Bruneau Valley Fault (980802-3A). These ages, and a muscovite $^{40}Ar/^{39}Ar$ age of 91.37 ± 0.64 Ma, support slow initial cooling within the footwall of the Bruneau Valley normal fault. Titanite (U-Th)/He (THe) and ZHe ages in the eastern block record later cooling than the corresponding thermochronometers from the western block. This area is characterized by ZHe ages of 53.7 ± 3.2 Ma in the western part of the block and 46.1± 3.2 Ma in the central part of the block, and a THe age of 37.2 ± 1.9 Ma in the east. These may record cooling and unroofing associated with Eocene extension (see below).

Exhumation and Basin Formation in the Copper Mountains

Discrete changes in sedimentary facies, provenance, and cooling rates signify the onset of rapid slip along the Copper Creek and Meadow Fork fault systems. The 115–100 Ma U-Pb grain age group matches zircon U-Pb crystallization ages obtained for the Coffeepot Stock, showing that the pluton acted as a primary sediment source to the basin. Additionally, rare-earth element (REE) compositions of apatite grains from Copper Basin strata are

indicative of granitic source rocks with La-enriched crystallization, and the bulk geochemistry, size, and shape of these grains are similar to apatite crystals within the Coffeepot Stock (Fig. 2.9; Seymour, 1980). These strata also contain abundant pebble–boulder clasts of quartz monzonite and granodiorite at multiple stratigraphic levels (Figs. 2.4 and 2.6). Confident identification of this plutonic detritus permits assessment of minimum and maximum lag time rates for these samples.

Lag time analysis can provide quantitative constraints on exhumation rates where precise stratigraphic (i.e., depositional) ages exist for the same samples. In Copper Basin, $^{40}Ar/^{39}Ar$ geochronology of interbedded tuffs (Figs. 2.3–2.4; Table 2) and detrital zircon maximum depositional ages of young (i.e., syndepositional) volcanic grains permits precise assessment of stratigraphic ages. A sample collected from the top of the Dead Horse Formation, 11 m above a tuff with an $^{40}Ar/^{39}Ar$ age of 38.95 ± 0.25 Ma (Fig. 2.5), contains a young population of plutonic AHe grain ages (42.5–39.8 Ma) that indicate a lag time of 2–5 m.y. and a corresponding cooling rate between 37 °C/m.y. and 14 °C/m.y. (Farley, 2000). Figure 2.12 shows *t-T* paths for this sample (NV12-176CB) using the estimated time of western Coffeepot Stock cooling through the biotite $^{40}Ar/^{39}Ar$ closure, mean ZHe and AHe grain ages of young cooling age populations, and the sample depositional age. The wide spectrum of AHe ages within this sample (106.5–39.8 Ma) implies the Copper Basin catchment may have contained sources with diverse thermal histories at this time. A sample collected from the Meadow Fork Formation, near the contact with the Dead Horse Formation, has younger AHe grain ages of 21.7–15.3 Ma that indicate post-depositional heating. This is likely a result of thermal resetting during eruption of proximal ca. 17–15 Ma Seventy Six Creek Basalt and Jarbidge Rhyolite (Fig. 2.4; Rahl et al., 2002; Brueseke et al., 2014). This is the stratigraphically deepest sample collected from the Meadow Fork Formation, indicating thermal resetting is a product of proximal volcanism and not heating produced by burial. Apatite extracted from a quartz monzonite clast at approximately the same stratigraphic level, near the contact of the Meadow Fork Formation and Dead Horse Formation, (010801-3) yields an AHe age of 42.8 ± 2.4 Ma (Fig. 2.2). The middle Eocene cooling age of this sample also suggests that the estimated rapid cooling rates during deposition of the upper Dead Horse Formation persisted during deposition of at least the

lowermost Meadow Fork Formation. The similar 15.7–12.8 Ma range of AHe ages from all other detrital apatite samples (050720-11, 050724-2A, and 050720-9D) taken from the upper Dead Horse Formation and at multiple stratigraphic levels within the Meadow Fork Formation (Fig. 2.3; Table 1), suggests Miocene volcanism had widespread thermal effects on Copper Basin strata.

The thick accumulation of late Eocene tuffaceous material in the Dead Horse Formation supports the interpretation that an east-west paleodrainage system connected this area with proximal calderas that were likely situated near the Bull Run Mountains, currently ~50 km to the west (Henry, 2008; Henry et al., 2011). We interpret the local accumulation of tuff and tuffaceous sediment in Copper Basin, however, primarily to accommodation generated during movement along the Copper Creek and Meadow Fork faults (Fig. 2.13). This fault-generated subsidence is supported by coarse-grained alluvial deposits in the Meadow Fork Formation that are conformably deposited above Dead Horse Formation strata. Chronostratigraphic correlation shows most lacustrine sedimentation within Copper Basin was confined to a narrow interval between eruption of 39.07 ± 0.25 Ma and 38.95 ± 0.25 Ma tuffs, which preceded a migration of lacustrine deposition to the northeast by ca. 38 Ma (Fig. 2.5). This lacustrine deposition indicates a period of increased basin subsidence and/or drainage obstruction that led to the deposition of lacustrine facies that are indicative of an overfilled lake basin, where the combined water and sediment fill rate exceeded the accommodation rate (Carroll and Bohacs, 1999). Detrital (U-Th)/(He-Pb) double dating of zircon and apatite sampled from near the top of the Dead Horse Formation shows rapid late Eocene cooling (≥14.4 °C/m.y.) and deposition of plutonic detritus in Copper Basin (Figs. 2.6 and 2.13). Detrital zircon extracted from the lower portion of the Meadow Fork Formation show cooling through the zircon (U-Th)/He partial retention zone by the Paleocene, which is consistent with cooling ages in the western part of the Coffeepot Stock (Figs. 2.1–2.2). In the eastern fault block, between the Bruneau Valley fault and Copper Creek Fault, the Coffeepot Stock is characterized by Eocene zircon and titanite He ages that decrease from 53.7 ± 3.2 to 37.2 ± 1.9 Ma, which supports >8 km of slip along the Copper Creek Fault during the Eocene (Figs. 2.11–2.12).

Characteristics of Eocene Extension in the Cordilleran Hinterland

The well-preserved structural and stratigraphic evidence of late Eocene–early Oligocene extension in the Copper Mountains of northern Nevada presented here provides one of the most complete near-surface records of extension currently recognized in the North American Cordilleran hinterland. Lag time analysis of double dated strata in Copper Basin reveals that rapid extension, with cooling rates of >14 °C/m.y., began by 38.0 ± 0.9 Ma. This is ~6 m.y. after the 45–44 Ma initiation of volcanism in northern Nevada (Henry et al., 2012; Smith et al., 2017), but initial volcanism in Nevada was relatively limited in volume and spatial distribution (Henry and Boden, 1998, Henry 2008; Smith et al., 2017). In contrast, intense magmatism associated with the proximal ca. 40.2 to 39.5 Ma Tuscarora volcanic field, <50 km to the southwest of Copper Basin, resulted in widespread volcanism (Henry and Boden, 1997; Henry et al., 1999; Henry, 2008) as well as emplacement of regional dike swarms and plutons (Ressel and Henry, 2006; du Bray, 2007). This peak phase of heating is also recorded by late Eocene Y-rich growth zones on metamorphic zircons in the East Humboldt Range (Hallett and Spear, 2015) and coeval Carlin-type Au mineralization across a large area of northeastern Nevada (Cline et al., 2005; Emsbo et al., 2006). Rapid extensional deformation in the Copper Mountains is contemporaneous with this peak phase of magmatism, which we interpret as an important driver for extension, both by rheological/thermal weakening of the lithosphere and isostatic effects of Farallon slab removal and possible subsequent delamination (Porter et al., 2016; Smith et al. 2017).

New temporal constraints reveal that high-magnitude extensional deformation in the Copper Mountains was concurrent with protracted metamorphic core complex development in the surrounding region (Fig. 2.14, and references therein). K-feldspar $^{40}Ar/^{39}Ar$ ages of 71.87 ± 1.65 Ma and 70.73 ± 1.41 Ma documented in the eastern part of the Coffeepot Stock are coeval with a 77.4 ± 2.8 to 68.2 ± 2.0 Ma cooling and melt crystallization event in the East Humboldt Range, recorded by zircon and monazite growth (Hallett and Spear, 2015). This may reflect widespread thermal effects of Late Cretaceous tectonism during orogenic plateau construction (e.g., Wells and Hoisch, 2008). The mechanisms that drove Late Cretaceous and Paleogene exhumation in the proximal Ruby Mountains-East Humboldt Range and Raft River-Albion-Grouse Creek metamorphic core complexes remains a matter

of debate, but some studies hypothesize that initial rapid exhumation may have resulted from isostatic adjustment and thermal weakening following regional mantle lithosphere delamination (Hodges and Walker, 1992; Wells and Hoisch, 2008, Wells et al., 2012) or rollback-driven magmatism (e.g., MacCready et al., 1997; Snoke et al., 1997, 2004; Hallett and Spear, 2015; Litherland and Klemperer, 2017; Smith et al., 2017), as interpreted here. Recently documented large magnitude late Eocene extension at Spruce Mountain (Pape et al., 2016) and in the southern East Humboldt Range (McGrew et al., 2018) support this finding. Paleogene extensional deformation in the Copper Mountains shares several important similarities with metamorphic core complexes, including a protracted (>50 m.y.) record of exhumation that initiated in the Late Cretaceous, low-angle faulting, high-magnitude (>8 km) slip, and a hanging wall of syntectonic sedimentary strata faulted down against a footwall of metamorphic rocks. The footwall of the Copper Creek Fault, however, is primarily comprised of low-grade metasedimentary rocks rather than exhumed middle–lower crustal rocks. This comparatively muted exhumation may reflect extension in an area with pre-existing crustal weaknesses developed during earlier polyphase deformation, as opposed to proximal metamorphic core complexes, which formed in the foreland of the Roberts Mountains allochthon (McGrew et al., 2000). The synchronicity of high-magnitude late Eocene extension in the Copper Mountains, and likely the Ruby Mountains-East Humboldt Range, with the southward propagation of volcanism and basin formation adds to growing evidence that Farallon slab removal and/or progressive delamination of the mantle lithosphere resulted in rapid exhumation and measurable surface deformation across multiple locations in the hinterland (i.e., Smith et al., 2014, 2017; Cassel et al., 2018; Canada et al., 2019). This is in agreement with previous models that indicate thermal weakening of the upper crust can be an essential driver for extension (e.g., Coney and Harms, 1984; Gans et al., 1989; Axen et al., 1993; Wells and Hoisch, 2008; Bendick and Baldwin, 2009), especially within areas of orogenically thickened crust.

CONCLUSIONS

Multi-system and multi-mineral thermochronology of Cretaceous intrusive rocks and Copper Basin strata show an excellent record of Late Cretaceous to early Oligocene exhumation partly accommodated by movement along several high-offset normal faults across the Copper Mountains that experienced up to 12 km of slip. The timing and magnitude of extensional deformation is precisely constrained by new detrital (U-Th)/(He-Pb) double dating and $^{40}Ar/^{39}Ar$ geochronology of Eocene–Oligocene strata. Detrital apatite grains derived from the Coffeepot Stock cooled through the apatite (U-Th)/He partial retention zone during the late Eocene and were deposited in Copper Basin within 2–5 m.y. This low-lag-time sedimentation reflects a 38.0 ± 0.9 Ma transition to rapid exhumation and surface-breaching extension in the Copper Mountains directly following widespread eruption of the ca. 40.2–39.8 Ma tuff of Nelson Creek and the tuff of Big Cottonwood Canyon, sourced from the Tuscarora volcanic field and proximal calderas, <50 km to the southwest of Copper Basin (Henry, 2008; Smith et al., 2017). The timing of extension in the Copper Mountains implies a close association with magmatism induced by removal of the Farallon slab and possibly subsequent removal of mantle lithosphere by delamination. Compressional stress release and advective heating of the lithosphere during associated volcanism also led to metamorphic fabric development within hinterland core complexes and heating that is inferred to reflect near-surface extensional deformation (Coney and Harms, 1984; Hallett and Spear, 2014, 2015). Despite heightened gravitational potential energy since as early as the Late Cretaceous and thermal weakening during late Eocene magmatism, the Cordilleran hinterland plateau maintained high elevations (2.7–3.1 km) and experienced minor late Oligocene surface uplift (up to 500 m; Cassel et al., 2014, 2018). Surface elevations most likely decreased during widely distributed high-magnitude (>1 km throw) normal faulting in the Miocene (Dickinson, 2006; Colgan and Henry, 2009). This indicates that orogen-wide extension and lithospheric thinning is not the immediate response of all high-elevation regions, specifically not those that are underlain by rheologically strong and thick lithosphere, such as the central Andes (Long, 2012) and the Eocene Cordilleran hinterland.

ACKNOWLEDGEMENTS

National Science Foundation grant EAR-1322073 and student grants from the Geological Society of America, American Association of Petroleum Geologists, and the Society for Sedimentary Geology (SEPM) supported this research. This work greatly benefited from discussions with S. Long and C. Henry as well as field assistance from E. White, A. Wilson, and N. Seymour. We would also like to acknowledge laboratory assistance by D. Barber, F. Galster, K. Thomson, and L. Stockli at the University of Texas at Austin. McGrew's contributions were funded by the American Chemical Society Petroleum Research Fund (Grant 40130-B8) and Grants-in-aid from the University of Dayton. In addition, McGrew wishes to acknowledge the valuable contributions of undergraduate research collaborators Jeffrey Rahl (1999) and Michael Rigby (2005), and the laboratory assistance of Fritz Hubacher and Jeff Linder at the Ohio State University.

REFERENCES

Armstrong, R.L., 1968, Sevier orogenic belt in Nevada and Utah: Geological Society of America Bulletin, v. 79, p. 429–458, doi:10.1130/0016-7606.

Armstrong, R.L., 1982, Cordilleran metamorphic core complexes - From Arizona to Southern Canada: Annual Reviews in Earth and Planetary Science Letters, v. 10, p. 129–154, doi:10.1146/annurev.ea.10.050182.001021.

Axelrod, D.I., 1966a, The Eocene Copper Basin flora of northeastern Nevada: University of California Publications in Geological Sciences, v. 59, 124 p.

Axelrod, D.I., 1996b, Diverse upland Eocene forests, western U.S.A.: Palaeobotanist, v. 45, p. 81–97.

Axelrod, D.I., 1997, Paleoelevation estimated from Tertiary floras: International Geology Review, v. 39, no. 12, p. 1124–1133, doi:10.1080/00206819709465319.

Axen, G.J., Taylor, W.J., and Bartley, J.M., 1993, Space-time patterns and tectonic controls of Tertiary extension and magmatism in the Great Basin of the western United States: Geological Society of America Bulletin, v. 105, p. 56–76, doi:10.1130/0016-7606(1993)105<0056:STPATC>2.3.CO;2.

Belousova, E.A., Griffin, W.L., O'Reilly, S.Y., and Fisher, N.I., 2002, Apatite as an indicator mineral for mineral exploration: trace-element compositions and their relationship to host rock type: Journal of Geochemical Exploration, v. 76, p. 45-69.

Belousova, E.A., Walters, S., Griffin, W.L., and O'Reilly, S.Y., 2001, Trace-element signatures of apatites in granitoids from the Mt Isa Inlier, northwestern Queensland: Australian Journal of Earth Sciences, v. 48, no. 4, p. 603-619.

Bendick, R., and Baldwin, J., 2009, Dynamic models for metamorphic core complex formation and scaling: The role of unchannelized collapse of thickened continental crust: Tectonophysics, v. 477, no. 1–2, p. 93–101, doi:10.1016/j.tecto.2009.03.017.

Best, M.J., Barr, D.L., Christiansen, E.H., Gromme, S., Deino, A.L., and Tingey, D.G., 2009, The Great Basin Altiplano during the middle Cenozoic ignimbrite flareup: insights from volcanic rocks: International Geology Review, v. 51, no. 7–8, p. 589–633, doi:10.1080/00206810902867690.

Best, M.G., Christiansen, E.H., de Silva, S., and Lipman, P.W., 2016, Slab-rollback ignimbrite flareups in the southern Great Basin and other Cenozoic American arcs: A distinct style of arc volcanism: Geosphere, v. 12, no. 4, p. 1097–1135, doi:10.1130/GES01285.1.

Brandon, M.T., and Vance, J.A., 1992, Tectonic evolution of the Cenozoic Olympic subduction complex, Washington State, as deduced from fission track ages for detrital zircons: American Journal of Science, v. 292, p. 565–636, doi:10.2475/ajs.292.8.565.

Branney, M.J., and Kokelaar, P., 2002, Pyroclastic density currents and the sedimentation of ignimbrites: Geological Society, London, Memoirs, v. 27, 152 p.

Brooks, W.E., Thorman, C.H., and Snee, L.W., 1995, The 40Ar/39Ar ages and tectonic setting of the middle Eocene northeast Nevada volcanic field: Journal of Geophysical Research: Solid Earth, v. 100, no. B7, p. 10,403–10,416, doi:10.1029/94JB03389.

Brueseke, M.E., Callicoat, J.S., Hames, W., and Larson, P.B., 2014, Mid-Miocene rhyolite volcanism in northeastern Nevada: The Jarbidge Rhyolite and its relationship to the Cenozoic evolution of the northern Great Basin (USA): Geological Society of America Bulletin, v. 126, no. 7/8, p. 1047–1067, doi:10.1130/B30736.1.

Bushnell, K.O., 1967, Geology of the Rowland Quadrangle, Elko County, Nevada: Nevada Bureau of Mines and Geology Bulletin v. 67, 38 p.

Camilleri, P.A., and Chamberlain, K.R., 1997, Mesozoic tectonics and metamorphism in the Pequop Mountains and Wood Hills region, northeast Nevada: Implications for the architecture and evolution of the Sevier orogeny: Geological Society of America Bulletin, v. 109, p. 74–94, doi:10.1130/0016-7606(1997)109<0074:MTAMIT>2.3.CO;2.

Camilleri, P., Deibert, J., and Perkins, M., 2017, Middle Miocene to Holocene tectonics, basin evolution, and paleogeography along the southern margin of the Snake River Plain in the Knoll Mountain–Ruby–East Humboldt Range region, northeastern Nevada and south-central Idaho: Geosphere v. 13, no. 6, p. 1901–1948, doi:10.1130/GES01318.1.

Canada, A.S., Cassel, E.J., Stockli, D.F., Smith, M.E., Jicha, B.R., and Singer B.S., 2019, in press, Accelerating exhumation in the Eocene North American Cordilleran hinterland:

Implications from detrital zircon (U-Th)/(He-Pb) double dating: Geological Society of America Bulletin, doi:10.1130/B35160.1.

Carroll, A.R., and Bohacs, K.M., 1999, Stratigraphic classification of ancient lakes: Balancing tectonic and climatic controls: Geology, v. 27, no. 2, p. 99–102, doi:10.1130/0091-7613(1999)027<0099:SCOALB>2.3.CO;2.

Cassel, E.J., Breecker, D.O., Henry, C.D., Larson, T.E., and Stockli, D.F., 2014, Profile of a paleo-orogen: High topography across the present-day Basin and Range from 40 to 23 Ma: Geology, v. 42, no. 11, p. 1007–1010, doi:10.1130/G35924.1.

Cassel, E.J., Calvert, A.T., and Graham, S.A., 2009, Age, geochemical composition, and distribution of Oligocene ignimbrites in the northern Sierra Nevada, California: implications for landscape morphology, elevation, and drainage divide geography of the Nevadaplano: International Geology Review, v. 51, no. 7–8, p. 723–742.

Cassel, E.J., Graham, S.A., Chamberlain, C.P., and Henry, C.D., 2012, Early Cenozoic topography, morphology, and tectonics of the northern Sierra Nevada and western Basin and Range: Geosphere, v. 8, no. 2, p. 229–249, doi:10.1080/00206810902880370.

Cassel, E.J., Smith, M.E., and Jicha, B.R., 2018, The impact of slab rollback on Earth's surface: Uplift and extension in the hinterland of the North American Cordillera: Geophysical Research Letters, v. 45, no. 20, p. 10,996–11,004, doi:10.1029/2018GL079887.

Chamberlain, C.P., Mix, H.T., Mulch, A., Hren, M.T., Kent-Corson, M.L., Davis, S.J., Horton, T.W., and Graham, S.A., 2012, The Cenozoic climatic and topographic evolution of the western North American Cordillera: American Journal of Science, v. 312, no. 2, p. 213–262, doi:10.2475/02.2012.05.

Chase, C.G., Gregory, K.M., Parrish, J.T., and DeCelles, P.G., 1998, Topographic history of the western Cordilleran of North America and the etiology of climate, in Crowley, T.J., and Burke, K., eds., Tectonic boundary conditions for climate reconstructions: Oxford Monographs on Geology and Geophysics, no. 39, p. 73–99.

Cline, J.S., Hofstra, A.H., Muntean, J.L., Tosdal, R.M., and Hickey, K.A., 2005, Carlin-type gold deposits in Nevada: Critical geologic characteristics and viable models:

Economic Geology and the Bulletin of the Society of Economic Geologists, v. 100, p. 451–484.

Coats, R.R., 1964, Geology of the Jarbidge quadrangle, Nevada-Idaho: U.S. Geological Survey Bulletin 1141-M, 24 p.

Coats, R.R., 1987, Geology of Elko County, Nevada: Nevada Bureau of Mines and Geology Bulletin 101, 112 p.

Coats, R.R., and McKee, E.H., 1972, Ages of plutons and types of mineralization, northwestern Elko County, Nevada, in Geological Survey Research 1972: U.S. Geological Survey Professional Paper 800-C, p. C165–C169.

Colgan, J.P., and Henry, C.D., 2009, Rapid middle Miocene collapse of the Sevier orogenic plateau in north-central Nevada: International Geology Review, v. 51, no. 9–11, p. 920–961, doi:10.1080/00206810903056731.

Colgan, J.P., Howard, K.A., Fleck, R.J., and Wooden, J.L., 2010, Rapid middle Miocene extension and unroofing of the southern Ruby Mountains, Nevada: Tectonics, v. 29, TC6022, doi:10.1029/2009TC002655.

Coney, P.J., and Harms, T.A., 1984, Cordilleran metamorphic core complexes: Cenozoic extensional relics of Mesozoic compression: Geology, v. 12, no. 9, p. 550–554, doi:10.1130/0091-7613(1984)12<550:CMCCCE>2.0.CO;2.

Crafford, E.J., 2008, Paleozoic tectonic domains of Nevada: An interpretive discussion to accompany the geologic map of Nevada: Geosphere, v. 4, no. 1, p. 260–291, doi:10.1130/GES00108.1.

Dallmeyer, R.D., Snoke, A., and McKee, E.H., 1986, The Mesozoic-Cenozoic tectonothermal evolution of the Ruby Mountains, East Humboldt Range, Nevada: A Cordilleran metamorphic core complex: Tectonics, v. 5, no. 6, p. 931–954, doi:10.1029/TC005i006p00931.

DeCelles, P.G., 2004, Late Jurassic to Eocene evolution of the Cordilleran thrust belt and foreland basin system, Western U.S.A.: American Journal of Science, v. 304, p. 105–168, doi:10.2475/ajs.304.2.105.

DeCelles, P.G., Ducea, M.N., Kapp, P., and Zandt, G., 2009, Cyclicity in Cordilleran orogenic systems: Nature Geoscience, v. 2, no. 4, p. 251–257, doi:10.1038/ngeo469.

Dechert, C.P., 1967, Bedrock geology of the northern Schell Creek Range, White Pine County, Nevada [Ph.D. thesis]: University of Washington, 266 p.

Dickinson, W.R., 1997, Tectonic implications of Cenozoic volcanism in coastal California: Geological Society of America Bulletin, v. 109, no. 8, p. 936–954, doi:10.1130/0016-7606(1997)109<0936:OTIOCV>2.3.CO;2.

Dickinson, W.R., 2006, Geotectonic evolution of the Great Basin: Geosphere, v. 2, no. 7, p. 353–368, doi:10.1130/GES00054.1.

Dokka, R.K., Mahaffie, M.J., and Snoke, A.W., 1986, Thermochronologic evidence of major tectonic denudation associated with detachment faulting, northern Ruby Mountains - East Humboldt Range, Nevada: Tectonics v. 5, no. 7, p. 995–1006, doi:10.1029/TC005i007p00995.

Druschke, P., Hanson, A.D., and Wells, M.L., 2009a, Structural, stratigraphic, and geochronologic evidence for extension predating Palaeogene volcanism in the Sevier hinterland, east-central Nevada: International Geology Review, v. 51, no. 7–8, p. 743–775, doi:10.1080/00206810902917941.

Druschke, P., Hanson, A.D., Wells, M.L., Rasbury, T., Stockli, D.F., and Gehrels, G., 2009b, Synconvergent surface-breaking normal faults of Late Cretaceous age within the Sevier hinterland, east-central Nevada: Geology, v. 37, no. 5, p. 447–450, doi:10.1130/G25546A.1.

Dubiel, R.F., Potter, C.J., Good, S.C., and Snee, L.W., 1996, Reconstructing an Eocene extensional basin: The White Sage Formation, eastern Great Basin, in Beratan, K.K., ed., Reconstructing the History of Basin and Range Extension Using Sedimentology and Stratigraphy: Geological Society of America Special Paper 303, p. 1–14, doi:10.1130/0-8137-2303-5.1.

du Bray, E.A., 2007, Time, space, and composition relations among northern Nevada intrusive rocks and their metallogenic implications: Geosphere, v. 3, no. 5, p. 381–405, doi:10.1130/GES00109.1.

Emsbo, P., Groves, D.I., Hofstra, A.H., and Bierlein, F.P., 2006, The giant Carlin gold province: a protracted interplay of orogenic, basinal, and hydrothermal processes above a lithospheric boundary: Mineralium Deposita, v. 41, no. 6, p. 517–525.

Farley, K.A., 2000, Helium diffusion from apatite: General behavior as illustrated by Durango fluorapatite: Journal of Geophysical Research, v. 105, no. B2, p. 2903–2914, doi:10.1029/1999JB900348.

Gans, P.B., Mahood, G.A., and Schermer, E, 1989, Synextensional magmatism in the Basin and Range Province: A case study from the eastern Great Basin: Geological Society of America Special Paper 253, 53 p., doi:10.1130/SPE233-p1.

Garver, J.I., Brandon, M.T., Roden-Tice, M.K., and Kamp, P.J.J., 1999, Exhumation history of orogenic highlands determined by detrital fission track thermochronology, in Ring, U., et al., eds., Exhumation Processes: Normal Faulting, Ductile Flow, and Erosion: Geological Society [London] Special Publication 154, p. 283–304.

Gaschnig, R.M., Vervoort, J.D., Lewis, R.S., and Tikoff, B., 2011, Isotopic evolution of the Idaho batholith and Challis intrusive province, northern US Cordillera: Journal of Petrology, v. 52, p. 2397–2429, doi:10.1093/petrology/egr050.

Haines, S.H., and van der Pluijm, B.A., 2010, Dating the detachment fault system of the Ruby Mountains, Nevada: Significance for the kinematics of low-angle normal faults: Tectonics, v. 29, TC4028, doi:10.1029/2009TC002552.

Hallett, B.W., and Spear, F.S., 2014, The P-T history of anatectic pelites of the northern East Humboldt Range, Nevada: Evidence for tectonic loading, decompression, and anatexis: Journal of Petrology, v. 55, no. 1, p. 3–36, doi:10.1093/petrology/egt057.

Hallett, B.W., and Spear, F.S., 2015, Monazite, zircon, and garnet growth in migmatitic pelites as a record of metamorphism and partial melting in the East Humboldt Range, Nevada: American Mineralogist, v. 100, no. 4, p. 951–972, doi:10.2138/am-2015-4839.

Haynes, S.R., 2003, Development of the Eocene Elko Basin, northeastern Nevada: Implications for paleogeography and regional tectonism [M.S. thesis]: Vancouver, British Columbia, Canada, University of British Columbia, 159 p.

Henry, C.D., 2008, Ash-flow tuffs and paleovalleys in northeastern Nevada: Implications for Eocene paleogeography and extension in the Sevier hinterland, northern Great Basin: Geosphere, v. 4, no. 1, p. 1–35, doi:10.1130/GES00122.1.

Henry, C.D., and Boden, D.R., 1997, Eocene magmatism of the Tuscarora volcanic field, Elko County, Nevada, and implications for Carlin-type mineralization, in Vikre, P., et al., eds., Guidebook for the Society of Economic Geologists Field Conference: Littleton, Colorado, Society of Economic Geologists, v. 28, p. 193–202, doi:10.1130/0091-7613(1998)026<1067:EMTHSF>2.3.CO;2.

Henry, C.D., and Boden, D.R., 1998, Geologic map of the southern part of the Mount Blitzen Quadrangle, Nevada: Nevada Bureau of Mines and Geology Map 110, scale 1:24,000, 20 p.

Henry, C.D., Boden, D.R., and Castor S.B., 1999, Geologic map of the Tuscarora Quadrangle, northeastern Nevada: Nevada Bureau of Mines and Geology Map 116, scale 1:24,000, 20 p.

Henry, C.D., and Faulds, J.E., 1999, Geologic map of the Emigrant Pass Quadrangle, Lander County, Nevada: Nevada Bureau of Mines and Geology Open-File Report 99-9, scale 1:24,000, 20 p.

Henry, C.D., Faulds, J.E., Boden, D.R., and Ressel, M.W., 2001, Timing and styles of Cenozoic extension near the Carlin Trend, northeastern Nevada: Implications for the formation of Carlin-type gold deposits, in Shaddrick, D.R., Zbinden, E., Mathewson, D.C., and Prenn, C., eds., Regional Tectonics & Structural Control of Ore: The Major Gold Trends of Northern Nevada: Geological Society of Nevada Special Publication 33, p. 115–128.

Henry, C.D., Hinz, N.H., Faulds, J.E., Colgan, J.P., John, D.A., Brooks, E.R., Cassel, E.J., Garside, L.J., Davis, D.A., and Castor, S.B., 2012, Eocene–early Miocene paleotopography of the Sierra Nevada–Great Basin–Nevadaplano based on widespread ash-flow tuffs and paleovalleys: Geosphere, v. 8, p. 1–27, doi:10.1130/GES00727.1.

Henry, C.D., and John, D.A., 2013, Magmatism, ash-flow tuffs, and calderas of the ignimbrite flareup in the western Nevada volcanic field, Great Basin, USA: Geosphere, v. 9, no. 3, p. 951–1008, doi:10.1130/GES00867.1.

Henry, C.D., McGrew, A.J., Colgan, J.P., Snoke, A.W., and Brueseke, M.E., 2011, Timing, distribution, amount, and style of Cenozoic extension in the northern Great Basin, in

Lee, J., and Evans, J.P., eds., Geologic field trips to the Basin and Range, Rocky Mountains, Snake River Plain, and terranes of the U.S. Cordillera: Geological Society of America Field Guide 21, p. 27–66, doi:10.1130/2011.0021(02).

Hickey, K., Tosdal, R., Haynes, S., and Moore, S., 2005, Tectonics, paleogeography, volcanic succession, and the depth of formation of Eocene sediment-hosted gold deposits of the northern Carlin Trend, Nevada: Geological Society of Nevada Symposium, GSN Symposium Field Trip Guidebook 3, p. 97–105.

Hodges, K.V., Snoke, A.W., and Hurlow, H.A., 1992, Thermal evolution of a portion of the Sevier hinterland: The northern Ruby Mountains–East Humboldt Range and Wood Hills, northeastern Nevada: Tectonics, v. 11, no. 1, p. 154–164, doi:10.1029/91TC01879.

Hodges, K.V., and Walker, J.D., 1992, Extension in the Cretaceous Sevier orogen, North American Cordillera: Geological Society of America Bulletin, v. 104, p. 560–569, doi:10.1130/0016-7606(1992)104<0560:EITCSO>2.3.CO;2.

Ketcham, R.A., 2005, Forward and inverse modeling of low-temperature thermochronology data: Reviews in Mineralogy and Geochemistry, v. 58, no. 1, p. 275–314, doi:10.2138/rmg.2005.58.11.

Kirkland, C.L., Yakymchuk, C., Szilas, K., Evans, N., Hollis, J., McDonald, B., and Gardiner, N. J., 2018, Apatite: a U-Pb thermochronometer or geochronometer?: Lithos, v. 318-319, p. 143-157, doi:10.1016/j.lithos.2018.08.007.

Kuiper, K.F., Deino, A., Hilgen, F.J., Krijgsman, W., Renne, P.R., and Wijbrans, J.R., 2008, Synchonizing rock clocks of Earth history: Science, v. 320, no. 5875, p. 500–504, doi:10.1126/science.1154339.

Kylander-Clark, A.R.C., Hacker, B.R., and Cottle, J.M., 2013, Laser-ablation split-stream ICP petrochronology: Chemical Geology, v. 345, p. 99–112, doi:10.1016/j.chemgeo.2013.02.019.

Lapointe, D.D., Tingley, J.V., and Jones, R.B., 1991, Mineral resources of Elko County Nevada: Nevada Bureau of Mines Geological Bulletin, v. 106, 236 p.

Linde, G.M., Trexler, J.H., Cashman, P.H., Gehrels, G., and Dickinson, W.R., 2016, Detrital zircon U-Pb geochronology and Hf isotope geochemistry of the Roberts Mountains

allochthon: New insights into the early Paleozoic tectonics of western North America: Geosphere, v. 12, no. 3, p. 1016–1031, doi:10.1130/GES01252.1.

Litherland, M.M., and Klemperer, S.L., 2017, Crustal structure of the Ruby Mountains metamorphic core complex, Nevada, from passive seismic imaging: Geosphere, v. 13, no. 5, p. 1–18, doi:10.1130/GES01472.1.

Long, S.P., 2019, Geometry and magnitude of extension in the Basin and Range Province (39°N), California, Nevada, and Utah, U.S.A: Constraints from a province-scale cross section: Geological Society of America Bulletin, v. 131, no. 1–2, p. 99–119, doi:10.1130/B31974.1.

Long, S.P., 2012, Magnitudes and spatial patterns of erosional exhumation in the Sevier hinterland, eastern Nevada and western Utah, USA: Insights from a Paleogene paleogeographic map: Geosphere, v. 8, no. 4, p. 881–901, doi:10.1130/GES00783.1.

Long, S.P., Heizler, M.T., Thomson, S.N., Reiners, P.W., and Fryxell, J.E., 2018, Rapid Oligocene to Early Miocene Extension Along the Grant Range Detachment System, Nevada, USA: Insights From Multipart Cooling Histories of Footwall Rocks: Tectonics, v. 37, doi:10.1029/2018TC005073.

Long, S.P., Henry, C.D., Muntean, J.L., Edmondo, G.P., and Cassel, E.J., 2014, Early Cretaceous construction of a structural culmination, Eureka, Nevada, U.S.A.: Implications for out-of-sequence deformation in the Sevier hinterland: Geosphere, v. 10, no. 3, p. 564–584, doi:10.1130/GES00997.1.

Long, S.P., Thomson, S.N., Reiners, P.W., and Di Fiori, R.V., 2015, Synorogenic extension localized by upper-crustal thickening: An example from the Late Cretaceous Nevadaplano: Geology, v. 43, no. 4, p. 351–354, doi:10.1130/G36431.1.

Ludwig, K.R., 1998, On the Treatment of Concordant Uranium-Lead Ages: Geochimica et Cosmochimica Acta, v. 62, p. 665–676, doi:10.1016/S0016-7037(98)00059-3.

Lund Snee, J.E., Miller, E.L., Grove, M., Hourigan, J.K., and Konstantinou, A., 2016, Cenozoic paleogeographic evolution of the Elko Basin and surrounding region, northeast Nevada: Geosphere, v. 12, no. 2, p. 464–500, doi:10.1130/GES01198.1.

MacCready, T., Snoke, A.W., Wright, J.E., and Howard, K.A., 1997, Mid-crustal flow during Tertiary extension in the Ruby Mountains core complex, Nevada: Geological Society

of America Bulletin, v. 109, no. 12, p. 1576–1594, doi:10.1130/0016-7606(1997)109<1576:MCFDTE>2.3.CO;2.

McGrew, A.J., Peters, M.T., and Wright, J.E., 2000, Thermobarometric constraints on the tectonothermal evolution of the East Humboldt Range metamorphic core complex, Nevada: Geological Society of America Bulletin, v. 112, no. 1, p. 45–60, doi:10.1130/0016-7606(2000)112<45:TCOTTE>2.0.CO;2.

McGrew, A.J., Rodgers, A., Metcalf, J.R., Bruno Meisner, C., and Webb, L.E., 2018, Tracking the escalator ride from mid-crustal depths to the surface: New constraints on the pace and episodicity of Late Eocene to Miocene exhumation from the southern East Humboldt Range metamorphic core complex, Elko County, Nevada: Geological Society of America Abstracts with Programs. v. 50, no. 6, doi:10.1130/abs/2018AM-318419.

McGrew, A.J., and Snee, L.W., 1994, 40Ar/39Ar thermochronologic constraints on the tectonothermal evolution of the northern East Humboldt Range metamorphic core complex, Nevada: Tectonophysics, v. 238, no. 1–4 p. 425–450, doi:10.1016/0040-1951(94)90067-1.

McGrew, A.J., and Snoke, A.W., 2015, Geologic map of the Welcome Quadrangle and an adjacent part of the Wells Quadrangle, Elko County, Nevada: Nevada Bureau of Mines and Geology Map 184, scale 1:24,000, 40 p.

Miller, E.L., and Gans, P.B., 1989, Cretaceous crustal structure and metamorphism in the hinterland of the Sevier thrust belt, western U.S. Cordillera: Geology, v. 17, p. 59–62, doi:10.1130/0091-7613(1989)017<0059:CCSAMI>2.3.CO;2.

Miller, D.M., and Hoisch, T.D., 1995, Jurassic tectonics of northeastern Nevada and northwestern Utah from the perspective of barometric studies, in Miller, D.M., and Busby, C., eds., Jurassic magmatism and tectonics of the North American Cordillera: Geological Society of America Special Paper 299, p. 267–294, doi:10.1130/SPE299-p267.

Miller, D.M., Nakata, J.K., and Glick, L.J., 1990, K-Ar ages of Jurassic to Tertiary plutonic and metamorphic rocks, northwestern Utah and northeastern Nevada: U.S. Geological Survey Bulletin, no. 1906, 18 p.

Misch, P., and Hazzard, J.C., 1962, Stratigraphy and metamorphism of late Precambrian rocks in central northeastern Nevada and adjacent Utah: American Association of Petroleum Geologists Bulletin, v. 46, no. 3, p. 289–343.

Mix, H.T., Mulch, A., Kent-Corson, M.L., and Chamberlain, C.P., 2011, Cenozoic migration of topography in the North American Cordillera: Geology, v. 39, no. 1, p. 87–90, doi:10.1130/G31450.1.

Mueller, K.J., Cerveny, P.K., Perkins, M.E., and Snee, L.W., 1999, Chronology of polyphase extension in the Windermere Hills, northeast Nevada: Geological Society of America Bulletin, v. 111, no. 1, p. 11–27, doi:10.1130/0016-7606(1999)111<0011:COPEIT>2.3.CO;2.

Norman, B.W., 2013, Structural evolution of the central Schell Creek Range, White Pine County, Nevada [M.S. thesis]: Santa Barbara, California, The University of California, Santa Barbara, 60 p.

Nutt, C.J., and Good, S.C., 1998, Recognition and significance of Eocene deformation in the Alligator Ridge area, central Nevada: U.S. Geological Survey Open-File Report 98–338, p. 141–150.

Painter, C.S., Carrapa, B., DeCelles, P.G., Gehrels, G.E., and Thomson, S.N., 2014, Exhumation of the North American Cordillera revealed by multi-dating of Upper Jurassic–Upper Cretaceous foreland basin deposits: Geological Society of America Bulletin, v. 126, no.11–12, p. 1439–1464, doi:10.1130/B30999.1.

Pape, J.R., Seedorff, E., Baril, T.C., and Thompson, T.B., 2016, Structural reconstruction and age of an extensionally faulted porphyry molybdenum system at Spruce Mountain, Elko County, Nevada: Geosphere, v. 12, no. 1, p. 237–263, doi:10.1130/GES01249.1.

Porter, R., Liu, Y., and Holt, W.E., 2016, Lithospheric records of orogeny within the continental U.S.: Geophysical Research Letters, v. 43, p. 144–153, doi:10.1002/2015GL066950.

Potter, C.J., Dubiel, R.F., Snee, L.W., and Good, S.C., 1995, Eocene extension of early Eocene lacustrine strata in a complexly deformed Cordilleran hinterland, northwest Utah and northeast Nevada: Geology, v. 23, no. 2, p. 181–184, doi:10.1130/0091-7613(1995)023<0181:EEOEEL>2.3.CO;2.

Premo, W.R., Moscati, R.J., McGrew, A.J., and Snoke, A.W., 2014, New U-Pb zircon geochronology of Precambrian paragneisses and late Phanerozoic orthogneisses of the Angel Lake–Lizzies Basin region of the East Humboldt Range, northeastern Nevada: A comparison with the thermal chronology at Lamoille Canyon in the adjacent Ruby Mountains: Geological Society of America Abstracts with Programs, v. 46, no. 5, p. 33.

Rahl, J.M., McGrew, A.J., and Foland, K.A., 2002, Transition from contraction to extension in the northeastern Basin and Range: New evidence from the Copper Mountains, Nevada: Journal of Geology, v. 110, no. 2, p. 179–194, doi:10.1086/338413.

Reiners, P.W., and Brandon, M.T., 2006, Using thermochronology to understand orogenic erosion: Annual Reviews in Earth and Planetary Science Letters, v. 34, p. 419–466, doi:10.1146/annurev.earth.34.031405.125202.

Reiners, P.W., Campbell, I.H., Nicolescu, S., Allen, C.M., Hourigan, J.K., Garver, J.I., Mattinson, J.M., and Cowan, D.S., 2005, (U-Th)/(He-Pb) double dating of detrital zircons: American Journal of Science, v. 305, p. 259–311, doi:10.2475/ajs.305.4.259.

Renne, P.R., Swisher, C.C., Deino, A.L., Karner, D.B., Owens, T.L., and DePaolo, D.J., 1998, Intercalibration of standards, absolute ages and uncertainties in 40Ar/39Ar dating: Chemical Geology, v. 145, p. 117–152, doi:10.1016/S0009-2541(97)00159-9.

Ressel, M.W., and Henry, C.D., 2006, Igneous geology of the Carlin Trend, Nevada: Development of the Eocene plutonic complex and significance for Carlin-Type gold deposits: Economic Geology and the Bulletin of the Society of Economic Geologists, v. 101, p. 347–383, doi:10.2113/gsecongeo.101.2.347.

Ruiz, G.M.H., Seward, D., and Winkler, W., 2004, Detrital thermochronology - a new perspective on hinterland tectonics, an example from the Andean Amazon Basin, Ecuador: Basin Research, v. 16, no. 3, p. 413–430, doi:10.1111/j.1365-2117.2004.00239.x.

Satarugsa, P., and Johnson, R.A., 2000, Cenozoic tectonic evolution of the Ruby Mountains metamorphic core complex and adjacent valleys, northeastern Nevada: Rocky Mountain Geology, v. 35, no. 2, p. 205–230, doi:10.2113/35.2.205.

Saylor, J.E., Stockli, D.F., Horton, B.K., Nie, J., and Mora, A., 2012, Discriminating rapid exhumation from syndepositional volcanism using detrital zircon double dating: Implications for the tectonic history of the Eastern Cordillera, Colombia: Geological Society of America Bulletin, v. 124, no. 5/6, p. 762–779, doi:10.1130/B30534.1.

Seymour, R.S., 1980, Petrology and geochemistry of the Coffeepot Stock, N.E. Nevada: A record of crystallization history and hydrothermal fluid migrations [M.S. thesis]: Eugene, Oregon, University of Oregon, 273 p.

Silberling, N.J., 1975, Age relationships of the Golconda thrust fault, Sonoma Range, North-Central Nevada: Boulder, Colorado: Geological Society of America Special Paper 163, 28 p., doi:10.1130/SPE163-p1.

Smith, M.E., Cassel, E.J., Jicha, B.R., Singer, B.S., and Canada, A.S., 2017, Hinterland drainage closure and lake formation in response to middle Eocene Farallon slab removal, Nevada, U.S.A.: Earth and Planetary Science Letters, v. 479, p. 156–167, doi:10.1016/j.epsl.2017.09.023.

Smith, M.E., Carroll, A.R., Jicha, B.R., Cassel, E.J., and Scott, J.J., 2014, Paleogeographic record of Eocene Farallon slab rollback beneath western North America: Geology, v. 42, no. 12, p. 1039–1042, doi:10.1130/G36025.1.

Snoke, A.W., Barnes, C.G., Howard, K.A., Wright, J.E., and Copeland, P., 2004, Late Eocene and Oligocene intrusions in the Ruby-East Humboldt Core Complex, Nevada: Magmatic processes in the middle crust in relation to tectonic extension: Geological Society of America Abstracts with Programs, v. 36, no. 4, p. 71.

Snoke, A.W., Howard, K.A., McGrew, A.J., Burton, B.R., Barnes, C.G., Peters, M.T., and Wright, J.E., 1997, The grand tour of the Ruby-East Humboldt metamorphic core complex, northeastern Nevada: Brigham Young University Geological Studies, v. 42, p. 225–269.

Snoke, A.W., and Miller, D.M., 1988, Metamorphic and tectonic history of the northeastern Great Basin, in Ernst, W.G., ed., Metamorphism and crustal evolution of the western United States: Englewood Cliffs, New Jersey, Prentice Hall, p. 606–648.

Stacey, J.S., and Kramers, J.D., 1975, Approximation of terrestrial lead isotope evolution by a 2-stage model: Earth and Planetary Science Letters, v. 26, no. 2, p. 207–221, doi:10.1016/0012-821X(75)90088-6.

Stewart, J.H., and Carlson, J.E., 1981, Geologic map of Nevada: U.S. Geological Survey and Nevada Bureau of Mines and Geology, scale 1:500,000, G81386.

Stockli, D.F., 2005, Application of low-temperature thermochronometry to extensional tectonic settings: Reviews in Mineralogy and Geochemistry, v. 58, no. 1, p. 411–448, doi:10.2138/rmg.2005.58.16.

Taylor, S.R., and McLennan, S.M., 1985, The continental crust: Its composition and evolution: Blackwell Scientific Publication, Carlton, 312 p.

Tera, F., and Wasserburg, G.J., 1972, U-Th-Pb systematics in three Apollo 14 basalts and the problem of initial Pb in lunar rocks: Earth and Planetary Science Letters, v. 14, p. 281–304, doi:10.1016/0012-821X(72)90128-8.

Thomson, S.N., Gehrels, G.E., Ruiz, J., and Buchwaldt, R., 2012, Routine low-damage U-Pb dating of apatite using laser ablation-multicollector-ICPMS: Geochemistry, Geophysics, Geosystems, v. 13, no. 2, 23 p., doi:10.1029/2011GC003928.

Thomson, K.D., Stockli, D.F., Clark, J.D., Puigdefàbregas, C., and Fildani, A., 2017, Detrital zircon (U-Th)/(He-Pb) double-dating constraints on provenance and foreland basin evolution of the Ainsa Basin, south-central Pyrenees, Spain: Tectonics, v. 36, no. 7, p. 1352–1375, doi:10.1002/2017TC004504.

Thorman, C.H., Ketner, K.B., Brooks, W.E., Snee, L.W., and Zimmermann, R.A., 1991, Late Mesozoic-Cenozoic Tectonics in Northeastern Nevada, in Raines, G.L., Lisle, R.E., Schafer, R.W., and Wilkinson, W.H., eds., Geology and Ore Deposits of the Great Basin: Geological Society of Nevada Symposium Proceedings, v. 1, p. 25–45.

Trexler, J.H., Cashman, P.H., Snyder, W.S., and Davydov, V.I., 2004, Late Paleozoic tectonism in Nevada: Timing, kinematics, and tectonic significance: Geological Society of America Bulletin, v. 116, no. 5–6, p. 525–538. doi:10.1130/B25295.1.

Trexler, J., and Nitchman, S.P., 1990, Sequence stratigraphy and evolution of the Antler foreland basin, east-central Nevada: Geology, v. 18, no. 5, p. 422–425, doi:10.1130/0091-7613(1990)018<0422:SSAEOT>2.3.CO;2

Vandervoort, D.S., and Schmitt, J.G., 1990, Cretaceous to early Tertiary paleogeography in the hinterland of the Sevier thrust belt, east-central Nevada: Geology, v. 18, p. 567–570, doi:10.1130/0091-7613(1990)018<0567:CTETPI>2.3.CO;2.

Vermeesch, P., 2018, IsoplotR: A free and open toolbox for geochronology: Geoscience Frontiers, v. 9, no. 5, p. 1479–1493, doi:10.1016/j.gsf.2018.04.001.

Wells, M.L., 1997, Alternating contraction and extension in the hinterlands of orogenic belts: An example from the Raft River Mountains, Utah: Geological Society of America Bulletin, v. 109, no. 1, p. 107–126, doi:10.1130/0016-7606(1997)109<0107:ACAEIT>2.3.CO;2.

Wells, M.L., Dallmeyer, R.D., and Allmendinger, R.W., 1990, Late Cretaceous extension in the hinterland of the Sevier thrust belt, northwestern Utah and southern Idaho: Geology, v. 18, p. 929–933, doi:10.1130/0091-7613(1990)018<0929:LCEITH>2.3.CO;2.

Wells, M.L., Hoisch, T.D., Cruz-Uribe, A.M., and Vervoort, J.D., 2012, Geodynamics of synconvergent extension and tectonic mode switching: Constraints from the Sevier-Laramide orogen: Tectonics, v. 31, no. 1, doi:10.1029/2011TC002913.

Wells, M.L., and Hoisch, T.D., 2008, The role of mantle delamination in widespread Late Cretaceous extension and magmatism in the Cordilleran orogen, western United States: Geological Society of America Bulletin, v. 120, no. 5–6, p. 515–530, doi:10.1130/B26006.1.

Wolfe, J.A., Forest, C.E., and Molnar, P., 1998, Paleobotanical evidence of Eocene and Oligocene paleoaltitudes in midlatitude western North America: Geological Society of America Bulletin, v. 110, no. 5, p. 664–678, doi:10.1130/0016-7606(1998)110<0664:PEOEAO>2.3.CO;2.

Wolfe, M.R., and Stockli, D.F., 2010, Zircon (U–Th)/He thermochronometry in the KTB drill hole, Germany, and its implications for bulk He diffusion kinetics in zircon: Earth and Planetary Science Letters, v. 295, p. 69–82, doi:10.1016/j.epsl.2010.03.025.

Woodward, L.A., 1967, Stratigraphy and correlation of Late Precambrian rocks of Pilot Range, Elko County, Nevada, and Box Elder County, Utah: American Association of Petroleum Geologists, v. 51, p. 235–243.

Wright, J.E., and Snoke, A.W., 1993, Tertiary magmatism and mylonitization in the Ruby–East Humboldt metamorphic core complex, northeastern Nevada: U-Pb geochronology and Sr, Nd, and Pb isotope geochemistry: Geological Society of America Bulletin, v. 105, no. 7, p. 935–952, doi:10.1130/0016-7606(1993)105<0935:TMAMIT>2.3.CO;2.

Young, J.C., 1960, Structure and stratigraphy in north central Schell Creek Range, in in Geology of east central Nevada: Intermountain Association of Petroleum Geologists Guidebook, 11th Annual Field Conference, p. 158–172.

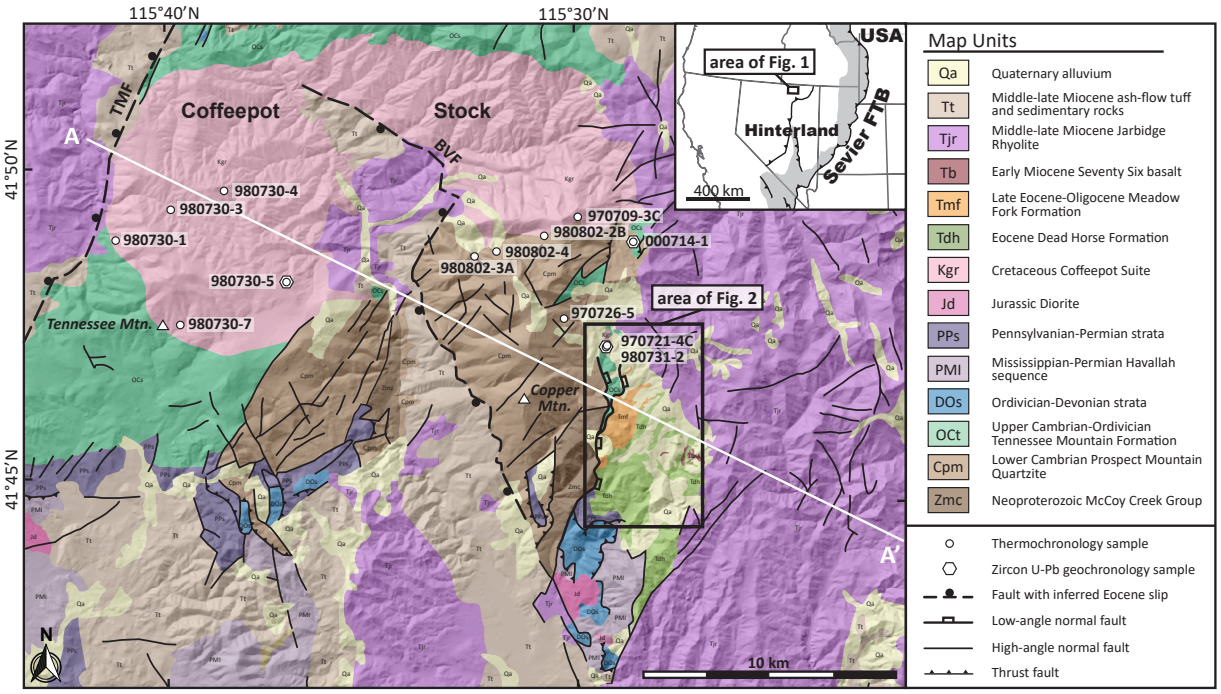

Figure 2.1. Geologic map of the Copper Mountains area showing geochronology and thermochronology sample locations. Geology modified from Bushnell (1967) and Coats (1964). Inset: map of western North America showing location of major fold-thrust belts from DeCelles (2004) and Long (2012). Abbreviations: TMF—Tennessee Mountain Fault; BVF—Bruneau Valley Fault.

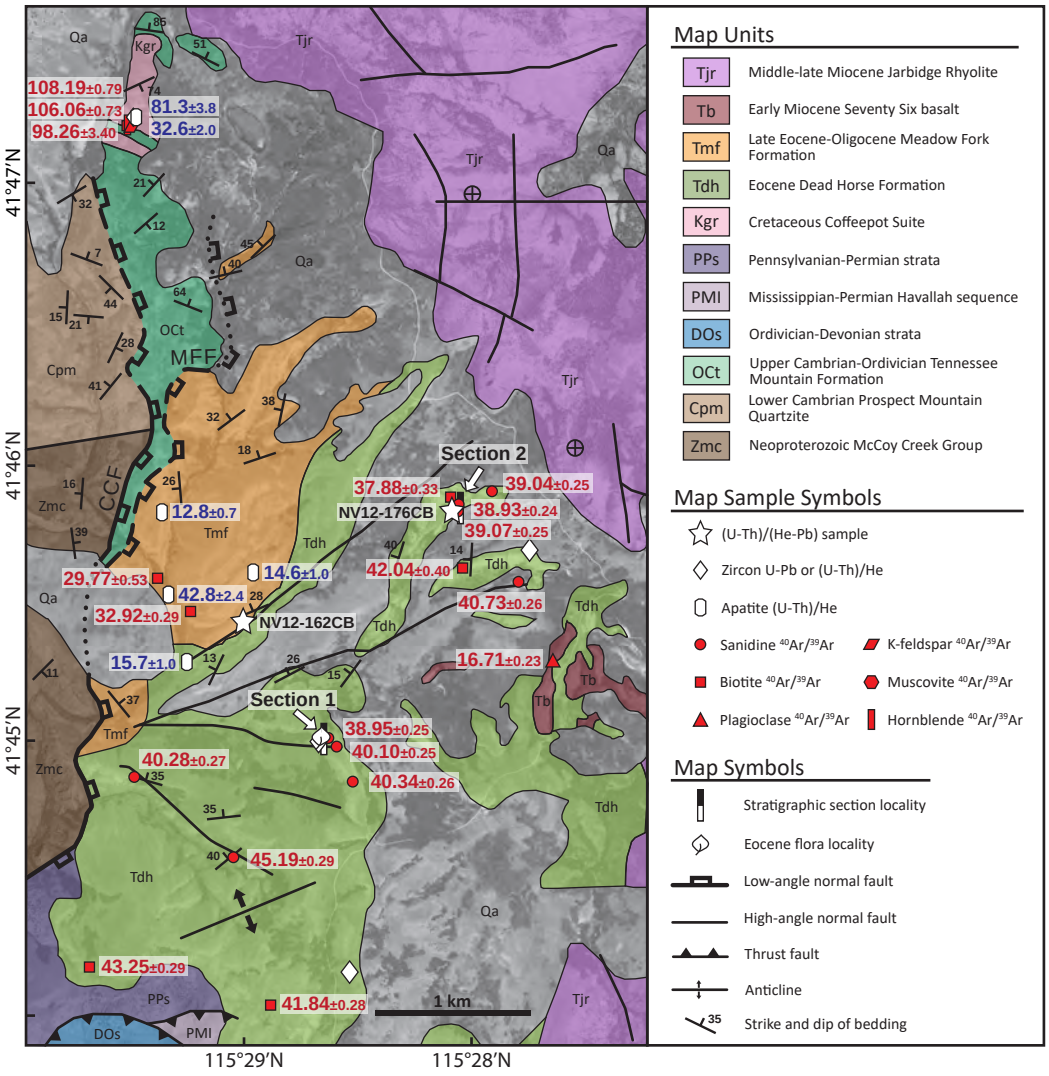

Figure 2.2. Geologic map of Copper Basin showing geochronology and thermochronology sample locations as well as $^{40}Ar/^{39}Ar$ and (U-Th)/He ages (see Tables 1 and 2 for full $^{40}Ar/^{39}Ar$ and (U-Th)/He results). Geology modified from Rahl et al. (2002) and Henry et al. (2011). Satellite imagery from USGS National Map. Abbreviations: CCF—Copper Creek Fault; MFF—Meadow Fork Fault.

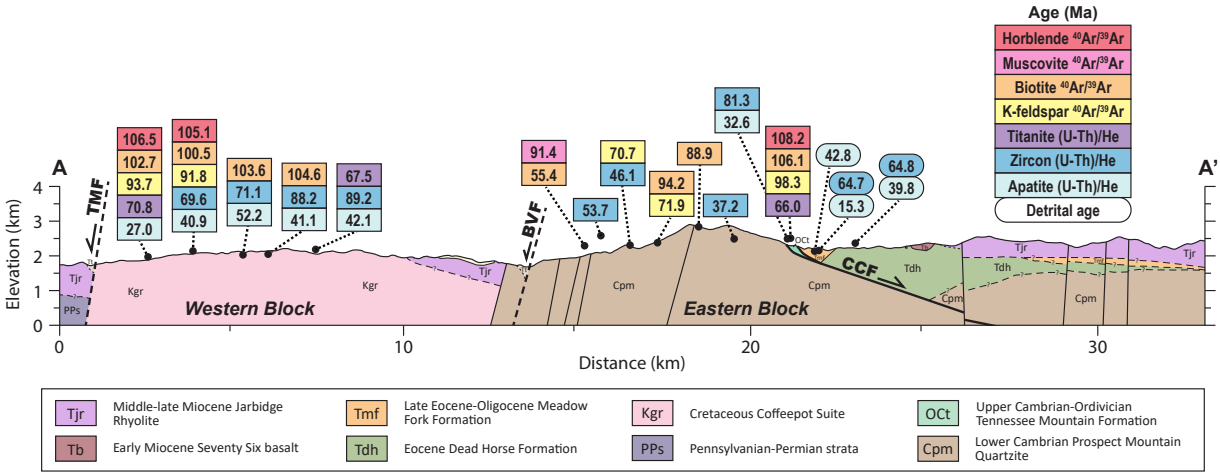

Figure 2.3. Cross section across the Copper Mountains and Copper Basin showing a summary of (U-Th)/He and $^{40}Ar/^{39}Ar$ data (see Tables 1 and 2). Eastern portion of cross section modified from Coats (1964). Abbreviations: TMF—Tennessee Mountain Fault; BVF—Bruneau Valley Fault; CCF—Copper Creek Fault.

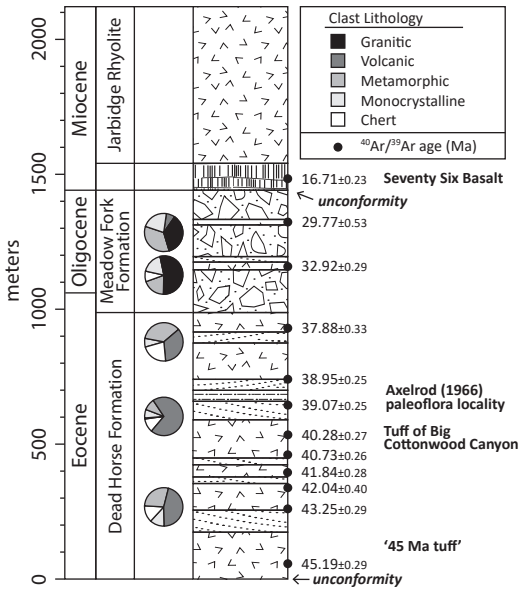

Figure 2.4. Generalized stratigraphic column of Copper Basin showing $^{40}Ar/^{39}Ar$ geochronology, and conglomerate clast lithology count data (n>100 counts each).

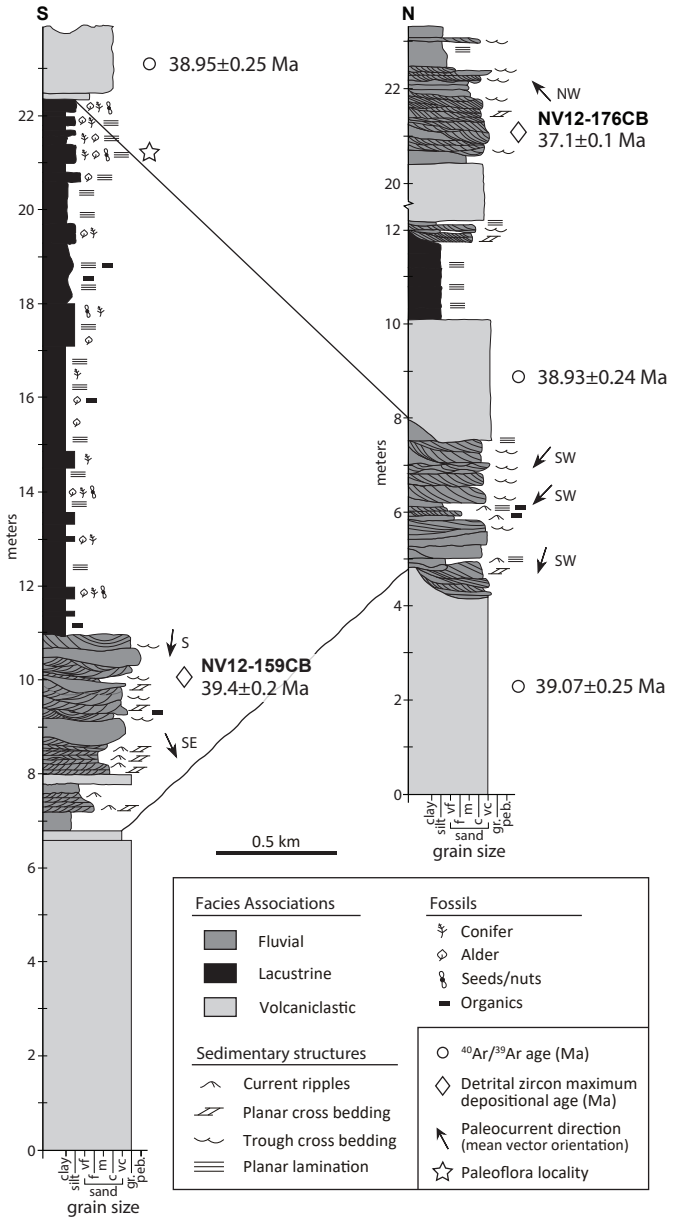

Figure 2.5. Two stratigraphic columns measured in the Dead Horse Formation showing facies association and chronostratigraphic correlation. See Figure 2 for section locations.

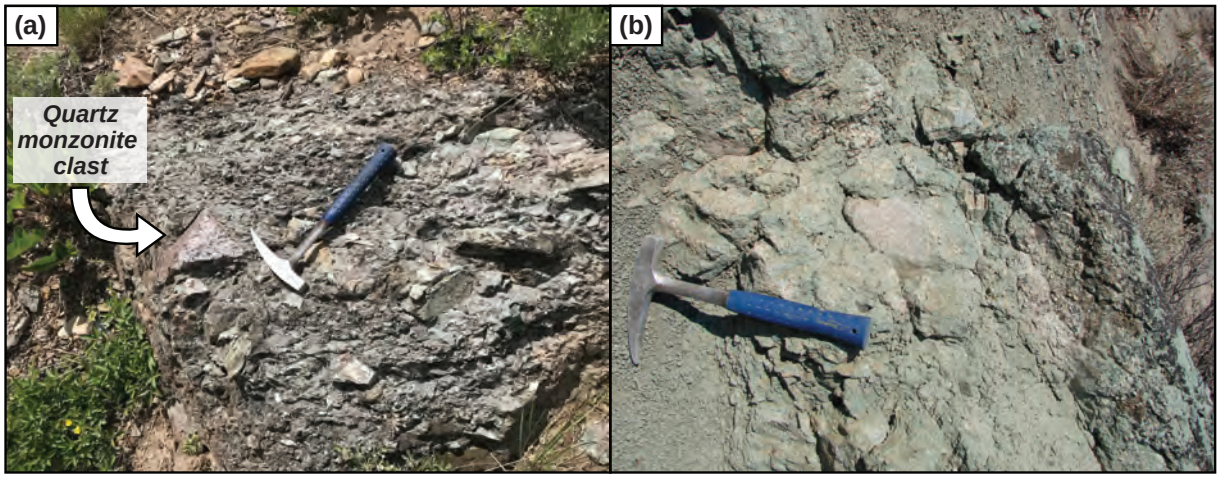

Figure 2.6. (A) Poorly sorted pebble conglomerate and sandstone of the Meadow Fork Formation. (B) Pebble–cobble conglomerate in the Meadow Fork Formation with quartz monzonite cobbles. Meadow Fork Formation outcrops often display pervasive blue-green alteration from partial feldspar replacement to chlorite.

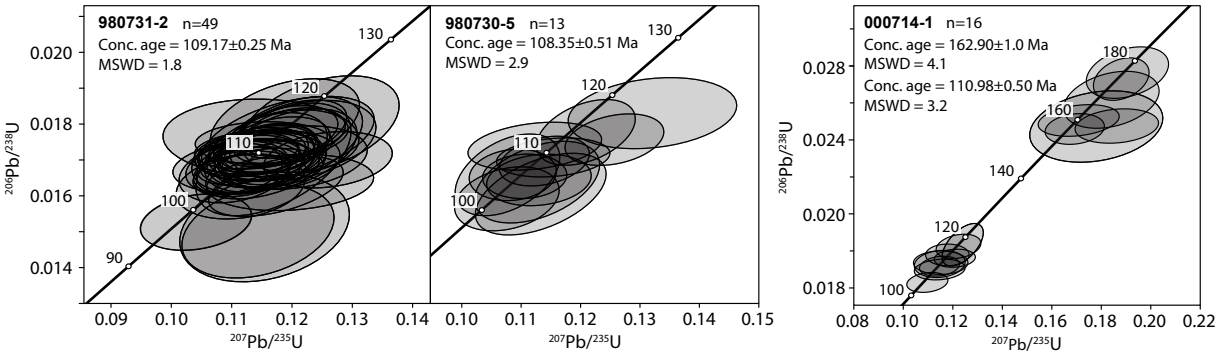

Figure 2.7. Concordia diagrams of zircon U-Pb ages for three samples of Coffeepot Stock intrusives plotted using Vermeesch (2018). Older zircon grain ages in sample 000714-1 (ca. 160–180 Ma) are interpreted to represent core ages of inherited zircons.

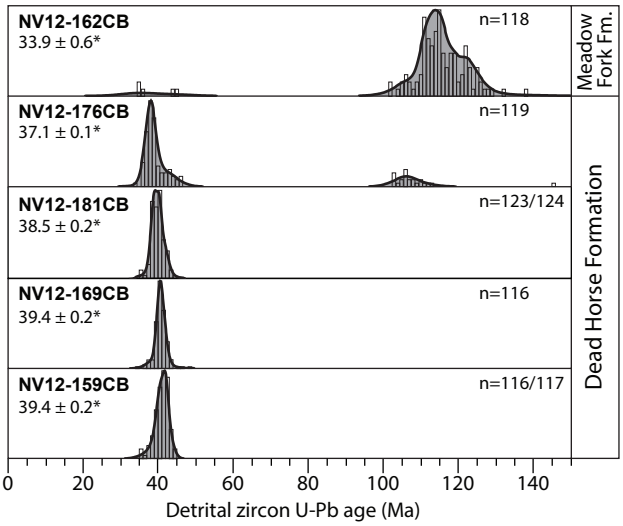

Figure 2.8. Detrital zircon kernel density estimates (KDE's) for sandstone samples from the Dead Horse Formation (NV12-181CB; NV12-169CB; NV12-159CB; NV12-176CB) and the Meadow Fork Formation (NV12-162CB) plotted using Vermeesch (2018). Asterisk denotes maximum depositional age determined from youngest age population (see Supplemental Figs. S2 and S3).

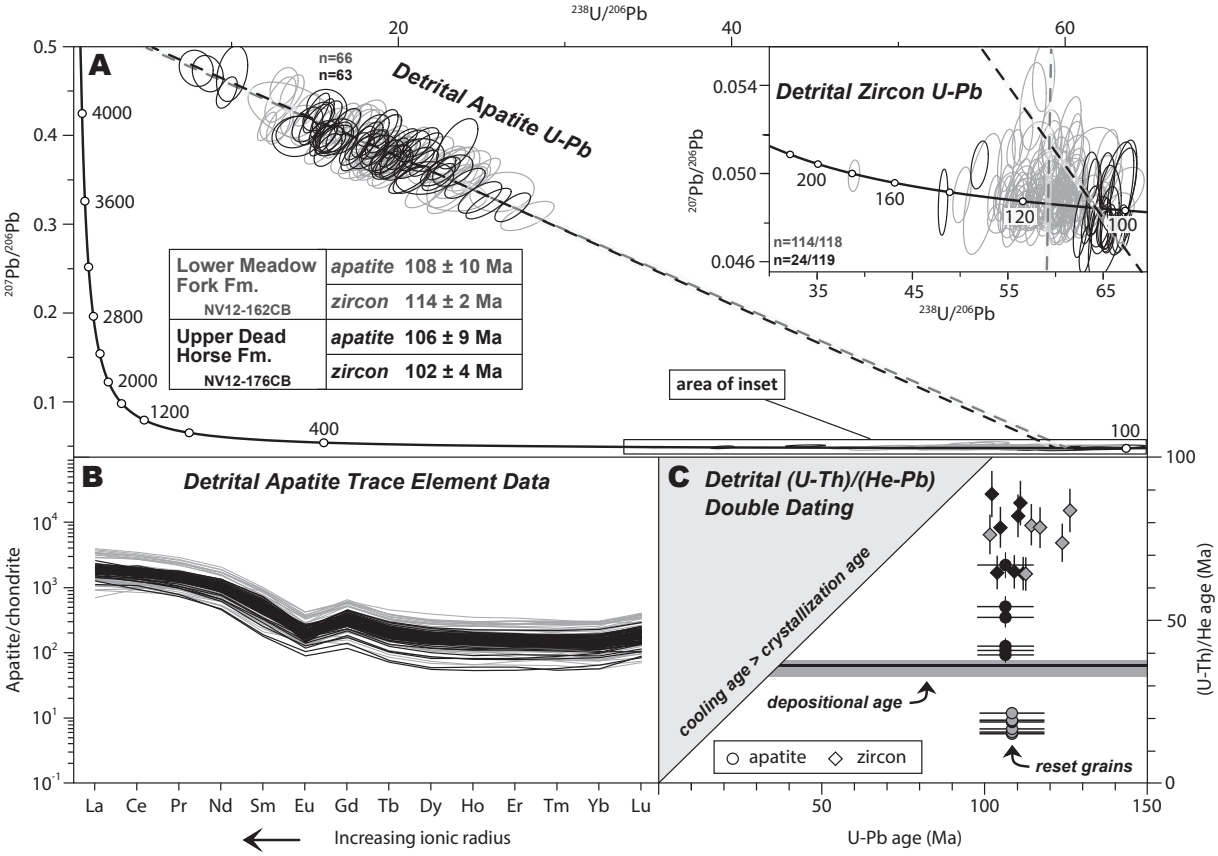

Figure 2.9. (A) Tera-Wasserburg plot of results from LA-ICPMS U-Pb dating of detrital zircon and apatite from samples NV12-162CB (gray) and NV12-176CB (black). Linear regressions of apatite and zircon U-Pb ages show excellent agreement with the ca. 109 Ma crystallization of the Coffeepot Stock. Error ellipses correspond to 2σ uncertainty of individual grain ages. (B) LASS-ICPMS rare earth element data for detrital apatite from the same samples. Chondrite REE values from Taylor and McLennan (1985). (C) (U-Th)/(He-Pb) double dating results for detrital zircon and apatite from the same samples.

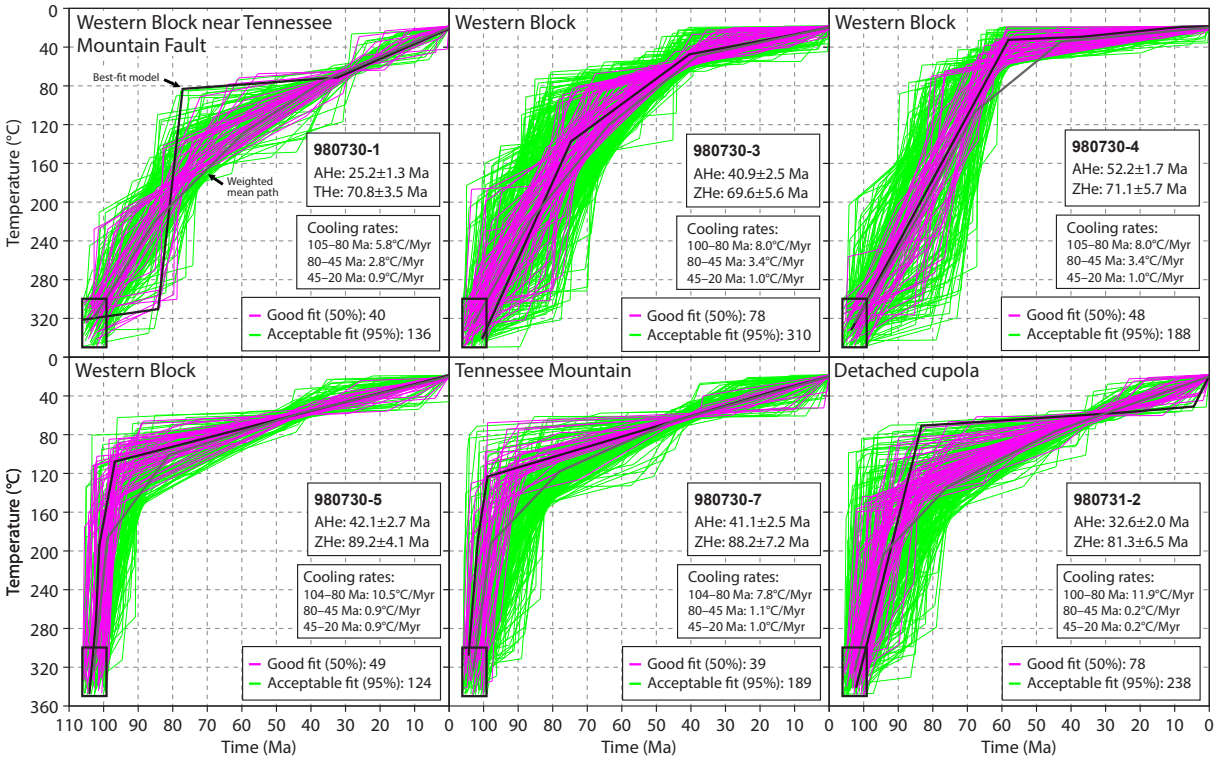

Figure 2.10. Results from inverse time-temperature HeFTy modeling (Ketcham, 2005) of apatite, titanite, and zircon (U-Th)/He data for six samples of the Coffeepot Stock. Cooling rates estimated from the best-fit model path. Model starting constraints (black box) corresponds to the range of biotite $^{40}Ar/^{39}Ar$ ages within the western fault block. Models with "good" fit corresponds to a mean goodness-of-fit value of 0.5 or higher, above the statistical precision limit, whereas "acceptable" models have a goodness-of-fit value above 0.05, where all statistics pass the 95% confidence test (Ketcham, 2005). See Supplemental Section 1 for model parameters.

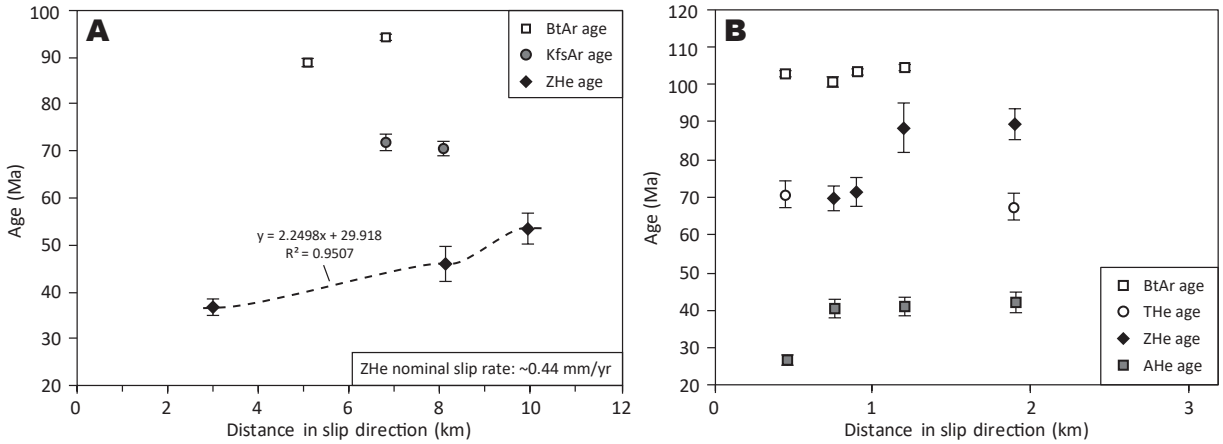

Figure 2.11. (A) Plot of zircon (U-Th)/He, biotite $^{40}Ar/^{39}Ar$, and k-feldspar $^{40}Ar/^{39}Ar$ age versus distance in slip direction from the Copper Creek Fault. Nominal slip rate calculated using a simple linear regression and inverse of the regression slope (e.g., Stockli, 2005). Equation and correlation coefficient shown for linear regression. Black dashed line is only used as a visual aid for changes in ages across the footwall. (B) Plot of apatite, zircon, and titanite (U-Th)/He and biotite $^{40}Ar/^{39}Ar$ age versus horizontal distance of samples in slip direction from the Tennessee Mountain Fault. Abbreviations: BtAr—biotite $^{40}Ar/^{39}Ar$ age, KfsAr—K-feldspar $^{40}Ar/^{39}Ar$ age, ZHe—zircon (U-Th)/He age, THe—titanite (U-Th)/He age, AHe—apatite (U-Th)/He age.

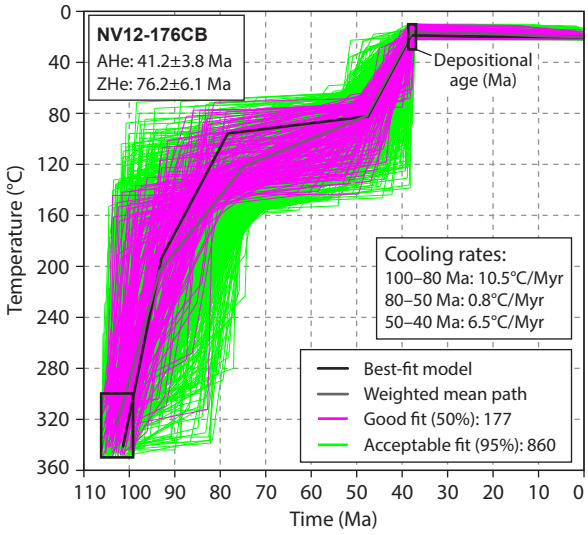

Figure 2.12. Inverse time-temperature model of upper Dead Horse Formation strata determined using detrital zircon and apatite (U-Th)/He ages and $^{40}Ar/^{39}Ar$ depositional age of sample NV12-176CB.

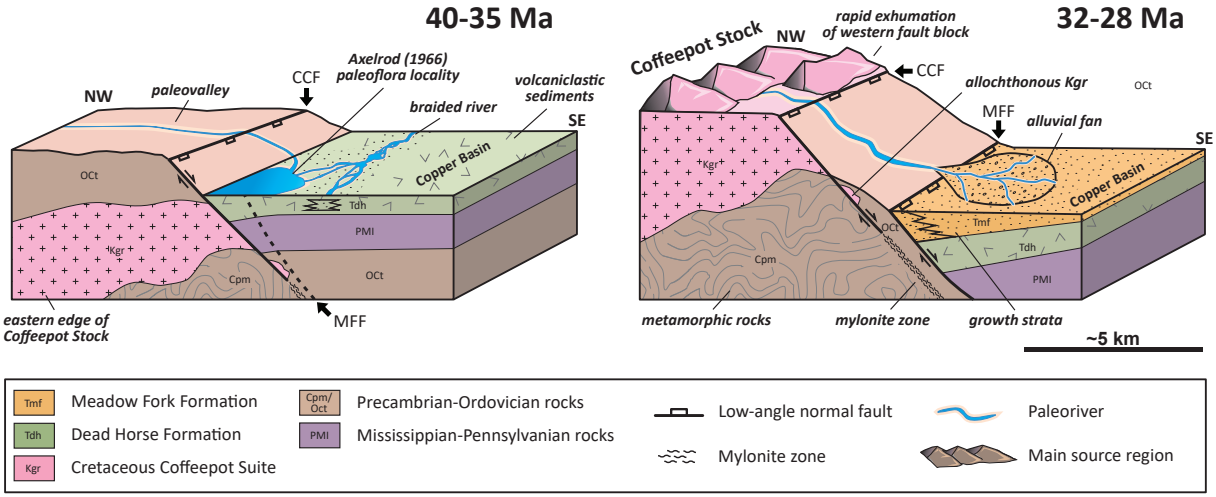

Figure 2.13. Schematic block diagrams showing development of Copper Basin during the middle to late Eocene and early Oligocene.

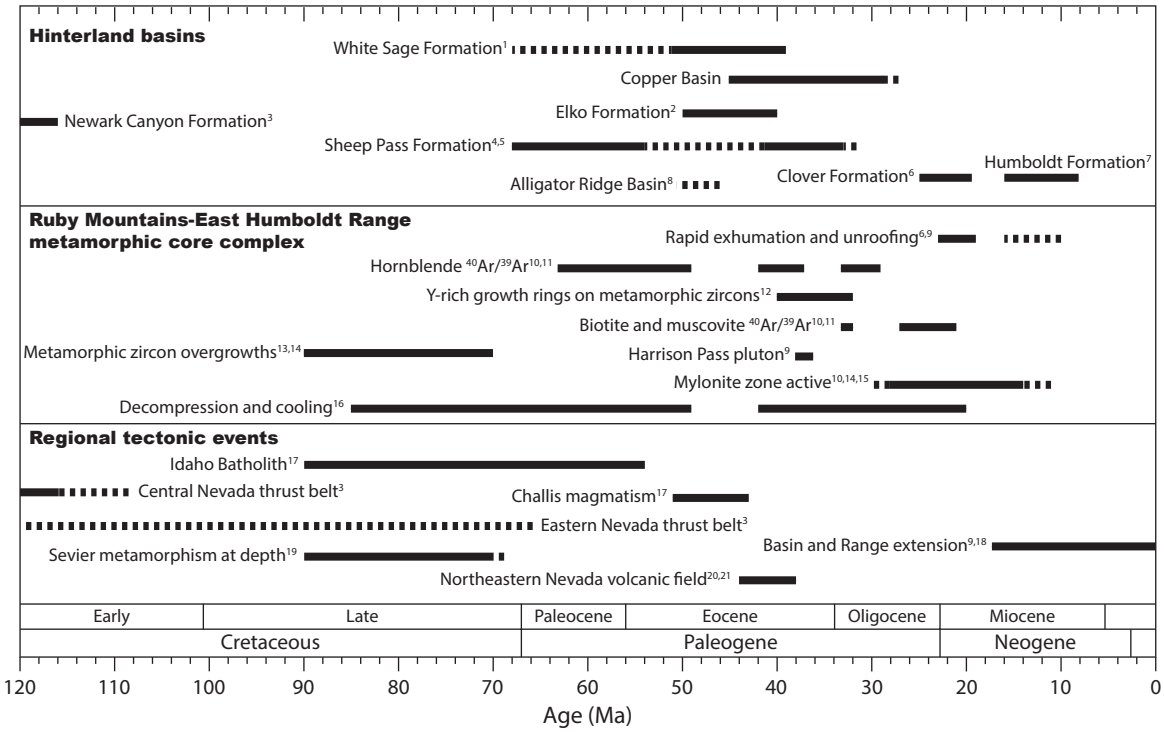

Figure 2.14. Summary of select geologic events in the North American Cordilleran hinterland. Dashed lines correspond to greater uncertainty. References: 1—Dubiel et al. (1996); 2—Smith et al. (2017); 3—Long et al. (2015); 4—Druschke et al. (2009a); 5—Druschke et al. (2009b); 6—McGrew and Snoke (2015); 7—Lund Snee et al. (2016); 8—Nutt and Good (1998); 9—Colgan et al. (2010); 10—McGrew and Snee (1994); 11—Dallmeyer et al. (1986); 12—Hallett and Spear (2015); 13—Premo et al. (2014); 14—Wright and Snoke (1993), Haines and van der Pluijm (2010); 15—McGrew et al. (2000); 16—Gaschnig et al. (2011); 17—Dickinson (1997); 18—Miller and Gans (1989); 19—Brooks et al. (1995); 20—Henry (2008).

TABLE 2.1. RESULTS FROM (U-Th)/He THERMOCHRONOLOGY

Sample number	Location		Elevation (m)	Lithology	Mineral(s) dated	n[†]	Age (Ma)	±2σ[§] (Ma)
	Latitude (°N)[*]	Longitude (°W)[*]						
980730-1[#]	41.8206	115.6900	1966	granodiorite	apatite	6	27.0	1.3
980730-1[#]	41.8206	115.6900	1966	granodiorite	titanite	4	70.8	3.5
980730-3[#]	41.8297	115.6674	2164	quartz monzonite	apatite	3	40.9	2.5
980730-3[#]	41.8297	115.6674	2164	quartz monzonite	zircon	3	69.6	3.2
980730-4	41.8352	115.6455	2195	quartz monzonite	apatite	1	52.2	1.7
980730-4[#]	41.8352	115.6455	2195	quartz monzonite	zircon	2	71.1	4.0
980730-5[#]	41.8067	115.6230	1825	quartz monzonite	apatite	4	42.1	2.7
980730-5[#]	41.8067	115.6230	1825	quartz monzonite	titanite	3	67.5	3.4
980730-5	41.8067	115.6230	1825	quartz monzonite	zircon	1	89.2	4.1
980730-7	41.7946	115.6643	2477	granodiorite	apatite	1	41.1	2.5
980730-7[#]	41.7946	115.6643	2477	granodiorite	zircon	3	88.2	6.6
980731-2[#]	41.7859	115.4934	2484	granodiorite	apatite	3	32.6	2.0
980731-2[#]	41.7859	115.4934	2484	granodiorite	zircon	3	81.3	3.8
980802-2B[#]	41.8198	115.5154	2591	quartz monzonite	zircon	3	46.1	3.7
980802-4[#]	41.8154	115.5350	2519	leucogranite	zircon	2	53.7	3.2
000714-1[#]	41.8161	115.4779	2487	quartz monzonite	titanite	4	37.2	1.9
970721-4C[#]	41.7856	115.4935	2475	granodiorite	titanite	2	66.0	3.3
NV12-162CB	41.7571	115.4835	2154	sandstone	detrital apatite	7	15.3-21.7	0.9-1.3
NV12-162CB	41.7571	115.4835	2154	sandstone	detrital zircon	7	64.7-139.6	5.2-11.2
NV12-176CB	41.7640	115.4679	2366	sandstone	detrital apatite	7	39.8-106.5	2.4-6.4
NV12-176CB	41.7640	115.4679	2366	sandstone	detrital zircon	7	64.8-89.6	5.2-7.2
010801-3[#]	41.7562	115.4873	2103	granitoid cobble	detrital apatite	3	42.8	2.4
050724-2A[#]	41.7603	115.4840	2170	granitoid cobble	detrital apatite	17	14.6	1.0
050720-9D[#]	41.7550	115.4886	2121	granitoid cobble	detrital apatite	12	15.7	1.0
050720-11[#]	41.7632	115.4907	2170	granitoid cobble	detrital apatite	16	12.8	0.7

[*]Locations reported relative to NAD 1983 projection.
[†]Number of grains analyzed in detrital sample or number of grains included in weighted mean age calculation.
[§]Fully propagated analytical uncertainty.
[#]Weighted mean age determined using Vermeesch (2018).

TABLE 2.2. RESULTS FROM $^{40}Ar/^{39}Ar$ GEOCHRONOLOGY

Sample number	Location		Lithology	Mineral(s)	n†	%^{40}Ar§	$^{40}Ar/^{39}Ar$ age (Ma)#	2σ**	2σ††	MSWD
	Latitude (°N)*	Longitude (°W)*								
960702-1A§§	41.7353	115.4823	ash-fall tuff	biotite	1	83	41.84	0.10	0.28	5
970728-3§§	41.7645	115.4687	ash-fall tuff	sanidine	1	86	37.88	0.23	0.33	1
970709-3C§§	41.8254	115.5016	quartz monzonite	biotite	1	88	94.21	0.30	0.66	12
970709-3C	41.8254	115.5016	quartz monzonite	k-feldspar	*21 of 40*		71.87##	1.59	1.65	43
970721-4C§§	41.7856	115.4935	quartz monzonite	hornblende	1	89	108.19	0.40	0.79	12
970721-4C§§	41.7856	115.4935	quartz monzonite	biotite	1	58	106.06	0.30	0.73	9
970721-4C	41.7856	115.4935	quartz monzonite	k-feldspar	*5 of 31*		98.26##	3.34	3.40	1.2
970726-5	41.7946	115.5080	muscovite-biotite schist	biotite	1	63	88.94	0.71	0.90	0.9
980730-1§§	41.8202	115.6911	granodiorite	hornblende	1	95	106.47	0.30	0.73	4.8
980730-1§§	41.8202	115.6911	granodiorite	biotite	1	89	102.72	0.30	0.71	2.7
980730-1	41.8202	115.6911	granodiorite	k-feldspar	*30 of 40*		93.70##	1.26	1.38	13
980730-3§§	41.8297	115.6674	quartz monzonite	hornblende	1	88	105.05	0.40	0.77	5.4
980730-3§§	41.8297	115.6674	quartz monzonite	biotite	1	66	100.49	1.21	1.37	7.6
980730-3	41.8297	115.6674	quartz monzonite	k-feldspar	*24 of 34*		91.82##	1.29	1.41	7.1
980730-4§§	41.8358	115.6456	quartz monzonite	biotite	1	91	103.63	0.30	0.71	1.9
980730-7§§	41.7946	115.6643	granodiorite	biotite	1	74	104.64	0.40	0.77	9.2
980802-2B	41.8198	115.5154	quartz monzonite	k-feldspar	*17 of 33*		70.73##	1.34	1.41	5.6
980802-3A	41.8133	115.5436	biotite-muscovite schist	biotite	2		55.39	2.38	2.39	35
980802-3A	41.8133	115.5436	biotite-muscovite schist	muscovite	2		91.37	0.56	0.64	3.6
990704-1§§	41.7560	115.4596	plagioclase-phyric basalt	plagioclase	1	83	16.71	0.20	0.23	4
010801-5	41.7600	115.4912	ignimbrite	biotite, hornblende	3		29.77	0.52	0.53	0.97
050719-4	41.7370	115.4964	andesite	biotite	1	89	43.25	0.10	0.29	2.7
050720-3B	41.7505	115.4784	ash-fall tuff	biotite	1	89	40.32	0.20	0.32	1.6
050720-10	41.7579	115.4887	ash-fall tuff	biotite	1	73	32.92	0.20	0.29	2.4
050721-11	41.7605	115.4674	ignimbrite	biotite	1	52	42.04	0.30	0.40	2.4
H06-123***	41.7439	115.4856	ash-fall tuff	sanidine	*9 of 10*		45.19##	0.07	0.29	1.17
H06-121***	41.7484	115.4930	ignimbrite	sanidine	*12 of 18*		40.28##	0.10	0.27	1.42
NV12-171CB†††	41.7649	115.4653	ignimbrite	sanidine	*19 of 19*		39.04##	0.07	0.25	1.12
NV12-175CB†††	41.7640	115.4679	ignimbrite	sanidine	*36 of 40*		38.93##	0.04	0.24	1.30
NV12-173CB†††	41.7637	115.4679	ignimbrite	sanidine	*20 of 20*		39.07##	0.07	0.25	1.09
NV12-165CB(B)†††	41.7597	115.4632	ignimbrite	sanidine	*19 of 19*		40.73##	0.06	0.26	0.86
ANV14-001COB†††	41.7502	115.4771	ignimbrite	sanidine	*30 of 31*		40.10##	0.05	0.25	0.98
NV12-160CB(A)†††	41.7508	115.4780	ignimbrite	sanidine	*24 of 24*		38.95##	0.06	0.25	0.76
NV12-157CB†††	41.7482	115.4759	ignimbrite	sanidine	*24 of 24*		40.34##	0.08	0.26	1.70

*Locations reported relative to NAD 1983 projection.

†Number of experiments. Italicized numbers represent number of crystals included in single crystal fusion weighted mean age, which corresponds to the number of fusion experiments containing >90% ^{40}Ar.

§Percentage of total ^{40}Ar in the plateau fraction. All plateaus are >70% concordant.

#Weighted mean age or plateau age calculated relative to the 28.201 Ma age for Fish Canyon Tuff sanidine (FCs) using the equations of Kuiper et al. (2008) and Renne et al. (1998). Where MSWD of weighted mean ages is >1, uncertainty has been multiplied by the square of the MSWD. For samples where MSWD exceeds 2, weighted mean uncertainties are the 100(1-α)% confidence interval calculated using Vermeesch (2018).

**Analytical uncertainty.

††Fully propagated uncertainty.

§§From Rahl et al. (2002).

##Weighted mean of single crystal analyses.

***From Henry (2008).

†††From Smith et al. (2017).

CHAPTER III

Geochemical Controls on Hinterland Lake Evolution: Eocene Elko Basin, Northeastern Nevada, U.S.A.

ABSTRACT

In northeastern Nevada, early–middle Eocene terrestrial strata of the Elko Formation record high-elevation lacustrine deposition across a large area of the North American Cordilleran hinterland. A new chronostratigraphic framework of the Elko Formation permits evaluation of geochemical variations in hinterland paleolakes. To identify if Eocene lakes were connected through time and differentiate intrinsic and external drivers for observed stratigraphic changes, we employ stable isotope geochemistry of lacustrine carbonates ($^{87}Sr/^{86}Sr$, $\delta^{13}C$, and $\delta^{18}O$) with δD analysis of volcanic glass (δD_{glass}) extracted from ash beds intercalated with lacustrine strata. $^{87}Sr/^{86}Sr$ ratios and Sr concentrations of 28 rock samples collected from lacustrine carbonates and marls and 6 stream water samples collected from watersheds draining a variety of potential sources to the Elko Basin also tests the provenance of source waters. When combined with lithostratigraphic correlations and single-crystal sanidine $^{40}Ar/^{39}Ar$ geochronology, these datasets highlight subtle changes in paleolake hydrology that are linked to organic preservation and allogenic controls on stratigraphic architecture.

Lacustrine lithofacies and geochemical data highlight two lake-type progressions from overfilled to balanced-fill conditions, one between ca. 49 and ca. 47 Ma and the other between ca. 45 and 41 Ma, that are correlative across northeastern Nevada and evident across multiple isotopic proxies. Samples collected from the Elko Formation generally have low $^{87}Sr/^{86}Sr$ ratios (mean = 0.7086; σ = 0.0007) indicating the Elko Basin catchment was predominantly comprised of sedimentary and volcanic rocks for the duration of lacustrine deposition. However, significantly elevated $^{87}Sr/^{86}Sr$ ratios of up to 0.7108 are present in samples from a range of stratigraphic and basin locations. Initial lacustrine deposition recorded in early Eocene strata in the northern Adobe Range is characterized by a sudden ~0.002 increase in

$^{87}Sr/^{86}Sr$ ratio, 15.5‰ decrease in $\delta^{18}O$, and 4.9‰ decrease in $\delta^{13}C$ values at ca. 48.9 Ma that is interpreted to record capture of a river. A separate river capture event likely occurred at ca. 41.3 Ma where $^{87}Sr/^{86}Sr$ ratios show a rapid ~0.002 increase and then progressive decrease until ca. 41.0 Ma. Between ca. 43 and 41 Ma, covariance in $^{87}Sr/^{86}Sr$, $\delta^{13}C$, and $\delta^{18}O$ occurs across multiple locations, implying prolonged lacustrine connectivity across a >1000 km^2 area. Lacustrine sediments deposited during this time have ~5‰ higher $\delta^{13}C$ values and ~9‰ higher $\delta^{18}O$ values (on average), which are correlative to enhanced evaporation and increased organic matter preservation that accompanied balanced-filled conditions. Intensified evaporation of hinterland lake waters after ca. 42.1 Ma is also recorded by a progressive 38–52‰ increase in δD_{glass} values in ash beds deposited directly prior to basin closure. At ca. 41.3 Ma, a 13‰ increase in $\delta^{18}O$ and 16.2‰ increase in $\delta^{13}C$ is interpreted to reflect drainage diversion induced by encroaching volcanism, which likely promoted basin closure by ca. 40 Ma. This detailed multi-proxy chemostratigraphic record indicates Eocene lakes were broadly connected and that the size and geochemistry of hinterland lakes was strongly influenced by drainage capture events and rollback-driven volcanism.

INTRODUCTION

Lacustrine basins contain sediments that can preserve detailed changes in geochemical, sedimentological, and climatic variation (e.g., Benson and Peterman, 1995; Carroll and Bohacs, 1999; Cohen et al., 2003; Pietras et al., 2003; Doebbert et al., 2014; Smith et al., 2014b). As a lake basin system evolves, changes in hydrology and climate drive variability in the distribution of sedimentary litho- and petrofacies, lake stratification, and accommodation, all of which are reflected by lake water geochemistry (e.g., Bohacs et al., 2000; Grove et al., 2003; Carroll et al., 2008; Smith et al., 2008a/b; Chamberlain et al., 2012; Gierlowski-Kordesch et al., 2014; Cohen et al., 2015). Lacustrine carbonates record the isotopic composition of lake water they precipitated from and thus provide a tool for reconstructing high-resolution records of ancient lacustrine systems (Capo et al., 1998; Bohacs, 2003; Gierlowski-Kordesch et al., 2008), with up to annual resolution (Andrews et al., 2010).

Strontium isotopes ($^{87}Sr/^{86}Sr$) can be powerful geochemical tracers of terrestrial processes, including weathering rates (e.g., Blum et al., 1993; Bain and Bacon, 1994; Brennan et al., 2014), surface and groundwater movement (e.g., Palmer and Edmond, 1992; Andersson et al., 1994; Johnson and DePaolo, 1994; Jacobson and Wasserburg, 2005; Peterman et al., 2012), soil genesis and biochemical cycling (e.g., Herut et al., 1993), and the paleohydrology of lakes (e.g., Benson and Peterman, 1995; Talbot and Williams, 2000). Strontium readily substitutes for calcium in a wide range of minerals and rock types because it has an ionic radius (1.18 Å) that is comparable to Ca (1.00 Å) and it is one of the most abundant trace elements in rocks (Sposito, 1989; Clow et al., 1997; Capo et al., 1998). The utility of strontium as a geochemical tracer stems from its high mass, which results in negligible mass-dependent fractionation from biological and geological processes in comparison to low-mass isotopic systems, such as $\delta^{13}C$ and $\delta^{18}O$ (Capo et al., 1998; Doebbert, 2006). As a result, measured $^{87}Sr/^{86}Sr$ ratios are solely a reflection of variations in the sources of radiogenic ^{87}Sr and are unaffected by biologic or temperature variations (Clow et al., 1997). Sources of watershed variability in Sr are primarily a function of the geochemical composition and age of bedrock (Palmer and Edmond, 1992; Blum et al., 1998; Grove et al., 2003; Bataille and Bowen, 2012). Slight stoichiometric and isotopic variability between source areas and derivative surface waters, however, is common because reactive minerals (i.e., calcite) have elevated weathering reactions compared to more recalcitrant minerals commonly present in K-rich silicate rocks (Blum et al., 1993; Jacobson et al., 2003; Brennan et al., 2014). Once Sr cations reach a reservoir, such as a lake, mass balance modeling has demonstrated that Sr has a short residence time (~10^3–10^4 years) in balance-fill and underfilled phases of lacustrine systems and that Sr isotope records can be retained with extremely high resolution, on the order of ~10^2 years (Doebbert et al., 2014). Despite this high sensitivity, the Sr evolution of lakes is widely variable and rates and magnitudes of $^{87}Sr/^{86}Sr$ variations are poorly defined for lakes in a variety of geologic settings (Gierlowski-Kordesch et al., 2004; Doebbert et al., 2014).

Hinterland and wedge-top basins, located between the magmatic arc and thrust front, can preserve a record of the paleogeographic evolution of elevated landscapes that often reflect unique records of climatic and tectonic evolution (Rahl et al., 2002; Kent-Corson et al., 2006; Druschke et al., 2009a; Chamberlain et al., 2012; Fan et al., 2017). Drainage

connectivity within hinterlands poses a fundamental control on the sources and character of sediment delivered to forearc and foreland basins (Dickinson and Suczek, 1979; DeCelles, 2004; Carroll et al., 2008; DeCelles and Graham, 2015) and hinterland basins frequently host kerogen-rich lacustrine facies that may be a viable target for resource production (Effimoff and Pinezick, 1981; Solomon, 1981; Moore et al., 1983; Anna et al., 2007). However, hinterlands are characteristically erosional and synorogenic stratigraphic records are often unpreserved or incomplete (e.g., Potter et al., 1995; Haynes, 2003; Leier et al., 2010; Long, 2012; Benvenuti et al., 2014). Pronounced structural deformation in orogenic belts also creates inherent stratigraphic complexity, which has led to fundamental uncertainties in spatial and temporal reconstructions of hinterland strata using lithostratigraphic correlation (Dubiel et al., 1996; Haynes, 2003; Henry, 2008; Druschke et al., 2009a; Umhoefer et al., 2010). As a result, there is no consensus regarding the driving mechanisms for hinterland basin formation in western North America; accommodation is ascribed to a range of geomorphic and tectonic controls (Fig. 3.3; e.g., Dubiel et al., 1996; Haynes, 2003; Henry, 2008; Druschke et al., 2009b; Smith et al., 2017). Globally, hinterland basin formation has been attributed to multiple tectonic processes, including large-scale synorogenic extension, slab or lithospheric delamination, slab rollback, and the growth of lithospheric roots (e.g., Wells et al., 2012; Benvenuti et al., 2014; Cohen et al., 2015; DeCelles et al., 2015; Brun et al., 2016).

In the North American Cordilleran hinterland, the Eocene Elko Formation records ~10 Myr of fluvial and lacustrine sedimentation and its strata are exposed across a 9,000 km^2 area of northeastern Nevada (Fig. 3.1; Cassel et al., 2014; 2018). Recent $^{40}Ar/^{39}Ar$ geochronology of the Elko Formation and equivalent hinterland strata (cf. Smith et al., 2017) provides a chronostratigraphic framework (Fig. 3.2) for interpreting geochemical variability of hinterland lakes. A combination of Sr ($^{87}Sr/^{86}Sr$) and O ($\delta^{18}O$) isotopic data is useful because O isotopes fractionate in response to temperature, elevation, and drainage and atmospheric patterns (Dansgaard, 1964; Stuiver, 1970; Rowley et al., 2001; Carroll et al., 2008; Ezquerro et al., 2014). Carbon isotopes ($\delta^{13}C$) also fractionate in response to climatic variations and reflect the local and global hydrologic cycles as well as variations in lake evolution that affect organic productivity and preservation (Gross and Tracey, 1966; Davis et al., 2009; Chamberlain et al., 2013; Sluijs et al., 2013). By comparing Sr, C, and O isotope data across

temporally constrained stratigraphic intervals, it is possible to reconstruct controls on lake basin evolution that led to the observed depositional variability. We use this approach to test limited existing models of the response of Sr isotopic variations to changes in lithofacies in a large and long-lived lacustrine basin situated in the hinterland of the Sevier orogenic belt. This combined geochemical approach permits evaluation of 1) the extent and connectivity of lacustrine systems through time, and 2) controls on depositional and geochemical variability.

GEOLOGIC SETTING

The Elko Basin formed within the Eocene hinterland of the North American Cordillera and contains a wide variety of fluvial and lacustrine facies that represent terrestrial sedimentation at elevations of ~2.8 km (Cassel et al., 2018). High Paleogene elevations in the interior of the Sevier orogen reflect contractional deformation and orogenic thickening during late Mesozoic subduction of the Farallon plate (Coney and Harms, 1984; DeCelles, 2004). In the Eocene and Oligocene, Farallon slab rollback induced drainage migration, basin formation, <1 km of surface uplift, and southwest-propagating volcanism (Figs. 3.1–3.2; Janecke and Snee, 1993; Smith et al., 2014a, 2017; Heller and Liu, 2016; Cassel et al., 2018). Starting in the Paleogene, collapse of a welt of 50–60-km-thick crust that developed within the Cordilleran hinterland (Coney and Harms, 1984; Camilleri and Chamberlain, 1997; Dilek and Moores, 1999) created a chain of metamorphic core complexes that exhumed medium- to high-grade metamorphic rocks along the North American craton margin (Armstrong, 1982; DeCelles, 2004; Rey et al., 2009). In northeastern Nevada, the Elko Basin is currently dissected by the Ruby Mountains-East Humboldt Range-Wood Hills-Pequop Mountains metamorphic core complex, which exposes upper-amphibolite-facies metamorphic rocks (McGrew et al., 2000) with radiogenic $^{87}Sr/^{86}Sr$ ratios between 0.7098 and 0.7436 (Wright and Snoke, 1993; Lee et al., 2003). Present $^{87}Sr/^{86}Sr$ ratios of basement rocks exposed proximal to the Elko Basin range from a minimum of 0.7051 for Eocene volcanic rocks (estimated from minimum $^{87}Sr/^{86}Sr$ ratios for correlative volcanic rocks in the Challis and Absaroka volcanic fields; Peterman et al., 1970; Meen and Eggler, 1987; Hiza, 1999; Feeley et al., 2002) to a maximum of 0.7615 for Late Cretaceous leucogranites that intrude metamorphic rocks in the East Humboldt Range (Wright and Snoke, 1993). Measurements of

$^{87}Sr/^{86}Sr$ ratios of modern surface and groundwaters are therefore expected to reflect this considerable isotopic variability, which can likewise be tested using isotope geochemistry of Elko Formation strata.

The Elko Formation ranges in age from ca. 50 to 40 Ma (Smith et al., 2017) and is divided into an early Eocene member consisting of diverse fluvial and lacustrine facies that is unconformably overlain by widespread middle Eocene fluvial and lacustrine facies. Below lacustrine strata, terrestrial strata of the Elko Basin include fluvial sandstones and pebble to cobble conglomerates deposited in paleovalleys that deeply incise Paleozoic bedrock (Henry, 2008; Cassel et al., 2014). The lowermost lacustrine interval of both early and middle Eocene strata contains micritic carbonate with freshwater molluscs, carbonaceous shale, and abundant plant matter indicative of overfilled lake-type conditions (Smith and Ketner, 1976; Carroll and Bohacs, 1999; Abruzzese et al. 2005). A major lake transgression at ca. 42.3 Ma coincides with increased salinity and alkalization of lacustrine waters reflected by balanced-fill facies, including organic-rich laminated mudstone and microbialitic carbonate (Smith and Ketner, 1976; Solomon et al., 1979; Moore et al., 1983; Smith et al., 2017). Volcanism progressively encroached the Elko Basin during the middle Eocene and led to a gradual increase in the abundance of volcaniclastic material within 43–40 Ma lacustrine facies (Haynes, 2003; Mulch et al., 2015). All Elko Formation sediment deposition occurred during the generally high atmospheric CO_2 levels and warm climate of the early and middle Eocene (Zachos et al., 2001; Sluijs et al., 2013; Mulch et al., 2015). Around this time, Green River Formation sediments accumulated in warm-temperature to subtropical conditions (Wilf, 2000) amidst elevated physical and chemical weathering rates (Smith et al., 2008a, 2014b). In comparison, fossil leaf and pollen floras of the Elko Formation indicate a warm-temperate climate, but likely cooler and drier conditions than the foreland because of higher mean surface elevations during the Eocene (Wingate, 1983; Axelrod, 1996; Chamberlain et al., 2012; Cassel et al., 2014, 2018). The diversity of facies and associated lake-types within the Elko Formation provide unique variety in the type, age, and location of paleoisotopic proxy material that can be used to reconstruct controls on lake formation and evolution. Primary controls on isotopic variability in lacustrine systems include drainage diversion and capture, unroofing of new sources and/or changes in source erodibility, and climatic changes (Benson and Peterman, 1995; Carroll et al., 2006, 2008; Kent-Corson et al., 2006; Davis et al., 2009; Smith et al.,

2014b). These potential allogenic and autogenic drivers of facies changes are poorly understood for the Elko Formation, but critical aspects of the basin history. Documentation of the trend and magnitude of variations of multiple geochemical tracers reveals depositional patterns, hydrologic inputs, and climatic variations across the retroarc system during the early and middle Eocene.

METHODS

Sampling Strategy

To characterize the geochemistry of Eocene lacustrine strata within the Elko Basin, carbonate and tuff samples were collected from multiple locations and water samples were collected from modern rivers draining a variety of bedrock catchment lithologies (Fig. 3.1). Water samples were collected from catchments draining pre-Elko Formation bedrock surrounding the basin. The current configuration of potential source regions surrounding the Elko Basin likely deviates significantly from the source distribution during the Eocene, due to Neogene basin segmentation and late Eocene–Miocene deposition of up to 5 km of volcanic and volcaniclastic strata above the Elko Formation (Satarugsa and Johnson, 2000; Colgan et al., 2010; Camilleri et al., 2017). To best reconstruct potential Eocene sediment sources, we targeted modern drainages with distinct catchment lithologies and combined this with other available geochemical data for rivers, streams, and wells in the study area (Table 3.1; Supplemental Materials). Water samples were passed through 0.45 μm filters, collected in acid-cleaned HDPE (High Density Polyethylene) bottles, and immediately acidified to a pH of 2 with concentrated nitric acid during collection. For geochemical sampling of Elko Formation strata, locations with well-characterized and chronostratigraphically correlative strata that span a considerable period of lacustrine deposition were targeted. Several isolated samples were also collected from distal locations to test geochemical and isotopic variation of paleolake waters across a large areal extent of the basin during the middle Eocene (Fig. 3.1). In addition, samples were selected to identify the stratigraphic range of isotope ratios. Previous strontium isotope studies of Paleogene lacustrine carbonates have found profundal carbonate-rich mudstone is the ideal sampling material because it is the least susceptible to diagenetic alteration and generally widespread in a variety of lacustrine facies (e.g., Rhodes et

al., 2002; Doebbert et al., 2014). Other paleoisotopic studies have successfully used primary fossil fragments of ostracods (Chamberlain et al., 2013), shells, or bone, but this material is not laterally and stratigraphically widespread within Elko Formation facies. Ostracode-bearing facies within the Green River Formation have been found to contain the most pervasive diagenetic alteration, so correlative facies were avoided here. In addition to micritic and dolomicritic facies, limestone and dolostone beds were sampled throughout the basin, particularly where carbonate-rich mudstone is absent. Samples of volcanic ash interbedded with lacustrine strata were also collected from select areas that preserve volcanic glass. While most Elko Basin ash beds contain zeolite or clay minerals from altered volcanic glass (cf. Cassel and Breecker, 2017; Smith et al., 2017), several locations preserve unaltered volcanic glass in ash beds intercalated within lacustrine intervals. The uppermost section of the Elko Formation, exposed within the Pinon Range, was targeted for volcanic glass sampling because it contains abundant tuffaceous interbeds (Fig. 3.2) as well as other complimentary geochemical and isotopic data that is used to help evaluate the efficacy of this proxy for lake water chemistry.

Carbonate Laboratory Procedures

Sample separation and petrology

All micritic samples were collected from trenched stratigraphic sections dug to expose minimally weathered and altered material. Limestone samples were collected from both trenched sections and outcrop exposures but were carefully sampled to avoid visible weathering and alteration. Thin sections were prepared from samples collected at regular stratigraphic intervals within sections sampled for isotopic analysis to identify authigenic calcite and carbonate textures and avoid zones of recrystallization and overgrowth that suggest diagenetic alteration. 10–50 g of samples that were not associated with visible diagenetic alteration were crushed in a porcelain mortar and wet-separated to a <70 μm fraction using deionized water purified to 18.2 MΩ at the University of Idaho. Carbonate powder was separated from select samples (n = 14) using a New Wave Research Micromill equipped with a 787 μm diameter carbide drill bit. Finely-laminated micritic samples, or samples that contain zones of alteration, were carefully milled to avoid sampling of diagenetic

material. Following carbonate powder separation, aliquots were separated for X-ray diffraction and isotopic analysis.

To quantitatively evaluate the effect of mineralogical variation on $^{87}Sr/^{86}Sr$, $\delta^{13}C$, and $\delta^{18}O$ ratios, X-ray diffraction (XRD) was completed on all sample separates at the University of Idaho using an X-ray diffractometer with a Cu Kα X-ray source (l = 1.5418 Å). Samples were scanned between 20º and 55º 2-θ at a step size of 0.02º and a step time of 1-2 s to obtain a strong count intensity and to measure all significant calcite and dolomite peaks. Select samples that are representative of a range of mineralogies were scanned across a wider 2–70º 2-θ range to test the presence of other minerals. To approximate the proportions of calcite and dolomite, the relative areas of the sums of calcite peaks (peaks between 29.30º and 30.00º 2-θ) and dolomite peaks (peaks between 30.40º and 31.10º 2-θ) was computed following background subtraction (see Supplemental Materials). Following the procedure of Pietras (2003), sample separates comprised of ≥80% calcite are classified as calcite, ≥80% dolomite are classified as dolomite, and all other samples as mixed mineralogy (Table 3.2; Supplemental Materials).

Stable isotope analysis

Stable isotopic analyses for $\delta^{13}C$ and $\delta^{18}O$ were completed at the Washington State University GeoAnalytical laboratory and the University of Texas at Austin Isotope Geochemistry Laboratory following the methods of McCrea (1950) and Swart et al. (1991) (see Supplemental Materials for detailed methods description). Separates consisting of 20–60 μg of carbonate powder were loaded in vials and roasted in vacuo at 200 °C for one hour to release volatile compounds. Samples and standards were then reacted under vacuum with 0.1 mL of 100% phosphoric acid (ρ=1.8913 g/cm^3) at 75 °C (e.g., Al-Aasam et al., 1990). Headspace sampling of released CO_2 was performed using a Finnigan Gas-Bench and CO_2 was transferred to a MAT253 Isotope Ratio Mass Spectrometer (IRMS) instrument eight times versus a calibrated CO_2 reference tank. Analyses were rejected if a >10% difference in voltage of the mass 44 beam was detected between the sample and reference gas, if the mass 44 signal of the sample was <600 mV, if the standard deviation of the 1-sigma ratios of a sample exceeds 0.07‰, or if a high leak rate (>400 mbar/minute) was detected prior to analysis (e.g., Talbot, 1990; Doebbert et al., 2010). No correction is applied for variable acid

fractionation between calcite and dolomite, which may cause measured $\delta^{18}O$ values in samples containing dolomite to be as much as 0.8‰ higher (Sharma and Clayton, 1965). Precision of all analyses is ±0.2‰ for $\delta^{13}C$ and ±0.3‰ $\delta^{18}O$ (1σ standard error) based on repeated analysis of interlaboratory and internal standards.

Strontium isotopic analysis

Laboratory methods for strontium isotopic analysis were modified from dissolution, leaching, extraction, and purification procedures outlined in Doebbert (2006) and Doebbert et al. (2014) (see Supplemental Materials for detailed description of methodology). Since many carbonate-rich samples contain variable amounts of clastic silica with high Rb/Sr and sometimes highly radiogenic Sr ratios, bulk 50–100 mg carbonate samples were first leached with 1M ammonium acetate to remove labile Rb and Sr from clay material prior to carbonate extraction with 1M acetic acid. Following separation, insoluble residues were discarded and ~10 mg aliquots were collected. This was followed by Sr separation through ion exchange chromatography using Sr-spec resin and cation exchange resin. Sample aliquots consisting of ~500 ng of Sr were then placed on Re filaments with Ta_2O_5 activator and analyzed using an Isotopix Phoenix Thermal Ionization Mass Spectrometer (TIMS) at the University of Idaho. Mass analysis of Sr was conducted using a three-jump multi-collector analysis routine. Calculated $^{87}Sr/^{86}Sr$ ratios are the average of ~150 ratios and all TIMS analyses have an analytical error (2σ) between 0.00004 and 0.00006.

Volcanic glass laboratory procedures

Volcanic glass was separated from Eocene ash beds using the procedures of Cassel and Breecker (2017). Of all tuff and ash bed samples collected within the Elko Basin, only ~15% preserve unaltered volcanic glass suitable for isotopic analysis. This poor preservation is likely a product of increased dissolution of Si-O bonds within alkaline lacustrine waters, and the resulting values reflect the least alkaline conditions (Pollard et al., 2003; Cassel and Breecker, 2017). Preserved volcanic glass was separated via crushing, wet-separation sieving, hydrochloric and hydrofluoric acid abrasion, magnetic separation, and lithium metatungstate density separation. Separates (3 mg aliquots) consisting of >98% glass shards were then loaded in Ag capsules and pyrolyzed in a Thermo Scientific TC/EA coupled with a Thermo

Scientific MAT 253 gas source IRMS in the University of Texas at Austin Isotope Geochemistry Laboratory. Water contents (wt.%) of each sample were calculated using the mass of each aliquot and the total amount of H measured through spectrometry. Volcanic glasses with high water contents (>10 wt.%) likely reflect considerable glass dissolution and/or the formation of hydrous secondary precipitates (Table 3.4; Cassel and Breecker, 2017) and were therefore excluded from interpretations. Reported δD values and water content estimates are the mean of three to five replicate analyses of each sample.

RESULTS

Modern River, Well, and Spring Isotope Geochemistry

Modern water samples collected from 6 rivers draining a variety of bedrock source lithologies have Sr concentrations between 0.014 and 0.022 ppm (Table 3.1). Rivers draining the Ruby Mountains-East Humboldt Range metamorphic core complex have significantly elevated $^{87}Sr/^{86}Sr$ (mean = 0.7120) in comparison to rivers draining Paleozoic sedimentary bedrock (mean = 0.7079). Rivers with higher Sr concentrations have lower $^{87}Sr/^{86}Sr$ ratios than rivers with low Sr concentrations. This relationship was anticipated for rivers in the Cordilleran hinterland, where Paleozoic carbonate and siliciclastic strata have low $^{87}Sr/^{86}Sr$ ratios of 0.707–0.709 and high Sr concentrations (Figs. 3.1 and 3.4; Brand, 2004; Paces et al., 2007; Brand et al., 2012; Edwards et al., 2015; Supplemental Materials) in comparison to igneous and metamorphic rocks in the Ruby Mountains-East Humboldt Range (Fig. 3.4; Kistler et al., 1981; Wright and Snoke, 1993). Eocene volcanic rocks in northeastern Nevada also have relatively low $^{87}Sr/^{86}Sr$ ratios (mean = 0.7069; Gans et al., 1989; Wright and Wooden, 1991; Stevens, 2013; Supplemental Materials). In contrast, Jurassic and Cretaceous backarc plutons in Nevada and Utah have variable $^{87}Sr/^{86}Sr$ ratios (Farmer et al., 1983; Kistler and Lee, 1989), but the highest $^{87}Sr/^{86}Sr$ ratios are well above $^{87}Sr/^{86}Sr$ ratios for any Paleozoic rocks in this area (Fig. 3.4).

A compilation of modern river, well, and spring data across this field area (Supplemental Table C1) shows δD values range from -141.8 to -91.0‰ and $\delta^{18}O$ values are from -16.7 to -1.6‰, with mean values of -124.3 and -13.9‰, respectively (Hershey et al., 2008). The most depleted $\delta^{18}O$ and δD values are sourced from the Ruby Mountains and East

Humboldt Range whereas enriched values are correlated to sample localities near the center of valleys, which likely reflect enhanced surface water evaporation in these areas. Modern waters have $\delta^{13}C$ values that vary from -2.0 to -18.2‰ and a mean of -8.5‰ (Hershey et al., 2008). This wide variability may reflect a variable flux of inorganic and organic solutes within rivers draining a variety of catchment lithologies.

Sr Concentration, $^{87}Sr/^{86}Sr$, $\delta^{13}C$, and $\delta^{18}O$ Geochemistry

Samples collected across the stratigraphic range of the Elko Formation have $^{87}Sr/^{86}Sr$ ratios that range from 0.7076 to 0.7108, with a mean of 0.7086 (Table 3.3; Fig. 3.4). All carbonate and water samples have low $^{87}Rb/^{86}Sr$ ratios (<0.001), indicating a lack of silicate contamination of Sr separates following sample leaching and dissolution (Table 3.3). Samples from early Eocene strata exposed in Coal Mine Canyon have considerably higher $^{87}Sr/^{86}Sr$ ratios (mean = 0.7090, σ = 0.0009) and greater $^{87}Sr/^{86}Sr$ variation compared to all other samples (mean = 0.7085, σ = 0.0006; Fig. 3.5). Samples collected in fluctuating-profundal zones have $^{87}Sr/^{86}Sr$ ratios that are on average ~0.001 higher than fluvial lacustrine zones. In the Pinon Range, Elko Formation strata record a progressive ~0.0008 decrease in $^{87}Sr/^{86}Sr$ ratio between 43.4 and 40.7 Ma. Correlative strata sampled from a slightly reduced (~2 Myr) interval of the EOS-3N core hole and outcrop sections in the Elko Hills shows a ~0.002 decrease in $^{87}Sr/^{86}Sr$ ratio (Fig. 3.2). Strata sampled from the K1L core are also broadly correlative to this interval and show a ~0.002 decrease in $^{87}Sr/^{86}Sr$ ratio across a <1 Ma duration, indicating a similar magnitude and rate of change to the Elko Hills Sr record (Fig. 3.2).

Elko Formation carbonate samples show wide variation between calcitic and dolomitic mineralogy as well as $\delta^{13}C$ and $\delta^{18}O$ values, even within lacustrine facies associated with the same lake-type (Figs. 3.5–3.6). Comparison of all samples reveals those with dolomitic mineralogy have average $\delta^{13}C$ values 1.5‰ higher and $\delta^{18}O$ values 6‰ higher than the mean of all samples with calcitic mineralogy (Fig. 3.4C). Elko Formation $\delta^{13}C$ values vary widely from -8.9‰ to 15.2‰ (mean = 1.9‰, σ = 4.4) and $\delta^{18}O$ values also have a large range from 6.9–33‰ (mean = 22.4‰, σ = 6). High-magnitude isotopic shifts are also found in both Elko Formation sections sampled at a high frequency. Directly above the lake-type boundary in the early Eocene section exposed at Coal Mine Canyon, a ~0.002 increase in $^{87}Sr/^{86}Sr$ that

coincides with a 4.9‰ decrease in $\delta^{13}C$ and a coeval 15.5‰ decrease in $\delta^{18}O$, both across a <3 m interval (at ca. 48.9 Ma; Fig. 3.5). The uppermost section of the Elko Formation, exposed in the Pinon Range, has considerably more variation in $\delta^{13}C$ values (~23‰) than samples collected from any other area (Fig. 3.6). In the upper portion of this section (ca. 41.3 Ma), a 16.2‰ increase in $\delta^{13}C$ and 13‰ increase in $\delta^{18}O$ is followed by a 9.1‰ decrease in $\delta^{13}C$ and a 0.9‰ decrease in $\delta^{18}O$ (Fig. 3.6). There is also a positive correlation between $\delta^{13}C$ values and $\delta^{18}O$ values in this section that is not observed elsewhere (Fig. 3.6). Covariance of $\delta^{13}C$ and $\delta^{18}O$ isotopic trends, however, is present across most sampled sections of the Elko Formation (Fig. 3.2).

Volcanic Glass δD Geochemistry

Volcanic glass separated from Eocene tuffs and ash beds in the field area have considerable variation in δD values (δD_{glass}), ranging from -60‰ to -175‰ (Table 3.4; Fig. 3.7). Ash beds intercalated with lacustrine intervals of the Elko Formation have δD_{glass} values from -60‰ to -118‰ whereas samples intercalated with fluvial strata, or outside of the basin, have δD_{glass} values from -160‰ to -175‰ (Cassel and Breecker, 2017; Smith et al., 2017; Figs. 3.2 and 3.7). Within lacustrine facies, fluvial lacustrine zones have δD_{glass} values of approximately -150 to -110‰ and fluctuating-profundal zones have δD_{glass} values from around -110‰ to -60‰. In the Pinon Range section, ash beds sampled across the uppermost 119 m of the Elko Formation show a gradual 51‰ increase in δD_{glass} value from -118‰ to -67‰ (Fig. 3.2). Correlative strata in the Elko Hills also record a comparable gradual 38‰ increase in δD_{glass} from -106‰ to -68‰ (Fig. 3.2).

Diagenetic Effects

Measured Sr, O, and C isotopic data and Sr concentrations are interpreted to reflect the primary composition of lake water from which carbonate precipitated, rather than diagenesis. The dolomitic composition of many samples is inferred to reflect primary dolomite precipitation from preferential concentration of Mg along lake bottoms in slightly anoxic lake waters (Wolfbauer and Surdam, 1974; Desborough, 1978; Baker and Kastner, 1981; Hamdall and Emad, 2016). Abruzzese et al. (2005) detailed the absence of carbonate recrystallization within Elko Formation limestone. We focused sampling on fine-grained and impermeable

profundal mudstone facies, which should have also prohibited the circulation of diagenetic solutions. Core samples, taken where possible, are from depths of up to 2800 m, where circulation of diagenetic fluids is unlikely. Samples taken from core exhibit a range of isotopic variation that is comparable to outcrop samples. Thin (<2 cm) beds of ostracode coquina are preserved in both outcrop and core and lack visible dissolution or calcification, implying an absence of diagenesis. Thin section petrography of a range of samples, including representative samples of all facies, shows all samples utilized in isotopic analysis preserve biogenic carbonate and lack fenestrae or secondary carbonate textures. In addition, a lack of late basin-scale diagenetic alteration that could affect Elko Formation carbonates sampled for this study is also evidenced by the dm-scale variation of isotopic values in all locations as well as the covariance of $\delta^{13}C$ and $\delta^{18}O$ records (e.g., Graf et al., 2015).

DISCUSSION

Controls on Geochemical Variation within Elko Formation Strata

Geochemical covariance in Elko Formation strata is related to the interpreted lake-type associated with lacustrine facies. Most locations near the center of the Elko Basin, have covariance in $^{87}Sr/^{86}Sr$, $\delta^{13}C$, and $\delta^{18}O$ between ca. 43 and 41 Ma (Table 3.2; Fig. 3.6). These basin-interior areas have slightly heavier $\delta^{13}C$ and $\delta^{18}O$ values associated with fluctuating-profundal facies than fluvial lacustrine facies. Among all sampled sections, fluctuating-profundal zones have a stronger overall correlation between $\delta^{13}C$ and $\delta^{18}O$ values and mineralogical variations may have a significant influence on isotopic covariation. Samples with dolomitic mineralogy are generally associated with fluctuating-profundal zones, where anoxic conditions lead to the decomposition of anaerobic algae and enhanced Mg and organic matter preservation (Desborough, 1978; Graf et al., 2015). Dolomitic samples, representative of balanced-fill conditions, have mean $\delta^{13}C$ values 1.5‰ higher and $\delta^{18}O$ values 6‰ higher than calcitic samples (Fig. 3.4C). This trend is also observed in Green River Formation strata (i.e., Doebbert, 2006; Graf et al., 2015) and may partially reflect enhanced fractionation and up to 3‰ heavier $\delta^{18}O$ values of dolomite when compared to calcite precipitated from the same water (Fritz and Smith, 1970). Higher $\delta^{18}O$ values in fluctuating-profundal zones likely signify enhanced evaporation and increased residence time in the lake, whereas lower $\delta^{18}O$

values are more similar to late Eocene meteoric water values observed in the Indian Wells Formation (Mulch et al., 2015; Smith et al., 2017) and correspond to a relatively high influx of stream and/or groundwater to the basin. Higher $\delta^{13}C$ values in fluctuating-profundal zones correlate to enhanced organic matter preservation because photosynthetic algae in lakes preferentially remove ^{12}C and therefore enrich lake water in ^{13}C if they are buried prior to decomposition (Pitman, 1996; Lettéron et al., 2018), but may also reflect an increased rate of primary productivity (Kirby et al., 2002). High $\delta^{13}C$ values also likely indicate stratified lake waters because unstratified lakes permit decomposition of organic matter (Picard, 1955; Bohacs, 1998), which releases ^{12}C by methanogenesis and decreases corresponding $\delta^{13}C$ values (Pitman, 1996; Sarg et al., 2013). Elko Formation strata have higher Fischer Assay values and gamma ray intensity within fluctuating profundal zones (Figs. 3.5–3.6; Moore et al., 1983; Johnson and Birdwell, 2016), which also correlate with higher $\delta^{13}C$ values. In the Coal Mine Canyon section, extremely high TOC values in fluvial-lacustrine facies (>15%) are likely from analysis of coal or carbonaceous mudstone (Fig. 3.5) and therefore not reflective of lake water chemistry. The abundance of carbonaceous shale facies in multiple locations, however, likely explains at least a portion of the high $\delta^{13}C$ values measured in fluvial-lacustrine zones and the relatively poor covariance among different lake-types in comparison to correlative records preserved in the Green River Formation (e.g., Talbot, 1990; Graf et al., 2015). Observed covariant trends in $\delta^{13}C$ and $\delta^{18}O$ values are interpreted to reflect deposition in a closed basin lake, where outgassing of ^{12}C-rich CO_2 is coupled with evaporation of ^{16}O-rich H_2O (Horton and Chamberlain, 2006). Based on Elko Formation smectite and carbonate $\delta^{13}C$ and $\delta^{18}O$ values from samples collected in the Pinon Range, Horton and Chamberlain (2006) and Mulch et al. (2015) interpreted strongly evaporative conditions during deposition of uppermost Elko Formation sediments.

Isotope geochemistry of hydrated volcanic glass extracted from middle Eocene ash beds intercalated with a variety of lacustrine facies illustrates a correlation with lake water chemistry. Fluvial-lacustrine facies were deposited prior to widespread proximal volcanism (before ca. 42.3 Ma) and are thus less tuffaceous then fluctuating-profundal facies, and available ash beds largely do not preserve unaltered volcanic glass. Limited volcanic glasses derived from this facies association have δD values between -147‰ and -106‰, indicating a >40‰ shift from paleoprecipitation values (Fig. 3.7). This positive shift likely reflects

increased residence time and limited evaporation in freshwater lakes. Fluctuating-profundal zones have δD_{glass} values between -108‰ and -60‰, which is indicative of long lake water residence times and enhanced evaporation (cf. Smith et al., 2017). Two correlative sections of the upper Elko Formation, exposed in the Elko Hills and Pinon Range, show a comparable progressive decrease in δD_{glass} values up-section. The Pinon Range section shows a 52‰ increase in δD_{glass} across a 119 m interval (Fig. 3.5) and the Elko Hills section shows a gradual 38‰ increase in δD_{glass} value within correlative strata (Fig. 3.2), indicating that progressively more evaporative conditions preceded basin closure. Mulch et al. (2015) interpret a large -14.7‰ shift in $\delta^{18}O$ values within ca. 40.2 to ca. 39.4 Ma Indian Wells Formation strata (cf. Smith et al., 2017) to changes in the $\delta^{18}O$ values of inflow waters due to regional uplift. We instead attribute this shift to reflect the large and systematic isotopic difference between fluvial and lacustrine depositional environments (Cassel and Breecker, 2017; Smith et al., 2017).

Lake Water Provenance and Connectivity

Samples taken across the stratigraphic extent of the Elko Formation have generally low $^{87}Sr/^{86}Sr$ ratios between 0.7076 to 0.7108 (±0.0002) with relatively little variation from a mean of 0.7086 ($\sigma = 0.0007$). These values are significantly lower than Green River Formation $^{87}Sr/^{86}Sr$ ratios, which primarily range between 0.712 and 0.715 (Pietras, 2003; Carroll et al., 2008; Doebbert et al., 2010, 2014). Heightened $^{87}Sr/^{86}Sr$ ratios in the Green River Formation likely reflect paleorivers draining radiogenic Precambrian-cored Laramide uplifts that bound the basin (Smith et al., 2008a; Rhodes and Carroll, 2015). The general absence of elevated $^{87}Sr/^{86}Sr$ within the Elko Basin suggests metamorphic rocks were not exposed in the catchment of the basin by middle Eocene time. Low $^{87}Sr/^{86}Sr$ ratios are inferred to reflect erosion and predominant sediment delivery from proximal Paleozoic carbonate-rich strata, which is consistent with prior provenance interpretations using Eocene clast assemblages and detrital zircon geo- and thermochronology (e.g., Smith and Ketner, 1976, Haynes, 2003; Canada et al., 2019). Elevated $^{87}Sr/^{86}Sr$ ratios within carbonate samples from the Coal Mine Canyon and Twin Bridges sections likely reflect predominant fluvial connectivity with Jurassic backarc plutonic rocks (Fig. 3.1; Supplemental Materials). Samples taken from a range of stratigraphic levels in these same locations contain detrital zircon with

Jurassic U-Pb ages that match proximal plutons (Canada et al., 2009; Supplemental Materials). The proximal Contact pluton and plutons in the Cortez Range intruded relatively shallow crustal depths (Schmidt, 1992; Miller and Hoisch, 1995) and could have provided a solute source to the Elko Basin during these time intervals (Canada et al., 2009; Camilleri et al., 2017). High $^{87}Sr/^{86}Sr$ ratios are mainly present in strata representing the initial and end phases of lacustrine deposition (Fig. 3.4), when Eocene lakes were relatively small and isolated. The significant increase in $^{87}Sr/^{86}Sr$ ratios during these lowstand conditions (Fig. 3.8) may have also resulted from a greater relative influx of groundwater. Groundwater commonly has higher ion concentrations than surface waters (e.g., Dowling et al., 2003; Hart et al., 2004; Crossey et al., 2006) and may have had high $^{87}Sr/^{86}Sr$, which would constitute a larger proportion of the Sr influx when the lake level was low (Doebbert et al., 2014). Increased volcaniclastic input to the basin after ca. 42 Ma may be recorded by diminished $^{87}Sr/^{86}Sr$ ratios in the Pinon Range section, which show a ~0.002 decrease from ca. 42.6 to 40.7 Ma. Eocene volcanic rocks are expected to have relatively low Sr concentrations and slightly lower $^{87}Sr/^{86}Sr$ ratios than Paleozoic strata (e.g., Peterman et al., 1970; Feeley et al., 2002; Rhodes et al., 2002). Drainage disruption caused by widespread eruption of Eocene ignimbrites from ca. 41–40 Ma (Henry et al., 2011, 2012) therefore likely drove the observed change in $^{87}Sr/^{86}Sr$ ratios during this interval of enhanced evaporation.

Comparison of coeval isotopic data in multiple locations reveals covariance during multiple phases of lacustrine evolution (Fig. 3.8). Geochemical data from across the basin is generally consistent with the paleohydrologic interpretations of Smith et al. (2017). At ca. 42.3 Ma, during the highstand phase of Lake Elko, $^{87}Sr/^{86}Sr$ ratios are correlative between the Elko Hills and Pinon Range and limited $\delta^{13}C$ and $\delta^{18}O$ data show slight variation between samples collected at localities near the basin interior (Fig. 3.8). At ca. 41.8 Ma, existing $^{87}Sr/^{86}Sr$ and $\delta^{18}O$ values are correlative across several locations in the southern portion of the basin and consistent with a transition to fluctuating-profundal conditions (Figs. 3.2 and 3.8). To the north and south of this area, lacustrine facies as well as $\delta^{13}C$, $\delta^{18}O$, and δD values indicate freshwater deposition. At ca. 41 Ma, increased salinity and evaporation of lake waters is recorded across the basin, and isotopic values are correlative within several sub-basins directly prior to basin closure (Fig. 3.8). Covariance of these isotopic datasets from ca. 43–41 Ma suggests Elko Basin lakes expanded across a broad area and were likely hydrologically

connected during the main ca. 43–41 Ma phase of deposition. Higher order isotopic and lithofacies variability that is correlative across multiple locations reflects lake expansion-contraction cycles (e.g., Fischer and Roberts, 1991; Aswasereelert et al., 2013), which may be paced by climatic changes.

Allogenic Controls on Lake Elko Evolution

The combined $^{87}Sr/^{86}Sr$, $\delta^{13}C$, $\delta^{18}O$, and δD record of the Elko Basin records drainage integration and diversion. In the Coal Mine Canyon section, a coeval 4.9‰ decrease in $\delta^{13}C$ values, 15.5‰ decrease in $\delta^{18}O$ values, and a ~0.002 increase in $^{87}Sr/^{86}Sr$ ratio at ca. 48.9 Ma suggests a drainage capture event. A sudden decrease in $\delta^{18}O$ suggests incorporation of a large source of isotopically depleted water to the basin. At the same time (ca. 48.9 Ma), a -6‰ shift in $\delta^{18}O$ values is documented across the lower LaClede-upper LaClede contact in the Laney Member of the Green River Formation and is interpreted to reflect the capture of a river at least the size of the modern Snake River (9.5×10^9 m^3/yr; Carroll et al., 2008; Doebbert et al., 2014). Early Eocene lakes in the Elko Basin are interpreted to be much smaller than contemporaneous foreland lakes, and drainage capture of a large river is therefore not required to drive the observed isotopic shift in the hinterland. The contemporaneous isotopic shifts observed within foreland and hinterland records, both constrained by high-precision geochronology, may indicate a regional-scale topographic or climatic change at ca. 48.9 Ma. For example, a temporary shift towards a wetter climate may have increased precipitation and reduced evaporation. Paleobotanical analysis of the ca. 50 Ma Little Mountain flora (Wyoming) and the ca. 47 Ma Bonanza flora (Utah) of the Green River Formation indicate a ca. 4–5 °C decrease in mean annual temperatures, but no significant change in mean annual precipitation (Wing and Greenwood, 1993; Wilf et al., 1998; Wilf, 2000). Changes in $^{87}Sr/^{86}Sr$ are not directly related to climate but could be induced by climatically induced changes that promoted the fill of upstream basins that drained into Elko Basin lakes (Rhodes et al., 2002). Climatic shifts may also accelerate differential weathering rates of lithologies within the basin catchment, where increased weathering rates generally correspond to decreased $^{87}Sr/^{86}Sr$ ratios in surface waters and increased $^{87}Sr/^{86}Sr$ ratios in residual clays relative to the parent rock (Singer and Navrot, 1973; Brass, 1975; Galy et al., 1999, Carroll et al., 2008). In arid environments, low lake levels may have been

accompanied by reduced differential weathering rates and increased exchange with clays during fluvial incision to drive higher $^{87}Sr/^{86}Sr$ ratios (Rhodes et al., 2002; Pietras, 2003; Doebbert et al., 2014). In the Laramide foreland, deposition of facies representing wetter conditions in Lake Gosiute of the Greater Green River Basin (LaClede Bed) and evaporative conditions in the Uinta Basin (Mahogany zone; Smith et al., 2008b) indicate it is unlikely that regional climate change produced the observed variability (Carroll et al., 2008). Similar to the drainage capture model for Lake Gosiute, the contemporaneous $\delta^{18}O$ and $^{87}Sr/^{86}Sr$ shifts in Elko Basin lakes are more likely associated with capture of a new source of low $\delta^{18}O$ water. The ~0.002 increase in $^{87}Sr/^{86}Sr$ ratios, directly prior to this negative $\delta^{13}C$ and $\delta^{18}O$ isotope excursion is consistent with an important change in the provenance of lake source water. This increase in $^{87}Sr/^{86}Sr$ ratios, near the inferred lake-type boundary, may reflect diminished solute delivery from proximal Paleozoic carbonate and clastic rocks, which are characterized by low $^{87}Sr/^{86}Sr$ ratios (Paces et al., 2007; Brand et al., 2012; Edwards et al., 2015). The contemporaneous 4.9‰ decrease in $\delta^{13}C$ values documented in hinterland strata is indicative of diminished organic matter preservation that may reflect mixing of lake waters in response to a large influx of fresh water. This is likely reflected by a short shift from dolomitic to calcitic carbonate mineralogy in strata exposed at Coal Mine Canyon (Fig. 3.4).

At ca. 41.3 Ma, a 13‰ increase in $\delta^{18}O$ and 16.2‰ increase in $\delta^{13}C$ is recorded in kerogen-rich fluctuating-profundal facies in the upper portion of the Pinon Range section. A contemporaneous $^{87}Sr/^{86}Sr$ ratio increase of ~0.002 and then progressive $^{87}Sr/^{86}Sr$ decrease until ca. 41.0 Ma is recorded in strata of both the K1L and EH section (Fig. 3.2). Mulch et al. (2015) attribute a -9.3‰ $\delta^{18}O$ shift in the Pinon Range section to regional uplift, but through comparison with δD_{glass} values of interbedded ash Smith et al. (2017) demonstrate that this change in $\delta^{18}O$ value can be entirely attributed to changes in carbonate-forming environments. We interpret these shifts in in $\delta^{18}O$, $\delta^{13}C$, and $^{87}Sr/^{86}Sr$ to reflect a separate drainage capture event during the initiation of proximal volcanism in the Tuscarora volcanic field (Fig. 3.8; Henry, 2001, 2008). Proximal volcanism may have diverted sources of fresh water to the basin and led to enhanced evaporation that is documented within all lake water proxies. This is supported by an order of magnitude increase in sediment accumulation rate during this time (Fig. 3.6) as well as abundant interbedded volcanic ash horizons across this interval. Diminished inflow to the basin would simultaneously enhance evaporation and lead to lake

stratification, increasing both $\delta^{18}O$ and $\delta^{13}C$ values recorded by lacustrine carbonates. Increased $\delta^{18}O$ and $\delta^{13}C$ values in ca. 42.4 and 40.4 Ma strata are interpreted to reflect enhanced primary productivity and intense evaporation in a closed lake basin. Lake segmentation during this phase (Fig. 3.8) would further augment the geochemical effects of drainage diversion.

CONCLUSIONS

(1) A sudden 15.5‰ decrease in $\delta^{18}O$, 4.9‰ decrease in $\delta^{13}C$, and ~0.002 increase in $^{87}Sr/^{86}Sr$ values at ca. 48.9 Ma likely reflects a drainage capture event during the early Eocene. Independent provenance data suggests this paleoriver had headwaters near the Challis volcanic field of central Idaho. A synchronous $\delta^{18}O$ shift documented in the Green River Formation indicates a separate drainage capture event with similar provenance. Together, these records indicate volcanism and potential surface uplift in the region of the Challis volcanic field strongly impacted both hinterland and foreland lacustrine sedimentation at this time.

(2) Covariance in $^{87}Sr/^{86}Sr$, $\delta^{13}C$, and $\delta^{18}O$ records between ca. 43 and 41 Ma across multiple locations near the center of the Elko Basin implies prolonged lacustrine connectivity across a >1000 km^2 area. Fluctuating profundal zones generally have higher $\delta^{13}C$ and $\delta^{18}O$ values than fluvial-lacustrine facies, corresponding to enhanced evaporation and increased organic matter preservation. At ca. 41.3 Ma $^{87}Sr/^{86}Sr$ ratios show a rapid ~0.002 increase and then progressive decrease until ca. 41.0 Ma, likely signifying a river capture event that signifies drainage reorganization during the final phase of lacustrine deposition in the Elko Basin.

(3) Generally low $^{87}Sr/^{86}Sr$ ratios for all Elko Formation strata (mean = 0.7086; σ = 0.0007) indicates proximal Paleozoic strata were the predominant source of sediment to the basin until widespread felsic volcanism from encroaching eruptions reached the basin at ca. 41 Ma. The low $^{87}Sr/^{86}Sr$ ratios likely indicate an absence of metamorphic rocks within the catchment of the Elko Basin, such as core-complex rocks of the Ruby Mountains-East Humboldt Range. High $^{87}Sr/^{86}Sr$ ratios (up to 0.7108) are present in samples from a range of

stratigraphic and basin locations and are directly correlated to lake size and the provenance of water that entered the Elko Basin.

(4) Enhanced evaporation of hinterland lake waters directly preceded basin closure and is recorded by δD_{glass} values for ca. 42 to 40 Ma volcaniclastic strata in two areas (separated by ~30 km), which gradually increase by 38–52‰ during this time. Covariant trends in $\delta^{13}C$ and $\delta^{18}O$ values also indicate evaporation within a closed lake basin. In addition, this trend is reflected by evaporative fluctuating-profundal facies as well as low $\delta^{13}C$ and $\delta^{18}O$ values in the upper Elko Formation. The initiation of proximal volcanism likely drove a 13‰ increase in $\delta^{18}O$ and 16.2‰ increase in $\delta^{13}C$ documented at ca. 41.3 Ma via drainage diversion and increased volcaniclastic sediment flux that triggered enhanced primary productivity and evaporation in the Elko Basin.

REFERENCES

Abruzzese, M. J., Waldbauer, J. R., and Chamberlain, C. P., 2005, Oxygen and hydrogen isotope ratios in freshwater chert as indicators of ancient climate and hydrologic regime: Geochimica et Cosmochimica Acta, v. 69, no. 6, p. 1377–1390, doi:10.1016/j.gca.2004.08.036.

Al-Aasam, I. S., Taylor, B. E., and South, B., 1990, Stable isotope evidence of multiple carbonate samples using selective acid extraction: Chemical Geology, v. 80, p. 119–125, doi:10.1016/0168-9622(90)90020-D.

Andersson, P. S., Wasserburg, G. J., Ingri, J., and Stordal, M. C., 1994, Strontium, dissolved and particulate loads in fresh and brackish waters: The Baltic Sea and Mississippi Delta: Earth and Planetary Science Letters, v. 124, p. 195–210, doi:10.1016/0012-821X(94)00062-X.

Andrews, S. D., Trewin, N. H., Hartley, A. J., and Weedon, G. P., 2010, Solar variance recorded in lacustrine deposits from the Devonian and Proterozoic of Scotland: Journal of the Geological Society, v. 167, no. 5, p. 847–856, doi:10.1144/0016-76492009-105.

Anna, L. O., Roberts, L. N. R., and Potter, C. J., 2007, Geologic Assessment of Undiscovered Oil and Gas in the Paleozoic-Tertiary Composite Total Petroleum System of the Eastern Great Basin, Nevada and Utah, Geologic Assessment of Undiscovered Oil and Gas Resources of the Eastern Great Basin Province, Nevada, Utah, Idaho, and Arizona, Volume DDS-69-L, U. S. Geological Survey Digital Data Series, 50 p.

Armstrong, R. L., 1982, Cordilleran metamorphic core complexes - From Arizona to Southern Canada: Annual Reviews in Earth and Planetary Science Letters, v. 10, p. 129–154, doi:10.1146/annurev.ea.10.050182.001021.

Aswasereelert, W., Meyers, S. R., Carroll, A. R., Peters, S. E., Smith, M. E., and Feigl, K. L., 2013, Basin-scale cyclostratigraphy of the Green River Formation, Wyoming: Geological Society of America Bulletin, v. 125, no. 1–2, p. 216–228, doi:10.1130/B30541.1.

Axelrod, D. I., 1966, The Eocene Copper Basin flora of northeastern Nevada, University of California Publications in Geological Sciences, v. 59–61, 129 p.

Axelrod, D. I., 1997, Paleoelevation estimated from Tertiary floras: International Geology Review, v. 39, no. 12, p. 1124–1133, doi:10.1080/00206819709465319.

Baddouh, M. B., Meyers, S. R., Carroll, A. R., Beard, B. L., and Johnson, C. M., 2016, Lacustrine 87Sr/86Sr as a tracer to reconstruct Milankovitch forcing of the Eocene hydrologic cycle: Earth and Planetary Science Letters, v. 448, p. 62–68, doi:10.1016/j.epsl.2016.05.007.

Baker, P. A., and Kastner, M., 1981, Constraints on the formation of sedimentary dolomite: Science, v. 213, no. 4504, p. 214–216, doi:10.1126/science.213.4504.214.

Bain, D. C., and Bacon, J. R., 1994, Strontium isotopes as indicators of mineral weathering in catchments: Catena, v. 22, no. 3, p. 201–214, doi:10.1016/0341-8162(94)90002-7.

Bataille, C. P., and Bowen, G. J., 2012, Mapping Sr-87/Sr-86 variations in bedrock and water for large scale provenance studies: Chemical Geology, v. 304, p. 39–52, doi:10.1016/j.chemgeo.2012.01.028.

Benson, L., and Peterman, Z., 1995, Carbonate deposition, Pyramid Lake subbasin, Nevada: 3. The use of 87Sr values in carbonate deposits (tufas) to determine the hydrologic state of paleolake systems: Palaeogeography Palaeoclimatology Palaeoecology: v. 119, no. 3–4, p. 201–213, doi:10.1016/0031-0182(95)00010-0.

Benvenuti, M., Del Conte, S., Scarselli, N., and Dominici, S., 2014, Hinterland basin development and infilling through tectonic and eustatic processes: latest Messinian-Gelasian Valdelsa Basin, Northern Apennines, Italy: Basin Research, v. 26, no. 3, p. 387–402, doi:10.1111/bre.12031.

Blum, J. D., Erel, Y., and Brown, K., 1993, 87Sr/86Sr ratios of Sierra Nevada stream waters: Implications for relative mineral weathering rates: Geochimica et Cosmochimica Acta, v. 57, p. 5019–5025, doi:10.1016/S0016-7037(05)80014-6.

Blum, J. D., Gazis, C. A., Jacobson, A. D., and Chamberlain, C. P., 1998, Carbonate versus silicate weathering in the Raikhot watershed within the high Himalayan crystalline series: Geology, v. 26, no. 5, p. 411–414, doi: 10.1130/0091-7613(1998)026<0411:CVSWIT>2.3.CO;2.

Bohacs, K. M., 1998, Contrasting expressions of depositional sequences in mudrocks from marine to non marine environs, *in* Schieber, J., Zimmerlie, W., and Sethi, P., eds.,

Mudstones and shales, v. 1, Characteristics at the basin scale: Stuttgart, Schweizerbart'sche Verlagsbuchhandlung, p. 32–77.

Bohacs, K. M., 2003, Lessons from large lake systems; thresholds, nonlinearity, and strange attractors: Geological Society of America Special Paper, v. 370, p. 75–90, doi:10.1130/0-8137-2370-1.75.

Bohacs, K. M., Carroll, A. R., Neal, J. E., and Mankiewicz, P. J., 2000, Lake-basin type, source potential, and hydrocarbon character: an integrated sequence-stratigraphic–geochemical framework, *in* Gierlowski-Kordesch, E. H., and Kelts, K. R., eds., Lake basins through space and time, AAPG Studies in Geology, v. 46, p. 3–34.

Bowen, G. J., Daniels, A. L., and Bowen, B. B., 2008, Paleoenvironmental isotope geochemistry and paragenesis of lacustrine and palustrine carbonates, Flagstaff Formation, central Utah, U.S.A: Journal of Sedimentary Research, v. 78, no. 3, p. 162–174, doi:10.2110/jsr.2008.021.

Brand, U., 2004, Carbon, oxygen and strontium isotopes in Paleozoic carbonate components: an evaluation of original seawater-chemistry proxies: Chemical Geology, v. 204, no. 1–2, p. 23–44, doi:10.1016/j.chemgeo.2003.10.013.

Brand, U., Jiang, G., Azmy, K., Bishop, J., and Montañez, I. P., 2012, Diagenetic evaluation of a Pennsylvanian carbonate succession (Bird Spring Formation, Arrow Canyon, Nevada, U.S.A.) – 1: Brachiopod and whole rock comparison: Chemical Geology, v. 308–309, p. 26–39, doi:10.1016/j.chemgeo.2012.03.017.

Brass, G. W., 1975, The effect of weathering on the distribution of strontium isotopes in weathering profiles: Geochimica et Cosmochimica Acta, v. 39, p. 1647–1653, doi:10.1016/0016-7037(75)90086-1.

Brennan, S. R., Fernandez, D. P., Mackey, G., Cerling, T. E., Bataille, C. P., Bowen, G. J., and Wooller, M. J., 2014, Strontium isotope variation and carbonate versus silicate weathering in rivers from across Alaska: Implications for provenance studies: Chemical Geology, v. 389, p. 167–181, doi:10.1016/j.chemgeo.2014.08.018.

Camilleri, P. A., and Chamberlain, K. R., 1997, Mesozoic tectonics and metamorphism in the Pequop Mountains and Wood Hills region, northeast Nevada: Implications for the architecture and evolution of the Sevier orogeny: Geological Society of America

Bulletin, v. 109, p. 74–94, doi:10.1130/0016-7606(1997)109<0074:MTAMIT>2.3.CO;2.

Camilleri, P., Deibert, J., and Perkins, M., 2017, Middle Miocene to Holocene tectonics, basin evolution, and paleogeography along the southern margin of the Snake River Plain in the Knoll Mountain–Ruby–East Humboldt Range region, northeastern Nevada and south-central Idaho: Geosphere v. 13, no. 6, p. 1901–1948, doi:10.1130/GES01318.1.

Canada, A. S., Cassel, E. J., Stockli, D. F., Smith, M. E., Jicha, B. R., and Singer B. S., 2019, *in press*, Accelerating exhumation in the Eocene North American Cordilleran hinterland: Implications from detrital zircon (U-Th)/(He-Pb) double dating: Geological Society of America Bulletin.

Capo, R. C., Stewart, B. W., and Chadwick, O. A., 1998, Strontium isotopes as tracers of ecosystem processes: theory and methods: Geoderma, v. 82, p. 197–225, doi:10.1016/S0016-7061(97)00102-X.

Carroll, A. R., and Bohacs, K. M., 1999, Stratigraphic classification of ancient lakes: Balancing tectonic and climatic controls: Geology, v. 27, no. 2, p. 99–102, doi:10.1130/0091-7613(1999)027<0099:SCOALB>2.3.CO;2

Carroll, A. R., and Bohacs, K. M., 2001, Lake-type controls on petroleum source rock potential in nonmarine basins: American Association of Petroleum Geologists Bulletin, v. 85, no. 6, p. 1033–1053, doi:10.1306/8626CA5F-173B-11D7-8645000102C1865D.

Carroll, A. R., Chetel, L. M., and Smith, M. E., 2006, Feast to famine: Sediment supply control on Laramide basin fill: Geology, v. 34, no. 3, p. 197–200, doi:10.1130/G22148.1.

Carroll, A. R., Doebbert, A. C., Booth, A. L., Chamberlain, C. P., Rhodes-Carson, M. K., Smith, M. E., Johnson, C. M., and Beard, B. L., 2008, Capture of high-altitude precipitation by a low-altitude Eocene lake, western U.S: Geology, v. 36, no. 10, p. 791–794, doi:10.1130/G24783A.1.

Cassel, E. J., and Breecker, D. O., 2017, Long-term stability of hydrogen isotope ratios in hydrated volcanic glass: Geochimica et Cosmochimica Acta, v. 200, p. 67–86, doi:10.1016/j.gca.2016.12.001

Cassel, E. J., Breecker, D. O., Henry, C. D., Larson, T. E., and Stockli, D. F., 2014, Profile of a paleo-orogen: High topography across the present-day Basin and Range from 40 to 23 Ma: Geology, v. 42, p. 1007–1010, doi:10.1130/G35924.1.

Cassel, E. J., Smith, M. E., and Jicha, B. R., 2018, The impact of slab rollback on Earth's surface: Uplift and extension in the hinterland of the North American Cordillera: Geophysical Research Letters, v. 45, p. 10,996–11,004, doi:10.1029/2018GL079887.

Chamberlain, C. P., Mix, H. T., Mulch, A., Hren, M. T., Kent-Corson, M. L., Davis, S. J., Horton, T. W., and Graham, S. A., 2012, The Cenozoic climatic and topographic evolution of the western North American Cordillera: American Journal of Science, v. 312, no. 2, p. 213–262, doi:10.2475/02.2012.05.

Chamberlain, C. P., Wan, X., Graham, S. A., Carroll, A. R., Doebbert, A. C., Sageman, B. B., Blisniuk, P., Kent-Corson, M. L., Wang, Z., and Chengshan, W., 2013, Stable isotopic evidence for climate and basin evolution of the Late Cretaceous Songliao basin, China: Palaeogeography, Palaeoclimatology, Palaeoecology, v. 385, p. 106–124, doi:10.1016/j.palaeo.2012.03.020

Cline, J. S., Hofstra, A. H., Muntean, J. L., Tosdal, R. M., and Hickey, K. A., 2005, Carlin-type gold deposits in Nevada: Critical geologic characteristics and viable models: Economic Geology, v. 100, p. 451–484, doi:10.5382/AV100.15.

Cohen, A. H., 2003, Paleolimnology: The history and evolution of lake systems, Oxford, Oxford University Press, 528 p.

Cohen, A., McGlue, M. M., Ellis, G. S., Zani, H., Swarzenski, P. W., Assine, M. L., and Silva, A., 2015, Lake formation, characteristics, and evolution in retroarc deposystems: A synthesis of the modern Andean orogen and its associated basins, *in* DeCelles, P. G., Ducea, M. N., Carrapa, B., and Kapp, P. A., eds., Geodynamics of a Cordilleran Orogenic System: The Central Andes of Argentina and Northern Chile: Geological Society of America Memoir, v. 212, p. 309–335, doi:10.1130/2015.1212(16).

Colgan, J. P., Howard, K. A., Fleck, R. J., and Wooden, J. L., 2010, Rapid middle Miocene extension and unroofing of the southern Ruby Mountains, Nevada: Tectonics, v. 29, no. 6, 38 p., doi:10.1029/2009TC002655.

Coney, P. J., and Harms, T. A., 1984, Cordilleran metamorphic core complexes: Cenozoic extensional relics of Mesozoic compression: Geology, v. 12, p. 550–554, doi:10.1130/0091-7613(1984)12<550:CMCCCE>2.0.CO;2.

Crossey, L. J., Fischer, T. B., Patchett, P. J., Karlstrom, K., Hilton, D. R., Newell, D. L., Huntoon, P., Reynolds, A., and DeLeeuw, G. A. M., 2006, Dissected hydrologic system at the Grand Canyon: interaction between deeply derived fluids and plateau aquifer waters in modern springs and travertine: Geology, v. 34, no. 1, p. 25–28, doi:10.1130/G22057.1.

Dansgaard, W., 1964, Stable isotopes in precipitation: Tellus, v. 16, p. 436–468, doi:10.1111/j.2153-3490.1964.tb00181.x.

Davis, S. J., Mix, H. T., Wiegand, B. A., Carroll, A. R., and Chamberlain, C. P., 2009, Synorogenic evolution of large-scale drainage patterns: Isotope paleohydrology of sequential Laramide basins: American Journal of Science, v. 309, no. 7, p. 549–602, doi:10.2475/07.2009.02.

Dawber, C. F., and Tripati, A. K., 2011, Constraints on glaciation in the middle Eocene (46–37 Ma) from Ocean Drilling Program (ODP) Site 1209 in the tropical Pacific Ocean: Paleoceanography, v. 26, PA2208, doi:10.1029/2010PA002037.

DeCelles, P. G., Carrapa, B., Horton, B. K., McNabb, J., Gehrels, G. E., and Boyd, J., 2015, The Miocene Arizaro Basin, central Andean hinterland: Response to partial lithosphere removal?, *in* DeCelles, P. G., Ducea, M. N., Carrapa, B., and Kapp, P. A., eds., Geodynamics of a Cordilleran Orogenic System: The Central Andes of Argentina and Northern Chile: Geological Society of America Memoir, v. 212, p. 359–386, doi:10.1130/2015.1212(18).

DeCelles, P. G., 2004, Late Jurassic to Eocene evolution of the Cordilleran Thrust Belt and foreland basin system, Western U.S.A.: American Journal of Science, v. 304, p. 105–168, doi:10.2475/ajs.304.2.105.

Desborough, G. A., 1978, A biogenic-chemical stratified lake model for the origin of oil shale of the Green River Formation: An alternative to the playa-lake model: Geological Society of America Bulletin, v. 89, p. 961–971, doi:10.1130/0016-7606(1978)89<961:ABSLMF>2.0.CO;2.

Dickinson, W. R., and Suczek, C. A., 1979, Plate tectonics and sandstone compositions: The American Association of Petroleum Geologists, v. 63, no. 12, p. 2164–2182, doi:10.1306/2F9188FB-16CE-11D7-8645000102C1865D.

Dilek, Y., and Moores, E. M., 1999, A Tibetan model for the early Tertiary western United States: Journal of the Geological Society, London, v. 156, p. 929–941, doi:10.1144/gsjgs.156.5.0929.

Doebbert, A. C., 2006, Geomorphic controls on lacustrine isotopic compositions: evidence from the Laney Member, Green River Formation (Wyoming) [Master of Science]: University of Wisconsin-Madison, 247 p.

Doebbert, A. C., Carroll, A. R., Mulch, A., Chetel, L. M., and Chamberlain, C. P., 2010, Geomorphic controls on lacustrine isotopic compositions: Evidence from the Laney Member, Green River Formation, Wyoming: Geological Society of America Bulletin, v. 122, no. 1–2, p. 236–252, doi:10.1130/B26522.1.

Doebbert, A. C., Johnson, C. M., Carroll, A. R., Beard, B. L., Pietras, J. T., Rhodes Carson, M., Norsted, B., and Throckmorton, L. A., 2014, Controls on Sr isotopic evolution in lacustrine systems: Eocene green river formation, Wyoming: Chemical Geology, v. 380, p. 172–189, doi:10.1016/j.chemgeo.2014.04.008.

Dowling, C. B., Poreda, R. J., and Basu, A. R., 2003, The groundwater geochemistry of the Bengal Basin: weathering, chemsorption, and trace metal flux to the oceans: Geochimica et Cosmochimica Acta, v. 67, no. 12, p. 2117–2136, doi:10.1016/S0016-7037(02)01306-6.

Druschke, P., Hanson, A.D., and Wells, M.L., 2009a, Structural, stratigraphic, and geochronologic evidence for extension predating Palaeogene volcanism in the Sevier hinterland, east-central Nevada: International Geology Review, v. 51, p. 743–775, doi:10.1080/00206810902917941.

Druschke, P., Hanson, A.D., Wells, M.L., Rasbury, T., Stockli, D.F., and Gehrels, G., 2009b, Synconvergent surface-breaking normal faults of Late Cretaceous age within the Sevier hinterland, east-central Nevada: Geology, v. 37, no. 5, p. 447–450, doi:10.1130/G25546A.1.

Dubiel, R. F., Potter, C. J., Good, S. C., and Snee, L. W., 1996, Reconstructing an Eocene extensional basin: The White Sage Formation, eastern Great Basin: Geological Society of America Special Paper, v. 303, p. 1–14, doi:10.1130/0-8137-2303-5.1.

Edwards, C. T., Saltzman, M. R., Leslie, S. A., Bergström, S. M., Sedlacek, A. R. C., Howard, A., Bauer, J. A., Sweet, W. C., and Young, S. A., 2015, Strontium isotope (87Sr/86Sr) stratigraphy of Ordovician bulk carbonate: Implications for preservation of primary seawater values: Geological Society of America Bulletin, v. 127, no. 9–10, p. 1275–1289, doi:10.1130/B31149.1.

Effimoff, I., and Pinezich, A. R., 1981, Tertiary structural development of selected valleys based on seismic data: Basin and Range province, Northeastern Nevada: Philosophical Transactions of the Royal Society of London, v. 300, p. 435–442, doi:10.1098/rsta.1981.0074.

Ezquerro, L., Luzón, A., Navarro, M., Liesa, C. L., and Simón, J. L., 2014, Climatic vs. tectonic signals in a continental extensional basin (Teruel, NE Spain) from stable isotope (δ18O) and sequence stratigraphical evolution: Terra Nova, v. 26, no. 5, p. 337–346, doi:10.1111/ter.12101.

Fan, M., Constenius, K. N., and Dettman, D. L., 2017, Prolonged high relief in the northern Cordilleran orogenic front during middle and late Eocene extension based on stable isotope paleoaltimetry: Earth and Planetary Science Letters, v. 457, p. 376–384, doi:10.1016/j.epsl.2016.10.038.

Farmer, G. L., and DePaolo, D. J., 1983, Origin of Mesozoic and Tertiary granite in the western United States and implications for pre-Mesozoic crustal structure 1. Nd and Sr isotopic studies in the geocline of the northern Great Basin: Journal of Geophysical Research, v. 88, no. B4, p. 3379–3401, doi:10.1029/JB088iB04p03379.

Feeley, T. C., Cosca, M. A., and Lindsay, C. R., 2002, Petrogenesis and implications of calc-alkaline cryptic hybrid magmas from Washburn Volcano, Absaroka Volcanic Province, U.S.A.: Journal of Petrology, v. 43, no. 4, p. 663–703, doi:10.1093/petrology/43.4.663.

Fischer, A. G., and Roberts, L. T., 1991, Cyclicity in the Green River Formation (lacustrine Eocene) of Wyoming: Journal of Sedimentary Petrology, v. 61, no. 7, p. 1146–1154, doi:10.1306/D4267852-2B26-11D7-8648000102C1865D.

Fritz, P., and Smith, D. G. W., 1970, The isotopic composition of secondary dolomites: Geochimica et Cosmochimica Acta, v. 34, p. 1161–1173, doi:10.1016/0016-7037(70)90056-6.

Galy, A., France-Lanord, C., and Derry, L. A., 1999, The strontium isotopic budget of Himalayan rivers in Nepal and Bangladesh: Geochimica et Cosmochimica Acta, v. 63, p. 1905–1925, doi:10.1016/S0016-7037(99)00081-2.

Gans, P. B., Mahood, G. A., and Schermer, E., 1989, Synextensional magmatism in the Basin and Range Province; A case study from the eastern Great Basin: Geological Society of America Special Paper, v. 233, p. 1–53, doi:10.1130/SPE233-p1.

Gierlowski-Kordesch, E., Finkelstein, D. B., Truchan Holland, J. J., and Kallini, K. D., 2014, Carbonate Lake Deposits Associated with Distal Siliciclastic Perennial-River Systems: Journal of Sedimentary Research, v. 83, no. 12, p. 1114–1129, doi:10.2110/jsr.2013.81.

Gierlowski-Kordesch, E. H., Jacobsen, A. D., Blum, J. D., and Valero Garces, B. L., 2004, Using Sr isotopes in basin analysis: Paleocene-Eocene Flagstaff Formation, Utah: Geological Society of America Abstracts with Programs, v. 36, no. 5, p. 35, doi:10.1130/B26070.1.

Gierlowski-Kordesch, E. H., Jacobson, A. D., Blum, J. D., and Valero Garces, B. L., 2008, Watershed reconstruction of a Paleocene-Eocene lake basin using Sr isotopes in carbonate rocks: Geological Society of America Bulletin, v. 120, no. 1–2, p. 85–95, doi:10.1130/B26070.1.

Graf, J. W., Carroll, A. R., and Smith, M. E., 2015 Lacustrine sedimentology, stratigraphy and stable isotope geochemistry of the Tipton Member of the Green River Formation, *in* Smith, M. E., and Carroll, A. R., eds., Stratigraphy and paleolimnology of the Green River Formation, Western U.S., Springer, Dordrecht, p. 40–69, doi:10.1007/978-94-017-9906-5_3.

Gross, M. G., and Tracey, J. I., 1966, Oxygen and Carbon Isotopic Composition of Limestones and Dolomites, Bikini and Eniwetok Atolls: Science, v. 151, no. 3714, p. 1082–1084, doi:10.1126/science.151.3714.1082.

Grove, M. J., Baker, P. A., Cross, S. L., Rigsby, C. A., and Seltzer, G. O., 2003, Application of strontium isotopes to understanding the hydrology and paleohydrology of the

Altiplano, Bolivia–Peru: Palaeogeography, Palaeoclimatology, Palaeoecology, v. 194, no. 1–3, p. 281–297, doi:10.1016/S0031-0182(03)00282-7.

Grunder, A. L., 1992, Two-stage contamination during crustal assimilation: isotopic evidence from volcanic rocks in eastern Nevada: Contributions to Mineralogy and Petrology, v. 112, p. 219–229, doi:10.1007/BF00310456.

Hamdall, W., and Emad, S., 2016, Abiotically-formed, primary dolomite in the mid-Eocene lacustrine succession at Gebel El-Goza El-Hamra, NE Egypt; an approach to the role of smectitic clays: Sedimentary Geology, v. 343, p. 132–140, doi:10.1016/j.sedgeo.2016.08.003.

Hart, W., Quade, J., Madsen, D., Kaufman, D., and Oviatt, C., 2004, The 87Sr/86Sr ratios of lacustrine carbonates and lake-level history of the Bonneville paleolake system: Geological Society of America Bulletin, v. 116, no. 9, p. 1107–1119, doi:10.1130/B25330.1.

Haynes, S. R., 2003, Development of the Eocene Elko Basin, northeastern Nevada: Implications for paleogeography and regional tectonism [M.S. thesis]: The University of British Columbia, 159 p.

Hegg, J. C., Kennedy, B. P., and Fremier, A. K., 2013, Predicting strontium isotope variation and fish location with bedrock geology: Understanding the effects of geologic heterogeneity: Chemical Geology, v. 360–361, p. 89–98, doi:10.1016/j.chemgeo.2013.10.010.

Heller, P. L., and Liu, L., 2016, Dynamic topography and vertical motion of the U.S. Rocky Mountain region prior to and during the Laramide orogeny: Geological Society of America Bulletin, v. 128, no. 5–6, p. 973–988, doi:10.1130/B31431.1.

Henry, C. D., Hinz, N. H., Faulds, J. E., Colgan, J. P., John, D. A., Brooks, E. R., Cassel, E. J., Garside, L. J., Davis, D. A., and Castor, S. B., 2012, Eocene–early Miocene paleotopography of the Sierra Nevada–Great Basin–Nevadaplano based on widespread ash-flow tuffs and paleovalleys: Geosphere, v. 8, p. 1–27, doi:10.1130/GES00727.1.

Henry, C. D., The Eocene Elko Basin and Elko Formation, NE Nevada: Paleotopographic controls on area, thickness, facies distribution, and petroleum potential: AAPG Search and Discovery Article 11102.

Henry, C. D., McGrew, A. J., Colgan, J. P., Snoke, A. W., and Brueseke, M. E., 2011, Timing, distribution, amount, and style of Cenozoic extension in the northern Great Basin, *in* Lee, J., and Evans, J.P., eds., Geologic field trips to the Basin and Range, Rocky Mountains, Snake River Plain, and terranes of the U.S. Cordillera: Geological Society of America Field Guides, no. 21, p. 27–66, doi:10.1130/2011.0021(02).

Henry, C. D., 2008, Ash-flow tuffs and paleovalleys in northeastern Nevada: Implications for Eocene paleogeography and extension in the Sevier hinterland, northern Great Basin: Geosphere, v. 4, no. 1, p. 1–35, doi:10.1130/GES00122.1.

Hershey, R. L., Rybarski, S., Thomas, J.M., and Pohll, G., 2014, Water-quality data, hydraulic fracturing in the upper Humboldt River Basin, aquifer quality assessment program, Report 2: Desert Research Institute, no. 41259, 54 p.

Herut, B., Starinsky, A., and Katz, A., 1993, Strontium in rainwater from Israel: Sources, isotopes and chemistry: Earth and Planetary Science Letters, v. 120, p. 77–84, doi:10.1016/0012-821X(93)90024-4.

Hiza, M. M., 1999, The geochemistry and geochronology of the Eocene Absaroka Volcanic Province, northern Wyoming and southwest Montana, USA [Ph.D. thesis]: Oregon State University, 249 p.

Horton, T. W., and Chamberlain, C. P., 2006, Stable isotopic evidence for Neogene surface downdrop in the central Basin and Range Province: Geological Society of America Bulletin, v. 118, no. 3/4, p. 475–490, doi:10.1130/B25808.

Horton, T. W., Sjostrom, D. J., Abruzzese, M. J., Poage, M. A., Waldbauer, J. R., Hren, M. T., Wooden, J., and Chamberlain, C. P., 2004, Spatial and temporal variation of Cenozoic surface elevation in the Great Basin and Sierra Nevada: American Journal of Science, v. 304, p. 862–888, doi:10.2475/ajs.304.10.862.

Jacobson, A. D., Blum, J. D., Chamberlain, C. P., Craw, D., and Koons, P. O., 2003, Climatic and tectonic controls on chemical weathering in the New Zealand Southern Alps: Geochimica et Cosmochimica Acta, v. 67, no. 1, p. 29–46, doi:10.1016/S0016-7037(02)01053-0.

Jacobson, A. D., and Wasserburg, G. J., 2005, Anhydrite and the Sr isotope evolution of groundwater in a carbonate aquifer: Chemical Geology, v. 214, no. 3–4, p. 331–350, doi:10.1016/j.chemgeo.2004.10.006.

Janecke, S. U., and Snee, L. W., 1993, Timing and episodicity of middle Eocene volcanism and onset of conglomerate deposition, Idaho: The Journal of Geology, v. 101, p. 603–621, doi:10.1086/648252.

Johnson, R. C., and Birdwell, J. E., 2016, Evolution of the Lower Tertiary Elko Lake Basin, a potential hydrocarbon source rock in Northeast Nevada, *in* Dolan, M. P., Higley, D. H., and Lillis, P. G., eds., Hydrocarbon Source Rocks in Unconventional Plays, Rocky Mountain Region, Rocky Mountain Association of Geologists, p. 261–294.

Johnson, T. M., DePaolo, D. J., 1994, Interpretation of isotopic data in groundwater–rock systems: Model development and application to Sr isotope data from Yucca Mountain: Water Resources Research, v. 30, p. 1571–1587, doi:10.1029/94WR00157.

Kent-Corson, M. L., Sherman, L. S., Mulch, A., and Chamberlain, C. P., 2006, Cenozoic topographic and climatic response to changing tectonic boundary conditions in Western North America: Earth and Planetary Science Letters, v. 252, no. 3–4, p. 453–466, doi:10.1016/j.epsl.2006.09.049.

Kirby, M. E., Mullins, H. T., and Patterson, W. P., 2002, Late glacial-Holocene atmospheric circulation and precipitation in the northeast United States inferred from modern calibrated stable oxygen and carbon isotopes: Geological Society of America Bulletin, v. 114, p. 1326–1340, doi:10.1130/0016-7606(2002)114<1326:LGHACA>2.0.CO;2.

Kistler, R. W., Ghent, E. D., and O'Neil, J. R., 1981, Petrogenesis of garnet two-mica granites in the Ruby Mountains, Nevada: Journal of Geophysical Research, v. 86, no. B11, p. 10,591–10,606, doi:10.1029/JB086iB11p10591.

Kistler, R. W., and Lee, D. E., 1989, Rubidium, strontium, and strontium isotopic data for a suite of granitoid rocks from the Basin and Range Province, Arizona, California, Nevada, and Utah: U.S. Geological Survey Open-File Report 89-199, 13 p., doi:10.3133/ofr89199.

Konstantinou, A., Strickland, A., Miller, E., Vervoort, J., Fisher, C. M., Wooden, J., and Valley, J., 2013, Synextensional magmatism leading to crustal flow in the Albion-Raft River-Grouse Creek metamorphic core complex, northeastern Basin and Range: Tectonics, v. 32, p. 1384–1403, doi:10.1002/tect.20085.

Lee, S. J., Barnes, C. G., Snoke, A. W., Howard, K. A., and Frost, C. D., 2003, Petrogenesis of Mesozoic, peraluminous granites in the Lamoille Canyon area, Ruby Mountains,

Nevada, USA: Journal of Petrology, v. 44, no. 4, p. 713–732, doi:10.1093/petrology/44.4.71.

Leier, A. L., McQuarrie, N., Horton, B. K., and Gehrels, G. E., 2010, Upper Oligocene Conglomerates of the Altiplano, Central Andes: The Record of Deposition and Deformation Along the Margin of a Hinterland Basin: Journal of Sedimentary Research, v. 80, no. 8, p. 750–762, doi:10.2110/jsr.2010.064.

Lettéron, A., Hamon, Y., Fournier, F., Séranne, M., Pellenard, P., and Joseph, P., 2018, Reconstruction of a saline, lacustrine carbonate system (Priabonian, St-Chaptes Basin, SE France): Depositional models, paleogeographic and paleoclimatic implications: Sedimentary Geology, v. 367, p. 20–47, doi:10.1016/j.sedgeo.2017.12.023.

Li, D., Shields-Zhou, G. A., Ling, H.-F., and Thirlwall, M., 2011, Dissolution methods for strontium isotope stratigraphy: Guidelines for the use of bulk carbonate and phosphorite rocks: Chemical Geology, v. 290, no. 3–4, p. 133–144, doi:10.1016/j.chemgeo.2011.09.004.

Long, S. P., 2012, Magnitudes and spatial patterns of erosional exhumation in the Sevier hinterland, eastern Nevada and western Utah, USA: Insights from a Paleogene paleogeographic map: Geosphere, v. 8, no. 4, p. 881–901, doi:10.1130/GES00783.1.

Lund Snee, J. E., Miller, E. L., Grove, M., Hourigan, J. K., and Konstantinou, A., 2016, Cenozoic paleogeographic evolution of the Elko Basin and surrounding region, northeast Nevada: Geosphere, v. 12, no. 2, p. 464–500, doi:10.1130/GES01198.1.

McCrea, J. M., 1950, On the isotopic chemistry of carbonates and a paleotemperature scale: The Journal of Chemical Physics, v. 18, p. 849‑857, doi:10.1063/1.1747785.

McGrew, A. J., Peters, M. T., and Wright, J. E., 2000, Thermobarometric constraints on the tectonothermal evolution of the East Humboldt Range metamorphic core complex, Nevada: Geological Society of America Bulletin, v. 112, no. 1, p. 45–60., doi:10.1130/0016-7606(2000)112<45:TCOTTE>2.0.CO;2.

Meen, J. K., and Eggler, D. H., 1987, Petrology and geochemistry of the Cretaceous Independence volcanic suite, Absaroka Mountains, Montana: Clues to the composition of the Archean sub-Montanan mantle: Geological Society of America Bulletin, v. 98, p. 238–247, doi:10.1130/0016-7606(1987)98<238:PAGOTC>2.0.CO;2.

Moore, S. W., Madrid, H. B., and Server, G. T., 1983, Results of Oil-Shale Investigations in Northeastern Nevada: U.S. Geological Survey Open-File Report 83–586, 56 p.

Mueller, K. J., Cerveny, P. K., Perkins, M. E., and Snee, L. W., 1999, Chronology of polyphase extension in the Windermere Hills, northeast Nevada: Geological Society of America Bulletin, v. 111, no. 1, p. 11–27, doi:10.1130/0016-7606(1999)111<0011:COPEIT>2.3.CO;2.

Mulch, A., Chamberlain, C. P., Cosca, M. A., Teyssier, C., Methner, K., Hren, M. T., and Graham, S. A., 2015, Rapid change in high-elevation precipitation patterns of western North America during the Middle Eocene Climatic Optimum (MECO): American Journal of Science, v. 315, no. 4, p. 317–336, doi:10.2475/04.2015.02.

Paces, J. B., Peterman, Z. E., Futa, K., Oliver, T. A., and Marshall, B. D., 2007, Strontium isotopic composition of Paleozoic carbonate rocks in the Nevada test site vicinity, Clark, Lincoln, and Nye Counties, Nevada, and Inyo County, California: U.S. Geological Survey Data Series 280, 42 p, doi:10.3133/ds280.

Palmer, S. E., 1984, Hydrocarbon source potential of organic facies of the lacustrine Elko Formation (Eocene/Oligocene), northeastern Nevada: Hydrocarbon Source Rocks of the Greater Rocky Mountain Region, *in* Woodard, J., Meissner, F. F., and Clayton, J. L., eds., Hydrocarbon Source Rocks of the Greater Rocky Mountain Region: Rocky Mountain Association of Geologists, p. 491–511.

Palmer, M. R., and Edmond, J. M., 1992, Controls over the strontium isotope composition of river water: Geochimica et Cosmochimica Acta, v. 56, p. 2099–2111, doi:10.1016/0016-7037(92)90332-D.

Peterman, Z. E., Doe, B. R., and Prostka, H. J., 1970, Lead and strontium isotopes in rocks of the Absaroka volcanic field, Wyoming: Contributions to Mineralogy and Petrology, v. 27, p. 121–130, doi:10.1007/BF00371979.

Peterman, Z. E., Thamke, J., Futa, K., and Preston, T., 2012, Strontium isotope systematics of mixing groundwater and oil-field brine at Goose Lake in northeastern Montana, USA: Applied Geochemistry, v. 27, no. 12, p. 2403–2408, doi:10.1016/j.apgeochem.2012.08.004.

Picard, M. D., 1955, Subsurface stratigraphy and lithology of the Green River Formation in the Uinta Basin, Utah: American Association of Petroleum Geologists Bulletin, v. 39, p. 75–102.

Pietras, J. T., 2003, High-resolution sequence stratigraphy and strontium isotope geochemistry of the lacustrine Wilkins Peak Member, Eocene Green River Formation, Wyoming, U.S.A. [Ph.D. Thesis]: University of Wisconsin-Madison, 381 p.

Pietras, J. T., Carroll, A. R., Singer, B. S., and Smith, M. E., 2003, 10 k.y. depositional cyclicity in the early Eocene: Stratigraphic and 40Ar/39Ar evidence from the lacustrine Green River Formation: Geology, v. 31, no. 7, p. 593–596, doi:10.1130/0091-7613(2003)031<0593:KDCITE>2.0.CO;2.

Pitman, J. K., 1996, Origin of primary and diagenetic carbonates in the lacustrine Green River Formation (Eocene), Colorado and Utah: U.S. Geological Survey Bulletin 2157, 17 p.

Pollard A. M., Blockley S. P. E. and Ward K. R., 2003, Chemical alteration of tephra in the depositional environment: theoretical stability modelling: Journal of Quaternary Science, v. 18, p. 385–394, doi:10.1002/jqs.760.

Potter, C. J., Dubiel, R. F., Snee, L. W., and Good, S. C., 1995, Eocene extension of early Eocene lacustrine strata in a complexly deformed Sevier-Laramide hinterland, northwest Utah and northeast Nevada: Geology, v. 23, no. 2, p. 181–184, doi:10.1130/0091-7613(1995)023<0181:EEOEEL>2.3.CO;2.

Rahl, J. M., McGrew, A. J., and Foland, K. A., 2002, Transition from Contraction to Extension in the Northeastern Basin and Range: New Evidence from the Copper Mountains, Nevada: The Journal of Geology, v. 110, no. 2, p. 179–194, doi:10.1086/338413.

Rey, P. F., Teyssier, C., and Whitney, D. L., 2009, The role of partial melting and extensional strain rates in the development of metamorphic core complexes: Tectonophysics, v. 477, no. 3–4, p. 135-144, doi:10.1016/j.tecto.2009.03.010.

Rhodes, M. K., and Carroll, A. R., 2015, Lake Type Transition from Balanced-Fill to Overfilled: Laney Member, Green River Formation, Washakie Basin, Wyoming, *in* Smith, M. E., and Carroll, A. R., eds., Stratigraphy and paleolimnology of the Green River Formation, Western U.S., Springer, Dordrecht, p. 103–125, doi:10.1007/978-94-017-9906-5_5.

Rhodes, M. K., Carroll, A. R., Pietras, J. T., Beard, B. L., and Johnson, C. M., 2002, Strontium isotope record of paleohydrology and continental weathering, Eocene Green River Formation, Wyoming: Geology, v. 30, no. 2, p. 167–170, doi:10.1130/0091-7613(2002)030<0167:SIROPA>2.0.CO;2.

Rowley, D. B., Pierrehumbert, R. T., and Currie, B. S., 2001, A new approach to stable isotope-based paleoaltimetry: Implications for paleoaltimetry and paleohypsometry of the High Himalaya since the late Miocene: Earth and Planetary Science Letters, v. 188, p. 253–268, doi:10.1016/S0012-821X(01)00324-7.

Salaviale, C., Gollain, B., and Mattioli, E., 2018, Calcareous nannofossil fluxes and size fluctuations in the middle Eocene (48–39 Ma) from Ocean Drilling Program (ODP) Site 1209 in the tropical Pacific Ocean: Palaeogeography, Palaeoclimatology, Palaeoecology, v. 490, p. 240–251, doi:10.1016/j.palaeo.2017.11.003.

Sarg, J. F., Suriamin, N., TÌnavsuu-Milkeviciene, K., and Humphrey, J. D., 2013, Lithofacies, stable isotopic composition, and stratigraphic evolution of microbial and associated carbonates, Green River Formation (Eocene), Piceance Basin, Colorado: AAPG Bulletin, v. 97, no. 11, p. 1937–1966, doi:10.1306/07031312188.

Satarugsa, P., and Johnson, R. A., 2000, Cenozoic tectonic evolution of the Ruby Mountains metamorphic core complex and adjacent valleys, northeastern Nevada: Rocky Mountain Geology, v. 35, no. 2, p. 205–230, doi:10.2113/35.2.205.

Schmidt, M. W.. 1992, Amphibole composition in tonalite as a function of pressure: An experimental calibration of the Al-in-hornblende barometer: Contributions to Mineralogy and Petrology, v. 110, p. 304–310, doi:10.1007/BF00310745.

Sharma, T., and Clayton, R. N., 1965, Measurement of O18/O16 ratios of total oxygen of carbonates: Geochimica et Cosmochimica Acta, v. 29, no. 12, p. 1347–1353, doi:10.1016/0016-7037(65)90011-6.

Singer, A., and Navrot, J., 1973, Some aspects of the Ca and Sr weathering cycle in the Lake Kinneret (Lake Tiberias) drainage basin: Chemical Geology, v. 12, p. 209–218, doi:10.1016/0009-2541(73)90089-2.

Sluijs, A., Zeebe, R. E., Bijl, P. K., and Bohaty, S. M., 2013, A middle Eocene carbon cycle conundrum: Nature Geoscience, v. 6, no. 6, p. 429–434, doi:10.1038/NGEO1807.

Smith, M. E., and Carroll, A. R., 2015, Stratigraphy and Paleolimnology of the Green River Formation, Syntheses in Limnogeology, 359 p, doi:10.1007/978-94-017-9906-5.

Smith, M., E., Carroll, A. R., and Mueller, E. R., 2008a, Elevated weathering rates in the Rocky Mountains during the Early Eocene Climatic Optimum: Nature Geoscience, v. 1, no. 6, p. 370–374, doi:10.1038/ngeo205.

Smith, M. E., Carroll, A. R., Jicha, B. R., Cassel, E. J., and Scott, J. J., 2014a, Paleogeographic record of Eocene Farallon slab rollback beneath western North America: Geology, v. 42, no. 12, p. 1039–1042, doi:10.1130/G36025.1.

Smith, M. E., Carroll, A. R., Scott, J. J., and Singer, B. S., 2014b, Early Eocene carbon isotope excursions and landscape destabilization at eccentricity minima: Green River Formation of Wyoming: Earth and Planetary Science Letters, v. 403, p. 393–406, doi:10.1016/j.epsl.2014.06.024.

Smith, M. E., Carroll, A. R., and Singer, B. S., 2008b, Synoptic reconstruction of a major ancient lake system: Eocene Green River Formation, western United States: Geological Society of America Bulletin, v. 120, no. 1–2, p. 54–84, doi:10.1130/B26073.1.

Smith, M. E., Cassel, E. J., Jicha, B. R., Singer, B. S., and Canada, A. S., 2017, Hinterland drainage closure and lake formation in response to middle Eocene Farallon slab removal, Nevada, U.S.A.: Earth and Planetary Science Letters, v. 479, p. 156–167, doi:10.1016/j.epsl.2017.09.023.

Smith, J. F. J., and Ketner, K. B., 1976, Stratigraphy of Post-Paleozoic Rocks and Summary of Resources in the Carlin-Pinon Range Area, Nevada: U.S. Geological Survey Professional Paper, v. 867-B, 48 p, doi:10.3133/pp867B

Solomon, B. J., 1981, Geology and oil shale resources near Elko, Nevada: Open-File Report 81-709, 154 p, doi:10.3133/ofr81709.

Solomon, B. J., McKee, E. H., and Andersen, D. W., 1979, Stratigraphy and depositional environments of Paleogene rocks near Elko, Nevada, *in* Armentrout, J. M., et al., ed., Cenozoic paleogeography of the western United States: Pacific Coast Paleogeography Symposium III, Pacific Section, Society of Economic Paleontologist and Mineralogists, p. 75–88.

Sposito, G., 1989, The Chemistry of Soils: Oxford University Press, New York, 277 p, doi:10.1017/S0016756800014059.

Stewart, J. H., and Carlson, J. E., 1981, Geologic Map of Nevada: U.S. Geological Survey and Nevada Bureau of Mines and Geology, 1:500,000, G81386.

Stevens, C., 2013, Petrography, geochemistry and isotopic analysis of Paleogene volcanism in the Fish Creek Mountains, Great Basin, north-central Nevada [M.S. Thesis]: Carleton University, 155 p.

Stuiver, M. I., 1970, Oxygen and carbon isotope ratios of fresh-water carbonates as climatic indicators: Journal of Geophysical Research, v. 75, no. 27, p. 5247–5257, doi:10.1029/JC075i027p05247.

Swart, P. K., Burns, S. J., and Leder, J. J., 1991, Fractionation of the stable isotopes of oxygen and carbon in carbon dioxide during the reaction of calcite with phosphoric acid as a function of temperature and technique: Chemical Geology: Isotope Geoscience section, v. 86, no. 2, p. 89–96, doi:10.1016/0168-9622(91)90055-2.

Talbot, M. R., 1990, A review of the paleohydrological interpretation of carbon and oxygen isotopic ratios in primary lacustrine carbonates: Chemical Geology, v. 80, p. 261–279, doi:10.1016/0168-9622(90)90009-2.

Talbot, M. R., Williams, M. A. J., 2000, Strontium isotopic evidence for late Pleistocene reestablishment of an integrated Nile drainage network: Geology, v. 28, p. 343–346, doi:10.1130/0091-7613(2000)28<343:SIEFLP>2.0.CO;2.

Tindall, J., Flecker, R., Valdes, P., Schmidt, D. N., Markwick, P., and Harris, J., 2010, Modelling the oxygen isotope distribution of ancient seawater using a coupled ocean–atmosphere GCM: Implications for reconstructing early Eocene climate: Earth and Planetary Science Letters, v. 292, no. 3–4, p. 265–273, doi:10.1016/j.epsl.2009.12.049.

Umhoefer, P. J., Beard, L. S. Martin, K. L. Blythe, N., 2010, From detachment to transtensional faulting: A model for the Lake Mead extensional domain based on new ages and correlation of subbasins, *in* Umhoefer, Paul J., Lamb, Melissa A., Beard, L.S., eds., Miocene Tectonics of the Lake Mead region: Geological Society of America Special Paper, v. 463, p. 371–394, doi:10.1130/2010.2463(17).

Vandenberghe, N., Hilgen, F. J., and Speijer, R. P., 2012, The Paleogene period, *in* Gradstein, F.M., et al., eds., The Geologic Time Scale 2012: Amsterdam, Elsevier, p. 855–921, doi:10.1016/b978-0-444-59425-9.00028-7.

Wells, M. L., Hoisch, T. D., Cruz-Uribe, A. M., and Vervoort, J. D., 2012, Geodynamics of synconvergent extension and tectonic mode switching: Constraints from the Sevier-Laramide orogen: Tectonics, v. 31, TC1002, no. 1, 20 p, doi:10.1029/2011TC002913.

White, A. F., Blum, A. E., Bullen, T. D., Vivit, D. V., Schulz, M., and Fitzpatrick, J., 1999, The effect of temperature on experimental and natural chemical weathering rates of granitoid rocks: Geochimica et Cosmochimica Acta, v. 63, p. 3277–3291, doi:10.1016/S0016-7037(99)00250-1.

Wilf, P., Wing, S. L., Greenwood, D. R., and Greenwood, C. L., 1998, Using fossil leaves as paleoprecipitation indicators: An Eocene example: Geology, v. 26, no. 3, p. 203–206, doi:10.1130/0091-7613(1998)026<0203:UFLAPI>2.3.CO;2

Wilf, P., 2000, Late Paleocene–early Eocene climate changes in southwestern Wyoming: Paleobotanical analysis: Geological Society of America Bulletin, v. 112, p. 292–307, doi:10.1130/0016-7606(2000)112<0292:LPEECC>2.3.CO;2.

Wing, S. L., and Greenwood, D. R., 1993, Fossils and fossil climate: The case for equable continental interiors in the Eocene: Royal Society of London Philosophical Transactions, ser. B, v. 341, p. 243–252, doi:10.1098/rstb.1993.0109.

Wingate, F. H., 1983, Palynology and Age of the Elko Formation (Eocene) near Elko, Nevada: Palynology, v. 7, p. 93–132, doi:10.1080/01916122.1983.9989254.

Wolfbauer, C. A., and Surdam, R. C., 1974, Origin of nonmarine dolomite in Eocene Lake Gosiute, Green River Basin, Wyoming: Geological Society of America Bulletin, v. 85, p. 1733–1740, doi:10.1130/0016-7606(1974)85<1733:OONDIE>2.0.CO;2.

Wright, J. E., and Snoke, A. W., 1993, Tertiary magmatism and mylonitization in the Ruby-East Humboldt metamorphic core complex, northeastern Nevada: U-Pb geochronology and Sr, Nd, and Pb isotope geochemistry: Geological Society of America Bulletin, v. 105, p. 935–952, doi:10.1130/0016-7606(1993)105<0935:TMAMIT>2.3.

Wright, J. E., and Wooden, J. L., 1991, New Sr, Nd, and Pb isotopic data from plutons in the northern Great Basin: implications for crustal structure and granite petrogenesis in the

hinterland of the Sevier thrust belt: Geology, v. 19, p. 457–460, doi:10.1130/0091-7613(1991)019<0457:NSNAPI>2.3.CO;2.

Zachos, J., Pagani, M., Sloan, L., Thomas, E., and Billups, K., 2001, Trends, rhythms, and aberrations in global climate 65 Ma to present: Science, v. 292, p. 686–693, doi:10.1016/S0031-0182(02)00449-2.

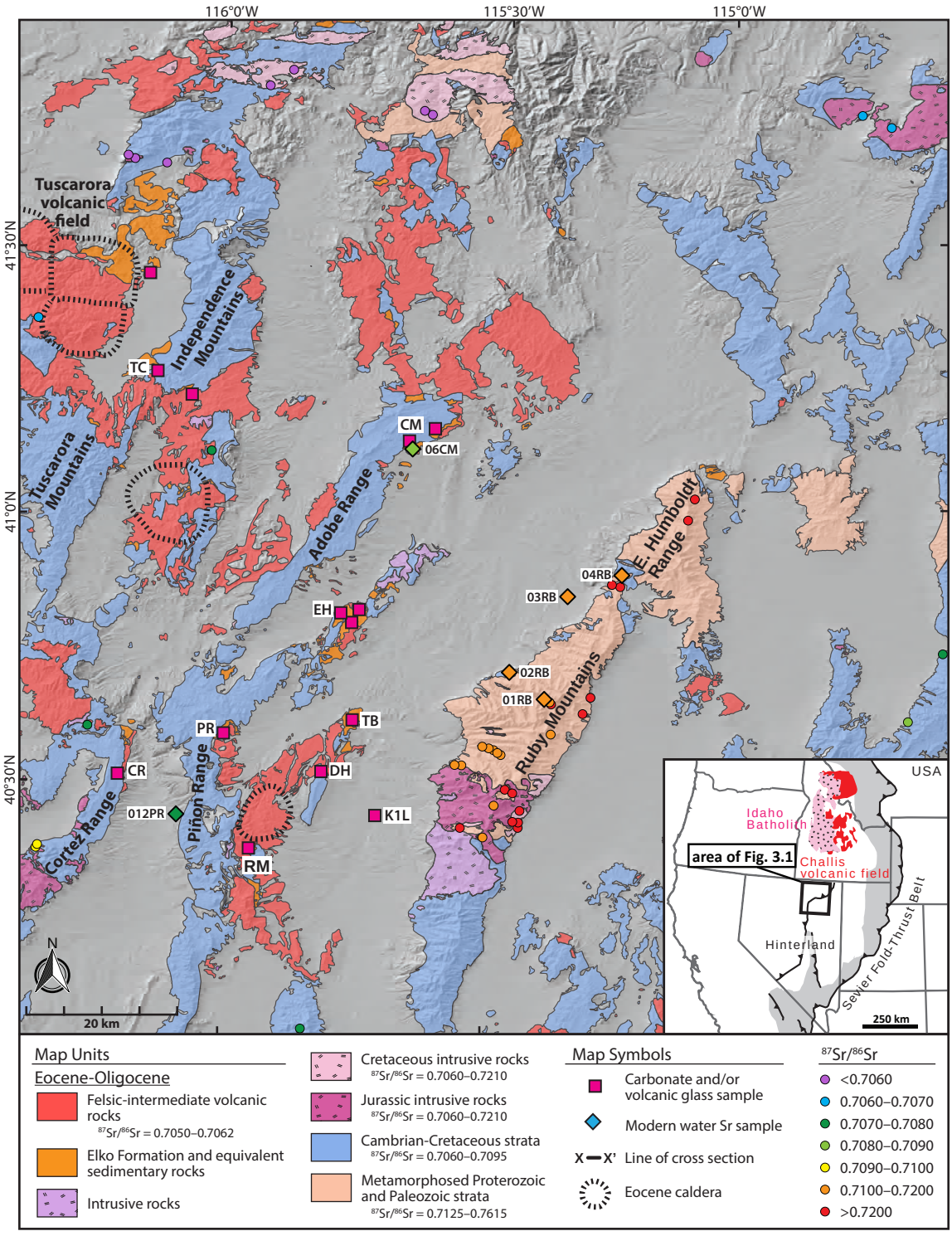
116°0'W
115°30'W
115°0'W
41°30'N
41°0'N
40°30'N
Tuscarora volcanic field
Independence Mountains
Tuscarora Mountains
Adobe Range
E. Humboldt Range
Ruby Mountains
Pinon Range
Cortez Range
TC
CM
06CM
EH
04RB
03RB
02RB
01RB
TB
PR
CR
DH
012PR
K1L
RM
N
20 km
USA
Idaho Batholith
area of Fig. 3.1
Challis volcanic field
Hinterland
Sevier Fold-Thrust Belt
250 km
Map Units
Eocene-Oligocene
Felsic-intermediate volcanic rocks
87Sr/86Sr = 0.7050–0.7062
Elko Formation and equivalent sedimentary rocks
Intrusive rocks
Cretaceous intrusive rocks
87Sr/86Sr = 0.7060–0.7210
Jurassic intrusive rocks
87Sr/86Sr = 0.7060–0.7210
Cambrian-Cretaceous strata
87Sr/86Sr = 0.7060–0.7095
Metamorphosed Proterozoic and Paleozoic strata
87Sr/86Sr = 0.7125–0.7615
Map Symbols
Carbonate and/or volcanic glass sample
Modern water Sr sample
X—X' Line of cross section
Eocene caldera
87Sr/86Sr
<0.7060
0.7060–0.7070
0.7070–0.7080
0.7080–0.7090
0.7090–0.7100
0.7100–0.7200
>0.7200

Figure 3.1. Simplified geologic map of northeastern Nevada showing sample locations. Distribution of map units from Stewart and Carlson (1981), Camilleri and Chamberlain (1997), and Lund Snee et al. (2016); Eocene caldera locations from Henry et al. (2011). Strontium ratios are compiled from Kistler and Lee (1989), Wright and Snoke (1993), Kistler et al. (1981), Farmer et al. (1983), Gans et al. (1989), and Brand et al. (2012). See Supplemental Materials for all sources of bedrock strontium geochemistry. Inset map: Overview of Idaho Batholith, Challis volcanic field, and Paleozoic and Mesozoic thrust belts from Long (2012), Konstantinou et al. (2013), and DeCelles and Graham (2015). Field area abbreviations: CR—Cortez Range, RM—Robinson Mountain, K1L—Noble Energy K1L well, DH—Dixie Hills, PR—Pinon Range, TB—Twin Bridges, EH—Elko Hills, CM—Coal Mine Canyon, TC—Taylor Canyon.

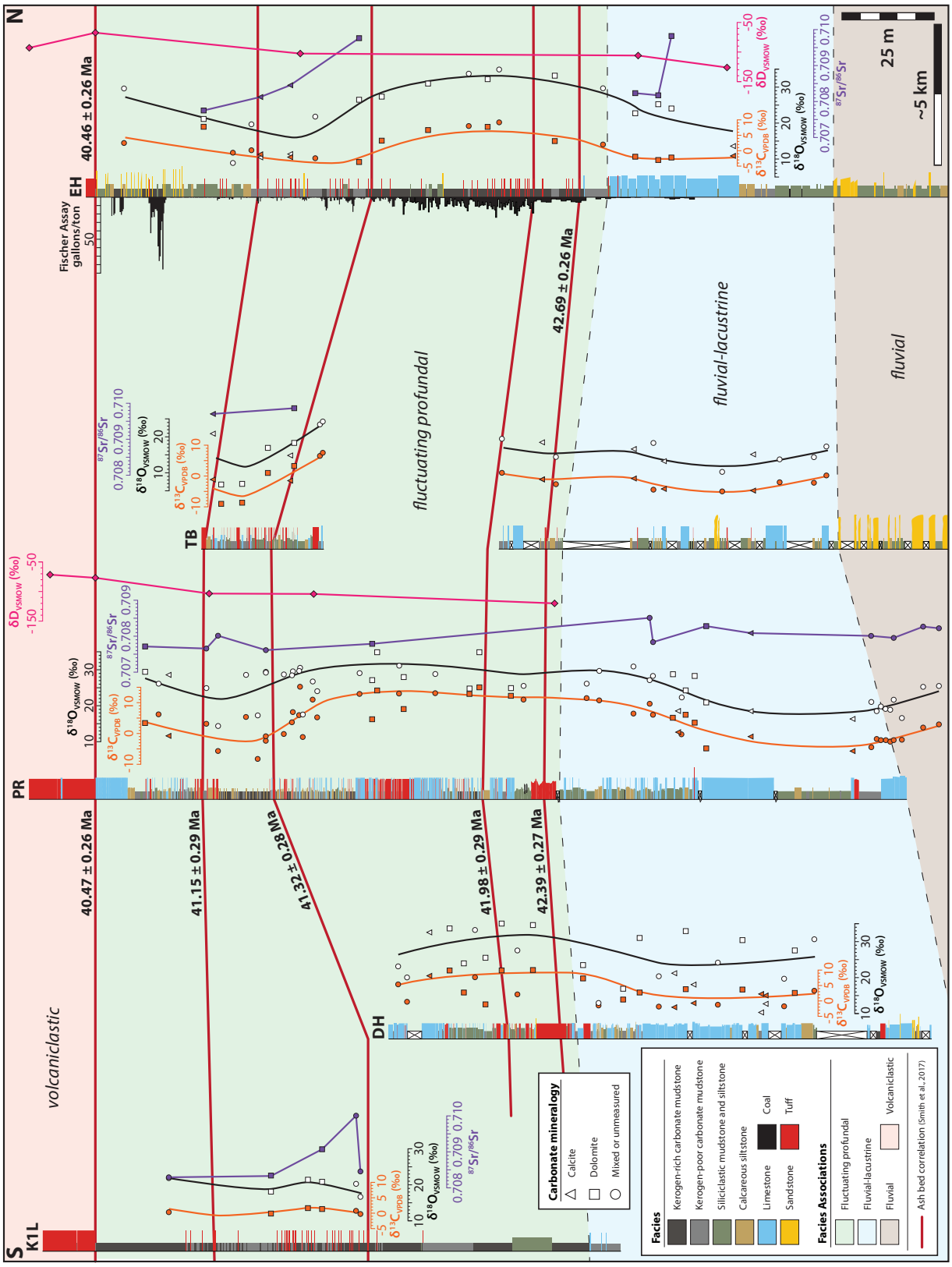
N
S
K1L
PR
EH
TB
DH
volcaniclastic
fluctuating profundal
fluvial-lacustrine
fluvial
40.47 ± 0.26 Ma
40.46 ± 0.26 Ma
41.15 ± 0.29 Ma
41.32 ± 0.28 Ma
41.98 ± 0.29 Ma
42.39 ± 0.27 Ma
42.69 ± 0.26 Ma
Fischer Assay gallons/ton
δ18OVSMOW (‰)
δ13CVPDB (‰)
87Sr/86Sr
δDVSMOW (‰)
25 m
~5 km
Carbonate mineralogy
Calcite
Dolomite
Mixed or unmeasured
Facies
Kerogen-rich carbonate mudstone
Kerogen-poor carbonate mudstone
Siliciclastic mudstone and siltstone
Calcareous siltstone
Limestone
Coal
Sandstone
Tuff
Facies Associations
Fluctuating profundal
Fluvial-lacustrine
Fluvial
Volcaniclastic
Ash bed correlation (Smith et al., 2017)

Figure 3.2. Chemostratigraphic correlation panel showing decimeter-scale stratigraphy and isotope geochemistry for the upper Elko Formation. See Fig. 3.1 for section locations and Table 3.2 for full geochemical data. $^{40}Ar/^{39}Ar$ ages from Smith et al. (2017); sample mineralogy from X-ray diffraction; Fischer assay oil yield data from Moore et al. (1983).

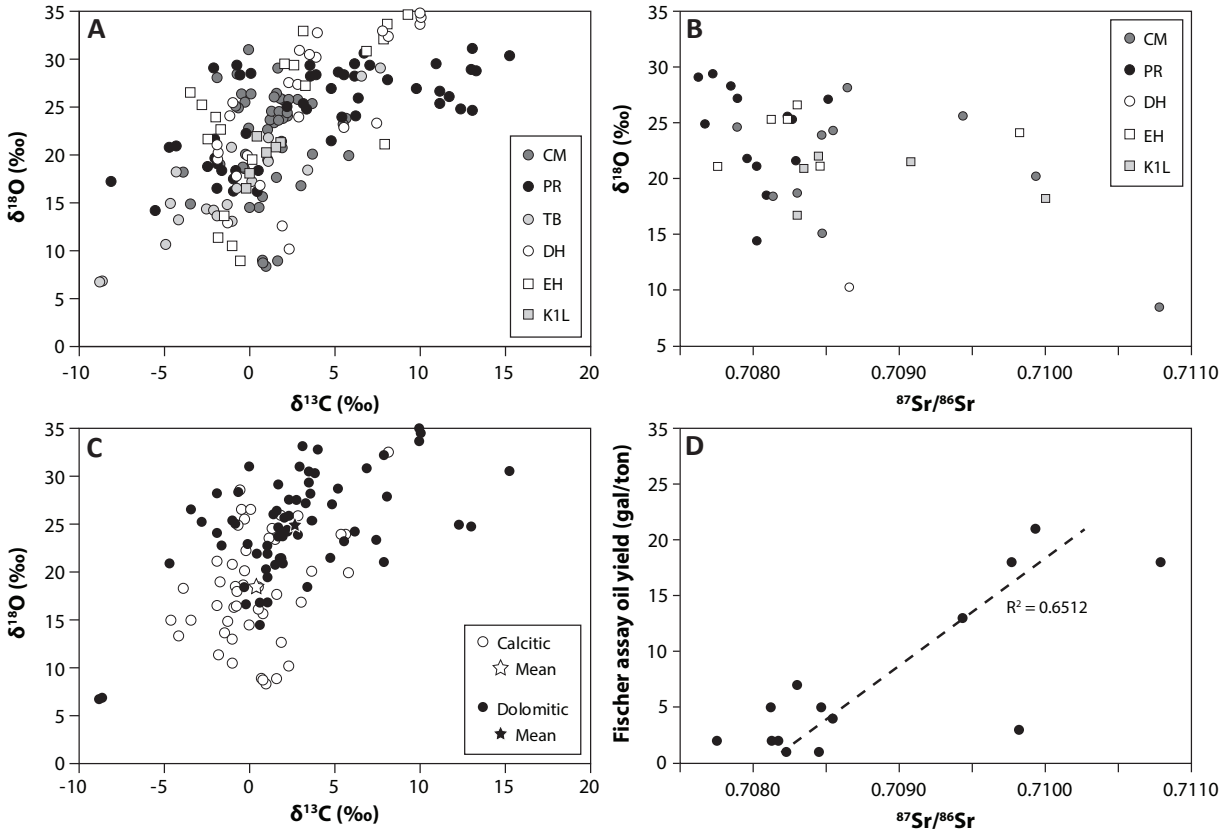

Figure 3.3. (A–C) Summary of $\delta^{13}C$, $\delta^{18}O$, and $^{87}Sr/^{86}Sr$ stable isotope geochemistry of Elko Formation lacustrine carbonates. Abbreviations correspond to field locations shown in Fig. 3.1. (D) Strontium ratios for Fischer assay oil yield data generated from proximal strata (within ≤ 1.5 m). Fischer assay data from Moore et al. (1983) and Johnson and Birdwell (2016).

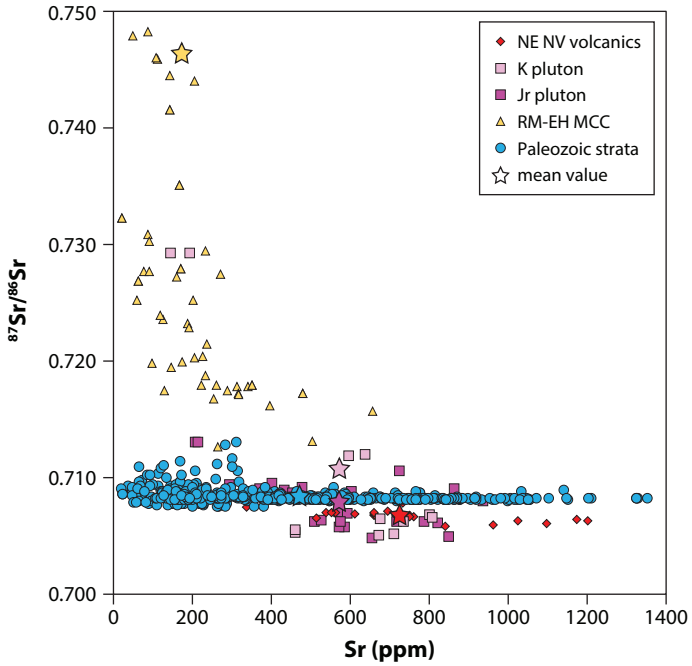

Figure 3.4. Strontium isotope geochemistry for potential sediment sources to the Elko Basin compiled from prior geochemical studies in eastern Nevada and western Utah. See Supplemental Materials and Figure C1 for sources of data.

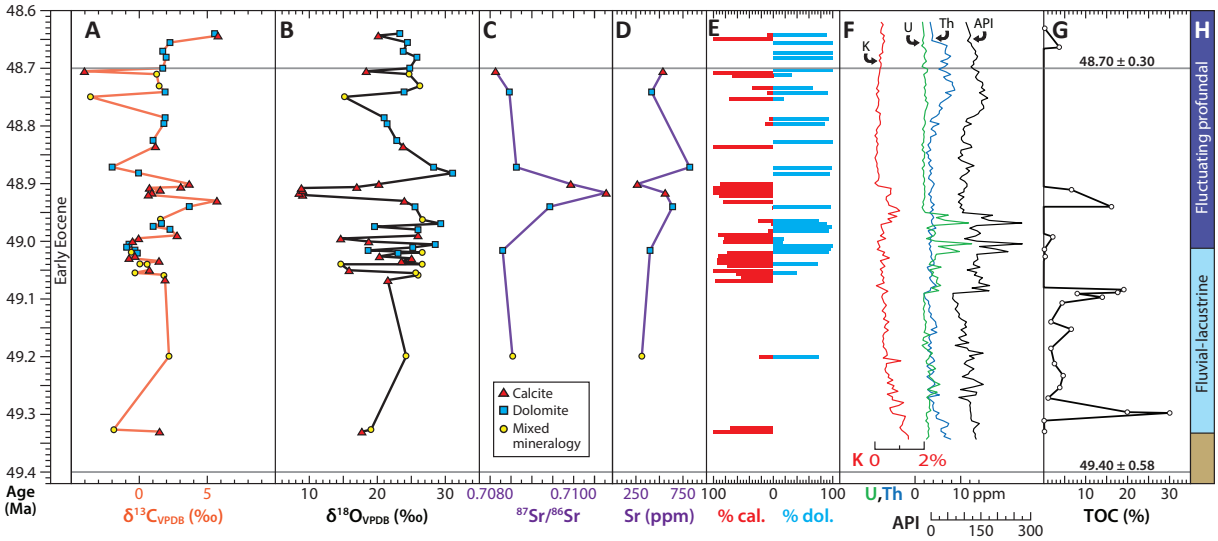

Figure 3.5. Summary of early Eocene geochemical and isotopic data for samples collected in Coal Mine Canyon (see Fig. 3.1 for section location). Interpolated ages and full results given in Table 3.2; gray bars show age control from $^{40}Ar/^{39}Ar$ geochronology (Smith et al., 2017) and detrital zircon U-Pb geochronology (Canada et al., 2019). (A–C) $\delta^{13}C$, $\delta^{18}O$, and $^{87}Sr/^{86}Sr$ stable isotope geochemistry of lacustrine carbonates with sample mineralogy data from powder X-ray diffraction. (D) Strontium concentration of carbonate separates (see Supplemental Methods). (E) Estimated percent calcitic and dolomitic mineralogy, based on X-ray diffraction (see Supplemental Materials). (F) Hand-held spectral gamma ray spectroscopy measured at 50 cm intervals. (G) Total organic carbon (TOC) data from Palmer (1984). (H) Lacustrine facies associations interpreted from decimeter-scale stratigraphy at Coal Mine Canyon.

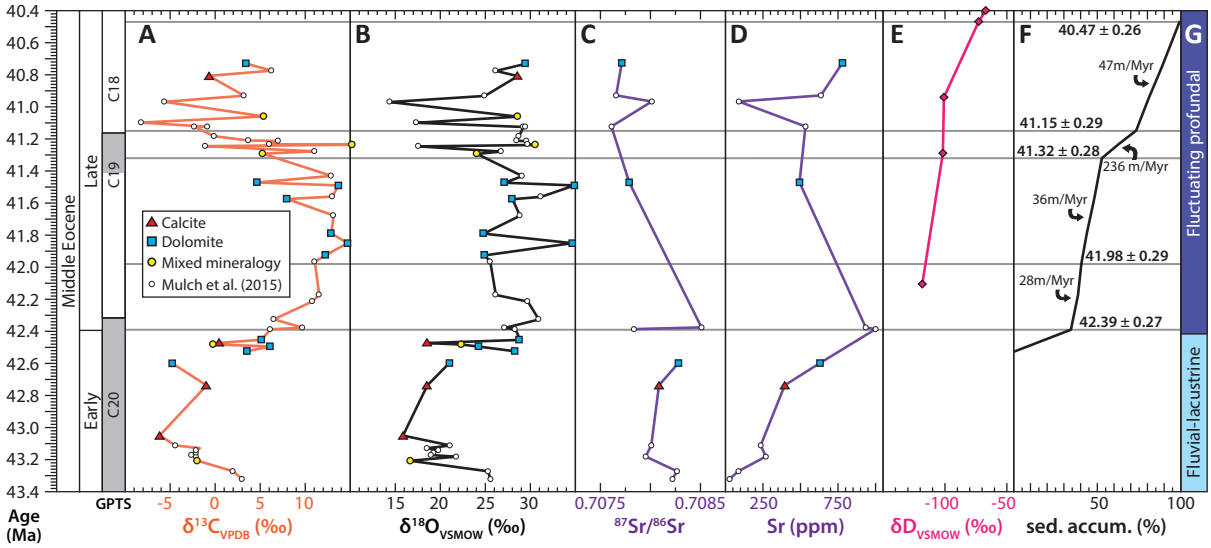

Figure 3.6. Summary of middle Eocene geochemical and isotopic data for samples collected in the Pinon Range, where the uppermost Elko Formation is preserved. GPTS scale from Smith et al. (2017). Interpolated ages and full results given in Table 3.2. (A–C) $\delta^{13}C$, $\delta^{18}O$, and $^{87}Sr/^{86}Sr$ stable isotope geochemistry of lacustrine carbonates with sample mineralogy data from X-ray diffraction. Select samples from Mulch et al. (2016). (D) Strontium concentration of carbonate separates. Select samples data (circles) from Mulch et al. (2016). (E) Volcanic glass δD values for hydrated volcanic glass separated from interbedded volcanic ash horizons (Smith et al., 2017). (F) Sediment accumulation rate for upper Pinon Range section based on interbedded single crystal sanidine $^{40}Ar/^{39}Ar$ ages (shown by gray bars). (G) Lacustrine facies associations interpreted from decimeter-scale stratigraphy in the Pinon Range.

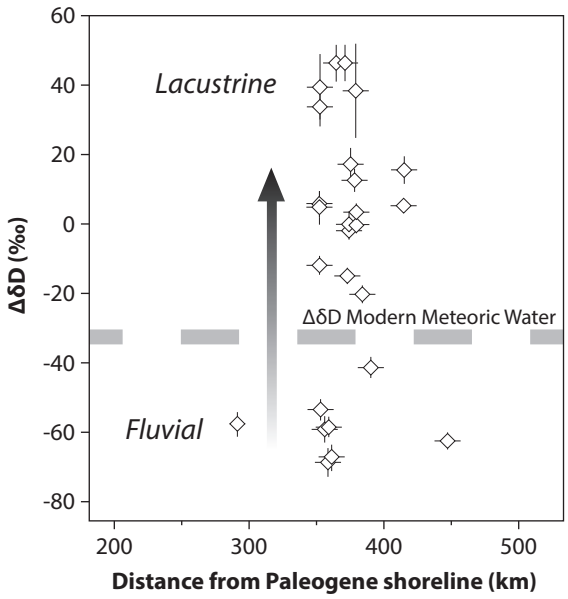

Figure 3.7. Comparison of δD values for Eocene volcanic glass in eastern Nevada normalized to a datum near paleo-sea level and plotted along a transect according to restored distance from the Paleogene shoreline (cf. Cassel et al., 2018). Refer to Table 3.4 for source of sample data and full results. Samples deposited in a lacustrine environment reflect deuterium-enriched lake waters, whereas samples deposited in fluvial facies show considerable distillation and depletion from the modern meteoric water, corresponding to higher mean surface elevations during the Eocene.

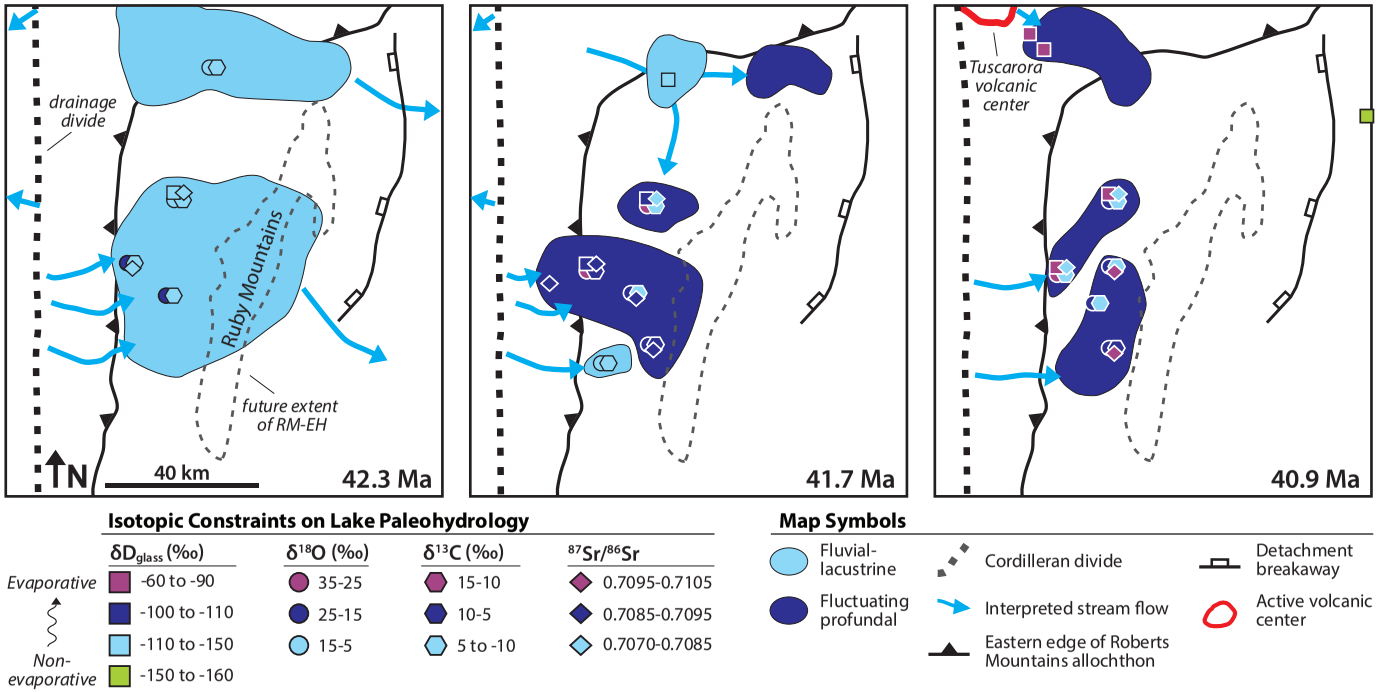

Figure 3.8. Schematic paleohydrologic reconstruction of the Elko Basin modified from Smith et al. (2017) showing mean isotopic values across the Elko Basin during several middle Eocene time slices. Location of eastern edge of Roberts Mountains allochthon from Long (2012).

TABLE 3.1. MODERN RIVER DATA

Sample	Date collected	Location	Main bedrock lithology	Latitude (N)	Longitude (W)	pH	Temp. (°C)	Sr (ppm)	$^{87}Sr/^{86}Sr$ measured	Analytical error (±2σ)	Included ratios
NV17-001RB	4/21/2017	Ruby Mountains	metamorphic	40.649°	-115.391°	7.1	4.4	0.0189	0.71172	0.00004	149
NV17-002RB	4/21/2017	Ruby Mountains	metamorphic	40.692°	-115.476°	6.6	5.8	0.0218	0.71338	0.00004	148
NV17-003RB	4/21/2017	Lamoille Valley	metamorphic	40.822°	-115.317°	6.8	10.4	0.0220	0.71174	0.00004	142
NV17-004RB	4/21/2017	Secret Pass	metamorphic	40.867°	-115.269°	7.3	10.6	0.0206	0.71124	0.00004	150
Core-complex average								**0.0208**	**0.71202**		
NV17-006CM	4/22/2017	Coal Mine Canyon	sedimentary	41.111°	-115.627°	7.2	5.4	0.0142	0.70806	0.00004	150
NV17-012PR	4/23/2017	Pinon Range	sedimentary	40.451°	-116.069°	7.0	16.8	0.0209	0.70779	0.00004	151
Paleozoic bedrock average								**0.0176**	**0.70792**		

TABLE 3.2. CARBONATE SAMPLE LOCATION, INTERPOLATED AGE, AND GEOCHEMISTRY RESULTS.

Location **Sample ID**	**Lithology**	**Height (m)†**	**TI age (Ma)§**	**Mineralogy#**			**$\delta^{13}C$ (‰, VPDB)**	**$\delta^{18}O$ (‰, VSMOW)**	**δD_{Glass} (‰, VSMOW)**	**±2σ**	**Sr (ppm)**	**$^{87}Sr/^{86}Sr$**	**Latitude (N)**	**Longitude (W)**
				Calcite	**Dolomite**	**Silica**								
Coal Mine Canyon *Base of section: 41.133°N, -115.640°W*														
NV12-040CM	sandstone	0	49.40**											
NV15-073CM	micrite	15	49.33	100%	0%	0%	1.5	17.7						
NV15-075CM	micrite	15.9	49.32	71%	0%	29%	-1.8	19.1						
NV14-005CMC	dolomicrite	41	49.20	23%	76%	0%	2.2	24.3			327	0.70854		
NV15-083CM	limestone	67.5	49.07	96%	0%	4%	1.8	21.5						
NV12-055CMA	limestone	69.5	49.06	53%	0%	47%	1.8	26.0						
NV15-084CM	micrite	70.1	49.05	61%	39%	0%	-0.4	25.6						
NV15-085CM	limestone	71	49.05	100%	0%	0%	0.7	15.8						
NV15-088CM	dolomicrite	73	49.04	5%	75%	20%	0.5	14.6						
NV12-057CM	limestone	73.2	49.04	76%	0%	23%	0.0	26.6						
NV15-089CM	micrite	74	49.03	93%	0%	7%	1.4	23.5						
NV15-090CM	limestone	75	49.03	93%	0%	7%	-0.8	25.1						
NV15-091CM	limestone	76	49.02	92%	0%	8%	-0.3	20.3						
NV15-092CM	dolomicrite	77	49.02	0%	93%	7%	-0.2	23.0						
NV12-058CM	limestone	77.3	49.02	76%	0%	24%	-0.6	26.6						
NV15-093CM	dolomicrite	78	49.01	0%	90%	10%	-0.4	18.7			418	0.70830		
NV15-094CM	dolomite	79	49.01	0%	96%	4%	-0.9	25.2						
NV15-095CM	dolomite	80	49.01	0%	100%	0%	-0.8	28.5						
NV15-096CM	micrite	81	49.00	84%	16%	0%	-0.5	18.8						
NV15-097CM	micrite	82	49.00	82%	18%	0%	-0.1	14.6						
NV15-098CM	micrite	83.2	48.99	91%	0%	9%	2.8	26.0						
NV15-100CM	dolomicrite	85	48.98	7%	93%	0%	2.2	26.0						
NV15-101CM	dolomicrite	86	48.98	0%	98%	2%	1.0	19.6						
NV12-061CMA	dolomite	87.3	48.97	2%	90%	8%	1.6	29.3						
NV15-102CM	dolomicrite	88.4	48.96	24%	76%	0%	1.5	26.6						
NV12-063CMA	dolomicrite	93	48.94	1%	97%	2%	3.6	25.6			671	0.70943		
NV15-104CM	micrite	95.2	48.93	84%	0%	16%	5.6	24.0						
NV15-106CM	micrite	97.2	48.92	90%	0%	10%	0.7	9.1						
NV15-107CM	micrite	98	48.92	100%	0%	0%	0.9	8.5			584	0.71078		
NV15-108CM	micrite	99	48.91	91%	0%	9%	1.5	9.0						
NV15-108CME	micrite	99.4	48.91	100%	0%	0%	0.7	8.9						
NV15-109CM	micrite	100	48.91	100%	0%	0%	3.0	17.0						
NV15-110CM	micrite	101	48.90	89%	0%	11%	3.6	20.2			276	0.70993		
NV12-067CMA	dolomicrite	104.8	48.88	0%	94%	6%	-0.1	31.1						
NV12-067CMB	dolomicrite	106.9	48.87	0%	99%	1%	-2.0	28.3			863	0.70864		
NV15-112CM	limestone	114	48.84	100%	0%	0%	1.1	23.8						
NV15-114CM	dolomicrite	116	48.83	0%	100%	0%	1.0	22.9						
NV15-117CM	dolomicrite	122	48.80	13%	87%	0%	1.8	21.5						

NV15-118CM	dolomicrite	124	48.79	6%	94%	0%	1.9	21.0					
NV12-070CM	limestone	131	48.75	73%	17%	0%	-3.5	15.1					
NV15-121CM	dolomicrite	133	48.74	9%	91%	0%	1.9	23.9			439	0.70846	
NV15-122CM	dolomicrite	135	48.73	34%	66%	0%	1.4	26.2					
NV15-123CM	micrite	139	48.71	69%	31%	0%	1.2	24.6					
NV12-071CM	limestone	140	48.71	97%	0%	3%	-4.0	18.4			564	0.70813	
NV15-124CM	dolomicrite	141	48.70	0%	100%	0%	1.7	24.7					
NV12-106CM	tuff	141.8	48.70††										
NV15-126CM	dolomicrite	145	48.68	0%	100%	0%	1.9	25.8					
NV15-127CM	dolomicrite	147	48.67	0%	100%	0%	1.7	23.8					
NV15-128CM	dolomicrite	150	48.66	0%	100%	0%	2.2	24.4					
NV15-129CM	micrite	152.4	48.65	100%	0%	0%	5.7	20.1					
NV15-130CM	dolomicrite	153	48.64	10%	90%	0%	5.5	23.3					
NV11-040CM	tuff		41.22††						-147.4††	6.3††		41.132°	-115.643°
NV16-034CM	limestone			100%	0%	0%	3.7	9.8				41.152°	-115.593°
Piñon Range	*Base of section 1: 40.580°N, -115.992°W*												
ANV14-021PR	dolomite	1.5	42.53	0%	96%	4%	3.5	28.4					
ANV14-014PR	dolomite	16.3	42.50	0%	100%	0%	6.1	24.3					
ANV14-018PR	limestone	23.5	42.48	62%	0%	38%	-0.3	22.4					
ANV14-012PR	micrite	27.5	42.48	100%	0%	0%	0.4	18.5					
ANV14-022PR	dolomite	38.2	42.45	0%	97%	3%	5.1	28.8					
NV-EF-3-07*	paleosol	70	42.39				6.1	28.4			1001	0.70784	
NV12-110SR	tuff	70.5	42.39††										
NV-EF-4-07*	limestone	71.5	42.38				9.7	27.1			940	0.70851	
NV-EF-5-07*	limestone	73	42.33				6.6	30.9					
NV-EF-6-07*	limestone	76.2	42.21				10.9	29.7					
NV-EF-7-07*	limestone	77.3	42.17				11.6	26.2					
ANV16-006PR	tuff	79.2	42.11						-118.1	2.8			
NV12-113SR	tuff	82.1	41.98††										
NV-EF-8-07*	micrite	82.5	41.97				11.1	25.5					
NV12-114SR	dolomite	84	41.93	2%	94%	4%	12.3	25.0					
NV16-101PR	dolomicrite	87	41.85	0%	100%	0%	14.8	34.8					
NV12-116SR	dolomite	89	41.79	0%	100%	0%	13.0	24.8					
NV-EF-9-07*	limestone	93	41.68				13.2	28.9					
NV12-119SR	dolomite	96.8	41.57	0%	99%	1%	8.0	27.9					
NV-EF-10-07*	limestone	97.3	41.56				13.0	31.2					
NV16-104PR	dolomite	99	41.49	0%	100%	0%	13.8	34.9					
NV12-120SR	dolomite	100.5	41.47	1%	95%	4%	4.7	27.2			487	0.70788	
NV-EF-11-07*	limestone	102	41.43				12.9	29.1					
NV12-121SR	tuff	106	41.32††										
NV12-122SR	limestone	112.3	41.29	69%	21%	10%	5.3	24.1					
ANV14-060PR	tuff	113	41.29						-101.5	4.9			
NV-EF-12-07*	limestone	116	41.28				11.1	26.8					

NV-EF-13-07*	micrite	123.5	41.25				-1.0	17.6						
NV12-123SR	dolomicrite	126	41.24	0%	70%	30%	15.2	30.6						
NV-EF-14-07*	micrite	126.5	41.23				6.1	29.7						
NV-EF-15-07*	limestone	131	41.21				7.0	29.6						
NV-EF-16-07*	limestone	132	41.21				3.8	28.5						
NV-EF-17-07*	sandstone	138	41.18				0.0	28.7						
NV12-129SR	tuff	146.1	41.15††											
NV-EF-18-07*	micrite	148	41.13				-2.2	29.2			537	0.70762		
NV-EF-19-07*	tuff	148	41.13				-0.8	29.5						
NV-EF-20-07*	tuff	150	41.10				-8.2	17.3						
NV12-131SR	dolomicrite	153	41.06	5%	59%	36%	5.5	28.6						
NV-EF-22-07*	micrite	160	40.97				-5.6	14.4			86	0.70802		
ANV14-062PR	tuff	162	40.94						-100.6	3.7				
NV-EF-23-07*	micrite	163	40.93				3.3	24.9			635	0.70766		
NV12-133SR	limestone	172.5	40.81	91%	5%	4%	-0.6	28.6						
NV-EF-24-07*	micrite	175	40.77				6.3	26.1						
NV12-135SR	dolomicrite	178.5	40.73	0%	96%	4%	3.5	29.5			782	0.70772		
NV12-099ES	tuff	181	40.40††						-66.7††	9.4††				
NV12-139SR	tuff	198.5	40.47††						-72.4††	5.6††				
NV14-077SR(A)	tuff								-159.5††	3.1††			40.573°	-115.978°
Piñon Range	*Base of section 2: 40.579°N, -115.998°W*													
TL12-02*	limestone	0	43.32				3.1	25.6			25	0.70823		
TL04-02*	limestone	5	43.27				2.1	25.3			79	0.70827		
ANV14-058PR	limestone	11.5	43.21	76%	18%	6%	-2.0	16.6						
CL-10*	limestone	14	43.18				-2.1	21.8			270	0.70796		
CL-11*	limestone	15	43.17				-2.5	18.9						
CL-12*	limestone	16.5	43.16				-2.0	19.2						
CL-15*	limestone	18	43.14				-2.1	19.8						
CL-16*	limestone	19.3	43.13				-1.7	18.5						
CL-17*	limestone	21	43.11				-4.4	21.1			227	0.70802		
NV16-099PR	limestone	26.9	43.05	100%	0%	0%	-6.1	15.9						
ANV14-056PR	limestone	58.5	42.74	83%	17%	0%	-0.9	18.5			397	0.70808		
ANV14-057PR	dolomicrite	72.2	42.60	2%	93%	5%	-4.8	21.0						
ANV14-010PR	tuff	84	42.23††											
NV12-098ES	dolomite			6%	89%	5%	4.7	21.6			635	0.70828	40.590°	-115.998°
NV12-095ES	micrite			100%	0%	0%	0.4	16.2					40.590°	-116.000°
Twin Bridges	*Base of section 1: 40.611°N, -115.734°W*													
NV16-039TB	limestone	32.5					0.1	17.4						
NV16-040TB	micrite	35.7					-2.2	14.4						
NV16-042TB	limestone	44.9					-2.0	13.8						
NV16-045TB	micrite	52		100%	0%	0%	-4.7	15.1						
NV16-046TB	micrite	60.4					-5.0	10.7						

NV16-047TB	limestone	76	100%	0%	0%	-4.2	13.4		
NV16-048TB	limestone	78.6				-4.4	18.4		
NV16-049TB	micrite	83.5	100%	0%	0%	-0.8	16.6		
NV16-050TB	micrite	104.5				-2.6	14.5		
NV16-051TB	micrite	108.2	100%	0%	0%	-1.1	13.2		
NV16-052TB	micrite	119.3				-1.0	19.5		
Twin Bridges	*Base of section 2: 40.613°N, -115.746°W*								
NV16-056TB	micrite	0				7.6	24.2		
NV16-057TB	micrite	1				6.5	23.4		
NV15-147TB	dolomite	8	0%	100%	0%	3.3	14.5	439	0.70970
NV15-152TB	micrite	9	100%	0%	0%	-1.3	10.0		
NV15-154TB	dolomicrite	15	0%	100%	0%	1.0	22.0		
NV15-160TB	dolomite	21.7	0%	100%	0%	-8.7	7.0		
NV15-163TB	dolomite	27.5	0%	100%	0%	-8.9	6.9		
NV15-165TB	limestone	29.8	100%	0%	0%	-1.1	21.0	298	0.70986
Dixie Hills	*Base of section: 40.513°N, -115.803°W*								
NV15-239DH	dolomite	1.2	0%	72%	28%	3.4	30.7		
NV15-238DH	dolomite	7.2	0%	89%	11%	2.7	27.6		
NV15-237DH	limestone	10.5				-1.9	19.6		
NV15-235DH	limestone	16	100%	0%	0%	1.8	12.8		
NV15-234DH	micrite	17.1	100%	0%	0%	2.3	10.3	332	0.70866
NV15-232DH	dolomicrite	23.5	0%	97%	3%	3.8	30.5		
NV15-231DH	limestone	30				-1.2	24.2		
NV15-227DH	limestone	37.5	100%	0%	0%	-0.8	18.0		
NV15-225DH	dolomite	41	0%	100%	0%	3.9	33.0		
NV15-224DH	limestone	44.5	100%	0%	0%	-2.0	21.2		
NV15-222DH	limestone	49.4				-1.9	20.4		
NV15-220DH	paleosol	55.3	0%	100%	0%	2.8	31.1		
NV15-216DH	dolomicrite	60.5	0%	82%	18%	0.5	17.0		
NV15-210DH	limestone	67.8	20%	0%	80%	-1.4	13.0		
NV15-206DH	dolomite	75.4	0%	100%	0%	7.4	23.5		
NV15-204DH	dolomicrite	88	0%	100%	0%	10.0	34.6		
NV15-202DH	dolomicrite	93.1	0%	76%	24%	2.2	27.6		
NV15-197DH	dolomite	98.2	0%	100%	0%	9.9	35.0		
NV15-195DH	dolomicrite	103	0%	100%	0%	-1.0	25.5		
NV15-193DH	dolomicrite	106.2				7.7	33.2		
NV15-190DH	dolomite	109.6	8%	92%	0%	2.8	24.0		
NV15-186DH	dolomite	114.5	0%	100%	0%	9.9	33.8		
NV15-182DH	limestone	121	100%	0%	0%	8.1	32.6		
NV15-180DH	dolomite	127.4	0%	48%	52%	-0.2	20.1		
NV15-178DH	dolomite	130.2	0%	31%	69%	5.4	23.1		

Elko Hills	*Base of section: 40.817°N, -115.746°W*												
NV16-075EH	dolomicrite	9				2.0	29.7						
NV16-077EH	dolomicrite	22.5		0%	100%	0%	3.1	33.2					
NV16-078EH	dolomite	37.5					9.2	34.9					
NV16-081EH	dolomicrite	41		0%	100%	0%	7.8	32.3					
NV16-082EH	dolomicrite	46.2					8.0	33.8					
NV16-083EH	dolomicrite	57.5		0%	100%	0%	6.8	31.0					
NV16-085EH	dolomite	70.2		0%	100%	0%	3.2	27.4					
NV16-086EH	dolomicrite	88.5					-2.5	21.8					
NV16-089EH	dolomicrite	106					0.1	19.7					
NV16-094EH	dolomite	141.1					2.5	29.6					
ANV14-051EH	limestone			99%	0%	1%	-1.9	11.5			514	0.70845	40.848°	-115.691°
ANV14-054EH	limestone			91%	0%	9%	-1.1	10.6			683	0.70812	40.848°	-115.690°
ANV14-055EH	dolomite			0%	100%	0%	-3.5	26.7			219	0.70976	40.848°	-115.690°
NV15-007EH	limestone			45%	0%	55%	-0.6	9.0					40.851°	-115.686°
ANV14-008EH	tuff		39.55[††]						-93.5[††]	3.2[††]			40.812°	-115.730°
										27.0[†]				
NV12-105EH	tuff		40.46[††]						-67.7[††]	[†]			40.816°	-115.722°
NV12-104EH	tuff		42.69[††]						-102.8[††]	2.5[††]			40.794°	-115.721°
NV16-073EH	tuff								-126.4	2.5			40.841°	-115.676°
NV16-026EH	tuff								-106.1	2.5			40.815°	-115.716°
EOS Core Hole	*Base of section: 40.794°N, -115.720°W*												
EOS3N-269-5	dolomicrite	82.1		0%	100%	0%	7.8	21.2			442	0.70775		
EOS3N-563	dolomicrite	171.6		0%	85%	15%	-1.7	22.8						
EOS3N-576	dolomicrite	175.6		0%	100%	0%	-2.9	25.4			657	0.70823		
EOS3N-578	dolomicrite	176.2		0%	89%	11%					292	0.70817		
EOS3N-588	dolomite	179.2		0%	82%	18%	-2.0	24.1			158	0.70982		
EOS3N-625	micrite	190.5		100%	0%	0%	-1.5	13.7						
Jiggs	*Well location: 40.420°N, -115.736°W*												
K1L-8996	dolomicrite	2742		0%	63%	37%	-0.2	16.7			720	0.70829		
K1L-9114-7	dolomicrite	2778.2		0%	83%	17%	0.9	20.3						
K1L-9158	dolomicrite	2791.4		0%	100%	0%	1.4	20.9			843	0.70834		
K1L-9174-5	dolomicrite	2796.4		0%	83%	17%	1.7	21.5			1034	0.70907		
K1L-9214	dolomicrite	2808.4		40%	45%	15%	-0.1	18.2			920	0.71000		
K1L-9219	dolomicrite	2810		7%	75%	18%	0.4	22.0			548	0.70845		
Robinson Mountain														
NV15-242RM	limestone			92%	0%	8%							40.360°	-115.933°
NV15-246RM	micrite			96%	0%	4%	1.3	11.2					40.359°	-115.932°
Cortez Range														
NV18-07CR	limestone			100%	0%	0%					689	0.70895	40.590°	-116.172°

NV11-051EP	dolomite		18%	40%	42%				40.686°	-116.287°
Taylor Canyon										
NV15-134TC	limestone		100%	0%	0%				41.280°	-116.109°
NV12-017TC	tuff	40.54[††]				-59.7[††]	5.3[††]		41.266°	-116.104°
NV14-069TC	tuff	40.30[††]				-121.0[††]	2.5[††]		41.281°	-116.113°
Pie Creek										
ANV14-063PC	tuff					-89.0	4.6		41.277°	-115.940°
ANV14-064PC	tuff	40.25[††]				-106.5[††]	4.0[††]		41.266°	-115.931°
ANV14-065PC	tuff	38.19[††]				-107.7[††]	3.1[††]		41.264°	-115.930°

[*] Analyses from Mulch et al. (2015).
[†] Stratigraphic height from base of section at reported coordinates.
[§] Ages determined using tiered interpolation between single crystal sanidine $^{40}Ar/^{39}Ar$ and detrital zircon U-Pb maximum depositional ages following the procedures outlined in Smith et al. (2011).
[#] Sample mineralogy from X-ray diffraction of replicate separates. See text for full methodology and Supplemental Material for full analytical results.
[**] Detrital zircon U-Pb maximum depositional age. See Supplementary Information.
[††] From Smith et al. (2017).

TABLE 3.3. Sr ISOTOPE COMPOSITIONS OF ELKO FORMATION SAMPLES.

Sample	Sr (ppm)	$^{87}Sr/^{86}Sr$ measured	Included ratios (*n*)	Analytical error (±2σ)	$^{87}Rb/^{86}Sr$	Lithology
ANV14-051EH	514	0.70845	147	0.00004	0.00001	limestone
ANV14-054EH	292	0.70812	151	0.00004	0.00001	limestone
ANV14-055EH	219	0.70976	151	0.00004	0.00005	dolomite
EOS-269	442	0.70775	150	0.00004	0.00003	dolomicrite
EOS-576	657	0.70823	149	0.00006	0.00001	dolomicrite
EOS-578	292	0.70817	150	0.00004	0.00001	dolomicrite
EOS-588	158	0.70982	150	0.00004	0.00001	dolomite
NV14-005CMC	327	0.70854	149	0.00004	0.00002	dolomicrite
NV12-063CMA	671	0.70943	151	0.00004	0.00010	dolomicrite
NV12-067CMB	863	0.70863	151	0.00004	0.00001	dolomicrite
NV12-071CM	564	0.70813	150	0.00004	0.00001	limestone
NV12-093CM	418	0.70830	151	0.00004	0.00001	dolomicrite
NV15-107CM	584	0.71078	150	0.00004	0.00001	micrite
NV15-110CM	276	0.70993	144	0.00004	0.00001	micrite
NV15-121CM	439	0.70846	150	0.00004	0.00001	dolomicrite
NV12-098ES	635	0.70828	150	0.00004	0.00001	dolomite
NV12-120SR	487	0.70788	149	0.00004	0.00001	dolomite
NV12-135SR	782	0.70772	156	0.00004	0.00001	dolomicrite
ANV14-056PR	397	0.70808	150	0.00004	0.00001	limestone
K1L-8996	720	0.70829	148	0.00004	0.00007	dolomicrite
K1L-9158	843	0.70834	150	0.00004	0.00001	dolomicrite
K1L-9174	1034	0.70907	149	0.00004	0.00001	dolomicrite
K1L-9214	920	0.71000	88	0.00004	0.00001	micrite
K1L-9219	548	0.70845	149	0.00004	0.00001	dolomicrite
NV15-147TB	439	0.70970	142	0.00006	0.00001	dolomite
NV15-165TB	298	0.70986	149	0.00004	0.00001	micrite
NV15-234DH	332	0.70866	150	0.00004	0.00001	micrite
NV18-070CR	689	0.70895	151	0.00004	0.00001	limestone

TABLE 3.4. EOCENE VOLCANIC GLASS δD AND RECONSTRUCTED DISTANCE FROM PALEOSHORELINE

Sample	Weighted mean age (Ma)*	Latitude (N)	Longitude (W)	Reconstructed distance (km)	δD_{glass} (‰)	± 2σ	Normalized δD_{glass} (‰)†	Water content (wt. %)
NV11036DC	33.90	39.983°	-116.796°	291.2	-163.7	3.5	-57.7	2.96
NV11022EU	36.40	39.510°	-115.967°	356.3	-165.2	4.0	-59.2	4.55
NV11020EU	36.50	39.407°	-115.918°	361.0	-173.3	3.7	-67.3	5.35
NV11019EU	36.63	39.448°	-115.938°	359.2	-164.5	2.8	-58.5	5.43
NV11021EU	36.92	39.481°	-115.940°	358.9	-174.8	4.1	-68.8	4.42
NV12099ES	40.40	40.579°	-115.990°	352.5	-66.7	9.4	39.3	0.10§
NV12139SR	40.47	40.580°	-115.990°	352.7	-72.4	5.6	33.6	8.91§
NV12018TC	40.55	41.282°	-116.113°	364.5	-59.7	5.3	46.3	0.78§
NV12105EH	40.46	40.816°	-115.722°	379.1	-67.7	13.5	38.3	0.17§
NV11044CM	41.22	41.126°	-115.637°	390.3	-147.4	3.1	-41.4	3.65
NV12175CB	38.93	41.764°	-115.468°	415.1	-90.6	4.0	15.4	2.20
NV12154NC	40.50	41.025°	-114.544°	447.3	-168.4	2.4	-62.4	2.98
ANV14065PC	38.19	41.264°	-115.930°	374.2	-107.7	3.1	-1.7	4.17
NV14-077SR	41.00	40.573°	-115.978°	353.0	-159.5	3.1	-53.5	3.44
ANV14-008EH	39.55	40.812°	-115.730°	378.3	-93.5	3.2	12.5	5.25
NV12-104EH	42.69	40.794°	-115.721°	379.6	-102.8	2.5	3.2	5.46
NV14-069TC	40.30	41.281°	-116.113°	372.8	-121.0	2.5	-15	6.93
ANV14-064PC	40.25	41.266°	-115.931°	374.2	-106.5	4.0	-0.5	2.09
ANV140-001COB	40.10	41.750°	-115.477°	414.9	-100.7	2.5	5.3	1.73
ANV16-006PR		40.580°	-115.991°	352.2	-118.1	2.8	-12.1	1.21
ANV14-060PR		40.580°	-115.991°	352.3	-101.5	4.9	4.5	10.39§
ANV14-062PR		40.578°	-115.990°	352.4	-100.6	3.7	5.4	1.11
NV16-073EH		40.841°	-115.676°	383.9	-126.4	2.5	-20.4	6.64
NV16-026EH		40.815°	-115.716°	379.4	-106.1	2.5	-0.1	5.22
ANV14-063PC		41.276°	-115.940°	375.4	-89.0	4.6	17	2.26

* From single crystal sanidine $^{40}Ar/^{39}Ar$ ages reported in Smith et al. (2017) and Cassel et al. (2018)

† Normalized to a low elevation Eocene (ca. 40 Ma) datum collected near paleo-sea-level (cf. Cassel et al., 2018)

§ High or low water content, signifying more or less fractionation into glass and greater uncertainty for corresponding δD values.

CHAPTER IV

Stratigraphy of an Evolving Hinterland Basin: Eocene Elko Formation, northeastern Nevada, U.S.A.

ABSTRACT

Hinterland basins contain important records of orogenic evolution, but associated stratigraphic records are often overprinted by later orogenic collapse. In the North American Cordilleran hinterland, the Eocene Elko Basin was filled by >1.2 km of lacustrine, fluvial, and volcaniclastic sediment at elevations of ~2800–3000 m. Following post-depositional extension, Eocene fluvial and lacustrine strata of the Elko Formation are spread across a >20,000 km^2 area of what is now northeastern Nevada and represent the evolution of a longstanding lacustrine system. Spatial disconnectivity of Elko Formation strata and a prior lack of correlation tools has deterred detailed stratigraphic characterization of the Elko Basin and prohibited a clear understanding of controls on basin formation and development. Decimeter-scale stratigraphy of early–middle Eocene Elko Formation strata, combined with correlation enabled by recent single crystal sanidine $^{40}Ar/^{39}Ar$ geochronology and detrital zircon U-Pb geochronology, permits synoptic reconstruction of the Elko Basin lake system at high spatial and temporal resolution.

Initial Elko Formation lacustrine strata were deposited in a relatively small lake basin at ca. 49 Ma, which was likely confined to a preexisting paleovalley. The most spatially extensive phase of lacustrine deposition initiated at 43.2 Ma and filled a large extent of the Elko Basin with interconnected freshwater lakes by 42.4 Ma. These lakes further segmented into a series of subbasins and developed increasingly saline and alkaline waters following a ca. 42.2 Ma transition to balanced-fill conditions. At the same time, the depocenter of Elko Formation lakes gradually migrated towards the west, prior to ca. 40.4 Ma basin closure marked by caldera-forming eruptions in the proximal Tuscarora volcanic field. This basin history reflects two distinct phases of tectonic subsidence at rates of ~0.1–0.3 mm/yr between both ca. 50–49 Ma and ca. 43–40 Ma. In both phases, braided streams occupying broad paleovalleys were ponded into a series of freshwater lakes with relatively low relief margins.

The most rapid sediment accumulation, at a rate of ~1.2 mm/yr, occurred between 41 and 40 Ma, when volcaniclastic sediments derived from the Tuscarora volcanic field filled the Elko Basin. This record reflects both internal and external controls on basin development over multiple timescales. This includes k.y. depositional variations from global climatic fluctuations and m.y. variations in drainage migration/sediment supply and accommodation changes, both likely controlled by the dynamic and isostatic effects of slab and lower lithosphere removal.

INTRODUCTION

Lakes are sensitive to changes in regional and global climate (e.g., Glenn and Kelts, 1991; Roehler, 1993; Leng and Marshall, 2004; Balch et al., 2005; Bowen et al., 2008; Tanavsuu-Milkeviciene et al., 2012; Chamberlain et al., 2013; Smith et al., 2014b; Ma et al., 2016), drainage patterns (e.g., Pietras et al., 2003; Carroll et al., 2006; Smith et al., 2008; Davis et al., 2009; Chetel et al., 2011), biologic diversity (e.g., Williams, 1998; Cohen, 2003; Gierlowski-Kordesch and Park, 2004), and tectonics (e.g., Olsen, 1990; Saez and Cabrera, 2002; Gierlowski-Kordesch and Buchheim, 2003; Smith et al., 2014a, 2017; Cassel et al., 2018), and lake deposits often contain important mineral and petroleum resources (e.g., Smoot and Lowenstein, 1991; Johnson et al., 2011; Katz and Lin, 2014). Several large and resource generative lacustrine systems, such as Eocene lakes of the Green River Formation, are well characterized following nearly a century of intense study (Fig. 4.1; e.g., Sears and Bradley, 1924; Bradley, 1925; Picard, 1955; Bradley, 1970; Sullivan, 1985; Mason and Surdam, 1992; Carroll and Bohacs, 1999; Bohacs et al., 2000; Smith et al., 2008, 2014b). Hinterland lakes, situated to the west of the Cordilleran thrust belt, are comparatively poorly understood, despite their initial recognition over a century ago (Fig. 4.1; King, 1876; 1878).

Hinterland basins often occupy the elevated interior of orogens and record the cumulative effects of surface uplift, erosion, and magmatism (Fig. 4.1; e.g., Horton et al., 2002; Evenchick et al., 2007; Leier et al., 2010; Moreno et al., 2011; Benvenuti et al., 2014; Cohen et al., 2015; DeCelles et al., 2015; Tenorio et al., 2018). These basins are commonly supported by thick crust and can contain a depositional history that spans large portions of the contractile phase of orogens (McQuarrie et al., 2005; DeCelles and Graham, 2015).

Hinterland basin formation is attributed to a wide range of tectonic and geomorphic controls, including removal of dense lower-crustal lithospheric roots (Molnar and Houseman, 2004), metamorphic core complex exhumation (Satarugsa and Johnson, 2000), backthrusting (Leier et al., 2010), gravitational collapse (Rahl et al., 2002), slab removal (Smith et al., 2014a; Brun et al., 2016; Cassel et al., 2018; Canada et al., 2019), and geomorphic/volcanic damming. Syn-contractional hinterland basins, such as the Ayaviri basin in Peru or the broader Altiplano intermontane basin preserve large quantities of synorogenic sediments and high magnitudes of erosional exhumation (Long, 2012; Perez and Horton, 2014). In comparison, post-contractional hinterland basins may record the initial stages of orogen collapse that accompany slab or lower lithosphere removal (Cassel et al., 2018). In the North American Cordillera, the largest, and likely most prolonged hinterland lacustrine systems occupied the broad Elko Basin (Fig. 4.2; Van Houten, 1956; Jaeger, 1987; Smith et al., 2017), which sustained relatively high elevations (2800–3000 m; Cassel et al., 2014, 2018) throughout the early and middle Eocene (Fig. 4.3). The mechanisms governing basin formation and depositional variability, however, are not well understood for hinterland basins across a range of ancient and modern orogens (Fig. 4.4).

This paper synthesizes detailed sedimentology and stratigraphy of early to middle Eocene Elko Formation strata, deposited across a large expanse of the North American Cordilleran hinterland, with recent geochronology (Fig. 4.3). Several previous efforts were taken to characterize Elko Formation strata (Van Houten, 1956; Smith and Ketner, 1976; Solomon et al., 1979a, 1979b; Solomon, 1981; Moore et al., 1983; Server and Solomon, 1983; Solomon, 1992; van de Kamp and Samoun, 1992; Haynes, 2003; Horner, 2015; McGowan, 2015; Johnson and Birdwell, 2016), but were limited by restricted age control. We integrate facies and geochemical analyses from decimeter-scale stratigraphic sections with recent ages derived from single crystal sanidine $^{40}Ar/^{39}Ar$ geochronology and detrital zircon U-Pb geochronology to correlate strata and reconstruct depositional variability through time (Fig. 4.3). In addition, newly cored intervals at several critical locations in the Elko Basin provide an opportunity to study complete sections of the Elko Formation within this age model for the first time.

CORDILLERAN HINTERLAND BASINS

Eocene Lake Basins in the Hinterland

The hinterland of the North American Cordillera, situated between the Sevier thrust front and Sierra magmatic arc, is characterized as a high-elevation (~3–4 km) orogenic plateau, supported by thick crust (Fig. 4.1; Coney and Harms, 1984; Camilleri and Chamberlain, 1997; Dickinson, 2004; Cassel et al., 2014, 2018; Bahadori et al., 2018). This region is often referred to as the 'Nevadaplano' from comparison with the Altiplano of Peru and Bolivia (Dilek and Moores, 1999; DeCelles, 2004; Mulch et al., 2006; Best et al., 2009, 2016; Cassel et al., 2012). In the Paleogene, the region was occupied by a series of terrestrial sedimentary basins situated adjacent to actively forming metamorphic core complexes (Fig. 4.1; Fouch et al., 1979b; Armstrong, 1982; McGrew and Snee, 1994; Bendick and Baldwin, 2009; Druschke et al., 2009a, 2009b, 2011; Konstantinou et al., 2012; Smith et al., 2017; Canada et al., 2019). Some previous workers interpret this record to signify Cretaceous and/or Paleogene extension and the initiation of orogenic gravitational collapse (Gans et al., 1989; Fouch et al., 1991; Axen et al., 1993; Liberty et al., 1994; Camilleri, 1996; Dubiel et al., 1996; Dickinson, 2006; Evans et al., 2015), whereas others support only minor extension in the hinterland until the Miocene (Henry, 2008; Colgan et al., 2010; Lund Snee et al., 2016). Widely distributed Miocene extension across the modern Basin and Range Province has overprinted prior records of surface deformation (Colgan and Henry, 2009; Long, 2019), but this critical prior history is preserved in the Eocene fluvial and lacustrine strata of the Elko Basin (Fig. 4.2).

Elko Basin Lithostratigraphy

Eocene fluvial and lacustrine strata of the Elko Formation are spread across a >20,000 km^2 area of northeastern Nevada and reflect a diverse array of terrestrial lithofacies deposited between ca. 50 and 40 Ma (Figs. 4.2–4.3; Cassel et al., 2014; Smith et al., 2017; Canada et al., 2019). Strata of the Elko Formation were first interpreted to be age equivalent to foreland strata of the Green River Formation because of its similar character (King, 1876; 1878; Winchester, 1916; 1923). Sharp (1939) reassigned these strata to the Miocene Humboldt Formation based on paleoflora and paleofauna assemblages. Van Houten (1956) later

proposed these rocks may be Eocene or Oligocene in age based on mollusk assemblages. The Elko Formation was first named and described in detail by Smith and Ketner (1976) and differentiated from overlying strata using K-Ar geochronology of interbedded tuffs (Evans and Ketner, 1971). Initial efforts to define the facies distribution and architecture of the Elko Formation was mainly fueled by interest in the characterization of 'oil shale' facies (kerogen-rich mudstone; Fig. 4.5; Winchester, 1923; Smith and Ketner, 1976; Fouch et al., 1979a; Solomon et al., 1979a; Solomon, 1981; Moore et al., 1983; Server and Solomon, 1983; Palmer, 1984; Poole and Claypool, 1984; Barker et al., 1990; Solomon, 1992; van de Kamp and Samoun, 1992; Horner, 2015; McGowan, 2015; Johnson and Birdwell, 2016). Previous studies introduced conflicting stratigraphic nomenclature, but generally subdivide the ~1000 m of Elko Formation strata (Ketner and Alpha, 1992; Haynes, 2003; Smith et al., 2017) into a basal conglomerate member, a lower 'cherty limestone' member, a middle 'oil shale' member, and an upper 'tuffaceous siltstone' member (e.g., Smith and Ketner, 1976; Solomon et al., 1979; Solomon and Moore, 1982; Moore et al., 1983; Wingate, 1983; Haynes, 2003; Horner, 2015). Outcrop and subsurface data indicate Eocene rocks unconformably overlie Mississippian strata of the Diamond Peak Formation and Chainman Shale (Fig. 4.5; Poole, 1974; Server and Solomon, 1983; Ketner and Alpha, 1992) and are overlain by late Eocene ignimbrites of the Indian Wells Formation (Smith and Ketner, 1976; Henry et al., 2001; Smith et al., 2017). Due to poor surface exposures across much of the basin extent, detailed description of Elko Formation strata has been predominantly limited to two trenched sections in the Adobe Range and Pinon Range (Fig. 4.2; Smith and Ketner, 1976; Moore et al., 1983; Horner, 2015) and limited exposures in the Elko Hills (Figs. 4.5–4.6; Haynes, 2003; Johnson and Birdwell, 2016). Previous workers have identified that Eocene lacustrine facies and overlying volcaniclastic deposits are generally thickest proximal to the Ruby Mountains-East Humboldt Range (Camilleri et al., 2017; Smith et al., 2017), which is interpreted by some to indicate deposition in the hanging wall of the Ruby Mountains detachment fault (Figs. 4.2, 4.4; Solomon et al., 1979a; Satarugsa and Johnson, 2000; Haynes, 2003; Cline et al., 2005). However, due to unconstrained lateral changes in Elko Formation thickness and facies and an absence of full stratigraphic integration within a new age model for this Eocene strata (c.f., Smith et al., 2017), the mechanisms that drove regional ponding and observed depositional variability remain controversial (Fig. 4.4).

METHODS

Stratigraphic Correlation

Ash horizons, sandstone beds, gamma ray logs (measured at 50 cm intervals in outcrop sections), and existing Fischer Assay oil yield data were used to correlate decimeter-scale stratigraphic sections of Elko Formation outcrops and core (Figs. 4.6–4.8). Most sections measured in the field were trenched to adequately characterize, measure, and sample these generally poorly exposed sedimentary rocks. Eocene strata lack abundant trace fossils and no biostratigraphic framework exists for Eocene strata in the hinterland. Gastropod (Solomon et al., 1979b; Nutt and Good, 1998), ostracode (Swain, 1964, 1999; Solomon et al., 1979b), and pelobatid (Henrici and Haynes, 2006) species as well as palynology (Table 4.2., Wingate, 1983) of the Elko Formation broadly indicate middle Eocene deposition, but are not useful for detailed intrabasinal stratigraphic correlation.

Lithostratigraphic Correlation

Two discrete types of marker beds permit basin-wide lithostratigraphic correlation. The lowermost lacustrine interval of the Elko Formation is recognized at many localities as the ‘cherty limestone’ unit (Table 4.1.; Fig. 4.9; Smith and Ketner, 1976). These beds are laterally continuous and are limited to near the basin depocenter. Outcrops of organic-rich dolomicritic mudstone occasionally weather to a light gray/blue color and are hence commonly referred to as ‘blue beds’ (cf. Rhodes and Carroll, 2015). These distinctive beds correspond to high TOC and Fischer Assay oil yields that are correlative within fluctuating profundal zones (Fig. 4.7).

Gamma Ray Spectrometry and Well Correlation

To correlate outcrops with subsurface data, the radioactivity of lithologic units within the Elko Basin was determined using spectral gamma ray measurements in outcrop (Figs. 4.6–4.7). The spectral gamma ray signal corresponds to discrete K, U, and Th concentrations that reflect mineralogical variations in strata (Gadeken et al., 1991; Blum et al., 1997). U-rich zones are inferred to reflect basin-wide geochemical changes associated with low pH and U-insoluble lake water (Mott and Drever, 1983; Smith and Carroll, 2015). Spikes in gamma ray

intensity should therefore be correlative across hydrologically connected areas and permit correlation between outcrop and subsurface data (e.g., Chamberlain, 1984; Aigner et al., 1995).

Chronostratigraphic Correlation

Ash beds and ignimbrites. Volcanic and volcaniclastic horizons are abundant within the Elko Formation and are intercalated at regular intervals within ca. 43–40 Ma strata. Intercalated ash beds range in thickness (1–50 cm) and were deposited across a large area, providing ideal material for chronostratigraphic correlation. Ash beds become increasingly more abundant towards the top of the Eocene sedimentary section, where they are commonly overlain by >10 m thick ignimbrites of the Indian Wells Formation (Figs. 4.6–4.8; Cook, 1960). Smith et al. (2017) performed single crystal sanidine $^{40}Ar/^{39}Ar$ geochronology of 26 ash beds and ignimbrites in northeastern Nevada, expanding the known range of Elko Basin deposition to ca. 50 to 40 Ma. Several tuffs are identifiable within multiple field areas and permit direct correlation. The 40.45 ± 0.25 Ma Tuff of Nelson Creek was deposited across a >10,000 km^2 area and directly overlies Elko Formation lacustrine strata in multiple field areas (Fig. 4.3; Smith et al., 2017). This tuff provides a pivotal tie point for disparate stratigraphic sections (Figs. 4.3, 4.7) and marks the approximate onset of lake basin closure.

Volcanic glasses preserved within ash beds can record the δD geochemistry of ambient water following deposition. Ash beds intercalated with Elko Formation lacustrine strata commonly contain clay or zeolite minerals produced during the alteration of constituent volcanic glass (Cassel et al., 2014; 2018; Johnson and Birdwell, 2016; Smith et al., 2017). However, several water-lain air fall tuffs preserve volcanic glass, particularly those deposited within fluctuating profundal zones. Preliminary comparison of δD_{glass} values with adjacent lithofacies (cf. Smith et al., 2017) indicates δD_{glass} values are correlative to inferred lake water chemistry reflected by varying lacustrine facies (Cassel and Breecker, 2017). This suggests that chemostratigraphic correlation may also be possible.

Detrital zircon geochronology. Fluvial strata within the Elko Basin contain sparse tuffaceous interbeds suitable for $^{40}Ar/^{39}Ar$ geochronology. Sandstone beds throughout the Elko Basin therefore provide alternative dateable material for detrital zircon U-Pb geochronology to constrain the duration of fluvial deposition. Several prior studies have used

this technique to reconstruct provenance and maximum depositional ages for the Elko Formation (Figs. 4.3, 4.5; e.g., Lund Snee et al., 2016; Hollingsworth et al., 2018; Canada et al., 2019). Depositional age assessment using this method is hindered, however, by an absence of coarse-grained strata across large intervals of the Elko Formation and a lack of volcaniclastic detritus within some samples. While certain samples contain detrital zircon grains with early Eocene U-Pb ages, consistent with derivation from the Challis volcanic field, most pre-43 Ma samples contain either limited or no volcanic grains. These samples largely consist of Precambrian U-Pb grain age populations (Canada et al., 2019) unfit for maximum depositional age assessment. A combination of recent detrital zircon U-Pb ages and sanidine $^{40}Ar/^{39}Ar$ ages therefore provides a new high-resolution age model for the Elko Formation.

ELKO BASIN SEDIMENTARY FACIES

A. Alluvial Macroassociation

(i) Axial Fluvial Association

Description. The axial fluvial association contains two broad coarse-grained lithofacies that comprise most of the base of the Elko Formation: *(1) conglomerate* and *(2) trough cross-stratified and planar- to ripple-laminated sandstone*. These lithofacies are observed within many field and core sections and are composed of poorly to moderately sorted sand and pebbles. Beds of Lithofacies 1 are approximately 15 cm–2.5 m thick, laterally continuous for up to 10 m, and comprised of matrix-supported subangular–rounded granules, pebbles, and cobbles. Modal grain size is highly variable, but basin marginal locations generally display the coarsest grain size and thickest bedding. Conglomerate containing subangular–angular boulders up to 1.2 m in diameter is found in a few field areas, including the Pinon Range, Tuscarora Mountains, and Elko Hills (Figs. 4.2, 4.6; Smith and Ketner, 1976; Haynes 2003). The coarsest deposits are found within 5–20 m wide channel forms incised into underlying strata, which contain aggradational sets up to 10 m–thick with multiple incision surfaces and convex-up boundaries. Beds often contain large-scale trough cross-bedding (40 cm–1.5 m thick sets) and imbrication that is concentrated within <50 cm

wide lenses, where clasts are tightly packed. Clasts are predominantly composed of chert, quartzite, and limestone within a matrix of quartz and minor calcitic sand. Both lithofacies 1 and 2 are commonly characterized by erosive bed contacts, scour and fill features, and lenticular bedforms. Lithofacies 2 is commonly interbedded with Lithofacies 1 and consists of laterally discontinuous, normally graded, subangular–subrounded litharenite sands with fine to coarse grain size. Beds are typically 5 cm–1.2 m thick and contain ripple marks, 0.1- to 0.6-m scale trough-cross beds, and planar cross beds at both a low and high angle. Bedsets are vertically and laterally aggraded and some bedding planes contain parting lineation and pebble–cobble lags. Lag deposits consist of the largest clast size gravel within beds and are sometimes imbricated. Channel bodies are clearly defined at several locations but elsewhere appear to be amalgamated by concave-up and sigmoidal lateral accretion surfaces. In a few locations, this facies contains convolute bedding and soft-sediment-deformation near the base of beds. Paleocurrents within Lithofacies 2 are highly variable and commonly range in direction by at least 90°.

Interpretation. Axial fluvial facies are characteristic of deposition in gravel-bed braided river depositional systems. Traction-structured conglomerate beds commonly fine upwards and are laterally discontinuous, representing braided channel deposits. These coarse, locally sourced, and often poorly sorted deposits suggest high-gradient tributary channels fed sediment into paleovalleys. Paleochannel slopes were in some places steep enough to transport boulders (Paola and Mohrig, 1996). Trough cross-stratified sandstone represents sinuous-crested or linguoid dunes deposited in unidirectional flow and potentially crevasse-splay deposits (Miall, 1978; 1996). Aggradational bed sets indicate sustained high sediment flux, whereas the erosional bases and lenticular geometry of beds suggests turbulent and channelized flow (Bridge, 1993; Leier et al., 2010; Cassel and Graham, 2011). Rare plane-parallel sandstone may be associated with migration of bedload sheets under relatively high flow velocities at upper flow regime conditions (Paola et al., 1989; Lunt et al., 2004). The high variance of paleocurrents within this facies may indicate deposition within sinuous channels at the midstream reaches of broad paleovalleys (Hein and Walker, 1977; Henry, 2008).

(ii) Floodplain Association

Description. This association consists of *(1) planar-bedded sandstone and siltstone*, and *(2) pedogenically modified siliciclastic mudstone–sandstone*. Lithofacies 1 is commonly found in thin interbeds between LAi1 and LAi2 and consists of faintly planar bedded siliciclastic siltstone and very fine to medium grained sandstone. Siltstone beds are 5 cm–1.3 m thick with mm- to cm-scale laminations and are laterally discontinuous for <5 m in most sections. Plant leaves and fragments as well as carbonaceous material are common within siltstone (Figs. 4.9–4.10). Sandstone in this lithofacies consists of moderately–well sorted subangular–subrounded sand grains that commonly fine upward from very fine to fine grain size. Sandstone beds are aggradational and contain faint cm-scale sub-horizontal laminations and occasional load structures. Lithofacies 2 consists of highly discontinuous 0.1–3.4 m thick beds of mottled red, green, and gray claystone and mudstone with variable amounts of unevenly distributed silt- and sand-sized grains (Fig. 4.11). These facies contain vertical burrows, carbonate concretions, slickensides, and calcic horizons as well as minor root traces. Beds of this lithofacies are often highly bioturbated and contain wavy and irregular contacts with adjacent strata (Fig. 4.11).

Interpretation. Laterally discontinuous and generally thin fine-grained sandstone and siltstone deposits indicate floodplain deposition within a relatively narrow channel belt (Bridge, 1984; Bentham et al., 1993). Thin sandstone beds likely indicate overbank deposition during flood intervals, potentially deposited as crevasse splays (Miall, 1992). Preserved leaves and carbonaceous matter indicate low shear stress during deposition (Bridge, 1993). Carbonate concretions and red and green color mottling are indicative of pedogenesis within a floodplain environment (Fig. 4.11; Retallack, 1988; Kraus 1999). Carbonate precipitation likely occurred in lowland areas that alternated between wet and dry conditions whereas pedogenesis indicates deposition further from active channels (Mack et al., 1993; Platt and Wright, 1992; Schnurrenberger et al., 2003; Valero-Garcés et al., 2014). Early paleosol development is supported by erosional tops of color mottled mudstone and siltstone (Müller et al., 2004), primarily observed within core (Fig. 4.11).

(iii) Distal–Overbank Association

Description. This association is comprised of *(1) structureless sandstone and*

siliciclastic mudstone, and (2) siliciclastic and carbonaceous mudstone and coal. Lithofacies 1 consists of structureless or weakly horizontally laminated mudstone and sandstone. Most beds are laterally continuous for >10 m, 10 cm to 60 cm thick, and weakly amalgamated. Sandstone beds are uncommon and are generally found as thin (<15 cm) interbeds within fine-grained strata. Sandstone is fine to coarse-grained and moderately to well sorted. Siliciclastic mudstone is red, green, and brown in color and commonly preserves leaf fossils, other plant matter, and sparse carbonaceous debris. Infrequent rhizoliths and peds also occur within color mottled mudstone. Rare near-vertical injection features comprised of fine-coarse sand cross-cut several beds of mudstone. Lithofacies 2 is comprised of 2–20 cm thick laterally continuous beds of brown to dark brown variegated planar-laminated mudstone with carbonaceous matter and interbedded coal (Figs. 4.9 and 4.11). Laminations range from mm- to cm-scale and are planar-parallel to wavy-parallel. Coal grades from lignitic to bituminous and commonly occurs in discontinuous <1.5 m-wide lenses with sulfidation (Fig. 4.11). Carbonaceous mudstone facies contain abundant sticks, leaves, root traces, and unidentifiable plant matter and varying proportions of silt and sand sized grains (Fig. 4.10).

Interpretation. Crudely bedded and weakly horizontally laminated mudstone and sandstone represent overbank sedimentation distal to the main distributary network. Occasional rhizoliths and peds indicate subaerial exposure and weak pedogenic development. Thin and laterally continuous sandstone beds may indicate deposition in crevasse splays and abandoned distributary channels. Carbonaceous mudstone and coal facies are interpreted to reflect deposition in an overbank and marginal lacustrine environment. The preservation of large amounts of organic matter indicates still water and reducing conditions (Scholz et al., 2011). The abundance of carbonaceous mudstone suggests high rates of sediment supply (Bohacs et al., 2003). Thin and laterally discontinuous coal beds (Fig. 4.9) imply paludal deposition during instable lake levels (Flores, 1981; Sáez and Cabrera 2002) or shoreline progradation (Bohacs et al., 2000). Root traces likely indicate subaerial exposure of the substrate (Scott, 2010).

B. Lacustrine Macroassociation

(i) Littoral Association

Description. This association consists of *(1) laminated stromatolitic carbonate mudstone*, and *(2) cherty microbialitic limestone*, and *(3) molluscan limestone*. Lithofacies 1 commonly occurs as laterally continuous 0.1 to 2 m thick beds consisting of light gray to tan micrite and dolomicrite with cm-scale algal laminations and mudcracks (Fig. 4.9). Carbonate mudstone contains mm- to cm-scale planar laminations and columnar microbial laminae that alternate between carbonate and organic-rich layers (Fig. 4.11). Mudcracks, ostracodes, and peloids are abundant and desiccation features are common near the top of beds. Lithofacies 2 is correlative across many sections and is distinguished by 0.1–0.7 m thick beds of microbialitic limestone with chert nodules up to 35 cm in width (Fig. 4.9). This facies is distinguished by gray to light tan resistant <2.8 m-high outcrops that are laterally continuous for up to >50 m and commonly appears light gray to tan. Upper and lower contacts with adjacent facies are indeterminate in outcrop but appear conformable in core. Ostracode, minor gastropod and charophyte fossils, as well as peloids and oncoids are present within this facies. Microbialitic limestone contains laterally extensive and finely laminated algal mats that lack the typical bioherm structure of stromatolites and thrombolites. Chert is predominantly comprised of granular microcrystalline quartz with minor chalcedony (Abruzzese et al., 2005) and often occurs in nodules that are concordant with bedding (Fig. 4.9; Knauth and Epstein, 1976, 1982), but is also present as pore- and fracture-filling cement (Horner, 2015). Limestone is mainly calcitic (Mulch et al., 2015; Johnson and Birdwell, 2016) with partial silicification. Lithofacies 3 consists of calcitic and dolomitic limestone with carbonate intraclasts and peloids as well as gastropods and bivalve fragments (Fig. 4.12). This lithofacies commonly contains thin (1–5 cm) and often plane-parallel grainstones and packstones that are predominantly comprised of ostracodes. Ostracodal grainstones and packstones are frequently interbedded with profundal facies at regular (5–10 cm) intervals and commonly contain disarticulated skeletal fragments (Fig. 4.11).

Interpretation. Laterally extensive stromatolitic and gastropod-bearing carbonate mudstone as well as cherty microbialitic limestone both contain fine algal laminations that suggest littoral deposition within relatively shallow lake water (Buchheim, 1978; Carter and

Pickerill, 1985; Casanova, 1986; Cohen, 1989; Benavente et al., 2015), likely along lake margins (Lowenstein et al., 2017). Alternating deposition of cyanobacterial films and carbonate mud reflect fluctuating levels of organic productivity (Sarg et al., 2013), often driven by sediment supply rate changes (Bohacs, 1998; Ghadeer and Macquaker, 2012). Most stromatolitic intervals are relatively thin, potentially reflecting an unstable flux of carbonate sediment to the basin. Abruzzese et al. (2005) interpret nodular chert in the Elko Formation to reflect early diagenesis and chert $\delta^{18}O$ values to reflect the geochemistry Eocene lake water. Early diagenesis of siliceous fluids was likely promoted by dissolution of volcanic glass from coeval volcanism (Abruzzese et al., 2005; Smith et al., 2017). Molluscan and charophyte-bearing limestone was deposited in freshwater and likely a shallow near-shore environment (Peck, 1953; Carroll, 1998). However, thin ostracodal packstones and grainstones interbedded with profundal facies containing soft-sediment-deformation structures (Figs 4.11–4.12) likely indicates transport by shoreline currents into deeper, sublittoral and profundal environments. The variable mineralogy of limestone facies may be correlative to water depth during deposition, where calcitic compositions are generally correlative to shallower depths (Mason and Surdam, 1992).

(ii) Sublittoral Association

Description. This association consists of *(1) laminated carbonate mudstone and marlstone*, and *(2) structureless carbonate mudstone and marlstone*. Lithofacies 1 is comprised of mm- to cm-scale laminations of dolomitic and calcitic carbonate mudstone. Beds are 3–40 cm thick with planar-parallel and wavy-parallel mm-scale laminations and are laterally continuous for >15 m. This facies contains abundant ostracodes and infrequent well-preserved leaves, seeds, and other plant matter (Fig. 4.10). Lithofacies 2 is comprised of structureless to faintly bedded carbonate mudstone with minimal–no organic matter and varying amounts of siliciclastic grains. Both lithofacies 1 and 2 have low kerogen content and low Fischer Assay oil yields ranging from 7 to 18 gal./ton (Moore et al., 1983; Barker et al., 1990; Johnson and Birdwell, 2016).

Interpretation. The preservation of fine laminations in Lithofacies 1 is indicative of deposition of carbonate mud within anoxic bottom waters (Wolfbauer and Surdam, 1974; Demaison and Moore, 1980). The input of clastic sediment and terrigenous organic matter

was likely minimal and episodic, promoting the accumulation of carbonate muds and algal organic matter (Bohacs, 1998; Gierlowski-Kordesch, 1998; Liu and Wang, 2013; Gierlowski-Kordesch et al., 2014). Preservation of leaves and an absence of trace fossils suggests minimal disturbance of the substrate. The absence of laminations and low kerogen content of carbonate mudstone in lithofacies 2 is likely a product of activity by benthic organisms (Pietras and Carroll, 2006). This lithofacies therefore implies oxygenated bottom waters and a lack of well-developed thermal or chemical stratification, potentially reflecting shallower water depths (Sagri et al., 1989; Pietras and Carroll, 2006).

(iii) Profundal–Sublittoral Association

Description. The profundal-sublittoral association contains *(1) microlaminated kerogen-rich carbonate mudstone and marlstone*, and *(2) laminated mudstone*. Lithofacies 1 consists of dark-brown to black mudstone with μm- to mm-scale laminations. Ostracodal grainstone lags and thin (1–10 cm) interbeds of tuff are common throughout this lithofacies. Fish fossils and bone fragments are infrequently present with ostracodes (Fig. 4.10). This facies commonly displays a wide range of soft-sediment-deformation structures, including load casts, ball-and-pillow structures, small-scale faulting, flame structures, and clastic dikes (Fig. 4.12). Lithofacies 1 is characterized by TOC values up to 37% (Poole and Claypool, 1984) and Fischer Assay oil yields ranging from 18 to 85 gal./ton (Smith and Ketner, 1976; Solomon, 1981). Lithofacies 2 is comprised of gray to brown mudstone with mm- to cm-scale laminations and varying proportions of silt. Bedding planes contain infrequent fish fossils and vertical burrows (Fig. 4.11). This lithofacies is characterized by highly variable TOC and Fischer Assay oil yield values of 12 to 25 gal./ton (Fig. 4.7; Moore et al., 1983; Palmer, 1984).

Interpretation. The preservations of fine (μm-scale) laminations and high kerogen content of lithofacies LBiii1 suggests fallout deposition in thermally stratified anoxic bottom waters (Sullivan, 1980; Bohacs, 1998; Strobl et al., 2014). High kerogen content suggests this lithofacies was likely deposited during lake highstands accompanied by increased oxygenation and production of particulate organic matter as well as diminished clastic dilution (Fu et al., 2014; Graf et al., 2015). The term “oil shale” has been widely applied to this lithofacies because of its high kerogen content and potential to produce oil (Winchester,

1923; Smith and Ketner, 1976; Fouch et al., 1979a; Solomon et al., 1979a; Solomon, 1981; Moore et al., 1983; Server and Solomon, 1983; Palmer, 1984; Poole and Claypool, 1984; Barker et al., 1990; Solomon, 1992; van de Kamp and Samoun, 1992; Johnson and Birdwell, 2016). The high rate of production and preservation of organic matter in this facies indicates persistent stratification (Renaut and Tiercelin, 1994; Picard, 1955), whereas its dolomitic composition indicates brackish to moderately saline conditions (Eugster and Hardie, 1978; Baker and Kastner, 1981; Pitman, 1996; Carroll and Bohacs, 2001; Smith et al., 2014b). Laminated mudstone of lithofacies 2 also suggests profundal deposition in low-oxygenated to anoxic conditions, but the variable organic content reflects diminished organic productivity or increased clastic dilution and inorganic sedimentation. Palmer (1984) identified small amounts of fine-grained reworked kerogen in this facies. Relatively low organic contents may also be associated with increased freshwater input to the lake, which may have decreased concentrations of dissolved bicarbonate and thereby diminished organic productivity (Kelts and Hsu, 1978; Horsfield et al., 1994).

(iv) Palustrine Association

Description. This association consists of *(1) bioturbated carbonate mudstone and siltstone*. Lithofacies 1 consists of calcareous mudstone that is crudely bedded and lacks pedogenic structures. This facies commonly contains vertical burrows with structureless or meniscate backfill as well as infrequent mudcracks and syneresis cracks. The degree of bioturbation (Bioturbation Index; cf. Droser and Bottjer, 1986) and the depths to which traces penetrate the substrate is highly variable.

Interpretation. The non-laminated nature of carbonate mudstone and abundant trace fossils/bioturbation are indicative of deposition in a well-oxygenated and subaerially exposed environment, likely in the supralittoral zone (Sagri et al., 1989; Cowan and James, 1992; Buatois and Mángano, 2009; Ingalls and Park, 2010). This environment is expected to have sustained a high influx of fine-grained carbonate material and/or diminished siliciclastic input (Freytet and Verrecchia, 2002).

DISCUSSION

Lithofacies Stacking Patterns

Correlated stratigraphic sections show variability in depositional cyclicity and thickness of Eocene fluvial and lacustrine facies, but also record basin-wide changes induced by a combination of autogenic and allogenic controls. Repetitive stacking of lithofacies is evident at multiple scales and at several basin locations (Figs. 4.6–4.8). Fluvial-lacustrine and fluctuating profundal facies both show cyclicity across basin-interior and peripheral locations that likely reflect expansion-contraction cycles during the main ca. 43–40 Ma phase of lacustrine deposition (Figs. 4.7–4.8). In fluvial-lacustrine zones, cycles consist of carbonaceous siliciclastic mudstone overlain by ostracodal and stromatolitic limestone and capped by finely laminated carbonate mudstone (Fig. 4.8). These cycles are 0.3–6.0 m thick and are most complete within basin-interior sections (Fig. 4.8). Lithofacies interpreted to represent deposition within fluctuating profundal conditions show cyclicity at a fine scale (0.1–3.5 m) that is commonly more complete. In the basin-interior, theses cycles are characterized by kerogen-poor carbonate mudstone, with frequent soft-sediment deformation (Fig. 4.12), overlain by thinly laminated kerogen-rich carbonate mudstone and capped by mudcracked carbonate mudstone and dolostone (Fig. 4.7). In the Robinson Mountain section, proximal to the basin margin, kerogen-rich ‘blue beds’ are regularly interbedded with ostracodal limestone in 0.6–4.5 m cycles, indicating more pronounced fluctuations between organic-rich and lean lithofacies (Fig. 4.7).

Evaluation of the pace of lithofacies variations is possible for ca. 42.4 to ca. 41.3 Ma strata in the Pinon Range, where depositional ages are well-constrained by single crystal sanidine $^{40}Ar/^{39}Ar$ geochronology of interbedded ash (Smith et al., 2017). Sediment accumulation rates were relatively constant at this time (0.03–0.04 mm/yr), permitting evaluation of potential climatic controls on depositional cyclicity. This ~1.1 m.y. interval records 12 cycles between basin-ward and shoreward facies, potentially paced by 100 k.y. orbital eccentricity variations (Zachos et al., 2010; Smith et al., 2014b). Basin-ward facies associations consist of thinly bedded kerogen-rich carbonate mudstone and calcareous siltstone. Shoreward facies associations contain kerogen-poor carbonate mudstone with common soft-sediment deformation structures, calcareous siltstone with plant matter and

occasional root traces, and mudcracked dolostone. These alternations therefore suggest periodic fluctuations between a profundal and littoral–supralittoral environment. A comparable pace of alternation is interpreted for correlative sedimentary rocks deposited to the south and west (Fig. 4.7; Robinson Mountain and K1L sections), suggesting hydrologic connectivity and/or a regional control on lakes occupying multiple subbasins.

Mapping, stratigraphy, and core data collected from well-exposed strata in the Elko Hills, near the center of the basin, preserve a near-complete record of Elko Formation deposition (Fig. 4.5). Fluvial strata are correlative across a >5 km transect of this area and are overlain by palustrine, littoral, and sublittoral facies. Palustrine facies mark the initiation of ponding in this area and show a northward migration across the period of lacustrine deposition. Across this interval, thin (0.1–1.2 m) interbedded tuffs influence the character of adjacent strata and disrupt the cyclicity observed in lower lacustrine strata. Kerogen-rich strata with high Fischer assay oil yield values and increased gamma ray productivity are commonly situated directly beneath these thin tuffs. Frequent soft-sediment deformation within this part of the section indicates that deposition of tuffaceous sediment and overlying material was likely rapid and may have promoted anoxic conditions that enabled organic matter preservation.

Basin Fill Sequence

Integration of stratigraphic and geochemical data with the new Smith et al. (2017) age model permits reconstruction of drainage system evolution and inter-basin relationships for the Elko Formation lake system. Data from new and existing wells in the field area is used to interpret the thickness, spatial extent, and lithology of Elko Formation and Indian Wells strata in the subsurface (Figs. 4.13–4.14). Contributions from intra- and extrabasinal flow are then compared with multiple constraints on sedimentary provenance to quantify past drivers of stratigraphic heterogeneity and paleolake evolution.

49.2–48.8 Ma

Volcanism was active in the Challis volcanic field at this time, where southeast-draining paleovalleys transported volcaniclastic sediment across the fold and thrust belt and to Green River Formation lakes that occupied the broken foreland (Janecke and Snee, 1993;

Palmer and Shawkey, 1997; Carroll et al., 2008; Smith et al., 2008; Chetel et al. 2011). Fluvial strata deposited in the Elko Basin at ca. 49.4 Ma contains detrital zircon grains with ca. 52–49 Ma U-Pb ages, indicating rivers with headwaters in the Challis volcanic field and Idaho Batholith may have also drained southward to the Elko Basin (Cassel et al., 2018; Canada et al., 2019). Two thin (<15 cm) air fall tuffs at the top of the Coal Mine Canyon section, both dated at 48.70 ± 0.30 Ma (cf. Smith et al., 2017), were likely derived from the Challis volcanic field. This indicates that early Eocene volcanic detrital zircon grains may also reflect erosion of recent air fall tuffs within the Elko Basin catchment (cf. Lund Snee et al., 2016).

At the onset of lacustrine deposition, streams draining from the Cordilleran divide ponded into an isolated lake basin situated between the modern East Humboldt Range and Adobe Range (Fig. 4.15A). The specific cause of ponding during this time is uncertain. A lack of temporally correlative deposits and variable paleocurrents measured from strata of this age suggest lacustrine deposition was relatively localized at this time. The small size of the lake basin and its spatial correlation with the wide and ≥ 1 km deep 'Central Paleovalley' of Henry (2008) suggests geomorphic damming may have ponded rivers. Initial overfilled conditions likely sustained an outlet stream that drained eastward towards the northern East Humboldt Range and the foreland. Continued outflow along this trajectory may partly explain anomalously thick Eocene strata in the subsurface north of the East Humboldt Range (Effimoff and Pinezich, 1986; Satarugsa and Johnson, 2000; Camilleri et al., 2017). Well data indicates that this area was also later filled with >750 m of ignimbrites of the Indian Wells Formation, suggesting it was a topographic low for the entire duration of Elko Formation deposition (see Supplemental Materials).

43.0–42.4 Ma

Two broad freshwater lakes occupied the Elko Basin at this time and both gradually expanded across this time interval (Fig. 4.15C). This expansion occurred concurrent with the onset of regional magmatism and accelerated source exhumation rates, likely associated with upper-crustal extensional faulting (Canada et al., 2019). The location and trajectories of outflow streams from these lakes is speculative, resulting from an absence of preserved alluvial strata of this age along the eastern and southern margins of the basin. Paleocurrent

measurements indicate wide variations in paleocurrent direction within individual field areas, but existing paleocurrent indicators suggest flow was predominantly oriented towards the basin interior. The two subbasins at this time, separated by the Lamoille Paleohigh (cf. Smith et al., 2017), likely sustained hydrologic connectivity as outflow from the northern subbasin intermittently drained southward.

42.4–40.4 Ma

The Elko Formation lakes were increasingly influenced by encroaching volcanism across this time interval. After ca. 42.4 Ma, the Elko Lake depocenter migrated to the west, towards the paleodivide, and lakes quickly transitioned to balanced-fill conditions (Fig. 4.15D). Stratigraphic and geochemical correlation indicates a series of lakes with varied geochemistry occupied the basin during this time. Relatively small freshwater lakes continued to occupy previous depocenters and intermittently drained to downstream saline and alkaline lakes. By ca. 41.0 Ma, the extent of all lakes substantially diminished and lacustrine deposition was primarily confined to the modern Huntington Valley region, west of the Ruby Mountains (Fig. 4.15E). A relatively small freshwater lake occupied the northern portion of the Elko Basin at this time and received a flux of volcaniclastic sediment derived from proximal volcanism (Fig. 4.15E). Incipient volcanism likely diverted sources of freshwater to the basin and ignimbrites may have temporarily dammed prior drainage pathways. Continued volcanism may have promoted microbialite growth at this time by changing the solute flux within the lake basin (Wright, 2012). Fluctuating-profundal facies deposited during this final phase of lacustrine deposition have sedimentary structures and geochemistry that reflects increasingly evaporative conditions and high sediment accumulation rates.

Lacustrine strata deposited across this time interval contain a wide variety of soft-sediment deformation structures, which are notably absent from older strata (Figs. 4.11–4.12). These features have been interpreted to reflect syndepositional structural deformation within the Elko Basin catchment (Haynes, 2003; Horner, 2015), but may also reflect high sediment accumulation rates and subsequent compaction of unlithified to partly lithified sediment. The Elko Formation lacks stratal geometries and coarse-grained alluvium clearly associated with potential bounding faults (Smith et al., 2017). In addition, detailed stratigraphic characterization demonstrates that Elko Formation strata does not contain coarse-grained

alluvial sediments intercalated with lacustrine intervals or deltaic deposits. This implies the Elko Basin lake system sustained low relief margins, which did not distribute coarse-grained clastic material from the basin margin to lake interiors. One exception to this interpretation is evident in ca. 40.5 Ma strata of the K1L core, where laminated mud rip-up clasts preserved in coarse-grained tuffaceous sediment (Figs. 4.7 and 4.12) likely signify deposition of newly erupted volcaniclastic material in a turbidity current (Dyni and Hawkins, 1981). At 40.4 Ma, caldera-forming eruptions in the Tuscarora volcanic field released a large volume of volcaniclastic debris that filled existing topographic lows over a >10,000 km^2 area (Fig. 4.15F; Brooks et al., 1995; Smith et al., 2017). Geologic mapping and well data indicate ignimbrites erupted at this time were concentrated within paleovalleys that drained eastward; one to the north of the East Humboldt Range and the other to Ruby Valley (Figs. 4.13–4.15). This ca. 40.4 Ma eruption of the Tuff of Nelson Creek (cf. Smith et al., 2017) marked an abrupt end to lacustrine deposition across the Elko Basin.

Sediment Accumulation Rates

The Elko Basin is characterized by two distinct intervals with high rates of sediment accumulation from ca. 51–49 Ma and ca. 43–40 Ma (Fig. 4.16). Both of these intervals are characterized by lacustrine deposition and a medial transition in lake-type from fluvial-lacustrine to fluctuating profundal conditions. Balanced-fill facies had the highest rate of sediment accumulation (≤ 0.35 mm/yr), but sedimentation rates were also high during deposition of overfilled facies (0.13–0.20 mm/yr). In the Greater Green River Basin, overfilled facies had the highest sediment accumulation rates, measured along the basin margin (up to ~0.35 mm/yr; Smith et al., 2008). High rates of sediment accumulation estimated for overfilled facies may reflect the basin marginal position of measured sections. Balanced-fill facies had more variable rates of sediment accumulation (0.05–0.35 mm/yr), reflecting periodic removal of solutes from the lake basin (Smith et al., 2008). Laminations in balanced-fill facies are commonly 0.1–0.5 mm thick, suggesting these laminae may reflect annual deposition. Increased sediment flux during deposition of balanced-fill facies may account for the highest rates of sediment accumulation, potentially triggered by the inception of proximal volcanism and/or the unroofing of new source areas within the basin catchment. Fluvial deposition between ca. 48 Ma and 43 Ma was distinguished by a comparatively slow

rate of sediment accumulation (~0.03 mm/yr), which likely represents diminished regional accommodation and a renewed period of sediment bypass.

New early and middle Eocene age data and detailed stratigraphy of the Elko Formation enable backstripping analysis of the Elko Basin to determine basin subsidence histories using Nestor Cardoza's OSXBackStrip program, which assumes Airy isostatic compensation (Fig. 4.16). Table 4.3 provides the parameters included for backstripping analysis of the Elko Basin. Backstripping was also performed on several other hinterland basins to derive and compare tectonic components of subsidence. These analyses are all affected by error associated with paleobathymetric and paleoelevation estimates (Jordan et al., 1988). Paleoelevations are well-quantified for the Elko Basin (Cassel et al., 2018), however, so the primary source of error is associated with uncertainty in changes to lake water depths. Comparison of tectonic subsidence histories for the Elko Basin and other basins from a range of settings reveals several similarities among common basin types. For example, post-contractional hinterland basins are characterized by rapid tectonic-derived subsidence over a short duration, in comparison to foreland basins and syn-contractional hinterland basins (Fig. 4.16). This phase of rapid sediment accumulation is also commonly followed by inversion and unconformity formation (e.g., DeCelles et al., 2015). These characteristics may reflect the relatively short-lived geodynamic influences on hinterland regions, which often influence basin formation (e.g., DeCelles et al., 2015; Wang et al., 2015). In comparison, foreland basins have prolonged and relatively gradual subsidence histories that can span much of the contractile phase of an orogen (DeCelles, 2004; Fan and Carrapa, 2014).

Climatic and Tectonic Controls on Basin Development

There is no present evidence for sudden large-scale climatic changes that strongly influenced development of the Elko Basin. Deep-sea oxygen isotope records of benthic foraminifera indicate global temperatures cooled across the depositional history of the Elko Formation following the high CO_2 concentrations and warmest Cenozoic climatic conditions attained during the ~53–51 Ma Early Eocene Climatic Optimum (EECO; Zachos et al., 2001, 2008). Smith et al. (2017) also determined that the end phase of Elko Formation deposition directly preceded heightened temperatures of the Middle Eocene Climatic Optimum (MECO). Paleotemperature estimates for the Elko Basin region based on floral assemblages and

palynology indicate warm-temperate climatic conditions (mean annual temperatures of ~8–15 °C; Axelrod, 1996a/b, 1997) that supported conifer-deciduous forests (Solomon et al., 1979b; Wingate, 1983). During the early and middle Eocene, the Elko Basin region had lower humidity and ~10 °C lower mean annual temperatures (MAT) than the subtropical to tropical climate that accompanied deposition of the Green River Formation to the east (Wolfe, 1978; Wingate, 1983; Wilf, 2000). In addition to flora assemblages, this clear difference in climate between hinterland and foreland regions is evident from comparison of lacustrine facies in the Green River Formation and Elko Formation. For example, the Green River Formation is characterized by abundant sodium carbonate evaporite deposits (i.e., trona, shortite, and nahcolite) interpreted to represent deposition in saline–hypersaline and alkaline density-stratified lakes in underfilled basins (Fahey, 1962; Bradley and Eugster, 1969; Eugster and Surdam, 1973; Smith et al., 2008; Lowenstein et al., 2017). Sodium carbonate evaporite deposits are linked to elevated chemical weathering in the basin catchment and inflow waters with total carbonate ($HCO_3^- + CO_3^{2-}$) concentrations greater than combined Ca^{2+} and Mg^{2+} concentrations (Hardie et al., 1978; Jagniecki and Lowenstein, 2015; Lowenstein et al., 2017). Elko Formation strata does not contain bedded evaporite or other diagnostic features of an underfilled basin (Carroll and Bohacs, 1999). These observations suggest mechanisms other than regional or global climate changes likely exerted the strongest controls on the long-term (m.y.) spatial and lake-type evolution of Elko Formation lakes. Expansion-contraction cycles observed at multiple scales, however, indicate short-term (k.y.) and seasonal climatic/temperature fluctuations likely affected the flux of calcium-rich inflow waters and lake levels (Fischer and Roberts, 1991; Ocakoğlu et al., 2012). The rate of cyclicity between basin-ward and shoreward facies (i.e., transgression and regression) within several sections may indicate pacing by 100 k.y. orbital eccentricity variations (Smith et al., 2014b; Ma et al., 2016).

Reorganization of the Elko Basin catchment from uplift of new source areas may alternatively account for the observed lake-type shifts, particularly the primary lake-type transition at 42.4 Ma. Thermochronology and lag time analysis of Elko Formation detrital grains indicates an acceleration in source exhumation rates at 43 Ma, which may signify the inception of surface-breaching extensional deformation within the Elko Basin catchment (Canada et al., 2019; Fig. 4.17). However, Elko Formation lithofacies, sedimentary stacking

patterns, and stratigraphic architecture all indicate distinctive differences in comparison to synextensional sedimentary rocks deposited in fault-bound basins, as discussed above. This implies an important distinction between the Elko Basin and other lake basins that represent a range of tectonic settings, which are commonly bound by faults and/or marginal source areas with moderate–high relief (e.g., Janecke et al., 1997, 1999; Gawthorpe and Leeder, 2000; Charrier et al., 2002; Oner and Dilek, 2011; Ezquerro et al., 2014; Hargave et al., 2014).

Synoptic reconstruction of the spatial distribution and connectivity of Elko Formation lakes indicates it is unlikely lakes were entirely confined to isolated grabens or existing paleovalleys. This interpretation is particularly well-supported for ca. 43–40 Ma lakes, which are constrained via correlative sedimentary facies and expansion-contraction cycles as well as covariance of multiple geochemical datasets. These ca. 43–40 Ma lakes had a broad extent, which does not directly overlap with interpreted paleovalley locations. It is important to note, however, that the dense distribution (and estimated depths) of paleovalleys in this region suggests they had considerable effects on paleolimnologic evolution. This is most evident in isopach reconstructions of Eocene sedimentary and volcanic strata, which show several depocenters were filled with anomalously thick strata (Fig. 4.2; Camilleri et al., 2017). While all depocenters contain thick accumulations of Eocene volcanic rocks of the Indian Wells Formation, well data indicates distinct differences in the character of Elko Formation strata in different areas. For example, the depocenter north of the modern East Humboldt Range is predominantly filled with coarse-grained sediments (i.e., conglomerate and sandstone) beneath >1 km of Eocene ignimbrites, representing mixed fluvial-alluvial deposition in a large paleovalley (see Supplemental Materials). In comparison, depocenters located on both sides of the modern Ruby Mountains are interpreted to contain a substantial amount of Eocene limestone and mudstone, particularly west of the Ruby Mountains (Figs. 4.13–4.14). This may indicate subsidence was localized and/or more pronounced in this area, which is consistent with the profundal association of facies in proximal sections (i.e., K1L section; Fig. 4.7).

The history of deposition within the Elko Basin may suggest middle Eocene removal of the Farallon slab and/or lower mantle lithosphere was a driving mechanism of basin development (Fig. 4.17). Recent studies indicate Farallon slab rollback was accompanied by trenchward-migrating dynamic subsidence from suction at the slab hinge and subsequent

volcanism and surface uplift (≤600 m) from isostatic effects of heating and delamination (Pysklywec and Cruden, 2004; Kent-Corson et al., 2006; Göğüş and Pysklywec, 2008; Humphreys, 2009; Smith et al., 2014a; 2017; Jones et al., 2015; Cassel et al., 2018). Regional magmatism associated with this influx of asthenosphere initiated at ca. 44 Ma in the northernmost region of what is now Nevada and migrated across the Elko Basin by ca. 38 Ma (Figs. 4.15, 4.17). Crustal heating during this phase of magmatism likely triggered extension and the initiation of rapid upper-crustal exhumation of the proximal RM-EH metamorphic core complex (McGrew and Snee, 1994; MacCready et al., 1997; Hallett and Spear, 2015; Canada et al., 2019; Fig. 4.17). The westward migration of Elko Formation lakes between ca. 42.4 Ma and 40.4 Ma is interpreted to reflect the surface response to the unroofing of this incipient core complex at depth (Fig. 4.17). Increasingly saline and alkaline lake conditions across this interval may reflect upstream diversions of sources of freshwater and/or topographic blockage of eastward-draining outflow, caused by newly developed topographic barriers above the incipient RM-EH core complex.

CONCLUSIONS

The Elko Formation reflects a diverse array of fluvial and lacustrine facies deposited across a >9,000 km^2 area of the North American Cordilleran hinterland between ca. 50 and 40 Ma. Decimeter-scale stratigraphy and detailed correlations of outcrop and well data, enabled by new geochronology and geochemistry, permit reconstruction of this lake system at high spatial and temporal resolution.

Stratigraphic and geochemical correlation illustrates the wide spatial extent and evolving chemistry of middle Eocene lakes in the Elko Basin. Initial lake development in the early Eocene was confined to a relatively small area and reflects ponding of extrabasinal rivers, potentially with headwaters near the Challis volcanic field to the north. The Elko Basin is characterized by two distinct phases of deposition during the early and middle Eocene. High sediment accumulation rates, between ~0.10 mm/yr and 0.35 mm/yr, accompanied deposition of fluvial-lacustrine and fluctuating profundal facies during both stages. The main phase of lacustrine deposition in the Elko Basin initiated abruptly at ca. 43.2 Ma, and freshwater lakes expanded to reach highstand conditions by ca. 42.4 Ma. A subsequent

transition to balanced-fill conditions occurred across the basin at ca. 42.2 Ma and was followed by westward-directed migration of lake depocenters and increasingly evaporative conditions that preceded ca. 40.4 Ma basin closure, signified by proximal caldera-forming eruptions in the Tuscarora volcanic field.

Synoptic reconstruction and backstripping analysis of Elko Formation strata indicates the Elko Basin shares several genetic similarities with other post-contractional hinterland basins. In particular, hinterland basins are characterized by rapid tectonic subsidence over relatively short durations, which is commonly followed by basin inversion and unconformity (e.g., Perez and Horton, 2014; DeCelles et al., 2015). Dynamic tectonic controls are therefore a fundamental influence on hinterland basin formation. In the Paleogene North American Cordillera, this is demonstrated by the interpreted link between Farallon slab rollback and Elko Basin development. Removal of the Farallon slab and lower mantle lithosphere during the middle–late Eocene is consistent with the observed trenchward-migration of volcanism, where crustal heating triggered extension and core complex exhumation that directly influenced the Elko Formation lake basin.

REFERENCES

Abruzzese, M. J., Waldbauer, J. R., and Chamberlain, C. P., 2005, Oxygen and hydrogen isotope ratios in freshwater chert as indicators of ancient climate and hydrologic regime: Geochimica et Cosmochimica Acta, v. 69, n. 6, p. 1377–1390, doi:10.1016/j.gca.2004.08.036

Aigner, T., Schauer, M., Junghans, W. D., and Reinhardt, L., 1995, Outcrop gamma-ray logging and its applications: examples from the German Triassic: Sedimentary Geology, v. 100, p. 47–61, doi:10.1016/0037-0738(95)00102-6.

Alonso-Zarza, A. M., and Calvo, J. P., 2000, Palustrine sedimentation in an episodically subsiding basin: the Miocene of the northern Teruel Graben (Spain): Palaeogeography, Palaeoclimatology, Palaeoecology, v. 160, p. 1–21, doi:10.1016/S0031-0182(00)00041-9.

Anadon, P., Cabrera, L., Julia, R., Roca, E., and Rosell, L., 1989, Lacustrine oil-shale basins in Tertiary grabens from NE Spain (Western European Rift System): Palaeogeography, Palaeoclimatology, Palaeoecology, v. 70, p. 7–28, doi:10.1016/0031-0182(89)90077-1.

Armstrong, R. L., 1982, Cordilleran metamorphic core complexes - From Arizona to Southern Canada: Annual Reviews in Earth and Planetary Science Letters, v. 10, p. 129–154, doi:10.1146/annurev.ea.10.050182.001021.

Axelrod, D. I., 1966a, The Eocene Copper Basin flora of northeastern Nevada, University of California Publications in Geological Sciences, 129 p.

Axelrod, D. I., 1996b, Diverse upland Eocene forests, western U.S.A.: Palaeobotanist, v. 45, p. 81–97.

Axelrod, D. I., 1997, Paleoelevation estimated from Tertiary floras: International Geology Review, v. 39, no. 12, p. 1124–1133.

Axen, G. J., Taylor, W. J., and Bartley, J. M., 1993, Space-time patterns and tectonic controls of Tertiary extension and magmatism in the Great Basin of the western United States: Geological Society of America Bulletin, v. 105, p. 56–76, doi:10.1130/0016-7606(1993)105<0056:STPATC>2.3.CO;2.

Bahadori, A., Holt, W. E., and Rasbury, E. T., 2018, Reconstruction modeling of crustal thickness and paleotopography of western North America since 36 Ma: Geosphere, v. 14, no. 3, p. 1207–1231, doi:10.1130/GES01604.1.

Baker, P. A., and Kastner, M., 1981, Constraints on the formation of sedimentary dolomite: Science, v. 213, no. 4504, p. 214–216, doi:10.1126/science.213.4504.214.

Balch, D. P., Cohen, A. S., Schnurrenberger, D. W., Haskell, B. J., Valero Garces, B. L., Beck, J. W., Cheng, H., and Edwards, R. L., 2005, Ecosystem and paleohydrological response to Quaternary climate change in the Bonneville Basin, Utah: Palaeogeography, Palaeoclimatology, Palaeoecology, v. 221, no. 1–2, p. 99–122, doi:10.1016/j.palaeo.2005.01.013.

Barker, C. E., Johnson, R. C., Poole, F. G., Daws, T. A., and Threlkeld, C. N., 1990, Rock-Eval pyrolysis data for petroleum-potential evaluation based on well cuttings and core samples from eastern Nevada collected during 1990: U.S. Geological Survey, Open-File Report 90-698, 15 p.

Benavente, C., Mancuso, A., Cabaleri, N., Gierlowski-Kordesch, E., and Ariztegui, D., 2015, Comparison of lacustrine successions and their palaeohydrological implications in two sub-basins of the Triassic Cuyana rift, Argentina: Sedimentology, v. 62, no. 7, p. 1771–1813, doi:10.1111/sed.12209.

Bendick, R., and Baldwin, J., 2009, Dynamic models for metamorphic core complex formation and scaling: The role of unchannelized collapse of thickened continental crust: Tectonophysics, v. 477, no. 1–2, p. 93–101, doi:10.1016/j.tecto.2009.03.017.

Bentham, P. A., Talling, P. J., and Burbank, D. W., 1993, Braided stream and flood-plain deposition in a rapidly aggrading basin: The Escanilla Formation, Spanish Pyrenees, *in* Best, J.L., and Bristow, C.S., eds., Braided Rivers: Geological Society of London Special Publication, v. 75, p. 177–194, doi:10.1144/GSL.SP.1993.075.01.11.

Benvenuti, M., Del Conte, S., Scarselli, N., and Dominici, S., 2014, Hinterland basin development and infilling through tectonic and eustatic processes: latest Messinian-Gelasian Valdelsa Basin, Northern Apennines, Italy: Basin Research, v. 26, no. 3, p. 387–402, doi:10.1111/bre.12031.

Best, M. G., Barr, D. L., Christiansen, E. H., Gromme, S., Deino, A. L., and Tingey, D. G., 2009, The Great Basin Altiplano during the middle Cenozoic ignimbrite flareup:

insights from volcanic rocks: International Geology Review, v. 51, no. 7–8, p. 589–633, doi:10.1080/00206810902867690.

Best, M. G., Christiansen, E. H., de Silva, S., and Lipman, P.W., 2016, Slab-rollback ignimbrite flareups in the southern Great Basin and other Cenozoic American arcs: A distinct style of arc volcanism: Geosphere, v. 12, no. 4, p. 1097–1135, doi:10.1130/GES01285.1.

Blum, P., Rabaute, A., Gaudon, P., and Allan, J. F., 1997. Analysis of natural gamma-ray spectra obtained from sediment cores with the shipboard scintillation detector of the Ocean Drilling Program: example from Leg 156 *in* Shipley, T. H., Ogawa, Y., Blum, P., and Bahr, J. M., eds., Proceedings ODP, Scientific Results, v. 156, p.183–195, doi:10.2973/odp.proc.sr.156.024.1997.

Bohacs, K. M., 1998, Contrasting expressions of depositional sequences in mudrocks from marine to non marine environs, *in* Schieber, J., Zimmerlie, W., and Sethi, P., eds., Mudstones and shales, v. 1, Characteristics at the basin scale: Stuttgart, Schweizerbart'sche Verlagsbuchhandlung, p. 32–77.

Bohacs, K. M., 2003, Lessons from large lake systems; thresholds, nonlinearity, and strange attractors: Geological Society of America Special Paper, v. 370, p. 75–90, doi:10.1130/0-8137-2370-1.75.

Bohacs, K. M., Carroll, A. R., Neal, J. E., and Mankiewicz, P. J., 2000, Lake-basin type, source potential, and hydrocarbon character: an integrated sequence-stratigraphic–geochemical framework, *in* Gierlowski-Kordesch, E. H., and Kelts, K. R., eds., Lake basins through space and time, American Association of Petroleum Geologists Studies in Geology, v. 46, p. 3–34.

Bowen, G. J., Daniels, A. L., and Bowen, B. B., 2008, Paleoenvironmental isotope geochemistry and paragenesis of lacustrine and palustrine carbonates, Flagstaff Formation, central Utah, U.S.A: Journal of Sedimentary Research, v. 78, no. 3, p. 162–174, doi:10.2110/jsr.2008.021.

Bradley, W. H., 1925, A contribution to the origin of the Green River Formation and its oil shale: American Association of Petroleum Geologists Bulletin, v. 9, p. 247–262.

Bradley, W. H., 1970, Green River oil shale—concept of origin extended: Geological Society of America Bulletin, v. 81, p. 985–1000, doi 10.1130/0016-7606(1970)81[985:GROSOO]2.0.CO;2:.

Bradley, W. H., and Eugster, H. P., 1969, Geochemistry and paleolimnology of the trona deposits and associated authigenic minerals of the Green River Formation of Wyoming: U. S. Geological Survey Professional Paper 496-B, 71 p.

Bridge, J. S., 1984, Large-scale facies sequences in alluvial overbank environments: Journal of Sedimentary Petrology, v. 54, p. 583–588, doi:10.1306/212F8477-2B24-11D7-8648000102C1865D.

Bridge, J. S., 1993, Description and interpretation of fluvial deposits; a critical perspective: Sedimentology, v. 40, p. 801–810, doi:10.1111/j.1365-3091.1993.tb01361.x.

Brooks, W. E., Thorman, C. H., and Snee, L. W., 1995, The 40Ar/39Ar ages and tectonic setting of the middle Eocene northeast Nevada volcanic field: Journal of Geophysical Research, v. 100, no. B7, p. 10403–10416, doi:10.1029/94JB03389.

Brun, J.-P., Faccenna, C., Gueydan, F., Sokoutis, D., Philippon, M., Kydonakis, K., Gorini, C., and Polat, A., 2016, The two-stage Aegean extension, from localized to distributed, a result of slab rollback acceleration: Canadian Journal of Earth Sciences, v. 53, no. 11, p. 1142–1157, doi:10.1139/cjes-2015-0203.

Buatois, L. A., and Mángano, M. G., 2009, Applications of ichnology in lacustrine sequence stratigraphy: Potential and limitations: Palaeogeography, Palaeoclimatology, Palaeoecology, v. 272, no. 3–4, p. 127–142, doi:10.1016/j.palaeo.2008.10.012.

Buchheim, H. P., 1978, Paleolimnology of the Laney Member of the Eocene Green River Formation [PhD thesis]: Laramie, University of Wyoming, 101 p.

Camilleri, P. A., 1996, Evidence for Late Cretaceous–Early Tertiary(?) extension in the Pequop Mountains, Nevada: Implications for the nature of the early Tertiary unconformity, *in* Taylor, W.J., and Holly, L., eds., Cenozoic structure and stratigraphy of central Nevada, Volume 1996 Field Conference Volume: Reno, Nevada Nevada, Petroleum Society Inc., p. 23–31.

Camilleri, P. A., and Chamberlain, K. R., 1997, Mesozoic tectonics and metamorphism in the Pequop Mountains and Wood Hills region, northeast Nevada: Implications for the

architecture and evolution of the Sevier orogeny: Geological Society of America Bulletin, v. 109, p. 74–94, doi:10.1130/0016-7606(1997)109<0074:MTAMIT>2.3.CO;2.

Camilleri, P., Deibert, J., and Perkins, M., 2017, Middle Miocene to Holocene tectonics, basin evolution, and paleogeography along the southern margin of the Snake River Plain in the Knoll Mountain–Ruby–East Humboldt Range region, northeastern Nevada and south-central Idaho: Geosphere v. 13, no. 6, p. 1901–1948, doi:10.1130/GES01318.1.

Canada, A. S., Cassel, E. J., Stockli, D. F., Smith, M. E., Jicha, B. R., and Singer B. S., 2019, *in press,* Accelerating exhumation in the Eocene North American Cordilleran hinterland: Implications from detrital zircon (U-Th)/(He-Pb) double dating: Geological Society of America Bulletin.

Carroll, A. R., 1998, Upper Permian lacustrine organic facies evolution, Southern Junggar Basin, NW China: Organic Geochemistry, v. 28, no. 11, p. 649–667, doi:10.1016/S0146-6380(98)00040-0.

Carroll, A. R., and Bohacs, K. M., 1999, Stratigraphic classification of ancient lakes: Balancing tectonic and climatic controls: Geology, v. 27, no. 2, p. 99–102, doi: 10.1130/0091-7613(1999)027<0099:SCOALB>2.3.CO;2.

Carroll, A. R., and Bohacs, K. M., 2001, Lake-type controls on petroleum source rock potential in nonmarine basins: American Association of Petroleum Geologists Bulletin, v. 85, no. 6, p. 1033–1053, doi:10.1306/8626CA5F-173B-11D7-8645000102C1865D.

Carroll, A. R., Chetel, L. M., and Smith, M. E., 2006, Feast to famine: Sediment supply control on Laramide basin fill: Geology, v. 34, no. 3, p. 197–200, doi:10.1130/G22148.1.

Carroll, A. R., Doebbert, A. C., Booth, A. L., Chamberlain, C. P., Rhodes-Carson, M. K., Smith, M. E., Johnson, C. M., and Beard, B. L., 2008, Capture of high-altitude precipitation by a low-altitude Eocene lake, western U.S.: Geology, v. 36, no. 10, p. 791–794, doi:10.1130/G24783A.1.

Carter, D. C., and Pickerill, R. K., 1985, Algal swamp, marginal and shallow evaporitic lacustrine lithofacies from the late Devonian – early Carboniferous Albert Formation,

southeastern New Brunswick, Canada: Maritime Sediments and Atlantic Geology, v. 21, p. 69–86, doi:10.4138/1588.

Casanova, J., 1986, East African Rift stromatolites, *in* Frostick, L.E., Renaut, R.W., Reid, I, and Tiercelin, J. J., eds., Sedimentation in the African Rifts: Geological Society Special Publication, no. 25, p. 201–210.

Cassel, E. J., and Breecker, D. O., 2017, Long-term stability of hydrogen isotope ratios in hydrated volcanic glass: Geochimica et Cosmochimica Acta, v. 200, p. 67–86, doi:10.1016/j.gca.2016.12.001.

Cassel, E. J., Breecker, D. O., Henry, C. D., Larson, T. E., and Stockli, D. F., 2014, Profile of a paleo-orogen: High topography across the present-day Basin and Range from 40 to 23 Ma: Geology, v. 42, no. 11, p. 1007–1010, doi:10.1130/G35924.1.

Cassel, E. J., and Graham, S. A., 2011, Paleovalley morphology and fluvial system evolution of Eocene–Oligocene sediments ("auriferous gravels"), northern Sierra Nevada, California: Implications for climate, tectonics, and topography: Geological Society of America Bulletin, v. 123, no. 9–10, p. 1699–1719, doi:10.1130/B30356.1.

Cassel, E. J., Graham, S. A., Chamberlain, C. P., and Henry, C. D., 2012, Early Cenozoic topography, morphology, and tectonics of the northern Sierra Nevada and western Basin and Range: Geosphere, v. 8, no. 2, p. 229–249, doi:10.1130/GES00671.1.

Cassel, E. J., Smith, M. E., and Jicha, B. R., 2018, The impact of slab rollback on Earth's surface: Uplift and extension in the hinterland of the North American Cordillera: Geophysical Research Letters, v. 45, no. 20, p. 10996–11004, doi:10.1029/2018GL079887.

Chamberlain, A. K., 1984, Surface gamma-ray logs: a correlation tool for frontier areas: American Association of Petroleum Geologists Bulletin, v. 68, no. 8, p. 1040–1043, doi:10.1306/AD4616C4-16F7-11D7-8645000102C1865D.

Chamberlain, C. P., Wan, X., Graham, S. A., Carroll, A. R., Doebbert, A. C., Sageman, B. B., Blisniuk, P., Kent-Corson, M. L., Wang, Z., and Chengshan, W., 2013, Stable isotopic evidence for climate and basin evolution of the Late Cretaceous Songliao basin, China: Palaeogeography, Palaeoclimatology, Palaeoecology, v. 385, p. 106–124, doi: 10.1016/j.palaeo.2012.03.020.

Charrier, R., Baeza, O., Elgueta, S., Flynn, J. J., Gans, P., Kay, S. M., Munoz, N., Wyss, A. R., and Zurita, E., 2002, Evidence for Cenozoic extensional basin development and tectonic inversion south of the flat-slab segment, southern Central Andes, Chile (33°–36°S.L.): Journal of South American Earth Sciences, v. 15, p. 117–139, doi:10.1016/S0895-9811(02)00009-3.

Chetel, L. M., Janecke, S. U., Carroll, A. R., Beard, B. L., Johnson, C. M., and Singer, B. S., 2011, Paleogeographic reconstruction of the Eocene Idaho River, North American Cordillera: Geological Society of America Bulletin, v. 123, no. 1–2, p. 71–88, doi:10.1130/B30213.1.

Cline, J. S., Hofstra, A. H., Muntean, J. L., Tosdal, R. M., and Hickey, K. A., 2005, Carlin-type gold deposits in Nevada: Critical geologic characteristics and viable models: Economic Geology, v. 100, p. 451–484, doi:10.5382/AV100.15.

Cohen, A., McGlue, M. M., Ellis, G. S., Zani, H., Swarzenski, P. W., Assine, M. L., and Silva, A., 2015, Lake formation, characteristics, and evolution in retroarc deposystems: A synthesis of the modern Andean orogen and its associated basins, *in* DeCelles, P. G., Ducea, M. N., Carrapa, B., and Kapp, P. A., eds., Geodynamics of a Cordilleran Orogenic System: The Central Andes of Argentina and Northern Chile, Geological Society of America Memoir, v. 212, p. 309–335, doi:10.1130/2015.1212(16).

Cohen, A. H., 2003, Paleolimnology: The history and evolution of lake systems, Oxford, Oxford University Press, 528 p.

Cohen, A. S., 1989, The taphonomy of gastropod shell accumulations in large lakes: An example from Lake Tanganyika, Africa: Paleobiology, v. 15, no. 1, p. 26–45, doi:10.1017/S0094837300009167.

Colgan, J. P., Howard, K. A., Fleck, R. J., and Wooden, J. L., 2010, Rapid middle Miocene extension and unroofing of the southern Ruby Mountains, Nevada: Tectonics, v. 29, TC6022, 38 p., doi:10.1029/2009TC002655.

Colgan, J. P., and Henry, C. D., 2009, Rapid middle Miocene collapse of the Sevier orogenic plateau in north-central Nevada: International Geology Review, v. 51, no. 9–11, p. 920–961, doi:10.1080/00206810903056731.

Coney, P. J., and Harms, T. A., 1984, Cordilleran metamorphic core complexes: Cenozoic extensional relics of Mesozoic compression: Geology, v. 12, no. 9, p. 550–554, doi:10.1130/0091-7613(1984)12<550:CMCCCE>2.0.CO;2.

Cook, E. F., 1960, Great basin ignimbrites, *in* Boettcher, J. W., and Sloan, W. W., eds., Guidebook to the geology of east central Nevada, Eleventh Annual Field Conference, Intermountain Association of Petroleum Geologists, p. 134–141.

Cowan, C. A., and James, N. P., 1992, Diastasis cracks: mechanically generated synaeresis-like cracks in Upper Cambrian shallow water oolite and ribbon carbonates: Sedimentology, v. 39, p. 1101–1118, doi:10.1111/j.1365-3091.1992.tb01999.x.

Davis, S. J., Mix, H. T., Wiegand, B. A., Carroll, A. R., and Chamberlain, C. P., 2009, Synorogenic evolution of large-scale drainage patterns: Isotope paleohydrology of sequential Laramide basins: American Journal of Science, v. 309, no. 7, p. 549–602, doi:10.2475/07.2009.02.

DeCelles, P. G., 2004, Late Jurassic to Eocene evolution of the Cordilleran Thrust Belt and foreland basin system, Western U.S.A.: American Journal of Science, v. 304, no. 2, p. 105–168, doi:10.2475/ajs.304.2.105.

DeCelles, P. G., and Graham, S. A., 2015, Cyclical processes in the North American Cordilleran orogenic system: Geology, v. 43, no. 6, p. 499–502, doi:10.1130/G36482.1.

DeCelles, P. G., Carrapa, B., Horton, B. K., McNabb, J., Gehrels, G. E., and Boyd, J., 2015, The Miocene Arizaro Basin, central Andean hinterland: Response to partial lithosphere removal?, *in* DeCelles, P. G., et al., eds., Geodynamics of a Cordilleran orogenic system: The Central Andes of Argentina and northern Chile: Geological Society of America Memoir, v. 212, p. 359–386, doi:10.1130/2015.1212(18).

Demaison, G. J., and Moore, J. T., 1980, Anoxic environments and oil source bed genesis: American Association of Petroleum Geologists Bulletin, v. 4, no. 8, p. 1179–1209, doi:10.1016/0146-6380(80)90017-0.

Dickinson, W. R., 2004, Evolution of the North American Cordillera: Annual Review of Earth and Planetary Sciences, v. 32, no. 1, p. 13–45, doi:10.1146/annurev.earth.32.101802.120257.

Dickinson, W. R., 2006, Geotectonic evolution of the Great Basin: Geosphere, v. 2, no. 7, p. 353–368, doi:10.1130/GES00054.1.

Dilek, Y., and Moores, E. M., 1999, A Tibetan model for the early Tertiary western United States: Journal of the Geological Society, London, v. 156, p. 929–941, doi:10.1144/gsjgs.156.5.0929.

Droser, M. L., and Bottjer, D. J., 1986, A semiquantitative field classification of ichnofabric: Journal of Sedimentary Petrology, v. 56, p. 558–559, doi:10.1306/212F89C2-2B24-11D7-8648000102C1865D.

Druschke, P., Hanson, A. D., and Wells, M. L., 2009a, Structural, stratigraphic, and geochronologic evidence for extension predating Palaeogene volcanism in the Sevier hinterland, east-central Nevada: International Geology Review, v. 51, no. 7–8, p. 743–775, doi:10.1080/00206810902917941.

Druschke, P., Hanson, A. D., Wells, M. L., Rasbury, T., Stockli, D. F., and Gehrels, G., 2009b, Synconvergent surface-breaking normal faults of Late Cretaceous age within the Sevier hinterland, east-central Nevada: Geology, v. 37, no. 5, p. 447–450, doi:10.1130/G25546A.1.

Druschke, P., Hanson, A. D., Wells, M. L., Gehrels, G. E., and Stockli, D., 2011, Paleogeographic isolation of the Cretaceous to Eocene Sevier hinterland, east-central Nevada: Insights from U-Pb and (U-Th)/He detrital zircon ages of hinterland strata: Geological Society of America Bulletin, v. 123, no. 5, p. 1141–1160, doi:10.1130/B30029.1.

Dubiel, R. F., Potter, C. J., Good, S. C., and Snee, L. W., 1996, Reconstructing an Eocene extensional basin: The White Sage Formation, eastern Great Basin: Geological Society of America Special Paper, no. 303, p. 1–14, doi:10.1130/0-8137-2303-5.1.

Dyni, J. R., and Hawkins, J. E., 1981, Lacustrine turbidites in the Green River Formation, northwestern Colorado: Geology, v. 9, p. 235–238, doi:10.1130/0091-7613(1981)9<235:LTITGR>2.0.CO;2.

Effimoff, I., and Pinezich, A. R., 1981, Tertiary structural development of selected valleys based on seismic data: Basin and Range Province, northeastern Nevada: Philosophical Transactions of the Royal Society of London, v. 300, no. 1454, p. 435–442, doi:10.1130/SPE208-p31.

Eugster, H. P., and Hardie, L. A., 1978, Saline lakes, *in* Lerman A. ed., Lakes: chemistry, geology, and physics: Springer, New York, p. 237–293.

Eugster, H. P., and Surdam, R. C., 1973, Depositional environment of the Green River Formation of Wyoming: A preliminary report: Geological Society of America Bulletin, v. 84, p. 1115–1120, doi:10.1130/0016-7606(1973)84<1115:DEOTGR>2.0.CO;2.

Evans, J. G., and Ketner, K. B., 1971, Geologic map of the Swales Mountain quadrangle and part of the Adobe Summit quadrangle, Elko County, Nevada: U.S. Geological Survey Miscellaneous Investigations Series Map I-667.

Evans, S. L., Styron, R. H., van Soest, M. C., Hodges, K. V., and Hanson, A. D., 2015, Zircon and apatite (U-Th)/He evidence for Paleogene and Neogene extension in the southern Snake Range, Nevada, USA: Tectonics, v. 34, no. 10, p. 2142–2164, doi:10.1002/2015TC003913.

Evenchick, C. A., McMechan, M. E., McNicoll, V. J., and Carr, S. D., 2007, A synthesis of the Jurassic–Cretaceous tectonic evolution of the central and southeastern Canadian Cordillera: Exploring links across the orogen, *in* Sears, J. W., Harms, T. A., and Evenchick, C. A., eds., Whence the mountains? Inquiries into the evolution of orogenic systems, a volume in honor of Raymond A. Price: Geological Society of America, Special Paper 443, p. 117–145, doi:10.1130/2007.2433(06).

Ezquerro, L., Luzón, A., Navarro, M., Liesa, C. L., and Simón, J. L., 2014, Climatic vs. tectonic signals in a continental extensional basin (Teruel, NE Spain) from stable isotope (δ18O) and sequence stratigraphical evolution: Terra Nova, v. 26, no. 5, p. 337–346, doi:10.1111/ter.12101.

Fahey, J. J., 1962, Saline minerals of the Green River Formation: U.S. Geological Survey Professional Paper 405, 57 p.

Fan, M., and Carrapa, B., 2014, Late Cretaceous–early Eocene Laramide uplift, exhumation, and basin subsidence in Wyoming: Crustal responses to flat slab subduction: Tectonics, v. 33, no. 4, p. 509–529, doi:10.1002/2012TC003221.

Fischer, A. G., and Roberts, L. T., 1991, Cyclicity in the Green River Formation (lacustrine Eocene) of Wyoming: Journal of Sedimentary Petrology, v. 61, no. 7, p. 1146–1154, doi:10.1306/D4267852-2B26-11D7-8648000102C1865D.

Flores, R. M., 1981, Coal deposition in fluvial paleoenvironments of the Paleocene Tongue River Member of the Fort Union Formation, Powder River Area, Powder River Basin, Wyoming and Montana, *in* Ethridge, F. G., and Flores, R. M., eds., Recent and ancient nonmarine depositional environments: models for exploration: Tulsa, Oklahoma, Society of Economic Paleontologists and Mineralogists Special Publication, no. 31, p. 169–190, doi:10.2110/pec.81.31.0169.

Fouch, T. D., 1979a, Character and paleogeographic distribution of upper Cretaceous (?) and Paleogene nonmarine sedimentary rocks in east-central Nevada, *in* Armentrout, J. M., Cole, M. R., and Terbest, H., eds., Cenozoic paleogeography of the western United States, Pacific Coast Paleogeography Symposium 3, Pacific Coast Section, Society of Economic Paleontologists and Mineralogists, p. 97–111.

Fouch, T. D., Hanley, J. H., and Forester, R. M., 1979b, Preliminary correlation of Cretaceous and Paleogene lacustrine and related nonmarine sedimentary and volcanic rocks in parts of the eastern Great Basin of Nevada and Utah, Proceedings Basin and Range Symposium and Great Basin Field Conference, 30th Annual Field Conference, Rocky Mountain Association of Geologists: Denver, Colorado, p. 305–312.

Fouch, T. D., Lund, K., Schmitt, J. G., Good, S. C., and Hanley, J. H., 1991, Late Cretaceous(?) and Paleogene sedimentary rocks and extensional(?) basins in the region of the Egan and Grant ranges, and White River and Railroad valleys, Nevada: their relation to Sevier and Laramide contractional basins in the southern Rocky Mountains and Colorado Plateau, *in* Flanigan, D. M. H., Flanigan, E., and Hansen, M., eds., Geology of White River Valley, the Grant Range, Eastern Railroad Valley and Western Egan Range, Nevada, Fieldtrip Guidebook: Reno, Nevada, Nevada Petroleum Society, p. 15–23.

Freytet, P., and Verrecchia, E. P., 2002, Lacustrine and palustrine carbonate petrography: an overview: Journal of Paleolimnology, v. 27, p. 221–237, doi:10.1023/A:1014263722766.

Fu, X., Jian, W., Chen, W., Feng, X., Wang, D., Song, C., and Zeng, S., 2014, Organic accumulation in lacustrine rift basin: constraints from mineralogical and multiple geochemical proxies: International Journal of Earth Sciences, v. 104, no. 2, p. 495–511, doi:10.1007/s00531-014-1089-3.

Gadeken, L. L., Gartner, M. L., Sharbak, D. E., and Wyatt, D. F., 1991, The interpretation of radioactive tracer logs using gamma ray spectroscopy measurements: The Log Analyst, v. 32, no. 1, p. 24–34.

Gans, P. B., Mahood, G. A., and Schermer, E., 1989, Synextensional magmatism in the Basin and Range Province; A case study from the eastern Great Basin: Geological Society of America Special Paper, v. 233, p. 1–53, doi:10.1130/SPE233-p1.

Gawthorpe, R. L., and Leeder, M. R., 2000, Tectono-sedimentary evolution of active extensional basins: Basin Research, v. 12, p. 195–218, doi:10.1111/j.1365-2117.2000.00121.x.

Ghadeer S. G., and Macquaker, J. H. S., 2012, The role of event beds in the preservation of organic carbon in fine-grained sediments: analyses of the sedimentological processes operating during deposition of the Whitby Mudstone Formation (Toarcian, Lower Jurassic) preserved in northeast England: Marine and Petroleum Geology, v. 35, no. 1, p. 309–320, doi:10.1016/j.marpetgeo.2012.01.001.

Gierlowski-Kordesch, E., Finkelstein, D. B., Truchan Holland, J. J., and Kallini, K. D., 2014, Carbonate lake deposits associated with distal siliciclastic perennial-river systems: Journal of Sedimentary Research, v. 83, no. 12, p. 1114–1129, doi:10.2110/jsr.2013.81.

Gierlowski-Kordesch, E. H., 1998, Carbonate deposition in an ephemeral siliciclastic alluvial system: Jurassic Shuttle Meadow Formation, Newark Supergroup, Hartford Basin, USA: Palaeogeography, Palaeoclimatology, Palaeoecology, v. 140, p. 161–184, doi:10.1016/S0031-0182(98)00039-X.

Gierlowski-Kordesch, E. H., and Buchheim, H. P., 2003, Lake basins as archives of continental tectonics and paleoclimate: introduction: Journal of Paleolimnology, v. 30, p. 113–114, doi:10.1023/A:1025563931270.

Gierlowski-Kordesch, E. H., and Park, L. E., 2004, Comparing species diversity in the modern and fossil record of lakes: The Journal of Geology, v. 112, p. 703–717, doi:10.1086/424578.

Glenn, C. R., and Kelts, K. R., 1991, Sedimentary rhythms in lake deposits, *in* Einsele et al., eds., Cycles and events in stratigraphy, Springer-Verlag Berlin Heidelberg, p. 188–221.

Göğüş, O. H., and Pysklywec, R. N., 2008, Near-surface diagnostics of dripping or delaminating lithosphere: Journal of Geophysical Research, v. 113, 11 p., doi:10.1029/2007JB005123.

Graf, J. W., Carroll, A. R., and Smith, M. E., 2015, Lacustrine sedimentology, stratigraphy and stable isotope geochemistry of the Tipton Member of the Green River Formation, *in* Smith, M. E., and Carroll, A. R., eds., Stratigraphy and Paleolimnology of the Green River Formation, Western USA: Synthesis in Limnogeology, no. 1, p. 31–60, doi:10.1007/978-94-017-9906-5_3.

Hallett, B. W., and Spear, F. S., 2015, Monazite, zircon, and garnet growth in migmatitic pelites as a record of metamorphism and partial melting in the East Humboldt Range, Nevada: American Mineralogist, v. 100, no. 4, p. 951–972, doi:10.2138/am-2015-4839.

Hardie, L. A., Smoot, J. P., and Eugster, H. P., 1978, Saline lakes and their deposits: a sedimentological approach: Special Publications - International Association of Sedimentologists, v. 2, p. 7–41, doi:10.1002/9781444303698.ch2.

Hargrave, J. E., Hicks, M. K., and Scholz, C. A., 2014, Lacustrine carbonates from Lake Turkana, Kenya: A depositional model of carbonates in an extensional basin: Journal of Sedimentary Research, v. 84, no. 3, p. 224–237, doi:10.2110/jsr.2014.22.

Haynes, S. R., 2003, Development of the Eocene Elko Basin, northeastern Nevada: Implications for paleogeography and regional tectonism [M.S. thesis]: Vancouver, The University of British Columbia, 159 p.

Hein, F. J., and Walker, R. G., 1977, Bar evolution and development of stratify cation in the gravelly braided, Kicking Horse River, British Columbia: Canadian Journal of Earth Sciences, v. 14, p. 562–570, doi:10.1139/e77-058.

Henrici, A. C., and Haynes, S. R., 2006, Elkobatrachus Brocki, a new Pelobatid (Amphibia: Anura) from the Eocene Elko Formation of Nevada: Annals of Carnegie Museum, v. 75, no. 1, p. 11–35, doi:10.2992/0097-4463(2006)75[11:EBANPA]2.0.CO;2.

Henry, C. D., 2018, The Eocene Elko Basin and Elko Formation, NE Nevada: Paleotopographic controls on area, thickness, facies distribution, and petroleum potential: American Association of Petroleum Geologists, Search and Discovery Article, no. 11102.

Henry, C. D., 2008, Ash-flow tuffs and paleovalleys in northeastern Nevada: Implications for Eocene paleogeography and extension in the Sevier hinterland, northern Great Basin: Geosphere, v. 4, no. 1, p. 1–35, doi:10.1130/GES00122.1.

Henry, C. D., Faulds, J. E., Boden, D. R., and Ressel, M. W., 2001, Timing and styles of Cenozoic extension near the Carlin Trend, northeastern Nevada: Implications for the formation of Carlin-type gold deposits: Geological Society of Nevada Special Publication, no. 33, p. 115–128.

Henry, C. D., Hinz, N. H., Faulds, J. E., Colgan, J. P., John, D. A., Brooks, E. R., Cassel, E. J., Garside, L. J., Davis, D. A., and Castor, S. B., 2012, Eocene–early Miocene paleotopography of the Sierra Nevada–Great Basin–Nevadaplano based on widespread ash-flow tuffs and paleovalleys: Geosphere, v. 8, no. 1, p. 1–27, doi:10.1130/GES00727.1.

Henry, C. D., McGrew, A. J., Colgan, J. P., Snoke, A. W., and Brueseke, M. E., 2011, Timing, distribution, amount, and style of Cenozoic extension in the northern Great Basin, *in* Lee, J., and Evans, J. P., eds., Geologic field trips to the Basin and Range, Rocky Mountains, Snake River Plain, and terranes of the U.S. Cordillera: Geological Society of America Field Guide 21, p. 27–66, doi:10.1130/2011.0021(02).

Hollingsworth, E., Ressel, M. W., and Henry, C., 2018, Early coarse clastic deposition in the western Elko Basin, Piñon Range, northeastern Nevada: Implications for basin evolution and petroleum potential: American Association of Petroleum Geologists Annual Convention and Exhibition, Salt Lake City, Utah, Search and Discovery Article no. 90323.

Horner, W. H., 2015, Tertiary lake sedimentation in the Elko Formation, Nevada - The Evolution of a small lake system in an extensional setting [M.S. Thesis]: Colorado State University, 102 p.

Horner, W. H., Egenhoff, S., Amerman, R., Bond, W., Burch, D., Hocker, M., and Stucker, R., 2015, Tertiary lake sedimentation in the Elko Formation, Nevada - The evolution of a lake system in an extensional setting, and the changing location of deep-lake source rock facies: American Association of Petroleum Geologists Annual Convention and Exhibition, Search and Discovery Article no. 90216.

Horsfield, B., Curry, D. J., Bohacs, K. M., Littke, R., Rullkötter J., Schenk, H. J., Radke, M., Schaefer, R. G., Carroll, A. R., Isaksen, G., and Witte, E. G., 1994, Organic geochemistry of freshwater and alkaline lacustrine sediments in the Green River Formation of the Washakie Basin, Wyoming, U.S.A.: Organic Geochemistry, v. 22, no. 3–5, p. 415–440, doi:10.1016/0146-6380(94)90117-1.

Horton, B. K., Hampton, B. A., LaReau, B. N., and Baldellon, E., 2002, Tertiary provenance history of the northern and central Altiplano (central Andes, Bolivia): A detrital record of plateau-margin tectonics: Journal of Sedimentary Research, v. 72, p. 711–726, doi:10.1306/020702720711.

Humphreys, E., 2009, Relation of flat subduction to magmatism and deformation in the western United States: Geological Society of America Memoir, v. 204, p. 85–98, doi:10.1130/2009.1204(04).

Ingalls, B. R., and Park, L. E., 2010, Biotic and taphonomic response to lake-level fluctuations in the Greater Green River Basin (Eocene), Wyoming: Palaios, v. 25, no. 5/6, p. 287–298, doi:10.2110/palo.2009.p09-048r.

Jaeger, K. B., 1987, Structural geology and stratigraphy of the Elko Hills, Elko County, Nevada [M.S. thesis]: Laramie, The University of Wyoming, 70 p.

Jagniecki, E. A., and Lowenstein, T. K., 2015, Evaporites of the Green River Formation, Bridger, and Piceance Creek basins: Deposition, diagenesis, paleobrine chemistry, and Eocene atmospheric CO_2, *in* Smith, M. E., and Carroll, A. R., eds., Stratigraphy and Paleolimnology of the Green River Formation, Western USA: Synthesis in Limnogeology, no. 1, p. 277–312, doi:10.1007/978-94-017-9906-5_11.

Janecke, S. U., Hammond, B. F., Snee, L. W., and Geissman, J. W., 1997, Rapid extension in an Eocene volcanic arc: Structure and paleogeography of an intra-arc half graben in central Idaho: Geological Society of America Bulletin, v. 109, no. 3, p. 253–267, doi:10.1130/0016-7606(1997)109<0253:REIAEV>2.3.CO;2.

Janecke, S. U., McIntosh, W., and Good, S., 1999, Testing models of rift basins: structure and stratigraphy of an Eocene–Oligocene supradetachment basin, Muddy Creek half graben, south-west Montana: Basin Research, v. 11, p. 143–165, doi:10.1046/j.1365-2117.1999.00092.x.

Janecke, S. U., and Snee, L. W., 1993, Timing and episodicity of middle Eocene volcanism and onset of conglomerate deposition, Idaho: The Journal of Geology, v. 101, no. 5, p. 603–621, doi:10.1086/648252.

Johnson, R. C., and Birdwell, J. E., 2016, Evolution of the lower Tertiary Elko Lake Basin, a potential hydrocarbon source rock in Northeast Nevada, *in* Dolan, M. P., Higley, D. H., and Lillis, P. G., eds., Hydrocarbon source rocks in unconventional plays, Rocky Mountain region, Rocky Mountain Association of Geologists, p. 261–294.

Johnson, R. C., Mercier, T. J., Ryder, R. T., Brownfield, M. E., and Self, J. G., 2011, Assessment of in-place oil shale resources of the Eocene Green River Formation, Greater Green River Basin, Wyoming, Colorado, and Utah, Oil shale resources of the Eocene Green River Formation, Greater Green River Basin, Wyoming, Colorado, and Utah, U.S. Geological Survey Digital Data Series DDS–69–DD.

Jones, C. H., Mahan, K. H., Butcher, L. A., Levandowski, W. B., and Farmer, G. L., 2015, Continental uplift through crustal hydration: Geology, v. 43, p. 355–358, doi:10.1130/G36509.1.

Jordan, T. E., Flemings, P. B., and Beer, J. A., 1988, Dating thrust fault activity by use of foreland basin strata, *in* Kleinspehn, K., and Paolo, C., eds., New Perspectives in Basin Analysis: Berlin, Springer-Verlag, p. 307–330, doi:10.1007/978-1-4612-3788-4_16.

Katz, B., and Lin, F., 2014, Lacustrine basin unconventional resource plays: Key differences: Marine and Petroleum Geology, v. 56, p. 255–265, doi:10.1016/j.marpetgeo.2014.02.013.

Kelts, K. R., and Hsu, K. J., 1978, Freshwater carbonate sedimentation, *in* Lerman, A., ed., Lakes: chemistry, geology, and physics: Berlin, Springer, p. 295–323, doi:10.1007/978-1-4757-1152-3_9.

Kent-Corson, M. L., Sherman, L. S., Mulch, A., and Chamberlain, C. P., 2006, Cenozoic topographic and climatic response to changing tectonic boundary conditions in Western North America: Earth and Planetary Science Letters, v. 252, no. 3–4, p. 453–466, doi:10.1016/j.epsl.2006.09.049.

Ketner, K. B., and Alpha, A. G., 1992, Mesozoic and Tertiary rocks near Elko, Nevada evidence for Jurassic to Eocene folding and low-angle faulting: U.S. Geological Survey Bulletin, 1988C, p. C1–C13.

King, C., 1876, Geological and topographical atlas accompanying the report of the geological exploration of the fortieth parallel: U.S. Army Professional Paper 18, scale: 1:250,000.

King, C., 1878, Report of the geological exploration of the fortieth parallel-systematic geology: U.S. Army Professional Paper 18, v. 1, 803 p.

Knauth, L. P., and Epstein S., 1976, Hydrogen and oxygen isotope ratios in nodular and bedded cherts: Geochimica et Cosmochimica Acta, v. 40, no. 9, p. 1095–1108, doi:10.1016/0016-7037(76)90051-X.

Knauth, L. P., and Epstein S., 1982, The nature of water in hydrous silica: American Mineralogist, v. 67, p. 510–520.

Konstantinou, A., Strickland, A., Miller, E. L., and Wooden, J. P., 2012, Multistage Cenozoic extension of the Albion-Raft River-Grouse Creek metamorphic core complex: Geochronologic and stratigraphic constraints: Geosphere, v. 8, no. 6, p. 1429–1466, doi:10.1130/GES00778.1.

Kraus, M. J., 1999, Paleosols in clastic sedimentary rocks: Their geologic applications: Earth-Science Reviews, v. 47, p. 41–70, doi:10.1016/S0012-8252(99)00026-4.

Leng, M. J., and Marshall, J. D., 2004, Palaeoclimate interpretation of stable isotope data from lake sediment archives: Quaternary Science Reviews, v. 23, no. 7–8, p. 811–831, doi:10.1016/j.quascirev.2003.06.012.

Leier, A. L., McQuarrie, N., Horton, B. K., and Gehrels, G. E., 2010, Upper Oligocene conglomerates of the Altiplano, Central Andes: The record of deposition and deformation along the margin of a hinterland basin: Journal of Sedimentary Research, v. 80, no. 8, p. 750–762, doi:10.2110/jsr.2010.064.

Liberty, L. M., Heller, P. L., and Smithson, S. B., 1994, Seismic reflection evidence for two-phase development of Tertiary basins from east-central Nevada: Geological Society of America Bulletin, v. 106, no. 12, p. 1621–1633, doi:10.1130/0016-7606(1994)106<1621:SREFTP>2.3.CO;2.

Liu, C., and Wang, P., 2013, The role of algal blooms in the formation of lacustrine petroleum source rocks — Evidence from Jiyang Depression, Bohai Gulf Rift Basin, eastern

China: Palaeogeography, Palaeoclimatology, Palaeoecology, v. 388, p. 15–22, doi:10.1016/j.palaeo.2013.07.024.

Litherland, M. M., and Klemperer, S. L., 2017, Crustal structure of the Ruby Mountains metamorphic core complex, Nevada, from passive seismic imaging: Geosphere, v. 13, no. 5, p. 1–18, doi:10.1130/GES01472.1.

Long, S. P., 2012, Magnitudes and spatial patterns of erosional exhumation in the Sevier hinterland, eastern Nevada and western Utah, USA: Insights from a Paleogene paleogeographic map: Geosphere, v. 8, no. 4, p. 881–901, doi:10.1130/GES00783.1.

Lowenstein, T. K., Jagniecki, E. A., Carroll, A. R., Smith, M. E., Renaut, R. W., and Owen, R. B., 2017, The Green River salt mystery: What was the source of the hyperalkaline lake waters?: Earth-Science Reviews, v. 173, p. 295–306, doi:10.1016/j.earscirev.2017.07.014.

Lund Snee, J. E., Miller, E. L., Grove, M., Hourigan, J. K., and Konstantinou, A., 2016, Cenozoic paleogeographic evolution of the Elko Basin and surrounding region, northeast Nevada: Geosphere, v. 12, no. 2, p. 464–500, doi:10.1130/GES01198.1.

Lunt, I. A., Bridge, J. S., and Tye, R. S., 2004, A quantitative, three-dimensional depositional model of gravelly braided rivers: Sedimentology, v. 51, p. 377–414, doi:10.1111/j.1365-3091.2004.00627.x.

Ma, Y., Fan, M., Lu, Y., Liu, H., Hao, Y., Xie, Z., Liu, Z., Peng, L., Du, X., and Hu, H., 2016, Climate-driven paleolimnological change controls lacustrine mudstone depositional process and organic matter accumulation: Constraints from lithofacies and geochemical studies in the Zhanhua Depression, eastern China: International Journal of Coal Geology, v. 167, p. 103–118, doi:10.1016/j.coal.2016.09.014.

MacCready, T., Snoke, A. W., Wright, J. E., and Howard, K. A., 1997, Mid-crustal flow during Tertiary extension in the Ruby Mountains core complex, Nevada: Geological Society of America Bulletin, v. 109, no. 12, p. 1576–1594, doi:10.1130/0016-7606(1997)109<1576:MCFDTE>2.3.CO;2.

Mack, G. H., James, W. C., and Monger, H. C., 1993, Classification of paleosols: Geological Society of America Bulletin, v. 105, p. 129–136, doi:10.1130/0016-7606(1993)105<0129:COP>2.3.CO;2.

Mason, G. M., and Surdam, R. C., 1992, Carbonate mineral distribution and isotope fractionation: An approach to depositional environment interpretation, Green River Formation, Wyoming, U.S.A.: Chemical Geology, v. 101, p. 311–321, doi:10.1016/0009-2541(92)90010-3.

McGowan, E. M., 2015, Spectral gamma ray characterization of the Elko Formation, Nevada - A case study for a small lacustrine basin [M.S. Thesis]: Colorado State University, 193 p.

McGrew, A. J., and Snee, L. W., 1994, $^{40}Ar/^{39}Ar$ thermochronologic constraints on the tectonothermal evolution of the northern East Humboldt Range metamorphic core complex, Nevada: Tectonophysics, v. 238, no. 1–4, p. 425–450, doi:10.1016/0040-1951(94)90067-1.

McQuarrie, N., Horton, B. K., Zandt, G., Beck, S., and DeCelles, P.G., 2005, Lithospheric evolution of the Andean fold-thrust belt, Bolivia, and the origin of the central Andean plateau: Tectonophysics, v. 399, p. 15–37, doi:10.1016/j.tecto.2004.12.013.

Miall, A. D., 1978, Lithofacies types and vertical profile models in braided river deposits: A summary, *in* Miall, A. D., ed., Fluvial Sedimentology: Memoirs of Canadian Society of Petroleum Geology, v. 5, p. 597–604.

Miall, A. D., 1992, Alluvial deposits, *in* Walker, R.G., and James, N.P., eds., Facies Models: Geological Association of Canada, p. 119–142.

Miall, A. D., 1996, The Geology of fluvial deposits: Berlin, Springer-Verlag, 582 p., doi:10.1007/978-3-662-03237-4.

Molnar, P., and Houseman, G. A., 2004, The effects of buoyant crust on the gravitational instability of thickened mantle lithosphere at zones of intracontinental convergence: Geophysical Journal International, v. 158, p. 1134–1150, doi:10.1111/j.1365-246X.2004.02312.x.

Moore, S. W., Madrid, H. B., and Server, G. T., 1983, Results of oil-shale investigations in northeastern Nevada: U.S. Geological Survey Open-File Report 83-586, 18 p.

Moreno, C. J., Horton, B. K., Caballero, V., Mora, A., Parra, M., and Sierra, J., 2011, Depositional and provenance record of the Paleogene transition from foreland to hinterland basin evolution during Andean orogenesis, northern Middle Magdalena

Valley Basin, Colombia: Journal of South American Earth Sciences, v. 32, no. 3, p. 246–263, doi:10.1016/j.jsames.2011.03.018.

Mott, L. V., and Drever, J. I., 1983, Origin of uraniferous phosphatic beds in Wilkins Peak Member of the Green River Formation: American Association of Petroleum Geologists Bulletin, v. 67, p. 70–82, doi:10.1306/03B5ACC3-16D1-11D7-8645000102C1865D.

Mulch, A., Chamberlain, C. P., Cosca, M. A., Teyssier, C., Methner, K., Hren, M. T., and Graham, S. A., 2015, Rapid change in high-elevation precipitation patterns of western North America during the Middle Eocene Climatic Optimum (MECO): American Journal of Science, v. 315, no. 4, p. 317–336, doi:10.2475/04.2015.02.

Mulch, A., Graham, S. A., and Chamberlain, C. P., 2006, Hydrogen isotopes in Eocene river gravels and paleoelevation of the Sierra Nevada: Science, v. 313, p. 87–89, doi:10.1126/science.1125986.

Müller, R., Nystuen, J. P., and Wright, V. P., 2004, Pedogenic mud aggregates and paleosol development in ancient dryland river systems; criteria for interpreting alluvial mudrock origin and floodplain dynamics: Journal of Sedimentary Research, v. 74, p. 537–551, doi:10.1306/010704740537.

Nutt, C. J., and Good, S. C., 1998, Recognition and significance of Eocene deformation in the Alligator Ridge area, central Nevada: U.S. Geological Survey Open-File Report 98–338, p. 141–150.

Ocakoğlu, F., Açıkalın, S., Yılmaz, İ. Ö., Şafak, Ü., and Gökçeoğlu, C., 2012, Evidence of orbital forcing in lake-level fluctuations in the middle Eocene oil shale-bearing lacustrine successions in the Mudurnu-Göynük Basin, NW Anatolia (Turkey): Journal of Asian Earth Sciences, v. 56, p. 54–71, doi:10.1016/j.jseaes.2012.04.021.

Olsen, P. E., 1990, Tectonic, climatic, and biotic modulation of lacustrine ecosystems; examples from Newark Supergroup of eastern North America, *in* Katz, B. J., ed., Lacustrine Exploration: Case studies and modern analogues: American Association of Petroleum Geologists, Memoir 50, p. 209–224, doi:10.1306/M50523C13.

Oner, Z., and Dilek, Y., 2011, Supradetachment basin evolution during continental extension: The Aegean province of western Anatolia, Turkey: Geological Society of America Bulletin, v. 123, no. 11–12, p. 2115–2141, doi:10.1130/B30468.1.

Palmer, B. A., and Shawkey, E. P., 1997, Lacustrine sedimentation processes and patterns during effusive and explosive volcanism, Challis Volcanic Field, Idaho: Journal of Sedimentary Research, v. 67, no. 1, p. 154–167, doi:10.1306/D426851D-2B26-11D7-8648000102C1865D.

Palmer, S. E., 1984, Hydrocarbon source potential of organic facies of the lacustrine Elko Formation (Eocene/Oligocene), northeastern Nevada: Hydrocarbon Source Rocks of the Greater Rocky Mountain Region, p. 491–511, doi:10.1306/AD4615A7-16F7-11D7-8645000102C1865D.

Paola, C., and Mohrig, D., 1996, Palaeohydraulics revisited: Palaeoslope estimation in coarse-grained braided rivers: Basin Research, v. 8, p. 243–254, doi:10.1046/j.1365-2117.1996.00253.x.

Paola, C., Wiele, S. M., and Reinhart, M. A., 1989, Upper-regime parallel lamination as the result of turbulent sediment transport and low-amplitude bed forms: Sedimentology, v. 36, p. 47–59, doi:10.1111/j.1365-3091.1989.tb00819.x.

Pape, J. R., 2010, Reconstructions of Cenozoic extensional faulting within the southern Ruby Mountains metamorphic core complex and adjacent areas, northeastern Nevada [M.S. Thesis]: University of Arizona, 137 p.

Peck, R. E., 1953, Fossil charophytes: Botanical Review, v. 19, no. 4, p. 209–227, doi:10.1007/BF02861826.

Perez, N. D., and Horton, B. K., 2014, Oligocene–Miocene deformational and depositional history of the Andean hinterland basin in the northern Altiplano plateau, southern Peru: Tectonics, v. 33, p. 1819–1847, doi:10.1002/2014TC003647.

Picard, M. D., 1955, Subsurface stratigraphy and lithology of the Green River Formation in the Uinta Basin, Utah: American Association of Petroleum Geologists Bulletin, v. 39, p. 75–102.

Pietras, J. T., and Carroll, A. R., 2006, High-resolution stratigraphy of an underfilled lake basin: Wilkins Peak Member, Eocene Green River Formation, Wyoming, U.S.A.: Journal of Sedimentary Research, v. 76, no. 11, p. 1197–1214, doi:10.2110/jsr.2006.096.

Pietras, J. T., Carroll, A. R., And Rhodes, M. K., 2003, Lake basin response to tectonic drainage diversion, Eocene Green River Formation, Wyoming: Journal of Paleolimnology, v. 30, p. 115–125, doi:10.1023/A:1025518015341.

Pitman, J. K., 1996, Origin of primary and diagenetic carbonates in the lacustrine Green River Formation (Eocene), Colorado and Utah: U.S. Geological Survey Bulletin 2157, 17 p.

Platt, N. H., and Wright, V. P., 1992, Palustrine carbonates and the Florida Everglades: towards an exposure index for the fresh-water environment: Journal of Sedimentary Petrology, v. 62, p. 1058–1071, doi:10.1306/D4267A4B-2B26-11D7-8648000102C1865D.

Poole, F. G., 1974, Flysch deposits of Antler Foreland Basin, western United States, *in* Dickinson, W. R., ed., Tectonics and Sedimentation, Volume 22, Society of Economic Paleontologists and Mineralogists, p. 58–82, doi:10.2110/pec.74.22.0058.

Poole, F. G., and Claypool, G. E., 1984, Petroleum source-rock potential and crude-oil correlation in the Great Basin, *in* Woodward, J., Meissner, F. F., and Clayton, J. L., eds., Hydrocarbon source rocks of the greater Rocky Mountain region: Denver, Colorado, Rocky Mountain Association of Geologists, p. 179–229.

Pysklywec, R. N., and Cruden, A. R., 2004, Coupled crust-mantle dynamics and intraplate tectonics: Two-dimensional numerical and three-dimensional analogue modeling: Geochemistry, Geophysics, Geosystems, v. 5, no. 10, 22 p, doi:10.1029/2004GC000748.

Rahl, J. M., McGrew, A. J., and Foland, K. A., 2002, Transition from contraction to extension in the northeastern Basin and Range: New evidence from the Copper Mountains, Nevada: Journal of Geology, v. 110, no. 2, p. 179–194, doi:10.1086/338413.

Renaut, R. W., and Tiercelin, J., 1994, Lake Bogoria, Kenya Rift Valley - A sedimentological overview, *in* Renaut, R. W., and Last, W. M., eds., Sedimentology and geochemistry of modern and ancient saline lakes: Tulsa, Oklahoma, Special Publication 50, SEPM (Society for Sedimentary Geology), p. 101–123, doi:10.2110/pec.94.50.0101.

Retallack, G. J., 1988, Field recognition of paleosols, *in* Reinhardt, J., and Sigleo, W.R., eds., Paleosols and Weathering through Geologic Time: Geology Society of America, Special Paper 216, p. 1–20, doi:10.1130/SPE216-p1.

Rhodes, M. K., and Carroll, A. R., 2015, Lake type transition from balanced-fill to overfilled: Laney Member, Green River Formation, Washakie Basin, Wyoming, *in* Smith, M. E., and Carroll, A. R., eds., Stratigraphy and Paleolimnology of the Green River Formation, Western USA: Synthesis in Limnogeology, no. 1, p. 103–125, doi:10.1007/978-94-017-9906-5_5.

Roehler, H. W., 1993, Eocene climates, depositional environments, and geography, Greater Green River Basin, Wyoming, Utah, and Colorado: U.S. Geological Survey Professional Paper 1506-F, 74 p.

Roperch, P., Hérail, G., and Fornari, M., 1999, Magnetostratigraphy of the Miocene Corque basin, Bolivia: Implications for the geodynamic evolution of the Altiplano during the late Tertiary: Journal of Geophysical Research, v. 104, no. B9, p. 20,415–20,429, doi:10.1029/1999JB900174.

Sáez, A., and Cabrera, L., 2002, Sedimentological and palaeohydrological responses to tectonics and climate in a small, closed, lacustrine system: Oligocene As Pontes Basin (Spain): Sedimentology, v. 49, p. 1073–1094, doi:10.1046/j.1365-3091.2002.00490.x.

Sagri, M., Abbate, E., and Bruni, P., 1989, Deposits of ephemeral and perennial lakes in the Tertiary Daban Basin (northern Somalia): Palaeogeography, Palaeoclimatology, Palaeoecology, v. 70, p. 225–233, doi:10.1016/0031-0182(89)90092-8.

Sarg, J. F., Suriamin, N., TÌnavsuu-Milkeviciene, K., and Humphrey, J. D., 2013, Lithofacies, stable isotopic composition, and stratigraphic evolution of microbial and associated carbonates, Green River Formation (Eocene), Piceance Basin, Colorado: American Association of Petroleum Geologists Bulletin, v. 97, no. 11, p. 1937–1966, doi:10.1306/07031312188.

Satarugsa, P., and Johnson, R. A., 2000, Cenozoic tectonic evolution of the Ruby Mountains metamorphic core complex and adjacent valleys, northeastern Nevada: Rocky Mountain Geology, v. 35, no. 2, p. 205–230, doi:10.2113/35.2.205.

Schnurrenberger, D., Russell, J., and Kelts, K., 2003, Classification of lacustrine sediments based on sedimentary components: Journal of Paleolimnology, v. 29, p. 141–154, doi:10.1023/A:1023270324800.

Scholz, C. A., Talbot, M. R., Brown, E. T., and Lyons, R. P., 2011, Lithostratigraphy, physical properties and organic matter variability in Lake Malawi drillcore sediments

over the past 145,000 years: Palaeogeography, Palaeoclimatology, Palaeoecology, v. 303, no. 1–4, p. 38–50, doi:10.1016/j.palaeo.2010.10.028.

Scott, J. J., 2010, Saline lake ichnology: composition and distribution of Cenozoic traces in the saline, alkaline lakes of the Kenya Rift Valley and Eocene Green River Formation: University of Saskatchewan, Saskatoon, 526 p.

Sears J. D., and Bradley, W. H., 1924, Relations of the Wasatch and Green River Formations in northwestern Colorado and southern Wyoming: U.S. Geological Survey Professional Paper 132-F, p. 93–107.

Server, G. T., and Solomon, B. J., 1983, Geology and oil shale deposits of the Elko Formation in the Pinon Range, Nevada: U.S. Geological Survey Miscellaneous Field Studies Map MF-1546, scale: 1:24,000.

Sharp, R. P., 1939, The Miocene Humboldt Formation in northeastern Nevada: The Journal of Geology, v. 47, no. 2, p. 133–160, doi:10.1086/624749.

Smith, M. E., Carroll, A. R., and Singer, B. S., 2008, Synoptic reconstruction of a major ancient lake system: Eocene Green River Formation, western United States: Geological Society of America Bulletin, v. 120, no. 1–2, p. 54–84, doi:10.1130/B26073.1.

Smith, M. E., Carroll, A. R., Jicha, B. R., Cassel, E. J., and Scott, J. J., 2014a, Paleogeographic record of Eocene Farallon slab rollback beneath western North America: Geology, v. 42, no. 12, p. 1039–1042, doi:10.1130/G36025.1.

Smith, M. E., Carroll, A. R., Scott, J. J., and Singer, B. S., 2014b, Early Eocene carbon isotope excursions and landscape destabilization at eccentricity minima: Green River Formation of Wyoming: Earth and Planetary Science Letters, v. 403, p. 393–406, doi:10.1016/j.epsl.2014.06.024.

Smith, M. E., Cassel, E. J., Jicha, B. R., Singer, B. S., and Canada, A. S., 2017, Hinterland drainage closure and lake formation in response to middle Eocene Farallon slab removal, Nevada, U.S.A.: Earth and Planetary Science Letters, v. 479, p. 156–169, doi:10.1016/j.epsl.2017.09.023.

Smith, J. F., and Ketner, K. B., 1976, Stratigraphy of post-Paleozoic rocks and summary of resources in the Carlin-Piñon Range area, Nevada: U.S. Geological Survey Professional Paper 867-B, p. B1–B48.

Smith, J. F., Ketner, K., Hernandez, G. X., Harris, A. G., Stamm, R. G., and Smith, M. C., 1990, Geologic Map of the Summer Camp Quadrangle and Part of the Black Butte Quadrangle, Elko County, Nevada: U.S. Geological Survey Miscellaneous Investigations Series Map I-2097, scale 1:24,000.

Smoot, J. P., Lowenstein, T. K., 1991, Depositional environments of non-marine evaporites, *in* Melvin J. L., ed., Evaporites, petroleum, and mineral resources: Developments in sedimentology, Elsevier, Amsterdam, p. 189–347, doi:10.1016/S0070-4571(08)70261-9.

Solomon, B. J., 1981, Geology and oil shale resources near Elko, Nevada: Open-File Report, v. 81–709, 154 p.

Solomon, B. J., 1992, The Elko Formation of Eocene and Oligocene (?) age–source rocks and petroleum potential *in* Trexler, J. H, et al., eds., Structural Geology and Petroleum Potential of Southwest Elko County, Nevada: 1992 Fieldtrip Guidebook, Nevada Petroleum Society, Inc., Reno, Nevada, p. 25–38.

Solomon, B. J., and Moore, S. W., 1982, Geologic map and oil shale deposits of the Elko East Quadrangle, Elko County, Nevada: U.S. Geological Survey Miscellaneous Field Studies Map MF-1421, scale 1:24,000.

Solomon, B. J., McKee, E. H., and Andersen, D. W., 1979a, Eocene and Oligocene lacustrine and volcanic rocks near Elko, Nevada: 1979 Basin and Range Symposium, p. 325–337.

Solomon, B. J., McKee, E. H., and Andersen, D. W., 1979b, Stratigraphy and depositional environments of Paleogene rocks near Elko, Nevada, *in* Armentrout, J. M., et al., ed., Cenozoic paleogeography of the western United States: Pacific Coast Paleogeography Symposium III, Pacific Section, Society of Economic Paleontologist and Mineralogists, p. 75–88.

Stewart, J. H., and Carlson, J. E., 1981, Geologic map of Nevada: U.S. Geological Survey and Nevada Bureau of Mines and Geology, scale 1:500,000, G81386, doi:10.3133/70046281.

Strobl, S. A. I., Sachsenhofer, R. F., Bechtel, A., Gratzer, R., Gross, D., Bokhari, S. N. H., Liu, R., Liu, Z., Meng, Q., and Sun, P., 2014, Depositional environment of oil shale

within the Eocene Jijuntun Formation in the Fushun Basin (NE China): Marine and Petroleum Geology, v. 56, p. 166–183, doi:10.1016/j.marpetgeo.2014.04.011.

Sullivan, R., 1980, A stratigraphic evaluation of the Eocene rocks of southwestern Wyoming: Geological Survey of Wyoming, Report of Investigations, no. 20, 50 p.

Sullivan, R., 1985, Origin of lacustrine rocks of Wilkins Peak Member, Wyoming: American Association of Petroleum Geologists Bulletin, v. 69, no. 6, p. 913–922, doi:10.1306/AD462B1E-16F7-11D7-8645000102C1865D.

Swain, F. M., 1964, Tertiary fresh-water ostracoda of the Uinta Basin and related forms from southern Wyoming, western Utah, Idaho, and Nevada: Guidebook to the geology and mineral resources of the Uinta Basin: Utah's Hydrocarbon Storehouse, 13th Annual Field Conference, p. 173–180.

Swain, F. M., 1999, Fossil nonmarine Ostracoda of the United States: Developments in Paleontology and Stratigraphy, 16, Elsevier Science, 401 p., doi:10.1669/0883-1351(2000)015<0170:BR>2.0.CO;2.

Tanavsuu-Milkeviciene, K., and Frederick Sarg, J., 2012, Evolution of an organic-rich lake basin - stratigraphy, climate and tectonics: Piceance Creek basin, Eocene Green River Formation: Sedimentology, v. 59, no. 6, p. 1735–1768, doi:10.1111/j.1365-3091.2012.01324.x.

Tenorio, G. E., Vanacker, V., Campforts, B., Álvarez, L., Zhiminaicela, S., Vercruysse, K., Molina, A., and Govers, G., 2018, Tracking spatial variation in river load from Andean highlands to inter-Andean valleys: Geomorphology, v. 308, p. 175–189, doi:10.1016/j.geomorph.2018.02.009.

Valero-Garcés, B., Morellón, M., Moreno, A., Corella, J. P., Martín-Puertas, C., Barreiro, F., Pérez, A., Giralt, S., and Mata-Campo, M. P., 2014, Lacustrine carbonates of Iberian karst lakes: Sources, processes and depositional environments: Sedimentary Geology, v. 299, p. 1–29, doi:10.1016/j.sedgeo.2013.10.007.

Van Houten, F. B., 1956, Reconnaissance of Cenozoic sedimentary rocks of Nevada: American Association of Petroleum Geologists Bulletin, v. 40, no. 12, p. 2801–2825.

Vandenberghe, N., Hilgen, F. J., and Speijer, R. P., 2012, The Paleogene period, *in* Gradstein, F.M., et al., eds., The Geologic Time Scale 2012: Amsterdam, Netherlands, Elsevier, p. 855–921, doi:10.1016/B978-0-444-59425-9.00028-7.

Wallace, A. R., Perkins, M. E., and Fleck, R. J., 2008, Late Cenozoic paleogeographic evolution of northeastern Nevada: Evidence from the sedimentary basins: Geosphere, v. 4, no. 1, 36 p., doi:10.1130/GES00114.1.

Wang, H., Currie, C. A., and DeCelles, P. G., 2015, Hinterland basin formation and gravitational instabilities in the central Andes: Constraints from gravity data and geodynamic models, *in* DeCelles, P. G., Ducea, M. N., Carrapa, B., and Kapp, P. A., eds., Geodynamics of a Cordilleran orogenic system: The Central Andes of Argentina and Northern Chile, Volume 212, Geological Society of America Memoir, p. 387–406, doi:10.1130/2015.1212(19).

Wilf, P, 2000, Late Paleocene–early Eocene climate changes in southwestern Wyoming: Paleobotanical analysis: Geological Society of America Bulletin, v. 112, p. 292–307, doi:10.1130/0016-7606(2000)112<292:LPECCI>2.0.CO;2.

Williams, W. D., 1998, Salinity as a determinant of the structure of biological communities in salt lakes, *in* Mianping, Z., Hurlbert, S. H., and Williams, W. D., eds., Saline Lakes VI, Volume 381: Belgium, Hydrobiologia, p. 191–201, doi:10.1023/A:1003287826503.

Winchester, D. E., 1916, Oil shale in northwestern Colorado and adjacent areas: U.S. Geological Survey Bulletin, v. 641-F, p. 139–198.

Winchester, D. E., 1923, Oil shale of the Rocky Mountain region: U.S. Geological Survey Bulletin 729, 220 p.

Wingate, F. H., 1983, Palynology and age of the Elko Formation (Eocene) near Elko, Nevada: Palynology, v. 7, p. 93–132, doi:10.1080/01916122.1983.9989254.

Wolfbauer, C. A., and Surdam, R. C., 1974, Origin of nonmarine dolomite in Eocene Lake Gosiute, Green River Basin, Wyoming: Geological Society of America Bulletin, v. 85, p. 1733–1740, doi:10.1130/0016-7606(1974)85<1733:OONDIE>2.0.CO;2.

Wolfe, J. A., 1978, A paleobotanical interpretation of Tertiary climates in the Northern Hemisphere: American Scientist, v. 66, p. 694–703, doi:10.2307/27848958.

Wright, V. P., 2012, Lacustrine carbonates in rift settings: the interaction of volcanic and microbial processes on carbonate deposition, *in* Garland, J., Neilson, J. E., Laubach, S. E., and Whidden, K. J., eds., Advances in carbonate exploration and reservoir analysis,

Geological Society, London, Special Publications, v. 370, p. 39–47, doi:10.1144/SP370.2.

Zachos, J. C., Dickens, G. R., and Zeebe, R. E., 2008, An early Cenozoic perspective on greenhouse warming and carbon-cycle dynamics: Nature, v. 451, no. 7176, p. 279–283, doi:10.1038/nature06588.

Zachos, J. C., McCarren, H., Murphy, B., Röhl, U., and Westerhold, T., 2010, Tempo and scale of late Paleocene and early Eocene carbon isotope cycles: Implications for the origin of hyperthermals: Earth and Planetary Science Letters, v. 299, no. 1–2, p. 242–249, doi:10.1016/j.epsl.2010.09.004.

Zachos, J., Pagani, M., Sloan, L., Thomas, E., and Billups, K., 2001, Trends, rhythms, and aberrations in global climate 65 Ma to present: Science, v. 292, p. 686–693, doi:10.1126/science.1059412.

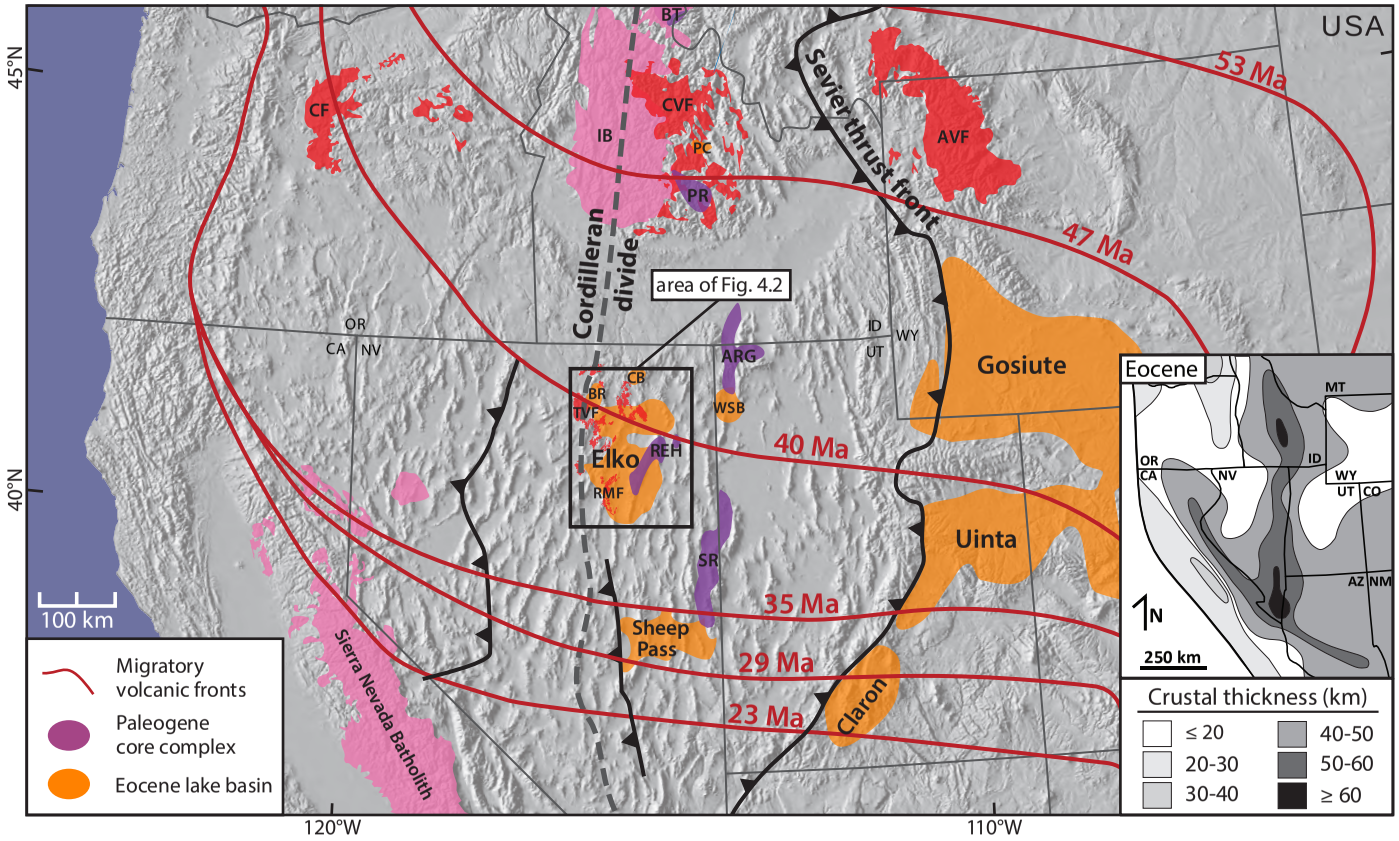

Figure 4.1. Overview map of the western USA showing Eocene terrestrial lake basins and migratory Eocene-Oligocene volcanic fronts modified from Smith et al. (2017). Extent of Eocene basins from Smith et al. (2017) and Janecke et al. (1997); distribution of metamorphic core complexes and early and middle Eocene volcanic centers from Konstantinou et al. (2012) and Stewart and Carlson (1981); location of thrust belts from Long et al. (2012); extent of Sierra Nevada Batholith from Cassel et al. (2012). Inset: Palinspastic and paleoisopach reconstruction of Eocene crustal thickness from Coney and Harms (1984). Abbreviations: SR—Snake Range; BR—Bull Run Basin; CB—Copper Basin; WSB—White Sage Basin; REH—Ruby Mountains-East Humboldt Range; RMF—Robinson Mountain volcanic field; TVF—Tuscarora volcanic field; ARG—Albion-Raft River-Grouse Creek; PR—Pioneer; IB—Idaho Batholith; PC—Panther Creek half graben; CF—Clarno Formation; CVF—Challis volcanic field; AVF—Absaroka volcanic field; BT—Bitterroot.

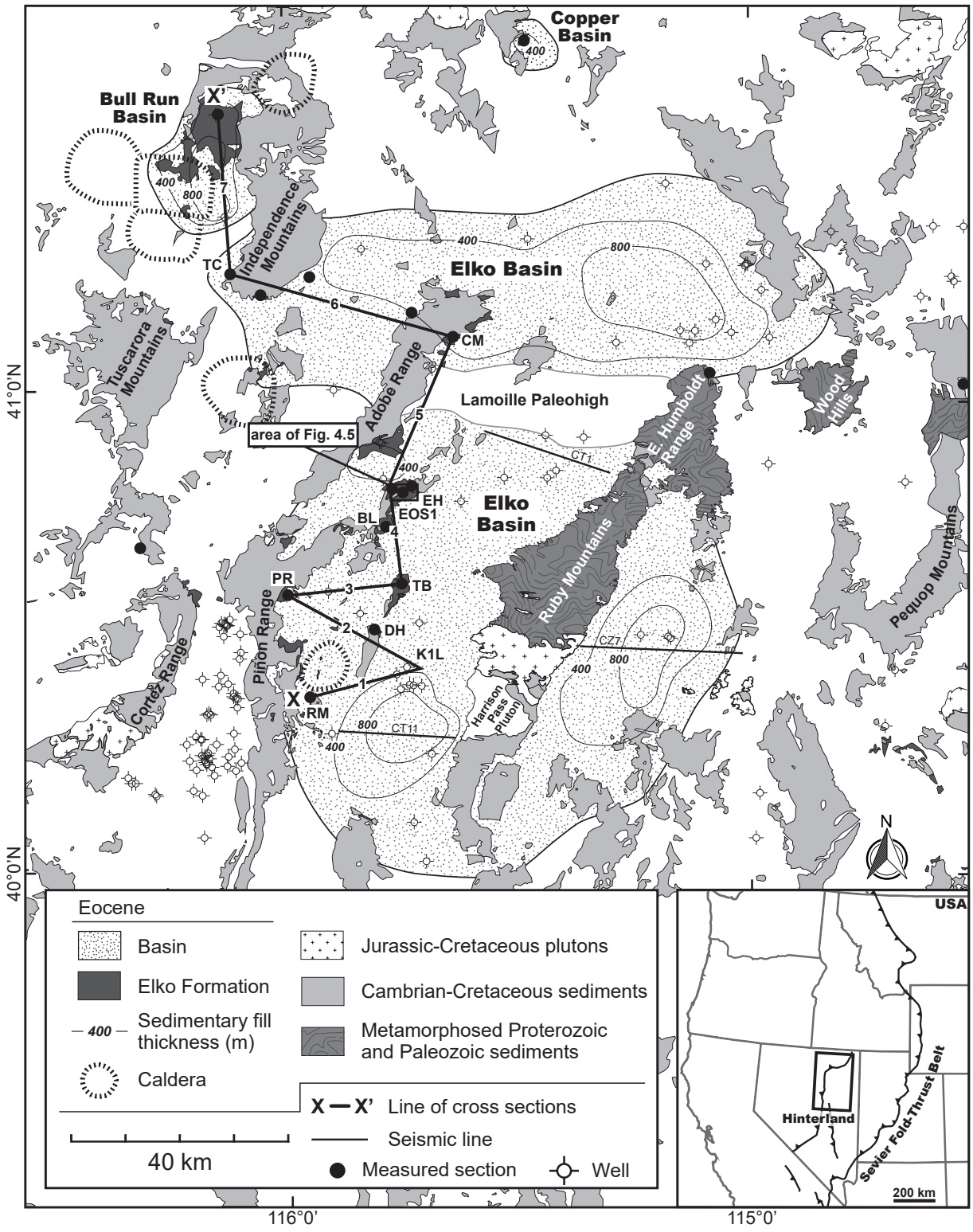
Copper Basin
400
Bull Run Basin
X'
400
800
7
Independence Mountains
TC
400
800
Elko Basin
6
CM
Tuscarora Mountains
Adobe Range
Lamoille Paleohigh
Wood Hills
E. Humboldt Range
area of Fig. 4.5
5
CT1
400
EH
EOS1
Elko Basin
BL
4
Ruby Mountains
Pequop Mountains
PR
3
TB
Piñon Range
2
DH
CZ7
800
400
K1L
Cortez Range
1
X
RM
800
CT11
400
Harrison Pass Pluton
41°0'N
40°0'N
116°0'
115°0'
N
Eocene
Basin
Elko Formation
400
Sedimentary fill thickness (m)
Caldera
Jurassic-Cretaceous plutons
Cambrian-Cretaceous sediments
Metamorphosed Proterozoic and Paleozoic sediments
X — X' Line of cross sections
Seismic line
40 km
Measured section
Well
USA
Hinterland
Sevier Fold-Thrust Belt
200 km

Figure 4.2. Simplified geologic map of northeastern Nevada showing the interpreted modern extent of the Elko Basin. Distribution of map units from Stewart and Carlson (1981), Smith et al. (1990), Camilleri and Chamberlain (1997), and Lund Snee et al. (2016); Eocene calderas from Henry et al. (2011); seismic lines from Satarugsa and Johnson (2000); well locations from the Nevada Bureau of Mines and Geology (NBMG). Abbreviations: TC—Taylor Canyon; CM—Coal Mine Canyon; EH—Elko Hills; BL—Bullion Road; PR—Pinon Range; TB—Twin Bridges; DH—Dixie Hills; K1L—Jiggs (Noble Energy K1L well); RM—Robinson Mountain. Inset: Overview map showing major thrust belt locations modified from DeCelles (2004) and Long et al. (2012).

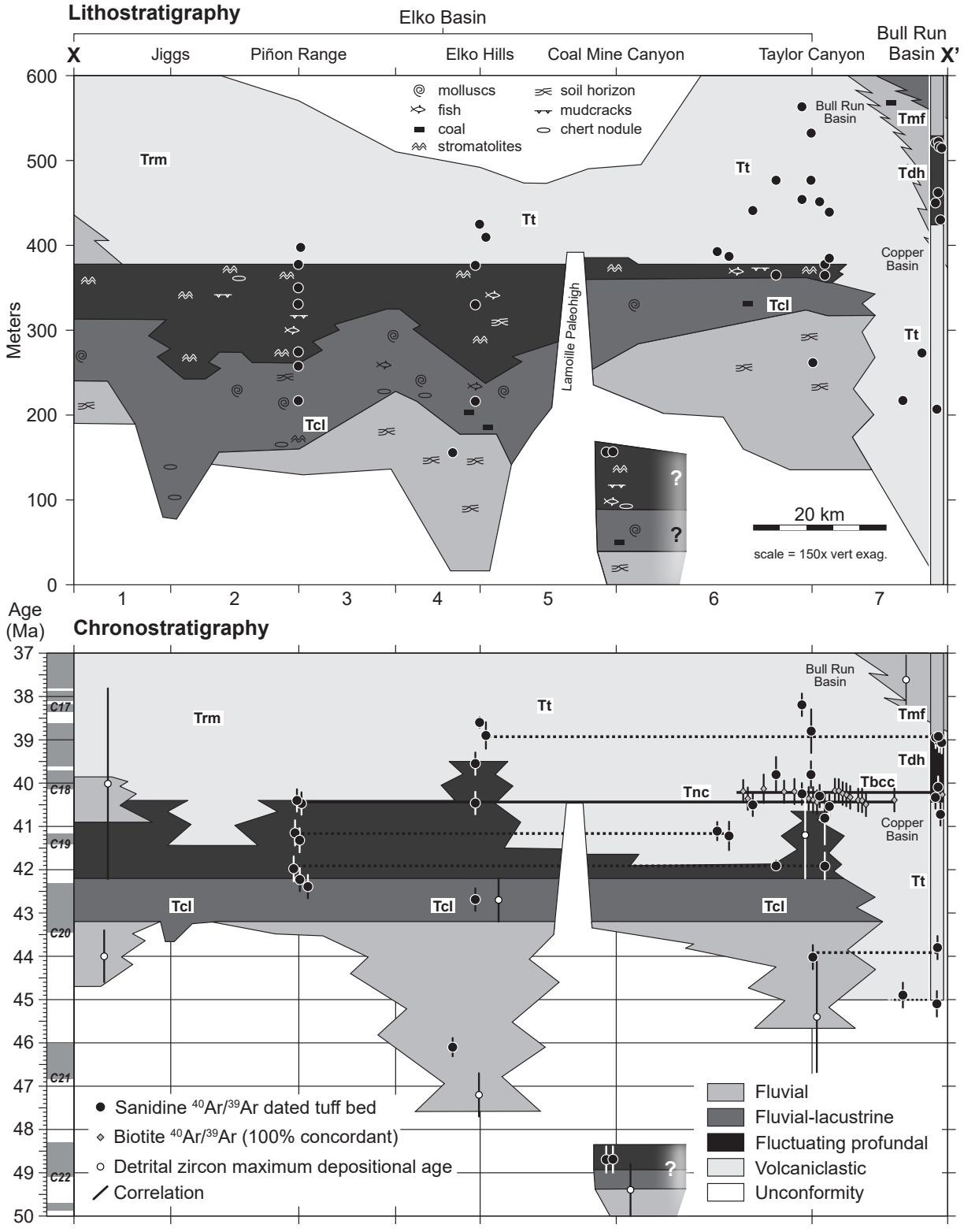
Lithostratigraphy
Elko Basin
X
Jiggs
Piñon Range
Elko Hills
Coal Mine Canyon
Taylor Canyon
Bull Run Basin
X'
molluscs
fish
coal
stromatolites
soil horizon
mudcracks
chert nodule
Trm
Tt
Tcl
Tmf
Tdh
Copper Basin
Lamoille Paleohigh
20 km
scale = 150x vert exag.
Meters
Age (Ma)
Chronostratigraphy
C17
C18
C19
C20
C21
C22
Tnc
Tbcc
Sanidine 40Ar/39Ar dated tuff bed
Biotite 40Ar/39Ar (100% concordant)
Detrital zircon maximum depositional age
Correlation
Fluvial
Fluvial-lacustrine
Fluctuating profundal
Volcaniclastic
Unconformity

Figure 4.3. Lithostratigraphic and chronostratigraphic panels for the Elko Formation and equivalent Eocene strata. Cross-section line shown in Figure 2. Sanidine and biotite $^{40}Ar/^{39}Ar$ ages from Smith et al. (2017) and references therein; detrital zircon U-Pb geochronology from Canada et al. (2019). See Supplemental Materials for detailed stratigraphic correlation panel. Geomagnetic polarity timescale from Vandenberghe et al. (2012) and Smith et al. (2017). Abbreviations: Tcl—Cherty Limestone; Trm—Robinson Mountain volcanics; Tt—Tuscarora volcanics; Tnc—Tuff of Nelson Creek; Tbcc—Tuff of Big Cottonwood Canyon; Tdh—Dead Horse Formation; Tmf—Meadow Fork Formation.

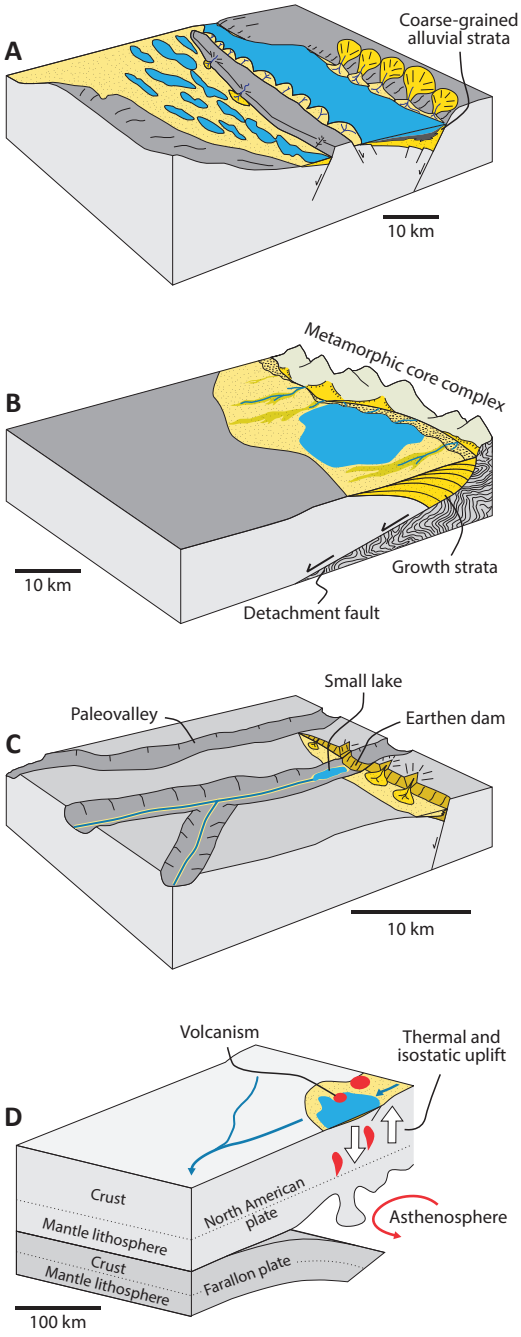
A
Coarse-grained alluvial strata
10 km
B
Metamorphic core complex
Growth strata
10 km
Detachment fault
C
Small lake
Paleovalley
Earthen dam
10 km
D
Volcanism
Thermal and isostatic uplift
Crust
Mantle lithosphere
North American plate
Asthenosphere
Crust
Mantle lithosphere
Farallon plate
100 km

Figure 4.4. Schematic block diagrams illustrating proposed basin forming mechanisms for the Elko Basin. (A) Formation of isolated horst and grabens (i.e., Cline et al., 2005; Colgan et al., 2010; Lund Snee et al., 2016). Block diagram modified from Haynes (2003). (B) Formation of a supradetachment basin during unroofing of the Ruby Mountains-East Humboldt Range metamorphic core complex (i.e., Satarugsa and Johnson, 2000; Johnson and Birdwell, 2016). (C) Lake development in paleovalleys dammed by geomorphic or volcanic processes, potentially augmented by limited extensional deformation (i.e., Henry, 2008; Henry et al., 2011). Block diagram modified from Henry (2018). (D) Basin formation in response to dynamic and isostatic effects associated with Farallon slab and lower lithosphere removal (i.e., Smith et al., 2014a; DeCelles et al., 2015; Smith et al., 2017).

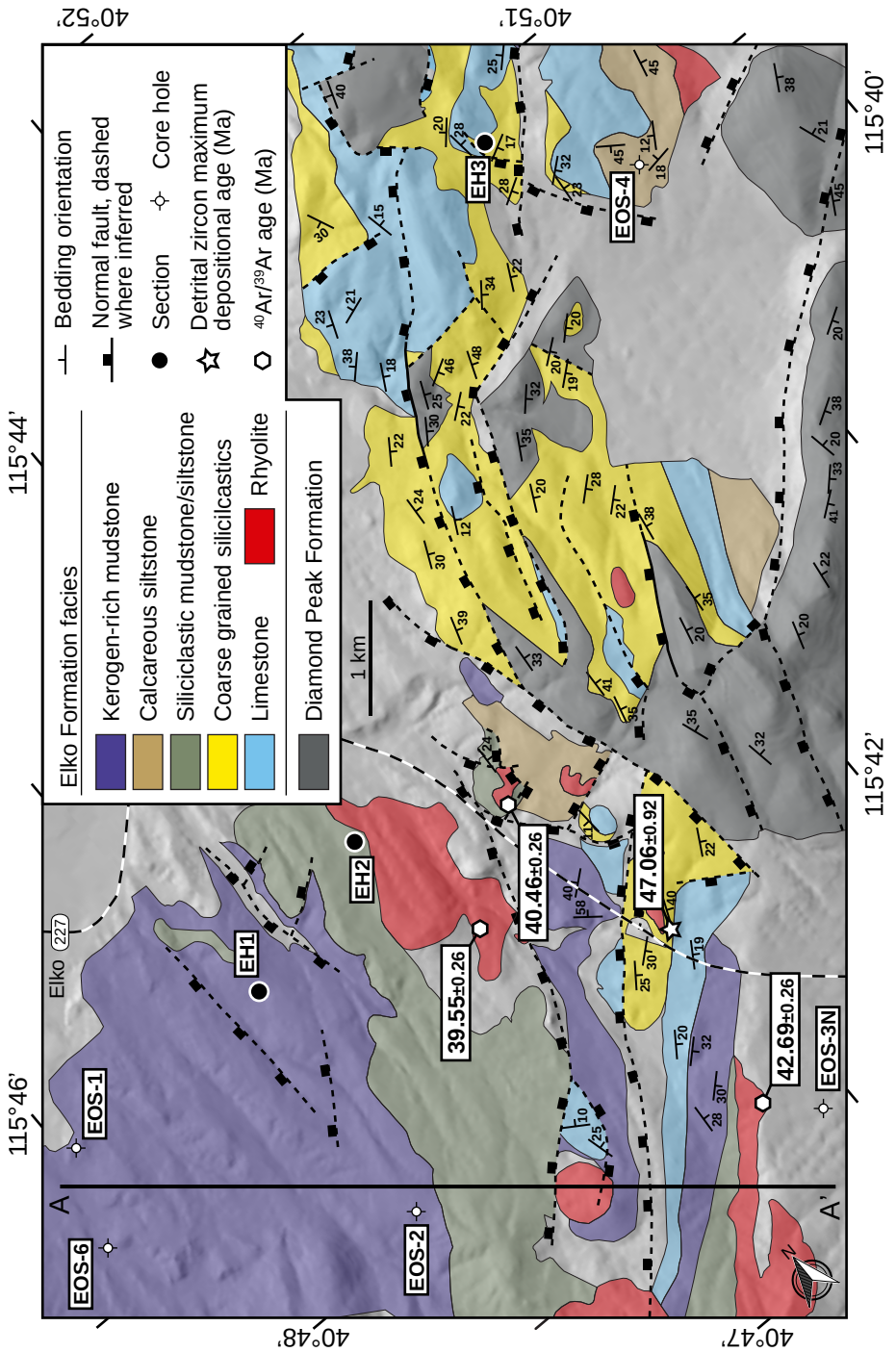

Figure 4.5. Geologic map of the Elko Hills modified from Haynes (2003) and Solomon and Moore (1982) showing the relationship of several predominant Elko Formation facies in this area. Age control from Smith et al. (2017) and Canada et al. (2019); EOS Core Hole locations from Moore et al. (1983) and the Nevada Bureau of Mines and Geology (NBMG).

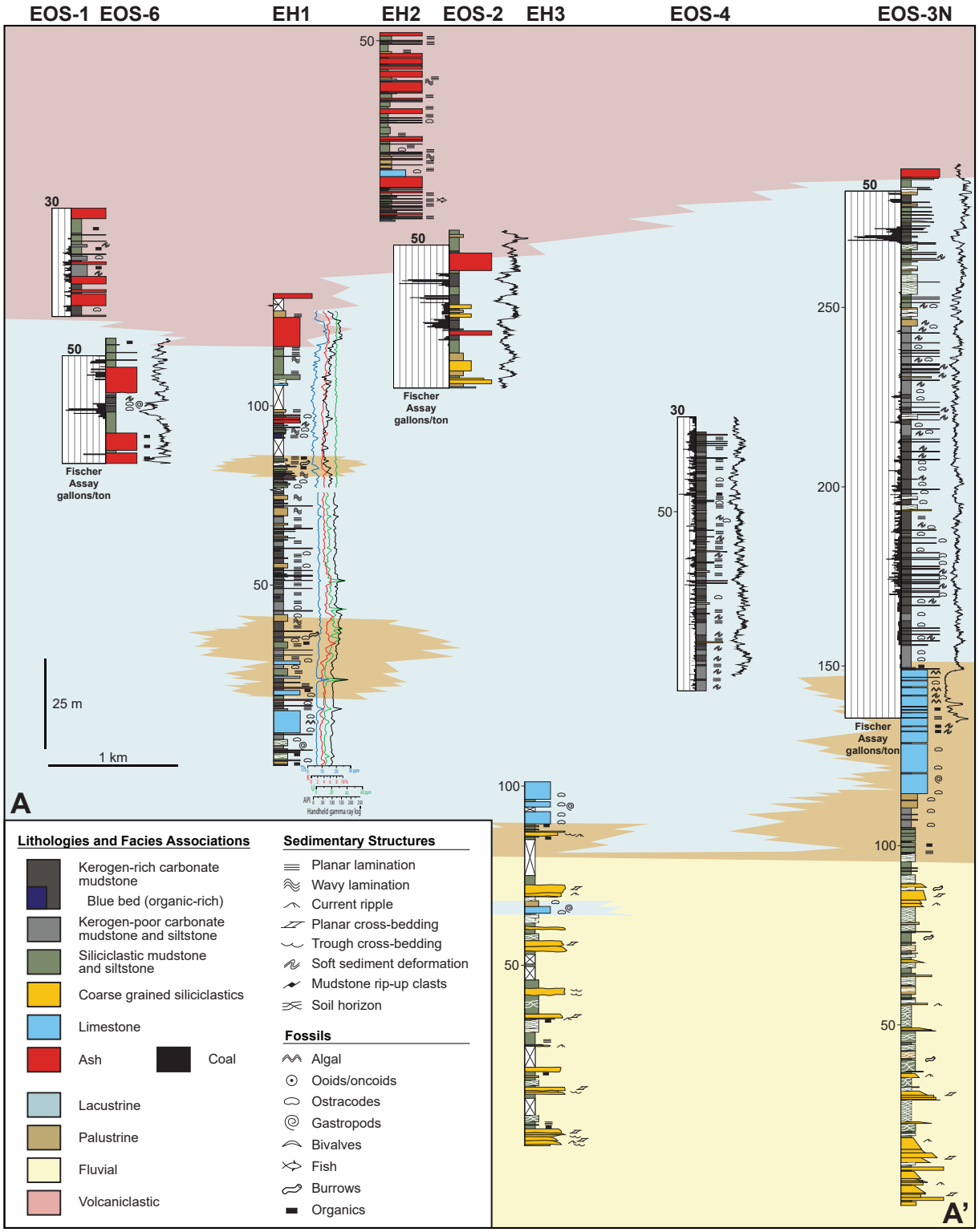

Figure 4.6. Cross-section through the Elko Hills near the center of the Elko Basin showing decimeter-scale stratigraphy and interpreted facies associations. Cross-section line shown in Figure 4.4. Fischer assay oil yields and EOS gamma ray logs from Moore et al. (1983) and Johnson and Birdwell (2016).

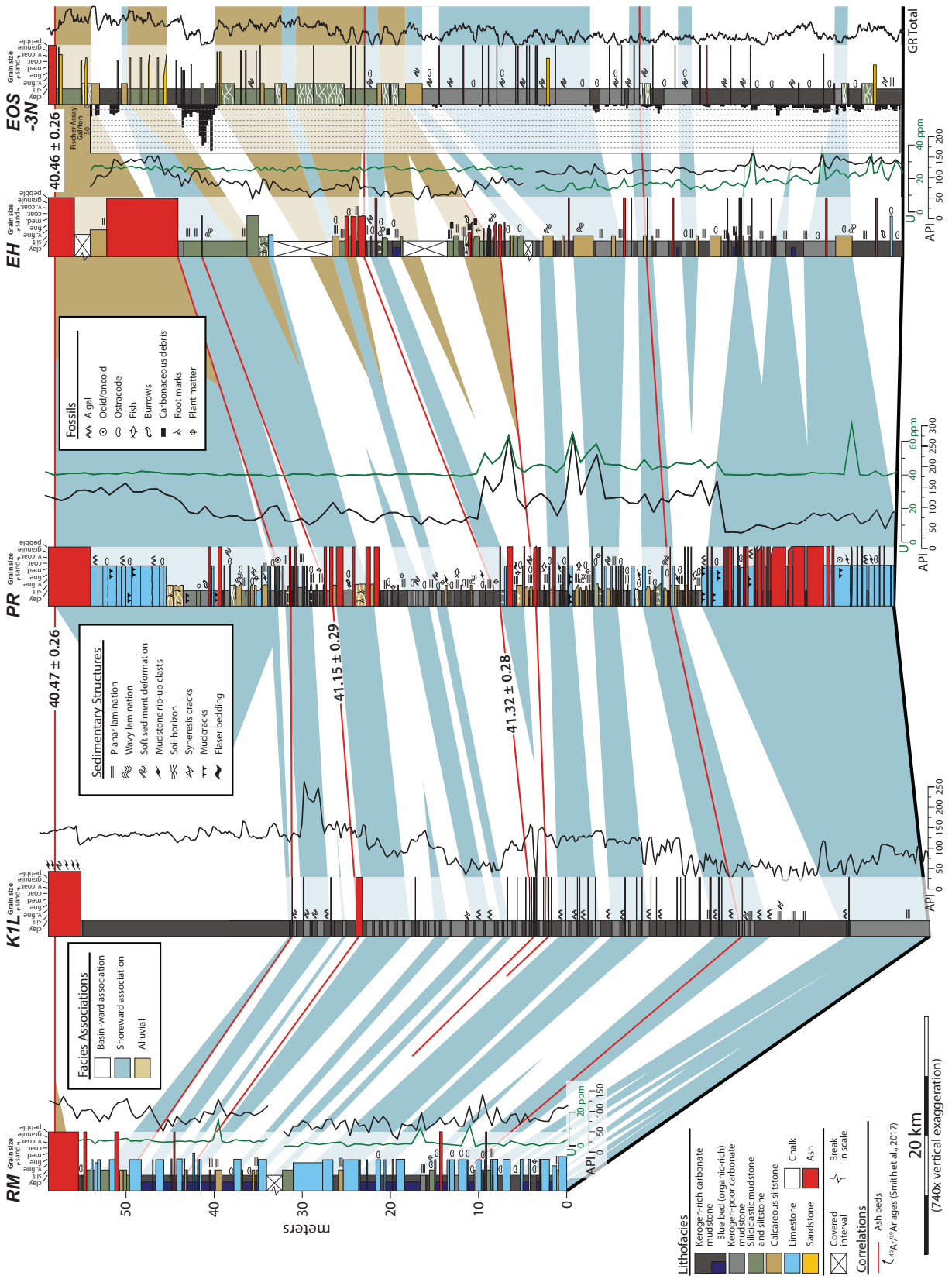
RM
K1L
PR
EH
EOS -3N
Grain size
clay
silt
v. fine
fine
med.
coar.
v. coar.
granule
pebble
sand
Fischer Assay Gal/ton
GR Total
API
U
ppm
meters
40.47 ± 0.26
41.15 ± 0.29
41.32 ± 0.28
40.46 ± 0.26
Facies Associations
Basin-ward association
Shoreward association
Alluvial
Sedimentary Structures
Planar lamination
Wavy lamination
Soft sediment deformation
Mudstone rip-up clasts
Soil horizon
Syneresis cracks
Mudcracks
Flaser bedding
Fossils
Algal
Ooid/oncoid
Ostracode
Fish
Burrows
Carbonaceous debris
Root marks
Plant matter
Lithofacies
Kerogen-rich carbonate mudstone
Blue bed (organic-rich) Kerogen-poor carbonate mudstone
Siliciclastic mudstone and siltstone
Calcareous siltstone
Limestone
Chalk
Sandstone
Ash
Covered interval
Break in scale
Correlations
Ash beds
$^{40}Ar/^{39}Ar$ ages (Smith et al., 2017)
20 km
(740x vertical exaggeration)

Figure 4.7. Detailed correlation panel of fluctuating profundal facies deposited between Robinson Mountain and the Elko Hills tied to the ca. 40.45 ± 0.25 Ma Tuff of Nelson Creek (cf. Smith et al., 2017). Cross-section follows southern half of cross-section line shown in Figure 4.2. K1L and EOS-3N sections are from core observations; gamma ray logs for K1L and EOS-3N sections are from Moore et al. (1983) and the Nevada Bureau of Mines and Geology (NBMG). Abbreviations correspond to locations shown in Figure 4.1.

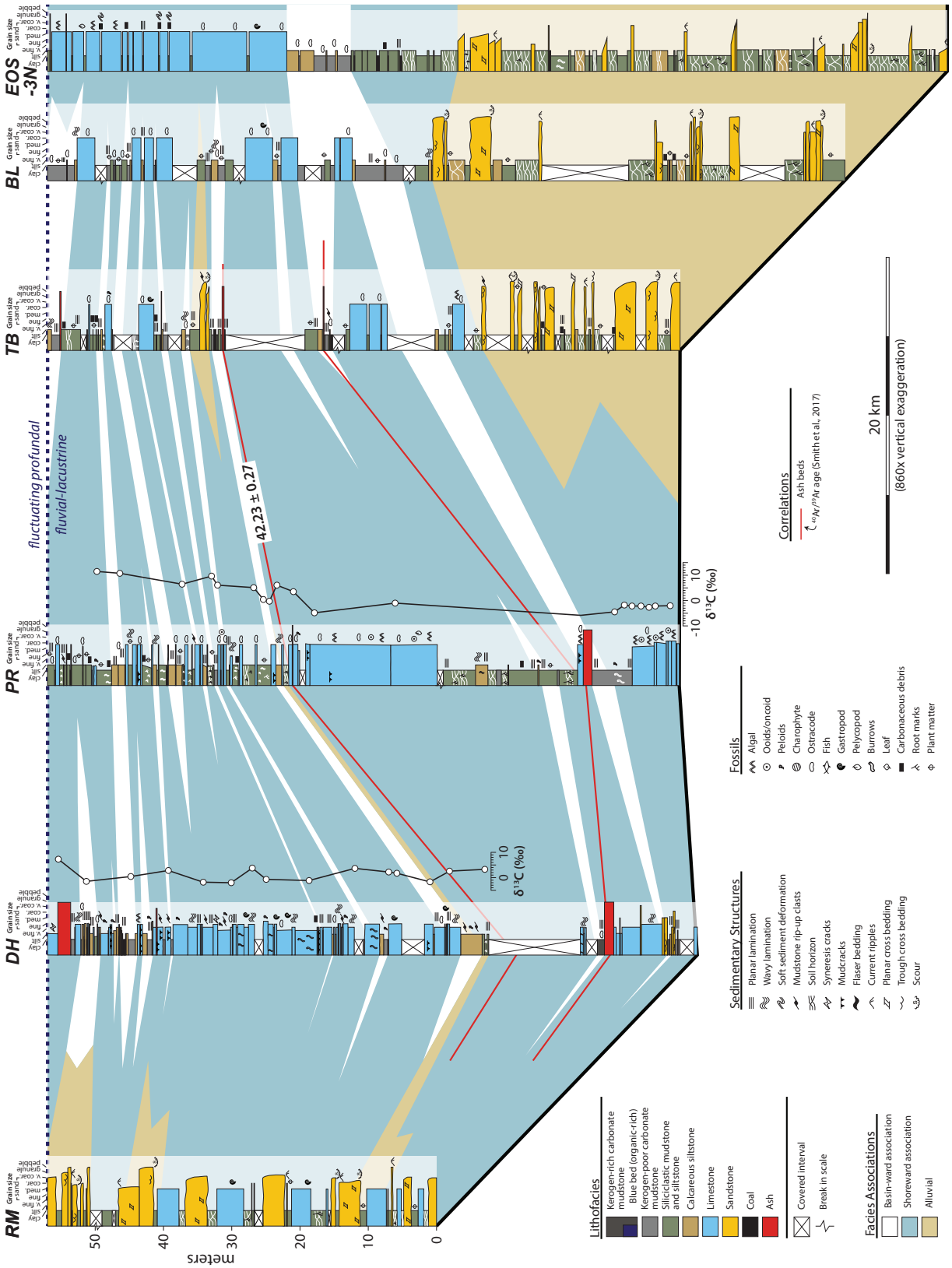
RM
DH
PR
TB
BL
EOS -3N
Grain size
clay
silt
v. fine
fine
med.
coar.
v. coar.
f. sand
granule
pebble
meters
0
10
20
30
40
50
fluctuating profundal
fluvial-lacustrine
42.23 ± 0.27
δ13C (‰)
-10 0 10
0 10
Lithofacies
Kerogen-rich carbonate mudstone
Blue bed (organic-rich) mudstone
Kerogen-poor carbonate mudstone
Siliciclastic mudstone and siltstone
Calcareous siltstone
Limestone
Sandstone
Coal
Ash
Covered interval
Break in scale
Facies Associations
Basin-ward association
Shoreward association
Alluvial
Sedimentary Structures
Planar lamination
Wavy lamination
Soft sediment deformation
Mudstone rip-up clasts
Soil horizon
Syneresis cracks
Mudcracks
Flaser bedding
Current ripples
Planar cross bedding
Trough cross bedding
Scour
Fossils
Algal
Ooids/oncoid
Peloids
Charophyte
Ostracode
Fish
Gastropod
Pelycopod
Burrows
Leaf
Carbonaceous debris
Root marks
Plant matter
Correlations
Ash beds
40Ar/39Ar age (Smith et al., 2017)
20 km
(860x vertical exaggeration)

Figure 4.8. Detailed correlation panel of fluvial-lacustrine facies deposited between Robinson Mountain and the Elko Hills tied to inferred fluctuating profundal-fluvial lacustrine transition. Cross-section follows southern half of cross-section line shown in Figure 4.2. Abbreviations correspond to locations shown in Figure 4.1.

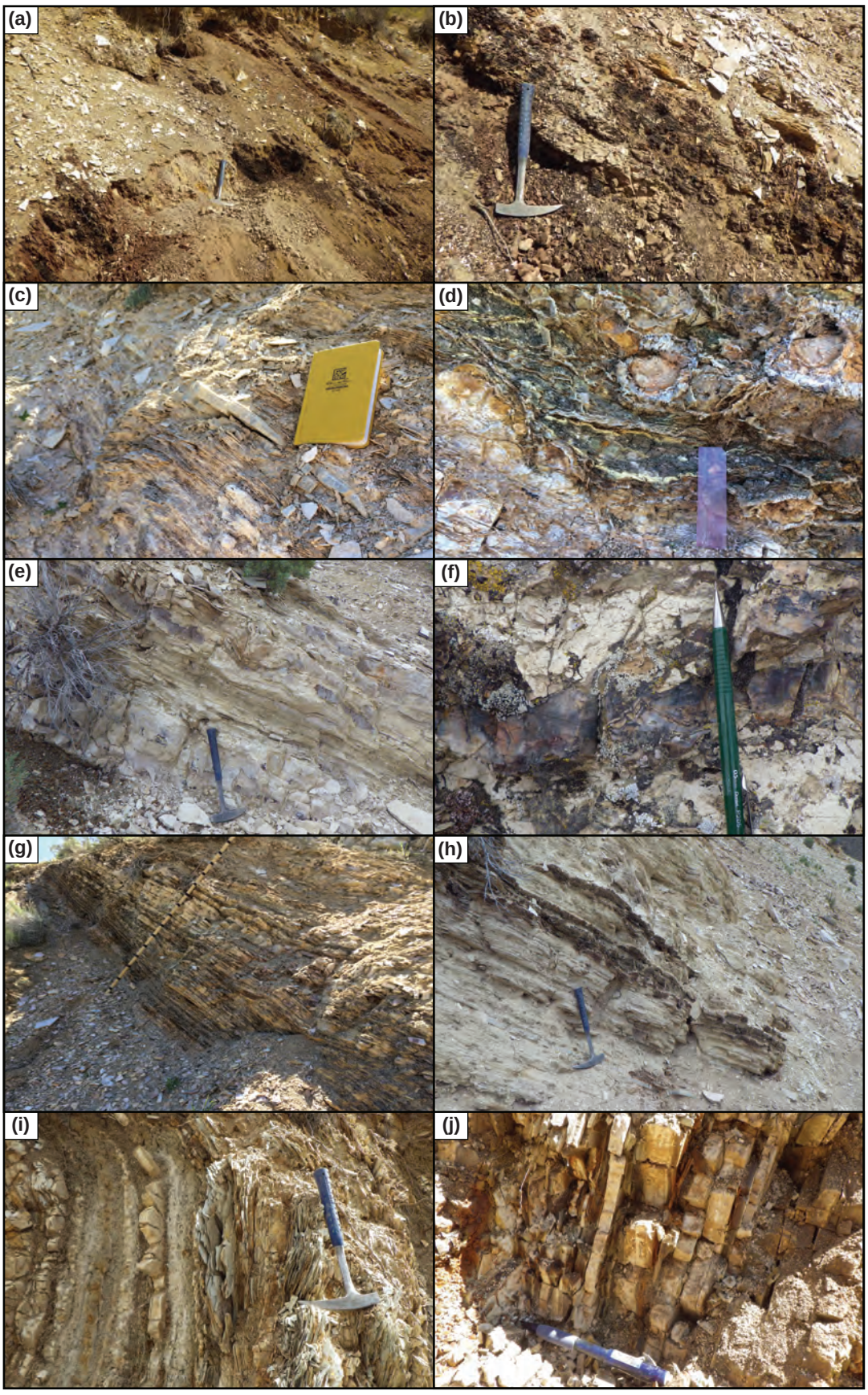
(a)
(b)
(c)
(d)
(e)
(f)
(g)
(h)
(i)
(j)

Figure 4.9. Representative photographs of Elko Formation facies. (A–B) Carbonaceous mudstone with discontinuous coal facies. (C–D) Gypsum and sulfur deposits within finely laminated kerogen-poor mudstone facies. Secondary replacement minerals commonly cross-cut bedding, but sometimes fill bedding-parallel fractures. (E–F) 'Cherty limestone' facies with nodular chert filling microbialitic limestone and dolostone. (G–I) Typical kerogen-rich 'oil shale' facies with interbedded limestone and air-fall tuffs. (J) Altered tuff and non-laminated carbonate mudstone.

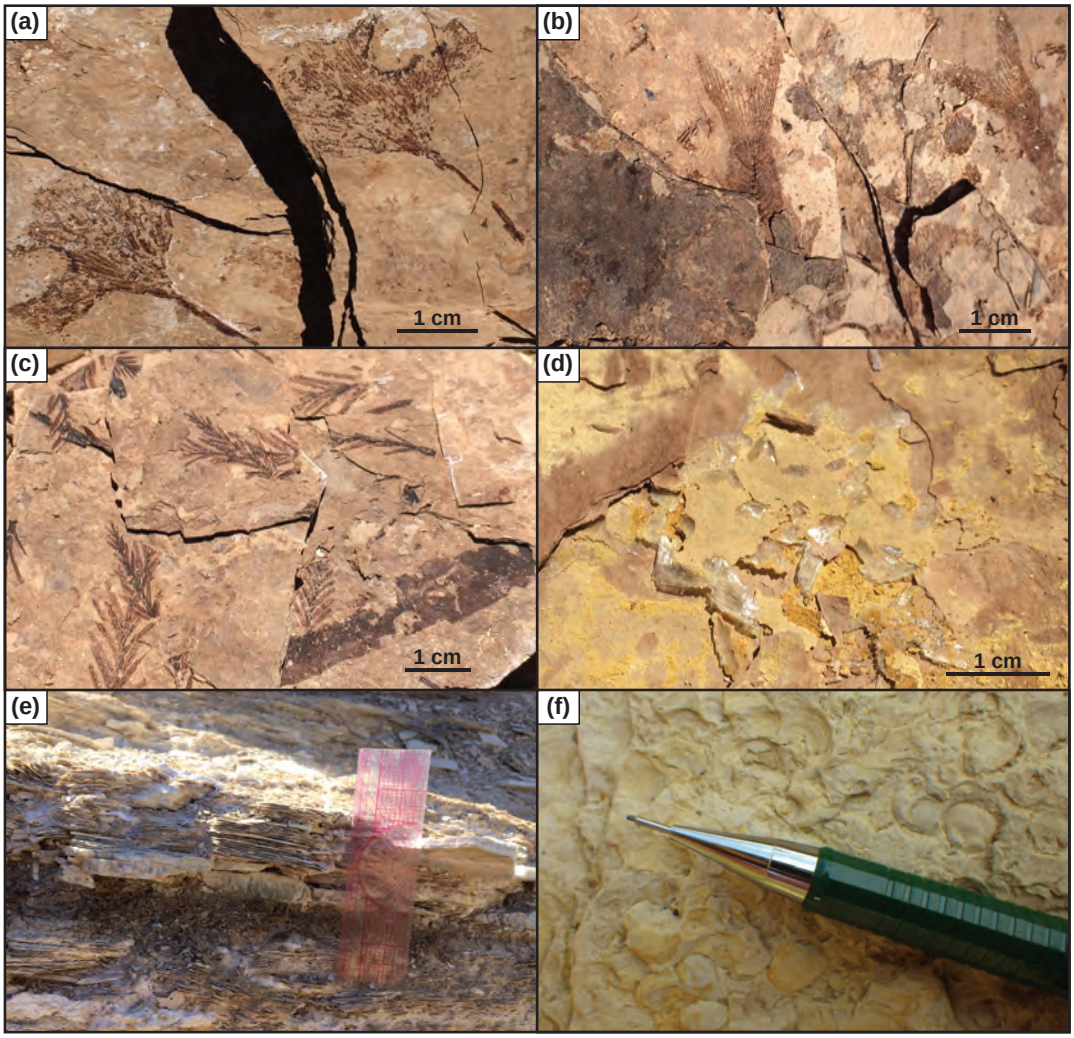

Figure 4.10. Photographs of several common features in Elko Formation strata: (A) Fossil angiosperm leaf; (B) fossil fish; (C) Metasequoia fossils; (D) halite crystals and sulfur on bedding plane of carbonaceous shale; (E) gypsum within finely-laminated kerogen-rich mudstone facies; and (F) gastropod fossils.

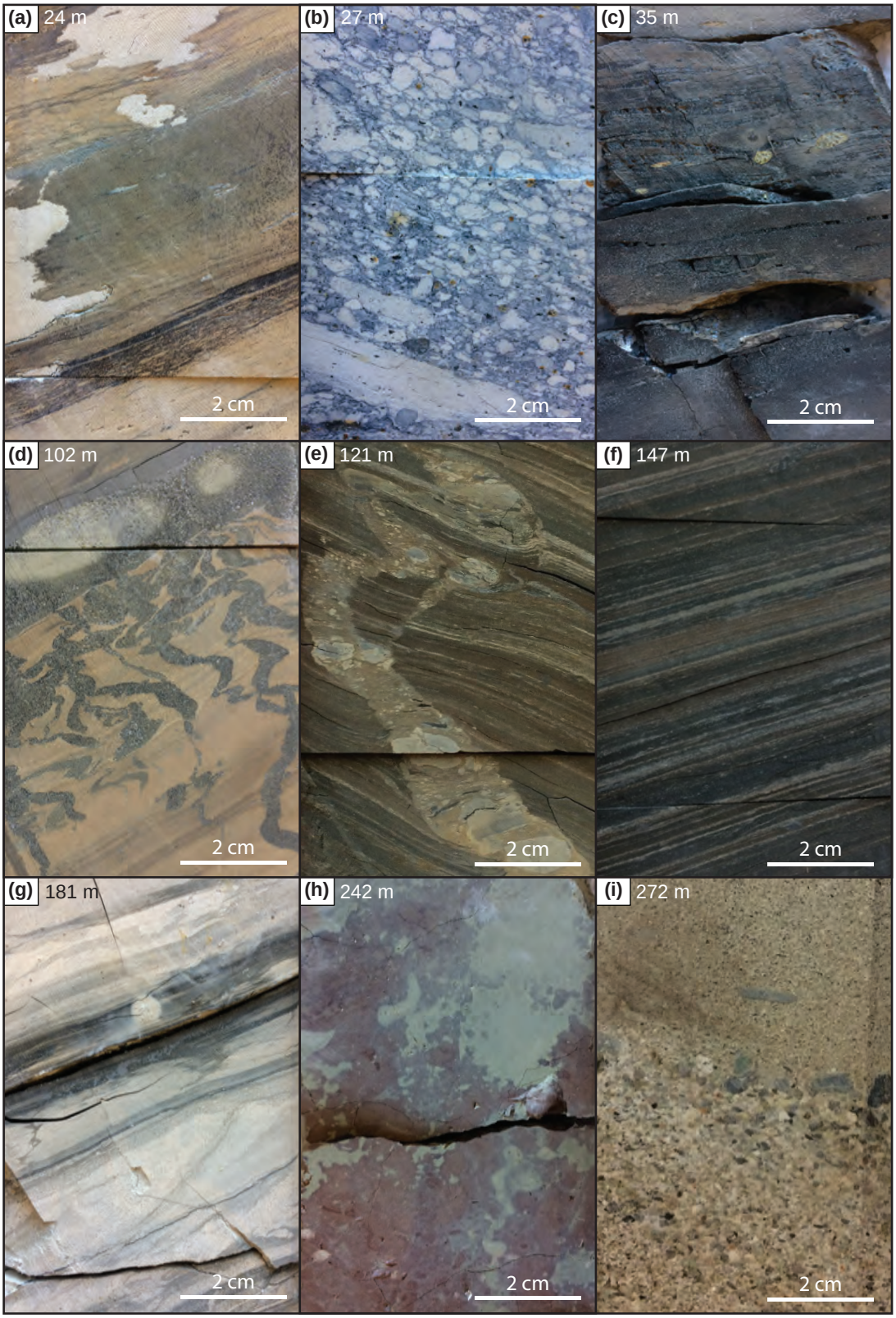
(a) 24 m
2 cm
(b) 27 m
2 cm
(c) 35 m
2 cm
(d) 102 m
2 cm
(e) 121 m
2 cm
(f) 147 m
2 cm
(g) 181 m
2 cm
(h) 242 m
2 cm
(i) 272 m
2 cm

Figure 4.11. Photographs of Elko Formation facies in the Noble Energy EOS-3N core hole completed in the Elko Hills (see Fig. 5): (A) siliciclastic mudstone with carbonaceous material and soft-sediment deformation; (B) pumiceous tuff; (C) sub-bituminous coal with disseminated sulfur; (D) bioturbated carbonate mudstone and concretions; (E) clastic dike and small-scale faults cross-cutting finely laminated kerogen-rich mudstone; (F) kerogen-rich carbonate mudstone with thin ostracode lags; (G) limestone with thin carbonaceous laminations; (G) paleosol with color mottling; and (H) tuffaceous sandstone. Numbers correspond to sample depth.

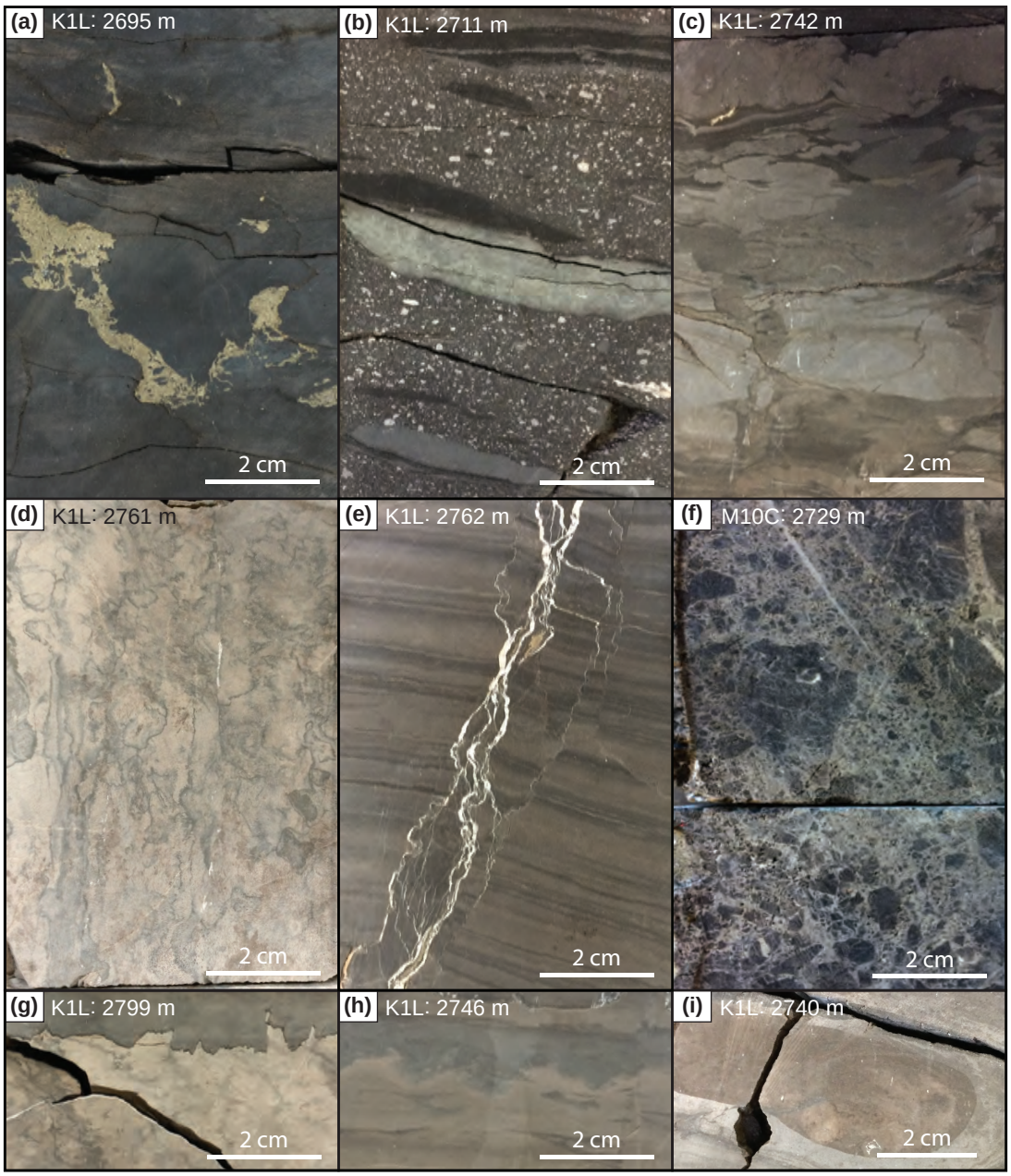

Figure 4.12. Photographs of Elko Formation core from the Noble Energy K1L well and M10C well in Huntington Valley: (A) kerogen-rich mudstone with disseminated pyrite; (B) rip-up clasts within tuffaceous mudstone; (C) kerogen-poor carbonate mudstone with soft-sediment deformation; (D) dolostone with dolomite veins; (E) laminated mudstone with bedding-perpendicular stylolites and small-scale faults; (F) brecciated carbonate mudstone; (G) Bedding-parallel stylolites; (H): flame structures; and (I): concretion in carbonate mudstone. Numbers correspond to sample depth.

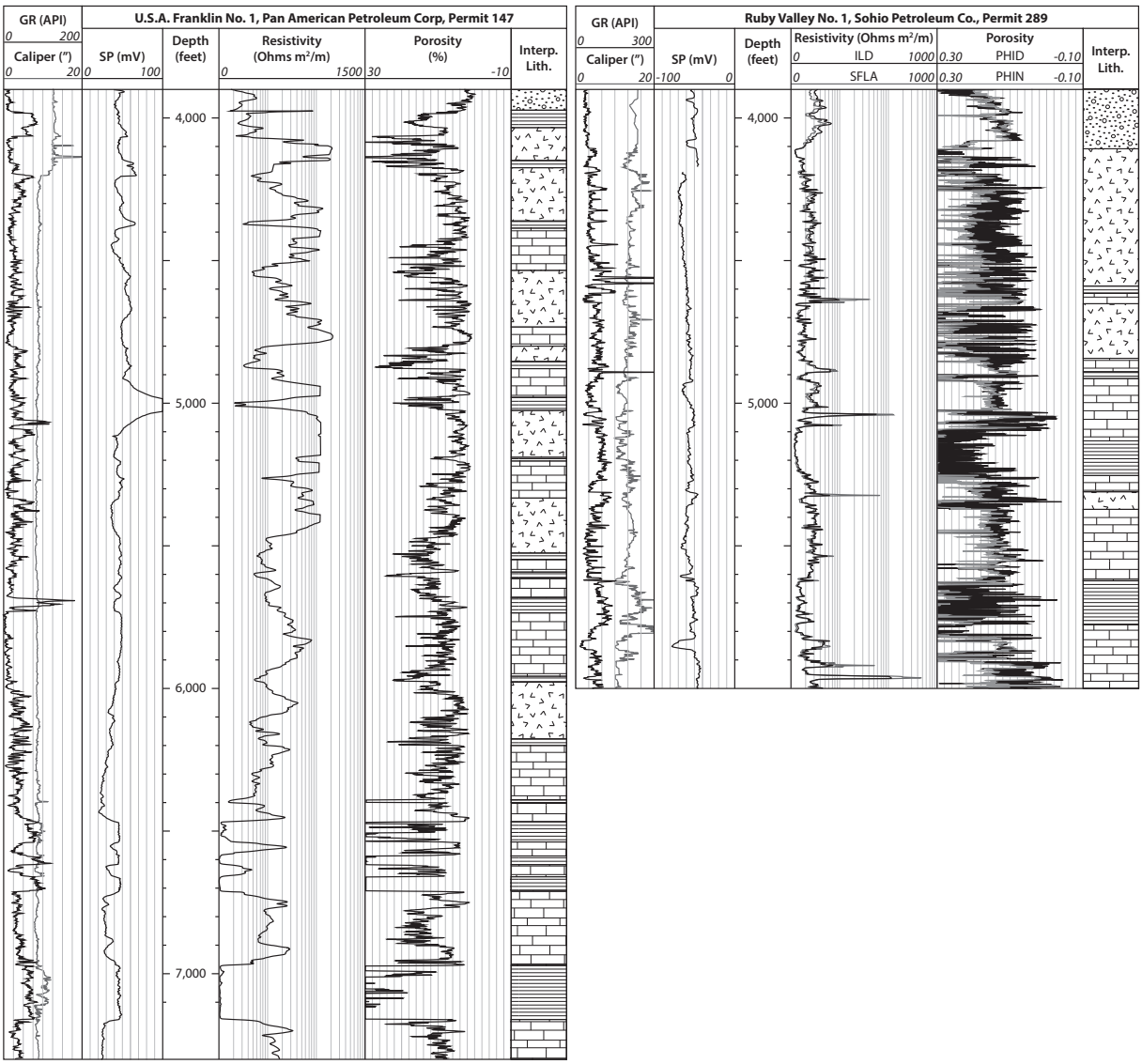

Figure 4.13. Petrophysical data and interpreted lithologies for USA Franklin No. 1 well and Ruby Valley No. 1 well in Ruby Valley. Both wells are interpreted to contain tuffaceous Elko Formation facies and tuffs of the overlying Indian Wells Formation based on well log data and cuttings observations (see Supplemental Materials).

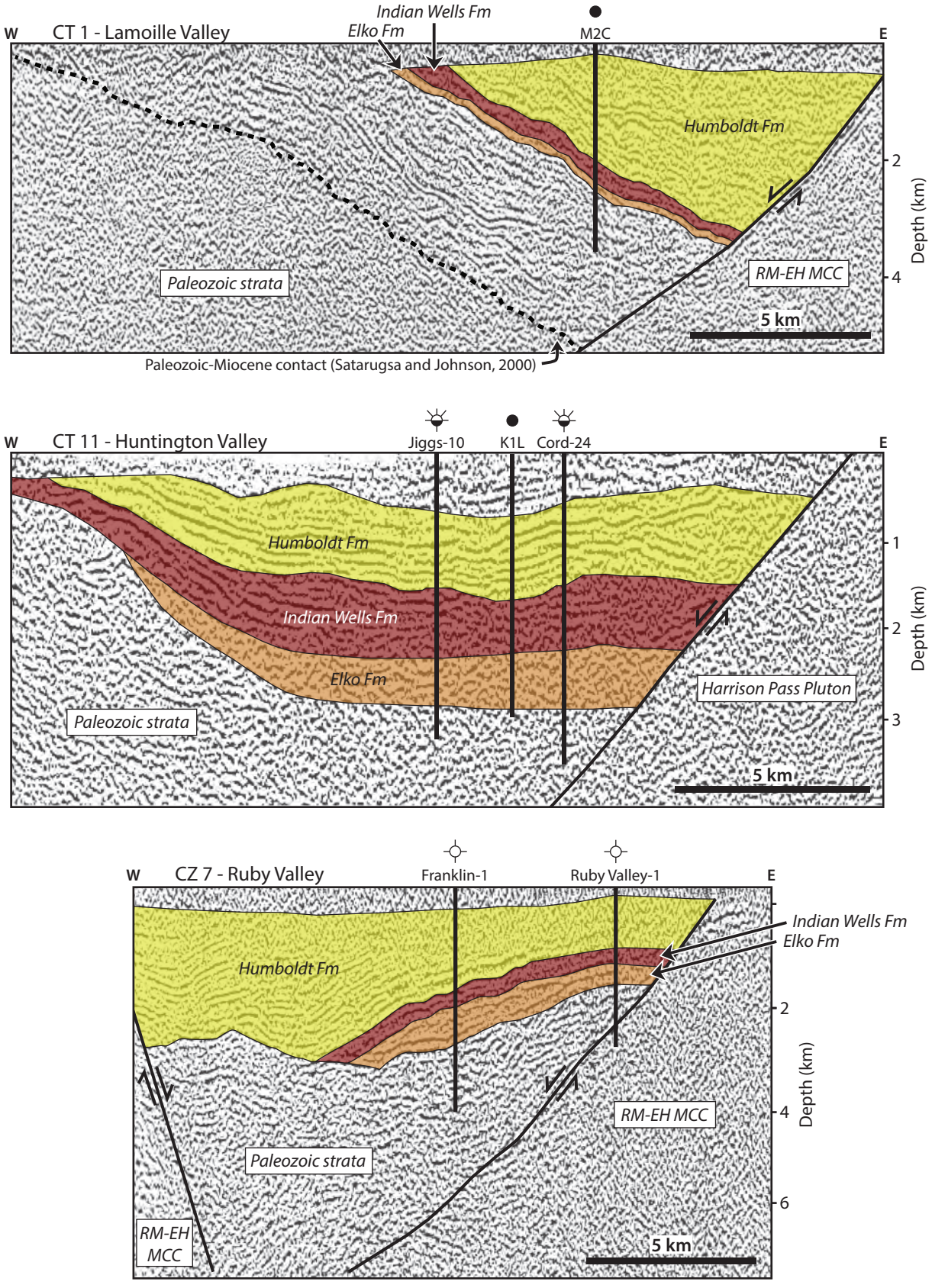
W
CT 1 - Lamoille Valley
Indian Wells Fm
Elko Fm
M2C
E
Humboldt Fm
Paleozoic strata
RM-EH MCC
5 km
Paleozoic-Miocene contact (Satarugsa and Johnson, 2000)
Depth (km)
2
4
W
CT 11 - Huntington Valley
Jiggs-10
K1L
Cord-24
E
Humboldt Fm
Indian Wells Fm
Elko Fm
Paleozoic strata
Harrison Pass Pluton
5 km
Depth (km)
1
2
3
W
CZ 7 - Ruby Valley
Franklin-1
Ruby Valley-1
E
Indian Wells Fm
Elko Fm
Humboldt Fm
RM-EH MCC
Paleozoic strata
RM-EH MCC
5 km
Depth (km)
2
4
6

Figure 4.14. Seismic reflection profiles from Satarugsa and Johnson (2000) with interpreted extent of Elko Formation, Indian Wells Formation, and Humboldt Formation from adjacent well data. See Figure 4.2 for profile locations.

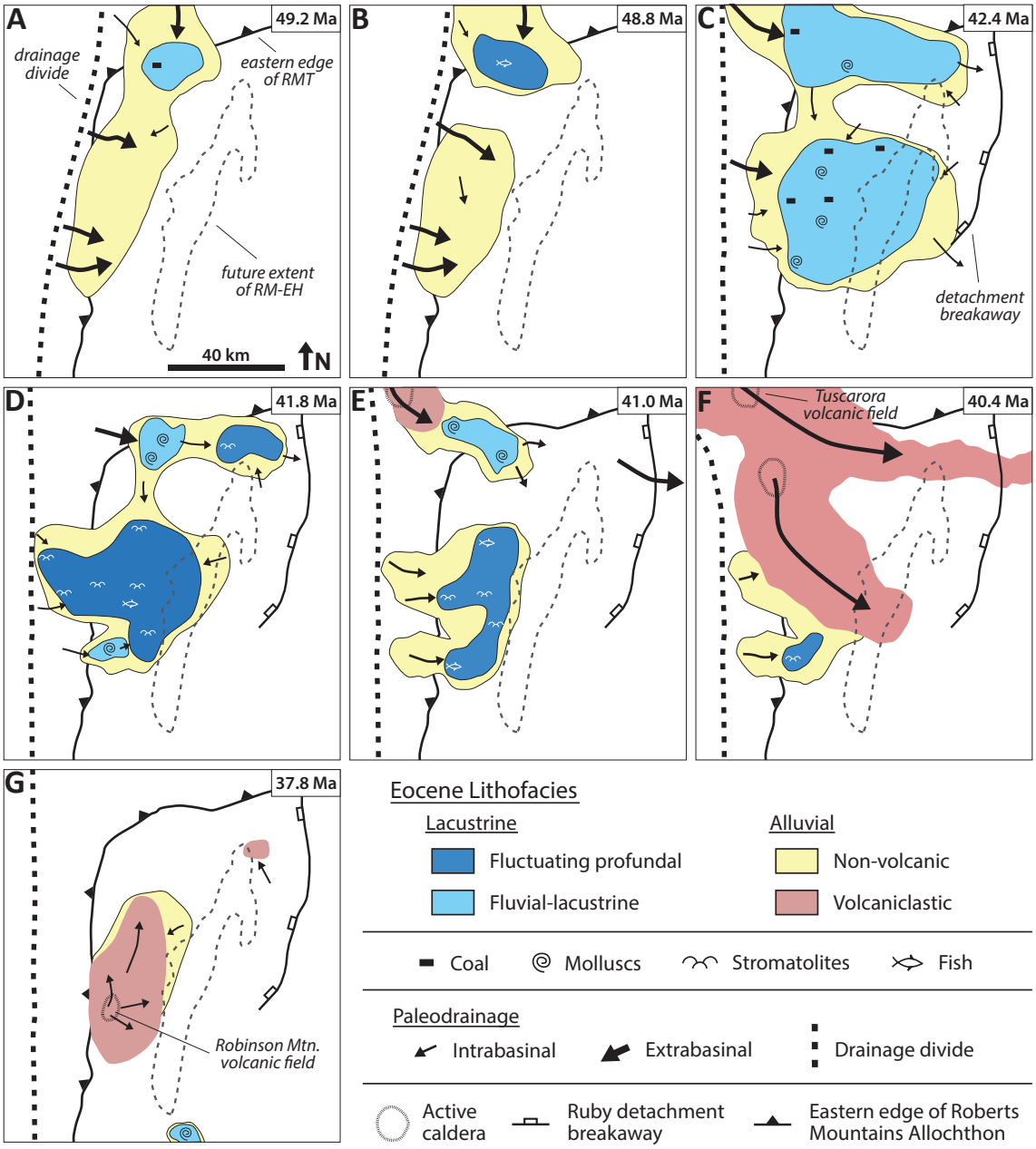

Figure 4.15. Schematic maps of northeastern Nevada at seven discrete time intervals showing the progression of Elko Formation lakes between 49.2 and 37.8 Ma. Landscape restored assuming 52% extension (Pape, 2010).

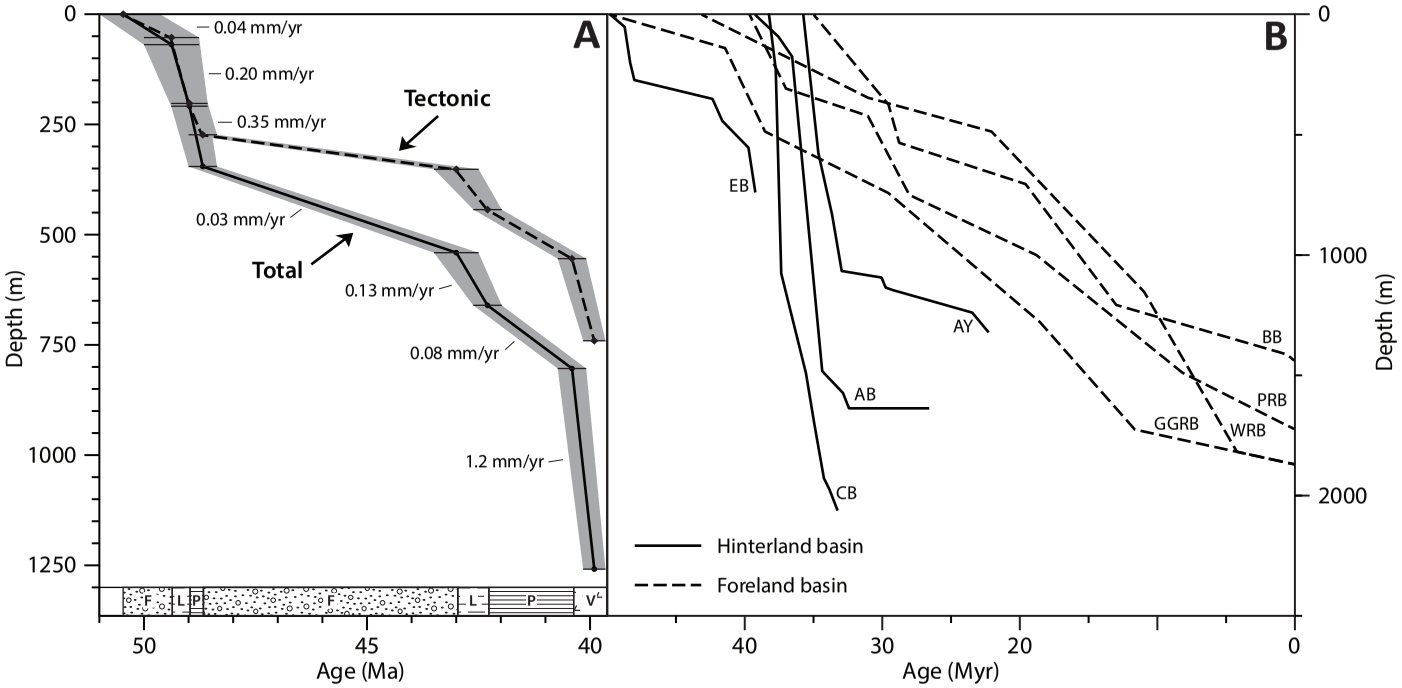

Figure 4.16. (A) Subsidence history curves for the Elko Basin showing total sediment accumulation and tectonic subsidence. Plots created using Nestor Cardozo's OSXBackstrip program assuming Airy isostatic compensation. See Table 4.3 for model input parameters. Abbreviations: F—fluvial; L—fluvial-lacustrine; P—fluctuating profundal; V—volcaniclastic. (B) Comparison of tectonic subsidence curves for several hinterland and foreland basins. Tectonic subsidence curves for the Sevier-Laramide depositional history of foreland basins from Fan and Carrapa (2014) and the Arizaro Basin from DeCelles et al. (2015); subsidence curves for the Ayaviri and Corque basins created using data provided in Roperch et al. (1999) and Perez and Horton (2014). Abbreviations: AY—Ayaviri Basin; AB—Arizaro Basin; CB—Corque Basin; GGRB—Greater Green River Basin; WRB—Wind River Basin; PRB—Powder River Basin; BB—Bighorn Basin.

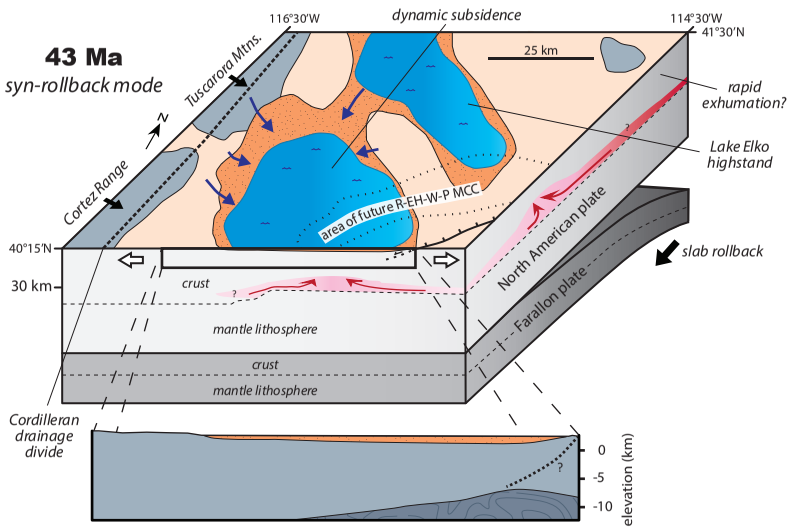
43 Ma
syn-rollback mode
116°30'W
114°30'W
41°30'N
40°15'N
Tuscarora Mtns.
Cortez Range
dynamic subsidence
25 km
rapid exhumation?
Lake Elko highstand
area of future R-EH-W-P MCC
North American plate
Farallon plate
slab rollback
30 km
crust
mantle lithosphere
crust
mantle lithosphere
Cordilleran drainage divide
0
-5
-10
elevation (km)

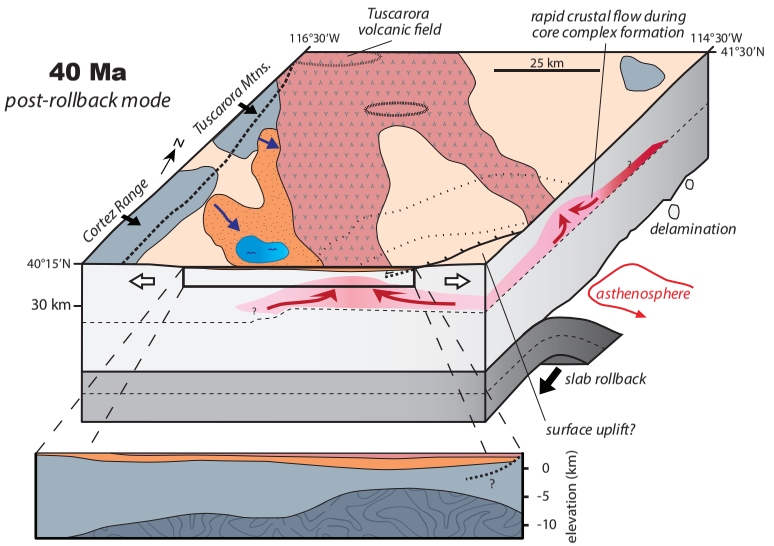
40 Ma
post-rollback mode
116°30'W
114°30'W
41°30'N
40°15'N
Tuscarora Mtns.
Cortez Range
Tuscarora volcanic field
rapid crustal flow during core complex formation
25 km
delamination
asthenosphere
slab rollback
surface uplift?
30 km
0
-5
-10
elevation (km)

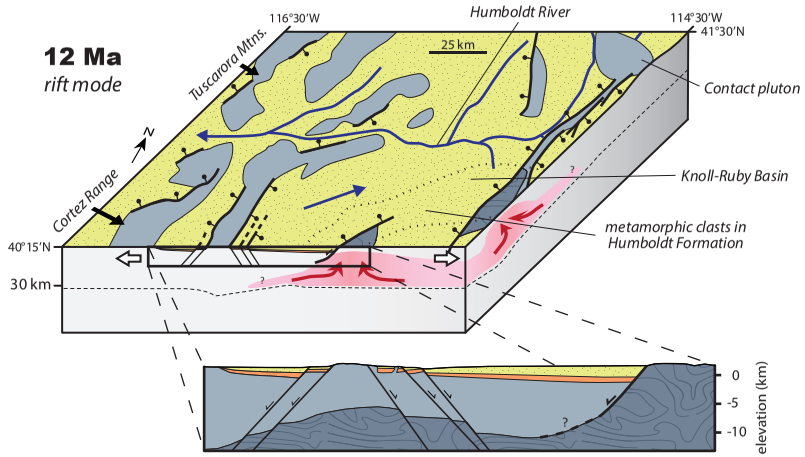
12 Ma
rift mode
116°30'W
114°30'W
41°30'N
40°15'N
Tuscarora Mtns.
Cortez Range
Humboldt River
25 km
Contact pluton
Knoll-Ruby Basin
metamorphic clasts in Humboldt Formation
30 km
0
-5
-10
elevation (km)

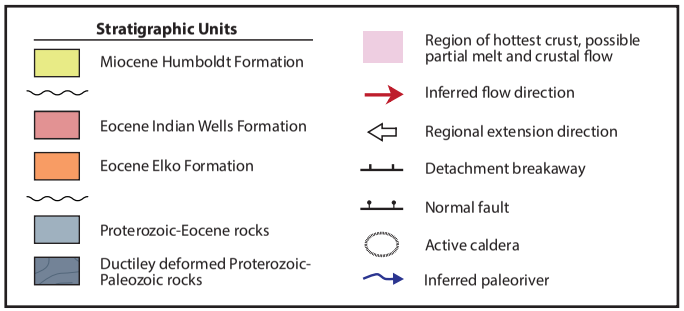
Stratigraphic Units
Miocene Humboldt Formation
Eocene Indian Wells Formation
Eocene Elko Formation
Proterozoic-Eocene rocks
Ductiley deformed Proterozoic-Paleozoic rocks
Region of hottest crust, possible partial melt and crustal flow
Inferred flow direction
Regional extension direction
Detachment breakaway
Normal fault
Active caldera
Inferred paleoriver

Figure 4.17. Schematic block diagrams of tectonic and paleogeographic evolution of the Elko Basin before and directly following Farallon slab removal and during Miocene Basin and Range-style extension. Interpretive cross-sections modified from Pape (2010) and Lund Snee et al. (2016); Miocene paleogeography modified from Wallace et al. (2008) and Camilleri et al. (2017); crustal-flow region and direction and paleo-Moho depth modified from Litherland and Klemperer (2017).

TABLE 4.1. ELKO FORMATION LITHOFACIES CLASSIFICATION

L*	Facies	Description	Interpretation	Occurrence
A.	Alluvial Macroassociation			
(i)	Axial Fluvial Association			
	1. Conglomerate	Traction-structured granule-cobble conglomerate; beds commonly fine upwards and are scoured at base	Braided river channel mouth bar	TC, CM, BL, EH, RM
	2. Trough cross-stratified and planar- to ripple- laminated sandstone	vF-C aggradational sandstone beds with trough cross-stratification; granule-pebble lag common	Braided river channel mouth bar	TC, CM, BL, EH, RM
(ii)	Floodplain Association			
	1. Planar-bedded sandstone and siltstone	Brown to green siliciclastic siltstone and vF-M sandstone; mm-scale laminations to structureless; convolute bedding and plant fossils common	River floodplain	EH, HV, CM, TB, TC
	2. Pedogenically altered siliciclastic mudstone and siltstone	Brightly colored mottled horizons of mudstone and siltstone; burrows, carbonate concretions, and calcic horizons common	River floodplain	EH, HV, PR, BL, TC
(iii)	Distal-Overbank Association			
	1. Siliciclastic mudstone-siltstone and structureless sandstone	Color mottled red, green, and brown siliciclastic mudstone-siltstone with thin F-C sandstone interbeds; sparse carbonaceous matter	River floodplain and distal lake-margin alluvial fan	EH, BL, TB, PR, DH, RM, TC
	2. Siliciclastic and carbonaceous mudstone and coal	Planar-laminated (mm-scale) brown mudstone with abundant carbonaceous matter and coal; plant matter; root traces	Marginal lacustrine environment with abundant organic matter; relatively high sediment supply	CM, EH, BR, BR
B.	Lacustrine Macroassociation			
(i)	Littoral Association			
	1. Laminated stromatolitic carbonate mudstone	Laterally continuous beds containing thin (cm-scale) algal mats, chert nodules, ostracodes, and ooids	Littoral, low relief lake floor	PR, DH, RM, TB, EH
	2. Cherty microbialitic limestone	Laterally continuous beds containing thin (cm-scale) algal mats, chert nodules, ostracodes, and ooids	Foreshore deposition in fresh water	PR, EH, TB, CM, DH, RM, BL
	3. Molluscan limestone	Tan to white dolomicritic limestone; structureless to faint plane-parallel laminations; gastropods, bivalves, carbonate intraclasts and peloids	Littoral shoal	DH, EH, PR, TC
(ii)	Sublittoral Association			
	1. Laminated carbonate mudstone and marlstone	Laminated (mm-scale) carbonate mudstone with calcitic to dolomitic composition and minimal organic matter	Sublittoral deposition in anoxic water	PR, CM, EH, BL, TB, DH
	2. Structureless carbonate mudstone and marlstone	Structureless carbonate mudstone; occasional plant fossils	Sublittoral deposition in Ca^{2+}-rich water	PR, CM, EH, TB, DH
(iii)	Profundal-Sublittoral Association			
	1. Microlaminated kerogen-rich carbonate mudstone and marlstone	Gray to black mudstone with µm to cm-scale laminations; high kerogen content	Profundal deposition in anoxic water	EH, PR, HV, CM
	2. Laminated mudstone	Brown to gray mudstone with µm to cm-scale laminations; abundant ostracodes and fish fossils	Profundal deposition in anoxic water	CM, PR, EH, TB
	3. Tuffaceous siltstone-sandstone	White to gray tuffaceous horizons with normal grading; rip-up clasts	Turbidite deposition of volcaniclastic debris and water-lain ash	HV, CM, PR, TB
(iv)	Palustrine Association			
	1. Bioturbated carbonate mudstone	Gray to tan mudstone with no visible laminations; color mottling; ostracode and plant fragments; infrequent root traces	Marginal lacustrine environment with abundant organic matter	CM, EH, PR, DH. BR

Notes: Facies description abbreviations correspond to sandstone modal grain size: vF-very fine; F-fine; M-medium; C-coarse.
*Lithofacies designation.
†Abbreviations: PR-Pinon Range; DH-Dixie Hills; RM-Robinson Mountain; TB-Twin Bridges; EH-Elko Hills; BR-Bullion Road; TC-Taylor Canyon; CM-Coal Mine Canyon; HV-Huntington Valley.

TABLE 4.2. CHARACTERISTIC ELKO FORMATION FLORA AND FAUNA

Common Name	Family	Genus	Lithofacies*	Interpretation	Reference
Fauna					
Bivalve	Sphaeriidae	Sphaerium	LBi3	Freshwater	Solomon et al., 1979; Solomon, 1981
Bivalve	Pisidiidae	Pisidium	LBi3	Freshwater	Solomon, 1981
Fish	Indeterminate	Indeterminate	LBii1, LBiii2	Stratified lake with fresh epilimnion	Moore et al., 1983; Haynes, 2003
Gastropod	Lymnaeidae	Stagnicola	LBi3	Freshwater	Smith and Ketner, 1976
Gastropod	Lymnaeidae	Lymnae	LBi2, LBi3	Freshwater	Solomon et al., 1979; Nutt and Good, 1998
Gastropod	Planorbidae	Biomphalaria	LBi2	Freshwater	Solomon et al., 1979
Ostracode	Candonidae	Candona	LAii1, LBi1, LBi2, LBi3, LBii1, LBiii1, LBiii2, LBiv1	Variable water chemistry	Solomon et al., 1979; Solomon, 1981; Swain, 1999
Toad	Pelobatidae	Elkobatrachus	LBi2	Shallow freshwater	Henrici and Haynes, 2006
Flora					
Algal microfossil	Dictyosphaeriaceae	Botryococcus	LBiv1, LAiii2	Fresh to relatively saline lake water	Wingate, 1983
Algal microfossil	Hydrodictyaceae	Pediastrum	LAiii2	Fresh water	Wingate, 1983
Algal microfossil	Zygnemataceae	Schizosporis	LAiii2	Open, stagnant, freshwater marsh	Solomon, 1981; Wingate, 1983
Algal microfossil		Sigmopollis	LAiii2	Shallow eutrophic freshwater, including areas of coal deposition	Wingate, 1983; Roehler and Martin, 1987
Algal microfossil	Zygnemataceae	Ovoidites	LAiii2	Shallow, oxygenated, freshwater	Solomon et al., 1979; Wingate, 1983
Angiosperm	Sparganiaceae	Sparganiaceaepollenites	LAiii2	Freshwater marsh	Wingate, 1983
Birch	Alnus	Alnipollenites	LAii1, LAii2, LAiii2, LBi3, LBiii1, LBii2, LBiv1	Fluvial and nearshore lacustrine	Wingate, 1983
Conifer	Cupresaceae	Metasequoia	LAii1, LAii2, LAiii2, LBii2, LBiii2, LBiv1		Axelrod, 1966; Smith and Ketner, 1976
Cypress	Cupresaceae	Taxodium	LAii1, LBii1		Smith and Ketner, 1976
Barberry	Berberidaceae	Mahonia			Smith and Ketner, 1976
Elm	Ulmaceae	Ulmus			Axelrod, 1966; Smith and Ketner, 1976
Maple	Aceraceae	Acer			Axelrod, 1966; Smith and Ketner, 1976; Wingate, 1983
Willow	Salicaceae	Salix			Axelrod, 1966; Smith and Ketner, 1976; Wingate, 1983

*Lithofacies where present.
†Abbreviations: PR-Pinon Range; DH-Dixie Hills; RM-Robinson Mountain; TB-Twin Bridges; EH-Elko Hills; BR-Bullion Road; TC-Taylor Canyon; CM-Coal Mine Canyon; HV-Huntington Valley.

TABLE 4.3. BACKSTRIPPING ANALYSIS INPUT DATA

Stratigraphic base (m)	Age base (Ma)	Stratigraphic top (m)	Age top (Ma)	Sediment properties		
				ϕ* (%)	$c^{\dagger}$ (km^{-1})	$\rho^{\S}$ (kg/m^3)
1262	50.5	1214	49.4	50	0.38	2650
1214	49.4	1135	49.0	63	0.72	2320
1135	49.0	1029	48.7	56	0.57	2720
1029	48.7	839	43.0	50	0.38	2650
839	43.0	746	42.3	63	0.72	2320
746	42.3	598	40.4	56	0.57	2720
598	40.4	0	39.9	45	0.38	2500

*initial porosity.
†compaction coefficient.
§mean density.

APPENDIX A

Supplemental Materials for Chapter I

METHODS

Zircon U-Pb Geochronology

For U-Pb analyses, approximately 1–3 kg of samples were crushed, and zircon and apatite were separated using conventional density separation techniques, including gemini table, heavy liquid (methylene iodide and bromoform), vibratory "wiggle-bug" separation, and magnetic separation at the University of Texas at Austin. Zircon grains were randomly poured onto epoxy pucks with double-sided sticky tape whereas all apatite grains that could be petrographically identified were picked from separates and mounted. U-Pb analyses of grains were conducted using laser ablation-high-resolution-inductively coupled plasma-mass spectrometry (LA-HR-ICP-MS) equipped with a PhotonMachine Analyte G.2 ArF excimer 193 nm laser and a two-volume Helex 9 sample cell, coupled to a ThermoFinnigan Element2 using a double-focusing magnetic sector ICP-MS. Zircon grains were ablated with a 30 μm laser spot size and apatite grains were ablated with a 40 μm spot size. Helium was used as the carrier gas and mixed with argon before entering the ICPMS. All analyses were conducted in static mode operated with an energy density of 1.43 J/cm2, and a pulse rate of 10 Hz. Analyses consisted of 6 cleaning shots, 25 seconds of baseline data collection, 30 seconds of laser dwell time, and 35 seconds of washout. Ablation rates of ~0.5μm/second mean that only the outer 15–17μm of zircons are typically sampled by this technique.

For all zircon samples, we attempted to analyze ~100 grains to identify with 95% confidence the grain age populations constituting >3% of the zircon population (Andersen, 2005). Elemental and isotopic fractionation of Pb/U and Pb isotopes, respectively, was corrected by interspersed analysis of primary zircon standard GJ1 ($^{206}Pb/^{238}U$ 601.7 ± 1.3 Ma; Jackson et al., 2004). The common unknown to standard measurement ratio is generally 4:1 at UT laboratory. Uncertainty resulting from calibration correction is generally 1–2% for both $^{206}Pb/^{207}Pb$ and $^{206}Pb/^{238}U$. An internal lab zircon standard (Pak 1) is used as a secondary reference. Standard correction is within 1–2% for $^{206}Pb/^{238}Pb$ and $^{206}Pb/^{207}Pb$ but increases for

younger grains due to low ^{207}Pb intensity. We therefore adopted the $^{206}Pb/^{238}Pb$ age of grains younger than 850 Ma and the $^{206}Pb/^{207}Pb$ age of grains older than 850 Ma. Age calculation was performed using Iolite (Igor Pro) and VizualAge (Petrus and Kamber, 2012), based on Isoplot V3 formulas (Ludwig, 2003), from baseline-subtracted intensities. No correction was applied for common Pb due to interferences in measurement of ^{204}Pb; however common Pb was evaluated graphically and high Pbc zones usually rejected. We excluded grains with >10% discordance and >10% uncertainty and only considered age peaks comprised of at least three grains. Following application of fractionation factor corrections, detrital zircon and apatite grains were checked for discordance using Isoplot 4.1 (Ludwig, 2008).

Zircon and Apatite (U-Th)/He Thermochronology

Following U-Pb geochronology, 4–7 zircon and apatite grains from each significant age population (consisting of >5 grains that were ~65–120 μm in width) were picked from epoxy mounts using a high-magnification polarizing microscope. Zircon and apatite grains that were metamict or had obvious cracks or inclusions were avoided. Grains were then measured to apply the alpha ejection correction factor (Farley, 2000), and individually packed in Pt packets at the University of Texas at Austin. Pt-wrapped grains were repeatedly laser heated using a 20W Nd:YAG laser for intervals of 10 min at ~1300°C until complete degassing of the aliquot was achieved (>99% ^{3}He extracted) at the University of Texas at Austin. Extracted gas was spiked using a ^{3}He tracer, cryogenically purified, and measured on a quadrupole noble gas mass spectrometer. Following complete degassing, zircon grains were removed from Pt packets whereas apatite grains were dissolved in Pt packets after being spiked with ^{230}Th, ^{235}U, ^{149}SM, and a REE tracer and digested in a pressure vessel with a HF-HNO_3 mixture for 72 hr at 255°C and 6 N HCL for 12 hr at 200°C. Parent nuclide concentrations were measured by isotope dilution on a Thermo Element2 HR-ICP-MS by comparing the spike to a gravimetric 1 ppb U-Th-Sm-REE normal solution. (U-Th)/He ages were calculated using standard FT corrections with estimated 8% analytical uncertainty (2σ) based on the Fish Canyon Tuff zircon (U-Th)/He standard.

Time-Temperature Path Modeling

Zircon (U-Th)/He ages and depositional ages from detrital zircon U-Pb geochronology and $^{40}Ar/^{39}Ar$ geochronology were used to inverse-model time-temperature (t-T) paths for grains with <10 Myr lag times using HeTYy version 1.9.1 (Ketcham, 2005). A closure temperature range of 180 ± 20°C was used for the zircon (U-Th)/He system (Reiners et al., 2004) and surface temperature was estimated at 20 ± 10°C. The following model parameters were used for each zircon grain: Calibration: "Guenthner et al., 2013 (Zircon)"; Abraded: "0 μm" (default); Model precision: "Good"; Stopping distances: "Ketcham et al. 2011"; Alpha calculation: "Ejection"; Age to report: "Corrected"; Alpha correction: "Ketcham et al. 2011"; Zoned? "No." Inverse modeling used the following parameters: Search Method: "Monte Carlo" (default); Subsegment spacing: "Random" (default); Ending condition: "Paths tried = 10000" (default); Result to display: "Paths"; Merit value for 'good' fit: "0.5" (default); Merit value for 'acceptable fit' = "0.05" (default). Segments: "monotonic consistent" (default); Randomizer style: "Episodic" (default).

ANDREW S. CANADA
Ph.D. Candidate
Geological Sciences
University of Idaho

University of Idaho

875 Perimeter Drive, MS 3022
Moscow, ID 83844-3022
(925) 389-6988
acanada@uidaho.edu

GSA
PO Box 9140
Boulder, CO 80301-9140

April 3, 2019

Dear Copyright Permissions Manager,

I am completing a doctoral dissertation at the University of Idaho this spring entitled "Eocene Exhumation and Lake Basin Development in the North American Cordilleran Hinterland, Northeastern Nevada, U.S.A." I would like your permission to reprint the following article in my dissertation, of which I am the primary author of the original material:

Canada, A.S., Cassel, E.J., Stockli, D.F., Smith, M.E., Jicha, B.R., and Singer B.S., 2019, Accelerating exhumation in the Eocene North American Cordilleran hinterland: Implications from detrital zircon (U-Th)/(He-Pb) double dating: Geological Society of America Bulletin, in press, doi:10.1130/B35160.1.

The article text, figures, and supplementary information submitted to the Geological Society of America Bulletin would be reproduced in my dissertation with no modifications and would include a complete article citation on the chapter title page. The material will be formatted in accordance with the University of Idaho dissertation guidelines. The requested permission extends to any future revisions and editions of my dissertation, including non-exclusive world rights in all languages, and to the prospective publication of my dissertation by ProQuest. ProQuest may produce and sell copies of my dissertation on demand and may make my dissertation available for free internet download at my request. These rights will in no way restrict republication of the material in any other form by you or by others authorized by you. Your signing of this letter will also confirm that the Geological Society of America owns the copyright to the above-described material.

If these arrangements meet with your approval, please sign the letter where indicated below and return it to me via the mail or email address above. Your prompt response is greatly appreciated. Thank you very much.

Sincerely,

Andrew Canada

Andrew S. Canada

PERMISSION GRANTED FOR THE USE REQUESTED ABOVE:

Geological Society of America

By: Jeanette Hammann

Title: GSA Director of Publications

Date: 4 April 2019

TABLE A.1. ESTIMATED DEPOSITIONAL AGES

Sample	Estimated depositional Age (Ma)	Source
NV11-049EP	44-40	Regional mapping by Henry and Faulds (1999) places Elko Formation calcareous siltstone and sandstone that overlies basal conglomerate strata (containing NV11-049EP) in the middle Eocene based on fossil flora taxa. The general absence of volcaniclastic material in this sequence indicates it was deposited before ca. 40 Ma (Smith et al., 2017). Correlative lithostratigraphic units in the Pinon Range were deposited after 44 Ma (Smith et al., 2017).
NV11-017EU	43-39	This sample is unconformably overlain by 36.69 ± 0.04 Ma dacite (Long et al., 2014). Detrital zircon grains from this sample define a Cretaceous maximum depositional age (73-70 Ma) and therefore may indicate this is a sample of the Newark Canyon Formation (Long et al., 2014). However, this sample is assumed to be an Elko Formation sample based on lithostratigraphic correlation and stratigraphic relation to sample NV11-014EU.
NV11-014EU	45-40	This sample is unconformably overlain by 36.69 ± 0.04 Ma dacite (Long et al., 2014). This sample contains one detrital zircon grain with a U-Pb age of 43 ± 1.1 Ma. Based on this age and lithostratigraphic correlation, this sample is inferred to be correlative with middle Eocene Elko Formation fluvial strata (Smith et al., 2017).

DETRITAL ZIRCON U-Pb ANALYSES

Elko Formation Samples

Analysis	U (ppm)	U/Th	207Pb/ 235U	±	206Pb/ 238U	±	err. corr.	207Pb/ 235U Age (Ma)	± (Ma)	206Pb/ 238U Age (Ma)	± (Ma)	207Pb/ 206Pb Age (Ma)	± (Ma)	Best age (Ma)	± (Ma)	Disc (%)
NV12-040CM: Coal Mine Canyon 41° 8' 2"N, 115° 38' 24"W																
12040CM_270	387	1.43	0.0480	0.0037	0.0065	0.0002	0.0017	47.5	3.6	41.7	1.4	478	75	41.7	1.4	12.2
12040CM_231	462	1.76	0.0455	0.0033	0.0065	0.0002	0.1822	45.1	3.2	41.8	1.5	420	84	41.8	1.5	7.3
12040CM_231	470	1.80	0.0453	0.0034	0.0065	0.0002	0.2299	44.9	3.3	41.9	1.5	431	84	41.9	1.5	6.7
12040CM_194	298	1.26	0.0580	0.0051	0.0070	0.0002	0.1059	57.0	4.8	45.2	1.5	790	110	45.2	1.5	20.7
12040CM_235	376	1.66	0.0511	0.0035	0.0071	0.0002	0.2695	50.5	3.4	45.3	1.4	494	79	45.3	1.4	10.3
12040CM_212	289	2.18	0.0544	0.0061	0.0071	0.0004	0.1198	53.7	5.8	45.9	2.3	550	130	45.9	2.3	14.5
12040CM_254	511	1.59	0.0513	0.0027	0.0072	0.0002	0.0153	50.8	2.6	46.5	1.5	357	58	46.5	1.5	8.5
12040CM_199	271.6	1.79	0.0614	0.0049	0.0073	0.0003	0.2692	60.3	4.6	46.6	1.8	634	99	46.6	1.8	22.7
12040CM_215	351	2.70	0.0525	0.0034	0.0073	0.0002	0.1164	51.8	3.2	46.6	1.4	475	75	46.6	1.4	10.0
12040CM_208	363.5	2.22	0.0530	0.0030	0.0073	0.0002	0.0150	52.4	2.9	46.8	1.3	499	83	46.8	1.3	10.7
12040CM_214	178.2	1.53	0.0567	0.0058	0.0074	0.0003	0.0935	55.7	5.5	47.5	2.2	740	130	47.5	2.2	14.7
12040CM_182	330	2.13	0.0549	0.0035	0.0074	0.0003	0.1190	54.1	3.3	47.6	1.6	513	75	47.6	1.6	12.0
12040CM_197	438	1.20	0.0511	0.0029	0.0074	0.0002	0.0741	50.6	2.8	47.8	1.5	359	51	47.8	1.5	5.5
12040CM_181	299	1.45	0.0516	0.0037	0.0075	0.0003	0.0032	51.0	3.6	47.9	1.9	440	100	47.9	1.9	6.1
12040CM_176	210.7	1.30	0.0700	0.0100	0.0075	0.0003	0.2623	68.0	9.3	48.0	1.7	950	140	48.0	1.7	29.4
12040CM_243	408	1.69	0.0592	0.0036	0.0075	0.0002	0.2209	58.3	3.4	48.1	1.3	597	78	48.1	1.3	17.5
12040CM_250	252	1.24	0.0529	0.0039	0.0075	0.0003	0.0145	52.2	3.8	48.2	1.9	452	79	48.2	1.9	7.7
12040CM_291	266	1.61	0.0632	0.0054	0.0075	0.0003	0.3924	61.9	5.1	48.3	1.7	920	110	48.3	1.7	22.0
12040CM_168	408	1.32	0.0578	0.0043	0.0075	0.0002	0.1614	56.9	4.2	48.5	1.4	549	90	48.5	1.4	14.8
12040CM_205	150.8	1.78	0.0605	0.0051	0.0076	0.0004	0.1119	59.4	4.9	48.5	2.4	626	92	48.5	2.4	18.4
12040CM_259	225.1	1.27	0.0546	0.0035	0.0076	0.0003	0.0131	53.9	3.3	48.5	1.9	549	71	48.5	1.9	10.0
12040CM_174	226.7	1.63	0.0554	0.0049	0.0076	0.0003	0.0532	54.5	4.7	48.6	1.6	570	110	48.6	1.6	10.8
12040CM_203	180.8	1.63	0.0590	0.0049	0.0076	0.0003	0.0434	58.0	4.7	48.6	2.1	660	110	48.6	2.1	16.2
12040CM_221	495	1.59	0.0563	0.0060	0.0076	0.0004	0.4186	55.5	5.8	48.6	2.8	450	120	48.6	2.8	12.4
12040CM_218	236	1.42	0.0544	0.0043	0.0076	0.0003	0.0161	53.6	4.2	48.7	2.1	510	100	48.7	2.1	9.1
12040CM_172	277	3.38	0.0501	0.0055	0.0076	0.0004	0.1073	49.5	5.3	48.8	2.4	520	150	48.8	2.4	1.4
12040CM_186	252	0.90	0.0610	0.0050	0.0076	0.0003	0.3073	59.9	4.8	48.9	1.8	610	110	48.9	1.8	18.4
12040CM_267	385	1.67	0.0504	0.0032	0.0076	0.0002	0.1061	49.8	3.1	48.9	1.5	298	53	48.9	1.5	1.8
12040CM_224	206.5	1.26	0.0559	0.0039	0.0077	0.0003	0.0371	55.1	3.7	49.2	1.8	541	83	49.2	1.8	10.7
12040CM_227	206.3	1.60	0.0614	0.0041	0.0077	0.0004	0.1179	60.3	3.9	49.2	2.3	659	84	49.2	2.3	18.4
12040CM_286	296	1.37	0.0543	0.0041	0.0077	0.0003	0.0340	53.5	4.0	49.2	1.7	480	70	49.2	1.7	8.0

12040CM_220	256.5	1.66	0.0581	0.0039	0.0077	0.0002	0.0608	57.2	3.7	49.4	1.5	574	73	49.4	1.5	13.6
12040CM_268	292	1.38	0.0586	0.0043	0.0077	0.0002	0.0664	58.2	4.0	49.4	1.6	605	75	49.4	1.6	15.1
12040CM_191	335	1.52	0.0568	0.0058	0.0077	0.0003	0.1054	55.8	5.4	49.5	1.8	470	100	49.5	1.8	11.3
12040CM_244	199	2.89	0.0621	0.0094	0.0077	0.0004	0.0593	60.4	8.3	49.5	2.2	553	93	49.5	2.2	18.0
12040CM_173	211.8	1.84	0.0522	0.0047	0.0077	0.0002	0.0246	51.5	4.5	49.6	1.5	468	91	49.6	1.5	3.7
12040CM_213	133	1.20	0.0584	0.0071	0.0077	0.0004	0.0113	56.1	6.4	49.6	2.7	730	120	49.6	2.7	11.6
12040CM_289	323	1.47	0.0587	0.0042	0.0077	0.0003	0.0547	57.7	4.1	49.6	1.6	553	70	49.6	1.6	14.0
12040CM_290	460	1.35	0.0554	0.0051	0.0078	0.0004	0.0704	54.7	4.9	49.8	2.3	450	140	49.8	2.3	9.0
12040CM_187	204	2.20	0.0549	0.0041	0.0078	0.0003	0.1318	54.1	4.0	49.9	1.9	550	93	49.9	1.9	7.8
12040CM_188	303	1.63	0.0658	0.0074	0.0078	0.0003	0.1446	64.3	6.9	50.0	1.6	770	160	50.0	1.6	22.2
12040CM_226	292	1.12	0.0557	0.0043	0.0078	0.0003	0.0671	54.9	4.1	50.0	1.6	640	120	50.0	1.6	8.9
12040CM_240	273	1.58	0.0600	0.0042	0.0078	0.0003	0.0629	59.0	4.0	50.1	1.6	630	74	50.1	1.6	15.1
12040CM_285	226	1.15	0.0671	0.0058	0.0078	0.0003	0.0478	65.7	5.5	50.2	2.2	870	130	50.2	2.2	23.6
12040CM_228	344	1.50	0.0572	0.0034	0.0079	0.0003	0.0441	56.3	3.3	50.4	1.6	536	81	50.4	1.6	10.5
12040CM_179	253	1.63	0.0631	0.0053	0.0079	0.0003	0.0276	61.9	5.0	50.5	1.8	684	93	50.5	1.8	18.4
12040CM_206	392	1.12	0.0560	0.0045	0.0079	0.0004	0.3829	55.2	4.3	50.5	2.2	371	59	50.5	2.2	8.5
12040CM_294	246	1.35	0.0559	0.0043	0.0079	0.0003	0.0442	55.0	4.1	50.5	1.8	555	92	50.5	1.8	8.2
12040CM_230	215.6	1.28	0.0578	0.0049	0.0079	0.0003	0.0290	56.9	4.7	50.7	2.0	630	100	50.7	2.0	10.9
12040CM_294	248	1.35	0.0557	0.0044	0.0079	0.0003	0.0435	54.9	4.2	50.7	1.9	557	95	50.7	1.9	7.7
12040CM_292	244	1.49	0.0590	0.0057	0.0079	0.0003	0.0653	57.9	5.5	50.9	1.9	750	120	50.9	1.9	12.1
12040CM_280	229	1.10	0.0592	0.0049	0.0080	0.0004	0.1059	58.2	4.7	51.2	2.3	515	88	51.2	2.3	12.0
12040CM_255	228.3	1.47	0.0677	0.0052	0.0080	0.0004	0.1971	66.2	4.9	51.3	2.2	820	110	51.3	2.2	22.5
12040CM_195	234	2.35	0.0713	0.0059	0.0080	0.0004	0.0801	69.7	5.5	51.4	2.3	970	120	51.4	2.3	26.3
12040CM_271	219.9	1.14	0.0576	0.0046	0.0080	0.0003	0.0711	56.7	4.4	51.4	1.9	604	91	51.4	1.9	9.3
12040CM_222	290	1.30	0.0605	0.0043	0.0080	0.0003	0.0584	59.4	4.1	51.5	1.8	559	87	51.5	1.8	13.3
12040CM_271	220.7	1.13	0.0584	0.0047	0.0080	0.0003	0.0471	57.5	4.5	51.6	1.9	624	92	51.6	1.9	10.3
12040CM_277	206	2.02	0.0627	0.0058	0.0080	0.0003	0.0162	61.4	5.5	51.6	2.1	730	110	51.6	2.1	16.0
12040CM_263	146.3	1.34	0.0663	0.0071	0.0081	0.0004	0.2659	64.8	6.7	52.0	2.7	1010	160	52.0	2.7	19.8
12040CM_253	224.2	1.31	0.0610	0.0046	0.0081	0.0004	0.3280	60.0	4.4	52.2	2.2	630	81	52.2	2.2	13.0
12040CM_293	160.3	1.17	0.0589	0.0050	0.0082	0.0004	0.1634	58.6	4.9	52.7	2.7	626	92	52.7	2.7	10.1
12040CM_192	223	1.40	0.0582	0.0045	0.0083	0.0003	0.0320	57.2	4.3	53.0	2.0	447	75	53.0	2.0	7.3
12040CM_246	281	1.44	0.0656	0.0047	0.0083	0.0004	0.1544	64.4	4.4	53.1	2.2	580	93	53.1	2.2	17.5
12040CM_256	193.4	1.32	0.0635	0.0090	0.0083	0.0005	0.0604	62.0	8.4	53.3	3.0	670	130	53.3	3.0	14.0
12040CM_274	282	1.44	0.0542	0.0042	0.0083	0.0003	0.0673	53.5	4.0	53.3	2.1	510	100	53.3	2.1	0.4
12040CM_272	188	1.89	0.0655	0.0065	0.0084	0.0004	0.1911	64.1	6.2	54.1	2.6	760	130	54.1	2.6	15.6
12040CM_281	204	1.58	0.0710	0.0074	0.0084	0.0004	0.0901	69.2	6.9	54.2	2.6	810	130	54.2	2.6	21.7
12040CM_190	250	1.59	0.0641	0.0046	0.0092	0.0003	0.0908	62.9	4.4	59.1	2.0	490	100	59.1	2.0	6.0
12040CM_217	106.5	2.14	0.0755	0.0082	0.0092	0.0004	0.0425	73.4	7.6	59.1	2.8	960	120	59.1	2.8	19.5
12040CM_265	300	1.54	0.0838	0.0052	0.0119	0.0004	0.0768	81.5	4.9	76.4	2.3	415	59	76.4	2.3	6.3
12040CM_171	514	3.07	0.1062	0.0040	0.0158	0.0003	0.0219	102.3	3.7	101.2	2.0	234	35	101.2	2.0	1.1

12040CM_177	128.2	0.86	0.5200	0.0190	0.0658	0.0015	0.2150	425.0	12.0	410.7	9.3	518	48	410.7	9.3	3.4
12040CM_257	288	0.91	1.7940	0.0270	0.1740	0.0021	0.3524	1042.3	9.8	1034.0	12.0	1057	20	1057.0	20.0	2.2
12040CM_239	128.1	0.59	2.0370	0.0340	0.1900	0.0026	0.3746	1127.0	11.0	1121.0	14.0	1120	18	1120.0	18.0	-0.1
12040CM_207	146	3.72	2.0320	0.0400	0.1866	0.0037	0.5011	1124.0	14.0	1105.0	20.0	1162	19	1162.0	19.0	4.9
12040CM_202	29.9	1.60	4.0800	0.1000	0.2997	0.0057	0.1108	1650.0	21.0	1689.0	28.0	1598	30	1598.0	30.0	-5.7
12040CM_283	77	1.45	4.3690	0.0840	0.3127	0.0051	0.3361	1704.0	16.0	1753.0	25.0	1637	21	1637.0	21.0	-7.1
12040CM_185	46.6	1.48	3.9590	0.0970	0.2723	0.0046	0.5979	1625.0	20.0	1552.0	23.0	1711	18	1711.0	18.0	9.3
12040CM_264	239	2.42	4.8200	0.0670	0.3255	0.0038	0.3485	1787.0	12.0	1816.0	19.0	1753	17	1753.0	17.0	-3.6
12040CM_245	159	2.84	4.9570	0.0750	0.3368	0.0053	0.4639	1810.0	13.0	1870.0	25.0	1757	17	1757.0	17.0	-6.4
12040CM_261	121	0.87	4.5080	0.0680	0.3019	0.0048	0.1619	1731.0	12.0	1700.0	24.0	1763	19	1763.0	19.0	3.6
12040CM_167	54.6	1.02	4.9220	0.0870	0.3220	0.0043	0.2010	1806.0	15.0	1799.0	21.0	1809	24	1809.0	24.0	0.6
12040CM_234	291.5	2.31	4.5730	0.0710	0.3009	0.0045	0.5095	1744.0	13.0	1695.0	22.0	1809	16	1809.0	16.0	6.3
12040CM_282	171	0.62	5.3570	0.0780	0.3511	0.0059	0.6646	1877.0	13.0	1939.0	28.0	1824	16	1824.0	16.0	-6.3
12040CM_193	44.7	1.89	5.0700	0.1200	0.3320	0.0067	0.4477	1830.0	20.0	1850.0	33.0	1826	26	1826.0	26.0	-1.3
12040CM_251	63.9	0.60	4.9070	0.0900	0.3240	0.0068	0.3459	1804.0	16.0	1812.0	34.0	1829	22	1829.0	22.0	0.9
12040CM_249	28.1	0.55	5.2500	0.1200	0.3437	0.0056	0.1953	1866.0	20.0	1904.0	27.0	1831	26	1831.0	26.0	-4.0
12040CM_204	89	1.80	5.1960	0.0960	0.3348	0.0063	0.4420	1850.0	16.0	1861.0	30.0	1832	18	1832.0	18.0	-1.6
12040CM_269	114.7	3.29	5.2260	0.0700	0.3381	0.0037	0.2553	1859.0	11.0	1877.0	18.0	1835	17	1835.0	17.0	-2.3
12040CM_209	35.3	0.49	5.2940	0.0990	0.3340	0.0052	0.3509	1865.0	16.0	1857.0	25.0	1856	21	1856.0	21.0	-0.1
12040CM_184	93.9	0.74	4.8770	0.0630	0.3114	0.0042	0.4514	1800.0	11.0	1747.0	21.0	1858	14	1858.0	14.0	6.0
12040CM_242	37	0.80	5.1000	0.1100	0.3280	0.0068	0.2629	1833.0	18.0	1827.0	33.0	1862	26	1862.0	26.0	1.9
12040CM_201	47.2	0.84	4.9200	0.0970	0.3143	0.0044	0.4143	1803.0	17.0	1761.0	22.0	1863	18	1863.0	18.0	5.5
12040CM_189	51.7	0.81	5.1900	0.1000	0.3293	0.0059	0.6810	1848.0	16.0	1834.0	28.0	1868	22	1868.0	22.0	1.8
12040CM_175	112.3	0.65	5.5510	0.0650	0.3473	0.0036	0.4352	1908.0	10.0	1921.0	17.0	1894	13	1894.0	13.0	-1.4
12040CM_170	80	0.48	5.6770	0.0900	0.3522	0.0047	0.4489	1928.0	13.0	1944.0	22.0	1916	15	1916.0	15.0	-1.5
12040CM_276	140.2	1.01	6.1510	0.0880	0.3703	0.0051	0.3577	1996.0	13.0	2030.0	24.0	1984	18	1984.0	18.0	-2.3
12040CM_247	49.6	1.08	7.1000	0.1100	0.4125	0.0071	0.3220	2128.0	14.0	2225.0	32.0	2035	19	2035.0	19.0	-9.3
12040CM_232	107.4	1.07	6.6910	0.0990	0.3790	0.0054	0.4910	2070.0	13.0	2071.0	25.0	2057	13	2057.0	13.0	-0.7
12040CM_169	76.5	1.06	6.5790	0.0920	0.3739	0.0057	0.4660	2055.0	12.0	2047.0	27.0	2058	14	2058.0	14.0	0.5
12040CM_278	41.7	1.03	6.5600	0.1400	0.3637	0.0068	0.3944	2057.0	19.0	1999.0	32.0	2138	24	2138.0	24.0	6.5
12040CM_216	49.9	1.18	7.2500	0.3100	0.3900	0.0110	0.8131	2137.0	39.0	2125.0	50.0	2168	28	2168.0	28.0	2.0
12040CM_216	52	0.61	7.8900	0.2100	0.4086	0.0077	0.5325	2218.0	25.0	2213.0	34.0	2205	29	2205.0	29.0	-0.4
12040CM_279	150.9	1.81	9.0700	0.1300	0.4493	0.0065	0.5564	2343.0	13.0	2391.0	29.0	2304	15	2304.0	15.0	-3.8
12040CM_212	79.1	1.06	8.5200	0.1200	0.4053	0.0051	0.7063	2286.0	12.0	2196.0	24.0	2362	13	2362.0	13.0	7.0
12040CM_295	232.2	2.12	11.6800	0.1100	0.5176	0.0056	0.5673	2579.8	8.6	2688.0	24.0	2514	10	2513.7	9.9	-6.9
12040CM_198	49.5	0.86	12.3200	0.1500	0.5024	0.0061	0.3858	2629.0	12.0	2623.0	26.0	2636	11	2636.0	11.0	0.5
12040CM_241	82.5	1.28	11.4600	0.2300	0.4555	0.0063	0.4977	2564.0	18.0	2419.0	28.0	2656	22	2656.0	22.0	8.9
12040CM_248	20.17	0.47	12.7400	0.2300	0.5100	0.0110	0.4139	2659.0	17.0	2654.0	47.0	2674	20	2674.0	20.0	0.7
12040CM_210	78.8	1.33	13.0000	0.1500	0.5155	0.0067	0.6049	2681.0	11.0	2679.0	28.0	2687	11	2687.0	11.0	0.3
12040CM_236	45.7	0.58	13.9100	0.2100	0.5425	0.0095	0.1049	2743.0	15.0	2792.0	40.0	2716	16	2716.0	16.0	-2.8

12040CM_236	45.7	0.58	13.9100	0.2100	0.5425	0.0095	0.1049	2743.0	15.0	2792.0	40.0	2716	16	2716.0	16.0	-2.8
12040CM_266	38.4	1.15	13.9500	0.2700	0.5262	0.0096	0.6070	2743.0	19.0	2723.0	41.0	2747	14	2747.0	14.0	0.9
12040CM_262	63.4	1.86	15.0700	0.2200	0.5662	0.0074	0.3129	2818.0	14.0	2891.0	31.0	2775	17	2775.0	17.0	-4.2

Analysis	U (ppm)	U/Th	207Pb/ 235U	±	206Pb/ 238U	±	err. corr.	207Pb/ 235U Age (Ma)	± (Ma)	206Pb/ 238U Age (Ma)	± (Ma)	207Pb/ 206Pb Age (Ma)	± (Ma)	Best age (Ma)	± (Ma)	Disc (%)
NV12-026CM: Coal Mine Canyon 41° 8' 5"N, 115° 38' 34"W																
NV12026CM_85	658	14.32	4.448	0.066	0.306	0.005	0.87632	1721.0	12.0	1721.0	23.0	1689	10	42.1	0.6	3.4
NV12026CM_112	396	43.90	0.816	0.015	0.097	0.002	0.54900	606.1	8.1	596.0	14.0	589	39	42.2	1.0	34.0
NV12026CM_3	252	1.87	0.048	0.002	0.007	0.000	0.05925	48.0	1.6	43.3	0.8	155	73	43.3	0.8	9.8
NV12026CM_55	369	1.93	0.052	0.001	0.008	0.000	0.10749	51.8	1.3	49.4	0.7	179	62	45.2	0.7	3.1
NV12026CM_2	307	1.63	0.048	0.001	0.007	0.000	0.16167	48.2	1.3	45.5	0.8	57	65	45.5	0.8	5.7
NV12026CM_110	183.6	1.66	4.691	0.054	0.299	0.003	0.67762	1764.8	9.7	1684.0	13.0	1839	11	45.5	1.1	10.8
NV12026CM_16	277	1.82	0.068	0.006	0.008	0.000	0.21355	66.8	5.5	49.4	1.0	660	150	46.1	0.7	0.5
NV12026CM_29	269	3.86	0.055	0.003	0.007	0.000	0.11049	54.4	2.6	46.1	0.8	400	110	46.2	0.7	1.9
NV12026CM_92	57	1.09	5.355	0.067	0.328	0.004	0.64136	1877.0	11.0	1828.0	20.0	1894	18	46.8	0.9	3.0
NV12026CM_79	74.9	2.31	6.190	0.170	0.343	0.007	0.81487	2002.0	24.0	1899.0	35.0	2103	26	46.9	0.6	2.9
NV12026CM_83	296	1.82	0.052	0.002	0.007	0.000	0.08074	51.3	1.4	47.5	0.7	274	62	46.9	1.3	6.6
NV12026CM_95	75.5	1.63	2.302	0.040	0.197	0.004	0.76029	1212.0	12.0	1157.0	22.0	1261	29	46.9	0.8	3.0
NV12026CM_34	399	1.46	5.217	0.049	0.315	0.005	0.67727	1855.0	8.0	1766.0	23.0	1946	15	47.0	0.8	2.4
NV12026CM_39	228	2.04	4.711	0.062	0.308	0.004	0.64617	1768.0	11.0	1728.0	18.0	1844	16	47.0	1.1	6.7
NV12026CM_41	350	2.06	0.050	0.001	0.008	0.000	0.23995	49.9	1.4	49.5	0.8	129	64	47.1	0.8	2.7
NV12026CM_12	317	1.26	1.955	0.045	0.119	0.003	0.93139	1100.0	16.0	724.0	19.0	1911	38	47.1	0.6	2.3
NV12026CM_1	442	2.08	0.052	0.002	0.007	0.000	0.09182	50.9	1.8	47.3	0.6	134	71	47.3	0.6	7.1
NV12026CM_68	335	1.57	0.050	0.001	0.008	0.000	0.11191	49.0	1.3	48.8	0.9	104	60	47.5	0.7	7.4
NV12026CM_6	378	2.16	0.051	0.001	0.007	0.000	0.07892	50.7	1.4	47.5	1.0	109	68	47.5	1.0	6.3
NV12026CM_99	91.3	0.79	13.010	0.140	0.499	0.005	0.55796	2680.0	10.0	2610.0	21.0	2711	13	47.8	0.9	2.5
NV12026CM_21	37.82	0.86	5.454	0.077	0.331	0.005	0.45152	1895.0	13.0	1843.0	22.0	1948	25	47.9	1.1	2.2
NV12026CM_47	189.3	1.80	0.051	0.003	0.007	0.000	0.07190	50.4	3.1	47.0	1.1	189	98	48.2	1.0	3.2
NV12026CM_46	184.7	2.55	14.110	0.170	0.507	0.006	0.84936	2756.0	12.0	2642.0	25.0	2863	11	48.3	0.8	1.1
NV12026CM_56	200	22.00	1.962	0.056	0.179	0.006	0.65240	1105.0	20.0	1059.0	35.0	1246	55	48.8	0.9	0.4
NV12026CM_19	552.8	2.71	0.061	0.002	0.008	0.000	0.13547	60.3	1.8	54.1	0.8	346	77	48.9	0.9	6.4
NV12026CM_102	116.7	1.37	0.055	0.003	0.008	0.000	0.02931	55.0	2.5	49.9	1.2	330	110	49.0	1.4	10.6
NV12026CM_93	280	1.92	0.058	0.003	0.008	0.000	0.01058	56.6	2.5	48.6	0.9	390	110	49.0	0.8	1.5
NV12026CM_121	272	1.02	0.049	0.002	0.007	0.000	0.00720	48.3	1.5	46.7	0.8	143	73	49.1	1.3	2.8
NV12026CM_40	359	2.45	0.049	0.001	0.007	0.000	0.11900	48.1	1.2	47.0	0.8	141	62	49.1	1.0	8.2
NV12026CM_71	349	2.17	0.051	0.001	0.008	0.000	0.39628	50.5	1.3	50.6	1.0	33	55	49.1	0.6	6.2
NV12026CM_51	209.9	2.03	0.046	0.001	0.007	0.000	0.06055	45.8	1.4	47.1	0.8	66	73	49.2	0.8	9.4
NV12026CM_73	272	3.00	0.056	0.002	0.008	0.000	0.34660	54.8	1.5	53.1	1.2	114	66	49.2	1.0	8.5
NV12026CM_8	592	1.91	0.051	0.001	0.008	0.000	0.02475	50.8	1.3	49.3	0.8	168	64	49.3	0.8	3.0
NV12026CM_96	355.1	0.81	0.198	0.006	0.023	0.000	0.69895	183.4	4.8	143.6	2.8	728	49	49.4	0.8	5.6
NV12026CM_44	459	2.15	0.059	0.002	0.008	0.000	0.06687	57.8	1.4	52.6	1.0	312	65	49.4	0.7	4.7

NV12026CM_54	346	2.00	0.058	0.002	0.008	0.000	0.07414	57.2	1.9	49.5	0.9	382	77	49.5	0.9	3.2
NV12026CM_35	277	2.36	4.648	0.072	0.307	0.004	0.75976	1756.0	13.0	1730.0	18.0	1792	13	49.5	0.8	0.8
NV12026CM_82	126.5	0.47	6.412	0.073	0.366	0.003	0.65011	2033.0	10.0	2012.0	15.0	2074	12	49.9	1.2	9.3
NV12026CM_30	45.5	0.74	12.670	0.170	0.488	0.005	0.69887	2654.0	13.0	2563.0	21.0	2717	13	49.9	0.7	1.2
NV12026CM_100	411	1.92	0.065	0.010	0.008	0.001	0.99192	61.3	8.3	54.1	4.5	273	91	50.0	1.1	0.6
NV12026CM_7	764	2.03	0.054	0.001	0.008	0.000	0.17580	53.6	1.1	50.6	0.8	161	53	50.6	0.8	5.7
NV12026CM_60	153.7	1.57	4.312	0.064	0.290	0.004	0.52066	1695.0	12.0	1639.0	19.0	1821	21	50.6	1.0	0.1
NV12026CM_13	340.4	1.39	0.049	0.001	0.007	0.000	0.32804	48.2	1.2	47.1	0.6	118	51	51.2	0.8	6.1
NV12026CM_69	96	1.91	4.844	0.058	0.310	0.004	0.59418	1794.0	10.0	1743.0	18.0	1851	17	51.2	1.2	2.0
NV12026CM_18	307.7	2.03	0.047	0.001	0.007	0.000	0.16239	46.3	1.4	46.1	0.7	107	60	51.4	1.1	7.2
NV12026CM_81	181	2.41	0.077	0.006	0.007	0.000	0.07279	74.8	5.5	45.0	1.4	1040	150	51.9	0.8	5.1
NV12026CM_101	482	2.37	0.055	0.001	0.008	0.000	0.29435	54.7	1.3	51.9	0.8	151	54	51.9	0.9	1.5
NV12026CM_64	14.01	0.81	11.710	0.190	0.463	0.007	0.71221	2579.0	15.0	2452.0	31.0	2711	18	52.0	0.8	6.2
NV12026CM_98	428	2.76	0.118	0.013	0.013	0.001	0.97279	112.0	12.0	84.0	6.7	633	90	52.1	0.8	3.6
NV12026CM_59	327	2.23	0.050	0.002	0.008	0.000	0.26304	49.8	1.6	48.2	1.0	138	71	52.1	0.8	4.1
NV12026CM_97	962	1.26	0.049	0.001	0.007	0.000	0.22708	48.3	0.7	46.9	0.6	132	38	52.1	1.4	3.9
NV12026CM_36	377	1.68	0.048	0.001	0.007	0.000	0.06082	47.1	1.2	46.2	0.7	136	61	52.6	1.0	8.9
NV12026CM_61	46.9	1.27	4.823	0.058	0.303	0.003	0.55487	1788.0	10.0	1706.0	14.0	1918	17	53.1	1.2	3.1
NV12026CM_14	543	1.87	0.055	0.002	0.008	0.000	0.05313	54.5	1.4	51.2	0.8	207	63	69.9	1.1	3.9
NV12026CM_22	397	1.71	0.056	0.002	0.008	0.000	0.35196	55.4	1.8	51.4	1.1	226	70	95.6	2.9	3.1
NV12026CM_108	285.7	2.02	0.061	0.003	0.007	0.000	0.44259	60.2	2.4	47.1	0.8	559	79	109.1	2.0	2.2
NV12026CM_124	462	2.53	0.055	0.002	0.008	0.000	0.53992	54.2	1.6	52.1	1.4	142	62	433.0	10.0	32.7
NV12026CM_5	820	1.17	0.620	0.009	0.075	0.001	0.61968	489.6	5.5	464.2	4.4	499	19	464.2	4.4	5.2
NV12026CM_109	61.8	1.58	1.847	0.036	0.171	0.002	0.64926	1067.0	13.0	1017.0	13.0	1088	27	575.0	15.0	7.0
NV12026CM_89	76.5	0.47	5.507	0.061	0.328	0.004	0.71404	1900.9	9.5	1828.0	18.0	1923	16	596.0	14.0	1.7
NV12026CM_88	432	1.94	0.061	0.003	0.008	0.000	0.25689	59.5	2.6	49.5	0.8	402	89	601.0	14.0	1.0
NV12026CM_90	91.7	1.32	4.834	0.060	0.302	0.004	0.72856	1790.0	10.0	1700.0	17.0	1820	14	601.0	13.0	1.1
NV12026CM_91	500	1.95	0.061	0.002	0.008	0.000	0.02110	59.8	2.0	50.8	0.7	375	80	603.0	12.0	0.9
NV12026CM_86	378	1.56	0.053	0.002	0.008	0.000	0.24032	52.4	1.8	49.1	0.6	187	70	1088.0	27.0	6.5
NV12026CM_111	399	44.20	0.818	0.015	0.098	0.002	0.46507	607.3	8.2	601.0	14.0	593	47	1260.0	40.0	10.8
NV12026CM_78	556	2.67	0.056	0.001	0.008	0.000	0.11830	55.4	1.4	52.0	0.8	237	60	1261.0	29.0	8.2
NV12026CM_113	408	43.15	0.818	0.016	0.098	0.002	0.50315	607.4	8.6	601.0	13.0	603	42	1513.0	24.0	8.0
NV12026CM_70	449	2.02	0.055	0.001	0.008	0.000	0.11579	54.3	1.3	52.1	0.8	149	53	1688.6	9.9	1.9
NV12026CM_66	377	1.94	0.052	0.002	0.008	0.000	0.25558	51.1	1.6	49.5	0.9	164	68	1707.0	18.0	3.3
NV12026CM_84	326	4.00	0.051	0.002	0.008	0.000	0.14636	50.2	1.6	51.2	1.2	178	74	1710.0	16.0	1.5
NV12026CM_114	402	43.25	0.821	0.014	0.098	0.002	0.49710	608.2	7.6	603.0	12.0	593	40	1731.0	32.0	3.2
NV12026CM_122	270	1.32	0.049	0.002	0.007	0.000	0.22693	48.4	1.5	46.9	0.8	161	73	1746.0	25.0	2.3
NV12026CM_118	291	3.24	0.060	0.004	0.008	0.000	0.32507	58.8	3.9	48.9	0.9	490	130	1762.0	32.0	0.3
NV12026CM_50	402	1.85	0.061	0.003	0.008	0.000	0.29321	60.2	2.6	48.7	1.0	541	97	1784.0	19.0	8.7
NV12026CM_28	95.4	1.46	4.510	0.100	0.297	0.006	0.90766	1732.0	19.0	1673.0	28.0	1797	21	1792.0	13.0	3.5

NV12026CM_23	359	1.96	0.053	0.002	0.008	0.000	0.08324	52.2	1.5	48.9	0.9	202	68	1797.0	21.0	6.9
NV12026CM_75	319	2.02	0.061	0.007	0.008	0.000	0.99788	59.9	6.4	50.8	3.1	384	83	1820.0	14.0	6.6
NV12026CM_48	274	1.88	0.080	0.008	0.008	0.000	0.51867	77.2	7.5	50.0	0.9	900	180	1821.0	21.0	10.0
NV12026CM_4	312	2.28	4.690	0.058	0.283	0.003	0.47485	1766.0	10.0	1608.0	13.0	1827	14	1827.0	14.0	12.0
NV12026CM_87	364	2.38	0.054	0.002	0.008	0.000	0.03370	53.8	2.1	49.2	1.0	255	83	1839.0	11.0	8.4
NV12026CM_32	254.1	1.70	0.057	0.003	0.007	0.000	0.35483	55.7	2.6	47.4	0.9	395	97	1844.0	16.0	6.3
NV12026CM_15	192.3	2.07	0.069	0.002	0.011	0.000	0.25905	67.3	1.9	69.9	1.1	-2	57	1851.0	16.0	7.5
NV12026CM_58	326	3.67	0.048	0.001	0.008	0.000	0.19776	47.8	1.2	48.3	0.8	78	59	1851.0	17.0	5.8
NV12026CM_11	120.2	2.17	4.779	0.056	0.311	0.003	0.67747	1780.3	9.7	1743.0	13.0	1865	14	1865.0	14.0	6.5
NV12026CM_63	377.5	2.20	0.055	0.002	0.008	0.000	0.20202	54.3	1.6	49.2	0.8	328	66	1867.0	15.0	3.9
NV12026CM_76	173.1	3.72	5.014	0.064	0.321	0.004	0.62703	1822.0	11.0	1794.0	17.0	1867	15	1894.0	18.0	3.5
NV12026CM_116	359.5	2.77	0.051	0.001	0.008	0.000	0.32210	50.8	1.2	49.3	0.7	122	54	1900.0	25.0	0.5
NV12026CM_49	264	2.20	0.054	0.003	0.008	0.000	0.58444	53.5	2.8	49.1	1.0	271	98	1918.0	17.0	11.1
NV12026CM_74	85.3	0.63	12.750	0.160	0.494	0.004	0.61202	2662.0	12.0	2586.0	18.0	2725	10	1923.0	16.0	4.9
NV12026CM_26	563	1.75	0.102	0.004	0.015	0.000	0.84527	98.7	3.2	95.6	2.9	116	41	1946.0	15.0	9.2
NV12026CM_17	50.6	4.33	4.663	0.056	0.304	0.003	0.62711	1760.0	10.0	1713.0	17.0	1851	16	1948.0	25.0	5.4
NV12026CM_67	291	1.46	0.047	0.002	0.007	0.000	0.35999	46.7	1.7	45.2	0.7	134	68	2074.0	12.0	3.0
NV12026CM_65	57.9	0.93	0.080	0.015	0.007	0.000	0.05637	77.0	13.0	47.8	1.3	780	230	2103.0	26.0	9.7
NV12026CM_123	418.7	2.25	0.053	0.001	0.008	0.000	0.39218	52.3	1.4	49.4	0.8	201	59	2689.0	33.0	6.9
NV12026CM_52	54.1	2.06	12.680	0.130	0.491	0.005	0.66863	2655.6	9.3	2573.0	23.0	2733	12	2711.0	18.0	9.6
NV12026CM_80	341.6	2.36	4.094	0.052	0.292	0.004	0.69690	1652.0	10.0	1650.0	21.0	1707	18	2711.0	13.0	3.7
NV12026CM_24	291	1.93	0.050	0.002	0.007	0.000	0.41301	49.0	1.6	47.9	1.1	95	69	2717.0	13.0	5.7
NV12026CM_62	59.4	0.93	4.265	0.047	0.287	0.003	0.37790	1687.1	8.9	1629.0	15.0	1784	19	2725.0	10.0	5.1
NV12026CM_43	320	2.35	0.075	0.006	0.008	0.000	0.20769	73.2	5.4	49.5	1.1	900	140	2733.0	12.0	5.9
NV12026CM_37	619	1.82	0.051	0.002	0.008	0.000	0.10651	50.5	1.6	49.9	0.7	145	49	2863.0	11.0	7.7
NV12026CM_120	451	1.74	0.050	0.001	0.008	0.000	0.22459	49.8	1.2	49.0	0.8	116	53	2963.0	37.0	12.9

Analysis	U (ppm)	U/Th	207Pb/ 235U	±	206Pb/ 238U	±	err. corr.	207Pb/ 235U Age (Ma)	± (Ma)	206Pb/ 238U Age (Ma)	± (Ma)	207Pb/ 206Pb Age (Ma)	± (Ma)	Best age (Ma)	± (Ma)	Disc (%)
NV12-102EH: Elko Hills 40°48'17"N, 115°43'5"W																
12102EH_97	145.8	0.91	0.04910	0.00310	0.00699	0.00019	0.07063	48.7	3.0	44.9	1.2	470	110	44.9	1.2	7.8
12102EH_92	186.1	1.43	0.07100	0.01700	0.00711	0.00015	0.26871	63.0	12.0	45.7	0.9	880	280	45.7	0.9	27.5
12102EH_61	495	0.55	0.04820	0.00220	0.00719	0.00012	0.06465	47.8	2.1	46.2	0.7	366	98	46.2	0.7	3.4
12102EH_75	229	1.28	0.05680	0.00610	0.00731	0.00018	0.15237	55.9	5.7	46.9	1.1	920	200	46.9	1.1	16.1
12102EH_53	286	0.88	0.04960	0.00180	0.00730	0.00013	0.02412	49.1	1.7	46.9	0.9	309	61	46.9	0.9	4.4
12102EH_58	433	0.62	0.05110	0.00240	0.00742	0.00012	0.15225	50.5	2.3	47.7	0.8	464	89	47.7	0.8	5.6
12102EH_60	370	0.81	0.05360	0.00220	0.00748	0.00011	0.33745	53.0	2.1	48.1	0.7	299	49	48.1	0.7	9.3
12102EH_107	247	0.73	0.05620	0.00340	0.00751	0.00012	0.04166	55.4	3.3	48.2	0.8	615	96	48.2	0.8	12.9
12102EH_69	166	1.10	0.08770	0.00780	0.00815	0.00022	0.14796	84.9	7.2	52.3	1.4	1150	150	52.3	1.4	38.4
12102EH_71	810	1.94	0.11730	0.00490	0.01704	0.00020	0.37828	112.5	4.4	108.9	1.2	222	57	108.9	1.2	3.2
12102EH_102	209.7	2.60	0.11750	0.00280	0.01753	0.00025	0.07866	112.8	2.6	112.0	1.6	202	39	112.0	1.6	0.7
12102EH_90	140.4	1.38	0.12180	0.00570	0.01755	0.00027	0.08281	116.5	5.2	112.2	1.7	354	53	112.2	1.7	3.7
12102EH_67	532	1.15	0.11770	0.00180	0.01780	0.00018	0.05846	112.9	1.6	113.7	1.2	131	23	113.7	1.2	0.7
12102EH_62	189.7	1.33	0.12370	0.00320	0.01834	0.00024	0.12524	118.3	2.9	117.1	1.5	204	30	117.1	1.5	1.0
12102EH_74	849	1.17	0.14770	0.00240	0.02063	0.00028	0.46445	139.8	2.1	131.7	1.7	258	22	131.7	1.7	5.8
12102EH_114	579	0.58	0.15180	0.00370	0.02215	0.00048	0.00402	143.4	3.2	141.2	3.0	201	24	141.2	3.0	1.5
12102EH_128	70.7	0.77	0.16900	0.01200	0.02248	0.00066	0.11775	158.0	10.0	143.3	4.1	435	97	143.3	4.1	9.3
12102EH_104	141.8	0.66	0.17190	0.00470	0.02385	0.00038	0.20905	160.9	4.1	151.9	2.4	320	41	151.9	2.4	5.6
12102EH_100	112.8	1.01	0.16100	0.00610	0.02404	0.00038	0.13179	151.4	5.3	153.1	2.4	207	49	153.1	2.4	1.1
12102EH_105	71	0.53	0.18200	0.01000	0.02418	0.00041	0.20754	169.4	8.5	154.0	2.5	439	73	154.0	2.5	9.1
12102EH_109	123	0.59	0.17030	0.00450	0.02443	0.00048	0.14525	159.5	3.9	155.6	3.0	265	31	155.6	3.0	2.4
12102EH_83	102	0.65	0.17260	0.00850	0.02468	0.00048	0.03898	159.9	6.9	157.1	3.0	349	57	157.1	3.0	1.8
12102EH_87	97.1	0.67	0.17210	0.00830	0.02471	0.00042	0.27478	160.8	7.2	157.3	2.6	303	47	157.3	2.6	2.2
12102EH_66	252	0.71	0.17180	0.00370	0.02480	0.00040	0.05875	160.9	3.2	157.9	2.5	241	30	157.9	2.5	1.9
12102EH_115	471	1.28	0.16990	0.00310	0.02485	0.00035	0.20725	159.3	2.7	158.2	2.2	198	26	158.2	2.2	0.7
12102EH_65	65.6	0.48	0.20100	0.01200	0.02515	0.00058	0.43565	185.0	10.0	160.1	3.7	589	99	160.1	3.7	13.5
12102EH_94	149	0.91	0.17330	0.00610	0.02516	0.00037	0.05291	162.0	5.3	160.2	2.4	296	48	160.2	2.4	1.1
12102EH_72	120	0.61	0.16990	0.00690	0.02526	0.00042	0.04414	159.1	5.9	160.8	2.6	310	100	160.8	2.6	1.1
12102EH_78	365	1.48	0.19800	0.01100	0.02571	0.00041	0.20166	182.6	9.1	163.7	2.6	435	86	163.7	2.6	10.4
12102EH_68	74.2	0.72	0.18000	0.00800	0.02599	0.00046	0.10532	167.6	6.9	165.4	2.9	378	82	165.4	2.9	1.3
12102EH_112	378	0.99	0.17830	0.00450	0.02615	0.00038	0.13370	167.1	4.0	166.4	2.4	203	37	166.4	2.4	0.4
12102EH_63	60.2	0.70	0.18200	0.01000	0.02624	0.00050	0.02919	169.3	8.6	167.0	3.1	375	72	167.0	3.1	1.4
12102EH_82	142.8	1.75	0.19010	0.00560	0.02647	0.00049	0.15499	176.5	4.7	168.4	3.1	295	35	168.4	3.1	4.6
12102EH_96	190.5	1.30	0.29300	0.01200	0.03833	0.00065	0.49439	260.3	9.0	242.4	4.0	426	57	242.4	4.0	6.9
12102EH_118	64.5	0.68	0.33000	0.01300	0.04484	0.00076	0.13673	289.0	10.0	282.7	4.7	404	62	282.7	4.7	2.2

12102EH_93	92.7	0.76	0.41000	0.01100	0.05484	0.00088	0.22341	348.7	7.7	344.1	5.4	436	51	344.1	5.4	1.3
12102EH_89	127.7	5.11	0.47140	0.00850	0.06162	0.00074	0.14103	391.8	5.8	385.4	4.5	434	29	385.4	4.5	1.6
12102EH_55	809	103.20	0.47760	0.00500	0.06315	0.00050	0.22175	396.4	3.4	394.7	3.0	411	13	394.7	3.0	0.4
12102EH_54	232	0.63	0.55130	0.00730	0.07145	0.00057	0.28892	445.7	4.8	444.9	3.4	465	17	444.9	3.4	0.2
12102EH_81	301	0.98	0.65900	0.01100	0.08090	0.00110	0.16235	513.9	6.5	501.2	6.4	571	23	501.2	6.4	2.5
12102EH_113	34.7	1.13	0.69200	0.02100	0.08330	0.00160	0.20879	536.0	12.0	516.9	9.9	608	40	516.9	9.9	3.6
12102EH_85	300	0.81	0.79300	0.01100	0.09330	0.00100	0.52291	592.8	6.3	575.0	6.2	669	17	575.0	6.2	3.0
12102EH_130	166.7	0.44	0.87300	0.01400	0.10170	0.00120	0.23868	638.7	7.6	624.1	7.2	675	21	624.1	7.2	2.3
12102EH_88	40.1	1.31	0.93800	0.02500	0.10690	0.00160	0.07442	670.0	13.0	654.7	9.5	723	37	654.7	9.5	2.3
12102EH_119	250.5	5.95	1.62600	0.01400	0.16210	0.00110	0.27334	980.0	5.4	968.1	6.0	1003	9	1002.7	9.0	3.5
12102EH_110	59.5	0.76	1.64700	0.03400	0.16440	0.00290	0.49238	990.0	14.0	981.0	16.0	1027	23	1027.0	23.0	4.5
12102EH_91	125.6	1.38	1.76700	0.02000	0.17300	0.00170	0.55583	1032.9	7.4	1028.6	9.4	1045	12	1045.0	12.0	1.6
12102EH_76	220.7	5.40	1.86600	0.03200	0.17980	0.00330	0.79540	1068.0	11.0	1066.0	18.0	1057	11	1057.0	11.0	0.9
12102EH_70	50.4	1.69	2.06200	0.02900	0.19110	0.00220	0.34214	1135.5	9.7	1129.0	11.0	1144	17	1144.0	17.0	1.3
12102EH_57	57	3.34	2.23300	0.03300	0.20300	0.00180	0.11794	1191.0	10.0	1191.3	9.7	1193	15	1193.0	15.0	0.1
12102EH_124	97.6	2.01	2.52200	0.02700	0.21620	0.00200	0.35499	1277.7	7.8	1262.0	10.0	1305	12	1305.0	12.0	3.3
12102EH_103	74.1	1.51	2.67700	0.03300	0.22650	0.00240	0.30075	1321.4	9.0	1316.0	13.0	1324	15	1324.0	15.0	0.6
12102EH_111	260	1.26	2.69600	0.01900	0.22600	0.00140	0.45565	1327.1	5.1	1313.6	7.5	1345	8	1345.3	7.7	2.4
12102EH_80	124.3	1.39	3.14700	0.02300	0.25060	0.00190	0.42693	1444.1	5.6	1441.5	9.9	1435	11	1435.0	11.0	0.5
12102EH_86	193	0.97	3.22000	0.02900	0.25530	0.00250	0.68958	1461.6	6.9	1466.0	13.0	1448	8	1447.5	8.1	1.3
12102EH_52	127.7	1.82	4.80500	0.03700	0.31980	0.00230	0.57509	1785.4	6.5	1788.0	11.0	1784	7	1784.0	6.6	0.2
12102EH_51	99	1.51	4.68700	0.05100	0.31100	0.00300	0.50976	1765.4	8.8	1745.0	15.0	1789	10	1789.0	9.5	2.5
12102EH_64	240	1.70	6.60100	0.04500	0.37500	0.00220	0.66514	2062.8	5.9	2053.0	10.0	2076	6	2076.1	5.8	1.1
12102EH_56	152.7	1.63	13.19000	0.11000	0.52040	0.00410	0.85280	2692.8	7.7	2700.0	18.0	2685	6	2684.9	5.5	0.6

Analysis	U (ppm)	U/Th	207Pb/ 235U	±	206Pb/ 238U	±	err. corr.	207Pb/ 235U Age (Ma)	± (Ma)	206Pb/ 238U Age (Ma)	± (Ma)	207Pb/ 206Pb Age (Ma)	± (Ma)	Best age (Ma)	± (Ma)	Disc (%)
NV11-049EP: Emigrant Pass 40° 41' 9"N , 116° 17' 17"W																
11049EP_33_2	141.8	1.30	0.29890	0.00830	0.03924	0.00052	0.27198	265.2	6.5	248.1	3.2	412	36	248.1	3.2	6.4
11049EP_33_1	170.5	1.45	0.28910	0.00690	0.04093	0.00069	0.11962	257.6	5.5	258.6	4.3	291	40	258.6	4.3	0.4
11049EP_96	204	1.26	0.62400	0.01200	0.07893	0.00095	0.09109	492.8	7.3	489.7	5.7	500	28	489.7	5.7	0.6
11049EP_97	220.4	1.47	0.63730	0.00660	0.08065	0.00082	0.05380	501.1	4.3	500.0	4.9	507	21	500.0	4.9	0.2
11049EP_111	216.1	0.83	0.77200	0.01100	0.09113	0.00095	0.20366	581.2	6.1	562.2	5.6	648	21	562.2	5.6	3.3
11049EP_87	149.1	0.40	1.84300	0.02400	0.17800	0.00180	0.15417	1060.1	8.5	1055.9	9.9	1081	18	1081.0	18.0	2.3
11049EP_76	51.6	0.85	1.79900	0.03300	0.17430	0.00230	0.32094	1044.0	12.0	1037.0	12.0	1092	20	1092.0	20.0	5.0
11049EP_62	49.7	1.90	2.48900	0.03800	0.21530	0.00260	0.40810	1271.0	11.0	1257.0	14.0	1274	15	1274.0	15.0	1.3
11049EP_81	123.5	1.93	3.04300	0.03200	0.24720	0.00250	0.20643	1420.0	7.6	1424.0	13.0	1413	12	1413.0	12.0	0.8
11049EP_28	182	1.63	3.14800	0.02600	0.25030	0.00200	0.43809	1444.2	6.4	1440.0	10.0	1444	10	1443.7	9.9	0.3
11049EP_26	74.9	1.16	4.04500	0.04800	0.29070	0.00270	0.32029	1643.9	9.9	1645.0	14.0	1645	12	1645.0	12.0	0.0
11049EP_112	92.7	1.14	4.09600	0.05400	0.29280	0.00290	0.57032	1654.0	11.0	1655.0	14.0	1653	13	1653.0	13.0	0.1
11049EP_2	128.6	1.03	4.14900	0.03200	0.29320	0.00230	0.40055	1664.5	6.1	1657.0	11.0	1683	9	1682.8	9.0	1.5
11049EP_90	85.5	1.42	4.18100	0.03500	0.29440	0.00270	0.19640	1669.8	6.9	1663.0	13.0	1686	10	1685.9	9.9	1.4
11049EP_60	389	4.80	3.83300	0.03100	0.26840	0.00280	0.59006	1599.4	6.5	1532.0	14.0	1686	10	1686.0	10.0	9.1
11049EP_50	77.4	1.92	4.30500	0.05400	0.29960	0.00340	0.49714	1695.0	11.0	1691.0	17.0	1696	10	1696.2	9.7	0.3
11049EP_82	211.1	1.30	3.88900	0.03500	0.27050	0.00290	0.45884	1611.0	7.2	1543.0	15.0	1709	12	1709.0	12.0	9.7
11049EP_100	11.4	1.21	4.07000	0.13000	0.28500	0.00610	0.46637	1648.0	25.0	1616.0	31.0	1722	38	1722.0	38.0	6.2
11049EP_89	220.5	1.16	4.32300	0.03900	0.29150	0.00230	0.54438	1697.3	7.4	1649.0	11.0	1770	10	1770.0	10.0	6.8
11049EP_105	43.2	0.57	4.77900	0.06600	0.31850	0.00440	0.40457	1782.0	12.0	1782.0	21.0	1782	17	1782.0	17.0	0.0
11049EP_49	89.5	2.43	4.83700	0.03800	0.31950	0.00260	0.37477	1791.0	6.6	1787.0	13.0	1783	9	1783.1	9.0	0.2
11049EP_66	28.42	0.80	5.07700	0.06900	0.33060	0.00500	0.32683	1831.0	12.0	1840.0	24.0	1825	17	1825.0	17.0	0.8
11049EP_102	64.2	0.50	4.92200	0.05400	0.32220	0.00300	0.31465	1806.8	9.1	1800.0	15.0	1825	14	1825.0	14.0	1.4
11049EP_48	111.2	1.27	5.01200	0.04400	0.32670	0.00280	0.36361	1820.9	7.4	1822.0	14.0	1825	10	1825.2	9.7	0.2
11049EP_24	78	1.06	5.15100	0.04800	0.33250	0.00310	0.59376	1844.0	7.9	1852.0	15.0	1834	9	1833.9	9.1	1.0
11049EP_77	155.3	0.93	5.08200	0.03600	0.32970	0.00230	0.31664	1832.7	6.0	1837.0	11.0	1835	10	1835.0	10.0	0.1
11049EP_93	79.5	0.89	5.15600	0.04900	0.33280	0.00300	0.27504	1844.8	8.1	1851.0	15.0	1838	11	1838.0	11.0	0.7
11049EP_52	89.1	0.74	5.11800	0.06500	0.32810	0.00400	0.56987	1839.0	11.0	1829.0	20.0	1839	13	1839.0	13.0	0.5
11049EP_8	50.5	1.23	5.03800	0.05400	0.32480	0.00360	0.51411	1827.3	9.4	1812.0	17.0	1841	13	1841.0	13.0	1.6
11049EP_64	159.8	1.06	5.22500	0.04500	0.33700	0.00230	0.44401	1856.1	7.3	1872.0	11.0	1842	9	1842.3	8.7	1.6
11049EP_83	112	0.90	4.82200	0.04900	0.31050	0.00260	0.50772	1789.1	8.3	1743.0	13.0	1844	8	1844.0	7.9	5.5
11049EP_39	80.8	0.51	5.16800	0.05300	0.33270	0.00340	0.59084	1847.9	8.5	1851.0	16.0	1844	10	1844.1	9.7	0.4
11049EP_63	105.3	1.91	5.12800	0.05900	0.32980	0.00430	0.66175	1840.4	9.7	1837.0	21.0	1844	9	1844.2	9.2	0.4
11049EP_31	56.1	25.50	5.22600	0.06000	0.33480	0.00270	0.27861	1856.0	9.8	1861.0	13.0	1846	13	1846.0	13.0	0.8
11049EP_19	45.9	1.59	5.10200	0.06000	0.32870	0.00360	0.38405	1836.0	10.0	1832.0	18.0	1848	12	1848.0	12.0	0.9

11049EP_84	101.6	1.94	5.09600	0.04900	0.32890	0.00320	0.46878	1835.8	8.2	1833.0	16.0	1850	10	1850.0	10.0	0.9
11049EP_42	49.5	0.67	4.98600	0.06500	0.31720	0.00380	0.30306	1817.0	11.0	1776.0	19.0	1852	12	1852.0	12.0	4.1
11049EP_73	63.8	0.45	5.09100	0.06700	0.32830	0.00410	0.45884	1833.0	11.0	1830.0	20.0	1853	13	1853.0	13.0	1.2
11049EP_85	115.2	0.90	5.14200	0.06100	0.32940	0.00370	0.62348	1842.0	10.0	1838.0	19.0	1855	9	1855.2	9.1	0.9
11049EP_43	153.9	1.69	5.27300	0.03900	0.33490	0.00240	0.61959	1864.1	6.3	1862.0	12.0	1867	8	1866.6	7.6	0.2
11049EP_1	117.8	1.24	4.95700	0.04600	0.31400	0.00280	0.70791	1811.5	7.9	1760.0	14.0	1869	9	1868.9	8.9	5.8
11049EP_101	78.3	1.23	5.15000	0.13000	0.32910	0.00850	0.70520	1844.0	22.0	1842.0	43.0	1869	19	1869.0	19.0	1.4
11049EP_70	59	2.09	5.25700	0.06200	0.33260	0.00400	0.46134	1861.0	10.0	1850.0	19.0	1876	12	1876.0	12.0	1.4
11049EP_38	112.3	1.60	5.45700	0.05300	0.34160	0.00340	0.66106	1893.1	8.4	1894.0	16.0	1898	9	1897.9	8.6	0.2
11049EP_98	15.85	0.62	4.96000	0.11000	0.31390	0.00560	0.15999	1812.0	17.0	1759.0	27.0	1909	24	1909.0	24.0	7.9
11049EP_65	30.97	0.94	5.35200	0.08000	0.33100	0.00440	0.21985	1877.0	12.0	1843.0	22.0	1915	16	1915.0	16.0	3.8
11049EP_95	126.8	1.91	5.44600	0.04200	0.33720	0.00300	0.43128	1891.7	6.6	1873.0	14.0	1919	9	1919.4	9.1	2.4
11049EP_91	57.4	0.97	5.46100	0.06500	0.33770	0.00340	0.32786	1893.0	10.0	1875.0	16.0	1926	13	1926.0	13.0	2.6
11049EP_75	57	0.79	5.67900	0.07100	0.34690	0.00340	0.46326	1927.0	11.0	1920.0	16.0	1940	12	1940.0	12.0	1.0
11049EP_44	49.9	1.63	5.48600	0.05900	0.33480	0.00330	0.47266	1897.5	9.2	1861.0	16.0	1942	12	1942.0	12.0	4.2
11049EP_37	161.3	0.78	4.85000	0.05000	0.28470	0.00330	0.70791	1794.4	8.4	1615.0	17.0	2001	11	2001.0	11.0	19.3
11049EP_67	97	0.60	6.12900	0.06700	0.36040	0.00280	0.34881	1993.5	9.5	1984.0	13.0	2008	13	2008.0	13.0	1.2
11049EP_108	133.6	0.80	6.50300	0.05400	0.37360	0.00330	0.65008	2047.2	7.7	2046.0	15.0	2049	9	2048.6	9.2	0.1
11049EP_27	222.8	2.52	6.82000	0.04600	0.38350	0.00230	0.37483	2088.1	6.0	2093.0	11.0	2080	8	2080.0	8.2	0.6
11049EP_51	69.7	0.49	6.62200	0.08100	0.37550	0.00400	0.30311	2062.0	11.0	2055.0	19.0	2084	14	2084.0	14.0	1.4
11049EP_56	144	1.74	6.81700	0.05300	0.38320	0.00330	0.67101	2087.5	6.9	2091.0	15.0	2085	7	2085.0	6.9	0.3
11049EP_18	576	1.33	3.95600	0.03500	0.22010	0.00190	0.44407	1624.9	7.2	1283.0	10.0	2100	12	2100.0	12.0	38.9
11049EP_20	109.4	1.05	5.26000	0.12000	0.28270	0.00600	0.68861	1861.0	20.0	1604.0	30.0	2145	22	2145.0	22.0	25.2
11049EP_36	67.7	1.02	7.06100	0.08300	0.38120	0.00420	0.39749	2118.0	10.0	2087.0	20.0	2162	13	2162.0	13.0	3.5
11049EP_41	91.4	0.46	9.12200	0.08400	0.41410	0.00330	0.54108	2349.6	8.4	2233.0	15.0	2459	9	2458.9	8.8	9.2
11049EP_110	204	1.22	11.39000	0.12000	0.48830	0.00620	0.66820	2555.4	9.9	2563.0	27.0	2553	10	2553.4	9.9	0.4
11049EP_79	75	1.43	11.46000	0.12000	0.48910	0.00500	0.53156	2562.0	10.0	2566.0	22.0	2556	9	2556.2	9.4	0.4
11049EP_29	172.2	1.19	11.42000	0.10000	0.48620	0.00550	0.64418	2557.7	8.4	2554.0	24.0	2568	7	2568.3	7.3	0.6
11049EP_40	111.8	1.37	12.66300	0.07800	0.50950	0.00350	0.51080	2656.1	5.5	2654.0	15.0	2656	6	2655.7	5.5	0.1
11049EP_78	54.2	0.72	12.66000	0.14000	0.50160	0.00690	0.61726	2654.0	10.0	2620.0	30.0	2668	10	2668.0	10.0	1.8
11049EP_58_1	58.6	1.05	12.70000	0.11000	0.50610	0.00470	0.62827	2657.9	8.1	2639.0	20.0	2674	8	2673.5	7.9	1.3
11049EP_58_2	59.8	0.74	13.02000	0.13000	0.51830	0.00590	0.63318	2680.2	9.3	2691.0	25.0	2677	9	2677.4	9.4	0.5
11049EP_34	72.8	0.61	12.90000	0.11000	0.51250	0.00460	0.54593	2673.0	8.2	2667.0	20.0	2679	9	2678.9	8.7	0.4
11049EP_106	85.9	1.59	13.70000	0.15000	0.53850	0.00480	0.71279	2728.0	10.0	2776.0	20.0	2688	6	2687.7	6.3	3.3
11049EP_59	115.7	1.26	12.86000	0.11000	0.50550	0.00370	0.73621	2669.9	7.8	2637.0	16.0	2695	6	2694.8	6.2	2.1
11049EP_54	51.2	2.06	13.37000	0.12000	0.52060	0.00620	0.61225	2705.2	8.3	2701.0	26.0	2705	10	2705.1	9.7	0.2
11049EP_53	102.1	0.59	13.51000	0.10000	0.52640	0.00430	0.67055	2716.2	7.1	2726.0	18.0	2707	5	2707.4	5.1	0.7
11049EP_109	52.8	1.45	13.62000	0.19000	0.52610	0.00530	0.50811	2722.0	13.0	2724.0	22.0	2721	12	2721.0	12.0	0.1
11049EP_3	41.1	0.51	13.66000	0.11000	0.53020	0.00530	0.45481	2725.7	7.7	2741.0	22.0	2722	7	2721.6	7.4	0.7
11049EP_94	35.9	0.42	12.86000	0.14000	0.49900	0.00560	0.48612	2670.0	10.0	2609.0	24.0	2722	12	2722.0	12.0	4.2

11049EP_71	18.43	2.46	11.95000	0.20000	0.46270	0.00740	0.64551	2598.0	16.0	2450.0	33.0	2726	14	2726.0	14.0	10.1
11049EP_61	50.6	0.80	13.67000	0.19000	0.52120	0.00820	0.62622	2726.0	13.0	2710.0	33.0	2739	14	2739.0	14.0	1.1
11049EP_47	37.69	0.59	13.98000	0.17000	0.52870	0.00660	0.61820	2747.0	11.0	2735.0	28.0	2757	10	2757.3	9.8	0.8
11049EP_104	123.5	1.73	13.74000	0.11000	0.52070	0.00400	0.38752	2732.4	7.4	2702.0	17.0	2761	7	2760.6	6.6	2.1
11049EP_16	51.4	0.88	14.26000	0.16000	0.53190	0.00620	0.62574	2766.0	11.0	2754.0	28.0	2779	10	2779.0	10.0	0.9
11049EP_86	24.1	0.69	14.42000	0.20000	0.53480	0.00760	0.51557	2781.0	14.0	2770.0	30.0	2794	15	2794.0	15.0	0.9
11049EP_32	63	0.67	16.07000	0.15000	0.56130	0.00610	0.60948	2880.2	9.1	2871.0	25.0	2874	10	2874.0	10.0	0.1
11049EP_7	40.4	0.83	16.49000	0.16000	0.55240	0.00610	0.45311	2904.7	9.2	2834.0	25.0	2964	8	2964.2	8.2	4.4
11049EP_23	59	0.64	23.60000	0.32000	0.65300	0.01100	0.71315	3251.0	13.0	3240.0	44.0	3255	10	3254.5	9.7	0.4

Analysis	U (ppm)	U/Th	207Pb/ 235U	±	206Pb/ 238U	±	err. corr.	207Pb/ 235U Age (Ma)	± (Ma)	206Pb/ 238U Age (Ma)	± (Ma)	207Pb/ 206Pb Age (Ma)	± (Ma)	Best age (Ma)	± (Ma)	Disc (%)
NV12-008TC: Taylor Canyon 41° 16' 2"N, 116° 6' 19"W																
NV12008TC_92	334	2.61	0.04470	0.00240	0.00633	0.00020	0.19180	44.3	2.3	40.7	1.3	200	110	40.7	1.3	8.1
NV12008TC_89	458	2.15	0.04250	0.00210	0.00639	0.00024	0.31678	42.3	2.1	41.0	1.5	130	120	41.0	1.5	3.1
NV12008TC_68	236.1	0.87	0.04570	0.00290	0.00641	0.00023	0.03514	45.3	2.8	41.2	1.5	310	160	41.2	1.5	9.1
NV12008TC_91	417	2.10	0.04630	0.00260	0.00646	0.00016	0.08025	45.9	2.6	41.5	1.0	260	130	41.5	1.0	9.6
NV12008TC_103	291	2.24	0.04210	0.00260	0.00646	0.00027	0.46186	41.8	2.5	41.5	1.8	48	99	41.5	1.8	0.7
NV12008TC_60	334	2.33	0.04260	0.00250	0.00646	0.00020	0.07009	42.3	2.4	41.6	1.3	80	100	41.6	1.3	1.7
NV12008TC_50	291.2	1.08	0.04530	0.00210	0.00650	0.00019	0.10772	45.2	2.0	41.7	1.2	220	100	41.7	1.2	7.7
NV12008TC_88	282	2.52	0.04210	0.00280	0.00650	0.00027	0.17782	41.8	2.7	41.7	1.8	10	120	41.7	1.8	0.2
NV12008TC_57	361	1.40	0.04360	0.00270	0.00651	0.00037	0.52088	43.3	2.7	41.8	2.4	130	110	41.8	2.4	3.5
NV12008TC_3	343	2.77	0.04420	0.00240	0.00652	0.00013	0.11041	43.9	2.3	41.9	0.9	170	100	41.9	0.9	4.6
NV12008TC_87	401	0.92	0.04470	0.00230	0.00654	0.00017	0.16879	44.3	2.2	42.0	1.1	130	100	42.0	1.1	5.2
NV12008TC_111	335	2.75	0.04440	0.00250	0.00654	0.00032	0.46367	44.0	2.4	42.0	2.1	170	110	42.0	2.1	4.5
NV12008TC_24	108.2	1.33	0.04550	0.00400	0.00655	0.00031	0.00013	45.1	3.9	42.1	2.0	230	200	42.1	2.0	6.7
NV12008TC_40	251	2.03	0.04430	0.00240	0.00655	0.00022	0.15798	43.9	2.3	42.1	1.4	180	110	42.1	1.4	4.1
NV12008TC_56	354.1	2.54	0.04630	0.00270	0.00656	0.00028	0.49199	45.9	2.6	42.1	1.8	250	110	42.1	1.8	8.3
NV12008TC_90	358	2.81	0.04430	0.00230	0.00663	0.00017	0.13132	43.9	2.2	42.6	1.1	131	99	42.6	1.1	3.0
NV12008TC_104	487	2.43	0.04390	0.00210	0.00663	0.00024	0.17862	43.6	2.0	42.6	1.6	118	99	42.6	1.6	2.3
NV12008TC_69	266	1.88	0.04620	0.00310	0.00665	0.00031	0.23054	45.8	3.0	42.7	2.0	140	160	42.7	2.0	6.8
NV12008TC_75	395	0.94	0.04770	0.00320	0.00668	0.00035	0.54027	47.3	3.1	42.9	2.2	280	120	42.9	2.2	9.3
NV12008TC_82	368	2.55	0.04770	0.00230	0.00667	0.00025	0.13444	47.3	2.2	42.9	1.6	211	95	42.9	1.6	9.3
NV12008TC_4	372	0.87	0.04370	0.00270	0.00671	0.00017	0.19495	43.4	2.6	43.1	1.1	50	100	43.1	1.1	0.7
NV12008TC_10	265	1.19	0.04440	0.00220	0.00671	0.00023	0.08662	44.1	2.2	43.1	1.4	130	120	43.1	1.4	2.3
NV12008TC_51	328	1.41	0.04420	0.00210	0.00671	0.00018	0.32649	43.9	2.0	43.1	1.1	55	93	43.1	1.1	1.8
NV12008TC_76	242	1.10	0.04560	0.00270	0.00672	0.00019	0.11828	45.2	2.6	43.2	1.2	250	130	43.2	1.2	4.4
NV12008TC_78	244	2.79	0.04800	0.00290	0.00674	0.00021	0.06669	47.6	2.8	43.3	1.4	270	140	43.3	1.4	9.0
NV12008TC_25	331	3.02	0.04720	0.00300	0.00676	0.00019	0.05178	46.8	2.9	43.4	1.2	160	130	43.4	1.2	7.3
NV12008TC_66	560	0.99	0.04490	0.00190	0.00676	0.00016	0.03319	44.6	1.8	43.4	1.0	146	98	43.4	1.0	2.7
NV12008TC_65	276	3.68	0.04580	0.00370	0.00677	0.00027	0.10301	45.4	3.6	43.5	1.7	130	150	43.5	1.7	4.2
NV12008TC_128	299	2.07	0.04340	0.00230	0.00678	0.00027	0.13856	43.1	2.2	43.6	1.7	60	110	43.6	1.7	1.2
NV12008TC_117	199.7	1.15	0.04650	0.00350	0.00682	0.00025	0.01045	46.1	3.4	43.8	1.6	160	160	43.8	1.6	5.0
NV12008TC_63	537	0.87	0.04460	0.00200	0.00683	0.00015	0.14348	44.3	1.9	43.9	1.0	83	84	43.9	1.0	0.9
NV12008TC_28	162	3.04	0.04830	0.00380	0.00683	0.00023	0.08539	47.8	3.7	43.9	1.5	200	160	43.9	1.5	8.2
NV12008TC_29	277	1.23	0.04390	0.00300	0.00683	0.00022	0.02093	43.6	2.9	43.9	1.4	60	130	43.9	1.4	0.7
NV12008TC_41	240	2.29	0.04710	0.00300	0.00686	0.00024	0.05985	46.6	2.9	44.1	1.5	150	130	44.1	1.5	5.4
NV12008TC_96	443	1.26	0.04590	0.00220	0.00686	0.00027	0.19406	45.6	2.1	44.1	1.8	140	110	44.1	1.8	3.3

NV12008TC_48	333	3.59	0.04920	0.00210	0.00688	0.00016	0.00642	48.7	2.0	44.2	1.0	320	100	44.2	1.0	9.2
NV12008TC_115	316	2.09	0.04610	0.00240	0.00688	0.00025	0.16058	45.7	2.4	44.2	1.6	140	110	44.2	1.6	3.3
NV12008TC_31	601	1.97	0.04590	0.00220	0.00689	0.00014	0.21236	45.6	2.1	44.3	0.9	90	89	44.3	0.9	2.9
NV12008TC_15	244	0.93	0.04510	0.00280	0.00691	0.00019	0.23713	44.8	2.7	44.4	1.2	110	140	44.4	1.2	0.9
NV12008TC_49	443	1.05	0.04790	0.00200	0.00698	0.00018	0.24976	47.4	2.0	44.8	1.2	116	84	44.8	1.2	5.5
NV12008TC_101	218.1	2.43	0.04540	0.00270	0.00699	0.00020	0.14164	45.0	2.6	44.9	1.3	100	120	44.9	1.3	0.2
NV12008TC_43	257	2.38	0.04750	0.00230	0.00701	0.00022	0.01353	47.1	2.3	45.0	1.4	210	120	45.0	1.4	4.5
NV12008TC_77	151.5	2.54	0.04620	0.00600	0.00701	0.00049	0.31256	47.0	6.3	45.0	3.2	210	270	45.0	3.2	4.3
NV12008TC_33	264	2.19	0.04750	0.00260	0.00702	0.00027	0.21170	47.1	2.5	45.1	1.7	200	130	45.1	1.7	4.2
NV12008TC_37	292	0.75	0.04670	0.00290	0.00705	0.00022	0.19491	46.2	2.8	45.3	1.4	180	130	45.3	1.4	1.9
NV12008TC_59	381	1.19	0.04890	0.00260	0.00705	0.00022	0.08879	48.4	2.5	45.3	1.4	200	120	45.3	1.4	6.4
NV12008TC_6	133	1.17	0.04870	0.00410	0.00707	0.00025	0.10992	48.2	4.0	45.4	1.6	190	170	45.4	1.6	5.8
NV12008TC_11	430	1.01	0.04600	0.00220	0.00707	0.00019	0.36284	45.7	2.1	45.4	1.2	128	93	45.4	1.2	0.7
NV12008TC_74	251.3	0.79	0.05100	0.00280	0.00709	0.00022	0.01461	50.4	2.7	45.5	1.4	300	120	45.5	1.4	9.7
NV12008TC_125	402	2.91	0.04730	0.00260	0.00709	0.00033	0.24644	46.9	2.5	45.5	2.1	110	110	45.5	2.1	3.0
NV12008TC_123	246.1	0.96	0.04940	0.00300	0.00710	0.00025	0.29971	48.9	2.9	45.6	1.6	210	120	45.6	1.6	6.7
NV12008TC_47	456	1.73	0.04690	0.00170	0.00711	0.00017	0.22343	46.5	1.7	45.7	1.1	103	82	45.7	1.1	1.7
NV12008TC_61	801	1.36	0.04730	0.00140	0.00713	0.00014	0.27456	47.1	1.3	45.8	0.9	108	60	45.8	0.9	2.8
NV12008TC_97	473	1.33	0.04830	0.00230	0.00718	0.00017	0.44723	47.9	2.2	46.1	1.1	137	84	46.1	1.1	3.8
NV12008TC_121	211.1	2.30	0.05090	0.00260	0.00720	0.00030	0.23200	50.3	2.6	46.3	1.9	270	120	46.3	1.9	8.0
NV12008TC_35	301	2.01	0.05040	0.00330	0.00736	0.00027	0.10075	49.9	3.2	47.3	1.7	180	140	47.3	1.7	5.2
NV12008TC_20	201	0.79	0.04910	0.00340	0.00751	0.00024	0.15572	48.6	3.3	48.2	1.6	100	150	48.2	1.6	0.8
NV12008TC_108	1170	0.99	0.05130	0.00180	0.00756	0.00016	0.59606	50.7	1.7	48.5	1.0	205	60	48.5	1.0	4.3
NV12008TC_19	397	2.15	0.05210	0.00190	0.00756	0.00016	0.20244	51.6	1.8	48.6	1.0	227	82	48.6	1.0	5.8
NV12008TC_18	237	3.37	0.05180	0.00460	0.00760	0.00033	0.17056	50.3	4.2	48.8	2.1	170	140	48.8	2.1	3.0
NV12008TC_54	623	0.97	0.05420	0.00250	0.00764	0.00020	0.25066	53.5	2.4	49.0	1.3	254	99	49.0	1.3	8.4
NV12008TC_124	699	0.97	0.04990	0.00180	0.00772	0.00023	0.14849	49.4	1.8	49.6	1.5	101	90	49.6	1.5	0.4
NV12008TC_102	262	1.21	0.05230	0.00280	0.00776	0.00025	0.17780	51.7	2.7	49.8	1.6	180	110	49.8	1.6	3.7
NV12008TC_114	757	1.61	0.05410	0.00340	0.00781	0.00034	0.13670	53.4	3.2	50.2	2.2	150	120	50.2	2.2	6.0
NV12008TC_122	356.9	2.04	0.05210	0.00210	0.00786	0.00017	0.11828	51.8	2.0	50.5	1.1	115	86	50.5	1.1	2.5
NV12008TC_27	482.5	1.11	0.19800	0.00610	0.02789	0.00073	0.40942	183.3	5.1	177.3	4.6	224	61	177.3	4.6	3.3
NV12008TC_70	67.4	0.78	0.55300	0.02700	0.06860	0.00250	0.28877	445.0	18.0	427.0	15.0	540	110	427.0	15.0	4.0
NV12008TC_38	128.8	1.81	0.58300	0.01700	0.06940	0.00150	0.22541	469.0	11.0	432.6	9.3	657	64	432.6	9.3	7.8
NV12008TC_55	575	1.62	1.53800	0.02900	0.15830	0.00390	0.73005	945.0	11.0	947.0	22.0	953	34	953.0	34.0	0.6
NV12008TC_112	58.6	1.75	2.30600	0.08400	0.20400	0.01000	0.54580	1211.0	25.0	1192.0	56.0	1246	84	1246.0	84.0	4.3
NV12008TC_110	155	2.73	2.85300	0.08000	0.23570	0.00770	0.71948	1371.0	21.0	1362.0	40.0	1398	48	1398.0	48.0	2.6
NV12008TC_85	104.4	1.68	3.25100	0.06900	0.25000	0.00520	0.63277	1470.0	16.0	1438.0	27.0	1507	34	1507.0	34.0	4.6
NV12008TC_16	83.4	1.33	4.04900	0.07600	0.28340	0.00570	0.76081	1646.0	16.0	1608.0	29.0	1731	33	1731.0	33.0	7.1
NV12008TC_109	106.3	2.78	4.12000	0.14000	0.28500	0.01200	0.66070	1654.0	27.0	1613.0	59.0	1732	58	1732.0	58.0	6.9
NV12008TC_73	785	2.82	4.82000	0.07400	0.32350	0.00590	0.70876	1789.0	13.0	1806.0	29.0	1764	22	1764.0	22.0	2.4

NV12008TC_127	117	1.76	4.81900	0.08100	0.32110	0.00570	0.63664	1790.0	14.0	1798.0	28.0	1794	25	1794.0	25.0	0.2
NV12008TC_9	105.6	1.99	4.66800	0.06000	0.31300	0.00440	0.54937	1761.0	11.0	1755.0	22.0	1795	21	1795.0	21.0	2.2
NV12008TC_105	132.6	1.12	5.23000	0.11000	0.33060	0.00990	0.81904	1856.0	19.0	1849.0	47.0	1884	30	1884.0	30.0	1.9
NV12008TC_62	112.2	1.63	10.59000	0.11000	0.47350	0.00650	0.74506	2487.0	9.9	2498.0	28.0	2464	20	2464.0	20.0	1.4
NV12008TC_93	78.3	1.68	11.58000	0.17000	0.48900	0.00780	0.43842	2570.0	14.0	2565.0	34.0	2559	22	2559.0	22.0	0.2

Analysis	U (ppm)	U/Th	207Pb/ 235U	±	206Pb/ 238U	±	err. corr.	207Pb/ 235U Age (Ma)	± (Ma)	206Pb/ 238U Age (Ma)	± (Ma)	207Pb/ 206Pb Age (Ma)	± (Ma)	Best age (Ma)	± (Ma)	Disc (%)
NV15-168RM: Robinson Mountain 40° 22' 2"N, 115° 55' 57"W																
NV15_168RM_8	446	1.19	0.03740	0.00180	0.00546	0.00016	0.29881	37.3	1.8	35.1	1.0	182	98	35.1	1.0	5.9
NV15_168RM_116	120.9	2.50	0.04110	0.00360	0.00582	0.00026	0.16813	40.8	3.5	37.4	1.7	210	160	37.4	1.7	8.3
NV15_168RM_29	154.9	1.64	0.04170	0.00260	0.00587	0.00020	0.00012	41.4	2.5	37.8	1.3	170	130	37.8	1.3	8.7
NV15_168RM_114	111.8	2.64	0.05180	0.00450	0.00616	0.00038	0.02940	51.1	4.3	39.6	2.5	480	210	39.6	2.5	22.5
NV15_168RM_93	105.5	1.90	0.04470	0.00310	0.00620	0.00034	0.13701	44.3	3.1	39.8	2.2	240	180	39.8	2.2	10.2
NV15_168RM_98	313	3.09	0.04130	0.00190	0.00622	0.00017	0.11359	41.3	1.8	40.0	1.1	90	100	40.0	1.1	3.1
NV15_168RM_82	166	2.52	0.04230	0.00310	0.00654	0.00042	0.17132	42.0	3.0	42.0	2.7	50	160	42.0	2.7	0.0
NV15_168RM_22	160.6	2.11	0.04500	0.00300	0.00655	0.00022	0.31661	44.6	3.0	42.1	1.4	180	130	42.1	1.4	5.6
NV15_168RM_32	115.6	2.17	0.04880	0.00380	0.00656	0.00026	0.11380	48.3	3.7	42.2	1.6	380	190	42.2	1.6	12.6
NV15_168RM_80	141.9	1.82	0.04500	0.00360	0.00657	0.00027	0.18923	44.6	3.5	42.2	1.8	180	160	42.2	1.8	5.4
NV15_168RM_90	166	2.69	0.04760	0.00280	0.00657	0.00025	0.02380	47.1	2.7	42.2	1.6	250	140	42.2	1.6	10.4
NV15_168RM_24	453	1.41	0.04720	0.00220	0.00699	0.00019	0.30220	46.8	2.2	44.9	1.2	96	92	44.9	1.2	4.1
NV15_168RM_112	406	3.99	0.04650	0.00230	0.00703	0.00027	0.35424	46.1	2.2	45.1	1.7	100	100	45.1	1.7	2.2
NV15_168RM_94	225	2.53	0.06090	0.00330	0.00726	0.00035	0.32706	60.3	3.2	46.6	2.3	590	120	46.6	2.3	22.7
NV15_168RM_64	134.9	0.89	0.04380	0.00340	0.00739	0.00031	0.03113	43.8	3.3	47.4	2.0	-80	150	47.4	2.0	8.2
NV15_168RM_9	321	2.82	0.19200	0.01000	0.01730	0.00130	0.58068	178.9	8.6	110.3	8.0	1278	86	110.3	8.0	38.3
NV15_168RM_54	490	2.00	0.16270	0.00780	0.01970	0.00140	0.41018	153.5	6.9	125.4	8.7	630	140	125.4	8.7	18.3
NV15_168RM_103	510	1.63	0.18530	0.00790	0.01990	0.00100	0.46405	173.8	6.6	126.8	6.6	804	98	126.8	6.6	27.0
NV15_168RM_79	208	1.94	0.16800	0.01000	0.01994	0.00087	0.41100	158.8	8.8	127.2	5.5	600	120	127.2	5.5	19.9
NV15_168RM_21	1000	1.93	0.20610	0.00990	0.02076	0.00084	0.49662	189.9	8.2	132.4	5.3	1011	82	132.4	5.3	30.3
NV15_168RM_28	406	1.65	0.15970	0.00400	0.02088	0.00056	0.46316	150.3	3.5	133.2	3.6	427	54	133.2	3.6	11.4
NV15_168RM_105	143.1	2.03	0.15760	0.00700	0.02113	0.00075	0.46181	149.1	6.0	134.7	4.7	260	92	134.7	4.7	9.7
NV15_168RM_68	400	1.52	0.15040	0.00690	0.02147	0.00097	0.31664	142.8	6.2	136.9	6.1	300	100	136.9	6.1	4.1
NV15_168RM_12	171	1.40	0.16120	0.00600	0.02155	0.00066	0.21133	151.5	5.3	137.4	4.1	416	95	137.4	4.1	9.3
NV15_168RM_33	184	1.19	0.15950	0.00500	0.02172	0.00066	0.13116	150.6	4.4	138.5	4.1	340	84	138.5	4.1	8.0
NV15_168RM_92	149	1.10	0.16300	0.00880	0.02190	0.00095	0.44824	152.7	7.7	139.6	6.0	380	110	139.6	6.0	8.6
NV15_168RM_34	621	4.75	0.16110	0.00700	0.02204	0.00088	0.77915	152.0	6.0	140.5	5.6	306	56	140.5	5.6	7.6
NV15_168RM_3	179	0.74	0.15360	0.00510	0.02258	0.00039	0.20176	144.9	4.5	143.9	2.5	135	66	143.9	2.5	0.7
NV15_168RM_17	121	1.32	0.16690	0.00880	0.02274	0.00092	0.49468	156.4	7.6	144.9	5.8	350	110	144.9	5.8	7.4
NV15_168RM_120	686	1.69	0.18030	0.00780	0.02275	0.00058	0.45041	169.9	7.1	145.0	3.6	556	81	145.0	3.6	14.7
NV15_168RM_101	182	1.23	0.18400	0.01100	0.02290	0.00090	0.16709	170.4	9.2	145.9	5.7	590	150	145.9	5.7	14.4
NV15_168RM_42	965	1.88	0.18490	0.00370	0.02297	0.00079	0.60376	172.2	3.1	146.3	5.0	513	59	146.3	5.0	15.0
NV15_168RM_65	85.2	1.14	0.16980	0.00790	0.02314	0.00090	0.04736	159.8	7.0	147.4	5.7	300	120	147.4	5.7	7.8
NV15_168RM_106	157.4	0.88	0.15910	0.00520	0.02327	0.00055	0.32155	149.7	4.5	148.3	3.4	137	70	148.3	3.4	0.9
NV15_168RM_36	86.3	0.70	0.17860	0.00970	0.02333	0.00093	0.25811	168.0	8.7	148.6	5.9	380	150	148.6	5.9	11.5

NV15_168RM_76	115.5	0.93	0.16290	0.00770	0.02360	0.00082	0.32620	152.8	6.7	150.3	5.1	200	96	150.3	5.1	1.6
NV15_168RM_113	154	0.93	0.17180	0.00850	0.02365	0.00084	0.12087	160.5	7.3	150.6	5.3	260	110	150.6	5.3	6.2
NV15_168RM_2	176	1.40	0.16180	0.00460	0.02383	0.00043	0.19444	152.7	3.9	151.8	2.7	163	65	151.8	2.7	0.6
NV15_168RM_110	200	1.45	0.17900	0.01000	0.02390	0.00096	0.48151	166.2	8.6	152.2	6.1	330	120	152.2	6.1	8.4
NV15_168RM_86	123.6	0.76	0.16300	0.00530	0.02396	0.00048	0.01697	153.1	4.7	152.6	3.0	180	81	152.6	3.0	0.3
NV15_168RM_1	454	4.21	0.16870	0.00330	0.02421	0.00045	0.23010	158.2	2.9	154.2	2.9	178	51	154.2	2.9	2.5
NV15_168RM_109	160	0.95	0.16850	0.00740	0.02412	0.00075	0.05609	158.5	6.3	154.2	4.8	180	100	154.2	4.8	2.7
NV15_168RM_78	97	1.42	0.17580	0.00980	0.02430	0.00100	0.14091	163.7	8.4	154.5	6.3	300	130	154.5	6.3	5.6
NV15_168RM_52	67.7	1.07	0.16900	0.00890	0.02429	0.00069	0.19240	158.0	7.7	154.7	4.3	220	110	154.7	4.3	2.1
NV15_168RM_35	136	1.34	0.16310	0.00780	0.02432	0.00072	0.42462	152.9	6.8	154.9	4.5	107	87	154.9	4.5	1.3
NV15_168RM_18	153.2	1.47	0.17250	0.00700	0.02440	0.00074	0.29159	161.4	6.0	155.4	4.7	223	87	155.4	4.7	3.7
NV15_168RM_41	155.5	0.86	0.16290	0.00660	0.02440	0.00056	0.05228	152.9	5.8	155.4	3.5	114	90	155.4	3.5	1.6
NV15_168RM_26	171	0.77	0.17020	0.00470	0.02445	0.00057	0.34588	159.5	4.1	155.7	3.6	210	66	155.7	3.6	2.4
NV15_168RM_25	149	0.98	0.17270	0.00550	0.02453	0.00053	0.30416	161.5	4.7	156.2	3.4	189	65	156.2	3.4	3.3
NV15_168RM_30	150	1.02	0.17450	0.00790	0.02454	0.00087	0.47564	163.8	7.0	156.2	5.5	253	93	156.2	5.5	4.6
NV15_168RM_38	77.2	0.90	0.16350	0.00830	0.02468	0.00083	0.29690	153.2	7.2	157.1	5.2	150	110	157.1	5.2	2.5
NV15_168RM_44	363	1.13	0.17850	0.00780	0.02469	0.00082	0.40053	166.4	6.7	157.2	5.2	263	82	157.2	5.2	5.5
NV15_168RM_104	221	1.03	0.17900	0.00690	0.02480	0.00100	0.38771	166.9	6.0	157.9	6.4	254	96	157.9	6.4	5.4
NV15_168RM_117	141	1.14	0.17740	0.00660	0.02480	0.00110	0.29746	165.5	5.7	157.9	7.1	260	100	157.9	7.1	4.6
NV15_168RM_45	175.8	1.03	0.17300	0.00600	0.02485	0.00071	0.29659	161.8	5.2	158.2	4.5	223	80	158.2	4.5	2.2
NV15_168RM_107	145	1.08	0.17430	0.00950	0.02490	0.00120	0.41941	162.5	8.2	158.2	7.7	220	120	158.2	7.7	2.6
NV15_168RM_27	121.6	1.19	0.16750	0.00630	0.02489	0.00063	0.31471	156.9	5.5	158.5	3.9	148	73	158.5	3.9	1.0
NV15_168RM_19	549	1.94	0.17470	0.00400	0.02492	0.00045	0.21506	163.4	3.4	158.7	2.9	186	57	158.7	2.9	2.9
NV15_168RM_43	130.8	0.95	0.21400	0.01200	0.02493	0.00056	0.06067	196.0	9.9	158.7	3.5	620	120	158.7	3.5	19.0
NV15_168RM_23	88.4	1.04	0.17250	0.00830	0.02494	0.00065	0.19593	161.1	7.2	158.8	4.1	147	99	158.8	4.1	1.4
NV15_168RM_83	241	1.78	0.17650	0.00660	0.02508	0.00072	0.32513	165.5	5.8	159.7	4.6	303	77	159.7	4.6	3.5
NV15_168RM_16	135.5	1.26	0.17850	0.00690	0.02511	0.00090	0.43088	166.4	6.0	159.8	5.6	277	96	159.8	5.6	4.0
NV15_168RM_111	139	1.02	0.17740	0.00800	0.02511	0.00090	0.38945	165.4	6.9	159.9	5.7	233	96	159.9	5.7	3.3
NV15_168RM_100	282	4.39	0.17800	0.00750	0.02520	0.00120	0.56574	165.9	6.4	160.1	7.5	241	76	160.1	7.5	3.5
NV15_168RM_6	338	4.15	0.17690	0.00510	0.02522	0.00053	0.28834	165.2	4.4	160.5	3.3	199	69	160.5	3.3	2.8
NV15_168RM_118	334	1.20	0.17890	0.00520	0.02526	0.00065	0.42264	167.5	4.4	160.8	4.1	204	65	160.8	4.1	4.0
NV15_168RM_51	172	2.32	0.16690	0.00690	0.02529	0.00071	0.28997	156.4	6.0	160.9	4.5	139	91	160.9	4.5	2.9
NV15_168RM_58	135	0.80	0.17560	0.00700	0.02531	0.00055	0.15535	164.8	5.9	161.1	3.5	208	89	161.1	3.5	2.2
NV15_168RM_74	98.7	1.18	0.24600	0.01700	0.02530	0.00130	0.29540	225.0	14.0	161.2	8.1	830	160	161.2	8.1	28.4
NV15_168RM_49	133.9	0.87	0.17000	0.00730	0.02541	0.00071	0.12860	159.1	6.3	161.7	4.4	161	98	161.7	4.4	1.6
NV15_168RM_99	186	1.09	0.19100	0.01300	0.02532	0.00083	0.23632	176.0	10.0	161.8	5.1	360	120	161.8	5.1	8.1
NV15_168RM_71	238	2.42	0.17400	0.00690	0.02550	0.00120	0.42139	163.5	6.2	162.0	7.3	140	91	162.0	7.3	0.9
NV15_168RM_4	224	1.07	0.17670	0.00520	0.02559	0.00063	0.23030	165.0	4.5	162.8	4.0	201	71	162.8	4.0	1.3
NV15_168RM_55	99.7	1.03	0.17190	0.00770	0.02560	0.00110	0.23386	160.7	6.7	162.8	6.7	120	100	162.8	6.7	1.3
NV15_168RM_85	101.8	1.23	0.28900	0.07400	0.02570	0.00130	0.73397	206.0	30.0	163.5	7.9	570	190	163.5	7.9	20.6

NV15_168RM_46	262	1.63	0.17810	0.00560	0.02573	0.00059	0.30509	166.2	4.8	163.7	3.7	214	74	163.7	3.7	1.5
NV15_168RM_119	410	2.50	0.17640	0.00760	0.02574	0.00096	0.60920	164.5	6.6	163.8	6.0	177	77	163.8	6.0	0.4
NV15_168RM_81	146	0.99	0.17040	0.00700	0.02576	0.00069	0.39816	159.4	6.1	163.9	4.3	124	82	163.9	4.3	2.8
NV15_168RM_102	182	1.57	0.18100	0.00850	0.02580	0.00140	0.48529	168.4	7.3	163.9	8.5	177	90	163.9	8.5	2.7
NV15_168RM_91	185	1.57	0.17610	0.00760	0.02590	0.00082	0.52215	164.3	6.6	164.8	5.1	150	78	164.8	5.1	0.3
NV15_168RM_75	686	1.13	0.18520	0.00520	0.02591	0.00077	0.49861	172.3	4.5	164.9	4.8	260	68	164.9	4.8	4.3
NV15_168RM_11	214	0.87	0.20200	0.01300	0.02595	0.00054	0.10262	185.0	11.0	165.1	3.4	420	130	165.1	3.4	10.8
NV15_168RM_97	127	1.11	0.19200	0.01200	0.02600	0.00120	0.52855	177.0	10.0	165.6	7.5	290	120	165.6	7.5	6.4
NV15_168RM_108	211	1.01	0.18170	0.00780	0.02607	0.00078	0.34288	170.8	6.8	165.8	4.9	215	87	165.8	4.9	2.9
NV15_168RM_47	225	1.50	0.18280	0.00670	0.02611	0.00084	0.48062	170.1	5.8	166.1	5.3	186	81	166.1	5.3	2.4
NV15_168RM_88	223	1.01	0.22800	0.01900	0.02614	0.00090	0.23529	207.0	15.0	166.3	5.7	580	140	166.3	5.7	19.7
NV15_168RM_5	558	1.09	0.28100	0.03100	0.02654	0.00068	0.54422	242.0	21.0	168.8	4.3	840	130	168.8	4.3	30.2
NV15_168RM_87	176	0.94	0.17780	0.00660	0.02657	0.00081	0.36830	165.9	5.7	169.0	5.1	148	82	169.0	5.1	1.9
NV15_168RM_50	125.2	1.18	0.18230	0.00760	0.02660	0.00120	0.25613	170.5	6.7	169.3	7.2	240	110	169.3	7.2	0.7
NV15_168RM_14	269	2.06	0.19590	0.00760	0.02670	0.00100	0.36353	181.3	6.4	169.5	6.4	326	84	169.5	6.4	6.5
NV15_168RM_95	203	1.84	0.18430	0.00530	0.02674	0.00091	0.33202	172.2	4.7	170.1	5.7	162	77	170.1	5.7	1.2
NV15_168RM_10	700	0.80	0.18930	0.00590	0.02681	0.00098	0.61001	175.8	5.0	170.5	6.2	190	62	170.5	6.2	3.0
NV15_168RM_60	85.3	1.34	0.19090	0.00950	0.02690	0.00150	0.27021	176.8	8.1	170.7	9.1	190	130	170.7	9.1	3.5
NV15_168RM_7	446	1.76	0.20120	0.00520	0.02688	0.00078	0.29944	185.9	4.4	171.0	4.9	323	72	171.0	4.9	8.0
NV15_168RM_63	148	1.71	0.20100	0.01200	0.02690	0.00130	0.38826	186.0	10.0	171.0	8.2	340	130	171.0	8.2	8.1
NV15_168RM_77	198	2.10	0.19580	0.00700	0.02700	0.00100	0.23163	182.0	5.8	171.6	6.5	319	97	171.6	6.5	5.7
NV15_168RM_72	87	1.62	0.20500	0.01600	0.02710	0.00180	0.40830	188.0	13.0	172.0	11.0	330	150	172.0	11.0	8.5
NV15_168RM_48	331	1.55	0.18400	0.01100	0.02720	0.00160	0.03818	171.2	9.4	172.8	9.7	170	180	172.8	9.7	0.9
NV15_168RM_40	430	2.33	0.19280	0.00570	0.02727	0.00090	0.37065	178.8	4.9	173.4	5.7	212	70	173.4	5.7	3.0
NV15_168RM_31	333	1.94	0.18640	0.00790	0.02730	0.00120	0.25996	173.1	6.8	173.6	7.8	180	110	173.6	7.8	0.3
NV15_168RM_70	156	1.31	0.25900	0.02100	0.02730	0.00130	0.08854	231.0	17.0	173.6	8.4	740	180	173.6	8.4	24.8
NV15_168RM_13	62.3	1.27	0.35400	0.03500	0.02750	0.00220	0.29837	309.0	27.0	175.0	14.0	1420	210	175.0	14.0	43.4
NV15_168RM_73	316.9	1.94	0.19320	0.00630	0.02830	0.00096	0.25136	179.1	5.3	179.8	6.0	166	75	179.8	6.0	0.4
NV15_168RM_69	126.8	1.31	0.18780	0.00890	0.02830	0.00140	0.33282	174.2	7.6	180.0	8.6	110	110	180.0	8.6	3.3
NV15_168RM_61	126	1.28	0.37200	0.01700	0.04820	0.00200	0.53262	320.0	12.0	303.0	13.0	410	100	303.0	13.0	5.3
NV15_168RM_115	266.8	1.41	0.37970	0.00830	0.05170	0.00100	0.22518	326.5	6.1	324.7	6.3	323	58	324.7	6.3	0.6
NV15_168RM_21	233	1.42	0.94500	0.06200	0.06520	0.00410	0.84955	673.0	33.0	407.0	25.0	1667	53	407.0	25.0	39.5
NV15_168RM_96	97.8	1.11	0.69400	0.02900	0.08390	0.00310	0.35353	536.0	17.0	519.0	18.0	584	95	519.0	18.0	3.2
NV15_168RM_37	462	3.71	1.31800	0.03700	0.09260	0.00390	0.42824	852.0	16.0	570.0	23.0	1675	63	570.0	23.0	33.1
NV15_168RM_48	97.5	1.23	1.56600	0.05600	0.12840	0.00380	0.45322	955.0	22.0	778.0	22.0	1327	60	778.0	22.0	18.5
NV15_168RM_37	202	2.84	1.49100	0.05300	0.13740	0.00640	0.65896	925.0	22.0	829.0	37.0	1119	66	829.0	37.0	10.4
NV15_168RM_56	225	2.47	1.87200	0.04100	0.16210	0.00290	0.47842	1072.0	14.0	968.0	16.0	1287	42	1287.0	42.0	24.8
NV15_168RM_66	315	1.11	2.89000	0.07400	0.24010	0.00790	0.65953	1376.0	19.0	1385.0	41.0	1324	47	1324.0	47.0	4.6
NV15_168RM_57	210	0.79	2.28400	0.03800	0.18690	0.00320	0.58843	1206.0	12.0	1104.0	17.0	1369	30	1369.0	30.0	19.4
NV15_168RM_59	221.8	1.37	3.32900	0.07000	0.25550	0.00690	0.68516	1488.0	16.0	1465.0	35.0	1520	39	1520.0	39.0	3.6

NV15_168RM_84	132	1.26	2.56100	0.06500	0.19530	0.00540	0.56994	1286.0	18.0	1149.0	29.0	1566	55	1566.0	55.0	26.6
NV15_168RM_89	410	6.27	4.54000	0.18000	0.29600	0.01100	0.90092	1727.0	36.0	1666.0	53.0	1809	38	1809.0	38.0	7.9
NV15_168RM_15	225	2.53	7.92000	0.23000	0.39880	0.00800	0.83862	2219.0	25.0	2161.0	37.0	2264	26	2264.0	26.0	4.5

Analysis	U (ppm)	U/Th	207Pb/ 235U	±	206Pb/ 238U	±	err. corr.	207Pb/ 235U Age (Ma)	± (Ma)	206Pb/ 238U Age (Ma)	± (Ma)	207Pb/ 206Pb Age (Ma)	± (Ma)	Best age (Ma)	± (Ma)	Disc (%)
NV15-241RM: Robinson Mountain 40° 21' 36"N 115° 55' 58"W																
NV15_241RM_21	131.9	1.38	0.04170	0.00300	0.00656	0.00036	0.23411	41.4	3.0	42.2	2.3	80	160	42.2	2.3	1.9
NV15_241RM_42	930	2.09	0.06170	0.00500	0.00661	0.00045	0.48331	60.6	4.8	42.5	2.9	750	150	42.5	2.9	29.9
NV15_241RM_16	251.4	1.58	0.04370	0.00240	0.00663	0.00022	0.15628	43.4	2.3	42.6	1.4	130	120	42.6	1.4	1.8
NV15_241RM_17	64.6	1.46	0.05130	0.00750	0.00669	0.00042	0.05355	50.4	7.1	43.0	2.7	280	270	43.0	2.7	14.7
NV15_241RM_34	169.6	1.37	0.04500	0.00290	0.00678	0.00028	0.06679	44.6	2.8	43.5	1.8	150	140	43.5	1.8	2.5
NV15_241RM_122	178	0.90	0.04810	0.00300	0.00682	0.00030	0.17760	47.6	2.9	43.8	1.9	240	130	43.8	1.9	8.0
NV15_241RM_12	182	1.00	0.04430	0.00350	0.00683	0.00034	0.28049	43.9	3.4	43.9	2.2	80	130	43.9	2.2	0.0
NV15_241RM_24	270	1.46	0.04500	0.00290	0.00684	0.00027	0.34747	44.6	2.8	44.0	1.7	140	130	44.0	1.7	1.3
NV15_241RM_19	119.6	1.11	0.05220	0.00510	0.00687	0.00037	0.12790	51.5	4.9	44.1	2.4	260	190	44.1	2.4	14.4
NV15_241RM_62	70.3	1.68	0.05900	0.01100	0.00692	0.00042	0.05212	56.9	9.5	44.4	2.7	380	230	44.4	2.7	22.0
NV15_241RM_94	178.1	1.81	0.04500	0.00310	0.00691	0.00029	0.18316	44.6	3.0	44.4	1.9	20	150	44.4	1.9	0.4
NV15_241RM_20	176	0.94	0.07100	0.00430	0.00694	0.00035	0.22167	69.5	4.1	44.6	2.2	1050	140	44.6	2.2	35.8
NV15_241RM_29	613	1.36	0.04510	0.00170	0.00699	0.00020	0.25093	45.0	1.6	44.9	1.3	46	76	44.9	1.3	0.2
NV15_241RM_83	361.7	1.28	0.04720	0.00200	0.00700	0.00023	0.30978	46.8	2.0	45.0	1.5	128	95	45.0	1.5	3.8
NV15_241RM_81	246	1.50	0.05370	0.00390	0.00703	0.00036	0.30096	53.0	3.7	45.2	2.3	340	150	45.2	2.3	14.7
NV15_241RM_54	174	1.37	0.05970	0.00430	0.00707	0.00031	0.39729	59.3	4.0	45.4	2.0	710	140	45.4	2.0	23.4
NV15_241RM_18	653	1.14	0.05960	0.00340	0.00712	0.00017	0.10400	58.6	3.2	45.7	1.1	570	130	45.7	1.1	22.0
NV15_241RM_67	80	1.68	0.04940	0.00560	0.00712	0.00050	0.14351	48.7	5.4	45.7	3.2	170	210	45.7	3.2	6.2
NV15_241RM_1	50.3	1.36	0.04680	0.00700	0.00722	0.00047	0.04889	47.0	6.9	46.4	3.0	70	260	46.4	3.0	1.3
NV15_241RM_31	119.7	1.42	0.04800	0.00370	0.00724	0.00042	0.26743	47.4	3.6	46.5	2.7	120	160	46.5	2.7	1.9
NV15_241RM_75	121.1	0.68	0.05320	0.00440	0.00732	0.00025	0.11427	52.5	4.2	47.0	1.6	350	170	47.0	1.6	10.5
NV15_241RM_80	199	1.21	0.04930	0.00270	0.00733	0.00025	0.16768	48.8	2.6	47.1	1.6	180	130	47.1	1.6	3.5
NV15_241RM_66	127	1.07	0.05680	0.00470	0.00735	0.00055	0.20466	55.9	4.5	47.2	3.5	360	170	47.2	3.5	15.6
NV15_241RM_8	167.2	1.40	0.04560	0.00370	0.00738	0.00041	0.22434	45.2	3.6	47.4	2.6	70	170	47.4	2.6	4.9
NV15_241RM_23	349	1.33	0.04870	0.00260	0.00743	0.00026	0.03015	48.2	2.5	47.7	1.7	120	120	47.7	1.7	1.0
NV15_241RM_59	100.1	1.44	0.05080	0.00570	0.00744	0.00049	0.21939	50.0	5.5	47.8	3.1	110	190	47.8	3.1	4.4
NV15_241RM_58	406	2.43	0.05090	0.00300	0.00749	0.00030	0.11774	50.3	2.9	48.1	1.9	180	120	48.1	1.9	4.4
NV15_241RM_3	126.3	0.99	0.05260	0.00400	0.00762	0.00052	0.00302	51.9	3.9	48.9	3.3	230	180	48.9	3.3	5.8
NV15_241RM_103	267.3	1.78	0.07020	0.00450	0.00766	0.00043	0.29158	69.3	4.2	49.2	2.7	820	110	49.2	2.7	29.0
NV15_241RM_91	177.7	1.52	0.05380	0.00390	0.00774	0.00036	0.24193	53.1	3.7	49.7	2.3	190	130	49.7	2.3	6.4
NV15_241RM_32	76.6	1.59	0.05520	0.00620	0.00777	0.00070	0.05800	54.2	5.9	49.9	4.5	200	230	49.9	4.5	7.9
NV15_241RM_45	144	0.60	0.06220	0.00470	0.00777	0.00041	0.39002	61.7	4.6	49.9	2.6	520	150	49.9	2.6	19.1
NV15_241RM_28	94.5	1.03	0.06240	0.00580	0.00781	0.00051	0.19660	61.2	5.5	50.1	3.3	410	180	50.1	3.3	18.1
NV15_241RM_15	107	1.09	0.04720	0.00480	0.00792	0.00043	0.07163	46.6	4.6	50.8	2.8	-50	190	50.8	2.8	9.0
NV15_241RM_57	105.9	1.56	0.06790	0.00630	0.00791	0.00051	0.19082	66.3	6.0	50.8	3.3	550	200	50.8	3.3	23.4

NV15_241RM_68	384	1.45	0.05250	0.00330	0.00803	0.00053	0.40443	51.9	3.2	51.6	3.4	50	120	51.6	3.4	0.6
NV15_241RM_113	183	3.16	0.05550	0.00430	0.00805	0.00041	0.18793	54.7	4.1	51.7	2.6	170	160	51.7	2.6	5.5
NV15_241RM_120	249	1.65	0.05290	0.00310	0.00810	0.00037	0.23821	52.7	2.9	52.0	2.4	110	120	52.0	2.4	1.3
NV15_241RM_78	116.9	1.34	0.06220	0.00610	0.00834	0.00070	0.32034	60.9	5.8	53.5	4.5	320	190	53.5	4.5	12.2
NV15_241RM_39	185.3	1.31	0.05190	0.00460	0.00844	0.00068	0.56137	51.2	4.4	54.2	4.3	10	140	54.2	4.3	5.9
NV15_241RM_47	265	1.53	0.06000	0.00430	0.00848	0.00056	0.50896	59.0	4.1	54.4	3.6	170	130	54.4	3.6	7.8
NV15_241RM_40	1520	1.56	0.06380	0.00390	0.00871	0.00063	0.42112	62.7	3.7	55.9	4.0	390	140	55.9	4.0	10.8
NV15_241RM_111	88	1.24	0.15380	0.00980	0.01741	0.00090	0.27244	147.2	8.6	111.2	5.7	730	150	111.2	5.7	24.5
NV15_241RM_93	409	2.00	0.15850	0.00990	0.01790	0.00130	0.27512	148.7	8.6	114.2	8.2	750	160	114.2	8.2	23.2
NV15_241RM_107	147	1.70	0.14700	0.01000	0.01920	0.00130	0.35770	138.4	8.8	122.4	8.0	480	160	122.4	8.0	11.6
NV15_241RM_7	160	1.93	0.15180	0.00760	0.02080	0.00100	0.35532	144.1	6.9	132.6	6.3	320	110	132.6	6.3	8.0
NV15_241RM_10	100	1.54	0.16470	0.00980	0.02300	0.00130	0.43804	155.2	8.4	146.4	8.3	300	120	146.4	8.3	5.7
NV15_241RM_50	59.9	1.85	0.17400	0.01500	0.02320	0.00130	0.08487	161.0	13.0	147.8	7.9	310	170	147.8	7.9	8.2
NV15_241RM_64	297	1.50	0.22600	0.01100	0.02360	0.00160	0.24157	206.5	8.9	150.0	10.0	820	170	150.0	10.0	27.4
NV15_241RM_44	54.6	1.18	0.19000	0.01600	0.02480	0.00200	0.36458	178.0	13.0	158.0	12.0	510	160	158.0	12.0	11.2
NV15_241RM_118	93	1.61	0.18500	0.01600	0.02480	0.00180	0.55551	171.0	13.0	158.0	12.0	400	140	158.0	12.0	7.6
NV15_241RM_35	182	1.22	0.17190	0.00630	0.02493	0.00085	0.20841	160.8	5.4	158.7	5.4	220	100	158.7	5.4	1.3
NV15_241RM_71	218	1.77	0.17990	0.00490	0.02496	0.00067	0.32895	167.8	4.2	158.9	4.2	291	69	158.9	4.2	5.3
NV15_241RM_41	60.1	0.94	0.18400	0.01300	0.02510	0.00220	0.38240	174.0	11.0	160.0	14.0	420	170	160.0	14.0	8.0
NV15_241RM_106	169	1.37	0.18100	0.00820	0.02520	0.00100	0.26599	168.5	7.1	160.6	6.6	290	100	160.6	6.6	4.7
NV15_241RM_74	183	1.16	0.18220	0.00710	0.02596	0.00093	0.32823	169.6	6.1	165.1	5.8	295	91	165.1	5.8	2.7
NV15_241RM_121	94	1.82	0.19100	0.01500	0.02610	0.00200	0.45008	176.0	12.0	166.0	13.0	310	160	166.0	13.0	5.7
NV15_241RM_110	365	4.20	0.18650	0.00940	0.02620	0.00150	0.49031	173.0	8.0	166.4	9.2	260	100	166.4	9.2	3.8
NV15_241RM_56	89	1.26	0.17000	0.01200	0.02630	0.00190	0.52399	159.0	10.0	167.0	12.0	150	130	167.0	12.0	5.0
NV15_241RM_51	94	1.08	0.19600	0.01100	0.02659	0.00095	0.04202	180.5	9.4	169.1	6.0	340	140	169.1	6.0	6.3
NV15_241RM_52	66.4	1.29	0.18600	0.01200	0.02660	0.00140	0.23193	171.9	9.9	169.2	8.6	220	140	169.2	8.6	1.6
NV15_241RM_36	121	1.25	0.19030	0.00980	0.02700	0.00180	0.47131	176.3	8.3	171.0	11.0	260	120	171.0	11.0	3.0
NV15_241RM_11	56.5	1.46	0.19400	0.01300	0.02710	0.00190	0.14147	182.0	12.0	172.0	12.0	340	170	172.0	12.0	5.5
NV15_241RM_43	135	1.74	0.20000	0.01400	0.02730	0.00190	0.52036	184.0	12.0	173.0	12.0	310	140	173.0	12.0	6.0
NV15_241RM_92	320	0.60	0.19290	0.00830	0.02730	0.00110	0.54042	178.7	7.1	173.8	7.1	260	93	173.8	7.1	2.7
NV15_241RM_26	148	1.88	0.19900	0.01100	0.02750	0.00150	0.52777	185.1	9.0	175.0	9.2	227	87	175.0	9.2	5.5
NV15_241RM_86	61.9	1.19	0.18800	0.01100	0.02780	0.00220	0.20198	175.7	9.1	177.0	14.0	210	170	177.0	14.0	0.7
NV15_241RM_48	87	1.51	0.20100	0.01200	0.02810	0.00160	0.40917	186.8	9.9	178.0	10.0	310	140	178.0	10.0	4.7
NV15_241RM_53	108	1.06	0.19700	0.01100	0.02810	0.00140	0.34666	181.8	9.2	178.6	9.0	270	130	178.6	9.0	1.8
NV15_241RM_82	236	1.24	0.20600	0.01100	0.02820	0.00130	0.47814	189.8	8.8	179.2	8.2	290	110	179.2	8.2	5.6
NV15_241RM_27	218	1.76	0.21300	0.01300	0.02830	0.00160	0.60360	195.0	11.0	180.0	9.7	340	110	180.0	9.7	7.7
NV15_241RM_98	61.5	1.62	0.22500	0.01400	0.02880	0.00170	0.51840	207.0	12.0	183.0	10.0	460	150	183.0	10.0	11.6
NV15_241RM_46	220.9	1.32	0.19800	0.01000	0.02890	0.00160	0.41137	182.9	8.6	184.0	10.0	250	110	184.0	10.0	0.6
NV15_241RM_108	123.5	1.50	0.18180	0.00950	0.02940	0.00120	0.48260	169.0	8.2	186.6	7.5	60	100	186.6	7.5	10.4
NV15_241RM_4	303	1.00	0.21800	0.01200	0.02990	0.00190	0.60285	199.0	10.0	190.0	12.0	380	120	190.0	12.0	4.5

NV15_241RM_125	544	2.69	0.20190	0.00920	0.02990	0.00160	0.71930	186.2	7.8	190.0	10.0	183	86	190.0	10.0	2.0
NV15_241RM_117	288	2.45	0.22700	0.01100	0.03010	0.00170	0.40313	206.8	9.5	191.0	11.0	350	120	191.0	11.0	7.6
NV15_241RM_55	105	2.67	0.20400	0.01300	0.03030	0.00220	0.39794	187.0	11.0	192.0	14.0	230	150	192.0	14.0	2.7
NV15_241RM_89	445	4.22	0.22070	0.00690	0.03080	0.00130	0.53440	202.2	5.8	195.4	8.4	296	79	195.4	8.4	3.4
NV15_241RM_112	257	3.73	0.22900	0.01400	0.03250	0.00220	0.42599	208.0	11.0	206.0	13.0	280	130	206.0	13.0	1.0
NV15_241RM_109	490	7.41	0.26500	0.01700	0.03380	0.00210	0.67279	242.0	14.0	214.0	13.0	495	97	214.0	13.0	11.6
NV15_241RM_27	71.5	1.30	0.64700	0.05800	0.07010	0.00680	0.69723	504.0	37.0	436.0	41.0	910	160	436.0	41.0	13.5
NV15_241RM_33	110.5	1.22	0.66600	0.02900	0.08130	0.00400	0.50611	515.0	18.0	506.0	23.0	530	110	506.0	23.0	1.7
NV15_241RM_38	112	6.50	0.76400	0.03700	0.09770	0.00340	0.51183	580.0	20.0	601.0	20.0	469	94	601.0	20.0	3.6
NV15_241RM_70	292	11.61	1.45500	0.04800	0.14160	0.00670	0.61641	914.0	19.0	853.0	38.0	1024	72	1024.0	72.0	16.7
NV15_241RM_14	37.7	1.71	1.55500	0.09500	0.14460	0.00900	0.45469	943.0	38.0	874.0	52.0	1110	110	1110.0	110.0	21.3
NV15_241RM_116	228	16.70	2.34000	0.09700	0.21160	0.00870	0.57984	1221.0	30.0	1234.0	46.0	1178	90	1178.0	90.0	4.8
NV15_241RM_79	118.9	3.57	2.42000	0.12000	0.22000	0.01300	0.54882	1251.0	34.0	1275.0	70.0	1180	110	1180.0	110.0	8.1

Analysis	U (ppm)	U/Th	207Pb/ 235U	±	206Pb/ 238U	±	err. corr.	207Pb/ 235U Age (Ma)	± (Ma)	206Pb/ 238U Age (Ma)	± (Ma)	207Pb/ 206Pb Age (Ma)	± (Ma)	Best age (Ma)	± (Ma)	Disc (%)
NV11-014EU: Eureka 39° 29' 6"N, 115° 56' 42"W																
NV11DZ014EU_102	2.2	0.04	0.0580	0.0110	0.00669	0.00017	0.150	10	43	1.1	44.2	260	-7	43.0	1.1	24.6
NV11DZ014EU_51	6.1	0.03	0.13690	0.00350	0.02000	0.00026	0.28115	3.2	127.7	1.7	131.9	57	70	127.7	1.7	1.9
NV11DZ014EU_66	6.9	0.03	0.16900	0.01100	0.02037	0.00032	0.09275	8.7	130.0	2.0	168.0	110	150	130.0	2.0	16.4
NV11DZ014EU_18	19	0.01	0.18020	0.00460	0.02535	0.00035	0.03268	3.9	161.4	2.2	161.2	60	0	161.4	2.2	4.0
NV11DZ014EU_99	18	0.14	0.6360	0.0300	0.07030	0.00230	0.462	19	438	14	711	99	-800	438.0	14.0	12.2
NV11DZ014EU_32	3.2	0.01	0.61000	0.02000	0.07410	0.00110	0.10686	12.0	460.8	6.4	486.0	71	-250	460.8	6.4	4.6
NV11DZ014EU_127	4.4	0.02	0.7320	0.0250	0.07550	0.00150	0.230	14	469.3	8.7	693	69	710	469.3	8.7	15.6
NV11DZ014EU_125	3.1	0.05	0.6270	0.0130	0.07600	0.00150	0.274	8.2	472	8.9	648	48	40	472.0	8.9	4.4
NV11DZ014EU_30	5.6	0.02	1.04600	0.05700	0.08750	0.00110	0.05637	28.0	540.8	6.5	663.0	110	460	540.8	6.5	25.1
NV11DZ014EU_124	1.2	0.03	1.2040	0.0520	0.09940	0.00180	0.137	23	611	10	958	73	130	611.0	10.0	23.3
NV11DZ014EU_89	17	3.00	1.6310	0.0270	0.15930	0.00260	0.508	10	952	14	1560	32	0	1037.0	32.0	8.2
NV11DZ014EU_63	17	0.18	2.24400	0.04200	0.20400	0.00330	0.79185	13.0	1196.0	18.0	1298.0	24	1500	1155.0	24.0	3.5
NV11DZ014EU_62	5	0.02	2.12700	0.03000	0.19640	0.00260	0.63461	9.8	1156.0	14.0	1152.0	22	-100	1156.0	22.0	0.0
NV11DZ014EU_55	5.2	0.02	2.57600	0.02300	0.22140	0.00250	0.60896	6.6	1289.0	13.0	1362.0	19	500	1294.0	19.0	0.4
NV11DZ014EU_120	2.7	0.04	2.9250	0.0300	0.24070	0.00320	0.369	7.8	1390	17	1581	28	300	1398.0	28.0	0.6
NV11DZ014EU_43	0.59	0.03	2.53800	0.07600	0.20290	0.00300	0.09526	21.0	1191.0	16.0	1449.0	64	370	1405.0	64.0	15.2
NV11DZ014EU_70	4.2	0.02	2.26300	0.04600	0.18190	0.00270	0.29554	14.0	1077.0	15.0	1175.0	41	450	1430.0	41.0	24.7
NV11DZ014EU_53	14	0.07	3.03200	0.03300	0.23970	0.00270	0.76612	8.1	1385.0	14.0	1426.0	15	3000	1451.0	15.0	4.5
NV11DZ014EU_101	13	0.02	3.3040	0.0350	0.25830	0.00280	0.773	8.2	1481	14	1509	13	1200	1484.0	13.0	0.2
NV11DZ014EU_10	3.6	0.06	2.86700	0.06000	0.22360	0.00420	0.56885	16.0	1300.0	22.0	1688.0	30	540	1500.0	30.0	13.3
NV11DZ014EU_119	1.5	0.01	3.2610	0.0640	0.24810	0.00330	0.425	15	1431	17	1750	30	200	1533.0	30.0	6.7
NV11DZ014EU_104	4.4	0.02	3.2680	0.0490	0.24630	0.00320	0.544	12	1419	16	1697	25	2360	1538.0	25.0	7.7
NV11DZ014EU_138	3.8	0.02	2.8980	0.0570	0.20840	0.00410	0.442	15	1220	22	1609	32	950	1643.0	32.0	25.7
NV11DZ014EU_80	12	0.02	3.96000	0.05000	0.27970	0.00460	0.62540	10.0	1589.0	23.0	1870.0	25	2300	1655.0	25.0	4.0
NV11DZ014EU_54	3.7	0.01	3.83800	0.04200	0.26950	0.00360	0.73804	8.7	1540.0	18.0	1660.0	15	-1100	1662.0	15.0	7.3
NV11DZ014EU_14	1.9	0.02	3.92200	0.03900	0.28390	0.00270	0.71898	8.0	1611.0	14.0	1638.0	16	300	1663.0	16.0	3.1
NV11DZ014EU_25	9.8	0.23	4.03200	0.06500	0.28970	0.00680	0.35467	13.0	1639.0	34.0	1707.0	20	2700	1664.0	20.0	1.5
NV11DZ014EU_7	3.1	0.04	4.04100	0.06900	0.28710	0.00600	0.72577	14.0	1626.0	30.0	1969.0	22	200	1694.0	22.0	4.0
NV11DZ014EU_28	3.8	0.02	4.55100	0.05400	0.30940	0.00420	0.77772	9.6	1737.0	21.0	1759.0	14	200	1773.0	14.0	2.0
NV11DZ014EU_71	6.8	0.01	4.43500	0.03800	0.29410	0.00300	0.51309	7.2	1662.0	15.0	1765.0	15	1600	1775.0	15.0	6.4
NV11DZ014EU_21	19	0.05	4.52400	0.05300	0.30860	0.00500	0.93689	10.0	1733.0	25.0	1821.0	11	-400	1779.0	11.0	2.6
NV11DZ014EU_56	14	0.07	4.80000	0.11000	0.31720	0.00710	0.84920	20.0	1781.0	34.0	1817.0	19	4900	1781.0	19.0	0.0
NV11DZ014EU_38	8.9	0.04	4.25600	0.07700	0.28660	0.00400	0.45898	15.0	1627.0	20.0	1945.0	31	1200	1783.0	31.0	8.7
NV11DZ014EU_123	9.6	0.14	4.4590	0.0640	0.29790	0.00460	0.845	12	1681	23	1752	15	1300	1783.0	15.0	5.7
NV11DZ014EU_4	12	0.05	4.39100	0.05100	0.29390	0.00400	0.75636	9.9	1660.0	20.0	2033.0	15	2900	1785.0	15.0	7.0
NV11DZ014EU_97	4.4	0.01	4.8170	0.0410	0.31830	0.00350	0.805	7.2	1781	17	1772	14	200	1786.0	14.0	0.3

NV11DZ014EU_17	8.5	0.25	4.56000	0.05200	0.31030	0.00430	0.83208	9.8	1741.0	21.0	1740.0	12	1100	1788.0	12.0	2.6
NV11DZ014EU_130	18	0.03	4.8630	0.0990	0.32330	0.00780	0.954	16	1804	38	1562	14	3100	1793.0	14.0	0.6
NV11DZ014EU_136	3.6	0.05	4.8230	0.0530	0.31900	0.00350	0.799	9.2	1785	17	1870	13	500	1798.0	13.0	0.7
NV11DZ014EU_140	5.4	0.09	3.9380	0.0630	0.26090	0.00390	0.523	13	1494	20	1873	28	2100	1799.0	28.0	17.0
NV11DZ014EU_22	9.4	0.03	4.09100	0.06000	0.27390	0.00570	0.75276	12.0	1560.0	29.0	1777.0	23	1700	1823.0	23.0	14.4
NV11DZ014EU_34	3.2	0.02	4.33600	0.08000	0.28260	0.00560	0.16431	15.0	1607.0	27.0	1852.0	42	1080	1828.0	42.0	12.1
NV11DZ014EU_128	1.3	0.02	4.3200	0.1100	0.27850	0.00270	0.007	22	1584	14	1679	55	630	1851.0	55.0	14.4
NV11DZ014EU_44	9.9	0.23	4.91800	0.05200	0.31640	0.00280	0.52865	9.0	1772.0	14.0	2050.0	18	2360	1854.0	18.0	4.4
NV11DZ014EU_76	4.4	0.02	4.89200	0.05600	0.31250	0.00360	0.70733	9.6	1753.0	18.0	1858.0	16	500	1861.0	16.0	5.8
NV11DZ014EU_15	2.2	0.01	4.87600	0.08500	0.31370	0.00520	0.70826	15.0	1758.0	25.0	1920.0	20	900	1867.0	20.0	5.8
NV11DZ014EU_20	13	0.08	5.07000	0.05400	0.32860	0.00360	0.68871	9.0	1831.0	17.0	1835.0	14	2600	1869.0	14.0	2.0
NV11DZ014EU_114	1.1	0.02	4.7880	0.0630	0.30090	0.00290	0.356	11	1695	14	1876	23	20	1878.0	23.0	9.7
NV11DZ014EU_95	1.9	0.04	5.3480	0.0650	0.33440	0.00380	0.596	10	1859	18	1836	18	790	1890.0	18.0	1.6
NV11DZ014EU_112	10	0.08	4.9850	0.0510	0.31240	0.00360	0.574	8.4	1755	17	2067	16	760	1899.0	16.0	7.6
NV11DZ014EU_107	0.68	0.01	5.1400	0.1300	0.31810	0.00390	0.248	19	1780	19	1898	43	160	1901.0	43.0	6.4
NV11DZ014EU_42	3.4	0.01	5.17400	0.09500	0.32370	0.00630	0.55508	15.0	1807.0	30.0	1874.0	30	720	1910.0	30.0	5.4
NV11DZ014EU_36	10	0.04	5.42900	0.07300	0.34110	0.00320	0.09030	11.0	1892.0	16.0	2108.0	28	1000	1916.0	28.0	1.3
NV11DZ014EU_15	12	0.02	3.97600	0.08900	0.24650	0.00590	0.35264	20.0	1420.0	31.0	2015.0	35	1100	1923.0	35.0	26.2
NV11DZ014EU_58	8.2	0.09	4.12700	0.05500	0.25150	0.00330	0.73961	11.0	1446.0	17.0	1865.0	18	1930	1926.0	18.0	24.9
NV11DZ014EU_39	2	0.01	5.04900	0.07400	0.31440	0.00350	0.40921	12.0	1762.0	17.0	1975.0	28	200	1929.0	28.0	8.7
NV11DZ014EU_105	0.47	0.01	5.2300	0.2100	0.32450	0.00580	0.114	27	1811	28	2103	84	40	1939.0	84.0	6.6
NV11DZ014EU_116	5.8	0.05	5.7180	0.0950	0.34900	0.00590	0.837	14	1929	28	2148	15	-500	1955.0	15.0	1.3
NV11DZ014EU_12	3.7	0.04	4.72900	0.07200	0.29050	0.00470	0.80851	13.0	1644.0	23.0	1756.0	16	2500	1956.0	16.0	16.0
NV11DZ014EU_117	1.5	0.03	5.5690	0.0950	0.32790	0.00450	0.016	15	1831	21	2188	34	10	1977.0	34.0	7.4
NV11DZ014EU_29	2.6	0.01	5.86700	0.06400	0.35390	0.00400	0.28274	9.4	1955.0	18.0	1966.0	16	700	1998.0	16.0	2.2
NV11DZ014EU_19	4.2	0.01	5.45200	0.07800	0.32430	0.00510	0.70128	12.0	1810.0	25.0	2065.0	21	760	2034.0	21.0	11.0
NV11DZ014EU_11	3.4	0.02	6.70000	0.15000	0.37950	0.00890	0.81063	20.0	2072.0	41.0	2228.0	24	560	2092.0	24.0	1.0
NV11DZ014EU_50	1.3	0.02	6.84300	0.09900	0.38240	0.00540	0.59197	13.0	2087.0	25.0	2331.0	21	1900	2107.0	21.0	0.9
NV11DZ014EU_5	5	0.02	6.74200	0.06700	0.37820	0.00470	0.69913	8.9	2068.0	22.0	2232.0	16	2600	2110.0	16.0	2.0
NV11DZ014EU_109	0.5	0.02	5.9300	0.2900	0.32400	0.01000	0.337	42	1814	49	2430	87	390	2133.0	87.0	15.0
NV11DZ014EU_90	0.61	0.01	7.1100	0.1600	0.38860	0.00640	0.629	20	2116	29	2446	30	490	2139.0	30.0	1.1
NV11DZ014EU_6	1.5	0.01	7.25000	0.17000	0.39130	0.00530	0.38884	20.0	2132.0	24.0	1716.0	38	100	2164.0	38.0	1.5
NV11DZ014EU_98	4.8	0.01	6.4200	0.1000	0.32220	0.00430	0.477	13	1800	21	1974	24	1930	2270.0	24.0	20.7
NV11DZ014EU_77	4.1	0.03	9.55000	0.11000	0.44950	0.00620	0.73707	11.0	2393.0	28.0	2575.0	20	2700	2390.0	20.0	0.1
NV11DZ014EU_87	7.9	0.03	8.5200	0.1500	0.39530	0.00690	0.921	16	2146	32	2161	12	4000	2408.0	12.0	10.9
NV11DZ014EU_26	8.8	0.01	11.10000	0.11000	0.48210	0.00500	0.87190	8.9	2536.0	22.0	2575.0	9	4500	2572.5	9.2	1.4
NV11DZ014EU_86	6.3	0.02	10.7100	0.1100	0.45040	0.00480	0.643	9.7	2397	21	2658	15	1500	2575.0	15.0	6.9
NV11DZ014EU_122	6.7	0.04	11.6700	0.1900	0.49050	0.00740	0.843	16	2572	32	2882	13	1300	2585.0	13.0	0.5
NV11DZ014EU_64	5.4	0.06	11.71000	0.24000	0.48300	0.01200	0.83970	19.0	2541.0	54.0	2541.0	26	2500	2597.0	26.0	2.2
NV11DZ014EU_84	5.5	0.01	11.9100	0.1400	0.47060	0.00580	0.881	11	2485	26	2739	9	2400	2678.7	9.1	7.2

NV11DZ014EU_1	0.64	0.00	12.96000	0.18000	0.51500	0.01100	0.64991	13.0	2677.0	46.0	2698.0	27	80000	2679.0	27.0	0.1
NV11DZ014EU_3	1.3	0.02	12.62300	0.09900	0.50240	0.00480	0.78885	7.4	2624.0	20.0	2714.0	10	3100	2681.5	9.9	2.1
NV11DZ014EU_135	1.1	0.01	12.8400	0.1600	0.50970	0.00610	0.389	11	2655	26	2991	22	540	2683.0	22.0	1.0
NV11DZ014EU_2	0.37	0.00	12.99000	0.21000	0.51420	0.00930	0.83938	15.0	2673.0	39.0	2810.0	19	30	2694.0	19.0	0.8
NV11DZ014EU_23	0.9	0.01	11.46000	0.14000	0.44720	0.00660	0.55014	12.0	2382.0	29.0	2757.0	21	1000	2733.0	21.0	12.8
NV11DZ014EU_33	11	0.02	13.26000	0.28000	0.51000	0.01200	0.49331	20.0	2657.0	48.0	3550.0	33	1400	2765.0	33.0	3.9
NV11DZ014EU_103	2.6	0.02	14.0700	0.1200	0.51610	0.00490	0.642	8.1	2682	21	2947	13	550	2815.0	13.0	4.7
NV11DZ014EU_115	8	0.02	15.0900	0.1600	0.54760	0.00650	0.521	10	2815	27	3380	15	2000	2826.0	15.0	0.4
NV11DZ014EU_60	3.2	0.01	15.92000	0.21000	0.54410	0.00670	0.74306	12.0	2800.0	28.0	2809.0	14	-400	2901.0	14.0	3.5
NV11DZ014EU_45	1.6	0.03	15.17000	0.37000	0.51700	0.01000	0.28569	23.0	2685.0	44.0	4690.0	37	440	2908.0	37.0	7.7

Analysis	U (ppm)	U/Th	207Pb/ 235U	±	206Pb/ 238U	±	err. corr.	207Pb/ 235U Age (Ma)	± (Ma)	206Pb/ 238U Age (Ma)	± (Ma)	207Pb/ 206Pb Age (Ma)	± (Ma)	Best age (Ma)	± (Ma)	Disc (%)
NV11-017EU: Eureka 39° 26' 18"N, 115° 57' 57"W																
11017EU_26_1	202.6	1.40	0.07290	0.00270	0.01092	0.00023	0.10017	71.3	2.6	70.0	1.5	258	50	70.0	1.5	1.8
11017EU_51	512	1.44	0.07250	0.00190	0.01124	0.00014	0.00507	71.3	1.8	72.1	0.9	150	36	72.1	0.9	1.1
11017EU_26_2	197.5	1.36	0.07550	0.00290	0.01130	0.00024	0.23985	73.8	2.7	72.5	1.5	200	42	72.5	1.5	1.8
11017EU_50_1	340	2.72	0.10460	0.00250	0.01541	0.00022	0.39625	100.9	2.3	98.8	1.4	187	27	98.8	1.4	2.1
11017EU_60	288	2.05	0.10690	0.00290	0.01577	0.00032	0.13655	103.5	2.8	100.9	2.0	279	52	100.9	2.0	2.5
11017EU_50_2	278.2	2.75	0.10480	0.00380	0.01583	0.00032	0.28007	101.1	3.5	101.3	2.0	195	39	101.3	2.0	0.2
11017EU_35_1	63.9	0.73	0.10610	0.00560	0.01601	0.00044	0.01451	102.9	5.0	102.4	2.8	371	78	102.4	2.8	0.5
11017EU_6	220	2.16	0.11110	0.00320	0.01607	0.00022	0.19233	107.3	2.9	102.8	1.4	232	34	102.8	1.4	4.2
11017EU_5_2	346	4.77	0.10720	0.00230	0.01612	0.00021	0.30175	103.4	2.1	103.1	1.3	147	21	103.1	1.3	0.3
11017EU_1	275	2.87	0.10930	0.00290	0.01623	0.00020	0.01542	105.3	2.7	103.8	1.3	213	31	103.8	1.3	1.4
11017EU_66_2	522	2.22	0.10940	0.00210	0.01634	0.00022	0.09564	105.4	2.0	104.5	1.4	184	22	104.5	1.4	0.9
11017EU_35_2	78.6	0.71	0.11320	0.00460	0.01636	0.00047	0.11216	108.8	4.2	104.6	3.0	316	44	104.6	3.0	3.9
11017EU_66_1	322	2.23	0.12370	0.00590	0.01640	0.00025	0.32787	118.2	5.3	104.9	1.6	478	88	104.9	1.6	11.3
11017EU_8	459	1.53	0.11030	0.00270	0.01645	0.00026	0.03187	106.2	2.5	105.3	1.6	224	39	105.3	1.6	0.8
11017EU_61	283.8	2.79	0.10810	0.00280	0.01654	0.00023	0.13610	104.1	2.6	105.8	1.4	176	36	105.8	1.4	1.6
11017EU_52_1	324.8	2.53	0.11100	0.00270	0.01684	0.00023	0.04590	106.8	2.5	107.7	1.4	190	31	107.7	1.4	0.8
11017EU_52_2	267	2.64	0.11050	0.00270	0.01692	0.00022	0.23313	106.4	2.5	108.2	1.4	148	25	108.2	1.4	1.7
11017EU_46	154	1.04	0.11470	0.00420	0.01704	0.00034	0.06506	110.7	4.0	108.9	2.1	320	49	108.9	2.1	1.6
11017EU_5_1	269.6	5.75	0.11520	0.00320	0.01708	0.00023	0.04966	110.6	2.9	109.2	1.4	215	37	109.2	1.4	1.3
11017EU_85	228	1.27	0.12260	0.00490	0.01709	0.00040	0.24537	117.3	4.4	109.2	2.5	340	47	109.2	2.5	6.9
11017EU_75	281.3	3.37	0.11470	0.00310	0.01710	0.00026	0.03868	110.2	2.9	109.3	1.6	220	37	109.3	1.6	0.8
11017EU_14	168	1.20	0.11370	0.00320	0.01713	0.00032	0.16953	109.3	2.9	109.5	2.0	237	36	109.5	2.0	0.2
11017EU_72_2	181	1.22	0.11710	0.00470	0.01717	0.00029	0.11165	112.2	4.3	109.7	1.8	289	48	109.7	1.8	2.2
11017EU_44_1	294	1.29	0.11500	0.00560	0.01723	0.00029	0.00190	108.5	3.5	110.1	1.8	212	46	110.1	1.8	1.5
11017EU_71_1	160	1.05	0.11980	0.00410	0.01723	0.00041	0.02937	114.7	3.7	110.1	2.6	313	43	110.1	2.6	4.0
11017EU_22	164.6	1.00	0.11570	0.00420	0.01729	0.00038	0.02108	111.1	3.8	110.5	2.4	281	50	110.5	2.4	0.5
11017EU_44_2	187	0.81	0.12230	0.00420	0.01740	0.00036	0.05590	117.5	3.9	111.2	2.3	282	44	111.2	2.3	5.4
11017EU_34_2	234	2.61	0.11680	0.00320	0.01741	0.00028	0.24149	112.1	2.9	111.3	1.8	198	32	111.3	1.8	0.7
11017EU_84	205.9	1.29	0.12630	0.00470	0.01744	0.00031	0.04072	120.6	4.3	111.5	2.0	378	55	111.5	2.0	7.5
11017EU_34_1	250.7	2.59	0.12320	0.00360	0.01753	0.00022	0.05470	117.9	3.3	112.0	1.4	231	37	112.0	1.4	5.0
11017EU_73	310	2.15	0.11900	0.00310	0.01760	0.00032	0.04031	114.2	2.8	112.4	2.0	234	39	112.4	2.0	1.6
11017EU_62	308	1.23	0.11880	0.00360	0.01775	0.00037	0.34253	113.9	3.3	113.4	2.3	207	31	113.4	2.3	0.4
11017EU_24_1	143	1.36	0.12510	0.00450	0.01797	0.00031	0.09493	119.6	4.1	114.8	2.0	271	42	114.8	2.0	4.0
11017EU_24_2	213	1.19	0.11980	0.00300	0.01804	0.00027	0.05885	114.9	2.7	115.3	1.7	187	25	115.3	1.7	0.3
11017EU_45	302	1.24	0.17250	0.00720	0.02477	0.00058	0.48536	161.3	6.2	157.7	3.6	275	44	157.7	3.6	2.2

11017EU_23	154.6	3.30	0.50000	0.01900	0.06350	0.00130	0.40941	411.0	13.0	397.1	7.9	451	43	397.1	7.9	3.4
11017EU_33	83.9	1.16	0.52100	0.01400	0.06550	0.00100	0.47646	424.7	9.4	408.9	6.3	463	34	408.9	6.3	3.7
11017EU_81	326	1.53	0.54440	0.00760	0.07067	0.00080	0.45921	441.2	5.0	440.2	4.8	428	16	440.2	4.8	0.2
11017EU_80	207.2	2.09	0.55290	0.00770	0.07221	0.00066	0.01956	446.7	5.0	449.9	3.9	422	21	449.9	3.9	0.7
11017EU_91	14.7	0.52	1.75300	0.05200	0.17130	0.00390	0.14435	1028.0	19.0	1021.0	21.0	1023	48	1023.0	48.0	0.2
11017EU_36	109.5	1.40	2.03500	0.02400	0.19180	0.00180	0.39385	1127.7	7.7	1130.8	9.6	1106	13	1106.0	13.0	2.2
11017EU_32_2	34.7	0.69	2.40300	0.05100	0.21210	0.00350	0.47786	1245.0	16.0	1242.0	18.0	1246	28	1246.0	28.0	0.3
11017EU_32_1	27.5	0.44	2.60500	0.09200	0.22470	0.00400	0.42419	1300.0	26.0	1306.0	21.0	1277	33	1277.0	33.0	2.3
11017EU_68.	82.7	1.90	2.48600	0.04400	0.21560	0.00240	0.48178	1269.0	12.0	1258.0	13.0	1301	20	1301.0	20.0	3.3
11017EU_30	113.7	1.82	3.66000	0.03200	0.28410	0.00240	0.50501	1562.3	6.9	1612.0	12.0	1478	10	1478.4	9.5	9.0
11017EU_13	197.6	1.31	3.31500	0.03200	0.25600	0.00210	0.37691	1484.3	7.5	1471.0	10.0	1498	11	1498.0	11.0	1.8
11017EU_65	260	1.33	3.98300	0.02600	0.28820	0.00180	0.60014	1630.5	5.3	1632.6	8.9	1637	6	1637.2	5.9	0.3
11017EU_29	22.98	0.65	4.92100	0.06900	0.32450	0.00480	0.10369	1805.0	12.0	1811.0	23.0	1772	21	1772.0	21.0	2.2
11017EU_88	57.3	1.27	4.76300	0.06600	0.31670	0.00560	0.61598	1779.0	11.0	1773.0	27.0	1777	16	1777.0	16.0	0.2
11017EU_86	71.5	1.57	4.50400	0.06000	0.30040	0.00390	0.54728	1732.0	11.0	1693.0	19.0	1780	11	1780.0	11.0	4.9
11017EU_94	87.9	1.48	4.35500	0.05600	0.28940	0.00310	0.48901	1705.0	10.0	1638.0	15.0	1782	11	1782.0	11.0	8.1
11017EU_19	49.1	0.65	4.97700	0.06200	0.32550	0.00380	0.45299	1814.0	11.0	1816.0	18.0	1818	12	1818.0	12.0	0.1
11017EU_93	255	0.89	5.04300	0.03300	0.32690	0.00210	0.46558	1826.4	5.5	1823.0	10.0	1818	8	1818.4	8.3	0.3
11017EU_7	63.7	0.99	4.88200	0.05900	0.31680	0.00320	0.27790	1800.0	11.0	1774.0	15.0	1819	14	1819.0	14.0	2.5
11017EU_57	48	0.73	4.77400	0.06300	0.30960	0.00410	0.47032	1779.0	11.0	1738.0	20.0	1821	14	1821.0	14.0	4.6
11017EU_87	82.9	1.20	4.90900	0.06700	0.31900	0.00410	0.70428	1803.0	12.0	1784.0	20.0	1822	10	1822.1	9.5	2.1
11017EU_48	113	1.32	4.91900	0.05900	0.32080	0.00270	0.36452	1805.0	10.0	1793.0	13.0	1824	14	1824.0	14.0	1.7
11017EU_82	105.4	0.90	4.93900	0.08100	0.31960	0.00630	0.84222	1808.0	14.0	1787.0	31.0	1827	15	1827.0	15.0	2.2
11017EU_76	48.3	0.99	4.86900	0.05900	0.31470	0.00320	0.50146	1796.0	10.0	1763.0	16.0	1830	13	1830.0	13.0	3.7
11017EU_64	54.3	1.15	4.79600	0.05000	0.31040	0.00380	0.45451	1783.6	8.8	1742.0	19.0	1832	13	1832.0	13.0	4.9
11017EU_56	62.4	1.04	4.88900	0.06900	0.31650	0.00430	0.72713	1803.0	12.0	1772.0	21.0	1832	10	1832.2	9.5	3.3
11017EU_27	24.2	0.81	5.23600	0.08500	0.33680	0.00540	0.45996	1864.0	15.0	1870.0	26.0	1834	16	1834.0	16.0	2.0
11017EU_10	48.59	1.02	5.04800	0.07300	0.32500	0.00330	0.50413	1828.0	13.0	1814.0	16.0	1838	16	1838.0	16.0	1.3
11017EU_55	64.6	1.21	4.69300	0.06700	0.30160	0.00370	0.64147	1765.0	12.0	1699.0	18.0	1846	12	1846.0	12.0	8.0
11017EU_37	26.3	1.13	5.12800	0.09500	0.32750	0.00610	0.53876	1839.0	16.0	1825.0	30.0	1849	16	1849.0	16.0	1.3
11017EU_38	118.8	1.94	5.33500	0.05200	0.34130	0.00310	0.70790	1873.9	8.3	1893.0	15.0	1851	9	1850.6	9.1	2.3
11017EU_92	95.9	1.27	4.74400	0.06500	0.30180	0.00350	0.47610	1774.0	12.0	1700.0	18.0	1851	12	1851.0	12.0	8.2
11017EU_59	107.1	1.07	5.05800	0.04400	0.32340	0.00250	0.50249	1828.6	7.4	1806.0	12.0	1858	8	1857.9	7.8	2.8
11017EU_31	61	2.38	5.38400	0.07300	0.33860	0.00430	0.62854	1881.0	12.0	1882.0	20.0	1858	12	1858.0	12.0	1.3
11017EU_83	60.7	1.75	5.00400	0.06100	0.31610	0.00370	0.60703	1824.0	9.8	1770.0	18.0	1868	10	1868.0	10.0	5.2
11017EU_4	36.4	0.51	5.43100	0.08300	0.33960	0.00420	0.50593	1889.0	13.0	1884.0	20.0	1879	13	1879.0	13.0	0.3
11017EU_89	68.3	1.15	5.41800	0.05900	0.33690	0.00280	0.52818	1887.3	9.4	1871.0	13.0	1887	9	1887.4	9.2	0.9
11017EU_9	93.7	1.37	5.33200	0.07400	0.33100	0.00260	0.17775	1875.0	12.0	1843.0	13.0	1898	25	1898.0	25.0	2.9
11017EU_16	156	0.60	5.45900	0.05000	0.34170	0.00370	0.76213	1896.8	8.1	1894.0	18.0	1907	7	1907.3	6.8	0.7
11017EU_42	43.3	0.43	5.40100	0.08900	0.33180	0.00540	0.47878	1884.0	14.0	1847.0	26.0	1927	15	1927.0	15.0	4.2

11017EU_2	166	0.54	5.69500	0.03000	0.34690	0.00180	0.54984	1930.4	4.5	1919.7	8.5	1942	6	1942.0	6.0	1.1
11017EU_49	38.6	0.81	5.99800	0.08900	0.35420	0.00450	0.30778	1974.0	13.0	1954.0	21.0	2003	19	2003.0	19.0	2.4
11017EU_25	65.3	0.72	6.42500	0.07900	0.36510	0.00490	0.66573	2035.0	11.0	2006.0	23.0	2050	15	2050.0	15.0	2.1
11017EU_28	23.69	1.06	6.66000	0.10000	0.37850	0.00630	0.68194	2068.0	13.0	2068.0	29.0	2055	11	2055.0	11.0	0.6
11017EU_3	51.8	1.00	6.43000	0.06100	0.36450	0.00290	0.45835	2035.9	8.3	2003.0	14.0	2062	10	2062.0	10.0	2.9
11017EU_58	127.9	0.97	6.16500	0.05300	0.34670	0.00340	0.71804	1999.0	7.6	1919.0	16.0	2075	8	2074.5	8.3	7.5
11017EU_40	100.6	1.19	6.43500	0.06700	0.35910	0.00350	0.70001	2036.4	9.2	1978.0	17.0	2075	8	2074.6	7.5	4.7
11017EU_67	106.6	0.36	6.40800	0.06800	0.35680	0.00390	0.67833	2032.7	9.3	1967.0	18.0	2090	10	2090.0	10.0	5.9
11017EU_20	15.64	0.57	6.55000	0.13000	0.36150	0.00500	0.26929	2053.0	17.0	1989.0	24.0	2124	25	2124.0	25.0	6.4
11017EU_90	74.9	1.23	7.25100	0.08200	0.38500	0.00430	0.51605	2144.0	9.6	2099.0	20.0	2183	12	2183.0	12.0	3.8
11017EU_47	91.9	1.02	10.29000	0.11000	0.46720	0.00470	0.75407	2460.4	9.6	2471.0	21.0	2465	8	2465.3	7.7	0.2
11017EU_78	23.25	0.80	11.76000	0.19000	0.48650	0.00580	0.53271	2584.0	15.0	2555.0	25.0	2596	11	2596.0	11.0	1.6
11017EU_39	52.9	0.60	11.72000	0.14000	0.47620	0.00600	0.69639	2583.0	11.0	2510.0	26.0	2628	8	2627.6	8.3	4.5
11017EU_74	103.1	0.94	12.93000	0.16000	0.47730	0.00520	0.69208	2674.0	12.0	2515.0	23.0	2791	9	2790.7	8.7	9.9
11017EU_41	47.9	1.09	16.57000	0.26000	0.53810	0.00930	0.58399	2909.0	15.0	2774.0	39.0	2994	11	2994.0	11.0	7.3

Diamond Peak Formation Sample

Analysis	U (ppm)	U/Th	207Pb/ 235U	±	206Pb/ 238U	±	err. corr.	207Pb/ 235U Age (Ma)	± (Ma)	206Pb/ 238U Age (Ma)	± (Ma)	207Pb/ 206Pb Age (Ma)	± (Ma)	Best age (Ma)	± (Ma)	Disc (%)
NV15-013PR: Piñon Range 40° 35' 6"N, 116° 0' 18"W																
NV15013PR_7	463	0.77	0.43920	0.00640	0.05877	0.00074	0.75746	369.5	4.5	368.1	4.5	350	23	368.1	4.5	0.4
NV15013PR_95	206	2.49	1.90800	0.02800	0.18230	0.00280	0.62368	1084.0	10.0	1081.0	15.0	1103	26	1103.0	26.0	2.0
NV15013PR_28	197.7	2.24	1.89100	0.03400	0.17840	0.00350	0.82530	1078.0	12.0	1060.0	19.0	1139	20	1139.0	20.0	6.9
NV15013PR_109	376	2.11	3.26000	0.06800	0.25720	0.00730	0.79169	1469.0	16.0	1478.0	36.0	1465	31	1465.0	31.0	0.9
NV15013PR_120	167	1.90	4.63700	0.04300	0.31230	0.00330	0.70044	1756.9	7.9	1754.0	15.0	1759	14	1759.0	14.0	0.3
NV15013PR_110	89.1	0.94	4.78700	0.05300	0.31880	0.00370	0.52837	1781.9	9.4	1783.0	18.0	1764	19	1764.0	19.0	1.1
NV15013PR_124	167.6	1.56	4.70400	0.04500	0.31590	0.00310	0.62457	1767.4	8.0	1770.0	15.0	1769	17	1769.0	17.0	0.1
NV15013PR_127	225	1.63	4.86900	0.03900	0.32730	0.00290	0.62747	1796.4	6.8	1825.0	14.0	1769	14	1769.0	14.0	3.2
NV15013PR_123	208	1.24	3.95200	0.07100	0.26810	0.00500	0.85817	1625.0	14.0	1530.0	25.0	1777	21	1777.0	21.0	13.9
NV15013PR_68	105.5	1.45	4.89100	0.07200	0.31960	0.00510	0.69335	1799.0	12.0	1787.0	25.0	1780	21	1780.0	21.0	0.4
NV15013PR_20	132.8	1.53	4.45400	0.04700	0.29610	0.00310	0.66486	1721.8	8.8	1674.0	16.0	1782	17	1782.0	17.0	6.1
NV15013PR_37	247	1.96	4.40600	0.03700	0.29010	0.00280	0.67393	1713.0	6.9	1643.0	14.0	1783	14	1783.0	14.0	7.9
NV15013PR_43	262	2.42	4.84400	0.04200	0.32150	0.00340	0.56454	1792.2	7.2	1797.0	16.0	1786	16	1786.0	16.0	0.6
NV15013PR_58	166	3.49	5.50300	0.08200	0.36820	0.00650	0.84265	1900.0	13.0	2023.0	30.0	1786	18	1786.0	18.0	13.3
NV15013PR_90	416	2.42	4.69000	0.06700	0.31020	0.00540	0.82177	1764.0	12.0	1744.0	27.0	1787	17	1787.0	17.0	2.4
NV15013PR_84	164	1.53	4.60000	0.05600	0.30900	0.00410	0.76898	1748.0	10.0	1738.0	21.0	1789	15	1789.0	15.0	2.9
NV15013PR_42	47.9	0.75	4.73700	0.06200	0.31480	0.00370	0.35606	1773.0	11.0	1766.0	18.0	1790	26	1790.0	26.0	1.3
NV15013PR_91	367	4.21	4.78100	0.04600	0.31530	0.00390	0.83020	1782.0	8.2	1766.0	19.0	1794	14	1794.0	14.0	1.6
NV15013PR_63	203	2.15	4.09500	0.08500	0.26950	0.00540	0.87722	1650.0	17.0	1537.0	27.0	1795	18	1795.0	18.0	14.4
NV15013PR_50	318	2.99	4.95000	0.05900	0.32880	0.00340	0.79165	1811.0	10.0	1832.0	16.0	1796	12	1796.0	12.0	2.0
NV15013PR_44	258	1.46	4.38000	0.13000	0.28980	0.00940	0.96031	1705.0	24.0	1644.0	46.0	1797	17	1797.0	17.0	8.5
NV15013PR_116	51.8	0.77	4.41000	0.10000	0.29340	0.00490	0.65894	1714.0	18.0	1658.0	24.0	1799	27	1799.0	27.0	7.8
NV15013PR_21	269	2.17	4.47300	0.04200	0.29480	0.00360	0.86945	1725.3	7.8	1665.0	18.0	1801	16	1801.0	16.0	7.6
NV15013PR_41	119.9	1.98	4.63800	0.04300	0.30450	0.00310	0.52783	1755.5	7.7	1713.0	15.0	1803	17	1803.0	17.0	5.0
NV15013PR_46	266	1.94	4.76100	0.04700	0.31460	0.00350	0.71451	1777.5	8.2	1763.0	17.0	1805	14	1805.0	14.0	2.3
NV15013PR_29	81.9	2.08	4.38400	0.05400	0.29060	0.00320	0.67901	1708.0	10.0	1644.0	16.0	1807	18	1807.0	18.0	9.0
NV15013PR_102	440	10.20	5.02000	0.11000	0.32730	0.00760	0.81407	1821.0	19.0	1824.0	37.0	1807	27	1807.0	27.0	0.9
NV15013PR_24	143.9	1.08	4.74800	0.06500	0.31260	0.00560	0.54653	1776.0	11.0	1752.0	28.0	1808	24	1808.0	24.0	3.1
NV15013PR_53	308	2.16	4.99400	0.07200	0.32710	0.00500	0.87829	1817.0	12.0	1826.0	25.0	1808	13	1808.0	13.0	1.0
NV15013PR_15	42.8	2.34	4.77800	0.07900	0.31210	0.00450	0.52570	1781.0	14.0	1750.0	22.0	1816	29	1816.0	29.0	3.6
NV15013PR_121	176	2.44	3.69000	0.32000	0.23700	0.02200	0.92547	1538.0	75.0	1360.0	110.0	1817	33	1817.0	33.0	25.2
NV15013PR_5	109.7	0.96	5.42900	0.08500	0.34630	0.00460	0.59323	1891.0	14.0	1916.0	22.0	1820	24	1820.0	24.0	5.3
NV15013PR_112	179.2	1.89	4.86500	0.05700	0.31710	0.00360	0.75850	1795.0	10.0	1775.0	18.0	1824	14	1824.0	14.0	2.7

NV15013PR_115	240	1.22	5.18800	0.06200	0.33980	0.00450	0.81788	1850.0	10.0	1885.0	22.0	1824	13	1824.0	13.0	3.3
NV15013PR_122	63	1.52	5.03800	0.06400	0.32590	0.00400	0.55505	1825.0	11.0	1818.0	19.0	1824	21	1824.0	21.0	0.3
NV15013PR_3	65.7	0.95	5.25300	0.06800	0.33390	0.00390	0.57252	1860.0	11.0	1857.0	19.0	1825	21	1825.0	21.0	1.8
NV15013PR_66	278	2.91	4.28600	0.08600	0.27970	0.00670	0.88941	1694.0	17.0	1589.0	34.0	1828	17	1828.0	17.0	13.1
NV15013PR_129	192.3	2.03	5.24100	0.07300	0.33490	0.00530	0.75381	1859.0	12.0	1861.0	26.0	1838	22	1838.0	22.0	1.3
NV15013PR_114	71.8	1.04	5.08500	0.05100	0.33120	0.00360	0.50431	1833.1	8.5	1844.0	18.0	1839	19	1839.0	19.0	0.3
NV15013PR_94	161	1.05	5.11500	0.07500	0.32870	0.00600	0.77727	1838.0	12.0	1831.0	29.0	1840	22	1840.0	22.0	0.5
NV15013PR_111	54.1	0.71	5.36000	0.06700	0.34310	0.00390	0.40220	1878.0	11.0	1901.0	19.0	1840	22	1840.0	22.0	3.3
NV15013PR_19	104.4	3.24	5.15200	0.05600	0.33170	0.00290	0.65323	1845.1	9.0	1846.0	14.0	1841	15	1841.0	15.0	0.3
NV15013PR_2	66.4	0.84	5.23800	0.06000	0.33220	0.00450	0.75594	1859.5	9.5	1849.0	22.0	1846	17	1846.0	17.0	0.2
NV15013PR_16	84.8	1.44	4.77700	0.07000	0.30690	0.00420	0.76890	1781.0	13.0	1725.0	21.0	1847	16	1847.0	16.0	6.6
NV15013PR_8	99.3	0.76	5.41000	0.07600	0.34070	0.00570	0.75432	1885.0	12.0	1889.0	27.0	1848	18	1848.0	18.0	2.2
NV15013PR_6	129	0.95	4.99800	0.06800	0.31370	0.00420	0.77859	1819.0	12.0	1758.0	21.0	1849	15	1849.0	15.0	4.9
NV15013PR_128	148	1.79	5.19800	0.04900	0.33160	0.00330	0.51520	1851.7	8.0	1848.0	16.0	1850	17	1850.0	17.0	0.1
NV15013PR_27	237	2.51	3.49100	0.06400	0.22700	0.00550	0.69033	1525.0	14.0	1318.0	29.0	1855	30	1855.0	30.0	28.9
NV15013PR_80	27.53	1.91	5.39000	0.21000	0.34900	0.01200	0.20339	1865.0	26.0	1923.0	57.0	1855	69	1855.0	69.0	3.7
NV15013PR_47	76.5	1.21	4.91100	0.09100	0.31400	0.00610	0.83431	1802.0	16.0	1759.0	30.0	1862	18	1862.0	18.0	5.5
NV15013PR_96	187	6.15	5.56000	0.18000	0.34700	0.01100	0.75437	1907.0	28.0	1918.0	51.0	1864	48	1864.0	48.0	2.9
NV15013PR_97	213	1.65	4.56300	0.07900	0.29200	0.00750	0.73654	1745.0	15.0	1651.0	38.0	1864	29	1864.0	29.0	11.4
NV15013PR_117	54.5	1.01	4.79100	0.09400	0.30780	0.00530	0.32699	1781.0	16.0	1729.0	26.0	1865	33	1865.0	33.0	7.3
NV15013PR_73	92.5	3.51	5.07000	0.15000	0.32030	0.00900	0.93420	1825.0	26.0	1788.0	44.0	1867	22	1867.0	22.0	4.2
NV15013PR_34	227	1.38	5.06000	0.08300	0.32060	0.00640	0.89030	1828.0	14.0	1792.0	32.0	1872	17	1872.0	17.0	4.3
NV15013PR_39	111	2.88	5.45300	0.06200	0.34310	0.00380	0.54773	1892.4	9.7	1901.0	18.0	1872	18	1872.0	18.0	1.5
NV15013PR_104	117	2.11	4.67000	0.14000	0.29160	0.00990	0.93852	1767.0	26.0	1647.0	49.0	1872	25	1872.0	25.0	12.0
NV15013PR_113	42.1	3.68	5.25700	0.07000	0.33480	0.00350	0.55681	1861.0	11.0	1861.0	17.0	1879	20	1879.0	20.0	1.0
NV15013PR_88	163.6	4.19	5.22300	0.08500	0.32840	0.00600	0.69587	1856.0	13.0	1829.0	29.0	1881	25	1881.0	25.0	2.8
NV15013PR_82	162.2	0.91	4.42000	0.10000	0.28270	0.00730	0.91616	1715.0	19.0	1603.0	37.0	1884	15	1884.0	15.0	14.9
NV15013PR_65	131	2.19	5.21800	0.05600	0.32550	0.00380	0.09961	1854.7	9.2	1816.0	18.0	1893	20	1893.0	20.0	4.1
NV15013PR_9	42.7	1.75	5.54300	0.09300	0.34380	0.00550	0.70175	1905.0	15.0	1904.0	26.0	1897	23	1897.0	23.0	0.4
NV15013PR_77	187	1.73	5.19700	0.06200	0.32640	0.00420	0.81163	1853.0	10.0	1820.0	20.0	1903	17	1903.0	17.0	4.4
NV15013PR_38	120.8	1.11	5.80200	0.05900	0.35830	0.00390	0.72932	1947.0	8.6	1974.0	19.0	1905	16	1905.0	16.0	3.6
NV15013PR_70	292	1.61	4.72000	0.11000	0.29000	0.00780	0.95692	1775.0	20.0	1644.0	38.0	1908	15	1908.0	15.0	13.8
NV15013PR_74	93	1.62	5.46100	0.06400	0.33870	0.00450	0.62445	1897.3	9.9	1879.0	22.0	1910	19	1910.0	19.0	1.6
NV15013PR_125	77.1	0.86	5.63200	0.06100	0.35270	0.00450	0.48402	1920.4	9.5	1950.0	22.0	1912	20	1912.0	20.0	2.0
NV15013PR_108	297	1.39	5.62400	0.06800	0.34600	0.00480	0.81800	1920.0	11.0	1917.0	22.0	1914	14	1914.0	14.0	0.2
NV15013PR_17	288.6	4.27	5.53000	0.19000	0.34300	0.01400	0.67028	1903.0	29.0	1904.0	67.0	1920	53	1920.0	53.0	0.8
NV15013PR_14	128.3	1.59	4.35000	0.10000	0.26620	0.00640	0.47772	1701.0	19.0	1520.0	32.0	1931	36	1931.0	36.0	21.3
NV15013PR_18	212.7	2.06	5.59000	0.09300	0.33340	0.00630	0.84798	1914.0	14.0	1853.0	30.0	1960	17	1960.0	17.0	5.5
NV15013PR_67	167	0.82	5.73000	0.05700	0.34110	0.00420	0.76797	1935.1	8.7	1894.0	21.0	1960	15	1960.0	15.0	3.4
NV15013PR_72	74.1	0.67	6.28000	0.10000	0.36690	0.00590	0.46048	2014.0	15.0	2013.0	28.0	1990	20	1990.0	20.0	1.2

NV15013PR_25	104.7	2.43	5.77000	0.13000	0.33950	0.00660	0.55338	1945.0	21.0	1883.0	32.0	1996	36	1996.0	36.0	5.7
NV15013PR_33	203	1.77	6.26200	0.05500	0.36880	0.00410	0.77549	2012.7	7.6	2023.0	19.0	2010	11	2010.0	11.0	0.6
NV15013PR_100	189	1.49	6.48000	0.14000	0.37400	0.01000	0.78266	2040.0	19.0	2044.0	48.0	2026	30	2026.0	30.0	0.9
NV15013PR_48	290	2.46	5.01900	0.07000	0.29160	0.00480	0.90442	1824.0	12.0	1649.0	24.0	2040	12	2040.0	12.0	19.2
NV15013PR_87	151	1.64	6.58000	0.16000	0.37470	0.00750	0.84945	2052.0	21.0	2054.0	34.0	2046	23	2046.0	23.0	0.4
NV15013PR_81	50.6	0.74	6.08600	0.08600	0.34820	0.00520	0.74250	1987.0	12.0	1925.0	25.0	2063	18	2063.0	18.0	6.7
NV15013PR_103	100.1	1.51	7.36000	0.29000	0.41000	0.02000	0.67070	2154.0	36.0	2202.0	91.0	2068	65	2068.0	65.0	6.5
NV15013PR_23	120.5	2.19	6.64200	0.07700	0.37640	0.00460	0.82468	2064.0	10.0	2059.0	22.0	2081	12	2081.0	12.0	1.1
NV15013PR_61	250	1.07	6.67700	0.06400	0.37690	0.00320	0.65193	2068.9	8.5	2061.0	15.0	2088	13	2088.0	13.0	1.3
NV15013PR_64	40.6	0.95	6.96000	0.11000	0.38940	0.00510	0.74452	2106.0	15.0	2119.0	24.0	2089	18	2089.0	18.0	1.4
NV15013PR_71	181	1.37	6.84500	0.08600	0.37460	0.00570	0.91517	2090.0	11.0	2050.0	27.0	2110	13	2110.0	13.0	2.8
NV15013PR_83	54.8	0.98	5.97100	0.08500	0.33760	0.00520	0.60618	1972.0	12.0	1874.0	25.0	2112	25	2112.0	25.0	11.3
NV15013PR_106	56.4	4.86	7.75000	0.13000	0.41460	0.00910	0.72048	2203.0	15.0	2241.0	43.0	2143	27	2143.0	27.0	4.6
NV15013PR_98	95.1	2.59	7.69000	0.41000	0.37000	0.01400	0.92158	2179.0	51.0	2022.0	67.0	2311	44	2311.0	44.0	12.5
NV15013PR_51	75.9	1.15	9.17000	0.18000	0.44220	0.00640	0.56195	2354.0	19.0	2359.0	29.0	2335	27	2335.0	27.0	1.0
NV15013PR_76	33.9	2.02	7.90000	0.31000	0.37900	0.01100	0.64501	2214.0	33.0	2077.0	50.0	2375	45	2375.0	45.0	12.5
NV15013PR_26	258	2.52	8.64000	0.62000	0.39300	0.01800	0.98158	2263.0	71.0	2130.0	86.0	2415	58	2415.0	58.0	11.8
NV15013PR_45	273.6	5.42	7.81000	0.19000	0.34300	0.01000	0.87293	2205.0	22.0	1900.0	48.0	2504	22	2504.0	22.0	24.1
NV15013PR_119	201	2.06	11.30000	0.15000	0.48420	0.00740	0.78615	2547.0	13.0	2545.0	32.0	2535	14	2535.0	14.0	0.4
NV15013PR_10	37.8	0.67	10.94000	0.16000	0.45840	0.00670	0.64088	2518.0	14.0	2431.0	30.0	2542	22	2542.0	22.0	4.4
NV15013PR_31	248	1.63	10.40000	0.24000	0.44930	0.00830	0.77693	2463.0	18.0	2390.0	37.0	2543	16	2543.0	16.0	6.0
NV15013PR_56	250.2	2.28	9.55000	0.31000	0.40800	0.01100	0.90297	2389.0	30.0	2201.0	52.0	2548	22	2548.0	22.0	13.6
NV15013PR_59	105.8	1.31	12.32000	0.22000	0.53600	0.00930	0.56524	2631.0	17.0	2764.0	39.0	2554	26	2554.0	26.0	8.2
NV15013PR_105	212	1.50	11.31000	0.28000	0.47500	0.01300	0.94109	2553.0	24.0	2501.0	57.0	2581	17	2581.0	17.0	3.1
NV15013PR_130	146.9	1.16	10.10000	0.16000	0.42010	0.00650	0.82878	2444.0	15.0	2260.0	29.0	2587	15	2587.0	15.0	12.6
NV15013PR_85	218	2.06	11.52000	0.16000	0.48550	0.00730	0.74989	2564.0	13.0	2550.0	32.0	2592	15	2592.0	15.0	1.6
NV15013PR_13	113.7	1.49	11.30000	0.26000	0.45480	0.00760	0.65060	2550.0	20.0	2416.0	34.0	2593	27	2593.0	27.0	6.8
NV15013PR_60	191	1.31	12.66000	0.29000	0.52800	0.01300	0.96977	2650.0	24.0	2730.0	57.0	2601	16	2601.0	16.0	5.0
NV15013PR_30	231	3.42	11.40000	0.23000	0.47500	0.01000	0.88951	2557.0	19.0	2505.0	46.0	2609	19	2609.0	19.0	4.0
NV15013PR_32	203	1.54	11.94000	0.22000	0.49400	0.01100	0.94225	2593.0	19.0	2586.0	48.0	2609	14	2609.0	14.0	0.9
NV15013PR_101	192.5	1.64	12.33000	0.23000	0.50300	0.01200	0.87781	2627.0	18.0	2623.0	49.0	2615	20	2615.0	20.0	0.3
NV15013PR_35	117.7	2.63	12.51000	0.20000	0.50430	0.00950	0.92595	2637.0	17.0	2630.0	41.0	2627	19	2627.0	19.0	0.1
NV15013PR_54	220	2.98	9.90000	0.34000	0.39900	0.01500	0.72428	2425.0	32.0	2167.0	72.0	2642	43	2642.0	43.0	18.0
NV15013PR_89	91.4	0.69	12.79000	0.13000	0.51170	0.00540	0.72191	2663.7	9.8	2663.0	23.0	2673	12	2673.0	12.0	0.4
NV15013PR_92	124.9	1.18	13.00000	0.14000	0.51500	0.00600	0.81064	2680.0	10.0	2677.0	25.0	2678	12	2678.0	12.0	0.0
NV15013PR_86	187	0.86	12.00000	0.45000	0.47500	0.01700	0.97984	2597.0	37.0	2498.0	75.0	2698	12	2698.0	12.0	7.4
NV15013PR_118	150.5	1.12	12.96000	0.10000	0.50800	0.00410	0.72419	2677.0	7.3	2648.0	18.0	2698	10	2698.0	10.0	1.9
NV15013PR_126	53.8	1.23	13.17000	0.14000	0.51850	0.00560	0.66094	2691.0	10.0	2692.0	24.0	2698	15	2698.0	15.0	0.2
NV15013PR_49	87	2.90	13.08000	0.25000	0.50810	0.00970	0.94992	2682.0	19.0	2646.0	42.0	2706	16	2706.0	16.0	2.2
NV15013PR_40	171.2	0.79	13.30000	0.14000	0.50070	0.00640	0.79447	2700.0	10.0	2616.0	27.0	2754	13	2754.0	13.0	5.0

NV15013PR_52	24.11	1.58	14.71000	0.21000	0.55900	0.01000	0.53005	2799.0	13.0	2860.0	43.0	2754	23	2754.0	23.0	3.8
NV15013PR_62	179	1.82	14.21000	0.14000	0.53150	0.00620	0.88100	2763.1	9.3	2751.0	25.0	2774	12	2774.0	12.0	0.8
NV15013PR_4	73	0.65	15.14000	0.24000	0.53470	0.00860	0.86473	2824.0	15.0	2759.0	36.0	2838	15	2838.0	15.0	2.8
NV15013PR_55	65.3	1.37	19.71000	0.19000	0.65160	0.00690	0.61816	3077.8	9.6	3233.0	27.0	2980	14	2980.0	14.0	8.5
NV15013PR_12	95.4	1.13	19.17000	0.19000	0.59730	0.00890	0.63871	3050.0	9.8	3019.0	36.0	3036	23	3036.0	23.0	0.6

DETRITAL ZIRCON AND APATITE (U-Th)/He

Sample	mineral	U (ppm)	Th (ppm)	147Sm (ppm)	[U]e	Th/U	He (nmol/g)	mass (µg)	Ft	ESR	Age (Ma)	err., Ma
Coal Mine Canyon												
zDD_NV12_040CM-242	zircon	62.5	34.6	1.4	70.5	0.55	89.2	5.86	0.78	52.74	295.9	23.67
zDD_NV12_040CM-209	zircon	27.7	23.3	2.3	33.0	0.84	88.7	14.60	0.83	71.84	571.3	45.70
zDD_NV12_040CM-189	zircon	62.6	40.7	3.7	72.0	0.65	144.2	10.85	0.81	64.28	440.9	35.27
zDD_NV12_040CM-269	zircon	131.8	34.1	6.6	139.7	0.26	115.7	5.51	0.78	52.33	194.6	15.57
zDD_NV12_040CM-175	zircon	97.8	77.9	2.5	115.8	0.80	428.0	10.70	0.81	64.37	790.0	63.20
zDD_NV12_040CM-169	zircon	45.6	28.2	2.0	52.1	0.62	79.8	7.67	0.79	58.02	347.8	27.83
zDD_NV12_040CM-278	zircon	48.7	35.1	2.7	56.8	0.72	151.5	8.55	0.80	60.90	587.8	47.03
zDD_NV12_040CM-232	zircon	49.3	22.5	2.7	54.5	0.46	56.8	5.77	0.78	52.95	244.0	19.52
zDD_NV12_040CM-247	zircon	27.0	20.4	2.2	31.7	0.75	19.7	1.77	0.68	36.19	166.8	13.34
zDD_NV12_040CM-212	zircon	157.1	45.2	17.2	167.6	0.29	212.0	4.21	0.75	45.69	306.6	24.53
zDD_NV12_040CM-241	zircon	123.8	63.5	5.5	138.5	0.51	202.3	2.86	0.73	42.09	363.9	29.12
zDD_NV12_040CM-236	zircon	43.7	39.5	3.0	52.8	0.91	73.5	5.31	0.77	52.24	326.5	26.12
zDD_NV12_040CM-290	zircon	318.2	93.0	1.4	339.6	0.29	66.8	2.86	0.71	39.25	51.1	4.09
zDD_NV12_040CM-286	zircon	163.2	61.1	1.0	177.3	0.37	33.2	4.18	0.75	45.78	46.4	3.71
zDD_NV12_040CM-181	zircon	201.6	66.6	1.1	216.9	0.33	36.1	1.84	0.68	35.55	44.9	3.59
zDD_NV12_040CM-197	zircon	395.9	152.4	3.9	431.0	0.39	86.6	3.16	0.72	40.59	51.7	4.13
zDD_NV12_026CM-11	zircon	66.6	33.4	3.4	74.3	0.50	65.4	4.77	0.76	49.20	211.0	16.88
zDD_NV12_026CM-17	zircon	50.0	20.8	2.2	54.8	0.42	59.0	1.82	0.69	36.26	285.1	22.81
zDD_NV12_026CM-62	zircon	21.5	14.5	1.0	24.8	0.68	153.7	6.19	0.78	53.88	1307.7	104.61
zDD_NV12_026CM-79	zircon	84.5	48.9	2.6	95.8	0.58	63.0	3.65	0.74	45.65	162.0	12.96
zDD_NV12_026CM-74	zircon	44.4	29.4	3.0	51.2	0.66	39.7	4.02	0.75	46.32	189.8	15.18
zDD_NV12_026CM-61	zircon	14.3	5.0	0.2	15.4	0.35	68.2	11.41	0.82	65.96	920.2	73.61
zDD_NV12_026CM-60	zircon	72.9	68.5	4.7	88.7	0.94	91.3	2.85	0.72	41.38	261.0	20.88

Elko Hills												
zDD_NV12_102EH-115	zircon	355.1	189.4	5.0	398.7	0.53	227.2	7.24	0.78	53.49	134.1	10.73
zDD_NV12_102EH-83	zircon	134.6	59.1	7.3	148.3	0.44	54.8	2.42	0.71	39.87	95.5	7.64
zDD_NV12_102EH-94	zircon	93.2	63.5	1.8	107.8	0.68	66.9	4.05	0.75	46.79	151.7	12.14
zDD_NV12_102EH-82	zircon	189.8	71.2	1.2	206.2	0.38	140.8	7.08	0.78	52.86	160.7	12.85
zDD_NV12_102EH-66	zircon	280.4	146.8	5.8	314.2	0.52	157.7	3.18	0.71	39.60	129.9	10.39
zDD_NV12_102EH-57	zircon	58.7	33.2	2.7	66.4	0.56	51.6	1.89	0.69	36.46	207.1	16.57
zDD_NV12_102EH-103	zircon	46.3	14.4	0.5	49.6	0.31	58.2	6.04	0.79	54.50	271.2	21.70
zDD_NV12_102EH-86	zircon	200.5	125.4	8.7	229.4	0.63	224.6	5.70	0.76	50.23	233.1	18.65
zDD_NV12_102EH-80	zircon	57.1	24.2	0.9	62.7	0.42	168.2	10.89	0.82	66.17	577.9	46.23
zDD_NV12_102EH-93	zircon	55.2	35.0	1.3	63.3	0.63	77.0	4.90	0.77	50.83	287.4	22.99
zDD_NV12_102EH-85	zircon	205.0	100.6	5.9	228.2	0.49	274.0	5.60	0.77	50.89	283.4	22.68
zDD_NV12_102EH-88	zircon	38.8	14.5	0.9	42.1	0.38	46.3	2.42	0.71	39.87	280.3	22.43
zDD_NV12_102EH-113	zircon	79.4	116.7	42.8	106.5	1.47	34.1	4.04	0.73	44.58	80.1	6.41
zDD_NV12_102EH-130	zircon	134.8	137.6	4.5	166.5	1.02	162.3	3.23	0.73	42.95	244.4	19.55
zDD_NV12_102EH-89	zircon	88.4	7.8	0.0	90.2	0.09	67.7	2.78	0.73	41.47	188.7	15.10
aNV12_103EH-1	apatite	11.3	33.5	289.4	20.5	2.96	0.8	3.17	0.67	47.42	10.3	0.62
aNV12_103EH-3	apatite	3.1	17.3	117.3	7.6	5.64	0.8	3.52	0.69	50.24	25.9	1.56
aNV12_103EH-4	apatite	14.8	114.2	332.9	42.8	7.70	2.1	6.29	0.74	61.97	11.6	0.69
aNV12_103EH-5	apatite	9.4	24.2	366.0	16.8	2.58	0.6	3.87	0.68	49.15	8.7	0.52
aNV12_103EH-6	apatite	8.2	127.4	261.2	38.8	15.60	1.5	4.36	0.71	56.22	9.6	0.57
aNV12_103EH-8	apatite	7.6	18.9	223.3	13.1	2.49	0.5	4.46	0.71	54.73	10.0	0.60
aNV12_103EH-9	apatite	3.5	20.8	138.6	8.9	5.98	0.7	3.49	0.67	48.29	19.7	1.18
aNV12_103EH-10	apatite	2.2	12.7	98.8	5.7	5.66	0.4	3.96	0.69	51.71	19.4	1.17
aNV12_103EH-11	apatite	2.2	15.0	95.2	6.1	6.93	0.4	4.45	0.71	55.54	17.9	1.07
Emigrant Pass												
zDD_NV11_049EP-64	zircon	92.3	43.6	0.9	102.4	0.47	397.0	3.44	0.74	44.82	903.5	72.28
zDD_NV11_049EP-93	zircon	63.6	36.1	1.3	72.0	0.57	444.0	10.71	0.81	64.34	1245.9	99.67
zDD_NV11_049EP-48	zircon	80.1	29.6	0.6	86.9	0.37	204.8	5.08	0.77	50.80	544.2	43.54

zDD_NV11_049EP-105	zircon	80.9	63.6	7.7	95.6	0.79	165.6	3.98	0.73	44.23	424.2	33.93
zDD_NV11_049EP-61	zircon	53.5	23.1	1.6	58.9	0.43	317.5	5.24	0.76	49.35	1180.1	94.41
zDD_NV11_049EP-3	zircon	59.9	34.7	1.1	67.9	0.58	324.7	2.69	0.72	41.20	1128.2	90.25
zDD_NV11_049EP-59	zircon	66.3	29.3	-0.4	73.0	0.44	412.2	2.40	0.71	39.52	1321.4	105.71
zDD_NV11_049EP-106	zircon	72.3	57.5	4.6	85.6	0.79	508.5	4.47	0.76	49.15	1297.9	103.83
zDD_NV11_049EP-90	zircon	63.0	25.6	0.9	68.9	0.41	375.7	7.04	0.79	56.51	1149.5	91.96
zDD_NV11_049EP-50	zircon	66.8	18.9	2.5	71.1	0.28	347.8	3.65	0.75	45.97	1100.8	88.06
zDD_NV11_049EP-2	zircon	31.1	17.2	1.0	35.0	0.55	184.6	7.30	0.79	57.64	1112.9	89.03
zDD_NV11_049EP-8	zircon	217.9	158.2	2.0	254.3	0.73	43.6	5.01	0.75	47.34	42.1	3.37
zDD_NV11_049EP-26	zircon	642.0	199.4	4.3	687.9	0.31	138.0	5.46	0.77	50.40	48.2	3.86
zDD_NV11_049EP-27	zircon	131.6	84.4	1.4	151.0	0.64	50.0	5.22	0.77	50.40	79.6	6.37
zDD_NV11_049EP-95	zircon	187.4	128.6	2.6	217.1	0.69	39.2	12.58	0.82	65.72	40.8	3.26
Taylor Canyon												
zDD_NV12_008TC-93	zircon	64.6	50.0	9.8	76.1	0.77	41.7	1.91	0.69	37.07	145.6	11.65
zDD_NV12_008TC-127	zircon	36.0	23.8	1.7	41.5	0.66	26.2	2.82	0.72	42.31	159.7	12.77
zDD_NV12_008TC-9	zircon	79.0	61.7	7.2	93.2	0.78	58.4	2.33	0.71	39.69	162.0	12.96
Robinson Mountain												
zDD_NV15_168RM-4	zircon	92.7	32.9	3.9	100.3	0.36	73.4	7.41	0.80	58.10	167.9	13.43
zDD_NV15_168RM-3	zircon	216.4	168.6	7.8	255.3	0.78	167.1	10.86	0.80	60.24	149.6	11.97
zDD_NV15_168RM-1	zircon	329.5	136.8	11.4	361.0	0.42	199.4	2.59	0.70	38.68	143.8	11.51
zDD_NV15_168RM-57	zircon	186.1	194.4	27.5	231.0	1.04	547.7	2.78	0.72	41.40	589.0	47.12
zDD_NV15_168RM-56	zircon	77.7	43.9	10.1	87.9	0.57	275.0	3.13	0.72	41.48	761.2	60.90
zDD_NV15_168RM-59	zircon	226.6	122.2	4.3	254.7	0.54	217.3	1.74	0.68	35.54	229.0	18.32
zDD_NV15_168RM-88	zircon	275.4	192.6	118.5	320.3	0.70	90.4	2.57	0.71	39.56	73.3	5.87
zDD_NV15_168RM-86	zircon	74.6	60.1	5.4	88.5	0.81	47.6	3.60	0.74	44.47	134.0	10.72
zDD_NV15_168RM-76	zircon	98.7	55.6	2.1	111.5	0.56	58.0	3.16	0.73	43.06	130.7	10.46
zDD_NV15_168RM-46	zircon	590.5	784.2	842.8	775.3	1.33	113.0	1.89	0.68	36.43	39.4	3.15
zDD_NV15_168RM-11	zircon	113.8	43.2	3.1	123.7	0.38	56.1	4.81	0.77	49.74	108.9	8.71

zDD_NV15_168RM-20	zircon	655.7	234.9	10.6	709.8	0.36	131.9	2.34	0.70	38.42	48.8	3.90
zDD_NV15_168RM-45	zircon	144.6	57.4	4.8	157.8	0.40	97.8	2.95	0.72	41.34	157.2	12.57
zDD_NV15_168RM-78	zircon	237.9	134.8	6.1	268.9	0.57	140.8	4.83	0.75	46.95	128.1	10.24
aNV15_168RM-2	apatite	0.63	41.37	4.4	21.8	179.0	10.3	4.99	1.4	1.64	38.4	2.30
aNV15_168RM-3	apatite	0.69	50.01	0.0	0.2	0.2	0.1	4.34	0.1	3.18	166.0	9.96
zDD_NV15_241RM-10	zircon	64.3	47.3	3.2	75.2	0.74	39.1	4.47	0.75	47.56	126.7	10.14
zDD_NV15_241RM-35	zircon	58.1	50.3	4.0	69.7	0.86	43.0	12.37	0.82	66.00	138.1	11.05
zDD_NV15_241RM-48	zircon	50.1	30.2	3.8	57.0	0.60	51.2	3.08	0.72	40.71	228.5	18.28
zDD_NV15_241RM-27	zircon	107.5	53.3	10.5	119.8	0.50	130.7	8.49	0.80	57.98	249.3	19.94
zDD_NV15_241RM-33	zircon	87.0	54.9	1.8	99.7	0.63	68.4	9.81	0.81	62.52	155.4	12.43
zDD_NV15_241RM-98	zircon	67.1	38.2	4.0	76.0	0.57	64.2	4.49	0.75	46.27	206.5	16.52
zDD_NV15_241RM-50	zircon	59.6	33.5	2.2	67.3	0.56	26.0	4.31	0.76	48.61	93.8	7.51
aNV15_241RM-1	apatite	0.74	63.31	29.8	353.6	195.0	112.2	11.87	25.7	6.97	55.5	3.33
aNV15_241RM-4	apatite	0.70	53.50	31.4	222.0	170.0	83.4	7.07	17.2	3.63	53.2	3.19
aNV15_241RM-8	apatite	0.66	46.72	31.1	204.3	208.1	79.2	6.57	18.2	2.57	62.6	3.75
Eureka												
zDD_NV11_014EU-114	zircon	23.2	10.2	1.8	25.6	0.44	68.5	9.14	0.81	61.93	585.9	46.87
zDD_NV11_014EU-90	zircon	220.2	88.7	3.4	240.7	0.40	235.2	2.59	0.72	40.85	247.6	19.81
zDD_NV11_014EU-107	zircon	63.2	46.0	8.3	73.8	0.73	40.6	6.53	0.78	54.31	129.2	10.33
zDD_NV11_014EU-71	zircon	510.4	773.4	212.6	689.5	1.52	267.6	1.91	0.68	36.81	104.3	8.34
zDD_NV11_014EU-76	zircon	50.5	57.9	7.2	63.9	1.15	401.5	10.21	0.81	64.90	1278.3	102.26
zDD_NV11_014EU-103	zircon	88.8	88.1	58.1	109.4	0.99	120.4	10.42	0.81	64.61	245.6	19.65
zDD_NV11_017EU-19	zircon	46.9	39.9	2.8	56.1	0.85	301.9	11.04	0.81	63.94	1113.1	89.05
zDD_NV11_017EU-37	zircon	31.0	17.3	2.0	34.9	0.56	164.6	11.36	0.82	66.44	976.4	78.11
zDD_NV11_017EU-59	zircon	53.1	29.7	2.3	59.9	0.56	309.3	18.87	0.84	76.36	1031.0	82.48
zDD_NV11_017EU-58	zircon	42.3	34.5	3.5	50.3	0.82	186.5	7.59	0.79	57.79	812.1	64.97
zDD_NV11_017EU-49	zircon	39.6	26.2	2.7	45.6	0.66	141.1	4.40	0.76	48.75	715.8	57.26
zDD_NV11_017EU-40	zircon	72.2	19.2	1.3	76.6	0.27	451.5	8.62	0.81	60.58	1203.6	96.29
zDD_NV11_017EU-28	zircon	44.0	24.4	1.2	49.6	0.55	203.8	12.12	0.82	68.28	856.8	68.54

zDD_NV11_017EU-22	zircon	185.3	211.6	2.6	234.1	1.14	38.1	3.02	0.72	42.10	41.6	3.33
zDD_NV11_017EU-42	zircon	38.1	47.6	2.4	49.1	1.25	232.1	6.12	0.78	53.87	1040.3	83.23
zDD_NV11_017EU-46	zircon	118.2	62.4	1.1	132.6	0.53	26.5	5.67	0.78	53.27	47.4	3.79
zDD_NV11_017EU-87	zircon	60.1	29.2	2.2	66.8	0.49	342.2	4.74	0.76	48.34	1136.5	90.92
zDD_NV11_017EU-82	zircon	83.9	52.8	8.0	96.1	0.63	491.3	7.38	0.79	57.29	1087.6	87.01
zDD_NV11_017EU-86	zircon	67.6	30.8	1.8	74.7	0.46	328.9	6.26	0.77	51.47	974.7	77.98
zDD_NV11_017EU-67	zircon	39.0	64.1	4.3	53.8	1.64	163.3	2.89	0.71	41.43	750.1	60.01
zDD_NV11_017EU-84	zircon	193.5	126.1	0.9	222.5	0.65	53.4	3.48	0.74	45.34	59.6	4.77
zDD_NV11_017EU-85	zircon	235.3	153.8	2.8	270.7	0.65	65.8	2.56	0.71	40.54	62.8	5.02
zDD_NV11_017EU-73	zircon	129.7	62.5	1.0	144.1	0.48	37.4	9.10	0.80	60.90	59.5	4.76
zDD_NV11_017EU-91	zircon	15.3	13.1	1.5	18.4	0.86	10.8	4.04	0.75	46.97	143.8	11.50
Piñon Range (Diamond Peak Formation)												
zDD_NV15_013PR-105	zircon	272.2	293.2	8.3	339.8	1.08	132.2	4.62	0.76	49.78	94.0	7.52
zDD_NV15_013PR-124	zircon	122.0	122.6	2.6	150.3	1.00	1127.5	2.05	0.69	37.23	1749.2	139.94
zDD_NV15_013PR-41	zircon	98.5	53.3	2.6	110.8	0.54	334.3	7.88	0.80	59.61	661.9	52.96
zDD_NV15_013PR-62	zircon	222.9	101.2	47.0	246.4	0.45	496.3	2.99	0.72	41.51	498.5	39.88
zDD_NV15_013PR-55	zircon	155.9	76.5	27.4	173.6	0.49	597.7	7.88	0.80	58.94	750.5	60.04
zDD_NV15_013PR-31	zircon	191.0	77.4	17.0	208.9	0.41	318.4	3.26	0.73	42.65	377.1	30.17
zDD_NV15_013PR-15	zircon	19.4	13.9	2.5	22.6	0.71	150.7	10.90	0.82	65.32	1330.4	106.44
zDD_NV15_013PR-20	zircon	70.2	41.9	53.1	80.1	0.60	313.5	16.65	0.83	72.90	808.3	64.66
zDD_NV15_013PR-23	zircon	82.3	50.7	4.0	94.0	0.62	500.1	6.01	0.78	52.83	1149.4	91.95
zDD_NV15_013PR-28	zircon	168.0	73.9	5.7	185.1	0.44	564.3	4.69	0.77	50.08	698.0	55.84
zDD_NV15_013PR-33	zircon	120.6	44.2	11.0	130.9	0.37	649.5	4.57	0.76	49.15	1096.1	87.69
zDD_NV15_013PR-36	zircon	94.9	82.2	12.5	113.9	0.87	308.0	6.61	0.78	55.51	609.9	48.79
zDD_NV15_013PR-37	zircon	282.5	118.4	39.4	309.9	0.42	562.1	3.41	0.73	43.54	443.3	35.46
zDD_NV15_013PR-38	zircon	55.4	44.5	5.5	65.6	0.80	327.9	4.35	0.75	48.19	1119.7	89.58
zDD_NV15_013PR-39	zircon	56.9	25.9	5.6	62.8	0.45	133.6	9.92	0.81	64.20	465.9	37.27
zDD_NV15_013PR-43	zircon	80.2	45.7	5.5	90.8	0.57	450.8	10.44	0.81	63.08	1035.1	82.81
zDD_NV15_013PR-48	zircon	169.5	73.1	34.5	186.5	0.43	238.8	7.87	0.80	58.83	290.5	23.24

zDD_NV15_013PR-49	zircon	65.9	43.0	6.5	75.9	0.65	391.7	4.54	0.76	48.18	1149.4	91.95
zDD_NV15_013PR-56	zircon	117.8	60.0	10.7	131.7	0.51	395.7	9.09	0.81	62.51	652.6	52.21
zDD_NV15_013PR-59	zircon	68.2	61.1	4.3	82.2	0.90	447.1	4.91	0.76	50.72	1192.3	95.39
zDD_NV15_013PR-64	zircon	74.3	52.2	19.4	86.4	0.70	463.2	10.57	0.82	65.47	1101.7	88.14
zDD_NV15_013PR-66	zircon	41.1	40.9	2.6	50.5	1.00	286.2	8.41	0.80	60.30	1184.1	94.73
zDD_NV15_013PR-77	zircon	158.7	97.7	24.5	181.3	0.62	267.8	3.92	0.75	46.78	356.1	28.49
zDD_NV15_013PR-81	zircon	209.7	172.5	59.3	249.7	0.82	659.5	2.99	0.72	42.45	645.1	51.61
zDD_NV15_013PR-89	zircon	134.2	40.0	37.4	143.6	0.30	295.8	10.45	0.81	63.28	452.3	36.18
aNV15_013PR-2	apatite	5.8	4.2	53.2	7.1	0.72	3.5	1.95	0.66	43.33	133.6	8.02
aNV15_013PR-6	apatite	7.1	27.6	119.0	14.0	3.90	1.8	2.75	0.69	50.27	34.0	2.04
aNV15_013PR-9	apatite	9.6	4.6	24.0	10.8	0.47	1.2	2.19	0.66	43.49	30.9	1.85
aNV15_013PR-10	apatite	6.1	6.1	11.1	7.6	1.00	3.5	1.43	0.63	39.65	135.7	8.14
aNV15_013PR-11	apatite	25.2	6.4	53.5	27.0	0.26	3.9	1.14	0.61	36.44	42.8	2.57
aNV15_013PR-12	apatite	7.2	20.1	102.9	12.4	2.78	3.0	1.41	0.60	37.83	72.3	4.34

DOUBLE DATING OF SELECT ELKO FORMATION VOLCANIC GRAINS

U-Pb Geochronology

Analysis	U (ppm)	U/Th	207Pb/ 235U	±%	206Pb/ 238U	±%	err. corr.	207Pb/ 235U Age (Ma)	± (Ma)	206Pb/ 238U Age (Ma)	± (Ma)	207Pb/ 206Pb Age (Ma)	± (Ma)	Best age (Ma)	± (Ma)	Disc (%)
NV12-109SR: Scott Ranch 40° 34' 49"N, 115° 59' 30"W																
12109SR_5	316	0.89	0.04090	0.00110	0.00619	0.00011	0.19888	40.7	1.1	39.8	0.7	171	38	39.8	0.7	2.2
12109SR_16	328	0.84	0.04310	0.00200	0.00643	0.00009	0.34791	42.8	2.0	41.3	0.6	267	62	41.3	0.6	3.5
12109SR_60	315	1.15	0.04390	0.00120	0.00656	0.00011	0.12159	43.6	1.2	42.2	0.7	192	28	42.2	0.7	3.3
12109SR_102	221	0.73	0.04310	0.00270	0.00636	0.00015	0.01323	42.8	2.6	40.8	0.9	354	85	40.8	0.9	4.6
NV11-045TC: Taylor Canyon 41° 16' 2"N, 116° 6' 21"W																
11045TC_54	217.7	0.71	0.04760	0.00240	0.00707	0.00020	0.10952	47.2	2.4	45.4	1.3	342	76	45.4	1.3	3.8
11045TC_57	567	0.94	0.05330	0.00270	0.00708	0.00015	0.22621	52.6	2.6	45.5	0.9	493	61	45.5	0.9	13.6
11045TC_117	86.8	1.20	0.04790	0.00640	0.00724	0.00042	0.08600	47.2	6.2	46.5	2.7	790	150	46.5	2.7	1.5
11045TC_166	121.9	0.69	0.04710	0.00570	0.00695	0.00032	0.04936	46.5	5.5	44.6	2.1	700	130	44.6	2.1	4.1
NV12-136SR: Scott Ranch 40° 34' 47"N, 115° 59' 24"W																
12136SR_78	124.3	1.10	0.03970	0.00170	0.00623	0.00013	0.34610	39.5	1.6	40.0	0.8	222	39	40.0	0.8	1.3
12136SR_106	60.3	0.89	0.03970	0.00600	0.00635	0.00031	0.13278	39.5	5.9	40.8	2.0	420	220	40.8	2.0	3.3
12136SR_119	198	0.75	0.04130	0.00180	0.00636	0.00013	0.27918	41.0	1.8	40.9	0.8	282	88	40.9	0.8	0.3

(U-Th)/He Thermochronology

Sample	mineral	U (ppm)	Th (ppm)	147Sm (ppm)	[U]e	Th/U	He (nmol/g)	mass (µg)	Ft	ESR	Age, Ma	err., Ma
Taylor Canyon												
zDD_NV11_045TC-54	zircon	0.84	73.74	70.5	54.6	2.1	83.1	0.77	15.8	16.79	42.0	3.36
zDD_NV11_045TC-117	zircon	0.75	46.87	88.3	40.6	2.4	97.7	0.46	16.1	5.02	40.6	3.25
zDD_NV11_045TC-166	zircon	0.83	72.32	108.9	74.8	2.5	126.1	0.69	23.5	16.47	41.2	3.30
zDD_NV11_045TC-57	zircon	139.3	109.3	3.0	164.5	0.78	32.8	28.02	0.84	75.62	43.8	3.50
Piñon Range												
zDD_NV12_136SR-106	zircon	62.4	43.6	2.7	72.4	0.70	12.4	4.35	0.75	47.83	41.9	3.35
zDD_NV12_136SR-78	zircon	49.9	33.2	1.9	57.6	0.66	8.9	4.58	0.76	49.07	37.6	3.00
zDD_NV12_136SR-119	zircon	96.1	70.2	5.2	112.3	0.73	19.3	2.64	0.72	41.21	44.1	3.53
zDD_NV12_109SR-16	zircon	193.7	111.3	2.0	219.4	0.57	41.4	13.20	0.82	67.95	42.3	3.38
zDD_NV12_109SR-102	zircon	304.8	171.6	4.6	344.3	0.56	62.2	12.83	0.82	65.59	40.8	3.26
zDD_NV12_109SR-5	zircon	224.0	180.2	2.2	265.5	0.80	49.6	7.37	0.78	55.76	43.9	3.51
zDD_NV12_109SR-60	zircon	193.7	111.3	2.0	219.4	0.57	41.4	13.20	0.82	67.95	42.3	3.38

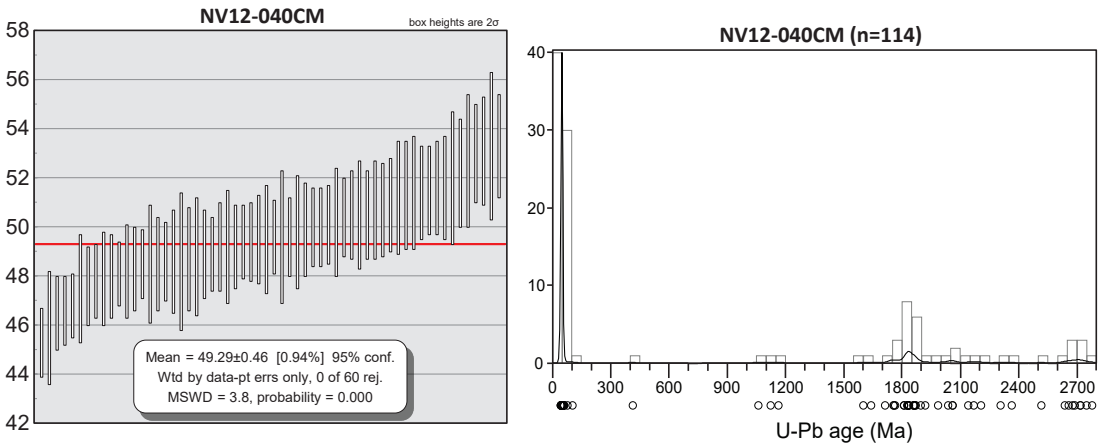

Figure A.1. Detrital zircon maximum depositional age and U-Pb age plots for sample NV12-040CM. U-Pb age plotted using a kernel density estimate function (Vermeesch, 2012) and maximum depositional age determined with Isoplot (Ludwig, 2008).

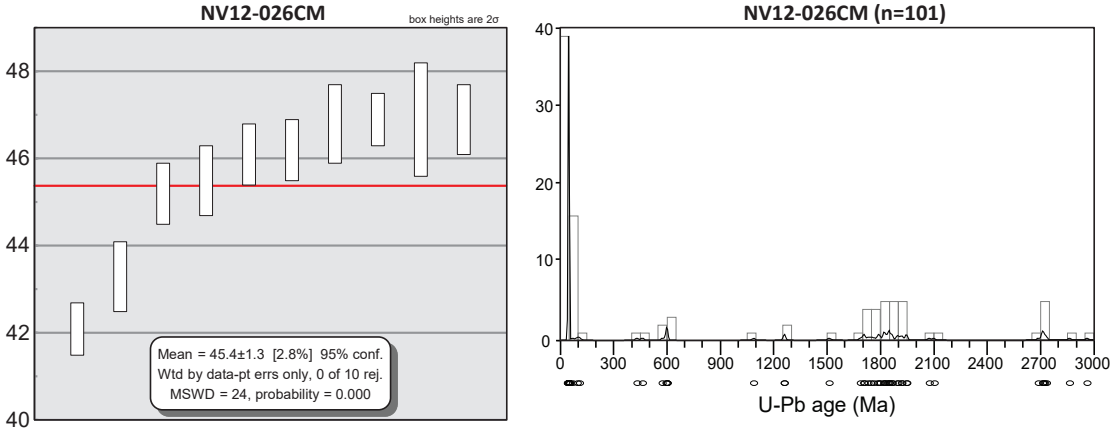

Figure A.2. Detrital zircon maximum depositional age and U-Pb age plots for sample NV12-026CM. U-Pb age plotted using a kernel density estimate function (Vermeesch, 2012) and maximum depositional age determined with Isoplot (Ludwig, 2008).

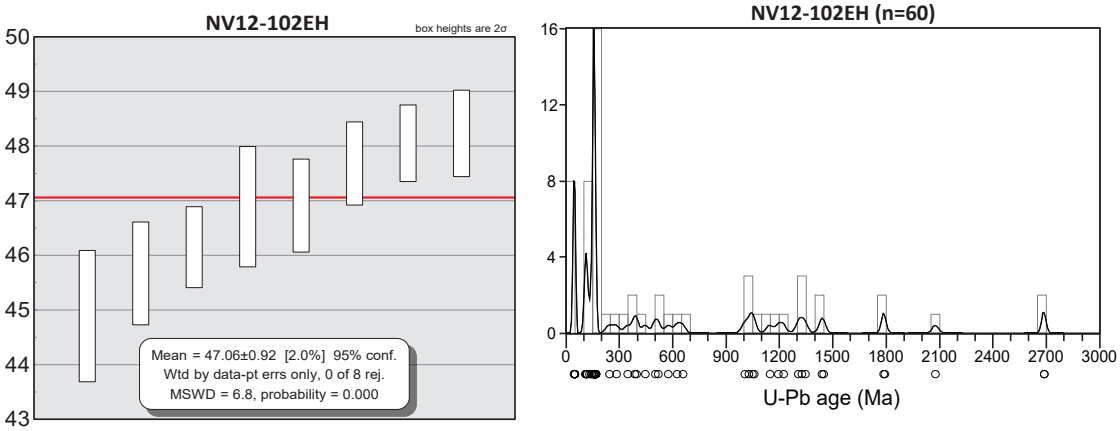

Figure A.3. Detrital zircon maximum depositional age and U-Pb age plots for sample NV12-102EH. U-Pb age plotted using a kernel density estimate function (Vermeesch, 2012) and maximum depositional age determined with Isoplot (Ludwig, 2008).

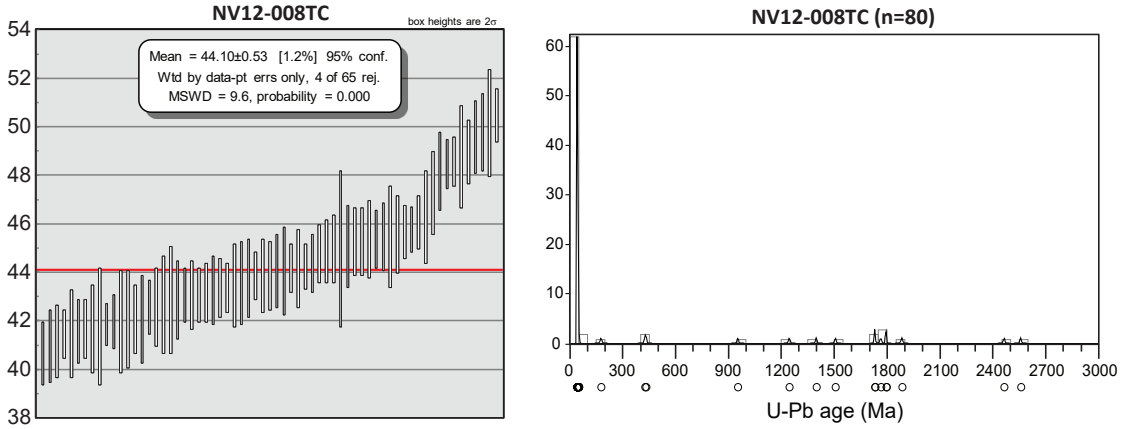

Figure A.4. Detrital zircon maximum depositional age and U-Pb age plots for sample NV12-008TC. U-Pb age plotted using a kernel density estimate function (Vermeesch, 2012) and maximum depositional age determined with Isoplot (Ludwig, 2008).

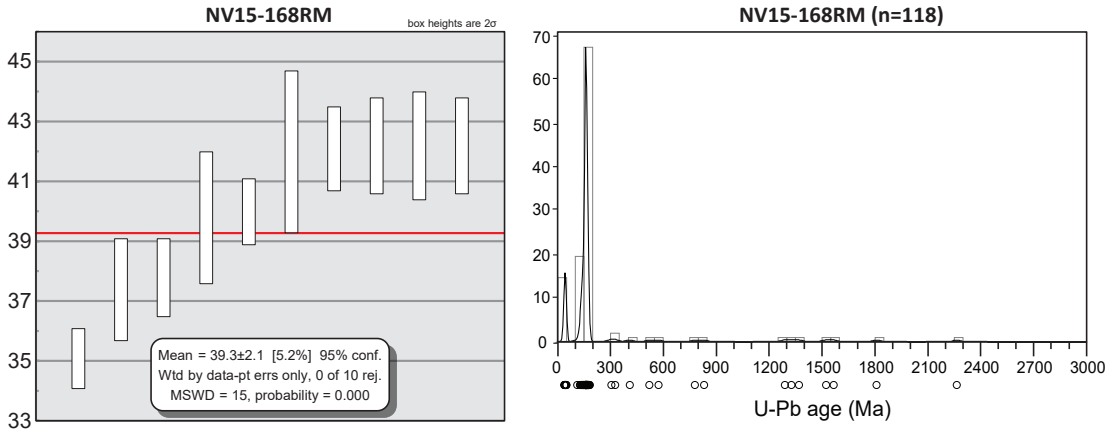

Figure A.5. Detrital zircon maximum depositional age and U-Pb age plots for sample NV15-168RM. U-Pb age plotted using a kernel density estimate function (Vermeesch, 2012) and maximum depositional age determined with Isoplot (Ludwig, 2008).

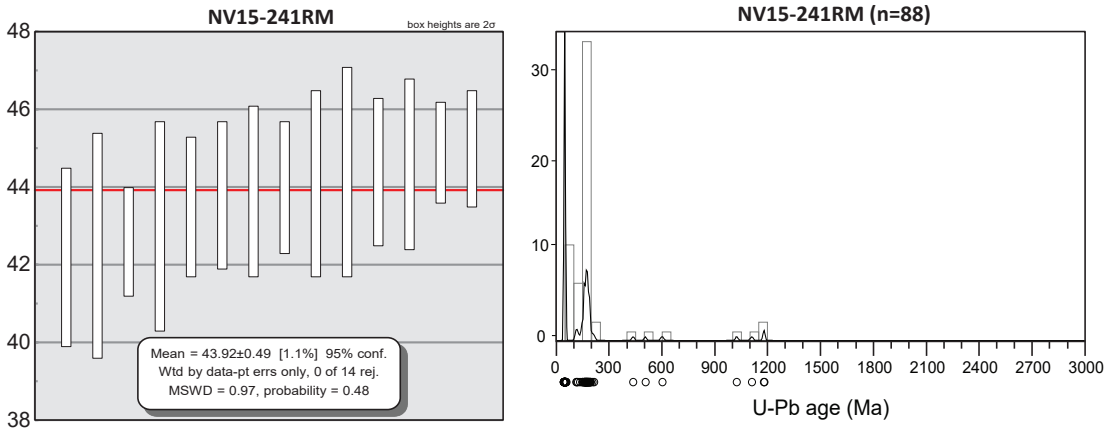

Figure A.6. Detrital zircon maximum depositional age and U-Pb age plots for sample NV12-102EH. U-Pb age plotted using a kernel density estimate function (Vermeesch, 2012) and maximum depositional age determined with Isoplot (Ludwig, 2008).

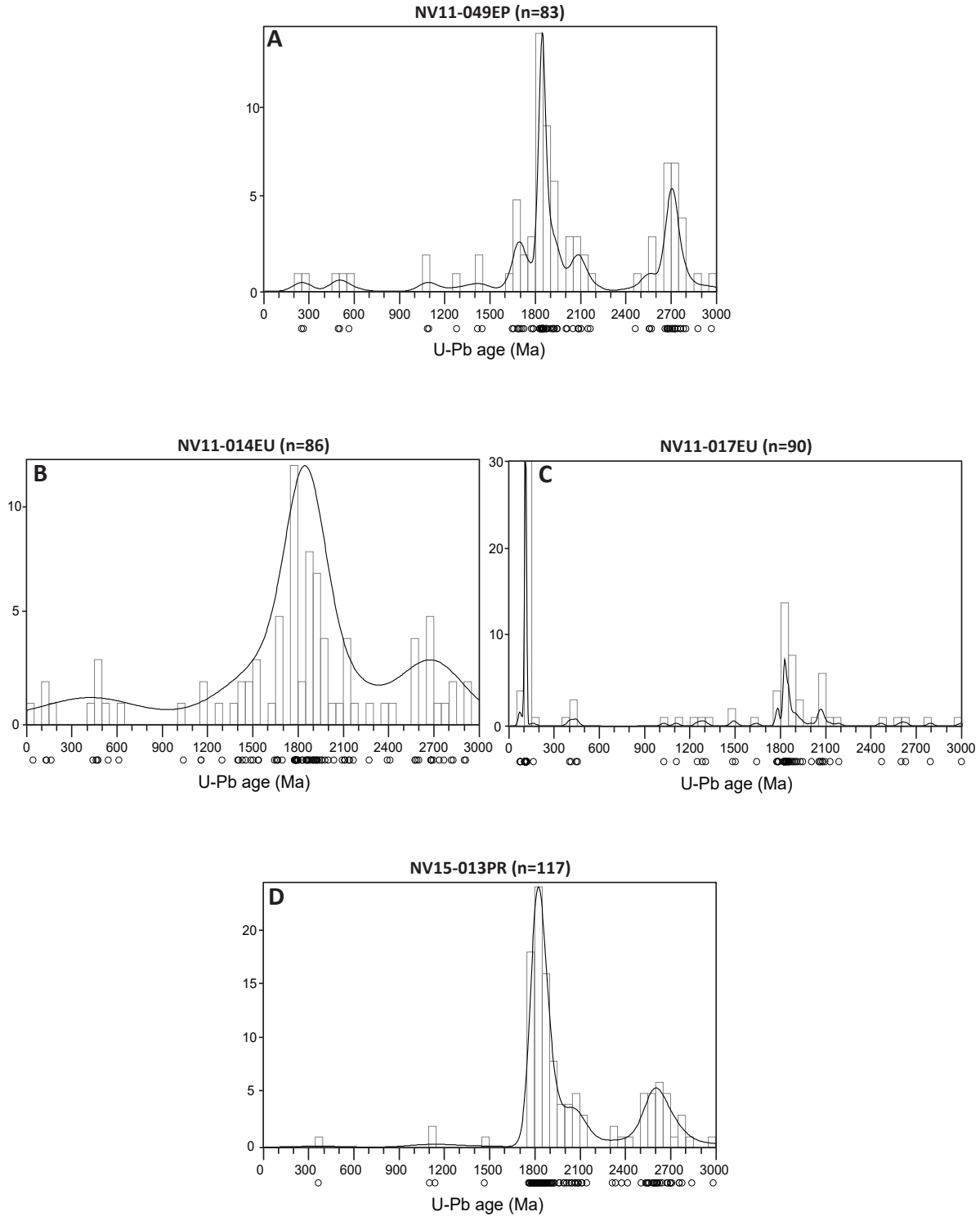

Figure A.7. Detrital zircon U-Pb age plots for samples A) NV11-049EP, B) NV11-014EU, C) NV11-017EU, and D) NV15-013PR. U-Pb ages plotted using a kernel density estimate function (Vermeesch, 2012)

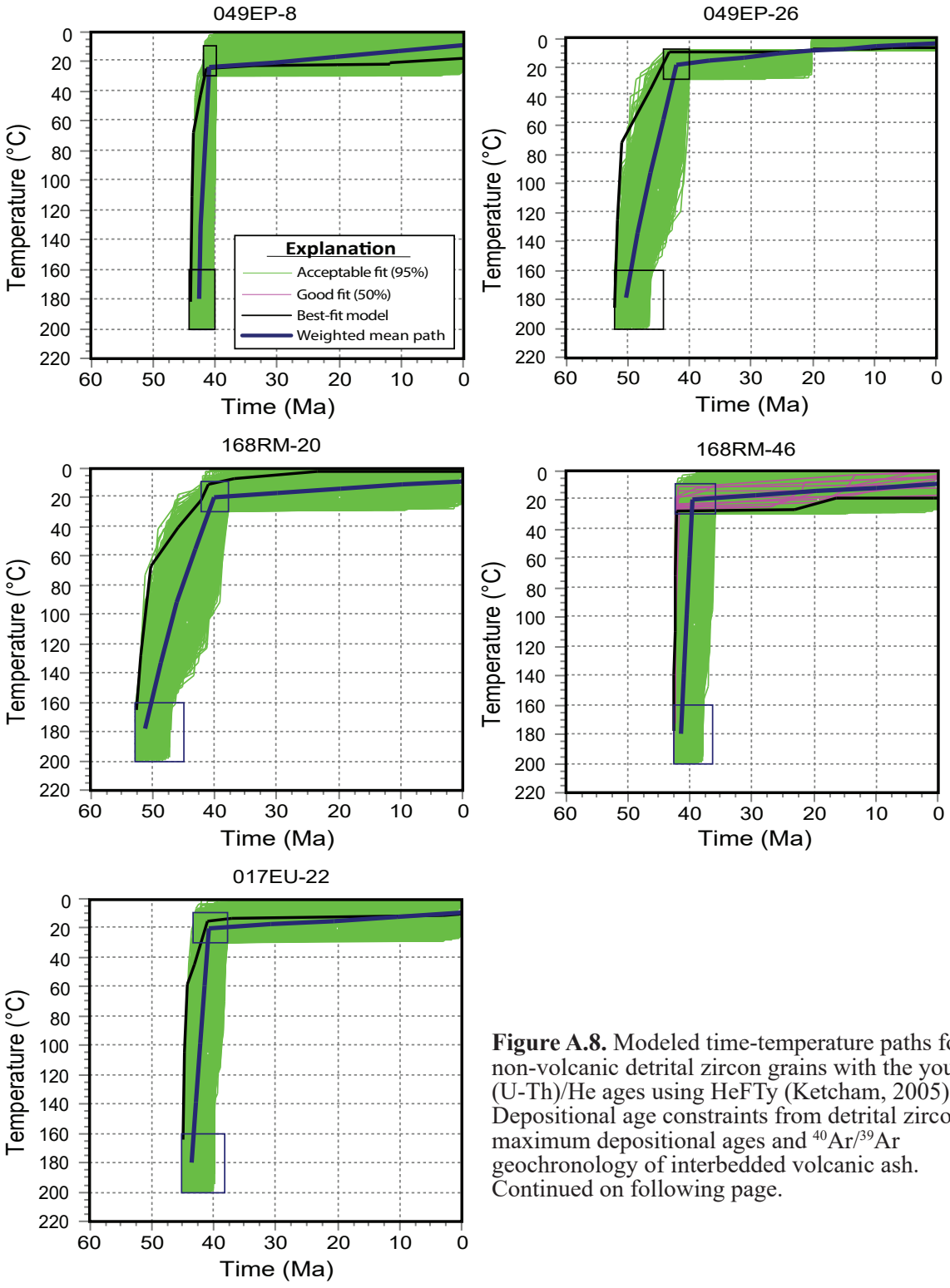

Figure A.8. Modeled time-temperature paths for non-volcanic detrital zircon grains with the youngest (U-Th)/He ages using HeFTy (Ketcham, 2005). Depositional age constraints from detrital zircon maximum depositional ages and $^{40}Ar/^{39}Ar$ geochronology of interbedded volcanic ash. Continued on following page.

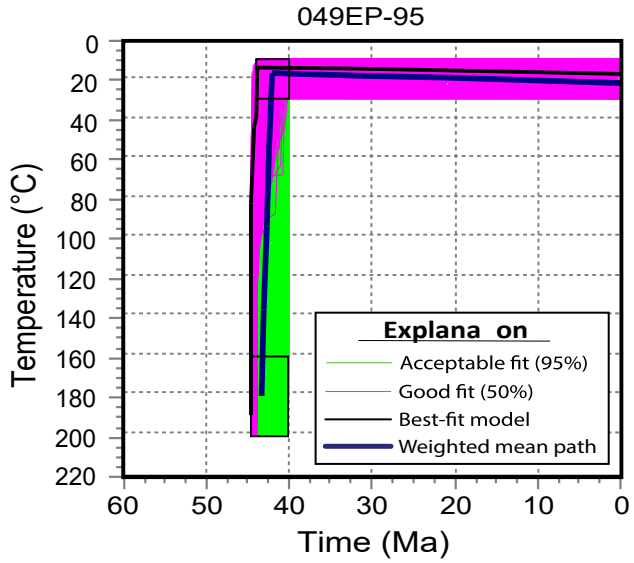
049EP-95
Temperature (°C)
Time (Ma)
Explana on
Acceptable fit (95%)
Good fit (50%)
Best-fit model
Weighted mean path

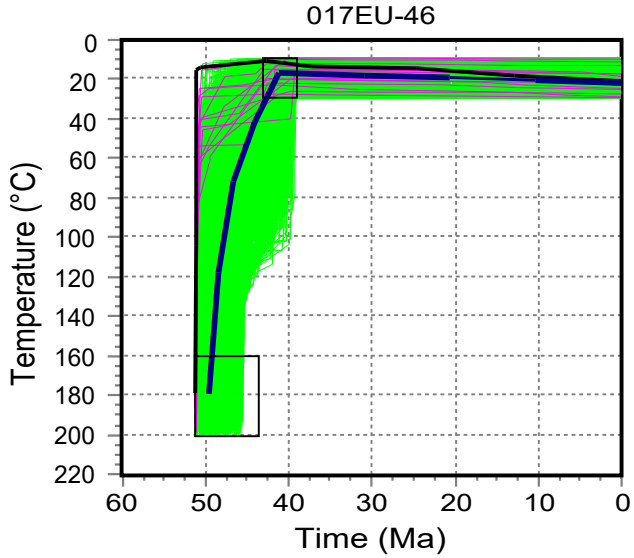
017EU-46
Temperature (°C)
Time (Ma)

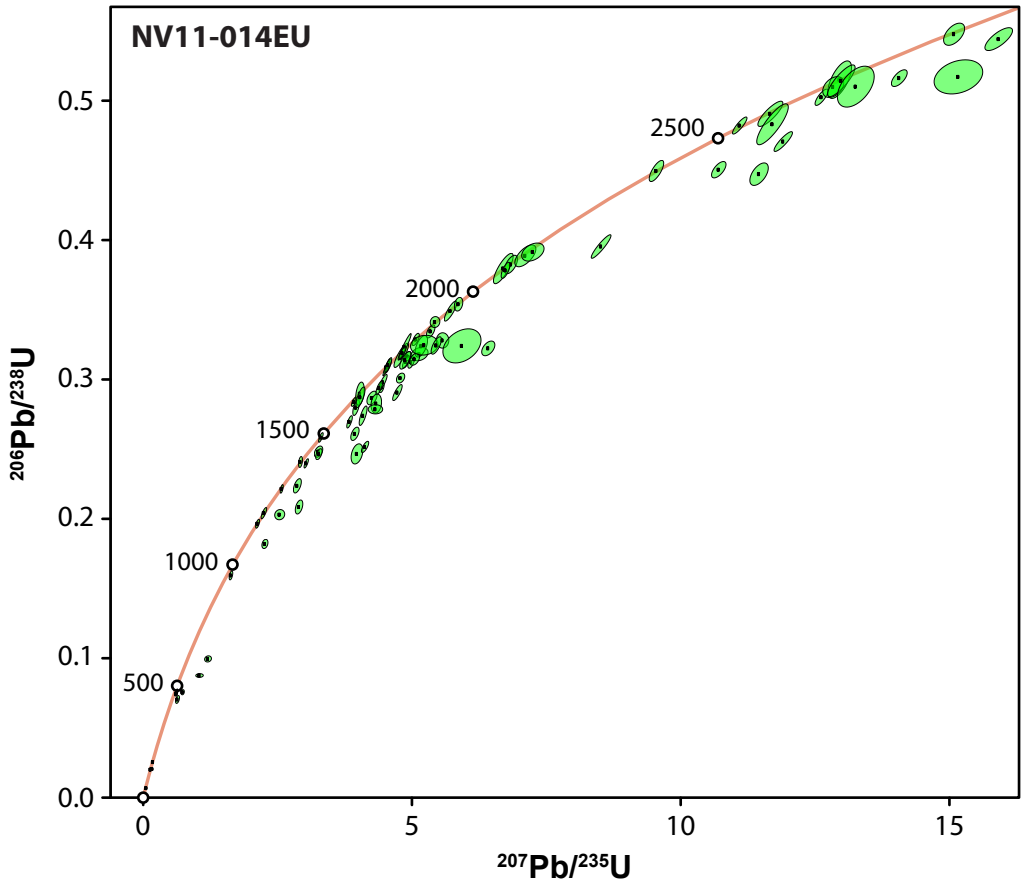
NV11-014EU
0.5
0.4
0.3
0.2
0.1
0.0
2500
2000
1500
1000
500
0
5
10
15
$^{206}Pb/^{238}U$
$^{207}Pb/^{235}U$

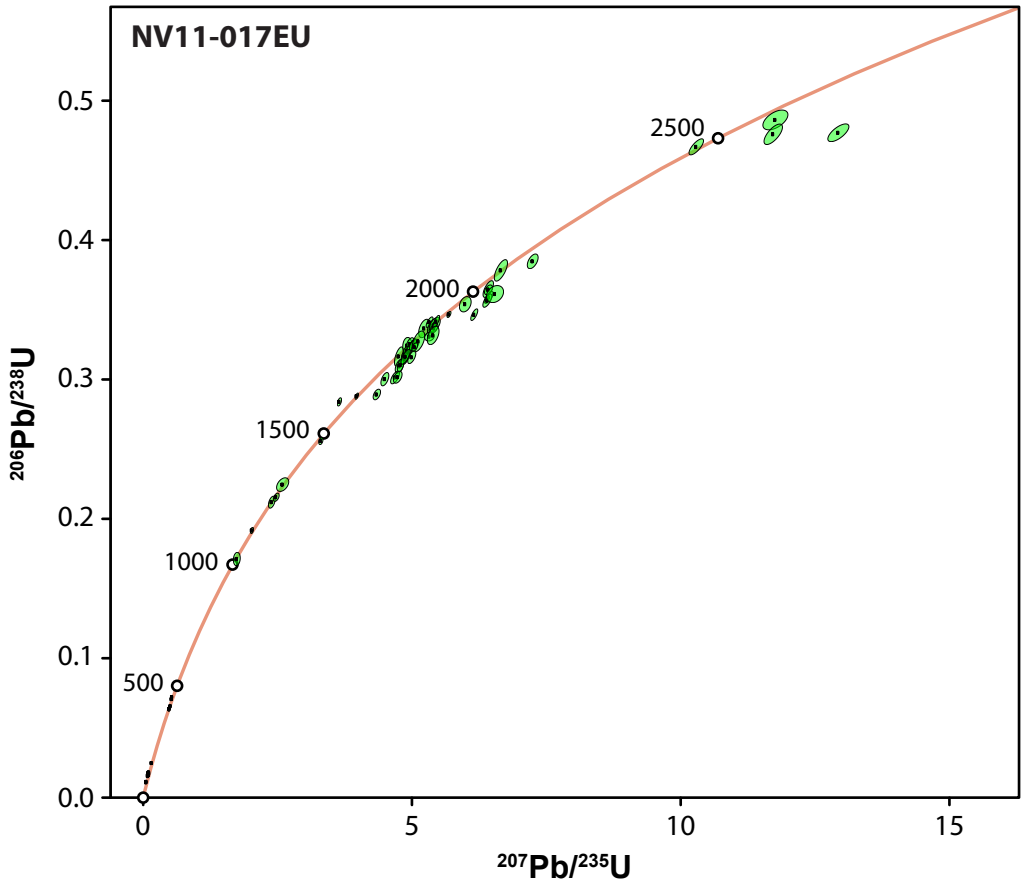
NV11-017EU
0.5
0.4
0.3
0.2
0.1
0.0
206Pb/238U
2500
2000
1500
1000
500
0
5
10
15
207Pb/235U

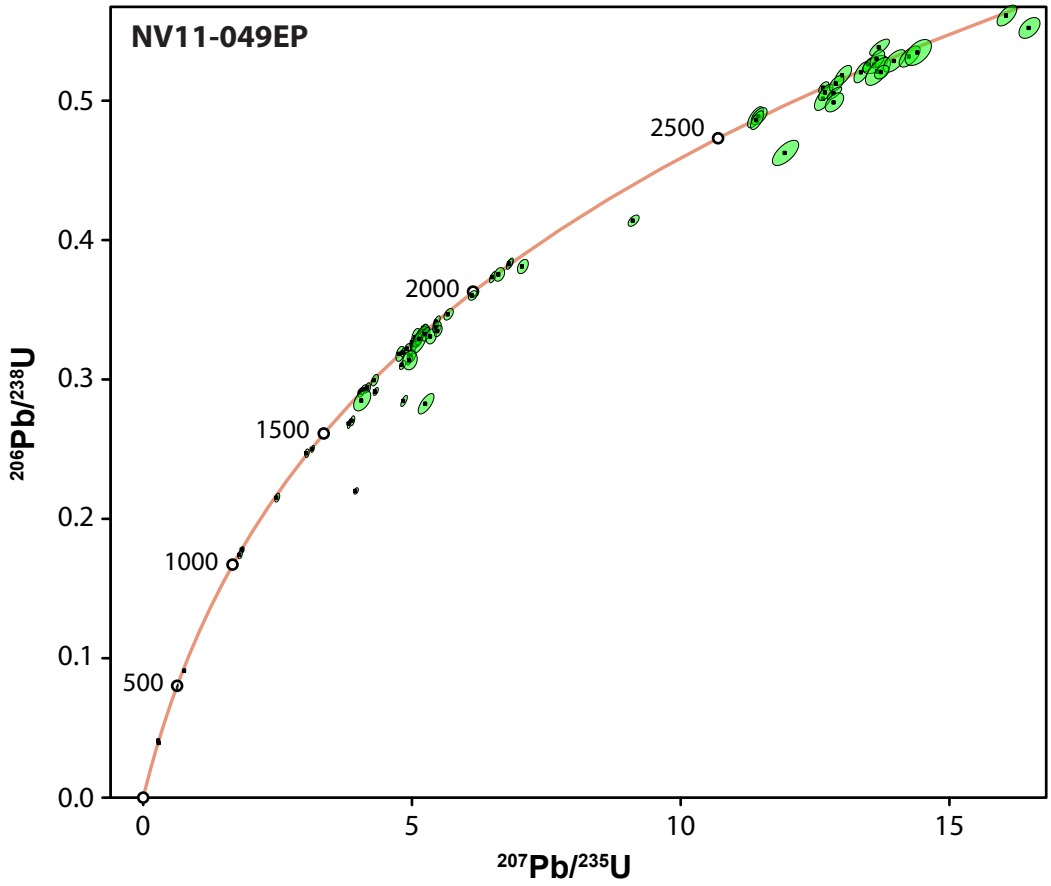
NV11-049EP
0.5
0.4
0.3
0.2
0.1
0.0
2500
2000
1500
1000
500
0
5
10
15
206Pb/238U
207Pb/235U

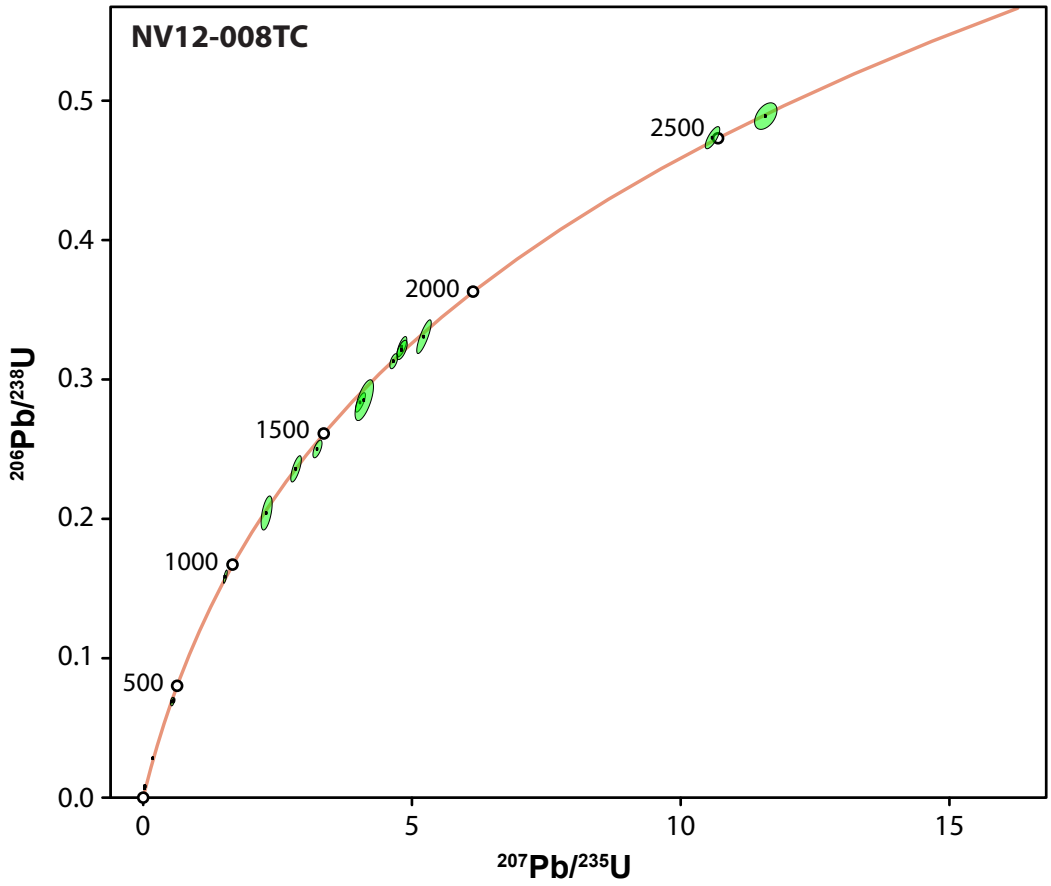
NV12-008TC
0.5
0.4
0.3
0.2
0.1
0.0
206Pb/238U
2500
2000
1500
1000
500
0
5
10
15
207Pb/235U

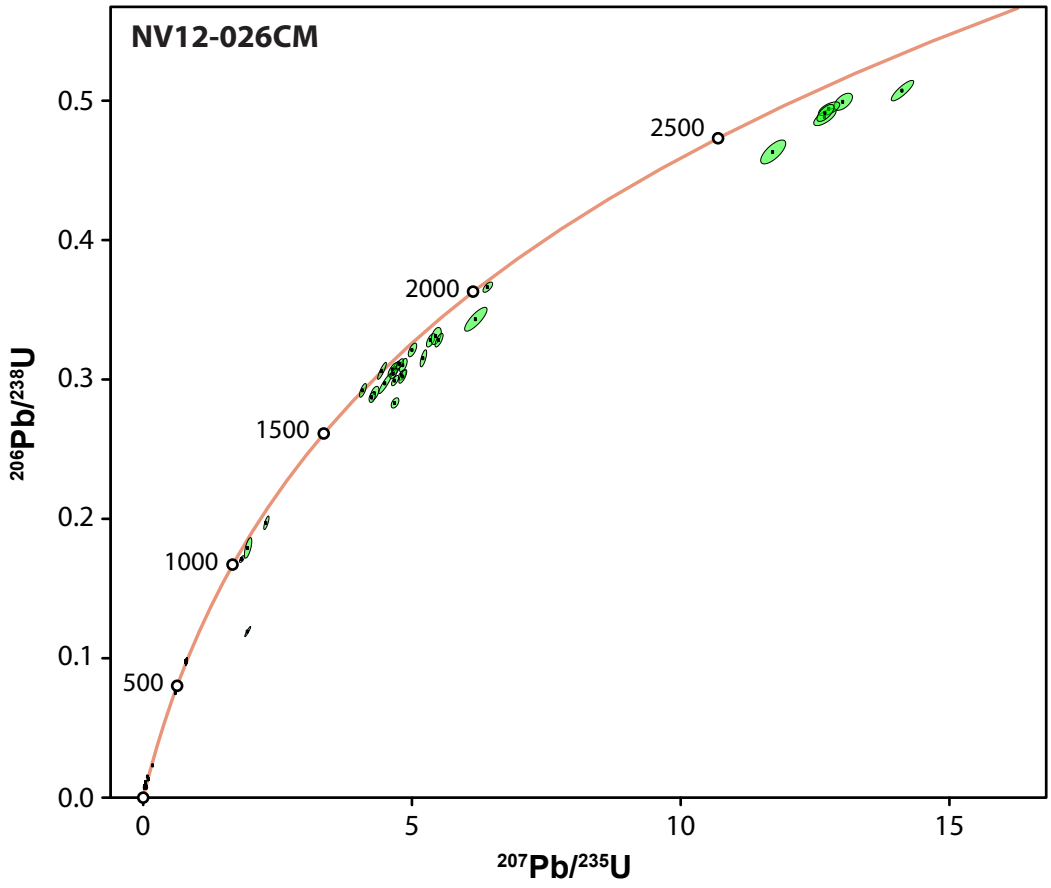
NV12-026CM
0.5
0.4
0.3
0.2
0.1
0.0
206Pb/238U
2500
2000
1500
1000
500
0
5
10
15
207Pb/235U

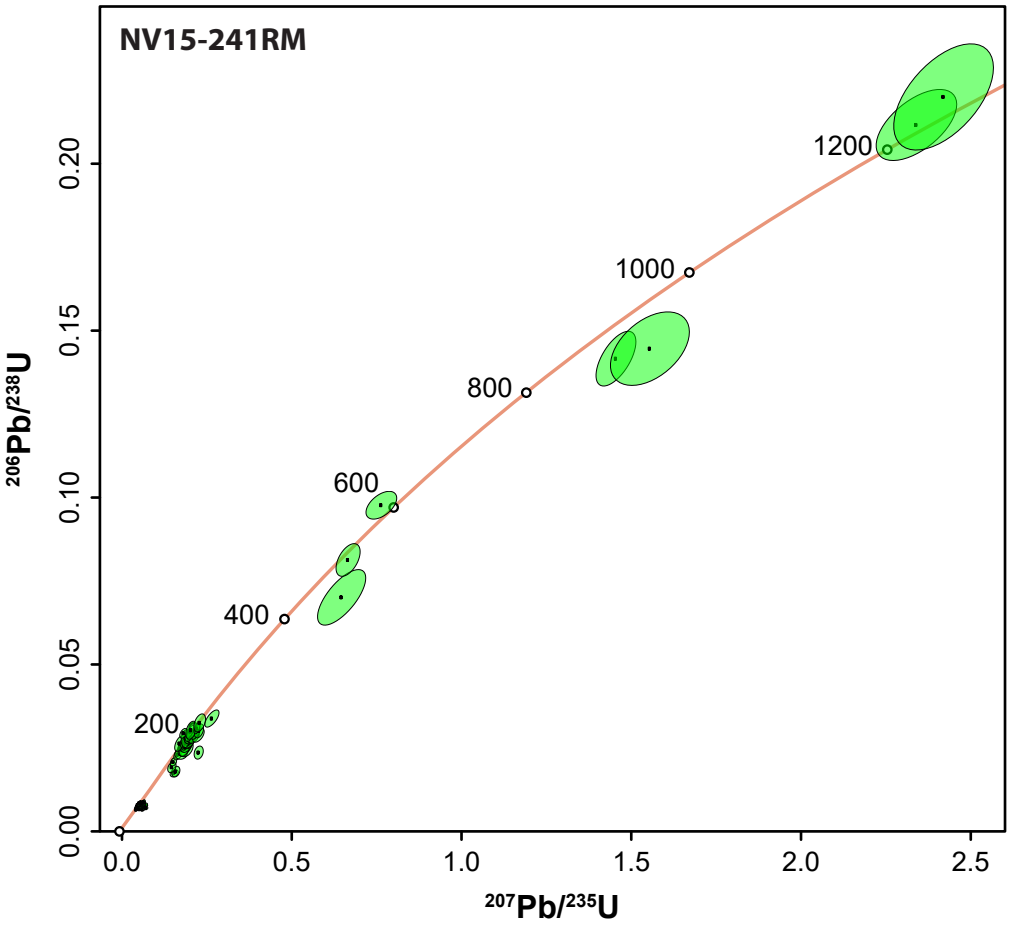
NV15-241RM
1200
1000
800
600
400
200
0.00
0.05
0.10
0.15
0.20
0.0
0.5
1.0
1.5
2.0
2.5
206Pb/238U
207Pb/235U

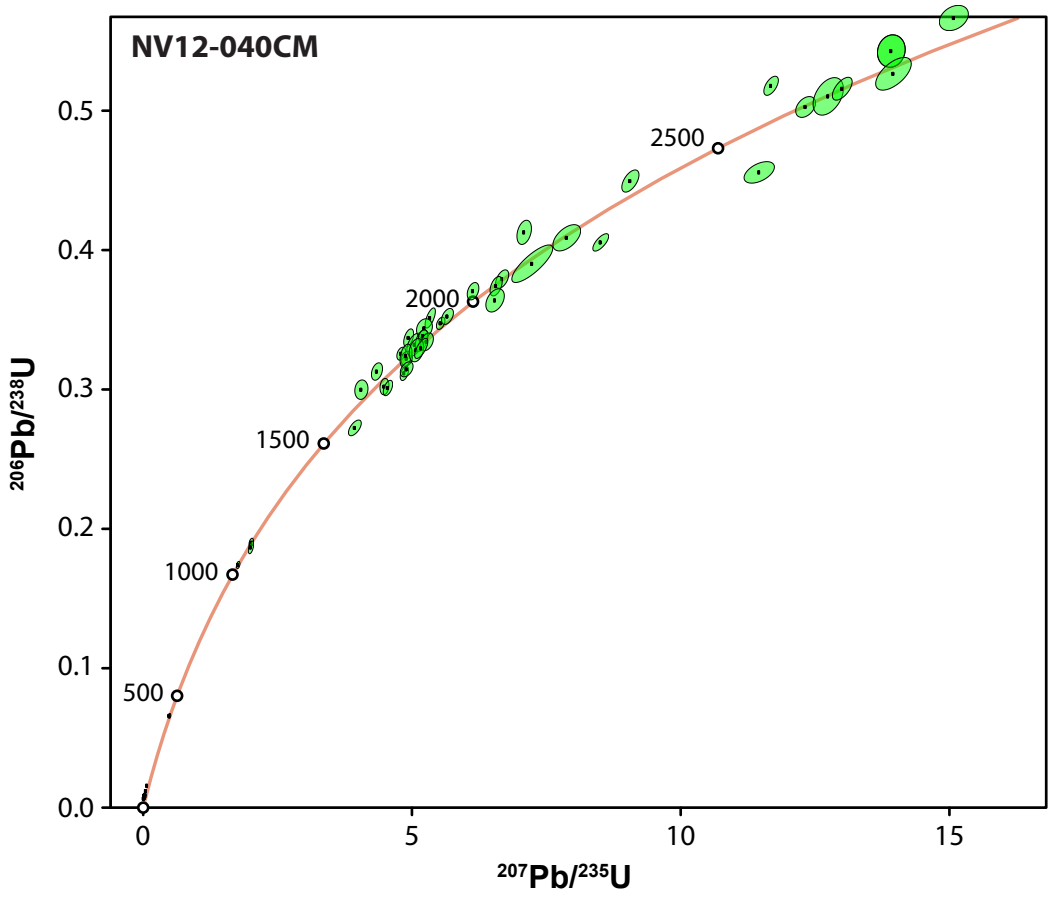
NV12-040CM
0.5
0.4
0.3
0.2
0.1
0.0
206Pb/238U
2500
2000
1500
1000
500
0
5
10
15
207Pb/235U

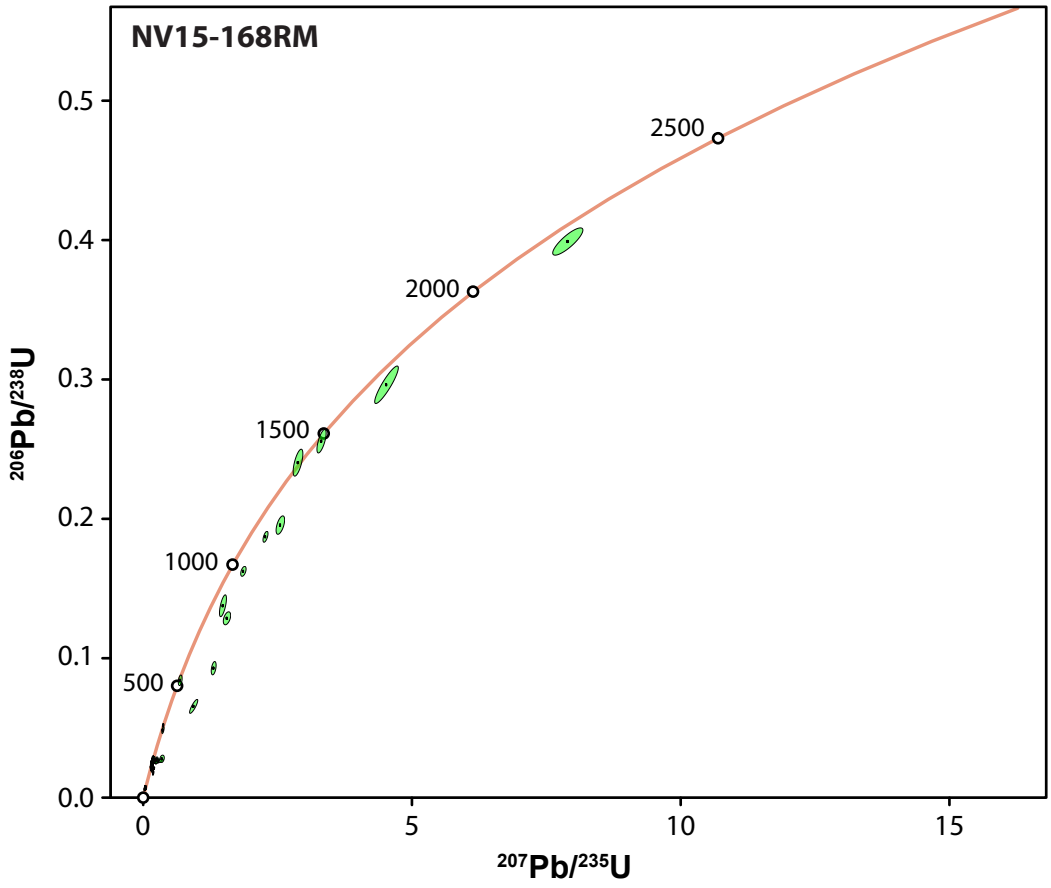
NV15-168RM
0.5
0.4
0.3
0.2
0.1
0.0
2500
2000
1500
1000
500
0
5
10
15
206Pb/238U
207Pb/235U

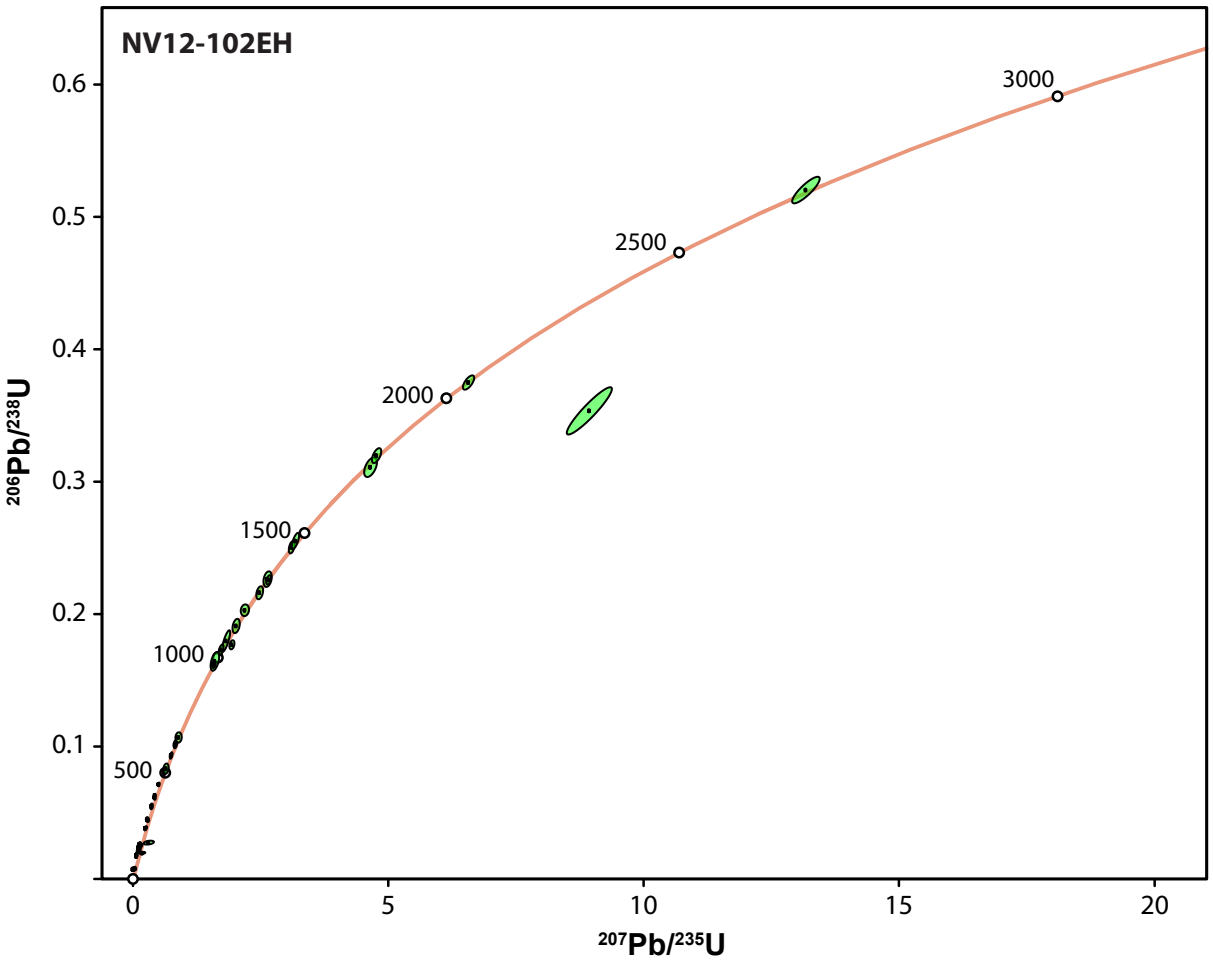
NV12-102EH
0.6
0.5
0.4
0.3
0.2
0.1
206Pb/238U
3000
2500
2000
1500
1000
500
0
5
10
15
20
207Pb/235U

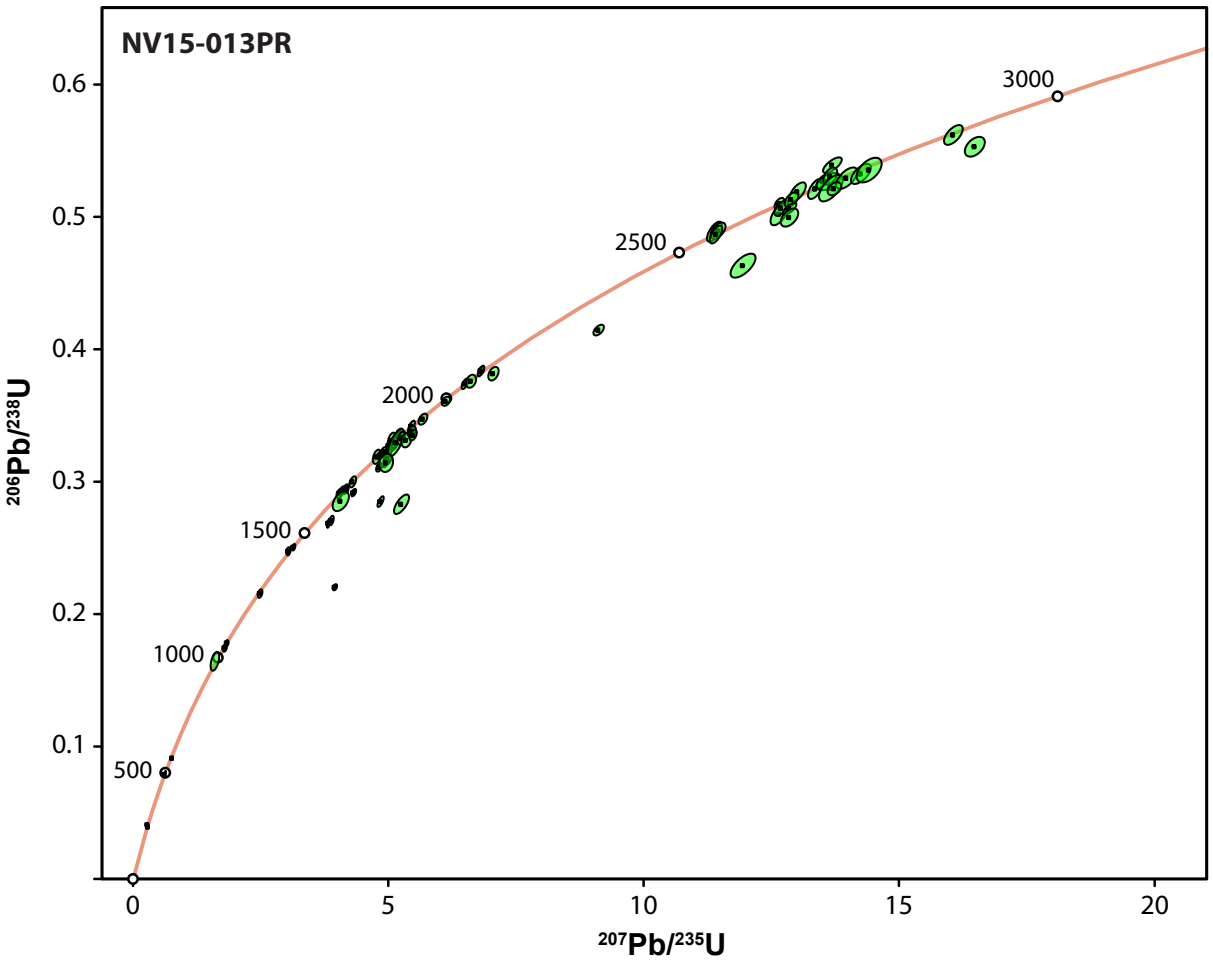
NV15-013PR
0.6
0.5
0.4
0.3
0.2
0.1
206Pb/238U
3000
2500
2000
1500
1000
500
0
5
10
15
20
207Pb/235U

REFERENCES

Andersen, T., 2005, Detrital zircons as tracers of sedimentary provenance: limiting conditions from statistics and numerical simulation: Chemical Geology, v. 216, p. 249–270.

Farley, K.A., 2000, Helium diffusion from apatite: General behavior as illustrated by Durango fluorapatite: Journal of Geophysical Research, v. 105, p. 2903–2914.

Henry, C.D., and Faulds, J.E., 1999, Preliminary geologic map of the Emigrant Pass Quadrangle, Nevada: Nevada Bureau of Mines and Geology Open-File Report 99-9, scale 1:24,000, 20 p.

Jackson, S.E., Pearson, N.J., Griffin, W.L., and Belousova, E.A., 2004, The application of laser ablation-inductively coupled plasma-mass spectrometry to in situ U/Pb zircon geochronology: Chemical Geology, v. 211, p. 47–69.

Ketcham, R.A., 2005, Forward and inverse modeling of low-temperature thermochronometry data, *in* Reiners, P.W., and Ehlers, T.A., eds., Low-Temperature Thermochronology: Techniques, Interpretations, and Applications: Reviews in Mineralogy and Geochemistry, v. 58, p. 275–314.

Long, S.P., Henry, C.D., Muntean, J.L., Edmondo, G.P., and Cassel, E.J., 2014, Early Cretaceous construction of a structural culmination, Eureka, Nevada, U.S.A.: Implications for out-of-sequence deformation in the Sevier hinterland: Geosphere, v. 10, no. 3, p. 564–584.

Ludwig, K.R., 2003, Isoplot/EX, version 3.0: A geochronological toolkit for Microsoft Excel. Berkeley Geochronology Center Special Publication 1a, California.

Ludwig, K.R., 2008, Manual for Isoplot 3.7: Berkeley Geochronology Center Special Publication 4, 77 p.

Petrus, J.A., and Kamber, B.S., 2012, VizualAge: A Novel Approach to Laser Ablation ICP-MS U-Pb Geochronology Data Reduction: Geostandards and Geoanalytics Research, v. 36, p. 247–270.

Smith, M.E., Cassel, E.J., Jicha, B.R., Singer, B.S., and Canada, A.S., 2017, Hinterland drainage closure and lake formation in response to middle Eocene Farallon slab removal, Nevada, U.S.A.: Earth and Planetary Science Letters, v. 479, p. 156–167.

Vermeesch, P., 2012, On the visualisation of detrital age distributions: Chemical Geology, v. 312, p. 190–194.

APPENDIX B

Supplemental Materials for Chapter II

METHODS

Zircon and Apatite U-Pb Geochronology

For U-Pb analyses, approximately 1-3 kg of samples were crushed, and zircon and apatite were separated using conventional density separation techniques, including gemini table, heavy liquid (methylene iodide and bromoform), vibratory "wiggle-bug" separation, and magnetic separation at the University of Texas at Austin and the University of Idaho. For detrital analyses, zircon grains were randomly poured onto epoxy pucks with double-sided sticky tape. All apatite and non-detrital zircon grains that could be petrographically identified were picked from separates and mounted. U-Pb analyses of grains were conducted using laser ablation-high-resolution-inductively coupled plasma-mass spectrometry (LA-HR-ICP-MS) equipped with a PhotonMachines® Analyte G.2 ArF excimer 193nm laser and a two-volume HeLex® 9 sample cell, coupled to a ThermoFisher® ElementII using a double-focusing magnetic sector ICP-MS. Zircon grains were ablated with a 30 μm laser spot size and apatite grains were ablated with a 40 μm spot size. Helium was used as the carrier gas and mixed with argon before entering the ICPMS. All analyses were conducted in static mode operated with an energy density of 1.43 J/cm^2, and a pulse rate of 10 Hz. Analyses consisted of 6 cleaning shots, 25 seconds of baseline data collection, 30 seconds of laser dwell time, and 35 seconds of washout. Ablation rates of ~0.5μm/second mean that only the outer 15–17μm of zircons are typically sampled by this technique.

We attempted to analyze ~100 detrital zircon grains to identify with 95% confidence the grain age populations constituting >3% of the zircon population (Andersen, 2005). For zircon, elemental and isotopic fractionation of Pb/U and Pb isotopes, respectively, was corrected by interspersed analysis of primary zircon standard GJ1 (^{206}Pb/^{238}U age of 601.7 ± 1.3 Ma; Jackson et al., 2004) and secondary zircon standard Plešovice (^{206}Pb/^{238}U age of 337.1 ± 0.4 Ma; Sláma et al., 2008) was used to monitor data quality. Standards were analyzed repeatedly before, after, and intermittently during all analyses of unknown

specimens so that mass fractionation and instrumental mass bias corrections could later be applied. Repeated analyses performed during all analytical sessions yielded a concordia U-Pb age of 600.4 ± 2.6 Ma for GJ1 (n = 438) and 332.3 ± 9.2 Ma for Plešovice (n = 55). The zircon Pak1 (in house standard) was also used for several samples and yielded a mean $^{206}Pb/^{238}U$ age of 42.8 ± 0.6 Ma (n = 18) over the course of all analytical sessions. The common unknown to standard measurement ratio is generally 4:1. The signals for masses ^{204}(Pb + Hg), ^{206}Pb, ^{207}Pb, ^{208}Pb, ^{232}Th, and ^{238}U were all acquired and ^{235}U was calculated from ^{235}U with the relationship $^{238}U/^{235}U = 137.88$. Uncertainty resulting from calibration correction is generally 1-2% for both $^{206}Pb/^{207}Pb$ and $^{206}Pb/^{238}U$. Standard correction is within 1–2% for $^{206}Pb/^{238}Pb$ and $^{206}Pb/^{207}Pb$ but increases for younger grains due to low ^{207}Pb intensity. We therefore adopted the $^{206}Pb/^{238}Pb$ age of grains younger than 850 Ma and the $^{206}Pb/^{207}Pb$ age of grains older than 850 Ma.

For split-stream analysis of apatite, the aerosol was split to deliver approximately even amounts to each ICP-MS from the ablation cell for U-Th-Pb isotope and trace element analysis. Apatite standards were also analyzed repeatedly before, after, and intermittently during all analyses of unknown specimens so that mass fractionation and instrumental mass bias corrections could later be applied. For apatite U-Pb geochronology, elemental and isotopic fractionation of Pb/U and Pb isotopes, respectively, was corrected by interspersed analysis of the Madagascar apatite (MAD-1; $^{206}Pb/^{238}Pb$ age of 486.6 ± 0.9 Ma; Thomson et al., 2012) and terrestrial fluorapatite from Bancroft, Canada (UWA-1; $^{206}Pb/^{238}U$ age of 1100 ± 96 Ma; Sano et al., 1999). Independent ID-TIMS dating of the UWA-1 standard at NIGL (NERC Isotope Geosciences Laboratories) yielded a mean age of 1009.9 ± 9.1 Ma (n = 14), which was used for data correction. Measured $^{206}Pr/^{204}Pb$ values were used to monitor and correct for ion counter gain. The $^{206}Pb/^{238}Pb$ age was determined following procedures outlined in Stacey and Kramers (1975) common lead evolution model.

Data reduction and age calculation was performed using Iolite (Igor Pro; Paton et al., 2011) and VizualAge (Petrus and Kamber, 2012), based on Isoplot V3 formulas (Ludwig, 2003), from baseline-subtracted intensities. Sequentially arranged raw count data were fit with a smoothed spline for background and reference standard characterization to enable time-resolved background subtraction and depth-dependent elemental fractionation corrections. No correction was applied for common Pb due to interferences in measurement of ^{204}Pb; however

common Pb was evaluated graphically and high Pbc zones usually rejected. We excluded zircon grains with >10% discordance and >10% uncertainty and only considered age peaks comprised of at least three grains. Following application of fractionation factor corrections, detrital zircon and apatite grains were checked for discordance using Isoplot 4.1 (Ludwig, 2008).

Apatite Trace Element Geochemistry

Simultaneous measurement of U-Th-Pb isotopic and trace element abundances was undertaken on the same ablation volume using Laser Ablation Split Stream (LASS) ICPMS analysis at the University of Texas at Austin. Trace element abundances were measured using a secondary ThermoFisher® Element II HR-ICPMS coupled to a Photon Machines® Analyte G.2 ArF 192 nm Excimer Laser. Simultaneous trace element analysis was completed by analyzing the NIST 612 glass standard as a primary reference material and the MAD and UWA-1 standards as secondary reference materials. The NIST 612 glass standard contains 61 trace elements in the range of 10 mg/kg to 80 mg/kg (NIST, 2012). The preferred values of element concentrations for the reference material are from the GeoReM database (Jochum et al., 2005). Trace element analyses included the masses ^{43}Ca, ^{44}Ca, ^{87}Sr, ^{89}Y, ^{137}Ba, ^{139}La, ^{140}Ce, ^{141}Pr, ^{146}Nd, ^{147}Sm, ^{153}Eu, ^{157}Gd, ^{159}Tb, ^{163}Dy, ^{165}Ho, ^{166}Er, ^{169}Tm, ^{172}Yb, ^{175}Lu, ^{232}Th, and ^{238}U, which were measured sequentially with a dwell time of ~0.02-0.03 s per analyte during each cycle. The LA-ICPMS data are in good agreement with the recommended standard values, and the analytical precision is within 5% for most of the measured elements. Ca content in apatite was used to correct matrix effects, signal differences, and differences in ablation yield between samples and reference materials. Chondrite-normalized TE abundances were calculated using the values from Taylor and McLennan (1985). Reduction of elemental data was performed off-line using trace element data reduction schemes in the Iolite software package (Paton et al., 2011).

Zircon, Apatite, and Titanite (U-Th)/He Thermochronology

Zircon, apatite, and titanite (U-Th)/He thermochronology was completed at the University of Texas at Austin and the University of Kansas. For detrital thermochronology, 4–7 zircon and apatite grains from each significant age population (consisting of >5 grains that

were ~65–120 μm in width) were picked from epoxy mounts, following U-Pb geochronology, using a high-magnification polarizing microscope. Zircon, apatite, and titanite grains that were metamict or had obvious cracks or inclusions were avoided. Grains were then measured to apply the alpha ejection correction factor (Farley, 2000), and individually packed in Pt packets. Pt-wrapped grains were repeatedly laser heated using a 20W Nd:YAG laser for intervals of 10 min at ~1300°C until complete degassing of the aliquot was achieved (>99% ^{3}He extracted). Extracted gas was spiked using a ^{3}He tracer, cryogenically purified, and measured on a quadrupole noble gas mass spectrometer. Following complete degassing, zircon grains were removed from Pt packets whereas apatite grains were dissolved in Pt packets after being spiked with ^{230}Th, ^{235}U, ^{149}SM, and a REE tracer and digested in a pressure vessel with a HF-HNO_3 mixture for 72 hr at 255°C and 6 N HCL for 12 hr at 200°C. Parent nuclide concentrations were measured by isotope dilution on a Thermo Element2 HR-ICP-MS by comparing the spike to a gravimetric 1 ppb U-Th-Sm-REE normal solution. (U-Th)/He ages were calculated using standard FT corrections with estimated 8% analytical uncertainty (2σ) based on the Fish Canyon Tuff zircon (U-Th)/He standard.

Methods and Supporting Data for Time-Temperature Path Modeling

Zircon, apatite, and titanite (U-Th)/He ages and depositional ages from ^{40}Ar/^{39}Ar geochronology were used to inverse model time-temperature (t-T) paths using HeTYy version 1.9.3 (Ketcham, 2005). Surface temperature was estimated at 20 ± 10°C. Inverse modeling used the following parameters: Search Method: “Monte Carlo” (default); Subsegment spacing: “Random” (default); Ending condition: “Paths tried = 10000” (default); Result to display: “Paths”; Merit value for ‘good’ fit: “0.5” (default); Merit value for ‘acceptable fit’ = “0.05” (default). Segments: “monotonic consistent” (default); Randomizer style: “Episodic” (default).

The following model parameters were used for the zircon (U-Th)/He model: Calibration: “Guenthner et al., 2013 (Zircon)”; Abraded: “0 μm” (default); Model precision: “Good”; Stopping distances: “Ketcham et al. 2011”; Alpha calculation: “Ejection”; Age to report: “Corrected”; Alpha correction: “Ketcham et al. 2011”; Zoned? “No.”

For the apatite (U-Th)/He model, the following model parameters were used: Calibration: “Shuster et al., 2006 (Do/a2) (Apatite)”; Abraded: “0 μm” (default); Model

precision: “Good”; Stopping distances: “Ketcham et al. 2011”; Alpha calculation: “Static ejection”; Measured age (uncorrected); Age to report: “Corrected”; Alpha correction: “Ketcham et al. 2011”; Zoned? “No.”

For the titanite (U-Th)/He model, the following model parameters were used: Calibration: “Reiners and Farley, 1999 (Titanite)”; Abraded: “0 μm” (default); Model precision: “Good”; Stopping distances: “Ketcham et al. 2011”; Alpha calculation: “Static ejection”; Measured age (uncorrected); Age to report: “Corrected”; Alpha correction: “Ketcham et al. 2011”; Zoned? “No.”

For the (U-Th)/He model of sample NV12-176CB, the weighted mean (U-Th)/He age of uncorrected ages was used along with the mean grain radius and the average U, Th, and Sm concentration of all grains used to calculate the weighted mean age of the sample.

$^{40}Ar/^{39}Ar$ Geochronology

The $^{40}Ar/^{39}Ar$ measurements were performed in the Radiogenic Isotopes Laboratory at Ohio State University using procedures discussed in Foland et al. (1993) except for the use of a newer noble gas mass analysis system. Samples were first prepared using standard crushing, sieving, magnetic, and heavy-liquid density separation techniques. Mineral aliquots (~1–15 mg) were irradiated in the L-67 position of the Ford Nuclear Reactor, Phoenix Memorial Laboratory, at the University of Michigan for 36 hours. Sample aliquots were then heated incrementally, in ≥20 steps, to successively higher temperatures using a custom-built, resistance-heating, high-vacuum, and low-blank furnace. Continuous step heating was conducted with ramp times of ~1 min and dwell times of ~30 min at each temperature. Incremental-heating fractions were analyzed by static gas mass analysis with a MAP 215-50 mass spectrometer. Corrections for interfering reactions producing Ar from K, Ca, and Cl during sample irradiation were made using factors determined using solids irradiated at the same time. An intralaboratory muscovite standard (“PM-1”) was used as a fluence monitor and has an $^{40}Ar/^{39}Ar$ age of 165.3 Ma with a ±1% uncertainty, determined using cross-calibration with several monitors including the 27.84 Ma Fish Canyon Tuff biotite standard (FCT-3).

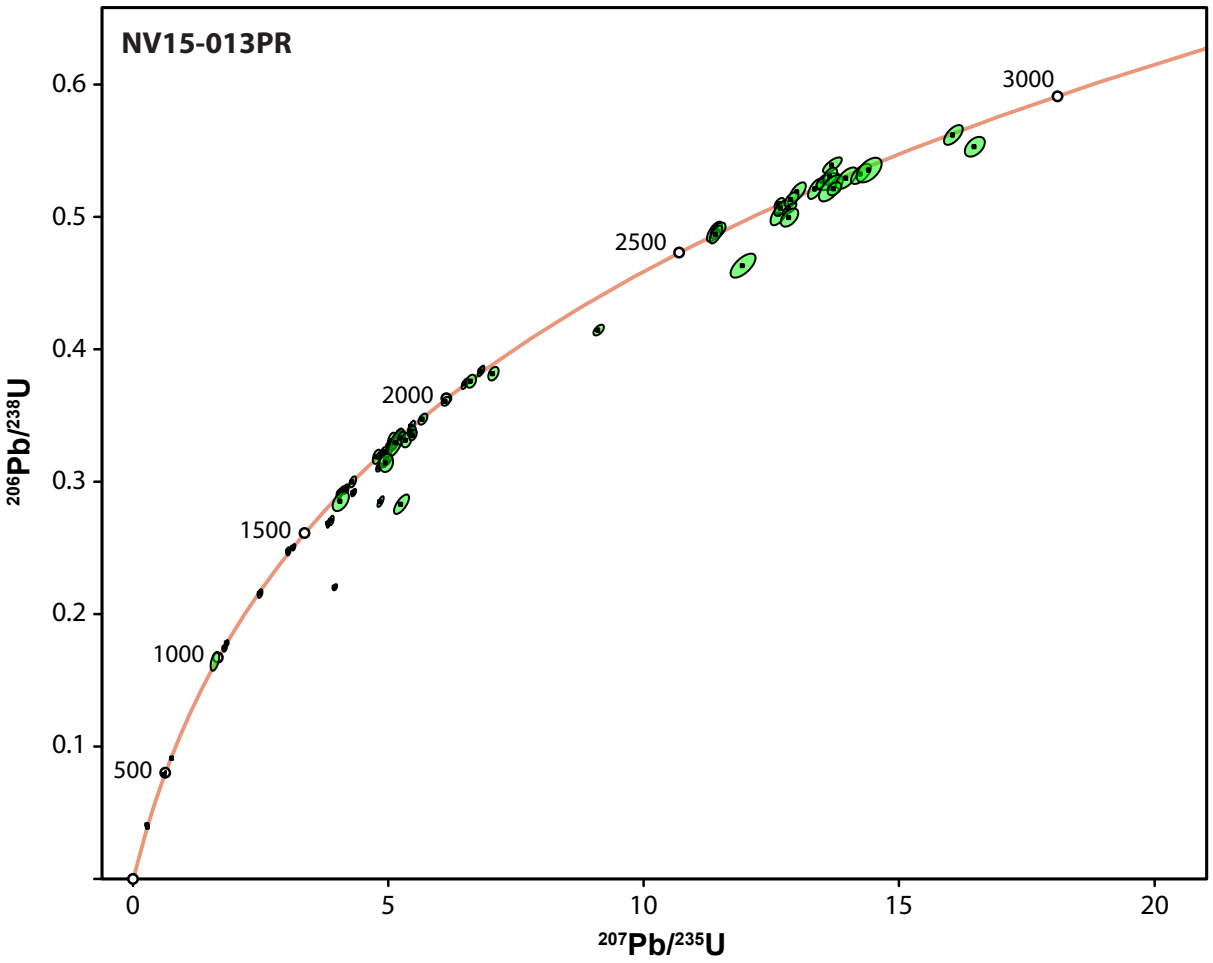
NV15-013PR
0.6
0.5
0.4
0.3
0.2
0.1
206Pb/238U
3000
2500
2000
1500
1000
500
0
5
10
15
20
207Pb/235U

ANDREW S. CANADA
Ph.D. Candidate
Geological Sciences
University of Idaho

University of Idaho

875 Perimeter Drive, MS 3022
Moscow, ID 83844-3022
(925) 389-6988
acanada@uidaho.edu

GSA
PO Box 9140
Boulder, CO 80301-9140

April 3, 2019

Dear Copyright Permissions Manager,

I am completing a doctoral dissertation at the University of Idaho this spring entitled "Eocene Exhumation and Lake Basin Development in the North American Cordilleran Hinterland, Northeastern Nevada, U.S.A." I would like your permission to reprint the following article in my dissertation, of which I am the primary author of the original material:

Canada, A.S., Cassel, E.J., McGrew, A.J., Smith, M.E., Stockli, D.F., Foland, K.A., Jicha, B.R., and Singer B.S., 2019, Eocene exhumation and extensional basin formation in the Copper Mountains, Nevada, U.S.A.: Geosphere, in review.

The article text, figures, and supplementary information submitted to Geosphere would be reproduced in my dissertation with no modifications and would include a complete article citation on the chapter title page. The material will be formatted in accordance with the University of Idaho dissertation guidelines. The requested permission extends to any future revisions and editions of my dissertation, including non-exclusive world rights in all languages, and to the prospective publication of my dissertation by ProQuest. ProQuest may produce and sell copies of my dissertation on demand and may make my dissertation available for free internet download at my request. These rights will in no way restrict republication of the material in any other form by you or by others authorized by you. Your signing of this letter will also confirm that the Geological Society of America owns the copyright to the above-described material.

If these arrangements meet with your approval, please sign the letter where indicated below and return it to me via the mail or email address above. Your prompt response is greatly appreciated. Thank you very much.

Sincerely,

Andrew Canada

Andrew S. Canada

PERMISSION GRANTED FOR THE USE REQUESTED ABOVE:

Geological Society of America

By: Jeanette Hammann for GSA

Title: Director of Publications, GSA

Date: 24 April 2019

This paper has been revised and of this writing is pending a formal decision by the science editor. An updated permission will be sent when we have that formal decision, with wording dependent on the outcome: Jeanette Hammann 4/24/19

TABLE B1. CHEMICAL ANALYSES OF THE COFFEEPOT STOCK

Sample:	980729-1	980730-1	980730-2	980730-4	980730-5	980730-6	980731-2	980731-4A	980731-4B	980802-71B	980802-72	980802-74
Location:	Coffeepot Stock	Coffeepot Stock	Coffeepot Stock	Coffeepot Stock	Coffeepot Stock	Coffeepot Stock	Coffeepot Stock	Coffeepot Stock	Coffeepot Stock	Copper Basin	Copper Basin	Copper Basin
Latitude:	41.7940°N	41.8202°N	41.8225°N	41.8358°N	41.8067°N	41.7922°N	41.7859°N	41.7872°N	41.7861°N	41.7625°N	41.7634°N	41.7553°N
Longitude:	115.6698°W	115.6911°W	115.6885°W	115.6456°W	115.6230°W	115.6448°W	115.4934°W	115.4926°W	115.4919°W	115.4903°W	115.4903°W	115.4874°W
SiO_2	74.11	65.23	75.16	65.48	71.58	74.18	72.52	73.73	70.73	71.77	70.98	69.79
Al_2O_3	12.10	17.67	12.69	17.79	16.21	12.10	14.58	13.49	14.38	16.33	14.72	15.10
Fe	0.70	3.86	0.52	3.42	1.72	0.61	2.55	0.27	2.42	1.03	2.82	0.49
Mg	0.07	1.05	0.04	1.08	0.47	0.11	0.55	0.06	0.60	0.41	0.71	0.01
Ca	0.36	3.93	0.79	3.42	2.36	0.35	0.85	0.85	0.82	2.92	3.66	0.29
Mn	0.03	0.11	0.05	0.11	0.05	0.01	0.05	0.01	0.06	0.03	0.06	0.00
K	4.75	4.15	3.78	4.51	3.24	3.87	2.74	6.82	4.68	4.04	2.65	9.07
Na	2.10	3.71	3.68	4.03	4.94	2.35	2.44	2.70	2.21	4.35	3.22	2.92
Ti	0.10	0.51	0.06	0.39	0.18	0.07	0.32	0.15	0.33	0.21	0.29	0.05
Sum	94.32	100.23	96.76	100.22	100.75	93.64	96.60	98.07	96.23	101.10	99.11	97.73
Sr	182	757	35	921	410	135	585	292	601	665	677	66
Ba	248	2087	56	1587	452	97	918	711	1571	950	779	145
Ni	16	5	5	12	15	N.D.	16	4	10	88	12	3
Sc	4	4	1	8	8	N.D.	9	0	6	6	6	0
Cr	24	1	2	9	11	N.D.	33	-	24	7	9	0
V	37	26	2	42	33	N.D.	53	0	38	25	34	2
Zn	58	72	47	81	57	42	81	38	63	52	66	30
Cu	3	4	4	9	16	N.D.	4	4	3	17	8	4

Note: Geochemistry data analyzed at USF Center for Geochemical Analysis following protocols described in Peterson and Ryan (2008). Sample analyses calibrated against USGS standards G-2, AGV-1, SDC-1, and SDC-1 and IWG standard AC-E. Intralaboratory LML-7 dacite standard used as a drift monitor. Uncertainties are 1% for major elements (>10%),1-3% for elements (<10% but >0.1%), 5% for Sr and Ba, and 10-20% for other trace elements, with greater uncertainties at lower concentrations.

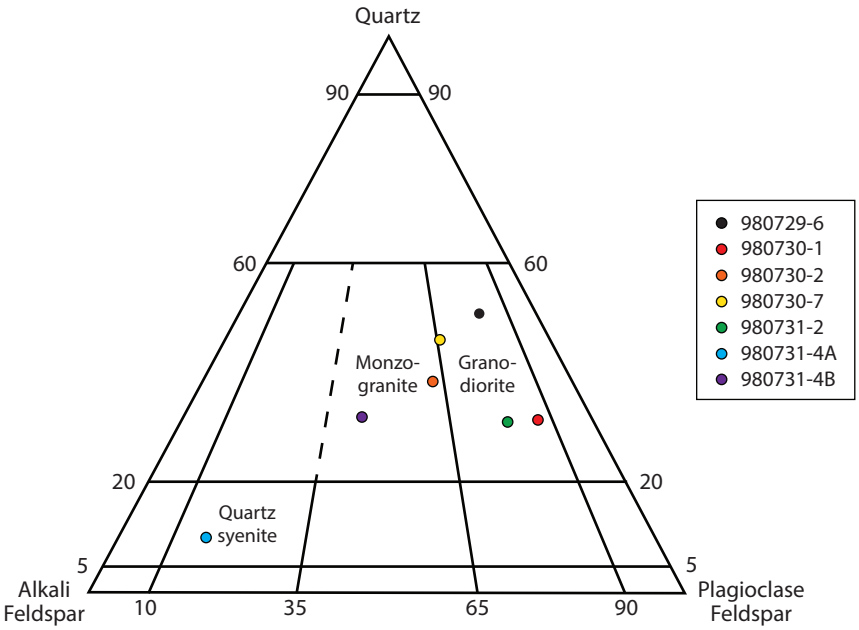

Figure B1. QAP plot showing the relative proportions of quartz, alkali feldspar, and plagioclase feldspar for Coffeepot Stock samples.

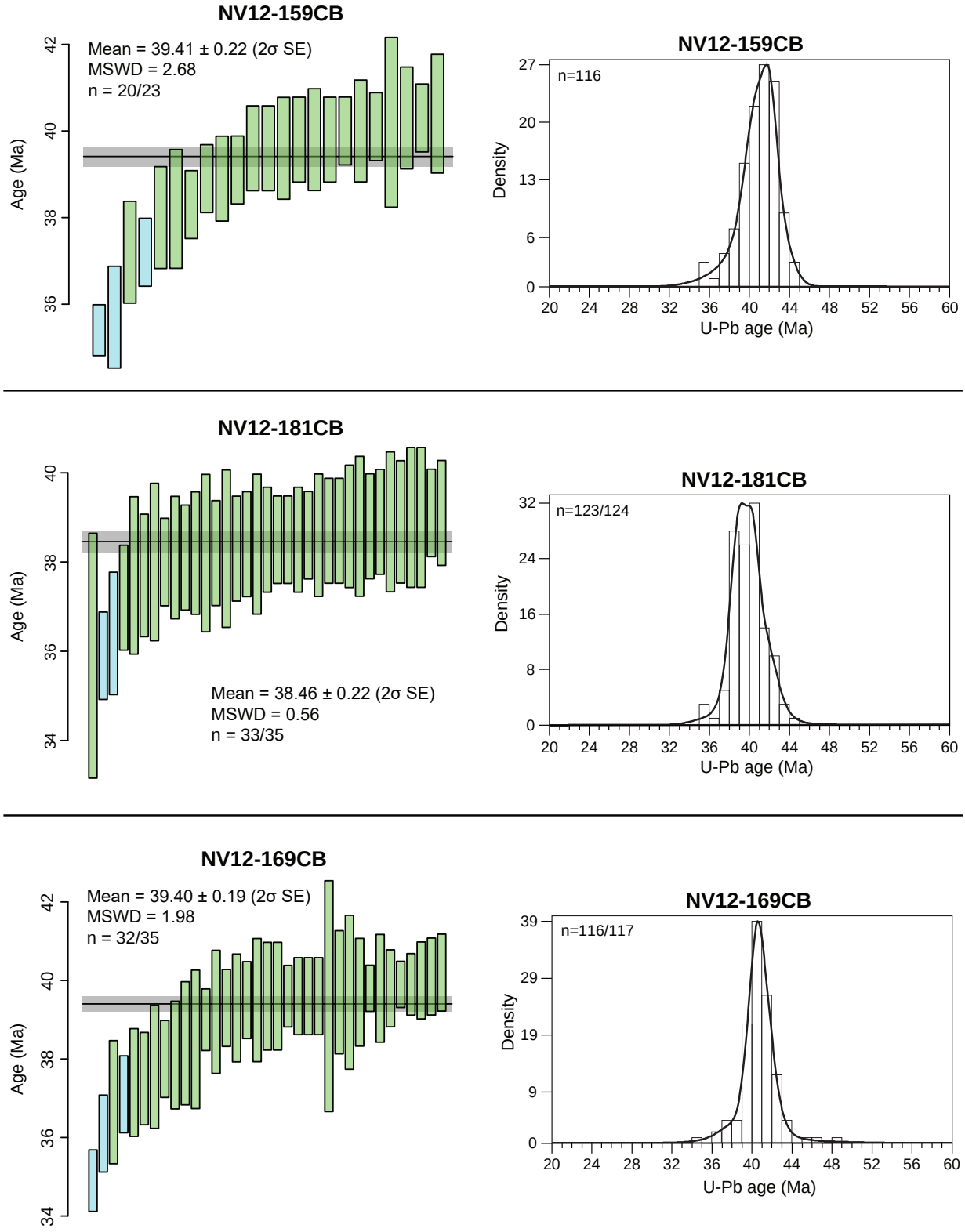

Figure B2. Detrital zircon maximum depositional ages (MDA) and U-Pb age plots for samples NV12-159CB, NV12-181CB, and NV12-169CB. U-Pb ages plotted using a kernal density estimate function (Vermeesch, 2012) and MDA determined with IsoplotR (Vermeesch, 2018). Grains with ≥10% discordance not included in maximum depositional age determination.

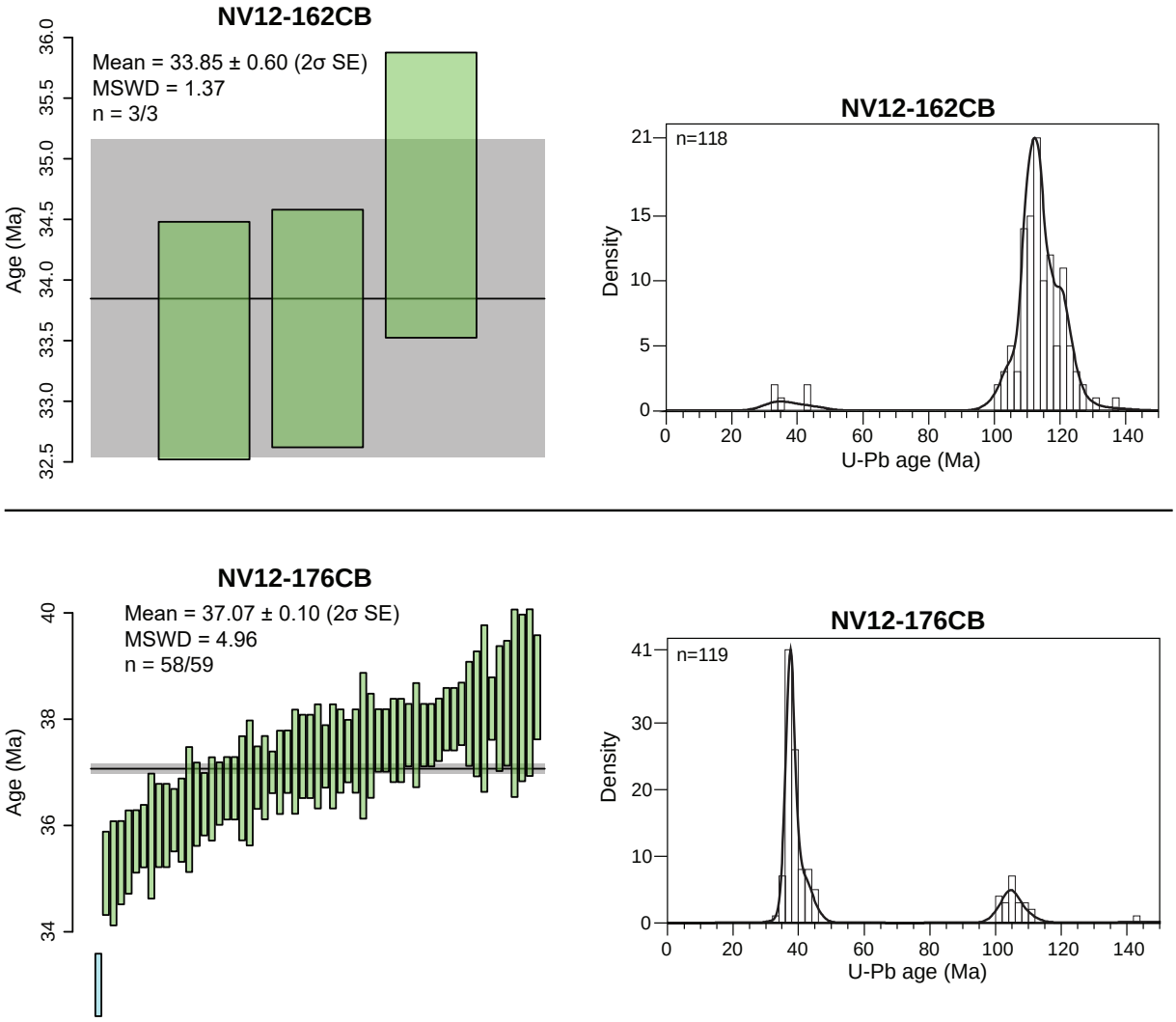

Figure B3. Detrital zircon maximum depositional ages (MDA) and U-Pb age plots for samples NV12-162CB and NV12-176CB. U-Pb age plotted using a kernal density estimate function (Vermeesch, 2012) and MDA determined with IsoplotR (Vermeesch, 2018). Grains with ≥10% discordance not included in maximum depositional age determination.

Sample number	Lithology	Mineral(s) dated	Location		Elevation (m)
			Latitude (°N) *	Longitude (°W) *	
NV12-159CB	sandstone	zircon	41.7505	115.4784	2176
NV12-162CB	sandstone	apatite, zircon	41.7571	115.4835	2154
NV12-169CB	sandstone	zircon	41.7615	115.4627	2374
NV12-176CB	sandstone	apatite, zircon	41.7640	115.4679	2366
NV12-181CB	sandstone	zircon	41.7370	115.4757	2264

*Locations reported relative to NAD 1983 projection.

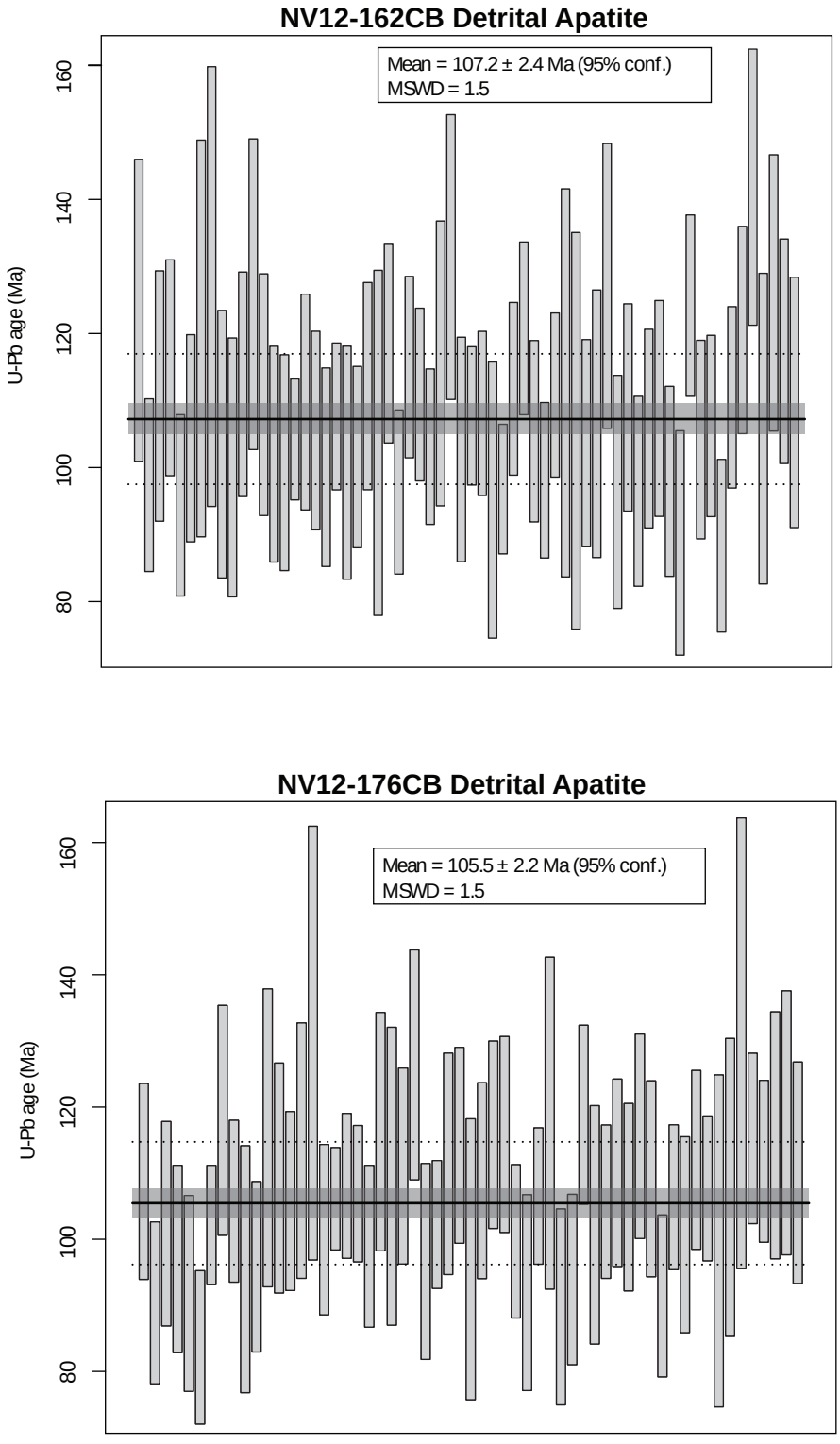

Figure B4. Weighted mean plots of ^{204}Pb-corrected U-Pb ages for detrital apatite extracted from samples NV12-162CB and NV12-176CB created using Vermeesch (2018).

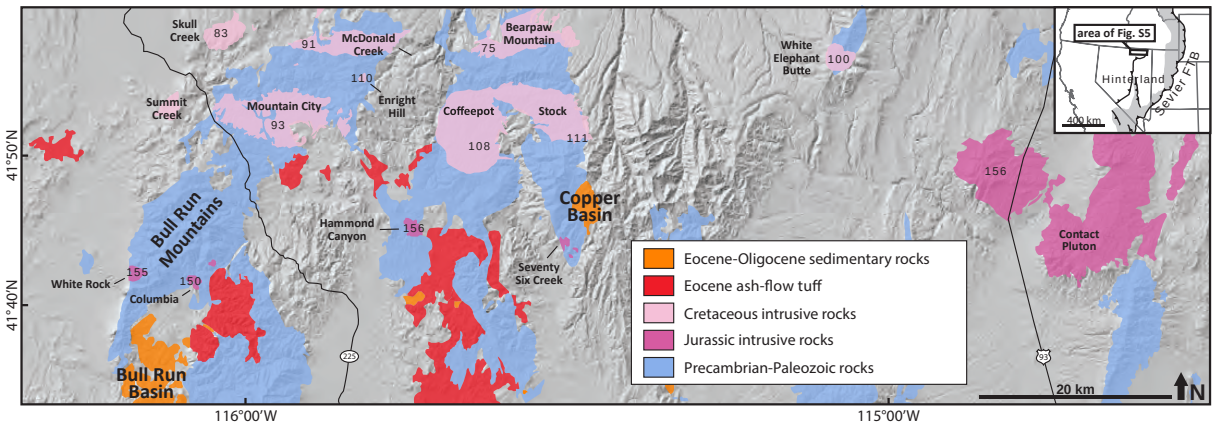

Figure B5. Simplified geologic map of northeastern Nevada showing ages of Jurassic and Cretaceous intrusive rocks proximal to the Copper Mountains. Geology modified from Coats (1987) and Henry et al. (2011). Crystallization ages from du Bray (2007).

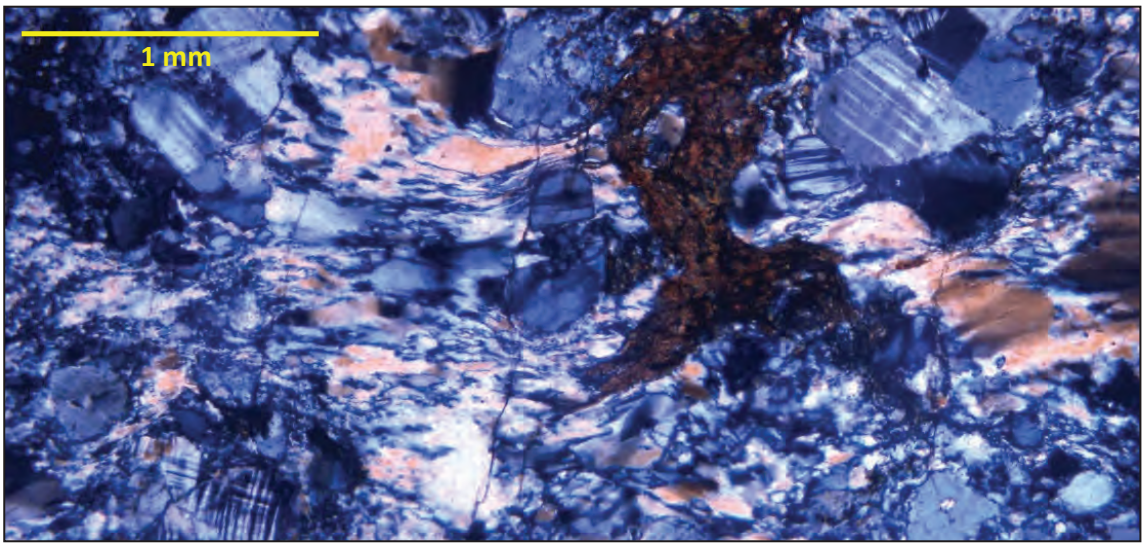

Figure B6. Photomicrograph of sample 000714-1 in XPL. Sample is of medium-coarse-grained biotite monzogranite with dynamically recrystallized quartz matrix. Feldspars are locally microfractured and/or cut by thin recrystallized veinlets. Biotite commonly occurs in recrystallized patches 1-2 mm in diameter intergrown with epidote. The absence of chlorite suggests recrystallization may have occurred in the epidote amphibolite facies.

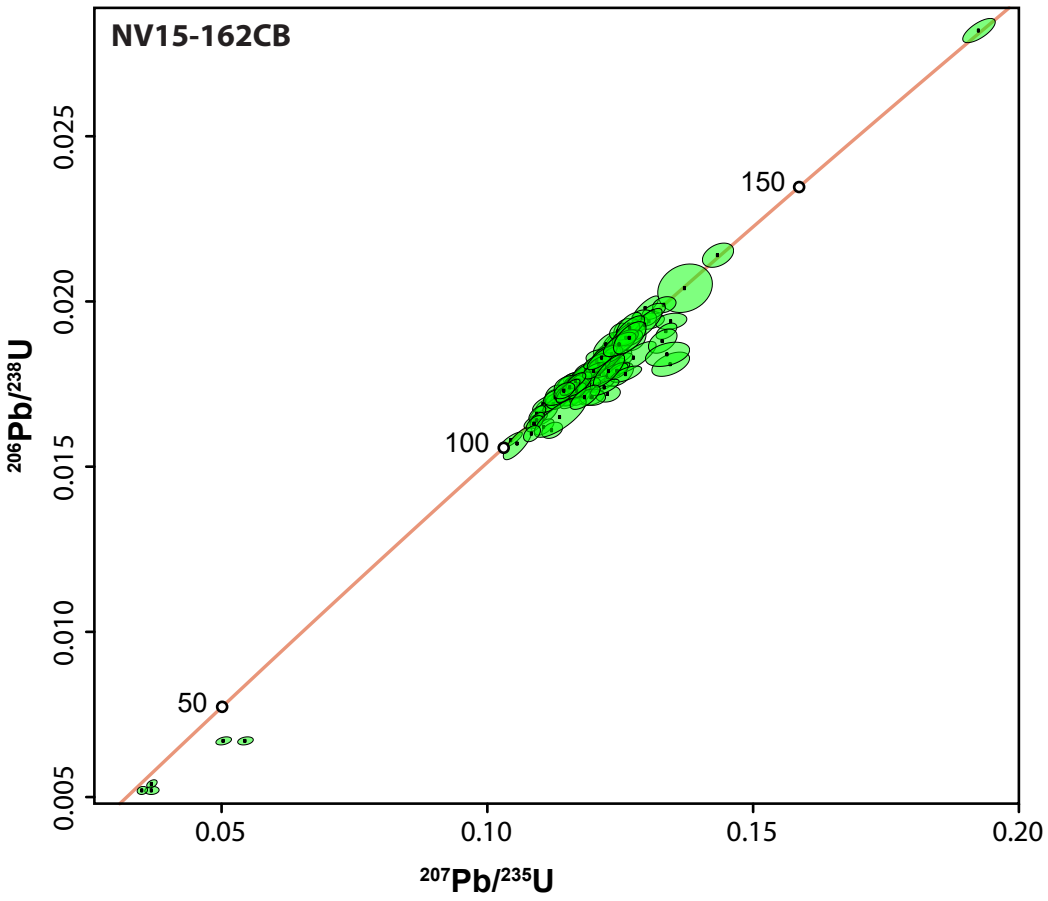
NV15-162CB
0.025
0.020
0.015
0.010
0.005
206Pb/238U
150
100
50
0.05
0.10
0.15
0.20
207Pb/235U

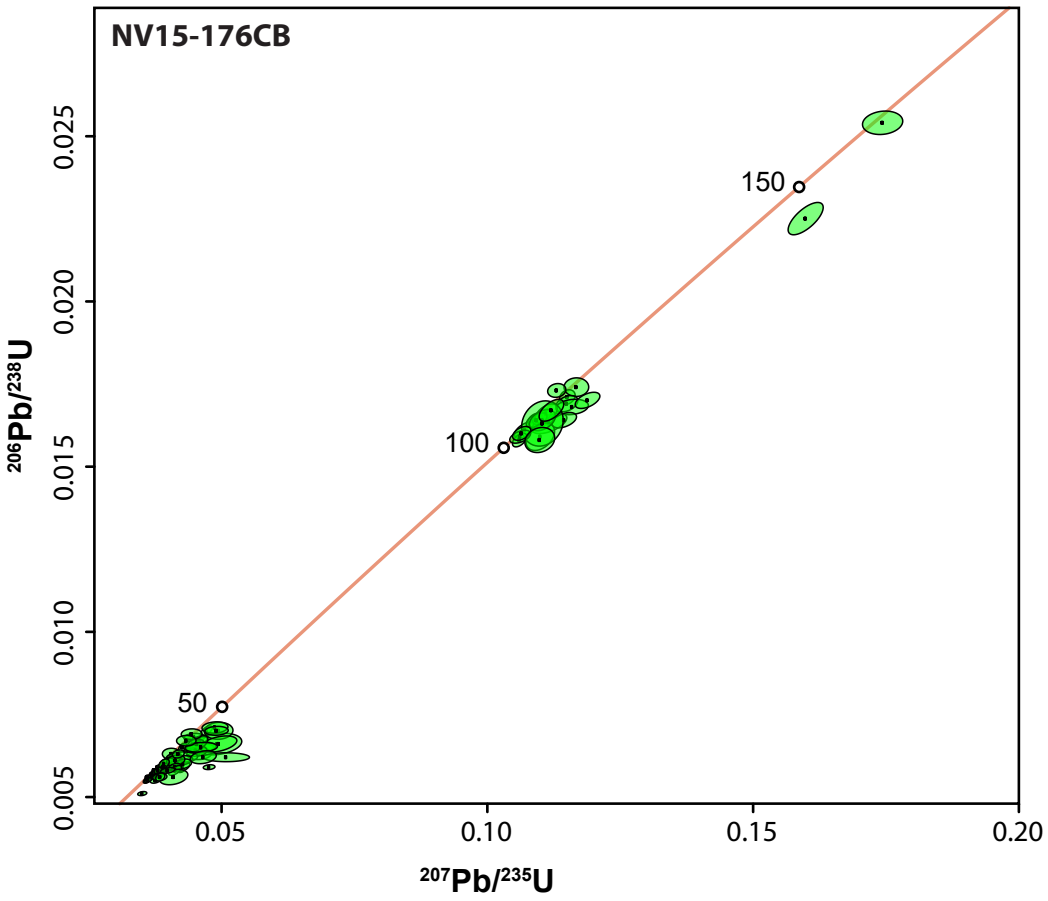
NV15-176CB
0.025
0.020
0.015
0.010
0.005
206Pb/238U
150
100
50
0.05
0.10
0.15
0.20
207Pb/235U

DETRITAL ZIRCON U-Pb GEOCHRONOLOGY

Analysis	U (ppm)	U/Th	207Pb/ 206Pb	2σ error	207Pb/ 235U	2σ error	206Pb/ 238U	2σ error	err. corr.	206Pb/ 238U Age (Ma)	2σ error (Ma)	207Pb/ 235U Age (Ma)	2σ error (Ma)	207Pb/ 206Pb Age (Ma)	2σ error (Ma)	Best age (Ma)	2σ error (Ma)	Disc. (%)
NV12-159CB																		
12159CB_1	262	1.0	0.0496	0.0021	0.0433	0.0019	0.0063	0.0001	0.14	40.5	0.7	43.0	1.8	328	73	40.5	0.7	5.8
12159CB_2	404	1.0	0.0595	0.0047	0.0509	0.0033	0.0064	0.0001	0.11	41.0	0.6	50.4	3.2	586	81	41.0	0.6	18.7
12159CB_4	437	0.9	0.0503	0.0014	0.0430	0.0012	0.0062	0.0001	0.33	39.8	0.5	42.8	1.2	238	36	39.8	0.5	7.0
12159CB_5	444	0.9	0.0486	0.0014	0.0422	0.0010	0.0063	0.0001	0.07	40.6	0.5	41.9	0.9	192	37	40.6	0.5	3.2
12159CB_6	310	1.7	0.0475	0.0016	0.0449	0.0015	0.0069	0.0001	0.20	44.3	0.8	44.6	1.4	222	57	44.3	0.8	0.7
12159CB_7	343	1.2	0.0505	0.0015	0.0416	0.0012	0.0060	0.0001	0.37	38.2	0.7	41.4	1.2	237	34	38.2	0.7	7.7
12159CB_8	248	1.4	0.0602	0.0017	0.0537	0.0016	0.0064	0.0001	0.06	41.3	0.6	53.1	1.5	633	45	41.3	0.6	22.2
12159CB_9	278	1.0	0.0531	0.0021	0.0468	0.0020	0.0064	0.0001	0.28	41.2	0.9	46.4	2.0	364	60	41.2	0.9	11.2
12159CB_10	359	0.7	0.0516	0.0014	0.0444	0.0012	0.0063	0.0001	0.41	40.4	0.7	44.1	1.2	315	45	40.4	0.7	8.4
12159CB_11	205	0.9	0.0635	0.0091	0.0595	0.0081	0.0068	0.0001	0.11	43.4	0.8	58.3	7.4	640	160	43.4	0.8	25.5
12159CB_12	147	0.8	0.0624	0.0063	0.0564	0.0065	0.0065	0.0002	0.48	41.9	1.2	55.5	6.1	770	170	41.9	1.2	24.5
12159CB_13	171	1.0	0.0565	0.0052	0.0454	0.0032	0.0059	0.0001	0.09	37.8	0.9	45.0	3.1	530	140	37.8	0.9	16.0
12159CB_14	409	0.6	0.0629	0.0031	0.0549	0.0029	0.0063	0.0001	0.30	40.6	0.5	54.2	2.8	760	110	40.6	0.5	25.1
12159CB_15	204	1.0	0.0655	0.0031	0.0582	0.0029	0.0065	0.0001	0.29	41.8	0.8	57.4	2.8	762	75	41.8	0.8	27.1
12159CB_16	216	1.0	0.0519	0.0029	0.0444	0.0023	0.0063	0.0002	0.13	40.2	1.0	44.1	2.2	346	84	40.2	1.0	8.8
12159CB_17	2070	2.4	0.0484	0.0007	0.0439	0.0007	0.0066	0.0001	0.24	42.2	0.6	43.7	0.7	154	28	42.2	0.6	3.4
12159CB_18	393	1.7	0.0542	0.0060	0.0467	0.0054	0.0063	0.0001	0.08	40.3	0.6	43.9	1.9	350	130	40.3	0.6	8.2
12159CB_19	463	0.8	0.0566	0.0015	0.0454	0.0013	0.0058	0.0001	0.14	37.2	0.5	45.1	1.3	516	53	37.2	0.5	17.5
12159CB_20	5387	1.9	0.0489	0.0005	0.0411	0.0005	0.0061	0.0001	0.59	39.1	0.4	40.9	0.5	148	16	39.1	0.4	4.4
12159CB_21	499	1.2	0.0495	0.0020	0.0396	0.0015	0.0058	0.0001	0.01	37.2	0.6	39.4	1.5	237	59	37.2	0.6	5.6
12159CB_23	1629	3.0	0.0504	0.0018	0.0438	0.0016	0.0063	0.0001	0.24	40.8	0.4	43.5	1.6	215	51	40.8	0.4	6.3
12159CB_24	714	1.5	0.0587	0.0043	0.0518	0.0045	0.0063	0.0001	0.18	40.3	0.5	51.1	4.2	540	130	40.3	0.5	21.2
12159CB_25	189	1.2	0.0519	0.0027	0.0461	0.0024	0.0065	0.0001	0.12	41.4	0.8	45.7	2.3	443	90	41.4	0.8	9.3
12159CB_26	287	1.5	0.0524	0.0019	0.0460	0.0017	0.0064	0.0001	0.06	40.8	0.7	45.7	1.6	357	58	40.8	0.7	10.7
12159CB_28	196	2.6	0.0486	0.0021	0.0429	0.0017	0.0064	0.0001	0.02	41.1	0.8	42.7	1.6	273	73	41.1	0.8	3.7
12159CB_29	3400	2.2	0.0526	0.0007	0.0408	0.0005	0.0055	0.0000	0.18	35.6	0.3	40.6	0.5	310	23	35.6	0.3	12.3
12159CB_30	582	1.3	0.0510	0.0016	0.0455	0.0015	0.0064	0.0001	0.33	41.4	0.5	45.1	1.5	264	50	41.4	0.5	8.1
12159CB_31	139	1.3	0.0579	0.0049	0.0509	0.0038	0.0065	0.0002	0.03	42.0	1.0	50.3	3.7	700	160	42.0	1.0	16.5
12159CB_32	203	1.0	0.0630	0.0034	0.0560	0.0026	0.0064	0.0001	0.01	41.3	0.8	55.3	2.5	720	72	41.3	0.8	25.3

12159CB_33	909	6.2	0.0488	0.0009	0.0419	0.0006	0.0063	0.0001	0.15	40.3	0.4	41.7	0.6	139	22	40.3	0.4	3.3
12159CB_34	1840	1.9	0.0466	0.0006	0.0394	0.0005	0.0061	0.0001	0.43	38.9	0.4	39.2	0.5	86	16	38.9	0.4	0.7
12159CB_35	205	1.4	0.0501	0.0019	0.0452	0.0015	0.0066	0.0001	0.10	42.1	0.6	44.8	1.4	299	64	42.1	0.6	6.0
12159CB_36	566	1.1	0.0527	0.0026	0.0448	0.0022	0.0062	0.0001	0.10	39.9	0.5	44.5	2.1	361	86	39.9	0.5	10.3
12159CB_37	434	1.0	0.0490	0.0012	0.0434	0.0011	0.0065	0.0001	0.29	41.8	0.6	43.1	1.0	160	30	41.8	0.6	3.1
12159CB_38	229	1.5	0.0591	0.0032	0.0533	0.0026	0.0065	0.0001	0.03	41.8	0.5	52.7	2.5	529	88	41.8	0.5	20.6
12159CB_39	500	1.0	0.0482	0.0010	0.0430	0.0008	0.0064	0.0001	0.17	41.3	0.5	42.8	0.8	164	23	41.3	0.5	3.4
12159CB_40	3571	1.9	0.0488	0.0006	0.0428	0.0005	0.0064	0.0001	0.24	40.9	0.3	42.5	0.5	129	21	40.9	0.3	3.7
12159CB_42	169	1.1	0.0524	0.0021	0.0460	0.0015	0.0064	0.0001	0.03	41.1	0.7	45.6	1.5	325	50	41.1	0.7	9.8
12159CB_43	248	1.5	0.0556	0.0035	0.0513	0.0036	0.0067	0.0001	0.05	43.0	0.7	50.7	3.3	414	81	43.0	0.7	15.2
12159CB_44	495	0.6	0.0508	0.0019	0.0436	0.0020	0.0062	0.0001	0.15	39.6	0.5	43.3	1.9	313	81	39.6	0.5	8.5
12159CB_45	687	1.3	0.0516	0.0011	0.0428	0.0009	0.0060	0.0001	0.04	38.9	0.5	42.6	0.9	251	30	38.9	0.5	8.7
12159CB_46	138	0.9	0.0627	0.0039	0.0526	0.0031	0.0060	0.0001	0.04	38.6	0.7	51.9	3.0	653	72	38.6	0.7	25.6
12159CB_47	436	0.6	0.0491	0.0015	0.0428	0.0013	0.0063	0.0001	0.34	40.7	0.6	42.5	1.3	216	60	40.7	0.6	4.2
12159CB_48	2650	2.5	0.0482	0.0006	0.0373	0.0005	0.0055	0.0001	0.27	35.4	0.3	37.2	0.5	133	21	35.4	0.3	4.7
12159CB_49	547	1.3	0.0583	0.0022	0.0497	0.0023	0.0062	0.0001	0.32	39.7	0.5	48.6	1.8	549	76	39.7	0.5	18.4
12159CB_50	516	0.9	0.0494	0.0015	0.0441	0.0013	0.0064	0.0001	0.01	41.3	0.6	43.8	1.3	206	36	41.3	0.6	5.6
12159CB_51	529	1.3	0.0496	0.0025	0.0449	0.0018	0.0067	0.0001	0.05	42.8	0.6	44.6	1.8	261	81	42.8	0.6	4.0
12159CB_52	317	0.8	0.0548	0.0031	0.0519	0.0024	0.0068	0.0002	0.22	43.8	1.2	51.3	2.3	469	54	43.8	1.2	14.6
12159CB_55	215	1.4	0.0562	0.0040	0.0542	0.0038	0.0069	0.0002	0.11	44.0	1.0	53.5	3.7	496	97	44.0	1.0	17.8
12159CB_56	285	1.9	0.0539	0.0031	0.0462	0.0023	0.0063	0.0001	0.02	40.5	0.6	45.9	2.2	461	87	40.5	0.6	11.9
12159CB_57	122	1.3	0.0527	0.0030	0.0491	0.0027	0.0068	0.0001	0.13	43.4	0.9	48.7	2.6	451	93	43.4	0.9	11.0
12159CB_58	1210	1.4	0.0493	0.0008	0.0425	0.0007	0.0062	0.0001	0.26	40.1	0.4	42.3	0.7	171	22	40.1	0.4	5.2
12159CB_59	488	1.5	0.0523	0.0029	0.0468	0.0026	0.0065	0.0001	0.20	41.7	0.8	46.4	2.5	340	100	41.7	0.8	10.2
12159CB_60	705	1.1	0.0498	0.0012	0.0411	0.0009	0.0060	0.0001	0.17	38.3	0.4	40.9	0.8	235	39	38.3	0.4	6.3
12159CB_61	188	1.4	0.0610	0.0027	0.0569	0.0021	0.0068	0.0001	0.05	43.7	0.9	56.1	2.0	631	51	43.7	0.9	22.1
12159CB_62	655	1.0	0.0481	0.0011	0.0422	0.0011	0.0064	0.0001	0.55	41.1	0.5	42.0	1.1	160	29	41.1	0.5	2.0
12159CB_63	341	1.3	0.0520	0.0029	0.0464	0.0024	0.0065	0.0002	0.15	41.8	1.1	46.0	2.3	317	95	41.8	1.1	9.1
12159CB_64	670	1.3	0.0481	0.0009	0.0414	0.0008	0.0062	0.0001	0.10	40.0	0.4	41.2	0.8	142	23	40.0	0.4	2.9
12159CB_65	152	1.1	0.0482	0.0018	0.0437	0.0015	0.0066	0.0001	0.12	42.3	0.9	43.4	1.5	253	41	42.3	0.9	2.5
12159CB_66	279	1.5	0.0533	0.0019	0.0489	0.0018	0.0066	0.0002	0.30	42.7	1.0	48.5	1.7	378	37	42.7	1.0	12.0
12159CB_67	146	1.3	0.0520	0.0027	0.0476	0.0019	0.0067	0.0002	0.05	42.8	1.0	47.2	1.9	422	67	42.8	1.0	9.3
12159CB_68	517	1.2	0.0507	0.0013	0.0452	0.0012	0.0065	0.0001	0.37	41.5	0.6	44.8	1.1	242	43	41.5	0.6	7.4
12159CB_69	83	0.9	0.0481	0.0023	0.0420	0.0018	0.0063	0.0002	0.13	40.4	1.0	41.7	1.8	328	85	40.4	1.0	3.0
12159CB_70	444	0.5	0.0522	0.0029	0.0415	0.0023	0.0057	0.0001	0.25	36.6	0.4	41.3	2.3	342	93	36.6	0.4	11.3

12159CB_71	895	3.9	0.0511	0.0011	0.0435	0.0009	0.0062	0.0001	0.38	40.0	0.6	43.2	0.9	253	31	40.0	0.6	7.4
12159CB_72	616	0.6	0.0480	0.0011	0.0415	0.0009	0.0063	0.0001	0.24	40.4	0.6	41.3	0.9	147	25	40.4	0.6	2.0
12159CB_73	2410	1.8	0.0517	0.0011	0.0442	0.0012	0.0061	0.0001	0.38	39.3	0.5	43.9	1.2	277	36	39.3	0.5	10.5
12159CB_74	650	1.0	0.0494	0.0015	0.0433	0.0012	0.0063	0.0001	0.04	40.7	0.4	43.0	1.1	235	58	40.7	0.4	5.3
12159CB_75	296	1.3	0.0567	0.0030	0.0514	0.0026	0.0066	0.0001	0.22	42.3	0.6	50.8	2.5	443	89	42.3	0.6	16.7
12159CB_76	620	1.2	0.0477	0.0008	0.0406	0.0007	0.0062	0.0001	0.23	39.6	0.5	40.4	0.7	117	19	39.6	0.5	1.8
12159CB_77	676	0.9	0.0550	0.0015	0.0478	0.0009	0.0062	0.0001	0.05	39.9	0.7	47.4	0.9	427	45	39.9	0.7	15.8
12159CB_78	311	1.3	0.0514	0.0022	0.0463	0.0020	0.0065	0.0001	0.17	41.9	0.5	45.9	1.9	322	54	41.9	0.5	8.6
12159CB_79	392	1.4	0.0502	0.0025	0.0456	0.0018	0.0066	0.0001	0.13	42.7	0.6	44.7	1.3	258	75	42.7	0.6	4.5
12159CB_80	539	1.2	0.0501	0.0021	0.0454	0.0019	0.0066	0.0001	0.01	42.3	0.6	45.1	1.8	256	67	42.3	0.6	6.3
12159CB_81	504	1.0	0.0494	0.0013	0.0439	0.0013	0.0064	0.0001	0.35	40.9	0.5	43.6	1.2	273	52	40.9	0.5	6.2
12159CB_82	319	1.1	0.0538	0.0017	0.0511	0.0016	0.0069	0.0001	0.18	44.1	0.7	50.6	1.6	360	43	44.1	0.7	12.8
12159CB_83	303	1.9	0.0573	0.0030	0.0533	0.0026	0.0067	0.0001	0.08	43.2	0.7	52.7	2.5	511	76	43.2	0.7	18.1
12159CB_84	1870	1.7	0.0652	0.0036	0.0543	0.0032	0.0060	0.0001	0.45	38.6	0.4	53.7	3.1	790	120	38.6	0.4	28.1
12159CB_86	342	0.8	0.0499	0.0016	0.0446	0.0012	0.0065	0.0001	0.01	41.5	0.7	44.3	1.2	310	76	41.5	0.7	6.4
12159CB_87	199	1.1	0.0553	0.0034	0.0472	0.0029	0.0061	0.0002	0.23	39.4	1.0	46.8	2.9	490	140	39.4	1.0	15.8
12159CB_88	533	0.8	0.0512	0.0016	0.0436	0.0013	0.0062	0.0001	0.16	39.8	0.6	43.3	1.3	275	49	39.8	0.6	8.1
12159CB_90	523	0.8	0.0530	0.0037	0.0449	0.0029	0.0061	0.0001	0.15	39.4	0.5	44.5	2.7	309	76	39.4	0.5	11.5
12159CB_91	287	1.6	0.0562	0.0025	0.0524	0.0026	0.0068	0.0001	0.26	43.6	0.8	51.8	2.5	456	60	43.6	0.8	15.9
12159CB_92	222	1.3	0.0559	0.0026	0.0502	0.0022	0.0066	0.0001	0.16	42.1	0.7	49.7	2.1	491	83	42.1	0.7	15.4
12159CB_93	265	1.5	0.0508	0.0015	0.0469	0.0014	0.0067	0.0001	0.02	42.9	0.7	46.5	1.3	275	39	42.9	0.7	7.8
12159CB_94	217	0.9	0.0516	0.0037	0.0495	0.0038	0.0068	0.0001	0.01	43.7	0.8	48.0	3.0	430	100	43.7	0.8	9.1
12159CB_95	440	0.8	0.0468	0.0014	0.0364	0.0009	0.0055	0.0001	0.09	35.7	0.6	36.3	0.9	145	35	35.7	0.6	1.7
12159CB_96	266	1.0	0.0501	0.0013	0.0411	0.0010	0.0059	0.0001	0.02	38.0	0.6	40.9	1.0	252	45	38.0	0.6	7.2
12159CB_97	516	1.3	0.0514	0.0017	0.0453	0.0015	0.0064	0.0001	0.29	41.3	0.4	45.0	1.4	274	51	41.3	0.4	8.3
12159CB_98	304	1.6	0.0503	0.0018	0.0456	0.0014	0.0066	0.0001	0.07	42.5	0.5	45.3	1.3	258	53	42.5	0.5	6.2
12159CB_99	1116	1.1	0.0612	0.0026	0.0524	0.0023	0.0061	0.0001	0.20	39.4	0.5	51.9	2.2	644	91	39.4	0.5	24.1
12159CB_100	696	1.0	0.0486	0.0013	0.0430	0.0010	0.0064	0.0001	0.42	41.0	0.5	42.7	1.0	159	39	41.0	0.5	4.1
12159CB_101	1650	1.9	0.0478	0.0007	0.0427	0.0007	0.0065	0.0001	0.30	41.6	0.4	42.5	0.7	102	17	41.6	0.4	2.0
12159CB_103	527	1.0	0.0483	0.0011	0.0419	0.0011	0.0062	0.0001	0.25	39.8	0.5	41.7	1.0	170	35	39.8	0.5	4.5
12159CB_104	800	1.7	0.0532	0.0031	0.0469	0.0029	0.0063	0.0001	0.25	40.4	0.9	46.4	2.8	390	120	40.4	0.9	13.0
12159CB_105	600	1.8	0.0508	0.0028	0.0462	0.0030	0.0066	0.0001	0.53	42.3	0.9	45.8	2.9	303	98	42.3	0.9	7.7
12159CB_106	251	0.8	0.0532	0.0023	0.0491	0.0022	0.0066	0.0001	0.19	42.5	0.9	48.7	2.1	402	52	42.5	0.9	12.7
12159CB_108	287	1.3	0.0517	0.0041	0.0466	0.0036	0.0065	0.0001	0.04	42.0	0.6	46.1	3.5	440	140	42.0	0.6	8.8
12159CB_109	234	1.3	0.0523	0.0020	0.0474	0.0017	0.0066	0.0001	0.16	42.1	0.8	47.0	1.6	346	64	42.1	0.8	10.5

12159CB_110	5400	1.5	0.0489	0.0004	0.0392	0.0005	0.0058	0.0001	0.49	37.2	0.4	39.0	0.5	148	16	37.2	0.4	4.6
12159CB_111	345	0.9	0.0512	0.0019	0.0460	0.0014	0.0066	0.0001	0.08	42.1	0.7	45.6	1.3	268	63	42.1	0.7	7.7
12159CB_112	194	1.2	0.0528	0.0036	0.0480	0.0033	0.0066	0.0001	0.03	42.3	0.9	47.6	3.1	450	100	42.3	0.9	11.2
12159CB_113	226	3.3	0.0513	0.0030	0.0471	0.0028	0.0066	0.0001	0.05	42.6	0.6	46.6	2.7	421	89	42.6	0.6	8.5
12159CB_116	157	0.8	0.0490	0.0022	0.0443	0.0019	0.0066	0.0001	0.11	42.2	0.8	43.9	1.9	304	63	42.2	0.8	3.8
12159CB_117	332	1.1	0.0482	0.0014	0.0435	0.0013	0.0065	0.0001	0.03	41.8	0.7	43.2	1.2	232	84	41.8	0.7	3.3
12159CB_118	258	2.0	0.0546	0.0029	0.0490	0.0025	0.0066	0.0001	0.28	42.3	0.7	48.5	2.4	499	94	42.3	0.7	12.7
12159CB_119	321	0.9	0.0548	0.0016	0.0498	0.0014	0.0065	0.0001	0.22	41.9	0.8	49.3	1.4	400	44	41.9	0.8	14.9
12159CB_121	297	1.3	0.0510	0.0019	0.0466	0.0016	0.0065	0.0001	0.00	42.0	0.6	46.2	1.6	353	45	42.0	0.6	9.0
12159CB_123	426	1.3	0.0515	0.0021	0.0462	0.0017	0.0065	0.0001	0.11	41.9	0.6	45.9	1.6	374	75	41.9	0.6	8.7
12159CB_124	351	1.0	0.0560	0.0036	0.0515	0.0035	0.0066	0.0001	0.06	42.5	0.8	51.0	3.3	680	150	42.5	0.8	16.6
12159CB_125	636	1.2	0.0491	0.0013	0.0429	0.0012	0.0064	0.0001	0.24	41.0	0.6	42.6	1.1	215	37	41.0	0.6	3.8
12159CB_126	481	1.5	0.0578	0.0012	0.0482	0.0009	0.0061	0.0001	0.23	39.0	0.5	47.8	0.9	517	31	39.0	0.5	18.5
12159CB_127	383	1.7	0.0499	0.0015	0.0438	0.0013	0.0063	0.0001	0.06	40.5	0.7	43.5	1.2	257	49	40.5	0.7	6.9
12159CB_128	401	1.3	0.0516	0.0017	0.0442	0.0015	0.0062	0.0001	0.11	39.6	0.6	43.8	1.5	342	56	39.6	0.6	9.7
12159CB_130	183	0.9	0.0486	0.0018	0.0450	0.0015	0.0066	0.0001	0.15	42.7	0.7	44.7	1.5	272	62	42.7	0.7	4.5
12159CB_131	58	1.1	0.0566	0.0053	0.0525	0.0043	0.0068	0.0002	0.12	43.4	1.5	51.9	4.2	560	130	43.4	1.5	16.4

Analysis	U (ppm)	U/Th	207Pb/ 206Pb	2σ error	207Pb/ 235U	2σ error	206Pb/ 238U	2σ error	err. corr.	206Pb/ 238U Age (Ma)	2σ error (Ma)	207Pb/ 235U Age (Ma)	2σ error (Ma)	207Pb/ 206Pb Age (Ma)	2σ error (Ma)	Best age (Ma)	2σ error (Ma)	Disc. (%)
NV12-162CB																		
12162CB_1	347	3.9	0.0484	0.0007	0.1173	0.0020	0.0175	0.0002	0.41	112.6	1.8	112.0	1.2	116	34	112.0	1.2	0.5
12162CB_2	535	2.1	0.0483	0.0005	0.1161	0.0016	0.0175	0.0002	0.60	111.5	1.4	111.9	1.1	110	25	111.9	1.1	0.4
12162CB_3	408	3.3	0.0482	0.0006	0.1109	0.0015	0.0168	0.0002	0.40	106.8	1.4	107.5	1.0	107	28	107.5	1.0	0.7
12162CB_4	386	3.3	0.0483	0.0008	0.1172	0.0023	0.0176	0.0002	0.52	112.5	2.1	112.7	1.4	112	36	112.7	1.4	0.2
12162CB_5	494	3.5	0.0481	0.0005	0.1106	0.0017	0.0169	0.0002	0.66	106.5	1.5	107.7	1.3	101	25	107.7	1.3	1.1
12162CB_6	481	2.5	0.0482	0.0007	0.1106	0.0022	0.0166	0.0003	0.58	106.4	2.0	106.0	1.7	107	31	106.0	1.7	0.4
12162CB_7	477	3.8	0.0483	0.0006	0.1144	0.0017	0.0173	0.0002	0.33	109.9	1.5	110.4	1.2	109	26	110.4	1.2	0.5
12162CB_8	759	2.8	0.0480	0.0004	0.1045	0.0017	0.0158	0.0002	0.81	100.9	1.6	100.8	1.6	100	20	100.8	1.6	0.1
12162CB_10	385	1.6	0.0488	0.0009	0.1305	0.0023	0.0194	0.0002	0.29	124.5	2.1	123.9	1.2	132	41	123.9	1.2	0.5
12162CB_11	454	2.8	0.0485	0.0007	0.1247	0.0020	0.0188	0.0003	0.53	119.3	1.8	120.0	1.6	124	31	120.0	1.6	0.6
12162CB_12	939	2.4	0.0482	0.0005	0.1190	0.0020	0.0178	0.0003	0.78	114.1	1.8	113.6	1.8	108	21	113.6	1.8	0.4
12162CB_13	609	1.8	0.0483	0.0004	0.1227	0.0019	0.0186	0.0002	0.78	117.5	1.7	118.9	1.4	115	21	118.9	1.4	1.2
12162CB_15	630	3.3	0.0482	0.0006	0.1165	0.0018	0.0176	0.0002	0.13	111.9	1.6	112.3	1.4	107	28	112.3	1.4	0.4
12162CB_16	685	2.5	0.0496	0.0008	0.1160	0.0022	0.0171	0.0002	0.52	111.4	2.0	109.1	1.5	173	35	109.1	1.5	2.1
12162CB_17	706	2.3	0.0484	0.0006	0.1221	0.0019	0.0184	0.0003	0.66	117.0	1.7	117.4	2.0	116	29	117.4	2.0	0.3
12162CB_18	608	2.1	0.0484	0.0005	0.1227	0.0013	0.0185	0.0002	0.63	117.5	1.2	118.3	1.1	115	23	118.3	1.1	0.7
12162CB_19	560	3.5	0.0484	0.0010	0.1160	0.0021	0.0175	0.0002	0.08	111.5	1.9	111.9	1.5	117	43	111.9	1.5	0.4
12162CB_20	419	3.4	0.0482	0.0007	0.1131	0.0018	0.0171	0.0002	0.09	108.8	1.6	109.3	1.2	107	31	109.3	1.2	0.5
12162CB_21	439	2.8	0.0489	0.0007	0.1207	0.0017	0.0180	0.0002	0.48	115.7	1.5	115.1	1.2	145	31	115.1	1.2	0.5
12162CB_22	360	4.1	0.0482	0.0009	0.1158	0.0024	0.0175	0.0003	0.48	111.2	2.2	112.1	1.6	108	42	112.1	1.6	0.8
12162CB_23	784	2.3	0.0484	0.0005	0.1196	0.0018	0.0178	0.0003	0.81	114.7	1.6	113.9	1.7	120	22	113.9	1.7	0.7
12162CB_24	508	3.2	0.0481	0.0006	0.1165	0.0017	0.0175	0.0002	0.14	111.8	1.5	112.0	1.4	106	27	112.0	1.4	0.2
12162CB_25	774	2.9	0.0483	0.0007	0.1147	0.0023	0.0172	0.0003	0.69	110.2	2.1	109.6	1.7	115	32	109.6	1.7	0.5
12162CB_26	276	4.9	0.0484	0.0007	0.1130	0.0017	0.0170	0.0002	0.30	108.6	1.6	108.3	1.0	116	31	108.3	1.0	0.3
12162CB_27	363	3.6	0.0490	0.0007	0.1246	0.0021	0.0183	0.0002	0.62	119.4	1.9	117.0	1.2	146	31	117.0	1.2	2.0
12162CB_28	360	2.1	0.0482	0.0006	0.1150	0.0017	0.0173	0.0002	0.48	110.5	1.6	110.4	1.3	111	29	110.4	1.3	0.1
12162CB_29	415	3.0	0.0493	0.0008	0.1162	0.0023	0.0172	0.0003	0.55	111.6	2.1	109.8	1.9	159	36	109.8	1.9	1.6
12162CB_30	793	1.9	0.0482	0.0005	0.1155	0.0015	0.0174	0.0003	0.69	110.9	1.4	111.3	1.7	108	24	111.3	1.7	0.4
12162CB_31	605	4.0	0.0481	0.0004	0.1125	0.0017	0.0169	0.0002	0.80	108.2	1.5	108.2	1.5	101	20	108.2	1.5	0.0
12162CB_32	596	3.8	0.0482	0.0005	0.1091	0.0018	0.0164	0.0002	0.70	105.2	1.6	104.8	1.3	106	24	104.8	1.3	0.4
12162CB_33	792	2.4	0.0487	0.0008	0.1057	0.0022	0.0157	0.0004	0.77	102.0	2.0	100.3	2.3	133	35	100.3	2.3	1.7
12162CB_34	543	2.7	0.0480	0.0005	0.1171	0.0014	0.0177	0.0002	0.62	112.6	1.3	113.1	1.2	96	24	113.1	1.2	0.4

12162CB_35	640	2.1	0.0483	0.0006	0.1174	0.0018	0.0176	0.0002	0.11	112.7	1.7	112.2	1.4	113	26	112.2	1.4	0.4
12162CB_36	304	0.8	0.0510	0.0018	0.0369	0.0011	0.0052	0.0001	0.11	36.8	1.1	33.5	0.5	130	34	33.5	0.5	9.0
12162CB_37	286	3.4	0.0487	0.0008	0.1372	0.0042	0.0204	0.0006	0.18	130.4	3.8	130.2	3.5	114	31	130.2	3.5	0.2
12162CB_38	309	3.1	0.0483	0.0007	0.1434	0.0024	0.0214	0.0003	0.38	136.5	2.1	136.2	1.8	79	20	136.2	1.8	0.2
12162CB_40	1060	1.8	0.0476	0.0004	0.1298	0.0020	0.0198	0.0003	0.81	124.1	1.8	126.2	1.8	114	30	126.2	1.8	1.7
12162CB_41	401	2.8	0.0483	0.0007	0.1333	0.0018	0.0199	0.0002	0.26	127.1	1.6	127.1	1.2	126	28	127.1	1.2	0.0
12162CB_42	423	2.1	0.0486	0.0006	0.1313	0.0018	0.0197	0.0002	0.48	125.3	1.6	125.5	1.2	115	23	125.5	1.2	0.2
12162CB_43	643	2.0	0.0484	0.0005	0.1285	0.0014	0.0193	0.0002	0.41	122.8	1.2	123.0	1.2	116	33	123.0	1.2	0.2
12162CB_44	391	2.8	0.0484	0.0007	0.1295	0.0019	0.0195	0.0002	0.05	123.6	1.7	124.2	1.3	95	29	124.2	1.3	0.5
12162CB_45	467	1.9	0.0479	0.0006	0.1242	0.0021	0.0188	0.0003	0.60	118.8	1.8	120.3	1.8	121	32	120.3	1.8	1.3
12162CB_46	632	2.1	0.0485	0.0007	0.1268	0.0025	0.0190	0.0004	0.01	121.2	2.2	121.4	2.3	94	24	121.4	2.3	0.2
12162CB_47	568	2.4	0.0480	0.0005	0.1246	0.0014	0.0188	0.0002	0.50	119.2	1.3	120.0	1.3	118	28	120.0	1.3	0.7
12162CB_48	658	3.0	0.0484	0.0006	0.1196	0.0020	0.0171	0.0002	0.33	114.7	1.8	109.4	1.4	155	34	109.4	1.4	4.6
12162CB_49	340	2.6	0.0492	0.0008	0.1248	0.0021	0.0182	0.0002	0.54	119.4	1.9	116.5	1.5	140	25	116.5	1.5	2.4
12162CB_50	833	1.7	0.0489	0.0005	0.1198	0.0017	0.0178	0.0002	0.68	114.8	1.5	113.8	1.3	108	26	113.8	1.3	0.9
12162CB_52	990	2.2	0.0482	0.0005	0.1173	0.0020	0.0177	0.0003	0.77	112.6	1.8	113.3	2.0	199	43	113.3	2.0	0.6
12162CB_53	484	3.0	0.0502	0.0010	0.1346	0.0024	0.0194	0.0002	0.27	128.2	2.2	124.0	1.5	97	26	124.0	1.5	3.3
12162CB_54	533	2.4	0.0480	0.0006	0.1224	0.0020	0.0187	0.0003	0.66	117.2	1.8	119.2	1.9	159	28	119.2	1.9	1.7
12162CB_55	690	3.6	0.0493	0.0006	0.1297	0.0026	0.0193	0.0004	0.78	123.8	2.4	123.1	2.3	203	32	123.1	2.3	0.6
12162CB_57	756	2.1	0.0502	0.0007	0.1220	0.0032	0.0178	0.0004	0.81	116.8	2.9	113.8	2.7	121	27	113.8	2.7	2.6
12162CB_58	683	2.1	0.0486	0.0006	0.1252	0.0023	0.0187	0.0003	0.75	120.0	2.0	119.5	1.9	144	31	119.5	1.9	0.4
12162CB_59	695	1.6	0.0490	0.0007	0.1211	0.0022	0.0179	0.0003	0.30	116.0	2.0	114.4	1.6	158	25	114.4	1.6	1.4
12162CB_60	678	2.1	0.0493	0.0005	0.1212	0.0023	0.0178	0.0003	0.79	116.1	2.1	113.8	1.9	114	44	113.8	1.9	2.0
12162CB_62	713	1.6	0.0483	0.0010	0.1129	0.0017	0.0171	0.0003	0.16	108.6	1.6	109.1	1.6	249	27	109.1	1.6	0.5
12162CB_63	766	1.7	0.0513	0.0006	0.1248	0.0022	0.0178	0.0003	0.46	119.4	2.0	113.9	1.6	145	34	113.9	1.6	4.6
12162CB_64	477	1.3	0.0489	0.0007	0.1276	0.0034	0.0183	0.0004	0.77	121.8	3.1	116.6	2.7	96	25	116.6	2.7	4.3
12162CB_65	552	2.0	0.0479	0.0005	0.1247	0.0014	0.0191	0.0002	0.35	119.3	1.3	121.6	1.0	123	30	121.6	1.0	1.9
12162CB_66	479	2.6	0.0485	0.0006	0.1267	0.0019	0.0193	0.0003	0.62	121.1	1.7	123.1	1.6	190	22	123.1	1.6	1.7
12162CB_67	369	1.2	0.0500	0.0005	0.1925	0.0025	0.0282	0.0003	0.70	178.7	2.1	179.0	1.9	233	38	179.0	1.9	0.2
12162CB_68	608	2.1	0.0510	0.0009	0.1212	0.0022	0.0175	0.0002	0.51	116.1	2.0	112.1	1.4	128	19	112.1	1.4	3.4
12162CB_69	2630	6.4	0.0486	0.0004	0.1246	0.0018	0.0179	0.0002	0.80	119.3	1.6	114.3	1.0	112	30	114.3	1.0	4.2
12162CB_70	497	2.7	0.0483	0.0006	0.1261	0.0021	0.0190	0.0003	0.66	120.6	1.9	121.2	1.7	159	22	121.2	1.7	0.5
12162CB_71	3430	1.9	0.0493	0.0005	0.1158	0.0017	0.0170	0.0002	0.66	111.3	1.5	108.7	1.4	103	37	108.7	1.4	2.3
12162CB_72	691	2.3	0.0481	0.0008	0.1129	0.0019	0.0171	0.0002	0.40	108.6	1.7	109.4	1.0	108	22	109.4	1.0	0.7
12162CB_73	651	2.7	0.0482	0.0005	0.1094	0.0013	0.0166	0.0002	0.57	105.4	1.2	105.8	1.1	146	35	105.8	1.1	0.4

12162CB_74	622	2.6	0.0490	0.0007	0.1170	0.0023	0.0173	0.0002	0.62	112.3	2.1	110.4	1.3	107	28	110.4	1.3	1.7
12162CB_76	419	2.6	0.0483	0.0006	0.1218	0.0020	0.0182	0.0003	0.62	116.6	1.8	116.3	1.6	120	27	116.3	1.6	0.3
12162CB_77	474	1.9	0.0484	0.0006	0.1270	0.0018	0.0189	0.0002	0.40	121.4	1.6	120.8	1.4	109	26	120.8	1.4	0.5
12162CB_78	853	1.9	0.0482	0.0006	0.1177	0.0019	0.0177	0.0002	0.68	113.0	1.7	113.2	1.3	112	25	113.2	1.3	0.2
12162CB_79	623	2.4	0.0483	0.0005	0.1202	0.0016	0.0181	0.0002	0.49	115.2	1.5	115.4	1.1	214	26	115.4	1.1	0.2
12162CB_80	670	2.0	0.0505	0.0006	0.1337	0.0016	0.0191	0.0002	0.51	127.4	1.5	121.9	1.3	238	37	121.9	1.3	4.3
12162CB_81	563	1.8	0.0509	0.0008	0.1330	0.0022	0.0188	0.0003	0.45	126.8	2.0	120.1	1.6	117	27	120.1	1.6	5.3
12162CB_83	549	2.4	0.0484	0.0006	0.1215	0.0024	0.0183	0.0002	0.06	116.4	2.2	117.0	1.5	115	29	117.0	1.5	0.5
12162CB_84	597	2.3	0.0483	0.0006	0.1183	0.0021	0.0178	0.0003	0.72	113.5	1.9	113.9	1.7	152	29	113.9	1.7	0.4
12162CB_85	600	2.5	0.0492	0.0006	0.1190	0.0019	0.0175	0.0002	0.15	114.1	1.7	111.9	1.4	379	43	111.9	1.4	1.9
12162CB_86	436	2.7	0.0541	0.0010	0.1345	0.0029	0.0181	0.0003	0.49	128.1	2.6	115.3	1.6	117	25	115.3	1.6	10.0
12162CB_87	610	2.2	0.0485	0.0005	0.1216	0.0018	0.0182	0.0002	0.69	116.5	1.6	116.5	1.5	120	41	116.5	1.5	0.0
12162CB_88	444	4.0	0.0484	0.0009	0.1223	0.0023	0.0183	0.0003	0.43	117.5	2.2	116.7	2.1	117	27	116.7	2.1	0.7
12162CB_89	473	3.9	0.0484	0.0006	0.1269	0.0022	0.0192	0.0003	0.70	121.3	2.0	122.3	1.8	108	35	122.3	1.8	0.8
12162CB_90	451	2.7	0.0482	0.0008	0.1186	0.0018	0.0179	0.0002	0.39	113.8	1.6	114.5	1.5	112	33	114.5	1.5	0.6
12162CB_91	910	2.1	0.0483	0.0007	0.1182	0.0023	0.0178	0.0003	0.68	113.4	2.1	113.5	2.0	233	23	113.5	2.0	0.1
12162CB_92	684	1.9	0.0508	0.0005	0.1245	0.0016	0.0179	0.0002	0.50	119.1	1.4	114.0	0.9	195	25	114.0	0.9	4.3
12162CB_94	462	2.0	0.0592	0.0013	0.0545	0.0012	0.0067	0.0001	0.27	53.8	1.2	43.1	0.7	108	22	43.1	0.7	19.8
12162CB_95	2040	3.7	0.0500	0.0006	0.1107	0.0015	0.0162	0.0002	0.56	106.6	1.3	103.5	1.2	138	23	103.5	1.2	2.9
12162CB_96	1038	2.1	0.0482	0.0005	0.1094	0.0011	0.0164	0.0002	0.52	105.4	1.0	104.9	1.1	117	31	104.9	1.1	0.5
12162CB_97	1049	1.7	0.0488	0.0005	0.1168	0.0014	0.0174	0.0002	0.51	112.1	1.2	110.9	1.1	199	27	110.9	1.1	1.1
12162CB_98	1003	2.0	0.0484	0.0007	0.1122	0.0016	0.0161	0.0002	0.34	107.9	1.5	103.1	1.3	132	50	103.1	1.3	4.4
12162CB_99	1114	1.9	0.0502	0.0006	0.1176	0.0014	0.0171	0.0002	0.58	112.9	1.3	109.2	1.4	122	26	109.2	1.4	3.3
12162CB_100	495	4.3	0.0487	0.0011	0.1160	0.0028	0.0174	0.0003	0.12	111.4	2.5	111.1	1.6	121	31	111.1	1.6	0.3
12162CB_101	763	1.7	0.0484	0.0005	0.1089	0.0013	0.0163	0.0002	0.54	104.9	1.2	104.2	1.2	237	34	104.2	1.2	0.7
12162CB_102	826	1.9	0.0485	0.0007	0.1145	0.0014	0.0172	0.0002	0.45	110.0	1.3	109.8	1.3	117	27	109.8	1.3	0.2
12162CB_103	872	2.2	0.0510	0.0008	0.1261	0.0024	0.0178	0.0002	0.64	120.6	2.1	113.7	1.4	163	34	113.7	1.4	5.7
12162CB_104	988	1.9	0.0499	0.0012	0.0369	0.0008	0.0054	0.0001	0.42	36.8	0.8	34.7	0.6	108	25	34.7	0.6	5.7
12162CB_105	544	2.3	0.0484	0.0006	0.1207	0.0021	0.0182	0.0002	0.69	115.7	1.9	116.3	1.3	138	43	116.3	1.3	0.5
12162CB_106	867	2.0	0.0494	0.0007	0.1227	0.0019	0.0172	0.0002	0.22	117.5	1.8	110.0	1.5	127	27	110.0	1.5	6.4
12162CB_107	733	2.0	0.0482	0.0005	0.1153	0.0019	0.0173	0.0003	0.77	110.8	1.7	110.8	1.8	241	27	110.8	1.8	0.0
12162CB_108	676	1.6	0.0489	0.0010	0.1198	0.0020	0.0171	0.0002	0.04	114.9	1.8	109.0	1.0	133	25	109.0	1.0	5.1
12162CB_109	685	1.9	0.0486	0.0006	0.1169	0.0014	0.0173	0.0002	0.46	112.3	1.3	110.8	1.0	118	28	110.8	1.0	1.3
12162CB_110	796	1.3	0.0510	0.0006	0.1221	0.0022	0.0174	0.0002	0.72	116.9	2.0	111.4	1.5	309	51	111.4	1.5	4.7
12162CB_111	549	2.1	0.0487	0.0005	0.1235	0.0016	0.0184	0.0002	0.54	118.4	1.4	117.4	1.3	115	34	117.4	1.3	0.8

12162CB_112	543	2.1	0.0484	0.0006	0.1211	0.0017	0.0181	0.0002	0.52	116.1	1.5	115.4	1.4	117	27	115.4	1.4	0.6
12162CB_113	529	2.0	0.0528	0.0013	0.1339	0.0034	0.0184	0.0003	0.37	127.5	3.1	117.6	2.0	109	26	117.6	2.0	7.8
12162CB_115	343	1.1	0.0525	0.0013	0.0504	0.0012	0.0067	0.0001	0.37	49.9	1.2	42.8	0.6	202	55	42.8	0.6	14.3
12162CB_116	594	2.3	0.0483	0.0007	0.1171	0.0021	0.0175	0.0003	0.67	112.4	1.9	112.1	2.0	119	28	112.1	2.0	0.3
12162CB_117	474	2.4	0.0484	0.0006	0.1201	0.0018	0.0179	0.0002	0.60	115.1	1.6	114.4	1.3	174	29	114.4	1.3	0.6
12162CB_118	820	1.8	0.0482	0.0006	0.1216	0.0023	0.0183	0.0003	0.78	116.5	2.0	117.1	2.1	114	23	117.1	2.1	0.5
12162CB_119	1110	4.5	0.0502	0.0012	0.1137	0.0040	0.0165	0.0005	0.76	109.3	3.7	105.5	3.3	78	30	105.5	3.3	3.5
12162CB_120	1155	1.7	0.0485	0.0006	0.1167	0.0015	0.0176	0.0002	0.65	112.1	1.3	112.6	1.3	128	39	112.6	1.3	0.4
12162CB_121	999	1.7	0.0495	0.0006	0.1229	0.0024	0.0179	0.0004	0.77	117.6	2.2	114.6	2.2	106	31	114.6	2.2	2.6
12162CB_122	1029	1.4	0.0483	0.0005	0.1156	0.0015	0.0174	0.0002	0.71	111.0	1.4	111.4	1.2	203	34	111.4	1.2	0.4
12162CB_123	322	2.2	0.0482	0.0013	0.0351	0.0008	0.0052	0.0001	0.16	35.0	0.8	33.6	0.5	116	36	33.6	0.5	4.0
12162CB_124	740	1.9	0.0476	0.0006	0.1145	0.0016	0.0173	0.0002	0.43	110.1	1.5	110.6	1.4	117	38	110.6	1.4	0.5
12162CB_125	1265	11.0	0.0486	0.0008	0.1084	0.0013	0.0160	0.0002	0.40	104.5	1.2	102.3	1.2	230	76	102.3	1.2	2.1
12162CB_126	532	1.8	0.0482	0.0007	0.1262	0.0018	0.0189	0.0002	0.46	120.7	1.6	120.7	1.2	300	130	120.7	1.2	0.0
12162CB_127	1270	3.3	0.0503	0.0008	0.1184	0.0023	0.0171	0.0003	0.68	113.6	2.1	109.3	2.2	114	58	109.3	2.2	3.8
12162CB_129	502	2.4	0.0484	0.0008	0.1249	0.0025	0.0187	0.0003	0.63	119.5	2.3	119.2	1.7	294	54	119.2	1.7	0.3
12162CB_130	481	2.5	0.0484	0.0008	0.1268	0.0025	0.0189	0.0004	0.61	121.2	2.3	120.4	2.3	184	51	120.4	2.3	0.7

Analysis	U (ppm)	U/Th	207Pb/ 206Pb	2σ error	207Pb/ 235U	2σ error	206Pb/ 238U	2σ error	err. corr.	206Pb/ 238U Age (Ma)	2σ error (Ma)	207Pb/ 235U Age (Ma)	2σ error (Ma)	207Pb/ 206Pb Age (Ma)	2σ error (Ma)	Best age (Ma)	2σ error (Ma)	Disc. (%)
NV12-169CB																		
12169CB_01	199	2.1	0.0482	0.0018	0.0410	0.0015	0.0062	0.0001	0.12	39.6	0.7	41.0	1.5	215	51	39.6	0.7	3.3
12169CB_02	217	1.2	0.0519	0.0024	0.0467	0.0023	0.0066	0.0001	0.39	42.2	0.8	46.3	2.3	330	62	42.2	0.8	8.8
12169CB_03	370	1.0	0.0486	0.0020	0.0413	0.0027	0.0060	0.0001	0.57	38.4	0.8	41.0	2.6	233	66	38.4	0.8	6.4
12169CB_04	119	1.6	0.1615	0.0010	9.6930	0.0720	0.4335	0.0027	0.67	2321.0	12.0	2407.0	6.6	2472	6	2471.9	6.0	6.1
12169CB_05	244	1.6	0.0456	0.0019	0.0394	0.0016	0.0063	0.0001	0.16	40.4	0.7	39.2	1.5	194	41	40.4	0.7	3.1
12169CB_06	384	1.0	0.0471	0.0014	0.0412	0.0011	0.0063	0.0001	0.00	40.6	0.5	41.0	1.1	168	26	40.6	0.5	1.0
12169CB_07	621	0.9	0.0475	0.0009	0.0402	0.0008	0.0061	0.0001	0.28	39.3	0.5	40.0	0.8	164	27	39.3	0.5	1.8
12169CB_08	341	1.1	0.0549	0.0035	0.0509	0.0036	0.0067	0.0001	0.03	43.1	0.7	50.3	3.4	440	100	43.1	0.7	14.3
12169CB_09	412	1.1	0.0473	0.0013	0.0416	0.0011	0.0065	0.0001	0.28	41.5	0.6	41.4	1.1	158	29	41.5	0.6	0.2
12169CB_10	137	2.2	0.0484	0.0029	0.0406	0.0022	0.0061	0.0001	0.06	39.2	0.8	40.4	2.1	309	69	39.2	0.8	3.0
12169CB_11	281	1.1	0.0486	0.0016	0.0452	0.0013	0.0068	0.0001	0.06	43.9	0.6	44.9	1.3	227	39	43.9	0.6	2.3
12169CB_13	1372	5.1	0.0481	0.0008	0.0420	0.0006	0.0064	0.0001	0.37	41.2	0.5	41.8	0.6	114	18	41.2	0.5	1.4
12169CB_16	638	0.5	0.0541	0.0021	0.0483	0.0016	0.0065	0.0001	0.36	41.6	0.6	47.8	1.6	392	65	41.6	0.6	13.0
12169CB_17	542	1.1	0.0494	0.0012	0.0431	0.0008	0.0064	0.0001	0.12	40.9	0.7	42.8	0.8	162	25	40.9	0.7	4.6
12169CB_18	629	2.9	0.0475	0.0010	0.0412	0.0012	0.0064	0.0002	0.67	41.0	1.0	41.0	1.1	120	20	41.0	1.0	0.0
12169CB_19	297	1.4	0.0493	0.0018	0.0420	0.0013	0.0063	0.0001	0.16	40.3	0.6	41.8	1.3	280	41	40.3	0.6	3.6
12169CB_20	270	1.8	0.0495	0.0019	0.0428	0.0015	0.0063	0.0001	0.19	40.7	0.6	42.5	1.5	321	65	40.7	0.6	4.3
12169CB_21	313	40.6	0.0485	0.0017	0.0423	0.0013	0.0064	0.0001	0.15	41.2	0.7	42.0	1.3	208	40	41.2	0.7	1.8
12169CB_22	512	1.7	0.0523	0.0019	0.0421	0.0011	0.0059	0.0001	0.33	37.8	0.8	41.9	1.1	333	48	37.8	0.8	9.8
12169CB_23	218	1.6	0.0495	0.0017	0.0429	0.0013	0.0063	0.0001	0.11	40.6	0.7	42.6	1.3	241	37	40.6	0.7	4.8
12169CB_24	222	1.7	0.0485	0.0019	0.0417	0.0016	0.0063	0.0001	0.18	40.4	0.7	41.4	1.6	226	41	40.4	0.7	2.3
12169CB_25	2990	3.8	0.0499	0.0009	0.0425	0.0009	0.0062	0.0001	0.35	39.8	0.3	42.3	0.9	218	35	39.8	0.3	5.9
12169CB_26	458	1.0	0.0471	0.0012	0.0405	0.0009	0.0063	0.0001	0.01	40.3	0.5	40.3	0.9	131	26	40.3	0.5	0.0
12169CB_27	100	0.8	0.0537	0.0048	0.0451	0.0035	0.0063	0.0002	0.08	40.4	1.0	44.7	3.4	520	110	40.4	1.0	9.6
12169CB_28	208	2.5	0.0463	0.0018	0.0402	0.0015	0.0062	0.0001	0.15	39.6	0.7	40.0	1.4	184	34	39.6	0.7	1.1
12169CB_29	250	1.6	0.0638	0.0042	0.0570	0.0035	0.0066	0.0002	0.16	42.3	1.4	56.3	3.4	768	90	42.3	1.4	24.9
12169CB_30	1780	3.4	0.0478	0.0006	0.0413	0.0006	0.0063	0.0001	0.40	40.6	0.4	41.1	0.6	117	18	40.6	0.4	1.4
12169CB_31	228	1.3	0.0503	0.0023	0.0452	0.0019	0.0064	0.0001	0.02	41.4	0.8	44.8	1.9	424	67	41.4	0.8	7.6
12169CB_32	292	2.0	0.0472	0.0016	0.0427	0.0014	0.0066	0.0001	0.07	42.1	0.8	42.5	1.3	192	31	42.1	0.8	1.0
12169CB_33	246	2.0	0.0468	0.0017	0.0395	0.0012	0.0062	0.0001	0.02	39.8	0.7	39.3	1.2	181	41	39.8	0.7	1.3
12169CB_34	177	1.5	0.0517	0.0032	0.0441	0.0031	0.0061	0.0001	0.03	39.3	0.7	43.7	2.9	379	70	39.3	0.7	10.0

12169CB_35	274	1.4	0.0482	0.0015	0.0426	0.0012	0.0064	0.0001	0.11	41.1	0.7	42.3	1.2	201	29	41.1	0.7	2.8
12169CB_36	198	0.9	0.0528	0.0028	0.0458	0.0024	0.0063	0.0001	0.19	40.2	0.8	45.4	2.3	430	70	40.2	0.8	11.4
12169CB_37	258	1.2	0.0511	0.0028	0.0467	0.0029	0.0065	0.0002	0.33	42.0	1.6	46.3	2.8	291	64	42.0	1.6	9.3
12169CB_38	701	1.0	0.0490	0.0011	0.0443	0.0009	0.0065	0.0001	0.08	41.8	0.5	44.0	0.9	218	31	41.8	0.5	5.0
12169CB_39	760	4.4	0.0477	0.0010	0.0420	0.0007	0.0064	0.0001	0.05	41.3	0.5	41.8	0.7	122	19	41.3	0.5	1.3
12169CB_40	489	1.4	0.0535	0.0020	0.0455	0.0019	0.0063	0.0001	0.19	40.3	0.9	45.1	1.8	322	53	40.3	0.9	10.6
12169CB_41	207	1.7	0.0485	0.0017	0.0429	0.0016	0.0063	0.0001	0.05	40.7	0.7	42.6	1.5	223	34	40.7	0.7	4.4
12169CB_42	373	1.3	0.0547	0.0027	0.0472	0.0027	0.0064	0.0001	0.32	40.8	0.9	46.8	2.6	404	94	40.8	0.9	12.8
12169CB_43	442	1.2	0.0476	0.0014	0.0406	0.0011	0.0062	0.0001	0.07	39.8	0.5	40.4	1.1	174	34	39.8	0.5	1.5
12169CB_44	556	1.3	0.0511	0.0015	0.0424	0.0014	0.0060	0.0001	0.26	38.5	0.9	42.1	1.3	252	43	38.5	0.9	8.7
12169CB_45	298	0.7	0.0516	0.0024	0.0438	0.0018	0.0062	0.0001	0.20	39.7	0.8	43.5	1.7	317	59	39.7	0.8	8.9
12169CB_46	323	1.3	0.0472	0.0014	0.0426	0.0012	0.0065	0.0001	0.13	41.8	0.5	42.3	1.1	163	31	41.8	0.5	1.1
12169CB_47	142	2.0	0.0508	0.0026	0.0460	0.0021	0.0065	0.0002	0.02	41.8	1.1	45.6	2.1	322	66	41.8	1.1	8.3
12169CB_48	500	1.4	0.0493	0.0010	0.0439	0.0010	0.0065	0.0001	0.36	41.5	0.5	43.6	1.0	164	26	41.5	0.5	4.7
12169CB_49	3518	3.6	0.0467	0.0004	0.0404	0.0004	0.0062	0.0000	0.49	39.9	0.3	40.2	0.4	65	10	39.9	0.3	0.6
12169CB_50	661	1.0	0.0491	0.0010	0.0394	0.0008	0.0058	0.0001	0.27	37.1	0.5	39.2	0.8	185	26	37.1	0.5	5.5
12169CB_51	1240	1.9	0.0510	0.0017	0.0447	0.0014	0.0063	0.0001	0.14	40.6	0.6	44.4	1.4	263	58	40.6	0.6	8.7
12169CB_52	370	1.3	0.0512	0.0021	0.0421	0.0016	0.0059	0.0001	0.14	38.1	0.7	41.8	1.6	287	53	38.1	0.7	8.9
12169CB_53	575	1.2	0.0475	0.0012	0.0406	0.0010	0.0062	0.0001	0.16	40.0	0.5	40.4	1.0	159	31	40.0	0.5	0.9
12169CB_55	147	1.0	0.0479	0.0021	0.0418	0.0017	0.0064	0.0001	0.16	40.8	0.8	41.5	1.7	239	45	40.8	0.8	1.8
12169CB_56	403	1.3	0.0496	0.0014	0.0434	0.0011	0.0063	0.0001	0.09	40.6	0.5	43.2	1.1	222	38	40.6	0.5	6.1
12169CB_57	247	1.9	0.0482	0.0021	0.0413	0.0016	0.0062	0.0002	0.12	39.7	1.0	41.0	1.5	208	40	39.7	1.0	3.1
12169CB_58	1010	1.1	0.0503	0.0012	0.0441	0.0010	0.0063	0.0001	0.29	40.6	0.5	43.8	1.0	242	37	40.6	0.5	7.2
12169CB_59	585	1.3	0.0496	0.0014	0.0444	0.0010	0.0065	0.0001	0.19	41.5	0.5	44.1	1.0	203	34	41.5	0.5	6.0
12169CB_60	763	0.9	0.0487	0.0010	0.0419	0.0009	0.0062	0.0001	0.19	39.6	0.4	41.7	0.9	181	31	39.6	0.4	5.1
12169CB_61	366	2.1	0.0463	0.0014	0.0485	0.0013	0.0076	0.0001	0.11	48.7	0.6	48.1	1.2	170	35	48.7	0.6	1.3
12169CB_62	434	1.2	0.0480	0.0012	0.0404	0.0010	0.0062	0.0001	0.10	39.6	0.5	40.2	1.0	133	24	39.6	0.5	1.5
12169CB_63	158	2.3	0.0492	0.0023	0.0427	0.0018	0.0063	0.0001	0.03	40.4	0.8	42.5	1.7	239	48	40.4	0.8	4.9
12169CB_64	359	1.2	0.0510	0.0017	0.0458	0.0015	0.0065	0.0001	0.18	42.0	0.6	45.7	1.5	292	48	42.0	0.6	8.0
12169CB_65	191	1.0	0.0472	0.0021	0.0409	0.0017	0.0063	0.0001	0.06	40.3	0.7	40.7	1.6	234	42	40.3	0.7	0.9
12169CB_66	199	1.0	0.0520	0.0018	0.0523	0.0016	0.0073	0.0001	0.25	46.6	0.8	51.7	1.6	306	43	46.6	0.8	9.8
12169CB_67	524	1.8	0.0493	0.0014	0.0445	0.0013	0.0066	0.0001	0.42	42.5	0.5	44.2	1.3	221	41	42.5	0.5	4.0
12169CB_68	1561	0.8	0.0480	0.0008	0.0359	0.0006	0.0054	0.0001	0.33	34.9	0.4	35.8	0.6	112	17	34.9	0.4	2.5
12169CB_69	226	1.0	0.0516	0.0028	0.0449	0.0025	0.0064	0.0002	0.74	40.9	0.9	44.5	2.4	362	69	40.9	0.9	8.2
12169CB_71	546	1.1	0.0518	0.0014	0.0471	0.0013	0.0066	0.0001	0.43	42.7	0.6	46.7	1.3	258	33	42.7	0.6	8.5

12169CB_72	769	0.8	0.0483	0.0012	0.0454	0.0009	0.0068	0.0001	0.17	43.9	0.7	45.2	0.9	184	32	43.9	0.7	2.7
12169CB_73	347	1.1	0.0496	0.0015	0.0452	0.0014	0.0066	0.0001	0.11	42.1	0.7	44.9	1.3	235	42	42.1	0.7	6.3
12169CB_74	1005	2.4	0.0467	0.0009	0.0405	0.0007	0.0063	0.0001	0.10	40.6	0.5	40.3	0.7	115	23	40.6	0.5	0.7
12169CB_75	312	2.0	0.0491	0.0020	0.0436	0.0017	0.0065	0.0002	0.25	41.5	1.0	43.3	1.7	229	47	41.5	1.0	4.3
12169CB_76	336	1.5	0.0508	0.0023	0.0453	0.0023	0.0064	0.0001	0.17	41.1	0.7	44.9	2.2	400	110	41.1	0.7	8.6
12169CB_77	599	1.3	0.0493	0.0022	0.0423	0.0018	0.0062	0.0001	0.03	40.2	0.5	42.0	1.7	190	44	40.2	0.5	4.4
12169CB_78	456	1.0	0.0473	0.0014	0.0414	0.0011	0.0064	0.0001	0.26	41.1	0.6	41.2	1.1	159	30	41.1	0.6	0.1
12169CB_79	304	1.6	0.0501	0.0039	0.0433	0.0030	0.0063	0.0002	0.10	40.3	1.5	43.0	2.9	350	120	40.3	1.5	6.3
12169CB_80	498	1.9	0.0478	0.0012	0.0416	0.0009	0.0064	0.0001	0.14	40.8	0.6	41.4	0.9	117	25	40.8	0.6	1.3
12169CB_82	118	0.7	0.0510	0.0028	0.0439	0.0020	0.0063	0.0002	0.14	40.5	1.1	43.6	2.0	361	63	40.5	1.1	7.1
12169CB_83	278	2.2	0.0476	0.0016	0.0433	0.0013	0.0065	0.0001	0.17	41.7	0.7	43.1	1.3	182	41	41.7	0.7	3.3
12169CB_84	94	0.8	0.0515	0.0036	0.0448	0.0027	0.0063	0.0002	0.07	40.3	1.2	44.5	2.6	379	59	40.3	1.2	9.4
12169CB_85	139	2.2	0.0477	0.0025	0.0418	0.0021	0.0063	0.0002	0.01	40.7	1.0	41.8	2.1	320	63	40.7	1.0	2.6
12169CB_86	211	2.4	0.0457	0.0017	0.0393	0.0014	0.0063	0.0001	0.11	40.4	0.8	39.1	1.3	218	41	40.4	0.8	3.4
12169CB_87	987	2.6	0.0506	0.0016	0.0431	0.0012	0.0062	0.0001	0.02	39.6	0.5	42.8	1.2	260	39	39.6	0.5	7.5
12169CB_88	143	1.7	0.0469	0.0031	0.0395	0.0024	0.0063	0.0001	0.00	40.4	0.8	39.3	2.3	360	100	40.4	0.8	2.7
12169CB_89	523	1.0	0.0464	0.0013	0.0412	0.0010	0.0065	0.0001	0.02	41.6	0.6	41.0	1.0	169	33	41.6	0.6	1.5
12169CB_90	486	1.6	0.0518	0.0028	0.0456	0.0023	0.0064	0.0001	0.03	41.4	0.5	45.2	2.2	296	55	41.4	0.5	8.4
12169CB_91	434	1.3	0.0467	0.0013	0.0415	0.0010	0.0065	0.0001	0.12	41.7	0.5	41.3	1.0	124	25	41.7	0.5	0.9
12169CB_92	294	1.1	0.0482	0.0019	0.0463	0.0017	0.0071	0.0001	0.07	45.3	0.9	45.9	1.7	204	50	45.3	0.9	1.2
12169CB_93	430	1.2	0.0484	0.0022	0.0439	0.0017	0.0066	0.0001	0.06	42.4	0.9	43.6	1.6	225	66	42.4	0.9	2.7
12169CB_94	369	1.2	0.0487	0.0016	0.0437	0.0013	0.0065	0.0001	0.04	41.6	0.6	43.4	1.2	276	42	41.6	0.6	4.2
12169CB_95	447	1.1	0.0485	0.0013	0.0425	0.0011	0.0064	0.0001	0.17	40.9	0.5	42.3	1.0	198	27	40.9	0.5	3.4
12169CB_97	743	0.7	0.0514	0.0014	0.0410	0.0011	0.0058	0.0001	0.31	37.4	0.7	40.8	1.1	250	37	37.4	0.7	8.3
12169CB_98	404	0.7	0.0482	0.0016	0.0426	0.0012	0.0064	0.0001	0.15	40.9	0.7	42.3	1.2	221	33	40.9	0.7	3.2
12169CB_101	414	1.5	0.0496	0.0015	0.0398	0.0011	0.0058	0.0001	0.14	37.5	0.6	39.6	1.1	201	35	37.5	0.6	5.4
12169CB_102	491	1.9	0.0481	0.0011	0.0429	0.0009	0.0064	0.0001	0.14	41.3	0.5	42.7	0.8	176	28	41.3	0.5	3.2
12169CB_104	558	3.0	0.0540	0.0022	0.0466	0.0020	0.0063	0.0002	0.44	40.6	1.3	46.2	1.9	385	69	40.6	1.3	12.1
12169CB_105	466	1.1	0.0510	0.0017	0.0443	0.0014	0.0063	0.0001	0.47	40.4	0.6	44.0	1.3	258	51	40.4	0.6	8.2
12169CB_107	767	0.9	0.0480	0.0009	0.0405	0.0008	0.0061	0.0001	0.33	39.5	0.5	40.3	0.8	126	21	39.5	0.5	1.9
12169CB_108	793	2.0	0.0493	0.0011	0.0439	0.0009	0.0065	0.0001	0.16	41.7	0.5	43.6	0.9	176	23	41.7	0.5	4.3
12169CB_109	502	1.1	0.0471	0.0011	0.0417	0.0009	0.0064	0.0001	0.24	41.2	0.6	41.5	0.9	137	28	41.2	0.6	0.8
12169CB_110	480	0.5	0.0486	0.0012	0.0446	0.0010	0.0067	0.0001	0.22	43.0	0.7	44.3	1.0	192	31	43.0	0.7	3.0
12169CB_112	495	1.6	0.0498	0.0019	0.0450	0.0017	0.0066	0.0001	0.07	42.1	0.7	44.7	1.6	230	46	42.1	0.7	5.9
12169CB_113	750	2.0	0.0466	0.0009	0.0364	0.0008	0.0056	0.0001	0.32	36.1	0.5	36.3	0.8	89	19	36.1	0.5	0.7

12169CB_115	635	1.3	0.0481	0.0013	0.0390	0.0010	0.0059	0.0001	0.06	38.0	0.5	38.8	1.0	160	29	38.0	0.5	2.1
12169CB_116	296	1.4	0.0482	0.0021	0.0441	0.0019	0.0067	0.0001	0.23	42.8	0.8	43.8	1.8	248	57	42.8	0.8	2.4
12169CB_117	499	1.0	0.0470	0.0014	0.0407	0.0011	0.0062	0.0001	0.05	40.1	0.5	40.5	1.0	174	33	40.1	0.5	1.0
12169CB_118	589	1.8	0.0471	0.0012	0.0407	0.0009	0.0063	0.0001	0.16	40.7	0.5	40.5	0.9	135	28	40.7	0.5	0.6
12169CB_119	230	1.3	0.0484	0.0018	0.0414	0.0014	0.0062	0.0001	0.08	39.7	0.7	41.2	1.3	260	37	39.7	0.7	3.6
12169CB_120	499	1.2	0.0465	0.0012	0.0397	0.0009	0.0062	0.0001	0.28	39.6	0.5	39.5	0.9	130	32	39.6	0.5	0.4
12169CB_121	329	1.4	0.0485	0.0015	0.0445	0.0013	0.0066	0.0001	0.24	42.5	0.8	44.2	1.3	187	33	42.5	0.8	4.0
12169CB_122	446	1.2	0.0554	0.0030	0.0488	0.0029	0.0065	0.0001	0.20	41.5	0.9	48.4	2.8	460	83	41.5	0.9	14.3
12169CB_123	424	1.2	0.0524	0.0018	0.0436	0.0016	0.0061	0.0001	0.34	39.5	0.8	43.3	1.6	336	47	39.5	0.8	8.8
12169CB_124	420	1.5	0.0481	0.0015	0.0420	0.0013	0.0063	0.0001	0.17	40.7	0.7	41.8	1.3	294	54	40.7	0.7	2.5
12169CB_125	128	1.7	0.0483	0.0044	0.0423	0.0046	0.0062	0.0002	0.45	39.6	1.5	42.0	4.4	390	110	39.6	1.5	5.7
12169CB_126	727	1.7	0.0514	0.0020	0.0404	0.0013	0.0057	0.0001	0.17	36.9	0.8	40.2	1.3	277	55	36.9	0.8	8.2
12169CB_128	2836	4.8	0.0474	0.0006	0.0396	0.0005	0.0061	0.0001	0.44	39.0	0.4	39.5	0.5	100	15	39.0	0.4	1.1
12169CB_129	449	0.9	0.0492	0.0015	0.0433	0.0012	0.0064	0.0001	0.06	41.0	0.5	43.0	1.2	201	35	41.0	0.5	4.7
12169CB_130	550	1.4	0.0479	0.0010	0.0411	0.0009	0.0062	0.0001	0.27	39.9	0.4	40.9	0.8	139	22	39.9	0.4	2.4
12169CB_131	215	0.8	0.0488	0.0019	0.042	0.0016	0.0063	0.0001	0.06	40.2	0.6	41.8	1.5	295	43	40.2	0.6	3.8

Analysis	U (ppm)	U/Th	207Pb/ 206Pb	2σ error	207Pb/ 235U	2σ error	206Pb/ 238U	2σ error	err. corr.	206Pb/ 238U Age (Ma)	2σ error (Ma)	207Pb/ 235U Age (Ma)	2σ error (Ma)	207Pb/ 206Pb Age (Ma)	2σ error (Ma)	Best age (Ma)	2σ error (Ma)	Disc. (%)
NV12-176CB																		
12176CB_1	1345	1.4	0.0488	0.0010	0.0471	0.0009	0.0070	0.00012	0.62	45.2	0.8	46.8	0.9	144	32	45.2	0.8	3.4
12176CB_2	218	1.2	0.0511	0.0023	0.0459	0.0021	0.0065	0.00010	0.05	42.0	0.6	45.5	2.0	303	80	42.0	0.6	7.8
12176CB_3	223	0.9	0.0480	0.0019	0.0448	0.0016	0.0068	0.00010	0.12	43.6	0.6	44.5	1.5	206	62	43.6	0.6	2.0
12176CB_4	6300	0.8	0.0485	0.0005	0.0403	0.0005	0.0060	0.00007	0.51	38.8	0.4	40.1	0.5	119	16	38.8	0.4	3.3
12176CB_5	2653	1.8	0.0475	0.0006	0.0395	0.0005	0.0060	0.00006	0.23	38.7	0.4	39.3	0.5	107	21	38.7	0.4	1.5
12176CB_6	5810	1.3	0.0472	0.0004	0.0396	0.0003	0.0061	0.00005	0.52	39.0	0.3	39.5	0.3	69	10	39.0	0.3	1.1
12176CB_7	160	0.6	0.0541	0.0038	0.0491	0.0038	0.0066	0.00027	0.24	42.4	1.7	48.7	3.7	385	90	42.4	1.7	12.9
12176CB_8	6094	1.0	0.0488	0.0005	0.0392	0.0004	0.0058	0.00005	0.27	37.6	0.3	39.0	0.4	144	17	37.6	0.3	3.6
12176CB_9	3314	2.0	0.0517	0.0008	0.0422	0.0007	0.0060	0.00009	0.29	38.3	0.6	41.9	0.6	274	19	38.3	0.6	8.7
12176CB_10	3003	1.7	0.0529	0.0007	0.0423	0.0005	0.0058	0.00005	0.36	37.4	0.3	42.1	0.5	333	24	37.4	0.3	11.2
12176CB_11	249	1.7	0.0473	0.0017	0.0405	0.0014	0.0063	0.00014	0.00	40.2	0.9	40.3	1.3	190	47	40.2	0.9	0.3
12176CB_12	207	1.5	0.0521	0.0024	0.0464	0.0020	0.0065	0.00013	0.19	41.5	0.8	46.1	1.9	362	60	41.5	0.8	9.9
12176CB_13	638	0.9	0.0496	0.0012	0.0458	0.0012	0.0067	0.00011	0.36	43.1	0.7	45.5	1.2	225	45	43.1	0.7	5.4
12176CB_14	628	2.5	0.0490	0.0006	0.1151	0.0012	0.0171	0.00018	0.23	109.4	1.1	110.6	1.1	159	19	109.4	1.1	1.1
12176CB_15	3940	1.3	0.0474	0.0005	0.0393	0.0004	0.0060	0.00005	0.50	38.7	0.3	39.1	0.4	78	10	38.7	0.3	1.2
12176CB_16	264	0.7	0.0535	0.0029	0.0457	0.0019	0.0063	0.00014	0.08	40.4	0.9	45.3	1.8	361	74	40.4	0.9	10.9
12176CB_17	493	2.4	0.0489	0.0008	0.1168	0.0019	0.0174	0.00023	0.01	111.0	1.5	112.1	1.7	153	24	111.0	1.5	1.0
12176CB_18	3630	1.5	0.0476	0.0005	0.0385	0.0004	0.0059	0.00005	0.35	37.7	0.3	38.3	0.4	81	14	37.7	0.3	1.6
12176CB_20	4970	1.7	0.0493	0.0007	0.0418	0.0004	0.0062	0.00008	0.35	39.6	0.5	41.6	0.4	161	23	39.6	0.5	4.9
12176CB_21	526	3.1	0.0496	0.0008	0.1150	0.0017	0.0169	0.00020	0.38	108.1	1.3	110.5	1.5	190	20	108.1	1.3	2.2
12176CB_22	613	1.7	0.0490	0.0007	0.1104	0.0017	0.0164	0.00014	0.25	105.1	0.9	106.3	1.5	161	20	105.1	0.9	1.1
12176CB_23	5190	1.2	0.0483	0.0005	0.0404	0.0004	0.0061	0.00007	0.63	38.9	0.5	40.2	0.4	123	11	38.9	0.5	3.3
12176CB_24	2900	2.4	0.0484	0.0005	0.0400	0.0005	0.0060	0.00006	0.46	38.7	0.4	39.8	0.5	115	16	38.7	0.4	2.7
12176CB_25	2120	2.0	0.0498	0.0007	0.0414	0.0007	0.0060	0.00008	0.46	38.6	0.5	41.1	0.6	193	20	38.6	0.5	6.2
12176CB_26	719	2.7	0.0487	0.0007	0.1071	0.0016	0.0161	0.00020	0.55	103.0	1.3	103.3	1.5	145	19	103.0	1.3	0.3
12176CB_27	3799	1.6	0.0473	0.0005	0.0372	0.0004	0.0057	0.00005	0.41	36.7	0.3	37.1	0.4	73	11	36.7	0.3	1.1
12176CB_28	609	2.8	0.0499	0.0009	0.1160	0.0025	0.0168	0.00019	0.19	107.7	1.2	111.4	2.3	212	34	107.7	1.2	3.3
12176CB_29	1324	1.2	0.0590	0.0011	0.0476	0.0009	0.0059	0.00006	0.18	37.6	0.4	47.2	0.9	599	31	37.6	0.4	20.3
12176CB_30	3528	1.8	0.0470	0.0005	0.0372	0.0003	0.0058	0.00004	0.39	37.0	0.2	37.1	0.3	82	13	37.0	0.2	0.1
12176CB_31	639	1.0	0.0494	0.0015	0.0446	0.0016	0.0066	0.00011	0.51	42.6	0.7	44.3	1.5	221	39	42.6	0.7	3.9
12176CB_32	4660	1.3	0.0471	0.0004	0.0379	0.0003	0.0059	0.00005	0.38	37.6	0.3	37.8	0.3	78	14	37.6	0.3	0.4
12176CB_33	4479	1.3	0.0472	0.0005	0.0385	0.0004	0.0059	0.00004	0.42	38.1	0.3	38.4	0.4	70	11	38.1	0.3	0.8

12176CB_34	6800	1.0	0.0471	0.0004	0.0376	0.0003	0.0058	0.00006	0.62	37.3	0.4	37.5	0.3	72	10	37.3	0.4	0.6
12176CB_35	5800	1.0	0.0478	0.0005	0.0385	0.0004	0.0058	0.00006	0.54	37.6	0.4	38.3	0.4	97	16	37.6	0.4	2.0
12176CB_36	186	0.9	0.0515	0.0023	0.0494	0.0022	0.0070	0.00021	0.06	44.7	1.3	49.0	2.1	325	63	44.7	1.3	8.8
12176CB_37	2827	1.8	0.0470	0.0005	0.0384	0.0003	0.0059	0.00005	0.22	38.0	0.3	38.3	0.3	60	10	38.0	0.3	0.7
12176CB_38	705	2.4	0.0484	0.0006	0.1094	0.0014	0.0164	0.00018	0.26	104.8	1.1	105.4	1.3	112	15	104.8	1.1	0.6
12176CB_39	153	0.7	0.0498	0.0010	0.1745	0.0031	0.0254	0.00029	0.14	161.4	1.8	163.2	2.7	217	31	161.4	1.8	1.1
12176CB_40	732	2.8	0.0500	0.0009	0.1117	0.0027	0.0163	0.00025	0.56	104.0	1.6	107.5	2.4	202	19	104.0	1.6	3.3
12176CB_43	3991	1.9	0.0517	0.0012	0.0426	0.0011	0.0059	0.00012	0.54	38.2	0.8	42.4	1.1	275	44	38.2	0.8	10.0
12176CB_44	981	1.8	0.0482	0.0005	0.1103	0.0014	0.0165	0.00019	0.58	105.6	1.2	106.3	1.3	118	18	105.6	1.2	0.7
12176CB_45	4710	1.3	0.0475	0.0004	0.0388	0.0004	0.0059	0.00005	0.25	38.2	0.3	38.7	0.3	82	14	38.2	0.3	1.3
12176CB_46	1430	2.1	0.0512	0.0009	0.1189	0.0019	0.0170	0.00020	0.52	108.3	1.3	114.1	1.7	243	26	108.3	1.3	5.1
12176CB_47	550	1.8	0.0534	0.0028	0.0494	0.0028	0.0066	0.00020	0.43	42.7	1.3	48.9	2.7	347	73	42.7	1.3	12.7
12176CB_48	5400	1.5	0.0479	0.0006	0.0393	0.0005	0.0059	0.00008	0.40	38.1	0.5	39.2	0.5	111	15	38.1	0.5	2.8
12176CB_49	140	1.2	0.0589	0.0043	0.0508	0.0036	0.0062	0.00011	0.00	39.7	0.7	50.2	3.4	522	69	39.7	0.7	20.9
12176CB_50	5690	1.1	0.0480	0.0004	0.0389	0.0004	0.0059	0.00006	0.67	37.6	0.4	38.7	0.4	103	13	37.6	0.4	2.8
12176CB_51	3264	1.5	0.0488	0.0007	0.0392	0.0004	0.0058	0.00005	0.44	37.3	0.4	39.0	0.4	145	20	37.3	0.4	4.2
12176CB_52	342	1.1	0.0514	0.0022	0.0451	0.0017	0.0064	0.00014	0.04	41.0	0.9	44.8	1.7	299	67	41.0	0.9	8.4
12176CB_53	5310	1.1	0.0505	0.0008	0.0421	0.0007	0.0060	0.00010	0.65	38.7	0.7	41.9	0.7	219	23	38.7	0.7	7.5
12176CB_54	5192	1.7	0.0476	0.0007	0.0378	0.0005	0.0058	0.00008	0.53	37.3	0.5	37.7	0.4	118	16	37.3	0.5	1.1
12176CB_55	3463	1.8	0.0472	0.0005	0.0370	0.0004	0.0057	0.00005	0.42	36.7	0.3	36.9	0.4	75	11	36.7	0.3	0.7
12176CB_56	769	1.9	0.0486	0.0007	0.1111	0.0017	0.0166	0.00024	0.53	106.4	1.5	106.9	1.6	125	18	106.4	1.5	0.5
12176CB_57	8570	0.9	0.0489	0.0008	0.0386	0.0008	0.0057	0.00009	0.59	36.8	0.6	38.5	0.7	148	34	36.8	0.6	4.3
12176CB_58	5520	1.0	0.0475	0.0004	0.0382	0.0003	0.0058	0.00006	0.56	37.4	0.4	38.0	0.3	81	12	37.4	0.4	1.5
12176CB_59	6090	0.9	0.0472	0.0004	0.0383	0.0003	0.0059	0.00004	0.50	37.8	0.3	38.1	0.3	68	10	37.8	0.3	1.0
12176CB_60	238	1.3	0.0500	0.0028	0.0425	0.0024	0.0062	0.00013	0.12	39.6	0.8	42.2	2.3	287	95	39.6	0.8	6.2
12176CB_61	4835	1.3	0.0474	0.0005	0.0372	0.0005	0.0057	0.00006	0.59	36.5	0.4	37.1	0.5	90	14	36.5	0.4	1.5
12176CB_62	5630	1.5	0.0472	0.0004	0.0379	0.0003	0.0058	0.00005	0.57	37.3	0.3	37.7	0.3	73	9	37.3	0.3	1.1
12176CB_63	6020	1.1	0.0474	0.0004	0.0378	0.0004	0.0058	0.00005	0.60	37.4	0.3	37.7	0.4	82	11	37.4	0.3	0.9
12176CB_64	539	1.6	0.0494	0.0018	0.0424	0.0017	0.0061	0.00012	0.33	39.5	0.8	42.2	1.6	186	42	39.5	0.8	6.4
12176CB_65	677	1.4	0.0479	0.0008	0.0399	0.0008	0.0061	0.00009	0.46	38.9	0.6	39.8	0.8	125	22	38.9	0.6	2.0
12176CB_66	5330	1.2	0.0491	0.0007	0.0385	0.0006	0.0057	0.00007	0.55	36.4	0.4	38.3	0.6	176	19	36.4	0.4	5.0
12176CB_67	421	3.5	0.0475	0.0007	0.1131	0.0014	0.0173	0.00017	0.13	110.2	1.1	108.7	1.3	106	17	110.2	1.1	1.4
12176CB_68	3250	1.8	0.0468	0.0005	0.0371	0.0004	0.0057	0.00005	0.49	36.9	0.3	37.0	0.4	63	11	36.9	0.3	0.2
12176CB_69	3353	1.7	0.0478	0.0006	0.0359	0.0004	0.0055	0.00006	0.50	35.3	0.4	35.9	0.4	98	15	35.3	0.4	1.7
12176CB_70	3060	2.4	0.0480	0.0005	0.0370	0.0004	0.0056	0.00004	0.54	36.1	0.3	36.8	0.4	100	13	36.1	0.3	2.1

12176CB_71	712	2.5	0.0507	0.0008	0.1145	0.0019	0.0164	0.00019	0.45	104.6	1.2	110.0	1.7	235	24	104.6	1.2	4.9
12176CB_72	3700	2.2	0.0487	0.0007	0.0388	0.0005	0.0058	0.00007	0.09	37.3	0.5	38.6	0.5	140	20	37.3	0.5	3.4
12176CB_73	841	0.3	0.0518	0.0016	0.0427	0.0013	0.0060	0.00012	0.26	38.4	0.8	42.4	1.3	296	53	38.4	0.8	9.5
12176CB_74	757	1.6	0.0479	0.0009	0.0386	0.0008	0.0059	0.00007	0.29	37.7	0.5	38.5	0.8	137	27	37.7	0.5	2.0
12176CB_75	794	2.6	0.0484	0.0006	0.1093	0.0016	0.0164	0.00018	0.52	104.8	1.2	105.3	1.5	135	16	104.8	1.2	0.5
12176CB_76	3470	1.5	0.0478	0.0005	0.0383	0.0004	0.0058	0.00005	0.35	37.2	0.3	38.1	0.4	104	16	37.2	0.3	2.4
12176CB_77	708	2.3	0.0501	0.0012	0.1100	0.0022	0.0159	0.00034	0.38	101.4	2.1	105.9	2.1	220	37	101.4	2.1	4.2
12176CB_78	3950	1.5	0.0470	0.0005	0.0376	0.0004	0.0058	0.00006	0.58	37.0	0.4	37.4	0.4	89	11	37.0	0.4	1.1
12176CB_79	3957	1.5	0.0474	0.0006	0.0367	0.0004	0.0056	0.00006	0.18	36.0	0.4	36.6	0.4	91	14	36.0	0.4	1.7
12176CB_80	641	2.3	0.0490	0.0009	0.1104	0.0020	0.0164	0.00026	0.39	104.5	1.7	106.3	1.8	165	27	104.5	1.7	1.7
12176CB_81	5280	1.1	0.0471	0.0004	0.0373	0.0003	0.0057	0.00006	0.65	36.9	0.4	37.2	0.3	68	11	36.9	0.4	0.8
12176CB_82	3226	1.6	0.0478	0.0005	0.0371	0.0004	0.0056	0.00005	0.65	35.8	0.3	36.9	0.4	101	13	35.8	0.3	3.0
12176CB_83	3732	1.8	0.0481	0.0005	0.0391	0.0004	0.0059	0.00005	0.25	37.7	0.3	38.9	0.4	107	16	37.7	0.3	3.1
12176CB_84	1091	1.1	0.0479	0.0008	0.0426	0.0006	0.0065	0.00010	0.46	41.6	0.6	42.3	0.6	129	21	41.6	0.6	1.8
12176CB_85	4440	1.5	0.0476	0.0005	0.0386	0.0003	0.0059	0.00005	0.34	37.7	0.3	38.5	0.3	85	13	37.7	0.3	2.1
12176CB_86	293	1.6	0.0497	0.0019	0.0400	0.0014	0.0060	0.00014	0.16	38.3	0.9	39.8	1.4	218	37	38.3	0.9	3.7
12176CB_87	5500	1.4	0.0482	0.0009	0.0394	0.0006	0.0059	0.00010	0.40	38.2	0.6	39.2	0.6	142	30	38.2	0.6	2.6
12176CB_88	4410	1.5	0.0489	0.0007	0.0385	0.0005	0.0057	0.00008	0.44	36.7	0.5	38.3	0.5	156	23	36.7	0.5	4.2
12176CB_89	478	1.2	0.0493	0.0019	0.0413	0.0014	0.0061	0.00014	0.25	39.2	0.9	41.1	1.3	240	42	39.2	0.9	4.7
12176CB_90	538	2.2	0.0501	0.0013	0.0412	0.0010	0.0059	0.00009	0.29	38.1	0.6	40.9	0.9	246	29	38.1	0.6	6.9
12176CB_91	3460	2.6	0.0480	0.0006	0.0380	0.0003	0.0057	0.00005	0.28	36.6	0.3	37.9	0.3	111	19	36.6	0.3	3.3
12176CB_92	2448	2.5	0.0476	0.0006	0.0371	0.0004	0.0056	0.00006	0.47	36.1	0.4	37.0	0.4	112	16	36.1	0.4	2.6
12176CB_93	2646	1.9	0.0473	0.0005	0.0368	0.0004	0.0057	0.00005	0.55	36.4	0.3	36.7	0.4	88	14	36.4	0.3	0.8
12176CB_94	1993	2.1	0.0469	0.0010	0.0391	0.0008	0.0060	0.00012	0.41	38.5	0.8	39.0	0.8	124	30	38.5	0.8	1.3
12176CB_95	4000	1.6	0.0481	0.0006	0.0386	0.0004	0.0058	0.00006	0.39	37.4	0.4	38.5	0.4	108	18	37.4	0.4	2.7
12176CB_96	6880	1.3	0.0514	0.0012	0.0412	0.0010	0.0058	0.00012	0.62	37.5	0.7	41.0	1.0	268	33	37.5	0.7	8.6
12176CB_97	5140	0.9	0.0508	0.0027	0.0409	0.0022	0.0056	0.00019	0.30	36.3	1.2	40.7	2.2	310	140	36.3	1.2	10.8
12176CB_98	2949	2.2	0.0474	0.0007	0.0380	0.0006	0.0058	0.00008	0.42	37.5	0.5	37.9	0.6	90	13	37.5	0.5	0.9
12176CB_99	553	3.0	0.0492	0.0017	0.1104	0.0032	0.0163	0.00056	0.15	103.9	3.6	106.3	2.9	198	53	103.9	3.6	2.3
12176CB_100	888	2.2	0.0509	0.0009	0.1600	0.0027	0.0225	0.00040	0.69	143.5	2.5	150.7	2.3	251	24	143.5	2.5	4.8
12176CB_101	396	2.0	0.0498	0.0023	0.0487	0.0020	0.0071	0.00014	0.12	45.6	0.9	48.3	1.9	299	62	45.6	0.9	5.7
12176CB_102	1470	1.7	0.0496	0.0015	0.0453	0.0017	0.0066	0.00021	0.59	42.5	1.4	45.0	1.6	217	47	42.5	1.4	5.6
12176CB_103	2954	1.5	0.0480	0.0007	0.0390	0.0004	0.0059	0.00004	0.28	38.0	0.3	38.9	0.4	90	24	38.0	0.3	2.2
12176CB_104	3140	1.8	0.0471	0.0006	0.0360	0.0004	0.0056	0.00005	0.14	35.7	0.3	36.0	0.4	85	12	35.7	0.3	0.7
12176CB_105	529	2.9	0.0485	0.0008	0.1121	0.0019	0.0167	0.00027	0.58	106.5	1.7	107.9	1.7	163	22	106.5	1.7	1.3

12176CB_106	206	0.9	0.0506	0.0020	0.0490	0.0018	0.0070	0.00011	0.10	45.0	0.7	48.6	1.7	270	42	45.0	0.7	7.4
12176CB_107	3129	1.9	0.0497	0.0010	0.0375	0.0008	0.0055	0.00007	0.40	35.1	0.4	37.4	0.7	180	27	35.1	0.4	6.2
12176CB_108	671	2.6	0.0486	0.0005	0.1061	0.0011	0.0158	0.00017	0.52	101.3	1.1	102.4	1.0	134	13	101.3	1.1	1.1
12176CB_109	307	1.2	0.0468	0.0020	0.0443	0.0016	0.0069	0.00013	0.04	44.4	0.8	44.0	1.5	179	49	44.4	0.8	1.0
12176CB_110	4310	1.6	0.0489	0.0008	0.0350	0.0007	0.0051	0.00005	0.31	33.0	0.3	34.9	0.6	143	28	33.0	0.3	5.5
12176CB_111	3946	2.2	0.0477	0.0005	0.0369	0.0003	0.0056	0.00006	0.30	36.0	0.4	36.8	0.3	105	16	36.0	0.4	2.3
12176CB_112	603	2.5	0.0485	0.0006	0.1062	0.0016	0.0159	0.00016	0.48	101.5	1.0	102.4	1.5	143	16	101.5	1.0	0.9
12176CB_113	5900	1.5	0.0472	0.0006	0.0358	0.0005	0.0055	0.00007	0.50	35.1	0.5	35.7	0.4	116	18	35.1	0.5	1.8
12176CB_114	137	1.6	0.0519	0.0031	0.0461	0.0025	0.0065	0.00012	0.17	41.4	0.8	45.7	2.5	368	89	41.4	0.8	9.4
12176CB_115	580	1.6	0.0499	0.0013	0.0398	0.0011	0.0058	0.00007	0.37	37.2	0.5	39.6	1.1	218	35	37.2	0.5	6.1
12176CB_116	231	1.0	0.0488	0.0013	0.0418	0.0009	0.0063	0.00010	0.22	40.2	0.6	41.5	0.9	192	27	40.2	0.6	3.2
12176CB_117	2595	2.1	0.0503	0.0020	0.0383	0.0011	0.0056	0.00009	0.18	35.8	0.6	38.2	1.1	192	41	35.8	0.6	6.3
12176CB_119	757	2.1	0.0480	0.0006	0.1065	0.0014	0.0160	0.00017	0.44	102.3	1.1	102.8	1.3	109	15	102.3	1.1	0.5
12176CB_120	547	1.8	0.0501	0.0013	0.1099	0.0023	0.0158	0.00031	0.17	101.0	1.9	105.8	2.1	193	45	101.0	1.9	4.5
12176CB_121	208	0.9	0.0530	0.0022	0.0465	0.0020	0.0062	0.00016	0.27	40.0	1.0	46.1	2.0	420	67	40.0	1.0	13.2
12176CB_122	2298	1.7	0.0494	0.0010	0.0384	0.0007	0.0056	0.00010	0.33	36.3	0.6	38.3	0.7	227	33	36.3	0.6	5.1
12176CB_123	555	1.2	0.0462	0.0017	0.0433	0.0015	0.0067	0.00013	0.02	43.3	0.8	43.0	1.4	132	60	43.3	0.8	0.6
12176CB_124	2207	1.9	0.0477	0.0006	0.0361	0.0005	0.0055	0.00006	0.55	35.5	0.4	36.0	0.5	108	20	35.5	0.4	1.4

Analysis	U (ppm)	U/Th	207Pb/ 206Pb	2σ error	207Pb/ 235U	2σ error	206Pb/ 238U	2σ error	err. corr.	206Pb/ 238U Age (Ma)	2σ error (Ma)	207Pb/ 235U Age (Ma)	2σ error (Ma)	207Pb/ 206Pb Age (Ma)	2σ error (Ma)	Best age (Ma)	2σ error (Ma)	Disc. (%)
NV12-181CB																		
12181CB_1	130	1.1	0.0529	0.0027	0.0408	0.0017	0.0056	0.0001	0.16	35.9	0.8	40.5	1.7	330	110	35.9	0.8	11.3
12181CB_2	350	1.1	0.0481	0.0013	0.0417	0.0011	0.0059	0.0001	0.46	38.1	0.7	41.5	1.1	106	57	38.1	0.7	8.3
12181CB_3	153	1.1	0.0543	0.0031	0.0447	0.0025	0.0060	0.0001	0.11	38.8	0.8	44.3	2.4	340	110	38.8	0.8	12.5
12181CB_4	220	1.1	0.0459	0.0016	0.0386	0.0012	0.0061	0.0001	0.17	39.3	0.8	38.4	1.2	10	68	39.3	0.8	2.4
12181CB_5	202	0.7	0.0466	0.0015	0.0390	0.0013	0.0060	0.0001	0.27	38.8	0.7	38.9	1.3	38	64	38.8	0.7	0.3
12181CB_6	233	0.9	0.0507	0.0014	0.0423	0.0011	0.0060	0.0001	0.28	38.5	0.6	42.1	1.0	226	60	38.5	0.6	8.6
12181CB_7	440	1.1	0.0466	0.0009	0.0438	0.0009	0.0065	0.0001	0.45	42.1	0.6	43.5	0.9	43	41	42.1	0.6	3.3
12181CB_8	175	1.9	0.0465	0.0016	0.0384	0.0012	0.0061	0.0001	0.10	39.0	0.8	38.2	1.2	42	69	39.0	0.8	2.1
12181CB_9	249	1.1	0.0492	0.0017	0.0406	0.0014	0.0060	0.0001	0.29	38.3	0.9	40.3	1.4	149	69	38.3	0.9	5.0
12181CB_10	260	1.5	0.0544	0.0026	0.0471	0.0024	0.0063	0.0002	0.34	40.6	1.0	46.7	2.3	400	110	40.6	1.0	13.0
12181CB_11	294	1.1	0.0503	0.0018	0.0461	0.0015	0.0064	0.0001	0.14	41.0	0.8	45.8	1.4	211	82	41.0	0.8	10.6
12181CB_12	431	1.0	0.0629	0.0023	0.0553	0.0018	0.0064	0.0001	0.26	41.4	0.5	54.7	1.8	701	81	41.4	0.5	24.3
12181CB_13	748	1.0	0.0540	0.0010	0.0513	0.0010	0.0066	0.0001	0.35	42.6	0.6	50.8	1.0	369	39	42.6	0.6	16.1
12181CB_14	598	0.8	0.0552	0.0011	0.0507	0.0010	0.0064	0.0001	0.44	41.0	0.5	50.2	1.0	413	44	41.0	0.5	18.3
12181CB_16	355	1.1	0.0485	0.0012	0.0448	0.0011	0.0066	0.0001	0.38	42.5	0.7	44.5	1.1	133	54	42.5	0.7	4.6
12181CB_17	258	1.5	0.0598	0.0053	0.0576	0.0058	0.0070	0.0004	0.35	44.9	2.7	56.8	5.5	540	190	44.9	2.7	21.0
12181CB_18	209	1.1	0.0507	0.0017	0.0425	0.0014	0.0060	0.0001	0.25	38.7	0.6	42.2	1.4	233	73	38.7	0.6	8.2
12181CB_19	200	1.4	0.0489	0.0016	0.0417	0.0014	0.0062	0.0001	0.22	39.9	0.6	41.5	1.4	141	68	39.9	0.6	3.8
12181CB_20	257	0.7	0.0558	0.0046	0.0474	0.0032	0.0062	0.0001	0.11	40.1	0.7	47.0	3.1	330	100	40.1	0.7	14.8
12181CB_22	514	0.9	0.0500	0.0009	0.0465	0.0010	0.0068	0.0001	0.59	43.5	0.7	46.2	1.0	195	39	43.5	0.7	6.0
12181CB_23	208	1.2	0.0602	0.0028	0.0550	0.0031	0.0065	0.0001	0.45	41.9	0.8	54.3	3.0	545	87	41.9	0.8	22.8
12181CB_24	235	1.2	0.0473	0.0015	0.0396	0.0011	0.0060	0.0001	0.16	38.7	0.6	39.5	1.1	74	62	38.7	0.6	2.0
12181CB_26	673	0.9	0.0517	0.0013	0.0479	0.0020	0.0065	0.0002	0.67	41.7	1.1	47.5	1.9	261	56	41.7	1.1	12.2
12181CB_27	248	1.1	0.0506	0.0032	0.0435	0.0025	0.0062	0.0001	0.09	39.8	0.7	43.2	2.4	200	120	39.8	0.7	7.9
12181CB_28	242	1.0	0.0488	0.0020	0.0425	0.0018	0.0063	0.0001	0.34	40.7	0.6	42.2	1.8	136	82	40.7	0.6	3.6
12181CB_29	274	1.0	0.0528	0.0032	0.0440	0.0024	0.0062	0.0002	0.24	39.5	0.9	43.7	2.4	290	130	39.5	0.9	9.6
12181CB_30	271	0.8	0.0517	0.0024	0.0456	0.0017	0.0065	0.0002	0.22	41.5	1.0	45.2	1.7	252	99	41.5	1.0	8.2
12181CB_31	247	1.2	0.0497	0.0038	0.0396	0.0030	0.0056	0.0002	0.38	35.9	1.4	39.5	2.9	180	160	35.9	1.4	9.1
12181CB_32	394	0.8	0.0475	0.0018	0.0417	0.0016	0.0061	0.0001	0.33	39.4	0.6	41.4	1.6	80	78	39.4	0.6	4.9
12181CB_33	228	1.0	0.0499	0.0024	0.0427	0.0019	0.0063	0.0001	0.14	40.3	0.8	42.5	1.8	177	97	40.3	0.8	5.3
12181CB_34	217	0.8	0.0651	0.0028	0.0571	0.0025	0.0063	0.0001	0.25	40.5	0.8	56.4	2.4	768	94	40.5	0.8	28.2
12181CB_35	354	1.1	0.0510	0.0016	0.0459	0.0013	0.0065	0.0001	0.01	41.7	0.8	45.6	1.3	235	68	41.7	0.8	8.6

12181CB_36	180	1.0	0.0470	0.0017	0.0410	0.0014	0.0063	0.0001	0.02	40.5	0.6	40.8	1.4	64	73	40.5	0.6	0.7
12181CB_37	250	1.3	0.0491	0.0020	0.0418	0.0011	0.0063	0.0001	0.10	40.2	0.8	41.6	1.1	126	72	40.2	0.8	3.5
12181CB_38	536	1.2	0.0534	0.0020	0.0463	0.0018	0.0064	0.0002	0.16	40.8	1.1	45.9	1.8	345	81	40.8	1.1	11.1
12181CB_40	287	0.7	0.0466	0.0014	0.0400	0.0011	0.0059	0.0001	0.06	38.1	0.6	39.8	1.1	44	60	38.1	0.6	4.3
12181CB_41	521	0.8	0.0531	0.0011	0.0483	0.0011	0.0066	0.0001	0.30	42.2	0.6	47.9	1.1	326	48	42.2	0.6	11.9
12181CB_42	171	1.0	0.0475	0.0029	0.0391	0.0013	0.0062	0.0001	0.11	39.8	0.7	39.0	1.3	34	74	39.8	0.7	1.9
12181CB_43	561	1.0	0.0520	0.0016	0.0477	0.0014	0.0066	0.0001	0.34	42.6	0.9	47.4	1.3	272	68	42.6	0.9	10.2
12181CB_44	261	0.9	0.0503	0.0014	0.0430	0.0011	0.0062	0.0001	0.23	40.0	0.7	42.8	1.1	195	59	40.0	0.7	6.5
12181CB_45	191	1.2	0.0516	0.0030	0.0401	0.0021	0.0059	0.0001	0.31	37.7	0.9	39.9	2.1	270	130	37.7	0.9	5.5
12181CB_46	274	1.1	0.0474	0.0013	0.0432	0.0011	0.0065	0.0001	0.33	41.9	0.8	43.0	1.1	78	55	41.9	0.8	2.5
12181CB_47	289	1.0	0.0466	0.0012	0.0405	0.0011	0.0063	0.0001	0.46	40.6	0.8	40.3	1.0	42	52	40.6	0.8	0.7
12181CB_48	304	1.0	0.0480	0.0017	0.0434	0.0016	0.0066	0.0001	0.30	42.7	0.8	43.1	1.6	94	66	42.7	0.8	1.0
12181CB_49	226	0.9	0.0485	0.0017	0.0429	0.0016	0.0064	0.0001	0.17	40.9	0.7	42.6	1.6	107	64	40.9	0.7	3.9
12181CB_50	191	1.1	0.0504	0.0019	0.0436	0.0017	0.0062	0.0001	0.09	40.0	0.7	43.3	1.6	231	83	40.0	0.7	7.6
12181CB_51	427	0.8	0.0508	0.0020	0.0417	0.0015	0.0062	0.0001	0.56	40.0	0.8	41.5	1.5	217	85	40.0	0.8	3.7
12181CB_52	183	1.3	0.0474	0.0016	0.0398	0.0012	0.0062	0.0001	0.19	39.6	0.6	39.7	1.2	78	68	39.6	0.6	0.2
12181CB_53	301	0.6	0.0624	0.0020	0.0554	0.0017	0.0065	0.0001	0.02	41.6	0.6	54.7	1.6	683	69	41.6	0.6	23.9
12181CB_54	190	1.1	0.0463	0.0020	0.0377	0.0016	0.0059	0.0001	0.11	38.2	0.7	37.6	1.5	31	85	38.2	0.7	1.5
12181CB_55	287	1.0	0.0467	0.0012	0.0423	0.0010	0.0064	0.0001	0.02	41.4	0.6	42.0	1.0	45	51	41.4	0.6	1.4
12181CB_56	349	1.0	0.0511	0.0015	0.0455	0.0012	0.0066	0.0001	0.34	42.3	0.6	45.4	1.2	235	63	42.3	0.6	6.9
12181CB_57	286	1.0	0.0503	0.0018	0.0442	0.0014	0.0064	0.0001	0.10	40.8	0.7	43.9	1.3	196	73	40.8	0.7	7.1
12181CB_58	227	1.1	0.0498	0.0017	0.0412	0.0014	0.0061	0.0001	0.16	39.1	0.5	41.0	1.3	180	71	39.1	0.5	4.7
12181CB_59	557	1.3	0.0490	0.0009	0.0441	0.0009	0.0065	0.0001	0.36	41.8	0.7	43.8	0.9	144	42	41.8	0.7	4.6
12181CB_60	287	0.8	0.0503	0.0012	0.0419	0.0010	0.0060	0.0001	0.22	38.5	0.5	41.7	1.0	216	53	38.5	0.5	7.7
12181CB_61	1350	0.7	0.0512	0.0012	0.0462	0.0010	0.0063	0.0001	0.19	40.4	0.5	45.8	1.0	243	54	40.4	0.5	11.8
12181CB_62	195	1.2	0.0524	0.0021	0.0436	0.0016	0.0061	0.0001	0.05	39.2	0.6	43.3	1.6	279	82	39.2	0.6	9.5
12181CB_63	343	1.4	0.0477	0.0010	0.0437	0.0008	0.0067	0.0001	0.27	43.0	0.6	43.5	0.8	89	44	43.0	0.6	1.0
12181CB_64	301	1.5	0.0526	0.0028	0.0447	0.0021	0.0063	0.0001	0.11	40.7	0.9	44.4	2.1	290	110	40.7	0.9	8.4
12181CB_65	230	0.9	0.0482	0.0016	0.0403	0.0012	0.0061	0.0001	0.02	39.1	0.6	40.3	1.2	120	67	39.1	0.6	3.0
12181CB_66	283	1.1	0.0515	0.0020	0.0418	0.0017	0.0059	0.0001	0.30	38.0	0.9	41.6	1.7	275	86	38.0	0.9	8.8
12181CB_67	188	0.9	0.0526	0.0028	0.0426	0.0024	0.0059	0.0001	0.09	37.6	0.7	42.3	2.4	280	110	37.6	0.7	11.1
12181CB_68	223	1.1	0.0493	0.0015	0.0410	0.0012	0.0061	0.0001	0.06	38.9	0.6	40.8	1.2	143	61	38.9	0.6	4.6
12181CB_69	296	0.9	0.0644	0.0025	0.0552	0.0021	0.0063	0.0001	0.07	40.3	0.8	54.6	2.0	740	79	40.3	0.8	26.2
12181CB_70	231	1.0	0.0516	0.0015	0.0400	0.0012	0.0056	0.0001	0.18	35.9	0.5	39.8	1.2	271	68	35.9	0.5	9.7
12181CB_71	344	1.0	0.0481	0.0015	0.0413	0.0011	0.0060	0.0001	0.21	38.8	0.8	41.1	1.1	107	62	38.8	0.8	5.6

12181CB_72	197	1.0	0.0464	0.0017	0.0394	0.0015	0.0063	0.0001	0.31	40.2	0.7	39.3	1.4	34	73	40.2	0.7	2.3
12181CB_73	940	0.7	0.0468	0.0008	0.0434	0.0008	0.0068	0.0001	0.57	43.6	0.6	43.1	0.8	43	35	43.6	0.6	1.2
12181CB_74	246	1.1	0.0521	0.0027	0.0437	0.0019	0.0061	0.0001	0.15	39.3	0.8	43.4	1.9	280	110	39.3	0.8	9.5
12181CB_75	739	1.0	0.0479	0.0013	0.0410	0.0010	0.0060	0.0001	0.07	38.6	0.5	40.8	1.0	93	55	38.6	0.5	5.5
12181CB_76	606	0.7	0.0517	0.0010	0.0462	0.0010	0.0062	0.0001	0.45	40.1	0.6	45.9	1.0	265	44	40.1	0.6	12.7
12181CB_77	258	1.3	0.0478	0.0018	0.0412	0.0015	0.0063	0.0002	0.23	40.4	0.9	40.9	1.5	98	76	40.4	0.9	1.2
12181CB_78	340	0.5	0.0598	0.0026	0.0510	0.0018	0.0063	0.0001	0.18	40.4	0.8	50.5	1.7	563	96	40.4	0.8	19.9
12181CB_80	179	1.1	0.0524	0.0034	0.0439	0.0028	0.0061	0.0001	0.04	39.3	0.6	43.6	2.7	199	86	39.3	0.6	9.8
12181CB_81	130	0.9	0.0482	0.0020	0.0418	0.0017	0.0062	0.0001	0.19	40.1	0.8	41.5	1.6	117	82	40.1	0.8	3.5
12181CB_82	192	0.9	0.0485	0.0016	0.0400	0.0012	0.0061	0.0001	0.01	39.1	0.7	39.8	1.2	127	67	39.1	0.7	1.8
12181CB_83	395	1.0	0.0563	0.0029	0.0528	0.0028	0.0065	0.0002	0.40	42.0	1.1	52.2	2.7	490	110	42.0	1.1	19.5
12181CB_84	222	1.0	0.0487	0.0019	0.0404	0.0013	0.0060	0.0001	0.13	38.8	0.6	40.2	1.3	129	78	38.8	0.6	3.6
12181CB_85	242	1.3	0.0477	0.0014	0.0417	0.0013	0.0064	0.0001	0.31	41.0	0.8	41.7	1.3	90	60	41.0	0.8	1.8
12181CB_86	169	1.1	0.0484	0.0017	0.0400	0.0013	0.0061	0.0001	0.17	39.3	0.6	40.0	1.3	121	73	39.3	0.6	1.8
12181CB_87	232	1.0	0.0469	0.0015	0.0403	0.0012	0.0063	0.0001	0.17	40.5	0.6	40.1	1.2	58	63	40.5	0.6	0.9
12181CB_88	188	1.0	0.0486	0.0026	0.0401	0.0018	0.0061	0.0001	0.12	39.0	0.8	39.9	1.8	120	100	39.0	0.8	2.3
12181CB_89	159	0.9	0.0506	0.0022	0.0401	0.0016	0.0058	0.0001	0.00	37.2	0.6	39.9	1.6	224	86	37.2	0.6	6.7
12181CB_90	257	1.0	0.0467	0.0012	0.0399	0.0010	0.0061	0.0001	0.11	39.3	0.6	39.7	1.0	40	51	39.3	0.6	1.1
12181CB_91	176	1.0	0.0493	0.0024	0.0400	0.0016	0.0060	0.0001	0.04	38.6	0.7	39.8	1.6	149	98	38.6	0.7	3.1
12181CB_92	173	0.9	0.0507	0.0026	0.0429	0.0018	0.0058	0.0001	0.10	37.4	0.8	42.6	1.8	250	110	37.4	0.8	12.1
12181CB_93	268	1.2	0.0485	0.0027	0.0423	0.0029	0.0059	0.0001	0.13	38.0	0.5	41.1	2.1	78	76	38.0	0.5	7.6
12181CB_94	135	1.4	0.0478	0.0017	0.0374	0.0015	0.0057	0.0001	0.29	36.4	0.7	37.2	1.5	96	74	36.4	0.7	2.1
12181CB_95	259	0.9	0.0489	0.0016	0.0418	0.0016	0.0062	0.0001	0.48	39.9	0.7	41.5	1.6	150	70	39.9	0.7	3.8
12181CB_96	160	1.1	0.0468	0.0019	0.0388	0.0014	0.0061	0.0001	0.07	38.9	0.8	38.6	1.4	39	75	38.9	0.8	0.8
12181CB_97	148	1.4	0.0592	0.0050	0.0485	0.0042	0.0060	0.0001	0.20	38.5	0.7	48.0	4.0	470	160	38.5	0.7	19.9
12181CB_98	201	1.0	0.0461	0.0017	0.0380	0.0013	0.0060	0.0001	0.05	38.4	0.6	37.8	1.3	34	73	38.4	0.6	1.7
12181CB_99	95	1.5	0.0538	0.0049	0.0423	0.0022	0.0060	0.0001	0.15	38.2	0.9	42.0	2.1	240	110	38.2	0.9	9.0
12181CB_100	252	1.0	0.0482	0.0019	0.0399	0.0017	0.0059	0.0001	0.03	38.2	0.6	39.7	1.6	110	82	38.2	0.6	3.8
12181CB_101	232	1.0	0.0479	0.0018	0.0397	0.0013	0.0061	0.0001	0.00	38.9	0.7	39.5	1.2	84	72	38.9	0.7	1.5
12181CB_102	645	0.6	0.0484	0.0009	0.0411	0.0009	0.0061	0.0001	0.31	39.3	0.4	40.9	0.9	120	41	39.3	0.4	3.7
12181CB_103	162	1.0	0.0477	0.0016	0.0402	0.0013	0.0061	0.0001	0.25	39.2	0.7	40.0	1.3	91	67	39.2	0.7	2.1
12181CB_104	218	1.2	0.0489	0.0016	0.0415	0.0013	0.0062	0.0001	0.28	39.5	0.5	41.3	1.3	141	68	39.5	0.5	4.3
12181CB_105	216	1.2	0.0500	0.0019	0.0415	0.0017	0.0060	0.0001	0.26	38.3	0.6	41.3	1.7	210	84	38.3	0.6	7.3
12181CB_106	672	0.7	0.0488	0.0010	0.0447	0.0009	0.0066	0.0001	0.44	42.2	0.7	44.4	0.9	130	43	42.2	0.7	4.9
12181CB_107	646	0.9	0.0559	0.0015	0.0475	0.0014	0.0061	0.0001	0.19	39.5	0.5	47.1	1.4	431	58	39.5	0.5	16.1

12181CB_108	400	0.5	0.0597	0.0025	0.0541	0.0023	0.0064	0.0001	0.04	40.8	0.7	53.4	2.2	574	93	40.8	0.7	23.6
12181CB_109	304	0.8	0.0648	0.0024	0.0567	0.0019	0.0063	0.0001	0.01	40.7	0.7	56.0	1.9	750	75	40.7	0.7	27.4
12181CB_110	128	1.2	0.0487	0.0024	0.0402	0.0017	0.0060	0.0001	0.05	38.4	0.8	40.2	1.7	146	89	38.4	0.8	4.6
12181CB_111	265	1.0	0.0520	0.0025	0.0436	0.0023	0.0061	0.0001	0.18	38.9	0.7	43.3	2.2	263	99	38.9	0.7	10.3
12181CB_112	289	1.5	0.0520	0.0036	0.0453	0.0030	0.0063	0.0002	0.24	40.3	1.0	45.0	2.9	260	140	40.3	1.0	10.4
12181CB_113	255	1.3	0.0499	0.0025	0.0429	0.0018	0.0063	0.0001	0.06	40.4	0.9	42.6	1.7	151	81	40.4	0.9	5.2
12181CB_115	181	0.9	0.0484	0.0016	0.0401	0.0013	0.0061	0.0001	0.23	39.1	0.8	39.9	1.2	120	66	39.1	0.8	2.1
12181CB_116	186	1.2	0.0513	0.0020	0.0427	0.0013	0.0061	0.0001	0.01	39.1	0.9	42.4	1.3	237	83	39.1	0.9	7.7
12181CB_117	353	1.3	0.0479	0.0015	0.0419	0.0012	0.0062	0.0001	0.16	39.7	0.6	41.7	1.2	100	66	39.7	0.6	4.8
12181CB_118	229	1.3	0.0492	0.0017	0.0429	0.0013	0.0064	0.0001	0.12	41.0	0.6	42.9	1.3	162	72	41.0	0.6	4.5
12181CB_119	326	1.2	0.0498	0.0017	0.0419	0.0015	0.0059	0.0001	0.23	37.7	0.7	41.7	1.5	181	72	37.7	0.7	9.5
12181CB_120	171	0.8	0.0527	0.0037	0.0465	0.0032	0.0063	0.0001	0.13	40.2	0.8	46.1	3.1	290	140	40.2	0.8	12.9
12181CB_121	339	1.3	0.0469	0.0010	0.0406	0.0010	0.0060	0.0001	0.23	38.5	0.5	40.4	0.9	53	45	38.5	0.5	4.7
12181CB_122	178	1.8	0.1097	0.0023	4.0330	0.0870	0.2679	0.0029	0.12	1530.0	15.0	1640.0	17.0	1792	36	1792.0	36.0	14.6
12181CB_123	200	1.6	0.0481	0.0022	0.0410	0.0016	0.0062	0.0001	0.04	40.1	0.7	40.8	1.5	102	92	40.1	0.7	1.7
12181CB_124	1100	14.1	0.0470	0.0012	0.0403	0.0012	0.0063	0.0001	0.46	40.2	0.8	40.1	1.2	39	46	40.2	0.8	0.3
12181CB_125	298	1.3	0.0481	0.0014	0.0408	0.0011	0.0062	0.0001	0.34	39.7	0.8	40.5	1.1	106	60	39.7	0.8	2.0
12181CB_126	305	1.0	0.0474	0.0016	0.0421	0.0012	0.0065	0.0001	0.06	41.8	0.7	41.9	1.2	64	63	41.8	0.7	0.2
12181CB_127	258	0.9	0.0517	0.0024	0.0456	0.0017	0.0063	0.0001	0.12	40.4	0.9	45.3	1.6	280	100	40.4	0.9	10.8
12181CB_128	173	1.1	0.0496	0.0023	0.0408	0.0018	0.0060	0.0001	0.09	38.5	0.6	40.6	1.7	138	82	38.5	0.6	5.1
12181CB_129	249	1.3	0.0521	0.0036	0.0438	0.0030	0.0063	0.0002	0.39	40.3	1.0	43.5	2.9	240	130	40.3	1.0	7.4
12181CB_130	276	1.1	0.0480	0.0014	0.0432	0.0013	0.0066	0.0001	0.29	42.7	0.6	42.9	1.3	89	61	42.7	0.6	0.6

ZIRCON U-Pb GEOCHRONOLOGY

Analysis	U (ppm)	U/Th	207Pb/ 206Pb	2σ error	207Pb/ 235U	2σ error	206Pb/ 238U	2σ error	err. corr.	206Pb/ 238U Age (Ma)	2σ error (Ma)	207Pb/ 235U Age (Ma)	2σ error (Ma)	207Pb/ 206Pb Age (Ma)	2σ error (Ma)	Best age (Ma)	2σ error (Ma)	Disc. (%)
000714-1																		
000714-1_3	940	7.4	0.0507	0.0014	0.1906	0.0068	0.0277	0.0006	0.24	175.8	3.6	176.9	5.8	182	74	175.8	3.6	0.6
000714-1_4	445	6.2	0.0643	0.0016	0.1709	0.0067	0.0251	0.0004	0.04	159.6	2.2	159.6	5.7	163	76	159.6	2.2	0.0
000714-1_6	595	10.0	0.0499	0.0018	0.1151	0.0045	0.0174	0.0003	0.27	110.9	1.7	110.3	4.0	113	79	110.9	1.7	0.5
000714-1_7	9400	10.4	0.0497	0.0019	0.1240	0.0034	0.0183	0.0005	0.14	117.1	3.0	118.6	3.0	156	55	117.1	3.0	1.3
000714-1_8	668	7.9	0.0594	0.0021	0.1147	0.0042	0.0170	0.0002	0.28	108.6	1.5	110.0	3.9	139	73	108.6	1.5	1.3
000714-1_9	936	10.3	0.0483	0.0020	0.1097	0.0034	0.0163	0.0002	0.36	104.2	1.4	105.5	3.1	138	62	104.2	1.4	1.2
000714-1_10	783	10.3	0.0492	0.0013	0.1223	0.0037	0.0182	0.0003	0.50	116.5	1.7	116.9	3.3	140	60	116.5	1.7	0.3
000714-1_11	1620	10.4	0.0488	0.0018	0.1208	0.0034	0.0176	0.0002	0.24	112.4	1.3	116.1	3.1	197	62	112.4	1.3	3.2
000714-1_12	3560	9.7	0.0487	0.0015	0.1881	0.0046	0.0273	0.0005	0.23	173.6	2.9	174.7	3.9	188	49	173.6	2.9	0.6
000714-1_13	1110	8.0	0.0489	0.0015	0.1147	0.0042	0.0173	0.0003	0.27	110.5	1.9	109.3	3.6	82	62	110.5	1.9	1.1
000714-1_14	516	5.4	0.0500	0.0015	0.1780	0.0110	0.0247	0.0008	0.23	157.5	4.9	165.7	9.3	270	130	157.5	4.9	4.9
000714-1_15	738	5.4	0.0501	0.0012	0.1693	0.0049	0.0246	0.0003	0.26	156.6	2.1	158.4	4.2	185	61	156.6	2.1	1.1
000714-1_16	933	7.9	0.0476	0.0015	0.1146	0.0033	0.0172	0.0002	0.21	109.7	1.4	110.0	3.0	123	58	109.7	1.4	0.3
000714-1_17	709	7.9	0.0524	0.0034	0.1841	0.0079	0.0262	0.0006	0.29	166.6	3.9	172.7	7.2	228	87	166.6	3.9	3.5
000714-1_18	836	8.9	0.0499	0.0015	0.1178	0.0036	0.0178	0.0002	0.32	113.6	1.5	112.9	3.2	120	65	113.6	1.5	0.6
000714-1_19	548	5.4	0.0547	0.0020	0.1863	0.0069	0.0248	0.0004	0.18	157.7	2.4	173.1	5.9	365	80	157.7	2.4	8.9

Analysis	U (ppm)	U/Th	207Pb/ 206Pb	2σ error	207Pb/ 235U	2σ error	206Pb/ 238U	2σ error	err. corr.	206Pb/ 238U Age (Ma)	2σ error (Ma)	207Pb/ 235U Age (Ma)	2σ error (Ma)	207Pb/ 206Pb Age (Ma)	2σ error (Ma)	Best age (Ma)	2σ error (Ma)	Disc. (%)
980730-5																		
980730-5_2	1125	23.4	0.0489	0.0014	0.1106	0.0029	0.0165	0.0003	0.41	175.8	3.6	106.4	2.7	182	74	175.8	3.6	0.6
980730-5_3	995	21.6	0.0474	0.0016	0.1077	0.0036	0.0166	0.0005	0.39	159.6	2.2	103.7	3.3	163	76	159.6	2.2	0.0
980730-5_4	1107	21.3	0.0505	0.0019	0.1127	0.0043	0.0164	0.0005	0.25	110.9	1.7	108.6	4.1	113	79	110.9	1.7	0.5
980730-5_5	1370	12.5	0.0499	0.0014	0.1209	0.0034	0.0178	0.0004	0.37	117.1	3.0	115.8	3.1	156	55	117.1	3.0	1.3
980730-5_6	840	21.9	0.0477	0.0015	0.1086	0.0030	0.0166	0.0003	0.41	108.6	1.5	104.6	2.8	139	73	108.6	1.5	1.3
980730-5_8	1220	33.5	0.0687	0.0033	0.1154	0.0039	0.0171	0.0002	0.36	104.2	1.4	110.7	3.6	138	62	104.2	1.4	1.2
980730-5_9	1337	20.9	0.0493	0.0017	0.1139	0.0031	0.0170	0.0003	0.13	116.5	1.7	109.7	2.7	140	60	116.5	1.7	0.3
980730-5_10	1491	22.9	0.0491	0.0014	0.1257	0.0034	0.0176	0.0003	0.36	112.4	1.3	120.1	3.1	197	62	112.4	1.3	3.2
980730-5_11	778	30.0	0.0519	0.0014	0.1123	0.0046	0.0174	0.0003	0.30	173.6	2.9	107.7	4.2	188	49	173.6	2.9	0.6
980730-5_12	911	19.5	0.0469	0.0019	0.1133	0.0045	0.0161	0.0005	0.12	110.5	1.9	108.7	4.1	82	62	110.5	1.9	1.1
980730-5_15	610	10.8	0.0514	0.0019	0.1321	0.0058	0.0183	0.0004	0.35	157.5	4.9	126.5	5.4	270	130	157.5	4.9	4.9
980730-5_16	1176	12.0	0.0525	0.0036	0.1076	0.0036	0.0159	0.0004	0.30	156.6	2.1	103.6	3.3	185	61	156.6	2.1	1.1
980730-5_18	1089	9.9	0.0532	0.0023	0.1130	0.0036	0.0164	0.0003	0.30	109.7	1.4	108.5	3.3	123	58	109.7	1.4	0.3

Analysis	U (ppm)	U/Th	207Pb/ 206Pb	2σ error	207Pb/ 235U	2σ error	206Pb/ 238U	2σ error	err. corr.	206Pb/ 238U Age (Ma)	2σ error (Ma)	207Pb/ 235U Age (Ma)	2σ error (Ma)	207Pb/ 206Pb Age (Ma)	2σ error (Ma)	Best age (Ma)	2σ error (Ma)	Disc. (%)
980731-2																		
980731-2_1	721	13.2	0.0485	0.0016	0.1157	0.0037	0.0173	0.0002	0.26	110.6	1.2	110.9	3.4	131	65	110.6	1.2	0.3
980731-2_2	1128	11.0	0.0474	0.0014	0.1132	0.0037	0.0170	0.0003	0.19	108.8	1.9	108.7	3.4	87	57	108.8	1.9	0.1
980731-2_3	886	11.9	0.0480	0.0015	0.1129	0.0035	0.0171	0.0002	0.20	109.2	1.3	108.5	3.2	102	61	109.2	1.3	0.6
980731-2_4	872	10.8	0.0493	0.0015	0.1161	0.0034	0.0172	0.0003	0.43	110.1	2.0	111.4	3.1	154	62	110.1	2.0	1.2
980731-2_5	1006	10.6	0.0491	0.0016	0.1128	0.0036	0.0167	0.0003	0.22	106.8	1.7	108.7	3.3	154	64	106.8	1.7	1.7
980731-2_6	842	10.6	0.0538	0.0018	0.1116	0.0033	0.0167	0.0003	0.33	106.7	1.7	107.2	3.0	125	59	106.7	1.7	0.5
980731-2_7	941	10.4	0.0486	0.0015	0.1153	0.0032	0.0171	0.0002	0.26	109.1	1.2	110.7	2.9	151	57	109.1	1.2	1.4
980731-2_8	445	11.6	0.0490	0.0013	0.1148	0.0067	0.0176	0.0004	0.24	112.5	2.8	110.0	6.1	90	120	112.5	2.8	2.3
980731-2_9	947	5.4	0.0478	0.0031	0.1173	0.0046	0.0163	0.0003	0.43	104.0	2.2	112.4	4.2	271	71	104.0	2.2	7.5
980731-2_10	1083	9.4	0.0520	0.0017	0.1206	0.0034	0.0178	0.0003	0.06	113.4	1.8	115.4	3.0	162	58	113.4	1.8	1.7
980731-2_11	835	14.0	0.0491	0.0013	0.1148	0.0033	0.0171	0.0002	0.29	109.3	1.3	110.1	3.0	145	60	109.3	1.3	0.7
980731-2_12	693	11.4	0.0486	0.0014	0.1137	0.0041	0.0173	0.0002	0.22	110.5	1.4	109.5	3.8	97	68	110.5	1.4	0.9
980731-2_13	753	11.3	0.0480	0.0017	0.1135	0.0042	0.0170	0.0004	0.18	108.6	2.4	108.9	3.8	142	74	108.6	2.4	0.3
980731-2_14	770	12.9	0.0491	0.0019	0.1173	0.0037	0.0174	0.0003	0.34	111.3	2.0	112.4	3.3	145	60	111.3	2.0	1.0
980731-2_15	884	10.0	0.0491	0.0015	0.1175	0.0043	0.0170	0.0003	0.37	108.6	2.1	112.6	3.9	175	71	108.6	2.1	3.6
980731-2_16	757	15.2	0.0500	0.0018	0.1114	0.0044	0.0163	0.0004	0.26	104.0	2.3	107.0	4.0	152	75	104.0	2.3	2.8
980731-2_17	1210	8.1	0.0555	0.0024	0.1103	0.0033	0.0168	0.0003	0.33	107.0	1.8	106.0	3.0	108	61	107.0	1.8	0.9
980731-2_18	1410	10.8	0.0494	0.0019	0.1196	0.0039	0.0178	0.0004	0.17	113.6	2.3	114.5	3.6	146	61	113.6	2.3	0.8
980731-2_19	739	13.2	0.0481	0.0015	0.1126	0.0034	0.0172	0.0002	0.31	110.1	1.2	108.2	3.1	87	61	110.1	1.2	1.8
980731-2_20	591	11.4	0.0491	0.0015	0.1188	0.0051	0.0180	0.0005	0.19	115.2	3.2	113.6	4.6	128	83	115.2	3.2	1.4
980731-2_21	944	8.4	0.0476	0.0015	0.1156	0.0041	0.0167	0.0003	0.17	106.9	2.1	110.8	3.7	188	61	106.9	2.1	3.5
980731-2_22	566	14.2	0.0486	0.0021	0.1193	0.0059	0.0176	0.0005	0.21	112.4	3.0	114.0	5.4	159	88	112.4	3.0	1.4
980731-2_23	856	12.3	0.0502	0.0015	0.1162	0.0037	0.0171	0.0003	0.11	109.4	1.8	111.4	3.4	168	65	109.4	1.8	1.8
980731-2_24	451	13.2	0.0491	0.0021	0.1197	0.0057	0.0164	0.0003	0.17	104.6	2.0	114.3	5.1	277	95	104.6	2.0	8.5
980731-2_25	547	13.3	0.0496	0.0016	0.1123	0.0050	0.0168	0.0003	0.31	107.5	1.9	107.7	4.6	130	85	107.5	1.9	0.2
980731-2_26	835	13.3	0.0529	0.0026	0.1124	0.0036	0.0172	0.0003	0.30	109.6	1.6	108.0	3.3	90	64	109.6	1.6	1.5
980731-2_28	771	16.2	0.0487	0.0022	0.1135	0.0036	0.0167	0.0002	0.19	106.9	1.4	109.0	3.3	162	67	106.9	1.4	1.9
980731-2_29	1121	11.8	0.0473	0.0015	0.1191	0.0035	0.0178	0.0003	0.28	113.5	1.9	114.1	3.2	140	58	113.5	1.9	0.5
980731-2_30	905	8.6	0.0495	0.0017	0.1196	0.0046	0.0173	0.0005	0.34	110.5	2.9	114.4	4.2	204	76	110.5	2.9	3.4
980731-2_31	4630	14.7	0.0488	0.0014	0.1218	0.0050	0.0176	0.0005	0.28	112.1	2.9	116.7	4.5	208	89	112.1	2.9	3.9
980731-2_32	796	16.5	0.0503	0.0019	0.1156	0.0042	0.0172	0.0005	0.25	109.9	2.8	110.8	3.8	140	70	109.9	2.8	0.8

980731-2_33	920	17.6	0.0497	0.0015	0.1201	0.0038	0.0177	0.0003	0.31	113.3	1.7	114.9	3.4	167	66	113.3	1.7	1.4
980731-2_34	648	13.3	0.0487	0.0017	0.1201	0.0051	0.0171	0.0004	0.36	109.0	2.3	114.9	4.6	234	88	109.0	2.3	5.1
980731-2_35	867	18.1	0.0495	0.0016	0.1039	0.0038	0.0153	0.0003	0.26	97.7	2.0	100.1	3.5	186	73	97.7	2.0	2.4
980731-2_36	762	20.4	0.0511	0.0022	0.1247	0.0054	0.0180	0.0006	0.21	114.9	3.5	118.8	4.9	177	82	114.9	3.5	3.3
980731-2_37	955	14.5	0.0503	0.0019	0.1151	0.0038	0.0171	0.0004	0.34	109.2	2.2	110.4	3.5	158	70	109.2	2.2	1.1
980731-2_38	987	16.8	0.0502	0.0021	0.1159	0.0033	0.0173	0.0003	0.35	110.7	1.7	111.2	3.0	138	58	110.7	1.7	0.4
980731-2_39	651	22.7	0.0491	0.0017	0.1169	0.0053	0.0170	0.0006	0.28	108.7	4.0	111.9	4.8	201	85	108.7	4.0	2.9
980731-2_40	730	19.4	0.0487	0.0014	0.1198	0.0049	0.0175	0.0005	0.32	112.0	3.2	114.5	4.4	188	76	112.0	3.2	2.2
980731-2_41	1070	15.1	0.0569	0.0032	0.1144	0.0034	0.0172	0.0003	0.42	109.9	1.7	109.8	3.1	127	59	109.9	1.7	0.1
980731-2_42	571	14.4	0.0505	0.0022	0.1153	0.0047	0.0175	0.0002	0.37	111.6	1.5	111.1	4.4	113	82	111.6	1.5	0.5
980731-2_43	1070	15.9	0.0502	0.0019	0.1104	0.0038	0.0167	0.0004	0.24	106.5	2.2	106.1	3.5	108	69	106.5	2.2	0.4
980731-2_44	670	22.6	0.0484	0.0014	0.1129	0.0037	0.0170	0.0002	0.15	108.5	1.5	108.4	3.3	124	67	108.5	1.5	0.1
980731-2_45	721	13.2	0.0477	0.0020	0.1157	0.0037	0.0173	0.0002	0.28	110.6	1.2	110.9	3.4	131	65	110.6	1.2	0.3
980731-2_46	1128	11.0	0.0481	0.0017	0.1132	0.0037	0.0170	0.0003	0.22	108.8	1.9	108.7	3.4	87	57	108.8	1.9	0.1
980731-2_47	886	11.9	0.0485	0.0016	0.1129	0.0035	0.0171	0.0002	0.38	109.2	1.3	108.5	3.2	102	61	109.2	1.3	0.6
980731-2_48	872	10.8	0.0490	0.0015	0.1161	0.0034	0.0172	0.0003	0.24	110.1	2.0	111.4	3.1	154	62	110.1	2.0	1.2
980731-2_49	1006	10.6	0.0487	0.0018	0.1128	0.0036	0.0167	0.0003	0.30	106.8	1.7	108.7	3.3	154	64	106.8	1.7	1.7
980731-2_50	842	10.6	0.0502	0.0016	0.1116	0.0033	0.0167	0.0003	0.20	106.7	1.7	107.2	3.0	125	59	106.7	1.7	0.5

DETRITAL APATITE U-Pb GEOCHRONOLOGY

Analysis	U (ppm)	U/Th	207Pb/ 206Pb	2σ error	207Pb/ 235U	2σ error	206Pb/ 238U	2σ error	err. corr.	207Pb/ 204Pb	206Pb/ 204Pb	206Pb/238U age (Ma)	2σ error (Ma)	Best age (Ma)	2σ error (Ma)	Disc. %
NV12-162CB																
ANV12_162CB_0	4.9	0.4	0.375	0.017	2.870	0.140	0.0565	0.004	0.79	15.60	18.67	123.4	7.2	123.4	7.2	111.8
ANV12_162CB_1	6.5	0.6	0.369	0.016	2.179	0.088	0.0431	0.002	0.50	15.61	18.67	97.4	5.7	97.4	5.7	108.2
ANV12_162CB_2	4.6	0.5	0.386	0.019	2.800	0.120	0.0542	0.003	0.53	15.60	18.67	110.7	6.7	110.7	6.7	113.2
ANV12_162CB_3	6.6	0.4	0.370	0.017	2.544	0.092	0.0511	0.003	0.41	15.60	18.67	114.9	6.1	114.9	6.1	109.4
ANV12_162CB_4	5.2	0.4	0.383	0.017	2.372	0.096	0.0454	0.002	0.52	15.61	18.67	94.4	5.8	94.4	5.8	110.9
ANV12_162CB_5	8.0	0.5	0.356	0.017	2.090	0.130	0.0430	0.002	0.10	15.61	18.67	104.4	6.7	104.4	6.7	104.5
ANV12_162CB_6	9.7	1.0	0.378	0.029	4.290	0.870	0.0730	0.012	0.96	15.59	18.67	157.0	17.5	157.0	17.5	110.2
ANV12_162CB_7	5.4	0.7	0.415	0.015	4.090	0.260	0.0714	0.005	0.84	15.59	18.67	119.3	7.2	119.3	7.2	123.0
ANV12_162CB_8	4.5	0.5	0.420	0.02	4.510	0.280	0.0790	0.005	0.79	15.59	18.67	127.0	7.7	127.0	7.7	123.7
ANV12_162CB_9	5.5	0.4	0.392	0.023	2.760	0.110	0.0527	0.003	0.44	15.60	18.67	103.5	7.6	103.5	7.6	113.3
ANV12_162CB_10	5.1	0.5	0.399	0.018	2.820	0.110	0.0534	0.003	0.53	15.60	18.67	100.0	6.8	100.0	6.8	115.0
ANV12_162CB_11	5.1	0.5	0.387	0.019	2.830	0.110	0.0554	0.003	0.41	15.60	18.67	112.4	6.2	112.4	6.2	113.4
ANV12_162CB_12	4.8	0.6	0.420	0.018	4.430	0.180	0.0783	0.004	0.57	15.59	18.67	125.9	5.9	125.9	5.9	124.7
ANV12_162CB_13	6.2	0.4	0.390	0.018	2.930	0.120	0.0557	0.003	0.53	15.60	18.67	110.9	6.3	110.9	6.3	114.4
ANV12_162CB_14	5.7	0.5	0.387	0.017	2.620	0.110	0.0503	0.003	0.54	15.60	18.67	102.0	6.1	102.0	6.1	113.2
ANV12_162CB_15	8.2	0.5	0.413	0.016	3.360	0.130	0.0595	0.003	0.54	15.60	18.67	100.7	5.4	100.7	5.4	121.4
ANV12_162CB_16	10.1	1.2	0.355	0.012	2.082	0.052	0.0427	0.001	0.47	15.61	18.67	104.2	4.2	104.2	4.2	105.8
ANV12_162CB_17	7.1	0.9	0.358	0.017	2.290	0.150	0.0457	0.003	0.72	15.61	18.67	109.8	6.6	109.8	6.6	107.3
ANV12_162CB_18	9.3	0.6	0.330	0.018	1.770	0.130	0.0382	0.002	0.69	15.61	18.67	105.5	7.2	105.5	7.2	99.2
ANV12_162CB_19	6.7	0.4	0.393	0.018	2.760	0.100	0.0513	0.002	0.45	15.60	18.67	100.0	5.9	100.0	5.9	115.6
ANV12_162CB_20	9.8	0.8	0.313	0.013	1.538	0.058	0.0361	0.002	0.49	15.61	18.67	107.6	5.5	107.6	5.5	95.1
ANV12_162CB_21	4.6	0.6	0.413	0.018	3.400	0.150	0.0595	0.003	0.55	15.60	18.67	100.7	5.9	100.7	5.9	121.4
ANV12_162CB_22	6.6	0.5	0.364	0.015	2.201	0.091	0.0437	0.002	0.59	15.61	18.67	101.6	5.8	101.6	5.8	107.8
ANV12_162CB_23	7.0	0.4	0.383	0.015	2.830	0.110	0.0539	0.002	0.51	15.60	18.67	112.1	5.5	112.1	5.5	114.4
ANV12_162CB_24	6.1	0.8	0.439	0.016	4.790	0.260	0.0763	0.004	0.75	15.59	18.67	103.7	6.2	103.7	6.2	130.6
ANV12_162CB_25	7.1	0.6	0.345	0.017	2.147	0.081	0.0461	0.002	0.45	15.61	18.67	118.5	6.2	118.5	6.2	104.3
ANV12_162CB_26	7.8	0.5	0.374	0.016	2.232	0.076	0.0439	0.002	0.44	15.61	18.67	96.3	5.5	96.3	5.5	110.0
ANV12_162CB_27	8.9	0.4	0.366	0.013	2.530	0.095	0.0500	0.002	0.62	15.60	18.67	115.0	5.0	115.0	5.0	110.5
ANV12_162CB_28	7.6	0.4	0.367	0.015	2.464	0.074	0.0485	0.002	0.45	15.60	18.67	110.9	5.2	110.9	5.2	110.8
ANV12_162CB_29	10.0	1.0	0.352	0.012	2.013	0.071	0.0416	0.002	0.68	15.61	18.67	103.1	5.0	103.1	5.0	105.5

ANV12_162CB_30	6.0	0.4	0.402	0.017	3.470	0.150	0.0629	0.003	0.64	15.60	18.67	115.5	6.3	115.5	6.3	120.8
ANV12_162CB_31	5.8	0.5	0.389	0.014	3.470	0.130	0.0655	0.003	0.71	15.59	18.67	131.4	5.8	131.4	5.8	118.9
ANV12_162CB_32	7.0	0.4	0.400	0.017	3.110	0.130	0.0552	0.003	0.59	15.60	18.67	102.7	5.9	102.7	5.9	118.4
ANV12_162CB_33	7.7	0.5	0.341	0.013	1.989	0.069	0.0411	0.002	0.41	15.61	18.67	107.7	4.8	107.7	4.8	103.9
ANV12_162CB_34	7.9	0.5	0.376	0.015	2.609	0.089	0.0498	0.002	0.43	15.60	18.67	108.1	5.0	108.1	5.0	112.6
ANV12_162CB_35	4.8	0.8	0.444	0.016	4.550	0.170	0.0736	0.003	0.61	15.59	18.67	95.1	5.5	95.1	5.5	131.9
ANV12_162CB_36	9.8	0.5	0.357	0.015	1.966	0.055	0.0401	0.002	0.18	15.61	18.67	96.8	4.9	96.8	4.9	105.4
ANV12_162CB_37	7.7	0.4	0.378	0.013	2.762	0.074	0.0521	0.002	0.54	15.60	18.67	111.7	4.7	111.7	4.7	114.2
ANV12_162CB_38	6.3	0.5	0.329	0.014	1.974	0.071	0.0435	0.002	0.47	15.61	18.67	120.8	5.5	120.8	5.5	100.9
ANV12_162CB_39	7.5	0.5	0.397	0.015	3.073	0.098	0.0555	0.002	0.47	15.60	18.67	105.4	4.9	105.4	4.9	118.5
ANV12_162CB_40	8.4	0.5	0.360	0.016	2.072	0.090	0.0413	0.002	0.53	15.61	18.67	98.1	5.5	98.1	5.5	106.9
ANV12_162CB_41	7.7	0.4	0.366	0.013	2.455	0.075	0.0482	0.002	0.46	15.60	18.67	110.8	4.8	110.8	4.8	110.7
ANV12_162CB_42	5.9	0.5	0.416	0.018	3.840	0.220	0.0680	0.005	0.77	15.59	18.67	112.6	7.6	112.6	7.6	123.4
ANV12_162CB_43	5.9	0.6	0.439	0.017	4.710	0.230	0.0776	0.005	0.63	15.59	18.67	105.5	6.9	105.5	6.9	130.1
ANV12_162CB_44	6.0	0.5	0.400	0.017	3.140	0.150	0.0557	0.002	0.60	15.60	18.67	103.6	5.6	103.6	5.6	118.9
ANV12_162CB_45	5.9	0.6	0.425	0.015	4.090	0.150	0.0692	0.003	0.65	15.59	18.67	106.5	5.4	106.5	5.4	127.3
ANV12_162CB_46	9.0	0.6	0.376	0.015	3.020	0.140	0.0585	0.003	0.73	15.60	18.67	127.1	6.5	127.1	6.5	114.0
ANV12_162CB_47	5.7	0.5	0.411	0.018	3.210	0.170	0.0561	0.003	0.71	15.60	18.67	96.4	6.1	96.4	6.1	121.1
ANV12_162CB_48	5.8	0.4	0.389	0.019	2.893	0.091	0.0544	0.002	0.51	15.60	18.67	109.0	5.9	109.0	5.9	115.3
ANV12_162CB_49	6.0	0.5	0.413	0.017	3.270	0.110	0.0570	0.002	0.45	15.60	18.67	96.5	5.2	96.5	5.2	121.4
ANV12_162CB_50	9.6	0.8	0.397	0.014	3.050	0.120	0.0557	0.002	0.62	15.60	18.67	105.8	5.1	105.8	5.1	118.1
ANV12_162CB_51	6.6	0.5	0.386	0.018	2.762	0.080	0.0533	0.003	0.34	15.60	18.67	108.8	6.0	108.8	6.0	114.6
ANV12_162CB_52	7.6	0.4	0.399	0.017	2.890	0.110	0.0523	0.002	0.36	15.60	18.67	97.9	5.5	97.9	5.5	117.1
ANV12_162CB_53	5.7	0.5	0.419	0.017	3.170	0.150	0.0550	0.003	0.60	15.60	18.67	88.7	5.9	88.7	5.9	121.5
ANV12_162CB_54	7.0	0.7	0.361	0.015	2.601	0.084	0.0525	0.002	0.48	15.60	18.67	124.2	5.1	124.2	5.1	110.0
ANV12_162CB_55	7.6	0.5	0.377	0.015	2.520	0.100	0.0483	0.002	0.61	15.60	18.67	104.2	5.7	104.2	5.7	111.9
ANV12_162CB_56	6.7	0.4	0.350	0.016	2.030	0.077	0.0424	0.002	0.53	15.61	18.67	106.2	6.0	106.2	6.0	104.5
ANV12_162CB_57	8.4	0.5	0.402	0.018	2.586	0.075	0.0482	0.002	0.34	15.60	18.67	88.3	5.6	88.3	5.6	115.3
ANV12_162CB_58	8.2	0.5	0.377	0.016	2.641	0.076	0.0512	0.002	0.30	15.60	18.67	110.5	5.3	110.5	5.3	112.5
ANV12_162CB_59	7.0	0.5	0.392	0.014	3.311	0.089	0.0613	0.002	0.44	15.60	18.67	120.5	4.9	120.5	4.9	119.1
ANV12_162CB_60	7.5	0.6	0.412	0.013	4.680	0.130	0.0828	0.003	0.58	15.58	18.67	141.8	4.7	141.8	4.7	125.4
ANV12_162CB_61	7.2	0.6	0.412	0.016	3.510	0.200	0.0620	0.004	0.76	15.60	18.67	105.8	6.7	105.8	6.7	121.9
ANV12_162CB_62	16.4	1.0	0.318	0.02	1.980	0.180	0.0432	0.003	0.88	15.61	18.67	126.1	8.6	126.1	8.6	97.6
ANV12_162CB_63	6.2	0.6	0.373	0.016	2.730	0.130	0.0531	0.003	0.60	15.60	18.67	117.3	5.9	117.3	5.9	112.2
ANV12_162CB_64	6.2	0.4	0.385	0.019	2.720	0.100	0.0534	0.003	0.58	15.60	18.67	109.7	6.7	109.7	6.7	113.1

Analysis	U (ppm)	U/Th	207Pb/ 206Pb	2σ error	207Pb/ 235U	2σ error	206Pb/ 238U	2σ error	err. corr.	207Pb/ 204Pb	206Pb/ 204Pb	206Pb/238U age (Ma)	2σ error (Ma)	Best age (Ma)	2σ error (Ma)	Disc. %
NV12-176CB																
ANV12_176CB_0	7.2	0.4	0.405	0.014	3.412	0.086	0.0613	0.002	0.54	15.60	18.67	108.7	4.8	108.7	4.8	120.9
ANV12_176CB_1	7.7	0.5	0.392	0.016	2.522	0.081	0.0466	0.002	0.58	15.61	18.67	90.4	5.3	90.4	5.3	114.3
ANV12_176CB_2	6.9	0.5	0.419	0.013	3.720	0.110	0.0643	0.002	0.20	15.60	18.67	102.3	4.6	102.3	4.6	124.4
ANV12_176CB_3	9.8	0.6	0.414	0.012	3.360	0.110	0.0586	0.002	0.67	15.60	18.67	97.0	4.5	97.0	4.5	122.3
ANV12_176CB_4	3.3	0.5	0.467	0.024	6.380	0.500	0.0985	0.007	0.75	15.57	18.67	95.5	9.0	95.5	9.0	135.5
ANV12_176CB_5	10.8	0.6	0.410	0.014	3.010	0.120	0.0538	0.002	0.62	15.60	18.67	91.8	5.2	91.8	5.2	120.0
ANV12_176CB_6	8.2	0.4	0.389	0.017	2.280	0.110	0.0423	0.002	0.16	15.61	18.67	83.6	5.5	83.6	5.5	112.5
ANV12_176CB_7	12.7	0.6	0.363	0.011	2.210	0.054	0.0441	0.001	0.49	15.61	18.67	102.2	3.9	102.2	3.9	108.0
ANV12_176CB_8	5.0	0.9	0.388	0.02	3.930	0.370	0.0714	0.006	0.87	15.59	18.67	142.7	9.5	142.7	9.5	117.2
ANV12_176CB_9	3.5	0.4	0.446	0.014	7.450	0.740	0.1150	0.010	0.94	15.56	18.67	144.0	9.2	144.0	9.2	130.5
ANV12_176CB_10	7.1	0.6	0.397	0.012	3.420	0.120	0.0628	0.003	0.68	15.60	18.67	118.0	5.0	118.0	5.0	119.3
ANV12_176CB_11	6.8	0.4	0.389	0.016	2.824	0.099	0.0534	0.002	0.49	15.60	18.67	105.8	4.9	105.8	4.9	115.2
ANV12_176CB_12	7.0	0.5	0.425	0.015	3.660	0.130	0.0631	0.003	0.64	15.60	18.67	95.5	5.5	95.5	5.5	124.5
ANV12_176CB_13	7.9	0.4	0.387	0.015	2.560	0.110	0.0478	0.002	0.61	15.60	18.67	95.8	5.2	95.8	5.2	113.1
ANV12_176CB_14	5.9	0.4	0.397	0.014	3.340	0.160	0.0614	0.004	0.78	15.60	18.67	115.3	6.4	115.3	6.4	119.2
ANV12_176CB_15	5.2	0.6	0.388	0.017	2.890	0.130	0.0548	0.003	0.61	15.60	18.67	109.3	6.1	109.3	6.1	114.6
ANV12_176CB_16	6.8	0.4	0.383	0.016	2.670	0.100	0.0514	0.002	0.48	15.60	18.67	105.8	5.3	105.8	5.3	113.1
ANV12_176CB_17	9.6	0.6	0.352	0.017	2.240	0.160	0.0461	0.003	0.81	15.61	18.67	113.4	7.5	113.4	7.5	105.2
ANV12_176CB_18	6.7	0.5	0.402	0.014	3.980	0.290	0.0714	0.005	0.87	15.59	18.67	129.7	7.7	129.7	7.7	121.1
ANV12_176CB_19	7.7	0.5	0.382	0.014	2.560	0.078	0.0490	0.002	0.51	15.60	18.67	101.4	5.0	101.4	5.0	112.8
ANV12_176CB_20	12.7	0.6	0.321	0.012	1.634	0.049	0.0371	0.001	0.12	15.61	18.67	106.1	4.2	106.1	4.2	97.2
ANV12_176CB_21	9.6	0.7	0.329	0.013	1.749	0.050	0.0392	0.002	0.33	15.61	18.67	108.1	5.2	108.1	5.2	99.3
ANV12_176CB_22	10.4	0.5	0.356	0.012	2.164	0.061	0.0444	0.002	0.42	15.61	18.67	106.9	4.4	106.9	4.4	106.1
ANV12_176CB_23	8.0	0.4	0.369	0.015	2.193	0.073	0.0442	0.002	0.56	15.61	18.67	98.9	5.3	98.9	5.3	108.1
ANV12_176CB_24	7.2	0.5	0.402	0.014	3.550	0.150	0.0641	0.003	0.74	15.60	18.67	116.3	5.3	116.3	5.3	120.1
ANV12_176CB_25	5.6	0.6	0.418	0.018	3.880	0.190	0.0682	0.004	0.70	15.59	18.67	109.5	6.3	109.5	6.3	123.4
ANV12_176CB_26	6.2	0.5	0.400	0.016	3.320	0.120	0.0604	0.002	0.57	15.60	18.67	111.1	5.1	111.1	5.1	118.4
ANV12_176CB_27	5.5	0.5	0.387	0.015	3.330	0.130	0.0629	0.003	0.54	15.60	18.67	126.4	5.3	126.4	5.3	116.6
ANV12_176CB_28	8.4	0.5	0.381	0.018	2.420	0.150	0.0464	0.002	0.77	15.61	18.67	96.6	6.2	96.6	6.2	110.7
ANV12_176CB_29	10.1	0.5	0.371	0.013	2.350	0.062	0.0462	0.002	0.41	15.61	18.67	102.2	4.3	102.2	4.3	109.9
ANV12_176CB_30	6.0	0.4	0.390	0.017	2.964	0.092	0.0566	0.003	0.47	15.60	18.67	111.4	5.8	111.4	5.8	115.5

ANV12_176CB_31	7.3	0.5	0.359	0.013	2.327	0.074	0.0482	0.002	0.67	15.60	18.67	114.2	5.5	114.2	5.5	107.4
ANV12_176CB_32	7.7	0.4	0.427	0.013	3.790	0.180	0.0652	0.003	0.80	15.59	18.67	97.0	5.7	97.0	5.7	125.4
ANV12_176CB_33	7.5	0.5	0.386	0.013	2.900	0.130	0.0539	0.002	0.69	15.60	18.67	108.9	5.1	108.9	5.1	115.4
ANV12_176CB_34	9.7	0.5	0.367	0.014	2.585	0.095	0.0511	0.002	0.62	15.60	18.67	115.8	5.2	115.8	5.2	110.4
ANV12_176CB_35	6.4	0.5	0.398	0.014	3.410	0.110	0.0621	0.002	0.57	15.60	18.67	115.8	4.7	115.8	4.7	119.3
ANV12_176CB_36	9.5	0.6	0.362	0.015	2.129	0.096	0.0428	0.002	0.58	15.61	18.67	99.7	5.3	99.7	5.3	106.8
ANV12_176CB_37	7.4	0.5	0.405	0.017	2.879	0.097	0.0519	0.002	0.40	15.60	18.67	91.9	5.7	91.9	5.7	118.0
ANV12_176CB_38	8.2	0.6	0.387	0.012	2.864	0.081	0.0531	0.002	0.39	15.60	18.67	106.5	3.9	106.5	3.9	115.8
ANV12_176CB_39	7.1	0.5	0.393	0.016	3.350	0.230	0.0609	0.004	0.81	15.60	18.67	117.6	7.2	117.6	7.2	117.4
ANV12_176CB_40	5.1	0.5	0.461	0.016	8.200	0.930	0.1250	0.013	0.95	15.55	18.67	132.1	10.9	132.1	10.9	132.5
ANV12_176CB_41	6.4	0.4	0.393	0.019	2.454	0.080	0.0466	0.002	0.45	15.61	18.67	89.8	6.3	89.8	6.3	113.2
ANV12_176CB_42	8.1	0.4	0.395	0.014	2.665	0.074	0.0494	0.002	0.54	15.60	18.67	93.9	5.0	93.9	5.0	115.6
ANV12_176CB_43	7.0	0.4	0.350	0.011	2.312	0.084	0.0478	0.002	0.60	15.60	18.67	118.8	5.0	118.8	5.0	107.1
ANV12_176CB_44	5.2	0.6	0.422	0.018	3.860	0.120	0.0658	0.003	0.35	15.59	18.67	102.2	5.7	102.2	5.7	126.6
ANV12_176CB_45	7.7	0.4	0.380	0.015	2.649	0.066	0.0504	0.002	0.39	15.60	18.67	105.7	4.8	105.7	4.8	113.1
ANV12_176CB_46	6.8	0.4	0.374	0.014	2.589	0.082	0.0506	0.002	0.49	15.60	18.67	110.1	5.3	110.1	5.3	112.0
ANV12_176CB_47	6.8	0.5	0.369	0.015	2.420	0.085	0.0475	0.002	0.57	15.61	18.67	106.4	5.6	106.4	5.6	110.4
ANV12_176CB_48	6.4	0.5	0.386	0.015	3.037	0.099	0.0572	0.002	0.49	15.60	18.67	115.6	5.2	115.6	5.2	116.6
ANV12_176CB_49	6.1	0.5	0.392	0.015	3.035	0.085	0.0562	0.002	0.39	15.60	18.67	109.1	5.2	109.1	5.2	117.4
ANV12_176CB_50	6.6	0.4	0.406	0.017	2.930	0.100	0.0520	0.002	0.31	15.60	18.67	91.4	5.1	91.4	5.1	118.6
ANV12_176CB_51	7.9	0.5	0.344	0.015	1.982	0.065	0.0415	0.002	0.44	15.61	18.67	106.4	5.2	106.4	5.2	103.3
ANV12_176CB_52	6.7	0.4	0.400	0.017	2.990	0.100	0.0548	0.002	0.43	15.60	18.67	100.7	5.5	100.7	5.5	118.1
ANV12_176CB_53	7.1	0.5	0.375	0.014	2.661	0.096	0.0518	0.002	0.58	15.60	18.67	112.0	5.0	112.0	5.0	113.2
ANV12_176CB_54	7.8	0.4	0.334	0.015	1.823	0.065	0.0400	0.002	0.38	15.61	18.67	107.7	5.4	107.7	5.4	100.4
ANV12_176CB_55	7.1	0.5	0.420	0.016	3.760	0.280	0.0632	0.004	0.85	15.60	18.67	99.8	7.0	99.8	7.0	124.1
ANV12_176CB_56	5.3	0.5	0.416	0.018	3.760	0.150	0.0661	0.004	0.56	15.59	18.67	107.8	6.5	107.8	6.5	123.6
ANV12_176CB_57	3.5	0.6	0.444	0.014	6.290	0.280	0.1017	0.005	0.79	15.57	18.67	129.6	6.0	129.6	6.0	134.2
ANV12_176CB_58	7.4	0.5	0.364	0.016	2.550	0.120	0.0500	0.002	0.50	15.60	18.67	115.2	5.3	115.2	5.3	109.9
ANV12_176CB_59	9.0	0.5	0.370	0.013	2.542	0.068	0.0502	0.002	0.42	15.60	18.67	111.8	4.7	111.8	4.7	110.9
ANV12_176CB_60	6.6	0.5	0.402	0.016	3.500	0.100	0.0638	0.003	0.42	15.60	18.67	115.7	5.6	115.7	5.6	120.3
ANV12_176CB_61	7.0	0.5	0.397	0.014	3.420	0.180	0.0626	0.003	0.81	15.60	18.67	117.6	5.8	117.6	5.8	119.0
ANV12_176CB_62	8.8	0.5	0.381	0.017	2.770	0.150	0.0528	0.003	0.66	15.60	18.67	110.1	6.1	110.1	6.1	113.1

DETRITAL APATITE REE CHEMISTRY

Analysis	La (ppm)	2σ	Ce (ppm)	2σ	Pr (ppm)	2σ	Nd (ppm)	2σ	Sm (ppm)	2σ	Eu (ppm)	2σ	Gd (ppm)	2σ	Tb (ppm)	2σ	Dy (ppm)	2σ
NV12-162CB																		
ANV12_162CB_0	736	29	1655	86	218	11	886	41	152	8	16	2	125	8	15	1	73	4
ANV12_162CB_1	555	26	1289	67	168	8	671	35	107	7	14	1	100	6	12	1	60	3
ANV12_162CB_2	515	18	1298	43	157	7	580	28	93	5	15	1	79	5	10	1	55	4
ANV12_162CB_3	716	22	1790	100	235	8	930	44	160	9	18	1	141	7	17	1	86	5
ANV12_162CB_4	629	33	1410	110	171	12	633	46	100	8	18	2	93	8	11	1	61	5
ANV12_162CB_5	495	35	1130	100	130	12	455	44	71	9	12	1	63	7	8	1	42	4
ANV12_162CB_6	648	42	1460	100	173	12	590	45	88	7	15	1	79	7	9	1	51	4
ANV12_162CB_7	490	18	1367	80	191	9	766	40	145	8	11	1	140	8	18	1	105	5
ANV12_162CB_8	622	49	1380	130	162	13	579	44	91	8	14	1	80	6	9	1	50	5
ANV12_162CB_9	736	27	1640	100	200	10	721	42	118	9	20	1	101	7	12	1	64	4
ANV12_162CB_10	607	36	1560	120	191	12	699	51	115	13	19	2	99	9	12	1	64	4
ANV12_162CB_11	479	14	1158	36	146	4	554	18	90	5	14	1	78	4	9	0	52	3
ANV12_162CB_12	471	18	997	49	107	5	371	22	54	4	12	1	48	4	5	0	28	2
ANV12_162CB_13	828	37	1831	81	223	8	810	28	130	7	21	1	113	6	13	0	72	3
ANV12_162CB_14	700	49	1700	150	210	16	791	62	127	12	19	2	116	9	14	1	76	6
ANV12_162CB_15	712	29	1674	89	196	9	698	32	110	7	18	1	98	6	12	1	70	3
ANV12_162CB_16	36	29	109	69	17	9	78	31	23	4	6	1	38	6	6	1	38	5
ANV12_162CB_17	335	15	811	37	109	4	434	17	74	4	17	1	67	4	8	0	42	3
ANV12_162CB_18	340	49	920	130	139	20	623	94	139	23	19	3	128	21	16	3	86	13
ANV12_162CB_19	608	47	1490	120	197	14	736	57	121	9	18	2	108	8	13	1	72	5
ANV12_162CB_20	604	39	1464	87	190	12	728	50	118	9	19	2	110	9	13	1	73	5
ANV12_162CB_21	571	39	1255	94	156	9	582	33	94	7	13	1	80	6	10	1	53	4
ANV12_162CB_22	508	13	986	29	108	4	373	16	48	3	14	1	41	3	5	0	26	2
ANV12_162CB_23	721	29	1850	110	239	9	913	35	157	8	19	1	131	7	16	1	82	4
ANV12_162CB_24	810	56	1840	180	214	19	779	75	125	12	21	2	105	9	13	1	67	7
ANV12_162CB_25	413	29	879	75	106	10	382	37	60	6	12	1	53	6	6	1	32	4
ANV12_162CB_26	504	25	1202	67	147	7	569	29	96	6	12	1	86	5	10	1	54	3
ANV12_162CB_27	684	37	1760	130	205	13	706	57	114	11	19	2	100	10	12	1	66	6
ANV12_162CB_28	822	36	1980	100	253	10	941	41	151	10	21	2	128	7	16	1	89	6
ANV12_162CB_29	814	41	1830	160	218	15	826	66	136	12	20	2	117	11	14	1	71	6
ANV12_162CB_30	258	17	908	64	161	6	802	34	204	9	24	1	191	9	26	1	150	6
ANV12_162CB_31	646	26	1675	78	222	8	882	35	158	9	25	1	133	6	17	1	89	4
ANV12_162CB_32	609	54	1560	160	178	16	629	63	103	12	17	2	91	9	11	1	63	6
ANV12_162CB_33	712	26	1603	72	194	10	710	32	121	8	19	1	103	6	12	1	69	3
ANV12_162CB_34	572	77	1240	190	144	22	516	82	78	14	14	2	68	12	8	2	48	10
ANV12_162CB_35	702	27	1508	88	174	10	641	38	101	7	14	1	91	6	11	1	56	3
ANV12_162CB_36	477	25	1087	80	131	7	505	33	84	6	11	1	69	5	8	0	40	4
ANV12_162CB_37	822	19	1915	56	237	6	884	24	141	7	21	1	128	7	15	1	86	4
ANV12_162CB_38	762	31	1884	99	249	9	988	39	169	8	23	1	145	6	17	1	92	4
ANV12_162CB_39	748	43	2010	200	240	15	830	49	141	11	22	2	115	9	14	1	78	6
ANV12_162CB_40	727	31	1680	100	195	10	707	45	115	10	18	2	100	8	12	1	65	5
ANV12_162CB_41	767	44	1760	140	213	13	799	50	133	12	20	2	112	7	13	1	73	5
ANV12_162CB_42	842	34	1930	120	230	11	848	43	134	10	21	2	109	6	13	1	71	4
ANV12_162CB_43	651	37	1640	120	210	13	802	48	142	10	21	2	117	9	15	1	80	6

ANV12_162CB_44	475	34	1095	99	144	11	558	49	97	9	15	2	89	8	11	1	54	5
ANV12_162CB_45	624	21	1495	91	192	7	763	38	139	9	19	1	123	6	15	1	76	3
ANV12_162CB_46	395	23	1046	93	145	10	593	48	107	10	13	1	90	6	11	1	57	5
ANV12_162CB_47	822	30	1641	75	177	11	622	38	91	9	19	1	79	5	9	1	46	4
ANV12_162CB_48	667	23	1549	80	186	8	698	28	111	6	18	1	94	6	11	1	61	3
ANV12_162CB_49	805	40	2100	150	245	14	836	53	139	10	22	2	118	8	14	1	74	5
ANV12_162CB_50	553	25	1317	71	163	8	623	29	100	7	15	1	84	5	11	1	58	4
ANV12_162CB_51	387	29	958	80	131	11	515	44	96	10	16	2	83	7	10	1	51	6
ANV12_162CB_52	656	36	1620	140	202	11	792	50	136	12	21	2	113	7	14	1	74	4
ANV12_162CB_53	778	35	1753	74	208	9	772	37	126	9	19	1	116	8	13	1	68	4
ANV12_162CB_54	554	42	1320	130	173	15	693	58	114	12	15	2	98	10	12	1	65	5
ANV12_162CB_55	461	30	1060	110	126	11	481	47	71	7	11	1	66	6	8	1	41	4
ANV12_162CB_56	767	56	1890	190	240	18	894	75	156	15	19	2	133	11	17	2	90	9
ANV12_162CB_57	682	33	1430	110	175	10	675	40	112	6	17	1	91	5	10	1	54	3
ANV12_162CB_58	737	21	1739	92	191	7	653	20	98	6	17	1	93	5	11	0	60	3
ANV12_162CB_59	658	27	1675	75	217	10	854	40	146	10	18	2	125	7	15	1	78	5
ANV12_162CB_60	717	27	1639	85	199	10	747	45	127	9	19	2	111	8	13	1	71	6
ANV12_162CB_61	458	19	1080	61	134	9	513	38	91	7	16	1	86	7	11	1	59	5
ANV12_162CB_62	670	25	1470	110	163	10	597	51	92	9	16	1	81	7	9	1	46	5
ANV12_162CB_63	492	29	1015	66	117	7	444	26	71	5	16	1	63	4	8	1	42	3
ANV12_162CB_64	641	41	1210	84	127	9	435	34	63	6	15	1	54	5	6	1	33	3

Analysis	Ho (ppm)	2σ	Er (ppm)	2σ	Tm (ppm)	2σ	Yb (ppm)	2σ	Lu (ppm)	2σ	Th (ppm)	2σ	U (ppm)	2σ
NV12-162CB														
ANV12_162CB_0	15	1	38	2	5	0	30	2	6	0	33	2	14.6	0.9
ANV12_162CB_1	12	1	33	3	5	0	31	2	6	0	32	2	18.3	1.1
ANV12_162CB_2	12	1	36	2	5	0	39	3	7	0	24	1	13.0	0.8
ANV12_162CB_3	16	1	45	3	6	0	35	3	7	0	35	2	15.4	0.9
ANV12_162CB_4	13	1	38	4	5	1	37	4	8	1	31	2	14.3	1.1
ANV12_162CB_5	10	1	29	3	4	1	32	4	6	1	35	2	20.8	1.3
ANV12_162CB_6	11	1	37	3	6	1	45	4	10	1	27	2	30.3	7.1
ANV12_162CB_7	23	1	70	5	11	1	70	5	14	1	20	2	14.6	1.7
ANV12_162CB_8	11	1	28	3	4	0	27	2	6	1	22	4	11.5	1.3
ANV12_162CB_9	14	1	39	3	5	1	37	2	7	1	35	2	14.8	0.8
ANV12_162CB_10	14	1	44	4	6	1	45	3	9	1	28	2	14.2	1.1
ANV12_162CB_11	11	0	33	2	5	0	30	2	5	0	22	1	11.7	0.5
ANV12_162CB_12	6	1	16	1	2	0	14	1	3	0	21	1	11.6	0.6
ANV12_162CB_13	15	1	45	2	6	0	44	2	9	1	34	2	13.8	0.9
ANV12_162CB_14	16	1	47	4	6	1	45	4	9	1	29	2	14.4	1.0
ANV12_162CB_15	15	1	47	3	6	1	51	4	10	1	34	3	16.4	1.1
ANV12_162CB_16	10	2	31	4	4	1	30	4	5	1	9	3	1.0	0.9
ANV12_162CB_17	9	0	24	1	3	0	21	2	4	0	20	1	21.7	0.9
ANV12_162CB_18	17	3	43	7	6	1	35	5	6	1	24	3	18.5	2.0
ANV12_162CB_19	15	1	42	3	6	1	40	5	7	1	35	2	21.1	2.6
ANV12_162CB_20	16	1	46	2	6	1	48	4	9	1	32	2	13.6	0.7
ANV12_162CB_21	11	1	31	3	4	0	28	2	5	0	29	3	22.0	1.6

ANV12_162CB_22	6	0	18	1	3	0	19	2	4	0	17	1	10.1	0.6
ANV12_162CB_23	18	1	49	4	7	1	46	3	10	1	35	3	16.4	1.1
ANV12_162CB_24	14	1	44	5	6	1	43	5	8	1	42	3	16.9	1.3
ANV12_162CB_25	7	1	20	3	3	0	19	3	4	0	19	2	14.3	0.8
ANV12_162CB_26	11	1	29	2	4	0	27	2	6	0	28	2	15.8	1.1
ANV12_162CB_27	15	1	46	4	7	1	60	6	13	1	36	3	18.4	1.5
ANV12_162CB_28	19	1	56	3	8	1	58	5	11	1	43	1	18.0	0.8
ANV12_162CB_29	15	2	43	4	6	1	38	4	7	1	43	2	17.5	1.6
ANV12_162CB_30	30	1	85	4	11	1	71	3	11	1	26	1	23.5	1.0
ANV12_162CB_31	18	1	50	2	7	0	40	2	7	0	32	2	13.3	0.7
ANV12_162CB_32	14	1	38	4	6	1	43	6	8	1	31	3	14.8	0.9
ANV12_162CB_33	15	1	40	3	6	1	42	3	8	0	31	2	13.9	0.8
ANV12_162CB_34	10	2	31	6	4	1	32	6	6	1	31	4	14.9	1.3
ANV12_162CB_35	13	1	35	3	5	0	37	2	9	1	30	2	15.4	0.7
ANV12_162CB_36	8	1	21	2	3	0	16	1	3	0	14	1	10.8	0.8
ANV12_162CB_37	19	1	57	2	8	1	58	3	12	1	41	2	19.6	0.7
ANV12_162CB_38	18	1	51	3	7	0	42	2	9	1	35	2	14.8	0.8
ANV12_162CB_39	16	1	46	4	6	1	39	4	6	1	28	3	14.8	1.6
ANV12_162CB_40	13	1	40	3	6	0	40	4	8	0	31	2	15.1	1.1
ANV12_162CB_41	15	1	43	4	6	1	39	3	6	0	34	3	17.6	1.5
ANV12_162CB_42	15	1	44	2	6	1	41	3	8	1	38	2	16.1	0.8
ANV12_162CB_43	16	1	49	4	7	1	47	3	8	1	29	2	13.5	0.9
ANV12_162CB_44	12	1	34	3	4	0	32	3	6	1	20	2	12.6	1.2
ANV12_162CB_45	16	1	43	3	6	0	44	3	9	0	29	2	12.9	0.8
ANV12_162CB_46	11	1	30	3	4	0	25	3	5	0	19	1	13.1	1.4
ANV12_162CB_47	10	1	27	2	4	0	23	2	5	0	29	2	17.5	1.1
ANV12_162CB_48	13	1	36	3	5	0	39	2	7	0	26	2	13.1	0.9
ANV12_162CB_49	16	1	46	3	6	0	44	3	9	0	38	2	16.7	1.2
ANV12_162CB_50	12	1	35	3	5	0	30	3	6	0	24	2	12.2	0.8
ANV12_162CB_51	11	1	29	4	4	1	29	4	6	1	25	3	18.2	1.3
ANV12_162CB_52	15	1	43	4	5	0	38	4	7	1	34	3	15.6	1.7
ANV12_162CB_53	14	1	39	3	6	0	39	2	8	0	34	2	15.1	0.8
ANV12_162CB_54	13	2	39	3	5	1	36	3	7	1	23	2	11.9	1.0
ANV12_162CB_55	9	1	27	3	4	0	28	3	6	0	20	1	14.5	1.0
ANV12_162CB_56	19	2	54	6	7	1	54	6	11	1	33	3	16.5	1.1
ANV12_162CB_57	11	1	26	2	4	0	19	2	3	0	30	2	13.9	0.8
ANV12_162CB_58	13	1	39	2	6	0	42	3	9	1	32	1	17.2	0.8
ANV12_162CB_59	16	1	46	3	6	0	43	2	9	1	33	1	16.3	0.9
ANV12_162CB_60	14	1	42	3	6	0	41	3	7	1	31	2	14.5	0.8
ANV12_162CB_61	13	1	40	4	6	1	45	4	9	1	20	1	13.4	0.8
ANV12_162CB_62	9	1	24	3	3	0	20	3	4	0	27	2	16.9	1.9
ANV12_162CB_63	9	1	26	3	4	1	29	5	5	1	34	6	37.0	11.0
ANV12_162CB_64	7	1	19	2	3	0	19	2	4	0	23	1	14.3	1.0

Analysis	La (ppm)	2σ	Ce (ppm)	2σ	Pr (ppm)	2σ	Nd (ppm)	2σ	Sm (ppm)	2σ	Eu (ppm)	2σ	Gd (ppm)	2σ	Tb (ppm)	2σ	Dy (ppm)	2σ
NV12-176CB																		
ANV12_176CB_0	778	30	1970	150	216	11	714	51	108	10	20	2	93	9	11	1	59	5
ANV12_176CB_1	688	47	1490	130	180	15	634	65	93	12	16	2	82	10	10	1	53	6
ANV12_176CB_2	602	21	1461	76	186	7	688	26	114	7	17	1	98	5	12	1	63	3
ANV12_176CB_3	697	32	1470	110	173	10	666	39	108	8	14	1	103	6	12	1	58	3
ANV12_176CB_4	530	33	1220	110	135	8	476	37	75	7	12	1	67	4	7	0	38	3
ANV12_176CB_5	639	27	1455	69	187	7	742	37	134	10	16	1	119	8	14	1	77	4
ANV12_176CB_6	858	48	1970	190	237	19	810	76	128	13	20	2	107	9	12	1	67	7
ANV12_176CB_7	771	28	1850	130	202	9	676	29	109	7	14	1	91	5	11	1	54	3
ANV12_176CB_8	414	43	1030	140	108	13	327	39	41	6	8	1	36	6	4	1	21	3
ANV12_176CB_9	554	31	1370	130	144	7	473	28	67	6	10	1	57	3	6	0	33	2
ANV12_176CB_10	653	27	1315	89	135	6	440	21	58	4	11	1	53	3	6	0	31	3
ANV12_176CB_11	798	20	1651	78	195	8	693	33	108	7	20	1	91	6	11	1	56	3
ANV12_176CB_12	770	37	1640	100	187	10	643	35	101	7	18	1	90	6	11	1	59	5
ANV12_176CB_13	823	49	1820	120	226	15	834	58	133	11	22	2	112	9	14	1	76	6
ANV12_176CB_14	698	45	1510	120	193	13	739	52	119	10	19	1	108	10	12	1	67	4
ANV12_176CB_15	578	24	1860	140	223	13	725	39	119	10	22	2	96	5	11	1	59	3
ANV12_176CB_16	707	27	1406	62	171	8	624	34	97	7	24	1	86	7	10	1	55	4
ANV12_176CB_17	691	67	1620	160	196	16	708	50	109	7	18	2	93	7	12	1	62	4
ANV12_176CB_18	758	30	1750	110	198	10	699	33	108	7	17	1	98	5	12	1	65	2
ANV12_176CB_19	680	22	1647	64	207	11	794	46	128	10	19	1	106	8	12	1	66	4
ANV12_176CB_20	716	43	1680	170	193	14	702	56	112	10	16	2	103	10	12	1	63	5
ANV12_176CB_21	664	18	1502	54	179	6	674	31	105	7	15	1	90	6	11	1	60	5
ANV12_176CB_22	681	19	1595	52	200	6	756	22	135	7	18	1	120	7	14	1	76	4
ANV12_176CB_23	771	38	1860	110	246	13	965	51	168	10	21	2	140	9	17	1	90	5
ANV12_176CB_24	659	38	1650	140	196	10	679	46	110	9	16	1	96	5	12	1	64	5
ANV12_176CB_25	529	49	1290	130	166	15	640	62	107	11	13	2	95	10	11	1	57	6
ANV12_176CB_26	663	27	1820	140	195	10	605	31	89	6	16	2	79	6	9	1	49	4
ANV12_176CB_27	695	60	###	300	223	18	710	81	107	14	19	2	87	8	11	1	56	6
ANV12_176CB_28	682	33	1780	140	234	12	897	51	155	13	20	2	127	8	15	1	76	4
ANV12_176CB_29	771	31	1620	83	199	9	753	34	127	8	13	1	107	7	12	1	64	3
ANV12_176CB_30	742	23	1711	83	222	7	863	33	145	8	20	1	127	5	15	1	79	4
ANV12_176CB_31	695	33	1650	130	201	10	737	42	120	10	19	2	100	8	12	1	67	4
ANV12_176CB_32	795	37	1820	100	223	10	844	40	139	8	23	1	121	7	14	1	76	4
ANV12_176CB_33	695	45	1560	140	189	13	675	58	109	9	18	2	98	8	11	1	61	6
ANV12_176CB_34	700	25	1623	83	196	7	731	30	122	7	13	1	108	6	12	1	67	3
ANV12_176CB_35	616	12	1443	46	184	5	698	17	117	5	17	1	101	4	12	0	66	3
ANV12_176CB_36	595	42	1310	110	156	15	557	60	80	10	15	2	72	11	9	1	45	6
ANV12_176CB_37	637	21	1467	89	178	7	632	31	100	8	17	2	84	7	10	1	56	5
ANV12_176CB_38	618	29	1560	130	180	10	615	41	91	9	15	1	78	6	9	1	51	5
ANV12_176CB_39	753	66	1530	140	177	14	634	43	92	7	17	1	86	7	10	1	55	4
ANV12_176CB_40	664	74	1500	190	182	22	675	76	117	13	18	2	100	11	12	2	61	7
ANV12_176CB_41	645	30	1520	110	202	10	773	36	133	10	18	1	109	6	13	1	69	3
ANV12_176CB_42	772	43	1810	180	227	17	844	74	140	14	24	2	118	8	14	1	79	7
ANV12_176CB_43	964	58	1900	140	215	10	778	44	122	9	19	1	110	6	13	1	69	4
ANV12_176CB_44	563	19	1197	47	144	6	535	23	78	5	13	1	72	4	8	1	45	3

ANV12_176CB_45	719	34	1670	130	202	12	762	51	122	11	20	2	103	7	12	1	66	4
ANV12_176CB_46	694	16	1619	36	194	5	710	19	113	4	18	1	101	3	12	1	69	2
ANV12_176CB_47	745	25	1729	70	217	9	825	32	141	7	15	1	126	6	15	1	79	4
ANV12_176CB_48	768	23	1683	88	204	11	752	50	126	9	16	1	110	8	12	1	67	6
ANV12_176CB_49	685	17	1635	64	194	6	711	23	114	5	19	1	98	5	12	1	66	4
ANV12_176CB_50	860	50	1900	170	236	18	922	58	151	13	22	2	133	10	16	1	84	5
ANV12_176CB_51	729	34	1880	160	247	15	958	59	165	12	22	2	137	7	17	1	93	6
ANV12_176CB_52	796	30	1783	93	212	10	780	31	123	8	20	1	113	7	13	1	72	4
ANV12_176CB_53	724	24	1545	75	184	9	707	39	115	7	16	1	102	7	13	1	69	4
ANV12_176CB_54	697	17	1703	53	234	6	907	29	156	7	26	1	135	4	16	1	87	4
ANV12_176CB_55	714	37	1599	75	199	9	764	40	127	6	20	1	111	6	13	1	75	4
ANV12_176CB_56	644	41	1580	100	210	13	822	45	143	10	19	2	119	7	14	1	77	5
ANV12_176CB_57	467	17	908	56	101	5	338	20	44	4	9	1	43	4	4	0	23	2
ANV12_176CB_58	686	36	1569	88	183	12	642	51	99	12	17	2	84	9	10	1	54	7
ANV12_176CB_59	786	17	1902	60	232	5	827	21	135	5	17	1	114	4	14	1	76	4
ANV12_176CB_60	699	20	1607	85	193	6	733	29	119	5	17	1	107	6	13	1	66	3
ANV12_176CB_61	663	34	1580	130	209	12	813	49	145	11	17	1	113	7	14	1	72	5
ANV12_176CB_62	654	27	1432	86	170	7	614	35	94	7	18	1	82	5	10	1	54	4

Analysis	Ho (ppm)	2σ	Er (ppm)	2σ	Tm (ppm)	2σ	Yb (ppm)	2σ	Lu (ppm)	2σ	Th (ppm)	2σ	U (ppm)	2σ
NV12-176CB														
ANV12_176CB_0	12	1	36	3	5	0	37	4	6	0	6	0	37	2
ANV12_176CB_1	10	1	31	5	4	1	30	3	6	1	6	1	32	2.4
ANV12_176CB_2	13	1	36	2	5	0	35	3	7	1	7	1	28	2
ANV12_176CB_3	12	1	34	3	4	0	32	3	6	0	6	0	34	2.1
ANV12_176CB_4	8	1	23	2	3	0	22	2	4	0	4	0	15	2.1
ANV12_176CB_5	16	1	49	3	7	0	49	3	9	1	9	1	37	1.9
ANV12_176CB_6	14	1	42	5	6	1	42	4	7	0	7	0	41	3.5
ANV12_176CB_7	12	1	33	2	4	0	33	2	7	0	7	0	48	2.4
ANV12_176CB_8	5	1	14	2	2	0	16	2	3	0	3	0	13	1.1
ANV12_176CB_9	7	0	20	2	3	0	21	2	4	0	4	0	18	2
ANV12_176CB_10	7	1	20	1	3	0	24	2	5	0	5	0	25	1.5
ANV12_176CB_11	12	1	36	3	5	0	40	3	8	1	8	1	32	1.5
ANV12_176CB_12	12	1	36	2	5	0	35	3	7	1	7	1	31	2.8
ANV12_176CB_13	16	1	45	4	6	0	44	3	8	1	8	1	43	3
ANV12_176CB_14	14	1	37	3	5	1	31	3	6	1	6	1	27	2.4
ANV12_176CB_15	12	1	33	3	4	0	26	2	4	0	4	0	23	1.3
ANV12_176CB_16	12	1	31	3	5	0	28	2	5	0	5	0	29	1.5
ANV12_176CB_17	13	1	39	3	5	1	38	4	7	1	7	1	30	3.6
ANV12_176CB_18	13	1	39	2	5	0	38	3	8	1	8	1	32	2.4
ANV12_176CB_19	13	1	38	3	5	0	33	2	7	0	7	0	29	1.2
ANV12_176CB_20	13	1	36	4	5	1	35	4	7	0	7	0	41	2.7
ANV12_176CB_21	12	1	37	3	5	0	39	3	7	0	7	0	26	1.1
ANV12_176CB_22	16	1	44	2	6	0	37	2	7	0	7	0	37	1.9
ANV12_176CB_23	18	1	49	3	6	1	41	3	8	1	8	1	34	2.3
ANV12_176CB_24	13	1	40	3	6	1	39	3	8	0	8	0	29	2.5

ANV12_176CB_25	12	1	32	4	4	0	31	3	5	0	5	0	18	1.9
ANV12_176CB_26	10	1	29	2	4	0	28	2	5	0	5	0	29	1.5
ANV12_176CB_27	12	2	38	6	5	1	37	5	7	1	7	1	30	2.5
ANV12_176CB_28	16	1	42	3	6	1	35	2	7	0	7	0	35	2.1
ANV12_176CB_29	13	1	35	3	5	0	28	2	5	0	5	0	40	2.2
ANV12_176CB_30	15	1	43	2	6	0	36	2	7	1	7	1	29	1.4
ANV12_176CB_31	13	1	39	4	5	1	34	3	6	1	6	1	34	2.6
ANV12_176CB_32	16	1	47	3	7	1	46	3	8	1	8	1	42	2.5
ANV12_176CB_33	13	2	37	4	5	1	37	4	7	1	7	1	31	2.7
ANV12_176CB_34	14	1	41	2	5	0	33	2	6	0	6	0	31	2.1
ANV12_176CB_35	13	1	37	2	5	0	31	2	5	0	5	0	25	1.1
ANV12_176CB_36	10	1	30	4	4	1	30	4	6	1	6	1	28	3.4
ANV12_176CB_37	11	1	34	3	4	0	30	2	6	0	6	0	30	1.2
ANV12_176CB_38	12	1	35	4	5	1	38	4	8	0	8	0	27	1.7
ANV12_176CB_39	11	1	33	3	4	0	33	3	6	1	6	1	32	4.2
ANV12_176CB_40	13	2	35	4	5	1	33	4	7	1	7	1	27	4.3
ANV12_176CB_41	14	1	36	2	5	0	33	3	6	0	6	0	28	2.2
ANV12_176CB_42	16	1	49	5	6	1	41	4	8	1	8	1	39	3.4
ANV12_176CB_43	14	1	40	3	5	0	36	2	8	1	8	1	32	2.1
ANV12_176CB_44	9	1	28	2	4	0	25	2	6	0	6	0	18	0.8
ANV12_176CB_45	15	1	46	4	6	1	45	4	9	1	9	1	37	2
ANV12_176CB_46	15	1	43	2	6	0	40	2	8	0	8	0	34	0.8
ANV12_176CB_47	17	1	47	3	6	0	47	3	10	1	10	1	28	1.6
ANV12_176CB_48	14	1	40	3	6	0	38	3	8	0	8	0	27	1
ANV12_176CB_49	14	1	39	2	5	0	36	2	6	0	6	0	28	1
ANV12_176CB_50	18	1	48	4	6	1	41	4	8	1	8	1	34	2.3
ANV12_176CB_51	19	1	55	4	8	1	57	5	11	1	11	1	37	2.4
ANV12_176CB_52	16	1	47	2	7	0	47	3	9	1	9	1	30	1.2
ANV12_176CB_53	15	1	43	3	6	0	40	3	8	0	8	0	30	1.6
ANV12_176CB_54	18	1	49	2	6	0	42	2	7	0	7	0	37	1.5
ANV12_176CB_55	15	1	44	3	6	0	36	2	6	1	6	1	35	2.7
ANV12_176CB_56	16	1	41	3	6	0	36	2	6	0	6	0	22	1.4
ANV12_176CB_57	5	0	15	1	2	0	14	1	3	0	3	0	12	0.8
ANV12_176CB_58	11	1	33	3	5	1	34	4	7	0	7	0	31	2.4
ANV12_176CB_59	16	1	46	2	6	0	43	2	9	0	9	0	34	0.9
ANV12_176CB_60	14	1	39	2	5	0	35	2	7	0	7	0	28	1.9
ANV12_176CB_61	14	1	40	4	5	0	34	3	7	0	7	0	28	2
ANV12_176CB_62	11	1	33	2	5	0	33	2	6	1	6	1	32	3.2

ZIRCON, APATITE, AND TITANITE (U-Th)/He

Sample	mineral	U (ppm)	Th (ppm)	147Sm (ppm)	[U]e	Th/U	He (nmol/g)	mass (µg)	Ft	Age, (Ma)	err., (Ma)
NV12-176CB											
aNV12_176CB-1	apatite	18.7	35.1	130.9	27.4	1.87	4.2	3.16	0.67	41.2	2.47
aNV12_176CB-2	apatite	14.0	28.7	114.5	21.2	2.05	3.7	6.43	0.74	42.5	2.55
aNV12_176CB-3	apatite	14.1	27.0	88.0	20.8	1.91	8.4	3.70	0.68	106.5	6.39
aNV12_176CB-4	apatite	16.8	36.1	114.2	25.6	2.15	3.7	2.63	0.65	39.8	2.39
aNV12_176CB-5	apatite	11.3	31.6	87.9	19.0	2.79	3.6	2.66	0.67	51.5	3.09
aNV12_176CB-6	apatite	11.1	22.0	76.5	16.5	1.98	3.4	3.46	0.68	54.8	3.29
aNV12_176CB-7	apatite	10.0	19.8	67.1	14.9	1.98	4.1	6.00	0.73	67.7	4.06
zDD_NV12_176CB-46	zircon	694.5	172.9	3.6	734.3	0.25	183.9	2.18	0.71	65.3	5.23
zDD_NV12_176CB-69	zircon	363.2	95.9	0.8	385.3	0.26	142.7	6.06	0.79	86.8	6.95
zDD_NV12_176CB-81	zircon	575.9	138.4	1.9	607.7	0.24	229.1	5.29	0.78	89.6	7.17
zDD_NV12_176CB-26	zircon	525.4	114.3	2.1	551.7	0.22	150.9	5.93	0.78	65.1	5.21
zDD_NV12_176CB-14	zircon	390.5	105.6	0.8	414.8	0.27	140.6	4.03	0.75	82.8	6.63
zDD_NV12_176CB-40	zircon	575.8	148.9	14.5	610.2	0.26	209.4	8.54	0.80	79.2	6.34
zDD_NV12_176CB-17	zircon	726.9	164.4	3.2	764.8	0.23	191.2	2.56	0.71	64.8	5.19
NV12-162CB											
aNV12_162CB-1	apatite	19.2	21.7	90.6	24.6	1.13	1.6	4.99	0.71	16.8	1.01
aNV12_162CB-2	apatite	13.4	21.0	103.5	18.8	1.57	1.7	7.25	0.74	21.7	1.30
aNV12_162CB-3	apatite	15.5	28.6	85.6	22.5	1.85	1.8	9.66	0.77	19.0	1.14
aNV12_162CB-4	apatite	15.6	28.0	109.4	22.6	1.80	1.5	11.87	0.77	15.8	0.95
aNV12_162CB-5	apatite	10.6	19.9	84.2	15.6	1.88	1.0	7.46	0.75	15.3	0.92
aNV12_162CB-7	apatite	25.3	27.3	86.9	32.1	1.08	2.8	6.04	0.73	21.7	1.30
aNV12_162CB-8	apatite	19.2	39.0	161.1	29.0	2.03	2.3	6.63	0.73	19.7	1.18
zDD_NV12_162CB-8	zircon	878.6	250.1	5.9	936.2	0.28	312.9	9.36	0.80	77.0	6.16
zDD_NV12_162CB-19	zircon	406.1	91.8	2.0	427.2	0.23	125.1	16.12	0.84	64.7	5.17
zDD_NV12_162CB-76	zircon	422.6	89.1	1.6	443.2	0.21	151.0	8.63	0.79	79.1	6.33

zDD_NV12_162CB-42	zircon	788.0	190.1	2.8	831.8	0.24	277.5	3.72	0.73	84.5	6.76
zDD_NV12_162CB-66	zircon	383.0	97.1	1.3	405.3	0.25	123.8	4.68	0.76	74.5	5.96
zDD_NV12_162CB-67	zircon	264.9	144.8	3.8	298.3	0.55	180.4	8.35	0.79	139.6	11.17
zDD_NV12_162CB-12	zircon	530.0	131.6	1.4	560.3	0.25	185.9	5.61	0.76	80.1	6.40
050724-2A											
050724-2A-1	apatite	22.7	32.3	130.4	30.3	1.4	50.3	4.7	0.74	17.8	1.07
050724-2A-2	apatite	18.3	28.9	135.1	25.1	1.6	33.1	11.8	0.80	13.0	0.78
050724-2A-3	apatite	19.2	26.1	61.8	25.3	1.4	35.5	5.6	0.75	15.0	0.90
050724-2A-4	apatite	16.8	29.4	161.8	23.7	1.8	28.7	5.6	0.75	12.6	0.76
050724-2A-5	apatite	20.1	28.7	95.7	26.8	1.4	30.3	3.1	0.71	12.7	0.76
050724-2A-6	apatite	22.2	32.0	129.0	29.7	1.4	38.8	6.1	0.76	13.7	0.82
050724-2A-7	apatite	22.2	28.0	72.3	28.8	1.3	48.4	4.1	0.73	18.5	1.11
050724-2A-8	apatite	18.8	28.0	124.1	25.4	1.5	32.9	11.7	0.80	12.8	0.77
050724-2A-9	apatite	15.5	27.5	131.6	22.0	1.8	31.7	13.7	0.81	13.9	0.83
050724-2A-10	apatite	18.2	28.0	128.7	24.8	1.5	30.4	3.8	0.72	13.4	0.8
050724-2A-11	apatite	17.0	26.9	117.6	23.3	1.6	24.3	4.1	0.72	11.4	0.7
050724-2A-12	apatite	18.2	39.2	147.2	27.4	2.2	33.2	3.3	0.71	13.4	0.8
050724-2A-13	apatite	31.7	28.1	81.4	38.3	0.9	54.2	4.0	0.73	15.7	0.9
050724-2A-14	apatite	26.6	30.4	86.4	33.8	1.1	45.7	3.7	0.72	15.1	0.9
050724-2A-15	apatite	17.5	27.2	114.4	23.9	1.6	39.7	3.0	0.70	18.7	1.1
050724-2A-16	apatite	18.1	27.9	148.5	24.6	1.5	34.3	8.0	0.78	14.0	0.8
050724-2A-17	apatite	20.4	31.3	113.7	27.7	1.5	47.8	5.1	0.75	18.4	1.1
050720-11											
050720-11-1	apatite	18.5	46.6	149.4	29.4	2.5	33.0	4.2	0.72	12.3	0.74
050720-11-2	apatite	18.1	35.0	127.3	26.3	1.9	27.2	4.9	0.74	11.1	0.67
050720-11-3	apatite	28.0	24.1	123.3	33.7	0.9	41.0	5.4	0.75	12.9	0.77
050720-11-4	apatite	17.1	32.2	119.1	24.7	1.9	28.2	6.5	0.74	12.2	0.73
050720-11-5	apatite	16.1	21.1	188.7	21.0	1.3	31.6	10.2	0.79	14.5	0.87

050720-11-6	apatite	17.1	36.7	119.9	25.7	2.1	44.0	3.8	0.72	18.7	1.12
050720-11-7	apatite	19.8	35.1	127.6	28.1	1.8	32.8	4.1	0.73	12.7	0.76
050720-11-8	apatite	23.0	43.5	183.9	33.3	1.9	36.3	5.0	0.74	11.5	0.69
050720-11-9	apatite	19.3	47.4	141.9	30.5	2.4	63.2	3.4	0.71	23.2	1.39
050720-11-10	apatite	37.6	31.5	143.6	45.0	0.8	55.3	4.8	0.75	13.2	0.79
050720-11-11	apatite	13.2	26.4	90.8	19.4	2.0	27.5	5.5	0.75	15.0	0.90
050720-11-12	apatite	16.7	33.1	133.6	24.5	2.0	35.5	9.1	0.78	14.5	0.87
050720-11-13	apatite	16.0	38.2	130.4	24.9	2.4	26.2	6.2	0.74	11.2	0.67
050720-11-14	apatite	21.2	46.3	174.1	32.1	2.2	38.8	5.5	0.75	12.7	0.76
050720-11-15	apatite	22.5	23.3	95.0	28.0	1.0	36.9	4.8	0.74	14.2	0.85
050720-11-16	apatite	15.2	28.1	118.5	21.8	1.9	31.6	7.3	0.75	15.1	0.91
050720-11-17	apatite	18.5	43.1	147.6	28.7	2.3	28.5	3.2	0.69	11.3	0.68
050720-11-18	apatite	18.1	30.1	128.4	25.2	1.7	26.7	5.9	0.74	11.3	0.68
050720-9D											
050720-9D-1	apatite	23.7	27.6	109.4	30.2	1.2	47.2	4.5	0.74	16.9	1.01
050720-9D-2	apatite	38.6	28.8	131.4	45.4	0.7	57.8	3.8	0.73	14.0	0.84
050720-9D-3	apatite	20.5	20.4	28.1	25.3	1.0	34.7	4.0	0.73	15.3	0.92
050720-9D-4	apatite	34.9	30.7	47.1	42.1	0.9	59.5	4.2	0.73	15.7	0.94
050720-9D-5	apatite	27.2	31.0	65.7	34.4	1.1	41.1	5.0	0.74	13.0	0.78
050720-9D-6	apatite	16.8	32.4	121.9	24.4	1.9	30.1	3.5	0.71	13.7	0.82
050720-9D-7	apatite	36.3	36.1	79.9	44.8	1.0	65.4	4.6	0.74	16.1	0.96
050720-9D-8	apatite	75.4	66.8	217.1	91.1	0.9	142.2	6.9	0.76	16.5	0.99
050720-9D-9	apatite	22.3	39.5	128.5	31.6	1.8	47.9	7.9	0.78	15.5	0.93
050720-9D-10	apatite	24.7	24.5	112.5	30.5	1.0	54.7	8.3	0.78	18.4	1.10
050720-9D-11	apatite	26.8	28.3	71.8	33.5	1.1	59.8	5.5	0.75	19.3	1.16
050720-9D-12	apatite	25.8	30.8	51.6	33.1	1.2	44.5	2.7	0.69	15.8	0.95
010801											
010801-3Ap1	apatite	14.0	24.5		19.8	1.74	84.12	22.4	0.83	42.0	2.1

010801-3Ap2	apatite	13.2	23.3		18.7	1.77	80.79	27.5	0.85	41.7	2.1
010801-3Ap3	apatite	12.9	23.8		18.5	1.85	82.77	13.7	0.81	45.2	2.3
980730-1 41.821°N, 115.690°W											
980730-1Ap1	apatite	13.3	24.7		19.1	1.86	341.36	36.7	0.87	166.6	8.3
980730-1Ap2	apatite	16.1	26.1		22.2	1.62	56.39	25.5	0.87	23.9	1.2
980730-1Ap3	apatite	11.6	18.4		15.9	1.59	59.65	32.5	0.88	34.9	1.7
980730-1Ap4	apatite	13.6	23.1		19.0	1.70	46.05	46.2	0.90	22.1	1.1
980730-1Ap5	apatite	10.4	18.2		14.7	1.75	32.15	40.1	0.90	20.0	1.0
980730-1Ap6	apatite	11.0	17.0		15.0	1.55	34.15	32.5	0.89	21.0	1.1
980730-1Ap7	apatite	12.8	17.6		16.9	1.38	52.86	25.7	0.88	29.2	1.5
980730-1Ap8	apatite	14.5	16.0		18.3	1.10	49.06	30.4	0.88	25.1	1.3
980730-1Ap9	apatite	12.4	19.0		16.9	1.53	45.57	30.3	0.88	25.1	1.3
980730-1sp1	titanite	32.2	82.0		5.6	2.5	431.3	122.3		68.5	3.4
980730-1sp2	titanite	25.4	73.8		936.0	2.9	355.8	73.7		68.1	3.4
980730-1sp3	titanite	79.3	46.0		238.2	0.6	818.2	99.5		74.1	3.7
980730-1sp4	titanite	17.2	63.8		59.4	3.7	286.5	87.5		72.6	3.6
980730-3 41.830°N, 115.667°W											
980730-3-1	apatite	16.9	28.2	107.9	23.5	1.7	101.4	11.7	0.80	42.6	2.56
980730-3-2	apatite	14.5	24.4	81.0	20.3	1.7	66.0	4.2	0.64	40.7	2.44
980730-3-3	apatite	18.4	30.5	119.6	25.6	1.7	92.7	5.6	0.72	39.6	2.37
Z980730-3.1	zircon	251.7	52.7		264.1	0.21	1488.8	4.6	0.76	60.6	4.8
Z980730-3.2	zircon	261.3	65.1		276.5	0.25	2080.7	6.4	0.77	79.6	6.4
Z980730-3.3	zircon	415.0	101.5		438.9	0.24	2975.4	9.1	0.81	68.7	5.5
980730-4 41.835°N, 115.646°W											
980730-4	apatite	18.5	30.6	98.1	25.7	1.7	124.9	10.3	0.7	52.2	1.7
Z980730-4-1	zircon	475.8	111.4		502.0	0.23	3285.0	8.9	0.80	67.0	5.4
Z980730-4-2	zircon	574.2	133.7		605.6	0.23	4311.7	7.3	0.77	75.2	6.0

980730-5 41.835°N, 115.622°W											
980730-5-1	apatite	19.3	34.3	111.4	27.3	1.8	118.2	7.8	0.77	44.4	2.66
980730-5-2	apatite	18.1	30.2	97.4	25.2	1.7	87.3	7.6	0.70	39.4	2.36
980730-5-3	apatite	25.1	33.4	97.2	32.9	1.3	107.3	6.4	0.69	37.7	2.26
980730-5-4	apatite	21.8	32.0	84.7	29.3	1.5	142.0	5.7	0.68	47.0	3.42
	zircon	721.5	158.1		758.7	0.22	6270.8	6.0	0.8	89.2	4.1
980730-5sp1	titanite	36.5	58.6		50.3	1.6	355.0	36.2		57.7	2.9
980730-5sp3	titanite	43.9	89.6		65.0	2.0	586.3	42.1		73.7	3.7
980730-5sp4	titanite	31.1	49.2		42.6	1.6	371.6	39.5		71.2	3.6
980730-7 41.795°N, 115.664°W											
980730-7	apatite	33.2	29.1	65.8	40.0	0.9	122.8	3.1	0.6	41.1	2.5
Z980730-7.1	zircon	350.0	82.5		369.4	0.25	3075.2	6.5	0.76	88.6	7.2
Z980730-7.2	zircon	347.0	76.5		364.9	0.22	3277.3	6.4	0.77	94.6	7.6
Z980730-7.3	zircon	359.4	99.5		382.8	0.28	3018.4	6.6	0.77	83.2	6.7
980731-2 ***41.786°N, 115.493°W***											
980731-2-1	apatite	17.7	23.9	77.8	23.4	1.3	68.2	5.4	0.68	34.3	2.06
980731-2-2	apatite	17.6	21.3	71.0	22.6	1.2	60.8	4.5	0.67	32.2	1.93
980731-2-3	apatite	16.6	21.9	64.1	21.7	1.3	54.7	3.5	0.64	31.3	1.88
Z980731-2.1	zircon	354.3	89.4		375.3	0.25	2922.4	3.7	0.74	86.2	6.9
Z980731-2.2	zircon	380.9	117.6		408.6	0.31	3081.7	2.7	0.71	86.6	6.9
Z980731-2.3	zircon	784.8	416.3		882.6	0.53	5548.5	3.5	0.72	71.0	5.7
980802-2B 41.820°N, 115.515°W											
980802-2B.1	zircon	851.2	369.3		938.0	0.43	3511.8	5.3	0.76	40.4	3.2
Z980802-2B.2	zircon	425.6	175.1		466.7	0.41	1598.6	1.2	0.63	51.2	4.9
Z980802-2B.3	zircon	627.6	175.1		668.7	0.41	2198.6	1.2	0.63	48.2	3.9

980802-4 41.815°N, 115.535°W										
980802-4-1	zircon	341.8	42.9	351.9	0.13	1867.7	2.2	0.71	61.4	4.9
980802-4-3	zircon	235.3	56.8	248.6	0.24	1071.2	2.2	0.70	50.0	4.0
000714-1 41.816°N, 115.478°W										
000714-1sp1	titanite	130.7	76.4	148.6	0.6	595.9	24.7		32.8	1.6
000714-1sp2	titanite	90.4	54.4	103.2	0.6	473.4	21.1		37.6	1.9
000714-1sp3	titanite	100.1	63.2	115.0	0.6	578.0	29.7		41.1	2.1
000714-1sp4	titanite	97.9	135.8	129.8	1.4	995.2	23.6		62.6	3.1
970721-4C 41.786°N, 115.494°W										
970721-4C-sp1	titanite	78.2	47.4	94.3	0.6	719.9	78.9		62.9	3.1
970721-4c-sp2	titanite	82.2	51.1	24.0	0.6	725.9	65.4		203.7	10.2
970721-4c-sp3	titanite	23.7	1.6	60.6	0.1	609.7	75.4		99.5	5.0
970721-4c-sp4	titanite	50.8	41.6	84.3	0.8	740.4	53.1		69.1	3.5

TABLE B3. SUMMARY OF RESULTS FROM $^{40}Ar/^{39}Ar$ STEP HEATING EXPERIMENTS

Sample number	Mineral	Run	K (wt %)	J value	%^{39}Ar	$^{40}Ar/^{39}Ar$ age (Ma)	2σ*	2σ†	MSWD
960702-1A	biotite	55C22	7.4	0.007360	83	41.84	0.10	0.28	5
970728-3	sanidine	60C13	4.0	0.015645	95	37.88	0.23	0.33	1
970709-3C	biotite	60C2	8.2	0.015723	88	94.21	0.30	0.66	12
970709-3C	k-feldspar	73A12		0.005985		71.87	1.59	1.65	43
970721-4C	hornblende	60C6	0.7	0.015702	89	108.19	0.40	0.79	12
970721-4C	biotite	60C4	8.1	0.015711	58	106.06	0.30	0.73	9
970721-4C	k-feldspar	73A21		0.005991		98.26	3.34	3.40	1.2
970726-5	biotite	60C11	1.2	0.015663	63	88.94	0.71	0.90	0.9
980730-1	hornblende	63B40	0.6	0.005187	95	106.47	0.30	0.73	4.8
980730-1	biotite	63B39	6.3	0.005188	89	102.72	0.30	0.71	2.7
980730-1	k-feldspar	73A30		0.005973		93.70	1.26	1.38	13
980730-3	hornblende	63B51	0.7	0.005173	88	105.05	0.40	0.77	5.4
980730-3	biotite	63B41	6.3	0.005188	66	100.49	1.21	1.37	7.6
980730-3	k-feldspar	73A3		0.005985		91.82	1.29	1.41	7.1
980730-4	biotite	63B43	6.3	0.005188	91	103.63	0.30	0.71	1.9
980730-7	biotite	63B44	6.0	0.005182	74	104.64	0.40	0.77	9.2
980802-2B	k-feldspar	73A46		0.005925		70.73	1.34	1.41	5.6
980802-3A	muscovite	63B46	7.5	0.005179	63	91.57	0.30	0.64	2.6
980802-3A	muscovite	63B55	7.8	0.005168	62	91.17	0.30	0.64	1.6
980802-3A	biotite	63B45	6.5	0.005181	59	54.50	0.71	0.78	35
980802-3A	biotite	63B54	6.8	0.005169	51	56.22	0.51	0.61	23
990704-1	plagioclase	66C17	0.3	0.005465	83	16.71	0.20	0.23	4
010801-5	hornblende	73C19	1.2	0.005971	71	29.58	0.20	0.27	2.6
010801-5	hornblende	73C20	1.3	0.005969	70	30.08	0.30	0.36	1.2
010801-5	biotite	73C17	2.1	0.005973	72	29.68	0.41	0.44	1.1
050719-4	biotite	76B2	5.8	0.007397	89	43.25	0.10	0.29	2.7
050720-3B	biotite	76B4	5.2	0.007400	89	40.32	0.20	0.32	1.6
050720-10	biotite	76B7	4.2	0.007406	73	32.92	0.20	0.29	2.4
050721-11	biotite	76B8	4.6	0.007409	52	42.04	0.30	0.40	2.4

$^{40}Ar/^{39}Ar$ STEP HEATING EXPERIMENTS

Experiment:	55C22						
Sample:	**960702-1A**	J-value:	0.007387	K wt. %:	7.4	Plateau range:	920-1160°C
Material:	Biotite	^{39}Ar %:	83	wt.:	1.72 mg	Uncalibrated plateau age (Ma):	41.3 ± 0.1

T (°C)	$^{40}Ar/^{39}Ar$	$^{38}Ar/^{39}Ar$	$^{37}Ar/^{39}Ar$	$^{36}Ar/^{39}Ar$	F	39Ar %	40Ar %	K/Ca	K/Cl	Apparent Age (Ma)	Error 2σ
500	31.870	0.3121	8.340	10.2900	1.458	2.14	4.57	6.3	18.5	19.2	2.0
601	11.700	0.1909	4.311	3.1160	2.470	2.84	21.11	12.1	30.0	32.4	0.7
650	11.330	0.1808	4.609	2.8220	2.969	1.48	26.21	11.3	31.7	38.9	0.8
700	61.480	0.2197	7.424	20.1800	1.814	2.04	2.95	7.0	30.5	23.9	3.4
725	33.970	0.1881	6.772	10.6700	2.433	0.85	7.16	7.8	33.2	32.0	2.8
750	11.900	0.1919	4.689	2.9950	3.034	0.95	25.49	11.2	29.7	39.8	1.2
775	8.821	0.1969	3.742	1.8210	3.417	0.95	38.74	14.0	28.6	44.7	0.9
800	9.198	0.1962	3.716	2.0180	3.213	0.99	34.94	14.1	28.7	42.1	0.8
830	8.006	0.1946	3.460	1.6300	3.166	1.22	39.54	15.1	28.9	41.5	0.6
860	6.620	0.1913	2.565	1.1770	3.118	1.60	47.10	20.4	29.3	40.9	0.5
890	5.319	0.1923	2.023	0.7058	3.210	2.23	60.35	25.9	29.0	42.0	0.3
920	4.744	0.1885	1.656	0.5357	3.137	3.22	66.12	31.6	29.5	41.1	0.2
950	4.350	0.1858	1.542	0.4028	3.136	4.44	72.08	33.9	30.0	41.1	0.2
980	4.182	0.1860	1.377	0.3540	3.112	5.13	74.41	38.0	29.9	40.8	0.2
1010	4.107	0.1855	1.511	0.3278	3.114	5.84	75.82	34.6	30.0	40.8	0.1
1050	4.071	0.1882	1.728	0.3066	3.141	8.52	77.16	30.3	29.5	41.2	0.1
1090	3.894	0.1850	1.988	0.2522	3.125	11.58	80.25	26.3	30.0	40.9	0.1
1130	3.762	0.1856	2.252	0.2105	3.116	12.82	82.84	23.2	29.9	40.8	0.1
1160	3.562	0.1854	2.548	0.1459	3.107	12.59	87.24	20.5	29.9	40.7	0.1
1200	3.414	0.1881	4.980	0.1066	3.078	13.60	90.14	10.5	29.5	40.3	0.1
1250	3.613	0.2428	40.870	0.1858	3.069	3.67	84.93	1.3	22.5	40.2	0.1
1300	6.434	0.3983	133.000	1.2000	2.958	0.50	45.97	0.4	13.5	38.8	0.6
1500	7.309	0.2865	64.160	1.4240	3.123	0.77	42.72	0.8	19.1	40.9	0.8

Experiment:	60C13										
Sample:	**970728-3**		J-value:	0.015645		K wt. %:	4.3		Plateau range:		950-1275°C
Material:	Sanidine		^{39}Ar %:	86		wt.:	1.47 mg		Uncalibrated plateau age (Ma):		37.4 ± 0.2

T (°C)	^{40}Ar/^{39}Ar	^{38}Ar/^{39}Ar	^{37}Ar/^{39}Ar	^{36}Ar/^{39}Ar	F	39Ar %	40Ar %	K/Ca	K/Cl	Apparent Age (Ma)	Error 2σ
650	4.589	0.0464	0.2753	1.134	1.238	1.60	27.10	1.9	156	34.6	2.9
700	60.320	0.3763	0.2986	19.460	2.812	1.22	4.70	1.8	16	77.7	24.9
750	2.290	0.2869	0.2248	0.137	1.890	1.76	83.40	2.3	19	52.6	7.6
800	1.852	0.0288	0.1085	0.155	1.378	2.63	75.40	4.8	297	38.5	1.6
850	1.868	0.0115	0.1231	0.156	1.394	2.86	75.60	4.3	1250	38.9	1.9
900	2.072	0.0132	0.1314	0.228	1.383	3.21	67.50	4.0	2660	38.6	1.2
950	2.086	0.0127	0.1707	0.245	1.352	3.75	65.60	3.1	3550	37.8	1.4
975	1.790	0.0130	0.2307	0.179	1.254	4.01	71.00	2.3	2840	35.1	1.7
1000	1.661	0.0120	0.1472	0.109	1.327	5.11	81.10	3.6	5210	37.1	0.8
1025	1.531	0.0115	0.0830	0.050	1.366	4.04	90.70	6.3	7880	38.2	0.9
1050	1.665	0.0122	0.0889	0.118	1.299	2.44	79.20	5.9	4260	36.3	1.6
1075	1.583	0.0118	0.1029	0.102	1.265	2.27	81.20	5.1	6510	35.4	1.5
1100	1.611	0.0119	0.0807	0.088	1.333	2.78	84.00	6.5	5310	37.2	1.2
1125	1.572	0.0119	0.0937	0.071	1.345	3.16	86.90	5.6	5080	37.6	1.1
1150	1.491	0.0120	0.0710	0.042	1.349	6.46	92.00	7.4	4570	37.7	0.7
1175	1.497	0.0117	0.0656	0.041	1.355	11.26	92.10	8.0	5980	37.9	0.3
1200	1.449	0.0121	0.0527	0.022	1.363	15.38	95.70	9.9	4070	38.1	0.3
1225	1.457	0.0118	0.0355	0.029	1.350	11.73	94.20	14.7	5610	37.7	0.4
1250	1.501	0.0119	0.0528	0.042	1.356	7.39	91.90	9.9	4900	37.9	0.5
1275	1.476	0.0119	0.0288	0.052	1.301	6.42	89.60	18.2	5080	36.4	0.9
1300	2.292	0.0122	0.0018	0.338	1.270	0.54	56.00	286.0	6320	35.5	6.3

Experiment:	60C2										
Sample:	**970709-3C**		J-value:	0.015723		K wt. %:	8.2		Plateau range:		700-1110°C
Material:	Biotite		^{39}Ar %:	88		wt.:	2.59 mg		Uncalibrated plateau age (Ma):		93.0 ± 0.3

T (°C)	^{40}Ar/^{39}Ar	^{38}Ar/^{39}Ar	^{37}Ar/^{39}Ar	^{36}Ar/^{39}Ar	F	39Ar %	40Ar %	K/Ca	K/Cl	Apparent Age (Ma)	Error 2σ
550	5.008	0.0428	0.0310	1.072	1.820	1.62	36.52	17	180	50.9	1.3
600	4.002	0.0408	0.0062	0.320	3.033	3.34	76.25	84	183	84.0	0.6
650	3.839	0.0410	0.0040	0.189	3.259	7.18	85.44	131	181	90.1	0.3
700	5.542	0.0430	0.0036	0.742	3.328	6.43	60.32	145	175	92.0	0.5
725	3.976	0.0411	0.0022	0.202	3.355	7.04	84.91	238	180	92.7	0.3
750	3.433	0.0409	0.0017	0.014	3.368	8.80	98.81	310	179	93.1	0.2
770	3.498	0.0414	0.0016	0.033	3.378	6.83	97.27	336	176	93.4	0.2
790	3.976	0.0416	0.0016	0.186	3.403	4.47	86.14	317	177	94.0	0.4
810	3.897	0.0420	0.0022	0.158	3.407	2.94	88.00	240	174	94.1	0.4
830	3.520	0.0415	0.0030	0.043	3.370	2.24	96.43	177	176	93.2	0.4
850	3.692	0.0411	0.0039	0.101	3.370	2.00	91.90	136	179	93.1	0.5
875	3.785	0.0417	0.0046	0.137	3.359	2.14	89.31	115	176	92.8	0.4
900	3.643	0.0416	0.0060	0.096	3.337	2.54	92.24	88	176	92.3	0.4
940	3.622	0.0398	0.0068	0.094	3.323	3.53	92.37	77	187	91.9	0.3
980	3.547	0.0400	0.0050	0.076	3.300	4.33	93.67	104	186	91.2	0.3
1010	3.495	0.0403	0.0041	0.049	3.327	5.32	95.89	127	184	92.0	0.2
1030	3.503	0.0401	0.0030	0.042	3.356	6.36	96.48	176	185	92.8	0.2
1050	3.505	0.0407	0.0040	0.040	3.364	6.16	96.67	131	181	93.0	0.2
1070	3.508	0.0414	0.0045	0.028	3.402	5.95	97.68	116	176	94.0	0.2
1090	3.515	0.0414	0.0046	0.035	3.388	6.89	97.07	113	177	93.6	0.2
1110	3.530	0.0417	0.0086	0.026	3.430	3.89	97.85	61	175	94.8	0.3

Experiment:	60C6										
Sample:	**970721-4C**		J-value:	0.015702		K wt. %:	0.72		Plateau range:		800-1350°C
Material:	Hornblende		^{39}Ar %:	89		wt.:	6.27 mg		Uncalibrated plateau age (Ma):		106.8 ± 0.4

T (°C)	^{40}Ar/^{39}Ar	^{38}Ar/^{39}Ar	^{37}Ar/^{39}Ar	^{36}Ar/^{39}Ar	F	39Ar %	40Ar %	K/Ca	K/Cl	Apparent Age (Ma)	Error 2σ
650	14.330	0.1404	1.7270	3.619	3.758	1.85	26.24	0.3	42.8	103.4	4.0
750	46.840	0.1463	0.2466	14.310	4.549	1.27	9.71	2.1	48.5	124.5	9.8
800	4.215	0.0944	0.1146	0.135	3.806	2.46	90.82	4.6	63.4	104.7	2.4
850	7.354	0.0924	0.1642	1.252	3.646	1.78	49.74	3.2	66.7	100.4	3.7
900	5.059	0.1081	0.4610	0.379	3.958	1.10	78.61	1.1	54.6	108.8	4.0
950	6.118	0.1332	0.9927	0.757	3.946	0.94	64.72	0.5	43.5	108.5	4.0
1000	5.635	0.1523	1.2230	0.596	3.958	1.98	70.49	0.4	37.4	108.8	2.2
1020	4.558	0.1707	1.2950	0.262	3.873	3.21	85.36	0.4	32.9	106.5	1.5
1040	4.270	0.2098	1.8150	0.183	3.865	4.48	90.93	0.3	26.4	106.3	1.2
1060	4.277	0.4230	5.1180	0.264	3.915	6.92	91.75	0.1	12.7	107.6	0.8
1075	4.063	0.5232	6.3810	0.239	3.886	13.60	95.81	0.1	10.2	106.8	0.4
1090	4.117	0.5410	6.2290	0.244	3.913	11.83	95.21	0.1	9.8	107.6	0.5
1105	3.995	0.5078	5.5890	0.204	3.853	9.68	96.68	0.1	10.5	106.0	0.5
1120	4.517	0.5140	6.1070	0.376	3.912	3.48	86.72	0.1	10.4	107.6	1.9
1140	4.298	0.6275	7.6030	0.369	3.840	4.06	89.40	0.1	8.4	105.6	1.5
1160	4.524	0.6431	7.8820	0.413	3.962	3.43	87.57	0.1	8.2	108.9	1.5
1180	4.354	0.6451	7.9460	0.388	3.869	2.25	88.89	0.1	8.2	106.4	2.1
1200	4.390	0.6404	8.1710	0.393	3.910	1.87	89.08	0.1	8.3	107.5	3.3
1225	4.489	0.6271	8.0830	0.454	3.820	1.56	85.09	0.1	8.5	105.1	2.8
1250	4.626	0.6568	9.0480	0.455	4.038	1.11	87.22	0.1	8.1	110.9	6.1
1275	4.573	0.6899	8.8110	0.536	3.726	1.52	81.41	0.1	7.7	102.6	2.6
1300	4.461	0.6906	8.4970	0.421	3.928	2.71	88.03	0.1	7.7	108.0	1.7
1350	4.119	0.7092	8.7220	0.320	3.905	8.74	94.80	0.1	7.4	107.4	0.8
1400	4.258	0.6845	8.1500	0.330	3.964	8.18	93.14	0.1	7.7	108.9	0.7

Experiment:	60C4										
Sample:	**970721-4C**		J-value:	0.015711		K wt. %:	8.1		Plateau range:		1010-1110°C
Material:	Biotite		^{39}Ar %:	58		wt.:	4.01 mg		Uncalibrated plateau age (Ma):		104.7 ± 0.3

T (°C)	^{40}Ar/^{39}Ar	^{38}Ar/^{39}Ar	^{37}Ar/^{39}Ar	^{36}Ar/^{39}Ar	F	39Ar %	40Ar %	K/Ca	K/Cl	Apparent Age (Ma)	Error 2σ
550	5.914	0.0808	0.0516	1.2030	2.341	0.58	39.76	10.1	78.2	65.2	1.7
600	4.225	0.0858	0.0243	0.2186	3.560	0.89	84.76	21.5	70.9	98.2	0.8
650	4.213	0.0867	0.0085	0.1573	3.728	2.69	89.01	61.6	69.9	102.7	0.4
700	6.956	0.0916	0.0057	1.0660	3.787	3.10	54.64	91.1	67.0	104.3	0.6
725	4.366	0.0879	0.0042	0.1770	3.822	3.55	88.05	123.0	68.8	105.2	0.4
740	4.139	0.0879	0.0040	0.1039	3.811	4.33	92.64	130.0	68.7	104.9	0.2
760	4.155	0.0882	0.0048	0.1160	3.792	4.50	91.81	108.0	68.5	104.4	0.2
780	4.002	0.0870	0.0052	0.0544	3.821	4.23	96.06	101.0	69.5	105.2	0.2
800	3.960	0.0876	0.0079	0.0477	3.799	3.66	96.53	66.0	68.9	104.6	0.4
825	3.915	0.0872	0.0124	0.0229	3.827	2.84	98.39	42.1	69.2	105.3	0.3
850	4.070	0.0881	0.0173	0.0774	3.822	2.19	94.48	30.2	68.5	105.2	0.3
875	4.155	0.0875	0.0254	0.1005	3.839	1.64	92.95	20.6	69.1	105.7	0.5
900	3.989	0.0871	0.0284	0.0374	3.860	1.89	97.36	18.4	69.3	106.2	0.4
940	4.018	0.0882	0.0187	0.0377	3.887	2.80	97.34	28.0	68.4	106.9	0.3
980	3.975	0.0864	0.0115	0.0279	3.872	3.32	98.03	45.4	70.0	106.5	0.2
1010	3.900	0.0871	0.0068	0.0212	3.817	3.96	98.50	77.2	69.3	105.1	0.3
1030	3.879	0.0866	0.0054	0.0162	3.811	4.91	98.87	97.0	69.8	104.9	0.2
1050	3.853	0.0862	0.0035	0.0092	3.805	6.83	99.40	150.0	70.1	104.8	0.2
1070	3.874	0.0863	0.0037	0.0124	3.817	10.51	99.16	143.0	70.0	105.1	0.4
1090	3.851	0.0863	0.0021	0.0146	3.787	19.22	98.98	248.0	70.1	104.3	0.3
1110	3.855	0.0871	0.0044	0.0084	3.810	12.34	99.46	119.0	69.3	104.9	0.6

Experiment:	60C11										
Sample:	**970726-5**		J-value:	0.015663		K wt. %:	1.2		Plateau range:		710-1060°C
Material:	Biotite		^{39}Ar %:	63		wt.:	3.06 mg		Uncalibrated plateau age (Ma):		87.8 ± 0.7

T (°C)	^{40}Ar/^{39}Ar	^{38}Ar/^{39}Ar	^{37}Ar/^{39}Ar	^{36}Ar/^{39}Ar	F	39Ar %	40Ar %	K/Ca	K/Cl	Apparent Age (Ma)	Error 2σ
550	6.096	0.1195	0.6350	1.955	0.347	19.78	5.70	0.8	49.7	9.8	1.2
600	10.390	0.1123	0.2492	2.837	2.006	3.07	19.40	2.1	54.3	55.8	5.1
650	9.864	0.0395	0.2038	2.696	1.889	3.85	19.20	2.6	221.0	52.6	4.3
675	25.330	0.0450	0.1333	7.571	2.939	3.09	11.60	3.9	261.0	81.2	7.4
690	28.500	0.0402	0.0550	8.400	3.655	2.39	12.80	9.5	383.0	100.4	7.1
710	3.295	0.0118	0.0381	0.087	3.016	2.68	92.20	13.7	6300.0	83.3	3.0
730	3.971	0.0122	0.0346	0.228	3.276	3.24	83.00	15.1	5490.0	90.3	2.2
750	3.545	0.0120	0.0314	0.158	3.055	4.12	86.80	16.6	5840.0	84.3	2.3
775	3.496	0.0121	0.0235	0.093	3.199	6.08	92.20	22.3	4570.0	88.2	0.9
800	3.562	0.0132	0.0282	0.115	3.200	6.08	90.50	18.5	2390.0	88.2	1.4
825	3.596	0.0132	0.0308	0.149	3.134	5.03	87.80	17.0	2480.0	86.5	1.3
850	3.681	0.0125	0.0330	0.177	3.135	4.62	85.70	15.8	3880.0	86.5	1.5
890	3.978	0.0131	0.0374	0.252	3.212	5.37	81.20	14.0	2830.0	88.5	2.3
930	3.869	0.0129	0.0344	0.235	3.154	6.36	82.00	15.2	3050.0	87.0	1.3
960	4.177	0.0133	0.0321	0.326	3.191	5.55	76.80	16.3	2670.0	88.0	1.4
980	4.326	0.0136	0.0363	0.338	3.307	4.17	76.90	14.4	2390.0	91.1	2.7
1000	4.370	0.0140	0.0489	0.375	3.241	3.22	74.60	10.7	2050.0	89.3	1.8
1020	4.724	0.0144	0.0568	0.562	3.042	2.71	64.70	9.2	2060.0	84.0	5.1
1040	5.469	0.0157	0.0791	0.703	3.373	2.09	62.00	6.6	1440.0	92.9	5.3
1060	3.950	0.0165	0.1325	0.210	3.317	1.62	84.50	4.0	976.0	91.4	7.8
1080	5.095	0.0173	0.1615	0.454	3.740	1.10	73.80	3.2	919.0	102.7	5.6
1110	5.646	0.0175	0.3454	0.653	3.721	0.68	66.20	1.5	957.0	102.2	10.2
1150	9.096	0.0288	0.4953	2.009	3.176	0.53	35.00	1.1	368.0	87.6	12.7
1200	7.027	0.0206	0.3198	1.308	3.163	0.89	45.20	1.6	708.0	87.2	7.7
1350	10.020	0.0268	0.7233	2.160	3.676	1.68	36.70	0.7	438.0	101.0	6.9

Experiment:	63B40						
Sample:	**980730-1**	J-value:	0.005187	K wt. %:	0.6	Plateau range:	950-1340°C
Material:	Hornblende	^{39}Ar %:	95	wt.:	6.88 mg	Uncalibrated plateau age (Ma):	105.3 ± 0.4

T (°C)	^{40}Ar/^{39}Ar	^{38}Ar/^{39}Ar	^{37}Ar/^{39}Ar	^{36}Ar/^{39}Ar	F	39Ar %	40Ar %	K/Ca	K/Cl	Apparent Age (Ma)	Error 2σ
575	86.49	0.7686	3.338	20.780	25.38	0.23	29.3	0.16	7.3	223.1	24.6
650	25.39	0.1223	4.314	5.280	10.13	0.45	38.0	0.12	51.4	92.4	12.1
750	307.60	0.2471	1.217	100.000	12.10	0.79	4.1	0.43	108.0	109.8	30.6
850	19.24	0.0471	1.851	3.226	9.84	2.22	24.4	0.28	173.0	89.8	7.4
950	22.61	0.1883	7.941	3.920	11.67	2.38	51.4	0.07	30.6	106.1	3.2
980	13.40	0.2702	6.363	0.808	11.54	5.45	83.5	0.08	20.2	104.8	1.0
1000	12.22	0.2612	6.378	0.398	11.56	16.78	94.2	0.08	20.9	105.1	0.4
1020	11.91	0.2909	6.164	0.300	11.52	17.01	96.4	0.08	18.6	104.7	0.4
1030	12.63	0.2985	6.329	0.575	11.44	4.60	92.4	0.08	18.2	104.0	0.9
1050	13.12	0.2829	6.686	0.722	11.53	2.90	88.0	0.08	19.2	104.8	1.8
1075	13.33	0.2788	6.513	0.746	11.66	4.57	87.3	0.08	19.5	106.0	1.1
1100	13.31	0.2686	6.633	0.809	11.46	4.20	86.1	0.08	20.3	104.2	1.3
1125	12.88	0.2421	6.917	0.475	12.04	1.93	91.8	0.08	22.6	109.3	2.2
1150	12.29	0.3177	6.289	0.374	11.70	3.60	95.0	0.08	17.0	106.3	1.3
1200	11.89	0.3032	6.372	0.282	11.58	21.89	97.2	0.08	17.8	105.2	0.4
1250	12.29	0.3000	6.574	0.338	11.83	4.32	96.6	0.08	18.0	107.4	1.0
1280	12.48	0.3177	6.282	0.370	11.90	1.83	95.3	0.08	17.0	108.0	2.7
1310	12.31	0.2949	6.397	0.436	11.54	1.85	93.8	0.08	18.4	104.9	2.3
1340	12.40	0.3236	6.439	0.463	11.56	1.66	93.1	0.08	16.7	105.0	2.5
1380	13.18	0.3205	6.087	0.600	11.90	0.97	90.6	0.09	16.9	108.0	4.2
1400	17.32	0.3041	6.395	1.792	12.55	0.35	75.6	0.08	18.0	113.8	11.0

Experiment:	63B39										
Sample:	**980730-1**		J-value:	0.005188		K wt. %:	6.3		Plateau range:		650-1060°C
Material:	Biotite		^{39}Ar %:	89		wt.:	3.12 mg		Uncalibrated plateau age (Ma):		101.7 ± 0.3
T (°C)	**^{40}Ar/^{39}Ar**	**^{38}Ar/^{39}Ar**	**^{37}Ar/^{39}Ar**	**^{36}Ar/^{39}Ar**	**F**	**39Ar %**	**40Ar %**	**K/Ca**	**K/Cl**	**Apparent Age (Ma)**	**Error 2σ**
550	21.100	0.1363	0.0769	3.7120	10.12	0.65	48.0	6.8	44	92.3	2.0
600	12.610	0.0256	0.0419	0.8490	10.09	2.21	78.5	12.5	395	92.1	0.7
650	12.270	0.0259	0.0229	0.3570	11.20	4.45	90.9	22.8	362	101.9	0.4
675	11.860	0.0258	0.0234	0.2280	11.17	3.80	94.0	22.3	357	101.6	0.4
700	19.130	0.0293	0.0186	2.6440	11.30	5.05	60.6	28.2	385	102.8	0.7
720	12.930	0.0258	0.0144	0.5870	11.18	4.51	82.2	36.3	375	101.7	0.5
740	11.500	0.0249	0.0137	0.0940	11.20	5.93	96.8	38.2	375	101.9	0.3
760	11.350	0.0247	0.0147	0.0550	11.17	6.36	98.5	35.6	378	101.7	0.2
780	11.300	0.0246	0.0163	0.0520	11.13	5.10	98.6	32.1	382	101.3	0.3
800	11.310	0.0245	0.0197	0.0490	11.16	4.87	98.7	26.5	384	101.5	0.3
820	11.400	0.0245	0.0283	0.0730	11.17	3.36	98.2	18.5	383	101.6	0.4
840	11.440	0.0235	0.0386	0.0890	11.16	2.26	97.8	13.5	417	101.5	0.4
860	11.590	0.0233	0.0436	0.1810	11.04	1.79	95.7	12.0	430	100.5	0.5
890	13.070	0.0244	0.0347	0.6120	11.25	2.38	86.7	15.1	417	102.3	0.6
830	11.990	0.0241	0.0248	0.2320	11.29	3.17	93.7	21.0	405	102.7	0.4
890	11.810	0.0250	0.0161	0.1840	11.26	6.56	95.4	32.6	376	102.4	0.3
1020	11.450	0.0251	0.0133	0.1070	11.12	13.18	97.2	39.5	371	101.2	0.5
1040	11.360	0.0240	0.0095	0.0400	11.23	8.66	98.7	55.3	396	102.1	0.2
1050	11.310	0.0239	0.0142	0.0580	11.12	5.38	98.6	36.7	401	101.2	0.3
1060	11.330	0.0227	0.0252	0.0680	11.12	2.59	98.3	20.8	443	101.2	0.4
1070	11.280	0.0222	0.0441	0.1150	10.93	1.31	97.2	11.8	464	99.5	0.7
1080	11.250	0.0199	0.1042	0.1980	10.66	0.64	95.2	5.0	594	97.1	1.2
1090	11.040	0.0131	0.1574	0.1800	10.50	0.35	95.2	3.3	2600	95.7	2.3
1100	11.200	0.0147	0.1906	0.2500	10.46	0.34	93.7	2.7	1500	95.3	2.2
1150	11.120	0.0133	0.1884	0.1510	10.67	0.79	96.0	2.8	2360	97.2	1.2
1200	11.070	0.0137	0.0860	0.0910	10.79	1.58	97.5	6.1	1910	98.3	0.6
1600	11.960	0.0153	0.1231	0.4350	10.66	2.74	89.7	4.3	1390	97.1	0.5

Experiment:	63B51						
Sample:	**980730-3**	J-value:	0.005173	K wt. %:	0.7	Plateau range:	1025-1360°C
Material:	Hornblende	^{39}Ar %:	88	wt.:	6.61 mg	Uncalibrated plateau age (Ma):	104.0 ± 0.5

T (°C)	^{40}Ar/^{39}Ar	^{38}Ar/^{39}Ar	^{37}Ar/^{39}Ar	^{36}Ar/^{39}Ar	F	39Ar %	40Ar %	K/Ca	K/Cl	Apparent Age (Ma)	Error 2σ
600	51.62	0.1226	1.353	16.010	4.407	1.01	8.5	0.39	63.9	40.7	8.1
700	556.10	0.4094	1.817	185.800	7.055	0.76	1.4	0.29	106.0	64.7	52.8
800	33.29	0.0506	0.699	7.978	9.761	2.11	12.7	0.75	211.0	88.9	10.9
900	87.62	0.0928	2.306	26.980	8.078	1.54	9.6	0.23	167.0	73.9	8.5
1000	15.81	0.2217	8.909	1.808	11.200	4.38	58.8	0.06	25.1	101.6	1.8
1025	12.79	0.2861	5.832	0.619	11.430	5.98	87.9	0.09	19.0	103.7	0.8
1040	12.16	0.2699	5.992	0.423	11.400	10.66	93.4	0.09	20.2	103.4	0.4
1050	12.17	0.2937	5.738	0.448	11.310	7.02	93.0	0.09	18.5	102.6	0.7
1060	12.51	0.2979	5.842	0.514	11.460	4.30	91.7	0.09	18.2	103.9	0.9
1070	13.21	0.3055	6.077	0.819	11.280	2.44	86.2	0.09	17.8	102.3	1.4
1080	13.96	0.3053	6.575	0.931	11.750	1.83	84.2	0.08	17.8	106.5	1.9
1090	14.33	0.2866	6.598	1.118	11.560	1.64	80.9	0.08	19.0	104.8	2.3
1105	13.89	0.2965	6.242	1.017	11.400	2.31	81.8	0.08	18.4	103.3	1.7
1120	14.47	0.2869	5.941	1.295	11.120	2.79	77.2	0.09	19.0	100.9	1.4
1145	17.63	0.3394	5.918	2.190	11.640	2.88	66.7	0.09	16.0	105.5	1.5
1170	16.61	0.3585	5.655	1.950	11.300	4.09	67.9	0.09	15.1	102.5	1.3
1195	14.62	0.3680	5.595	1.239	11.410	7.41	77.4	0.09	14.7	103.5	0.8
1220	15.74	0.3488	5.968	1.541	11.670	5.95	74.5	0.09	15.5	105.8	1.0
1245	15.03	0.3337	6.061	1.386	11.430	7.30	75.8	0.09	16.3	103.7	0.8
1280	13.64	0.3408	5.980	0.860	11.590	11.94	84.3	0.09	15.9	105.0	0.6
1310	18.25	0.3090	7.049	2.377	11.800	4.45	68.4	0.07	17.7	106.9	1.1
1360	17.10	0.3343	5.757	2.062	11.480	4.60	66.8	0.09	16.3	104.0	1.2
1400	30.23	0.3443	5.804	6.286	12.130	1.69	43.9	0.09	16.2	109.8	3.5
1600	76.25	0.3009	5.744	21.860	12.130	0.92	17.4	0.09	20.9	109.8	7.6

Experiment:	63B41										
Sample:	**980730-3**		J-value:	0.005188		K wt. %:	6.3		Plateau range: 700-800°C, 1050-1090°C		
Material:	Biotite		^{39}Ar %:	66		wt.:	3.12 mg		Uncalibrated plateau age (Ma):		101.3 ± 0.3

T (°C)	^{40}Ar/^{39}Ar	^{38}Ar/^{39}Ar	^{37}Ar/^{39}Ar	^{36}Ar/^{39}Ar	F	39Ar %	40Ar %	K/Ca	K/Cl	Apparent Age (Ma)	Error 2σ
600	28.91	0.0519	0.0551	7.408	7.01	2.73	24.3	9.5	192	64.4	1.8
650	15.88	0.0238	0.0200	1.905	10.23	7.10	61.7	26.2	555	93.3	0.6
700	19.63	0.0264	0.0183	2.874	11.12	7.86	57.2	28.6	508	101.2	0.7
725	16.57	0.0238	0.0172	1.821	11.17	7.48	66.2	30.4	546	101.6	0.6
750	12.06	0.0211	0.0168	0.276	11.23	8.53	90.5	31.1	530	102.1	0.3
775	12.20	0.0212	0.0203	0.330	11.21	7.73	92.1	25.8	533	101.9	0.4
800	12.77	0.0217	0.0294	0.574	11.06	5.19	87.4	17.8	530	100.7	0.4
826	15.39	0.0227	0.0461	1.573	10.73	3.06	71.9	11.3	583	97.7	0.6
850	20.65	0.0240	0.0656	3.649	9.86	2.16	49.8	8.0	822	90.0	1.4
875	24.14	0.0290	0.0755	4.993	9.38	1.87	39.7	6.9	590	85.7	1.3
900	23.98	0.0278	0.0811	4.817	9.73	1.48	40.4	6.5	657	88.8	2.2
950	19.84	0.0255	0.0676	3.367	9.89	3.33	49.4	7.7	623	90.2	1.1
1000	13.59	0.0214	0.0398	0.917	10.87	6.20	77.8	13.2	589	98.9	0.4
1050	11.84	0.0216	0.0294	0.237	11.13	17.97	93.6	17.8	504	101.2	0.5
1070	11.47	0.0207	0.0285	0.157	11.00	7.96	95.6	18.4	543	100.1	0.3
1090	11.60	0.0195	0.0678	0.148	11.15	3.06	96.2	7.7	620	101.4	0.5
1110	11.68	0.0176	0.1732	0.280	10.85	1.29	93.6	3.0	827	98.7	0.9
1130	11.83	0.0163	0.2333	0.362	10.76	0.78	91.4	2.2	1080	98.0	1.3
1150	11.52	0.0147	0.2055	0.263	10.75	0.76	93.2	2.5	1510	97.8	1.6
1170	11.42	0.0135	0.1481	0.222	10.77	0.81	94.3	3.5	2270	98.0	1.2
1190	11.35	0.0133	0.1172	0.204	10.74	0.87	94.7	4.5	2500	97.8	1.1
1220	11.85	0.0132	0.0610	0.370	10.75	1.05	91.1	8.6	2960	97.8	1.2
1250	11.37	0.0142	0.0680	0.196	10.78	0.74	94.4	7.7	1710	98.1	1.4

Experiment:	63B43						
Sample:	**980730-4**	J-value:	0.005188	K wt. %:	6.3	Plateau range:	675-1050°C
Material:	Biotite	^{39}Ar %:	91	wt.:	3.12 mg	Uncalibrated plateau age (Ma):	102.6 ± 0.3

T (°C)	^{40}Ar/^{39}Ar	^{38}Ar/^{39}Ar	^{37}Ar/^{39}Ar	^{36}Ar/^{39}Ar	F	39Ar %	40Ar %	K/Ca	K/Cl	Apparent Age (Ma)	Error 2σ
550	17.24	0.0688	0.1455	3.967	5.51	0.63	32.0	3.6	103	50.8	2.2
600	11.93	0.0253	0.0648	1.439	7.66	1.64	62.5	8.1	440	70.3	0.8
625	12.79	0.0231	0.0218	0.740	10.59	2.90	82.0	23.9	476	96.4	0.5
650	12.30	0.0223	0.0162	0.394	11.12	3.50	89.9	32.2	485	101.1	0.4
675	11.94	0.0214	0.0095	0.223	11.27	4.94	94.2	55.2	509	102.4	0.3
700	17.88	0.0254	0.0068	2.183	11.41	4.88	65.8	77.1	494	103.6	0.6
720	11.70	0.0214	0.0063	0.135	11.28	6.19	92.9	83.5	504	102.5	0.3
740	12.01	0.0215	0.0062	0.244	11.28	6.08	94.2	83.9	509	102.5	0.3
760	11.99	0,0217	0.0061	0.250	11.24	5.19	93.8	85.4	499	102.1	0.3
780	11.85	0.0214	0.0077	0.177	11.32	3.95	95.4	68.0	509	102.8	0.3
800	11.99	0.0221	0.0100	0.210	11.36	2.78	94.9	52.1	476	103.2	0.4
820	12.10	0.0208	0.0134	0.282	11.26	2.15	93.3	39.2	549	102.3	0.5
840	13.99	0.0225	0.0119	0.903	11.31	1.68	82.1	44.1	519	102.8	0.8
860	23.74	0.0278	0.0252	4.204	11.30	1.82	49.3	20.8	574	102.7	1.2
890	12.97	0.0215	0.0277	0.531	11.39	3.21	83.9	18.9	536	103.5	0.5
930	12.28	0.0218	0.0165	0.313	11.34	7.34	92.3	31.7	502	103.1	0.3
980	13.44	0.0231	0.0138	0.751	11.20	17.06	83.8	38.0	479	101.8	0.5
1020	11.62	0.0216	0.0145	0.094	11.33	13.65	95.7	36.1	492	103.0	0.5
1030	11.68	0.0215	0.0149	0.118	11.31	6.06	97.1	35.1	498	102.8	0.2
1040	11.53	0.0213	0.0328	0.055	11.35	2.47	98.3	15.9	502	103.1	0.4
1050	11.66	0.0201	0.0725	0.115	11.31	1.12	97.4	7.2	573	102.8	0.8
1060	11.95	0.0211	0.1589	0.100	11.65	0.48	97.5	3.3	514	105.8	1.6
1075	12.80	0.0165	0.5403	0.643	10.93	0.17	88.1	1.0	1160	99.4	4.2
1100	13.84	0.0137	0.9046	0.516	12.37	0.10	89.0	0.6	2770	112.1	7.2

Experiment:	63B44						
Sample:	**980730-7**	J-value:	0.005182	K wt. %:	6.0	Plateau range: 675-800°C, 980-1070°C	
Material:	Biotite	^{39}Ar %:	74	wt.:	3.89 mg	Uncalibrated plateau age (Ma):	104.0 ± 0.3

T (°C)	^{40}Ar/^{39}Ar	^{38}Ar/^{39}Ar	^{37}Ar/^{39}Ar	^{36}Ar/^{39}Ar	F	39Ar %	40Ar %	K/Ca	K/Cl	Apparent Age (Ma)	Error 2σ
600	16.96	0.0361	0.0504	3.107	7.76	2.08	45.80	10.4	268	71.2	1.0
625	13.24	0.0284	0.0117	0.928	10.48	6.25	77.80	44.8	329	95.4	0.4
650	12.42	0.0270	0.0090	0.441	11.10	5.85	88.40	58.1	340	100.9	0.3
675	12.19	0.0267	0.0072	0.235	11.48	6.16	93.90	72.6	337	104.2	0.3
700	15.84	0.0286	0.0074	1.431	11.60	7.54	74.50	71.1	345	105.3	0.4
720	12.02	0.0259	0.0068	0.143	11.58	7.55	93.60	76.8	351	105.1	0.3
740	13.25	0.0270	0.0068	0.573	11.55	4.96	88.30	76.4	344	104.8	0.3
760	12.27	0.0269	0.0098	0.252	11.51	3.64	93.10	53.6	334	104.5	0.4
780	12.31	0.0261	0.0148	0.292	11.43	2.44	93.10	35.3	352	103.8	0.4
800	12.80	0.0278	0.0208	0.480	11.36	1.67	89.40	25.1	324	103.2	0.6
820	13.39	0.0272	0.0253	0.758	11.14	1.35	83.90	20.7	347	101.2	0.7
840	13.87	0.0270	0.0306	0.919	11.14	1.14	80.70	17.1	360	101.2	0.7
860	14.23	0.0281	0.0306	1.106	10.95	1.25	77.30	17.1	342	99.6	0.9
890	14.07	0.0272	0.0362	1.065	10.91	2.02	77.60	14.5	363	99.2	0.6
930	13.00	0.0276	0.0248	0.615	11.17	5.13	85.70	21.1	333	101.5	0.4
980	12.50	0.0268	0.0179	0.390	11.33	5.62	90.30	29.2	342	103.0	0.3
1000	12.17	0.0263	0.0213	0.290	11.30	5.84	92.80	24.6	349	102.7	0.3
1010	11.92	0.0269	0.0304	0.183	11.37	6.00	95.30	17.2	330	103.2	0.3
1020	11.80	0.0274	0.0575	0.130	11.40	5.35	96.70	9.1	320	103.6	0.3
1030	11.76	0.0292	0.1259	0.109	11.43	5.70	97.30	4.2	286	103.9	0.3
1040	11.73	0.0282	0.0940	0.102	11.42	5.06	97.50	5.6	303	103.8	0.3
1050	11.75	0.0265	0.0431	0.094	11.46	3.65	97.70	12.1	335	104.1	0.3
1060	11.81	0.0266	0.0573	0.099	11.51	1.86	97.60	9.1	334	104.5	0.5
1070	11.87	0.0271	0.1290	0.132	11.48	0.94	96.90	4.1	325	104.2	0.8
1100	12.01	0.0284	0.3988	0.139	11.62	0.72	96.80	1.3	302	105.5	1.0
1200	12.78	0.0357	1.7640	0.629	11.05	0.22	89.30	0.3	221	100.5	3.3

Experiment:	63B45						
Sample:	**980802-3A**	J-value:	0.005181	K wt. %:	6.5	Plateau range:	600-780°C
Material:	Biotite	^{39}Ar %:	59	wt.:	4.28 mg	Uncalibrated plateau age (Ma):	104.0 ± 0.3

T (°C)	^{40}Ar/^{39}Ar	^{38}Ar/^{39}Ar	^{37}Ar/^{39}Ar	^{36}Ar/^{39}Ar	F	39Ar %	40Ar %	K/Ca	K/Cl	Apparent Age (Ma)	Error 2σ
550	7.618	0.0405	0.0075	1.274	3.84	10.15	50.5	70.0	191	35.5	0.3
600	8.208	0.0395	0.0056	0.883	5.58	12.31	66.8	93.3	193	51.4	0.2
650	8.444	0.0394	0.0061	0.833	5.97	9.66	70.5	86.4	193	54.9	0.2
675	8.462	0.0394	0.0058	0.810	6.05	9.42	71.6	90.5	193	55.7	0.3
700	11.440	0.0409	0.0051	1.815	6.06	7.97	54.5	102.0	196	55.8	0.4
720	8.771	0.0392	0.0059	0.975	5.87	7.28	65.3	88.0	196	54.1	0.3
740	8.401	0.0378	0.0057	0.920	5.67	5.79	67.5	92.1	206	52.2	0.3
760	8.326	0.0357	0.0065	0.907	5.63	4.04	67.7	80.3	225	51.9	0.4
780	8.461	0.0320	0.0075	0.863	5.90	2.72	69.6	69.9	267	54.3	0.5
800	9.059	0.0268	0.0057	0.648	7.13	2.31	78.0	91.2	353	65.4	0.4
820	9.117	0.0267	0.0089	0.641	7.21	2.08	79.2	58.5	355	66.1	0.6
840	9.310	0.0282	0.0067	0.732	7.13	2.16	77.0	78.1	325	65.5	0.4
860	9.578	0.0228	0.0056	0.506	8.07	3.52	84.0	93.0	472	73.9	0.3
890	9.752	0.0194	0.0050	0.335	8.75	5.12	89.5	104.0	652	80.0	0.2
930	10.130	0.0218	0.0119	0.564	8.45	4.63	84.2	43.8	522	77.3	0.3
980	9.944	0.0279	0.0135	0.769	7.66	2.41	78.3	38.7	333	70.2	0.5
1000	10.250	0.0279	0.0165	0.841	7.75	1.65	75.9	31.6	336	71.0	0.6
1010	10.610	0.0280	0.0237	0.961	7.76	1.21	73.5	22.1	338	71.1	0.7
1020	10.350	0.0257	0.0306	0.723	8.20	0.84	78.6	17.1	383	75.1	1.0
1030	10.200	0.0231	0.0373	0.524	8.64	0.69	84.2	14.0	461	79.0	1.0
1040	9.982	0.0205	0.0360	0.369	8.88	0.69	88.7	14.5	577	81.1	0.9
1050	10.120	0.0181	0.0299	0.240	9.40	0.60	92.6	17.5	763	85.8	1.0
1060	10.330	0.0149	0.0378	0.274	9.51	0.57	92.3	13.8	1430	86.7	1.1
1070	10.350	0.0134	0.0318	0.164	9.85	0.68	95.1	16.5	2260	89.8	0.9
1150	10.500	0.0128	0.0388	0.097	10.20	1.21	97.2	13.5	2840	92.9	0.6
1200	11.990	0.0122	0.1780	0.383	10.86	0.30	92.9	2.9	8070	98.8	1.8

Experiment:	63B54										
Sample:	**980802-3A**		J-value:	0.005169		K wt. %:	6.8		Plateau range:		640-750°C
Material:	Biotite		^{39}Ar %:	51		wt.:	3.75 mg		Uncalibrated plateau age (Ma):		55.5 ± 0.5

T (°C)	^{40}Ar/^{39}Ar	^{38}Ar/^{39}Ar	^{37}Ar/^{39}Ar	^{36}Ar/^{39}Ar	F	39Ar %	40Ar %	K/Ca	K/Cl	Apparent Age (Ma)	Error 2σ
500	9.214	0.0411	0.0182	2.009	3.26	2.96	35.5	28.7	196	30.2	0.6
550	7.699	0.0396	0.0068	1.200	4.14	5.00	52.6	77.2	196	38.2	0.4
600	8.234	0.0396	0.0054	0.946	5.42	9.70	65.5	96.7	193	49.9	0.3
640	8.627	0.0397	0.0063	0.844	6.12	11.80	70.7	83.4	191	56.2	0.2
675	8.649	0.0392	0.0055	0.836	6.16	11.95	71.4	94.8	195	56.6	0.2
700	11.980	0.0411	0.0063	1.977	6.13	7.96	53.2	82.7	196	56.3	0.4
710	8.461	0.0379	0.0060	0.834	5.98	6.69	67.9	87.2	204	54.9	0.3
720	8.648	0.0375	0.0058	0.938	5.86	4.83	68.2	89.9	209	53.8	0.4
730	8.756	0.0370	0.0075	1.007	5.77	3.42	66.2	69.8	215	53.0	0.4
740	9.504	0.0367	0.0097	1.225	5.87	2.30	62.4	54.1	221	53.9	0.6
750	8.933	0.0343	0.0087	0.980	6.02	1.83	66.9	60.0	241	55.3	0.6
760	9.102	0.0305	0.0093	0.884	6.48	1.67	70.9	56.0	289	59.4	0.6
775	9.312	0.0285	0.0099	0.862	6.75	1.64	72.5	52.9	324	61.9	0.6
790	9.845	0.0284	0.0105	0.951	7.02	1.62	71.5	49.7	329	64.3	0.7
810	12.030	0.0313	0.0091	1.688	7.03	1.67	59.4	57.5	300	64.4	0.8
825	9.751	0.0269	0.0112	0.818	7.32	1.41	72.9	46.7	358	67.0	0.6
850	10.090	0.0250	0.0089	0.754	7.85	1.80	77.7	59.1	407	71.7	0.6
875	10.080	0.0195	0.0054	0.414	8.85	3.15	87.3	97.4	653	80.7	0.4
900	10.090	0.0200	0.0066	0.437	8.79	2.89	87.3	79.8	621	80.1	0.3
930	10.240	0.0192	0.0093	0.433	8.94	2.79	87.5	56.1	689	81.5	0.4
960	10.410	0.0215	0.0145	0.542	8.79	2.37	84.9	36.0	536	80.2	0.5
990	10.430	0.0269	0.0157	0.749	8.20	2.00	79.4	33.3	354	74.9	0.5
1010	10.480	0.0270	0.0142	0.811	8.07	1.57	77.3	36.7	356	73.7	0.6
1040	10.540	0.0259	0.0199	0.769	8.25	1.50	78.3	26.2	381	75.3	0.6
1070	10.820	0.0228	0.0223	0.643	8.90	1.54	82.1	23.5	483	81.2	0.6
1100	10.970	0.0155	0.0216	0.352	9.92	2.05	90.0	24.2	1280	90.2	0.4
1180	11.670	0.0140	0.0545	0.481	10.24	1.88	88.1	9.6	2240	93.0	0.5

Experiment:	63B46										
Sample:	**980802-3A**		J-value:	0.005179		K wt. %:	7.5		Plateau range:		830-1030°C
Material:	Muscovite		^{39}Ar %:	63		wt.:	3.19 mg		Uncalibrated plateau age (Ma):		90.4 ± 0.3

T (°C)	^{40}Ar/^{39}Ar	^{38}Ar/^{39}Ar	^{37}Ar/^{39}Ar	^{36}Ar/^{39}Ar	F	39Ar %	40Ar %	K/Ca	K/Cl	Apparent Age (Ma)	Error 2σ
550	12.840	0.0106	0.1869	0.535	11.26	0.03	87.8	2.8	455	102.2	21.9
600	9.968	0.0201	0.0286	0.465	8.58	0.38	86.2	18.3	619	78.4	1.9
650	9.459	0.0187	0.0161	0.298	8.56	0.73	90.5	32.5	713	78.3	1.0
700	14.450	0.0237	0.0138	2.049	8.38	1.14	59.4	37.9	575	76.6	1.2
750	11.130	0.0161	0.0065	0.791	8.78	1.82	77.4	80.4	1370	80.2	0.7
775	9.498	0.0120	0.0053	0.122	9.12	1.91	94.4	99.3	4980	83.3	0.5
800	9.828	0.0122	0.0026	0.080	9.58	4.53	97.6	204.0	3940	87.3	0.2
830	10.070	0.0119	0.0029	0.041	9.93	16.57	98.8	179.0	4990	90.5	0.3
860	10.050	0.0123	0.0016	0.053	9.87	9.84	98.5	330.0	3780	90.0	0.2
890	10.150	0.0121	0.0021	0.066	9.94	10.03	98.1	245.0	4230	90.5	0.2
920	10.070	0.0121	0.0028	0.040	9.94	8.71	98.8	188.0	4000	90.5	0.2
950	10.080	0.0123	0.0035	0.057	9.90	5.66	98.4	151.0	3650	90.2	0.2
970	10.170	0.0123	0.0061	0.104	9.85	3.77	97.2	86.2	4040	89.7	0.3
1010	10.130	0.0123	0.0080	0.056	9.95	4.41	98.3	65.6	3730	90.6	0.2
1030	10.130	0.0127	0.0087	0.048	9.98	3.79	98.6	59.9	2820	90.9	0.2
1050	10.160	0.0129	0.0112	0.029	10.06	4.22	99.1	46.8	2530	91.6	0.2
1070	10.180	0.0120	0.0089	0.030	10.08	5.07	99.1	58.5	4610	91.8	0.2
1080	10.190	0.0120	0.0074	0.016	10.12	4.45	99.5	70.9	4440	92.2	0.2
1090	10.280	0.0126	0.0084	0.030	10.18	4.00	99.2	62.2	2910	92.7	0.3
1100	10.290	0.0119	0.0107	0.020	10.21	2.96	99.4	48.7	5000	93.0	0.3
1120	10.340	0.0124	0.0142	0.016	10.28	2.63	99.5	36.9	3200	93.6	0.3
1140	10.420	0.0123	0.0186	0.046	10.27	2.17	98.8	28.2	3750	93.5	0.4
1160	10.560	0.0118	0.0623	0.033	10.45	0.94	99.0	8.4	5480	95.1	0.8
1200	11.570	0.0127	0.3403	0.443	10.27	0.25	91.7	1.5	4950	93.5	2.5

Experiment:	63B55										
Sample:	**980802-3A**		J-value:	0.005168		K wt. %:	7.8			Plateau range:	800-1060°C
Material:	Muscovite		^{39}Ar %:	62		wt.:	3.16 mg			Uncalibrated plateau age (Ma):	90.0 ± 0.3

T (°C)	^{40}Ar/^{39}Ar	^{38}Ar/^{39}Ar	^{37}Ar/^{39}Ar	^{36}Ar/^{39}Ar	F	39Ar %	40Ar %	K/Ca	K/Cl	Apparent Age (Ma)	Error 2σ
600	12.500	0.0258	0.0143	1.650	7.61	1.32	61.0	36.7	437	69.6	0.7
700	28.170	0.0292	0.0146	6.566	8.75	1.84	32.0	35.9	852	79.8	1.5
750	9.658	0.0133	0.0070	0.224	8.98	2.76	81.5	74.3	2530	81.8	0.5
780	10.090	0.0127	0.0045	0.201	9.48	4.21	94.1	117.0	3410	86.3	0.3
800	10.180	0.0123	0.0016	0.102	9.86	11.44	96.9	336.0	4020	89.7	0.2
810	10.380	0.0124	0.0055	0.237	9.66	3.84	94.3	94.5	4260	87.9	0.3
820	10.430	0.0131	0.0063	0.248	9.68	2.54	93.0	83.4	2740	88.1	0.4
830	10.580	0.0125	0.0079	0.277	9.74	2.23	92.3	66.5	4330	88.6	0.4
840	10.570	0.0122	0.0068	0.258	9.80	2.37	92.7	77.0	5330	89.1	0.4
850	10.740	0.0126	0.0049	0.267	9.94	2.59	92.7	107.0	3930	90.4	0.3
860	10.510	0.0125	0.0053	0.195	9.92	2.72	94.3	97.8	3720	90.2	0.3
870	10.480	0.0124	0.0041	0.193	9.90	2.73	94.5	128.0	4050	90.0	0.3
880	10.540	0.0126	0.0059	0.234	9.84	2.58	93.5	89.3	3730	89.5	0.4
890	10.620	0.0123	0.0082	0.233	9.92	2.26	93.5	63.5	4610	90.2	0.4
900	10.690	0.0125	0.0091	0.253	9.93	1.97	93.1	57.2	4030	90.3	0.5
940	10.480	0.0127	0.0045	0.170	9.96	3.73	95.1	117.0	3330	90.5	0.3
980	10.350	0.0122	0.0039	0.128	9.95	6.09	96.3	133.0	4240	90.5	0.2
1020	10.360	0.0124	0.0051	0.122	9.99	6.25	96.5	102.0	3700	90.8	0.2
1060	10.300	0.0123	0.0054	0.095	10.00	8.89	97.2	97.2	3950	90.9	0.2
1100	10.350	0.0129	0.0079	0.074	10.12	13.58	97.9	66.1	2680	92.0	0.4
1140	10.500	0.0130	0.0108	0.056	10.32	11.65	98.4	48.2	2430	93.8	0.4
1180	12.730	0.0124	0.0686	0.848	10.21	1.93	88.4	7.6	2540	92.8	0.5
1250	18.020	0.0180	0.2076	2.597	10.35	0.48	61.1	2.5	2260	94.0	1.6

Experiment:	73C19							
Sample:	**010801-5**	J-value:	0.005971	K wt. %:	1.2	Plateau range:	923-1258°C	
Material:	Hornblende	^{39}Ar %:	71	wt.:	13.35 mg	Uncalibrated plateau age (Ma):	29.2 ± 0.2	

T (°C)	^{40}Ar/^{39}Ar	^{38}Ar/^{39}Ar	^{37}Ar/^{39}Ar	^{36}Ar/^{39}Ar	F	39Ar %	40Ar %	K/Ca	K/Cl	Apparent Age (Ma)	Error 2σ
427	12.310	0.7125	0.2254	3.595	1.692	4.93	13.77	2.32	7.5	18.1	0.9
605	11.320	0.1237	0.1760	3.127	2.065	7.99	18.30	2.97	49.2	22.1	0.8
653	17.360	0.1103	0.1422	5.008	2.551	2.62	14.72	3.68	58.6	27.3	1.4
701	10.270	0.1142	0.1886	2.678	2.342	1.47	22.87	2.77	53.6	25.0	1.9
752	11.310	0.1293	0.3369	2.914	2.703	0.89	23.95	1.55	46.6	28.9	2.9
804	12.650	0.1323	0.3467	3.211	3.164	1.19	25.07	1.51	45.6	33.8	2.4
831	12.800	0.1258	0.3078	3.542	2.332	1.05	18.26	1.70	48.6	25.0	2.8
857	12.740	0.1269	0.3237	3.378	2.756	1.31	21.68	1.62	48.0	29.4	2.4
884	12.060	0.1342	0.3586	3.309	2.285	1.56	18.99	1.46	44.9	24.4	2.0
901	11.290	0.1357	0.3710	2.912	2.690	1.80	23.89	1.41	44.1	28.7	1.8
911	10.640	0.1444	0.4075	2.776	2.446	1.99	23.05	1.28	41.0	26.2	1.6
923	10.240	0.1527	0.4841	2.530	2.782	2.52	27.23	1.08	38.3	29.7	1.3
934	9.845	0.1618	0.5722	2.455	2.615	3.29	26.63	0.91	35.9	27.9	1.1
944	9.520	0.1799	0.7321	2.356	2.596	3.90	27.34	0.71	31.9	27.7	0.9
955	9.099	0.2180	1.1500	2.167	2.774	5.48	30.56	0.46	25.8	29.6	0.7
967	8.187	0.2851	1.7850	1.873	2.790	4.93	34.15	0.29	19.3	29.8	0.7
978	6.742	0.4009	2.9780	1.452	2.695	4.32	40.07	0.18	13.5	28.8	0.8
989	4.341	0.5891	4.7890	0.705	2.667	4.05	61.65	0.11	9.0	28.5	0.7
1000	3.440	0.6642	5.4910	0.407	2.714	5.31	79.25	0.10	8.0	29.0	0.5
1012	3.260	0.6679	5.4860	0.334	2.748	7.25	84.73	0.10	7.9	29.4	0.4
1023	3.160	0.6745	5.6590	0.298	2.772	7.91	88.18	0.09	7.9	29.6	0.4
1055	3.077	0.6634	5.6390	0.290	2.710	11.33	88.58	0.09	8.0	29.0	0.3
1080	3.419	0.6752	5.7650	0.363	2.847	4.00	83.66	0.09	7.9	30.4	0.6
1109	3.680	0.8081	6.6660	0.496	2.797	2.21	76.27	0.08	6.5	29.9	1.0
1139	4.234	0.7832	7.5520	0.753	2.673	0.81	63.23	0.07	6.7	28.6	2.5
1198	4.020	0.7630	8.1890	0.634	2.866	1.71	71.40	0.06	6.9	30.6	1.5

1258	4.277	0.6975	7.3730	0.722	2.789	2.29	65.34	0.07	7.6	29.8	1.2
1318	6.279	0.6711	6.3080	1.258	3.113	0.63	49.60	0.08	7.9	33.2	3.2
1442	6.969	0.4239	4.2420	0.812	4.936	0.78	70.92	0.12	12.7	52.4	3.2
1629	13.000	0.0701	0.5089	1.698	8.001	0.47	61.66	1.03	94.7	84.2	5.2

Experiment:	73C20						
Sample:	**010801-5**	J-value:	0.005969	K wt. %:	1.3	Plateau range:	933-1198°C
Material:	Hornblende	^{39}Ar %:	70	wt.:	14.12 mg	Uncalibrated plateau age (Ma):	29.7 ± 0.3

T (°C)	^{40}Ar/^{39}Ar	^{38}Ar/^{39}Ar	^{37}Ar/^{39}Ar	^{36}Ar/^{39}Ar	F	39Ar %	40Ar %	K/Ca	K/Cl	Apparent Age (Ma)	Error 2σ
427	16.990	0.7731	0.2134	5.151	1.775	5.24	10.47	2.45	6.9	19.0	1.8
558	11.150	0.2093	0.1327	3.118	1.929	6.49	17.34	3.94	27.2	20.7	1.3
604	11.830	0.0987	0.1655	3.187	2.397	3.81	20.32	3.16	64.6	25.6	2.0
652	15.770	0.1165	0.1331	4.420	2.690	2.94	17.09	3.93	54.2	28.7	2.7
805	13.960	0.1300	0.3177	3.848	2.586	2.76	18.56	1.65	47.1	27.6	2.8
912	13.420	0.1311	0.3462	3.708	2.470	5.79	18.44	1.51	46.5	26.4	1.5
933	12.010	0.1571	0.5238	3.171	2.657	4.65	22.18	1.00	37.4	28.4	1.7
955	10.170	0.1759	0.6654	2.507	2.802	7.72	27.60	0.79	32.7	29.9	1.1
972	9.180	0.2281	1.2670	2.186	2.810	10.75	30.68	0.41	24.6	30.0	0.8
989	7.824	0.3518	2.4720	1.741	2.881	8.26	36.90	0.21	15.5	30.8	1.0
1007	4.762	0.6443	5.3110	0.834	2.762	9.16	58.14	0.10	8.2	29.5	0.8
1018	4.103	0.6698	5.6270	0.629	2.738	9.00	66.94	0.09	7.9	29.2	0.8
1030	4.105	0.6688	5.5610	0.641	2.698	8.35	65.94	0.09	7.9	28.8	0.9
1046	5.050	0.6704	5.6150	0.962	2.701	5.09	53.59	0.09	7.9	28.9	1.4
1092	6.402	0.6994	6.1360	1.370	2.895	4.17	45.24	0.09	7.6	30.9	1.8
1198	9.081	0.8038	8.2540	2.361	2.838	3.36	31.17	0.06	6.6	30.3	2.3
1318	16.450	0.7036	7.1850	4.717	3.147	2.45	19.07	0.07	7.6	33.6	3.1

Experiment:	73C17										
Sample:	**010801-5**		J-value:	0.005973		K wt. %:	2.1		Plateau range:		604-1034°C
Material:	Biotite		^{39}Ar %:	72		wt.:	4.30 mg		Uncalibrated plateau age (Ma):		29.3 ± 0.4

T (°C)	^{40}Ar/^{39}Ar	^{38}Ar/^{39}Ar	^{37}Ar/^{39}Ar	^{36}Ar/^{39}Ar	F	39Ar %	40Ar %	K/Ca	K/Cl	Apparent Age (Ma)	Error 2σ
325	18.050	0.1589	0.1802	5.726	1.122	0.58	6.22	2.9	38.3	12.1	9.2
389	10.280	0.0931	0.1256	3.065	1.206	1.18	11.77	4.2	69.1	13.0	4.4
428	8.719	0.0874	0.0928	2.295	1.917	2.18	22.06	5.6	73.3	20.5	2.5
470	6.897	0.0867	0.0855	1.775	1.631	4.63	23.74	6.1	72.9	17.5	1.2
495	6.129	0.0789	0.0828	1.448	1.831	5.35	30.01	6.3	81.1	19.6	1.1
522	6.681	0.0832	0.0860	1.512	2.193	4.96	32.96	6.1	76.2	23.5	1.1
549	7.479	0.0915	0.0805	1.820	2.080	4.39	27.92	6.5	68.5	22.3	1.2
577	7.827	0.0976	0.0747	1.829	2.400	4.01	30.78	7.0	63.4	25.7	1.2
604	7.964	0.1011	0.0731	1.797	2.634	4.20	33.19	7.2	60.8	28.2	1.3
653	18.280	0.1131	0.0731	5.200	2.893	4.48	15.85	7.2	57.1	30.9	1.6
702	9.403	0.1068	0.0865	2.248	2.742	2.28	29.25	6.0	57.5	29.3	2.1
737	9.761	0.1097	0.1291	2.304	2.936	1.05	30.17	4.1	55.8	31.4	4.0
773	9.182	0.1077	0.1402	2.314	2.331	1.16	25.46	3.7	57.1	24.9	4.1
809	9.540	0.1054	0.2276	2.234	2.932	1.70	30.82	2.3	58.4	31.3	3.0
846	9.021	0.1081	0.1182	2.197	2.511	4.23	27.93	4.4	56.7	26.9	1.4
884	8.899	0.1091	0.1412	2.078	2.743	5.66	30.92	3.7	55.9	29.3	1.1
900	8.946	0.1121	0.1641	2.061	2.843	5.38	31.88	3.2	54.2	30.4	1.0
918	8.700	0.1140	0.1591	2.022	2.713	6.44	31.28	3.3	53.1	29.0	0.9
933	8.661	0.1163	0.1537	1.924	2.963	6.70	34.33	3.4	51.7	31.7	1.2
950	8.343	0.1164	0.1461	1.898	2.721	7.30	32.73	3.6	51.7	29.1	0.8
968	8.000	0.1138	0.1603	1.796	2.681	7.34	33.63	3.3	52.9	28.7	0.8
1000	7.624	0.1177	0.2082	1.651	2.736	9.87	36.02	2.5	50.8	29.2	0.7
1034	6.905	0.1693	0.7859	1.470	2.605	4.46	37.87	0.7	33.7	27.9	1.1
1080	7.186	0.4639	3.4110	1.493	3.060	0.45	42.65	0.2	11.6	32.7	5.0

Experiment:	76B2						
Sample:	**050719-4**	J-value:	0.007397	K wt. %:	5.8	Plateau range:	861-1150°C
Material:	Biotite	^{39}Ar %:	89	wt.:	3.35 mg	Uncalibrated plateau age (Ma):	42.7 ± 0.1

T (°C)	^{40}Ar/^{39}Ar	^{38}Ar/^{39}Ar	^{37}Ar/^{39}Ar	^{36}Ar/^{39}Ar	F	39Ar %	40Ar %	K/Ca	K/Cl	Apparent Age (Ma)	Error 2σ
500	8.888	0.0756	0.0426	2.1400	2.542	0.45	28.69	0.08	0.01	33.6	3.8
551	4.649	0.0544	0.0328	0.6884	2.591	0.43	56.09	0.06	0.01	34.3	3.2
575	4.311	0.0566	0.1061	0.5097	2.788	0.26	65.10	0.20	0.01	36.8	3.5
601	5.026	0.0537	0.2128	0.7510	2.798	0.21	56.00	0.41	0.01	37.0	4.0
621	4.846	0.0672	0.0719	0.6811	2.813	0.20	58.41	0.14	0.01	37.2	4.9
640	4.802	0.0769	0.0108	0.4367	3.487	0.21	73.06	0.02	0.01	45.9	4.3
660	5.180	0.0930	0.0124	0.8778	2.563	0.23	49.75	0.02	0.02	33.9	4.0
701	27.570	0.1465	0.0282	7.8990	4.207	0.71	15.28	0.05	0.02	55.3	4.5
741	4.685	0.1271	0.0109	0.4365	3.374	1.39	72.46	0.02	0.02	44.5	1.1
781	3.731	0.1225	0.0114	0.1444	3.282	2.22	88.68	0.02	0.02	43.3	0.6
821	3.640	0.1207	0.0057	0.0780	3.387	3.65	93.81	0.01	0.02	44.6	0.4
861	3.473	0.1178	0.0044	0.0694	3.245	6.42	94.24	0.01	0.02	42.8	0.3
906	3.436	0.1168	0.0037	0.0650	3.222	19.63	94.56	0.01	0.02	42.5	0.1
931	3.467	0.1160	0.0034	0.0670	3.246	11.56	94.43	0.01	0.02	42.8	0.2
960	3.525	0.1153	0.0056	0.0948	3.222	8.47	92.18	0.01	0.02	42.5	0.2
990	3.616	0.1167	0.0076	0.1273	3.218	9.14	89.71	0.02	0.02	42.4	0.2
1010	3.836	0.1197	0.0084	0.1835	3.272	7.52	85.95	0.02	0.02	43.1	0.3
1030	4.025	0.1186	0.0100	0.2565	3.245	5.25	81.21	0.02	0.02	42.8	0.3
1050	4.099	0.1191	0.0110	0.2785	3.254	5.05	79.96	0.02	0.02	42.9	0.4
1071	4.032	0.1185	0.0083	0.2458	3.283	4.58	82.03	0.02	0.02	43.3	0.4
1090	3.843	0.1185	0.0123	0.2110	3.198	4.44	83.84	0.02	0.02	42.2	0.4
1120	3.784	0.1225	0.0205	0.1830	3.222	4.56	85.82	0.04	0.02	42.5	0.3
1150	3.643	0.1305	0.0326	0.1379	3.216	2.84	89.00	0.06	0.02	42.4	0.6
1200	4.046	0.1474	0.0918	0.2528	3.286	0.59	81.80	0.18	0.03	43.3	2.3

Experiment:	76B4										
Sample:	**050720-3B**		J-value:	0.0074		K wt. %:	5.2		Plateau range:		861-1150°C
Material:	Biotite		^{39}Ar %:	89		wt.:	3.33 mg		Uncalibrated plateau age (Ma):		39.8 ± 0.2

T (°C)	^{40}Ar/^{39}Ar	^{38}Ar/^{39}Ar	^{37}Ar/^{39}Ar	^{36}Ar/^{39}Ar	F	39Ar %	40Ar %	K/Ca	K/Cl	Apparent Age (Ma)	Error 2σ
500	13.790	0.1504	0.0158	3.837	2.435	1.96	17.69	0.03	0.03	32.2	2.0
551	11.820	0.1510	0.0327	3.119	2.581	1.38	21.90	0.06	0.03	34.1	2.2
576	10.480	0.1559	0.0140	2.626	2.695	0.68	25.80	0.03	0.03	35.6	3.1
601	9.378	0.1670	0.0258	2.136	3.050	0.63	32.62	0.05	0.03	40.3	3.3
631	7.664	0.1721	0.0204	1.352	3.650	0.75	47.81	0.04	0.03	48.1	2.3
661	6.420	0.1807	0.0219	1.190	2.887	0.98	45.17	0.04	0.03	38.1	1.8
690	11.800	0.2097	0.0141	2.926	3.138	2.65	26.66	0.03	0.04	41.4	1.5
710	3.998	0.2023	0.0049	0.298	3.101	3.77	78.14	0.01	0.04	40.9	0.6
740	3.454	0.2001	0.0019	0.136	3.036	5.47	88.64	0.00	0.04	40.1	0.3
781	3.407	0.1925	0.0035	0.121	3.033	7.57	89.80	0.01	0.04	40.0	0.3
831	3.588	0.1868	0.0035	0.190	3.009	9.36	84.55	0.01	0.03	39.7	0.2
881	3.838	0.1901	0.0038	0.261	3.050	8.69	80.08	0.01	0.03	40.3	0.3
906	4.120	0.1983	0.0095	0.360	3.039	10.18	74.29	0.02	0.04	40.1	0.3
931	3.592	0.2045	0.0094	0.176	3.056	5.44	85.78	0.02	0.04	40.3	0.3
960	3.340	0.2025	0.0062	0.112	2.993	4.78	90.40	0.01	0.04	39.5	0.4
990	3.260	0.1983	0.0111	0.096	2.960	4.88	91.61	0.02	0.04	39.1	0.5
1020	3.169	0.2025	0.0120	0.064	2.965	6.03	94.44	0.02	0.04	39.2	0.4
1050	3.168	0.2056	0.0105	0.057	2.983	8.91	95.03	0.02	0.04	39.4	0.2
1080	3.133	0.1895	0.0154	0.040	2.999	8.86	96.64	0.03	0.03	39.6	0.3
1121	3.156	0.1558	0.0334	0.060	2.962	5.34	94.72	0.06	0.03	39.1	0.4
1181	3.274	0.1353	0.0935	0.070	3.054	1.69	94.13	0.18	0.02	40.3	0.9

Experiment:	76B7						
Sample:	**050720-10**	J-value:	0.007406	K wt. %:	4.3	Plateau range:	731-1140°C
Material:	Biotite	^{39}Ar %:	73	wt.:	2.72 mg	Uncalibrated plateau age (Ma):	32.5 ± 0.2

T (°C)	^{40}Ar/^{39}Ar	^{38}Ar/^{39}Ar	^{37}Ar/^{39}Ar	^{36}Ar/^{39}Ar	F	39Ar %	40Ar %	K/Ca	K/Cl	Apparent Age (Ma)	Error 2σ
500	17.030	0.1829	0.0475	5.1070	1.926	1.49	11.33	0.09	0.03	25.6	3.4
551	11.450	0.0709	0.0253	3.3580	1.504	3.00	13.17	0.05	0.01	20.0	1.9
576	8.469	0.0687	0.0263	2.2200	1.886	2.86	22.35	0.05	0.01	25.0	1.6
601	7.285	0.0668	0.0258	1.7820	1.995	3.10	27.49	0.05	0.01	26.5	1.3
620	6.470	0.0669	0.0341	1.4670	2.112	3.17	32.79	0.07	0.01	28.0	1.3
640	5.829	0.0661	0.0305	1.2250	2.185	3.19	37.67	0.06	0.01	29.0	1.2
661	5.263	0.0660	0.0298	1.0870	2.027	3.28	38.73	0.06	0.01	26.9	1.1
680	8.016	0.0725	0.0244	1.9640	2.187	3.50	27.39	0.05	0.01	29.0	1.2
700	4.827	0.0685	0.0241	0.8292	2.353	3.24	49.04	0.05	0.01	31.2	1.1
731	4.240	0.0680	0.0228	0.5930	2.463	3.77	58.50	0.04	0.01	32.6	0.9
761	3.798	0.0668	0.0188	0.4440	2.462	4.13	65.32	0.04	0.01	32.6	0.8
801	3.352	0.0681	0.0197	0.3099	2.412	4.29	72.59	0.04	0.01	31.9	0.7
840	3.365	0.0673	0.0201	0.3072	2.433	4.45	72.94	0.04	0.01	32.2	0.6
881	3.737	0.0646	0.0233	0.4033	2.521	3.99	68.00	0.05	0.01	33.4	0.7
901	4.074	0.0685	0.0288	0.5025	2.566	5.12	63.43	0.06	0.01	34.0	0.8
921	4.032	0.0687	0.0312	0.5186	2.476	3.80	61.86	0.06	0.01	32.8	0.8
941	4.036	0.0690	0.0259	0.5411	2.413	3.10	60.23	0.05	0.01	32.0	0.9
960	4.038	0.0677	0.0351	0.5099	2.509	3.53	62.57	0.07	0.01	33.2	0.8
990	3.995	0.0675	0.0291	0.4981	2.499	5.99	63.03	0.06	0.01	33.1	0.6
1020	3.813	0.0678	0.0349	0.4686	2.405	8.45	63.57	0.07	0.01	31.9	0.5
1050	3.642	0.0683	0.0468	0.4048	2.424	9.36	67.09	0.09	0.01	32.1	0.4
1080	3.455	0.0712	0.1286	0.3238	2.483	7.57	72.50	0.25	0.01	32.9	0.5
1110	3.138	0.0777	0.3165	0.2541	2.390	4.08	76.86	0.61	0.01	31.7	0.7
1140	3.041	0.0886	0.2572	0.2297	2.361	1.24	78.36	0.49	0.01	31.3	1.9
1181	3.719	0.2364	1.7740	0.5861	2.130	0.30	57.65	3.40	0.04	28.2	8.2

Experiment:	76B8										
Sample:	**050721-11**		J-value:	0.007409		K wt. %:	4.6		Plateau range:		871-990°C
Material:	Biotite		^{39}Ar %:	52		wt.:	3.96 mg		Uncalibrated plateau age (Ma):		41.5 ± 0.3

T (°C)	^{40}Ar/^{39}Ar	^{38}Ar/^{39}Ar	^{37}Ar/^{39}Ar	^{36}Ar/^{39}Ar	F	39Ar %	40Ar %	K/Ca	K/Cl	Apparent Age (Ma)	Error 2σ
500	10.770	0.1145	0.0262	3.030	1.797	8.28	16.73	0.05	0.02	23.9	0.9
551	9.917	0.1131	0.0224	2.643	2.084	6.97	21.08	0.04	0.02	27.6	0.9
576	10.090	0.1159	0.0212	2.607	2.361	4.39	23.48	0.04	0.02	31.3	1.0
600	9.844	0.1183	0.0223	2.432	2.637	3.45	26.86	0.04	0.02	34.9	1.2
620	9.499	0.1209	0.0235	2.360	2.503	2.77	26.43	0.05	0.02	33.2	1.2
641	9.380	0.1202	0.0234	2.258	2.687	2.20	28.73	0.05	0.02	35.6	1.4
660	9.481	0.1241	0.0186	2.276	2.734	1.71	28.93	0.04	0.02	36.2	1.7
680	20.140	0.1391	0.0230	5.782	3.033	1.42	15.08	0.04	0.02	40.1	2.7
695	10.480	0.1368	0.0276	2.356	3.500	1.05	33.48	0.05	0.02	46.2	2.3
711	9.900	0.1462	0.0203	2.164	3.484	0.92	35.30	0.04	0.03	46.0	2.5
725	14.440	0.1595	0.0182	3.713	3.447	0.82	23.92	0.04	0.03	45.5	3.1
751	9.603	0.1607	0.0202	2.172	3.166	1.06	33.07	0.04	0.03	41.8	2.2
791	9.240	0.1687	0.0224	1.971	3.397	2.41	36.88	0.04	0.03	44.8	1.3
831	9.449	0.1663	0.0225	2.063	3.334	2.97	35.39	0.04	0.03	44.0	1.2
871	9.550	0.1644	0.0267	2.131	3.234	4.03	33.97	0.05	0.03	42.7	1.0
895	9.270	0.1621	0.0267	2.052	3.187	4.88	34.48	0.05	0.03	42.1	0.9
916	8.960	0.1650	0.0267	1.948	3.184	12.48	35.65	0.05	0.03	42.1	0.6
931	8.700	0.1626	0.0256	1.894	3.084	8.10	35.57	0.05	0.03	40.8	0.6
950	8.485	0.1619	0.0235	1.803	3.139	6.54	37.12	0.05	0.03	41.5	0.7
970	8.182	0.1616	0.0240	1.712	3.103	8.15	38.05	0.05	0.03	41.0	0.7
990	7.916	0.1655	0.0231	1.634	3.070	7.51	38.92	0.04	0.03	40.6	0.6
1010	7.241	0.1709	0.0268	1.333	3.285	4.34	45.55	0.05	0.03	43.4	0.8
1035	5.965	0.1822	0.0441	1.034	2.893	2.10	48.73	0.08	0.03	38.3	1.1
1060	4.686	0.1959	0.1088	0.510	3.169	0.99	68.05	0.21	0.04	41.9	1.7
1084	4.200	0.2241	0.2951	0.384	3.075	0.48	73.71	0.56	0.04	40.6	3.5

$^{40}Ar/^{39}Ar$ SINGLE-GRAIN FUSION EXPERIMENTS

Experiment: 73A12 Material: K-feldspar
Sample: 970709-3C J-value: 0.005988

	wt. (μg)	$^{40}Ar/^{39}Ar$	$^{38}Ar/^{39}Ar$	$^{37}Ar/^{39}Ar$	$^{36}Ar/^{39}Ar$	F	^{39}Ar (%)	% $^{40}Ar^{*}$	K/Ca	% K	Age (Ma)	2σ Error (Ma)	Included in Wtd. Mean
1	18.7	18.930	0.0334	0.1524	3.6740	8.064	0.04	42.65	3.4	0.20	85.2	43.8	
2	33.1	44.020	0.1201	3.8310	7.2990	22.820	0.15	51.74	0.1	0.48	231.0	13.0	
3	28.4	7.347	0.0140	0.0029	0.1533	6.865	3.31	93.82	181.0	12.04	72.8	0.5	x
4	27.1	36.250	0.0903	1.6650	6.1990	18.070	0.28	49.83	0.3	1.07	186.0	8.0	
5	7.2	7.761	0.0161	0.0099	0.2724	6.928	0.87	89.60	52.9	12.49	73.4	1.9	x
6	18.8	7.331	0.0140	0.0593	0.1004	7.010	1.88	96.01	8.8	10.32	74.3	0.9	x
7	28.9	33.770	0.0743	1.2820	6.5090	14.630	0.39	43.32	0.4	1.38	152.0	6.0	
8	29.5	6.674	0.0134	0.0034	0.1932	6.074	3.59	91.41	153.0	12.57	64.6	0.5	x
9	21.9	7.249	0.0137	0.0043	0.0567	7.053	2.49	97.69	123.0	11.78	74.8	0.7	x
10	28.0	7.277	0.0141	0.0007	0.0906	6.980	3.38	96.31	726.0	12.50	74.0	0.5	x
11	23.5	6.804	0.0149	0.0109	0.2019	6.180	1.09	91.21	48.1	4.79	65.7	1.5	x
12	10.8	7.129	0.0144	0.0046	0.1537	6.646	1.35	93.61	114.0	12.91	70.5	1.2	x
13	9.6	67.080	0.2145	3.3810	13.5800	27.300	0.05	40.63	0.2	0.55	274.0	38.0	
14	16.2	31.570	0.0371	0.5218	8.0650	7.761	0.40	24.59	1.0	2.57	82.1	5.7	
15	30.0	8.198	0.0139	0.0011	0.5019	6.686	3.34	81.85	493.0	11.50	70.9	0.6	
16	25.2	70.290	0.1605	3.1560	16.0600	23.120	0.14	32.84	0.2	0.56	234.0	19.0	
17	17.4	7.573	0.0143	0.0817	0.3100	6.636	2.00	87.95	6.4	11.87	70.4	0.8	
18	15.2	296.000	0.4484	3.4500	86.8800	39.660	0.01	13.37	0.2	0.10	385.0	350.0	
19	25.1	6.949	0.0139	0.0036	0.2070	6.308	2.87	91.16	144.0	11.82	67.0	0.6	x
20	16.2	6.379	0.0133	0.0060	0.0431	6.224	1.63	98.00	87.9	10.43	66.1	1.0	x
21	42.3	8.020	0.0166	0.0620	0.3732	6.893	2.06	86.27	8.4	5.03	73.1	0.8	
22	50.8	7.775	0.0143	0.0021	0.2899	6.889	4.47	88.94	246.0	9.10	73.0	0.5	
23	48.9	8.066	0.0140	0.0018	0.3848	6.900	4.51	85.85	293.0	9.54	73.2	0.5	
24	40.2	7.546	0.0145	0.0017	0.1099	7.192	2.94	95.68	301.0	7.57	76.2	0.6	x
25	33.4	7.690	0.0169	0.2440	0.0917	7.413	0.90	96.75	2.1	2.80	78.5	1.8	x

26	42.4	7.112	0.0136	0.0008	0.1086	6.763	3.44	95.47	655.0	8.39	71.7	0.5	x
27	35.7	10.930	0.0260	0.1882	1.0760	7.740	1.89	70.99	2.8	5.48	81.9	1.2	
28	39.4	11.520	0.0291	0.3848	1.0970	8.285	1.47	72.09	1.4	3.86	87.5	1.3	
29	45.8	6.780	0.0132	0.0031	0.0955	6.469	3.49	95.82	169.0	7.89	68.7	0.5	x
30	42.5	7.304	0.0149	0.0616	0.1115	6.951	2.98	95.54	8.5	7.25	73.7	0.6	x
31	34.7	6.632	0.0133	0.0049	0.0841	6.354	3.36	96.24	106.0	10.01	67.5	0.5	x
32	54.1	7.018	0.0133	0.0018	0.0988	6.697	6.71	95.82	285.0	12.82	71.1	0.3	x
33	56.0	9.055	0.0206	0.1244	0.5347	7.458	2.65	82.62	4.2	4.90	78.9	0.8	
34	51.0	9.780	0.0207	0.1416	0.5755	8.063	1.50	82.69	3.7	3.04	85.2	1.2	
35	76.7	31.480	0.0491	0.1477	6.7460	11.530	0.33	36.65	3.5	0.44	121.0	7.0	
36	88.5	7.507	0.0164	0.1392	0.2220	6.834	6.08	91.39	3.8	7.11	72.5	0.4	x
37	62.1	6.637	0.0140	0.0249	0.1475	6.174	6.85	93.44	21.0	11.41	65.6	0.3	x
38	37.1	7.396	0.0154	0.0651	0.1840	6.829	3.36	92.70	8.0	9.37	72.4	0.6	x
39	72.9	6.942	0.0135	0.0099	0.1025	6.610	8.76	95.63	52.9	12.43	70.1	0.3	x
40	47.7	11.610	0.0213	0.1010	1.5350	7.052	2.98	60.89	5.2	6.45	74.7	0.9	
							Weighted mean age (21 of 40): 71.87 ± 1.59					MSWD: 43	

Experiment:	73A21		Material:	K-feldspar									
Sample:	970721-4C		J-value:	0.005991									
	wt. (µg)	**$^{40}Ar/^{39}Ar$**	**$^{38}Ar/^{39}Ar$**	**$^{37}Ar/^{39}Ar$**	**$^{36}Ar/^{39}Ar$**	**F**	**^{39}Ar (%)**	**% $^{40}Ar^{*}$**	**K/Ca**	**% K**	**Age (Ma)**	**2σ Error (Ma)**	**Included in Wtd. Mean**
1	11.4	284.300	0.2659	3.3630	90.4100	17.470	0.43	6.13	0.2	0.48	180.0	116.0	
2	11.2	296.900	0.2348	3.1650	94.2600	18.670	0.42	6.27	0.2	0.48	191.0	122.0	
3	9.4	17.770	0.0228	0.0075	3.0080	8.853	7.87	49.90	70.0	10.70	93.2	2.1	
4	8.3	28.810	0.0257	0.0028	6.6730	9.062	7.30	31.49	187.0	11.23	95.4	2.8	
5	10.4	14.590	0.0245	0.3271	2.0640	8.497	3.21	58.32	1.6	3.95	89.6	2.9	
6	13.2	40.550	0.0378	0.0240	10.4600	9.624	11.01	23.75	21.8	10.65	101.0	3.0	
7	10.1	19.780	0.0276	0.2403	3.5080	9.412	3.39	47.64	2.2	4.29	99.0	3.8	
8	11.3	10.430	0.0158	0.0426	0.4717	9.013	8.33	86.64	12.3	9.41	94.9	1.2	
9	13.8	10.030	0.0143	0.0190	0.2770	9.188	12.09	91.83	27.5	11.19	96.7	0.8	x
10	16.8	27.150	0.0543	3.4660	7.9690	3.889	0.09	14.31	0.2	0.07	41.6	82.7	
11	5.6	9.274	0.0158	0.0796	0.0591	9.078	2.32	98.19	6.6	5.30	95.5	3.4	x
12	4.5	12.220	0.0335	2.3560	0.9270	9.674	0.60	79.24	0.2	1.69	102.0	12.0	
13	11.2	193.100	0.5029	5.6200	41.1800	72.140	0.01	37.23	0.1	0.01	648.0	107.0	
14	7.2	39.730	0.0955	12.7300	2.8200	32.770	0.09	81.84	0.0	0.16	323.0	74.0	
15	8.4	52.150	0.2140	13.7300	14.1500	11.640	0.09	22.12	0.0	0.13	122.0	122.0	
16	8.6	12.740	0.0166	0.5353	1.2700	9.003	1.66	70.83	1.0	2.47	94.8	4.9	
17	5.4	10.440	0.0215	0.4056	0.4135	9.232	1.53	88.62	1.3	3.62	97.1	4.7	
18	7.6	10.300	0.0209	0.0055	0.2446	9.551	7.13	92.97	95.7	11.98	100.0	1.0	x
19	7.4	10.940	0.0223	0.6045	0.6699	8.993	1.22	82.36	0.9	2.11	94.7	6.1	
20	6.9	42.850	0.0596	12.8400	7.7140	21.340	0.06	49.41	0.0	0.11	217.0	155.0	
21	11.2	11.050	0.0219	0.4259	0.6650	9.092	3.05	82.51	1.2	3.48	95.7	3.0	
22	9.7	10.050	0.0170	0.0739	0.2782	9.209	4.57	91.87	7.1	6.02	96.9	1.7	x
23	13.5	12.010	0.0158	0.4011	0.5634	10.350	3.74	86.40	1.3	3.54	109.0	2.0	
24	14	10.390	0.0179	0.2707	0.4635	9.015	4.51	87.01	1.9	4.12	94.9	1.8	
25	7.7	12.330	0.0163	1.6990	0.3569	11.400	0.60	92.64	0.3	1.00	119.0	12.0	x
26	14.1	13.960	0.0178	0.1593	1.6460	9.078	6.09	65.18	3.3	5.51	95.5	1.9	
27	12	460.100	0.3092	0.0792	149.4000	18.780	5.01	4.08	6.6	5.33	192.0	51.0	

28	9.7	55.160	0.0618	0.8222	15.2700	10.080	1.36	18.27	0.6	1.78	106.0	14.0
29	12	129.400	0.0986	0.2781	39.4600	12.750	1.54	9.85	1.9	1.64	133.0	25.0
30	6.7	307.000	0.2091	0.4441	95.1900	25.700	0.58	8.37	1.2	1.10	258.0	85.0
31	8.2	1072.000	0.7397	8.0940	357.5000	16.240	0.08	1.51	0.1	0.12	167.0	40.0
							Weighted mean age (5 of 31): 98.26 ± 3.34					MSWD: 1.2

Experiment:	73A30		Material:	K-feldspar									
Sample:	980730-1		J-value:	0.005973									
	wt. (µg)	**$^{40}Ar/^{39}Ar$**	**$^{38}Ar/^{39}Ar$**	**$^{37}Ar/^{39}Ar$**	**$^{36}Ar/^{39}Ar$**	**F**	**^{39}Ar (%)**	**% $^{40}Ar^{*}$**	**K/Ca**	**% K**	**Age (Ma)**	**2σ Error (Ma)**	**Included in Wtd. Mean**
1	7.5	20.580	0.0598	4.6500	2.2310	14.420	0.05	69.92	0.1	0.51	149.0	43.0	
2	10.7	55.650	0.2068	8.6590	12.5400	19.430	0.04	34.74	0.1	0.27	198.0	61.0	
3	8.2	9.353	0.0147	0.0091	0.0639	9.135	1.20	97.98	57.2	12.01	95.8	1.7	x
4	12.8	8.919	0.0150	0.0047	0.3419	7.880	1.78	88.64	112.0	11.46	83.0	1.2	
5	5.8	9.453	0.0219	0.0012	0.2243	8.761	0.76	92.97	426.0	10.72	92.0	2.7	x
6	9.4	9.273	0.0139	0.0099	0.1844	8.700	1.31	94.11	52.6	11.45	91.4	1.6	x
7	7.4	9.351	0.0173	0.0105	0.2535	8.573	1.09	91.97	49.8	12.18	90.1	1.9	x
8	14.9	9.179	0.0129	0.0018	0.0102	9.120	2.07	99.67	290.0	11.44	95.7	1.0	x
9	9.2	9.328	0.0180	0.0046	0.1486	8.860	1.28	95.28	113.0	11.46	93.0	1.7	x
10	12.2	9.020	0.0136	0.0003	0.2923	8.128	1.69	90.40	1830.0	11.43	85.5	1.2	x
11	10.4	10.760	0.0197	0.2595	0.6536	8.819	0.58	82.21	2.0	4.56	92.6	3.5	
12	9.2	9.246	0.0181	0.0037	0.1102	8.892	1.23	96.47	142.0	11.03	93.4	1.8	x
13	7.8	8.574	0.0143	0.0019	0.0701	8.338	1.01	97.58	277.0	10.70	87.7	2.0	x
14	6.8	18.920	0.0613	4.4030	0.9687	16.460	0.03	86.90	0.1	0.39	169.0	57.0	
15	8.4	129.500	0.6808	7.3020	14.5900	87.420	0.00	67.21	0.1	0.02	758.0	109.0	
16	6.0	9.052	0.0163	0.0142	0.2366	8.326	0.71	92.27	36.8	9.74	87.6	3.2	x
17	8.0	10.620	0.0180	0.0401	0.7445	8.393	0.71	79.26	13.0	7.33	88.3	2.8	
18	5.1	9.642	0.0191	0.0008	0.3875	8.468	0.67	88.09	652.0	10.82	89.0	3.2	
19	8.1	9.609	0.0151	0.0089	0.2221	8.924	1.02	93.16	58.9	10.41	93.7	2.0	x
20	6.8	9.686	0.0125	0.1861	0.1165	9.330	0.42	96.60	2.8	5.14	97.8	4.4	x
21	33.7	9.346	0.0154	0.0430	0.2640	8.541	3.73	91.67	12.2	9.12	89.8	0.7	x
22	28.9	8.974	0.0157	0.0241	0.1793	8.417	3.53	94.10	21.7	10.06	88.5	0.7	x
23	25.8	9.588	0.0182	0.0057	0.0915	9.289	3.55	97.18	92.4	11.32	97.4	0.6	x
24	21.4	9.946	0.0173	0.1291	0.0410	9.808	1.21	98.90	4.1	4.67	103.0	2.0	x
25	17.7	8.900	0.0158	0.0036	0.2378	8.169	2.53	92.08	144.0	11.78	85.9	0.9	x
26	32.8	9.062	0.0156	0.0031	0.1283	8.654	4.70	95.81	168.0	11.80	90.9	0.5	x
27	25.4	10.190	0.0182	0.0145	0.4075	8.954	3.15	88.16	36.2	10.21	94.0	0.8	

28	26.5	9.545	0.0183	0.0507	0.2472	8.790	2.65	92.37	10.3	8.23	92.3	0.9	x
29	27.3	9.343	0.0185	0.0053	0.0989	9.022	3.92	96.87	98.4	11.82	94.7	0.6	x
30	25.6	9.541	0.0177	0.0038	0.1900	8.951	2.67	94.10	139.0	8.57	94.0	0.9	x
31	39.6	9.415	0.0176	0.0020	0.0896	9.122	5.92	97.18	263.0	12.31	95.7	0.4	x
32	34.3	9.238	0.0140	0.0062	0.1970	8.627	4.49	93.69	83.8	10.77	90.6	0.5	x
33	36.9	9.167	0.0142	0.0027	0.0920	8.866	5.24	97.03	193.0	11.68	93.1	0.5	x
34	43.4	9.158	0.0162	0.0096	0.1022	8.828	5.75	96.70	54.5	10.91	92.7	0.4	x
35	33.1	9.355	0.0172	0.0303	0.1562	8.867	4.04	95.08	17.3	10.04	93.1	0.6	x
36	35.9	9.704	0.0197	0.0401	0.3170	8.742	4.24	90.36	13.0	9.72	91.8	0.6	x
37	33.9	9.194	0.0154	0.0018	0.0757	8.941	5.07	97.56	298.0	12.32	93.9	0.5	x
38	40.6	9.626	0.0169	0.0010	0.0482	9.455	6.25	98.52	518.0	12.67	99.1	0.4	x
39	38.6	9.385	0.0166	0.0227	0.1577	8.892	5.31	95.04	23.0	11.32	93.4	0.5	x
40	41.7	10.450	0.0158	0.0558	0.5276	8.872	4.39	85.09	9.4	8.66	93.2	0.6	
							Weighted mean age (30 of 40): 93.70 ± 1.26					MSWD: 13	

Experiment:	73A3		Material:	K-feldspar									
Sample:	980730-3		J-value:	0.005985									
	wt. (µg)	**$^{40}Ar/^{39}Ar$**	**$^{38}Ar/^{39}Ar$**	**$^{37}Ar/^{39}Ar$**	**$^{36}Ar/^{39}Ar$**	**F**	**^{39}Ar (%)**	**% $^{40}Ar^{*}$**	**K/Ca**	**% K**	**Age (Ma)**	**2σ Error (Ma)**	**Included in Wtd. Mean**
1	5.2	8.938	0.0144	0.0161	0.1369	8.506	1.90	95.48	32.5	13.02	89.6	1.9	x
2	5.8	9.226	0.0161	0.0070	0.1924	8.629	2.50	93.83	74.9	15.35	90.8	1.5	x
3	6.4	8.751	0.0124	0.0083	0.1002	8.426	2.14	96.61	62.6	11.89	88.8	1.7	x
4	6.5	9.009	0.0125	0.0175	0.1889	8.423	1.96	93.80	29.9	10.74	88.7	1.9	x
5	11.7	9.792	0.0177	0.0236	0.0178	9.713	4.91	99.49	22.1	14.93	102.0	1.0	x
6	7.5	9.700	0.0159	0.0171	0.1476	9.237	3.00	95.51	30.5	14.25	97.1	1.3	x
7	8.7	11.260	0.0201	0.8665	1.0710	8.148	0.56	72.50	0.6	2.28	85.9	6.2	
8	6.9	9.502	0.0131	0.0147	0.1553	9.015	4.63	95.17	35.6	13.89	94.8	0.9	x
9	4.8	9.581	0.0136	0.0046	0.1438	9.127	2.57	95.56	113.0	9.06	96.0	1.5	x
10	11.3	9.213	0.0165	0.0100	0.1917	8.618	4.09	93.84	52.3	12.90	90.7	1.0	x
11	10.4	35.530	0.0657	0.6753	6.6240	15.990	0.06	45.03	0.8	0.21	165.0	59.0	
12	10.8	8.933	0.0167	0.0169	0.1138	8.570	4.08	96.24	31.0	13.44	90.2	0.9	x
13	8.8	9.037	0.0159	0.0096	0.1342	8.612	3.49	95.61	54.6	14.14	90.7	1.1	x
14	8.0	9.131	0.0145	0.0318	0.1069	8.789	2.80	96.56	16.4	12.44	92.5	1.3	x
15	6.8	103.200	0.3246	2.9030	6.3150	84.930	0.01	82.17	0.2	0.03	741.0	512.0	
16	9.6	8.877	0.0167	0.0097	0.0979	8.560	3.63	96.74	53.9	13.45	90.1	1.0	x
17	12.1	46.200	0.0633	10.7400	9.8570	18.120	0.06	38.97	0.0	0.18	186.0	60.0	
18	10.4	9.834	0.0149	0.0610	0.5198	8.275	3.32	84.39	8.6	11.37	87.2	1.3	
19	8.9	9.015	0.0137	0.0492	0.3728	7.889	2.68	87.79	10.6	10.73	83.2	1.3	
20	14.2	9.485	0.0152	0.0087	0.3665	8.374	4.70	88.56	59.8	11.78	88.2	0.9	
21	7.6	8.594	0.0126	0.0292	0.1333	8.174	2.62	95.43	17.9	12.26	86.2	1.3	x
22	11.6	8.936	0.0150	0.0095	0.1698	8.406	4.05	94.38	55.0	12.43	88.6	1.0	x
23	11.0	9.312	0.0155	0.0265	0.1934	8.714	4.23	93.87	19.8	13.69	91.7	0.9	x
24	15.7	8.956	0.0138	0.0093	0.1264	8.555	5.54	95.83	56.2	12.56	90.1	0.7	x
25	7.6	9.572	0.0184	0.0194	0.0756	9.322	2.73	97.68	26.9	12.78	97.9	1.3	x
26	7.4	10.370	0.0202	0.0339	0.5388	8.749	2.57	84.63	15.4	12.35	92.1	1.5	
27	9.7	8.791	0.0135	0.0060	0.1431	8.340	3.58	95.18	87.0	13.14	87.9	1.0	x

28	9.2	8.889	0.0141	0.0273	0.1941	8.289	3.22	93.55	19.1	12.45	87.3	1.2	x
29	11.0	9.103	0.0145	0.0609	0.3430	8.066	2.89	88.89	8.6	9.35	85.1	1.4	
30	6.4	9.309	0.0128	0.0448	0.3331	8.300	1.72	89.44	11.7	9.56	87.5	2.2	
31	12.0	9.117	0.0144	0.0360	0.1965	8.511	3.76	93.65	14.5	11.16	89.6	1.1	x
32	8.3	8.934	0.0152	0.0435	0.1743	8.394	2.70	94.26	12.0	11.60	88.4	1.3	x
33	11.2	8.819	0.0123	0.0159	0.0375	8.681	3.31	98.76	32.9	10.53	91.4	1.1	x
34	12.8	8.890	0.0142	0.0126	0.2462	8.134	3.99	91.80	41.4	11.11	85.8	1.0	x
								Weighted mean age (24 of 34): 91.82 ± 1.29				MSWD: 7.1	

Experiment:	73A46		Material:	K-feldspar								
Sample:	980802-2B		J-value:	0.005925								
	wt. (µg)	**$^{40}Ar/^{39}Ar$**	**$^{38}Ar/^{39}Ar$**	**$^{37}Ar/^{39}Ar$**	**$^{36}Ar/^{39}Ar$**	**F**	**^{39}Ar (%)**	**% $^{40}Ar^{*}$**	**K/Ca**	**% K**	**Age (Ma)**	**2σ Error (Ma)**	**Included in Wtd. Mean**
1	8.1	8.677	0.0170	0.4861	1.1880	5.181	0.72	59.89	1.1	1.87	54.5	6.4	
2	8.6	6.804	0.0132	0.0327	0.1269	6.403	4.24	94.51	16.0	10.43	67.2	1.1	x
3	8.5	8.840	0.0141	0.0257	0.7194	6.688	6.07	75.90	20.3	15.10	70.1	0.9	
4	12.8	7.124	0.0134	0.0167	0.0950	6.816	6.43	96.06	31.3	10.62	71.4	0.8	x
5	8.2	21.970	0.0386	3.1470	2.6480	14.430	0.18	65.61	0.2	0.48	148.0	24.0	
6	5.1	14.410	0.0180	1.0070	1.5180	9.990	0.32	69.43	0.5	1.32	104.0	13.0	
7	7.8	6.900	0.0131	0.0232	0.2068	6.262	3.40	91.13	22.5	9.21	65.7	1.5	x
8	6.1	18.400	0.0207	0.0288	3.9160	6.797	2.97	37.01	18.2	10.31	71.2	2.8	
9	6.8	21.730	0.0483	0.9102	4.3910	8.817	0.39	40.60	0.6	1.21	91.9	14.5	
10	12.2	6.698	0.0128	0.0357	0.0051	6.658	5.17	99.82	14.6	8.96	69.8	0.9	x
11	5.6	7.233	0.0127	0.0475	0.0885	6.947	2.64	96.43	11.0	9.96	72.8	1.7	x
12	7.8	7.030	0.0120	0.0379	0.0068	6.985	4.08	99.76	13.8	11.05	73.2	1.2	x
13	7.9	6.635	0.0124	0.0226	0.0549	6.446	4.05	97.58	23.2	10.83	67.6	1.2	x
14	6.7	7.110	0.0131	0.0213	0.0589	6.909	3.44	97.57	24.6	10.86	72.4	1.3	x
15	7.1	8.544	0.0144	0.0021	0.4769	7.106	3.33	83.45	244.0	9.92	74.4	1.5	
16	7.2	7.961	0.0140	0.0214	0.3994	6.754	3.72	85.14	24.5	10.94	70.8	1.4	
17	13.4	7.310	0.0127	0.0213	0.2506	6.542	6.39	89.85	24.6	10.08	68.6	0.8	
18	6.8	7.420	0.0124	0.0200	0.2111	6.769	3.45	91.58	26.1	10.74	70.9	1.5	x
19	6.3	43.640	0.0538	1.7700	7.9660	20.260	0.20	46.39	0.3	0.67	205.0	25.0	
20	4.6	10.410	0.0153	0.0116	1.4860	5.987	2.48	57.69	45.1	11.40	62.9	2.4	
21	5.3	6.498	0.0130	0.0191	0.2312	5.788	2.46	89.47	27.3	9.83	60.8	1.8	
22	7.4	54.500	0.1211	6.4920	13.4000	15.520	0.09	28.37	0.1	0.26	159.0	61.0	
23	9.4	6.683	0.0129	0.0075	0.0668	6.457	4.40	97.04	69.5	9.91	67.7	1.1	x
24	4.2	7.053	0.0126	0.0768	0.1828	6.491	2.38	92.41	6.8	11.97	68.1	2.0	x
25	3.8	30.290	0.0395	3.0410	8.5170	5.370	0.13	17.71	0.2	0.72	56.5	36.1	
26	8.6	7.240	0.0128	0.0439	0.0313	7.123	4.48	98.77	11.9	11.01	74.6	1.0	x
27	7.5	12.630	0.0160	0.0087	1.9800	6.751	3.31	53.58	60.0	9.35	70.8	1.8	

28	7.2	6.695	0.0124	0.0252	0.1457	6.238	2.85	93.57	20.8	8.38	65.5	1.6	x
29	5.6	7.341	0.0127	0.0854	0.1857	6.771	2.48	92.60	6.1	9.35	71.0	1.8	x
30	9.4	7.182	0.0136	0.0317	0.0673	6.957	4.36	97.26	16.5	9.80	72.9	1.0	x
31	8.2	6.973	0.0128	0.0295	0.1571	6.482	3.57	93.35	17.7	9.20	68.0	1.2	x
32	15.3	38.450	0.0636	2.4180	9.1520	11.610	0.46	30.16	0.2	0.63	120.0	15.0	
33	9.9	6.894	0.0129	0.0291	0.1526	6.417	5.37	93.47	18.0	11.47	67.3	1.0	x
								Weighted mean age (17 of 33): 70.73 ± 1.34				MSWD: 5.6	

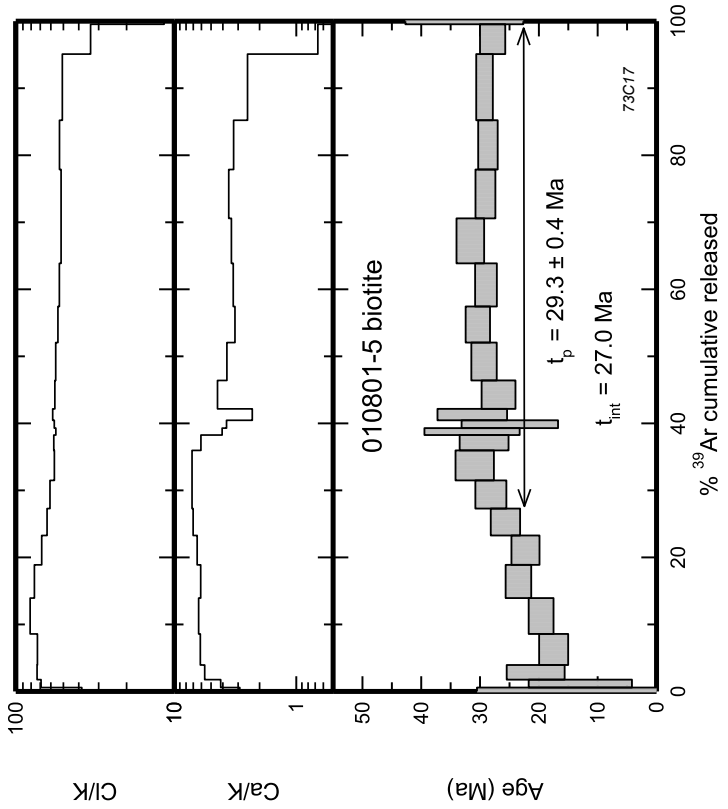
010801-5 biotite
73C17
Cl/K
Ca/K
Age (Ma)
t_p = 29.3 ± 0.4 Ma
t_{int} = 27.0 Ma
% ^{39}Ar cumulative released
t_{ic} = 27.8 ± 1.0 Ma
N = 16
MSWD = 1.1
AIR
^{36}Ar/ ^{40}Ar
^{39}Ar/ ^{40}Ar

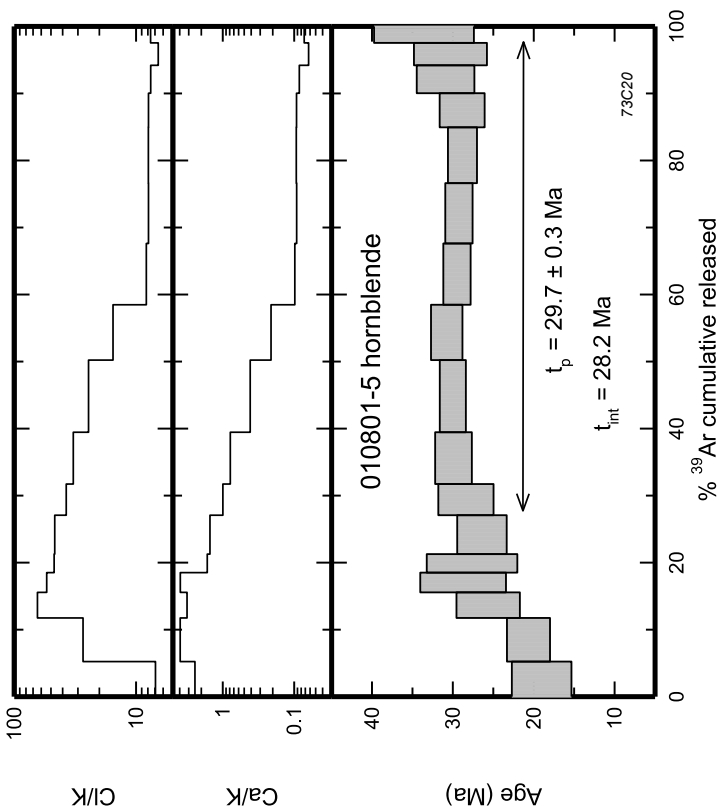
010801-5 hornblende
73C20
Cl/K
Ca/K
Age (Ma)
t_p = 29.7 ± 0.3 Ma
t_{int} = 28.2 Ma
% ^{39}Ar cumulative released
t_{ic} = 29.5 ± 0.4 Ma
N = 14
MSWD = 1.2
AIR
^{36}Ar/ ^{40}Ar
^{39}Ar/ ^{40}Ar

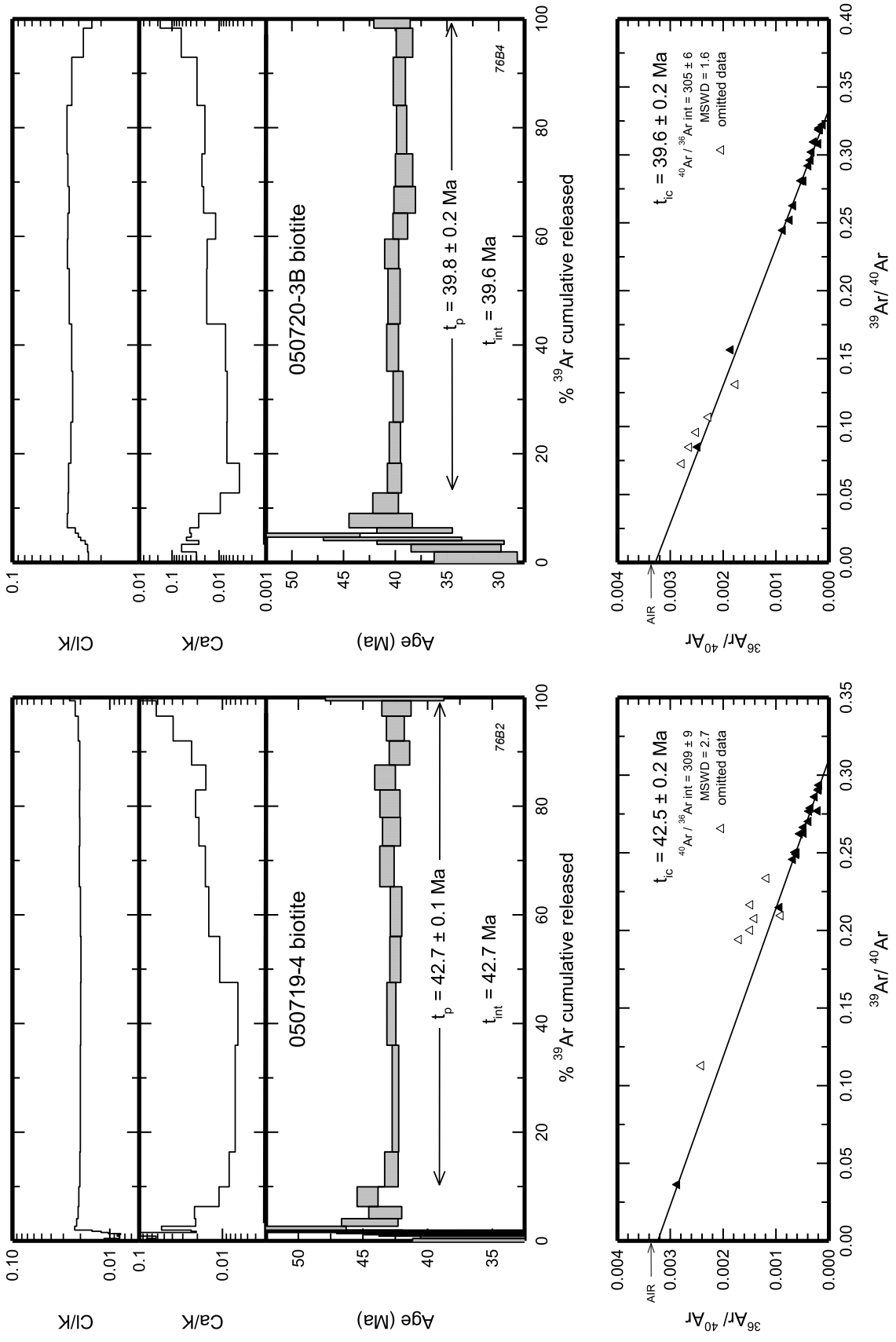
050719-4 biotite
050720-3B biotite
Cl/K
Ca/K
Age (Ma)
% 39Ar cumulative released
tp = 42.7 ± 0.1 Ma
tint = 42.7 Ma
tp = 39.8 ± 0.2 Ma
tint = 39.6 Ma
76B2
76B4
tic = 42.5 ± 0.2 Ma
tic = 39.6 ± 0.2 Ma
40Ar / 36Ar int = 309 ± 9
40Ar / 36Ar int = 305 ± 6
MSWD = 2.7
MSWD = 1.6
omitted data
AIR
36Ar/ 40Ar
39Ar/ 40Ar

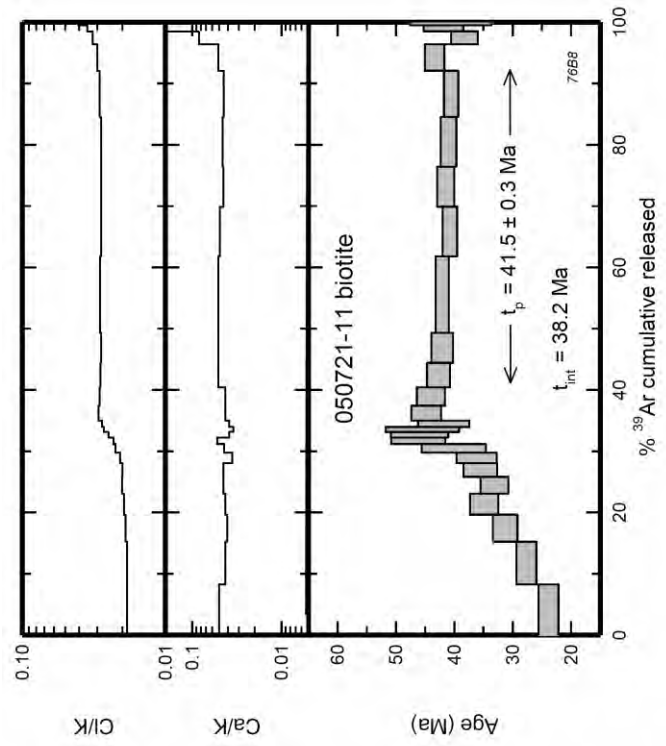
050721-11 biotite
t_p = 41.5 ± 0.3 Ma
t_{int} = 38.2 Ma
7688
Cl/K
Ca/K
Age (Ma)
% ^{39}Ar cumulative released
t_{ic} = 40.0 ± 1.3 Ma
^{40}Ar / ^{36}Ar int = 303 ± 5
MSWD = 2.4
omitted data
AIR
^{36}Ar/ ^{40}Ar
^{39}Ar/ ^{40}Ar

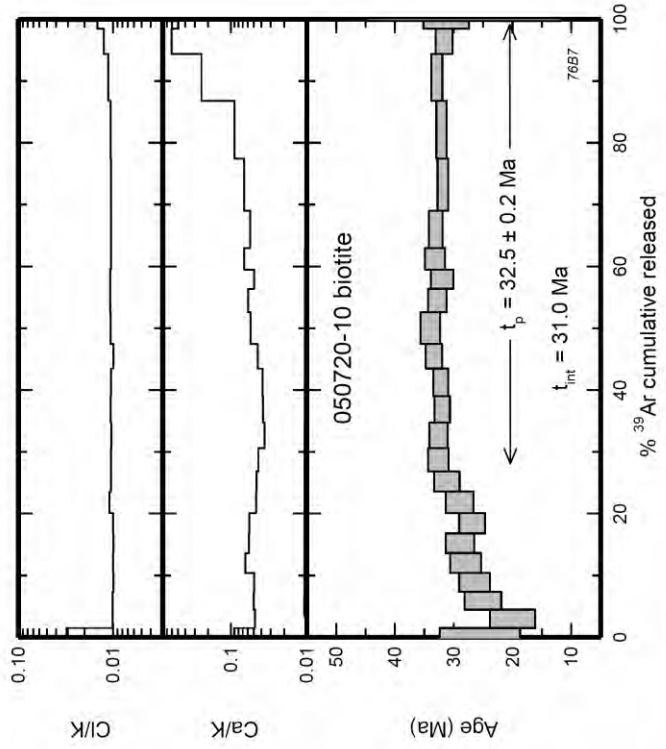
050720-10 biotite
t_p = 32.5 ± 0.2 Ma
t_{int} = 31.0 Ma
7687
Cl/K
Ca/K
Age (Ma)
% ^{39}Ar cumulative released
t_{ic} = 33.7 ± 0.3 Ma
^{40}Ar / ^{36}Ar int = 271 ± 4
MSWD = 2.4
omitted data
AIR
^{36}Ar/ ^{40}Ar
^{39}Ar/ ^{40}Ar

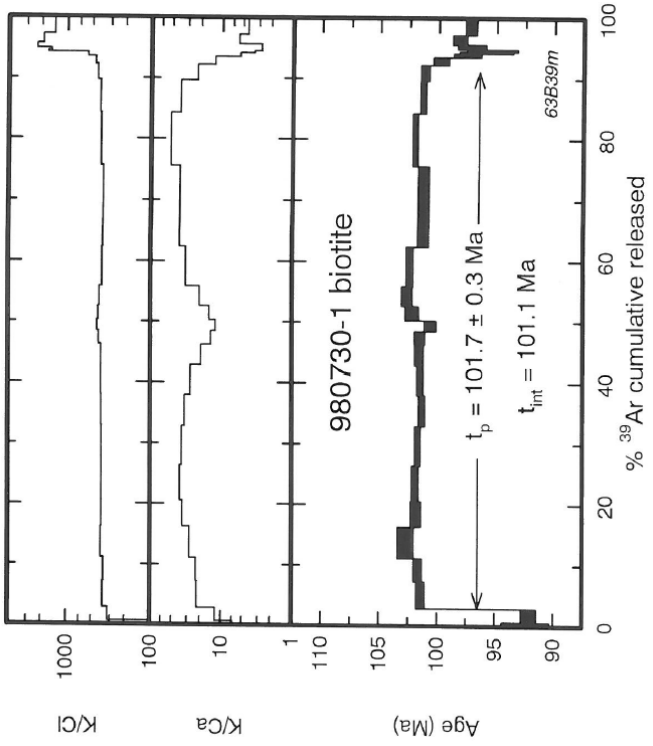
980730-1 biotite
t_p = 101.7 ± 0.3 Ma
t_{int} = 101.1 Ma
63B39m
K/Cl
K/Ca
Age (Ma)
% ^{39}Ar cumulative released

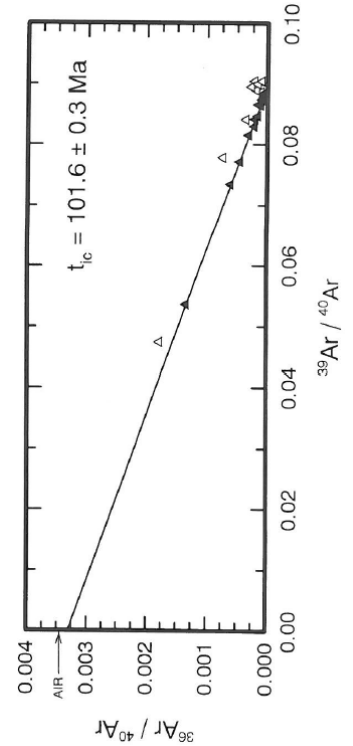
t_{ic} = 101.6 ± 0.3 Ma
AIR
^{36}Ar / ^{40}Ar
^{39}Ar / ^{40}Ar

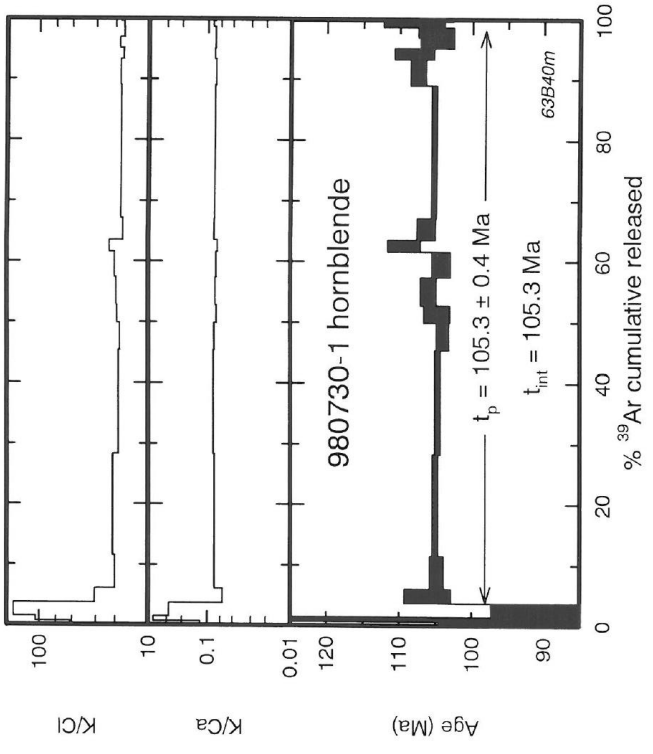
980730-1 hornblende
t_p = 105.3 ± 0.4 Ma
t_{int} = 105.3 Ma
63B40m
K/Cl
K/Ca
Age (Ma)
% ^{39}Ar cumulative released

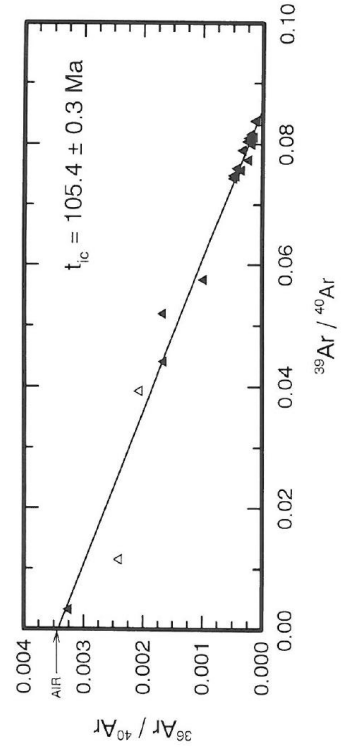
t_{ic} = 105.4 ± 0.3 Ma
AIR
^{36}Ar / ^{40}Ar
^{39}Ar / ^{40}Ar

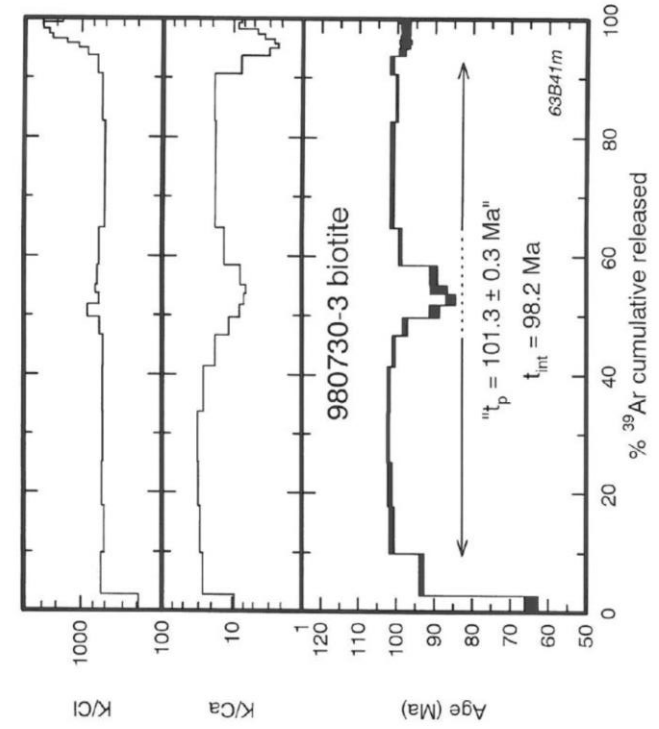
980730-3 biotite
63B41m
t_p = 101.3 ± 0.3 Ma"
t_{int} = 98.2 Ma
t_{ic} = 101.1 ± 0.4 Ma
AIR
K/Cl
K/Ca
Age (Ma)
% ^{39}Ar cumulative released
^{36}Ar / ^{40}Ar
^{39}Ar / ^{40}Ar

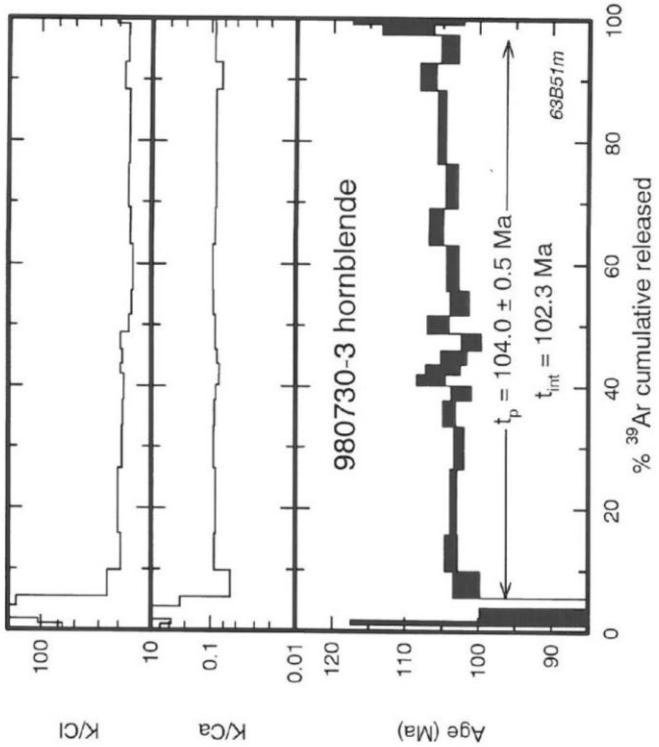
980730-3 hornblende
63B51m
t_p = 104.0 ± 0.5 Ma
t_{int} = 102.3 Ma
t_{ic} = 103.9 ± 0.4 Ma
AIR
K/Cl
K/Ca
Age (Ma)
% ^{39}Ar cumulative released
^{36}Ar / ^{40}Ar
^{39}Ar / ^{40}Ar

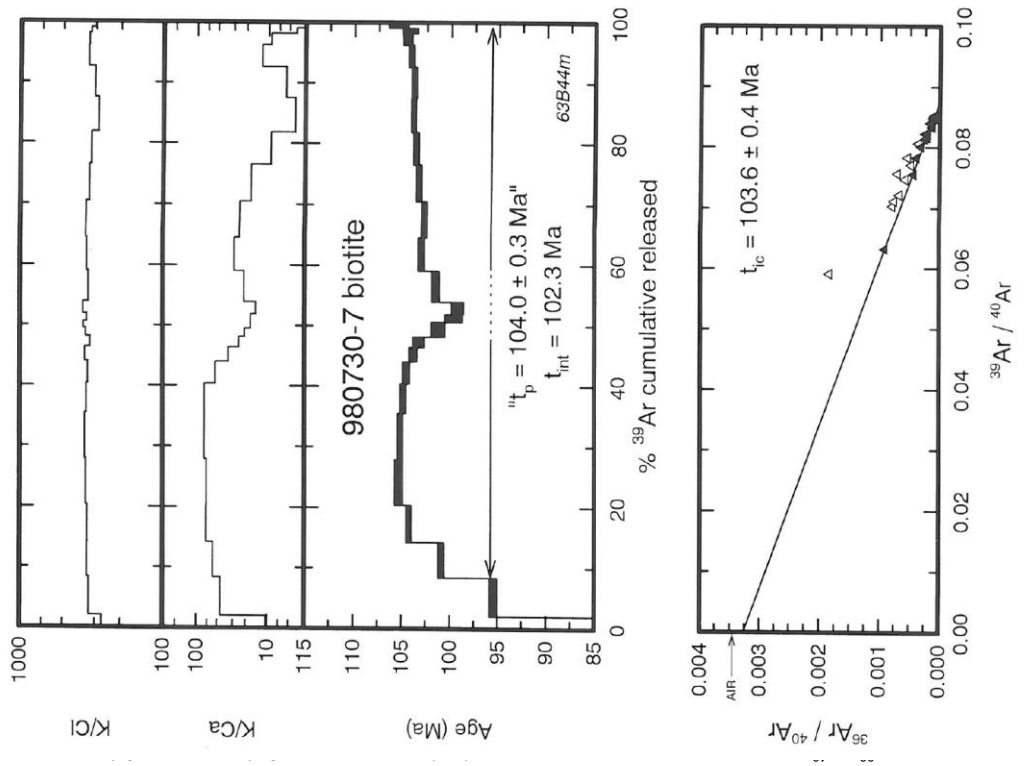
980730-7 biotite
"t_p = 104.0 ± 0.3 Ma"
t_{int} = 102.3 Ma
63B44m
K/Cl
K/Ca
Age (Ma)
% ^{39}Ar cumulative released
t_{ic} = 103.6 ± 0.4 Ma
AIR
^{36}Ar / ^{40}Ar
^{39}Ar / ^{40}Ar

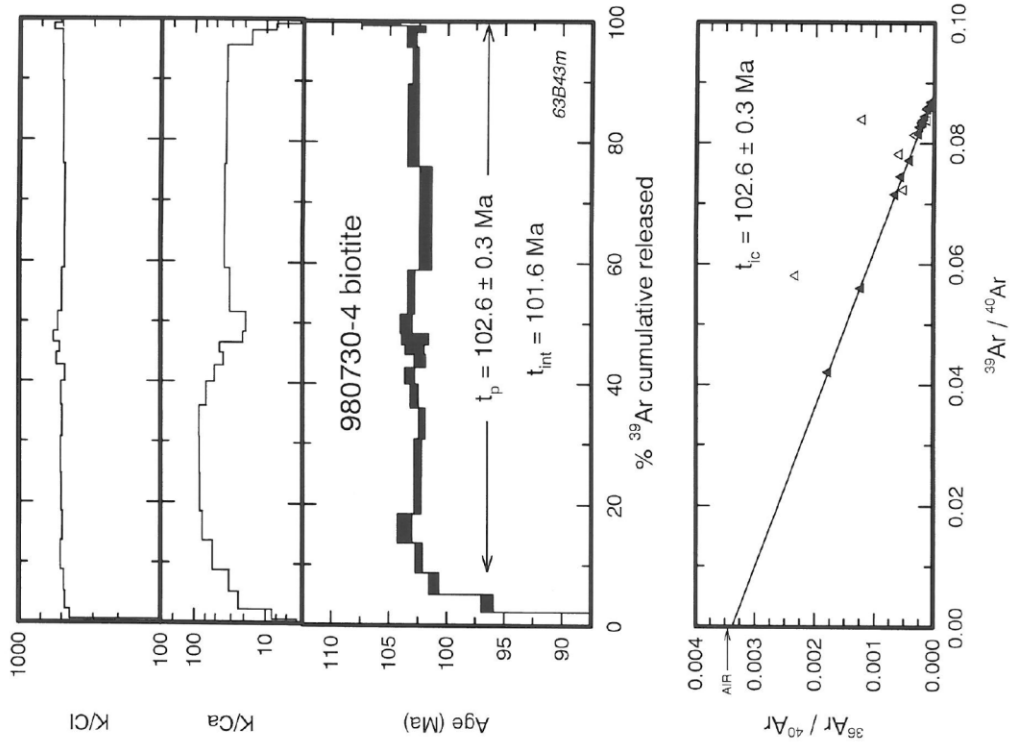
980730-4 biotite
t_p = 102.6 ± 0.3 Ma
t_{int} = 101.6 Ma
63B43m
K/Cl
K/Ca
Age (Ma)
% ^{39}Ar cumulative released
t_{ic} = 102.6 ± 0.3 Ma
AIR
^{36}Ar / ^{40}Ar
^{39}Ar / ^{40}Ar

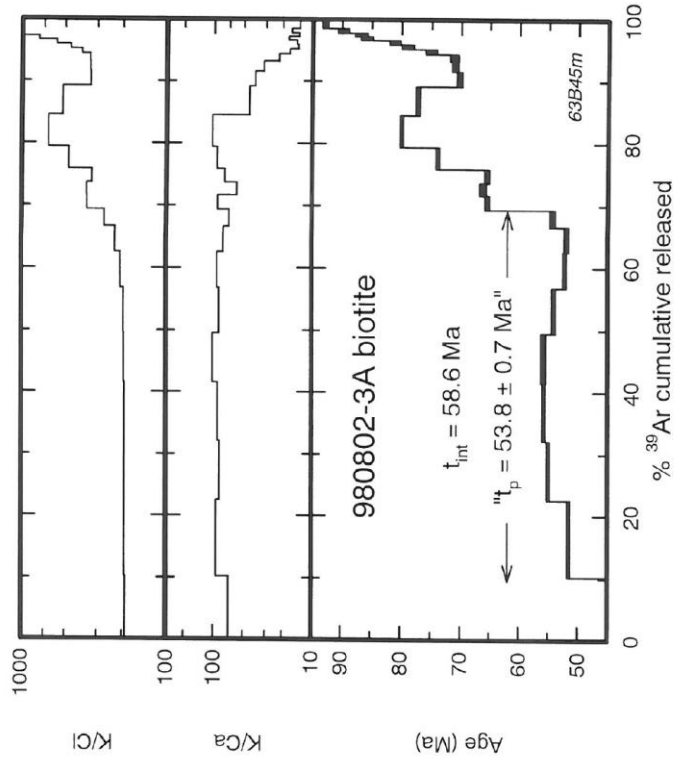
980802-3A biotite
t_{int} = 58.6 Ma
"t_p = 53.8 ± 0.7 Ma"
63B45m
Age (Ma)
K/Ca
K/Cl
% ^{39}Ar cumulative released
t_{ic} = 52.0 ± 0.2 Ma
AIR
^{36}Ar / ^{40}Ar
^{39}Ar / ^{40}Ar

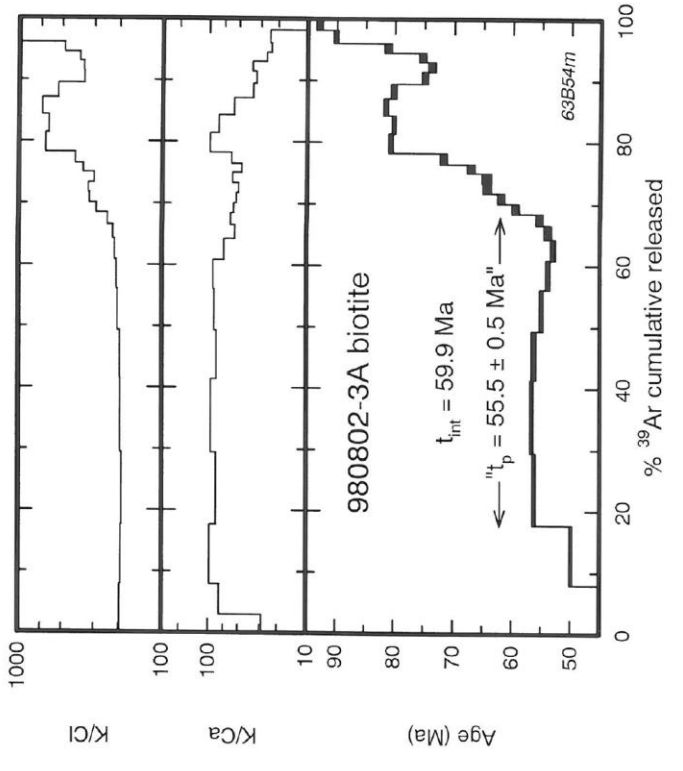
980802-3A biotite
t_{int} = 59.9 Ma
"t_p = 55.5 ± 0.5 Ma"
63B54m
Age (Ma)
K/Ca
K/Cl
% ^{39}Ar cumulative released
t_{ic} = 54.8 ± 1.7 Ma
AIR
^{36}Ar / ^{40}Ar
^{39}Ar / ^{40}Ar

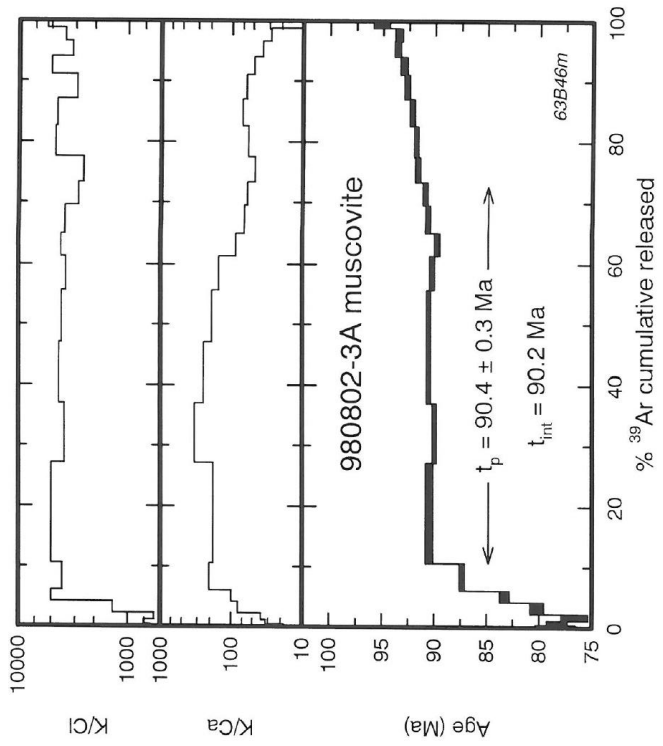
980802-3A muscovite
t_p = 90.4 ± 0.3 Ma
t_{int} = 90.2 Ma
63B46m
K/Cl
K/Ca
Age (Ma)
% ^{39}Ar cumulative released

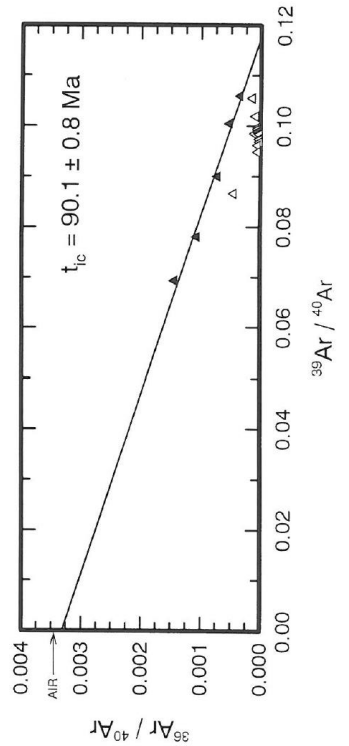
t_{ic} = 90.1 ± 0.8 Ma
AIR
^{36}Ar / ^{40}Ar
^{39}Ar / ^{40}Ar

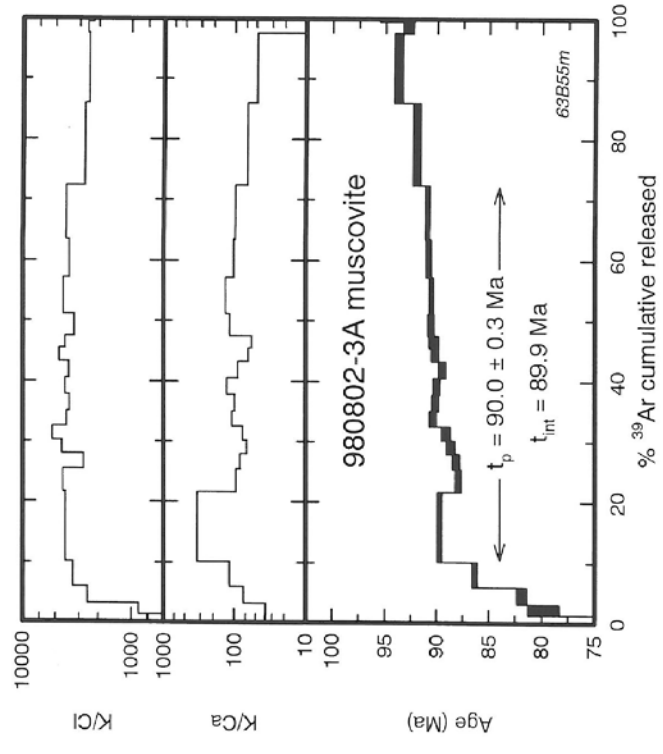
980802-3A muscovite
t_p = 90.0 ± 0.3 Ma
t_{int} = 89.9 Ma
63B55m
K/Cl
K/Ca
Age (Ma)
% ^{39}Ar cumulative released

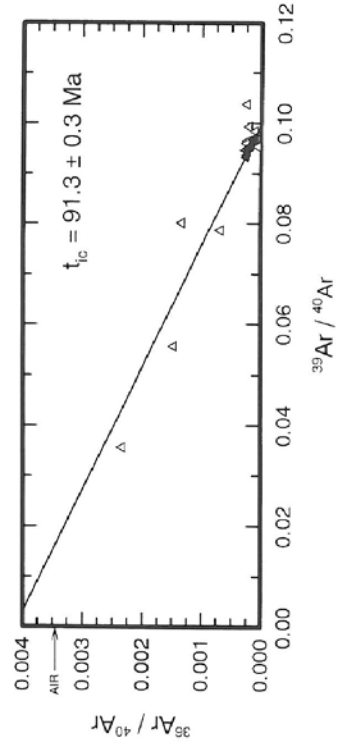
t_{ic} = 91.3 ± 0.3 Ma
AIR
^{36}Ar / ^{40}Ar
^{39}Ar / ^{40}Ar

REFERENCES

Andersen, T., 2005, Detrital zircons as tracers of sedimentary provenance: limiting conditions from statistics and numerical simulation: Chemical Geology, v. 216, p. 249–270.

Coats, R.R., 1987, Geology of Elko County, Nevada: Nevada Bureau of Mines and Geology Bulletin 101, 112 p.

du Bray, E.A., 2007, Time, space, and composition relations among northern Nevada intrusive rocks and their metallogenic implications: Geosphere, v. 3, no. 5, p. 381–405, doi:10.1130/GES00109.1.

Farley, K.A., 2000, Helium diffusion from apatite: General behavior as illustrated by Durango fluorapatite: Journal of Geophysical Research, v. 105, p. 2903–2914.

Foland, K.A., Fleming, T.H., Heimann, A., and Elliot, D.H., 1993, Potassium-Argon dating of fine-grained basalts with massive Ar loss: application of the $^{40}Ar/^{39}Ar$ technique to plagioclase and glass from the Kirkpatrick Basalt, Antarctica: Chemical Geology, v. 107, p. 173–190.

Henry, C.D., McGrew, A.J., Colgan, J.P., Snoke, A.W., and Brueseke, M.E., 2011, Timing, distribution, amount, and style of Cenozoic extension in the northern Great Basin, *in* Lee, J., and Evans, J.P., eds., Geologic field trips to the Basin and Range, Rocky Mountains, Snake River Plain, and terranes of the U.S. Cordillera: Geological Society of America Field Guides, no. 21, p. 27–66, doi:10.1130/2011.0021(02).

Jackson, S.E., Pearson, N.J., Griffin, W.L., and Belousova, E.A., 2004, The application of laser ablation-inductively coupled plasma-mass spectrometry to in situ U/Pb zircon geochronology: Chemical Geology, v. 211, p. 47–69.

Jochum, K.P., Nohl, U., Herwig, K., Lammel, E., Stoll, B., Hofmann, A.W., 2005, GeoRem: a new geochemical database for reference materials and isotopic standards: Geostandards and Geoanalytical Research, v. 29, p. 333–338.

Ketcham, R.A., 2005, Forward and inverse modeling of low-temperature thermochronometry data, *in:* Reiners, P.W., and Ehlers, T.A., eds., Low-Temperature Thermochronology: Techniques, Interpretations, and Applications: Reviews in Mineralogy and Geochemistry, v. 58, p. 275–314.

Ludwig, K.R., 2003, Isoplot/EX, version 3.0: A geochronological toolkit for Microsoft Excel: Berkeley Geochronology Center Special Publication 1a, California.

Ludwig, K.R., 2008, Manual for Isoplot 3.7: Berkeley Geochronology Center Special Publication 4, 77 pp.

Paton, C., Hellstrom, J., Paul, B., Woodhead, J., and Hergt, J., 2011, Iolite: Freeware for the visualisation and processing of mass spectrometric data: Journal of Analytical Atomic Spectrometry, v. 26, p. 2508–2518.

Peterson, V.L., Ryan, J.G., and the 1997-1998 REU Site Program Participants, 2008, Geochemistry and petrogenesis of the Buck Creek mafic/ultramafic complex, western North Carolina: Geological Society of America Bulletin, v. 129, p. 615–629.

Petrus, J.A., and Kamber, B.S., 2012, VizualAge: A Novel Approach to Laser Ablation ICP-MS U-Pb Geochronology Data Reduction: Geostandards and Geoanalytics Research, v. 36, p. 247–270.

Sano, Y., Oyama, T., Terada, K., and Hidaka, H., 1999, Ion microprobe U-Pb dating of apatite: Chemical Geology, v. 153, p. 249–258.

Slama, J., Kosler, J., Condon, D.J., Crowley, J.L., Gerdes, A., Hanchar, J.M., Horstwood,M.S.A., Morris, G.A., Nasdala, L., Norberg, N., Schaltegger, U., Schoene, B., Tubrett, M.N., and Whitehouse, M.J., 2008, Plesovice zircon — a new natural reference material for U–Pb and Hf isotopic microanalysis: Chemical Geology, v. 249, p. 1–35.

Stacey, J.S., and Kramers, J.D., 1975, Approximation of terrestrial lead isotope evolution by a two stage model: Earth and Planetary Science Letters, v. 26, p. 207–221.

Taylor, S.R., and McLennan, S.M., 1985, The continental crust: Its composition and evolution: Blackwell Scientific Publication, Carlton, 312 p.

Thomson, S.N., Gehrels, G.E., Ruiz, J., and Buchwaldt, R., 2012, Routine low-damage apatite U-Pb dating using laser ablation-multicollector-ICPMS: Geochemistry, Geophysics, Geosystems, v. 13, no. 2, 23 p.

Vermeesch, P., 2012, On the visualisation of detrital age distributions: Chemical Geology, v. 312, p. 190-194.

Vermeesch, P., 2018, IsoplotR: a free and open toolbox for geochronology: Geoscience Frontiers, v. 9, p. 1479–1493, doi:10.1016/j.gsf.2018.04.001.

APPENDIX C

Supplemental Materials for Chapter III

CARBONATE LABORATORY AND ANALYTICAL METHODS

Carbon and Oxygen Isotope Analyses:

Carbon and oxygen isotope data were obtained in stable isotope laboratories at Washington State University and the University of Texas at Austin. The grain sizes of all carbonate powders are <70µm and commonly range from 40µm to 60µm. CO_2 was extracted from samples using a Finnigan Gas-Bench following reaction with anhydrous phosphoric acid under the methods of McCrea (1950) and Swart et al. (1991). Released CO_2 was measured 8 times versus a calibrated CO_2 reference tank using a MAT253 Isotope Ratio Mass Spectrometer. Two or three replicate analyses were completed for most samples (n=63/97) and the reported value reflects the 2σSE of all aliquots. We utilized a combination of two inter-laboratory standards (NBS18, NBS19) and two intra-laboratory calcite standards (UTM, WSU). Standards were used for linearity and drift corrections, which reflect variations in machine performance, and to normalize measured values to the international V-PDB and V-SMOW scales. From repeated measurements of standards, the precision of all included analyses is 0.2‰ for $\delta^{13}C$ and ±0.3‰ $\delta^{18}O$ (1σ standard error).

Sr Laboratory Procedures:

Carbonate separation, dissolution, and Sr analyses was completed in laboratories at the University of Idaho and Washington State University. Laboratory procedures for $^{87}Sr/^{86}Sr$ separation and analyses closely followed the approach of Doebbert (2006) and Doebbert et al. (2014). 50-100 mg of carbonate powder were leached with 1M ammonium acetate and centrifuged. Following centrifuging, both leachate and carbonate extract were separated by pipetting and multiple DI water rinses. Samples were then dissolved in 1M acetic acid, centrifuged, and solution was pipetted from clay-rich sediment. The dry sample mass was measured both after leaching and after carbonate extraction to estimate the amount of dissolved carbonate material. Following evaporation to dryness, extracted carbonate was

redissolved in nitric acid and 0.5 mL aliquots collected for ion exchange chromatography. Concentrations of Sr were measured using an Agilent model 7700 ICP-MS in the WSU GeoAnalytical Lab and reflect the amount of Sr in the acetic acid extracted mass (µg Sr per g of carbonate).

Ion exchange chromatography was completed using Sr-Spec (Crown Ether) resin 100-150µm and a series of elution and Sr collection steps with 3N and 0.05N nitric acid. 2 µL of ultra-pure 20% HNO_3 (Seastar Chemical, Baseline) were added to dried samples and aliquots of ~500 ng of Sr extracted. Sample and standard aliquots were then loaded on outgassed Re filaments prepared with a Ta_2O_5 activator. Mass analysis of Sr was completed using a three-jump multi-collector analysis routine on an Isotopix Phoenix Thermal Ionization Mass Spectrometer (TIMS) at the University of Idaho. All analyses were completed using the same analytical methods. Residual Rb was monitored by measuring the ^{85}Rb intensity and interference corrections of ^{87}Rb on ^{87}Sr completed where necessary. $^{87}Rb/^{86}Sr$ ratios were calculated using the natural isotope abundances of Rb and the isotopic compositions of samples. Procedural blanks were evaluated to test for sample cross-contamination. Reported $^{87}Sr/^{86}Sr$ ratios are the average of ~150 ratios and reported errors reflect 2 standard errors of the individual analyses. Analysis of the NIST SRM 987 Sr standard performed over the course of this study (March 2018-February 2019) yields a value of 0.710252 ± 0.00001 (2σSE), which is in good agreement with published values (literature value = 0.710248).

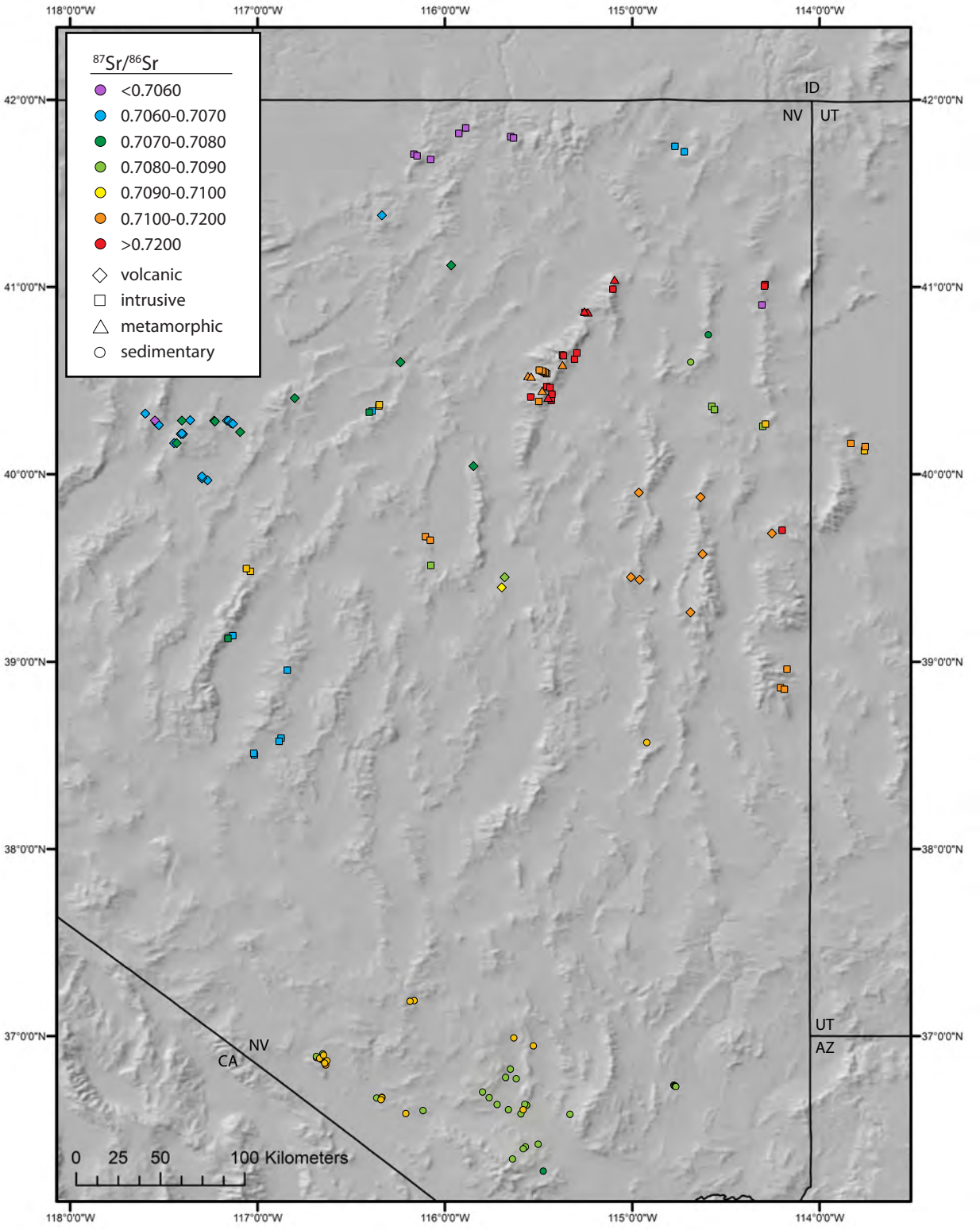

Figure C1. Compilation of Sr geochemical data for Precambrian-Paleozoic metamorphic rocks, Paleozoic sedimentary rocks, Jurassic-Cretaceous intrusive rocks, and Eocene volcanic rocks in Nevada and Utah. See below tables for sources of data.

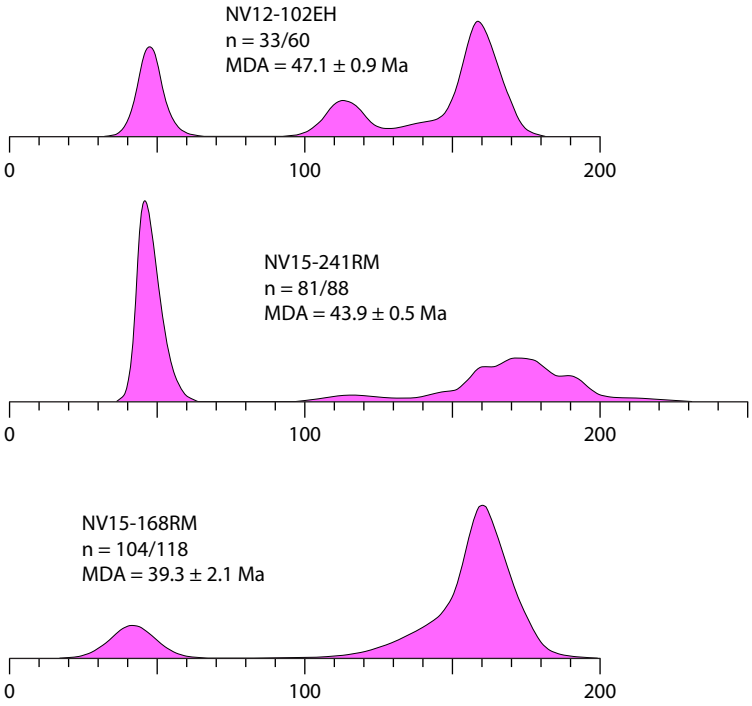

Figure C2. Detrital zircon U-Pb age plots and maximum depositional ages for samples NV12-102EH, NV15-241RM, and NV15-168RM from Canada et al. (2019).

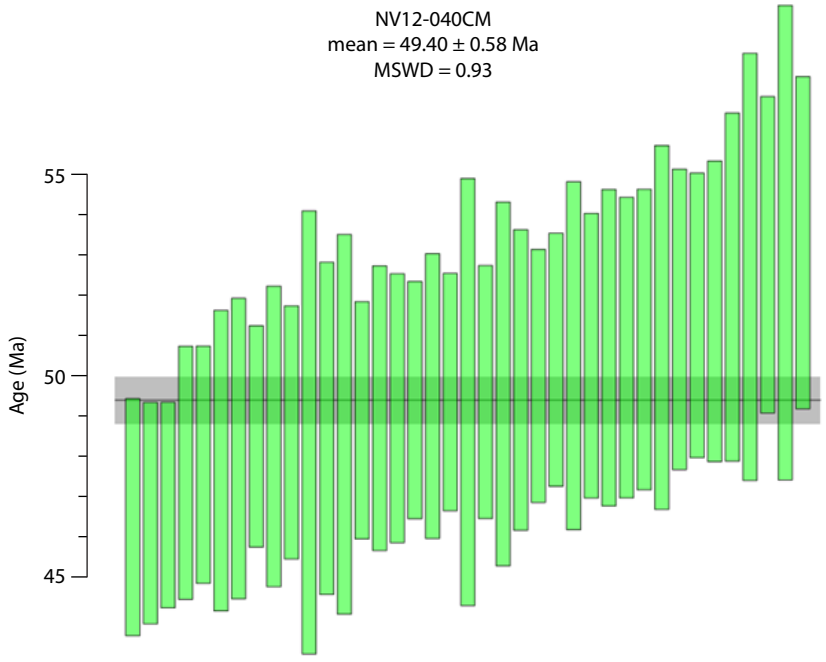

Figure C3. Weighted mean plot of detrital zircon U-Pb ages for sample NV12-040CM from Canada et al. (2019). Plotted using Vermeesch (2018).

TABLE C1: MODERN RIVER, SPRING, AND WELL DATA

Data source Sample	Date Collected	Location	Main bedrock lithology	Latitude	Longitude	pH	Temp. (°C)	Sr (ppm)	$^{87}Sr/^{86}Sr$	$\delta^{13}C$ (‰)	$\delta^{18}O$ (‰)	δD (‰)
Northeastern Nevada												
This study												
NV17-001RB	4/21/2017	Ruby Mountains	metamorphic	40.649°	-115.391°	7.1	4.4	0.0189	0.71172			
NV17-002RB	4/21/2017	Ruby Mountains	metamorphic	40.692°	-115.476°	6.6	5.8	0.0218	0.71338			
NV17-003RB	4/21/2017	Lamoille Valley	metamorphic	40.822°	-115.317°	6.8	10.4	0.0220	0.71174			
NV17-004RB	4/21/2017	Secret Pass	metamorphic	40.867°	-115.269°	7.3	10.6	0.0206	0.71124			
NV17-005RB	4/21/2017	East Humboldt Range	metamorphic	41.027°	-115.052°	7.0	7.2	0.0179				
NV17-006CM	4/22/2017	Coal Mine Canyon	sedimentary	41.111°	-115.627°	7.2	5.4	0.0142	0.70806			
NV17-007HP	4/23/2017	Harrison Pass Pluton	igneous	40.326°	-115.517°	7.3	7.6	0.0256				
NV17-008HP	4/23/2017	Harrison Pass Pluton	igneous	40.327°	-115.555°	7.7	8.0	0.0235				
NV17-009HV	4/23/2017	Diamond Range	sedimentary	39.967°	-115.730°	8.4	13.0	0.0241				
NV17-010DR	4/23/2017	Diamond Range	sedimentary	39.701°	-115.768°	8.1	12.1	0.0205				
NV17-011DR	4/23/2017	Sulphur Spring Range	sedimentary	39.975°	-116.173°	8.2	14.5					
NV17-012PR	4/23/2017	Pinon Range	sedimentary	40.451°	-116.069°	7.0	16.8	0.0209	0.70779			
NV17-013PR	4/23/2017	Pinon Range	sedimentary	40.540°	-116.124°	6.0	17.4	0.0203				
DRI water-quality data*												
1-1#	3/31/2014	Huntington Valley	metamorphic	40.486°	-115.664°	6.35	10.6	0.0321		-12.80	-15.28	-120.1
1-2#	3/31/2014	Huntington Valley	metamorphic	40.486°	-115.665°	7.10	2.9	0.0229		-14.91	-15.28	-117.3
1-3#	3/31/2014	Huntington Valley	metamorphic	40.493°	-115.693°	7.40	6.7	0.0609		-9.82	-14.51	-117.0
1-4#	3/31/2014	Huntington Valley	sedimentary	40.522°	-115.657°	7.45	9.4	0.0227		-13.37	-16.19	-123.9
1-5#	3/31/2014	Huntington Valley	sedimentary	40.514°	-115.683°	7.96	18.3	0.0150		-13.27	-16.45	-126.0
1-6§	3/31/2014	Huntington Valley	sedimentary	40.523°	-115.658°	7.62	13.3	0.0174				
1-7#	4/1/2014	Huntington Valley	sedimentary	40.525°	-115.670°	7.42	10.0	0.0330		-13.44	-15.61	-121.6
1-8§	4/1/2014	Huntington Valley	sedimentary	40.523°	-115.658°	7.89	10.0	0.0495		-13.01	-15.51	-119.4
1-9#	4/1/2014	Huntington Valley	sedimentary	40.525°	-115.666°	7.55	13.3	0.0234				
1-10§	4/1/2014	Huntington Valley	igneous	40.383°	-115.643°	7.48	6.6	0.0271				
1-11§	4/1/2014	Huntington Valley	igneous	40.381°	-115.665°	7.05	11.7	0.0291				
1-12§	4/2/2014	Huntington Valley				7.54	17.1			-8.50	-16.73	-124.8
1-13#	4/7/2014	Huntington Valley	metamorphic	40.489°	-115.594°	7.54	17.1	0.0092		-14.32	-16.56	-127.9
1-14#	4/18/2014	Huntington Valley	sedimentary	40.564°	-115.713°	6.72	13.1	0.0509		-10.22	-16.67	-1130.9
1-15#	4/18/2014	Huntington Valley	igneous	40.385°	-115.668°	8.76	22.2			-10.04	-14.25	-117.8
1-16§	9/22/2014	Huntington Valley	sedimentary	40.416°	-115.640°	7.60	12.5	0.0093		-14.57	-16.81	-127.0
1-17§	9/22/2014	Huntington Valley	sedimentary	40.424°	-115.669°	7.70	15.1	0.0342		-14.50	-15.68	-120.4
1-18§	9/22/2014	Huntington Valley	metamorphic	40.438°	-115.619°	6.66	14.4	0.0190		-17.56	-15.89	-121.3
1-19**	9/23/2014	Huntington Valley	sedimentary	40.504°	-115.727°	7.55	15.7	0.0418		-4.00	-14.51	-117.8
1-20§	9/23/2014	Huntington Valley	metamorphic	40.462°	-115.646°	7.55	19.8	0.0197		-17.69	-15.68	-118.5
1-21#	9/23/2014	Huntington Valley	sedimentary	40.265°	-115.629°	7.28	12.4			-12.04	-15.84	-119.4
1-22#	9/24/2014	Huntington Valley	igneous	40.386°	-115.629°	7.74	13.9			-13.23	-16.33	-127.3
1-23**	9/24/2014	Huntington Valley	metamorphic	40.444°	-115.621°	7.56	17.4			-11.91	-15.31	-116.4
1-24§	9/29/2014	Huntington Valley	sedimentary	40.445°	-115.664°	7.14	13.8	0.0223		-12.13	-16.38	-128.2
1-25§	9/29/2014	Huntington Valley	sedimentary	40.425°	-115.704°	7.49	17.6	0.0118		-6.17	-18.28	-140.1
1-26§	10/7/2014	Huntington Valley	sedimentary	40.554°	-115.675°	8.08	16.4	0.0196		-12.32	-17.34	-135.7
1-27§	10/7/2014	Huntington Valley	sedimentary	40.420°	-115.773°	7.98	14.5	0.0246		-10.38	-16.65	-128.7

1-28§	10/20/2014	Huntington Valley	metamorphic	40.467°	-115.655°	7.22	12.1	0.0164	-14.78	-15.99	-121.1
1-29§	10/20/2014	Huntington Valley	sedimentary	40.347°	-115.768°	8.31	12.7	0.0144	-11.94	-16.70	-127.4
1-30§	10/21/2014	Huntington Valley	sedimentary	40.350°	-115.681°	8.31	16.9	0.0446	-10.61	-16.53	-126.9
1-31§	10/20/2014	Huntington Valley	sedimentary	40.379°	-115.745°	8.30	13.7	0.0226			
1-32§	9/23/2014	Huntington Valley	metamorphic	40.439°	-115.620°	7.48	15.7	0.0167			
1-33§	9/22/2014	Huntington Valley	sedimentary	40.419°	-115.659°	7.33	13.2	0.0176			
1-35§	9/23/2014	Huntington Valley	metamorphic	40.462°	-115.646°	7.46	12.3	0.0152			
1-36§	11/12/2014	Huntington Valley	sedimentary	40.428°	-115.665°	7.55	13.1	0.0872			
1-37§	11/12/2014	Huntington Valley	metamorphic	40.429°	-115.616°	7.26	11.6	0.0809			
2-1§	9/4/2013	Lamoille Valley	sedimentary	40.857°	-115.463°	9.96	11.7	0.0069	-4.35	-17.90	-136.0
2-2§	6/23/2014	Lamoille Valley	sedimentary	40.927°	-115.463°	7.79	17.4	0.0313	-13.84	-15.09	-116.1
2-3§	6/23/2014	Lamoille Valley	sedimentary	40.927°	-115.462°	7.54	16.8	0.0368			
2-4§	9/4/2013	Lamoille Valley	metamorphic	40.808°	-115.411°	8.16	12.8	0.0295	-10.33	-16.46	-126.6
2-5§	6/25/2014	Lamoille Valley	metamorphic	40.807°	-115.335°	7.25	12.5	0.0161			
2-6§	6/25/2014	Lamoille Valley	metamorphic	40.811°	-115.345°	7.09	12.6	0.0146			
2-7§	7/1/2014	Lamoille Valley	metamorphic	40.811°	-115.346°	8.93	17.4	0.0211			
2-8§	6/25/2014	Lamoille Valley	metamorphic	40.748°	-115.493°	7.58	13.9	0.0241			
2-9§	6/25/2014	Lamoille Valley	metamorphic	40.767°	-115.493°	7.70	15.6	0.0278			
2-10**	6/23/2014	Lamoille Valley	metamorphic	40.763°	-115.481°	7.96	16.8		-6.94	-16.27	-121.9
2-11#	6/25/2014	Lamoille Valley	metamorphic	40.858°	-115.292°	7.90	21.8		-11.83	-15.83	-127.7
2-12#	6/24/2014	Lamoille Valley	metamorphic	40.848°	-115.289°	8.01	19.4		-11.55	-15.62	-122.1
2-13**	6/24/2014	Lamoille Valley	sedimentary	40.930°	-115.469°	8.32	22.8		-11.12	-15.51	-121.2
2-15#	9/5/2014	Lamoille Valley	metamorphic	40.781°	-115.414°	7.88	13.0		-12.21	-16.08	-125.3
2-16§	9/25/2014	Lamoille Valley	metamorphic	40.862°	-115.410°	9.64	19.5		-6.33	-18.25	-138.3
3-1#	9/3/2014	Tabor Flats	sedimentary	41.222°	-115.144°	7.97	14.3	0.0202	-11.57	-14.01	-105.6
3-2§	9/3/2014	Tabor Flats	sedimentary	41.215°	-115.234°	8.13	16.2	0.0141	-18.13	-10.67	-141.8
3-3§	9/3/2014	Tabor Flats	sedimentary	41.198°	-115.189°	9.47	14.8	0.0013	-18.17	-3.37	-139.0
3-4**	9/4/2014	Bishop Flats	sedimentary	41.172°	-115.034°	8.59	17.6		-16.13	-1.66	-130.1
3-5#	9/5/2014	Tabor Flats	sedimentary	41.180°	-115.175°	9.69	15.1		-7.98	-7.66	-91.0
3-6**	9/30/2014	Bishop Flats	sedimentary	41.230°	-114.976°	7.55	15.9	0.0349	-6.42	-16.53	-128.3
3-7§	9/30/2014	Tabor Flats	sedimentary	41.267°	-115.178°	7.99	11.9	0.0179	-10.18	-17.18	-130.5
3-8#	9/30/2014	Snake Mountains	sedimentary	41.244°	-114.938°	7.16	38.2		-3.80	-17.24	-130.7
3-9§	10/8/2014	Tabor Flats	sedimentary	41.303°	-115.157°	7.90	15.0	0.0231	-10.27	-17.19	-131.2
3-10§	10/21/2014	Bishop Flats	sedimentary	41.247°	-115.037°	5.67	12.6	0.0260	-10.73	-16.90	-129.4
3-11§	10/21/2014	Tabor Flats	sedimentary	41.130°	-115.159°	8.22	13.8	0.0345	-10.90	-15.67	-121.7
3-12#	10/22/2014	Tabor Flats	sedimentary	41.111°	-115.207°	7.86	12.4	0.0417	-12.89	-15.66	-119.0
3-13#	10/22/2014	Tabor Flats	metamorphic	41.125°	-115.098°	9.04	15.4		-1.96	-16.60	-140.5
3-14#	10/21/2014	Tabor Flats	sedimentary	41.115°	-115.190°	8.10	11.9	0.0290			
3-15§	10/21/2014	Bishop Flats	sedimentary	41.230°	-114.976°	8.44	17.3	0.0451			
3-16#	12/8/2014	Bishop Flats	sedimentary	41.192°	-115.031°	8.35	12.2	0.0102			
3-17#	12/8/2014	Bishop Flats	sedimentary	41.211°	-115.029°	8.00	8.2	0.0284			
3-18#	12/8/2014	Bishop Flats	sedimentary	41.213°	-115.032°	7.90	6.2	0.0278			
3-19§	12/8/2014	Tabor Flats	metamorphic	41.102°	-115.156°	7.98	71.7	0.0395			
3-20§	12/8/2014	Tabor Flats	sedimentary	41.135°	-115.144°	7.80	11.0	0.0629			
USGS stream gage data†											
10324500	1990-2000	Tuscarora Mountains	sedimentary	40.830°	-116.588°	8.7	12.5	0.0255		-10.91	-106.0
10322535	2013-2014	Sulphur Spring Range	sedimentary	39.869°	-116.167°	8.8	8.4	0.0197			

10323425	1991-1994	Tuscarora Mountains	sedimentary	40.706°	-116.530°	8.5	14.4	0.0377				
10321950	1990-1991	Tuscarora Mountains	sedimentary	40.803°	-116.199°	8.4	9	0.024				
10322500	1990-1991	Cortez Mountains	sedimentary	40.603°	-116.197°	8.4	17.8	0.0417				
10245970	2011-2018	Sulphur Spring Range	sedimentary	39.790°	-116.301°	8.3	12	0.0181				
10322150	1990-1991	Pinon Range	sedimentary	40.710°	-116.124°	8.0	14.8	0.0278				
10318500	1987-1989	Elko Hills	sedimentary	40.937°	-115.624°	8.1	14.2	0.1003				
10324700	3/9/1993	Tuscarora Mountains	sedimentary	40.955°	-116.439°	7.9	7	0.0074				
10322510	05-09/2013	Simpson Park Range	sedimentary	39.905°	-116.413°	8.4	17.5	0.0122				
10321000	1985-1998	Pinon Range	sedimentary	40.728°	-116.008°	8.2	13	0.0353			-14.07	-114.0
10316500	1987-1989	Ruby Mountains	sedimentary	40.686°	-115.476°	8.5	8.7	0.0103				
Central Idaho												
Idaho Batholith – Big Creek Watershed [††]												
		Beaver Creek	igneous	45.170°	-115.243°				0.713606			
		Big (downstream of Beaver)	igneous	45.161°	-115.236°				0.713726			
		Big (downstream of Cabin)	igneous	45.124°	-114.929°				0.714152			
		Big (downstream of Crooked)	igneous	45.162°	-115.130°				0.713875			
		Big (downstream of Logan)	igneous	45.124°	-115.319°				0.710600			
		Big (downstream of Monumental)	igneous	45.158°	-115.120°				0.713574			
		Big Ramey Creek	igneous	45.183°	-115.163°				0.708361			
		Big (upstream of Beaver)	igneous	45.160°	-115.255°				0.714780			
		Big (upstream of Cabin)	igneous	45.131°	-114.945°				0.714791			
		Big (upstream of Crooked)	igneous	45.171°	-115.137°				0.714331			
		Big (upstream Rush)	igneous	45.105°	-114.868°				0.714375			
		Cabin Creek	igneous	45.137°	-114.934°				0.708462			
		Crooked Creek	igneous	45.166°	-115.122°				0.706769			
		Lower Big Creek	igneous	45.104°	-114.856°				0.713762			
		Logan Creek	igneous	45.118°	-115.328°				0.711463			
		Monumental Creek	igneous	45.154°	-115.139°				0.720223			
		Rush Creek	igneous	45.096°	-114.867°				0.710239			
		Upper Big Creek	igneous	45.088°	-115.339°				0.709448			

[*] From Hershey et al. (2014)
[†] From U.S. Geological Survey (2016)
[§] Well data
[#] Spring data
[**] Stream data
[††] From Hegg et al. (2013)

TABLE C2. BEDROCK Sr DATA FOR EASTERN NEVADA AND WESTERN UTAH

Data source Sample	Lithology	Latitude (°)	Longitude (°)	Age (Ma)	Rb (ppm)	Sr (ppm)	$^{87}Rb/^{86}Sr$	$^{87}Sr/^{86}Sr$
Kistler and Lee, 1989								
GR-03	granite	39.188	-113.385	169	176	356	1.43	0.70945
GR-04	granite	39.185	-113.436	169	181	370	1.42	0.70983
GR-15	granite	39.717	-112.593	147	183	453	1.17	0.70995
GR-16	granite	38.740	-112.593	147	179	348	1.49	0.71055
GR-17	granite	39.899	-112.111	147	125	624	0.58	0.70926
GR-18	granite	39.908	-112.129	147	141	622	0.65	0.70868
GR-25	granite	41.006	-114.294	80	167	193	2.15	0.72938
GR-26	granite	41.010	-114.292	80	183	144	3.68	0.72940
GR-27	granite	41.796	-115.634	109	110	710	0.45	0.70522
GR-28	granite	41.804	-115.649	109	93	671	0.40	0.70519
GR-29	granite	41.821	-115.927	93	129	458	0.81	0.70541
GR-30	granite	41.851	-115.890	93	127	460	0.80	0.70557
GR-31	granite	41.679	-116.070	150	39	654	0.17	0.70489
GR-32	granite	41.682	-116.078	150	54	847	0.18	0.70505
GR-33	granite	39.647	-116.078	156	148	204	2.10	0.71314
GR-34	granite	39.665	-116.102	156	144	213	1.96	0.71309
GR-37	granite	39.494	-117.059	155	136	432	0.91	0.70905
GR-38	granite	39.479	-117.038	155	145	475	0.88	0.70923
GR-39	granite	39.136	-117.132	155	91	718	0.37	0.70634
GR-40	granite	39.121	-117.158	155	139	570	0.71	0.70710
GR-47	granite	38.858	-114.207	86	102	593	0.50	0.71191
GR-48	granite	38.849	-114.184	86	113	637	0.51	0.71203
GR-57	granite	41.749	-114.769	156	128	785	0.47	0.70630
GR-58	granite	41.724	-114.722	156	112	821	0.39	0.70624
GR-59	granite	41.702	-116.150	155	70	586	0.34	0.70580
GR-60	granite	41.708	-116.166	155	75	572	0.38	0.70581
GR-93	granite	40.146	-113.753	155	128	722	0.51	0.71067
GR-94	granite	40.124	-113.757	155	169	864	0.56	0.70918
GR-103	granite	40.364	-116.351	150	115	368	0.90	0.70915
GR-104	granite	40.369	-116.349	150	113	291	1.12	0.70944
GR-105	granite	40.331	-116.403	150	79	592	0.39	0.70702
GR-106	granite	40.336	-116.389	150	46	507	0.26	0.70626
GR-109	granite	38.508	-117.021	80	120	735	0.47	0.70630
GR-110	granite	38.500	-117.018	80	113	676	0.48	0.70653
GR-111	granite	38.573	-116.885	85	174	799	0.63	0.70688
GR-112	granite	38.590	-116.874	85	150	806	0.54	0.70671
GR-113	granite	38.953	-116.843	155	73	575	0.37	0.70631
GR-114	granite	38.953	-116.843	155	71	524	0.39	0.70645
GR-123	granite	40.265	-114.286	150	151	399	1.10	0.70965
GR-124	granite	40.254	-114.300	150	137	452	0.88	0.70880
GR-125	granite	40.342	-114.558	150	211	934	0.65	0.70812
GR-126	granite	40.361	-114.574	150	149	602	0.72	0.70889
Wright and Snoke, 1993								
RM-18	granite	40.989	-115.104	73	129	247	1.51	0.76156
RM-4	granite	40.634	-115.369	80	121	272	1.29	0.72756
RM-9	gneiss	41.031	-115.092	2500	168	99	5.04	0.98111
Kistler et al., 1981								
Lam Can'	granite	40.637	-115.372	PC	117	188	1.81	0.72328
LC-1	granite	40.637	-115.372	PC	150	227	1.92	0.72050
LC-5	granite	40.637	-115.372	PC	135	193	2.03	0.72287
LC-7	granite	40.637	-115.372	PC	160	200	2.32	0.72522
LC-8	granite	40.637	-115.372	PC	173	237	2.11	0.72147
SPIA	pegmatite	40.860	-115.237	PC	256	204	3.66	0.74415
RM-3-66	granite	40.516	-115.540	Jr	140	659	0.61	0.71570
RM-9-66	granite	40.387	-115.497	Jr	146	161	2.67	0.72730
RM-36-66	granite	40.469	-115.457	Jr	177	141	3.63	0.74460
RM-24A-67	granite	40.865	-115.253	PC	120	313	1.12	0.71787

RM-7B-67	granite	40.865	-115.253	PC	111	315	1.02	0.71728
RM6-67	granite	40.865	-115.253	PC	131	261	1.45	0.71800
RM-42-66	granite	40.548	-115.474	PC	69	319	0.58	0.71714
RM-40-66	granite	40.539	-115.460	PC	154	340	1.30	0.71782
RM-44-66	granite	40.552	-115.483	PC	70	128	1.59	0.71753
RM-24B67	diabase	40.865	-115.253	PC	8	70	0.33	0.70983
RM-24D67	diabase	40.865	-115.253	PC	78	505	0.45	0.71318
RM-37-66	granite	40.463	-115.440	Jr	201	103	5.68	0.75132
RM-41-66	granite	40.543	-115.466	PC	93	234	1.15	0.71875
RM-45-66	granite	40.555	-115.495	PC	85	395	0.62	0.71615
SPI-C	schist	40.860	-115.237	PC	95	143	1.91	0.74164
RM-19-67	schist	40.407	-115.443	PC	316	161	5.72	0.76651
SP-2	schist	40.860	-115.237	PC	207	63	9.58	0.78142
RM-27-66	schist	40.575	-115.370	PC	212	479	1.28	0.71727
RM-12-68	schist	40.575	-115.370	PC	158	350	1.31	0.71796
RM-24G-67	quartzite	40.865	-115.253	PC	25	20	3.51	0.73233
RM-24C-67	quartzite	40.865	-115.253	PC	50	62	2.34	0.72693
RM-7A-67	schist	40.865	-115.253	PC	118	170	2.01	0.72792
RM-27F-67	schist	40.865	-115.253	PC	85	168	1.47	0.73519
RM-24H-67	granite	40.865	-115.253	PC	67	263	0.74	0.71262
RM-43-68	granite	40.647	-115.294	PC	144	233	1.79	0.72945
RM-17-66(1)	granite	40.395	-115.433	K	283	86	9.50	0.74831
RM-17-66(2)	granite	40.395	-115.433	K	287	80	10.46	0.75065
RM-19-66(1)	granite	40.427	-115.429	K	273	112	7.11	0.74603
RM-19-66(2)	granite	40.427	-115.429	K	285	108	7.64	0.74608
J4a	granite	40.412	-115.543	K	158	34	13.65	0.75314
RM-19-66M	granite	40.427	-115.429	K	624	13	137.70	0.89194
RM-17-66M	granite	40.395	-115.433	K	710	9	231.10	1.02694
RM-15-67P	granite	40.405	-115.432	K	126	35	10.36	0.77582
RM-15-67K	granite	40.405	-115.432	K	1067	61	51.01	0.82249
RM-19-67	schist	40.407	-115.443	K	316	161	5.72	0.76651
RM-20-67	granite	40.407	-115.443	K	172	34	15.00	0.77766
RM-2-79A	granite	40.865	-115.253	K	299	77	11.19	0.72779
RM-2-79C	granite	40.865	-115.253	K	284	92	9.00	0.72778
RM-2-79E	granite	40.865	-115.253	K	185	99	5.40	0.71986
RM-45-68	granite	40.615	-115.309	K	257	58	12.81	0.72530
RM-45-68K	granite	40.615	-115.309	K	595	85	20.18	0.73094
R1-65	granite	40.517	-115.553	Jr	179	254	2.03	0.71683
R2-65	granite	40.517	-115.553	Jr	210	205	2.98	0.72031
64W66	granite	40.517	-115.553	Jr	204	173	3.42	0.71992
RM-11-66	granite	40.387	-115.497	Jr	232	91	7.45	0.73032
RM-31-66	granite	40.438	-115.479	Jr	129	147	2.55	0.71952
RM-47-66	granite	40.412	-115.543	Jr	188	126	4.32	0.72361
Jb4	granite	40.412	-115.543	Jr	262	48	15.82	0.74802
J1	granite	40.387	-115.497	Jr	199	33	17.36	0.75301
RM-10-66	granite	40.387	-115.497	Jr	152	289	1.54	0.71753
RM-38-66	granite	40.463	-115.440	Jr	413	44	27.39	0.77741
LC-2	granite	40.637	-115.372	Jr	245	118	8.00	0.72402
LC-6	granite	40.637	-115.372	Jr	276	224	3.27	0.71797
Farmer et al., 1983								
79NVSZ-2	granite	40.904	-114.305	124				0.70592
79UTGH-2	granite	40.163	-113.829	152				0.71139
NV77-10	granite	39.699	-114.197	79				0.72248
SnRng95	granite	38.957	-114.171	80				0.71804
Gans et al., 1989								
4SW-23B	tuff	39.561	-114.632	34	249	218	3.58	0.71468
4SE-14A	tuff	39.561	-114.632		166	411	1.14	0.71375
NS-3	dacite	S. Kern Mountains, NV			173	413	1.27	0.71390
WP-1	andesite	39.462	-115.466	34	93	549	0.47	0.70861
WP-3	andesite	39.403	-115.472	36	64	502	0.34	0.70972
H-2	andesite	Egan Range, NV			179	636	0.78	0.71198

HR-2	andesite	39.900	-114.992		71	506	0.41	0.71282
DC-33	rhyolite	Duck Creek Valley, NV			260	153	5.01	0.71783
Grunder, 1993								
MT-87-87	volcanic	39.45	-115.05		114	517	0.64	0.71181
AG-87-38	volcanic	39.45	-115.05		78	533	0.42	0.71343
MT-87-63	volcanic	39.45	-115.05		138	457	0.87	0.71246
RH-86-6	volcanic	39.45	-115.05		102	486	0.60	0.71326
AG-87-46	volcanic	39.45	-115.05		132	381	1.00	0.71432
MT-87-86	volcanic	39.45	-115.05		179	379	1.37	0.71303
AG-87-45	volcanic	39.45	-115.05		75	700	0.31	0.71119
Tht	volcanic	39.45	-115.05		670	38	50.96	0.72213
Wright and Wooden, 1991								
S117-8	volcanic	40.02	115.84	37				0.70800
NS1D-9	volcanic	41.12	115.96	39				0.70780
NS1-9	volcanic	41.12	115.96	39				0.70780
NS3-9	volcanic	40.61	116.26	39				0.70770
NS2-9	volcanic	41.33	116.33	39				0.70610
NS5-9	volcanic	40.41	116.78	39				0.70780
Stevens, 2013								
10-BV-06	dacite	40.284	-117.405					0.70752
10-BV-07	andesite	40.218	-117.406					0.70638
10-BV-08	andesite	40.217	-117.408					0.70639
10-BV-10	andesite	40.217	-117.400					0.70604
10-BV-11	dacite	40.164	-117.445					0.70690
10-BV-12A	rhyolite	40.166	-117.434					0.70706
10-BV-16	andesite	40.283	-117.229					0.70787
10-BV-29	andesite	40.271	-117.136					0.70683
10-BV-30	andesite	40.271	-117.141					0.70691
10-BV-31	andesite	40.284	-117.159					0.70684
10-BV-32	andesite	40.284	-117.161					0.70682
10-BV-34A	andesite	40.287	-117.360					0.70710
10-BV-34B	dacite	40.287	-117.360					0.70678
10-BV-39	andesite	40.263	-117.529					0.70631
10-BV-40	andesite	40.275	-117.542					0.70591
10-BV-41	andesite	40.287	-117.550					0.70583
10-BV-42	andesite	40.322	-117.600					0.70650
10-BV-44	dacite	39.966	-117.267					0.70665
10-BV-45	andesite	39.987	-117.296					0.70683
10-BV-46B	dacite	39.980	-117.296					0.70673
10-BV-47	rhyolite	39.978	-117.295					0.70708
10-BV-48A	dacite	39.974	-117.296					0.70698
10-BV-48B	rhyolite	39.974	-117.296					0.70707
10-BV-49	andesite	40.224	-117.094					0.70706
H10-53	rhyolite	40.283	-117.230					0.70748
Paces et al., 2007								
5466027	carbonate	40.599	-114.689	Pn		227		0.70825
5466055	carbonate	40.599	-114.689	Pn		635		0.70813
5466063	carbonate	40.599	-114.689	Pn		392		0.70818
5466069	carbonate	40.599	-114.689	Pn		352		0.70810
5466076	carbonate	40.599	-114.689	Pn		259		0.70836
5466088	carbonate	40.599	-114.689	Pn		256		0.70823
5466094	carbonate	40.599	-114.689	Pn		203		0.70841
5466107	carbonate	40.599	-114.689	Pn		533		0.70846
5466118	carbonate	40.599	-114.689	Pn		314		0.70832
5466127	carbonate	40.599	-114.689	Pn		277		0.70818
5466136	carbonate	40.599	-114.689	Pn		280		0.70814
5466158	carbonate	40.599	-114.689	Pn		285		0.70819
5153159	carbonate	40.599	-114.689	P		215		0.70810
5153170	carbonate	40.599	-114.689	P		336		0.70814

5153180	carbonate	40.599	-114.689	P	418	0.70811
5153183	carbonate	40.599	-114.689	P	187	0.70819
5153192	carbonate	40.599	-114.689	P	191	0.70828
5153203	carbonate	40.599	-114.689	P	547	0.70813
5153209	carbonate	40.599	-114.689	P	399	0.70819
5153220	carbonate	40.599	-114.689	P	172	0.70817
5153234	carbonate	40.599	-114.689	P	133	0.70820
5153242	carbonate	40.599	-114.689	P	135	0.70805
5153248	carbonate	40.599	-114.689	P	215	0.70790
5153257	carbonate	40.599	-114.689	P	95	0.70825
5153266	carbonate	40.599	-114.689	P	88	0.70835
5153275	carbonate	40.599	-114.689	P	197	0.70794
5153280	carbonate	40.599	-114.689	P	165	0.70789
5153291	carbonate	40.599	-114.689	P	159	0.70788
5153300	carbonate	40.599	-114.689	P	91	0.70828
5153309	carbonate	40.599	-114.689	P	86	0.70791
5153318	carbonate	40.599	-114.689	P	77	0.70819
5153328	carbonate	40.599	-114.689	P	141	0.70791
5153338	carbonate	40.599	-114.689	P	150	0.70786
5153348	carbonate	40.599	-114.689	P	139	0.70784
5153351	carbonate	40.599	-114.689	P	225	0.70778
5153354	carbonate	40.599	-114.689	P	177	0.70783
5153360	carbonate	40.599	-114.689	P	225	0.70780
5153368	carbonate	40.599	-114.689	P	218	0.70784
5153371	carbonate	40.599	-114.689	P	172	0.70780
5153379	carbonate	40.599	-114.689	P	272	0.70781
5153385	carbonate	40.599	-114.689	P	223	0.70784
5153388	carbonate	40.599	-114.689	P	286	0.70784
5153396	carbonate	40.599	-114.689	P	95	0.70849
5153405	carbonate	40.599	-114.689	P	93	0.70814
5153409	carbonate	40.599	-114.689	P	198	0.70784
5153419	carbonate	40.599	-114.689	P	144	0.70781
5466169	carbonate	40.599	-114.689	P	148	0.70804
5466184	carbonate	40.599	-114.689	P	137	0.70775
5466189	carbonate	40.599	-114.689	P	108	0.70778
5466203	carbonate	40.599	-114.689	P	2163	0.70773
5153437	carbonate	40.743	-114.591	P	154	0.70791
5153442	carbonate	40.743	-114.591	P	42	0.70893
5153453	carbonate	40.743	-114.591	P	152	0.70843
5153500	carbonate	40.743	-114.591	P	353	0.70765
5153508	carbonate	40.743	-114.591	P	263	0.70767
5153511	carbonate	40.743	-114.591	P	281	0.70763
5153517	carbonate	40.743	-114.591	P	158	0.70770
5153527	carbonate	40.743	-114.591	P	378	0.70761
5153529	carbonate	40.743	-114.591	P	262	0.70765
5466210	carbonate	40.743	-114.591	P	198	0.70761

Edwards et al., 2015

257.5	carbonate	Antelope Range, NV	466	236	0.70883
311.5	carbonate	Antelope Range, NV	463	260	0.70884
330	carbonate	Antelope Range, NV	462	313	0.70869
335	carbonate	Antelope Range, NV	462	200	0.70866
360	carbonate	Antelope Range, NV	460	197	0.70848
379.5	carbonate	Antelope Range, NV	459	293	0.70843
402	carbonate	Antelope Range, NV	457	220	0.70827
409.5	carbonate	Antelope Range, NV	457	154	0.70824
423	carbonate	Antelope Range, NV	455	716	0.70809
445.5	carbonate	Antelope Range, NV	454	199	0.70818
466	carbonate	Antelope Range, NV	454	545	0.70809
SP-82	carbonate	Shingle Pass, NV	486	187	0.70912
SP300	carbonate	Shingle Pass, NV	480	203	0.70904
SP573	carbonate	Shingle Pass, NV	480	143	0.70935
SP-630	carbonate	Shingle Pass, NV	480	260	0.71121
SP991	carbonate	Shingle Pass, NV	480	110	0.71049

SP1042	carbonate	Shingle Pass, NV		480		204	0.71062
SP1200	carbonate	Shingle Pass, NV		479		168	0.70964
SP1277	carbonate	Shingle Pass, NV		479		167	0.70974
SP1402	carbonate	Shingle Pass, NV		478		186	0.70939
SP1540	carbonate	Shingle Pass, NV		478		191	0.70917
SP1760	carbonate	Shingle Pass, NV		476		143	0.70915
SP1820	carbonate	Shingle Pass, NV		475		163	0.70933
SP1980	carbonate	Shingle Pass, NV		474		196	0.70935
SP2404	carbonate	Shingle Pass, NV		471		207	0.70956
SP-2620	carbonate	Shingle Pass, NV		470		214	0.70918
SP2653	carbonate	Shingle Pass, NV		470		181	0.70902
SP2848	carbonate	Shingle Pass, NV		469		177	0.70912
SPK4980	carbonate	Shingle Pass, NV		468		158	0.70955
SPK 4999	carbonate	Shingle Pass, NV		467		202	0.70946
SPK 5007	carbonate	Shingle Pass, NV		467		189	0.70950
SPK5011	carbonate	Shingle Pass, NV		467		110	0.70938
SPK5019	carbonate	Shingle Pass, NV		467		167	0.70975
SPK 5036	carbonate	Shingle Pass, NV		466		312	0.71067
SPK 5051	carbonate	Shingle Pass, NV		466		227	0.70906
SPK5058	carbonate	Shingle Pass, NV		465		233	0.70927
SPK5063	carbonate	Shingle Pass, NV		465		117	0.70891
SPK5069	carbonate	Shingle Pass, NV		465		122	0.70887
SPK5072	carbonate	Shingle Pass, NV		465		163	0.70900
SPK5074	carbonate	Shingle Pass, NV		465		163	0.70877
SPK 5078	carbonate	Shingle Pass, NV		464		149	0.70887
SPK5081	carbonate	Shingle Pass, NV		464		385	0.70868
SPK5088	carbonate	Shingle Pass, NV		464		177	0.70871
SPK5090	carbonate	Shingle Pass, NV		464		264	0.70873
SPK5095	carbonate	Shingle Pass, NV		464		149	0.70879
SPK5099	carbonate	Shingle Pass, NV		463		21	0.70864
SPK5101	carbonate	Shingle Pass, NV		463		19	0.70890
MP 109	carbonate	Meiklejohn Peak, NV		464		182	0.70879
MP 126	carbonate	Meiklejohn Peak, NV		464		120	0.70881
MP 139	carbonate	Meiklejohn Peak, NV		464		180	0.70891
MP 154	carbonate	Meiklejohn Peak, NV		464		131	0.70885
MP-164	carbonate	Meiklejohn Peak, NV		464		222	0.70902
MP 166	carbonate	Meiklejohn Peak, NV		464		152	0.70916
MP 170	carbonate	Meiklejohn Peak, NV		464		286	0.70904
MP 182	carbonate	Meiklejohn Peak, NV		463		714	0.70873
MP 196	carbonate	Meiklejohn Peak, NV		463		585	0.70878
MP 207	carbonate	Meiklejohn Peak, NV		463		549	0.70872
MP-219	carbonate	Meiklejohn Peak, NV		463		407	0.70886
MP 225	carbonate	Meiklejohn Peak, NV		463		659	0.70882
MP 235	carbonate	Meiklejohn Peak, NV		463		775	0.70875
MP-245	carbonate	Meiklejohn Peak, NV		462		534	0.70875
MP 253	carbonate	Meiklejohn Peak, NV		462		375	0.70886
MP-255	carbonate	Meiklejohn Peak, NV		462		546	0.70869
MP 261	carbonate	Meiklejohn Peak, NV		462		587	0.70870
MP-269	carbonate	Meiklejohn Peak, NV		462		137	0.70901
MP-270	carbonate	Meiklejohn Peak, NV		461		155	0.70889
MP 278	carbonate	Meiklejohn Peak, NV		457		178	0.70868
Paces et al., 2007							
HD-513	carbonate	36.854	-116.643	O	2	96	0.70946
HD-515	carbonate	36.855	-116.643	O	1	58	0.70875
HD-516A	carbonate	36.855	-116.643	Sr	2	71	0.70981
HD-517	carbonate	36.856	-116.643	Sr	16	311	0.71319
HD-518	carbonate	36.857	-116.643	Sr	8	63	0.71105
HD-519	carbonate	36.858	-116.644	D/Sr	2	64	0.70882
HD-520	carbonate	36.853	-116.642	D/Sr	1	55	0.70861
HD-533	carbonate	36.845	-116.638	O	1	300	0.71175
HD-534	carbonate	36.843	-116.638	O	5	298	0.71101
HD-527	carbonate	36.887	-116.685	D	1	60	0.70816
HD-528	carbonate	36.883	-116.688	D	1	166	0.71152

HD-1142	carbonate	36.879	-116.668	O	6	390	0.70876
HD-1144	carbonate	36.878	-116.671	D	2	35	0.70935
HD-1146	carbonate	36.867	-116.651	M/D	0	283	0.71292
HD-1147a	carbonate	36.865	-116.641	D	14	197	0.70926
HD-1147b	carbonate	36.865	-116.641	D	2	120	0.71088
HD-522	carbonate	36.866	-116.632	D	1	63	0.70976
HD-523	carbonate	36.867	-116.633	D	7	172	0.71029
HD-1138	carbonate	36.902	-116.652	O	9	777	0.70884
HD-1139	carbonate	36.901	-116.653	D/Sr	2	65	0.70935
HD-1141	carbonate	36.896	-116.649	O	10	1140	0.70906
HD-546	carbonate	36.665	-116.363	D	1	45	0.70886
HD-548	carbonate	36.671	-116.338	O	9	382	0.70921
HD-549	carbonate	36.669	-116.338	O	11	315	0.70979
HD-550	carbonate	36.668	-116.338	O	4	297	0.70921
HD-551A	carbonate	36.658	-116.343	O	1	47	0.70929
HD-1432	carbonate	36.582	-116.208	D	2	555	0.70931
HD-1434	carbonate	36.598	-116.116	D	0	51	0.70804
HD-229	carbonate	36.418	-115.501	M/P	0	743	0.70831
HD-230	carbonate	36.403	-115.569	M/P	2	132	0.70827
HD-231	carbonate	36.396	-115.580	M	2	564	0.70844
HD-236	carbonate	36.339	-115.637	O	0	66	0.70859
HD-238	carbonate	36.274	-115.473	M/P	8	263	0.70790
HD-1000	carbonate	36.577	-115.331	D	1	104	0.70834
HD-995	carbonate	36.580	-115.593	O	0	67	0.70845
HD-996	carbonate	36.602	-115.581	O	2	327	0.70912
HD-997	carbonate	36.626	-115.561	O	0	422	0.70884
HD-998	carbonate	36.632	-115.572	O	3	345	0.70880
HD-1001	carbonate	36.944	-115.526	O	1	233	0.70912
HD-1006	carbonate	36.987	-115.631	O	1	16	0.70918
HD-990	carbonate	36.602	-115.660	O	2	56	0.70841
HD-1002	carbonate	36.768	-115.618	O	1	44	0.70853
HD-991	carbonate	36.630	-115.721	O	1	63	0.70813
HD-993	carbonate	36.668	-115.762	D	0	22	0.70862
HD-994	carbonate	36.697	-115.797	M	0	470	0.70817
HD-1004	carbonate	36.775	-115.674	O	4	204	0.70884
HD-1003	carbonate	36.819	-115.650	D	4	164	0.70826
HD-1007	carbonate	37.186	-116.162	O	2	258	0.70994
HD-1008	carbonate	37.183	-116.185	D	9	59	0.70915
Brand et al., 2012							
A43B-2	carbonate	36.736	-114.778	M		497	0.70824
AC1-1	carbonate	36.736	-114.778	M		567	0.70816
AC1-2	carbonate	36.736	-114.778	M		391	0.70820
AC1-22	carbonate	36.736	-114.778	M		415	0.70824
AC1-3	carbonate	36.736	-114.778	M		461	0.70819
AC1-32	carbonate	36.736	-114.778	M		488	0.70818
AC1-4	carbonate	36.736	-114.778	M		564	0.70820
AC1-42	carbonate	36.736	-114.778	M		534	0.70818
AC1-43	carbonate	36.736	-114.778	M		513	0.70820
AC1-2C	carbonate	36.736	-114.778	M		144	0.70823
AC1-22C	carbonate	36.736	-114.778	M		162	0.70818
AC1-3C	carbonate	36.736	-114.778	M		167	0.70819
AC1-1M	carbonate	36.736	-114.778	M		681	0.70829
AC1-2M	carbonate	36.736	-114.778	M		708	0.70826
A44-10	carbonate	36.736	-114.778	M		608	0.70821
A44-8M	carbonate	36.736	-114.778	M		335	0.70824
A47-1	carbonate	36.736	-114.778	M		719	0.70816
AC2-2	carbonate	36.736	-114.778	M		861	0.70818
AC2-43	carbonate	36.736	-114.778	M		750	0.70815
AC2-1M	carbonate	36.736	-114.778	M		329	0.70826
AC3-3	carbonate	36.736	-114.778	M		998	0.70814
AC3-1M	carbonate	36.736	-114.778	M		419	0.70825
AC4-2	carbonate	36.736	-114.778	M		776	0.70821
AC4-1V	carbonate	36.736	-114.778	M		125	0.71110

AC4-1C	carbonate	36.736	-114.778	M	108	0.70829
AC4-1M	carbonate	36.736	-114.778	M	304	0.70839
AC5-3	carbonate	36.736	-114.778	M	1024	0.70821
AC5-6C	carbonate	36.736	-114.778	M	118	0.70829
AC5-32M	carbonate	36.736	-114.778	M	376	0.70831
A51-6	carbonate	36.736	-114.778	M	379	0.70819
A51-3M	carbonate	36.736	-114.778	M	498	0.70830
A51-3C	carbonate	36.736	-114.778	M	177	0.70820
AC6-6	carbonate	36.736	-114.778	M	1151	0.70816
AC6-2M	carbonate	36.736	-114.778	M	393	0.70835
AC7-13	carbonate	36.736	-114.778	M	517	0.70820
AC7-23	carbonate	36.736	-114.778	M	523	0.70829
AC7-12C	carbonate	36.736	-114.778	M	153	0.70823
AC7-3C	carbonate	36.736	-114.778	M	188	0.70820
AC7-2M	carbonate	36.736	-114.778	M	502	0.70852
AC8-1a	carbonate	36.736	-114.778	M	552	0.70826
AC8-1M	carbonate	36.736	-114.778	M	189	0.70825
AC9-1	carbonate	36.736	-114.778	M	822	0.70818
AC9-3	carbonate	36.736	-114.778	M	770	0.70815
AC9-34	carbonate	36.736	-114.778	M	764	0.70819
AC9-2M	carbonate	36.736	-114.778	M	367	0.70844
A56-4	carbonate	36.736	-114.778	Pn	425	0.70862
A56-5	carbonate	36.736	-114.778	Pn	385	0.70842
A56-3M	carbonate	36.736	-114.778	Pn	264	0.70838
A56-5M	carbonate	36.736	-114.778	Pn	256	0.70836
AC13-12	carbonate	36.736	-114.778	Pn	958	0.70817
AC13-22	carbonate	36.736	-114.778	Pn	503	0.70818
AC13-1M	carbonate	36.736	-114.778	Pn	308	0.70843
AC15-1	carbonate	36.736	-114.778	Pn	841	0.70822
AC15-3	carbonate	36.736	-114.778	Pn	846	0.70825
AC15-4	carbonate	36.736	-114.778	Pn	758	0.70819
AC15-5	carbonate	36.736	-114.778	Pn	522	0.70830
AC15-1M	carbonate	36.736	-114.778	Pn	476	0.70851
A58-2	carbonate	36.736	-114.778	Pn	1034	0.70895
A58-4	carbonate	36.736	-114.778	Pn	932	0.70823
A58-6	carbonate	36.736	-114.778	Pn	918	0.70846
A58-7	carbonate	36.736	-114.778	Pn	1053	0.70826
A58-2M	carbonate	36.736	-114.778	Pn	286	0.70833
A58A-5	carbonate	36.736	-114.778	Pn	879	0.70827
A58A-1M	carbonate	36.736	-114.778	Pn	262	0.70834
A59-1	carbonate	36.736	-114.778	Pn	527	0.70833
A59-3m	carbonate	36.736	-114.778	Pn	287	0.70847
A59A-12	carbonate	36.736	-114.778	Pn	905	0.70824
A61-18m	carbonate	36.736	-114.778	Pn	415	0.70853
A61-20	carbonate	36.736	-114.778	Pn	329	0.70842
A63C-38m	carbonate	36.736	-114.778	Pn	561	0.70866
A63C-45	carbonate	36.736	-114.778	Pn	521	0.70825
A64A-28	carbonate	36.736	-114.778	Pn	725	0.70825
A64-2	carbonate	36.736	-114.778	Pn	805	0.70825
A64-4	carbonate	36.736	-114.778	Pn	878	0.70822
A64-4M	carbonate	36.736	-114.778	Pn	510	0.70832
A66B-61	carbonate	36.736	-114.778	Pn	568	0.70823
A66C-66C	carbonate	36.736	-114.778	Pn	194	0.70844
A66C-67m	carbonate	36.736	-114.778	Pn	359	0.70836
A66C-71	carbonate	36.736	-114.778	Pn	597	0.70824
A67-6	carbonate	36.736	-114.778	Pn	878	0.70825
A67-1M	carbonate	36.736	-114.778	Pn	635	0.70843
A67-1M	carbonate	36.736	-114.778	Pn		0.70842
A69-73	carbonate	36.736	-114.778	Pn	541	0.70825
A70-81	carbonate	36.736	-114.778	Pn	555	0.70823
A73B-96	carbonate	36.736	-114.778	Pn	709	0.70827
A75-111	carbonate	36.736	-114.778	Pn	861	0.70822
A76-116m	carbonate	36.736	-114.778	Pn	419	0.70867
A76-117	carbonate	36.736	-114.778	Pn	538	0.70824

A80-124	carbonate	36.736	-114.778	Pn	684	0.70825
A80B-134	carbonate	36.736	-114.778	Pn	560	0.70830
A80B-141	carbonate	36.736	-114.778	Pn	641	0.70826
A81-5	carbonate	36.736	-114.778	Pn	917	0.70822
A86-1C	carbonate	36.736	-114.778	Pn	244	0.70825
A86-2m	carbonate	36.736	-114.778	Pn	444	0.70825
A86-3	carbonate	36.736	-114.778	Pn	790	0.70834
A91-1	carbonate	36.736	-114.778	Pn		0.70832
A91a-1	carbonate	36.736	-114.778	Pn	1016	0.70824
A91a-2m	carbonate	36.736	-114.778	Pn	571	0.70829
A93-2	carbonate	36.736	-114.778	Pn	764	0.70827
A95-4	carbonate	36.736	-114.778	Pn	592	0.70824
A96-2	carbonate	36.736	-114.778	Pn	531	0.70825
A96-4m	carbonate	36.736	-114.778	Pn	675	0.70843
A96-5	carbonate	36.736	-114.778	Pn	523	0.70828
A96a-1	carbonate	36.736	-114.778	Pn	467	0.70827
A96b-1	carbonate	36.736	-114.778	Pn	727	0.70826
A100-1m	carbonate	36.736	-114.778	Pn	754	0.70835
A100-3	carbonate	36.736	-114.778	Pn	1047	0.70826
A103-1	carbonate	36.736	-114.778	Pn	1329	0.70827
A104-2	carbonate	36.736	-114.778	Pn	1354	0.70829
A106-3	carbonate	36.736	-114.778	Pn	951	0.70829
A106a-2	carbonate	36.736	-114.778	Pn	807	0.70827
A107-1	carbonate	36.736	-114.778	Pn	675	0.70828
A107-4m	carbonate	36.736	-114.778	Pn	735	0.70826
A113-4	carbonate	36.736	-114.778	Pn	1053	0.70825
A113-5m	carbonate	36.736	-114.778	Pn	878	0.70834
A113-6	carbonate	36.736	-114.778	Pn		0.70836
A116-1	carbonate	36.736	-114.778	Pn	708	0.70826
A116-2	carbonate	36.736	-114.778	Pn	877	0.70837
A116-3	carbonate	36.736	-114.778	Pn	649	0.70824
A118-1	carbonate	36.732	-114.776	Pn		0.70828
A118-2	carbonate	36.732	-114.776	Pn	181	0.70838
A118-3	carbonate	36.732	-114.776	Pn	541	0.70825
A118-4m	carbonate	36.732	-114.776	Pn	515	0.70830
A122-2	carbonate	36.732	-114.776	Pn		0.70826
A122-3	carbonate	36.732	-114.776	Pn		0.70827
A123-1	carbonate	36.732	-114.776	Pn	572	0.70826
A126-1	carbonate	36.732	-114.776	Pn	682	0.70827
A127-2	carbonate	36.732	-114.776	Pn	762	0.70826
A127-4m	carbonate	36.732	-114.776	Pn	645	0.70829
A130-2	carbonate	36.732	-114.776	Pn	1806	0.70826
A130a-2	carbonate	36.732	-114.776	Pn	712	0.70828
A134-1	carbonate	36.732	-114.776	Pn	408	0.70830
A134-4m	carbonate	36.732	-114.776	Pn	721	0.70857
A134-5	carbonate	36.732	-114.776	Pn	407	0.70826
A134a-1	carbonate	36.732	-114.776	Pn	1211	0.70826
A146-2	carbonate	36.732	-114.776	Pn	573	0.70828
A147-2	carbonate	36.732	-114.776	Pn	876	0.70829
A147-4m	carbonate	36.732	-114.776	Pn	445	0.70840
A155-4	carbonate	36.732	-114.776	Pn	764	0.70894
A156-1m	carbonate	36.732	-114.776	Pn	414	0.70843
A156-2	carbonate	36.732	-114.776	Pn	374	0.70831
A156-4	carbonate	36.732	-114.776	Pn	1070	0.70828
A156-5	carbonate	36.732	-114.776	Pn	663	0.70827
A159-3	carbonate	36.732	-114.776	Pn	838	0.70826
A159-5	carbonate	36.732	-114.776	Pn		0.70825
A159a-1	carbonate	36.732	-114.776	Pn	967	0.70826
A159a-3	carbonate	36.732	-114.776	Pn	594	0.70825
A160-3	carbonate	36.732	-114.776	Pn	579	0.70832
A160-5m	carbonate	36.732	-114.776	Pn	567	0.70833
A181-15m	carbonate	36.732	-114.776	Pn	372	0.70848
A181-18	carbonate	36.732	-114.776	Pn	319	0.70830
A189-20m	carbonate	36.732	-114.776	Pn	450	0.70837

A189-21	carbonate	36.732	-114.776	Pn	451	0.70843
A189-25	carbonate	36.732	-114.776	Pn	404	0.70849
A214-30m	carbonate	36.732	-114.776	Pn	578	0.70843
A214-31	carbonate	36.732	-114.776	Pn	1104	0.70834
A214-35	carbonate	36.732	-114.776	Pn	1047	0.70834
A216-42m	carbonate	36.732	-114.776	Pn		0.70836
A216-45	carbonate	36.732	-114.776	Pn		0.70830
A216-37m	carbonate	36.732	-114.776	Pn	646	0.70835
A216-38	carbonate	36.732	-114.776	Pn		0.70825
A216-39	carbonate	36.732	-114.776	Pn	898	0.70834
A216-40	carbonate	36.732	-114.776	Pn		0.70842
A224-49	carbonate	36.729	-114.769	Pn	771	0.70830
A226-51m	carbonate	36.729	-114.769	Pn	519	0.70841
A226-56	carbonate	36.729	-114.769	Pn	264	0.70836
A238-58m	carbonate	36.729	-114.769	Pn	510	0.70839
A238-59	carbonate	36.729	-114.769	Pn	1202	0.70830
A238-61	carbonate	36.729	-114.769	Pn	876	0.70833
A238-62	carbonate	36.729	-114.769	Pn	872	0.70827
A264-610m	carbonate	36.729	-114.769	Pn	283	0.70838
A264-614	carbonate	36.729	-114.769	Pn	495	0.70831
A264-616	carbonate	36.729	-114.769	Pn	508	0.70832
A267-620	carbonate	36.729	-114.769	Pn	461	0.70835
A274-219m	carbonate	36.729	-114.769	Pn	498	0.70856
A274-221	carbonate	36.729	-114.769	Pn	536	0.70848
A278-224m	carbonate	36.729	-114.769	Pn	517	0.70848
A278-226	carbonate	36.729	-114.769	Pn	1005	0.70829
A278-228	carbonate	36.729	-114.769	Pn	839	0.70825
A279-229m	carbonate	36.729	-114.769	Pn	453	0.70840
A279-233	carbonate	36.729	-114.769	Pn	644	0.70847
A284-234m	carbonate	36.731	-114.771	Pn	392	0.70841
A284-238	carbonate	36.731	-114.771	Pn	1001	0.70824
A290-239m	carbonate	36.731	-114.771	Pn	515	0.70830
A290-240	carbonate	36.731	-114.771	Pn	1325	0.70827
A290-243	carbonate	36.731	-114.771	Pn	1324	0.70830
A295-244m	carbonate	36.731	-114.771	Pn	451	0.70830
A295-246	carbonate	36.731	-114.771	Pn	597	0.70829
A295-248	carbonate	36.731	-114.771	Pn	415	0.70826
A297-249m	carbonate	36.731	-114.771	Pn	436	0.70842
A297-252	carbonate	36.731	-114.771	Pn	729	0.70826
A306-254m	carbonate	36.731	-114.771	Pn	608	0.70838
A306-255	carbonate	36.731	-114.771	Pn	727	0.70827
A307-259m	carbonate	36.731	-114.771	Pn	814	0.70858
A307-260	carbonate	36.731	-114.771	Pn	872	0.70827
A307-263	carbonate	36.731	-114.771	Pn		0.70828
A307-265m	carbonate	36.731	-114.771	Pn	596	0.70839
A307-267	carbonate	36.731	-114.771	Pn	539	0.70829
A309-269m	carbonate	36.731	-114.771	Pn	490	0.70836
A309-270	carbonate	36.731	-114.771	Pn	655	0.70830
A309-273m	carbonate	36.731	-114.771	Pn	647	0.70834
A309-278	carbonate	36.731	-114.771	Pn	1035	0.70830
A310-279m	carbonate	36.731	-114.771	Pn	594	0.70832
A310-281	carbonate	36.731	-114.771	Pn	815	0.70832
A315-283m	carbonate	36.731	-114.771	Pn	504	0.70833
A315-286	carbonate	36.731	-114.771	Pn	1473	0.70832
A315-288	carbonate	36.731	-114.771	Pn	883	0.70830
A317-289m	carbonate	36.731	-114.771	Pn	462	0.70844
A317-292	carbonate	36.731	-114.771	Pn	704	0.70829
A318-294m	carbonate	36.731	-114.771	Pn	871	0.70847
A318-299	carbonate	36.731	-114.771	Pn	730	0.70833
A323-300m	carbonate	36.731	-114.771	Pn	749	0.70835
A323-301v	carbonate	36.731	-114.771	Pn	784	0.70838
A323-304	carbonate	36.731	-114.771	Pn	809	0.70831
A324-306m	carbonate	36.731	-114.771	Pn	775	0.70838
A324-307	carbonate	36.731	-114.771	Pn	785	0.70833

A332-311m	carbonate	36.731	-114.771	Pn	429	0.70843
A332-313	carbonate	36.731	-114.771	Pn		0.70830
A332-316	carbonate	36.731	-114.771	Pn	720	0.70830
A338-317m	carbonate	36.731	-114.771	Pn	460	0.70850
A338-318	carbonate	36.731	-114.771	Pn	1148	0.70829
A339-321m	carbonate	36.731	-114.771	Pn	407	0.70847
A339-323	carbonate	36.731	-114.771	Pn	913	0.70830
A341-326v	carbonate	36.731	-114.771	Pn	236	0.70854
A341-327	carbonate	36.731	-114.771	Pn	857	0.70831
A343-330m	carbonate	36.731	-114.771	Pn	1017	0.70836
A343-333	carbonate	36.731	-114.771	Pn	991	0.70830
A343-337m	carbonate	36.731	-114.771	Pn	674	0.70843
A343-339	carbonate	36.731	-114.771	Pn	830	0.70831
A345-347	carbonate	36.731	-114.771	Pn		0.70833
A350-350	carbonate	36.731	-114.771	Pn	797	0.70830
A350-352m	carbonate	36.731	-114.771	Pn	408	0.70831
A350-353	carbonate	36.731	-114.771	Pn	916	0.70829
A350-355	carbonate	36.731	-114.771	Pn	870	0.70830
A356-358m	carbonate	36.731	-114.771	Pn	554	0.70862
A356-360	carbonate	36.731	-114.771	Pn	982	0.70827
A359-63m	carbonate	36.731	-114.771	Pn	577	0.70858
A359-67	carbonate	36.731	-114.771	Pn	864	0.70829
A360-68m	carbonate	36.731	-114.771	Pn	538	0.70845
A360-71	carbonate	36.731	-114.771	Pn	734	0.70829
A360-72	carbonate	36.731	-114.771	Pn	208	0.70834
A360-73C	carbonate	36.731	-114.771	Pn	833	0.70828
A376-76m	carbonate	36.731	-114.771	Pn	490	0.70834
A376-77	carbonate	36.731	-114.771	Pn	650	0.70831
A376-78	carbonate	36.731	-114.771	Pn	685	0.70828
A376-80	carbonate	36.731	-114.771	Pn	765	0.70826
A381-81m	carbonate	36.731	-114.771	Pn	317	0.70847
A381-83	carbonate	36.731	-114.771	Pn	434	0.70834
A408-91m	carbonate	36.729	-114.769	Pn	461	0.70892
A408-94	carbonate	36.729	-114.769	Pn	420	0.70864
A408-95	carbonate	36.729	-114.769	Pn	342	0.70895
A408-85m	carbonate	36.729	-114.769	Pn	327	0.70860
A408-86	carbonate	36.729	-114.769	Pn	1031	0.70825
A408-87	carbonate	36.729	-114.769	Pn	771	0.70826
A408-89c	carbonate	36.729	-114.769	Pn	84	0.71027
A415-98	carbonate	36.729	-114.769	Pn		0.70835
A419-99m	carbonate	36.729	-114.769	Pn	441	0.70832
A419-100	carbonate	36.729	-114.769	Pn	270	0.70827
A434-103m	carbonate	36.729	-114.769	Pn	283	0.70910
A434-104	carbonate	36.729	-114.769	Pn	765	0.70830
A434-106	carbonate	36.729	-114.769	Pn	839	0.70825
A434-110	carbonate	36.729	-114.769	Pn	854	0.70827
A438-114m	carbonate	36.729	-114.769	Pn	328	0.70841
A438-115C	carbonate	36.729	-114.769	Pn	210	0.70872
A438-120	carbonate	36.729	-114.769	Pn	1049	0.70825
A440-121m	carbonate	36.729	-114.769	Pn	257	0.70854
A440-126	carbonate	36.729	-114.769	Pn	788	0.70825
A442-129C	carbonate	36.729	-114.769	Pn	132	0.71003
A447-130m	carbonate	36.729	-114.769	Pn	271	0.70876
A447-131v	carbonate	36.729	-114.769	Pn	91	0.71035
A447-133	carbonate	36.729	-114.769	Pn	679	0.70827
A450-143	carbonate	36.729	-114.769	Pn	722	0.70823
A454-147	carbonate	36.729	-114.769	Pn		0.70826
A454-152	carbonate	36.729	-114.769	Pn	643	0.70823
A454-155m	carbonate	36.729	-114.769	Pn	419	0.70850
A454-157	carbonate	36.729	-114.769	Pn	506	0.70825
A458-164	carbonate	36.729	-114.769	Pn	754	0.70821
A458-170	carbonate	36.729	-114.769	Pn	627	0.70821
A470-180m	carbonate	36.729	-114.769	Pn	353	0.70899
A470-183	carbonate	36.729	-114.769	Pn	688	0.70829

A470-184	carbonate	36.729	-114.769	Pn		0.70826
A471-185m	carbonate	36.729	-114.769	Pn	302	0.70860
A471-188	carbonate	36.729	-114.769	Pn	742	0.70824
A471-189	carbonate	36.729	-114.769	Pn	848	0.70823
A492-195	carbonate	36.728	-114.768	Pn	843	0.70820
A492-202	carbonate	36.728	-114.768	Pn	425	0.70821
A492-205	carbonate	36.728	-114.768	Pn	591	0.70819
A493-209	carbonate	36.728	-114.768	Pn	390	0.70820
A493-217	carbonate	36.728	-114.768	Pn		0.70941
A493-218	carbonate	36.728	-114.768	Pn	536	0.70822
A494-625m	carbonate	36.728	-114.768	Pn	169	0.70858
A494-631	carbonate	36.728	-114.768	Pn	754	0.70822
A494-633m	carbonate	36.728	-114.768	Pn	246	0.70849
A495-634v	carbonate	36.728	-114.768	Pn	127	0.70858
A495-635m	carbonate	36.728	-114.768	Pn	270	0.70852
A495-636	carbonate	36.728	-114.768	Pn	513	0.70824
A495-639	carbonate	36.728	-114.768	Pn	764	0.70821
A500-645m	carbonate	36.728	-114.768	Pn	193	0.70830
A500-646c	carbonate	36.728	-114.768	Pn	89	0.70934
A507-672m	carbonate	36.728	-114.768	Pn	75	0.70890
A515--667m	carbonate	36.728	-114.768	Pn	49	0.70798
A521-656m	carbonate	36.728	-114.767	P	55	0.70798
A522-654m	carbonate	36.728	-114.767	P	79	0.70793

Abbreviations: PC-Precambrian; O-Ordovician; Sr-Silurian; D-Devonian; Mississippian; Pn-Pennsylvanian; P-Permian; Jr-Jurassic; K-Cretaceous

X-RAY DIFFRACTION RESULTS

Position (°)	D-spacing (Å)	Background Intensity (cps)	Intensity (cps)	Relative Intensity (%)	Area	Area (%)	FWHM (°)	P/N
EOS3N-269-5								
24.264	3.6652	8.2	52	5.8	11.3	6.2	0.187	6.1
26.899	3.3119	7.4	52	5.9	12.3	6.7	0.200	6.2
29.705	3.0051	10.9	32	2.8	2.6	1.4	0.089	3.7
31.149	2.8690	9.2	769	100.0	183.4	100.0	0.174	27.4
33.724	2.6556	13.5	39	3.4	4.9	2.7	0.139	4.1
35.494	2.5271	12.8	49	4.8	6.2	3.4	0.123	5.2
37.592	2.3907	8.6	105	12.7	20.7	11.3	0.155	9.4
41.318	2.1833	9.8	206	25.8	48.9	26.6	0.180	13.7
44.001	2.0562	11.5	43	4.1	4.5	2.4	0.103	4.8
45.119	2.0079	9.6	116	14.0	30.1	16.4	0.204	9.9
50.734	1.7980	29.6	98	9.0	20.8	11.4	0.220	6.9
51.208	1.7825	10.4	134	16.3	51.9	28.3	0.357	10.7
57.649	1.5977	5.9	10	0.5	0.5	0.3	0.096	1.3
59.089	1.5621	10.0	33	3.0	5.7	3.1	0.179	4.0
EOS3N-563								
20.931	4.2407	17.0	54	5.2	8.1	4.3	0.157	5.0
24.105	3.6891	14.1	63	6.9	10.8	5.8	0.160	6.2
26.743	3.3309	12.7	274	37.1	55.9	30.2	0.155	15.8
29.538	3.0217	13.7	48	4.9	4.3	2.3	0.090	5.0
30.950	2.8869	13.9	719	100.0	185.3	100.0	0.190	26.3
33.488	2.6737	14.4	36	3.1	5.1	2.8	0.172	3.6
35.308	2.5399	18.8	41	3.2	4.8	2.6	0.157	3.5
37.435	2.4004	15.3	82	9.5	18.4	10.0	0.200	7.4
39.590	2.2746	10.8	37	3.7	4.5	2.4	0.123	4.3
41.120	2.1934	11.2	181	24.1	55.8	30.1	0.237	12.6
43.830	2.0638	14.8	29	2.0	2.6	1.4	0.134	2.6
44.955	2.0148	13.1	117	14.7	26.6	14.3	0.185	9.6
46.780	1.9404	4.7	9	0.6	0.5	0.3	0.100	1.4
50.305	1.8123	17.3	84	9.5	48	25.9	0.611	7.3
50.959	1.7906	14.5	102	12.4	56.5	30.5	0.548	8.7
58.809	1.5689	13.0	32	2.7	4	2.2	0.153	3.4
EOS3N-576								
21.084	4.2102	10.5	67	8.6	16.3	8.1	0.208	6.9
24.196	3.6753	10.6	68	8.7	10.5	5.2	0.132	7.0
26.843	3.3186	10.6	329	48.3	73.2	36.5	0.166	17.6
29.653	3.0102	13.1	88	11.3	8.7	4.3	0.098	8.0
31.017	2.8808	10.2	670	100.0	200.3	100.0	0.219	25.5
35.397	2.5338	14.2	34	3.0	5.7	2.8	0.206	3.4
36.744	2.4440	13.9	34	3.1	3.1	1.5	0.109	3.5
37.490	2.3970	9.8	97	13.2	26.4	13.2	0.219	8.9
39.679	2.2696	8.5	29	3.1	4.9	2.4	0.172	3.8
41.211	2.1888	9.7	196	28.2	59	29.4	0.229	13.3
42.609	2.1202	8.5	27	2.8	3.7	1.8	0.144	3.6
43.931	2.0594	12.7	28	2.3	3.5	1.8	0.167	2.9
45.011	2.0124	11.3	140	19.5	32.2	16.1	0.181	10.9
50.493	1.8060	14.9	101	13.0	46.8	23.4	0.462	8.6
51.058	1.7874	10.9	122	16.8	61.7	30.8	0.472	10.1

Position (°)	D-spacing (Å)	Background Intensity (cps)	Intensity (cps)	Relative Intensity (%)	Area	Area (%)	FWHM (°)	P/N
EOS3N-578								
21.192	4.1890	14.0	47	4.4	6.2	2.7	0.136	4.8
24.308	3.6587	8.7	76	9.1	14.1	6.1	0.151	7.7
26.949	3.3058	10.4	250	32.3	50.6	22.1	0.153	15.2
31.150	2.8689	10.1	752	100.0	229.5	100.0	0.223	27.1
35.550	2.5232	19.5	36	2.2	3.2	1.4	0.138	2.8
37.600	2.3902	10.3	103	12.5	26.7	11.6	0.208	9.1
41.344	2.1820	12.0	207	26.3	59.5	25.9	0.220	13.6
43.977	2.0573	12.1	30	2.4	4.7	2.1	0.190	3.3
45.106	2.0084	13.5	131	15.8	34.9	15.2	0.214	10.3
49.450	1.8417	15.4	42	3.6	6.7	2.9	0.182	4.1
50.597	1.8025	16.1	109	12.5	54.9	23.9	0.503	8.9
51.154	1.7842	11.9	130	15.9	72.3	31.5	0.520	10.4
EOS3N-588								
20.894	4.2482	12.4	73	8.1	17.1	7.8	0.204	7.1
22.067	4.0250	11.6	28	2.2	2.2	1.0	0.098	3.1
24.055	3.6966	10.8	67	7.5	14.9	6.8	0.191	6.9
26.692	3.3371	10.3	358	46.3	82.8	37.6	0.172	18.4
30.898	2.8917	12.8	763	100.0	220.4	100.0	0.212	27.2
33.404	2.6803	12.8	39	3.5	7.7	3.5	0.212	4.2
35.295	2.5409	17.5	33	2.1	4.4	2.0	0.202	2.7
37.351	2.4056	9.8	102	12.3	25.4	11.5	0.199	9.1
39.497	2.2797	10.5	28	2.3	4.1	1.9	0.171	3.3
41.099	2.1945	13.3	224	28.1	59.4	27.0	0.204	14.1
43.728	2.0684	11.5	32	2.7	5.1	2.3	0.181	3.6
44.899	2.0172	12.9	135	16.3	31.5	14.3	0.187	10.5
49.204	1.8503	16.7	42	3.4	4.1	1.9	0.118	3.9
50.259	1.8139	15.6	99	11.1	61.3	27.8	0.625	8.4
50.995	1.7894	8.6	123	15.2	74.0	33.6	0.550	10.3
58.848	1.5680	12.1	35	3.1	6.3	2.9	0.199	3.9
EOS3N-625								
21.155	4.1962	5.8	51	5.6	8.3	4.6	0.134	6.3
22.463	3.9549	4.0	10	0.7	0.8	0.4	0.094	1.9
23.408	3.7972	5.9	82	9.5	16.4	9.1	0.155	8.4
26.940	3.3068	6.6	213	25.8	43.5	24.1	0.152	14.1
29.784	2.9973	6.6	808	100.0	180.6	100.0	0.163	28.2
31.804	2.8114	6.0	67	7.6	13.9	7.7	0.165	7.5
33.908	2.6416	3.7	10	0.8	1.6	0.9	0.182	2.0
36.354	2.4692	6.6	100	11.7	24.4	13.5	0.189	9.3
39.795	2.2633	5.5	160	19.3	39.5	21.9	0.185	12.2
43.544	2.0768	6.3	96	11.2	24.6	13.6	0.198	9.2
47.553	1.9106	8.6	52	5.4	17.6	9.8	0.345	6.0
47.860	1.8991	9.5	159	18.7	54.2	30.0	0.308	11.9
48.867	1.8622	14.2	143	16.1	34.0	18.8	0.191	10.8
50.434	1.8080	7.5	25	2.2	3.9	2.2	0.162	3.5
51.529	1.7721	3.9	9	0.6	0.6	0.3	0.087	1.7
57.796	1.5940	5.7	61	6.9	23.0	12.7	0.354	7.1

Position (°)	D-spacing (Å)	Background Intensity (cps)	Intensity (cps)	Relative Intensity (%)	Area	Area (%)	FWHM (°)	P/N
K1L-8996								
20.992	4.2286	13.8	93	20.0	18.6	16.1	0.170	8.2
26.789	3.3252	13.8	410	100.0	115.7	100.0	0.211	19.6
30.952	2.8868	15.0	389	94.4	113.8	98.4	0.220	19.0
33.187	2.6973	13.8	50	9.1	8.2	7.1	0.163	5.1
33.498	2.6730	9.2	32	5.8	6.5	5.6	0.205	4.0
35.296	2.5408	13.4	42	7.2	10.7	9.3	0.318	4.4
36.668	2.4488	16.4	47	7.7	5.7	4.9	0.134	4.5
37.352	2.4056	10.5	63	13.3	28.7	24.8	0.464	6.6
39.604	2.2738	8.5	47	9.7	8.4	7.3	0.158	5.6
41.153	2.1917	16.2	104	22.2	27.9	24.1	0.229	8.6
42.552	2.1228	12.5	31	4.7	4.3	3.7	0.167	3.3
44.916	2.0164	11.1	81	17.6	17.9	15.5	0.185	7.8
45.884	1.9761	11.7	29	4.4	3.2	2.8	0.134	3.2
50.386	1.8096	11.6	96	21.3	51.1	44.2	0.515	8.6
51.046	1.7878	11.8	77	16.5	38.6	33.4	0.503	7.4
56.438	1.6291	12.6	35	5.7	5.2	4.5	0.167	3.8
K1L-9114-7								
21.160	4.1953	9.5	64	13.8	16.8	11.5	0.223	6.8
23.839	3.7296	12.1	61	12.4	13.6	9.3	0.202	6.3
24.243	3.6684	13.4	50	9.3	6.0	4.1	0.118	5.2
25.968	3.4284	12.9	44	7.9	7.3	5.0	0.169	4.7
26.899	3.3119	29.1	244	54.4	44.6	30.4	0.150	13.8
27.897	3.1956	10.6	58	12.0	24.0	16.4	0.430	6.2
30.110	2.9656	10.4	48	9.5	11.3	7.7	0.218	5.4
31.057	2.8772	9.7	405	100.0	146.4	100.0	0.315	19.6
33.635	2.6624	9.8	30	5.1	5.5	3.8	0.197	3.7
34.656	2.5863	8.8	24	3.8	4.0	2.8	0.193	3.1
35.055	2.5578	8.8	40	7.9	12.4	8.5	0.338	4.9
37.538	2.3940	8.8	66	14.5	25.1	17.1	0.373	7.0
39.668	2.2703	10.3	28	4.5	2.4	1.7	0.099	3.3
41.292	2.1847	11.8	104	23.3	34.5	23.6	0.318	9.0
45.065	2.0101	12.2	81	17.4	18.8	12.9	0.198	7.6
50.401	1.8091	15.6	65	12.5	45.1	30.8	0.777	6.1
51.101	1.7859	12.4	81	17.4	61.6	42.0	0.763	7.6
K1L-9158								
21.143	4.1986	11.5	79	16.9	18.0	12.1	0.192	7.6
24.265	3.6650	11.8	36	6.0	8.1	5.4	0.242	4.0
26.905	3.3111	14.1	265	62.7	84.1	56.4	0.242	15.4
27.844	3.2015	16.0	39	5.7	6.7	4.5	0.210	3.7
29.704	3.0052	9.8	83	18.3	22.6	15.2	0.223	8.0
31.103	2.8731	9.6	410	100.0	149.1	100.0	0.316	19.8
35.552	2.5231	10.2	32	5.4	9.5	6.4	0.372	3.9
37.585	2.3912	11.3	61	12.4	18.7	12.6	0.320	6.4
39.693	2.2689	12.9	34	5.3	3.4	2.3	0.115	3.6
41.301	2.1842	11.7	113	25.3	37.8	25.4	0.317	9.5
42.744	2.1138	8.3	32	5.9	5.0	3.3	0.151	4.2
45.091	2.0090	9.8	65	13.8	17.9	12.0	0.234	6.8
50.365	1.8103	18.8	76	14.3	28.1	18.8	0.417	6.6
51.152	1.7843	10.3	71	15.2	47.1	31.6	0.660	7.2

Position (°)	D-spacing (Å)	Background Intensity (cps)	Intensity (cps)	Relative Intensity (%)	Area	Area (%)	FWHM (°)	P/N
K1L-9174-5								
21.239	4.1798	10.0	71	14.0	12.4	8.1	0.147	7.2
24.342	3.6536	15.2	43	6.4	5.9	3.9	0.153	4.2
26.993	3.3005	11.5	272	59.8	47.8	31.4	0.133	15.8
27.991	3.1851	10.5	27	3.8	2.9	1.9	0.128	3.2
31.164	2.8676	12.6	448	100.0	152.3	100.0	0.253	20.6
37.651	2.3872	9.5	83	16.9	22.0	14.4	0.216	8.1
39.832	2.2613	9.6	27	4.0	3.1	2.0	0.127	3.4
41.358	2.1813	8.8	118	25.1	47.5	31.2	0.370	10.1
42.779	2.1121	8.3	25	3.8	2.5	1.6	0.108	3.3
45.234	2.0030	9.7	74	14.8	21.8	14.3	0.245	7.5
50.499	1.8058	12.6	66	12.3	66.7	43.8	1.061	6.6
51.247	1.7812	11.5	88	17.6	62.9	41.3	0.699	8.2
54.357	1.6864	6.0	10	0.9	1.1	0.7	0.201	1.3
55.943	1.6423	6.6	9	0.6	3.9	2.6	1.366	0.8
59.172	1.5602	9.9	28	4.2	3.7	2.4	0.147	3.4
K1L-9214-5								
20.971	4.2327	8.6	62	11.9	16.6	17.2	0.224	6.8
23.198	3.8312	9.1	54	10.0	13.1	13.6	0.211	6.1
23.629	3.7622	9.1	45	8.0	9.6	10.0	0.194	5.3
24.141	3.6835	13.7	27	3.0	2.0	2.0	0.106	2.6
25.905	3.4366	16.6	36	4.3	2.8	2.9	0.104	3.2
26.768	3.3277	14.6	316	67.1	52.9	54.9	0.127	17.0
27.705	3.2173	15.5	60	9.9	9.7	10.0	0.157	5.7
29.543	3.0212	14.6	464	100.0	96.3	100.0	0.155	20.9
29.988	2.9774	16.9	55	8.5	6.9	7.1	0.130	5.1
30.995	2.8829	14.0	240	50.3	70.9	73.6	0.227	14.6
36.127	2.4843	13.3	69	12.4	9.9	10.3	0.129	6.7
37.436	2.4004	13.7	45	7.0	10.4	10.8	0.240	4.7
39.562	2.2761	9.1	108	22.0	22.0	22.8	0.161	9.5
41.201	2.1893	14.4	75	13.5	16.7	17.4	0.200	7.0
43.310	2.0874	11.3	71	13.3	19.7	20.4	0.238	7.1
44.962	2.0145	12.3	47	7.7	8.2	8.6	0.172	5.1
47.313	1.9197	18.3	40	4.8	4.0	4.1	0.132	3.4
47.642	1.9072	12.9	63	11.1	21.9	22.8	0.372	6.3
48.623	1.8710	11.9	81	15.4	24.0	24.9	0.251	7.7
50.740	1.7978	8.3	53	10.0	40.7	42.2	0.773	6.1
51.139	1.7847	8.3	54	10.2	38.4	39.9	0.714	6.2
53.110	1.7230	3.7	10	1.4	1.2	1.2	0.137	2.0
54.400	1.6852	5.0	10	1.1	0.9	0.9	0.126	1.6
57.531	1.6007	12.0	49	8.2	5.1	5.3	0.100	5.3

Position (°)	D-spacing (Å)	Background Intensity (cps)	Intensity (cps)	Relative Intensity (%)	Area	Area (%)	FWHM (°)	P/N
NV15-147TB								
24.264	3.6652	7.2	73	8.1	12.2	5.8	0.134	7.7
26.885	3.3135	7.3	22	1.8	1.5	0.7	0.088	3.1
31.071	2.8760	12.0	829	100.0	211.2	100.0	0.187	28.4
33.596	2.6654	8.4	52	5.3	12.7	6.0	0.211	6.0
35.469	2.5288	13.5	39	3.1	5.5	2.6	0.157	4.1
37.544	2.3937	8.5	92	10.2	20.8	9.8	0.179	8.7
41.292	2.1846	7.7	188	22.1	53.4	25.3	0.214	13.1
43.966	2.0578	8.4	35	3.3	5.1	2.4	0.140	4.5
45.064	2.0102	9.6	99	10.9	28.6	13.5	0.231	9.0
49.272	1.8479	14.6	36	2.6	4.8	2.3	0.162	3.6
50.449	1.8075	20.0	101	9.9	27.4	13.0	0.244	8.1
51.097	1.7861	16.1	138	14.9	52.2	24.7	0.364	10.4
55.727	1.6482	4.1	8	0.5	1.8	0.9	0.396	1.4
59.053	1.5630	10.4	28	2.2	4.4	2.1	0.182	3.3
NV15-149TB								
20.052	4.4246	22.6	81	31.8	40.8	98.7	0.594	6.5
21.187	4.1901	31.0	76	24.5	15.0	36.4	0.241	5.2
26.947	3.3061	38.3	222	100.0	41.3	100.0	0.163	12.3
50.410	1.8088	14.2	42	15.1	5.6	13.5	0.145	4.3
NV15-152TB								
23.402	3.7983	7.4	87	9.3	15.2	9.5	0.138	8.5
25.320	3.5147	7.2	10	0.3	1.5	0.9	0.449	0.9
29.758	2.9999	8.8	860	100.0	160.9	100.0	0.137	29.0
31.063	2.8767	7.9	136	15.0	24.4	15.2	0.138	11.0
33.711	2.6566	4.8	10	0.6	3.8	2.3	0.616	1.6
36.340	2.4702	7.2	106	11.6	21.0	13.1	0.154	9.6
37.521	2.3951	7.2	22	1.7	2.7	1.7	0.132	3.2
39.767	2.2648	6.7	144	16.1	35.9	22.3	0.189	11.4
41.211	2.1887	8.0	26	2.1	1.9	1.2	0.090	3.5
42.400	2.1301	6.2	10	0.4	1.6	1.0	0.362	1.2
42.965	2.1034	5.4	10	0.5	1.5	0.9	0.239	1.5
43.514	2.0781	5.4	131	14.8	32.8	20.4	0.189	11.0
47.468	1.9138	8.0	45	4.3	10.2	6.3	0.198	5.5
47.864	1.8989	10.8	128	13.8	37.7	23.4	0.232	10.4
48.934	1.8599	11.2	122	13.0	31.7	19.7	0.207	10.0
51.013	1.7888	8.9	22	1.5	3.0	1.9	0.166	2.8
53.401	1.7143	5.9	8	0.3	0.5	0.3	0.184	0.8
55.643	1.6505	3.5	9	0.6	2.2	1.4	0.338	1.8
56.955	1.6155	8.4	33	2.9	5.8	3.6	0.169	4.3
57.789	1.5942	7.6	49	4.9	12.4	7.7	0.216	5.9
NV15-154TB								
20.149	4.4034	17.2	82	32.4	41.9	88.9	0.549	7.2
21.166	4.1942	17.2	79	30.9	25.8	54.9	0.355	7.0
26.984	3.3016	31.1	231	100.0	47.1	100.0	0.170	13.1
28.058	3.1777	33.2	108	37.4	10.1	21.5	0.098	7.2
29.875	2.9884	32.6	69	18.2	7.6	16.2	0.151	4.4
50.452	1.8074	12.2	38	12.9	5.2	11.1	0.146	4.2

Position (°)	D-spacing (Å)	Background Intensity (cps)	Intensity (cps)	Relative Intensity (%)	Area	Area (%)	FWHM (°)	P/N
NV15-160TB								
22.312	3.9812	12.4	37	2.5	2.7	1.2	0.095	4.0
24.321	3.6567	7.9	71	6.3	14.1	6.2	0.162	7.5
31.202	2.8643	11.8	1010	100.0	229.3	100.0	0.166	31.4
33.789	2.6506	6.9	56	4.9	13.2	5.7	0.194	6.6
35.558	2.5227	7.3	56	4.9	15.2	6.6	0.225	6.5
37.614	2.3894	8.1	101	9.3	21.3	9.3	0.165	9.2
41.368	2.1808	7.2	272	26.5	71.4	31.1	0.195	16.1
44.056	2.0538	8.9	42	3.3	7.1	3.1	0.155	5.1
45.193	2.0047	6.8	149	14.2	41.4	18.0	0.210	11.7
49.503	1.8398	10.4	47	3.7	7.8	3.4	0.155	5.3
50.753	1.7974	13.5	132	11.9	39.8	17.3	0.242	10.3
51.300	1.7795	18.3	188	17.0	50.5	22.0	0.215	12.4
54.974	1.6690	5.3	10	0.5	1.1	0.5	0.174	1.5
59.146	1.5608	9.2	48	3.9	7.2	3.1	0.134	5.6
NV15-163TB								
21.837	4.0667	6.3	10	0.5	2.7	1.4	0.603	1.2
22.374	3.9704	6.7	26	2.4	3.9	2.0	0.144	3.8
24.409	3.6438	8.0	66	7.1	11.2	5.8	0.139	7.1
29.850	2.9908	12.9	42	3.6	4.9	2.5	0.121	4.5
31.297	2.8557	11.3	826	100.0	192.0	100.0	0.170	28.3
33.854	2.6456	7.6	47	4.8	8.4	4.4	0.155	5.7
35.684	2.5141	7.6	53	5.6	8.9	4.7	0.142	6.2
37.702	2.3840	7.2	93	10.5	18.7	9.7	0.157	8.9
41.461	2.1762	7.5	240	28.5	60.0	31.2	0.186	15.0
44.142	2.0500	8.1	50	5.1	7.5	3.9	0.130	5.9
45.264	2.0018	6.3	140	16.4	34.6	18.0	0.187	11.3
49.615	1.8359	12.2	44	3.9	6.3	3.3	0.143	4.8
50.806	1.7956	9.5	123	13.9	35.7	18.6	0.228	10.2
51.397	1.7764	20.0	172	18.7	40.8	21.2	0.194	11.6
59.170	1.5602	10.2	33	2.8	4.8	2.5	0.151	4.0
NV15-165TB								
22.170	4.0065	14.8	88	10.1	7.7	5.5	0.089	7.8
23.295	3.8154	13.1	80	9.3	18.9	13.5	0.204	7.5
26.884	3.3136	10.9	42	4.3	5.7	4.1	0.133	4.8
28.044	3.1792	18.4	43	3.4	8.0	5.7	0.235	3.8
29.663	3.0092	16.3	740	100.0	139.7	100.0	0.139	26.6
30.975	2.8847	19.8	49	4.0	5.0	3.6	0.125	4.2
31.657	2.8241	13.4	30	2.3	3.3	2.3	0.142	3.0
36.227	2.4776	12.4	94	11.3	20.3	14.5	0.180	8.4
39.669	2.2702	9.8	119	15.1	26.3	18.8	0.174	10.0
43.419	2.0824	7.4	109	14.0	26.5	19.0	0.188	9.7
47.464	1.9140	16.8	44	3.8	6.7	4.8	0.177	4.1
47.805	1.9011	22.9	113	12.5	23.8	17.0	0.190	8.5
48.794	1.8649	11.3	128	16.1	28.4	20.3	0.176	10.3
53.026	1.7256	6.3	10	0.5	1.5	1.0	0.334	1.2
57.658	1.5975	8.0	63	7.6	17.4	12.4	0.228	6.9

Position (°)	D-spacing (Å)	Background Intensity (cps)	Intensity (cps)	Relative Intensity (%)	Area	Area (%)	FWHM (°)	P/N
NV16-045TB								
21.149	4.1974	6.5	76	3.3	12.8	3.1	0.133	8.0
23.401	3.7984	6.7	118	5.3	22.3	5.4	0.145	10.2
26.936	3.3074	7.8	327	15.2	65.9	15.8	0.149	17.7
29.759	2.9997	7.7	2107	100.0	416.1	100.0	0.143	45.7
31.772	2.8141	7.3	35	1.3	6.4	1.5	0.168	4.7
36.341	2.4701	5.4	146	6.7	36.5	8.8	0.188	11.6
36.804	2.4401	9.0	30	1.0	3.1	0.7	0.107	3.8
39.791	2.2635	6.4	158	7.2	48.0	11.5	0.229	12.1
42.740	2.1139	6.6	19	0.6	1.7	0.4	0.097	2.9
43.543	2.0768	7.1	126	5.7	36.8	8.8	0.224	10.6
47.599	1.9088	13.0	63	2.4	20.8	5.0	0.354	6.3
47.857	1.8992	14.2	151	6.5	53.0	12.7	0.329	11.1
48.861	1.8625	17.6	164	7.0	42.3	10.2	0.209	11.4
50.367	1.8102	9.2	41	1.5	7.3	1.7	0.165	5.0
56.941	1.6159	9.0	28	0.9	5.6	1.3	0.211	3.6
57.706	1.5962	5.6	64	2.8	27.8	6.7	0.405	7.3
NV16-047TB								
21.149	4.1974	5.6	66	3.0	15.7	3.7	0.188	7.4
23.399	3.7988	5.9	102	4.7	23.2	5.5	0.174	9.5
26.914	3.3101	7.4	338	16.3	64.2	15.3	0.140	18.0
29.760	2.9997	8.3	2041	100.0	420.0	100.0	0.149	45.0
31.857	2.8068	10.1	38	1.4	5.1	1.2	0.131	4.5
33.033	2.7095	4.9	10	0.3	2.0	0.5	0.337	1.6
36.343	2.4700	7.2	111	5.1	30.5	7.3	0.212	9.9
36.806	2.4400	9.0	30	1.0	3.7	0.9	0.126	3.8
39.762	2.2651	6.3	166	7.9	51.2	12.2	0.232	12.4
42.724	2.1147	8.7	25	0.8	2.5	0.6	0.110	3.3
43.510	2.0783	7.4	153	7.2	35.2	8.4	0.175	11.8
47.466	1.9139	12.0	55	2.1	12.2	2.9	0.204	5.8
47.860	1.8990	16.1	142	6.2	47.9	11.4	0.323	10.6
48.862	1.8624	15.0	174	7.8	43.4	10.3	0.197	12.1
50.374	1.8100	13.1	34	1.0	2.8	0.7	0.097	3.6
53.051	1.7248	4.9	10	0.3	1.1	0.3	0.154	1.6
57.760	1.5949	7.4	72	3.2	28.3	6.7	0.372	7.6

Position (°)	D-spacing (Å)	Background Intensity (cps)	Intensity (cps)	Relative Intensity (%)	Area	Area (%)	FWHM (°)	P/N
NV16-049TB								
21.149	4.1974	7.4	72	3.0	10.8	2.5	0.121	7.6
22.369	3.9713	3.2	10	0.3	1.3	0.3	0.142	2.1
23.390	3.8001	6.9	134	5.9	23.9	5.6	0.136	11.0
26.915	3.3099	5.2	315	14.3	65.2	15.4	0.152	17.5
29.761	2.9996	6.4	2176	100.0	423.9	100.0	0.141	46.5
31.873	2.8055	9.1	32	1.1	4.9	1.2	0.154	4.1
32.904	2.7199	4.0	10	0.3	1.4	0.3	0.174	1.9
36.343	2.4700	5.1	123	5.4	32.4	7.6	0.199	10.6
36.819	2.4391	7.3	28	1.0	3.8	0.9	0.133	3.9
39.760	2.2652	6.9	177	7.8	49.5	11.7	0.210	12.8
43.545	2.0767	6.5	135	5.9	38.4	9.1	0.216	11.1
47.502	1.9125	6.8	71	3.0	26.5	6.2	0.351	7.6
47.866	1.8988	20.9	145	5.7	48.6	11.5	0.333	10.3
48.864	1.8623	10.4	162	7.0	49.3	11.6	0.235	11.9
50.363	1.8104	10.7	38	1.3	4.8	1.1	0.126	4.4
55.092	1.6657	7.5	20	0.6	1.4	0.3	0.093	2.8
56.866	1.6178	9.2	32	1.1	5.3	1.3	0.169	4.0
57.757	1.5950	6.7	75	3.1	26.4	6.2	0.329	7.9
NV16-051TB								
23.407	3.7975	19.3	120	11.7	16.6	8.1	0.119	9.2
26.912	3.3103	11.6	64	6.1	18.3	8.9	0.252	6.6
29.765	2.9991	10.7	873	100.0	204.7	100.0	0.172	29.2
36.352	2.4694	10.5	122	12.9	36.2	17.7	0.234	10.1
36.848	2.4373	11.5	27	1.8	3.4	1.7	0.159	3.0
39.769	2.2647	11.0	147	15.8	36.4	17.8	0.194	11.2
43.556	2.0762	10.3	125	13.3	34.3	16.7	0.216	10.3
47.552	1.9106	8.2	60	6.0	21.3	10.4	0.350	6.7
47.941	1.8960	27.9	137	12.7	33.6	16.4	0.222	9.3
48.936	1.8598	8.0	144	15.8	51.3	25.1	0.321	11.3
50.992	1.7895	8.3	10	0.2	0.7	0.3	0.342	0.5
57.892	1.5916	8.2	68	6.9	25.0	12.2	0.356	7.3

Position (°)	D-spacing (Å)	Background Intensity (cps)	Intensity (cps)	Relative Intensity (%)	Area	Area (%)	FWHM (°)	P/N
NV15-178DH								
21.137	4.1998	15.9	300	21.2	83.4	23.4	0.212	16.4
23.936	3.7147	15.8	47	2.3	10.6	3	0.246	4.5
24.290	3.6614	14.0	38	1.8	5.3	1.5	0.160	3.9
26.112	3.4098	16.5	37	1.5	4.6	1.3	0.163	3.4
26.897	3.3120	14.3	1354	100	356.7	100	0.192	36.4
28.125	3.1702	12.4	43	2.3	11.8	3.3	0.328	4.7
30.239	2.9532	13.6	33	1.4	4.1	1.1	0.151	3.4
31.147	2.8691	12.9	293	20.9	96.1	26.9	0.248	16.4
33.552	2.6688	11.4	27	1.2	4.0	1.1	0.184	3.0
36.763	2.4427	13.2	96	6.2	22.5	6.3	0.196	8.5
37.563	2.3925	16.8	51	2.6	6.4	1.8	0.134	4.8
39.702	2.2684	12.5	96	6.2	22.8	6.4	0.197	8.5
40.521	2.2244	15.6	57	3.1	8.2	2.3	0.144	5.5
41.340	2.1822	15.6	98	6.2	24.3	6.8	0.213	8.3
42.696	2.1160	12.6	69	4.2	16.9	4.7	0.216	6.8
45.136	2.0071	10.7	75	4.8	16.0	4.5	0.180	7.4
46.042	1.9697	13.7	48	2.6	9.3	2.6	0.196	4.9
50.385	1.8097	9.1	176	12.5	100.0	28	0.509	12.6
51.199	1.7828	11.5	70	4.4	43.3	12.1	0.629	7.0
55.072	1.6662	10.0	47	2.8	12.7	3.5	0.247	5.4
NV15-180DH								
21.263	4.1753	17.2	80	23.4	65.9	92.0	0.892	7.0
21.896	4.0559	17.2	62	16.7	27.3	38.1	0.518	5.7
22.096	4.0197	17.2	66	18.2	71.6	100.0	1.246	6.0
22.797	3.8977	17.2	36	7.0	5.7	7.9	0.218	3.1
23.887	3.7221	11.0	63	19.3	26.3	36.7	0.429	6.6
26.139	3.4064	11.8	34	8.2	3.8	5.3	0.125	3.8
26.959	3.3046	12.4	114	37.8	56.0	78.2	0.468	9.5
27.496	3.2413	12.4	47	12.9	6.5	9.1	0.135	5.1
28.040	3.1796	12.6	52	14.7	12.4	17.3	0.227	5.5
29.766	2.9990	14.2	230	80.3	42.4	59.3	0.142	14.2
31.148	2.8691	14.2	283	100.0	65.7	91.8	0.177	16.0
33.709	2.6567	10.6	25	5.3	3.3	4.5	0.163	2.9
36.350	2.4695	16.6	54	13.9	9.1	12.7	0.176	5.1
37.590	2.3909	17.0	36	7.1	3.3	4.6	0.124	3.2
39.776	2.2643	11.1	44	12.2	7.7	10.7	0.168	5.0
41.341	2.1822	11.1	84	27.1	19.9	27.9	0.198	8.0
43.525	2.0776	12.6	48	13.2	5.2	7.3	0.106	5.1
45.146	2.0067	12.1	48	13.4	8.5	11.9	0.171	5.2
48.896	1.8612	11.9	38	9.7	5.2	7.3	0.145	4.2
50.551	1.8041	14.0	34	7.4	6.7	9.4	0.242	3.4
51.195	1.7829	17.6	55	13.9	13.6	19.0	0.309	5.0
57.750	1.5951	11.5	26	5.4	3.4	4.7	0.168	2.8

Position (°)	D-spacing (Å)	Background Intensity (cps)	Intensity (cps)	Relative Intensity (%)	Area	Area (%)	FWHM (°)	P/N
NV15-185DH								
20.802	4.2667	14.4	65	7.8	38.5	18.8	0.646	6.3
21.157	4.1958	22.4	196	26.7	98.1	47.9	0.480	12.4
22.049	4.0282	33.9	75	6.3	25.0	12.2	0.516	4.7
23.857	3.7268	16.0	80	9.8	25.2	12.3	0.335	7.2
26.056	3.4170	15.6	44	4.4	8.1	4.0	0.207	4.3
26.912	3.3103	15.6	666	100.0	204.8	100.0	0.227	25.2
28.048	3.1787	12.4	72	9.2	23.0	11.3	0.329	7.0
30.215	2.9555	15.6	55	6.1	9.6	4.7	0.177	5.3
31.188	2.8655	13.2	167	23.6	52.7	25.7	0.248	11.9
32.811	2.7274	11.4	31	3.0	4.5	2.2	0.165	3.5
36.804	2.4401	15.2	59	6.7	11.4	5.6	0.189	5.7
39.750	2.2658	15.0	46	4.8	6.1	3.0	0.141	4.6
41.356	2.1814	14.7	49	5.3	8.0	3.9	0.167	4.9
42.742	2.1138	14.9	53	5.9	8.2	4.0	0.155	5.2
50.375	1.8100	10.6	81	10.8	48.3	23.6	0.583	7.8
51.146	1.7845	10.6	37	4.1	13.8	6.7	0.445	4.3
NV15-190DH								
20.880	4.2510	26.0	51	3.6	6.7	4.3	0.194	3.5
22.300	3.9834	15.8	77	8.9	72.2	45.9	1.003	7.0
24.367	3.6499	19.0	55	5.2	5.6	3.6	0.112	4.9
29.815	2.9942	12.0	294	41.1	38.4	24.4	0.098	16.4
31.253	2.8597	11.0	697	100.0	157.2	100.0	0.166	26.0
33.847	2.6462	10.7	36	3.7	6.6	4.2	0.189	4.2
35.607	2.5193	20.2	47	3.9	4.9	3.1	0.132	3.9
37.650	2.3872	9.1	74	9.5	18.2	11.6	0.203	7.5
41.444	2.1770	9.3	197	27.4	48.4	30.8	0.186	13.4
45.244	2.0026	10.7	100	13.0	24.3	15.5	0.197	8.9
49.591	1.8367	10.8	32	3.1	6.4	4.1	0.217	3.8
50.807	1.7956	11.6	88	11.1	34.5	21.9	0.383	8.1
51.351	1.7779	8.4	109	14.7	50.1	31.9	0.423	9.6
54.422	1.6846	7.3	10	0.4	1.4	0.9	0.428	0.9
59.165	1.5603	14.6	35	3.0	3.6	2.3	0.127	3.4
NV15-195DH								
22.045	4.0289	46.4	84	5.2	16.0	8.9	0.361	4.1
22.353	3.9741	17.6	69	7.2	52.8	29.4	0.873	6.2
24.425	3.6414	11.9	52	5.6	7.4	4.1	0.133	5.6
31.299	2.8556	11.0	729	100.0	179.7	100.0	0.181	26.6
33.860	2.6452	9.4	46	5.1	9.4	5.2	0.185	5.4
35.666	2.5153	14.6	53	5.4	7.1	4.0	0.134	5.3
37.707	2.3837	10.8	74	8.8	16.9	9.4	0.193	7.3
41.462	2.1761	8.6	210	28.1	54.7	30.4	0.196	13.9
45.259	2.0020	9.8	113	14.4	27.7	15.4	0.194	9.7
49.697	1.8331	11.3	38	3.7	6.8	3.8	0.184	4.3
50.893	1.7928	21.3	104	11.5	25.3	14.1	0.221	8.1
51.399	1.7763	9.4	117	15.0	47.7	26.5	0.377	9.9
59.289	1.5574	13.2	27	1.9	2.9	1.6	0.153	2.7

Position (°)	D-spacing (Å)	Background Intensity (cps)	Intensity (cps)	Relative Intensity (%)	Area	Area (%)	FWHM (°)	P/N
NV15-186DH								
23.134	3.8416	6.9	10	0.6	3.7	2.5	1.011	1.0
24.353	3.6520	6.7	52	8.8	10.5	7.0	0.168	6.3
26.977	3.3024	11.1	34	4.4	4.5	3.0	0.141	3.9
29.705	3.0051	12.6	28	3.0	3.3	2.2	0.155	2.9
31.200	2.8644	9.8	527	100.0	150.4	100.0	0.210	22.5
33.698	2.6575	11.6	29	3.4	2.8	1.9	0.116	3.2
35.504	2.5264	12.5	33	4.0	4.7	3.1	0.166	3.6
37.598	2.3903	8.0	64	10.8	23.1	15.4	0.351	7.0
41.353	2.1816	8.1	165	30.3	52.4	34.8	0.241	12.2
45.146	2.0067	7.9	103	18.4	30.5	20.3	0.232	9.4
46.809	1.9392	7.2	10	0.5	0.5	0.4	0.138	0.9
48.221	1.8857	7.2	10	0.5	1.3	0.9	0.411	0.9
50.654	1.8007	13.4	99	16.5	45.2	30.1	0.449	8.6
51.291	1.7798	11.9	133	23.4	51.0	33.9	0.358	10.5
59.055	1.5630	10.9	42	6.0	6.5	4.3	0.152	4.8
NV15-197DH								
24.380	3.6481	7.6	40	5.9	7.9	5.1	0.176	5.1
26.983	3.3018	8.6	37	5.2	5.5	3.6	0.141	4.7
29.845	2.9913	11.9	38	4.8	3.8	2.5	0.106	4.2
31.199	2.8645	8.6	554	100.0	153.9	100.0	0.204	23.2
33.713	2.6564	9.5	29	3.6	5.4	3.5	0.199	3.6
35.585	2.5208	10.3	41	5.6	6.8	4.4	0.159	4.8
37.610	2.3897	9.6	59	9.1	16.7	10.9	0.245	6.4
41.391	2.1797	6.8	168	29.6	52.1	33.9	0.234	12.4
45.152	2.0065	8.9	94	15.6	28.8	18.7	0.244	8.8
50.652	1.8007	10.4	84	13.5	55.7	36.2	0.644	8.0
51.256	1.7809	10.3	105	17.4	58.8	38.2	0.528	9.2

Position (°)	D-spacing (Å)	Background Intensity (cps)	Intensity (cps)	Relative Intensity (%)	Area	Area (%)	FWHM (°)	P/N
NV15-204DH								
22.264	3.9898	14.7	32	1.5	2.4	0.8	0.100	3.1
24.292	3.6610	13.0	95	6.9	17.1	6.0	0.151	8.4
26.907	3.3108	19.2	89	5.9	11.8	4.1	0.122	7.4
29.705	3.0051	12.6	48	3.0	7.9	2.8	0.161	5.1
31.151	2.8688	13.2	1202	100.0	286.5	100.0	0.174	34.3
31.821	2.8099	10.8	80	5.8	21.8	7.6	0.227	7.7
33.688	2.6584	11.8	58	3.9	11.9	4.2	0.186	6.1
35.500	2.5267	13.6	64	4.2	20.0	7.0	0.338	6.3
37.626	2.3886	12.8	114	8.5	29.7	10.4	0.212	9.5
41.313	2.1836	11.6	324	26.3	87.7	30.6	0.203	17.4
44.003	2.0561	18.1	55	3.1	6.3	2.2	0.124	5.0
45.146	2.0067	12.6	179	14.0	45.5	15.9	0.197	12.4
47.477	1.9135	10.4	72	5.2	12.7	4.4	0.148	7.3
47.928	1.8965	11.0	31	1.7	3.2	1.1	0.116	3.6
48.872	1.8621	23.9	239	18.1	34.2	12.0	0.115	13.9
49.420	1.8427	16.2	55	3.3	11.1	3.9	0.207	5.2
50.649	1.8008	24.1	147	10.3	41.1	14.3	0.242	10.1
51.160	1.7840	57.9	190	11.1	34.6	12.1	0.189	9.6
59.059	1.5629	13.8	52	3.2	9.3	3.3	0.177	5.3
59.955	1.5416	10.1	99	7.5	32.0	11.2	0.306	8.9
63.589	1.4620	11.8	62	4.2	17.0	5.9	0.245	6.4
67.514	1.3862	11.9	64	4.4	18.5	6.5	0.302	6.5
K1L-9219-5								
20.941	4.2388	8.4	135	19.3	23.0	10.3	0.131	10.9
22.091	4.0206	8.4	21	1.9	2.8	1.3	0.162	2.8
24.067	3.6948	10.4	58	7.2	11.3	5.1	0.172	6.3
26.740	3.3312	8.0	615	92.3	94.6	42.3	0.113	24.5
29.507	3.0248	10.0	156	22.2	25.2	11.2	0.124	11.7
30.951	2.8868	8.4	666	100.0	223.8	100.0	0.246	25.5
35.304	2.5403	15.7	38	3.4	4.9	2.2	0.160	3.6
36.650	2.4500	11.4	65	8.1	7.3	3.3	0.098	6.6
37.403	2.4024	10.3	91	12.3	23.1	10.3	0.207	8.5
39.555	2.2765	7.0	57	7.6	11.1	5.0	0.160	6.6
41.153	2.1917	9.2	194	28.1	68.1	30.4	0.313	13.3
42.529	2.1239	10.2	26	2.4	2.2	1.0	0.100	3.1
44.951	2.0149	9.7	120	16.8	34.5	15.4	0.226	10.1
45.869	1.9768	9.1	40	4.7	4.9	2.2	0.114	4.9
48.649	1.8701	8.8	39	4.6	7.4	3.3	0.176	4.8
50.361	1.8105	13.8	87	11.1	49.5	22.1	0.574	7.8
51.048	1.7877	10.5	117	16.2	87.9	39.3	0.701	9.8
55.991	1.6410	6.8	10	0.5	0.6	0.3	0.146	1.0

Position (°)	D-spacing (Å)	Background Intensity (cps)	Intensity (cps)	Relative Intensity (%)	Area	Area (%)	FWHM (°)	P/N
NV15-202DH								
20.078	4.4189	10.8	28	3.3	3.6	2.5	0.152	3.3
21.171	4.1931	14.1	172	30.2	24.6	16.8	0.113	12.0
23.798	3.7360	13.4	60	8.9	8.3	5.7	0.128	6.0
24.352	3.6522	12.6	43	5.8	5.3	3.6	0.127	4.6
26.962	3.3042	17.0	333	60.4	75.1	51.3	0.172	17.3
27.993	3.1848	13.0	71	11.1	15.4	10.5	0.191	6.9
31.216	2.8630	8.4	532	100.0	146.3	100.0	0.202	22.7
33.835	2.6471	7.5	35	5.2	7.5	5.1	0.196	4.6
35.631	2.5177	11.6	40	5.4	8.2	5.6	0.209	4.5
37.680	2.3854	11.1	77	12.6	13.6	9.3	0.149	7.5
41.407	2.1789	9.6	157	28.1	45.1	30.9	0.221	11.8
44.118	2.0511	11.8	32	3.9	4.1	2.8	0.146	3.6
45.215	2.0038	11.4	85	14.0	18.1	12.4	0.178	8.0
50.501	1.8057	24.9	54	5.6	3.7	2.5	0.092	4.0
50.754	1.7973	12.4	74	11.8	41.5	28.4	0.573	7.2
51.305	1.7793	11.7	107	18.2	58.1	39.7	0.518	9.2
54.315	1.6876	7.4	10	0.5	0.8	0.6	0.233	0.8
NV15-206DH								
24.326	3.6560	9.1	60	5.4	9.3	4.3	0.132	6.6
26.895	3.3123	9.9	30	2.1	4.7	2.2	0.167	3.7
31.204	2.8641	12.8	957	100.0	215.6	100.0	0.165	30.5
33.763	2.6526	8.4	56	5.0	10.9	5.1	0.165	6.4
35.531	2.5245	8.6	58	5.2	13.2	6.1	0.193	6.5
37.616	2.3893	7.5	108	10.6	26.3	12.2	0.189	9.7
41.398	2.1793	7.5	275	28.3	70.4	32.7	0.190	16.1
44.090	2.0523	9.3	45	3.8	8.2	3.8	0.167	5.3
45.195	2.0047	7.1	160	16.2	36.0	16.7	0.170	12.1
49.539	1.8385	16.2	54	4.0	5.0	2.3	0.096	5.1
50.751	1.7974	19.3	173	16.3	39.6	18.4	0.186	11.7
51.301	1.7795	21.2	163	15.0	41.0	19.0	0.209	11.1
59.141	1.5609	9.6	31	2.3	5.4	2.5	0.181	3.8
NV15-210DH								
21.237	4.1802	13.0	165	23.3	45.9	21.5	0.218	11.8
22.866	3.8860	11.2	30	2.9	2.6	1.2	0.101	3.4
23.887	3.7223	13.6	58	6.8	8.0	3.8	0.131	5.8
26.085	3.4134	16.3	53	5.6	4.6	2.1	0.090	5.0
26.962	3.3043	14.6	668	100.0	213.6	100.0	0.236	25.3
28.004	3.1836	11.0	68	8.7	17.8	8.3	0.225	6.9
29.831	2.9926	11.8	133	18.5	28.9	13.5	0.172	10.5
30.200	2.9569	10.4	55	6.8	7.9	3.7	0.127	6.0
31.146	2.8692	11.0	31	3.1	6.6	3.1	0.237	3.6
32.779	2.7299	7.7	25	2.7	3.9	1.8	0.164	3.5
36.937	2.4316	19.8	48	4.3	5.6	2.6	0.143	4.1
39.804	2.2628	8.9	88	12.1	23.0	10.8	0.210	8.4
42.750	2.1135	12.0	44	4.9	8.9	4.2	0.201	4.8
43.582	2.0750	8.5	63	8.3	15.4	7.2	0.204	6.9
46.107	1.9671	9.8	33	3.6	6.5	3.0	0.202	4.0
47.953	1.8956	10.2	30	3.0	5.0	2.3	0.181	3.6
48.968	1.8587	9.4	50	6.2	9.0	4.2	0.159	5.7
50.372	1.8101	9.7	71	9.4	29.8	13.9	0.413	7.3

Position (°)	D-spacing (Å)	Background Intensity (cps)	Intensity (cps)	Relative Intensity (%)	Area	Area (%)	FWHM (°)	P/N
NV15-216DH								
21.192	4.1891	8.5	60	7.9	15.3	8.7	0.215	6.7
24.347	3.6530	9.5	56	7.1	9.0	5.1	0.140	6.2
26.938	3.3072	15.2	205	29.1	55.5	31.4	0.211	13.3
31.247	2.8602	10.7	662	100.0	176.7	100.0	0.196	25.3
33.774	2.6517	10.3	38	4.3	7.7	4.3	0.200	4.5
37.656	2.3868	9.8	81	10.9	17.3	9.8	0.176	7.9
41.414	2.1785	9.1	164	23.8	47.6	26.9	0.222	12.1
45.206	2.0042	10.2	96	13.2	23.3	13.2	0.196	8.8
49.511	1.8395	10.4	32	3.3	6.0	3.4	0.201	3.8
50.808	1.7956	30.9	122	14.0	22.0	12.5	0.175	8.2
51.362	1.7775	43.5	126	12.7	21.2	12.0	0.186	7.3
59.153	1.5606	11.3	27	2.4	3.8	2.1	0.174	3.0
NV15-220DH								
10.904	8.1072	78.6	107	2.1	3.2	1.2	0.095	2.7
21.185	4.1905	6.6	52	3.4	6.5	2.5	0.104	6.3
22.356	3.9734	9.6	33	1.7	2.7	1.0	0.096	4.1
24.398	3.6454	7.3	77	5.2	8.7	3.4	0.090	7.9
26.960	3.3045	6.1	188	13.5	29.0	11.3	0.115	13.3
31.305	2.8550	5.3	1348	100.0	256.1	100.0	0.138	36.6
33.890	2.6429	8.5	47	2.9	7.3	2.8	0.136	5.6
35.656	2.5160	6.1	69	4.7	13.1	5.1	0.150	7.6
37.709	2.3836	5.5	154	11.1	29.8	11.6	0.145	12.0
41.467	2.1759	5.9	292	21.3	67.4	26.3	0.170	16.7
42.747	2.1136	4.5	14	0.7	1.8	0.7	0.141	2.5
44.153	2.0495	5.8	50	3.3	11.0	4.3	0.180	6.2
45.266	2.0017	8.0	169	12.0	33.0	12.9	0.148	12.4
49.611	1.8360	6.0	53	3.5	9.2	3.6	0.141	6.5
50.867	1.7936	40.1	126	6.4	18.0	7.0	0.151	7.7
51.410	1.7759	8.5	216	15.5	65.0	25.4	0.226	14.1
59.201	1.5595	7.0	42	2.6	6.5	2.5	0.134	5.4
NV15-225DH								
21.207	4.1862	6.4	35	2.1	4.8	1.8	0.121	4.8
22.360	3.9728	6.8	32	1.8	4.6	1.7	0.132	4.5
24.397	3.6455	4.5	70	4.8	14.5	5.3	0.160	7.8
26.960	3.3045	4.4	126	8.9	21.5	7.9	0.128	10.8
31.306	2.8550	5.9	1372	100.0	271.3	100.0	0.143	36.9
33.870	2.6444	5.4	69	4.7	12.4	4.6	0.141	7.7
35.683	2.5141	5.4	63	4.2	14.2	5.2	0.178	7.3
37.707	2.3837	6.2	139	9.7	22.4	8.3	0.122	11.3
41.465	2.1759	7.8	339	24.2	74.3	27.4	0.162	18.0
44.113	2.0513	6.5	55	3.6	8.6	3.2	0.128	6.5
45.265	2.0017	6.6	180	12.7	40.3	14.9	0.168	12.9
49.620	1.8357	7.7	42	2.5	6.9	2.5	0.145	5.3
50.864	1.7937	13.4	161	10.8	41.1	15.2	0.201	11.6
51.405	1.7761	30.7	224	14.2	48.3	17.8	0.181	12.9
59.210	1.5592	6.1	50	3.2	8.5	3.1	0.140	6.2

Position (°)	D-spacing (Å)	Background Intensity (cps)	Intensity (cps)	Relative Intensity (%)	Area	Area (%)	FWHM (°)	P/N
NV15-232DH								
21.128	4.2017	7.2	28	1.4	3.4	1.2	0.119	3.9
22.302	3.9829	7.0	51	3.0	7.9	2.8	0.130	6.2
24.354	3.6519	7.4	79	4.9	14.2	5.1	0.144	8.1
26.900	3.3117	6.5	93	5.9	19.2	6.8	0.160	9.0
31.241	2.8607	7.7	1473	100.0	281.7	100.0	0.139	38.2
33.853	2.6457	6.8	67	4.1	14.6	5.2	0.175	7.3
35.617	2.5187	7.2	90	5.7	17.9	6.4	0.156	8.7
37.645	2.3875	6.1	139	9.1	29.1	10.3	0.158	11.3
39.708	2.2681	7.3	21	0.9	3.1	1.1	0.164	3.0
41.411	2.1787	7.0	470	31.6	94.2	33.4	0.147	21.4
44.070	2.0532	8.8	83	5.1	14.4	5.1	0.141	8.1
45.213	2.0039	9.9	211	13.7	48.7	17.3	0.175	13.8
49.553	1.8381	7.3	70	4.3	12.0	4.3	0.139	7.5
50.847	1.7943	17.8	203	12.6	49.3	17.5	0.192	13.0
51.357	1.7777	28.9	258	15.6	57.5	20.4	0.181	14.3
53.728	1.7047	3.6	10	0.4	1.8	0.6	0.200	2.0
59.189	1.5597	7.3	53	3.1	12.8	4.6	0.203	6.3
60.069	1.5390	9.8	116	7.2	28.2	10.0	0.192	9.9
63.703	1.4597	7.3	85	5.3	22.1	7.8	0.206	8.4
64.753	1.4385	9.9	56	3.1	6.1	2.2	0.096	6.2
65.411	1.4256	18.0	55	2.5	6.3	2.2	0.122	5.0
67.652	1.3838	5.5	101	6.5	34.9	12.4	0.310	9.5
NV15-234DH								
23.244	3.8236	6.0	101	8.4	20.5	8.8	0.156	9.5
26.781	3.3262	9.0	38	2.6	6.6	2.8	0.163	4.7
29.570	3.0185	5.8	1131	100.0	232.6	100.0	0.149	33.5
36.152	2.4826	5.4	116	9.8	22.2	9.5	0.145	10.3
39.604	2.2738	5.8	169	14.5	46.4	20.0	0.206	12.6
43.349	2.0857	4.7	119	10.2	32.0	13.7	0.202	10.5
45.116	2.0080	4.5	9	0.4	0.8	0.4	0.132	1.5
47.273	1.9212	9.2	53	3.9	14.1	6.0	0.232	6.0
47.706	1.9048	21.5	144	10.9	33.2	14.3	0.196	10.2
48.701	1.8682	9.7	173	14.5	41.5	17.8	0.184	12.4
51.834	1.7624	4.1	9	0.4	2.1	0.9	0.355	1.6
53.403	1.7143	3.3	10	0.6	3.7	1.6	0.471	2.1
54.386	1.6856	3.7	8	0.4	0.9	0.4	0.152	1.5
56.719	1.6217	10.0	32	2.0	3.6	1.5	0.118	3.9
57.563	1.5999	4.7	84	7.0	27.3	11.7	0.249	8.7

Position (°)	D-spacing (Å)	Background Intensity (cps)	Intensity (cps)	Relative Intensity (%)	Area	Area (%)	FWHM (°)	P/N
NV15-235DH								
22.278	3.9872	5.2	10	0.4	0.5	0.3	0.098	1.5
23.403	3.7981	3.5	94	8.3	21.1	10.0	0.169	9.3
26.112	3.4098	5.1	9	0.4	1.7	0.8	0.377	1.3
29.761	2.9996	5.2	1097	100.0	210.8	100.0	0.140	33.0
31.796	2.8120	11.5	28	1.5	2.4	1.1	0.105	3.1
34.289	2.6131	4.1	8	0.4	1.9	0.9	0.403	1.4
36.351	2.4695	4.9	142	12.6	22.9	10.9	0.121	11.5
39.797	2.2632	3.9	156	13.9	38.4	18.2	0.182	12.2
41.799	2.1593	5.5	8	0.2	1.8	0.9	0.620	0.9
43.548	2.0766	5.5	412	37.2	70.2	33.3	0.125	20.0
47.465	1.9139	9.4	57	4.4	14.5	6.9	0.220	6.3
47.863	1.8990	10.9	142	12.0	44.5	21.1	0.245	11.0
48.864	1.8623	9.6	170	14.7	39.5	18.7	0.178	12.3
51.251	1.7811	4.2	9	0.4	2.4	1.1	0.422	1.6
56.942	1.6158	6.2	33	2.5	4.8	2.3	0.130	4.7
57.794	1.5940	4.5	77	6.6	24.9	11.8	0.249	8.3
59.043	1.5633	3.9	7	0.3	0.6	0.3	0.139	1.2
59.321	1.5566	3.9	9	0.5	0.6	0.3	0.086	1.7
NV15-238DH								
21.181	4.1912	7.0	102	7.3	14.0	5.5	0.106	9.4
22.347	3.9751	6.1	34	2.1	4.2	1.7	0.109	4.8
24.393	3.6461	6.6	71	4.9	9.5	3.8	0.107	7.6
26.957	3.3048	7.5	293	21.8	52.8	20.8	0.134	16.7
31.294	2.8560	7.7	1318	100.0	254.0	100.0	0.140	36.1
33.901	2.6421	5.4	50	3.4	10.9	4.3	0.177	6.3
35.674	2.5148	8.2	60	4.0	10.0	3.9	0.139	6.7
36.872	2.4357	6.4	31	1.9	4.0	1.6	0.119	4.4
37.701	2.3841	4.8	97	7.0	19.8	7.8	0.155	9.4
39.782	2.2640	5.2	22	1.3	2.9	1.1	0.123	3.6
41.458	2.1763	7.9	261	19.3	54.7	21.5	0.156	15.7
44.112	2.0513	10.0	40	2.3	6.5	2.6	0.157	4.7
45.254	2.0022	6.3	146	10.7	29.6	11.6	0.153	11.6
49.599	1.8365	7.7	51	3.3	8.4	3.3	0.141	6.1
50.419	1.8085	8.4	81	5.5	20.6	8.1	0.205	8.1
50.865	1.7937	32.3	142	8.4	28.3	11.1	0.186	9.2
51.406	1.7761	48.4	186	10.5	28.1	11.0	0.147	10.1
59.196	1.5596	8.2	43	2.7	6.1	2.4	0.126	5.3

Position (°)	D-spacing (Å)	Background Intensity (cps)	Intensity (cps)	Relative Intensity (%)	Area	Area (%)	FWHM (°)	P/N
NV15-227DH								
21.144	4.1984	8.4	68	2.9	9.6	2.4	0.116	7.2
23.405	3.7978	6.3	111	5.1	25.0	6.2	0.173	9.9
26.933	3.3077	5.9	327	15.7	70.2	17.3	0.158	17.8
29.760	2.9997	9.3	2052	100.0	406.0	100.0	0.144	45.1
31.855	2.8070	8.6	36	1.3	5.8	1.4	0.152	4.6
36.348	2.4697	5.4	112	5.2	31.6	7.8	0.215	10.1
36.842	2.4377	5.4	30	1.2	5.4	1.3	0.158	4.5
39.762	2.2651	6.7	163	7.7	51.8	12.8	0.239	12.2
43.541	2.0769	7.5	130	6.0	34.6	8.5	0.204	10.7
47.507	1.9124	13.4	62	2.4	17.3	4.3	0.302	6.2
47.897	1.8977	28.8	155	6.2	35.5	8.7	0.203	10.1
48.861	1.8625	14.8	164	7.3	44.9	11.1	0.217	11.7
50.344	1.8110	7.4	40	1.6	6.9	1.7	0.153	5.2
52.842	1.7311	3.1	9	0.3	2.3	0.6	0.337	2.0
57.716	1.5960	5.5	69	3.1	29.6	7.3	0.396	7.6
NV15-182DH								
23.412	3.7966	16.2	99	10.1	16.0	8.0	0.140	8.3
26.876	3.3147	11.5	63	6.3	18.1	9.0	0.254	6.5
29.792	2.9965	9.9	829	100.0	201.0	100.0	0.177	28.5
31.813	2.8106	12.3	36	2.9	3.6	1.8	0.110	3.9
36.351	2.4695	13.1	125	13.7	30.1	15.0	0.195	10.0
36.846	2.4374	14.7	37	2.7	2.4	1.2	0.091	3.7
39.773	2.2645	12.2	156	17.6	36.5	18.2	0.184	11.5
43.550	2.0765	9.0	138	15.7	35.6	17.7	0.200	11.0
47.506	1.9124	9.8	60	6.1	20.6	10.2	0.349	6.5
47.944	1.8959	23.6	142	14.5	43.1	21.5	0.310	9.9
48.901	1.8611	12.4	151	16.9	42.3	21.0	0.220	11.3
57.801	1.5939	8.5	57	5.9	24.6	12.2	0.430	6.4
NV14-224DH								
21.150	4.1972	8.2	87	3.2	17.4	3.4	0.160	8.4
23.396	3.7992	7.3	125	4.7	28.4	5.5	0.174	10.5
26.935	3.3075	8.4	389	15.3	78.9	15.2	0.150	19.3
29.759	2.9997	10.2	2503	100.0	518.4	100.0	0.150	49.8
31.823	2.8097	10.0	49	1.6	8.2	1.6	0.151	5.6
36.315	2.4718	8.3	141	5.3	42.8	8.3	0.233	11.2
36.843	2.4376	8.8	40	1.3	7.2	1.4	0.166	4.9
39.792	2.2635	6.8	223	8.7	62.7	12.1	0.210	14.5
42.739	2.1140	10.2	27	0.7	3.5	0.7	0.151	3.2
43.511	2.0782	7.7	166	6.4	48.9	9.4	0.223	12.3
47.468	1.9138	8.2	70	2.5	25.5	4.9	0.350	7.4
47.860	1.8991	28.0	173	5.8	54.4	10.5	0.319	11.0
48.864	1.8624	9.2	213	8.2	66.8	12.9	0.237	14.0
50.373	1.8100	11.6	41	1.2	7.7	1.5	0.190	4.6
57.761	1.5949	9.1	84	3.0	40.5	7.8	0.460	8.2
60.185	1.5363	9.4	29	0.8	5.1	1.0	0.189	3.6
61.098	1.5155	9.8	56	1.9	36.6	7.1	0.672	6.2
61.302	1.5110	9.8	45	1.4	23.1	4.5	0.557	5.3
64.967	1.4343	12.4	48	1.4	11.7	2.2	0.236	5.1
65.997	1.4144	11.2	46	1.4	9.1	1.7	0.188	5.1

Position (°)	D-spacing (Å)	Background Intensity (cps)	Intensity (cps)	Relative Intensity (%)	Area	Area (%)	FWHM (°)	P/N
NV15-239DH								
21.187	4.1901	9.9	142	11.1	22.3	9.6	0.122	11.1
22.366	3.9718	8.2	33	2.1	3.1	1.3	0.091	4.3
24.404	3.6445	6.9	55	4.1	8.4	3.6	0.126	6.5
26.953	3.3053	8.4	664	55.3	117.4	50.6	0.129	25.4
31.307	2.8548	7.5	1193	100.0	232.2	100.0	0.142	34.3
33.897	2.6424	5.9	72	5.6	11.9	5.1	0.130	7.8
35.696	2.5132	10.1	53	3.6	9.1	3.9	0.154	5.9
36.876	2.4355	8.1	51	3.6	7.6	3.3	0.128	6.0
37.710	2.3836	7.5	83	6.4	12.6	5.4	0.121	8.3
39.789	2.2636	5.3	45	3.3	7.7	3.3	0.140	5.9
40.636	2.2184	6.5	28	1.8	4.5	1.9	0.151	4.1
41.493	2.1745	5.7	212	17.4	46.2	19.9	0.162	14.2
42.754	2.1133	7.1	35	2.4	5.8	2.5	0.150	4.7
44.151	2.0496	8.0	38	2.5	5.3	2.3	0.127	4.9
45.298	2.0003	8.5	145	11.5	29.9	12.9	0.158	11.3
49.603	1.8363	9.0	32	1.9	4.3	1.9	0.136	4.1
50.458	1.8072	8.8	93	7.1	16.1	6.9	0.138	8.7
50.918	1.7920	32.8	158	10.6	23.2	10.0	0.134	10.0
51.447	1.7747	32.6	166	11.3	27.6	11.9	0.150	10.4
55.179	1.6632	8.8	24	1.3	2.8	1.2	0.133	3.1
NV16-037RM								
12.650	6.9922	51.7	169	5.7	35.9	8.4	0.221	9.0
20.241	4.3836	11.4	57	2.2	13.0	3.0	0.206	6.0
20.657	4.2962	10.4	58	2.3	27.4	6.4	0.489	6.3
21.154	4.1965	15.1	392	18.4	106.2	24.9	0.204	19.0
21.581	4.1145	26.2	50	1.2	3.9	0.9	0.117	3.4
25.188	3.5328	16.0	83	3.3	16.4	3.8	0.176	7.4
26.942	3.3066	16.4	2064	100.0	427.4	100.0	0.151	45.1
35.306	2.5401	14.5	39	1.2	6.0	1.4	0.178	3.9
36.816	2.4393	14.4	135	5.9	27.3	6.4	0.164	10.4
38.877	2.3146	17.0	46	1.4	7.1	1.7	0.177	4.3
39.753	2.2656	21.8	141	5.8	21.7	5.1	0.131	10.0
40.594	2.2206	14.0	55	2.0	9.0	2.1	0.158	5.5
42.708	2.1154	8.7	95	4.2	23.9	5.6	0.200	8.9
46.092	1.9677	10.3	61	2.5	18.1	4.2	0.304	6.5
50.399	1.8092	9.3	201	9.4	58.7	13.7	0.221	13.5
55.114	1.6650	10.0	68	2.8	27.5	6.4	0.403	7.0
55.554	1.6529	20.6	42	1.0	4.9	1.1	0.165	3.3

Position (°)	D-spacing (Å)	Background Intensity (cps)	Intensity (cps)	Relative Intensity (%)	Area	Area (%)	FWHM (°)	P/N
NV15-242RM								
21.152	4.1968	9.7	85	7.4	21.8	10.0	0.209	8.2
23.394	3.7994	7.9	110	10.0	18.6	8.6	0.132	9.7
26.948	3.3059	8.5	430	41.3	94.1	43.3	0.161	20.3
29.755	3.0001	8.3	1029	100.0	217.3	100.0	0.154	31.8
31.766	2.8147	7.6	34	2.6	5.2	2.4	0.141	4.5
36.347	2.4697	9.6	133	12.1	26.1	12.0	0.153	10.7
39.792	2.2635	9.0	190	17.7	43.0	19.8	0.172	13.1
42.188	2.1403	6.6	10	0.3	0.6	0.3	0.130	1.1
43.543	2.0768	7.3	155	14.5	34.6	15.9	0.169	11.9
46.094	1.9676	6.2	21	1.5	4.1	1.9	0.199	3.2
47.464	1.9140	13.7	51	3.7	8.7	4.0	0.168	5.2
47.859	1.8991	20.4	145	12.2	34.7	16.0	0.201	10.3
48.891	1.8614	13.0	165	14.9	39.3	18.1	0.187	11.8
50.438	1.8079	7.0	53	4.5	14.6	6.7	0.230	6.3
56.946	1.6157	10.1	32	2.1	5.4	2.5	0.179	3.9
57.750	1.5951	6.0	74	6.7	29.5	13.6	0.369	7.9
NV15-246RM								
23.392	3.7997	6.3	115	9.4	17.7	8.4	0.118	10.1
26.931	3.3080	8.2	97	7.7	17.1	8.1	0.139	9.0
29.751	3.0006	7.9	1159	100.0	209.8	100.0	0.132	33.8
31.793	2.8124	6.6	28	1.9	3.6	1.7	0.120	4.0
34.130	2.6249	3.2	10	0.6	1.3	0.6	0.135	2.2
34.684	2.5842	4.5	9	0.4	1.9	0.9	0.367	1.5
35.749	2.5097	6.3	10	0.3	4.1	1.9	0.924	1.2
36.308	2.4723	6.7	123	10.1	27.4	13.1	0.170	10.5
39.762	2.2651	6.8	211	17.7	42.8	20.4	0.151	14.1
43.510	2.0783	6.5	130	10.7	28.3	13.5	0.165	10.8
44.572	2.0312	4.3	8	0.3	0.7	0.3	0.137	1.3
47.507	1.9123	9.7	60	4.4	23.4	11.2	0.396	6.5
47.856	1.8992	10.2	129	10.3	45.6	21.7	0.326	10.5
48.825	1.8638	11.2	196	16.1	42.1	20.0	0.164	13.2
56.879	1.6175	6.1	27	1.8	6.2	3.0	0.215	4.0
57.757	1.5950	5.0	68	5.5	20.8	9.9	0.239	7.6
NV18-07CR								
22.322	3.9795	4.9	161	13.1	16.7	6.7	0.091	12.3
23.413	3.7964	5.1	93	7.4	16.8	6.8	0.138	9.1
27.870	3.1986	3.7	9	0.4	3.1	1.3	0.501	1.8
29.796	2.9961	6.8	1202	100.0	247.6	100.0	0.150	34.5
36.358	2.4690	5.7	131	10.5	29.5	11.9	0.170	10.9
39.804	2.2628	6.0	122	9.7	29.4	11.9	0.183	10.5
43.580	2.0751	5.6	131	10.5	32.8	13.2	0.189	11.0
47.516	1.9120	14.5	47	2.7	5.4	2.2	0.120	4.7
47.941	1.8960	14.5	107	7.7	34.8	14.1	0.320	8.9
48.900	1.8611	14.2	117	8.6	23.8	9.6	0.167	9.5
51.072	1.7869	3.7	8	0.4	0.8	0.3	0.136	1.5
52.919	1.7288	4.3	7	0.2	1.1	0.4	0.331	1.0
57.759	1.5949	6.7	67	5.0	18.8	7.6	0.225	7.4

Position (°)	D-spacing (Å)	Background Intensity (cps)	Intensity (cps)	Relative Intensity (%)	Area	Area (%)	FWHM (°)	P/N
NV11-051EP								
21.167	4.1940	13.0	147	15.2	39.9	17.9	0.215	11.1
26.980	3.3021	14.0	895	100.0	223.3	100.0	0.183	29.4
29.800	2.9957	13.3	177	18.6	38.1	17.0	0.168	12.3
31.145	2.8693	15.9	226	23.9	70.3	31.5	0.242	14.0
33.539	2.6698	10.6	31	2.3	6.2	2.8	0.217	3.7
36.350	2.4696	17.3	46	3.3	4.0	1.8	0.100	4.2
36.887	2.4348	10.5	61	5.7	28.1	12.6	0.473	6.5
39.826	2.2616	12.4	96	9.5	20.9	9.4	0.181	8.5
41.351	2.1817	14.3	68	6.1	14.5	6.5	0.195	6.5
42.786	2.1118	11.4	46	3.9	8.3	3.7	0.174	5.1
45.109	2.0083	10.9	47	4.1	6.8	3.0	0.136	5.3
46.062	1.9689	9.2	31	2.5	6.3	2.8	0.209	3.9
47.872	1.8986	9.9	73	7.2	18.2	8.1	0.208	7.4
48.847	1.8630	14.7	37	2.5	3.7	1.6	0.119	3.7
50.443	1.8077	12.9	127	12.9	53.1	23.8	0.396	10.1
51.131	1.7850	23.4	43	2.2	3.8	1.7	0.140	3.0
55.151	1.6640	10.0	47	4.2	9.1	4.1	0.178	5.4
NV16-134TC								
21.202	4.1872	5.8	50	4.9	9.5	4.3	0.155	6.3
23.483	3.7854	5.6	80	8.2	14.3	6.5	0.139	8.3
24.130	3.6852	2.9	10	0.8	2.7	1.2	0.327	2.2
26.998	3.2999	8.0	230	24.6	44.7	20.4	0.145	14.6
29.835	2.9923	5.8	910	100.0	219.6	100.0	0.176	30.0
31.858	2.8067	7.1	30	2.5	2.9	1.3	0.090	4.2
36.399	2.4663	5.8	92	9.5	21.7	9.9	0.182	9.0
39.847	2.2605	6.3	123	12.9	36.3	16.5	0.225	10.5
43.599	2.0743	5.6	102	10.7	27.2	12.4	0.204	9.5
47.651	1.9069	22.2	42	2.2	2.9	1.3	0.107	3.1
47.993	1.8941	14.6	122	11.9	52.8	24.0	0.418	9.7
48.948	1.8593	16.7	109	10.2	26.8	12.2	0.209	8.8
50.461	1.8071	6.7	27	2.2	5.1	2.3	0.180	3.9
56.996	1.6144	7.8	25	1.9	4.2	1.9	0.176	3.4
57.849	1.5927	4.4	46	4.6	21.1	9.6	0.431	6.1

Position (°)	D-spacing (Å)	Background Intensity (cps)	Intensity (cps)	Relative Intensity (%)	Area	Area (%)	FWHM (°)	P/N
NV12-149BR-A								
20.191	4.3944	9.8	79	23.9	73.0	100.0	0.897	7.8
20.747	4.2779	11.2	62	17.6	52.3	71.6	0.875	6.5
21.199	4.1877	15.0	101	29.7	72.4	99.2	0.716	8.6
21.559	4.1185	15.0	48	11.4	6.9	9.4	0.150	4.8
25.212	3.5295	22.9	312	100.0	54.9	75.2	0.137	16.4
26.955	3.3051	29.7	303	94.5	58.9	80.6	0.156	15.7
28.288	3.1523	20.6	92	24.7	18.0	24.6	0.182	7.4
29.873	2.9885	19.0	58	13.5	6.0	8.2	0.111	5.1
35.393	2.5340	11.4	60	16.8	40.5	55.5	0.709	6.3
35.797	2.5064	11.4	37	8.9	10.1	13.8	0.335	4.2
36.313	2.4719	20.8	50	10.1	7.8	10.7	0.194	4.1
38.051	2.3629	21.0	71	17.3	7.3	10.0	0.105	5.9
39.604	2.2738	17.7	41	8.1	10.2	14.0	0.372	3.6
39.749	2.2658	12.6	38	8.8	13.4	18.3	0.447	4.1
50.405	1.8090	11.6	37	8.8	6.3	8.6	0.178	4.2
55.114	1.6650	10.3	134	42.8	33.9	46.5	0.198	10.7
NV15-007EH								
21.178	4.1918	11.9	152	16.8	33.5	15.5	0.173	11.4
23.404	3.7979	9.1	62	6.3	8.2	3.8	0.112	6.7
26.951	3.3056	6.9	842	100.0	215.7	100.0	0.187	28.8
29.755	3.0002	7.5	535	63.2	122.5	56.8	0.168	22.8
31.108	2.8727	10.5	67	6.8	14.6	6.8	0.187	6.9
36.377	2.4677	6.6	65	7.0	22.4	10.4	0.326	7.2
36.849	2.4372	6.3	51	5.4	23.2	10.8	0.442	6.3
39.763	2.2651	9.5	139	15.5	37.1	17.2	0.207	11.0
42.751	2.1134	7.0	49	5.0	13.2	6.1	0.227	6.0
43.512	2.0782	8.4	68	7.1	17.2	8.0	0.208	7.2
47.892	1.8979	12.1	92	9.6	26.3	12.2	0.237	8.3
48.866	1.8623	11.8	74	7.4	19.6	9.1	0.228	7.2
50.410	1.8088	7.3	106	11.8	34.0	15.8	0.249	9.6
53.612	1.7081	4.0	7	0.4	1.8	0.8	0.517	1.1
55.105	1.6653	4.0	26	2.6	10.7	5.0	0.413	4.3
57.793	1.5941	9.0	36	3.2	8.0	3.7	0.215	4.5
ANV14-051EH								
20.891	4.2486	6.0	62	15.6	9.5	16.1	0.123	7.1
20.978	4.2313	6.0	50	12.3	4.6	7.8	0.089	6.2
26.729	3.3325	19.6	378	100.0	59.1	100.0	0.119	18.4
29.510	3.0245	10.7	225	59.8	34.2	57.9	0.115	14.3
29.560	3.0195	15.1	177	45.2	31.8	53.8	0.142	12.2
36.053	2.4892	8.2	27	5.2	0.8	1.4	0.038	3.6
39.512	2.2789	6.1	60	15.0	9.8	16.5	0.131	7.0
39.620	2.2729	5.7	52	12.9	10.0	16.8	0.155	6.4
43.302	2.0878	14.4	37	6.3	1.5	2.6	0.058	3.7
50.199	1.8159	19.8	41	5.9	1.7	2.8	0.067	3.3

Position (°)	D-spacing (Å)	Background Intensity (cps)	Intensity (cps)	Relative Intensity (%)	Area	Area (%)	FWHM (°)	P/N
NV16-077EH								
24.382	3.6477	7.7	42	6.7	7.5	5.0	0.159	5.3
26.964	3.3040	9.0	37	5.5	6.3	4.2	0.163	4.6
31.201	2.8643	9.7	523	100.0	150.4	100.0	0.212	22.4
35.513	2.5258	9.3	32	4.4	7.9	5.3	0.252	4.0
37.601	2.3902	8.5	66	11.2	22.1	14.7	0.327	7.1
41.349	2.1818	8.8	159	29.3	49.6	33.0	0.239	11.9
45.186	2.0050	8.0	97	17.3	37.0	24.6	0.353	9.0
49.544	1.8384	13.6	33	3.8	4.5	3.0	0.168	3.4
50.746	1.7976	10.4	98	17.1	78.1	51.9	0.758	8.9
51.248	1.7812	10.6	123	21.9	80.0	53.2	0.605	10.1
53.950	1.6982	6.2	10	0.7	6.1	4.0	1.346	1.2
54.556	1.6807	5.4	10	0.9	6.3	4.2	1.169	1.5
59.133	1.5611	12.0	31	3.7	4.9	3.3	0.186	3.4
NV16-081EH								
24.384	3.6474	8.3	40	6.4	7.7	5.1	0.175	5.0
26.939	3.3070	10.6	40	6.0	6.1	4.0	0.150	4.7
29.769	2.9987	12.2	37	5.0	5.8	3.8	0.169	4.1
31.197	2.8647	8.9	501	100.0	151.6	100.0	0.223	22.0
33.775	2.6517	9.7	27	3.5	4.0	2.7	0.169	3.3
35.557	2.5227	12.0	42	6.1	5.4	3.5	0.129	4.6
37.611	2.3896	12.3	64	10.5	14.3	9.5	0.200	6.5
41.392	2.1796	8.1	143	27.4	49.9	32.9	0.314	11.3
45.188	2.0049	8.6	93	17.1	29.4	19.4	0.252	8.8
49.487	1.8404	11.7	33	4.3	4.4	2.9	0.150	3.7
50.661	1.8004	21.6	102	16.3	22.8	15.0	0.204	8.0
51.292	1.7798	9.2	125	23.5	58.6	38.6	0.430	10.4
55.185	1.6631	5.3	10	0.9	2.1	1.4	0.378	1.5
58.274	1.5820	7.3	10	0.5	0.7	0.5	0.197	0.8
59.057	1.5629	10.0	34	4.9	6.2	4.1	0.188	4.1
NV16-083EH								
22.291	3.9849	8.0	23	3.0	2.2	1.4	0.108	3.1
24.353	3.6521	10.0	51	8.3	8.4	5.4	0.148	5.7
26.981	3.3020	8.3	31	4.6	5.8	3.7	0.185	4.1
29.800	2.9957	9.5	39	5.9	6.6	4.3	0.162	4.7
31.199	2.8645	6.9	503	100.0	155.6	100.0	0.227	22.1
33.787	2.6508	8.7	37	5.7	6.0	3.8	0.152	4.7
37.603	2.3901	9.5	70	12.2	16.8	10.8	0.201	7.2
41.310	2.1837	9.3	144	27.1	49.2	31.6	0.310	11.2
45.188	2.0050	9.0	89	16.1	30.1	19.4	0.320	8.5
49.478	1.8407	15.3	41	5.2	2.6	1.7	0.085	4.0
50.741	1.7978	10.6	92	16.4	59.6	38.3	0.622	8.5
51.295	1.7797	10.6	119	21.8	76.6	49.3	0.601	9.9
57.613	1.5986	7.8	24	3.3	3.2	2.0	0.141	3.3
59.015	1.5639	8.9	32	4.7	7.4	4.7	0.230	4.1

Position (°)	D-spacing (Å)	Background Intensity (cps)	Intensity (cps)	Relative Intensity (%)	Area	Area (%)	FWHM (°)	P/N
ANV14-054EH								
20.885	4.2499	6.0	34	4.1	3.1	2.4	0.094	4.8
23.154	3.8384	5.2	73	10.0	10.9	8.3	0.116	7.9
26.698	3.3363	3.4	158	22.8	25.5	19.5	0.119	12.3
29.512	3.0243	4.8	684	100.0	131.0	100.0	0.139	26.0
36.100	2.4860	2.8	85	12.1	23.0	17.6	0.203	8.9
39.552	2.2767	6.3	112	15.6	24.5	18.7	0.167	10.0
43.308	2.0875	3.4	115	16.4	28.0	21.4	0.181	10.4
47.656	1.9067	7.5	124	17.1	38.1	29.1	0.236	10.5
48.661	1.8696	9.3	142	19.5	32.1	24.5	0.175	11.1
57.564	1.5998	4.1	52	7.1	15.7	12.0	0.237	6.6
64.899	1.4356	3.7	54	7.4	12.8	9.8	0.184	6.8
ANV14-055EH								
31.090	2.8743	13.6	249	100.0	44.7	100.0	0.137	14.9
41.290	2.1847	5.0	77	30.6	13.8	30.8	0.138	8.2
45.109	2.0083	5.7	48	18.0	6.7	14.9	0.114	6.1
50.634	1.8013	17.6	34	7.0	1.7	3.9	0.090	2.8
50.799	1.7959	11.8	29	7.3	1.0	2.3	0.050	3.2
51.130	1.7850	12.8	36	9.9	1.8	4.0	0.065	3.9
51.192	1.7830	10.6	56	19.3	8.0	17.9	0.127	6.1
NV16-085EH								
22.283	3.9864	7.4	30	4.6	4.2	2.9	0.133	4.1
24.383	3.6476	7.4	52	9.1	8.8	6.1	0.142	6.2
26.989	3.3010	8.2	35	5.4	6.4	4.5	0.173	4.5
29.776	2.9981	13.1	40	5.5	4.5	3.1	0.121	4.3
31.199	2.8645	10.6	502	100.0	143.6	100.0	0.211	21.9
35.550	2.5232	11.0	34	4.7	5.0	3.5	0.157	3.9
37.603	2.3901	7.8	69	12.5	20.9	14.6	0.247	7.4
41.393	2.1795	7.3	151	29.2	50.7	35.3	0.255	11.7
44.060	2.0536	10.3	33	4.6	4.5	3.2	0.145	3.9
45.198	2.0045	9.2	102	18.9	26.8	18.7	0.209	9.2
49.501	1.8399	13.5	41	5.6	6.2	4.3	0.164	4.3
50.651	1.8008	10.9	91	16.3	64.0	44.6	0.679	8.4
51.252	1.7810	11.3	120	22.1	75.7	52.7	0.592	9.9
59.139	1.5609	9.8	32	4.5	6.2	4.3	0.202	3.9

Position (°)	D-spacing (Å)	Background Intensity (cps)	Intensity (cps)	Relative Intensity (%)	Area	Area (%)	FWHM (°)	P/N
NV15-073CM								
23.257	3.8216	8.1	81	10.9	20.9	9.4	0.207	8.1
26.743	3.3308	7.1	59	7.8	7.5	3.4	0.105	6.8
29.646	3.0109	8.3	677	100.0	222.4	100.0	0.240	25.7
31.584	2.8304	11.0	32	3.1	4.8	2.1	0.164	3.7
34.461	2.6005	3.9	10	0.9	2.9	1.3	0.398	1.9
36.209	2.4788	6.8	89	12.3	31.7	14.2	0.327	8.7
39.698	2.2686	5.7	99	14.0	42.8	19.2	0.390	9.4
41.295	2.1845	4.8	9	0.6	1.8	0.8	0.354	1.4
43.543	2.0768	7.4	86	11.8	33.5	15.1	0.363	8.5
47.411	1.9160	21.5	42	3.1	3.3	1.5	0.117	3.2
47.669	1.9062	7.0	125	17.6	66.9	30.1	0.482	10.6
47.945	1.8959	29.7	91	9.2	36.0	16.2	0.499	6.4
48.800	1.8647	15.9	95	11.8	41.7	18.7	0.448	8.1
53.845	1.7012	4.5	9	0.7	1.0	0.5	0.164	1.5
57.698	1.5964	21.1	49	4.2	6.1	2.7	0.158	4.0
NV15-075CM								
20.949	4.2372	13.8	120	19.4	26.6	17.4	0.181	9.7
23.243	3.8238	12.2	83	13.0	14.5	9.5	0.148	7.8
26.739	3.3313	12.5	481	85.7	80.7	52.8	0.124	21.4
29.605	3.0150	13.4	560	100.0	152.9	100.0	0.202	23.1
36.167	2.4816	13.3	87	13.5	19.0	12.5	0.186	7.9
36.642	2.4505	15.8	41	4.6	4.6	3.0	0.132	3.9
39.609	2.2735	10.9	105	17.2	33.6	21.9	0.303	9.2
43.403	2.0832	10.5	108	17.8	24.9	16.3	0.184	9.4
47.881	1.8983	20.3	79	10.7	24.6	16.1	0.357	6.6
48.796	1.8648	15.2	92	14.0	25.6	16.7	0.240	8.0
50.216	1.8153	11.0	59	8.8	8.9	5.8	0.134	6.2
57.676	1.5970	16.1	41	4.6	6.0	3.9	0.173	3.9
NV15-083CM								
23.192	3.8321	16.3	77	13.0	15.7	8.9	0.187	6.9
26.651	3.3421	11.6	70	12.5	10.9	6.2	0.135	7.0
29.554	3.0200	12.9	480	100.0	176.4	100.0	0.321	21.3
36.100	2.4861	13.1	85	15.4	28.8	16.3	0.340	7.8
39.648	2.2714	9.3	97	18.8	37.1	21.0	0.360	8.9
43.403	2.0832	8.5	78	14.9	37.3	21.1	0.456	7.9
47.412	1.9159	9.8	57	10.1	44.5	25.2	0.801	6.3
47.840	1.8998	26.4	84	12.3	23.3	13.2	0.344	6.3
48.753	1.8664	12.6	78	14.0	32.9	18.6	0.427	7.4
57.723	1.5958	18.0	48	6.4	6.0	3.4	0.144	4.3
NV15-084CM								
26.681	3.3384	15.4	38	6.5	3.5	4.1	0.113	3.7
29.555	3.0200	20.9	369	100.0	87.2	100.0	0.181	18.1
30.885	2.8929	17.7	164	42.0	43.0	49.3	0.212	11.4
36.173	2.4812	17.6	93	21.7	37.2	42.7	0.420	7.8
39.563	2.2761	13.5	63	14.2	18.6	21.3	0.319	6.2
41.077	2.1956	17.0	52	10.0	7.7	8.8	0.158	4.8
43.354	2.0854	17.7	74	16.2	16.7	19.1	0.214	6.5
44.804	2.0212	16.3	37	5.9	5.3	6.1	0.185	3.4
47.738	1.9036	18.6	60	11.9	14.7	16.9	0.302	5.3
48.783	1.8653	18.6	59	11.6	14.1	16.1	0.251	5.3

Position (°)	D-spacing (Å)	Background Intensity (cps)	Intensity (cps)	Relative Intensity (%)	Area	Area (%)	FWHM (°)	P/N
NV15-085CM								
23.272	3.8192	9.7	74	11.9	15.8	9.5	0.177	7.5
29.607	3.0148	7.5	547	100.0	165.3	100.0	0.221	23.1
32.591	2.7452	7.4	10	0.5	0.9	0.5	0.250	0.8
36.199	2.4795	9.7	86	14.1	22.5	13.6	0.213	8.2
39.615	2.2732	7.8	114	19.7	38.3	23.2	0.306	9.9
43.443	2.0813	7.7	113	19.5	33.4	20.2	0.229	9.9
47.361	1.9179	14.6	54	7.3	9.3	5.6	0.170	5.4
47.748	1.9032	19.5	97	14.4	38.7	23.4	0.424	7.9
48.840	1.8632	14.2	124	20.4	38.9	23.5	0.301	9.9
51.958	1.7585	6.2	10	0.7	0.4	0.3	0.099	1.2
55.891	1.6437	6.3	9	0.5	1.9	1.1	0.574	0.9
56.844	1.6184	8.4	32	4.4	5.8	3.5	0.178	4.2
57.831	1.5931	6.7	49	7.8	26.0	15.7	0.522	6.0
NV15-088CM								
19.893	4.4597	13.4	45	8.0	11.3	8.0	0.303	4.7
20.977	4.2316	25.2	65	10.1	6.0	4.2	0.108	4.9
24.084	3.6922	14.2	62	12.1	9.2	6.5	0.138	6.1
26.747	3.3304	18.3	302	72.0	59.1	42.0	0.150	16.3
29.567	3.0188	18.4	151	33.7	15.2	10.8	0.097	10.8
30.861	2.8951	17.0	411	100.0	140.8	100.0	0.304	19.4
37.323	2.4073	15.7	78	15.8	18.7	13.2	0.216	7.1
39.637	2.2720	14.0	33	4.8	5.2	3.7	0.197	3.3
41.061	2.1964	13.0	121	27.4	39.2	27.9	0.309	9.8
44.824	2.0204	11.4	73	15.6	22.3	15.8	0.307	7.2
50.251	1.8142	16.8	83	16.8	35.7	25.3	0.458	7.3
50.848	1.7942	13.0	89	19.3	63.2	44.9	0.707	8.1
58.797	1.5692	12.0	28	4.1	4.0	2.8	0.179	3.0
59.619	1.5495	15.4	38	5.7	7.5	5.3	0.241	3.7
NV15-089CM								
19.910	4.4559	18.8	35	3.9	3.6	2.4	0.159	2.7
20.713	4.2849	30.9	99	16.5	16.3	10.7	0.173	6.8
21.148	4.1977	30.4	91	14.7	65.0	42.9	0.912	6.4
21.797	4.0741	30.4	186	37.7	151.6	100.0	0.828	11.4
22.569	3.9365	41.5	62	5.0	4.0	2.7	0.142	2.6
23.211	3.8290	24.5	81	13.7	15.7	10.3	0.200	6.3
26.735	3.3318	16.4	61	10.8	9.0	5.9	0.145	5.7
29.648	3.0107	12.8	425	100.0	120.0	79.2	0.210	20.0
36.203	2.4792	18.8	99	19.5	36.6	24.1	0.387	8.1
39.698	2.2687	13.1	88	18.2	26.6	17.5	0.302	8.0
43.453	2.0809	14.1	78	15.5	22.3	14.7	0.252	7.2
47.578	1.9097	21.6	49	6.6	6.8	4.5	0.180	3.9
47.855	1.8992	17.6	64	11.3	22.6	14.9	0.414	5.8
48.896	1.8612	13.2	82	16.7	22.4	14.8	0.235	7.6
57.861	1.5923	17.1	45	6.8	7.7	5.0	0.198	4.2

Position (°)	D-spacing (Å)	Background Intensity (cps)	Intensity (cps)	Relative Intensity (%)	Area	Area (%)	FWHM (°)	P/N
NV15-090CM								
20.555	4.3174	20.7	102	22.4	46.1	26.0	0.482	8.0
21.654	4.1007	20.7	176	42.7	177.6	100.0	0.972	11.7
23.052	3.8550	24.1	95	19.5	23.1	13.0	0.236	7.3
29.491	3.0264	17.3	381	100.0	122.5	69.0	0.243	18.6
35.952	2.4959	14.1	98	23.1	42.8	24.1	0.434	8.5
39.503	2.2794	16.9	81	17.6	22.2	12.5	0.250	7.1
43.288	2.0884	14.6	82	18.5	20.2	11.4	0.217	7.4
47.267	1.9215	18.0	42	6.6	6.3	3.5	0.188	3.7
47.648	1.9070	19.8	68	13.3	22.3	12.5	0.393	5.8
48.596	1.8720	8.0	76	18.7	31.4	17.7	0.393	7.8
57.465	1.6024	17.7	45	7.5	9.1	5.1	0.240	4.1
NV15-091CM								
23.251	3.8225	13.6	108	10.2	19.0	9.5	0.145	9.1
26.788	3.3253	8.5	76	7.3	26.5	13.2	0.333	7.7
29.616	3.0139	8.9	935	100.0	200.6	100.0	0.157	30.3
31.669	2.8231	10.3	36	2.8	4.8	2.4	0.135	4.3
36.234	2.4772	11.4	103	9.9	29.5	14.7	0.233	9.0
39.649	2.2713	13.1	166	16.5	34.9	17.4	0.165	11.9
43.406	2.0830	8.3	114	11.4	32.1	16.0	0.220	9.9
47.473	1.9136	25.2	51	2.8	5.9	3.0	0.167	3.6
47.753	1.9031	13.4	133	12.9	48.5	24.2	0.345	10.4
48.789	1.8650	13.0	121	11.7	34.9	17.4	0.233	9.8
56.867	1.6178	10.5	36	2.8	6.2	3.1	0.176	4.3
57.732	1.5956	8.9	67	6.3	20.9	10.4	0.306	7.1
NV15-092CM								
19.764	4.4884	14.2	34	3.3	8.3	5.1	0.356	3.4
20.808	4.2655	14.2	54	6.6	19.6	12.0	0.419	5.4
21.806	4.0725	14.2	68	8.9	37.8	23.1	0.597	6.5
24.038	3.6991	18.6	69	8.3	7.1	4.3	0.102	6.1
26.690	3.3373	15.2	119	17.2	26.7	16.3	0.185	9.5
30.890	2.8924	18.9	622	100.0	163.6	100.0	0.196	24.2
33.369	2.6830	13.2	40	4.4	5.8	3.6	0.158	4.2
35.084	2.5557	16.6	40	3.9	8.1	4.9	0.249	3.7
37.350	2.4057	16.0	85	11.4	16.3	10.0	0.171	7.5
41.058	2.1965	15.8	162	24.2	42.8	26.1	0.211	11.5
43.739	2.0680	12.9	35	3.7	4.8	2.9	0.157	3.7
44.863	2.0187	11.7	108	16.0	28.7	17.5	0.215	9.3
49.150	1.8522	14.0	31	2.8	5.9	3.6	0.251	3.1
50.347	1.8109	15.7	77	10.2	39.4	24.1	0.546	7.0
50.866	1.7937	13.5	118	17.3	66.0	40.4	0.537	9.6
58.844	1.5681	13.7	31	2.9	3.5	2.1	0.147	3.1

Position (°)	D-spacing (Å)	Background Intensity (cps)	Intensity (cps)	Relative Intensity (%)	Area	Area (%)	FWHM (°)	P/N
NV15-093CM								
20.522	4.3244	19.2	38	2.2	5.4	2.5	0.208	3.0
24.050	3.6973	14.8	68	6.3	7.6	3.5	0.103	6.5
26.657	3.3413	12.6	44	3.7	8.5	4.0	0.195	4.7
30.903	2.8913	13.5	852	100.0	214.3	100.0	0.185	28.7
33.410	2.6798	13.5	40	3.2	6.0	2.8	0.163	4.2
35.259	2.5434	15.6	42	3.2	5.6	2.6	0.152	4.1
37.354	2.4054	15.4	97	9.7	15.1	7.1	0.134	8.3
41.136	2.1926	13.0	214	24.0	59.2	27.6	0.213	13.7
43.762	2.0669	13.0	35	2.6	4.9	2.3	0.162	3.7
44.901	2.0171	11.3	126	13.7	32.0	14.9	0.201	10.2
49.206	1.8502	14.2	40	3.1	6.8	3.2	0.189	4.1
50.403	1.8091	16.8	89	8.6	35.4	16.5	0.416	7.7
50.955	1.7907	13.0	130	14.0	57.2	26.7	0.416	10.3
58.822	1.5686	13.3	37	2.8	3.8	1.8	0.114	3.9
NV15-094CM								
22.049	4.0281	16.2	54	3.7	5.7	2.4	0.109	5.1
24.076	3.6933	11.5	87	7.5	17.5	7.5	0.167	8.1
26.709	3.3350	10.8	110	9.8	15.9	6.8	0.116	9.5
29.542	3.0213	14.1	197	18.1	26.9	11.5	0.106	13.0
30.946	2.8873	14.9	1024	100.0	234.3	100.0	0.168	31.5
33.502	2.6726	7.6	58	5.0	13.3	5.7	0.190	6.6
37.367	2.4046	13.0	124	11.0	17.7	7.5	0.115	10.0
39.553	2.2766	9.5	25	1.5	3.3	1.4	0.154	3.1
41.116	2.1936	10.4	248	23.6	68.1	29.1	0.207	15.1
43.823	2.0642	13.2	51	3.7	6.5	2.8	0.124	5.3
44.916	2.0164	10.0	145	13.4	35.2	15.0	0.188	11.2
49.281	1.8476	14.9	43	2.8	6.1	2.6	0.157	4.3
50.448	1.8075	15.4	106	9.0	46.2	19.7	0.434	8.8
51.008	1.7890	11.2	176	16.3	62.3	26.6	0.321	12.4
58.854	1.5678	9.2	37	2.8	7.4	3.2	0.193	4.6
NV15-095CM								
20.648	4.2981	12.3	69	7.7	22.2	9.9	0.332	6.8
21.897	4.0558	23.8	102	10.6	51.8	23.1	0.564	7.7
24.001	3.7048	11.4	65	7.3	11.8	5.3	0.159	6.6
29.490	3.0264	14.7	136	16.5	16.8	7.5	0.100	10.4
30.815	2.8993	16.2	752	100.0	224.1	100.0	0.220	26.8
33.388	2.6815	12.6	37	3.3	6.4	2.9	0.190	4.0
35.192	2.5481	15.6	34	2.5	3.1	1.4	0.122	3.2
36.053	2.4892	15.1	42	3.7	6.8	3.0	0.183	4.1
37.300	2.4088	10.7	85	10.1	20.6	9.2	0.200	8.1
41.040	2.1975	9.3	214	27.8	66.7	29.7	0.235	14.0
44.809	2.0210	13.8	118	14.2	32.4	14.4	0.225	9.6
50.108	1.8190	32.1	57	3.4	3.8	1.7	0.111	3.3
50.394	1.8093	17.1	78	8.3	58.1	25.9	0.812	6.9
50.806	1.7956	13.5	113	13.5	80.5	35.9	0.687	9.4
58.751	1.5703	12.6	30	2.4	5.3	2.4	0.220	3.2

Position (°)	D-spacing (Å)	Background Intensity (cps)	Intensity (cps)	Relative Intensity (%)	Area	Area (%)	FWHM (°)	P/N
NV15-096CM								
23.181	3.8339	8.3	108	6.7	21.2	8.7	0.154	9.6
26.745	3.3306	5.4	10	0.3	0.7	0.3	0.103	1.5
29.529	3.0226	10.8	1496	100.0	244.6	100.0	0.119	38.4
30.901	2.8915	12.1	110	6.6	30.8	12.6	0.227	9.3
36.119	2.4848	6.9	137	8.8	31.9	13.0	0.177	11.1
39.568	2.2758	8.6	184	11.8	37.0	15.1	0.152	12.9
41.060	2.1965	11.2	46	2.3	6.2	2.5	0.128	5.1
43.313	2.0873	6.2	177	11.5	44.9	18.3	0.190	12.8
44.853	2.0191	8.8	26	1.2	4.6	1.9	0.192	3.4
47.228	1.9230	13.0	52	2.6	5.8	2.4	0.108	5.4
47.729	1.9040	26.1	128	6.9	29.0	11.9	0.206	9.0
48.736	1.8670	15.1	145	8.7	38.9	15.9	0.216	10.8
56.744	1.6210	9.3	35	1.7	5.9	2.4	0.164	4.3
57.524	1.6009	5.8	93	5.9	35.2	14.4	0.344	9.0
NV15-097CM								
23.114	3.8448	9.7	70	7.1	13.7	6.9	0.164	7.2
29.473	3.0282	9.3	858	100.0	199.1	100.0	0.169	29.0
30.850	2.8961	9.0	134	14.7	43.7	22.0	0.253	10.8
36.057	2.4889	6.9	125	13.9	31.3	15.7	0.192	10.6
39.511	2.2789	8.2	166	18.6	40.2	20.2	0.184	12.2
41.092	2.1948	10.3	43	3.9	9.3	4.7	0.205	5.0
43.251	2.0901	7.8	120	13.2	32.3	16.2	0.208	10.2
44.849	2.0193	8.6	37	3.3	7.4	3.7	0.188	4.7
47.264	1.9216	13.6	51	4.4	9.3	4.7	0.180	5.2
47.597	1.9089	12.4	151	16.3	45.7	22.9	0.238	11.3
48.601	1.8718	18.9	141	14.4	33.7	16.9	0.199	10.3
53.350	1.7159	4.2	9	0.6	0.5	0.3	0.089	1.6
57.510	1.6012	7.6	65	6.8	22.4	11.3	0.332	7.1
NV15-098CM								
21.982	4.0402	33.2	56	4.6	4	2.7	0.127	3.0
23.378	3.8020	18.3	59	8.2	9.4	6.3	0.168	5.3
26.793	3.3247	8.4	72	12.8	24.7	16.6	0.330	7.5
29.708	3.0048	13.9	510	100.0	148.7	100.0	0.217	22.0
30.859	2.8953	19.3	58	7.8	7.1	4.8	0.132	5.1
36.303	2.4726	14.3	83	13.8	21.8	14.7	0.230	7.5
39.800	2.2631	15.1	102	17.5	29.6	19.9	0.246	8.6
43.593	2.0745	11.8	78	13.4	22.3	15.0	0.244	7.5
47.482	1.9133	14.9	37	4.5	4.1	2.8	0.134	3.6
47.947	1.8958	22.4	89	13.4	26.6	17.9	0.340	7.1
48.950	1.8593	15.2	124	21.9	29.4	19.8	0.195	9.8
53.117	1.7228	7.8	10	0.4	0.8	0.6	0.324	0.7
57.896	1.5915	12.0	48	7.3	9.6	6.5	0.193	5.2

Position (°)	D-spacing (Å)	Background Intensity (cps)	Intensity (cps)	Relative Intensity (%)	Area	Area (%)	FWHM (°)	P/N
NV15-100CM								
24.138	3.6841	11.2	88	8.2	12.2	5.5	0.115	8.2
26.780	3.3263	11.9	43	3.3	3.4	1.5	0.092	4.7
29.559	3.0196	12.4	141	13.7	15.5	7.0	0.087	10.8
30.992	2.8831	12.7	949	100.0	221.3	100.0	0.171	30.4
33.513	2.6718	11.0	45	3.6	7.7	3.5	0.163	5.1
35.335	2.5381	17.6	50	3.5	5.2	2.3	0.116	4.6
36.131	2.4840	12.6	33	2.2	4.8	2.1	0.168	3.6
37.411	2.4019	9.0	118	11.6	25.4	11.5	0.168	10.0
41.161	2.1913	10.6	242	24.7	60.7	27.4	0.190	14.9
44.961	2.0145	10.8	152	15.1	36.3	16.4	0.186	11.5
48.699	1.8683	14.2	41	2.9	4.8	2.2	0.130	4.2
49.297	1.8470	16.6	48	3.4	5.9	2.6	0.135	4.5
50.459	1.8072	23.3	111	9.4	27.3	12.3	0.225	8.3
51.054	1.7875	14.3	142	13.6	61.7	27.9	0.411	10.7
NV15-101CM								
20.748	4.2777	19.0	38	2.3	8.8	3.8	0.394	3.1
21.574	4.1157	24.2	52	3.3	4.1	1.8	0.107	3.9
24.042	3.6986	12.2	65	6.3	11.4	4.9	0.155	6.6
26.702	3.3358	11.0	54	5.1	7.8	3.3	0.130	5.9
30.887	2.8927	13.8	851	100.0	233.7	100.0	0.202	28.7
33.398	2.6808	11.2	48	4.4	9.0	3.8	0.175	5.3
35.184	2.5487	14.1	45	3.7	5.7	2.4	0.134	4.6
37.348	2.4058	10.7	103	11.0	26.2	11.2	0.205	9.1
41.088	2.1951	12.0	217	24.5	66.1	28.3	0.233	13.9
43.267	2.0894	13.9	31	2.0	2.4	1.0	0.099	3.1
43.759	2.0671	14.9	34	2.3	4.2	1.8	0.159	3.3
44.862	2.0187	10.9	133	14.6	35.6	15.3	0.211	10.6
50.395	1.8093	17.5	101	10.0	43.4	18.6	0.441	8.3
50.860	1.7938	13.2	139	15.0	69.7	29.8	0.471	10.7
58.804	1.5690	10.4	31	2.5	6.0	2.6	0.212	3.7
NV15-102CM								
23.213	3.8287	15.2	78	10.1	8.2	5.3	0.094	7.1
24.133	3.6848	14.7	50	5.7	4.8	3.1	0.099	5.0
29.555	3.0199	13.3	636	100.0	104.6	68.1	0.121	24.7
30.950	2.8870	13.2	538	84.3	153.6	100.0	0.211	22.6
33.503	2.6726	10.0	28	2.9	5.2	3.4	0.209	3.4
36.139	2.4834	14.5	73	9.4	6.9	4.5	0.086	6.8
37.398	2.4027	8.5	72	10.2	17.2	11.2	0.196	7.5
39.591	2.2745	7.7	70	10.0	16.7	10.9	0.193	7.4
41.148	2.1920	8.1	128	19.2	41.4	26.9	0.249	10.6
43.317	2.0871	10.5	87	12.3	14.9	9.7	0.141	8.2
44.953	2.0149	10.1	97	13.9	23.9	15.5	0.199	8.8
47.266	1.9215	9.9	30	3.2	4.4	2.9	0.159	3.7
47.656	1.9067	11.6	77	10.5	18.8	12.2	0.207	7.5
48.661	1.8696	16.2	89	11.7	11.6	7.6	0.115	7.7
50.402	1.8091	12.1	72	9.6	40.2	26.2	0.570	7.1
51.001	1.7892	10.1	95	13.6	60.6	39.5	0.606	8.7
56.379	1.6306	6.1	10	0.6	3.8	2.5	0.832	1.2
57.546	1.6003	11.3	38	4.3	4.4	2.8	0.118	4.3

Position (°)	D-spacing (Å)	Background Intensity (cps)	Intensity (cps)	Relative Intensity (%)	Area	Area (%)	FWHM (°)	P/N
NV15-104CM								
19.854	4.4682	17.4	43	3.7	9.9	7.1	0.329	3.9
20.871	4.2527	24.0	76	7.5	15.5	11.0	0.215	6.0
23.150	3.8390	22.9	119	13.9	14.2	10.1	0.107	8.8
23.639	3.7607	12.8	27	2.1	4.3	3.0	0.217	2.7
26.692	3.3370	15.7	214	28.7	41.9	29.9	0.153	13.6
29.514	3.0241	16.1	708	100.0	140.2	100.0	0.146	26.0
36.108	2.4855	15.7	113	14.1	27.3	19.5	0.203	9.2
39.547	2.2769	11.3	159	21.4	37.8	26.9	0.185	11.7
43.311	2.0874	12.9	92	11.4	22.4	15.9	0.204	8.2
47.269	1.9214	17.5	49	4.6	7.4	5.3	0.170	4.5
47.651	1.9069	15.6	94	11.3	35.7	25.5	0.387	8.1
48.666	1.8695	16.0	130	16.5	30.0	21.4	0.190	10.0
50.226	1.8150	11.4	30	2.7	3.8	2.7	0.147	3.4
57.508	1.6013	14.8	47	4.7	9.9	7.1	0.223	4.7
NV15-106CM								
23.136	3.8412	7.8	150	14.1	22.8	14.5	0.116	11.6
26.713	3.3345	8.1	139	13.0	22.6	14.3	0.125	11.1
29.505	3.0250	8.2	1017	100.0	157.6	100.0	0.113	31.6
30.928	2.8890	10.3	24	1.4	3.3	2.1	0.172	2.8
31.558	2.8327	9.9	35	2.5	3.0	1.9	0.100	4.2
36.070	2.4880	8.7	234	22.3	30.0	19.0	0.096	14.7
38.889	2.3139	5.6	10	0.4	1.2	0.8	0.199	1.4
39.518	2.2785	8.0	327	31.6	50.0	31.7	0.113	17.6
43.266	2.0895	8.0	141	13.2	25.6	16.3	0.139	11.2
45.359	1.9978	6.3	9	0.3	2.8	1.8	0.888	0.9
47.206	1.9238	6.6	45	3.8	7.5	4.8	0.141	5.7
47.625	1.9079	10.3	138	12.7	31.8	20.2	0.180	10.9
48.616	1.8713	7.5	176	16.7	38.2	24.2	0.164	12.7
53.531	1.7105	5.4	9	0.4	1.5	1.0	0.362	1.2
54.197	1.6910	5.3	9	0.4	1.4	0.9	0.315	1.2
56.689	1.6224	7.4	35	2.7	6.0	3.8	0.157	4.7
57.503	1.6014	5.5	61	5.5	20.5	13.0	0.313	7.1
NV15-107CM								
23.093	3.8483	7.3	108	10.2	22.5	13.8	0.162	9.7
26.732	3.3322	6.9	129	12.3	23.0	14.1	0.136	10.7
29.506	3.0249	6.2	997	100.0	163.3	100.0	0.119	31.4
30.687	2.9111	5.5	10	0.5	2.1	1.3	0.393	1.4
36.085	2.4870	5.6	229	22.5	33.8	20.7	0.109	14.8
39.525	2.2781	8.5	207	20.0	31.7	19.4	0.116	13.8
41.821	2.1582	5.8	9	0.3	0.7	0.4	0.161	1.1
42.191	2.1402	5.0	9	0.4	2.0	1.2	0.419	1.3
43.283	2.0886	7.3	75	6.8	13.4	8.2	0.143	7.8
44.701	2.0256	4.7	9	0.4	1.7	1.1	0.347	1.4
47.650	1.9069	20.2	260	24.2	40.9	25.0	0.123	14.9
48.624	1.8710	9.7	203	19.5	37.1	22.7	0.139	13.6
52.762	1.7336	3.9	8	0.4	0.6	0.3	0.098	1.4
55.439	1.6560	4.8	10	0.5	2.7	1.7	0.449	1.6
56.666	1.6231	6.1	28	2.2	3.7	2.3	0.123	4.1
57.522	1.6009	5.1	171	16.7	37.0	22.7	0.161	12.7

Position (°)	D-spacing (Å)	Background Intensity (cps)	Intensity (cps)	Relative Intensity (%)	Area	Area (%)	FWHM (°)	P/N
NV15-108CM								
20.965	4.2340	7.8	71	4.8	7.0	3.3	0.094	7.5
23.177	3.8346	6.2	152	11.2	19.2	9.1	0.095	11.8
26.749	3.3301	8.2	138	9.9	20.4	9.7	0.114	11.1
29.559	3.0196	6.2	1312	100.0	211.4	100.0	0.117	36.1
30.977	2.8845	6.2	9	0.2	0.5	0.3	0.135	0.9
31.599	2.8291	6.8	30	1.8	4.3	2.1	0.135	4.2
36.125	2.4844	9.6	143	10.2	20.8	9.8	0.113	11.2
39.564	2.2760	4.9	457	34.6	69.1	32.7	0.11	21.1
43.318	2.0871	6.1	223	16.6	34.2	16.2	0.114	14.5
47.253	1.9220	9.5	41	2.4	6.9	3.3	0.158	4.9
47.665	1.9064	8.4	668	50.5	78.2	37.0	0.086	25.5
48.664	1.8695	8.6	219	16.1	34.3	16.2	0.118	14.2
50.245	1.8143	7.0	28	1.6	2.4	1.1	0.096	4.0
54.108	1.6936	5.1	10	0.4	1.7	0.8	0.302	1.6
56.721	1.6216	7.1	53	3.5	5.9	2.8	0.093	6.3
57.557	1.6000	6.3	116	8.4	29.8	14.1	0.197	10.2
NV15-108CM-E								
23.205	3.8300	6.9	349	14.9	39.4	9.7	0.098	18.3
26.738	3.3315	11.0	35	1.0	3.4	0.8	0.101	4.1
29.557	3.0197	7.2	2303	100.0	405.2	100.0	0.128	47.8
31.612	2.8280	8.7	26	0.8	3.0	0.7	0.126	3.4
36.138	2.4835	7.6	184	7.7	35.8	8.8	0.147	13.0
39.576	2.2753	7.5	332	14.1	60.9	15.0	0.136	17.8
43.310	2.0874	6.5	248	10.5	46.2	11.4	0.138	15.3
47.270	1.9214	10.0	123	4.9	22.9	5.7	0.146	10.2
47.666	1.9063	13.6	708	30.2	99.6	24.6	0.104	26.1
48.662	1.8696	13.3	545	23.2	75.9	18.7	0.103	22.8
54.310	1.6878	5.6	10	0.2	2.4	0.6	0.464	1.4
56.718	1.6217	6.5	53	2.0	7.2	1.8	0.111	6.4
57.555	1.6001	5.4	98	4.0	25.7	6.3	0.2	9.4
60.824	1.5217	6.8	76	3.0	15.5	3.8	0.162	7.9
61.102	1.5154	7.6	60	2.3	19.1	4.7	0.309	6.8
61.489	1.5068	16.7	45	1.2	3.4	0.8	0.086	4.2
63.213	1.4698	7.1	38	1.3	6.6	1.6	0.154	5.0
64.828	1.4370	10.4	28	0.8	3.3	0.8	0.135	3.3
65.804	1.4181	10.9	51	1.7	8.1	2.0	0.146	5.6
69.337	1.3542	6.5	24	0.8	2.5	0.6	0.103	3.6
NV15-109CM								
23.324	3.8108	12.6	109	10.0	22.1	10.6	0.165	9.2
26.825	3.3208	8.8	55	4.8	10.6	5.1	0.165	6.2
29.669	3.0087	10.0	971	100.0	208.5	100.0	0.157	30.8
36.288	2.4736	8.1	163	16.1	40.3	19.3	0.188	12.1
39.738	2.2665	8.8	173	17.1	41.5	19.9	0.183	12.5
43.493	2.0790	9.2	151	14.8	35.2	16.9	0.179	11.5
47.448	1.9146	12.4	63	5.3	12.0	5.8	0.172	6.4
47.727	1.9040	15.0	241	23.5	64.0	30.7	0.205	14.6
48.883	1.8617	11.6	151	14.5	39.1	18.8	0.203	11.3
56.931	1.6161	11.0	35	2.5	6.2	3.0	0.186	4.1
57.795	1.5940	8.7	70	6.4	25.3	12.1	0.35	7.3

Position (°)	D-spacing (Å)	Background Intensity (cps)	Intensity (cps)	Relative Intensity (%)	Area	Area (%)	FWHM (°)	P/N
NV15-110CM								
21.670	4.0976	40.2	71	5.4	7.6	5.3	0.178	3.7
23.013	3.8615	13.8	86	12.6	20.1	14.0	0.202	7.8
26.516	3.3588	13.9	104	15.7	29.5	20.5	0.237	8.8
29.399	3.0357	13.0	588	100.0	144.3	100.0	0.181	23.7
35.958	2.4955	16.0	117	17.6	26.8	18.6	0.192	9.3
39.374	2.2866	12.4	132	20.8	32.2	22.3	0.194	10.4
43.162	2.0943	9.7	134	21.6	31.3	21.7	0.182	10.7
47.116	1.9273	12.1	54	7.3	10.7	7.4	0.184	5.7
47.552	1.9106	14.6	111	16.8	33.8	23.4	0.254	9.1
48.555	1.8735	11.5	116	18.2	29.6	20.5	0.205	9.7
50.968	1.7903	5.7	10	0.7	4.7	3.3	0.934	1.4
57.452	1.6027	8.7	56	8.2	17.7	12.2	0.317	6.3
NV15-112CM								
18.231	4.8623	3.6	6	1.3	0.8	2.5	0.230	1.0
18.518	4.7874	3.8	7	1.8	0.8	2.5	0.171	1.2
23.967	3.7099	5.2	9	2.1	1.4	4.7	0.316	1.3
29.472	3.0283	4.8	183	100.0	29.5	100.0	0.120	13.2
30.483	2.9301	5.6	8	1.4	2.7	9.1	0.946	0.9
31.499	2.8379	5.7	10	2.4	1.2	4.1	0.201	1.4
32.339	2.7661	4.1	8	2.2	0.8	2.7	0.151	1.4
33.039	2.7091	3.4	6	1.5	0.4	1.2	0.099	1.1
33.788	2.6507	3.9	7	1.8	2.2	7.4	0.596	1.2
34.586	2.5914	4.4	9	2.6	1.5	5.1	0.235	1.5
35.000	2.5617	4.8	10	2.9	1.0	3.2	0.132	1.7
35.463	2.5292	4.9	9	2.3	3.4	11.6	0.712	1.4
37.862	2.3743	2.8	7	2.4	0.9	3.2	0.161	1.6
39.459	2.2818	4.0	28	13.5	5.6	18.8	0.167	4.5
43.257	2.0899	5.1	21	8.9	2.6	8.9	0.120	3.5
44.935	2.0156	3.5	9	3.1	0.9	2.9	0.113	1.8
46.090	1.9678	4.4	7	1.5	0.3	1.1	0.091	1.0
46.468	1.9527	3.7	8	2.4	1.2	3.9	0.193	1.5
46.850	1.9376	5.1	10	2.8	1.2	4.0	0.174	1.6
48.603	1.8717	5.6	24	10.3	4.7	15.9	0.185	3.8
51.205	1.7826	4.1	9	2.8	0.5	1.8	0.094	1.6
52.134	1.7530	4.1	10	3.3	1.0	3.5	0.124	1.9
56.031	1.6399	4.5	9	2.5	1.0	3.3	0.156	1.5
57.666	1.5973	5.3	10	2.6	0.9	3.2	0.144	1.5
58.536	1.5756	2.6	8	3.0	1.1	3.6	0.143	1.9
59.403	1.5546	2.6	6	1.9	0.4	1.4	0.091	1.4

Position (°)	D-spacing (Å)	Background Intensity (cps)	Intensity (cps)	Relative Intensity (%)	Area	Area (%)	FWHM (°)	P/N
NV15-114CM								
21.799	4.0738	24.9	90	6.9	48.4	19.7	0.632	6.9
22.045	4.0288	24.9	90	6.9	32.5	13.2	0.425	6.9
24.056	3.6964	15.8	86	7.5	11.1	4.5	0.114	7.6
30.907	2.8909	15.4	957	100.0	245.7	100.0	0.189	30.4
33.407	2.6800	14.2	43	3.1	8.4	3.4	0.209	4.4
35.204	2.5473	18.1	43	2.6	5.6	2.3	0.163	3.8
37.356	2.4053	15.0	97	8.7	18.8	7.7	0.166	8.3
41.108	2.1940	12.2	228	22.9	66.1	26.9	0.221	14.3
43.777	2.0662	15.8	63	5.0	6.5	2.7	0.100	5.9
44.902	2.0171	11.4	153	15.0	42.6	17.3	0.217	11.4
49.164	1.8517	13.9	34	2.1	7.8	3.2	0.329	3.5
50.402	1.8091	19.1	118	10.5	34.8	14.2	0.254	9.1
51.041	1.7879	18.1	134	12.3	48.7	19.8	0.357	10.0
NV15-117CM								
20.734	4.2805	18.4	40	2.7	4.0	2.0	0.134	3.4
21.017	4.2236	18.4	45	3.3	4.8	2.3	0.129	4.0
21.792	4.0751	39.0	86	5.9	16.6	8.2	0.300	5.1
23.148	3.8394	17.9	40	2.7	2.9	1.4	0.093	3.5
24.052	3.6970	14.6	70	6.9	8.1	4.0	0.106	6.6
29.479	3.0276	14.6	231	27.0	35.3	17.4	0.118	14.2
30.907	2.8909	14.8	817	100.0	202.8	100.0	0.183	28.1
33.486	2.6739	11.2	37	3.2	6.4	3.2	0.179	4.2
35.250	2.5440	14.0	41	3.4	8.5	4.2	0.226	4.2
36.065	2.4884	18.0	53	4.4	5.5	2.7	0.113	4.8
37.366	2.4047	12.1	91	9.8	17.9	8.8	0.164	8.3
39.522	2.2783	8.4	54	5.7	9.3	4.6	0.148	6.2
41.106	2.1941	9.1	191	22.7	57.3	28.3	0.228	13.2
43.250	2.0902	15.3	53	4.7	3.6	1.8	0.082	5.2
44.905	2.0169	11.8	105	11.6	30.6	15.1	0.237	9.1
47.274	1.9212	8.7	25	2.0	3.2	1.6	0.144	3.3
47.609	1.9085	12.1	36	3.0	7.7	3.8	0.231	4.0
48.600	1.8718	15.2	47	4.0	6.1	3.0	0.139	4.6
50.405	1.8090	13.6	88	9.3	34.1	16.8	0.390	7.9
50.952	1.7908	10.3	115	13.1	77.1	38.0	0.625	9.8

Position (°)	D-spacing (Å)	Background Intensity (cps)	Intensity (cps)	Relative Intensity (%)	Area	Area (%)	FWHM (°)	P/N
NV15-118CM								
20.642	4.2994	20.4	46	3.5	12.4	6.3	0.410	3.8
23.155	3.8382	21.4	53	4.3	4.2	2.2	0.097	4.3
24.090	3.6912	17.3	66	6.6	8.5	4.3	0.126	6.0
26.730	3.3324	12.6	30	2.4	2.3	1.2	0.094	3.2
29.509	3.0246	15.5	381	49.6	37.7	19.2	0.088	18.7
30.947	2.8872	16.9	754	100.0	196.2	100.0	0.192	26.8
33.419	2.6791	15.1	43	3.8	5.6	2.8	0.144	4.3
35.283	2.5417	15.2	38	3.1	7.5	3.8	0.237	3.7
36.121	2.4847	15.8	58	5.7	10.9	5.6	0.187	5.5
37.397	2.4028	12.8	90	10.5	18.1	9.2	0.169	8.1
39.521	2.2784	10.2	52	5.7	5.8	3.0	0.101	5.8
41.153	2.1917	11.7	179	22.7	52.1	26.5	0.225	12.5
43.823	2.0642	14.1	38	3.2	4.7	2.4	0.141	3.9
44.948	2.0151	13.2	125	15.2	26.3	13.4	0.170	10.0
47.603	1.9087	15.1	38	3.1	4.3	2.2	0.136	3.7
48.593	1.8721	12.4	65	7.1	8.5	4.3	0.117	6.5
49.243	1.8489	15.2	40	3.4	4.6	2.4	0.134	3.9
50.546	1.8043	13.6	100	11.7	51.6	26.3	0.508	8.6
51.050	1.7876	13.4	117	14.1	51.2	26.1	0.420	9.6
57.487	1.6018	12.2	31	2.6	2.3	1.2	0.089	3.4
58.830	1.5684	11.7	38	3.6	5.2	2.6	0.142	4.3
NV15-121CM								
24.054	3.6967	9.4	78	8.5	12.3	5.2	0.130	7.8
29.494	3.0261	16.4	252	29.0	34.9	14.9	0.107	14.8
30.897	2.8918	15.0	826	100.0	234.5	100.0	0.209	28.2
33.443	2.6772	12.6	42	3.6	5.5	2.3	0.135	4.5
35.346	2.5373	13.0	43	3.7	8.7	3.7	0.210	4.6
37.345	2.4060	9.4	120	13.6	25.0	10.7	0.163	10.1
39.486	2.2803	9.5	37	3.4	4.4	1.9	0.115	4.5
41.097	2.1946	8.9	247	29.4	69.2	29.5	0.210	15.2
43.225	2.0913	12.4	39	3.3	3.2	1.4	0.087	4.3
43.764	2.0668	13.9	39	3.1	5.3	2.2	0.152	4.0
44.899	2.0172	12.7	129	14.3	32.9	14.0	0.204	10.2
47.572	1.9099	12.9	30	2.1	3.4	1.5	0.145	3.1
48.603	1.8717	13.6	40	3.3	4.0	1.7	0.108	4.2
49.228	1.8494	16.0	39	2.8	6.3	2.7	0.196	3.7
50.309	1.8122	17.0	85	8.4	45.7	19.5	0.571	7.4
50.904	1.7924	13.3	121	13.3	86.0	36.7	0.679	9.8
53.520	1.7108	6.2	10	0.5	0.9	0.4	0.179	1.2
56.630	1.6240	6.0	29	2.8	3.7	1.6	0.117	4.3
58.839	1.5682	11.1	43	3.9	8.5	3.6	0.192	4.9

Position (°)	D-spacing (Å)	Background Intensity (cps)	Intensity (cps)	Relative Intensity (%)	Area	Area (%)	FWHM (°)	P/N
NV15-122CM								
21.807	4.0722	28.0	98	13.3	44.6	34.7	0.541	7.1
23.149	3.8391	17.5	76	11.1	11.5	8.9	0.142	6.7
24.060	3.6958	16.6	47	5.8	5.7	4.4	0.136	4.4
26.726	3.3329	12.1	30	3.4	3.1	2.4	0.123	3.3
29.511	3.0243	12.1	537	100.0	81.1	63.2	0.112	22.7
30.940	2.8879	11.9	454	84.2	128.4	100.0	0.210	20.7
36.067	2.4883	15.2	97	15.6	23.3	18.1	0.206	8.3
37.402	2.4025	14.2	65	9.7	10.2	7.9	0.145	6.3
39.523	2.2783	10.1	91	15.4	16.4	12.8	0.146	8.5
41.112	2.1938	9.0	124	21.9	38.2	29.7	0.240	10.3
43.298	2.0880	11.8	88	14.5	17.8	13.8	0.168	8.1
44.943	2.0153	12.5	77	12.3	15.7	12.2	0.176	7.3
47.213	1.9235	9.8	34	4.6	7.3	5.7	0.219	4.2
47.650	1.9069	10.1	77	12.8	21.9	17.0	0.236	7.6
48.623	1.8710	14.9	92	14.7	15.8	12.3	0.148	8.0
50.370	1.8102	15.2	55	7.6	14.4	11.2	0.307	5.4
50.961	1.7905	24.8	72	9.0	23.0	17.9	0.415	5.6
57.501	1.6015	17.0	46	5.5	5.0	3.9	0.126	4.3
58.902	1.5667	9.8	31	4.0	3.3	2.6	0.113	3.8
NV15-123CM								
21.705	4.0912	26.0	82	6.5	30.2	21.1	0.458	6.2
23.200	3.8308	17.2	150	15.4	19.0	13.3	0.103	10.8
24.058	3.6962	14.7	33	2.1	2.5	1.8	0.100	3.2
29.556	3.0199	13.9	875	100.0	143.1	100.0	0.120	29.1
30.911	2.8905	12.3	226	24.8	58.7	41.0	0.198	14.2
36.140	2.4834	14.1	157	16.6	31.3	21.8	0.158	11.4
37.403	2.4024	12.2	38	3.0	4.9	3.4	0.137	4.2
39.569	2.2757	9.3	155	16.9	29.2	20.4	0.145	11.7
41.143	2.1922	8.9	61	6.0	17.2	12.0	0.239	6.7
43.327	2.0867	11.9	139	14.8	23.1	16.1	0.131	10.8
44.868	2.0185	13.4	36	2.6	6.3	4.4	0.201	3.8
47.311	1.9198	13.1	59	5.3	8.9	6.2	0.140	6.0
47.666	1.9063	30.3	138	12.5	16.7	11.7	0.112	9.2
48.669	1.8694	15.9	140	14.4	25.8	18.1	0.150	10.5
50.347	1.8109	9.6	31	2.5	6.5	4.6	0.221	3.8
50.909	1.7922	9.6	36	3.1	10.6	7.4	0.341	4.4
56.709	1.6219	10.7	41	3.5	5.5	3.9	0.132	4.7
57.535	1.6006	11.6	58	5.4	12.4	8.6	0.193	6.1

Position (°)	D-spacing (Å)	Background Intensity (cps)	Intensity (cps)	Relative Intensity (%)	Area	Area (%)	FWHM (°)	P/N
NV15-124CM								
21.801	4.0735	30.2	107	10.6	59.4	29.2	0.657	7.4
22.088	4.0212	30.2	81	7.0	29.2	14.4	0.489	5.6
24.122	3.6864	12.8	60	6.5	11.1	5.4	0.170	6.1
30.956	2.8864	12.6	734	100.0	203.7	100.0	0.204	26.6
35.304	2.5403	14.8	45	4.2	9.9	4.9	0.238	4.5
37.397	2.4027	15.5	98	11.4	17.2	8.4	0.150	8.3
41.156	2.1916	12.0	214	28.0	57.3	28.1	0.205	13.8
43.869	2.0621	18.1	45	3.7	3.5	1.7	0.093	4.0
44.914	2.0165	14.1	133	16.5	28	13.7	0.170	10.3
49.293	1.8472	16.2	43	3.7	5.3	2.6	0.143	4.1
50.500	1.8058	14.6	90	10.5	59.9	29.4	0.676	7.9
51.048	1.7877	13.2	118	14.5	72.9	35.8	0.591	9.7
58.893	1.5669	12.7	31	2.5	5.1	2.5	0.201	3.3
NV15-126CM								
23.929	3.7158	16.0	67	7.8	14.1	7.1	0.200	6.2
26.656	3.3414	13.8	43	4.5	7.4	3.7	0.182	4.5
30.843	2.8967	16.7	672	100.0	198.2	100.0	0.218	25.3
33.401	2.6805	11.9	47	5.4	8.3	4.2	0.171	5.1
35.230	2.5454	16.9	43	4.0	7	3.6	0.195	4.0
37.283	2.4099	11.1	96	13.0	24.4	12.3	0.208	8.7
41.006	2.1992	11.3	169	24.1	59.1	29.8	0.319	12.1
43.731	2.0683	13.8	37	3.5	5.3	2.7	0.165	3.8
44.841	2.0196	12.4	127	17.5	29.1	14.7	0.183	10.2
50.312	1.8121	17.8	90	11.0	35.9	18.1	0.423	7.6
50.904	1.7924	14.0	124	16.8	76.8	38.8	0.594	9.9
58.762	1.5701	9.9	38	4.3	6.3	3.2	0.163	4.6
NV15-127CM								
20.655	4.2967	19.9	72	8.9	25.9	13.0	0.423	6.1
21.798	4.0739	19.9	130	18.8	127.9	64.1	0.987	9.7
21.946	4.0468	19.9	118	16.8	106.4	53.4	0.922	9.0
24.018	3.7022	15.8	66	8.6	10.4	5.2	0.150	6.2
30.858	2.8954	15.7	601	100.0	199.3	100.0	0.246	23.9
35.960	2.4954	16.2	44	4.7	10	5.0	0.305	4.2
36.085	2.4871	16.2	40	4.1	10	5.0	0.357	3.8
37.305	2.4085	13.4	104	15.5	22.1	11.1	0.176	8.9
41.014	2.1988	11.6	153	24.2	55.7	27.9	0.335	11.4
43.724	2.0686	16.0	34	3.1	5.1	2.5	0.203	3.1
44.851	2.0192	11.2	111	17.1	39.3	19.7	0.335	9.5
50.300	1.8125	16.2	68	8.9	51.3	25.7	0.841	6.3
50.902	1.7925	16.7	103	14.7	68.5	34.4	0.675	8.5

Position (°)	D-spacing (Å)	Background Intensity (cps)	Intensity (cps)	Relative Intensity (%)	Area	Area (%)	FWHM (°)	P/N
NV15-128CM								
21.789	4.0757	35.1	117	9.8	46.2	20.8	0.480	7.6
22.038	4.0301	27.0	104	9.2	62	27.9	0.684	7.6
23.126	3.8429	16.6	52	4.2	7.3	3.3	0.150	4.9
24.059	3.6959	15.6	84	8.1	9.7	4.4	0.103	7.5
29.474	3.0281	13.8	70	6.7	9.2	4.1	0.118	6.7
30.912	2.8905	14.6	854	100.0	222.4	100.0	0.191	28.7
33.414	2.6795	13.2	45	3.8	7.6	3.4	0.174	4.7
35.254	2.5437	15.6	51	4.2	10.2	4.6	0.208	5.0
37.382	2.4037	15.2	97	9.7	19.6	8.8	0.173	8.3
41.106	2.1941	9.9	224	25.5	69.5	31.2	0.234	14.3
43.809	2.0648	12.9	47	4.1	6.2	2.8	0.131	5.0
44.907	2.0168	10.8	138	15.2	37.4	16.8	0.212	10.8
49.176	1.8513	14.4	40	3.0	6.3	2.8	0.179	4.0
50.498	1.8058	14.1	101	10.4	60	27.0	0.587	8.6
51.042	1.7879	11.5	127	13.8	89.4	40.2	0.658	10.2
58.856	1.5678	14.4	31	2.0	5.3	2.4	0.229	3.0
NV15-129CM								
19.822	4.4753	32.1	71	11.5	7.3	4.1	0.136	4.6
20.568	4.3147	56.0	107	15.1	7	4.0	0.100	4.9
20.864	4.2541	64.0	131	19.8	30.4	17.1	0.385	5.9
21.752	4.0825	74.8	284	61.8	177.5	100.0	0.721	12.4
26.697	3.3364	26.5	124	28.8	14.3	8.1	0.106	8.8
29.492	3.0263	21.5	360	100.0	65.3	36.8	0.139	17.8
36.051	2.4893	30.1	107	22.7	31.3	17.6	0.346	7.4
39.499	2.2796	19.0	83	18.9	11.8	6.7	0.134	7.0
43.221	2.0915	20.6	79	17.3	13.8	7.8	0.171	6.6
47.565	1.9101	16.5	81	19.0	15.2	8.6	0.170	7.2
48.564	1.8731	15.0	87	21.3	14.2	8.0	0.142	7.7
NV15-130CM								
22.006	4.0360	26.6	56	3.3	8.2	3.8	0.202	3.9
24.144	3.6831	12.3	67	6.1	9.3	4.3	0.123	6.7
29.614	3.0141	12.1	272	29.2	38.9	17.8	0.108	15.8
31.008	2.8817	14.0	905	100.0	218.1	100.0	0.177	29.6
33.621	2.6635	10.8	46	4.0	7.7	3.5	0.157	5.2
35.418	2.5323	13.2	39	2.9	5.7	2.6	0.161	4.1
37.454	2.3992	9.2	110	11.3	20.3	9.3	0.146	9.6
39.616	2.2732	13.9	44	3.4	4.2	1.9	0.102	4.5
41.200	2.1893	9.4	244	26.3	60.6	27.8	0.187	15.0
43.865	2.0623	14.7	39	2.7	4.9	2.2	0.145	3.9
44.997	2.0130	9.4	137	14.3	34.6	15.9	0.196	10.9
47.810	1.9009	9.3	27	2.0	3.7	1.7	0.152	3.4
49.307	1.8467	15.5	48	3.6	7.3	3.4	0.163	4.7
50.537	1.8046	27.3	119	10.3	26	11.9	0.205	8.4
51.095	1.7861	19.6	164	16.2	42.7	19.6	0.214	11.3
58.902	1.5667	7.8	36	3.2	8.9	4.1	0.228	4.7

Position (°)	D-spacing (Å)	Background Intensity (cps)	Intensity (cps)	Relative Intensity (%)	Area	Area (%)	FWHM (°)	P/N
NV12-055CMA								
26.848	3.3180	9.6	84	100.0	13.3	94.5	0.129	8.1
29.581	3.0174	14.8	60	60.7	8.2	58.6	0.132	5.8
29.640	3.0116	5.8	80	99.7	14.1	100.0	0.137	8.3
29.690	3.0066	10.9	58	63.3	11.8	84.0	0.181	6.2
29.819	2.9939	10.9	37	35.1	3.8	27.3	0.106	4.3
39.625	2.2727	4.9	19	18.9	2.8	19.7	0.142	3.2
47.668	1.9062	6.5	18	15.5	0.8	5.9	0.061	2.7
50.279	1.8132	2.7	14	15.2	1.5	10.6	0.096	3.0
NV12-057CM								
29.611	3.0144	29.0	57	21.3	0.8	3.1	0.024	3.7
29.740	3.0017	15.6	147	100.0	24.2	92.6	0.133	10.8
29.790	2.9967	11.8	119	81.6	26.1	100.0	0.176	9.8
39.865	2.2595	7.8	23	11.6	1.1	4.3	0.063	3.2
NV12-058CM								
28.388	3.1414	1.5	10	9.5	0.4	1.8	0.040	2.7
29.631	3.0125	10.4	87	85.3	20.2	91.3	0.190	8.2
29.690	3.0065	11.2	101	100.0	20.2	91.7	0.163	8.9
29.799	2.9959	6.4	87	89.8	22.1	100.0	0.198	8.6
NV12-061CMA								
31.051	2.8778	6.8	79	100.0	18.6	100.0	0.187	8.1
41.290	2.1848	6.8	32	34.9	5.2	27.9	0.149	4.5
41.360	2.1812	10.1	31	28.9	3.1	16.7	0.108	3.8
45.082	2.0094	5.7	21	21.2	2.8	14.8	0.131	3.3
51.082	1.7866	11.7	24	17.0	1.2	6.3	0.081	2.5
63.509	1.4636	4.1	15	15.1	0.6	3.3	0.048	2.8
NV12-062CM								
30.932	2.8886	13.2	143	100.0	30.8	96.9	0.171	10.9
30.990	2.8833	16.6	141	95.8	29.7	93.4	0.172	10.5
31.049	2.8780	12.0	140	98.6	31.8	100.0	0.179	10.8
41.138	2.1925	8.7	52	33.4	6.7	21.2	0.113	6.0
41.257	2.1864	8.7	40	24.1	1.8	5.6	0.049	4.9
NV12-063CM								
26.826	3.3207	1.5	10	7.1	0.7	2.8	0.072	2.7
30.873	2.8940	19.1	35	13.4	0.5	1.8	0.025	2.7
31.090	2.8743	19.7	138	100.0	25.2	100.0	0.154	10.1
31.199	2.8645	23.6	94	59.5	20.4	81.0	0.209	7.3
41.290	2.1847	6.4	52	38.5	8.2	32.7	0.131	6.3
41.390	2.1797	6.4	35	24.2	0.7	2.9	0.022	4.8
NV12-067CMA								
30.910	2.8906	13.8	173	100.0	38.9	100.0	0.177	12.1
41.081	2.1954	11.3	58	29.4	8.8	22.6	0.136	6.1

Position (°)	D-spacing (Å)	Background Intensity (cps)	Intensity (cps)	Relative Intensity (%)	Area	Area (%)	FWHM (°)	P/N
NV12-067CMB								
31.051	2.8778	11.8	145	88.2	34.2	100.0	0.186	11.1
31.119	2.8716	13.7	154	92.9	33.6	98.0	0.173	11.3
31.168	2.8672	12.0	163	100.0	34.0	99.4	0.163	11.8
31.274	2.8578	20.2	52	21.1	1.5	4.5	0.041	4.4
41.259	2.1863	26.5	50	15.6	1.2	3.6	0.044	3.3
51.065	1.7871	14.0	30	10.6	1.2	3.5	0.064	2.9
NV12-070CM								
23.168	3.8360	3.3	52	13.5	5.0	8.0	0.087	6.8
29.521	3.0234	13.0	374	100.0	62.6	100.0	0.125	18.7
36.081	2.4873	3.4	54	14.0	7.0	11.2	0.100	6.9
36.133	2.4839	16.4	40	6.5	1.3	2.1	0.048	3.7
39.559	2.2763	3.0	69	18.3	11.5	18.4	0.126	7.9
39.621	2.2729	3.7	53	13.7	11.0	17.6	0.162	6.8
43.271	2.0892	5.9	55	13.6	7.4	11.9	0.109	6.6
43.355	2.0854	18.8	43	6.7	1.1	1.7	0.037	3.7
47.670	1.9062	11.1	72	16.9	9.6	15.3	0.113	7.2
48.640	1.8704	9.1	53	12.2	9.6	15.3	0.157	6.0
48.720	1.8675	7.8	51	12.0	10.5	16.7	0.175	6.1
69.504	1.3513	1.3	9	2.1	0.7	1.1	0.079	2.6
NV12-071CM								
19.728	4.4964	5.3	9	0.5	0.4	0.3	0.099	1.2
23.187	3.8330	5.3	74	9.0	13.6	8.9	0.143	8.0
24.818	3.5846	4.4	9	0.6	0.8	0.5	0.126	1.5
29.552	3.0203	4.8	765	100.0	152.4	100.0	0.145	27.5
31.613	2.8279	4.2	18	1.8	3.0	2.0	0.158	3.3
34.453	2.6010	2.3	8	0.7	0.9	0.6	0.119	2.0
36.138	2.4835	2.9	101	12.9	26.4	17.3	0.194	9.8
38.430	2.3405	3.1	5	0.3	0.4	0.3	0.146	0.9
39.565	2.2759	3.5	152	19.5	32.5	21.3	0.158	12.0
40.842	2.2077	2.7	7	0.6	1.5	1.0	0.247	1.6
41.446	2.1769	2.9	7	0.5	1.1	0.7	0.192	1.6
43.318	2.0871	3.5	141	18.1	28.8	18.9	0.151	11.6
47.260	1.9218	6.8	52	6.0	12.8	8.4	0.204	6.3
47.705	1.9049	15.1	101	11.3	26.0	17.1	0.219	8.5
48.665	1.8695	10.0	135	16.4	31.6	20.8	0.183	10.8
53.426	1.7136	3.2	8	0.6	0.5	0.4	0.095	1.7
56.753	1.6208	7.1	28	2.7	3.6	2.4	0.125	3.9
57.568	1.5997	3.7	52	6.4	20.9	13.7	0.367	6.7
60.831	1.5215	11.0	38	3.6	6.1	4.0	0.163	4.4
62.942	1.4755	3.2	9	0.8	2.8	1.8	0.410	1.9
64.105	1.4515	5.2	10	0.6	2.2	1.5	0.393	1.5
64.943	1.4348	5.2	31	3.4	8.4	5.5	0.234	4.6
66.861	1.3982	1.9	5	0.4	0.8	0.5	0.180	1.4
67.254	1.3910	2.3	6	0.5	1.0	0.6	0.191	1.5
68.865	1.3623	2.7	5	0.3	0.9	0.6	0.347	1.0
72.555	1.3018	1.7	7	0.7	1.1	0.7	0.144	2.0
73.147	1.2928	6.0	19	1.7	3.3	2.2	0.185	3.0
73.591	1.2860	3.3	10	0.9	5.5	3.6	0.699	2.1

Position (°)	D-spacing (Å)	Background Intensity (cps)	Intensity (cps)	Relative Intensity (%)	Area	Area (%)	FWHM (°)	P/N
NV12-095ES								
23.057	3.8542	5.7	89	6.8	23.4	9.4	0.203	8.8
26.597	3.3488	7.6	63	4.5	13.1	5.3	0.171	7.0
29.445	3.0310	10.2	1228	100.0	247.6	100.0	0.147	34.8
31.446	2.8425	6.6	31	2.0	4.3	1.7	0.127	4.4
36.034	2.4904	6.7	139	10.9	29.5	11.9	0.161	11.2
39.484	2.2804	6.3	181	14.3	49.7	20.1	0.206	13.0
41.241	2.1873	4.7	9	0.4	1.4	0.5	0.225	1.4
43.212	2.0920	4.9	159	12.7	42.8	17.3	0.201	12.2
47.171	1.9252	9.3	58	4.0	26.3	10.6	0.459	6.4
47.595	1.9090	25.6	171	11.9	38.8	15.7	0.193	11.1
48.593	1.8721	12.1	179	13.7	45.4	18.3	0.197	12.5
52.250	1.7494	4.1	8	0.3	1.0	0.4	0.195	1.4
54.171	1.6918	3.8	9	0.4	2.2	0.9	0.351	1.7
56.628	1.6241	9.0	32	1.9	5.6	2.3	0.176	4.1
57.498	1.6015	5.4	67	5.1	30.5	12.3	0.420	7.5
NV14-005CMC								
29.551	3.0204	5.6	109	83.9	15.0	57.4	0.105	9.9
29.637	3.0118	7.3	68	49.3	5.4	20.9	0.076	7.4
30.911	2.8905	12.8	124	90.2	26.0	100.0	0.169	10.0
30.980	2.8842	18.8	142	100.0	23.2	89.3	0.136	10.3
39.561	2.2762	13.0	34	17.0	0.9	3.3	0.035	3.6
41.297	2.1844	10.2	31	16.9	0.9	3.4	0.036	3.7
NV16-034CM								
23.367	3.8038	5.5	87	4.2	21.4	5.9	0.190	8.7
26.942	3.3067	5.4	51	2.3	11.3	3.1	0.179	6.4
29.714	3.0041	5.8	1952	100.0	360.6	100.0	0.134	44.0
33.017	2.7108	2.4	9	0.3	1.9	0.5	0.208	2.2
36.304	2.4726	7.0	147	7.2	31.3	8.7	0.162	11.5
39.758	2.2653	6.7	166	8.2	42.3	11.7	0.192	12.4
43.507	2.0784	8.4	148	7.2	35.7	9.9	0.185	11.5
47.499	1.9127	10.6	64	2.7	18.0	5.0	0.244	6.7
47.849	1.8995	23.7	199	9.0	48.1	13.3	0.198	12.4
48.852	1.8628	12.7	172	8.2	39.3	10.9	0.178	12.1
55.994	1.6409	4.8	8	0.2	1.5	0.4	0.386	1.1
56.906	1.6168	7.4	39	1.6	6.4	1.8	0.147	5.1
57.751	1.5951	5.5	78	3.7	24.8	6.9	0.247	8.2

Position (°)	D-spacing (Å)	Background Intensity (cps)	Intensity (cps)	Relative Intensity (%)	Area	Area (%)	FWHM (°)	P/N
NV16-101PR								
23.845	3.7216	16.0	58	7.4	14.1	6.8	0.202	6.0
26.656	3.3291	13.8	42	4.3	7.4	3.9	0.184	4.3
30.741	2.9003	16.7	680	100.0	198.2	100.0	0.220	25.6
33.329	2.6915	11.9	42	5.2	8.3	4.0	0.165	4.9
35.230	2.4351	16.9	39	3.9	7.1	3.5	0.189	3.8
37.192	2.0019	11.1	98	12.8	23.9	11.9	0.208	8.9
41.986	2.1756	11.3	172	23.2	58.7	28.6	0.319	12.3
43.801	2.0573	13.8	35	3.3	5.1	2.4	0.171	4.2
44.752	2.0074	12.4	131	17.7	29.3	13.8	0.183	10.4
50.299	1.7011	17.8	84	10.8	36.2	17.6	0.418	7.7
50.922	1.8213	14.0	126	16.4	78.1	39.1	0.590	9.7
NV16-099PR								
23.402	3.7983	7.4	87	9.3	15.2	9.5	0.138	8.5
25.320	3.5147	7.2	10	0.3	1.5	0.9	0.449	0.9
29.758	2.9999	8.8	860	100.0	160.9	100.0	0.137	29.0
31.063	2.8767	7.9	136	15.0	24.4	15.2	0.138	11.0
33.711	2.6566	4.8	10	0.6	3.8	2.3	0.616	1.6
36.340	2.4702	7.2	106	11.6	21.0	13.1	0.154	9.6
37.521	2.3951	7.2	22	1.7	2.7	1.7	0.132	3.2
39.767	2.2648	6.7	144	16.1	35.9	22.3	0.189	11.4
41.211	2.1887	8.0	26	2.1	1.9	1.2	0.090	3.5
42.400	2.1301	6.2	10	0.4	1.6	1.0	0.362	1.2
42.965	2.1034	5.4	10	0.5	1.5	0.9	0.239	1.5
43.514	2.0781	5.4	131	14.8	32.8	20.4	0.189	11.0
47.468	1.9138	8.0	45	4.3	10.2	6.3	0.198	5.5
47.864	1.8989	10.8	128	13.8	37.7	23.4	0.232	10.4
48.934	1.8599	11.2	122	13.0	31.7	19.7	0.207	10.0
51.013	1.7888	8.9	22	1.5	3.0	1.9	0.166	2.8
53.401	1.7143	5.9	8	0.3	0.5	0.3	0.184	0.8
55.643	1.6505	3.5	9	0.6	2.2	1.4	0.338	1.8
56.955	1.6155	8.4	33	2.9	5.8	3.6	0.169	4.3

Position (°)	D-spacing (Å)	Background Intensity (cps)	Intensity (cps)	Relative Intensity (%)	Area	Area (%)	FWHM (°)	P/N
ANV14-012PR								
18.215	4.8663	4.4	9	1.1	1.3	1.3	0.203	1.5
18.699	4.7415	3.3	7	0.9	0.9	0.9	0.167	1.4
21.016	4.2237	8.2	39	7.1	4.4	4.3	0.103	4.9
23.311	3.8128	13.7	45	7.2	3.3	3.3	0.091	4.7
26.807	3.3230	7.1	216	48.4	34.4	34.1	0.119	14.2
29.684	3.0072	5.1	437	100.0	100.8	100.0	0.169	20.7
30.981	2.8842	6.4	35	6.6	6.0	6.0	0.153	4.8
33.173	2.6984	4.3	9	1.1	1.6	1.6	0.244	1.6
33.443	2.6773	3.3	9	1.3	4.0	3.9	0.595	1.9
33.840	2.6468	3.5	10	1.5	2.9	2.8	0.373	2.1
36.252	2.4760	9.0	66	13.2	11.8	11.7	0.149	7.0
38.013	2.3652	4.9	10	1.2	0.5	0.5	0.092	1.6
39.673	2.2700	6.0	117	25.7	25.3	25.1	0.165	10.3
40.413	2.2301	4.3	10	1.3	2.7	2.7	0.401	1.8
43.460	2.0805	6.1	78	16.6	16.1	15.9	0.162	8.1
46.008	1.9711	4.9	10	1.2	0.5	0.5	0.083	1.6
47.455	1.9143	9.2	32	5.3	4.7	4.7	0.149	4.0
47.811	1.9009	8.0	72	14.8	22.7	22.5	0.301	7.5
48.808	1.8644	9.8	91	18.8	20.7	20.6	0.184	8.5
50.270	1.8135	5.8	20	3.3	4.6	4.5	0.233	3.2
52.251	1.7493	3.9	8	0.9	0.6	0.6	0.098	1.4
52.607	1.7383	3.9	7	0.7	0.6	0.6	0.129	1.2
53.186	1.7207	3.7	6	0.5	0.5	0.5	0.169	0.9
55.526	1.6537	4.1	7	0.7	1.6	1.6	0.482	1.1
56.909	1.6167	5.5	27	5.0	3.0	3.0	0.102	4.1
57.830	1.5931	7.7	34	6.1	6.8	6.7	0.186	4.5
60.050	1.5394	4.3	16	2.7	3.4	3.4	0.209	2.9
64.051	1.4526	4.7	8	0.8	2.0	2.0	0.519	1.2
64.956	1.4345	5.4	26	4.8	5.9	5.9	0.208	4.0
68.879	1.3621	2.4	8	1.3	2.1	2.1	0.325	2.0
69.179	1.3569	2.2	7	1.1	1.1	1.1	0.165	1.8
79.225	1.2081	3.2	9	1.3	0.5	0.5	0.081	1.9
ANV14-014PR								
24.123	3.6864	2.2	33	7.5	3.9	5.4	0.091	5.4
30.999	2.8826	4.8	418	100.0	72.2	100.0	0.126	20.2
35.356	2.5367	6.7	20	3.2	1.2	1.6	0.073	3.0
37.422	2.4012	2.4	44	10.1	7.4	10.3	0.129	6.3
41.181	2.1903	2.8	114	26.9	20.4	28.2	0.132	10.4
41.295	2.1845	3.3	76	17.6	13.9	19.2	0.138	8.3
43.876	2.0618	4.8	17	2.9	1.6	2.2	0.092	3.0
44.981	2.0137	3.4	85	19.7	10.5	14.5	0.093	8.9
49.305	1.8467	5.8	19	3.2	1.6	2.2	0.088	3.0
50.553	1.8040	21.0	50	7.0	4.2	5.9	0.105	4.1
51.120	1.7853	9.6	78	16.6	11.7	16.2	0.124	7.7
51.237	1.7815	8.1	57	11.8	7.8	10.7	0.115	6.5
59.844	1.5442	11.4	33	5.2	1.5	2.1	0.059	3.8
67.438	1.3876	7.5	26	4.5	2.2	3.1	0.086	3.6

Position (°)	D-spacing (Å)	Background Intensity (cps)	Intensity (cps)	Relative Intensity (%)	Area	Area (%)	FWHM (°)	P/N
ANV14-018PR								
26.830	3.3202	10.5	91	62.1	16.6	75.8	0.149	8.4
26.890	3.3129	9.5	139	100.0	21.9	100.0	0.122	11.0
29.720	3.0036	13.0	108	73.4	18.6	84.8	0.141	9.1
29.769	2.9988	8.6	114	81.4	21.0	96.1	0.144	9.9
29.819	2.9938	7.6	84	59.0	21.4	97.6	0.202	8.3
ANV14-021PR								
22.059	4.0263	2.0	10	2.9	1.0	1.8	0.090	2.5
26.709	3.3349	3.2	46	15.3	5.6	10.3	0.094	6.3
26.757	3.3291	13.0	28	5.4	0.6	1.0	0.032	2.8
30.970	2.8851	14.9	295	100.0	54.3	100.0	0.140	16.3
37.430	2.4007	3.4	44	14.5	5.5	10.2	0.098	6.1
41.141	2.1923	8.3	82	26.3	13.7	25.2	0.134	8.1
44.912	2.0166	19.3	37	6.3	0.5	0.9	0.024	2.9
44.961	2.0145	5.9	52	16.4	8.1	15.0	0.128	6.4
45.098	2.0087	9.8	39	10.4	1.6	2.9	0.046	4.7
51.009	1.7890	23.2	41	6.4	0.7	1.3	0.035	2.8
ANV14-022PR								
30.982	2.8841	8.1	351	100.0	64.9	100.0	0.137	18.3
37.403	2.4024	2.2	50	13.9	7.2	11.1	0.109	6.8
37.527	2.3947	2.2	29	7.8	5.2	8.0	0.140	5.0
41.179	2.1904	3.3	90	25.3	19.4	29.8	0.161	9.1
43.881	2.0616	3.9	18	4.1	1.6	2.5	0.099	3.3
44.961	2.0145	3.3	52	14.2	9.2	14.2	0.137	6.8
45.076	2.0096	8.6	34	7.4	6.4	9.8	0.181	4.4
50.383	1.8097	9.6	25	4.5	4.6	7.0	0.214	3.1
50.511	1.8054	9.6	46	10.6	6.3	9.8	0.126	5.4
50.614	1.8020	15.0	41	7.6	2.0	3.1	0.065	4.1
51.046	1.7878	10.9	63	15.2	10.9	16.9	0.152	6.6
51.174	1.7836	9.8	52	12.3	8.6	13.3	0.147	5.9
ANV14-057PR								
24.051	3.6972	9.6	55	9.0	5.7	3.6	0.091	6.1
26.708	3.3350	7.6	93	16.9	14.7	9.3	0.124	8.9
30.896	2.8919	6.9	513	100.0	156.8	100.0	0.224	22.3
37.315	2.4079	6.7	72	12.9	13.9	8.8	0.154	7.7
41.059	2.1965	5.3	126	23.8	42.4	27.1	0.254	10.8
44.898	2.0172	7.0	82	14.8	22.3	14.2	0.214	8.3
50.300	1.8125	12.0	75	12.4	34.8	22.2	0.469	7.3
50.901	1.7925	8.4	99	17.9	46.8	29.9	0.439	9.1
59.657	1.5486	10.7	36	5.0	8.2	5.3	0.235	4.2
67.306	1.3900	9.8	42	6.4	7.4	4.7	0.166	5.0

Position (°)	D-spacing (Å)	Background Intensity (cps)	Intensity (cps)	Relative Intensity (%)	Area	Area (%)	FWHM (°)	P/N
ANV14-058PR								
20.949	4.2370	6.0	27	2.3	3.4	2.1	0.117	4.0
23.189	3.8327	4.8	82	8.4	13.6	8.3	0.127	8.5
26.706	3.3353	4.4	151	15.9	26.6	16.2	0.131	11.9
29.551	3.0204	4.5	925	100.0	164.0	100.0	0.129	30.3
31.604	2.8287	3.9	27	2.5	4.0	2.4	0.124	4.4
36.123	2.4845	4.0	106	11.1	22.6	13.8	0.160	9.9
39.568	2.2758	3.0	133	14.1	36.0	22.0	0.200	11.3
43.318	2.0870	4.2	110	11.5	29.1	17.7	0.198	10.1
47.704	1.9049	11.1	109	10.6	33.7	20.6	0.249	9.4
48.672	1.8692	10.7	131	13.1	29.3	17.9	0.176	10.5
57.601	1.5989	3.7	54	5.5	19.4	11.8	0.328	6.8
60.937	1.5191	11.3	32	2.2	7.3	4.4	0.254	3.7
64.931	1.4350	5.9	38	3.5	8.2	5.0	0.184	5.2
65.852	1.4171	4.4	17	1.4	4.1	2.5	0.235	3.0
NV12-098ES								
24.228	3.6706	5.6	17	10.1	0.6	2.2	0.044	2.8
26.791	3.3249	12.0	41	25.6	2.3	8.5	0.066	4.5
31.012	2.8813	9.7	123	100.0	26.6	100.0	0.169	10.2
41.223	2.1882	16.4	43	23.5	3.0	11.4	0.097	4.1
45.002	2.0128	12.6	30	15.4	0.7	2.7	0.035	3.2
NV12-114SR								
24.187	3.6767	11.3	26	5.5	1.1	1.8	0.061	2.9
30.825	2.8984	23.3	39	5.8	0.6	1.0	0.033	2.5
31.011	2.8814	19.2	289	100.0	58.9	100.0	0.158	15.9
37.422	2.4012	10.8	36	9.3	2.6	4.4	0.087	4.2
37.472	2.3981	19.0	40	7.8	1.7	2.8	0.068	3.3
41.229	2.1878	8.6	93	31.3	16.0	27.1	0.137	8.7
44.993	2.0132	17.0	49	11.9	3.6	6.0	0.094	4.6
51.181	1.7834	11.0	58	17.4	10.0	16.9	0.153	6.2
NV16-104PR								
23.410	3.7969	10.8	51	4.3	4.1	1.9	0.088	5.6
24.298	3.6602	10.0	75	6.9	18.1	8.3	0.201	7.5
26.933	3.3077	10.7	74	6.7	11.3	5.1	0.129	7.4
29.694	3.0062	11.7	45	3.5	6.2	2.8	0.134	5.0
30.556	2.9233	14.6	31	1.7	2.5	1.1	0.110	2.9
31.151	2.8688	10.6	950	100.0	219.7	100.0	0.169	30.5
33.721	2.6558	12.4	44	3.4	7.3	3.3	0.166	4.8
35.539	2.5240	14.4	49	3.7	6.9	3.2	0.145	5.0
37.595	2.3906	7.9	113	11.2	33.1	15.1	0.227	9.9
41.338	2.1823	11.5	241	24.4	63.6	28.9	0.200	14.8
44.047	2.0542	11.5	38	2.8	5.7	2.6	0.155	4.3
45.114	2.0081	13.0	156	15.2	31.4	14.3	0.158	11.4
47.472	1.9137	9.8	66	6.0	11.3	5.1	0.145	6.9
48.827	1.8637	12.0	59	5.0	9.0	4.1	0.138	6.1
50.692	1.7994	12.2	114	10.8	62.2	28.3	0.519	9.5
51.203	1.7826	11.9	150	14.7	73.9	33.6	0.454	11.3
59.126	1.5613	14.5	49	3.7	6.0	2.7	0.125	4.9

Position (°)	D-spacing (Å)	Background Intensity (cps)	Intensity (cps)	Relative Intensity (%)	Area	Area (%)	FWHM (°)	P/N
NV12-116SR								
19.304	4.5942	3.9	10	0.5	0.9	0.4	0.105	1.9
19.783	4.4840	5.2	9	0.3	2.5	1.3	0.570	1.3
20.250	4.3817	5.2	10	0.4	2.5	1.3	0.452	1.5
20.555	4.3175	5.2	10	0.4	2.5	1.3	0.452	1.5
23.371	3.8033	5.1	9	0.3	0.7	0.4	0.138	1.3
23.724	3.7474	4.7	10	0.5	1.6	0.8	0.218	1.7
24.150	3.6822	4.7	62	5.0	9.0	4.5	0.114	7.3
28.580	3.1208	3.9	9	0.4	4.2	2.1	0.707	1.7
31.045	2.8784	4.5	1146	100.0	198.8	100.0	0.126	33.7
33.612	2.6642	4.9	65	5.3	10.5	5.3	0.126	7.5
35.412	2.5327	5.1	85	7.0	9.5	4.8	0.086	8.7
37.464	2.3986	5.9	126	10.5	18.0	9.0	0.108	10.7
40.189	2.2420	4.3	10	0.5	1.5	0.8	0.194	1.8
41.221	2.1883	4.5	300	25.9	56.4	28.4	0.138	17.1
43.912	2.0602	7.3	44	3.2	5.5	2.8	0.108	5.5
45.020	2.0120	6.5	166	14.0	29.9	15.1	0.136	12.4
49.369	1.8445	7.1	36	2.5	6.6	3.3	0.165	4.8
50.608	1.8022	8.6	142	11.7	31.4	15.8	0.170	11.2
51.154	1.7842	26.7	182	13.6	30.3	15.3	0.141	11.5
55.082	1.6659	3.4	8	0.4	1.0	0.5	0.153	1.6
56.488	1.6278	3.4	8	0.4	0.7	0.3	0.108	1.6
58.977	1.5648	5.7	34	2.5	6.2	3.1	0.159	4.8
59.905	1.5428	4.0	96	8.1	20.0	10.0	0.157	9.4
63.509	1.4637	5.8	52	4.0	11.9	6.0	0.186	6.4
66.162	1.4113	5.6	22	1.4	3.8	1.9	0.167	3.5
66.818	1.3990	3.8	8	0.4	1.3	0.7	0.231	1.5
67.481	1.3868	4.5	74	6.1	14.4	7.2	0.149	8.1
68.466	1.3693	4.4	10	0.5	0.7	0.3	0.090	1.8
70.567	1.3336	5.8	24	1.6	4.8	2.4	0.191	3.7
74.784	1.2685	3.6	21	1.5	5.3	2.7	0.219	3.8
77.056	1.2366	7.3	23	1.4	3.0	1.5	0.138	3.3

Position (°)	D-spacing (Å)	Background Intensity (cps)	Intensity (cps)	Relative Intensity (%)	Area	Area (%)	FWHM (°)	P/N
NV12-119SR								
17.808	4.9766	5.0	9	0.6	1.0	0.7	0.172	1.3
24.200	3.6747	5.1	48	6.3	10.2	7.0	0.171	6.2
26.762	3.3285	7.7	38	4.5	5.1	3.6	0.122	4.9
28.759	3.1017	5.6	9	0.5	1.0	0.7	0.217	1.1
31.059	2.8771	7.9	685	100.0	144.6	100.0	0.154	25.9
33.602	2.6649	4.8	47	6.2	9.3	6.4	0.159	6.2
35.394	2.5340	9.7	37	4.0	4.4	3.0	0.116	4.5
37.502	2.3962	5.8	79	10.8	17.8	12.3	0.176	8.2
39.448	2.2824	5.3	9	0.6	0.9	0.6	0.181	1.2
41.224	2.1881	5.9	173	24.7	42.2	29.2	0.182	12.7
43.918	2.0599	7.5	31	3.5	3.7	2.6	0.115	4.2
45.058	2.0104	7.6	105	14.4	19.3	13.4	0.143	9.5
46.351	1.9573	3.6	7	0.5	0.5	0.3	0.105	1.3
46.770	1.9408	3.8	7	0.5	0.5	0.4	0.120	1.2
47.728	1.9040	3.7	7	0.5	2.8	1.9	0.709	1.2
48.274	1.8837	4.1	8	0.6	0.9	0.6	0.169	1.4
49.351	1.8451	4.7	32	4.0	5.8	4.0	0.154	4.8
50.595	1.8026	28.9	86	8.4	12.5	8.7	0.159	6.2
51.146	1.7845	5.8	146	20.7	40.9	28.3	0.211	11.6
52.589	1.7389	4.6	8	0.5	0.6	0.4	0.125	1.2
54.159	1.6921	3.5	8	0.7	0.7	0.5	0.115	1.6
54.609	1.6792	3.8	6	0.3	0.8	0.6	0.314	0.9
55.168	1.6635	3.7	9	0.8	1.9	1.3	0.253	1.8
55.630	1.6508	4.1	10	0.9	0.7	0.5	0.097	1.9
57.765	1.5948	3.5	9	0.8	0.7	0.4	0.085	1.8
58.969	1.5650	6.6	33	3.9	5.6	3.9	0.153	4.6
59.900	1.5429	6.2	53	6.9	10.5	7.2	0.161	6.4
63.491	1.4640	5.3	41	5.3	9.0	6.2	0.181	5.6
64.480	1.4439	6.5	26	2.9	3.8	2.6	0.140	3.8
65.190	1.4299	6.5	20	2.0	3.1	2.2	0.167	3.0
66.680	1.4015	4.9	10	0.8	0.5	0.4	0.090	1.6
67.452	1.3874	6.3	45	5.7	9.4	6.5	0.175	5.8
68.118	1.3754	3.8	10	0.9	2.8	1.9	0.381	2.0
71.187	1.3235	2.3	8	0.8	1.6	1.1	0.208	2.0
73.107	1.2934	4.1	9	0.7	3.0	2.1	0.525	1.6
73.793	1.2830	3.8	8	0.6	0.4	0.3	0.078	1.5
74.256	1.2762	4.1	9	0.7	5.6	3.9	0.975	1.6
NV12-120SR								
30.941	2.8878	12.8	248	100.0	46.3	100.0	0.142	14.9
31.038	2.8790	9.6	135	53.3	20.6	44.4	0.118	10.8
41.131	2.1929	5.8	96	38.3	14.1	30.4	0.113	9.2
44.905	2.0169	16.0	37	8.9	1.1	2.4	0.044	3.5
44.969	2.0142	4.5	53	20.6	7.8	16.8	0.116	6.7
51.012	1.7889	19.2	42	9.7	2.6	5.5	0.095	3.5
79.665	1.2026	1.9	10	3.5	0.6	1.3	0.062	2.6

Position (°)	D-spacing (Å)	Background Intensity (cps)	Intensity (cps)	Relative Intensity (%)	Area	Area (%)	FWHM (°)	P/N
NV12-122SR								
22.708	3.9127	10.1	24	10.0	4.0	9.2	0.211	2.8
26.296	3.3865	7.0	25	13.0	4.3	9.7	0.170	3.6
29.098	3.0664	9.8	148	100.0	44.0	100.0	0.230	11.4
30.357	2.9420	12.5	121	78.5	30.0	68.0	0.199	9.9
33.525	2.6709	6.9	10	2.3	1.3	2.9	0.346	1.0
35.680	2.5143	8.3	32	17.2	5.6	12.8	0.171	4.2
38.599	2.3307	4.8	10	3.7	1.4	3.1	0.189	1.6
39.116	2.3010	8.0	29	15.2	6.1	13.8	0.210	3.9
40.590	2.2208	9.4	37	20.0	5.5	12.6	0.145	4.5
41.499	2.1742	4.5	10	3.9	1.0	2.2	0.126	1.7
42.932	2.1049	10.4	30	14.2	3.9	8.9	0.145	3.6
47.209	1.9237	7.7	52	32.1	12.1	27.4	0.196	6.1
48.211	1.8860	10.5	40	21.3	8.8	19.9	0.215	4.7
49.748	1.8313	11.4	25	9.9	2.8	6.4	0.150	2.7
52.315	1.7473	3.1	8	3.5	0.6	1.3	0.086	1.7
53.385	1.7148	4.5	6	1.1	0.8	1.8	0.450	0.6
54.656	1.6779	3.8	7	2.3	0.3	0.8	0.090	1.2
ANV14-056PR								
23.233	3.8254	11.0	33	7.2	1.6	3.4	0.062	3.8
26.739	3.3313	5.2	88	27.3	12.3	26.4	0.107	8.8
29.611	3.0144	17.3	321	100.0	46.5	100.0	0.111	17.0
36.173	2.4812	11.2	39	9.2	2.3	5.0	0.071	4.5
39.650	2.2712	4.6	59	17.9	9.9	21.3	0.132	7.1
39.719	2.2675	6.8	53	15.2	8.6	18.4	0.134	6.4
43.353	2.0855	13.7	36	7.3	1.1	2.3	0.040	3.7
43.402	2.0832	4.8	52	15.5	7.0	15.1	0.108	6.5
48.760	1.8661	8.1	53	14.8	7.6	16.4	0.123	6.2
48.825	1.8638	19.6	40	6.7	0.8	1.6	0.031	3.2

Position (°)	D-spacing (Å)	Background Intensity (cps)	Intensity (cps)	Relative Intensity (%)	Area	Area (%)	FWHM (°)	P/N
NV12-123SR								
20.537	4.3212	14.3	43	3.7	5.7	3.9	0.142	4.4
21.659	4.0998	21.5	110	11.5	78.6	54.4	0.755	8.4
21.944	4.0472	17.6	113	12.4	85.6	59.3	0.763	9.0
24.157	3.6813	10.6	56	5.9	8.4	5.8	0.133	6.1
31.044	2.8785	7.9	779	100.0	144.5	100.0	0.135	27.6
33.611	2.6642	8.1	42	4.4	5.5	3.8	0.118	5.2
35.419	2.5323	12.2	45	4.3	5.0	3.5	0.11	4.9
36.058	2.4889	12.3	31	2.4	5.3	3.7	0.205	3.4
37.467	2.3985	6.4	108	13.2	15.4	10.7	0.109	9.8
39.523	2.2782	5.6	10	0.6	0.7	0.5	0.114	1.4
41.217	2.1885	7.2	223	28.0	45.1	31.2	0.151	14.4
45.021	2.0120	10.2	120	14.2	20.1	13.9	0.132	10.0
47.908	1.8973	4.2	9	0.6	0.9	0.6	0.132	1.6
48.499	1.8755	5.5	10	0.6	1.2	0.8	0.198	1.4
49.349	1.8452	9.7	44	4.4	4.4	3.0	0.092	5.2
50.592	1.8027	7.2	101	12.2	27.6	19.1	0.213	9.3
51.148	1.7844	12.1	142	16.8	25.9	17.9	0.144	10.9
52.186	1.7514	4.1	8	0.5	2.0	1.4	0.436	1.4
52.869	1.7303	5.4	9	0.5	0.7	0.5	0.132	1.2
58.967	1.5651	7.9	24	2.1	4.0	2.8	0.181	3.3
59.907	1.5428	9.0	59	6.5	9.1	6.3	0.131	6.5
61.276	1.5115	5.3	9	0.5	1.8	1.3	0.412	1.2
62.520	1.4844	5.3	10	0.6	1.3	0.9	0.19	1.5
63.620	1.4614	10.0	37	3.5	6.2	4.3	0.166	4.4
67.459	1.3872	6.9	50	5.6	11.1	7.6	0.185	6.1
68.472	1.3692	5.5	10	0.6	1.2	0.9	0.199	1.4
71.733	1.3147	4.3	10	0.7	1.1	0.8	0.139	1.8
73.516	1.2872	4.8	10	0.7	0.5	0.4	0.083	1.7
77.002	1.2374	7.9	21	1.7	3.3	2.2	0.179	2.9
NV12-131SR								
31.069	2.8762	9.6	179	100.0	42.5	100.0	0.181	12.7
37.509	2.3958	9.0	29	11.8	0.9	2.1	0.039	3.7
41.229	2.1878	7.1	62	32.4	10.6	25.0	0.14	7.0
NV12-133SR								
21.716	4.0891	8.6	20	15.9	1.0	6.7	0.075	2.6
26.566	3.3526	8.4	23	20.3	2.0	13.2	0.098	3.0
26.640	3.3434	6.3	23	23.3	3.2	21.4	0.14	3.5
26.718	3.3339	6.3	24	24.7	3.1	20.8	0.128	3.6
30.961	2.8860	10.9	58	65.7	13.0	86.3	0.199	6.2
31.021	2.8805	7.4	79	100.0	15.0	100.0	0.151	8.1
31.098	2.8735	12.9	63	70.0	11.5	76.6	0.166	6.3
33.565	2.6678	2.1	10	11.1	0.7	4.4	0.071	2.5
37.413	2.4018	3.3	13	13.5	1.5	9.7	0.109	2.7
37.472	2.3981	3.2	12	12.3	1.6	10.4	0.129	2.5
41.160	2.1914	4.3	25	28.9	4.5	30.0	0.157	4.1
41.239	2.1873	5.2	33	38.9	4.0	26.9	0.105	4.8
44.999	2.0129	4.1	16	16.6	1.6	10.8	0.098	3.0
45.079	2.0095	2.9	15	16.9	2.1	13.9	0.124	3.1
51.171	1.7837	7.3	18	15.0	1.5	10.1	0.102	2.5

Position (°)	D-spacing (Å)	Background Intensity (cps)	Intensity (cps)	Relative Intensity (%)	Area	Area (%)	FWHM (°)	P/N
NV15-135SR								
20.926	4.2417	5.8	10	0.4	0.8	0.4	0.136	1.3
24.169	3.6794	5.6	55	4.6	6.1	3.3	0.089	6.7
31.067	2.8763	5.5	1068	100.0	186.6	100.0	0.127	32.5
33.656	2.6608	5.3	64	5.5	9.3	5.0	0.115	7.3
35.421	2.5321	5.6	48	4.0	10.3	5.5	0.176	6.1
37.470	2.3983	4.3	110	9.9	20.9	11.2	0.143	10.1
41.256	2.1865	5.6	328	30.3	58.1	31.1	0.130	17.8
42.611	2.1200	4.7	9	0.4	0.5	0.3	0.092	1.5
43.909	2.0603	5.0	52	4.4	7.9	4.2	0.122	6.5
45.063	2.0102	4.7	156	14.2	31.4	16.8	0.150	12.1
49.378	1.8442	5.6	56	4.7	9.1	4.9	0.131	6.7
50.655	1.8006	11.1	150	13.1	29.2	15.7	0.152	11.3
51.164	1.7839	23.3	160	12.9	30.6	16.4	0.162	10.8
59.009	1.5641	5.2	39	3.2	7.0	3.8	0.150	5.4
59.946	1.5419	3.6	63	5.6	19.7	10.6	0.240	7.5
63.556	1.4627	4.9	50	4.2	10.3	5.5	0.166	6.4
65.256	1.4286	7.1	26	1.8	4.6	2.5	0.176	3.7
67.492	1.3866	4.1	61	5.4	14.5	7.7	0.183	7.3
70.605	1.3329	4.6	22	1.6	6.1	3.3	0.254	3.7
77.087	1.2362	7.2	26	1.8	4.4	2.4	0.169	3.7
78.316	1.2199	3.4	8	0.4	0.7	0.4	0.112	1.6
NV15-137SR								
19.104	4.6420	8.4	94	34.3	15.8	17.3	0.133	8.8
20.421	4.3455	10.7	36	10.1	2.9	3.2	0.099	4.2
22.413	3.9635	12.7	262	100.0	91.2	100.0	0.311	15.4
22.752	3.9052	14.3	163	59.6	69.4	76.0	0.397	11.6
25.061	3.5504	16.9	48	12.5	4.8	5.3	0.111	4.5
26.058	3.4168	13.9	114	40.1	38.4	42.1	0.326	9.4
26.249	3.3924	13.9	58	17.7	19.1	21.0	0.369	5.8
26.888	3.3132	12.2	69	22.8	16.2	17.7	0.206	6.8
28.187	3.1634	13.8	96	33.0	26.5	29.1	0.233	8.4
28.582	3.1206	14.8	64	19.7	15.1	16.5	0.222	6.1
30.055	2.9708	15.7	132	46.7	52.5	57.5	0.383	10.1
30.954	2.8866	14.2	49	14.0	10.2	11.2	0.212	5.0
32.004	2.7942	16.8	108	36.6	16.1	17.6	0.127	8.8
32.716	2.7351	13.2	51	15.2	9.9	10.8	0.188	5.3
35.430	2.5315	18.5	38	7.8	5.1	5.6	0.190	3.2
37.086	2.4222	17.6	41	9.4	8.0	8.8	0.249	3.7

X-RAY DIFFRACTION ANALYSES

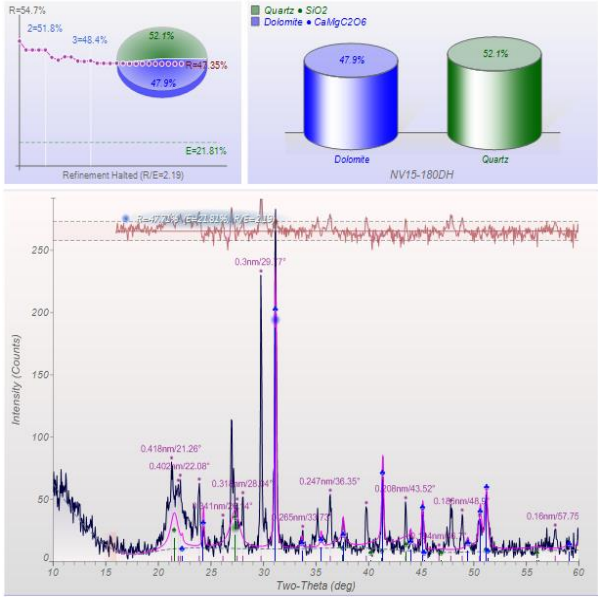

NV15-180DH

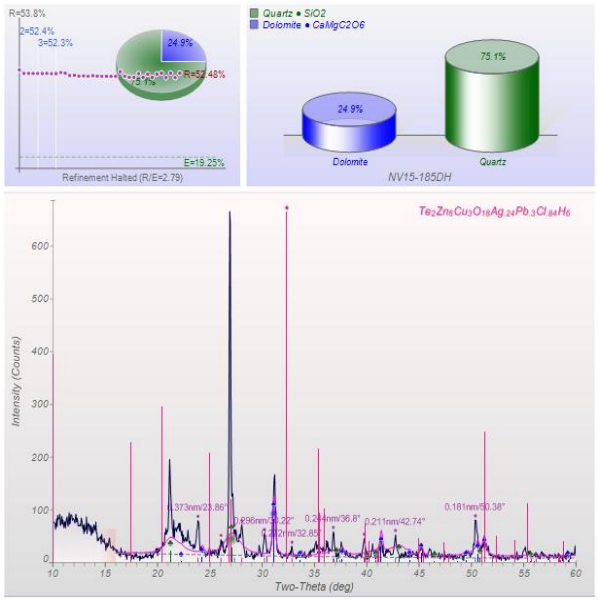

NV15-185DH

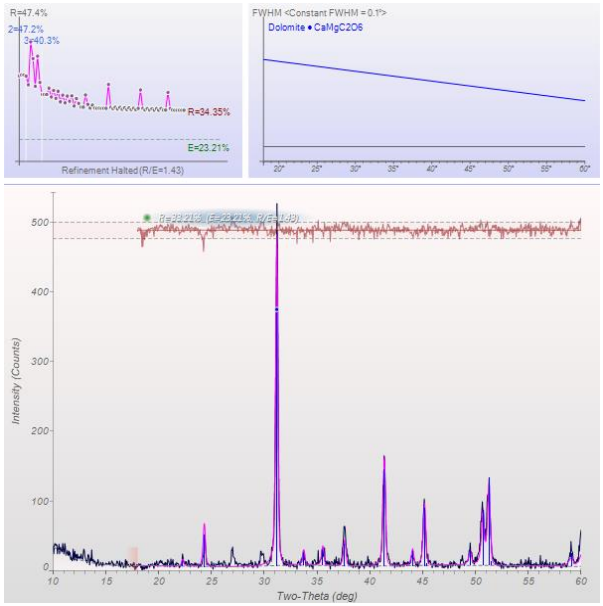

NV15-186DH

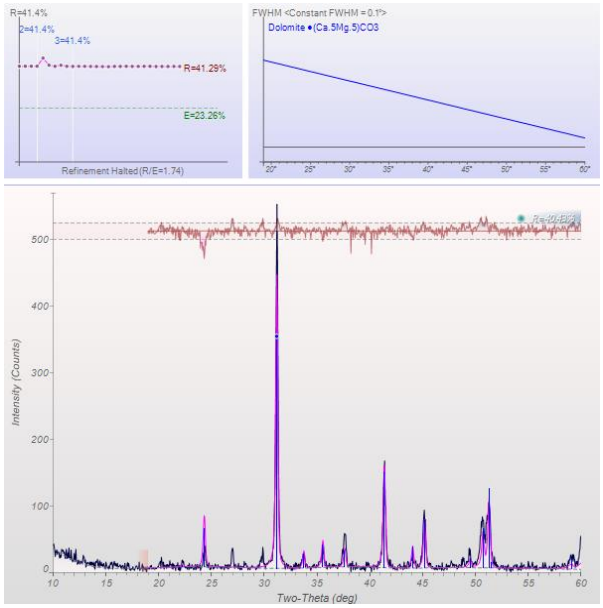

NV15-197DH

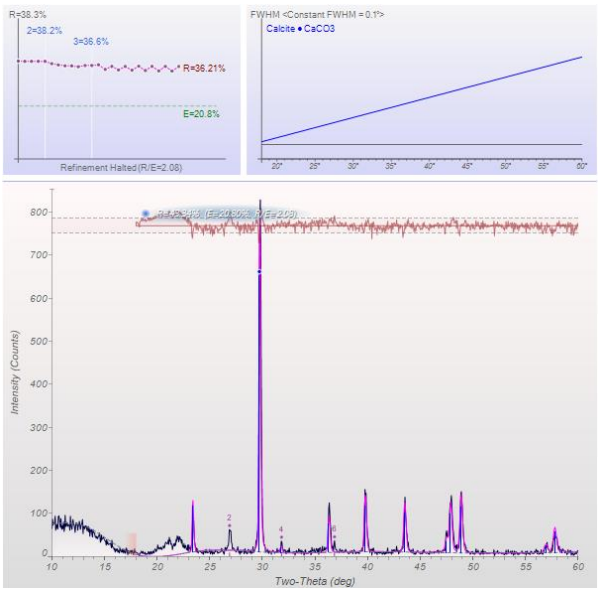

NV15-182DH

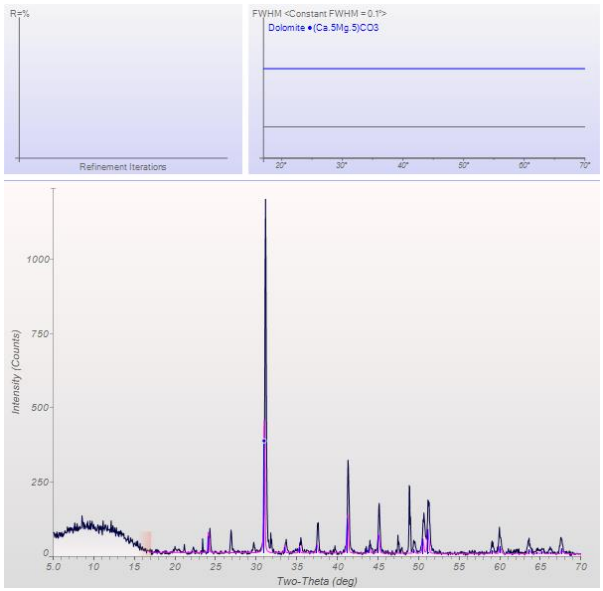

NV15-204DH

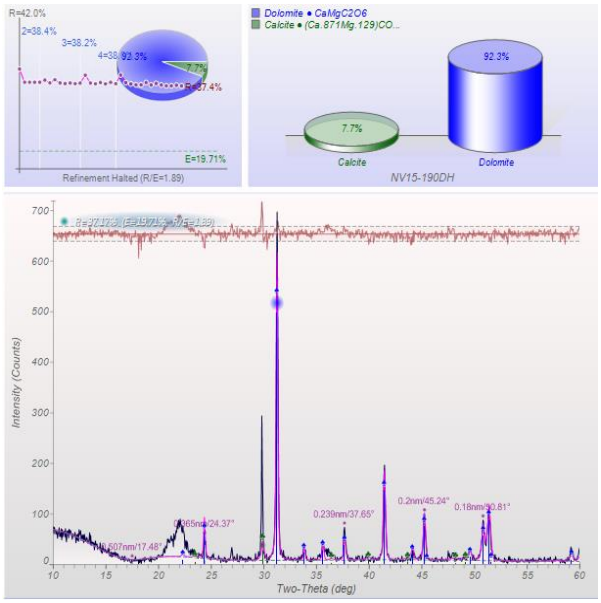

NV15-190DH

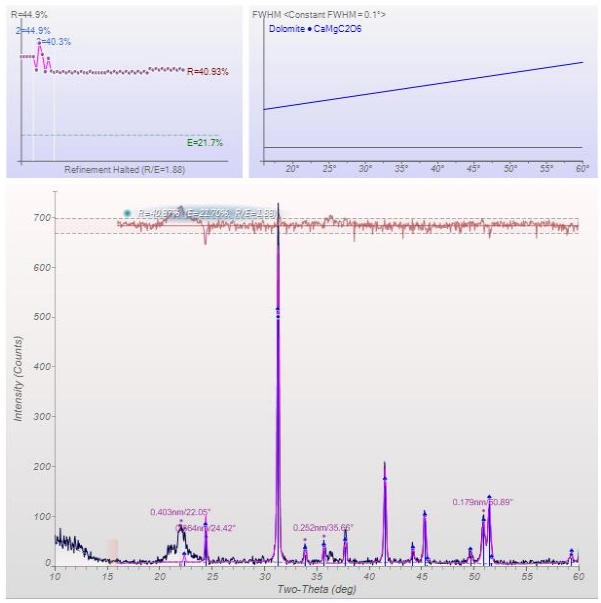

NV15-195DH

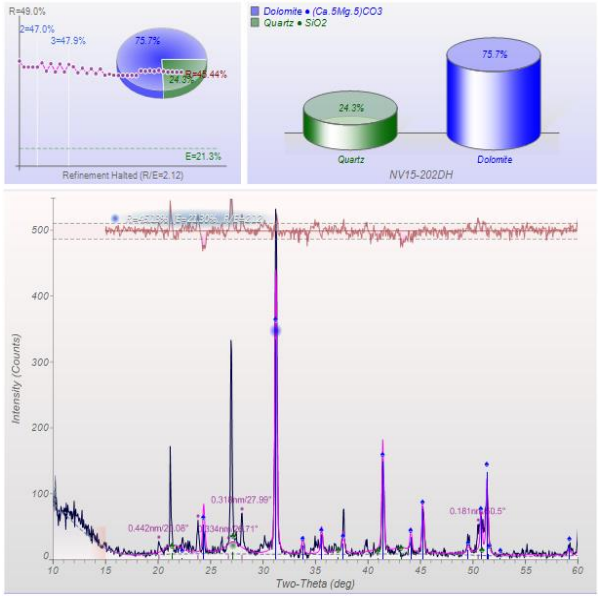

NV15-202DH

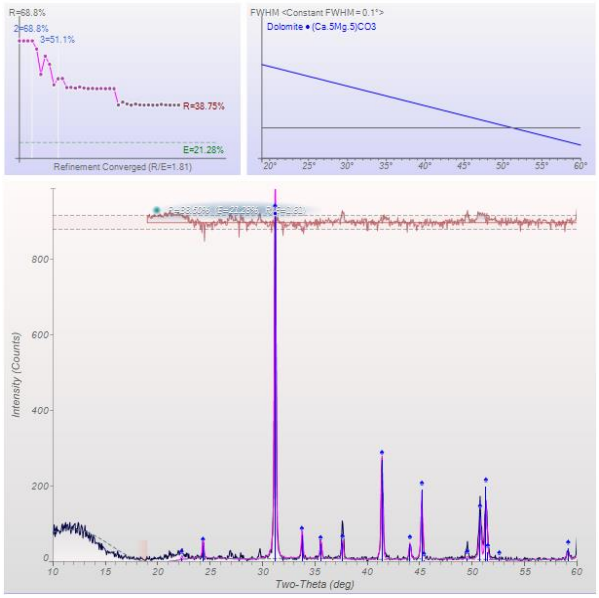

NV15-206DH

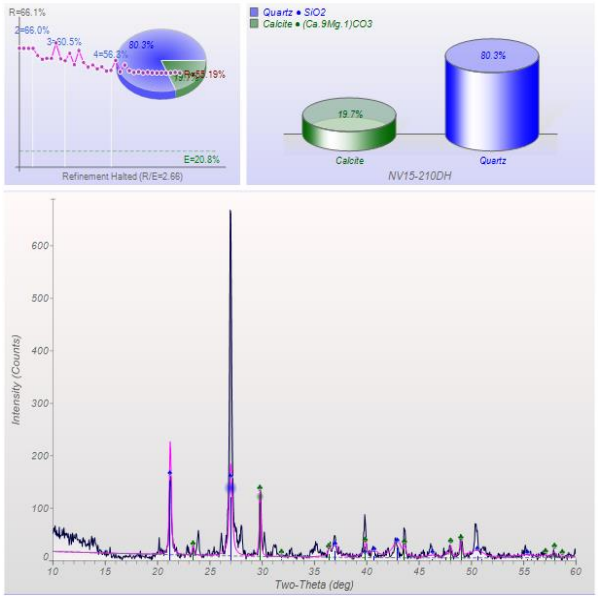

NV15-210DH

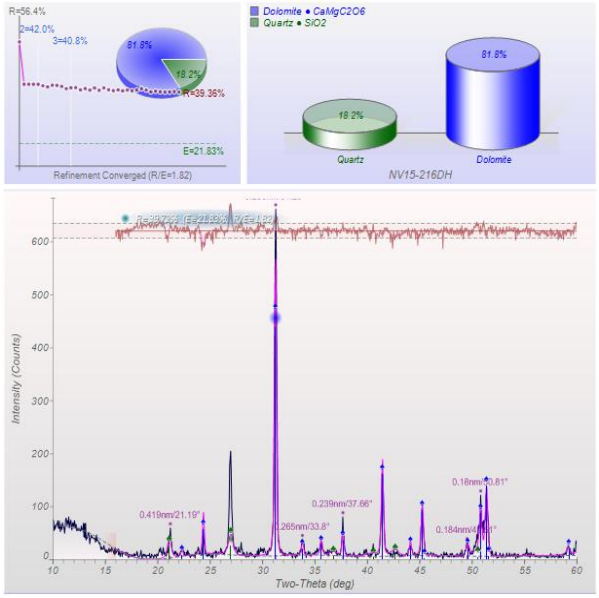

NV15-216DH

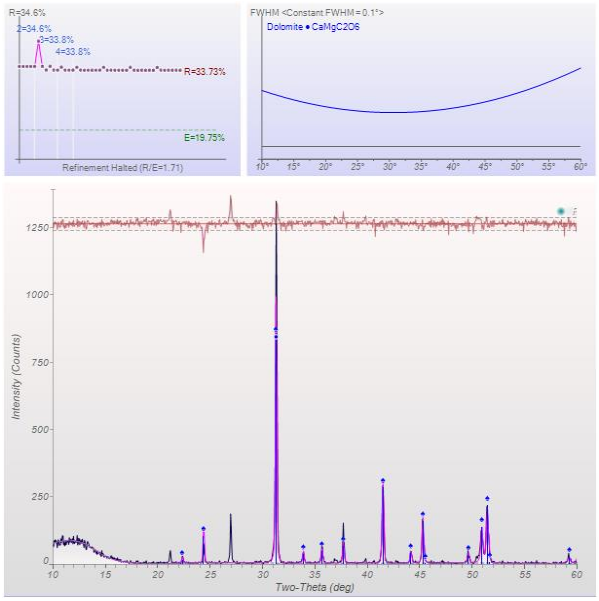

NV15-220DH

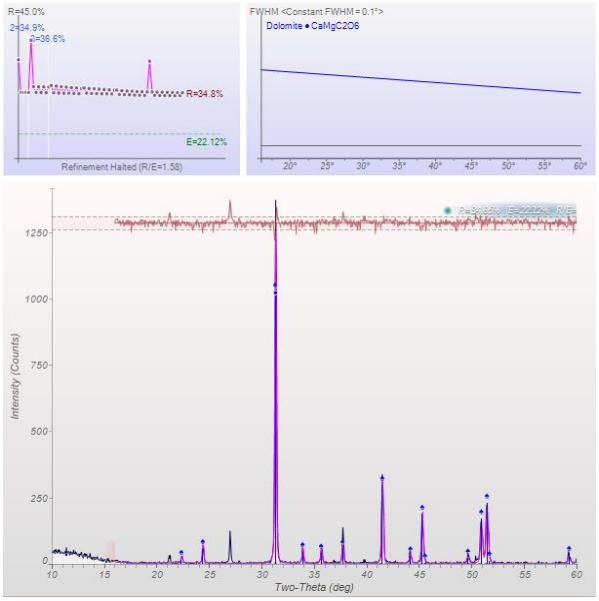

NV15-225DH

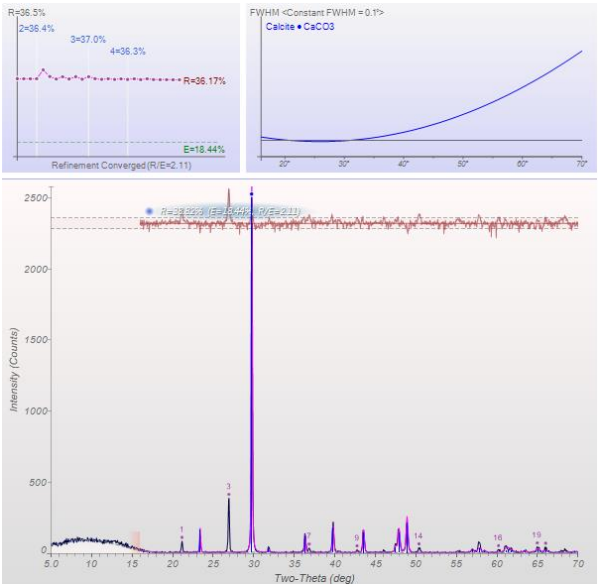

NV15-224DH

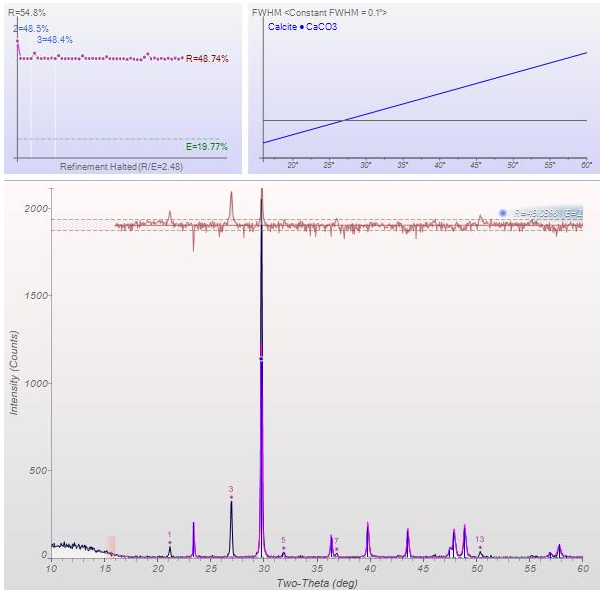

NV15-227DH

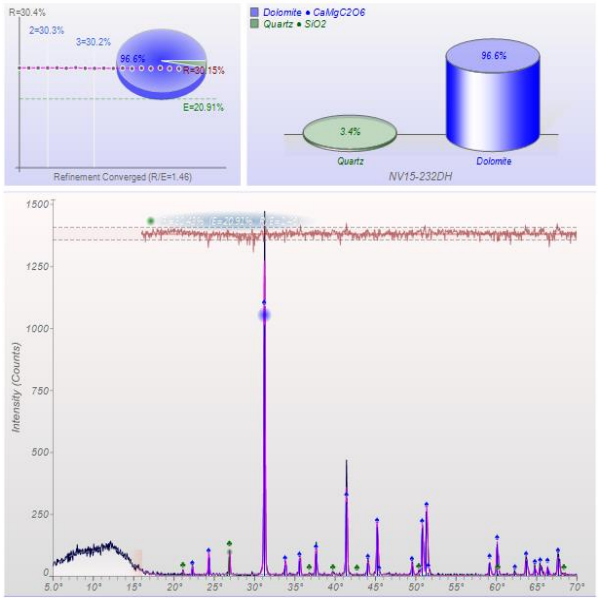

NV15-232DH

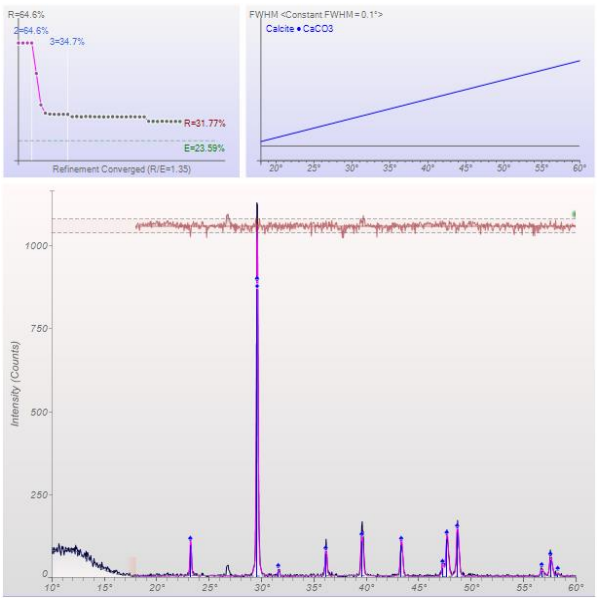

NV15-234DH

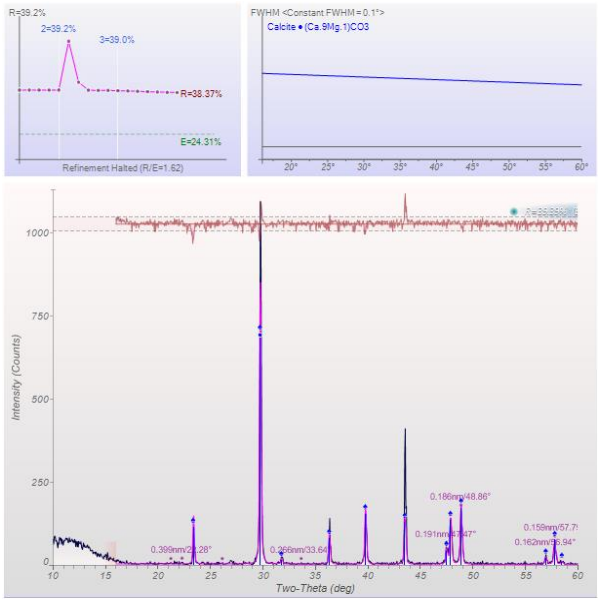

NV15-235DH

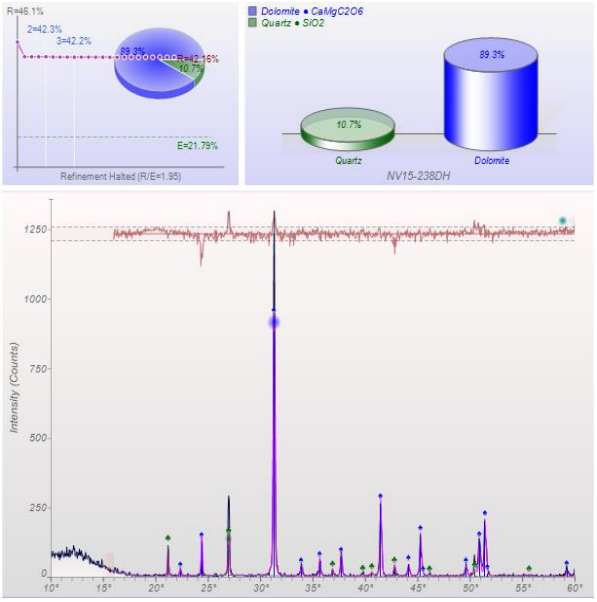

NV15-238DH

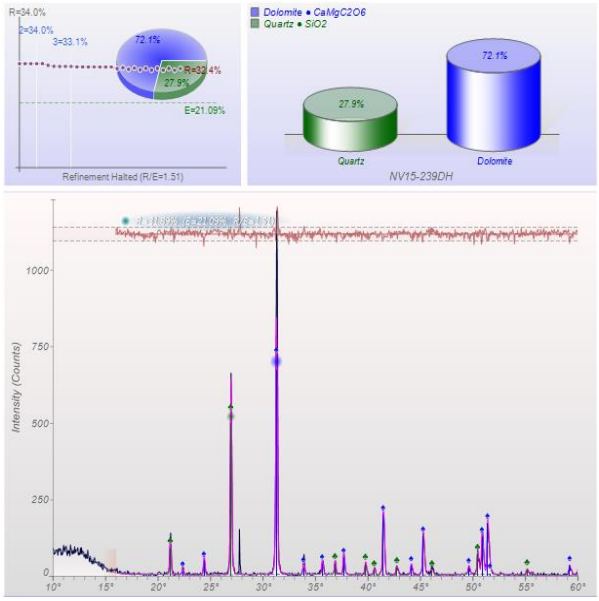

NV15-239DH

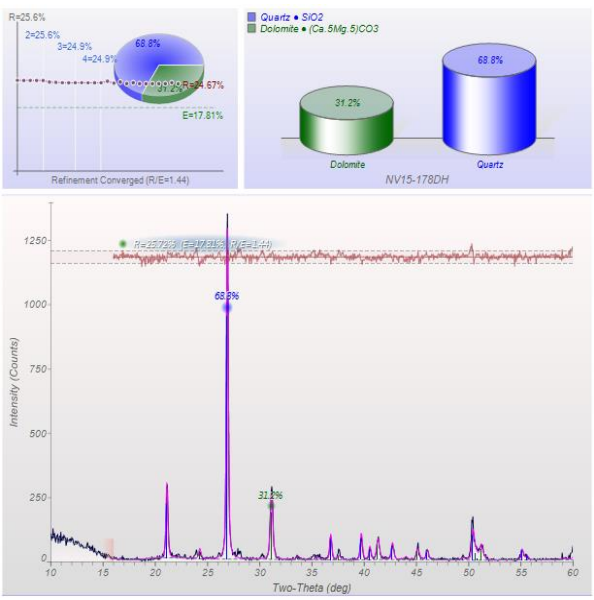

NV15-178DH

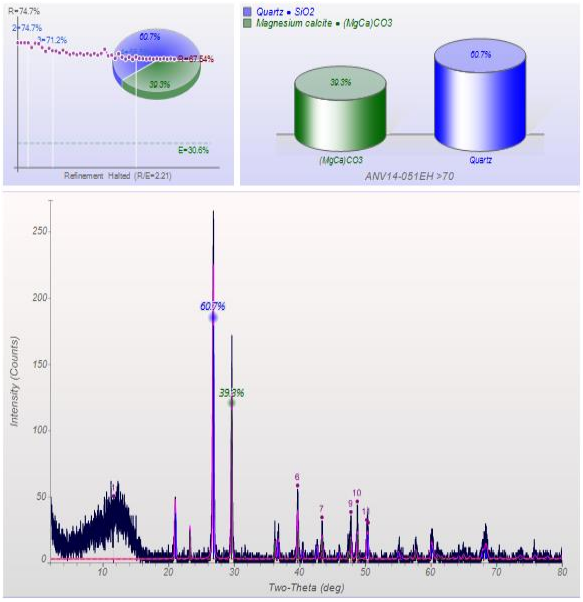

ANV14-051EH

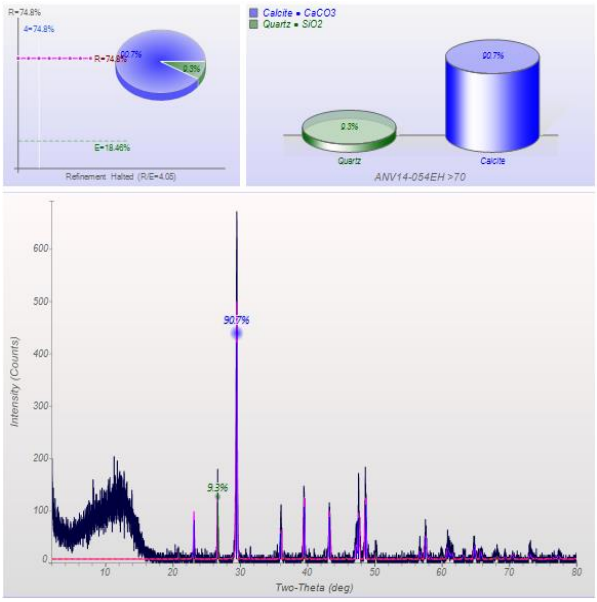

ANV14-054EH

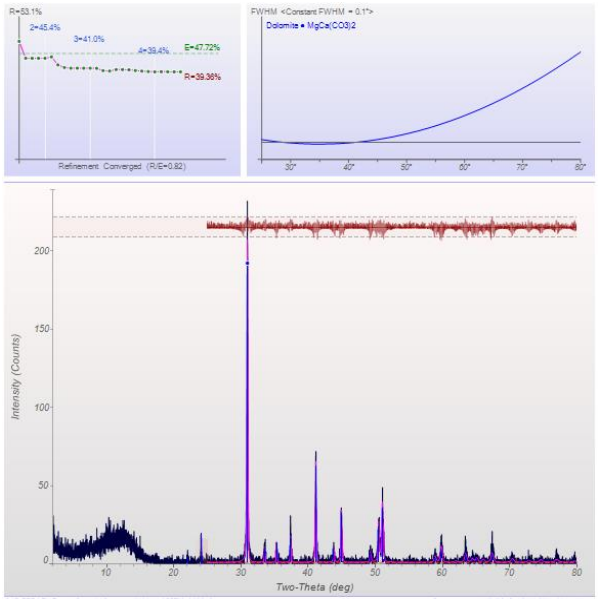

ANV14-055EH

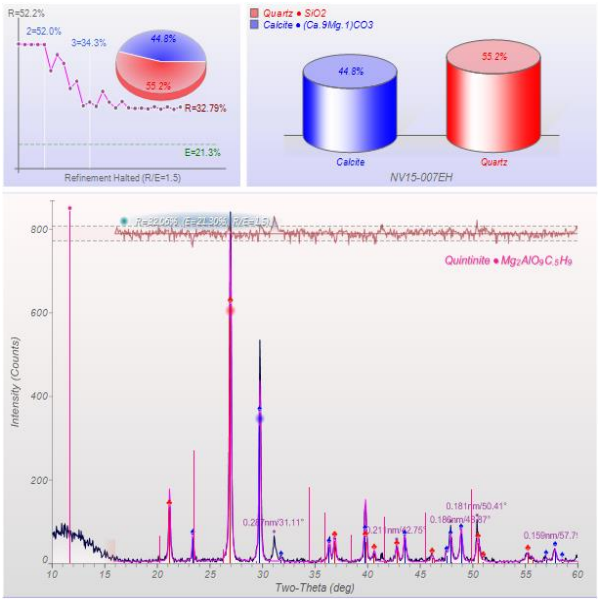

NV15-007EH

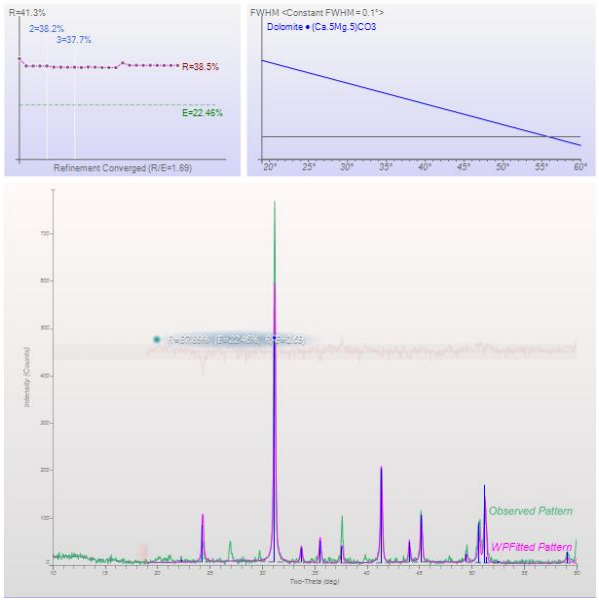

EOS3N-269.5

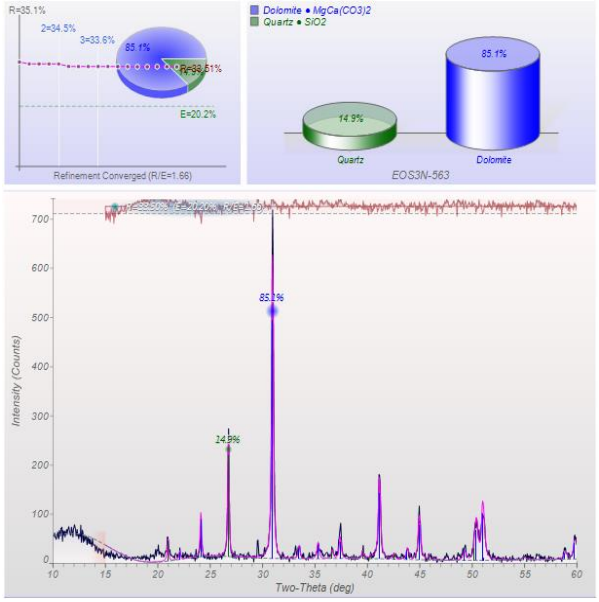

EOS3N-563

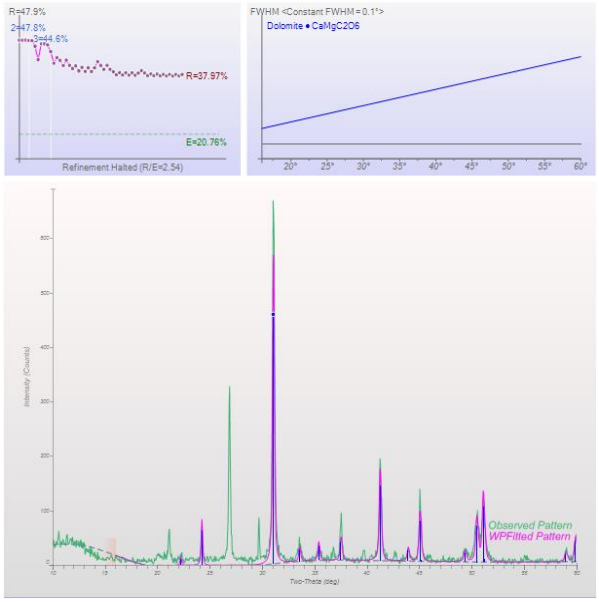

EOS3N-576

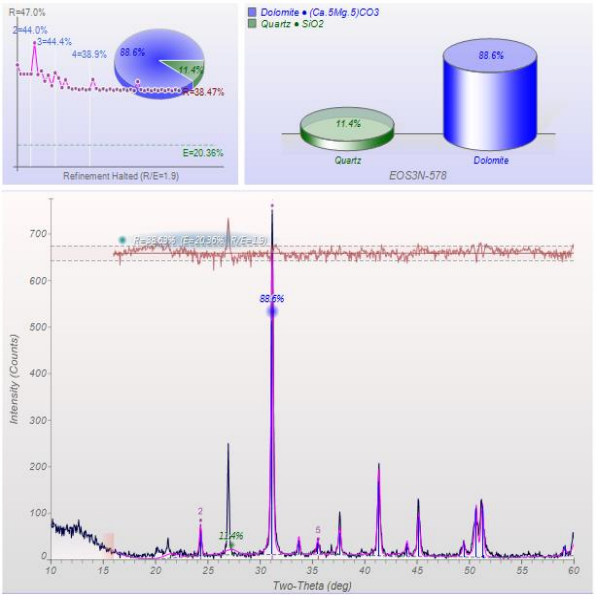

EOS3N-578

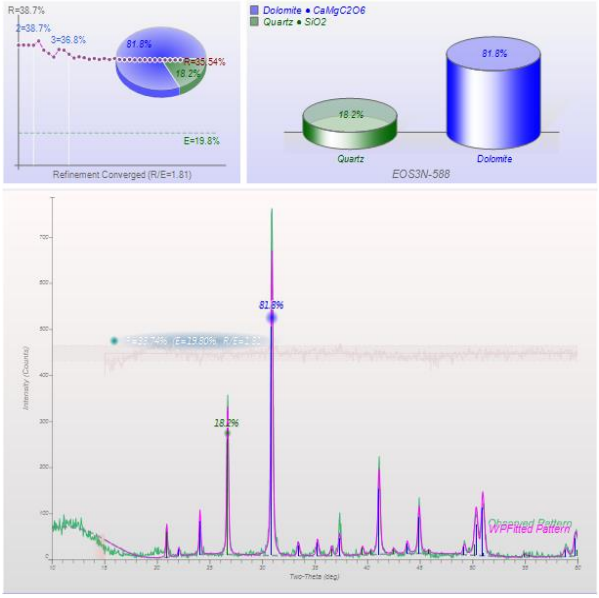

EOS3N-588

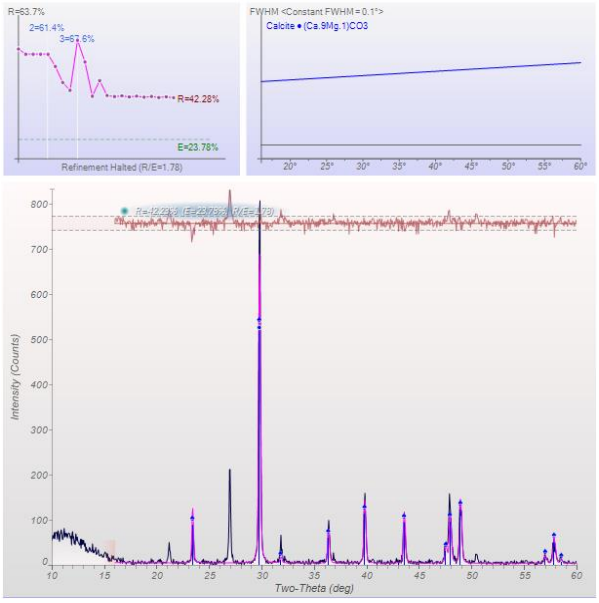

EOS3N-625

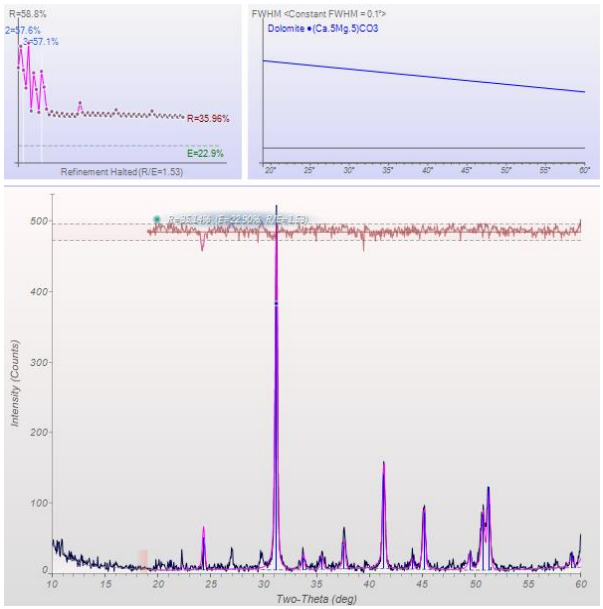

NV16-077EH

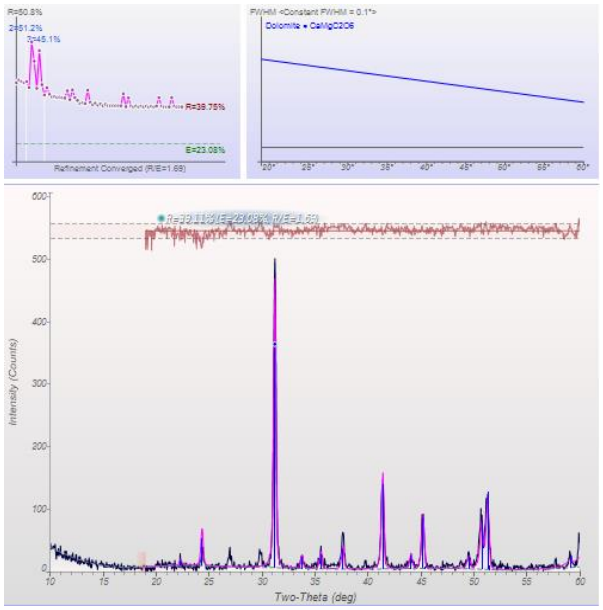

NV16-081EH

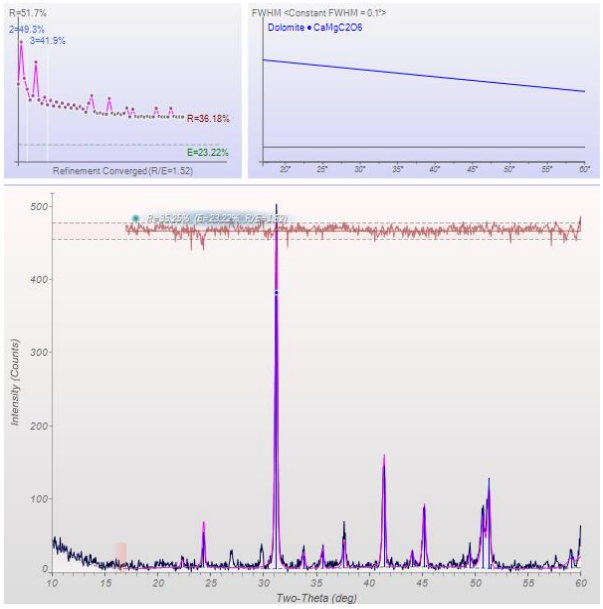

NV16-083EH

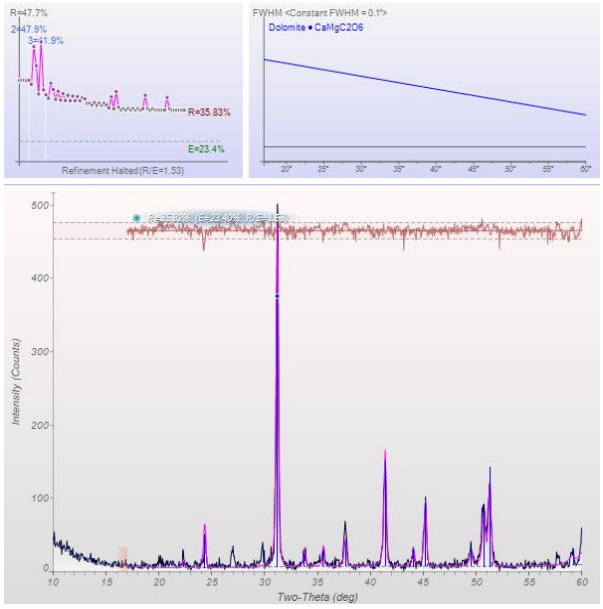

NV16-085EH

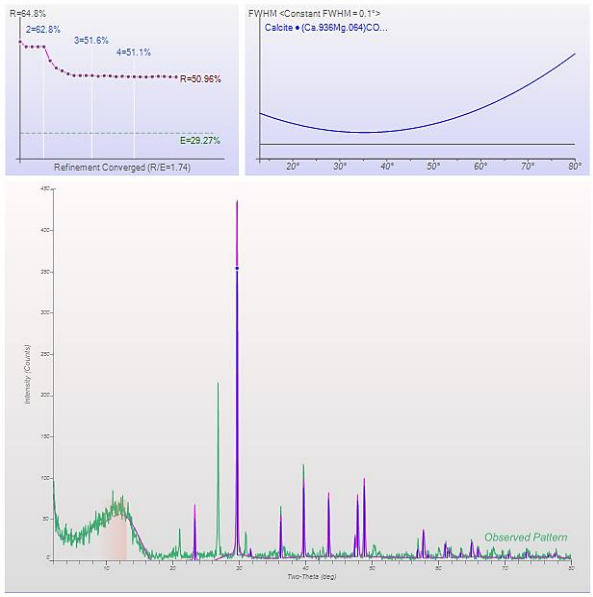

ANV14-012PR

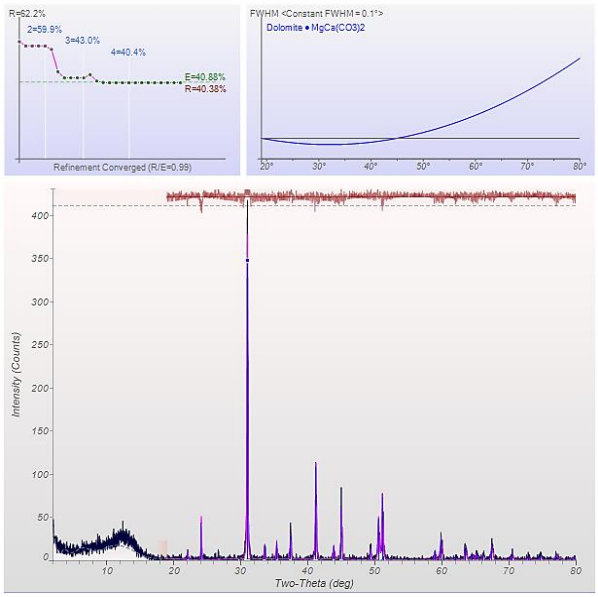

ANV14-014PR

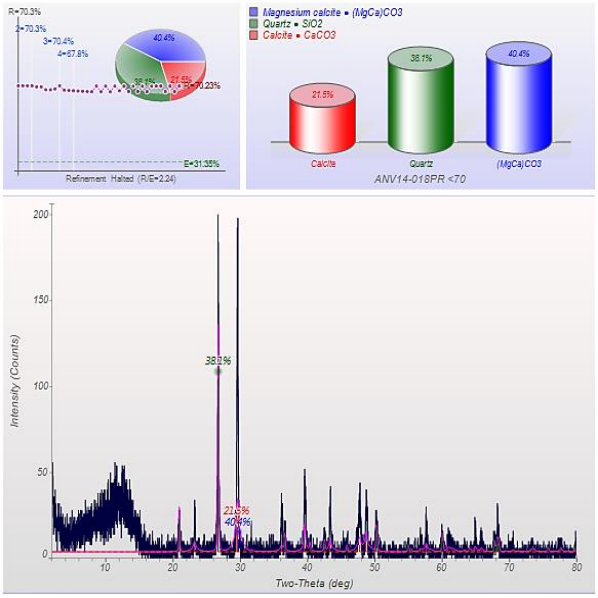

ANV14-018PR

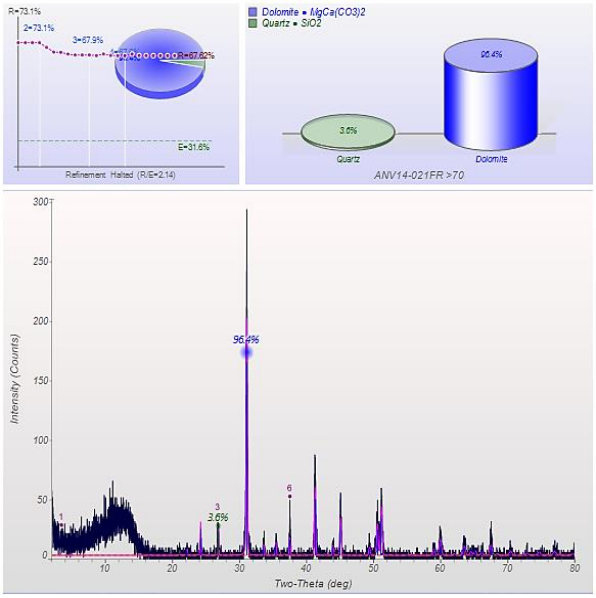

ANV14-021PR

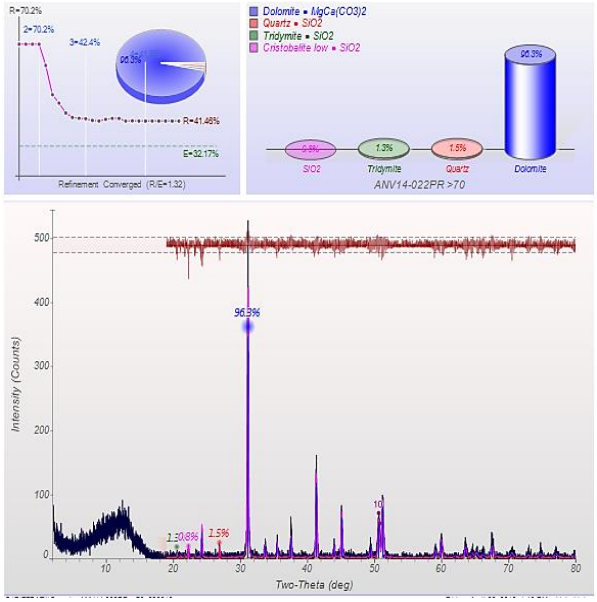

ANV14-022PR

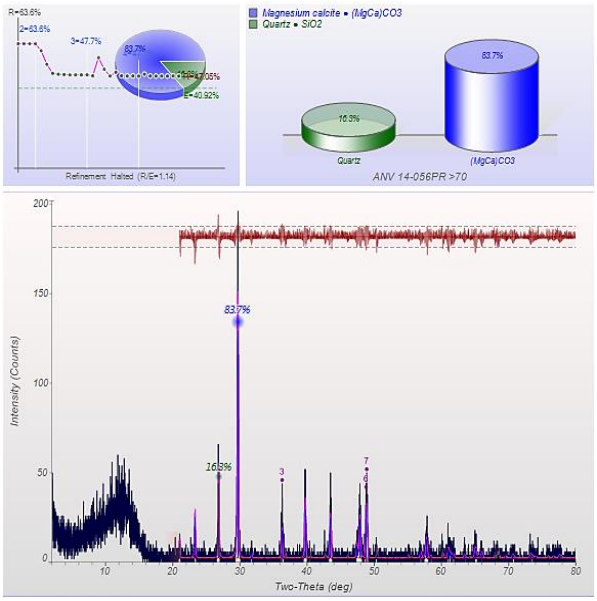

ANV14-056PR

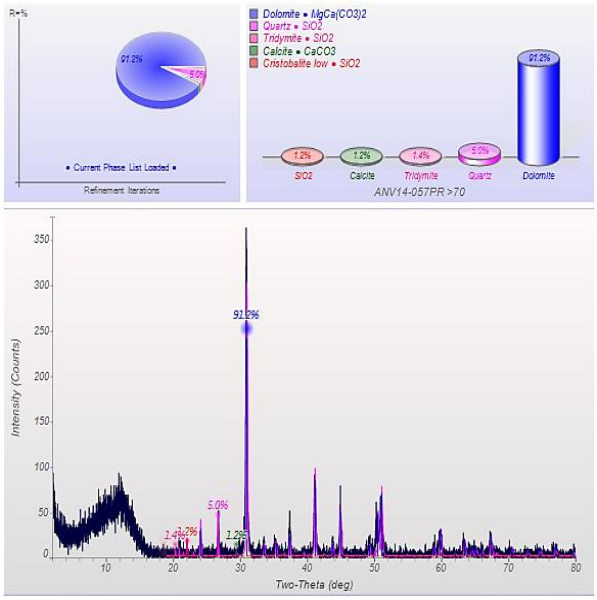

ANV14-057PR

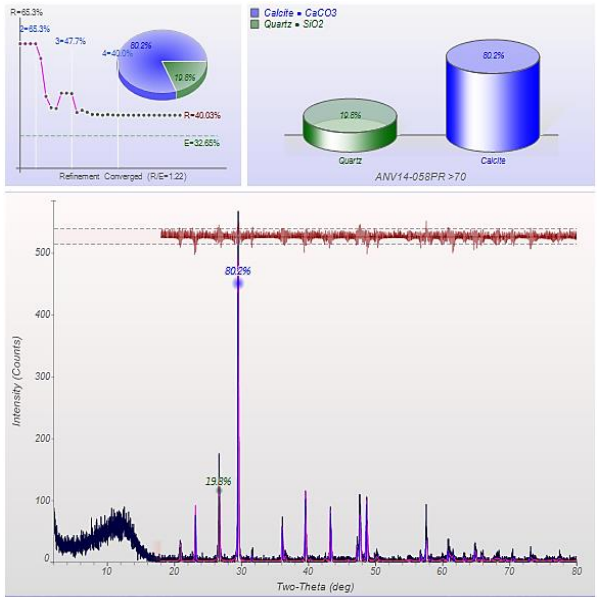

ANV14-058PR

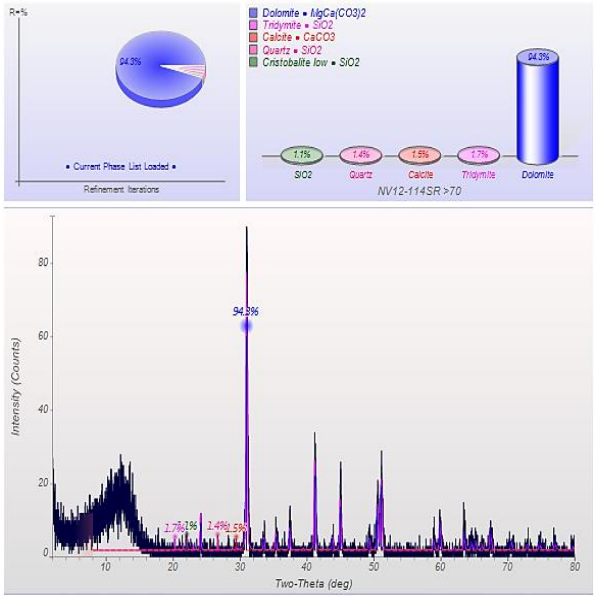

NV12-114SR

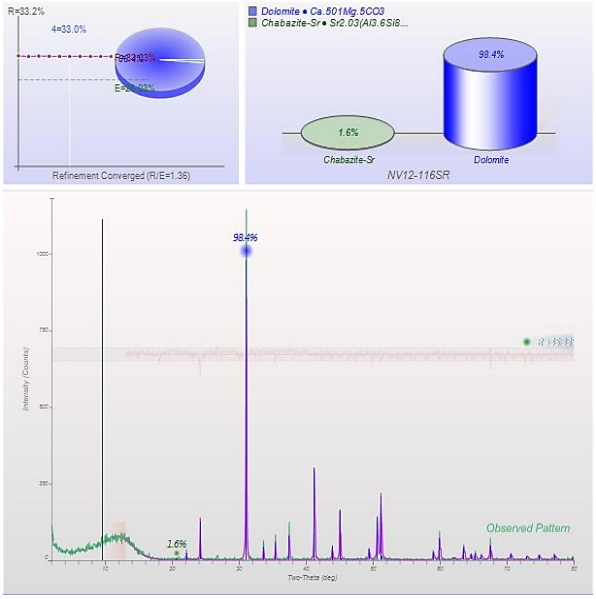

NV12-116SR

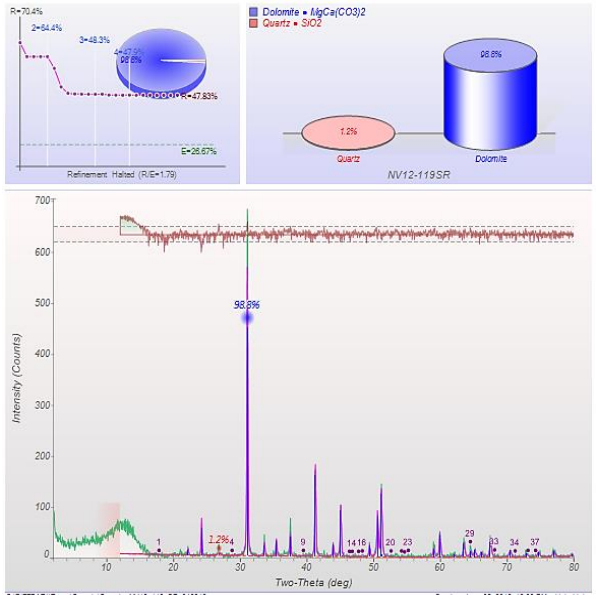

NV12-119SR

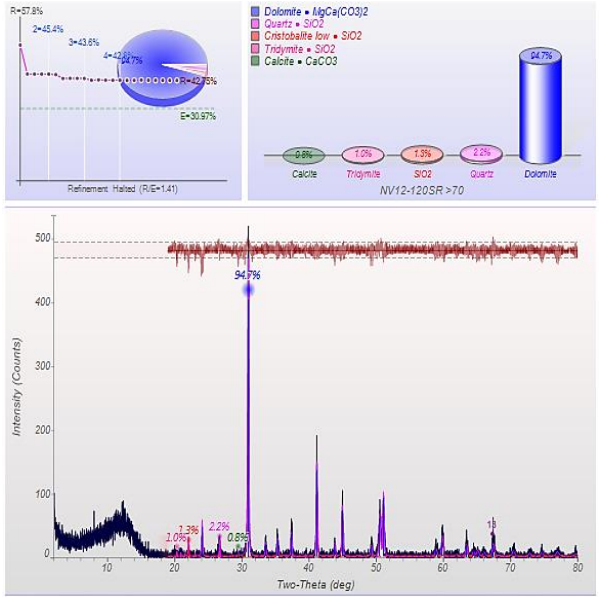

NV12-120SR

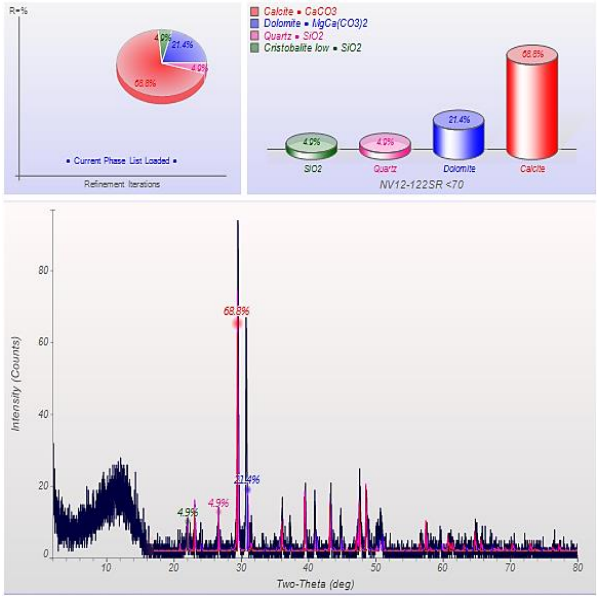

NV12-122SR

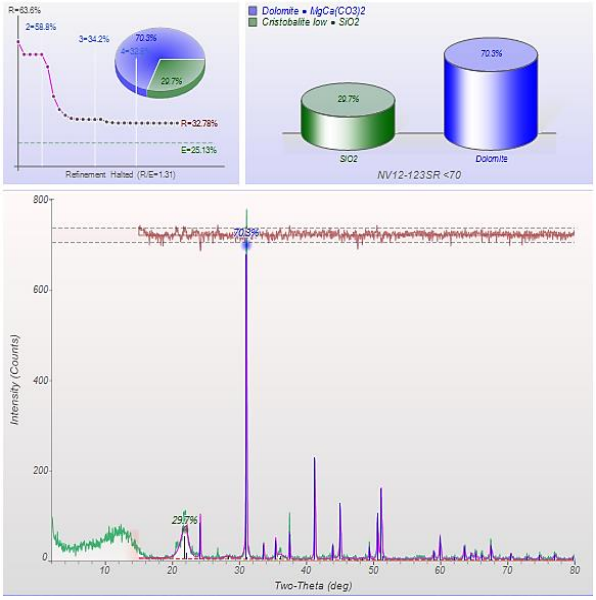

NV12-123SR

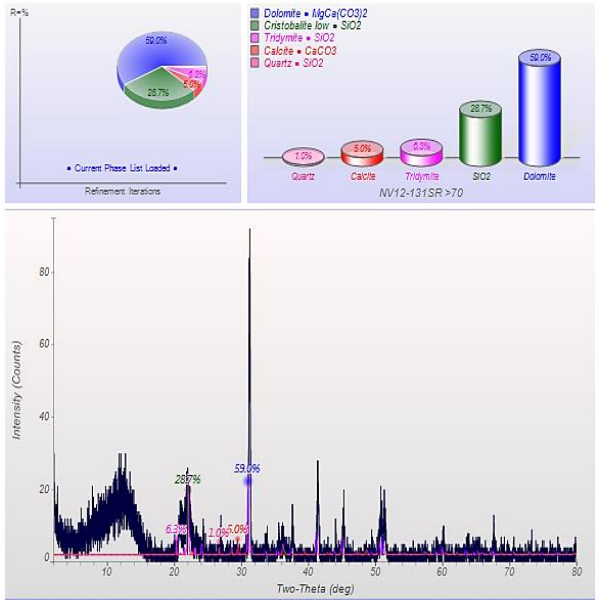

NV12-131SR

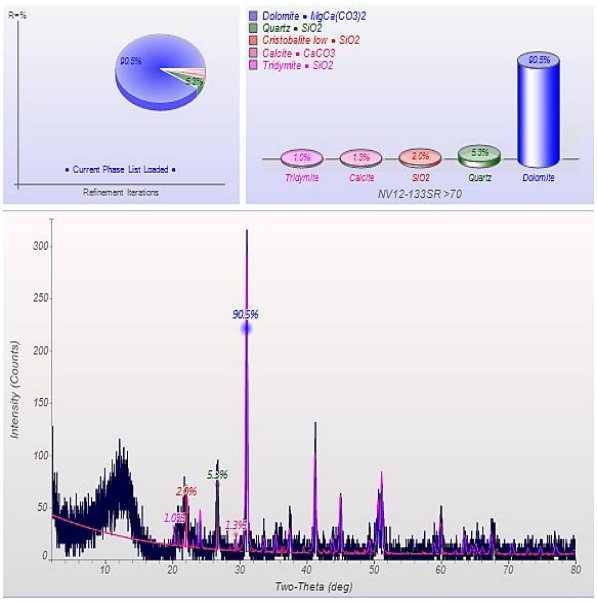

NV12-133SR

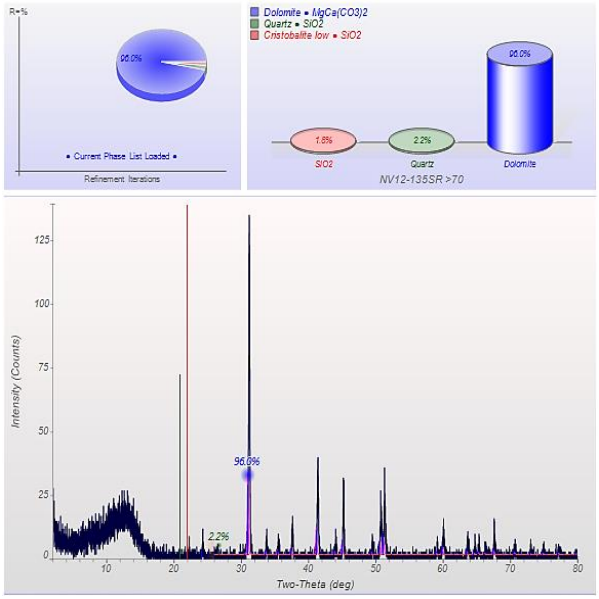

NV12-135SR

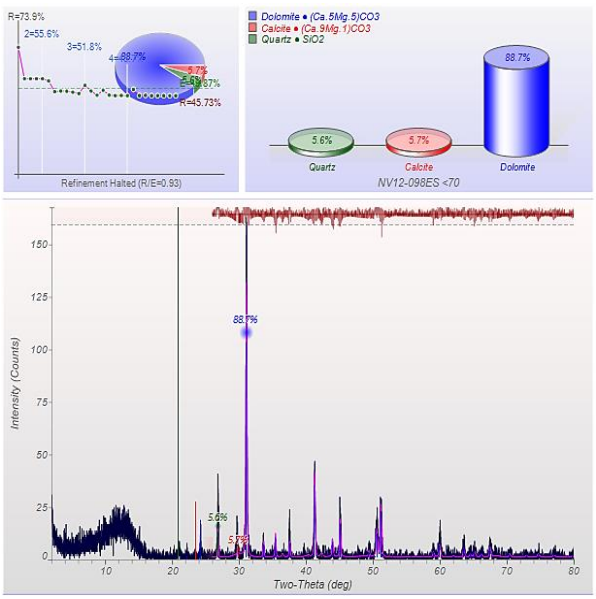

NV12-098ES

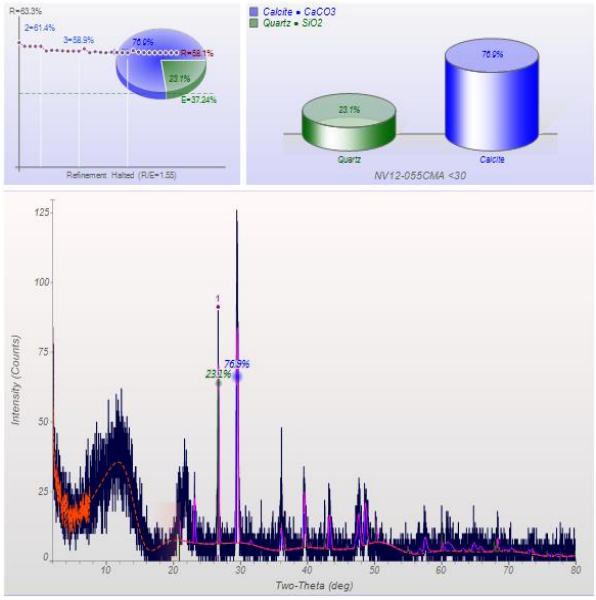

NV12-055CMA

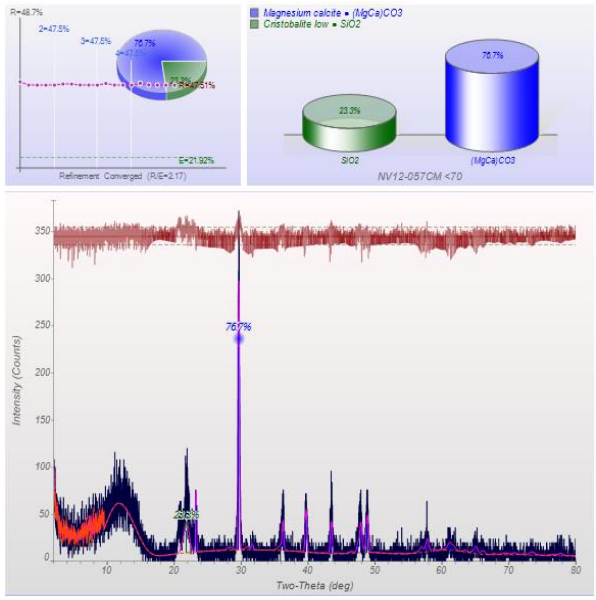

NV12-057CM

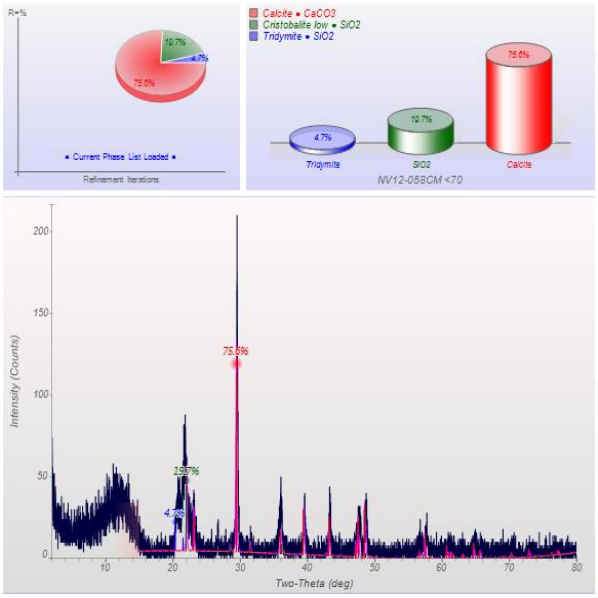

NV12-058CM

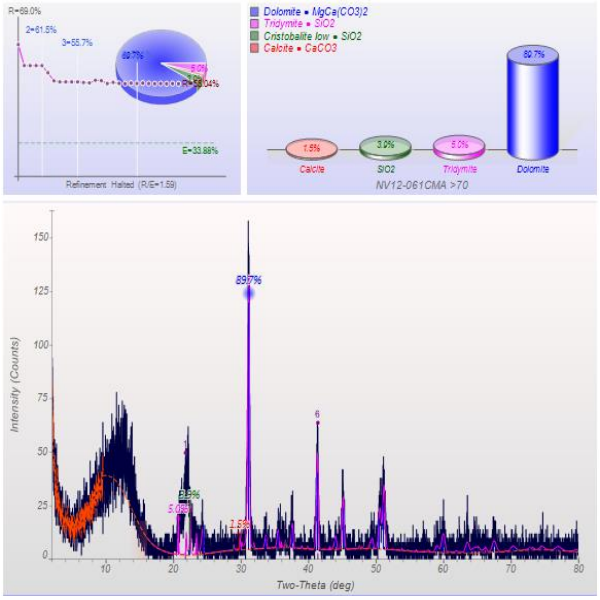

NV12-061CM

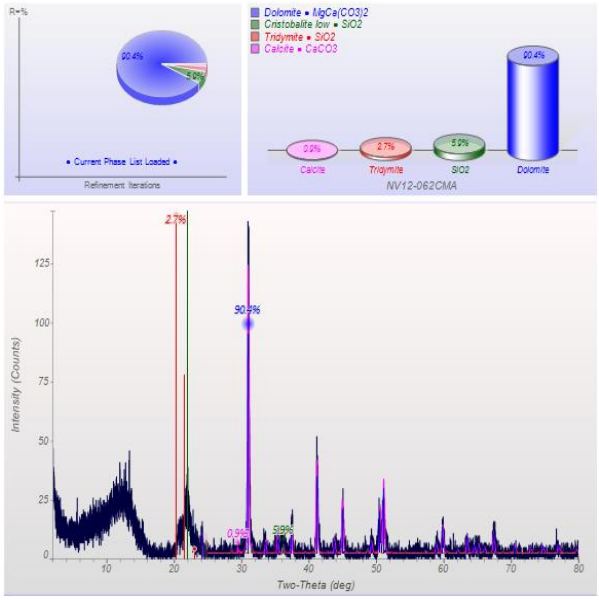

NV12-062CM

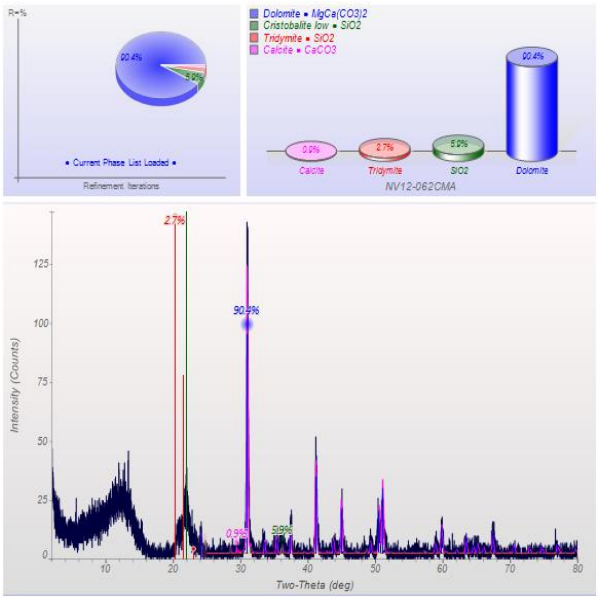

NV12-063CM

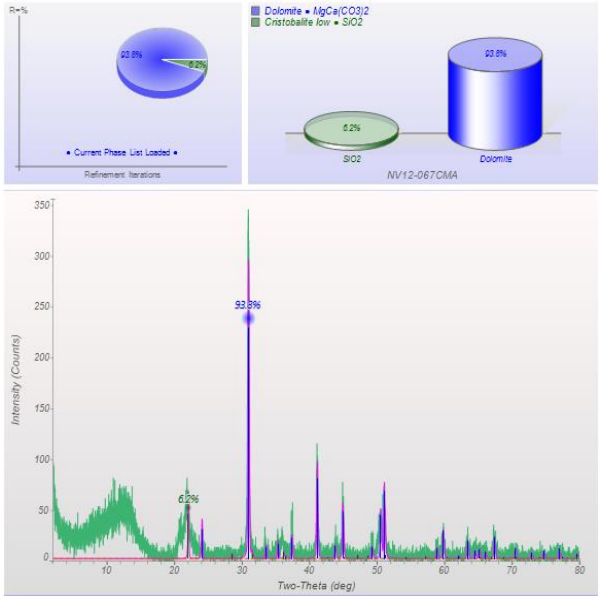

NV12-067CMA

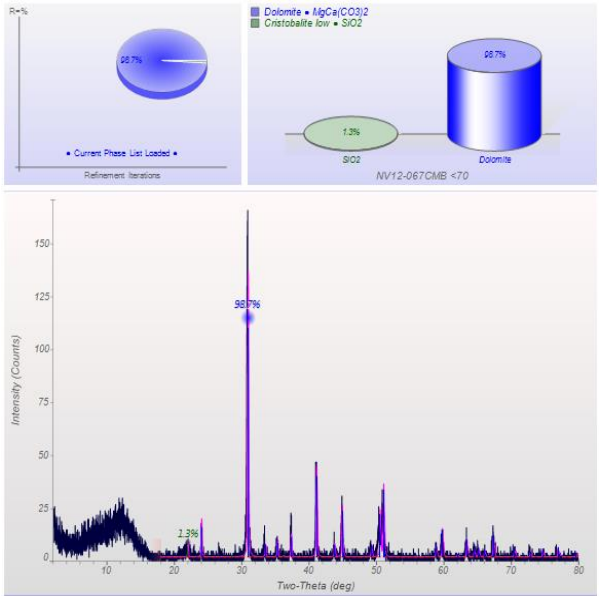

NV12-067CMB

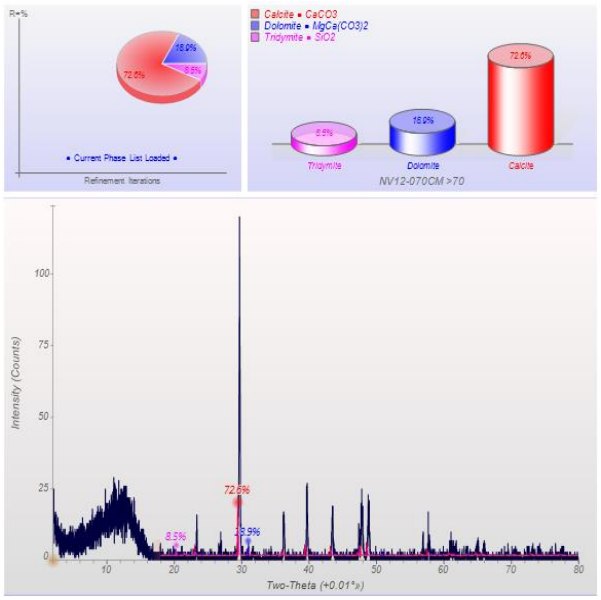

NV12-070CM

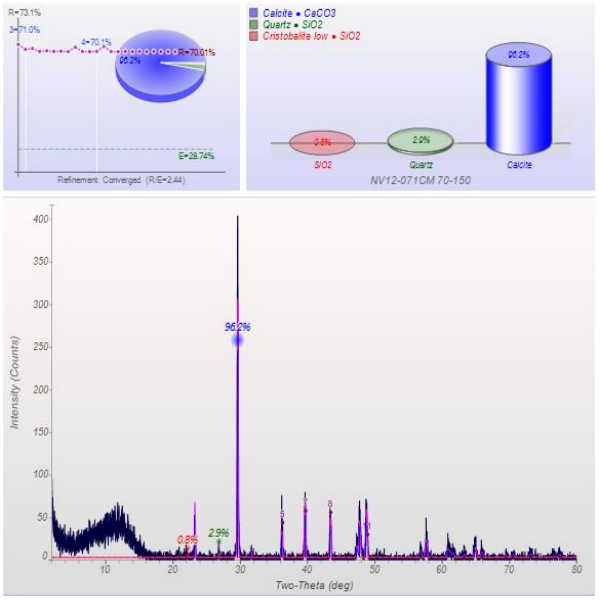

NV12-071CM

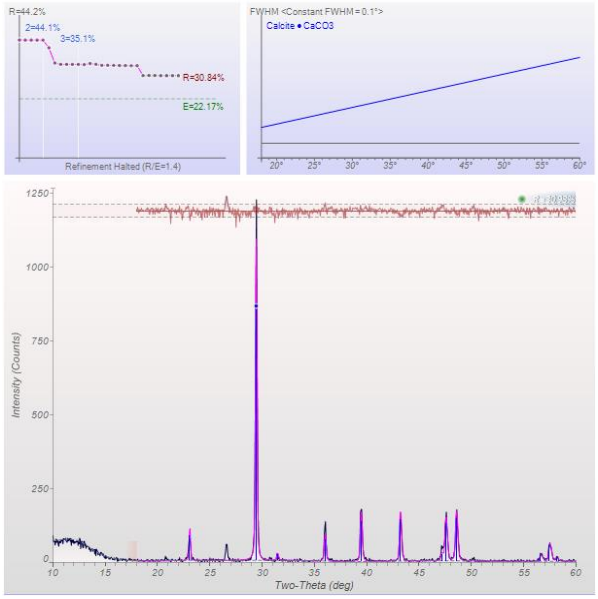

NV12-095CM

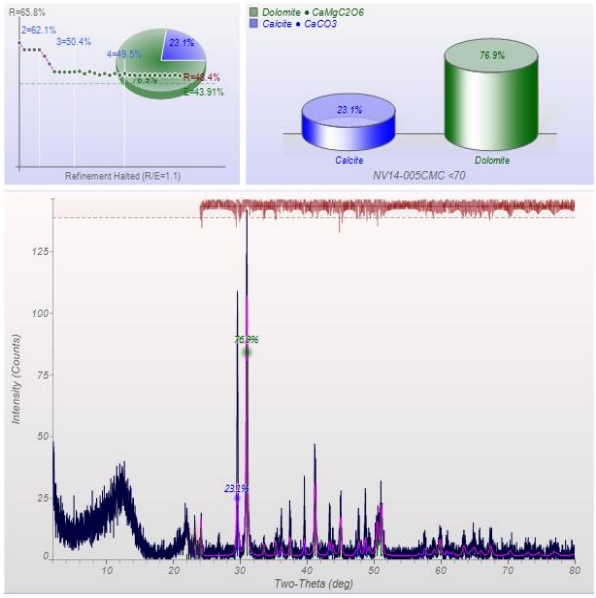

NV14-005CMC

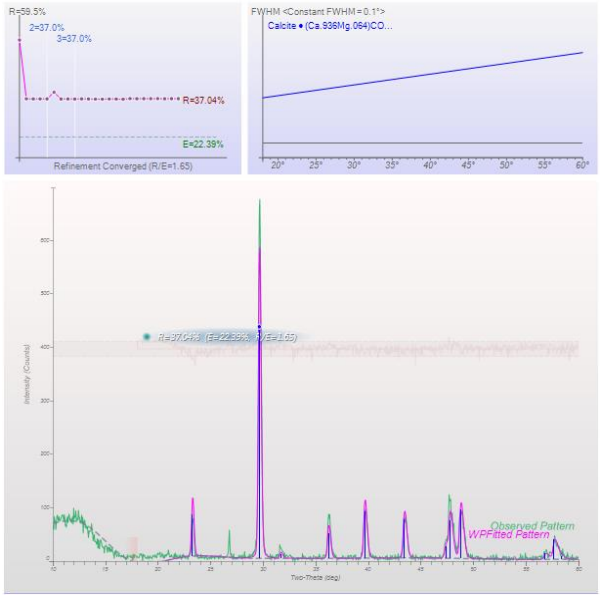

NV15-073CM

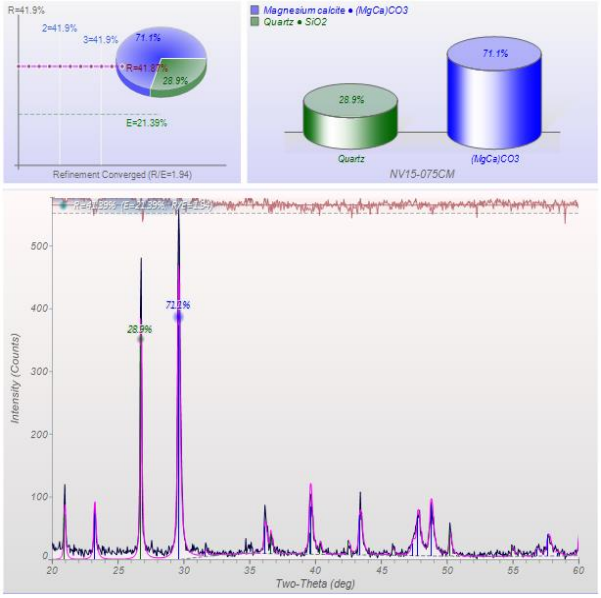

NV15-075CM

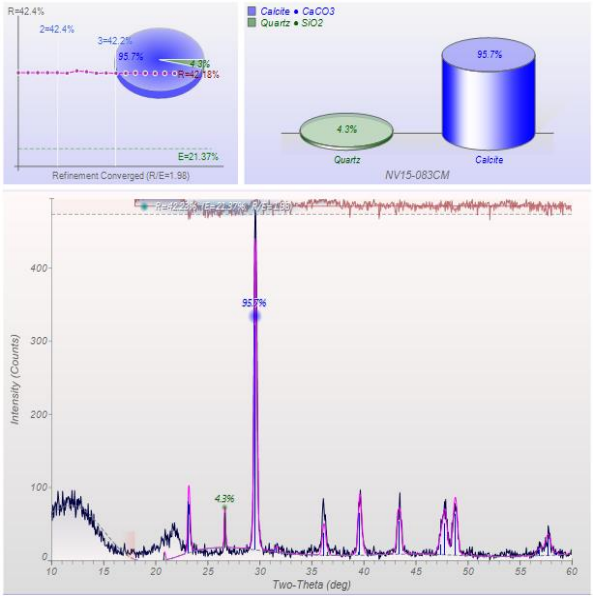

NV15-083CM

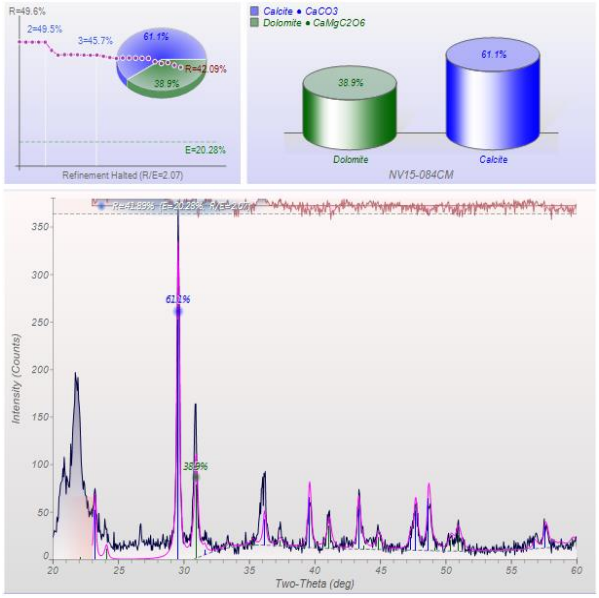

NV15-084CM

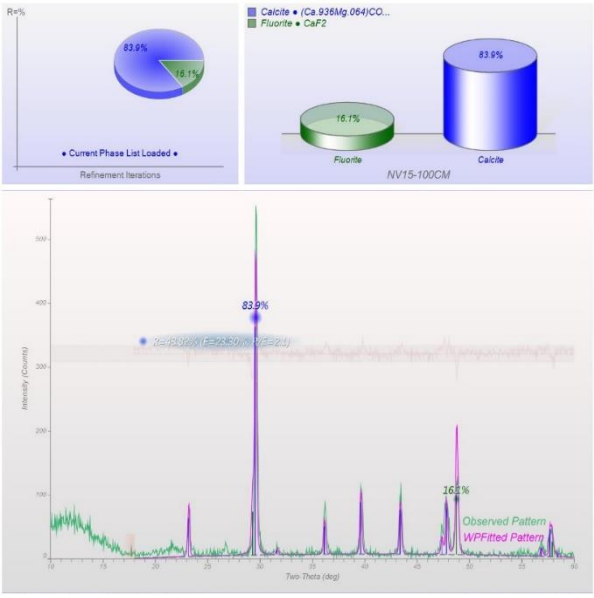

NV15-085CM

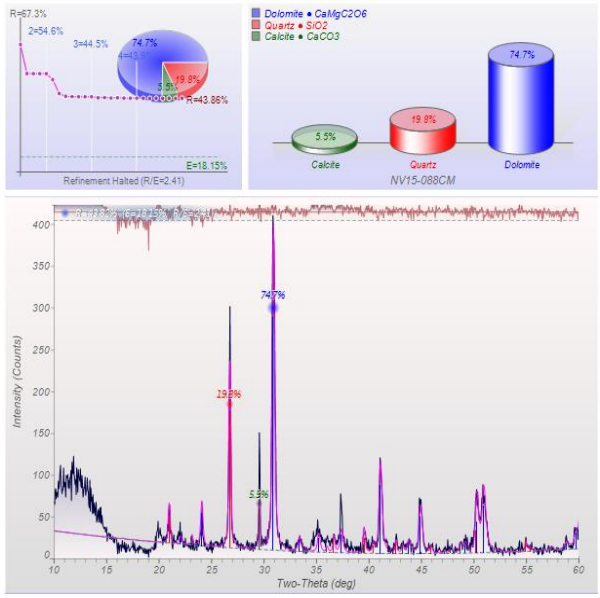

NV15-088CM

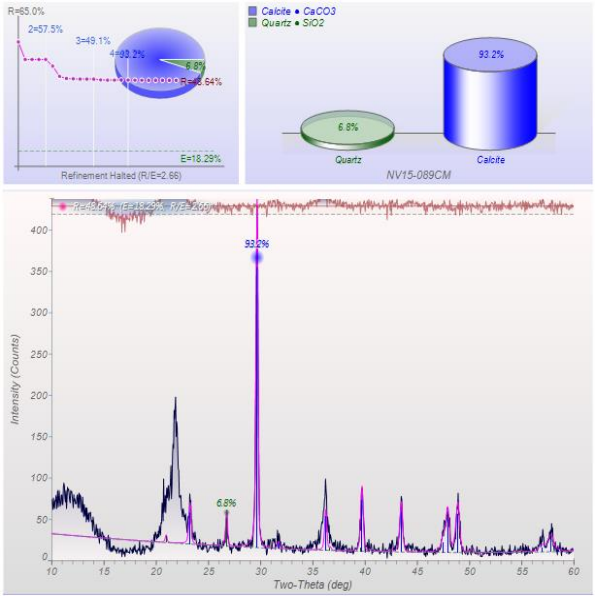

NV15-089CM

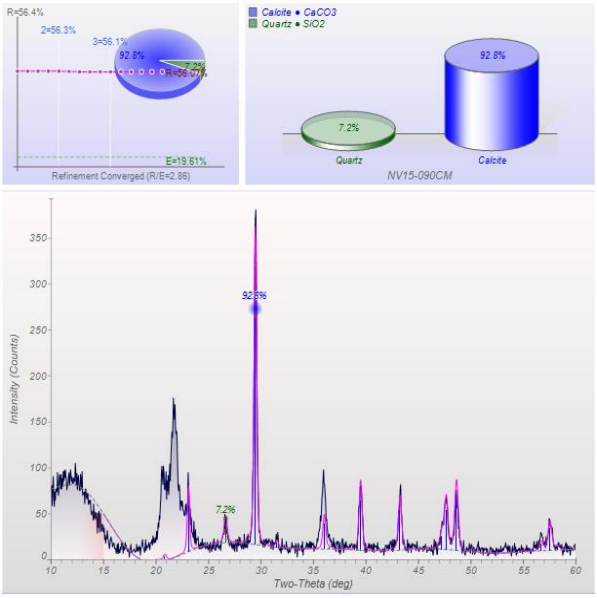

NV15-090CM

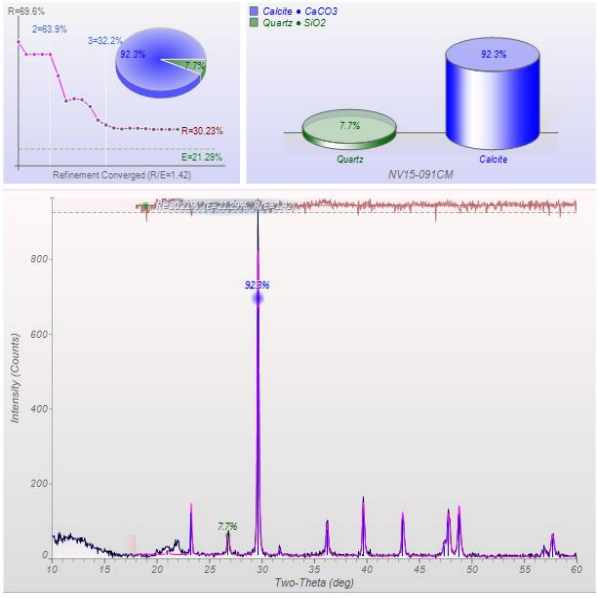

NV15-091CM

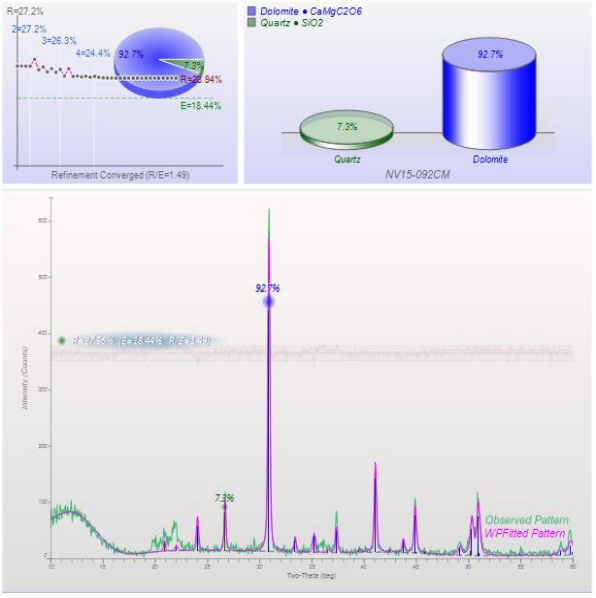

NV15-092CM

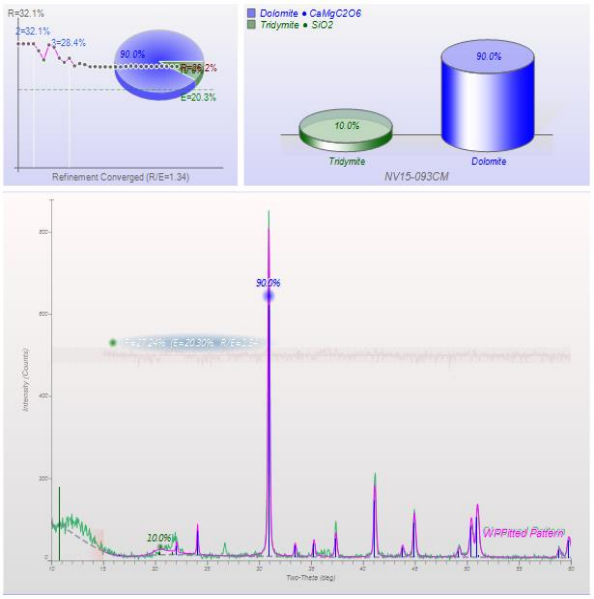

NV15-093CM

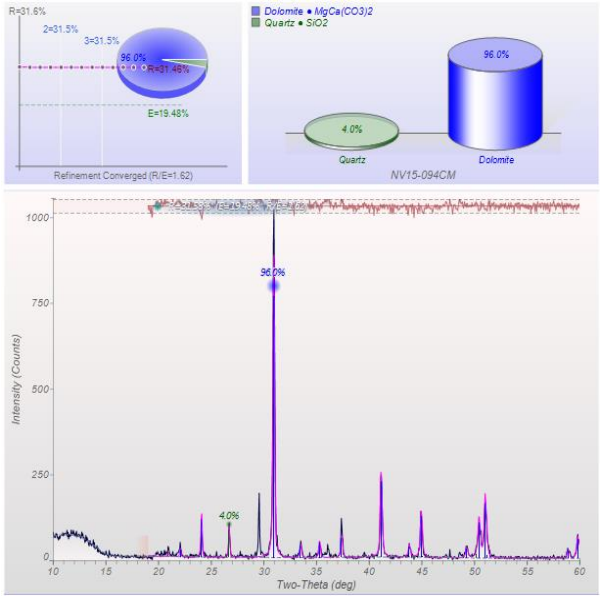

NV15-094CM

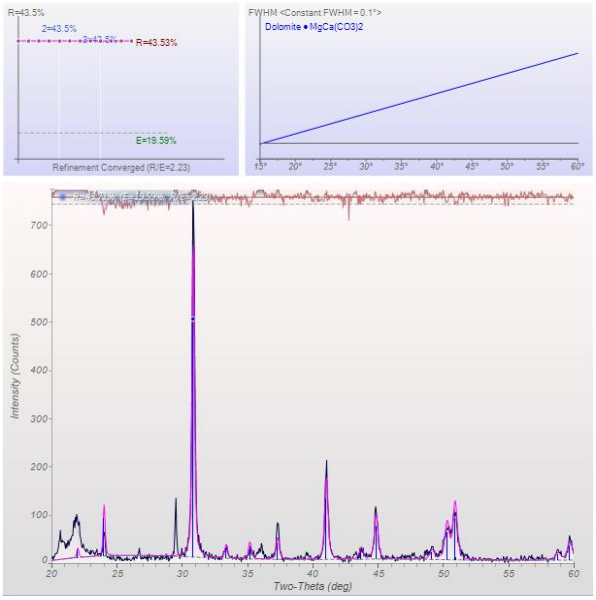

NV15-095CM

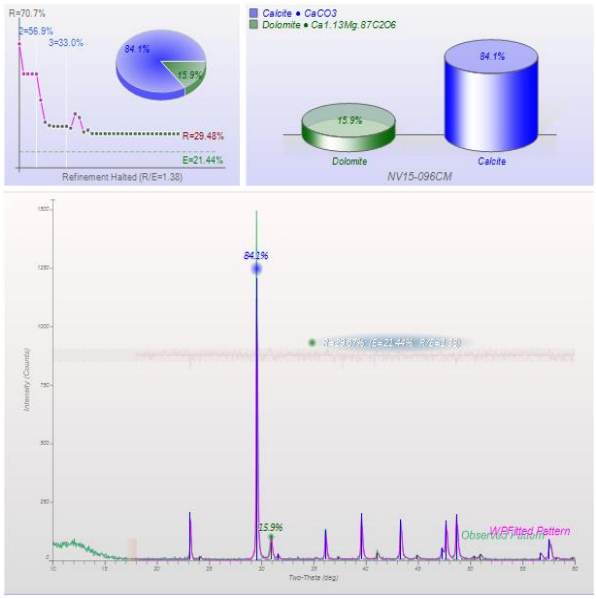

NV15-096CM

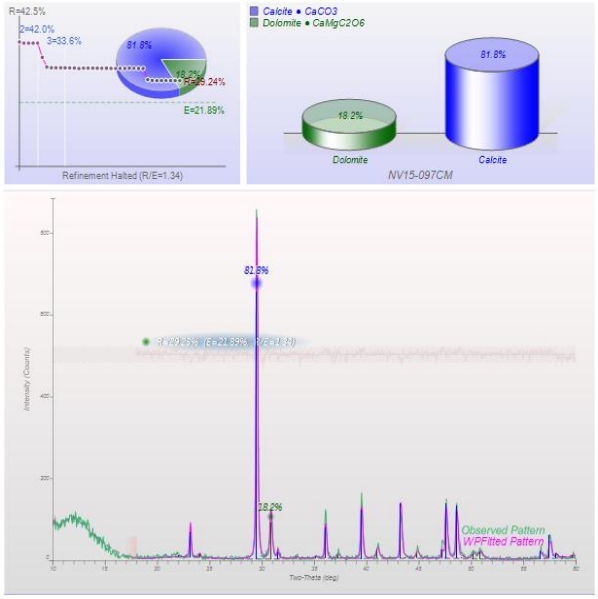

NV15-097CM

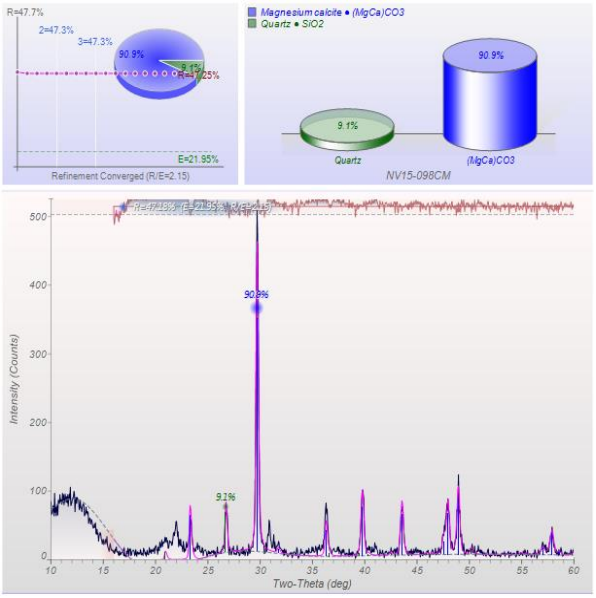

NV15-098CM

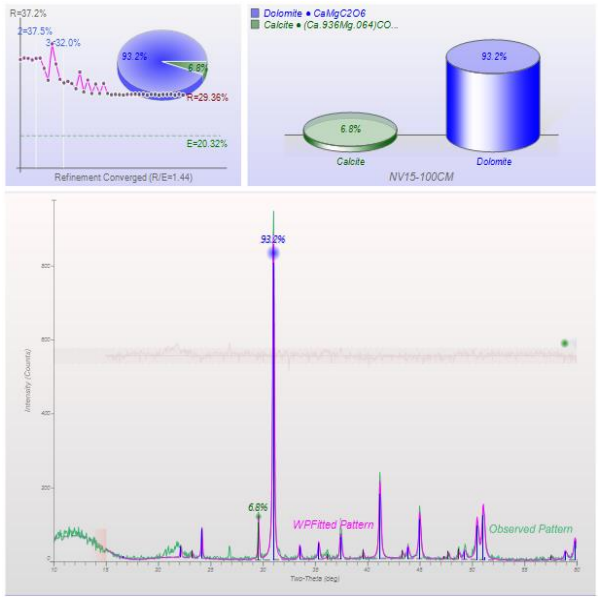

NV15-100CM

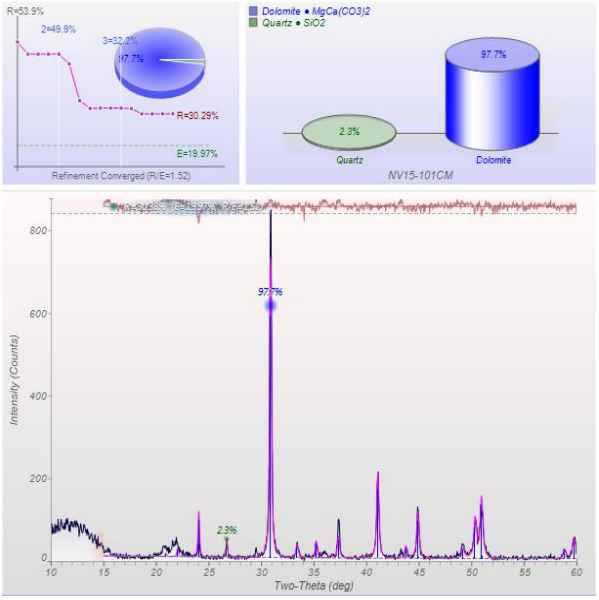

NV15-101CM

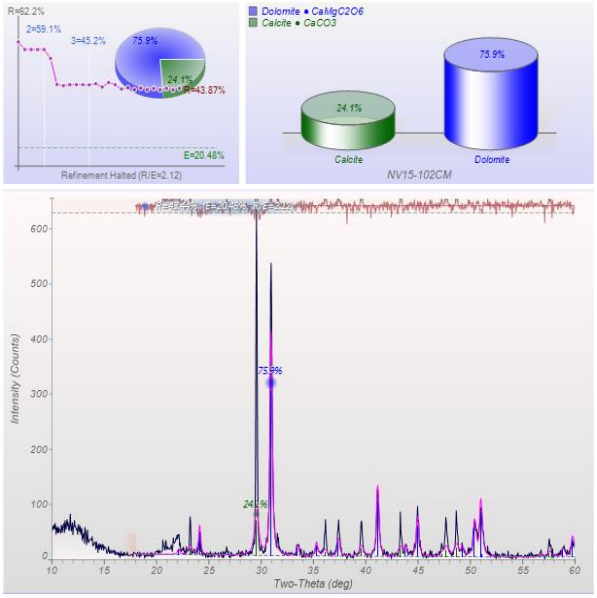

NV15-102CM

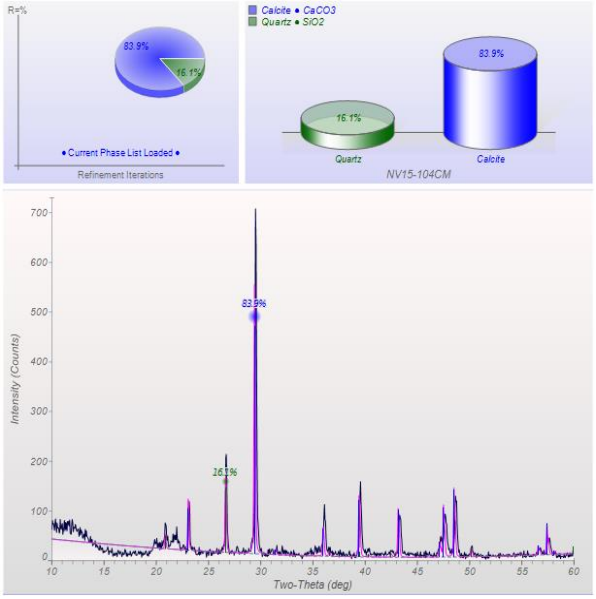

NV15-104CM

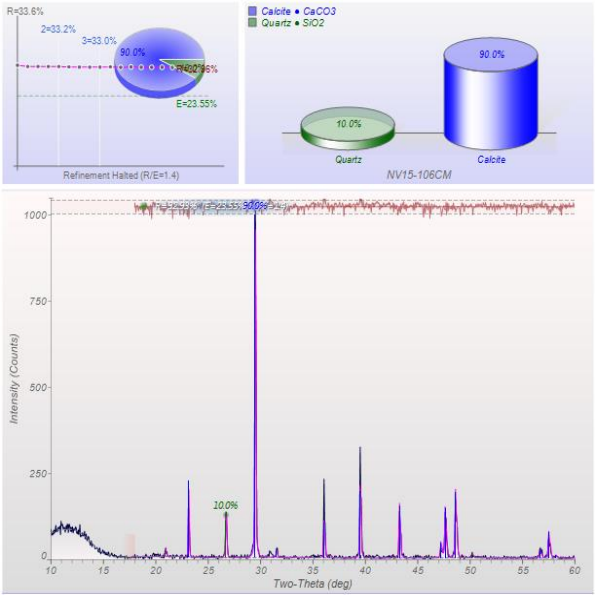

NV15-106CM

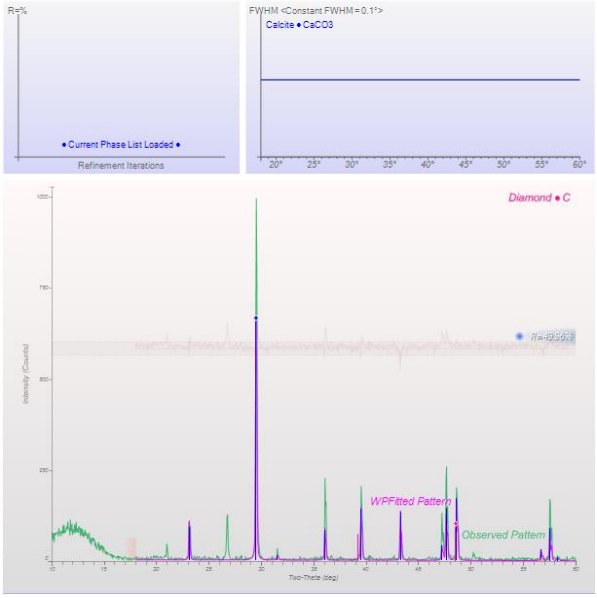

NV15-107CM

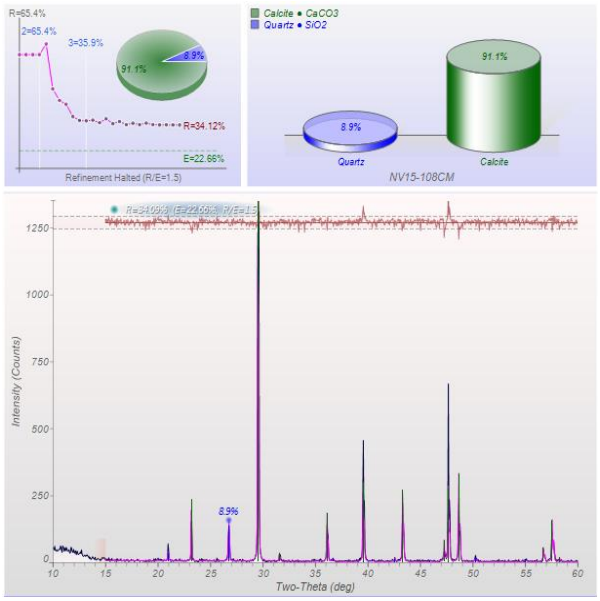

NV15-108CM

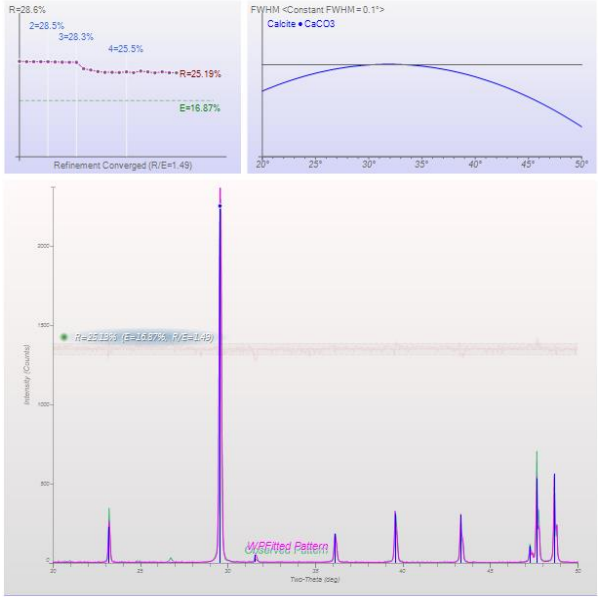

NV15-108CME

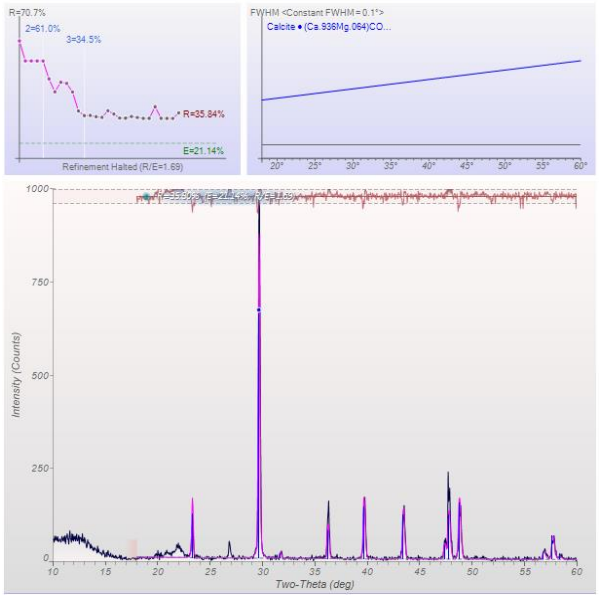

NV15-109CM

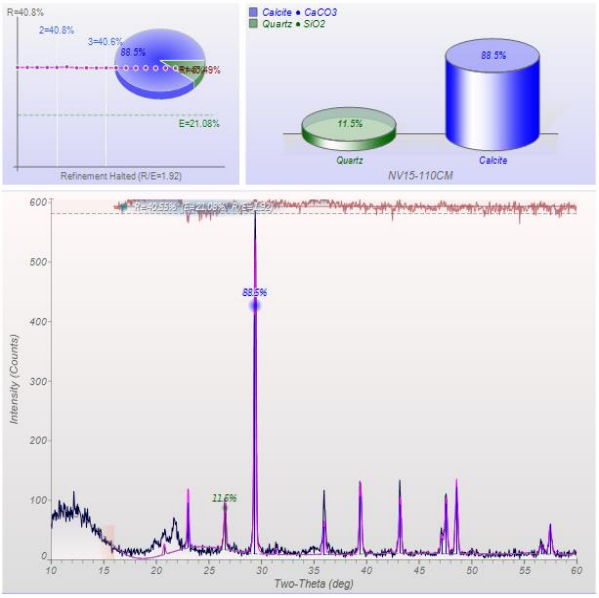

NV15-110CM

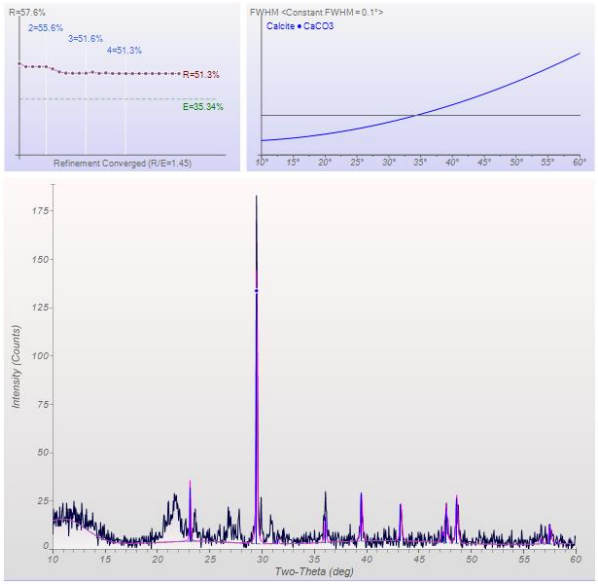

NV15-112CM

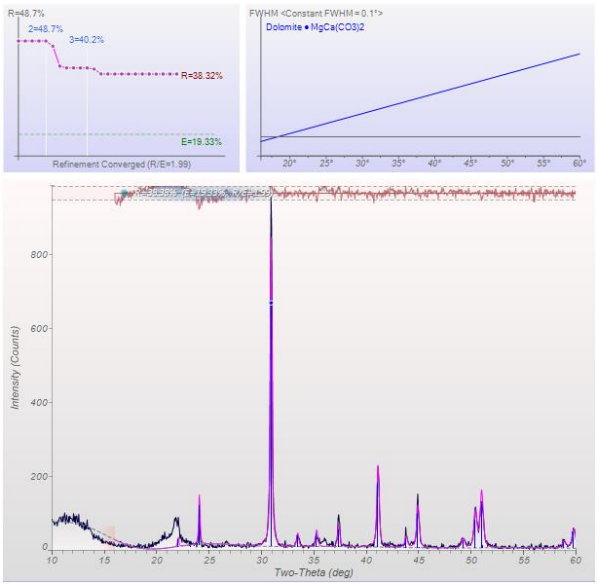

NV15-114CM

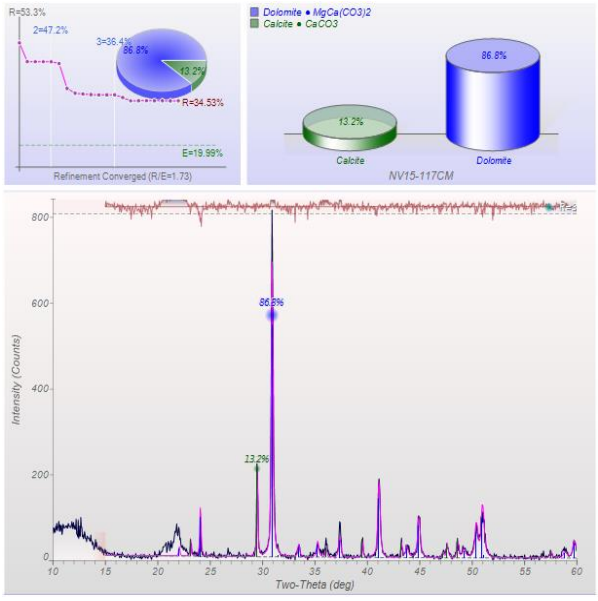

NV15-117CM

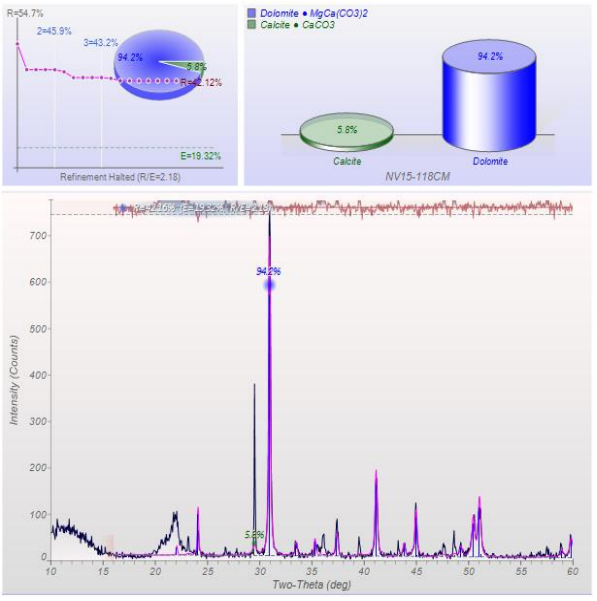

NV15-118CM

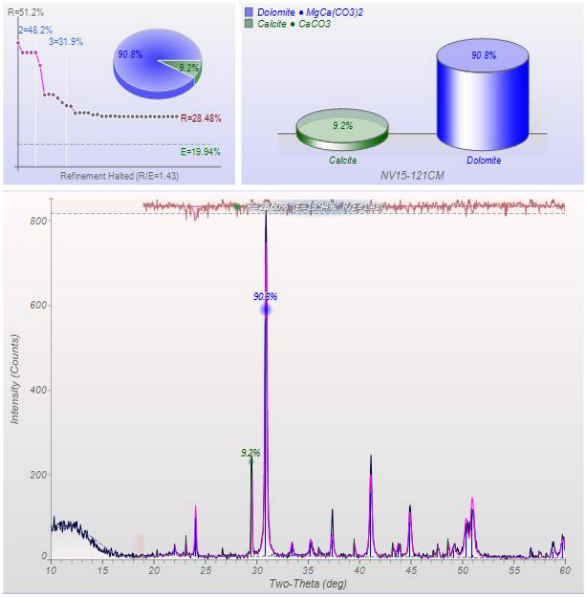

NV15-122CM

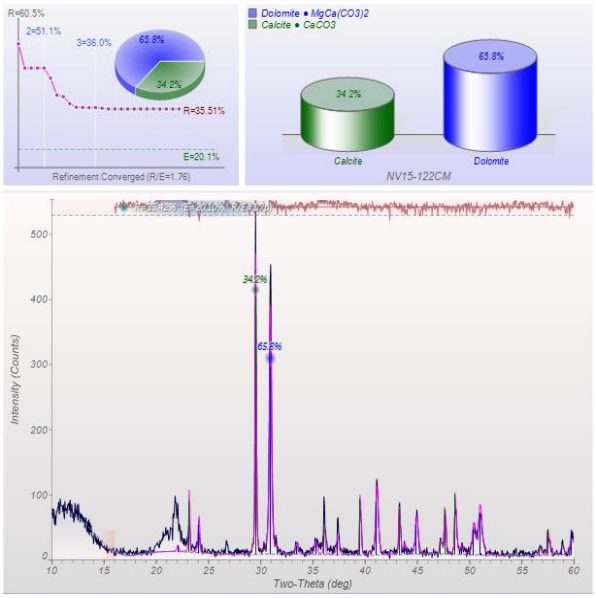

NV15-121CM

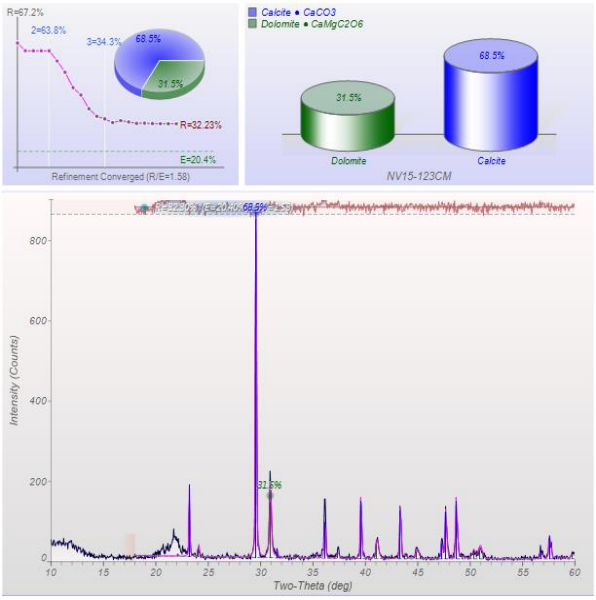

NV15-123CM

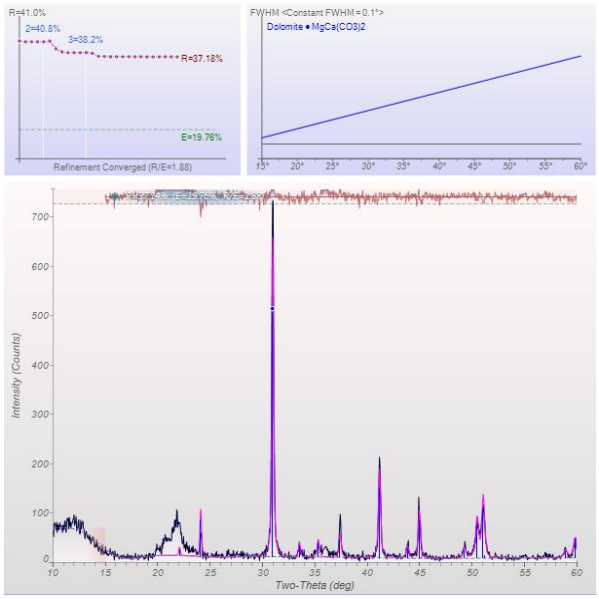

NV15-124CM

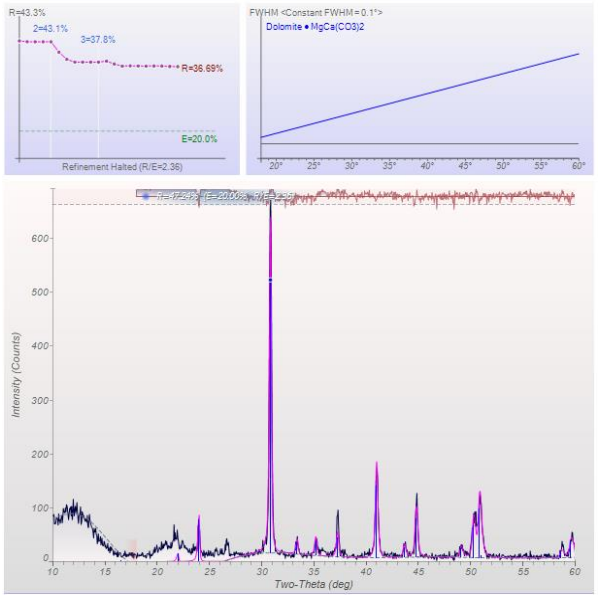

NV15-126CM

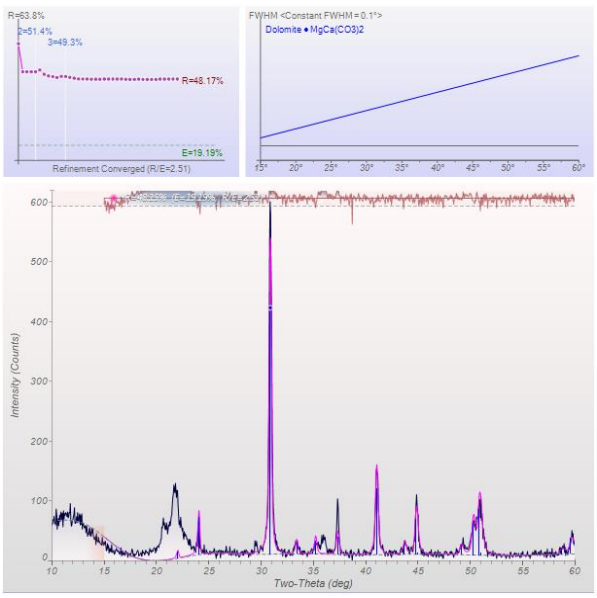

NV15-128CM

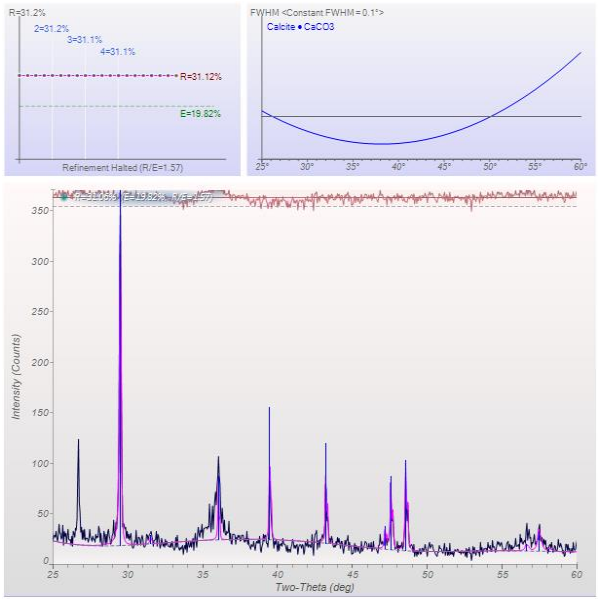

NV15-129CM

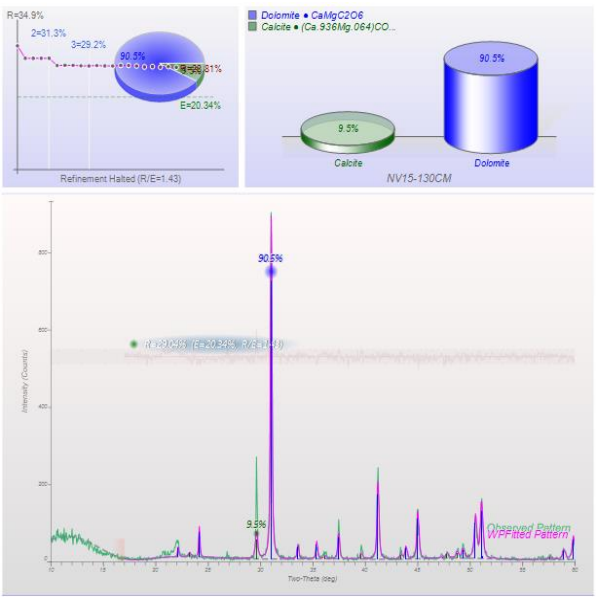

NV15-130CM

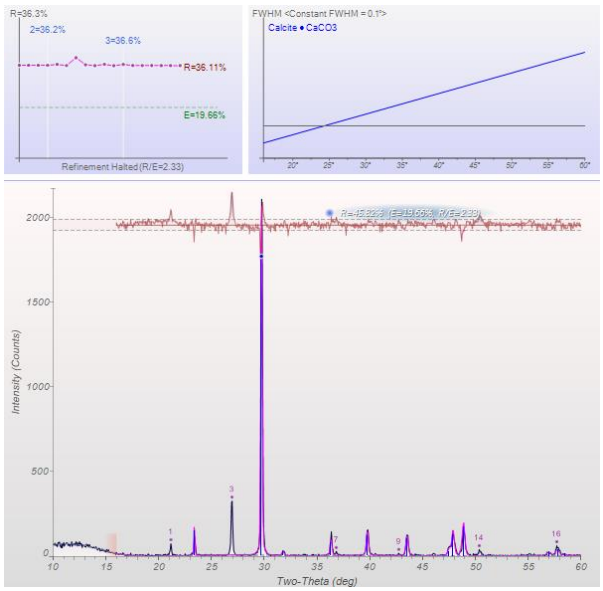

NV16-045TB

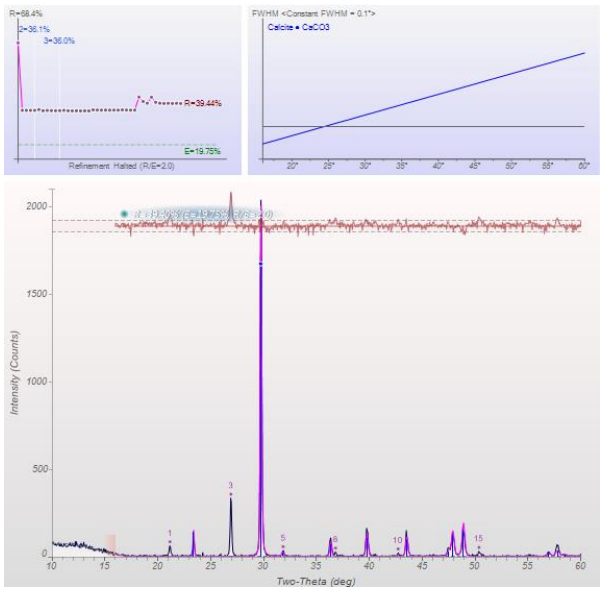

NV16-047TB

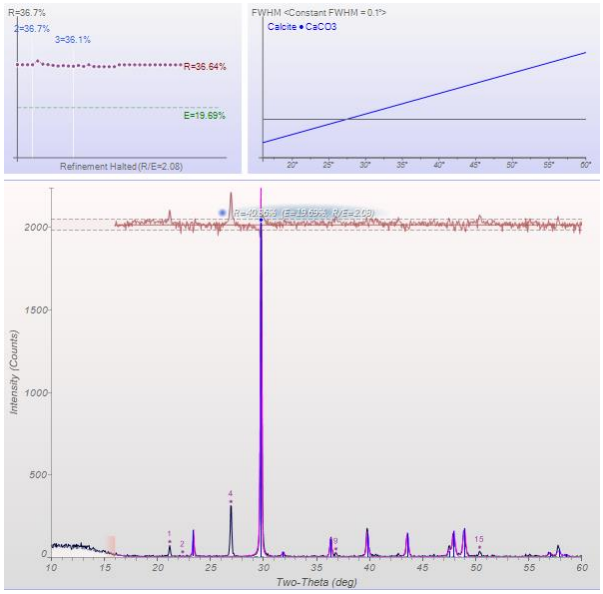

NV16-049TB

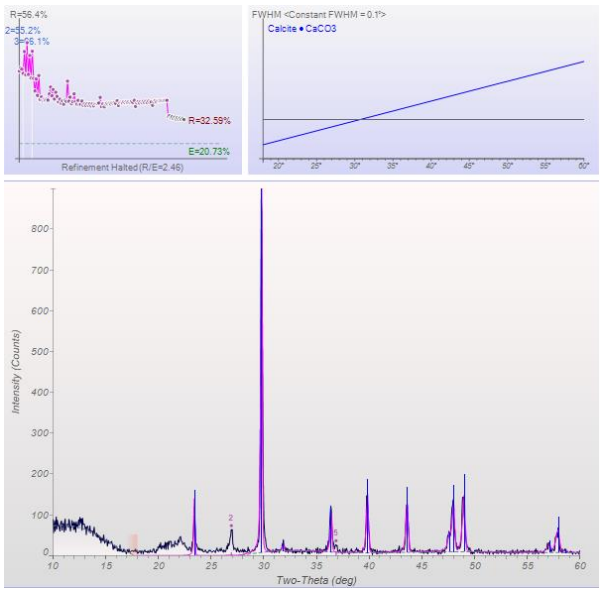

NV16-051TB

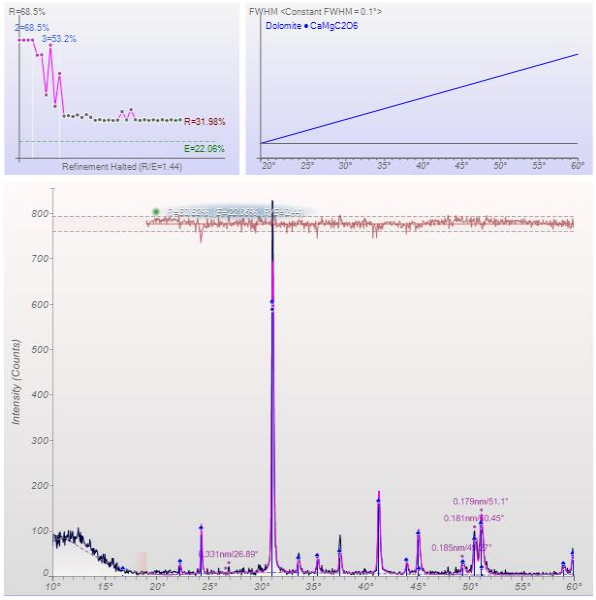

NV15-147TB

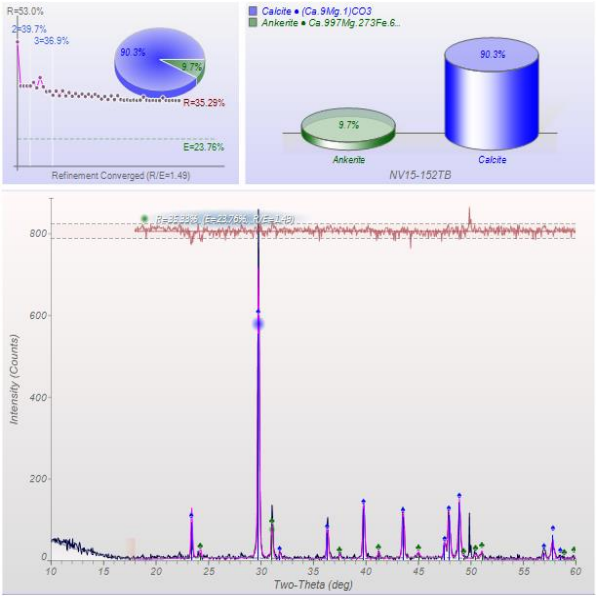

NV15-152TB

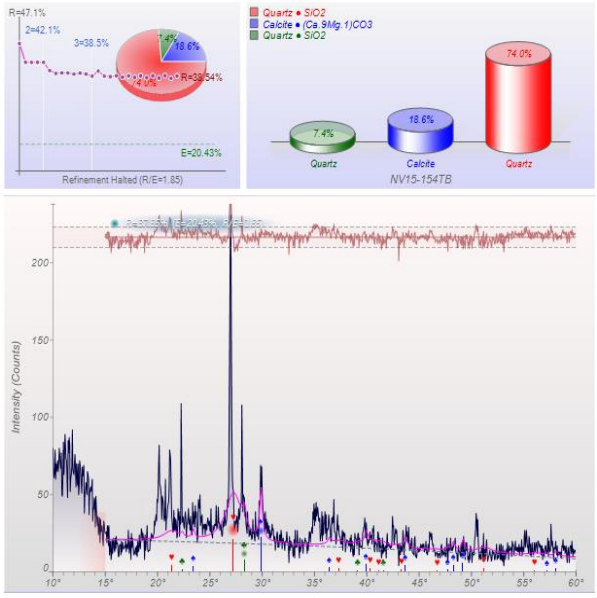

NV15-154TB

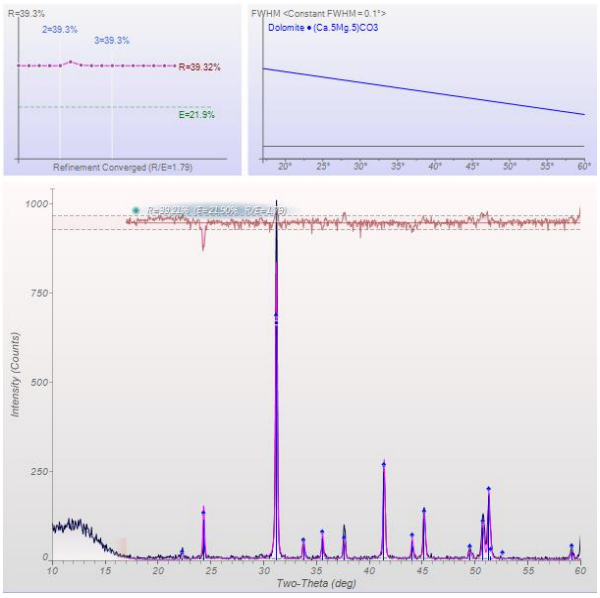

NV15-160TB

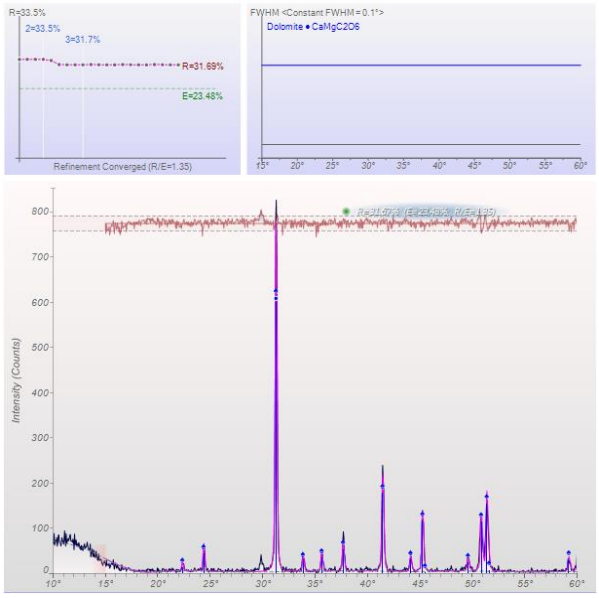

NV15-163TB

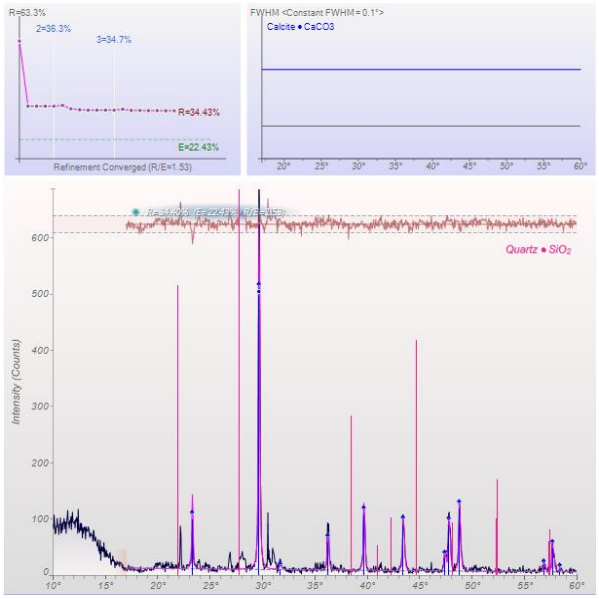

NV15-165TB

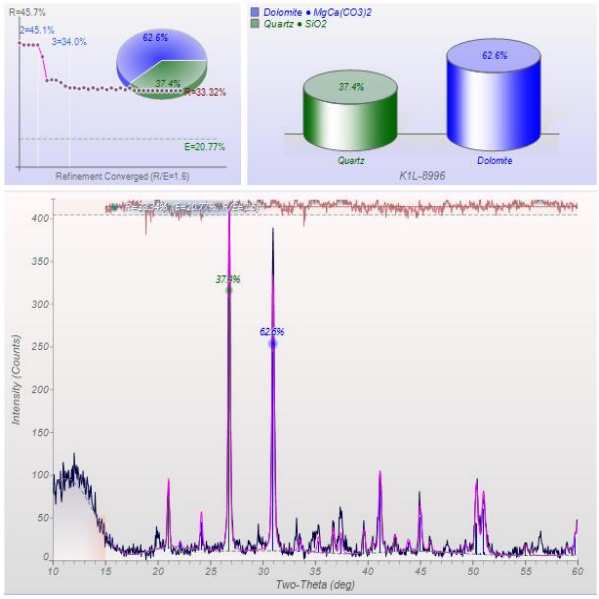

K1L-8996

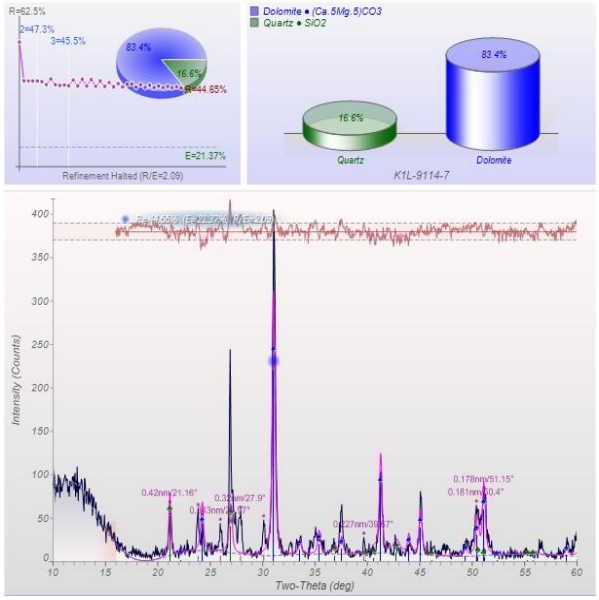

K1L-9114.7

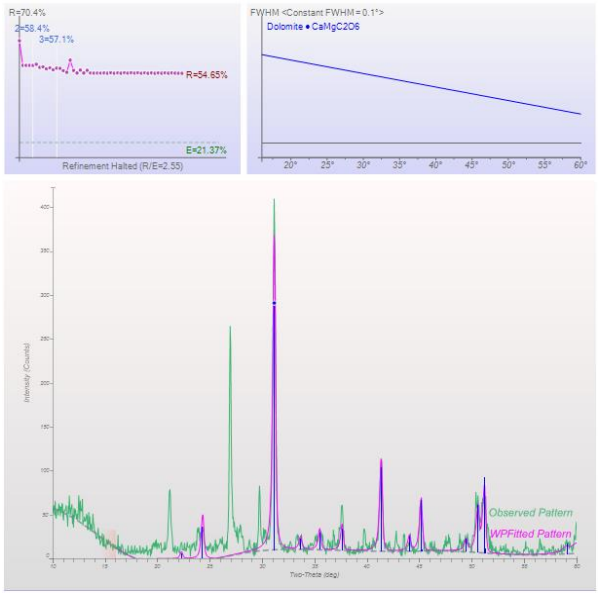

K1L-9158

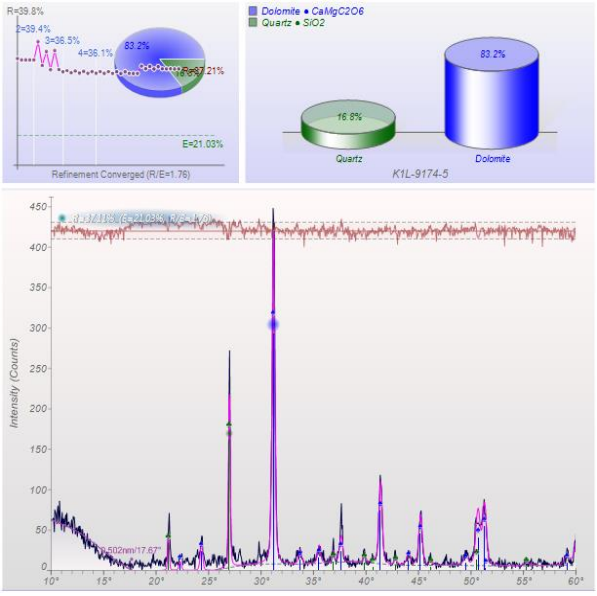

K1L-9174.5

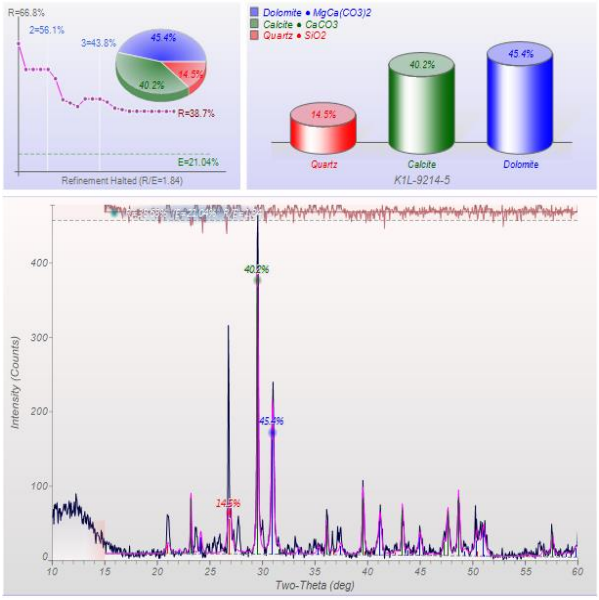

K1L-9214.5

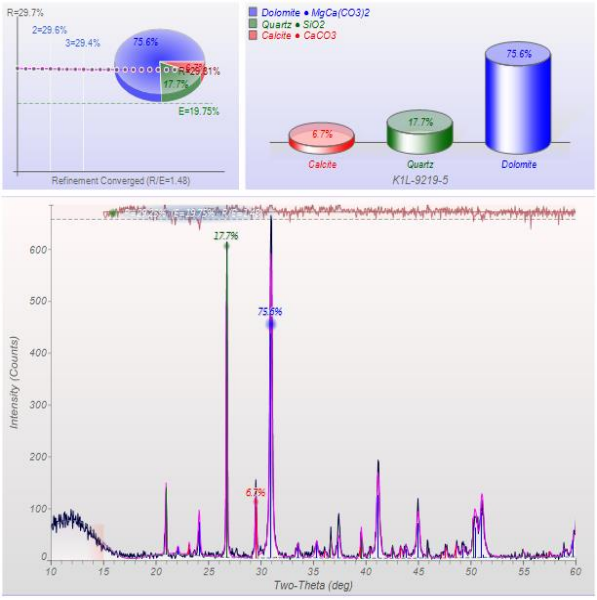

K1L-9219.5

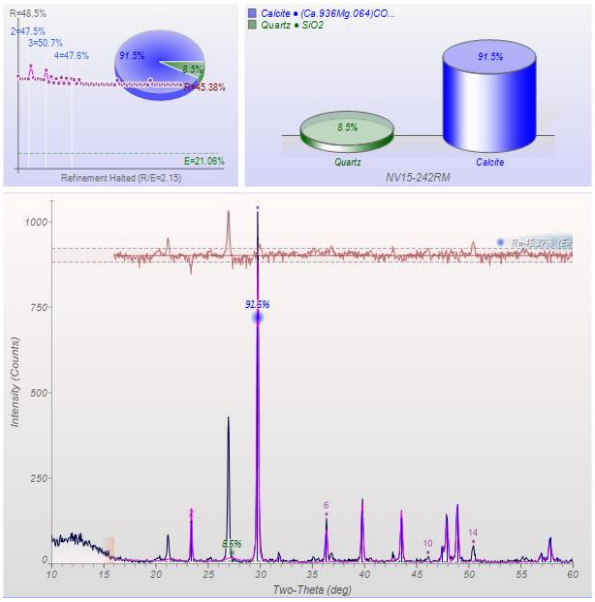

NV15-242RM

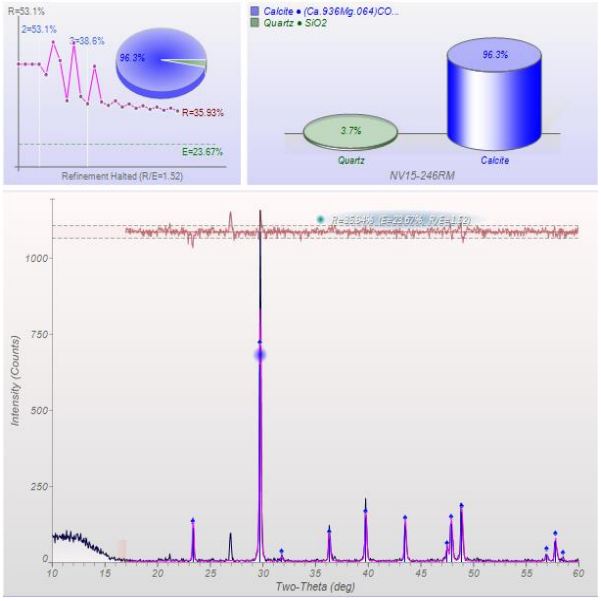

NV15-246RM

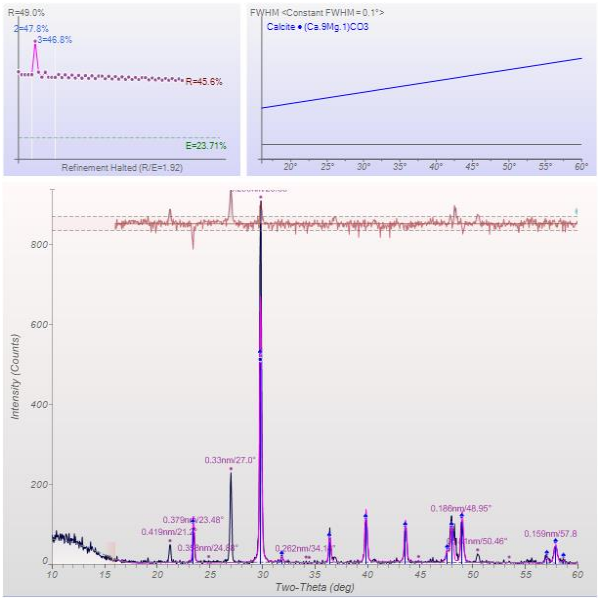

NV15-134TC

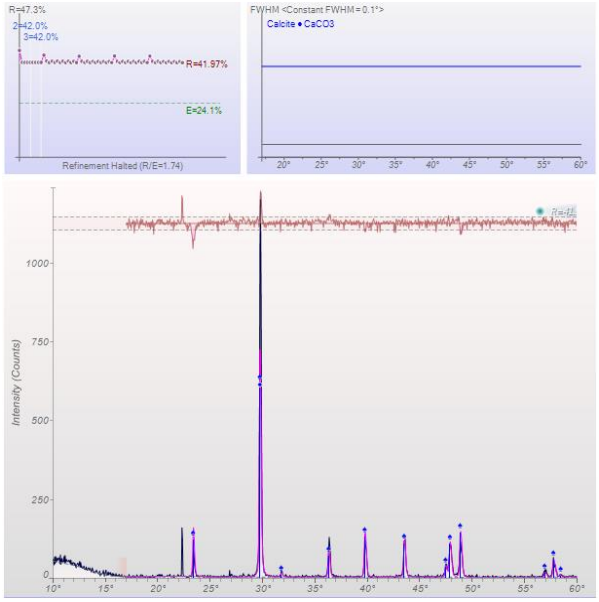

NV18-007CR

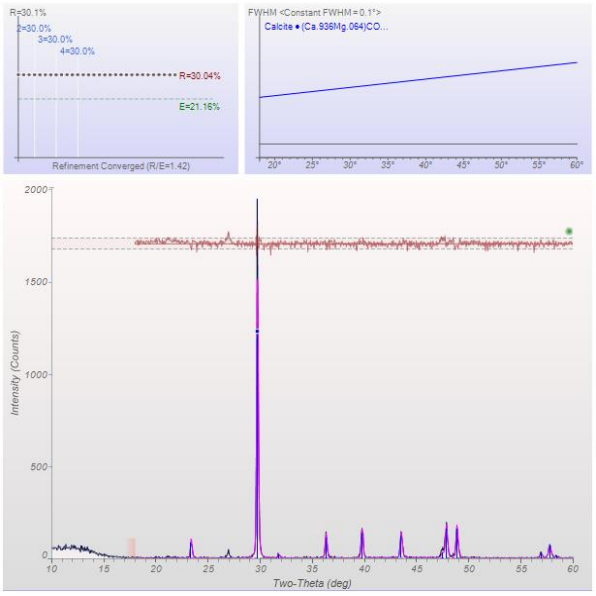

NV16-034CM

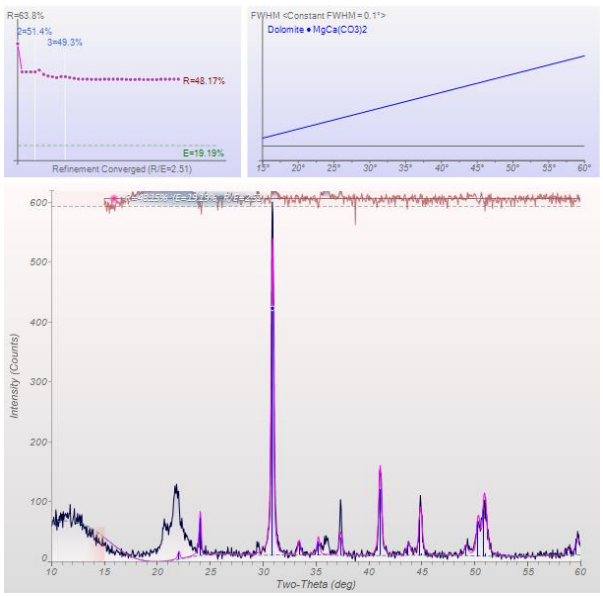

NV15-127CM

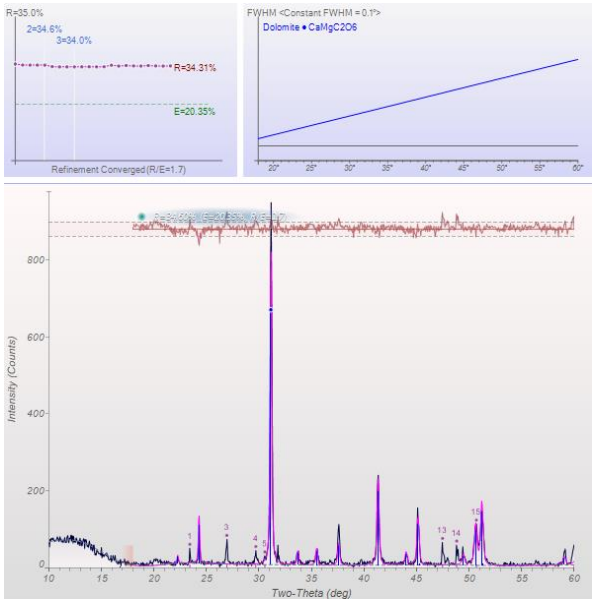

NV16-104PR

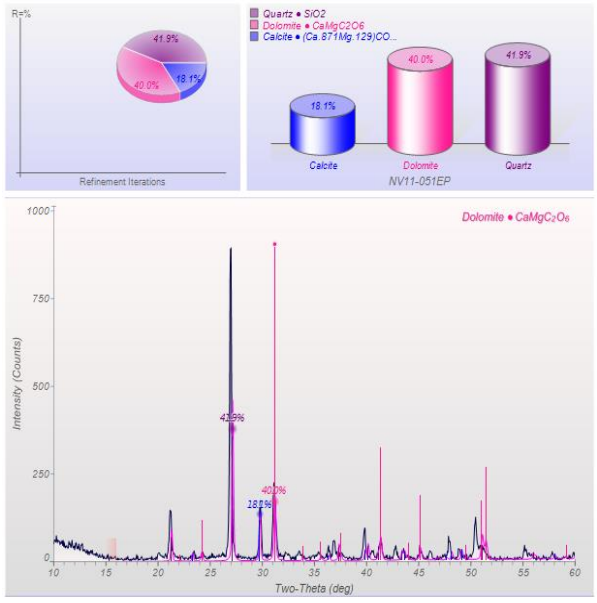

NV11-051EP

REFERENCES

Brand, U., Jiang, G., Azmy, K., Bishop, J., and Montañez, I. P., 2012, Diagenetic evaluation of a Pennsylvanian carbonate succession (Bird Spring Formation, Arrow Canyon, Nevada, U.S.A.) — 1: Brachiopod and whole rock comparison: Chemical Geology, v. 308-309, p. 26-39.

Canada, A. S., Cassel, E. J., Stockli, D. F., Smith, M. E., Jicha, B. R., and Singer B. S., 2019, *in press*, Accelerating exhumation in the Eocene North American Cordilleran hinterland: Implications from detrital zircon (U-Th)/(He-Pb) double dating: Geological Society of America Bulletin.

Doebbert, A. C., 2006, Geomorphic controls on lacustrine isotopic compositions: evidence from the Laney Member, Green River Formation (Wyoming) [MS Thesis]: University of Wisconsin-Madison, 247 p.

Doebbert, A. C., Johnson, C. M., Carroll, A. R., Beard, B. L., Pietras, J. T., Rhodes Carson, M., Norsted, B., and Throckmorton, L. A., 2014, Controls on Sr isotopic evolution in lacustrine systems: Eocene green river formation, Wyoming: Chemical Geology, v. 380, p. 172-189, doi:10.1016/j.chemgeo.2014.04.008.

Edwards, C. T., Saltzman, M. R., Leslie, S. A., Bergström, S. M., Sedlacek, A. R. C., Howard, A., Bauer, J. A., Sweet, W. C., and Young, S. A., 2015, Strontium isotope (87Sr/86Sr) stratigraphy of Ordovician bulk carbonate: Implications for preservation of primary seawater values: Geological Society of America Bulletin, v. 127, no. 9-10, p. 1275-1289.

Farmer, G. L., and DePaolo, D. J., 1983, Origin of Mesozoic and Tertiary granite in the Western United States and implications for pre-Mesozoic crustal structure 1. Nd and Sr isotopic studies in the geocline of the northern Great Basin, v. 88, no. B4, p. 3379-3401.

Gans, P. B., Mahood, G. A., and Schermer, E., 1989, Synextensional magmatism in the Basin and Range Province; A case study from the eastern Great Basin: Geological Society of America Special Paper, v. 233, p. 1-53.

Grunder, A. L., 1992, Two-stage contamination during crustal assimilation: isotopic evidence from volcanic rocks in eastern Nevada: Contributions to Mineralogy and Petrology, v. 112, p. 219-229.

Hegg, J. C., Kennedy, B. P., and Fremier, A. K., 2013, Predicting strontium isotope variation and fish location with bedrock geology: Understanding the effects of geologic heterogeneity: Chemical Geology, v. 360-361, p. 89-98.

Hershey, R. L., Rybarski, S., Thomas, J.M., and Pohll, G., 2014, Water-quality data, hydraulic fracturing in the upper Humboldt River Basin, aquifer quality assessment program, Report 2: Desert Research Institute, no. 41259, 54 p.

Kistler, R. W., Ghent, E. D., and O'Neil, J.R., 1981, Petrogenesis of two-mica granites in the Ruby Mountains, Nevada: Journal of Geophysical Research, v. 86, no. B11, p. 10591-10606.

Kistler, R. W., and Lee, D. E., 1989, Rubidium, strontium, and strontium isotopic data for a suite of granitoid rocks from the Basin and Range Province, Arizona, California, Nevada, and Utah: U.S. Geological Survey Open-File Report 89-199, 15 p.

McCrea, J. M., 1950, On the isotopic chemistry of carbonates and a paleotemperature scale: The Journal of Chemical Physics, v. 18, p. 849–857.

Paces, J. B., Peterman, Z. E., Futa, K., Oliver, T. A., and Marshall, B. D., 2007, Strontium isotopic composition of Paleozoic carbonate rocks in the Nevada Test Site vicinity, Clark, Lincoln, and Nye counties, Nevada, and Inyo County, California: U.S. Geological Survey Data Series 280, 42 p.

Swart, P. K., Burns, S. J., and Leder, J. J., 1991, Fractionation of the stable isotopes of oxygen and carbon in carbon dioxide during the reaction of calcite with phosphoric acid as a function of temperature and technique: Chemical Geology: Isotope Geoscience section, v. 86, no. 2, p. 89-96.

Stevens, C., 2013, Petrography, geochemistry and isotopic analysis of Paleogene volcanism in the Fish Creek Mountains, Great Basin, north-central Nevada [MS Thesis]: Carleton University, Ottowa, Ontario, 155 p.

U.S. Geological Survey, 2016, National Water Information System data available on the World Wide Web: USGS Water Data for the Nation, doi:10.5066/F7P55KJN.

Vermeesch, P., 2018, IsoplotR: A free and open toolbox for geochronology: Geoscience Frontiers, v. 9, p. 1479-1493.

Wright, J. E., and Snoke, A. W., 1993, Tertiary magmatism and mylonitization in the Ruby-East Humboldt metamorphic core complex, northeastern Nevada: U-Pb geochronology and Sr, Nd, and Pb isotope geochemistry: Geological Society of America Bulletin, v. 105, p. 935-952.

Wright, J.E., and Wooden, J.L., 1991, New Sr, Nd, and Pb isotopic data from plutons in the northern Great Basin: Implications for crustal structure and granite petrogenesis in the hinterland of the Sevier thrust belt: Geology, v. 19, p. 457-460.

APPENDIX D

Supplemental Materials for Chapter IV

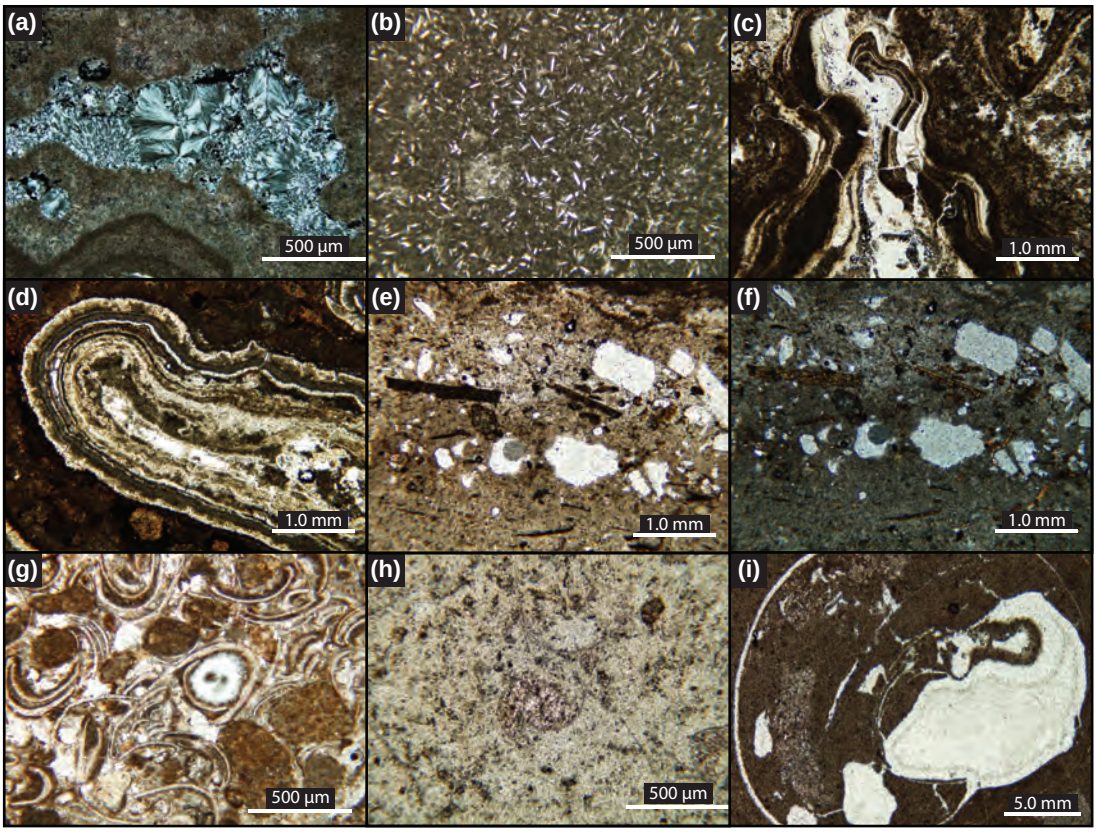

Figure D1. Thin section photomicrographs of Elko Formation carbonate facies: (A) chalcedony in stromatolitic dolomicrite; (B) micrite with lenticular gypsum laths; (C–D) algal laminations in limestone; (E–F) carbonaceous material and lithic quartz in carbonate mudstone; (G) ostracode packstone; (H) ostracode in dolostone; and (I) gastropod in carbonate mudstone.

			Location		Elko Formation	
Permit #	Operator	Name	Latitude	Longitude	Depth to top (m)	Estimated thickness (m)
3	Gulf Refining Co.	Wilkins Ranch No. 1	41°10'11"N	115°04'57"W	1190	1053
24	Richfield Oil Corp.	Rabbit Creek Unit No. 1	40°51'02"N	115°31'16"W	727	208
32	Richfield Oil Corp.	Scott-Ogilvie No. 1	41°36'23"N	116°07'30"W	338	241
147	Pan American Petroleum Corp.	U.S.A. Franklin No. 1	40°29'35"N	115°14'14"W	1189	994
149	Pan American Petroleum Corp.	U.S.A. Jiggs No. 1	40°23'13"N	115°42'14"W	2921	436
178	Ladd Petroleum Corp.	Federal No. 1-31-N	41°19'07"N	115°49'40"W	853	436
182	Ladd Petroleum Corp.	Nevelko No. 1	40°50'03"N	115°46'57"W	1317	357
207	Filson Exploration Co.	Ellison No. 1	41°23'37"N	116°07'50"W	1219	79
220	Gulf Refining Co.	Mary's River Federal No. 1	41°08'57"N	115°07'41"W	2181	1515
246	Wexpro Co.	Cord No. 24-1	40°23'13"N	115°43'19"W	2743	545
259	Aminoil U.S.A., Inc.	S.P. Land Company No. 1-23	40°27'51"N	116°05'03"W	1280	419
263	Wexpro Co.	Jiggs No. 10-1	40°24'34"N	115°45'32"W	2760	148
289	Sohio Petroleum Co.	Ruby Valley Unit No. 1	40°29'19"N	115°10'21"W	1250	530
332	Cities Service Co.	Federal BL No. 1	40°23'20"N	115°43'48"W	2297	470
377	Diamond Shamrock Exploration Co.	Kimbark Federal No. 1-28	41°03'52"N	115°40'24"W	52	86
428	Diamond Shamrock Exploration Co.	Magnuson Fee No. 22-21	40°54'28"N	115°47'17"W	304	281
429	Sun Exploration and Production Co.	Elko Hills No. 1	40°47'31"N	115°37'12"W	363	159
489	Quintana Petroleum Corp.	Magnuson Fee No. 1-21	40°54'33"N	115°47'26"W	408	141
492	Foreland Corp.	Foreland-Southern Pacific Land Co. No. 1-5	40°30'58"N	116°07'34"W	566	85
505	Exxon Corp.	Aspen Unit No. 1	40°17'46"N	115°53'33"W	946	194
716	Frontier Exploration Co.	Federal No. 16-5	40°14'44"N	115°40'54"W	521	606
729	Petroleum Corp. of Nevada	No. AV-10	41°01'26"N	115°53'27"W	465	83
818	Foreland Corp.	Dixie Flats Federal No. 1-4	40°35'47"N	115°54'12"W	322	290
826	V. F. Neuhaus Properties	Tomera Ranch No. 33-1	40°31'12"N	116°07'21"W	444	30
909	Charter Oak Production Co.	Ruby Valley No. 1-11	40°29'32"N	115°10'42"W	942	552
922	Tetuan Resources	Mary River No. 34-26	41°08'35"N	115°02'53"W	1679	357
955	Noble Energy	S25G	41°08'58"N	115°15'41"W	2469	925
960	Noble Energy	K1L	40°25'13"N	115°44'13"W	2417	457
946	Noble Energy	M10C	40°51'01"N	115°25'38"W	2594	168
942	Noble Energy	M2C	40°51'49"N	115°24'24"W	2420	130

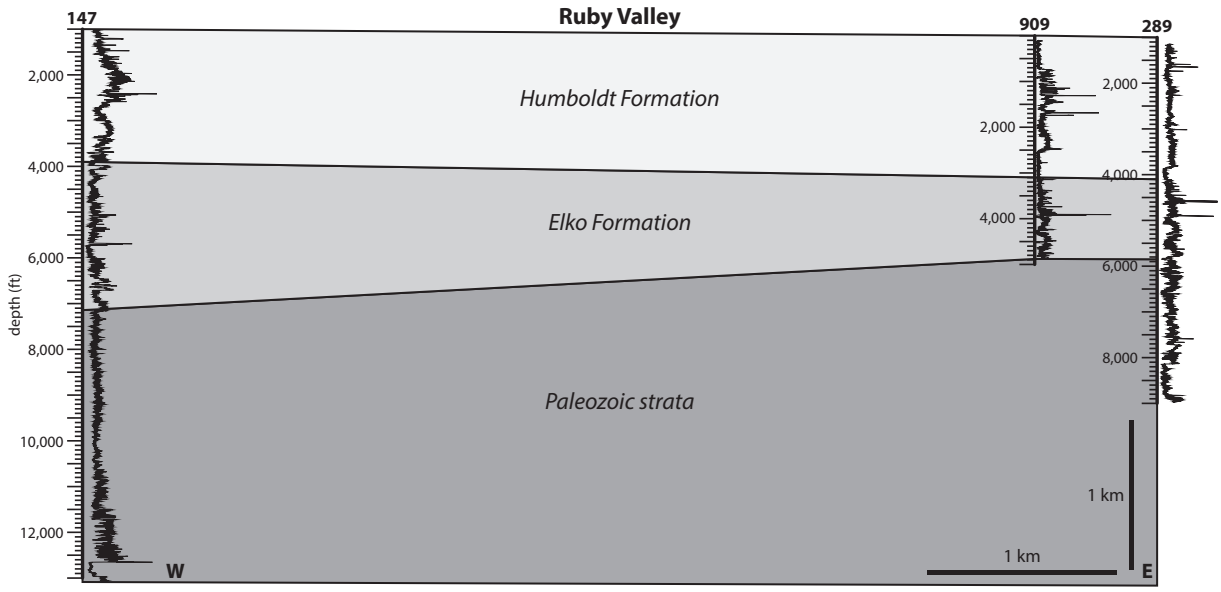

Figure D2. Gamma ray correlation and interpreted cross-section across Ruby Valley based on well and seismic data. Well data from the Nevada Bureau of Mines and Geology (NBMG); seismic data from Satarugsa and Johnson (2000). Well permit numbers: 147—USA Franklin No. 1; 289—Ruby Valley No. 1; 909—Ruby Valley Federal No. 1-11.

Figure D3. Photo of cuttings showing representative Elko Formation lithologies in USA Franklin No. 1 well. Sample collected at a depth of ~5,100'.

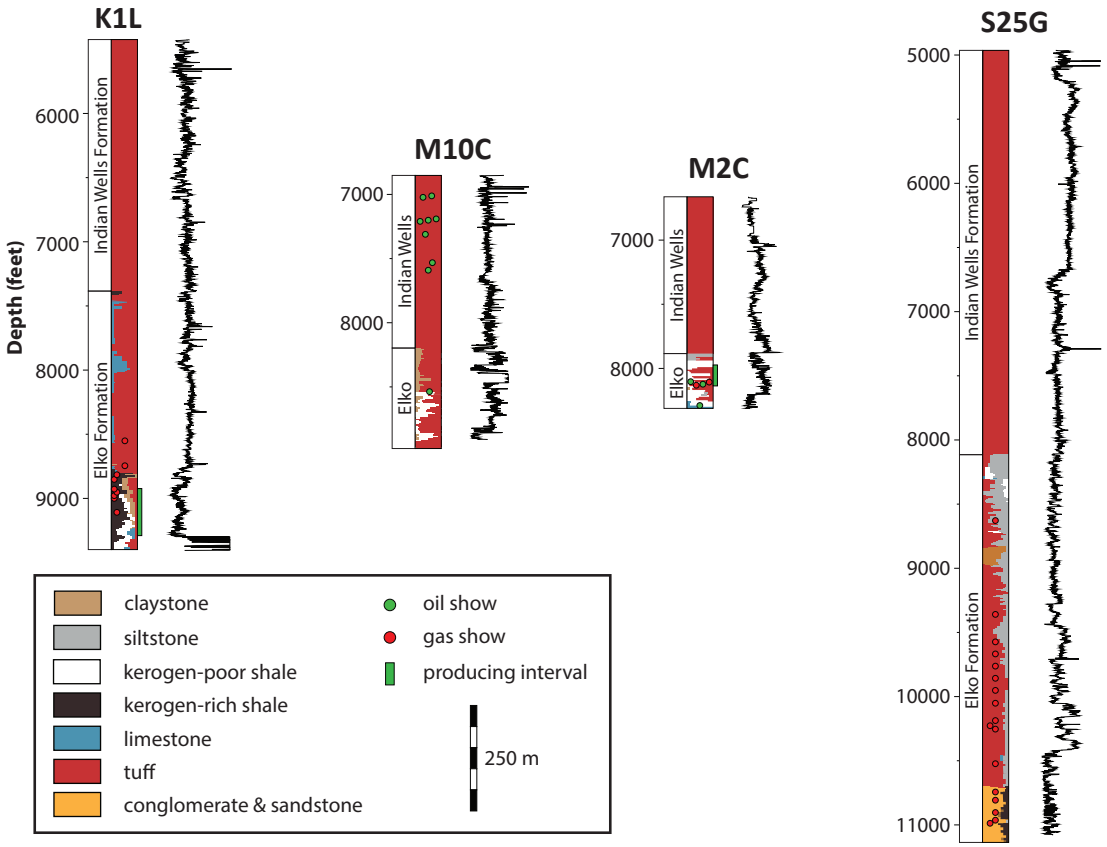

Figure D4. Interpreted percent lithology, formation tops, and gamma ray logs for Noble Energy wells drilled in 2013–2014. All data compiled from Nevada Bureau of Mines and Geology (NBMG).

Robinson Mountain
Elko Formation

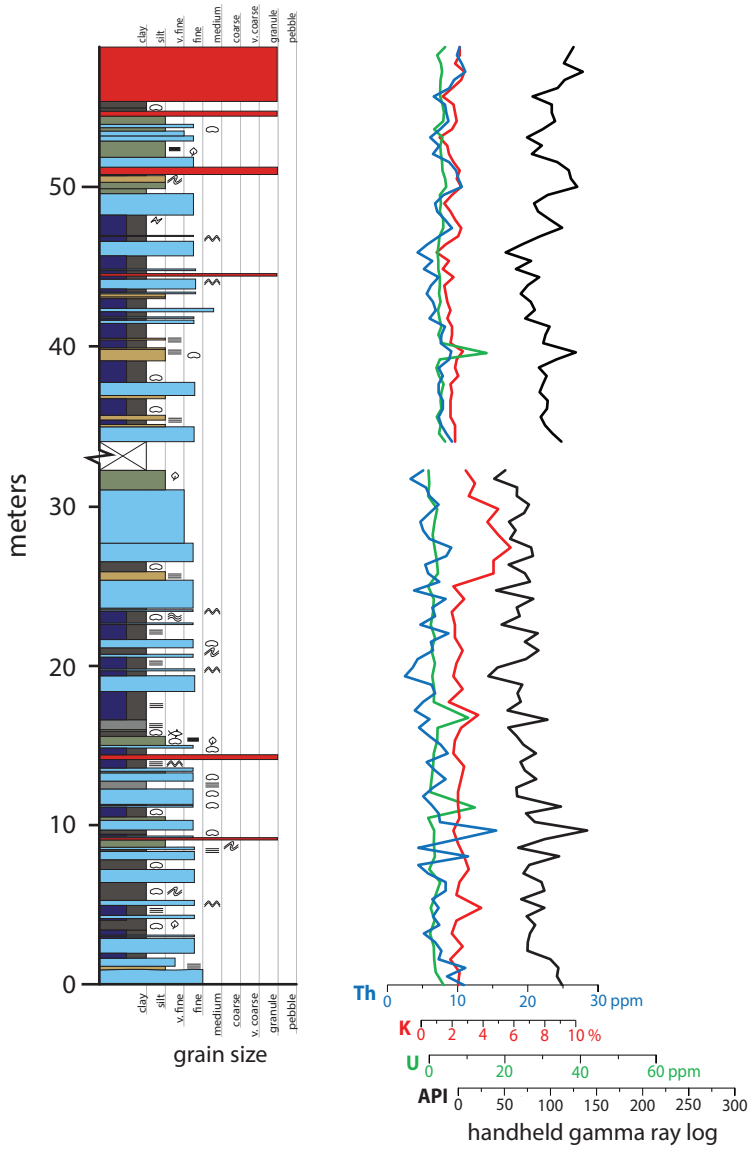

Lithofacies
- Kerogen-rich carbonate mudstone
  Blue bed (organic-rich
- Kerogen-poor carbonate mudstone
- Siliciclastic mudstone and siltstone
- Calcareous siltstone
- Limestone
- Ash

Sedimentary Structures
- Planar lamination
- Wavy lamination
- Soft sediment deformation
- Syneresis cracks

Fossils
- Algal
- Ostracodes
- Fish
- Carbonaceous
- Plant matter

Bullion Road
Elko Formation

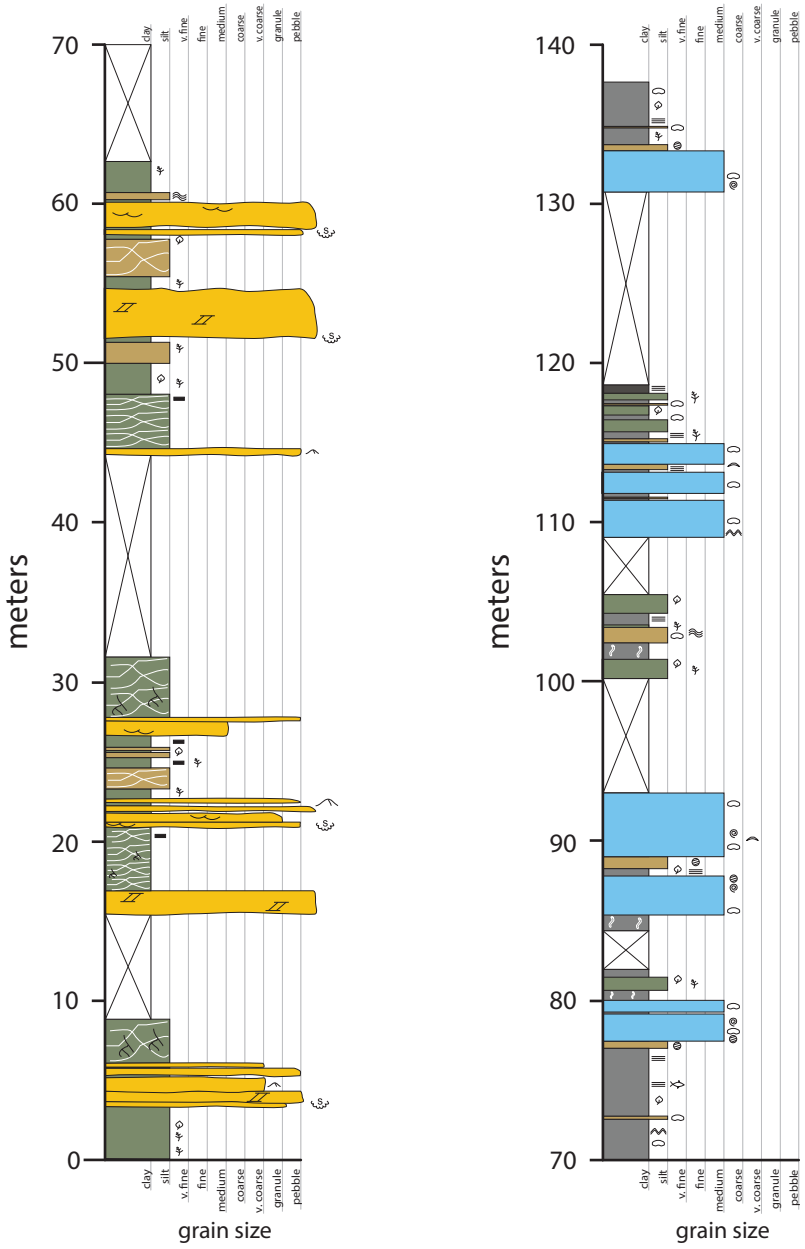

Lithofacies
- Kerogen-rich carbonate mudstone
- Kerogen-poor carbonate mudstone
- Siliciclastic mudstone and siltstone
- Calcareous siltstone
- Limestone
- Sandstone and conglomerate

Sedimentary Structures
- Planar lamination
- Wavy lamination
- Planar cross-bedding
- Trough cross-bedding
- Current ripple
- Scour
- Soil horizon

Fossils
- Algal
- Ostracodes
- Gastropods
- Bivalves
- Fish
- Carbonaceous
- Leaves
- Metasequoia
- Charophyte
- Roots
- Burrows

Huntington Valley - Dixie Hills

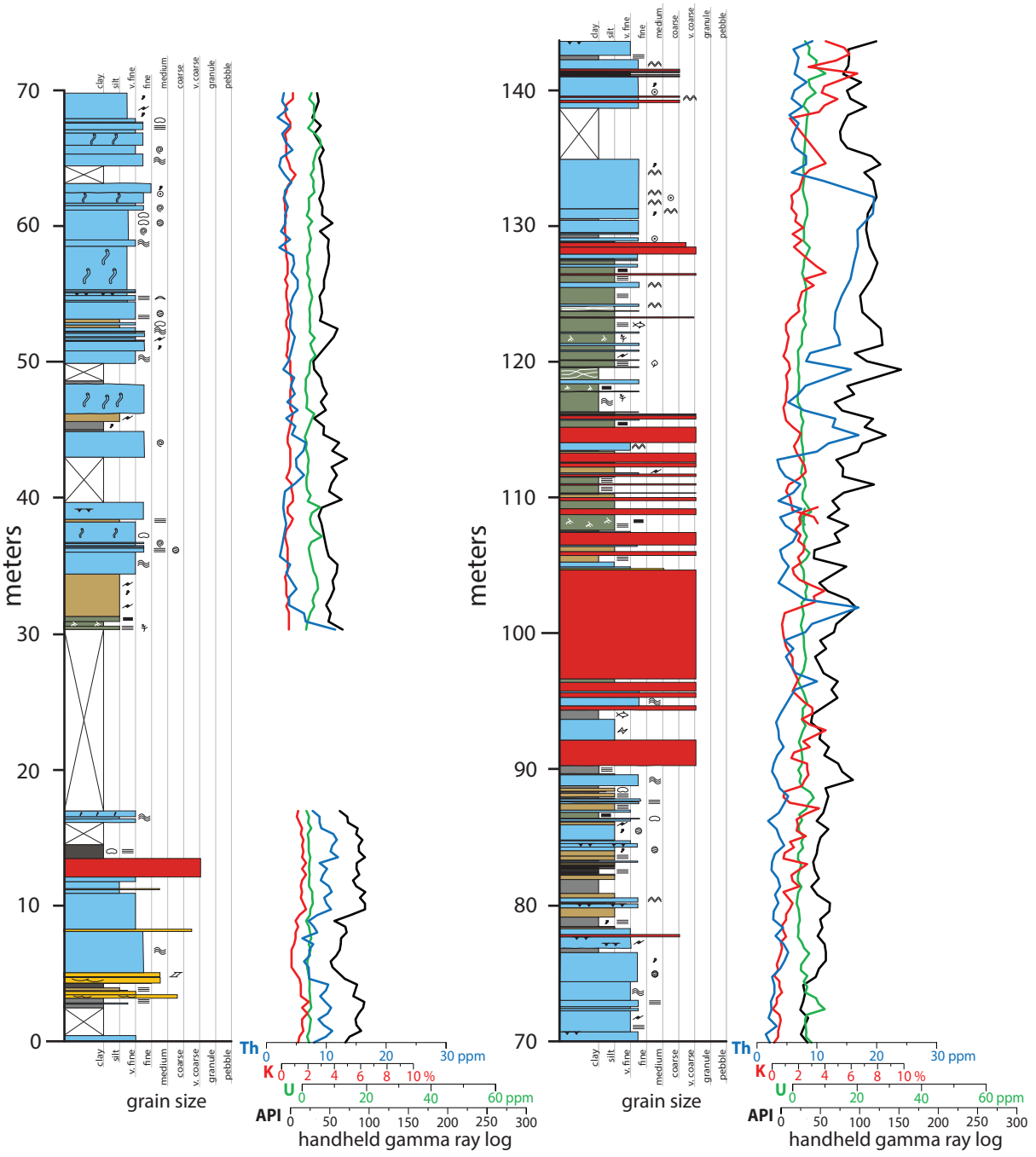

Lithofacies

- Kerogen-rich carbonate mudstone
- Kerogen-poor carbonate mudstone
- Siliciclastic mudstone and siltstone
- Calcareous siltstone
- Sandstone and conglomerate
- Limestone
- Ash

Sedimentary Structures

- Planar lamination
- Wavy lamination
- Planar cross-bedding
- Trough cross-bedding
- Mudcracks
- Soil horizon

Fossils

- Algal
- Ostracodes
- Gastropods
- Bivalves
- Fish
- Ooids/oncoids
- Leaves
- Metasequoia
- Charophyte
- Roots
- Burrows
- Carbonaceous

Northern Adobe Range
Elko Formation

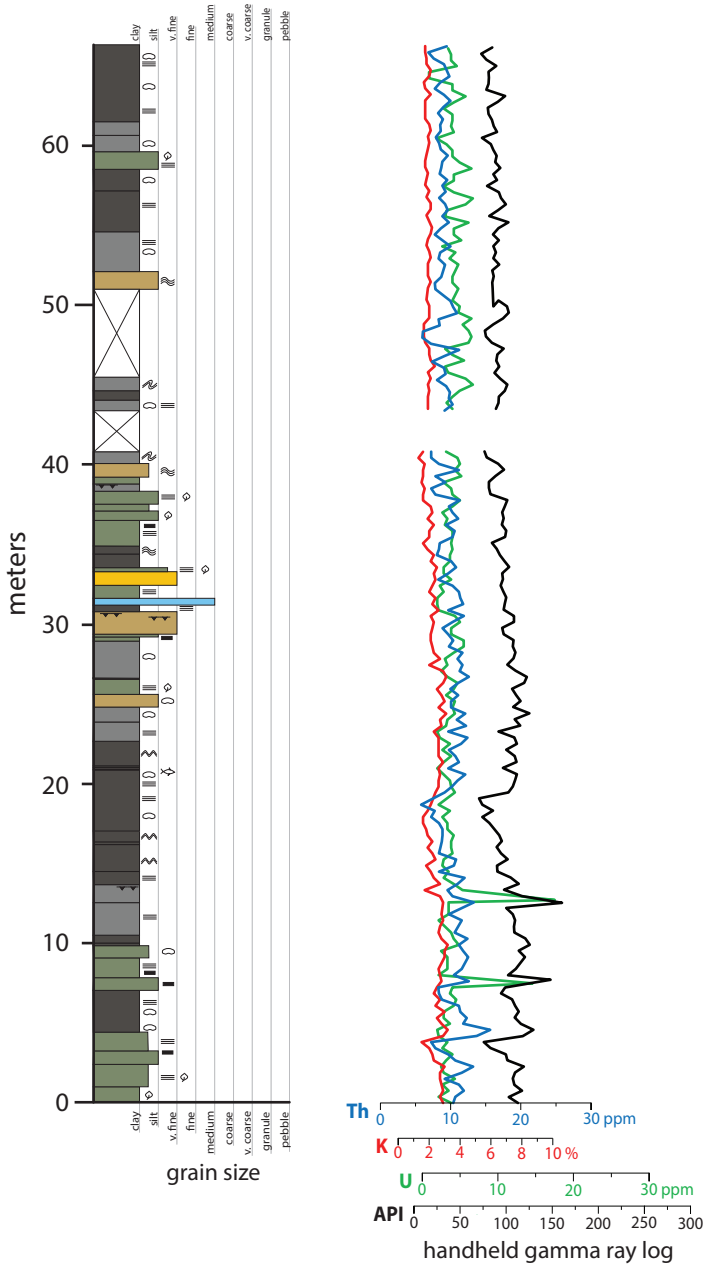

Lithofacies
- Kerogen-rich carbonate mudstone
- Kerogen-poor carbonate mudstone
- Siliciclastic mudstone and siltstone
- Calcareous siltstone
- Limestone
- Sandstone

Sedimentary Structures
- Planar lamination
- Wavy lamination
- Soft sediment deformation
- Mudcracks

Fossils
- Algal
- Ostracodes
- Fish
- Carbonaceous
- Plant matter

Coal Mine Canyon, Adobe Range
Elko Formation

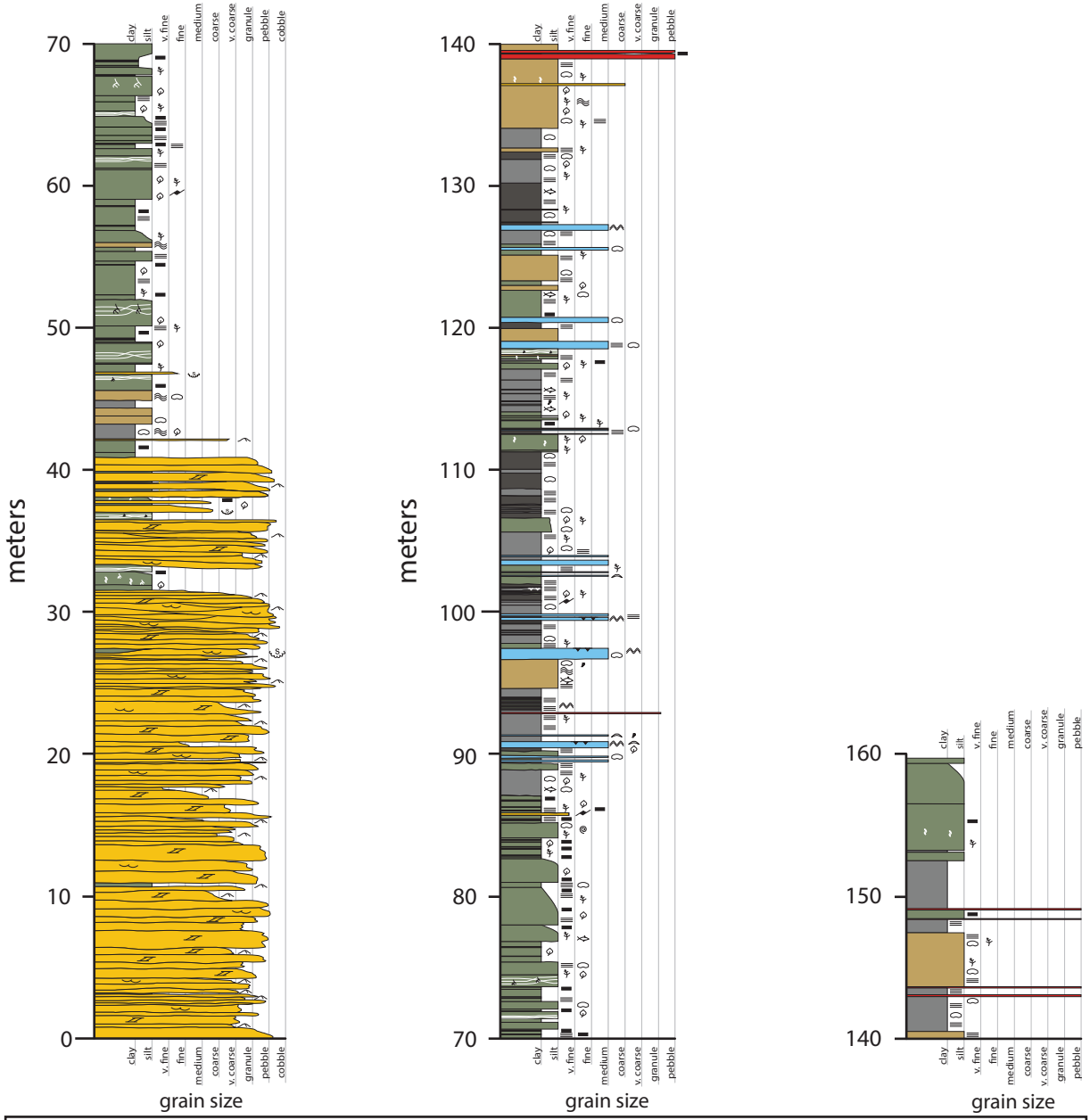

Lithofacies
- Kerogen-rich carbonate mudstone
- Kerogen-poor carbonate mudstone
- Siliciclastic mudstone and siltstone
- Calcareous siltstone
- Limestone
- Sandstone and conglomerate
- Coal
- Ash

Sedimentary Structures
- Planar lamination
- Wavy lamination
- Planar cross-bedding
- Trough cross-bedding
- Current ripple
- Scour
- Soil horizon
- Mudcracks
- Mudstone rip-up clasts
- Soft sediment deformation

Fossils
- Algal
- Metasequoia
- Ostracodes
- Roots
- Gastropods
- Burrows
- Bivalves
- Fish
- Peloids
- Carbonaceous
- Leaves

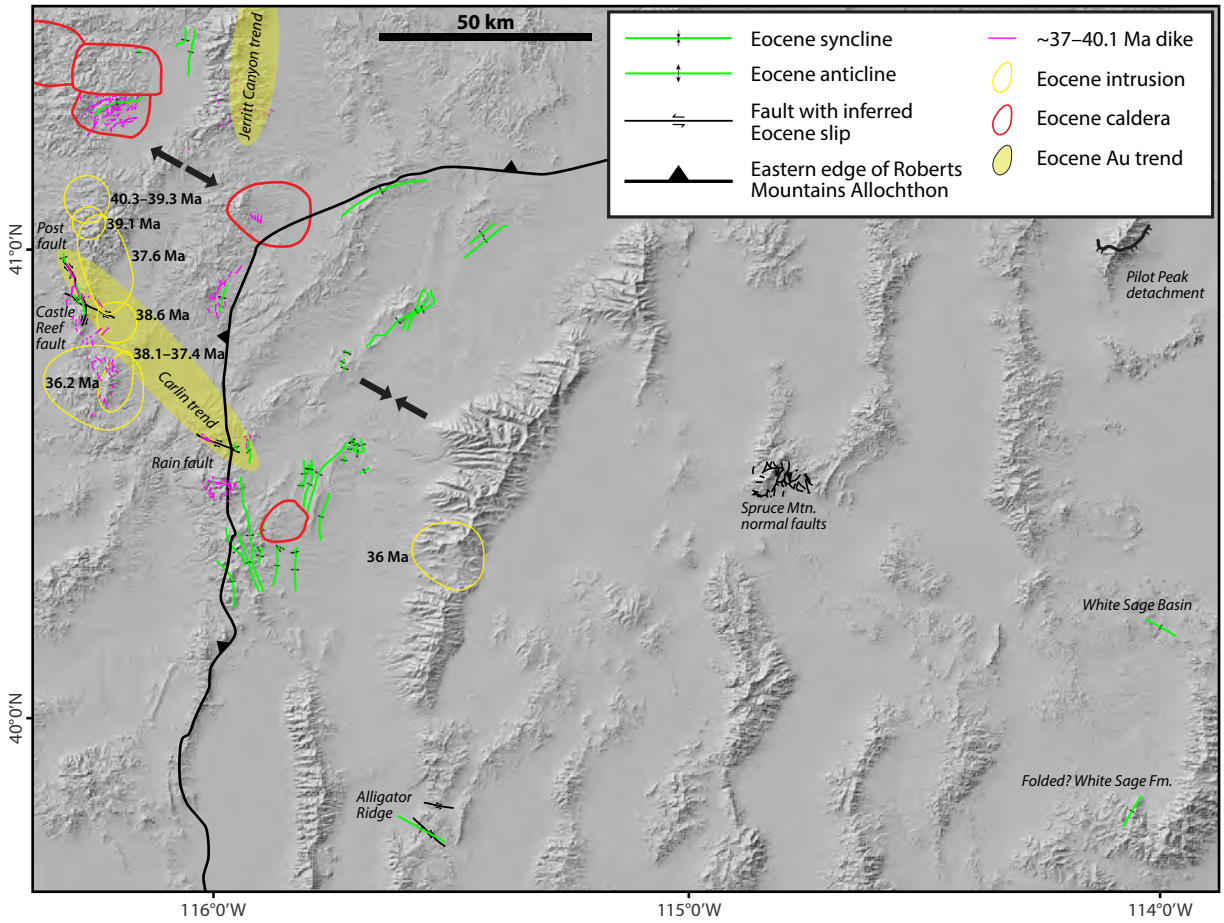
50 km
Eocene syncline
Eocene anticline
Fault with inferred Eocene slip
Eastern edge of Roberts Mountains Allochthon
~37–40.1 Ma dike
Eocene intrusion
Eocene caldera
Eocene Au trend
Jerritt Canyon trend
40.3–39.3 Ma
39.1 Ma
37.6 Ma
Post fault
Castle Reef fault
38.6 Ma
38.1–37.4 Ma
36.2 Ma
Carlin trend
Rain fault
36 Ma
Spruce Mtn. normal faults
Pilot Peak detachment
White Sage Basin
Folded? White Sage Fm.
Alligator Ridge
41°0′N
40°0′N
116°0′W
115°0′W
114°0′W

APPENDIX E

Detrital Zircon U-Pb Data for the White Sage Formation and Additional Elko Formation Provenance Data

DETRITAL ZIRCON U-Pb ANALYSES

White Sage Formation Samples

Analysis	U (ppm)	U/Th	207Pb/ 235U	±	206Pb/ 238U	±	err. corr.	207Pb/ 235U Age (Ma)	± (Ma)	206Pb/ 238U Age (Ma)	± (Ma)	207Pb/ 206Pb Age (Ma)	± (Ma)	Best age (Ma)	± (Ma)	Disc (%)
NV16-006WSB: White Sage Basin 40°12'30"N, 113°59'30"W																
NV16006_1.FIN2	339	0.92	0.160	0.0055	0.0238	0.0005	0.465	150.0	4.8	151.6	3.2	125	63	151.6	3.2	1.1
NV16006_2.FIN2	41.9	1.94	1.737	0.0470	0.1661	0.0035	0.629	1019.0	18.0	989.0	20.0	1099	43	1099.0	43.0	10.0
NV16006_3.FIN2	100.6	2.61	1.530	0.0410	0.1582	0.0035	0.655	944.0	16.0	948.0	19.0	953	43	953.0	43.0	0.5
NV16006_4.FIN2	31.78	0.32	13.300	0.3700	0.5100	0.0120	0.729	2708.0	26.0	2665.0	52.0	2727	31	2727.0	31.0	2.3
NV16006_5.FIN2	87	0.24	12.620	0.2800	0.4960	0.0110	0.815	2650.0	21.0	2593.0	47.0	2688	21	2688.0	21.0	3.5
NV16006_6.FIN2	941	1.12	0.175	0.0051	0.0244	0.0005	0.492	163.8	4.4	155.2	3.2	282	53	155.2	3.2	5.3
NV16006_7.FIN2	249.3	0.96	13.020	0.2600	0.5080	0.0100	0.857	2686.0	19.0	2648.0	43.0	2713	17	2713.0	17.0	2.4
NV16006_8.FIN2	73.1	0.48	5.820	0.1300	0.3454	0.0068	0.721	1948.0	19.0	1913.0	32.0	2006	28	2006.0	28.0	4.6
NV16006_9.FIN2	738	1.75	0.171	0.0050	0.0250	0.0005	0.507	159.9	4.4	159.3	3.3	177	54	159.3	3.3	0.4
NV16006_10.FIN2	1063	1.39	0.163	0.0054	0.0243	0.0007	0.520	154.6	4.5	154.6	4.1	153	59	154.6	4.1	0.0
NV16006_11.FIN2	691	0.96	0.161	0.0055	0.0240	0.0005	0.441	152.5	4.7	153.1	2.8	145	63	153.1	2.8	0.4
NV16006_12.FIN2	944	5.05	3.600	0.1200	0.2467	0.0081	0.871	1555.0	26.0	1420.0	41.0	1766	30	1766.0	30.0	19.6
NV16006_14.FIN2	512	1.51	0.174	0.0074	0.0244	0.0006	0.514	163.1	6.5	155.3	3.6	247	86	155.3	3.6	4.8
NV16006_15.FIN2	479	1.04	3.638	0.0770	0.2655	0.0056	0.800	1554.0	17.0	1516.0	29.0	1615	24	1615.0	24.0	6.1
NV16006_16.FIN2	86.1	1.59	5.080	0.1300	0.3232	0.0067	0.624	1828.0	22.0	1809.0	32.0	1875	36	1875.0	36.0	3.5
NV16006_17.FIN2	484	1.08	4.340	0.1100	0.2976	0.0081	0.741	1698.0	21.0	1677.0	40.0	1731	33	1731.0	33.0	3.1
NV16006_18.FIN2	557	3.05	2.193	0.0480	0.1883	0.0039	0.768	1177.0	15.0	1113.0	21.0	1287	30	1287.0	30.0	13.5
NV16006_19.FIN2	77.6	1.35	1.550	0.1100	0.1567	0.0068	0.538	941.0	44.0	937.0	38.0	940	120	940.0	120.0	0.3
NV16006_20.FIN2	448	1.31	0.168	0.0074	0.0243	0.0007	0.350	157.3	6.4	154.8	4.3	234	94	154.8	4.3	1.6
NV16006_21.FIN2	157	1.18	3.022	0.0790	0.2439	0.0064	0.647	1410.0	20.0	1410.0	34.0	1446	42	1446.0	42.0	2.5
NV16006_22.FIN2	311.3	1.35	4.090	0.1200	0.2905	0.0065	0.764	1657.0	22.0	1651.0	33.0	1661	34	1661.0	34.0	0.6

NV16006_23.FIN2	157.7	1.12	2.105	0.0470	0.1948	0.0037	0.626	1148.0	15.0	1148.0	20.0	1128	36	1128.0	36.0	1.8
NV16006_24.FIN2	46.5	0.62	13.940	0.3600	0.5350	0.0120	0.753	2743.0	25.0	2761.0	51.0	2731	29	2731.0	29.0	1.1
NV16006_25.FIN2	300	1.08	1.812	0.0390	0.1693	0.0038	0.607	1052.0	14.0	1009.0	21.0	1112	35	1112.0	35.0	9.3
NV16006_26.FIN2	72.6	1.70	1.377	0.0490	0.1453	0.0043	0.500	884.0	22.0	874.0	24.0	934	71	934.0	71.0	6.4
NV16006_27.FIN2	106.7	1.33	2.113	0.0530	0.1943	0.0043	0.545	1150.0	18.0	1143.0	23.0	1166	46	1166.0	46.0	2.0
NV16006_28.FIN2	293.1	0.88	4.549	0.0900	0.3124	0.0063	0.780	1739.0	17.0	1750.0	31.0	1734	24	1734.0	24.0	0.9
NV16006_29.FIN2	230.9	2.05	2.081	0.0440	0.1948	0.0035	0.740	1144.0	14.0	1147.0	19.0	1139	29	1139.0	29.0	0.7
NV16006_30.FIN2	106.9	0.24	12.420	0.3500	0.4790	0.0150	0.728	2633.0	27.0	2521.0	67.0	2692	36	2692.0	36.0	6.4
NV16006_31.FIN2	178	1.39	0.458	0.0150	0.0618	0.0014	0.271	384.0	10.0	386.2	8.2	359	74	386.2	8.2	0.6
NV16006_32.FIN2	149.5	1.09	1.839	0.0470	0.1758	0.0039	0.658	1062.0	16.0	1043.0	21.0	1095	41	1095.0	41.0	4.7
NV16006_33.FIN2	282	1.62	11.530	0.2200	0.4492	0.0079	0.747	2564.0	18.0	2393.0	35.0	2705	22	2705.0	22.0	11.5
NV16006_34.FIN2	778	1.11	0.163	0.0046	0.0245	0.0006	0.463	153.0	4.0	156.3	3.5	162	55	156.3	3.5	2.2
NV16006_35.FIN2	535	1.28	4.090	0.1700	0.2864	0.0096	0.837	1657.0	32.0	1622.0	48.0	1731	41	1731.0	41.0	6.3
NV16006_36.FIN2	900	0.91	0.168	0.0078	0.0248	0.0008	0.335	157.6	6.8	158.2	5.1	170	110	158.2	5.1	0.4
NV16006_37.FIN2	152.4	1.22	12.540	0.2800	0.4770	0.0100	0.846	2645.0	21.0	2516.0	44.0	2761	20	2761.0	20.0	8.9
NV16006_38.FIN2	1116	8.95	2.131	0.0500	0.2004	0.0048	0.835	1158.0	16.0	1179.0	25.0	1105	26	1105.0	26.0	6.7
NV16006_39.FIN2	488	3.74	1.467	0.0330	0.1509	0.0029	0.778	918.0	14.0	907.0	16.0	946	30	946.0	30.0	4.1
NV16006_40.FIN2	291.9	5.32	0.586	0.0160	0.0756	0.0018	0.491	471.0	10.0	470.0	11.0	462	59	470.0	11.0	0.2
NV16006_41.FIN2	427	9.11	1.679	0.0330	0.1635	0.0030	0.724	999.0	13.0	976.0	17.0	1037	27	1037.0	27.0	5.9
NV16006_42.FIN2	74.3	1.93	1.755	0.0490	0.1751	0.0034	0.597	1031.0	18.0	1039.0	18.0	975	48	975.0	48.0	6.6
NV16006_43.FIN2	31.98	1.16	3.860	0.1300	0.2745	0.0070	0.448	1601.0	26.0	1561.0	35.0	1645	55	1645.0	55.0	5.1
NV16006_44.FIN2	193.1	1.26	15.360	0.3600	0.5600	0.0120	0.812	2832.0	22.0	2873.0	48.0	2833	23	2833.0	23.0	1.4
NV16006_46.FIN2	135.5	0.98	1.224	0.0430	0.1301	0.0033	0.424	808.0	20.0	788.0	19.0	900	71	788.0	19.0	2.5
NV16006_47.FIN2	147.7	1.63	1.433	0.0430	0.1490	0.0040	0.513	900.0	18.0	894.0	22.0	898	59	898.0	59.0	0.4
NV16006_48.FIN2	95.5	1.38	2.432	0.0610	0.1953	0.0042	0.659	1258.0	18.0	1151.0	23.0	1412	38	1412.0	38.0	18.5
NV16006_49.FIN2	195	1.30	3.933	0.0850	0.2820	0.0050	0.738	1621.0	17.0	1600.0	25.0	1658	27	1658.0	27.0	3.5
NV16006_50.FIN2	275	1.38	3.009	0.0590	0.2376	0.0043	0.735	1408.0	15.0	1375.0	22.0	1457	24	1457.0	24.0	5.6
NV16006_51.FIN2	358	1.86	2.063	0.0440	0.1919	0.0041	0.844	1138.0	14.0	1130.0	22.0	1156	28	1156.0	28.0	2.2
NV16006_52.FIN2	468	1.01	3.636	0.0780	0.2626	0.0055	0.833	1558.0	18.0	1504.0	29.0	1623	26	1623.0	26.0	7.3
NV16006_53.FIN2	72.7	0.46	1.494	0.0360	0.1583	0.0032	0.467	929.0	15.0	948.0	17.0	927	52	927.0	52.0	2.3
NV16006_54.FIN2	436	4.32	1.733	0.0320	0.1733	0.0030	0.768	1022.0	12.0	1030.0	17.0	1003	26	1003.0	26.0	2.7
NV16006_55.FIN2	77.6	0.75	0.530	0.0200	0.0701	0.0015	0.261	433.0	13.0	436.3	9.0	392	71	436.3	9.0	0.8
NV16006_56.FIN2	365	1.42	12.360	0.3000	0.4470	0.0110	0.759	2630.0	23.0	2381.0	48.0	2818	30	2818.0	30.0	15.5
NV16006_57.FIN2	1029	1.34	1.591	0.0250	0.1592	0.0026	0.698	967.3	9.5	952.0	15.0	993	25	993.0	25.0	4.1
NV16006_58.FIN2	327	2.17	3.529	0.0780	0.2641	0.0049	0.823	1531.0	17.0	1509.0	25.0	1566	24	1566.0	24.0	3.6
NV16006_59.FIN2	142.4	1.23	2.239	0.0490	0.1990	0.0045	0.649	1193.0	15.0	1168.0	24.0	1230	39	1230.0	39.0	5.0
NV16006_60.FIN2	232	0.65	3.719	0.0880	0.2641	0.0051	0.647	1574.0	19.0	1509.0	26.0	1645	33	1645.0	33.0	8.3
NV16006_61.FIN2	210	1.55	1.721	0.0430	0.1664	0.0032	0.653	1017.0	16.0	992.0	18.0	1035	38	1035.0	38.0	4.2
NV16006_62.FIN2	261.8	2.22	2.238	0.0470	0.1950	0.0041	0.782	1193.0	15.0	1147.0	22.0	1272	28	1272.0	28.0	9.8
NV16006_63.FIN2	923	1.11	0.163	0.0047	0.0237	0.0005	0.538	153.2	4.1	151.1	3.0	199	49	151.1	3.0	1.4

NV16006_64.FIN2	684	1.50	3.765	0.0670	0.2710	0.0048	0.795	1587.0	14.0	1547.0	24.0	1639	20	1639.0	20.0	5.6
NV16006_65.FIN2	321	1.10	3.780	0.0960	0.2670	0.0059	0.772	1589.0	21.0	1526.0	29.0	1663	26	1663.0	26.0	8.2
NV16006_66.FIN2	160.6	0.57	0.821	0.0260	0.0968	0.0020	0.415	611.0	15.0	595.0	12.0	660	67	595.0	12.0	2.6
NV16006_67.FIN2	999	1.09	0.548	0.0130	0.0632	0.0013	0.696	443.6	8.3	394.7	8.0	675	37	394.7	8.0	11.0
NV16006_68.FIN2	305.7	3.20	4.764	0.0930	0.3105	0.0058	0.792	1776.0	16.0	1741.0	29.0	1805	23	1805.0	23.0	3.5
NV16006_69.FIN2	792	0.92	0.161	0.0047	0.0238	0.0005	0.527	151.2	4.1	151.5	2.9	162	52	151.5	2.9	0.2
NV16006_70.FIN2	165.8	0.53	3.490	0.1200	0.2457	0.0064	0.665	1519.0	26.0	1415.0	33.0	1662	42	1662.0	42.0	14.9
NV16006_73.FIN2	416	2.65	4.410	0.1000	0.3030	0.0063	0.795	1711.0	19.0	1704.0	31.0	1720	25	1720.0	25.0	0.9
NV16006_74.FIN2	242.5	1.44	1.848	0.0400	0.1748	0.0035	0.581	1062.0	14.0	1038.0	19.0	1108	38	1108.0	38.0	6.3
NV16006_75.FIN2	187.3	0.55	3.977	0.0730	0.2810	0.0050	0.703	1629.0	15.0	1595.0	25.0	1667	26	1667.0	26.0	4.3
NV16006_76.FIN2	488	1.90	2.157	0.0460	0.1949	0.0040	0.762	1165.0	15.0	1147.0	22.0	1184	26	1184.0	26.0	3.1
NV16006_77.FIN2	118.9	0.71	3.920	0.1000	0.2835	0.0072	0.693	1616.0	20.0	1607.0	36.0	1631	38	1631.0	38.0	1.5
NV16006_78.FIN2	134.5	0.72	4.360	0.1500	0.2854	0.0061	0.437	1685.0	24.0	1616.0	30.0	1777	41	1777.0	41.0	9.1
NV16006_79.FIN2	315	0.97	1.220	0.0250	0.1314	0.0022	0.684	813.0	12.0	795.0	13.0	851	35	795.0	13.0	2.2
NV16006_80.FIN2	265.9	1.46	2.070	0.0450	0.1922	0.0038	0.750	1140.0	15.0	1132.0	20.0	1173	29	1173.0	29.0	3.5
NV16006_81.FIN2	120.4	0.45	3.762	0.0830	0.2634	0.0043	0.605	1585.0	18.0	1506.0	22.0	1691	32	1691.0	32.0	10.9
NV16006_82.FIN2	257	1.27	3.684	0.0840	0.2698	0.0053	0.727	1564.0	19.0	1540.0	27.0	1630	30	1630.0	30.0	5.5
NV16006_83.FIN2	32.9	1.36	13.470	0.3500	0.4880	0.0120	0.754	2712.0	26.0	2555.0	53.0	2828	30	2828.0	30.0	9.7
NV16006_84.FIN2	368.8	1.90	3.694	0.0770	0.2403	0.0047	0.852	1569.0	17.0	1387.0	25.0	1827	23	1827.0	23.0	24.1
NV16006_86.FIN2	87.2	0.69	1.822	0.0460	0.1717	0.0035	0.472	1052.0	17.0	1020.0	19.0	1109	47	1109.0	47.0	8.0
NV16006_87.FIN2	388	1.73	3.460	0.1500	0.2470	0.0110	0.791	1515.0	34.0	1432.0	58.0	1652	45	1652.0	45.0	13.3
NV16006_88.FIN2	130	0.73	1.453	0.0430	0.1453	0.0030	0.587	908.0	18.0	874.0	17.0	958	47	958.0	47.0	8.8
NV16006_90.FIN2	508	1.38	4.170	0.0850	0.2832	0.0063	0.828	1665.0	17.0	1609.0	31.0	1733	23	1733.0	23.0	7.2
NV16006_91.FIN2	238	1.97	1.875	0.0440	0.1767	0.0036	0.732	1070.0	15.0	1048.0	19.0	1144	34	1144.0	34.0	8.4
NV16006_92.FIN2	341	1.05	3.850	0.2500	0.2510	0.0130	0.855	1599.0	52.0	1442.0	66.0	1814	60	1814.0	60.0	20.5
NV16006_93.FIN2	223	0.91	4.429	0.0840	0.3016	0.0055	0.770	1722.0	15.0	1698.0	27.0	1738	24	1738.0	24.0	2.3
NV16006_94.FIN2	167.7	0.91	2.083	0.0460	0.1911	0.0033	0.664	1143.0	15.0	1126.0	18.0	1184	33	1184.0	33.0	4.9
NV16006_95.FIN2	104.1	0.60	3.536	0.0880	0.2501	0.0052	0.692	1531.0	20.0	1437.0	27.0	1644	36	1644.0	36.0	12.6
NV16006_96.FIN2	595	1.53	0.164	0.0049	0.0237	0.0004	0.383	153.8	4.3	151.0	2.7	224	60	151.0	2.7	1.8
NV16006_97.FIN2	101.2	0.39	0.608	0.0320	0.0749	0.0026	0.468	480.0	20.0	466.0	15.0	580	110	466.0	15.0	2.9
NV16006_98.FIN2	136.1	1.07	3.330	0.0750	0.2546	0.0049	0.592	1486.0	18.0	1461.0	25.0	1512	35	1512.0	35.0	3.4
NV16006_99.FIN2	770	1.14	0.158	0.0072	0.0220	0.0006	0.432	148.7	6.3	140.2	4.0	287	81	140.2	4.0	5.7
NV16006_100.FIN2	406	2.07	4.325	0.0930	0.2961	0.0070	0.797	1698.0	17.0	1669.0	35.0	1726	24	1726.0	24.0	3.3
NV16006_101.FIN2	191.8	0.97	5.790	0.1300	0.3454	0.0072	0.796	1945.0	19.0	1909.0	34.0	1986	24	1986.0	24.0	3.9
NV16006_102.FIN2	336	1.74	1.814	0.0440	0.1749	0.0035	0.722	1050.0	15.0	1038.0	19.0	1104	32	1104.0	32.0	6.0
NV16006_103.FIN2	76.4	0.61	1.765	0.0590	0.1663	0.0040	0.598	1029.0	22.0	993.0	23.0	1088	54	1088.0	54.0	8.7
NV16006_104.FIN2	133.2	0.83	3.453	0.0710	0.2584	0.0048	0.673	1516.0	16.0	1480.0	24.0	1557	29	1557.0	29.0	4.9
NV16006_105.FIN2	254.3	1.38	3.042	0.0590	0.2409	0.0043	0.777	1418.0	14.0	1390.0	23.0	1474	25	1474.0	25.0	5.7
NV16006_106.FIN2	167.2	1.38	3.288	0.0720	0.2502	0.0049	0.681	1475.0	17.0	1438.0	25.0	1520	30	1520.0	30.0	5.4
NV16006_107.FIN2	489	0.81	3.942	0.0840	0.2823	0.0057	0.774	1621.0	17.0	1604.0	28.0	1661	25	1661.0	25.0	3.4

NV16006_108.FIN2	781	1.41	0.168	0.0050	0.0236	0.0005	0.538	157.1	4.3	150.2	2.8	263	53	150.2	2.8	4.4
NV16006_109.FIN2	912	1.47	0.168	0.0061	0.0234	0.0006	0.568	157.6	5.2	149.2	4.1	261	66	149.2	4.1	5.3
NV16006_110.FIN2	250.5	1.60	4.019	0.0840	0.2732	0.0055	0.738	1640.0	17.0	1560.0	27.0	1762	27	1762.0	27.0	11.5
NV16006_111.FIN2	1420	1.54	0.165	0.0049	0.0237	0.0005	0.596	155.1	4.3	150.9	2.8	211	52	150.9	2.8	2.7
NV16006_112.FIN2	513	1.16	0.368	0.0092	0.0498	0.0008	0.514	318.3	6.8	313.4	4.9	374	48	313.4	4.9	1.5
NV16006_113.FIN2	419.5	0.93	2.742	0.0550	0.2225	0.0041	0.729	1339.0	15.0	1294.0	22.0	1402	28	1402.0	28.0	7.7
NV16006_114.FIN2	298.2	1.47	3.275	0.0680	0.2469	0.0048	0.815	1473.0	16.0	1421.0	25.0	1551	22	1551.0	22.0	8.4
NV16006_115.FIN2	166	1.31	4.030	0.0840	0.2653	0.0050	0.665	1637.0	17.0	1520.0	26.0	1795	28	1795.0	28.0	15.3
NV16006_116.FIN2	1130	2.54	1.502	0.0230	0.1537	0.0024	0.813	931.0	9.1	921.0	13.0	945	20	945.0	20.0	2.5
NV16006_117.FIN2	1307	1.83	3.860	0.1000	0.2683	0.0064	0.842	1605.0	21.0	1531.0	33.0	1713	26	1713.0	26.0	10.6
NV16006_118.FIN2	988	1.11	3.783	0.0780	0.2702	0.0055	0.828	1590.0	17.0	1543.0	28.0	1654	22	1654.0	22.0	6.7
NV16006_119.FIN2	822	1.82	0.162	0.0046	0.0233	0.0004	0.506	152.1	4.0	148.7	2.5	249	58	148.7	2.5	2.2
NV16006_120.FIN2	1051	1.15	0.169	0.0055	0.0244	0.0005	0.639	158.3	4.7	155.1	3.1	209	54	155.1	3.1	2.0
NV16006_121.FIN2	975	1.00	0.156	0.0050	0.0233	0.0004	0.389	146.9	4.4	148.7	2.4	142	57	148.7	2.4	1.2
NV16006_122.FIN2	561	1.08	0.530	0.0120	0.0675	0.0011	0.678	430.8	8.0	420.8	6.8	474	38	420.8	6.8	2.3
NV16006_123.FIN2	498	1.45	3.248	0.0600	0.2496	0.0045	0.782	1468.0	14.0	1435.0	23.0	1519	21	1519.0	21.0	5.5
NV16006_124.FIN2	1281	1.31	0.156	0.0037	0.0228	0.0004	0.583	146.9	3.3	145.3	2.5	184	43	145.3	2.5	1.1
NV16006_125.FIN2	196.3	1.83	5.690	0.1100	0.3407	0.0060	0.796	1927.0	16.0	1894.0	30.0	1973	23	1973.0	23.0	4.0

Analysis	U (ppm)	U/Th	207Pb/ 235U	±	206Pb/ 238U	±	err. corr.	207Pb/ 235U Age (Ma)	± (Ma)	206Pb/ 238U Age (Ma)	± (Ma)	207Pb/ 206Pb Age (Ma)	± (Ma)	Best age (Ma)	± (Ma)	Disc (%)
NV16-007WSB: White Sage Basin 40°12'27"N, 113°59'31"W																
NV16007_1.FIN2	95.8	1.30	3.465	0.0840	0.2623	0.0048	0.685	1523.0	18.0	1500.0	24.0	1543	34	1543.0	34.0	2.8
NV16007_2.FIN2	81.3	1.50	5.110	0.1300	0.3291	0.0070	0.494	1833.0	21.0	1831.0	34.0	1836	34	1836.0	34.0	0.3
NV16007_3.FIN2	85.5	0.82	2.039	0.0530	0.1886	0.0037	0.486	1126.0	17.0	1113.0	20.0	1150	42	1150.0	42.0	3.2
NV16007_4.FIN2	590	1.85	0.475	0.0240	0.0620	0.0025	0.658	393.0	17.0	388.0	15.0	447	77	388.0	15.0	1.3
NV16007_5.FIN2	49	0.90	5.970	0.1500	0.3602	0.0073	0.500	1969.0	22.0	1983.0	35.0	1954	37	1954.0	37.0	1.5
NV16007_6.FIN2	106.5	1.93	3.232	0.0690	0.2521	0.0049	0.598	1466.0	16.0	1450.0	25.0	1442	37	1442.0	37.0	0.6
NV16007_7.FIN2	280	12.61	2.014	0.0660	0.1883	0.0035	0.102	1110.0	19.0	1111.0	19.0	1102	44	1102.0	44.0	0.8
NV16007_8.FIN2	446	1.77	0.176	0.0100	0.0248	0.0008	0.300	165.7	8.9	158.1	4.7	260	120	158.1	4.7	4.6
NV16007_9.FIN2	59.8	26.00	0.825	0.0520	0.0916	0.0021	0.058	602.0	27.0	564.0	13.0	680	120	564.0	13.0	6.3
NV16007_10.FIN2	45.3	3.08	4.770	0.1200	0.3153	0.0066	0.546	1778.0	21.0	1768.0	33.0	1803	42	1803.0	42.0	1.9
NV16007_11.FIN2	150.2	1.64	2.103	0.0530	0.1956	0.0043	0.554	1151.0	17.0	1150.0	23.0	1153	42	1153.0	42.0	0.3
NV16007_12.FIN2	220	1.08	5.970	0.1200	0.3751	0.0066	0.727	1972.0	17.0	2054.0	31.0	1891	24	1891.0	24.0	8.6
NV16007_13.FIN2	56.5	1.55	6.620	0.1800	0.3772	0.0082	0.305	2053.0	24.0	2068.0	39.0	2040	43	2040.0	43.0	1.4
NV16007_14.FIN2	72.9	1.34	13.550	0.2600	0.5318	0.0088	0.710	2723.0	18.0	2749.0	37.0	2710	22	2710.0	22.0	1.4
NV16007_15.FIN2	256.4	2.35	0.186	0.0130	0.0240	0.0007	0.331	173.0	11.0	153.1	4.5	400	130	153.1	4.5	11.5
NV16007_17.FIN2	79.5	1.11	5.520	0.1400	0.3469	0.0078	0.582	1903.0	21.0	1921.0	38.0	1899	38	1899.0	38.0	1.2
NV16007_18.FIN2	240	2.46	1.996	0.0480	0.1886	0.0043	0.697	1118.0	17.0	1114.0	23.0	1117	36	1117.0	36.0	0.3
NV16007_19.FIN2	76.5	2.08	4.380	0.1200	0.3021	0.0063	0.683	1702.0	23.0	1700.0	31.0	1701	40	1701.0	40.0	0.1
NV16007_20.FIN2	123.1	1.13	4.090	0.1200	0.2855	0.0064	0.547	1640.0	21.0	1616.0	32.0	1665	37	1665.0	37.0	2.9
NV16007_22.FIN2	73.4	1.46	14.790	0.4000	0.5420	0.0110	0.370	2787.0	23.0	2789.0	45.0	2796	30	2796.0	30.0	0.3
NV16007_23.FIN2	469	0.64	4.600	0.1400	0.2974	0.0082	0.778	1748.0	24.0	1693.0	40.0	1820	30	1820.0	30.0	7.0
NV16007_24.FIN2	51.5	0.66	4.180	0.1100	0.3005	0.0060	0.622	1666.0	22.0	1691.0	30.0	1623	37	1623.0	37.0	4.2
NV16007_25.FIN2	78.7	2.05	3.216	0.0960	0.2366	0.0064	0.588	1469.0	24.0	1366.0	33.0	1607	46	1607.0	46.0	15.0
NV16007_38.FIN2	210.1	1.02	1.814	0.0540	0.1719	0.0054	0.650	1052.0	19.0	1022.0	30.0	1128	54	1128.0	54.0	9.4
NV16007a_1.FIN2	124.2	1.31	2.151	0.0390	0.1912	0.0030	0.055	1163.0	12.0	1127.0	16.0	1210	38	1210.0	38.0	6.9
NV16007a_2.FIN2	52.5	1.00	2.090	0.0470	0.1879	0.0024	0.199	1142.0	15.0	1111.0	13.0	1198	39	1198.0	39.0	7.3
NV16007a_3.FIN2	136.7	1.08	10.360	0.1400	0.4525	0.0066	0.611	2467.0	13.0	2405.0	29.0	2514	22	2514.0	22.0	4.3
NV16007a_4.FIN2	78.43	0.51	2.206	0.0440	0.1945	0.0029	0.535	1181.0	14.0	1147.0	16.0	1240	35	1240.0	35.0	7.5
NV16007a_5.FIN2	80.2	1.65	4.140	0.1200	0.2701	0.0084	0.823	1661.0	23.0	1540.0	42.0	1819	38	1819.0	38.0	15.3
NV16007a_6.FIN2	578	6.30	6.050	0.1000	0.3609	0.0055	0.483	1982.0	15.0	1996.0	28.0	1977	31	1977.0	31.0	1.0
NV16007a_7.FIN2	298	1.29	2.708	0.0300	0.2267	0.0020	0.420	1329.5	8.2	1317.0	11.0	1350	20	1350.0	20.0	2.4
NV16007a_8.FIN2	48.3	0.68	5.150	0.0840	0.3314	0.0046	0.046	1842.0	14.0	1846.0	22.0	1845	29	1845.0	29.0	0.1
NV16007a_9.FIN2	246	6.11	5.360	0.0750	0.3355	0.0039	0.535	1878.0	12.0	1864.0	19.0	1881	23	1881.0	23.0	0.9
NV16007a_10.FIN2	84.6	1.79	4.040	0.1100	0.2714	0.0060	0.331	1642.0	21.0	1551.0	30.0	1744	47	1744.0	47.0	11.1
NV16007a_11.FIN2	44.2	0.53	4.380	0.1100	0.2973	0.0038	0.039	1699.0	18.0	1677.0	19.0	1691	39	1691.0	39.0	0.8
NV16007a_12.FIN2	97	0.25	0.917	0.0400	0.1044	0.0022	0.056	651.0	18.0	640.0	13.0	650	75	640.0	13.0	1.7

NV16007a_13.FIN2	110	1.04	2.872	0.0410	0.2340	0.0028	0.438	1374.0	11.0	1355.0	15.0	1382	28	1382.0	28.0	2.0
NV16007a_14.FIN2	153.7	1.67	12.860	0.2000	0.4626	0.0084	0.633	2669.0	15.0	2454.0	36.0	2843	26	2843.0	26.0	13.7
NV16007a_15.FIN2	123.6	0.57	4.061	0.0550	0.2880	0.0038	0.395	1648.0	11.0	1631.0	19.0	1649	28	1649.0	28.0	1.1
NV16007a_16.FIN2	109.5	0.43	4.021	0.0610	0.2915	0.0041	0.541	1639.0	12.0	1648.0	20.0	1616	27	1616.0	27.0	2.0
NV16007a_17.FIN2	281	1.82	1.689	0.0330	0.1621	0.0034	0.542	1005.0	12.0	967.0	19.0	1074	38	1074.0	38.0	10.0
NV16007a_18.FIN2	84.9	1.92	3.415	0.0870	0.2559	0.0054	0.357	1494.0	18.0	1467.0	28.0	1531	45	1531.0	45.0	4.2
NV16007a_19.FIN2	493	0.41	0.165	0.0057	0.0233	0.0003	0.337	154.7	5.0	148.5	1.9	268	68	148.5	1.9	4.0
NV16007a_20.FIN2	154	1.25	20.330	0.3500	0.6202	0.0090	0.533	3105.0	17.0	3108.0	36.0	3102	24	3102.0	24.0	0.2
NV16007a_21.FIN2	141	1.65	4.698	0.0710	0.3217	0.0053	0.521	1764.0	13.0	1796.0	26.0	1747	28	1747.0	28.0	2.8
NV16007a_22.FIN2	109.3	0.55	1.998	0.0680	0.1762	0.0060	0.283	1109.0	22.0	1047.0	32.0	1279	65	1279.0	65.0	18.1
NV16007a_23.FIN2	114	69.20	1.775	0.0430	0.1757	0.0028	0.023	1032.0	16.0	1043.0	15.0	996	47	996.0	47.0	4.7
NV16007a_24.FIN2	112.8	1.04	1.929	0.0430	0.1797	0.0026	0.341	1088.0	15.0	1065.0	14.0	1132	39	1132.0	39.0	5.9
NV16007a_25.FIN2	194	0.55	0.557	0.0200	0.0688	0.0016	0.047	449.0	13.0	428.8	9.7	549	96	428.8	9.7	4.5
NV16007a_26.FIN2	74	1.15	4.080	0.1700	0.2698	0.0090	0.288	1642.0	34.0	1538.0	46.0	1791	84	1791.0	84.0	14.1
NV16007a_27.FIN2	205.3	0.67	13.680	0.2900	0.5270	0.0130	0.489	2727.0	20.0	2723.0	54.0	2703	39	2703.0	39.0	0.7
NV16007a_28.FIN2	69.8	0.89	0.795	0.0370	0.0929	0.0025	0.119	588.0	21.0	572.0	15.0	654	97	572.0	15.0	2.7
NV16007a_29.FIN2	41.6	0.73	4.372	0.0920	0.2962	0.0053	0.417	1705.0	17.0	1671.0	26.0	1759	38	1759.0	38.0	5.0
NV16007a_30.FIN2	160.4	1.28	3.209	0.0510	0.2496	0.0041	0.608	1459.0	13.0	1435.0	21.0	1483	27	1483.0	27.0	3.2
NV16007a_31.FIN2	199.2	1.55	12.720	0.2000	0.5145	0.0077	0.686	2663.0	14.0	2673.0	33.0	2647	20	2647.0	20.0	1.0
NV16007a_32.FIN2	344	1.91	5.252	0.0500	0.3319	0.0029	0.532	1860.1	8.1	1847.0	14.0	1864	16	1864.0	16.0	0.9
NV16007a_33.FIN2	50.5	1.02	17.220	0.2200	0.5881	0.0068	0.457	2948.0	12.0	2985.0	28.0	2927	19	2927.0	19.0	2.0
NV16007a_34.FIN2	98.4	1.51	2.176	0.0730	0.1916	0.0050	0.538	1175.0	22.0	1129.0	27.0	1266	63	1266.0	63.0	10.8
NV16007a_35.FIN2	89	1.14	0.996	0.0330	0.1014	0.0020	0.535	701.0	16.0	622.0	12.0	1011	58	622.0	12.0	11.3
NV16007a_36.FIN2	38.6	1.10	3.060	0.1100	0.2323	0.0055	0.375	1419.0	27.0	1345.0	29.0	1511	68	1511.0	68.0	11.0
NV16007a_37.FIN2	66.8	1.09	2.330	0.1300	0.1924	0.0058	0.146	1216.0	41.0	1140.0	30.0	1340	100	1340.0	100.0	14.9
NV16007a_38.FIN2	130.4	1.48	2.601	0.0550	0.2189	0.0038	0.530	1298.0	16.0	1276.0	20.0	1344	37	1344.0	37.0	5.1
NV16007a_39.FIN2	144.6	0.42	12.630	0.2100	0.4868	0.0079	0.600	2659.0	15.0	2564.0	34.0	2725	22	2725.0	22.0	5.9
NV16007a_40.FIN2	195	1.92	1.721	0.0310	0.1661	0.0030	0.531	1014.0	12.0	990.0	17.0	1060	36	1060.0	36.0	6.6
NV16007a_41.FIN2	58.4	1.16	0.698	0.0300	0.0885	0.0017	0.318	535.0	18.0	548.0	11.0	471	90	548.0	11.0	2.4
NV16007a_42.FIN2	154.3	0.98	0.896	0.0180	0.1054	0.0013	0.198	649.0	9.7	645.7	7.4	673	48	645.7	7.4	0.5
NV16007a_43.FIN2	124.1	1.80	3.261	0.0550	0.2588	0.0036	0.509	1470.0	13.0	1483.0	18.0	1470	30	1470.0	30.0	0.9
NV16007a_44.FIN2	188.5	0.90	2.983	0.0480	0.2389	0.0037	0.520	1402.0	12.0	1380.0	19.0	1442	27	1442.0	27.0	4.3
NV16007a_45.FIN2	178	0.85	3.913	0.0600	0.2773	0.0036	0.467	1616.0	12.0	1577.0	18.0	1682	28	1682.0	28.0	6.2
NV16007a_46.FIN2	56	0.49	5.432	0.0820	0.3453	0.0044	0.339	1888.0	13.0	1913.0	21.0	1879	29	1879.0	29.0	1.8
NV16007a_47.FIN2	269	25.50	0.569	0.0210	0.0718	0.0016	0.433	457.0	14.0	446.9	9.9	502	89	446.9	9.9	2.2
NV16007a_48.FIN2	33.27	2.30	4.070	0.1300	0.2896	0.0061	0.059	1634.0	23.0	1637.0	31.0	1669	54	1669.0	54.0	1.9
NV16007a_49.FIN2	296.5	2.24	5.100	0.1100	0.3187	0.0065	0.589	1832.0	18.0	1781.0	32.0	1879	35	1879.0	35.0	5.2
NV16007a_51.FIN2	66.5	0.61	5.120	0.1600	0.3118	0.0052	0.349	1837.0	26.0	1749.0	26.0	1947	54	1947.0	54.0	10.2
NV16007a_52.FIN2	221.9	1.75	2.110	0.0530	0.1963	0.0046	0.659	1154.0	18.0	1155.0	25.0	1134	38	1134.0	38.0	1.9
NV16007a_53.FIN2	84.2	0.53	4.350	0.1000	0.2930	0.0035	0.469	1701.0	19.0	1658.0	18.0	1769	35	1769.0	35.0	6.3

NV16007a_54.FIN2	269.9	137.00	1.840	0.0530	0.1741	0.0054	0.385	1057.0	19.0	1033.0	30.0	1106	63	1106.0	63.0	6.6
NV16007a_55.FIN2	493	0.68	0.168	0.0056	0.0245	0.0004	0.293	157.0	4.9	156.0	2.4	188	67	156.0	2.4	0.6
NV16007a_56.FIN2	145.1	23.49	1.796	0.0280	0.1759	0.0022	0.450	1043.0	10.0	1045.0	12.0	1054	30	1054.0	30.0	0.9
NV16007a_57.FIN2	352	3.86	2.972	0.0340	0.2390	0.0026	0.307	1399.7	8.6	1381.0	13.0	1440	23	1440.0	23.0	4.1
NV16007a_58.FIN2	133.5	2.09	2.198	0.0460	0.1917	0.0038	0.374	1183.0	14.0	1132.0	20.0	1306	43	1306.0	43.0	13.3
NV16007a_59.FIN2	62.7	1.28	2.078	0.0530	0.1981	0.0033	0.302	1143.0	17.0	1164.0	18.0	1106	53	1106.0	53.0	5.2
NV16007a_60.FIN2	58.3	1.27	4.669	0.0890	0.3132	0.0048	0.430	1760.0	16.0	1755.0	24.0	1773	33	1773.0	33.0	1.0
NV16007a_61.FIN2	264.6	0.66	2.656	0.0290	0.2341	0.0026	0.519	1316.3	8.0	1357.0	13.0	1265	20	1265.0	20.0	7.3
NV16007a_62.FIN2	302.3	1.95	4.260	0.1000	0.2882	0.0057	0.688	1682.0	19.0	1632.0	29.0	1757	34	1757.0	34.0	7.1
NV16007a_63.FIN2	218	1.87	3.522	0.0440	0.2738	0.0033	0.550	1533.0	10.0	1559.0	17.0	1506	21	1506.0	21.0	3.5
NV16007a_64.FIN2	201	1.57	4.112	0.0790	0.2948	0.0059	0.681	1659.0	15.0	1664.0	29.0	1651	34	1651.0	34.0	0.8
NV16007a_65.FIN2	126	1.15	0.515	0.0140	0.0672	0.0010	0.022	420.7	9.3	419.0	6.2	440	61	419.0	6.2	0.4
NV16007a_66.FIN2	40.8	0.99	2.778	0.0680	0.2392	0.0035	0.320	1351.0	18.0	1384.0	18.0	1309	49	1309.0	49.0	5.7
NV16007a_67.FIN2	56.9	0.51	4.950	0.1000	0.3130	0.0061	0.456	1807.0	18.0	1753.0	30.0	1872	39	1872.0	39.0	6.4
NV16007a_68.FIN2	148.5	1.23	2.899	0.0640	0.2358	0.0050	0.514	1379.0	17.0	1364.0	26.0	1412	40	1412.0	40.0	3.4
NV16007a_69.FIN2	145	0.75	4.530	0.1500	0.3130	0.0084	0.597	1734.0	27.0	1753.0	41.0	1718	52	1718.0	52.0	2.0
NV16007a_70.FIN2	113.4	1.34	10.080	0.1500	0.4397	0.0073	0.565	2441.0	14.0	2348.0	33.0	2526	25	2526.0	25.0	7.0
NV16007a_71.FIN2	202.5	1.63	0.549	0.0180	0.0694	0.0018	0.327	443.0	12.0	432.0	11.0	513	78	432.0	11.0	2.5
NV16007a_72.FIN2	452.2	0.79	0.199	0.0070	0.0248	0.0006	0.200	183.7	5.9	157.7	3.5	521	79	157.7	3.5	14.2
NV16007a_73.FIN2	343.7	1.86	0.570	0.0120	0.0691	0.0011	0.420	457.5	8.0	431.0	6.5	627	46	431.0	6.5	5.8
NV16007a_74.FIN2	434	0.84	2.622	0.0430	0.2176	0.0036	0.569	1307.0	12.0	1269.0	19.0	1394	29	1394.0	29.0	9.0
NV16007a_75.FIN2	167	0.89	0.501	0.0200	0.0669	0.0019	0.497	412.0	14.0	418.0	11.0	405	82	418.0	11.0	1.5
NV16007a_76.FIN2	247	1.83	4.084	0.0530	0.2962	0.0029	0.420	1652.0	10.0	1672.0	14.0	1632	20	1632.0	20.0	2.5
NV16007a_77.FIN2	61.8	1.07	0.829	0.0310	0.0967	0.0023	0.455	614.0	17.0	594.0	14.0	678	70	594.0	14.0	3.3
NV16007a_78.FIN2	28.42	1.76	2.212	0.0870	0.1897	0.0041	0.022	1176.0	27.0	1119.0	22.0	1303	77	1303.0	77.0	14.1
NV16007a_79.FIN2	225.7	1.14	1.713	0.0320	0.1677	0.0024	0.304	1011.0	12.0	999.0	13.0	1043	37	1043.0	37.0	4.2
NV16007a_80.FIN2	12.22	0.36	4.430	0.1400	0.2859	0.0063	0.230	1711.0	27.0	1619.0	31.0	1811	59	1811.0	59.0	10.6
NV16007a_81.FIN2	37.82	2.20	1.970	0.0820	0.1861	0.0040	0.076	1102.0	28.0	1100.0	22.0	1119	97	1119.0	97.0	1.7
NV16007a_83.FIN2	84.3	1.71	1.539	0.0290	0.1545	0.0019	0.341	944.0	12.0	926.0	10.0	989	37	989.0	37.0	6.4
NV16007a_84.FIN2	80.9	0.95	3.796	0.0720	0.2694	0.0035	0.247	1589.0	15.0	1537.0	18.0	1647	34	1647.0	34.0	6.7
NV16007a_85.FIN2	239	0.94	3.915	0.0490	0.2822	0.0033	0.514	1616.2	9.9	1602.0	16.0	1630	22	1630.0	22.0	1.7
NV16007a_86.FIN2	69.8	1.36	3.850	0.1100	0.2808	0.0071	0.305	1601.0	24.0	1594.0	36.0	1590	47	1590.0	47.0	0.3
NV16007a_87.FIN2	57.9	1.49	2.986	0.0870	0.2299	0.0057	0.272	1401.0	22.0	1332.0	30.0	1535	59	1535.0	59.0	13.2
NV16007a_88.FIN2	39.7	0.72	5.530	0.1800	0.3410	0.0120	0.536	1904.0	27.0	1883.0	57.0	1909	56	1909.0	56.0	1.4
NV16007a_89.FIN2	66.2	2.19	12.500	0.7800	0.4370	0.0310	0.706	2623.0	55.0	2300.0	140.0	2927	81	2927.0	81.0	21.4
NV16007a_90.FIN2	157.1	1.94	3.850	0.1200	0.2748	0.0083	0.402	1599.0	24.0	1562.0	42.0	1657	51	1657.0	51.0	5.7
NV16007a_91.FIN2	107.8	0.50	3.800	0.0690	0.2748	0.0045	0.582	1592.0	14.0	1564.0	23.0	1612	27	1612.0	27.0	3.0
NV16007a_92.FIN2	343	1.53	0.179	0.0056	0.0259	0.0004	0.020	166.8	4.8	164.6	2.6	201	68	164.6	2.6	1.3
NV16007a_93.FIN2	140.4	0.83	4.094	0.0710	0.2894	0.0040	0.416	1652.0	14.0	1638.0	20.0	1651	29	1651.0	29.0	0.8
NV16007a_94.FIN2	24.62	0.54	0.815	0.0420	0.0934	0.0023	0.011	604.0	23.0	575.0	14.0	690	110	575.0	14.0	4.8

NV16007a_95.FIN2	59.43	0.74	5.278	0.0880	0.3335	0.0040	0.454	1864.0	13.0	1855.0	19.0	1871	25	1871.0	25.0	0.9
NV16007a_96.FIN2	142.3	2.11	5.350	0.1600	0.3238	0.0097	0.454	1883.0	25.0	1812.0	46.0	1933	48	1933.0	48.0	6.3
NV16007a_97.FIN2	53.7	1.12	12.080	0.3300	0.4500	0.0140	0.664	2609.0	27.0	2390.0	60.0	2781	39	2781.0	39.0	14.1
NV16007a_98.FIN2	52.7	2.46	3.530	0.1600	0.2550	0.0120	0.708	1538.0	38.0	1458.0	59.0	1662	65	1662.0	65.0	12.3
NV16007a_99.FIN2	101.7	1.20	1.830	0.0360	0.1764	0.0024	0.424	1056.0	12.0	1047.0	13.0	1071	34	1071.0	34.0	2.2
NV16007a_100.FIN2	145.4	1.63	3.013	0.0430	0.2456	0.0027	0.470	1410.0	11.0	1415.0	14.0	1398	27	1398.0	27.0	1.2
NV16007a_101.FIN2	195	1.79	1.731	0.0280	0.1691	0.0020	0.332	1021.0	10.0	1007.0	11.0	1062	32	1062.0	32.0	5.2
NV16007a_102.FIN2	28.41	0.54	2.340	0.0720	0.2008	0.0029	0.059	1222.0	22.0	1179.0	16.0	1295	64	1295.0	64.0	9.0
NV16007a_103.FIN2	105.1	0.87	3.911	0.0650	0.2788	0.0037	0.509	1615.0	14.0	1585.0	19.0	1657	27	1657.0	27.0	4.3
NV16007a_104.FIN2	376	0.64	0.169	0.0051	0.0238	0.0005	0.283	158.0	4.4	151.6	3.4	230	67	151.6	3.4	4.1
NV16007a_105.FIN2	111.6	0.64	5.168	0.0630	0.3205	0.0044	0.544	1848.0	11.0	1794.0	21.0	1900	23	1900.0	23.0	5.6

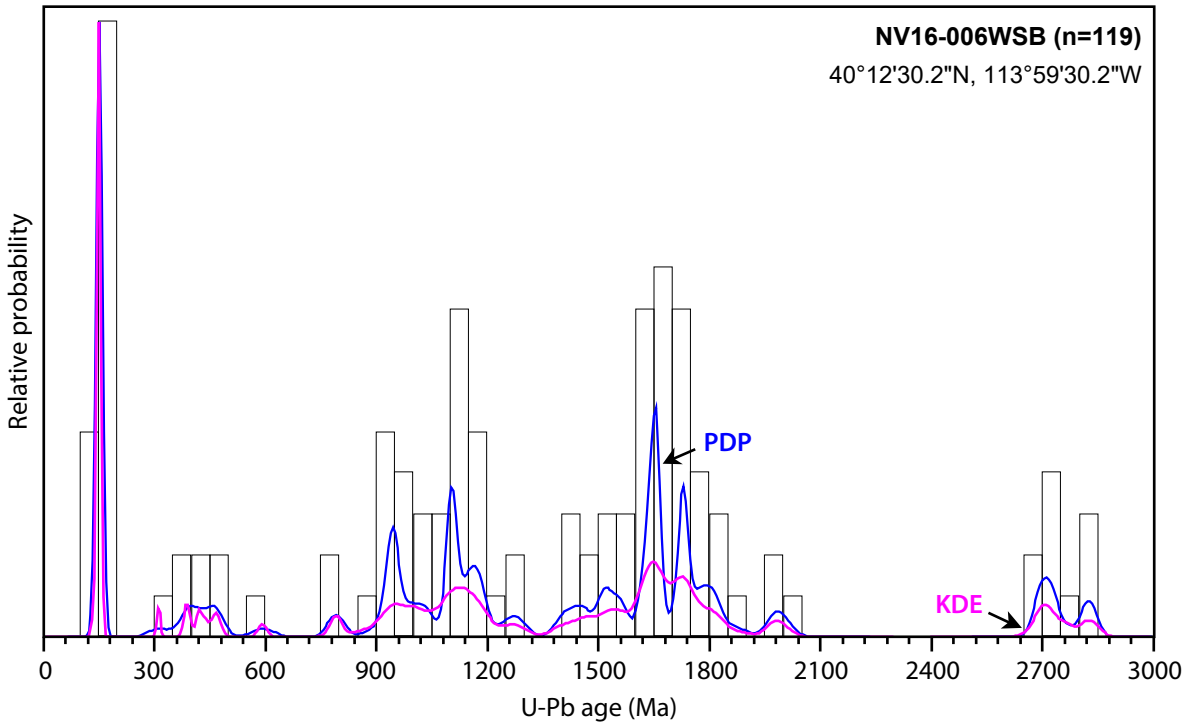
NV16-006WSB (n=119)
40°12'30.2"N, 113°59'30.2"W
Relative probability
PDP
KDE
0
300
600
900
1200
1500
1800
2100
2400
2700
3000
U-Pb age (Ma)

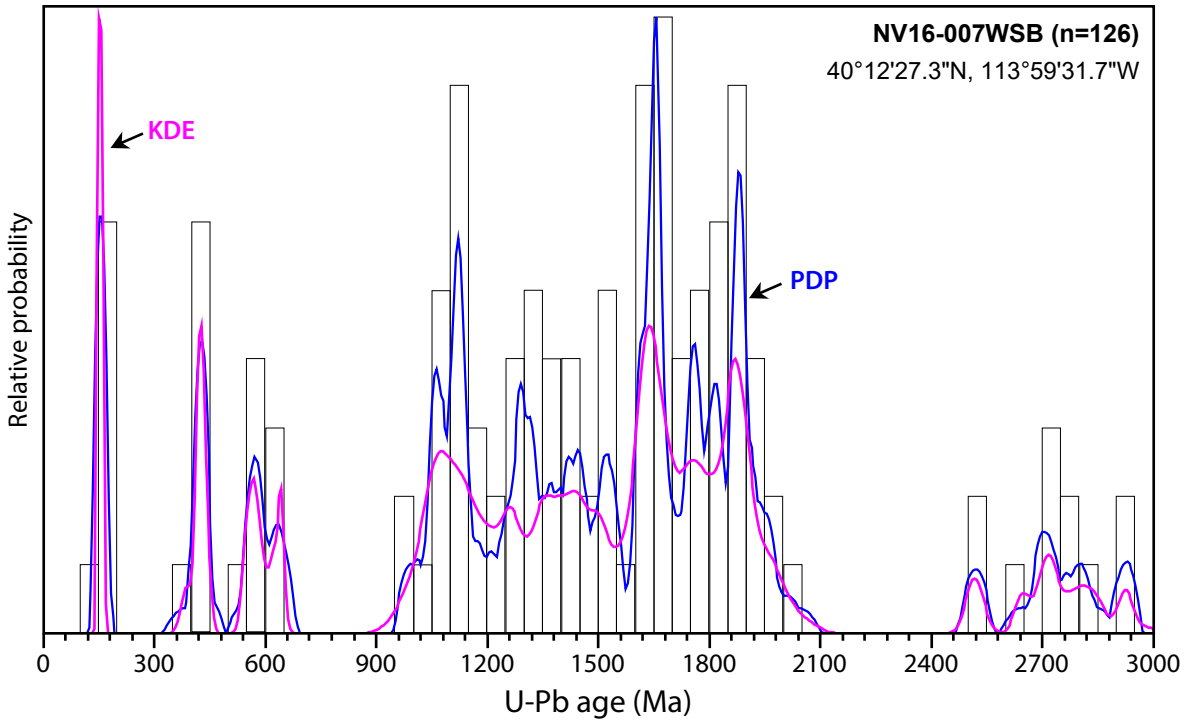
NV16-007WSB (n=126)
40°12'27.3"N, 113°59'31.7"W
KDE
PDP
Relative probability
0
300
600
900
1200
1500
1800
2100
2400
2700
3000
U-Pb age (Ma)

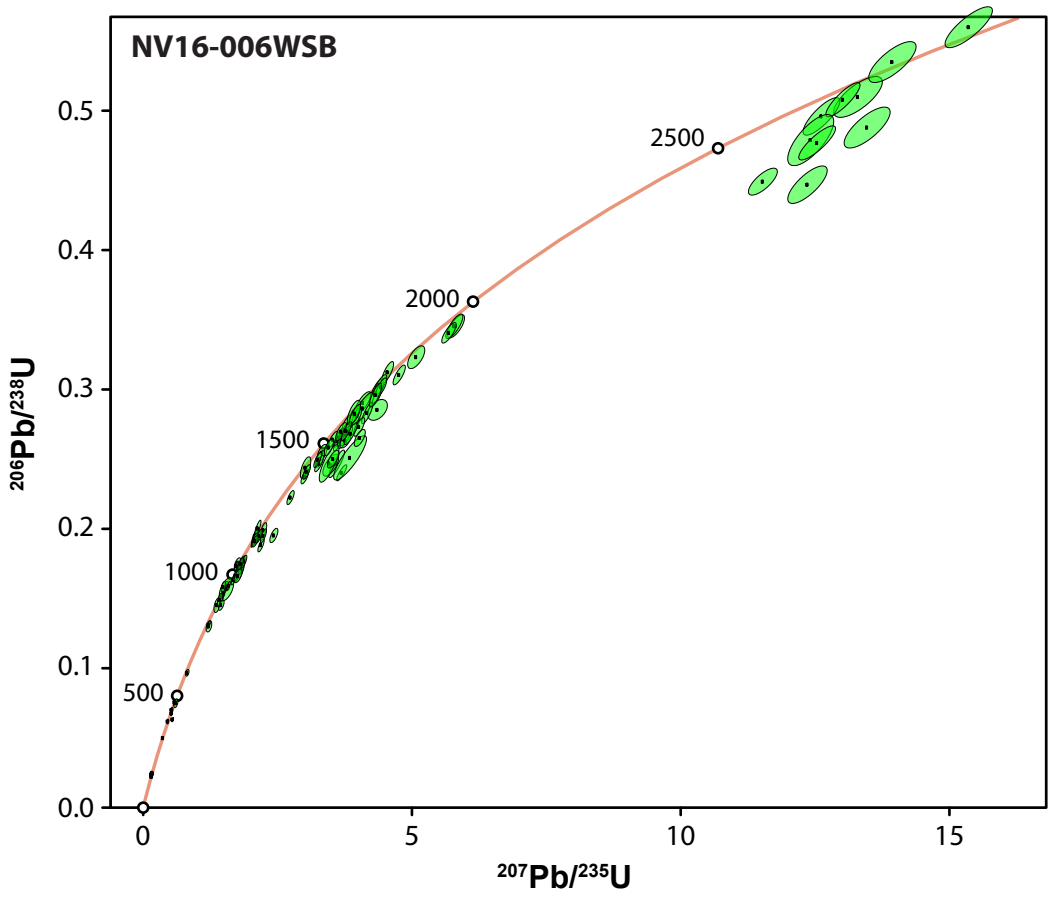
NV16-006WSB
0.5
0.4
0.3
0.2
0.1
0.0
2500
2000
1500
1000
500
0
5
10
15
206Pb/238U
207Pb/235U

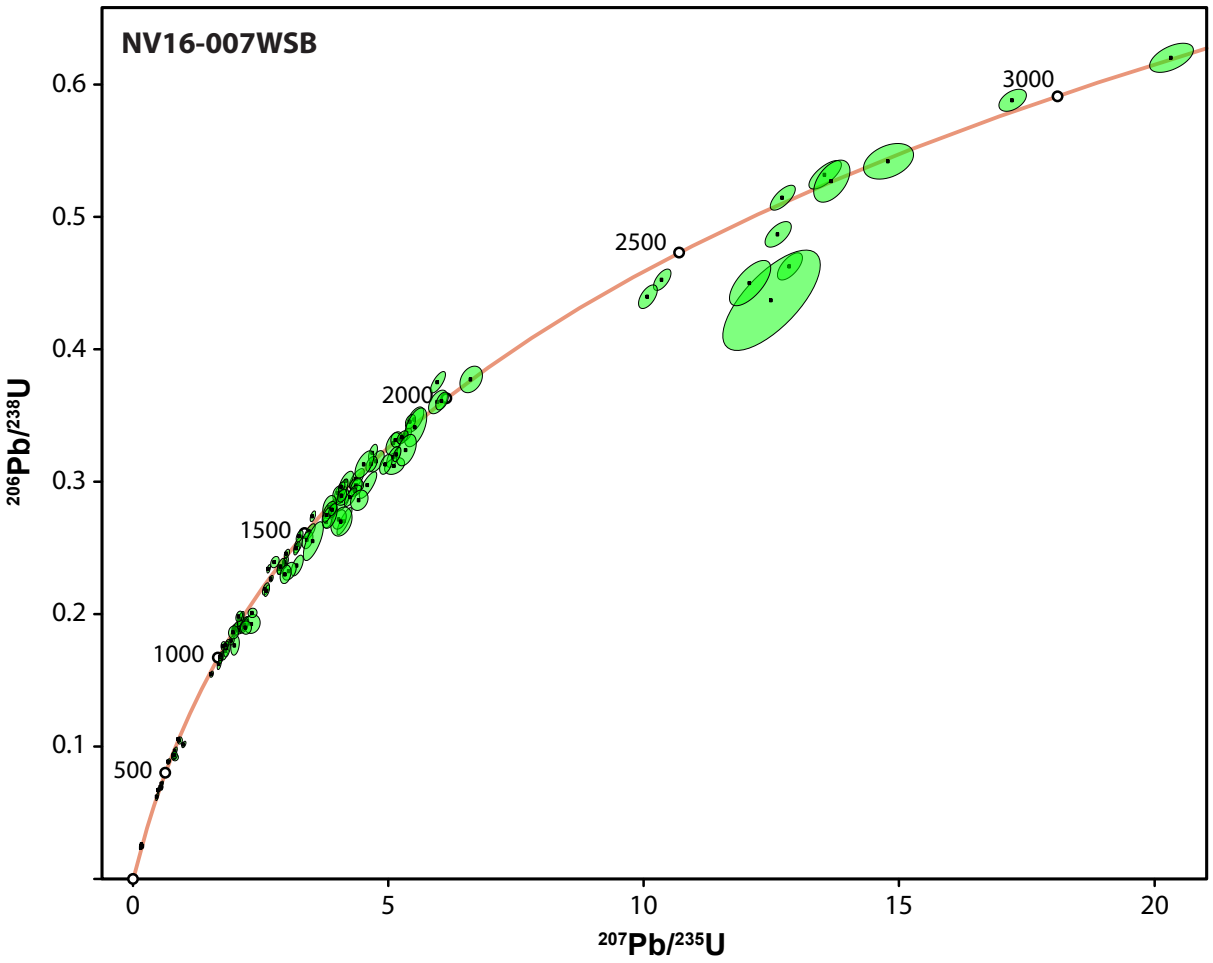
NV16-007WSB
0.6
0.5
0.4
0.3
0.2
0.1
0
5
10
15
20
500
1000
1500
2000
2500
3000
206Pb/238U
207Pb/235U

HEAVY MINERAL ANALYSIS

EDS ANALYSIS OF HEAVY MINERAL SEPARATES

	Elemental Composition														
Analysis	**O**	**Al**	**Si**	**Zr**	**Mg**	**Na**	**Ca**	**Ti**	**Fe**	**K**	**F**	**P**	**S**	**Ba**	**Mineral**
NV12-145BR 41°36.46'N, 116°08.25'W															
145BR_0	47%	14%	26%			3%	9%		1%						labadorite
145BR_1	46%	5%	28%	10%	1%			4%	5%	1%					
145BR_2	40%							60%							rutile
145BR_4	48%	9%	31%	6%	1%		1%		3%	1%					
145BR_6	35%		15%	51%											zircon
145BR_7	39%	2%	17%	29%				7%	7%	0%					
145BR_8	36%	2%	17%	43%							2%				ziircon
145BR_9	47%	9%	25%		1%		1%	9%	6%	1%					
145BR_10	38%		0%				44%				2%	15%			flourapatite
145BR_11	67%					2%				1%	1%		4%		
145BR_12	39%						44%		1%			16%			apatite
145BR_13	35%	0%	14%	48%				2%	2%						ziircon
NV11-031DCA 39° 57.77'N, 116° 50.08'W															
031DCA_1	41%	3%	3%					51%	2%						rutile
031DCA_2	40%	1%	1%					55%	3%						rutile
031DCA_3	40%	0%	0%					58%			2%				rutile
031DCA_4	45%	28%	18%								10%				topaz
031DCA_5	39%	0%	1%				40%				2%	17%			flourapatite
031DCA_6	47%	53%													corundum
031DCA_7	40%	0%	0%					57%	2%						rutile
031DCA_8	50%	15%	27%					7%	0%	0%					
031DCA_9	38%	5%	17%	39%											zircon
031DCA_10	39%	6%	18%	38%											zircon
031DCA_11	35%		14%	50%											zircon
031DCA_12	35%		15%	49%				1%							zircon
031DCA_13	39%	4%	5%				0%	32%	19%						illminite
031DCA_14	35%	0%	15%	49%											zircon
031DCA_15	35%		15%	51%											zircon
031DCA_16	51%	15%	32%					1%	1%	0%					
031DCA_17	35%		15%	51%											zircon
031DCA_18	51%	4%	30%		1%				3%	1%					
031DCA_19	52%	12%	35%		0%			1%	1%						

031DCA_20	51%	18%	30%					1%		0%						
031DCA_21	52%	13%	35%													
NV12-102EH																
102EH_1	35%		16%	49%												zircon
102EH_2	25%									0%				12%	63%	barite
102EH_3	40%	0%	0%					59%								rutile
102EH_4	24%													11%	64%	barite
102EH_5	35%		15%	51%												zircon
102EH_6	26%	0%												13%	60%	barite
102EH_7	22%		0%											9%	68%	barite
102EH_8	40%		0%					59%			0%					rutile
102EH_9	45%	20%	21%						1%					1%	12%	kyanite
102EH_10	25%													12%	63%	barite
102EH_10(2)	27%													13%	58%	barite
102EH_11	23%	0%	0%											10%	67%	barite
102EH_3	34%	0%	15%	50%							1%					zircon
102EH_6	53%	6%	41%													
102EH_7	34%		15%	50%							1%					zircon
102EH_8	34%		15%	51%												zircon
NV12-109CM																
109CM_0	23%													10%	67%	barite
109CM_1	25%													12%	63%	barite
109CM_2	21%		1%											8%	70%	barite
109CM_3	34%		15%	49%											2%	zircon
109CM_4	35%		15%	51%												zircon
109CM_5	38%		1%				41%				1%	16%			1%	fluorapatite
109CM_6	35%		15%	50%												zircon
109CM_7	36%		14%	49%												zircon
109CM_8	24%		1%											10%	65%	barite
109CM_9	25%													12%	63%	barite
109CM_10	37%		14%	47%												zircon
109CM_1	39%	0%	1%				38%				3%	18%				fluorapatite
109CM_2	35%	0%	16%	49%												zircon
109CM_4	39%	0%	1%				39%				2%	18%				fluorapatite
109CM_5	48%	12%	30%			5%	4%		1%	1%						
109CM_7	38%	0%	1%				45%					15%				fluorapatite
109CM_8	46%	1%	35%		0%		12%			0%	5%			1%		

109CM_9	49%	8%	33%		2%	0%	3%		4%	1%					
NV11-023EU															
023EU_2	40%	2%	19%		0%		1%		25%	1%		1%			chromite
023EU_5	38%						42%				3%	17%			flourapatite
NV11-014EU															
014EU_1	27%												13%	60%	barite
014EU_2	27%												14%	59%	barite
014EU_2(2)	27%												13%	60%	barite
014EU_3	23%	0%	1%										9%	66%	barite
014EU_4	34%		15%	50%							1%				zircon
014EU_5	27%												13%	60%	barite
014EU_6	25%								4%				11%	60%	barite
014EU_7	27%								1%				13%	58%	barite
014EU_8	28%	1%	2%						6%	0%			9%	50%	barite
014EU_10	27%												13%	60%	barite
014EU_11	23%												0%	67%	barite
NV11-045TC															
045TC_1	35%		15%	51%				0%							zircon
045TC_2	49%	17%	25%					6%	2%	1%					
045TC_3	48%	13%	29%		2%			0%	2%	6%					
045TC_4	35%	0%	15%	50%							0%				zircon
045TC_7	50%	21%	27%						1%						kyanite
045TC_10	51%	7%	37%		1%			1%	2%						
NV11-049EP															
049EP_1	38%	0%	0%			0%	41%				3%	17%			flourapatite
049EP_2	46%	1%	23%		0%	0%	19%		2%	0%		9%			garnet
049EP_3	32%	1%	4%		0%		1%		61%	0%		0%			
049EP_4	37%	1%	3%		0%		22%		25%	0%		10%			garnet
049EP_5	27%	1%	1%										12%	60%	barite
049EP_6	38%	0%	0%			0%	37%		1%		4%	17%			flourapatite
049EP_7	25%	0%	1%										11%	62%	barite
049EP_8	39%		0%				40%				2%	18%			
049EP_9	31%	2%	7%		0%				2%	1%			10%	46%	
049EP_10	38%	0%	1%			0%	44%		1%		1%	15%			flourapatite
049EP_11	37%	0%	1%		0%	1%	37%		1%		7%	16%			

049EP_12	44%	0%	19%		0%	21%			4%	10%				
049EP_13	39%	2%	14%	0%		5%	36%	1%		2%				
049EP_14	39%	0%	4%		0%	33%	9%	0%		13%				
049EP_15	28%	0%	1%			0%	13%			0%	10%	47%	barite	
049EP_16	30%		1%				68%						hematite	
049EP_17	25%						1%				12%	62%	barite	
049EP_18	32%	1%	4%			0%	56%			1%	1%	4%		
049EP_19	25%						2%				11%	62%	barite	
049EP_20	31%	1%	2%				66%			0%				
049EP_21	31%		2%				60%				1%	5%		
049EP_22	32%	0%	4%			0%	63%			0%				

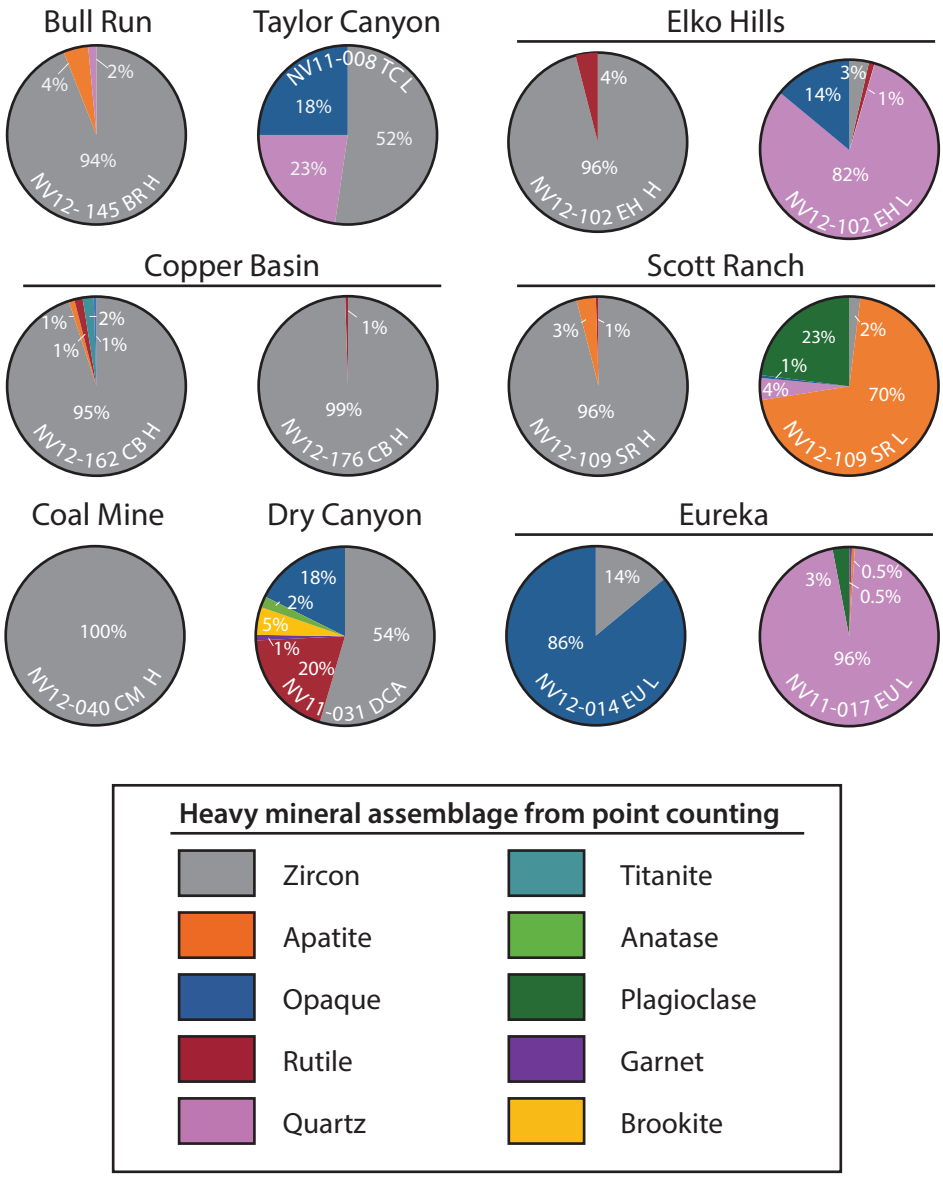
Bull Run
4%
2%
94%
NV12- 145 BR H
Taylor Canyon
NV11-008 TC L
18%
52%
23%
Elko Hills
4%
96%
NV12-102 EH H
3%
14%
1%
82%
NV12-102 EH L
Copper Basin
1%
2%
1%
1%
95%
NV12-162 CB H
1%
99%
NV12-176 CB H
Scott Ranch
3%
1%
96%
NV12-109 SR H
23%
2%
1%
4%
70%
NV12-109 SR L
Coal Mine
100%
NV12-040 CM H
Dry Canyon
18%
2%
5%
1%
20%
54%
NV11-031 DCA
Eureka
14%
86%
NV12-014 EU L
3%
0.5%
0.5%
96%
NV11-017 EU L
Heavy mineral assemblage from point counting
Zircon
Apatite
Opaque
Rutile
Quartz
Titanite
Anatase
Plagioclase
Garnet
Brookite

CONGLOMERATE CLAST LITHOLOGY COUNT DATA

Location	Total clasts counted	Clast lithology				
		Chert (%)	Limestone (%)	Quartzite (%)	Shale (%)	Tuff (%)
Bullion Road	250	71	11	16	2	0
Coal Mine Canyon	900	56	3	38	3	0
Elko Hills	750	74	3	20	1	2
Emigrant Pass	620	83	8	9	0	0
Taylor Canyon	825	71	5	14	1	9
Pie Creek	200	79	9	10	2	0
Robinson Mountain	350	68	10	21	1	0

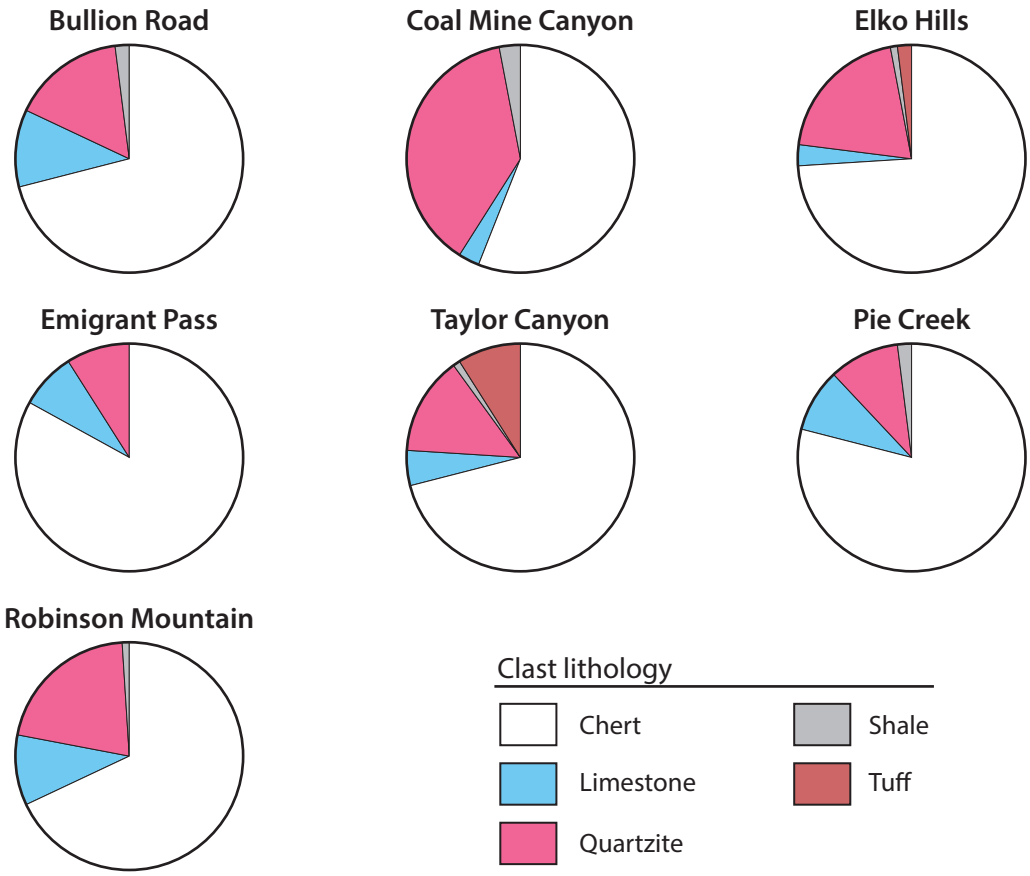

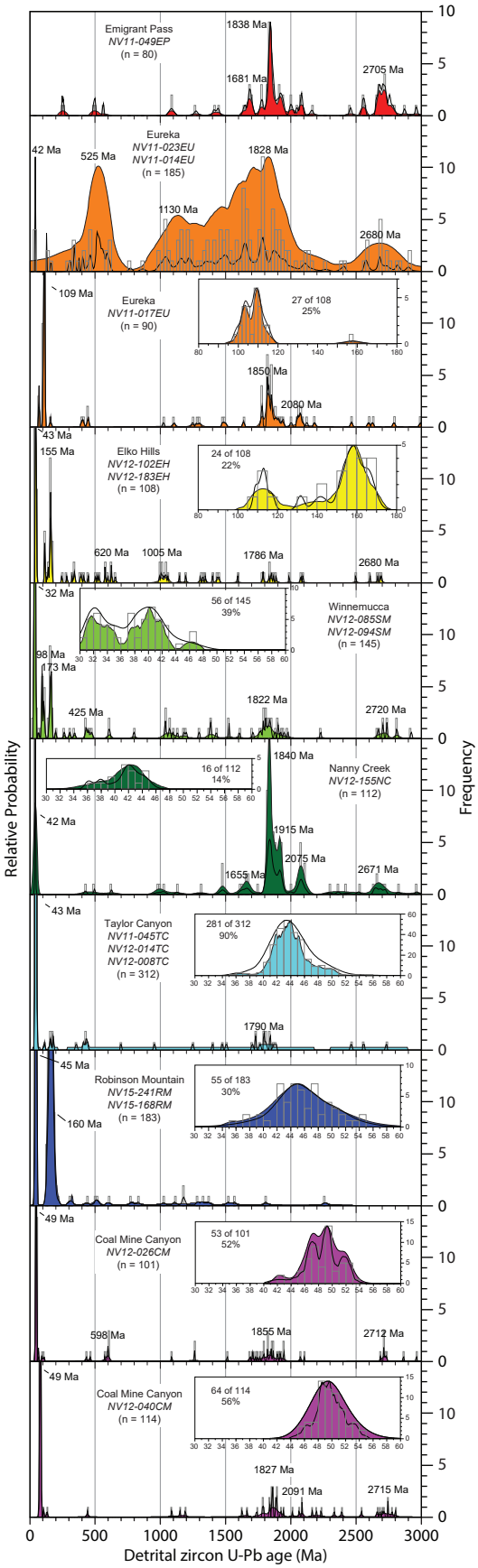
Emigrant Pass
NV11-049EP
(n = 80)
1838 Ma
1681 Ma
2705 Ma
Eureka
NV11-023EU
NV11-014EU
(n = 185)
42 Ma
525 Ma
1828 Ma
1130 Ma
2680 Ma
Eureka
NV11-017EU
(n = 90)
109 Ma
27 of 108
25%
1850 Ma
2080 Ma
Elko Hills
NV12-102EH
NV12-183EH
(n = 108)
43 Ma
155 Ma
24 of 108
22%
620 Ma
1005 Ma
1786 Ma
2680 Ma
Winnemucca
NV12-085SM
NV12-094SM
(n = 145)
32 Ma
56 of 145
39%
98 Ma
173 Ma
425 Ma
1822 Ma
2720 Ma
Nanny Creek
NV12-155NC
(n = 112)
16 of 112
14%
1840 Ma
42 Ma
1915 Ma
2075 Ma
1655 Ma
2671 Ma
Taylor Canyon
NV11-045TC
NV12-014TC
NV12-008TC
(n = 312)
43 Ma
281 of 312
90%
1790 Ma
Robinson Mountain
NV15-241RM
NV15-168RM
(n = 183)
45 Ma
55 of 183
30%
160 Ma
Coal Mine Canyon
NV12-026CM
(n = 101)
49 Ma
53 of 101
52%
598 Ma
1855 Ma
2712 Ma
Coal Mine Canyon
NV12-040CM
(n = 114)
49 Ma
64 of 114
56%
1827 Ma
2091 Ma
2715 Ma
Relative Probability
Frequency
Detrital zircon U-Pb age (Ma)
0
500
1000
1500
2000
2500
3000

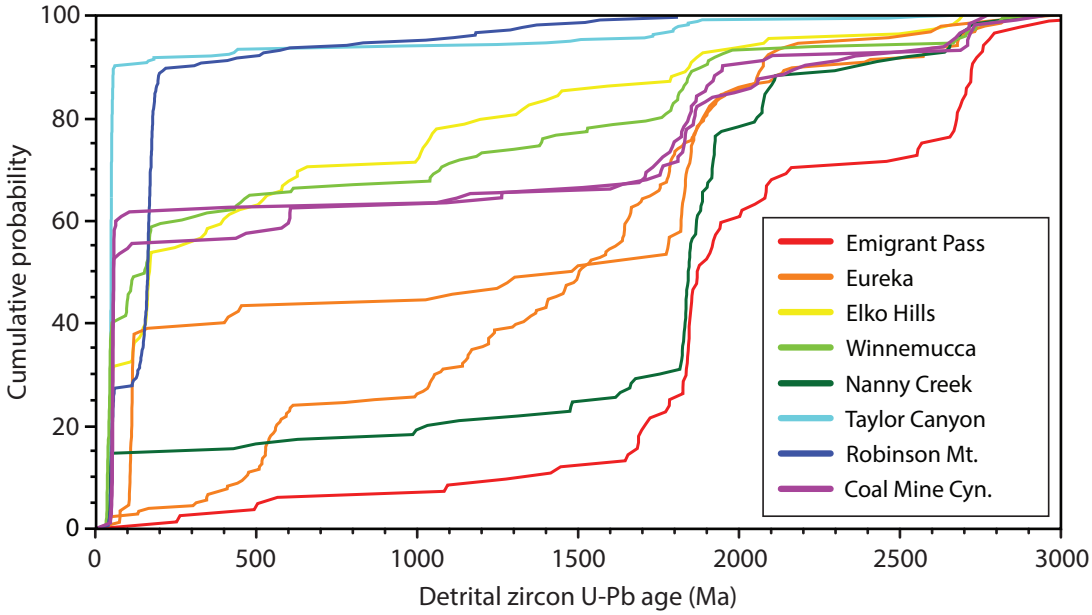
Cumulative probability
Detrital zircon U-Pb age (Ma)
0
20
40
60
80
100
0
500
1000
1500
2000
2500
3000
Emigrant Pass
Eureka
Elko Hills
Winnemucca
Nanny Creek
Taylor Canyon
Robinson Mt.
Coal Mine Cyn.

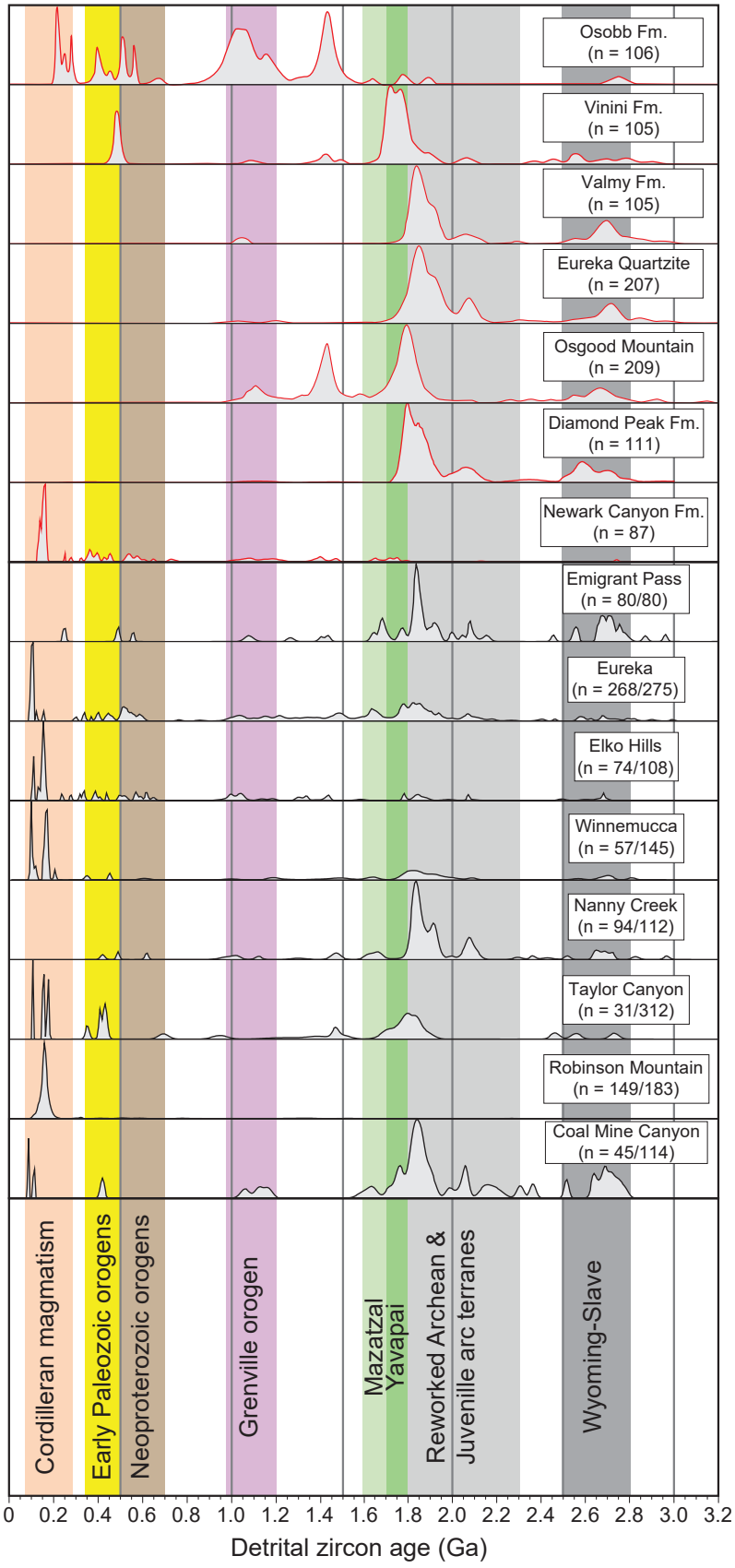
Osobb Fm.
(n = 106)
Vinini Fm.
(n = 105)
Valmy Fm.
(n = 105)
Eureka Quartzite
(n = 207)
Osgood Mountain
(n = 209)
Diamond Peak Fm.
(n = 111)
Newark Canyon Fm.
(n = 87)
Emigrant Pass
(n = 80/80)
Eureka
(n = 268/275)
Elko Hills
(n = 74/108)
Winnemucca
(n = 57/145)
Nanny Creek
(n = 94/112)
Taylor Canyon
(n = 31/312)
Robinson Mountain
(n = 149/183)
Coal Mine Canyon
(n = 45/114)
Cordilleran magmatism
Early Paleozoic orogens
Neoproterozoic orogens
Grenville orogen
Mazatzal
Yavapai
Reworked Archean &
Juvenille arc terranes
Wyoming-Slave
0
0.2
0.4
0.6
0.8
1.0
1.2
1.4
1.6
1.8
2.0
2.2
2.4
2.6
2.8
3.0
3.2
Detrital zircon age (Ga)

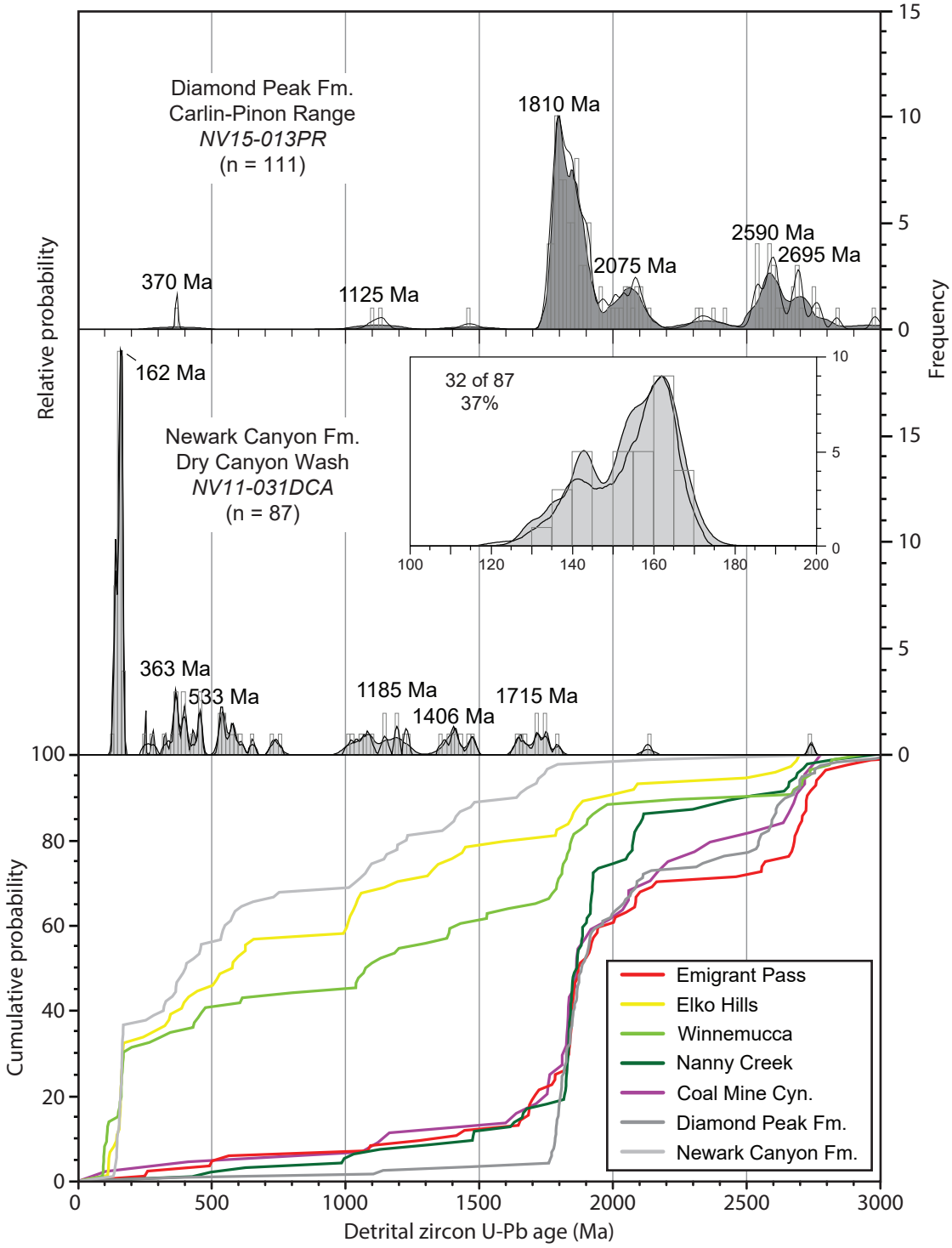
Diamond Peak Fm.
Carlin-Pinon Range
NV15-013PR
(n = 111)
1810 Ma
2075 Ma
2590 Ma
2695 Ma
370 Ma
1125 Ma
Relative probability
Frequency
Newark Canyon Fm.
Dry Canyon Wash
NV11-031DCA
(n = 87)
162 Ma
32 of 87
37%
363 Ma
533 Ma
1185 Ma
1406 Ma
1715 Ma
Cumulative probability
Detrital zircon U-Pb age (Ma)
Emigrant Pass
Elko Hills
Winnemucca
Nanny Creek
Coal Mine Cyn.
Diamond Peak Fm.
Newark Canyon Fm.

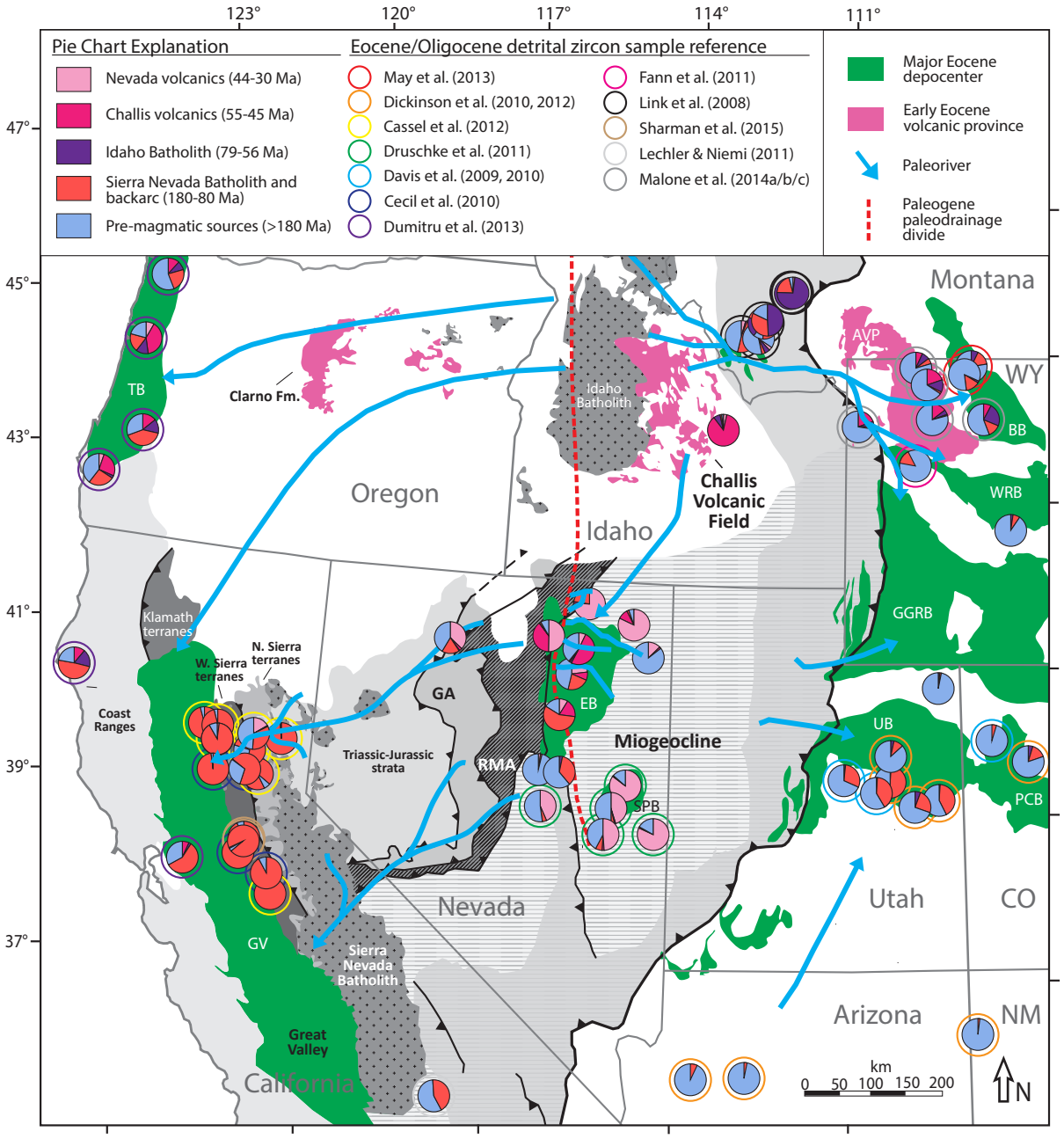
123°
120°
117°
114°
111°
47°
45°
43°
41°
39°
37°
Pie Chart Explanation
Nevada volcanics (44-30 Ma)
Challis volcanics (55-45 Ma)
Idaho Batholith (79-56 Ma)
Sierra Nevada Batholith and backarc (180-80 Ma)
Pre-magmatic sources (>180 Ma)
Eocene/Oligocene detrital zircon sample reference
May et al. (2013)
Dickinson et al. (2010, 2012)
Cassel et al. (2012)
Druschke et al. (2011)
Davis et al. (2009, 2010)
Cecil et al. (2010)
Dumitru et al. (2013)
Fann et al. (2011)
Link et al. (2008)
Sharman et al. (2015)
Lechler & Niemi (2011)
Malone et al. (2014a/b/c)
Major Eocene depocenter
Early Eocene volcanic province
Paleoriver
Paleogene paleodrainage divide
Montana
Oregon
Idaho
Nevada
Utah
CO
Arizona
NM
California
WY
TB
Clarno Fm.
Idaho Batholith
Challis Volcanic Field
AVP
BB
WRB
GGRB
Klamath terranes
W. Sierra terranes
N. Sierra terranes
Coast Ranges
GA
EB
Miogeocline
RMA
SPB
UB
PCB
Triassic-Jurassic strata
GV
Sierra Nevada Batholith
Great Valley
km
0 50 100 150 200
N

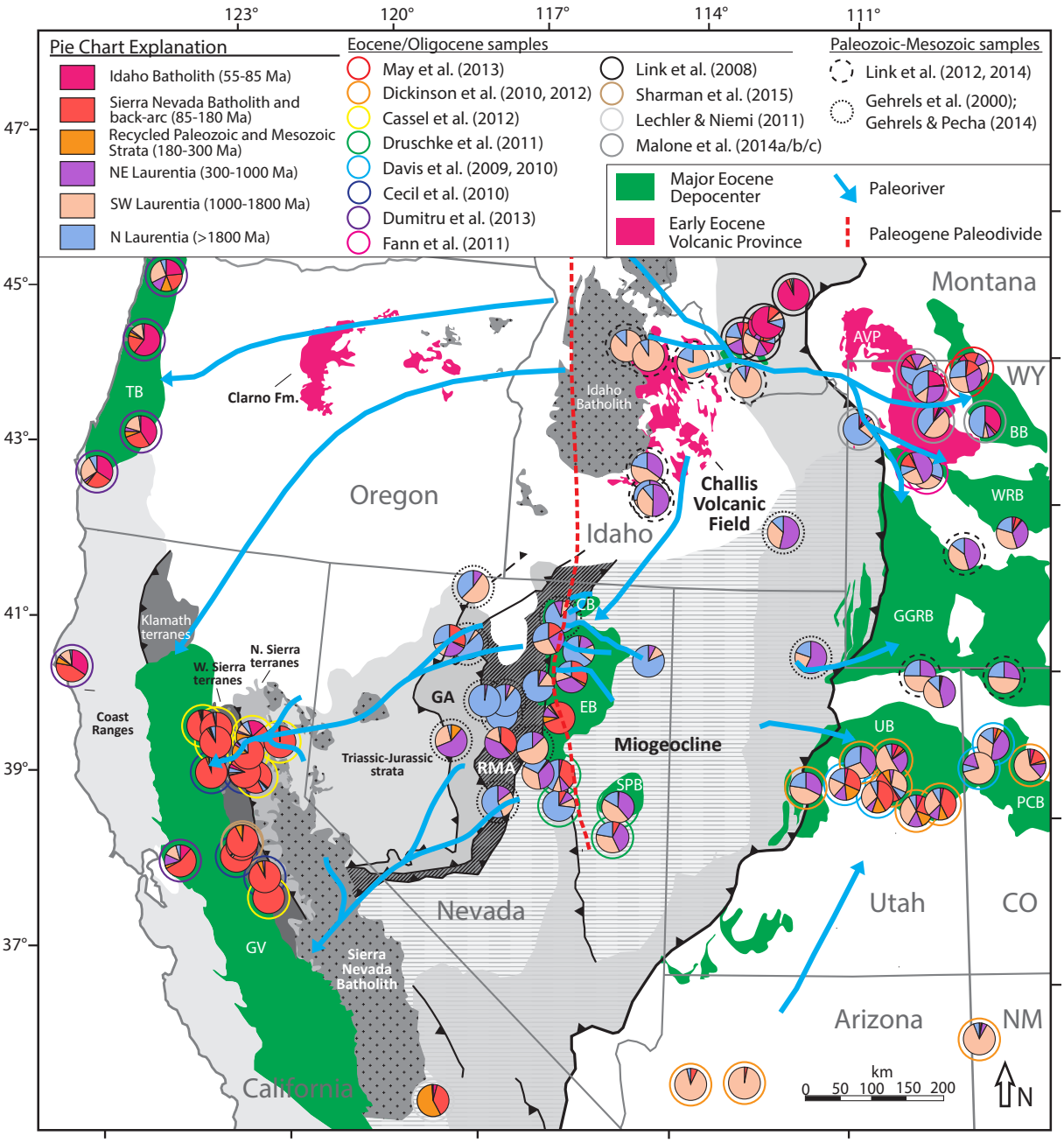
123°
120°
117°
114°
111°
47°
45°
43°
41°
39°
37°
Pie Chart Explanation
Idaho Batholith (55-85 Ma)
Sierra Nevada Batholith and back-arc (85-180 Ma)
Recycled Paleozoic and Mesozoic Strata (180-300 Ma)
NE Laurentia (300-1000 Ma)
SW Laurentia (1000-1800 Ma)
N Laurentia (>1800 Ma)
Eocene/Oligocene samples
May et al. (2013)
Dickinson et al. (2010, 2012)
Cassel et al. (2012)
Druschke et al. (2011)
Davis et al. (2009, 2010)
Cecil et al. (2010)
Dumitru et al. (2013)
Fann et al. (2011)
Link et al. (2008)
Sharman et al. (2015)
Lechler & Niemi (2011)
Malone et al. (2014a/b/c)
Paleozoic-Mesozoic samples
Link et al. (2012, 2014)
Gehrels et al. (2000); Gehrels & Pecha (2014)
Major Eocene Depocenter
Early Eocene Volcanic Province
Paleoriver
Paleogene Paleodivide
Montana
Oregon
Idaho
Nevada
Utah
CO
Arizona
NM
California
WY
TB
Clarno Fm.
Idaho Batholith
AVP
BB
WRB
Challis Volcanic Field
GGRB
CB
Klamath terranes
N. Sierra terranes
W. Sierra terranes
Coast Ranges
GA
EB
Miogeocline
Triassic-Jurassic strata
RMA
SPB
UB
PCB
GV
Sierra Nevada Batholith
km
0 50 100 150 200
N

DOUBLE DATING OF ADDITIONAL CRETACEOUS–OLIGOCENE STRATA

Detrital Zircon (U-Th)/He Thermochronology

Sample	mineral	U (ppm)	Th (ppm)	147Sm (ppm)	[U]e	Th/U	He (nmol/g)	mass (µg)	Ft	ESR	Age (Ma)	err., Ma
Winnemucca												
zDD_NV12_085SM-110	zircon	636.6	330.1	5.0	712.6	0.52	291.9	8.72	0.80	61.17	93.6	7.49
zDD_NV12_085SM-113	zircon	168.5	105.4	1.3	192.8	0.63	61.2	22.30	0.84	77.29	69.3	5.54
zDD_NV12_085SM-114	zircon	188.7	90.9	1.6	209.7	0.48	29.5	2.51	0.72	40.47	36.3	2.91
zDD_NV12_085SM-116	zircon	149.8	62.6	1.2	164.2	0.42	23.5	10.77	0.82	65.76	32.3	2.59
zDD_NV12_085SM-119	zircon	61.8	47.4	3.6	72.8	0.77	31.1	4.67	0.76	49.98	103.1	8.25
zDD_NV12_085SM-103	zircon	152.5	84.8	2.0	172.0	0.56	24.7	6.44	0.77	52.22	34.3	2.74
zDD_NV12_085SM-107	zircon	157.5	81.2	2.2	176.2	0.52	24.4	13.27	0.82	68.59	31.0	2.48
zDD_NV12_085SM-68	zircon	132.3	72.7	2.0	149.1	0.55	15.4	8.12	0.79	56.97	24.1	1.93
zDD_NV12_085SM-50	zircon	242.7	195.9	3.4	287.8	0.81	88.9	4.88	0.76	48.62	75.1	6.01
zDD_NV12_085SM-2	zircon	157.8	82.2	9.2	176.8	0.52	58.1	8.11	0.80	58.50	75.9	6.07
zDD_NV12_085SM-78	zircon	38.1	22.8	-1.4	43.3	0.60	18.7	1.49	0.66	32.90	120.7	9.66
zDD_NV12_085SM-48	zircon	44.0	50.0	1.2	55.6	1.13	9.2	4.16	0.75	48.09	40.5	3.24
zDD_NV12_085SM-98	zircon	260.0	151.2	5.0	294.8	0.58	96.1	6.24	0.77	52.32	77.5	6.20
zDD_NV12_085SM-102	zircon	239.5	83.4	4.0	258.7	0.35	55.3	5.60	0.77	51.87	51.0	4.08
Winnemucca – Pansy Lee Conglomerate 41° 02.15'N, 117° 57.98'W												
zDD_NV12_094SM-40	zircon	35.7	36.6	2.0	44.2	1.02	12.4	1.45	0.65	32.99	79.4	6.35
zDD_NV12_094SM-99	zircon	78.0	27.5	10.3	84.4	0.35	20.8	3.27	0.74	44.30	61.5	4.92
zDD_NV12_094SM-28	zircon	30.5	17.0	0.7	34.5	0.56	10.1	2.69	0.72	41.44	74.9	6.00
zDD_NV12_094SM-19	zircon	135.7	28.0	2.9	142.2	0.21	45.4	2.70	0.73	41.63	81.0	6.48
zDD_NV12_094SM-96	zircon	98.6	48.1	4.0	109.7	0.49	23.5	1.47	0.67	33.80	59.2	4.74
zDD_NV12_094SM-48	zircon	86.4	54.1	2.3	98.8	0.63	45.0	2.60	0.72	40.97	116.6	9.33
zDD_NV12_094SM-16	zircon	0.7	0.7	0.0	0.8	1.09	0.1	0.87	0.61	28.60	32.3	2.58

zDD_NV12_094SM-39	zircon	24.4	20.1	0.0	29.1	0.82	7.7	1.90	0.68	36.61	71.3	5.71
Dry Canyon – Newark Canyon Formation 39° 57.77'N, 116° 50.08'W												
zDD_NV11_031DCA-365	zircon	89.5	9.9	1.2	91.8	0.11	75.3	5.92	0.79	54.16	190.7	15.26
zDD_NV11_031DCA-358	zircon	290.7	40.7	2.8	300.1	0.14	310.1	6.16	0.78	53.32	240.1	19.21
zDD_NV11_031DCA-342	zircon	130.3	102.0	5.3	153.8	0.78	146.7	2.03	0.69	37.07	252.3	20.19
zDD_NV11_031DCA-388	zircon	235.8	111.7	5.9	261.5	0.47	285.1	2.84	0.73	42.18	273.2	21.86
zDD_NV11_031DCA-386	zircon	61.0	37.2	1.2	69.5	0.61	115.8	2.75	0.72	41.36	416.8	33.34
zDD_NV11_031DCA-364	zircon	40.7	19.3	2.2	45.2	0.47	135.3	4.55	0.76	49.22	690.3	55.23
zDD_NV11_031DCA-337	zircon	339.4	118.3	12.9	366.7	0.35	263.3	3.61	0.75	45.71	176.0	14.08
zDD_NV11_031DCA-375	zircon	228.6	82.1	8.7	247.5	0.36	196.5	5.20	0.77	50.19	189.1	15.13
zDD_NV11_031DCA-309	zircon	277.8	76.1	15.0	295.4	0.27	240.8	3.83	0.75	46.33	198.4	15.87
zDD_NV11_031DCA-307	zircon	92.1	31.2	2.8	99.3	0.34	101.1	2.82	0.73	42.09	254.8	20.39

U-Pb Geochronology

Analysis	U (ppm)	U/Th	207Pb/ 235U	±%	206Pb/ 238U	±%	err. corr.	207Pb/ 235U Age (Ma)	± (Ma)	206Pb/ 238U Age (Ma)	± (Ma)	207Pb/ 206Pb Age (Ma)	± (Ma)	Best age (Ma)	± (Ma)	Disc (%)
NV15-022WH: Windermere Hills 41°14.58'N, W114° 37.53'W																
NV15022WH_1	170	1.35	0.06100	0.00340	0.00696	0.00017	0.08198	60.0	3.2	44.7	1.1	690	120	44.7	1.1	25.5
NV15022WH_2	229	2.15	0.06320	0.00720	0.00645	0.00017	0.07545	61.9	6.7	41.4	1.1	740	160	41.4	1.1	33.1
NV15022WH_3	259	2.38	0.08450	0.00580	0.00694	0.00022	0.02946	82.1	5.4	44.6	1.4	1300	130	44.6	1.4	45.7
NV15022WH_4	292	2.58	0.04360	0.00180	0.00620	0.00016	0.01077	43.3	1.8	39.8	1.0	278	94	39.8	1.0	8.0
NV15022WH_5	345	2.14	0.05410	0.00290	0.00631	0.00012	0.27298	53.4	2.8	40.5	0.8	670	110	40.5	0.8	24.1
NV15022WH_7	552	1.48	0.05910	0.00390	0.00657	0.00015	0.04316	58.2	3.7	42.2	1.0	670	100	42.2	1.0	27.5
NV15022WH_8	368	1.78	0.06190	0.00360	0.00629	0.00015	0.24824	60.9	3.5	40.4	1.0	910	110	40.4	1.0	33.6
NV15022WH_9	220.2	2.51	0.06350	0.00340	0.00663	0.00016	0.04886	62.5	3.2	42.6	1.0	880	120	42.6	1.0	31.8
NV15022WH_10	122	1.80	0.05240	0.00420	0.00584	0.00017	0.02587	51.8	4.0	37.5	1.1	780	170	37.5	1.1	27.6
NV15022WH_13	261.5	2.52	0.04180	0.00220	0.00561	0.00012	0.15545	41.6	2.2	36.0	0.8	370	110	36.0	0.8	13.4
NV15022WH_15	247	1.37	0.04470	0.00140	0.00583	0.00012	0.05085	44.3	1.4	37.5	0.7	438	84	37.5	0.7	15.5
NV15022WH_16	456	3.37	0.05930	0.00360	0.00640	0.00013	0.03117	58.4	3.4	41.1	0.9	780	120	41.1	0.9	29.6
NV15022WH_18	393	2.58	0.04490	0.00140	0.00623	0.00012	0.49170	44.6	1.4	40.1	0.8	297	72	40.1	0.8	10.2
NV15022WH_19	296	2.44	0.07070	0.00380	0.00626	0.00015	0.12990	69.3	3.6	40.3	1.0	1220	130	40.3	1.0	41.9
NV15022WH_20	256.4	1.91	0.06670	0.00480	0.00624	0.00013	0.02267	65.4	4.5	40.1	0.8	1100	150	40.1	0.8	38.7
NV15022WH_21	338	1.10	0.07530	0.00550	0.00617	0.00011	0.14691	73.5	5.1	39.6	0.7	1360	130	39.6	0.7	46.1
NV15022WH_22	433	2.19	0.04430	0.00150	0.00604	0.00011	0.32077	43.9	1.4	38.9	0.7	315	78	38.9	0.7	11.5
NV15022WH_23	389	1.74	0.04470	0.00210	0.00607	0.00012	0.19413	44.7	2.1	39.0	0.8	304	94	39.0	0.8	12.7
NV15022WH_24	342.4	2.18	0.04390	0.00170	0.00606	0.00010	0.17362	43.6	1.7	38.9	0.6	338	93	38.9	0.6	10.7
NV15022WH_25	239.3	2.43	0.04550	0.00210	0.00629	0.00011	0.00896	45.2	2.0	40.4	0.7	360	110	40.4	0.7	10.6
NV15022WH_26	437	2.25	0.06020	0.00650	0.00640	0.00012	0.15977	59.0	6.1	41.1	0.8	680	170	41.1	0.8	30.3
NV15022WH_28	302.4	1.80	0.04720	0.00210	0.00616	0.00015	0.12478	46.8	2.1	39.6	1.0	450	110	39.6	1.0	15.4
NV15022WH_29	365	2.51	0.04360	0.00170	0.00614	0.00014	0.38465	43.3	1.7	39.4	0.9	255	74	39.4	0.9	8.9
NV15022WH_30	326	1.38	0.05120	0.00220	0.00600	0.00011	0.01745	50.9	2.1	38.6	0.7	680	100	38.6	0.7	24.2
NV15022WH_31	242	2.40	0.04630	0.00230	0.00592	0.00013	0.09430	45.9	2.2	38.0	0.9	420	110	38.0	0.9	17.1
NV15022WH_32	372	1.88	0.04360	0.00140	0.00629	0.00013	0.04797	43.3	1.4	40.5	0.8	235	81	40.5	0.8	6.6
NV15022WH_33	737	1.84	0.06360	0.00350	0.00661	0.00016	0.08630	62.5	3.3	42.5	1.0	850	110	42.5	1.0	32.0
NV15022WH_34	403	2.03	0.04190	0.00200	0.00584	0.00013	0.24621	41.7	2.0	37.6	0.9	290	110	37.6	0.9	9.9
NV15022WH_35	302	2.02	0.04790	0.00190	0.00622	0.00014	0.12459	47.5	1.8	40.0	0.9	424	99	40.0	0.9	15.8
NV15022WH_37	296	1.85	0.05060	0.00330	0.00627	0.00016	0.13190	50.1	3.1	40.3	1.0	480	130	40.3	1.0	19.6
NV15022WH_40	146	1.61	0.05540	0.00300	0.00633	0.00026	0.22334	54.7	2.9	40.7	1.7	690	120	40.7	1.7	25.6
NV15022WH_43	154.6	1.54	0.05340	0.00380	0.00701	0.00021	0.18131	52.7	3.7	45.1	1.4	360	140	45.1	1.4	14.4
NV15022WH_44	234.1	2.85	0.04270	0.00190	0.00598	0.00017	0.16303	42.7	1.8	38.4	1.1	283	99	38.4	1.1	10.1
NV15022WH_46	245	2.80	0.04840	0.00310	0.00666	0.00032	0.25416	47.9	3.0	42.8	2.0	280	140	42.8	2.0	10.6

NV15022WH_48	404	0.62	0.51800	0.01200	0.06080	0.00150	0.70403	423.3	7.7	380.3	9.4	666	40	380.3	9.4	10.2
NV15022WH_49	190.9	1.95	0.10050	0.00380	0.01295	0.00054	0.58468	97.6	3.4	82.9	3.4	464	84	82.9	3.4	15.1
NV15022WH_50	432	1.86	0.06340	0.00260	0.00642	0.00012	0.42864	62.4	2.5	41.2	0.8	968	72	41.2	0.8	33.9
NV15022WH_51	387	2.04	0.04850	0.00190	0.00660	0.00017	0.03116	48.3	1.9	42.4	1.1	336	94	42.4	1.1	12.2
NV15022WH_52	354	2.40	0.05270	0.00260	0.00626	0.00011	0.02352	52.1	2.5	40.2	0.7	600	110	40.2	0.7	22.8
NV15022WH_53	478	2.12	0.05050	0.00160	0.00684	0.00018	0.43822	50.0	1.5	44.0	1.1	344	67	44.0	1.1	12.0
NV15022WH_54	741	2.88	0.07780	0.00420	0.00748	0.00025	0.39633	76.0	3.9	48.0	1.6	1071	96	48.0	1.6	36.8
NV15022WH_55	244	1.69	0.04370	0.00180	0.00612	0.00016	0.09889	43.4	1.8	39.3	1.0	300	110	39.3	1.0	9.4
NV15022WH_56	116	1.96	0.06090	0.00400	0.00652	0.00017	0.23135	59.9	3.8	41.9	1.1	870	150	41.9	1.1	30.1
NV15022WH_57	134.3	2.25	0.04200	0.00270	0.00665	0.00018	0.15761	41.7	2.6	42.7	1.2	0	120	42.7	1.2	2.4
NV15022WH_58	155	1.61	0.04260	0.00250	0.00632	0.00016	0.27782	43.0	2.5	40.6	1.0	180	120	40.6	1.0	5.6
NV15022WH_59	351	2.22	0.04740	0.00190	0.00656	0.00018	0.12971	47.0	1.9	42.1	1.2	270	88	42.1	1.2	10.4
NV15022WH_60	222.6	2.60	0.05480	0.00480	0.00665	0.00021	0.29166	54.0	4.4	42.7	1.3	440	110	42.7	1.3	20.9
NV15022WH_61	696	3.21	0.04240	0.00100	0.00655	0.00008	0.22497	42.3	1.0	42.1	0.5	73	53	42.1	0.5	0.5
NV15022WH_64	216	0.82	0.04840	0.00360	0.00617	0.00017	0.16936	47.9	3.4	39.7	1.1	430	140	39.7	1.1	17.1
NV15022WH_66	341	2.70	0.05190	0.00280	0.00647	0.00014	0.31016	51.3	2.7	41.6	0.9	480	110	41.6	0.9	18.9
NV15022WH_67	229	1.10	0.04660	0.00290	0.00620	0.00015	0.05578	46.2	2.8	39.8	1.0	350	130	39.8	1.0	13.8
NV15022WH_68	299	1.73	0.04850	0.00230	0.00668	0.00014	0.03993	48.0	2.2	42.9	0.9	290	100	42.9	0.9	10.6
NV15022WH_69	574	1.82	0.05910	0.00380	0.00663	0.00012	0.24083	58.2	3.6	42.6	0.8	760	130	42.6	0.8	26.8
NV15022WH_70	571	1.67	0.06590	0.00370	0.00615	0.00010	0.07366	64.7	3.5	39.5	0.7	1100	110	39.5	0.7	38.9
NV15022WH_71	437	2.21	0.05780	0.00360	0.00631	0.00015	0.48211	57.6	3.6	40.5	1.0	820	120	40.5	1.0	29.6
NV15022WH_72	426	2.17	0.05810	0.00350	0.00694	0.00031	0.61382	57.2	3.4	44.6	2.0	480	110	44.6	2.0	22.0
NV15022WH_75	350.9	1.41	5.04700	0.04700	0.32770	0.00290	0.72911	1826.7	7.8	1827.0	14.0	1815	12	1815.0	12.0	0.7
NV15022WH_76	612	3.57	0.12250	0.00210	0.01829	0.00025	0.32345	117.3	1.9	116.8	1.6	121	40	116.8	1.6	0.4
NV15022WH_78	514	2.12	0.04520	0.00130	0.00635	0.00013	0.16897	44.8	1.3	40.8	0.9	275	73	40.8	0.9	8.9
NV15022WH_79	240.3	2.70	0.06210	0.00330	0.00791	0.00032	0.24624	61.1	3.2	50.8	2.1	530	130	50.8	2.1	16.9
NV15022WH_80	127.5	2.54	0.05870	0.00420	0.00691	0.00025	0.21415	57.8	4.0	44.4	1.6	640	160	44.4	1.6	23.2
NV15022WH_82	122	1.50	0.04620	0.00290	0.00604	0.00017	0.24246	45.8	2.9	38.8	1.1	420	130	38.8	1.1	15.3
NV15022WH_84	408	2.61	0.04430	0.00140	0.00627	0.00011	0.07044	44.0	1.3	40.3	0.7	254	76	40.3	0.7	8.5
NV15022WH_86	239	1.05	0.04310	0.00210	0.00625	0.00016	0.24273	42.8	2.0	40.2	1.0	210	100	40.2	1.0	6.1
NV15022WH_87	343	1.92	0.04500	0.00190	0.00653	0.00014	0.09911	44.6	1.9	41.9	0.9	232	98	41.9	0.9	6.0
NV15022WH_88	511	0.75	0.73500	0.03200	0.08300	0.00390	0.78620	557.0	19.0	513.0	23.0	820	62	513.0	23.0	7.9
NV15022WH_90	546	1.89	0.06130	0.00430	0.00661	0.00014	0.68973	60.2	4.1	42.5	0.9	760	130	42.5	0.9	29.5
NV15022WH_91	130.7	2.09	0.05910	0.00360	0.00669	0.00036	0.28758	58.7	3.4	43.0	2.3	740	150	43.0	2.3	26.7
NV15022WH_92	1760	0.84	0.05470	0.00260	0.00714	0.00016	0.25683	54.0	2.5	45.9	1.0	405	97	45.9	1.0	15.0
NV15022WH_93	95.2	1.45	0.04410	0.00290	0.00631	0.00018	0.11075	43.8	2.8	40.6	1.1	230	150	40.6	1.1	7.3
NV15022WH_94	396	2.43	0.04590	0.00180	0.00664	0.00021	0.14904	45.8	1.7	42.7	1.3	188	77	42.7	1.3	6.8
NV15022WH_96	405	2.87	0.04590	0.00160	0.00648	0.00016	0.19883	45.5	1.5	41.6	1.0	244	82	41.6	1.0	8.6
NV15022WH_97	172.8	1.22	0.06350	0.00470	0.00722	0.00031	0.44803	62.3	4.5	46.4	2.0	680	140	46.4	2.0	25.5
NV15022WH_99	199	1.40	0.08460	0.00610	0.00680	0.00020	0.29837	82.2	5.6	43.7	1.3	1400	120	43.7	1.3	46.8

NV15022WH_101	469	1.67	0.05470	0.00370	0.00672	0.00021	0.22616	53.9	3.5	43.2	1.3	440	100	43.2	1.3	19.9
NV15022WH_102	385	2.15	0.04880	0.00200	0.00655	0.00015	0.37009	48.4	2.0	42.1	1.0	359	86	42.1	1.0	13.1
NV15022WH_106	320.2	2.54	0.04730	0.00250	0.00625	0.00017	0.40904	46.9	2.4	40.2	1.1	410	120	40.2	1.1	14.3
NV15022WH_107	77.2	1.83	0.09900	0.02900	0.00707	0.00051	0.09268	82.0	13.0	45.4	3.2	1140	260	45.4	3.2	44.6
NV15022WH_108	402	2.43	0.04750	0.00190	0.00638	0.00024	0.43851	47.1	1.9	41.0	1.5	318	90	41.0	1.5	13.0
NV15022WH_109	348.9	2.26	0.07970	0.00340	0.00656	0.00019	0.39975	77.8	3.2	42.1	1.2	1363	81	42.1	1.2	45.9
NV15022WH_110	258	2.76	4.33000	0.37000	0.24500	0.02000	0.93073	1655.0	75.0	1390.0	110.0	2043	62	2043.0	62.0	32.0
NV15022WH_112	423	1.80	0.04850	0.00210	0.00637	0.00020	0.50762	48.3	2.0	41.0	1.3	391	94	41.0	1.3	15.1
NV15022WH_113	429	1.54	0.04700	0.00290	0.00588	0.00011	0.01944	46.6	2.8	37.8	0.7	410	100	37.8	0.7	18.9
NV15022WH_114	263	2.71	0.04880	0.00230	0.00561	0.00013	0.04061	48.4	2.3	36.1	0.8	650	110	36.1	0.8	25.5
NV15022WH_115	208.6	2.32	0.04670	0.00200	0.00590	0.00015	0.09107	46.3	2.0	37.9	1.0	440	110	37.9	1.0	18.2
NV15022WH_116	614	5.68	0.14900	0.02400	0.01340	0.00200	0.97281	137.0	20.0	86.0	13.0	1004	75	86.0	13.0	37.2
NV15022WH_117	188.9	1.45	0.04570	0.00200	0.00616	0.00015	0.20513	45.3	1.9	39.6	1.0	343	97	39.6	1.0	12.6
NV15022WH_118	489	2.05	0.05600	0.00250	0.00649	0.00013	0.23702	55.2	2.4	41.7	0.8	720	100	41.7	0.8	24.5
NV15022WH_119	798	1.48	0.06510	0.00380	0.00675	0.00015	0.55355	64.0	3.6	43.4	1.0	883	95	43.4	1.0	32.2
NV15022WH_120	450	2.98	0.04380	0.00150	0.00640	0.00013	0.08844	43.5	1.4	41.1	0.8	193	80	41.1	0.8	5.5
NV15022WH_122	310	1.88	0.05250	0.00290	0.00597	0.00011	0.02855	51.8	2.8	38.4	0.7	640	100	38.4	0.7	25.9
NV15022WH_124	237	1.04	0.06980	0.00550	0.00654	0.00018	0.23282	68.2	5.2	42.0	1.1	1070	160	42.0	1.1	38.4
NV15022WH_125	289	2.91	0.05690	0.00330	0.00627	0.00017	0.07607	56.1	3.2	40.3	1.1	740	120	40.3	1.1	28.2
NV15022WH_127	307	1.99	0.05000	0.00230	0.00642	0.00013	0.25882	49.5	2.2	41.2	0.8	475	96	41.2	0.8	16.7
NV15022WH_128	321	2.09	0.04590	0.00170	0.00621	0.00011	0.04899	45.5	1.6	39.9	0.7	330	78	39.9	0.7	12.3
NV15022WH_129	417	19.60	0.44800	0.02700	0.05670	0.00310	0.96691	373.0	18.0	355.0	18.0	533	38	355.0	18.0	4.8
NV15022WH_130	882	1.02	0.31600	0.00960	0.03820	0.00190	0.91341	278.4	7.5	242.0	12.0	606	52	242.0	12.0	13.1

DOUBLE DATED DETRITAL ZIRCON GRAIN DIMENSIONS

Sample	mineral	length (μm)	width (μm)	UFt	ThFt	mass (μg)	ESR
zDD_NV11_017EU-19	zircon	204.8	107.7	0.82	0.80	11.04	63.94
zDD_NV11_017EU-22	zircon	122.0	72.9	0.74	0.71	3.02	42.10
zDD_NV11_017EU-28	zircon	164.4	125.9	0.83	0.81	12.12	68.28
zDD_NV11_017EU-31	zircon	156.8	110.0	0.81	0.79	8.83	61.09
zDD_NV11_017EU-37	zircon	170.5	119.7	0.83	0.81	11.36	66.44
zDD_NV11_017EU-40	zircon	156.4	108.9	0.81	0.79	8.62	60.58
zDD_NV11_017EU-42	zircon	143.2	95.9	0.79	0.76	6.12	53.87
zDD_NV11_017EU-46	zircon	118.3	101.5	0.79	0.76	5.67	53.27
zDD_NV11_017EU-49	zircon	115.6	90.4	0.77	0.74	4.40	48.75
zDD_NV11_017EU-58	zircon	155.8	102.3	0.80	0.78	7.59	57.79
zDD_NV11_017EU-59	zircon	246.6	128.3	0.85	0.83	18.87	76.36
zDD_NV11_017EU-60	zircon	160.6	116.5	0.82	0.80	10.13	64.11
zDD_NV11_017EU-61	zircon	181.1	101.1	0.81	0.79	8.61	59.27
zDD_NV11_017EU-67	zircon	121.6	71.5	0.73	0.70	2.89	41.43
zDD_NV11_017EU-73	zircon	175.1	105.7	0.81	0.79	9.10	60.90
zDD_NV11_017EU-75	zircon	188.6	98.6	0.81	0.78	8.53	58.64
zDD_NV11_017EU-82	zircon	153.6	101.7	0.80	0.78	7.38	57.29
zDD_NV11_017EU-84	zircon	98.2	87.3	0.75	0.73	3.48	45.34
zDD_NV11_017EU-85	zircon	101.0	73.8	0.73	0.69	2.56	40.54
zDD_NV11_017EU-86	zircon	193.2	83.4	0.78	0.75	6.26	51.47
zDD_NV11_017EU-87	zircon	152.7	81.7	0.77	0.74	4.74	48.34
zDD_NV11_017EU-91	zircon	123.3	83.9	0.76	0.73	4.04	46.97
zDD_NV11_031DCA-307	zircon	98.6	78.4	0.74	0.71	2.82	42.09
zDD_NV11_031DCA-309	zircon	117.1	83.9	0.76	0.73	3.83	46.33
zDD_NV11_031DCA-337	zircon	106.4	85.4	0.75	0.73	3.61	45.71
zDD_NV11_031DCA-375	zircon	151.6	85.9	0.77	0.75	5.20	50.19
zDD_NV11_045TC-37	zircon	132.7	82.1	0.76	0.73	4.16	47.03
zDD_NV11_045TC-54	zircon	232.0	124.8	0.84	0.82	16.79	73.74
zDD_NV11_045TC-117	zircon	195.1	74.4	0.76	0.73	5.02	46.87
zDD_NV11_045TC-166	zircon	246.4	119.9	0.84	0.82	16.47	72.32
zDD_NV11_049EP-2	zircon	139.7	106.0	0.80	0.78	7.30	57.64
zDD_NV11_049EP-3	zircon	103.3	74.8	0.73	0.70	2.69	41.20
zDD_NV11_049EP-8	zircon	186.6	76.0	0.76	0.74	5.01	47.34
zDD_NV11_049EP-26	zircon	164.5	84.5	0.77	0.75	5.46	50.40
zDD_NV11_049EP-27	zircon	149.1	86.8	0.77	0.75	5.22	50.40
zDD_NV11_049EP-28	zircon	184.1	98.0	0.80	0.78	8.22	58.05
zDD_NV11_049EP-34	zircon	123.7	83.9	0.76	0.73	4.05	46.99
zDD_NV11_049EP-48	zircon	130.9	91.4	0.78	0.75	5.08	50.80
zDD_NV11_049EP-50	zircon	103.9	86.9	0.75	0.73	3.65	45.97
zDD_NV11_049EP-59	zircon	103.4	70.7	0.72	0.69	2.40	39.52
zDD_NV11_049EP-61	zircon	168.8	81.7	0.77	0.75	5.24	49.35
zDD_NV11_049EP-64	zircon	108.9	82.3	0.75	0.72	3.44	44.82
zDD_NV11_049EP-67	zircon	110.5	80.5	0.75	0.72	3.33	44.24
zDD_NV11_049EP-90	zircon	148.5	101.0	0.80	0.77	7.04	56.51
zDD_NV11_049EP-93	zircon	184.1	111.8	0.82	0.80	10.71	64.34
zDD_NV11_049EP-94	zircon	114.8	78.4	0.75	0.72	3.28	43.85
zDD_NV11_049EP-95	zircon	231.9	108.0	0.82	0.81	12.58	65.72

zDD_NV11_049EP-105	zircon	166.8	71.7	0.75	0.72	3.98	44.23
zDD_NV11_049EP-106	zircon	112.4	92.5	0.77	0.74	4.47	49.15
zDD_NV11_049EP-112	zircon	132.2	84.3	0.76	0.74	4.37	47.96
zDD_NV12_008TC-9	zircon	84.8	76.9	0.72	0.69	2.33	39.69
zDD_NV12_008TC-93	zircon	81.2	71.1	0.70	0.67	1.91	37.07
zDD_NV12_008TC-127	zircon	86.6	83.7	0.74	0.71	2.82	42.31
zDD_NV12_040CM-169	zircon	155.5	0.0	0.80	0.78	7.67	58.02
zDD_NV12_040CM-175	zircon	183.2	112.1	0.82	0.80	10.70	64.37
zDD_NV12_040CM-181	zircon	107.0	60.9	0.69	0.66	1.84	35.55
zDD_NV12_040CM-189	zircon	191.3	110.5	0.82	0.80	10.85	64.28
zDD_NV12_040CM-190	zircon	102.3	64.5	0.70	0.67	1.98	36.77
zDD_NV12_040CM-192	zircon	144.1	80.1	0.76	0.73	4.30	47.03
zDD_NV12_040CM-197	zircon	160.0	65.1	0.73	0.70	3.16	40.59
zDD_NV12_040CM-198	zircon	132.5	62.7	0.71	0.68	2.42	38.00
zDD_NV12_040CM-209	zircon	194.4	127.1	0.84	0.82	14.60	71.84
zDD_NV12_040CM-212	zircon	159.7	75.3	0.75	0.73	4.21	45.69
zDD_NV12_040CM-232	zircon	137.7	94.9	0.79	0.76	5.77	52.95
zDD_NV12_040CM-236	zircon	107.8	102.9	0.78	0.76	5.31	52.24
zDD_NV12_040CM-241	zircon	105.2	76.5	0.74	0.71	2.86	42.09
zDD_NV12_040CM-242	zircon	148.6	92.1	0.78	0.76	5.86	52.74
zDD_NV12_040CM-247	zircon	76.8	70.3	0.70	0.66	1.77	36.19
zDD_NV12_040CM-266	zircon	92.4	63.7	0.69	0.66	1.74	35.53
zDD_NV12_040CM-269	zircon	131.3	95.0	0.78	0.76	5.51	52.33
zDD_NV12_040CM-278	zircon	143.4	113.3	0.81	0.79	8.55	60.90
zDD_NV12_040CM-279	zircon	176.2	80.3	0.77	0.74	5.29	49.07
zDD_NV12_040CM-286	zircon	156.4	75.8	0.75	0.73	4.18	45.78
zDD_NV12_040CM-290	zircon	155.6	62.9	0.72	0.69	2.86	39.25
zDD_NV12_102EH-54	zircon	109.1	97.7	0.78	0.75	4.84	50.59
zDD_NV12_102EH-57	zircon	95.9	65.1	0.70	0.67	1.89	36.46
zDD_NV12_102EH-66	zircon	177.8	62.0	0.72	0.69	3.18	39.60
zDD_NV12_102EH-80	zircon	149.1	125.3	0.83	0.81	10.89	66.17
zDD_NV12_102EH-82	zircon	213.8	84.4	0.79	0.76	7.08	52.86
zDD_NV12_102EH-83	zircon	97.1	73.2	0.72	0.69	2.42	39.87
zDD_NV12_102EH-85	zircon	165.2	85.4	0.78	0.75	5.60	50.89
zDD_NV12_102EH-86	zircon	181.8	82.1	0.77	0.75	5.70	50.23
zDD_NV12_102EH-88	zircon	97.1	73.2	0.72	0.69	2.42	39.87
zDD_NV12_102EH-89	zircon	109.4	74.0	0.73	0.70	2.78	41.47
zDD_NV12_102EH-91	zircon	122.7	92.4	0.77	0.75	4.87	50.34
zDD_NV12_102EH-93	zircon	107.8	98.8	0.78	0.75	4.90	50.83
zDD_NV12_102EH-94	zircon	127.6	82.6	0.76	0.73	4.05	46.79
zDD_NV12_102EH-103	zircon	116.0	105.8	0.79	0.77	6.04	54.50
zDD_NV12_102EH-110	zircon	146.6	96.8	0.79	0.77	6.38	54.56
zDD_NV12_102EH-111	zircon	129.5	86.8	0.77	0.74	4.54	48.76
zDD_NV12_102EH-113	zircon	165.8	72.4	0.75	0.72	4.04	44.58
zDD_NV12_102EH-115	zircon	211.8	85.8	0.79	0.76	7.24	53.49
zDD_NV12_102EH-130	zircon	127.3	73.9	0.74	0.71	3.23	42.95
zDD_NV12_109CM-2	zircon	392.1	84.2	0.80	0.78	12.91	57.00
zDD_NV12_109CM-3	zircon	209.3	89.9	0.79	0.77	7.87	55.52
zDD_NV12_109CM-5	zircon	181.2	93.6	0.80	0.77	7.37	55.76
zDD_NV12_109CM-16	zircon	215.7	114.7	0.83	0.81	13.20	67.97

zDD_NV12_109CM-60	zircon	215.9	114.7	0.83	0.81	13.20	67.95
zDD_NV12_109CM-102	zircon	242.3	106.7	0.82	0.81	12.83	65.59
zDD_NV12_109CM-117	zircon	283.5	97.3	0.81	0.80	12.48	62.29
zDD_NV12_136SR-78	zircon	126.7	88.2	0.77	0.74	4.58	49.07
zDD_NV12_136SR-106	zircon	133.1	83.9	0.76	0.74	4.35	47.83
zDD_NV12_136SR-119	zircon	95.9	77.0	0.73	0.70	2.64	41.21
zDD_NV12_085SM-2	zircon	170.3	101.2	0.80	0.78	8.11	58.50
zDD_NV12_085SM-48	zircon	105.7	92.0	0.76	0.74	4.16	48.09
zDD_NV12_085SM-50	zircon	157.5	81.6	0.77	0.74	4.88	48.62
zDD_NV12_085SM-68	zircon	197.5	94.1	0.80	0.78	8.12	56.97
zDD_NV12_085SM-78	zircon	103.6	55.7	0.67	0.63	1.49	32.90
zDD_NV12_085SM-98	zircon	178.7	86.7	0.78	0.76	6.24	52.32
zDD_NV12_085SM-102	zircon	90.3	0.0	0.78	0.76	5.60	51.87
zDD_NV12_085SM-103	zircon	190.9	85.2	0.78	0.76	6.44	52.22
zDD_NV12_085SM-107	zircon	207.3	117.3	0.83	0.81	13.27	68.59
zDD_NV12_085SM-110	zircon	147.8	112.6	0.81	0.79	8.72	61.17
zDD_NV12_085SM-113	zircon	316.4	123.1	0.85	0.83	22.30	77.29
zDD_NV12_085SM-114	zircon	95.5	75.2	0.73	0.69	2.51	40.47
zDD_NV12_085SM-116	zircon	154.8	122.3	0.82	0.81	10.77	65.76
zDD_NV12_085SM-119	zircon	109.2	95.9	0.77	0.75	4.67	49.98
zDD_NV12_094SM-5	zircon	95.0	66.6	0.70	0.67	1.96	36.97
zDD_NV12_094SM-16	zircon	59.8	56.0	0.63	0.59	0.87	28.60
zDD_NV12_094SM-19	zircon	92.1	79.4	0.73	0.70	2.70	41.63
zDD_NV12_094SM-28	zircon	96.8	77.3	0.73	0.70	2.69	41.44
zDD_NV12_094SM-39	zircon	93.9	66.0	0.70	0.67	1.90	36.61
zDD_NV12_094SM-40	zircon	95.7	57.1	0.67	0.63	1.45	32.99
zDD_NV12_094SM-48	zircon	96.3	76.3	0.73	0.70	2.60	40.97
zDD_NV12_094SM-96	zircon	81.6	62.3	0.68	0.64	1.47	33.80
zDD_NV12_094SM-99	zircon	100.4	83.7	0.75	0.72	3.27	44.30
zDD_NV12_162CB-8	zircon	224.6	94.7	0.81	0.78	9.36	58.63
zDD_NV12_162CB-12	zircon	196.0	78.5	0.77	0.74	5.61	49.04
zDD_NV12_162CB-19	zircon	240.2	120.2	0.84	0.82	16.12	72.08
zDD_NV12_162CB-42	zircon	183.4	66.1	0.73	0.70	3.72	41.98
zDD_NV12_162CB-66	zircon	163.8	78.4	0.76	0.74	4.68	47.45
zDD_NV12_162CB-67	zircon	195.3	95.9	0.80	0.78	8.35	57.75
zDD_NV12_162CB-76	zircon	228.7	90.1	0.80	0.77	8.63	56.45
zDD_NV12_176CB-14	zircon	124.7	83.3	0.76	0.73	4.03	46.85
zDD_NV12_176CB-17	zircon	124.6	66.4	0.72	0.69	2.56	39.33
zDD_NV12_176CB-26	zircon	172.4	86.0	0.78	0.76	5.93	51.63
zDD_NV12_176CB-40	zircon	195.9	96.8	0.80	0.78	8.54	58.22
zDD_NV12_176CB-46	zircon	90.5	72.0	0.71	0.68	2.18	38.64
zDD_NV12_176CB-69	zircon	122.7	103.1	0.79	0.77	6.06	54.45
zDD_NV12_176CB-81	zircon	126.9	94.7	0.78	0.76	5.29	51.71

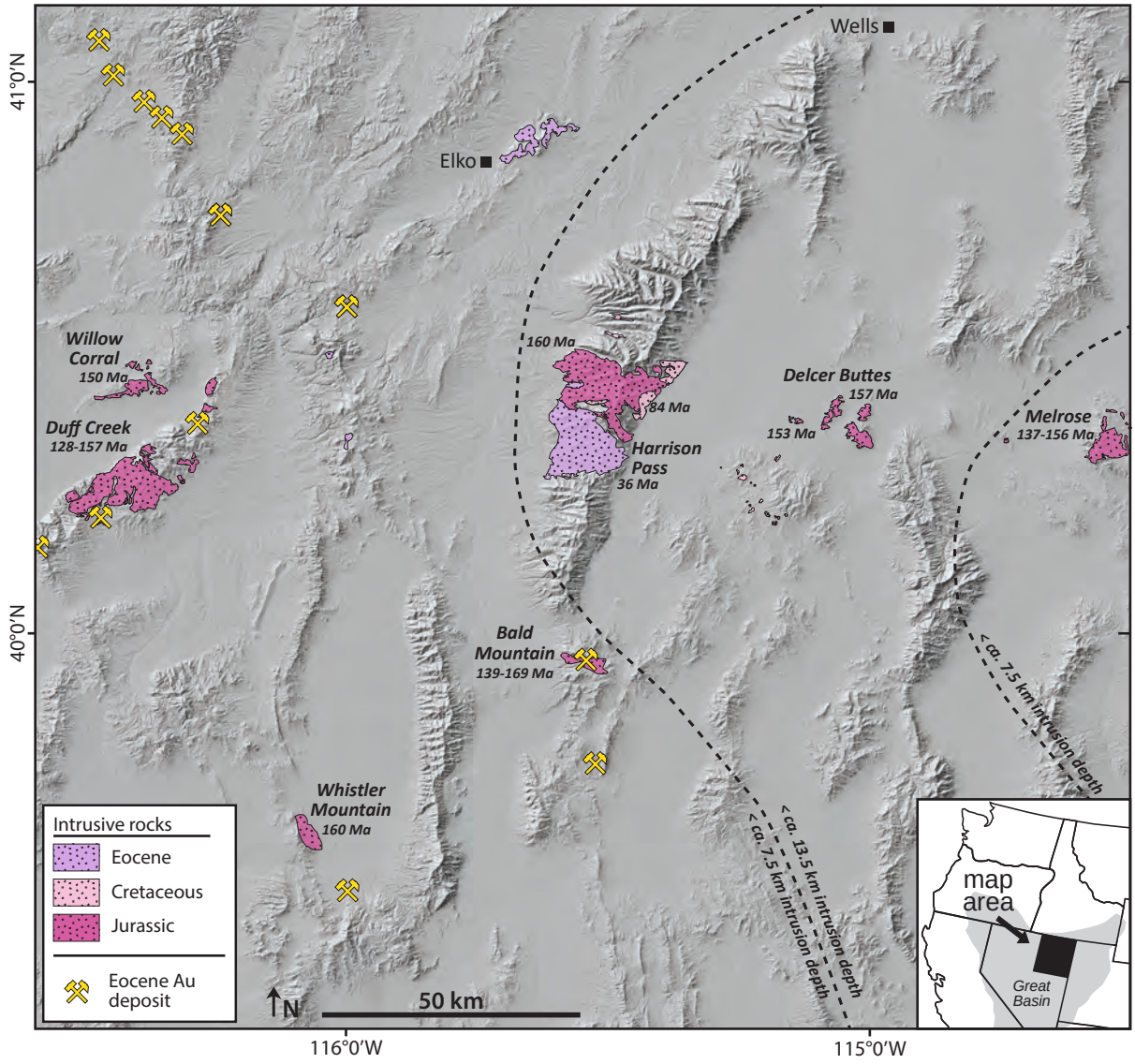
Wells
Elko
Willow Corral
150 Ma
Duff Creek
128-157 Ma
160 Ma
84 Ma
Harrison Pass
36 Ma
Delcer Buttes
157 Ma
153 Ma
Melrose
137-156 Ma
Bald Mountain
139-169 Ma
Whistler Mountain
160 Ma
< ca. 7.5 km intrusion depth
< ca. 13.5 km intrusion depth
< ca. 7.5 km intrusion depth
Intrusive rocks
Eocene
Cretaceous
Jurassic
Eocene Au deposit
N
50 km
map area
Great Basin
41°0′N
40°0′N
116°0′W
115°0′W

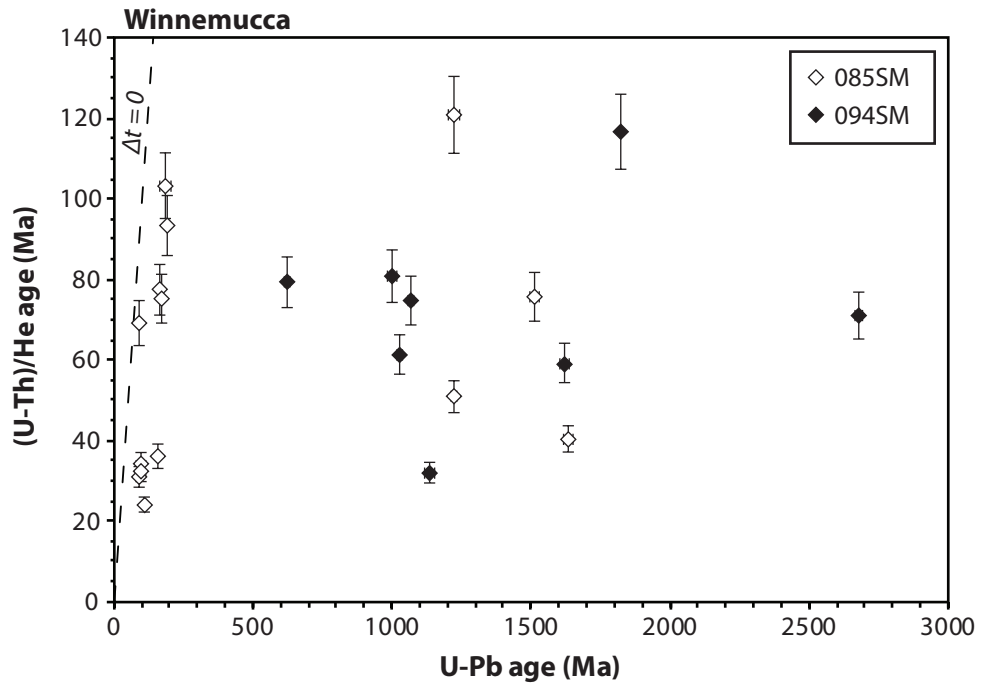
Winnemucca
085SM
094SM
Δt = 0
(U-Th)/He age (Ma)
U-Pb age (Ma)
0
20
40
60
80
100
120
140
0
500
1000
1500
2000
2500
3000

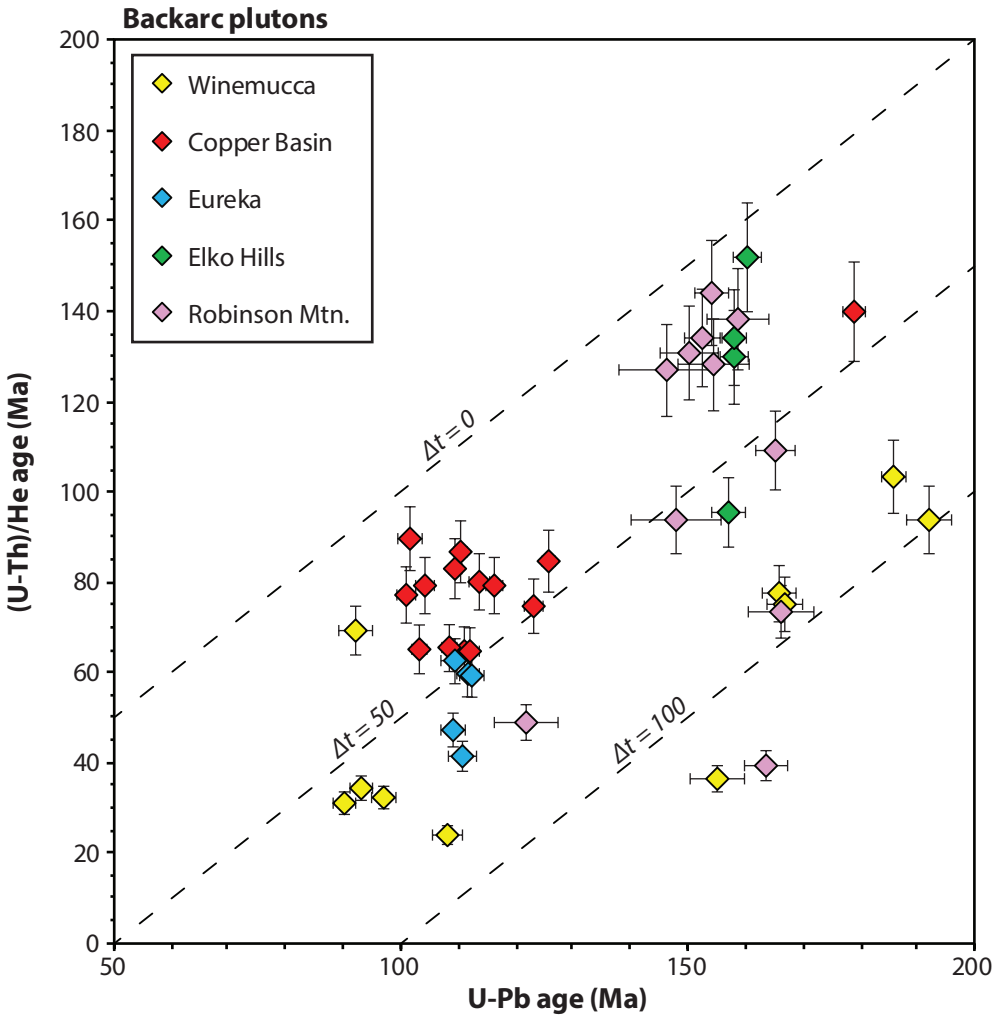
Backarc plutons
Winemucca
Copper Basin
Eureka
Elko Hills
Robinson Mtn.
Δt = 0
Δt = 50
Δt = 100
(U-Th)/He age (Ma)
U-Pb age (Ma)
0
20
40
60
80
100
120
140
160
180
200
50
100
150
200